

uace2019

underwater acoustics conference & exhibition

CONFERENCE PROCEEDINGS

ISSN: 2408-0195

HERSONISSOS, CRETE - GREECE | 30.06 - 05.07.2019



5th Underwater Acoustics Conference and Exhibition

UACE2019

Sunday 30th June through Friday 5th July, 2019
Hersonissos, Crete, Greece

Conference Proceedings

Edited by
John S. Papadakis

ISSN: 2408-0195

Conference logo by Yorgis Androulakis, IACM-FORTH

Preface

The Proceedings at hand include the papers presented at the 5th Underwater Acoustics Conference, UACE2019.

A brief history: Leif Bjørnø had the original idea and has been a co-organiser and a co-chairman with John S. Papadakis, for a series of Conferences starting in early 2000. Specifically, John and Leif have organized four conferences under the title 'Underwater Acoustic Measurements: Technologies and Results', (Heraklion in 2005 and 2007 –Nafplion in 2009 –Kos in 2011), and three conferences under the title 'Underwater Acoustics Conference and Exhibition', (Corfu in 2013, Rhodes in 2014 and Chania in 2015). The 4th Underwater Acoustics Conference and Exhibition was organized by John in the island of Skiathos in 2017 and was dedicated in the memory of Leif Bjørnø. During the meeting of the Organizing Committee in Skiathos, it was decided that David Bradley would Co-Chair the 2019 Conference with John S. Papadakis. It is the ambition of the Scientific Committee and the Organizers of UACE2019 to be able to continue the long history of successes of the ECUA, UAM and UACE Conferences, which have always attracted a large number of scientists and engineers from Europe, the United States, Canada, China, Japan etc, and have become an established forum for the presentation of the latest developments in all major areas of Underwater Acoustics.

The success of the conference is due to the joint efforts of many people. I would like to thank the Structured Session Organizers and the Scientific Committee for their valuable contribution. Our gratefulness also goes to the Office of Naval Research Global, for their continuous support and financial contributions throughout the history of these Conferences. I also appreciate the sponsoring of UACE2019 by two major societies, EAA and ASA. And of course, I would like to acknowledge the continuous support of IACM-FORTH. Last but not least, we are grateful to all the speakers for their great and important work prepared for and presented in this conference.

These Proceedings includes 139 papers offering significant contributions to the most important fields of Underwater Acoustics. We trust that these proceedings represent the state-of-the-art of most areas of Underwater Acoustics and will be a valuable reference to future works in this field.

John S. Papadakis and David Bradley,

Conference Chairmen

Organizing Committee

- *John S. Papadakis, FORTH, Greece (Chairman)*
- *David Bradley, ARL, Penn State University, USA (Chairman)*
- *Philippe Blondel, University of Bath, UK*
- *Mike Buckingham, MPL, Scripps, USA*
- *Ross Chapman, University of Victoria, Canada*
- *Qihu Li, Institute of Acoustics, Acad. Sinica, China*
- *Michael Taroudakis, University of Crete & FORTH, Greece*

Technical Issues

Yorgis Androulakis, IACM - FORTH

Secretariat

Yiota Rigopoulou, IACM – FORTH

Partner Agency in Organization

Cretan Conference and Business Services Greece (CCBS Greece)

Supported by

- *Office of Naval Research Global, London, UK*
- *IACM-FORTH*

Endorsed by

- *European Acoustics Association, EAA*
- *Acoustical Society of America, ASA*

Scientific Committee

- *John S. Papadakis, FORTH, Greece (Chairman)*
- *David Bradley, ARL, Penn State University, USA (Chairman)*
- *Michael Ainslie, TNO, The Netherlands*
- *Tuncay Akal, Tubitak, Turkey*
- *Philippe Blondel, University of Bath, UK*
- *Mike Buckingham, MPL, Scripps, USA*
- *Andrea Caiti, ISME/DII, Italy*
- *Chris Capus, Heriot-Watt Univ., Edinburgh, Scotland*
- *Ross Chapman, University of Victoria, Canada*
- *Chi-Fang Chen, National Taiwan University, Taiwan*
- *Nick Chotiros, Office of Naval, Research Global, London*
- *Alexander Gavrilov, Curtin University, Australia*
- *Peter Gerstoft, MPL, Scripps, USA*
- *Grazyna Grelowska, Naval Academy, Gdynia, Poland*
- *Hiroyuki Hachiya, Tokyo Inst. Technology, Japan*
- *Roy Edgar Hansen, FFI, Norway*
- *Georgios Haralabus, CTBTO, Austria*
- *Charles Holland, ARL, Penn State Univ., State College, USA*
- *Marcia Isakson, Univ. Texas at Austin, USA*
- *Kirk Jenne, NSWC HQ, Washington DC, USA*
- *Sergio Jesus, Univ. Algarve, Faro, Portugal*
- *Arata Kaneko, Hiroshima University, Japan*
- *Eugeniusz Kozaczka, Techn. Univ. Gdansk, Poland*
- *Tim Leighton, University of Southampton, UK*
- *Tony Lyons, University of New Hampshire, USA*
- *Qihu Li, Institute of Acoustics, Acad. Sinica, China*
- *Alain Maguer, CMRE, NATO Sci. & Techn. Org., Italy*
- *Jennifer Miksis-Olds, University of New Hampshire, USA*
- *Purnima Ratilal, Northeastern Univ., Boston, USA*
- *Jean-Pierre Sessarego, CNRS-LMA, Marseille, France*
- *Martin Siderius, Portland State University, USA*
- *Dick Simons, Delft Univ. Technology, The Netherlands*
- *Emmanuel Skarsoulis, F.O.R.T.H., Greece*
- *Michael Taroudakis, University of Crete & F.O.R.T.H., Greece*
- *Alessandra Tesei, NATO - STO CMRE, Italy*
- *Peter Thorne, National Oceanographic Centre, Liverpool, UK*

Structured Session Organisers

- *Megan Ballard, ARL, Univ. Texas at Austin, USA*
- *David Barclay, Department of Oceanography, Dalhousie University*
- *Philippe Blondel, University of Bath, UK*
- *Ross Chapman, University of Victoria, Canada*
- *Mathieu Colin, TNO, The Netherlands*
- *Frank Ehlers, WTD 71 –FWG, Germany*
- *Dale Ellis, Canada*
- *Victor Evora, USA*
- *Dominique Fattaccioli, DGA Techniques Navales, France*
- *Alexander Gavrilov, Curtin University, Australia*
- *Peter Gerstoft, MPL, Scripps, USA*
- *Johannes Groen, Atlas Elektronik, GmbH*
- *Aaron Gunderson, ARL, Univ. Texas at Austin, USA*
- *Georgios Haralabus, CTBTO*
- *Kevin Heaney, OASIS Inc, USA*
- *Victor Humphrey, University of Southampton*
- *Marcia Isakson, Univ. Texas at Austin, USA*
- *Wolfgang Jans, WTD 71, Germany*
- *Kevin Lee, Univ. Texas at Austin, USA*
- *Paul Lepper, Loughborough University, UK*
- *Markus Linné, Swedish Decence Research Agency, FOI*
- *Jennifer Miksis-Olds, University of New Hampshire, USA*
- *Paul Mitchell, University of York, UK*
- *Vincent Myers, DRDC Atlantic, Canada*
- *Peter Nielsen, CTBTO*
- *Marten Nijhof, TNO, The Netherlands*
- *David Nunn , Dstl Porton Down, UK*
- *Yan Pailhas, Heriot-Watt University, UK*
- *Konstantinos Pelekanakis, NATO - STO CMRE, Italy*
- *Mark Prior, TNO, The Netherlands*
- *Purnima Ratilal, Northeastern Univ., Boston, USA*
- *Gaultier Real, DGA Techniques Navales, France*
- *Mike Richardson, USA*
- *Stephen Robinson, Acoustics Group, National Physical Laboratory Teddington, UK*
- *Arne Schulz, WTD 71 –FWG, Germany*
- *Jean-Pierre Sessarego, CNRS-LMA, Marseille, France*
- *Dick Simons, Delft Univ. Technology, The Netherlands*
- *Emmanuel Skarsoulis, IACM-FORTH, Greece*
- *Mirjam Snellen, TU Delft OCW*
- *Michael Taroudakis, University of Crete and IACM-FORTH, Greece*
- *Jaroslaw Tegowski, Institute of Oceanography, University of Gdansk, Poland*
- *Alessandra Tesei, NATO - STO CMRE, Italy*
- *Charalampos Tsimenidis, Newcastle University, UK*
- *Duncan Williams, Dstl Porton Down, UK*

- *Angeliki Xenaki, NATO - STO CMRE, Italy*
- *Desen Yang, Harbin Engineering University, China*
- *Mario Zampolli, CTBTO*

Table of Contents

SESSION 01: MEMORIAL SESSION FOR JEAN-PIERRE HERMAND	1
10 YEARS, 30 PUBLICATIONS, AND A LOT OF MILEAGE!	3
HIGH-FREQUENCY ACOUSTICS OF MARINE VEGETATION – ROLE OF FREQUENCIES AND IMAGING ANGLES	9
ADVENT OF DEEP ARGO DATA & AN ATTEMPT AT ANALYZING THE DEEPER SOUND SPEED PROFILES FOR EXTRAPOLATION CORRECTIONS	17
SESSION 02: UNDERWATER ACOUSTIC CALIBRATION, TESTING, FACILITIES AND STANDARDS	23
STANDARDS FOR PROJECT JOMOPANS: OCEAN NOISE MONITORING FOR THE NORTH SEA	25
LOW FREQUENCY HYDROPHONE CALIBRATION WITH A LASER INTERFEROMETER	33
METHOD FOR LOW FREQUENCY CALIBRATION IN CONFINED MEASUREMENT TANK	41
NEAR-FIELD PARTICLE VELOCITY MEASUREMENT OF THE HIGH FREQUENCY PROJECTORS USING LASER VIBROMETRY METHOD	47
PLANE/CYLINDRICAL WAVE SYNTHESIS IN A SMALL TANK APPLIED TO FAR-FIELD BEAM PATTERN MEASUREMENT OF A 300KHZ SONAR TRANSDUCER	55
PECULIARITIES OF FREE-FIELD CALIBRATION OF A VECTOR RECEIVER IN A REVERBERANT SOUND FIELD OF A WATER TANK	61
STUDY OF A TRUE FREE FIELD CALIBRATION METHOD OF AN ACCELEROMETER BASED VECTOR SENSOR FOR UNDERWATER USE	67
STANDARD FACILITY FOR FREE-FIELD CALIBRATION OF HYDROPHONES AND VECTOR RECEIVERS IN THE REVERBERANT LABORATORY WATER TANK	75
CALIBRATION METHODS OF VECTOR RECEIVERS IN THE FREQUENCY RANGE 5 HZ TO 10 KHZ AND THEIR COMPARISON VERIFICATIONS	81
MEASUREMENTS OF ACOUSTIC BACKSCATTERING FROM SYNTACTIC-FOAM SPHERES	89
ACOUSTIC NOISE MEASUREMENT OF VESSELS WITH ADAPTIVE CHANNEL EQUALIZATION	95
SESSION 03: ACOUSTIC MONITORING OF OCEAN ENVIRONMENTS AND PROCESSES: BIOLOGY, ECOLOGY, GEOPHYSICS AND MAN-MADE ACTIVITIES	101
MECHANORECEPTORS IN EARLY DEVELOPMENTAL STAGES OF THE PYCNOGONIDA	103
OBSERVATIONS OF THE SOUNDS PRODUCED BY SWIMMING IN THE SPANISH LOBSTER, SCYLLARIDES AEQUINOCTIALIS (LUND)	109
ACOUSTIC CHARACTERIZATION OF AN ARTIFICIAL CO2 SEEP USING SPLIT-BEAM ECHO SOUNDERS	115
DIVERSE ACOUSTIC MANIFESTATIONS OF SHALLOW GAS IN THE GDAŃSK BAY (SOUTHERN BALTIC SEA)	123
ECOLOGICAL CATASTROPHE IN ARCTIC: AN ANOMALOUS GULF STREAM HEATING AND SHIFT TO GREENLAND DUE TO OCEAN POLLUTION BY RAINBOW OIL FILM	129
SESSION 4: TOWARDS AUTOMATIC TARGET RECOGNITION. DETECTION, CLASSIFICATION AND MODELLING	139
WAVEFORM DESIGN FOR LOW FREQUENCY SYNTHETIC APERTURE SONAR	141
CALIBRATION TARGET FOR EXTRACTION OF FREQUENCY DEPENDENCY IN SYNTHETIC APERTURE SONAR	147
2D AND 3D, CENTERED AND OFFSET, CIRCULAR SYNTHETIC APERTURE SONAR POINT SPREAD FUNCTION	155
IMPACT OF TEMPORAL DOPPLER ON CSAS IMAGERY	163
THE ALGORITHM OF THE UNDERWATER ACOUSTIC SOURCE COORDINATES DETERMINATION USING THE CORRELATION FUNCTION OF THE SIGNAL	171

IMPROVED DEEP-LEARNING BASED CLASSIFICATION OF MINE-LIKE CONTACTS IN SONAR IMAGES FROM AUTONOMOUS UNDERWATER VEHICLES 179
ON THE BENEFIT OF MULTIPLE REPRESENTATIONS WITH CONVOLUTIONAL NEURAL NETWORKS FOR IMPROVED TARGET CLASSIFICATION USING SONAR DATA 187
ATR PERFORMANCE FOR TARGET CLUSTERING 195
MBES WATER COLUMN DATA PROCESSING FOR SMALL UNDERWATER TARGET RECOGNITION 203
ENVIRONMENTALLY ADAPTIVE AUTOMATIC DETECTION OF LINEAR SEAFLOOR FEATURES IN SIDESCAN SONAR IMAGERY: THE CASE OF TRAWL MARKS DETECTION 211
BAYESIAN SEAFLOOR CHARACTERIZATION FROM SAS IMAGERY 219
TARGET CLASSIFICATION USING MULTI-VIEW SYNTHETIC APERTURE SONAR IMAGERY 227
THREATENING DEGREE ASSESSMENT METHOD OF SONAR TARGETS BASED ON MULTI-SOURCE INFORMATION FUSION 235
SESSION 5: UNDERWATER COMMUNICATIONS AND NETWORKING 241
ROBUST DIGITAL SELF-INTERFERENCE CANCELLATION FOR FULL-DUPLEX UWA SYSTEMS: LAKE EXPERIMENTS 243
FULL-DUPLEX CHANNEL ANALYSIS FOR UNDERWATER ACOUSTIC COMMUNICATIONS 251
A PARALLEL DECODING APPROACH FOR MITIGATING NEAR-FAR PROBLEMS IN UNDERWATER ACOUSTIC COMMUNICATIONS NETWORKS 259
SPREAD SPECTRUM MULTI-CARRIER COMMUNICATION IN INTERFERENCE-LIMITED ACOUSTIC REGIMES 265
TOWARDS PHYSICAL LAYER CRYPTOGRAPHY FOR UNDERWATER ACOUSTIC NETWORKING 271
DATA COLLECTION IN SHALLOW FRESH WATER SCENARIOS WITH LOW COST UNDERWATER ACOUSTIC MODEMS 281
A FULLY CUSTOM RECONFIGURABLE MIMO UNDERWATER ACOUSTIC TRANSMITTER 289
HIGH DATA RATE CARRIERLESS IMPULSIVE COMMUNICATIONS FOR UNDERWATER ACOUSTIC NETWORKS 297
ROUTING STRATEGIES FOR DUAL-HOP TDA-MAC: TRADE-OFF BETWEEN NETWORK THROUGHPUT AND RELIABILITY 303
EXPLOITING SPATIAL DIVERSITY TO IMPROVE QOS-ENABLED UNDERWATER COMMUNICATIONS 311
ROBUST DIRECTION FINDING IN THE FLUCTUATING OCEANS BY COMPLEX L1-NORM PRINCIPAL-COMPONENT ANALYSIS 319
THE INFLUENCE OF UPWELLING IN UNDERWATER COMMUNICATION OFF CABO FRIO ISLAND 327
AUV TRACKING UTILIZING A THRUSTER COMMUNICATION LINK 335
SESSION 6: UNDERWATER NOISE - MODELLING AND MEASUREMENTS 341
LOW FREQUENCY NOISE SOUTH OF AUSTRALIA FROM DISTANT SOURCES IN THE SOUTHERN OCEAN 343
THE SOUNDSCAPE OF THE INNER IONIAN ARCHIPELAGO AS EVINCED THROUGH THE WEST PATRAIKOS GULF AMBIENT AND SEISMIC NOISE MONITORING PROJECT. 351
UNDERWATER NOISE FROM WIND AT THE HIGH NORTH LOVE OCEAN OBSERVATORY 359
MONITORNING OF ANTHROPOGENIC UNDERWATER NOISE IN THE VENICE LAGOON, ITALY 367
FEASIBILITY AND ACCURACY OF PREDICTION OF OCEAN NOISE ON A SHORT-TIME SCALE 375
UNDERWATER ACOUSTIC RADIATION FROM PARTIALLY IMMERSED CYLINDRICAL SHELLS 383

STRONG VARIATIONS OF THE ACOUSTIC NOISE SPECTRA ACCOMPANYING INTERNAL WAVE SOLITONS	391
NUMERICAL ANALYSIS OF PILE DRIVING DISTURBANCES INTO WATER AND SOIL FOR OFFSHORE WINDFARM CONSTRUCTIONS	397
SESSION 7: UNDERWATER UNEXPLODED ORDNANCE (UXO) DETECTION AND REMEDIATION	403
SERDP/ESTCP MUNITIONS RESPONSE PROGRAM: UNDERWATER REMEDIATION OF UNEXPLODED ORDNANCE (UXO)	405
FROM BASIC RESEARCH TO A PROTOTYPE TOWBODY PLATFORM: PROGRESS ON UNDERWATER UNEXPLODED ORDNANCE REMEDIATION	413
ACOUSTIC-COLOR-BASED CONVOLUTIONAL NEURAL NETWORKS FOR UXO CLASSIFICATION WITH LOW-FREQUENCY SONAR	421
COMPARISON OF SYNTHETIC APERTURE SONAR IMAGES AND OPTICAL IMAGES OF UXOS FROM THE SKAGERRAK CHEMICAL MUNITIONS DUMPSITE	429
TEST OF A SUBMARINE TRANSIENT ELECTROMAGNETIC SENSOR FOR UXO CLASSIFICATION BY REMOTELY OPERATED VEHICLES (SUBTEM-ROV)	437
MOBILISATION OF UXO, CAUSED BY HYDRODYNAMICS	443
SESSION 8: COMPREHENSIVE NUCLEAR TEST-BAN TREATY MONITORING	451
EFFICIENT MODELING OF 3D ACOUSTIC PATHS TO IMPROVE SOURCE TRIANGULATION	453
FLUCTUATION DRIVERS AND VARIABILITY OF VERY LOW FREQUENCY LONG TERM OCEAN AMBIENT NOISE	461
EVALUATION OF LONG-TERM TRENDS IN DEEP-OCEAN NOISE IN THE SOUTHERN OCEAN USING CTBTO HYDROACOUSTIC DATA	467
SESSION 9: ACOUSTICS IN POLAR ENVIRONMENTS	475
INTERNATIONAL QUIET OCEAN EXPERIMENT – ARCTIC ACOUSTIC ENVIRONMENTS	477
LONG-RANGE SOUND PROPAGATION IN THE CANADA BASIN	483
SOUNDSCAPE CONTRIBUTIONS OF GLACIER ICE BLOCKS – INSIGHTS FROM LABORATORY MEASUREMENTS	491
A STUDY ON THE YEARLONG RECORD OF SOUND PROPAGATION FROM THE CANADA BASIN TO THE CHUKCHI SHELF	499
SESSION 10: DESIGN OF NEW EXPERIMENTAL FACILITIES TO ADDRESS FUTURE PROBLEMS IN UNDERWATER ACOUSTICS	507
A BRIEF FIVE-YEAR PROGRESS REPORT ON THE DGA "ALMA" PROJECT: SCIENTIFIC PROGRAM AND PROJECTS, AT-SEA CAMPAIGNS AND DATA COLLECTED, SYSTEM EVOLUTIONS AND IMPROVEMENTS	509
AT-SEA EXPERIMENTAL EVALUATION OF THE INFLUENCE OF ENVIRONMENTAL FLUCTUATIONS ON THE ACOUSTIC COHERENCE RADIUS	519
ALMA 2015 : STUDY AND MODELING OF THE IMPULSE RESPONSE VERTICAL DE-COHERENCE OF A FLUCTUATING SHALLOW CHANNEL	527
SOUND WAVES PROPAGATING IN FLUCTUATING MEDIA: EXPERIMENTAL ANALYSIS USING ALMA DATA	535
HOLOGRAPHIC ARRAY FOR DETERMINING STRUCTURAL ACOUSTIC PROPERTIES	543
DEVELOPMENT OF A MOORED ACOUSTIC ARRAY SYSTEM FOR EXPERIMENTAL ACOUSTIC IMAGING OF UNDERWATER ENVIRONMENT	551
SESSION 11: LARGE TIME-BANDWIDTH ACOUSTIC SIGNALS FOR TARGET DETECTION AND TRACKING	559
PASSIVE DETECTION AND BEARING-ONLY TRACKING OF LARGE TIME-BANDWIDTH SIGNALS USING AN AUV MOUNTED VECTOR SENSOR	561
HIGH DUTY CYCLE SONAR TRACKING PERFORMANCE AS A FUNCTION OF COHERENT PROCESSING INTERVAL FOR LCAS'15 DATA	569
OPTIMIZING A SLIDING M-OF-N TRACK INITIALIZER IN CLUTTER	577
IMPROVED TRACKING OF A SURROGATE TARGET USING CONTINUOUS ACTIVE SONAR	585

IMPROVED ACTIVE SONAR EXPERIMENT FOR MEASURING MATCHED-FILTER LOSS VS BANDWIDTH AND DURATION 593
HIGH DUTY CYCLE ACTIVE SONAR USING BROADBAND DOPPLER-SENSITIVE WAVEFORMS: EXPLOITING A TRIPLET ARRAY FOR ATTENUATING DIRECT PATH INTERFERENCE 599
SESSION 13: MACHINE LEARNING, COMPRESSIVE SENSING AND SIGNAL PROCESSING 607
VON MISES PRIOR FOR PHASE-NOISY DOA ESTIMATION: THE VITAMIN ALGORITHM 609
HIGH-RESOLUTION LOW-FREQUENCY COMPRESSIVE SAS IMAGING WITH DISTRIBUTED OPTIMIZATION 615
SESSION 14: ENVIRONMENTAL ACOUSTICS AND NOISE 623
AMBIENT NOISE OBSERVATIONS DURING A LARGE STORM EVENT IN SBCEX17 625
IDENTIFICATION OF HIGH NOISE ZONES WITH A 3D PILE DRIVING NOISE MODEL 631
AN EFFICIENT MODEL FOR OFFSHORE PILE DRIVING NOISE TAKING INTO ACCOUNT THE HAMMER CHARACTERISTICS. 639
SESSION 15: ACOUSTICS OF MARINE RENEWABLE ENERGY DEVELOPMENTS 645
DEVELOPMENT OF ACOUSTIC DOPPLER FISH MONITORING FOR APPLICATIONS IN HIGH-ENERGY TIDAL CHANNELS 647
PERFORMANCE CHARACTERISTICS OF A VECTOR SENSOR ARRAY IN AN ENERGETIC TIDAL CHANNEL 653
WAVE PROPAGATION IN SOFT SOLID HALF SPACES AND EVANESCENT PRESSURES IN OVERLYING WATERD 659
UNDERWATER NOISE GENERATED BY OFFSHORE PILE DRIVING: A PILE-SOIL-WATER VIBROACOUSTIC MODEL BASED ON A MODE MATCHING METHOD 667
SESSION 16: ADVANCES IN ACOUSTIC MEASUREMENT SYSTEMS: TECHNOLOGIES AND APPLICATIONS 675
LOW-FREQUENCY PASSIVE ACOUSTIC SURVEY OF SHIP TRAFFIC USING A GLIDER EQUIPPED WITH DIRECTIONAL SENSORS 677
PASSIVE ACOUSTIC MONITORING USING A TOWED ARRAY FROM A WAVE-PROPELLED USV 685
MODEL-BASED 3D MICRO-NAVIGATION AND BATHYMETRY ESTIMATION FOR INTERFEROMETRIC SYNTHETIC APERTURE SONAR 691
TRANSMISSION PATTERN OPTIMIZATION MODEL FOR CONFORMAL CONTOUR DESIGN 697
SYNTHETIC APERTURE SONAR FOR A LOW-COST AGILE PLATFORM: PRELIMINARY RESULTS 703
MULTI-BEAM DOPPLER SONAR FOR MEASURING 2-D VELOCITIES IN A SWATH: SWATHDOP 709
SESSION 17: MODELING TECHNIQUES FOR UNDERWATER ACOUSTIC SCATTERING AND PROPAGATION 715
SEMI-ANALYTIC MODELING OF SOUND PROPAGATION AND NOISE CROSS-CORRELATIONS IN A COASTAL OCEAN 717
EXCITATION AND PROPAGATION OF WHISPERING GALLERY WAVES IN THE VICINITY OF CURVILINEAR ISOBATHS IN SHALLOW WATER 723
ACOUSTIC WAVE SCATTERING FROM DYNAMIC ROUGH SEA-SURFACES USING THE FINITE-DIFFERENCE TIME-DOMAIN METHOD AND PIERSON-MOSKOWITZ FREQUENCY SPECTRUM 727
SEA-SURFACE SCATTERING OF A CONTINUOUS WAVE IN THE 1 TO 200 HZ FREQUENCY RANGE 735
SOUND SPEED AND ATTENUATION PREDICTIONS USING THE CORRECTED BIOT MODEL FOR GAS-BEARING MARINE SEDIMENTS 741
ACOUSTIC SCATTERING FROM AN OBJECT IN A MUD LAYER OF A SHALLOW WATER WAVEGUIDE 749
THREE-DIMENSIONAL FINITE ELEMENT MODELING TECHNIQUES FOR UNDERWATER ACOUSTIC SCATTERING SIMULATIONS 757

SESSION 18: MULTIBEAM ECHO SOUNDING: BATHYMETRY AND SEDIMENT CLASSIFICATION	765
SEAFLOOR SEDIMENT CHARACTERIZATION USING MULTIBEAM ECHOSOUNDERS WITHOUT GRAB SAMPLING: OPPORTUNITIES AND CHALLENGES	767
SEABED SCATTERING CROSS SECTION ESTIMATION USING THE RESON SEABAT T50: A NUMERICAL EVALUATION OF THE FOOTPRINT ERROR WHEN USING A ZERO-SLOPE ASSUMPTION IN THE ALONG-TRACK DIRECTION	775
ASSESSMENT OF RELIABILITY OF MULTI-BEAM ECHO-SOUNDER BATHYMETRIC UNCERTAINTY PREDICTION MODELS	783
MULTIBEAM AND SINGLEBEAM MULTIFREQUENCY CLASSIFICATION OF BOTTOM HABITATS - THE COMPLEMENTATION OF TWO APPROACHES	791
MBES DATA SIMULATION: ASSESSMENT BY DIRECT COMPARISON WITH A HIGH-RESOLUTION MULTI-SETTINGS WRECK SURVEY.	799
SESSION 19: SITUATION-ADAPTIVE DISTRIBUTED NETWORKED SYSTEMS	807
DISTRIBUTED FUSION IN UNDERWATER SENSOR NETWORKS: FUSING BEARING INFORMATION	809
A BAYESIAN INFORMATION FUSION APPROACH TO PLANNING AND EVALUATION FOR SYSTEM OF SYSTEMS IN AUTONOMOUS NAVAL MINE-HUNTING OPERATIONS	817
ACOUSTIC MODELLING KNOWLEDGE FOR DESIGN AND SPECIFICATION OF SITUATION-ADAPTIVE DISTRIBUTED NETWORKED SYSTEMS	825
SESSION 20: SONAR PERFORMANCE MODELING AND VERIFICATION. APPLICATIONS TO ACTIVE AND PASSIVE SONAR	833
PREDICTING INTERNAL WAVE PACKET CHARACTERISTICS AND ACOUSTIC SIGNAL COHERENCE	835
ESTIMATING RANGE DEPENDENT SEDIMENT THICKNESS AND REFLECTION COEFFICIENTS FROM BATHYMETRIC DATA FOR IMPROVED SONAR PERFORMANCE MODELLING	843
MODEL BENCHMARKING RESULTS FOR SHIP NOISE IN SHALLOW WATER	851
MODELLING NOISE FROM WIND, RAIN AND DISTANT SHIPPING IN SCENARIOS OF VARYING COMPLEXITY	859
VERTICAL ARRAY GAIN IN SHALLOW WATER	867
ENVIRONMENT DEPENDENT TRANSITION FREQUENCIES FOR RAM AND BELLHOP	875
REVERBERATION MODEL-DATA COMPARISONS AND ESTIMATED SCATTERING STRENGTHS IN THE VICINITY OF THE TREX13 SITE	883
UNCERTAINTY ANALYSIS IN SONAR PERFORMANCE MODELLING BY LATIN HYPERCUBE SAMPLING	891
SESSION 21: TARGET ECHO STRENGTH-MEASUREMENTS AND MODELLING	897
PRELIMINARY TARGET MEASUREMENTS FROM A PROTOTYPE MULTISPECTRAL SYNTHETIC APERTURE SONAR	899
COMPARING TARGET ECHO STRENGTH MODELS FOR A GENERIC SUBMARINE	905
ACOUSTIC SCATTERING FROM THIN-WALLED CYLINDERS: EXPERIMENTAL VALIDATION OF A NOVEL BOUNDARY ELEMENT METHOD	913
TARGET ECHO STRENGTH OF A SCALED STEEL BODY WITH INNER STRUCTURE AND THIN HULL	919
INFLUENCE OF FLUID-STRCTURE COUPLING ON TARGET ECHO STRENGTH SIMULATION	925
ANECHOIC COATING DESIGN KNOWLEDGE FIELDS	933
SESSION 22: VECTOR HYDROPHONE RESEARCH	937
AN ESTIMATION ALGORITHM OF DOA FOR VECTOR SENSOR ARRAY BASED ON TENSOR THEORY	939
A NEW ACOUSTIC PAYLOAD FOR GLIDERS	947
DEVELOPMENT OF LOW-NOISE VECTOR SENSOR USING BENDING MODE RELAXOR FERROELECTRIC SINGLE CRYSTAL MATERIALS	955

SESSION 23: MINE COUNTERMEASURES	963
EVALUATING HUMAN/MACHINE INTERACTION FOR UNDERWATER THREAT DETECTION AND CLASSIFICATION: A CASE STUDY.	965
ENABLING AUTONOMOUS MINE COUNTERMEASURES FOR THE NATO ALLIANCE	975
MARINE ECOSYSTEM ENGINEERS: A CHALLENGE FOR MINE COUNTERMEASURE.	987
SESSION 24: INVERSION METHODS IN UNDERWATER ACOUSTICS	993
ENHANCED SONAR IMAGE RESOLUTION USING COMPRESSIVE SENSING MODELLING	995
APPLICATION OF MARKOV-CHAIN MONTE CARLO PARAMETER-SET IDENTIFICATION TO DESIGN AND INVERSION	1001
SESSION 25: SIGNAL AND IMAGE PROCESSING	1007
OUT OF BAND SIGNAL PROCESSING FOR LOCALIZING DISTANT SOURCES IN A NOISY DEEP OCEAN	1009
SUBSPACE TRACKING FOR DOMINANT MODE REJECTION BEAMFORMING	1015
DEEP LEARNING BASED TECHNIQUE FOR ENHANCED SONAR IMAGING	1021
SESSION 26: SOUND PROPAGATION IN SHALLOW AND DEEP WATER	1029
STUDY ON PHASE OF REFLECTION COEFFICIENT OF THE MEDIUM WITH GRADIENT CHANGE OF ACOUSTIC IMPEDANCE	1031
VARIABILITY OF THE SOUND FIELD IN THE PRESENCE OF INTERNAL KELVIN WAVES IN A STRATIFIED LAKE	1037
ACOUSTICAL SIGNAL HORIZONTAL REFRACTION IN THE COAST WEDGE	1043
PARAMETRIC ARRAY SIGNAL COMPRESSION IN SHALLOW WATER WAVEGUIDE	1049
COUPLING 3D ACOUSTIC PROPAGATION TO OPERATIONAL OCEAN CIRCULATION MODELS.	1055
TIME-FREQUENCY AND WARPING ANALYSIS OF THE SOUND FIELD MODAL COMPOSITION IN VARIABLE SHALLOW WATER ENVIRONMENT. SWARM'95 EXPERIMENT AS A CASE STUDY	1061
FIRST AUTHORS' INDEX	1067

Structured Session 1
Memorial Session for Jean-Pierre Hermand

Organiser(s): Chapman Ross

10 YEARS, 30 PUBLICATIONS, AND A LOT OF MILEAGE

Mark Asch[a], Maxence Ferrari[b], Hervé Glotin[b], Franck Malige[b], Ricard Marxer[b], Julie Patris[b]

[a]LAMFA-CNRS, Université de Picardie Jules Verne, France.
[b]LIS-CNRS, Université de Toulon, France.

Contact: Prof. Mark Asch mark.asch@u-picardie.fr

Abstract: *I had the honor and great pleasure of collaborating closely with Jean-Pierre Hermand over a period of 10 years (2002-2012). This paper briefly recalls our work on adjoint methods for underwater geoacoustics, where we coupled acoustic wave propagation with semi-automatic differentiation to solve inverse problems. In the second part, we present recent work on underwater acoustic monitoring of whales. Here we are coupling classical pde-based acoustic modelling (direct and inverse) with modern machine learning approaches.*

Keywords: *inverse problems, adjoint modelling, geoacoustics, machine learning, passive acoustic monitoring, biodiversity.*

1. JEAN-PIERRE HERMAND – IN MEMORIAM

1.1. Earlier work



In 2002, Jean-Pierre was invited by me to chair a thesis defence jury. In the thesis and subsequent publications [1, 2], we had just started to investigate the feasibility of an adjoint approach to the following inverse problem: from surface/antenna measurements of underwater acoustic signals, can we recover the sound speed profile of the water column as well as the properties of the underlying seafloor? The knowledge of both seafloor and water column properties are indispensable in shallow water environments, where the acoustic wave propagation is strongly influenced by sea *and* sediments. Jean-Pierre immediately saw in this approach an alternative to the more classical model-based matched filter approach, with which he was familiar. This was the start of our extremely fruitful scientific collaboration that covered 10 years and produced 30-odd publications.

1.2. Later work

Having exhausted the analytical approach for deriving the adjoint equations, we decided in 2006 to explore automatic, or rather semi-automatic adjoint derivations. The former, known as “automatic differentiation”, was deemed less well adapted than a novel approach based on the construction of a modular graph. This approach, YAO [3, 4, 5], provided more flexibility but required that the user provide a modular graph describing the computational steps of the inversion algorithm. The results obtained enabled us to perform coupled inversions (sound-speed profile plus bottom sediments) in realistic environments – see Fig. 1.

The last paper we co-authored, dealt with applications of underwater acoustics to archaeology [6]. And our last common project was financed by CNRS and concerned the elaboration of a passive acoustic underwater monitoring system, inspired by Jean-Pierre’s pioneering work on Posidonia characterization [7, 8].

Oh yes, the “mileage” in the title? Well, working with Jean-Pierre always entailed lots of travelling – to workshops, meetings, partners, oceans and continents!

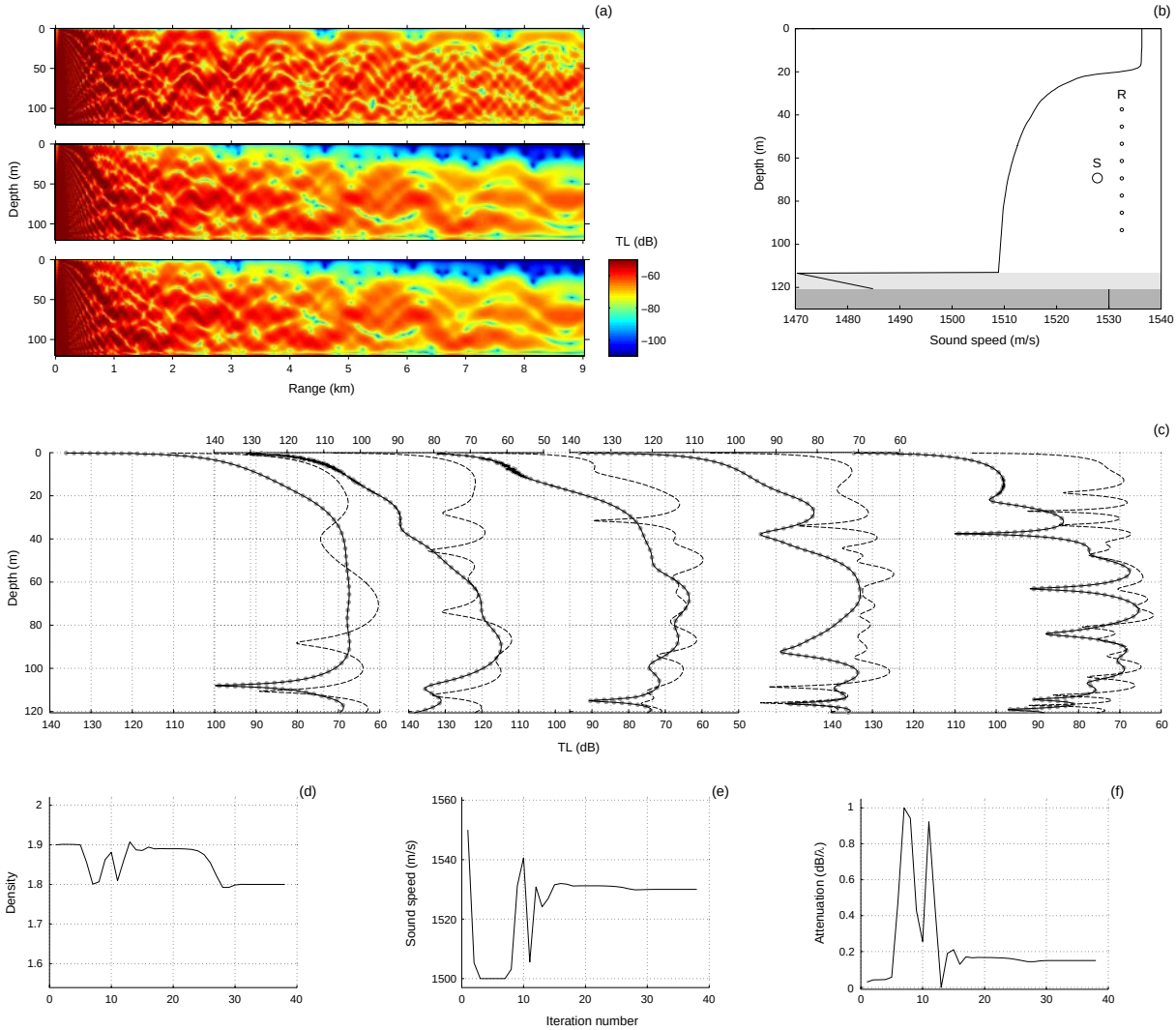


Fig.1: Coupled inversion of sound speed profile and sediment properties (two-layer case) [3].

2. PASSIVE ACOUSTIC MONITORING FOR BIODIVERSITY

2.1. Introduction and context

The conservation of cetaceans has been a major environmental concern for the last 50 years. The population of most large whales probably went down to the verge of extinction during the 20th century due to non-sustainable whaling. Since then, new dangers are arising for large and small cetaceans, such as the general level of man-made noise in the oceans.

One of the first and the most difficult tasks for cetacean preservation is to estimate their actual number. In this context, passive acoustic monitoring has been increasingly used to estimate cetacean populations although it is still a challenging technique for most species.

2.2. Instrumentation and measurement campaigns

Our initial studies were dedicated to blue whale *(Balaenoptera musculus*) populations. A field experiment close to the Chanaral Island Natural Reserve, 600 km north of Santiago de Chile was set up. This field experiment comprised: the mooring of a fixed hydrophone for one

and a half months during the summer of 2017, a visual follow-up of the zone between the island and the shore, and measurements of physical and biological properties to run an adapted computer simulation.

Subsequent studies have concerned sperm whales (*Physeter macrocephalus*). Measurement campaigns have been run in the Mediterranean (Bombyx Platform, Sphyrna drone), in the Caribbean (Jason – Fig. 2), and Mauritius (3-hydrophone, hand-held antenna + GoPro – Fig. 3).

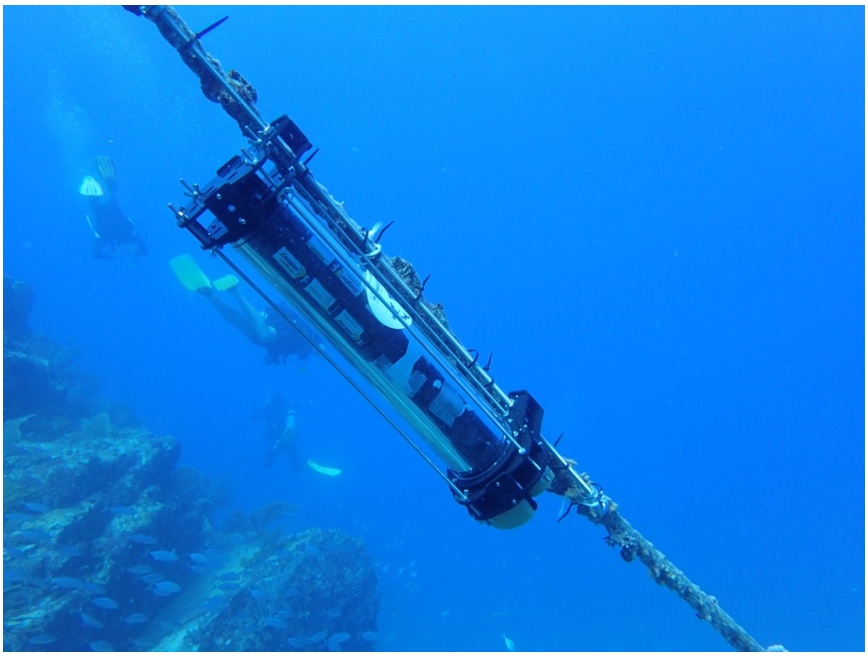


Fig. 2: JASON High Blue Recorder

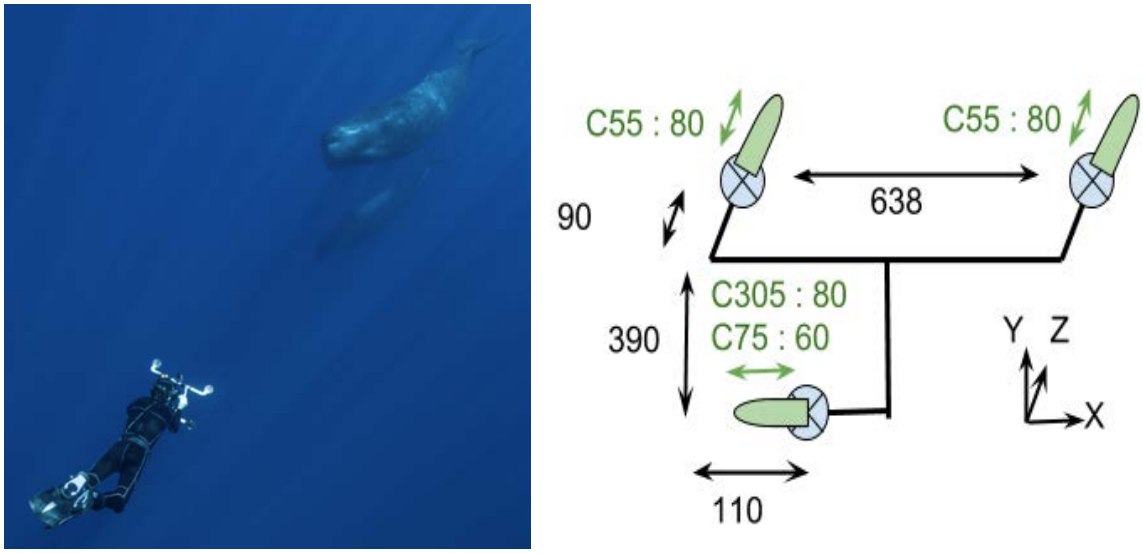


Fig. 3: The 3-hydrophone audiovisual antenna, 3 x 600 kHz, held by F. Sarano in 2018 (credit R. Heuzey)

3. CLASSICAL APPROACHES BASED ON FINITE ELEMENT MODELLING

A spectral finite element method was used to simulate the acoustic field, based on real bathymetry and water column measurements. Then correlations are computed to identify the emitters (whales) from field recordings using the Bombyx Platform. The initial results obtained [9] are promising.

4. MACHINE LEARNING ON BIOACOUSTIC SIGNALS

With the extraction of the TDoA from multichannel recordings, we were able to compute the DOA (Direction of Arrival), which allowed us to pinpoint the source location on each simultaneously recorded audio and video clip. The divers' visual identification of each animal allows us to tie each click to an individual. This database can be used to understand more deeply which features could be tied to an individual, and which are invariant and define the *Physeter macroencephalus* sonar [10].

Moreover, we propose a new kind of autoencoder that we call a stereo autoencoder (SAE) and represent in Fig. 4. This model is simply a double input autoencoder with double output. We chose as inputs the first two channels because they are the least noisy and are recorded with the same hydrophone, which could help the network to learn. The output of this SAE is composed of two branches, one that will reconstruct the signal, and one that will offset it to match each channel. The aim is (i) to study the features captured by the autoencoder, which could be features describing the individual that emitted the click, and (ii) to get features describing the type of click that has been emitted, according to their TDoA, angle of arrival etc. We show that this SAE generates an embedding space that efficiently clusters in 3D the clicks with respect to these features. The other goal of the autoencoder was to have an unsupervised method for computing the TDOA. By computing TDOA in that manner, the aim is to obtain better localisation results than with usual methods, such as the generalized cross correlation (see Section 3).

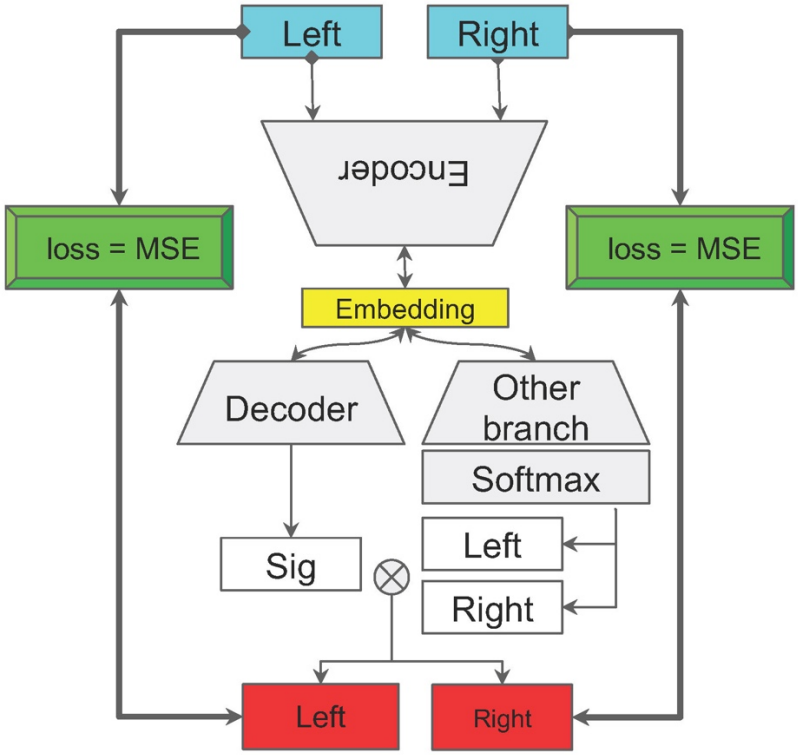


Fig. 4: Autoencoder with extra branch for denoising stereo signals.

REFERENCES

[1] **M. Asch, JC. Le Gac, P. Helluy**, An adjoint method for geoacoustic inversions. In *PICOF'02*, Tunisia, 2002.

[2] **M. Meyer, JP. Hermand, M. Asch, JC. Le Gac**, An analytic multiple frequency adjoint-based inversion algorithm for parabolic-type approximations in ocean acoustics, *Inverse Problems in Science and Engineering,* 14 (3), 245-265, 2006.

[3] **J.-P. Hermand, M. Meyer, M. Asch, and M. Berrada**, Adjoint-based acoustic inversion for the physical characterization of a shallow water environment, *J. Acoust. Soc. Amer.*, vol. 119, pp. 3860–3871, June 2006.

[4] **J.-P. Hermand, M. Meyer, M. Asch, M. Berrada, C. Sorror, S. Thiria, F. Badran, and Y. Stéphan**, Semi-automatic adjoint PE modeling or geoacoustic inversion, In *Theoretical and Computational Acoustics* (A. Tolstoy, E.-C. Shang, and Y.-C. Teng, eds.), pp. 53–64, World Scientific Publishing, 2006.

[5] **F. Badran, M. Berrada, J. Brajard, M. CrÅLepon, C. Sorror, S. Thiria, J.-P. Hermand, M. Meyer, L. Perichon, and M. Asch**, Inversion of satellite ocean colour imagery and geoacoustic characterization of seabed properties: Variational data inversion using a semi-automatic adjoint approach (invited paper), *J. Mar. Sys.*, vol. 69, pp. 126–136, Jan. 2008.

[6] **J.-P. Hermand, O. Gron, M. Asch, and Q.-Y. Ren,** Modelling flint acoustics for detection of submerged Stone Age sites, In *Proc. OCEANS '11 MTS/IEEE Kona Conf. (Oceans of Opportunity: International cooperation and partnership across the Pacific),* IEEE, Sept. 2011.

[7] **J.-P. Hermand, J.R. Johnson, O. Debeir, P.S. Wilson**, Acoustics of seagrass photosynthesis, *Journal of the Acoustical Society of America,* Volume 143, Issue 3, Pages 1796-1796, 2018.

[8] **J.-P. Hermand**, "Acoustic remote sensing of photosynthetic activity in seagrass beds (book chapter)," in *Scaling Methods in Aquatic Ecology. Measurement, Analysis, Simulation* (L. Seuront and P. G. Strutton, eds.), chapter 5, pp. 65–96, Boca Raton, Florida: CRC Press LLC, Sept. 2004.

[9] **J. Patris, D. Komatitsch, M. Sepulveda, F. Malige, M. santos, S . Buchan, H. Glotin, M. Asch.** Mono-hydrophone localization of baleen whales: a study of propagation using a spectral element method applied in Northern Chile, In *OCEANS 2019*, Marseilles (to appear), IEEE.

[10] **M. Ferrari, H. Glotin, R. Marxer, V. Barchasz, F. Sarano, V. Sarano, V. Giés, M. Asch, F. Sarano**. High-frequency near-field *Physeter macrocephalus* monitoring, stereo-autoencoder and model of sonar organ. In *OCEANS 2019*, Marseilles (to appear), IEEE.

HIGH-FREQUENCY ACOUSTICS OF MARINE VEGETATION – ROLE OF FREQUENCIES AND IMAGING ANGLES

Philippe Blondel[a], Aleksandra Kruss[b], Jaroslaw Tęgowski[c], Jennifer L. Wladichuk[d]

[a]University of Bath; Bath, United Kingdom
[b]ISMAR; Venice, Italy
[c]University of Gdansk; Gdansk, Poland
[d]JASCO Applied Sciences & University of Victoria; Victoria BC, Canada

Philippe Blondel, Department of Physics, University of Bath; Bath BA2 7AY, UK;
P.Blondel@bath.ac.uk

Abstract: *Marine vegetation is extremely varied and an essential component of shallow-water habitats. This paper will present two independent strands of work, using a variety of high-frequency acoustic sources to image macrophytes for different purposes. The first series of studies focuses on gas-filled kelp Nereocystis luetkeana, a seaweed ranging along the west coast of North America from California to Alaska, and is an important component of its diverse coastal ecosystems. As part of an investigation into grey whale habitats, we have measured propagation and attenuation through kelp beds of different densities, using broadband (1-20 kHz) white noise (Wladichuk, 2010, and other works). These field measurements in British Columbia (Canada) were compared with Monte Carlo simulations of sound propagation through kelp beds of increasing densities. The second series of measurements (started in Kruss et al., 2007 and continued through to Kruss et al., 2017) looked at gas-free macrophytes in shallow polar habitats; namely Saccharina latissima (L.) and Laminaria digitata (Huds.) in Svalbard fjords. These were mapped with traditional single-beam echo-sounders (such as the Biosonics DTX, 420 kHz) and with multibeam echo-sounders (such as the Imagenex 837 Delta-T, 260 kHz), investigating the ranges of angles at which macrophytes could be reliably mapped and what signal processing approaches were the most adapted. These two types of work are combined to show how they can be interpreted in the light of the seminal work done by Jean-Pierre Hermand on seagrass acoustics, for example Hermand et al. (2000) and Hermand (2004), and how his scientific legacy influences future efforts in acoustic mapping of marine vegetation.*

Keywords: *seagrass acoustics, Nereocystis luetkeana, Laminaria digitata, Saccharina latissima, acoustic propagation, single-beam echo-sounder (SBES), multibeam echo-sounder (MBES), acoustic emissions, Arctic fjords, temperate marine habitats*

1. RATIONALE

Macrophytes comprise all aquatic plants large enough to see with the naked eye, for example seaweed, algae and kelp. They rely on photosynthesis and can therefore be found at shallow depths all around the world, including coastal waters, estuaries, lakes and rivers. They are an important component of marine habitats, as they support biodiversity (including fish), stabilise bottom sediments and maintain coastal water quality and clarity. Some algae are also extensively used in the chemical, pharmaceutical and food industry. Kelps (*Laminariales, Phaeophycae*) are the largest marine crop, with over 4 million tonnes harvested annually [1]. As a source of ecosystem services and natural capital, macrophytes are valued at \$19k ha^{-1} yr^{-1} [2], accounting for at least 11.4% of the worldwide value of all ecosystems. These environments are directly threatened by coastal development, growing human populations and climate change [3-5]. These variations are strongly affecting local food webs and ecosystems [6]. For example, eutrophication is the result of nutrient run-off (usually related to intensive agriculture) and can increase macrophyte concentration and biomass until marine life disappears. In waterways, it can make navigation difficult or more costly. Siltation (increased concentrations of very fine, loose sediment) is closely related to deforestation and soil erosion, and will instead decrease macrophyte concentration [6]. Destructive fishing practices (e.g. trawling) will physically affect the seabed and macrophyte-based habitats [7]. Fish stocks will be directly influenced by these processes. Macrophyte concentrations also act as physical security, buffering shores from waves and extreme weather [6,8]. This is best achieved with acoustic tools, analysing propagation through large bodies of macrophytes, interpreting echoes from the seabed and from any overlying vegetation [7,9].

2. SOUND GENERATION AND ACOUSTIC PROPAGATION IN KELP BEDS

The first study presented in this article formed part of a larger research effort, aimed at understanding the underwater soundscapes of British Columbia. This area corresponds to the summer feeding grounds of grey whales migrating along the western North American and Mexican shores, and an open research question was how they can use the different sources of noise as aids to navigation ([10,11]. Whale behaviours were compared with environmental and acoustic conditions along a 40-km stretch of coast, with open water, rocky and sandy shores and beaches. Kelp beds are important to grey whales, as they contain large quantities of mysid shrimps, their main food in the study area.

These kelp beds mainly consist of bull kelp, *Nereocystis luetkeana*. Individual kelp can grow to 36 m long, with a holdfast (foot) of approximately 40 cm and a single stipe (Fig. 1) Each stipe is topped with a mostly CO-filled pneumatocyst, from which sprout the numerous blades. In sufficiently shallow areas, the top of the stipe can lay at the sea surface at low tides (Fig. 1c). Kelp beds are often dense enough to form what are called “kelp forests” (Fig. 1d). Bull kelp is common along the Pacific Coast of North America, from Southern California to the Aleutian Islands and Alaska, and can form large “forests” (Fig. 1d).

Because of their rich biodiversity [12], in particular very high numbers of mysid shrimps, kelp beds might contribute acoustically to the soundscapes. Movements of the stipes with tides and currents, and their effects on waves at the surface, might also have an effect. This was tested by measuring broadband noise spectra with SQ26-07 hydrophones (Cetacean Research Technology) and digital recorders (sampling at 99.6 kHz and 44.1 kHz), using silent platforms (kayaks). Average frequency spectral levels were taken in kelp beds (of varying densities) and in open shallow water nearby, in similar oceanographic conditions (a few hours apart at most). Typical spectra (Fig.2, top) show that, in the absence of dominant sound

sources in the vicinity (e.g. surf noise), sound levels in kelp increase across all frequencies > 250 Hz, with a maximum of 2.9 dB above open-water background at 3.1 kHz. Repeat measurements over different kelp beds showed water depth only affected frequencies > 7 kHz. These contributions to the soundscape are rather small, of the order of a few dB; however due to the mid-frequency composition, have the ability to propagate well. Since grey whale vocalizations are also in the mid-frequency range (0.09-2 kHz) [22, 23], their auditory sensitivity is likely acute at these frequencies. Therefore, it is plausible that grey whales could use these acoustic "hotspots" produced by the kelp beds and their inhabitants for finding their food but a small increase in the ambient noise could mask this.

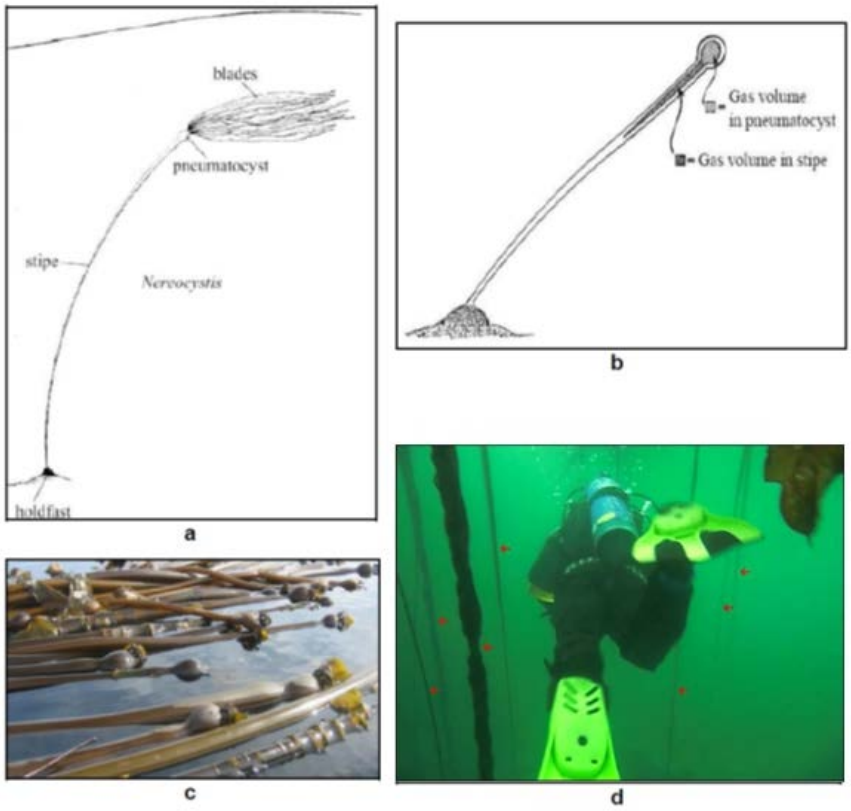


Fig.1: (a) general geometry of bull kelp; (b) distribution of gas in stipes; (c) and (d) field photographs of bull kelp at the sea surface and within a kelp bed. From [10].

As an example, Fig. 2 (inset) shows the relative variations measured as a ship passed behind the kelp bed. There is a 7-dB drop as the ship moves to the other side of the kelp bed and a further drop of 2.5 dB as it gets shielded by the denser part of the kelp bed. More systematic measurements were made, transmitting broadband noise (0.1 – 20 kHz) across kelp beds of different densities, at water depths of ca. 12 m, Fig.2 (bottom) shows the noise measured 1 m from the source, and averages over similar ranges through open water and kelp. The presence of kelp beds significantly reduces sound at nearly all frequencies (0-19 kHz), with higher transmission losses around 1.1, 2.3, 5.3 and 7.7 kHz [10,11]. Corrected for other effects (e.g. attenuation, spreading), broadband transmission losses were measured to vary between 0.4 and 1.2 dB/m, depending on kelp density (0.1 to 0.8 stipes/m^2 in the study area).

Kelp densities will vary with areas and they will show strong seasonal differences, increasing to up to 3.5 stipes/m^2 [12]. The individual arrangements of stipes will also affect sound propagation through kelp beds. We used Monte Carlo simulations of sound attenuation through different densities (0.1 – 10 stipes/m^2), for frequencies of 0.01 to 20 kHz (at 10 Hz steps), over a 10 × 10-m grid (with a cell resolution of 1 cm). Individual stipes were modelled as cylinders, with sizes and physical properties based on previous field measurements [10], with kelp tissue (sound speed 604 m/s, attenuation coefficient 10^{-5} dB/m, density 1,077

kg/m^3) surrounding a CO-O_2 gas mixture (sound speed 354 m/s, attenuations coefficient 52 – 1045 dB/m, density 1.145 kg/m^3). These simulations confirmed field measurements and extended them to higher kelp densities, with a positive linear increase with plant density. The actual slopes vary with gas content in the stipes, ranging from 0.34 to 4.84 dB m.

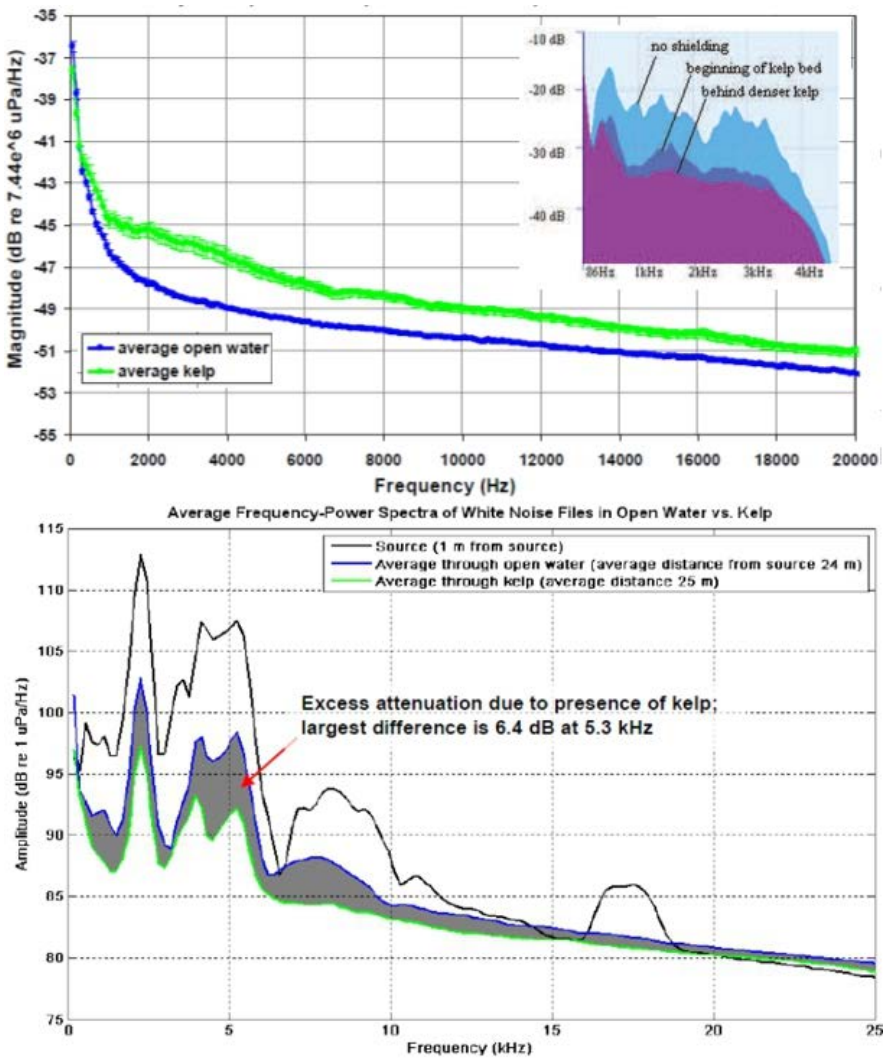


Fig.2: (top) broadband ambient noise measured in a typical kelp bed, and in open waters of similar depths and proximity to shore [10]; (inset) attenuation of ship noise through a kelp bed [13]; (bottom) systematic broadband attenuation through a typical kelp bed [10].

3. MULTI-ANGLE IMAGING OF MACROPHYTES

Climate change is at its most visible in the Arctic, and the results presented in this section form part of a larger research project, understanding how fjord habitats and ecosystems change with global warming. Macrophytes are important indicators of habitat health and glacier melting, and direct sampling [14,15] provides the most information, but it relies on previous knowledge of where the macrophytes are. Their large-scale extent is usually assessed from satellite or aerial imagery, if the water is clear enough, or using acoustics tools such as sidescan sonar [7,9]. These tools are good to map the areal extent of marine vegetation but cannot provide information on volumes or biomass. This is traditionally achieved using Single-Beam Echo-Sounders (SBES) [16], detecting both the seabed and the heights of the marine vegetation (or the top of the canopy if dense enough). Multi-Beam Echo-Sounders (MBES) extend this approach cross-track, and have proved very useful for

other studies [17], bur their potential for marine vegetation had not been systematically compared until recently.

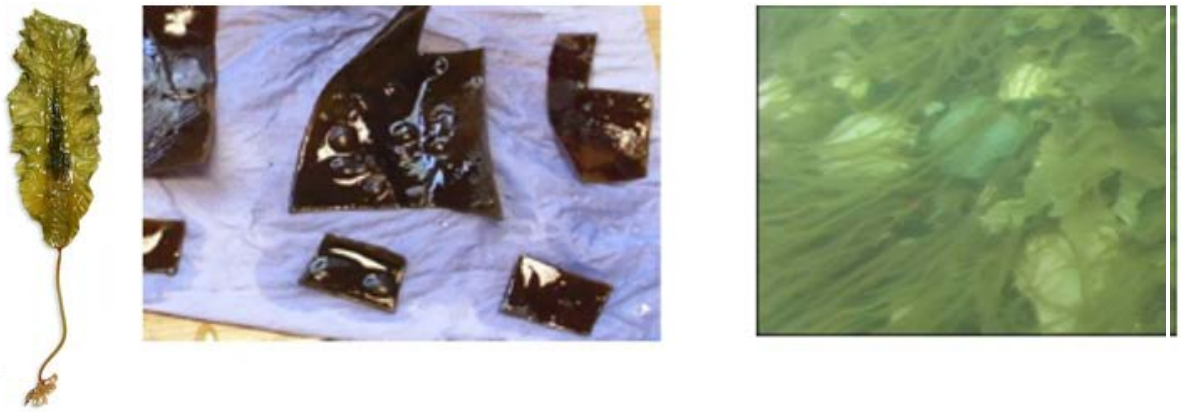


Fig.3: (left) full view of Saccharina latissima; (middle) samples measured in the laboratory; (right) shallow macrophytes in Svalbard. From[18].

Laminaria saccharina (Linnaeus) Lamouroux are very common macrophytes in Arctic fjords, at depths shallower than 20 m. They are also common in other parts of the world (www.habitas.org.uk/marinelife/species.asp?item=ZR6360), including temperate Europe, North America and other polar regions. *Laminaria* have thallus up to 4 m long, and they are attached to rocks by strong stipes (Fig.3). The blades are about 15 cm wide, "flat but wrinkly with wavy margins". Conversely, *Laminaria digitata* is a seaweed common on North Atlantic shores, and it can grow up to 2-3 m (www.seaweed.ie/descriptions/Laminaria_digitata.php). Its stipe is flexible and oval in cross-section, up to 2.5 cm in diameter. The blade is laminate, large (up to 2.5 m) and palm-shaped. The large sizes of the macrophytes mean they can be mapped with different types of sonars (e.g. [16]) but the very thin blades, with little to no gas content, mean their acoustic response is likely to vary significantly with imaging angles.

MBES provide acoustic profiles with narrow beams, at angles from vertical to highly oblique. They cover more ground than SBES along-track, and less across-track (Fig. 4), with similar measurements of vegetation heights (Fig. 5). Depending on the MBES used, up to 30% of measurements in the centre beams can be affected by noise or lost, but this is corrected by averaging over several pings, taking advantage of the higher imaging rate. Our analyses show that MBES beams at angles > 55.5° from the vertical ae noisy enough to be safely rejected before further analyses. Angles of 50.5°–55.5° fared little better, with faint seabed traces and no indication of the presence (or not) of macrophytes. Between 15.5°–30.5°, acoustic returns from macrophytes also seem to disappear. Theoretical simulations [18] showed this was mostly explained by the physical characteristics of the macrophytes present in the Arctic, thin and with no gas content and therefore very close acoustically to the surrounding seawater. On a positive note, though, angles less than 15.5° from the vertical, and between 30.5° and 50.5°, were extremely helpful in identifying macrophytes, their partial extent and their respective heights above the seabed. The Arctic results were corroborated with measurements in controlled conditions, using freshly collected samples of similar macrophytes and also looking at the role of gas vesicles in the acoustic returns [18]. The Arctic measurements (2007), the laboratory tank measurements (2011-2012) and the open-water measurements (2011) all used the same sonar, and found the same results. Another MBES, working at a higher frequency (i.e. higher resolution), confirmed the conclusions from the tank experiments, with slightly different angular ranges for the "dark zone" at which acoustic returns from macrophytes disappear.

In conclusion, the angles at which macrophytes can be detected with MBES extends further away (±15°) from the vertical than would be possible with SBES, and encompasses a further range of angles (30°–50° from the vertical, on either side of the MBES), but there is a

"dark zone" between these angles, explained by the acoustic characteristics of the macrophytes, and data beyond 50° angles is not useful at all. Anecdotal evidence from other teams indicates this is a common observation.

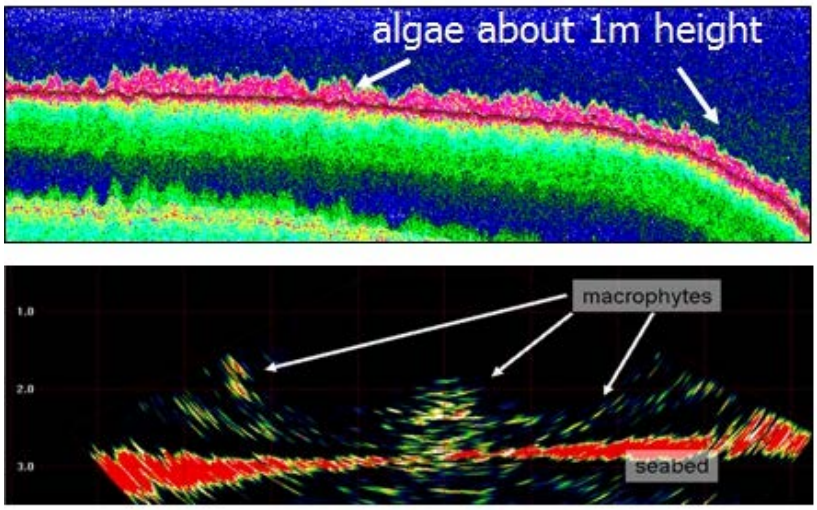


Fig.4: Typical views of along-track SBES measurements of macrophytes (top) and across-track MBES measurements over a wide range of angles (bottom). From [18].

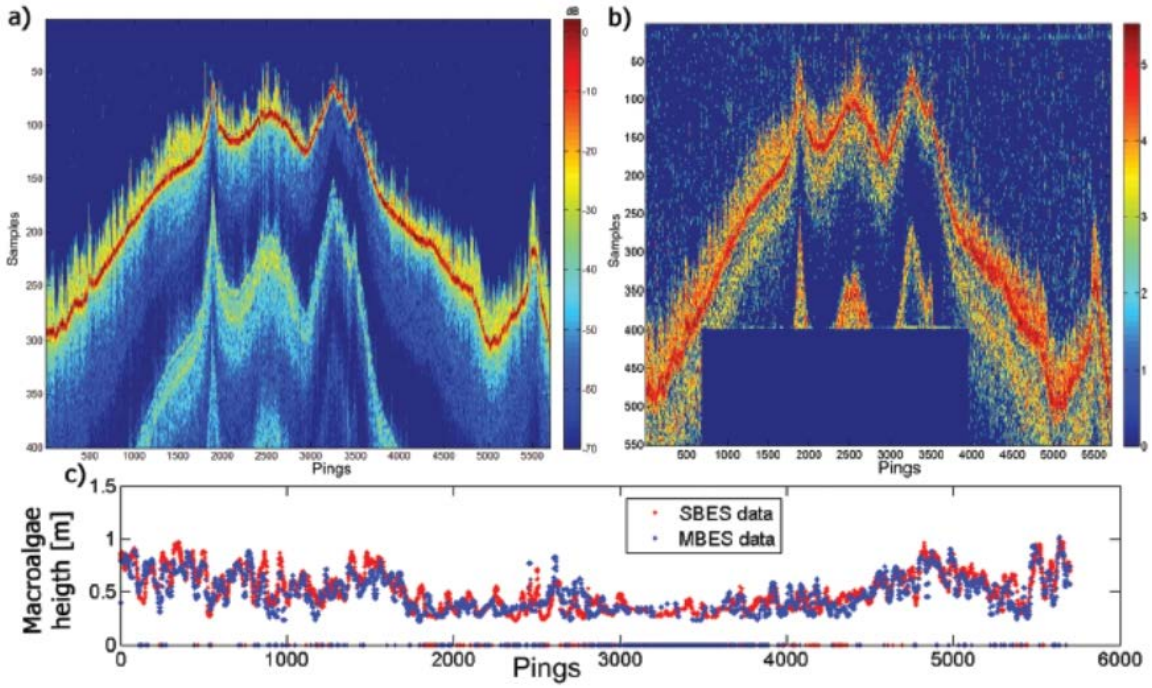


Fig.5: SBES (a) and central-beam MBES (b) measurements, with derived heights (c) [19].

4. CONCLUSIONS

Measurements and simulations of kelp beds (*Nereocystis luetkeana*) in British Columbia showed they were associated with acoustic emissions, relatively low above the open-water background (ca. 3 dB) but within the estimated hearing range of grey whales.. Sound attenuation (ca. 6 dB) strongly depends on kelp bed density and is frequency-dependent. The overarching study [10] concluded grey whales can use the different attenuation of natural sounds (surf noise, winds, waves) through kelp beds as an aid to underwater navigation. Any

temporal variability due to the presence of kelp is masked by these natural processes, in particular weather-related sounds.

Measurements and simulations of gas-free macrophytes (*Laminaria digitata* and *Saccharina latissima*), in Arctic fjords and in controlled experiments in laboratory and open water, showed how adequate processing of SBES and MBES measurements can provide useful measurements of vegetation heights, biovolumes and (for MBES) areal extents [19]. Cross-validation of SBES and MBES measurements show the latter are comparable within ±15° and ±(30°–50°) from the vertical, with a "dark zone" between these angles, explained by the acoustic characteristics of the macrophytes, and data beyond 50° angles is not useful at all.

These field observations inscribe themselves within the scientific legacy of Jean-Pierre Hermand and his famous experiments on seagrass acoustics (e.g. [20,21]), which inspired many researchers. Broadband propagation (0.2 – 16 kHz) through meadows of *Posidonia oceanica* and individual plants showed frequency variations related to the physical make-up of each plant and gas circulation (in microbubbles and in plants) associated to photosynthesis The modelling of multipath propagation over different ranges (50 – 1,500 m) also showed the importance of intermediate grazing angles [21]. As work on acoustic scattering by different types of marine vegetation progresses, it will be very important to see how these elements contribute to multi-path scattering, and for example assess whether the "dark zones" of MBES imaging can be filled up with multi-aspect sonars). Jean-Pierre's work will continue to inspire scientists in the field, and in the laboratory, for many years to come.

5. ACKNOWLEDGEMENTS

Fieldwork by JLW, PB (Section 2) was supported by the Earthwatch Institute and the Coastal Ecosystems Research Foundation (CERF). Fieldwork by AK, JT, PB (Section 3) was supported by ARCFAC-026129-70, IOPAS and the Ministry of Education and Science of Poland (#N306-425034) (led by JT). AK acknowledges Marie Curie Fellowship #PIEF-GA-2009-251832 (Bath) and Marie Curie Bandiera Cofund ARMSC (ISMAR). We thank C. Wiencke (AWI, Bremerhaven, Germany) and his divers for the samples in Kongsfjord.

REFERENCES

[1] **Asensi, A., E.A. Gall, D. Marie, C. Billot, P. Dion, B. Kloareg**, Clonal Propagation of *Laminaria digitata* (*Phaeophyceae*) Sporophytes through a Diploid Cell-Filament Suspension, *J. Phycol.*, 37, pp. 411-417, 2001.

[2] **Costanza, R., et al.**, The Value of the World's Ecosystem Services and Natural Capital, Nature, 387, pp. 253 - 260, 1997.

[3] **IPCC (Intergovernmental Panel on Climate Change)**, Climate Change 2007, Synthesis Report, *United Nations,* 52 pp., 2007.

[4] **Halpern, B.S. et al.**, A Global Map of Human Impact on Marine Ecosystems, *Science*, 319(5865), pp. 948-952, 2008.

[5] **Waycott, M. et al**., Accelerating Loss of Seagrasses across the Globe Threatens Coastal Ecosystems, *PNAS*, 106 (30), pp. 12,377-12,381, 2009.

[6] **GEO-4**, Global Environment Outlook – Environment for Development, *United Nations Environment Programme*, 572 pp., 2007.

[7] **Blondel, Ph**., *Handbook of Sidescan Sonar*, Springer-Praxis, 345 pp., 2009.

[8] **Kelly, E. (ed.)**, The Role of Kelp in the Marine Environment, Irish Wildlife Manuals, No. 17. National Parks and Wildlife Service, 2005

[9] **Gumusay, M.U., T. Bakirman, I.T. Kizilkaya, N.O. Aykut,** A Review of Seagrass Detection, Mapping and Monitoring Applications using Acoustic Systems, *Eur. J. Remote Sensing*, 52(1), pp. 1-29, 2019.

[10] **Wladichuk, J.**, Investigation of Ambient Noise in the Underwater Coastal Environment and its Potential for Use as a Navigational Aid by Grey Whales *Eschrichtius robustus*, Foraging in British Columbia, Canada, PhD thesis, U. Bath (UK), 201 pp., 2010

[11] **Wladichuk, J., W. Megill, Ph. Blondel**, Ambient Soundscape of Grey Whale Feeding Grounds in British Columbia, Canada, In Proc. *8th DCLDE*, 2018.

[12] **Shaffer, J.A.**, Seasonal Variation in Understory Kelp Bed Habitats of the Strait of Juan de Fuca, *J. Coastal Research*, 16(3), pp. 768-775, 2000.

[13] **Wladichuk, J., W. Megill, Ph. Blondel**, A Bioinspired Approach to Sound Localization in the Underwater Coastal Environment; *Proc. Underwater Acoustic Measurements UAM-2007*, pp. 917-924, 2007.

[14] **Woelfel, J., R. Schumann, F. Peine, A. Flohr, A. Kruss, J. Tegowski, P. Blondel, C. Wiencke, U. Karsten**, Microphytobenthos of Arctic Kongsfjorden (Svalbard, Norway): Biomass and Potential Primary Production along the Shore Line, *Polar Biology*, 33(9), pp. 1,239-1,253, 2010.

[15] **Bartsch, I. et al.,** Changes in Kelp Forest Biomass and Depth Distribution in Kongsfjorden, Svalbard, Between 1996–1998 and 2012–2014 Reflect Arctic Warming, *Polar Biology*, 39(11), pp. 2,201-2,036. 2016.

[16] **Kruss A., Tęgowski J., Wiktor J., Tatarek A.**, Acoustic Estimation of Macrophytes in Hornsund fjord (Svalbard), *Hydroacoustics*, 9, pp. 89-96, 2006.

[17] **Brown, C., Ph. Blondel**, Developments in the Application of Multibeam Sonar Backscatter Data for Seafloor Habitat Mapping, *Applied Acoustics*, 70(10), pp. 1242-1247, 2009.

[18] **Kruss, A., Ph. Blondel, J. Tegowski**, Acoustic Properties of Macrophytes: Comparison of Single-Beam and Multibeam Imaging with Modelling Results, In *Proc. 11th European Conference on Underwater Acoustics ECUA-2012*, pp. 168-175, 2012.

[19] **Kruss, A., J. Tegowski, A. Tatarek, J. Wiktor, Ph. Blondel**, Spatial Distribution of Macroalgae along the Shores of Kongsfjorden (West Spitsbergen) Using Acoustic Imaging, *Polish Polar Research*, 38(2), pp. 205-229, 2017.

[20] **Hermand J.P., Nascetti P., Cinelli F.**, Inverse Acoustical Determination of Photosynthetic Oxygen Productivity of *Posidonia* Seagrass, In: *Experimental Acoustic Inversion Methods for Exploration of the Shallow Water Environment*, A. Caiti J.P. Hermand, S.M. Jesus, M.B. Porter (eds). Springer, pp. 125-144, 2000.

[21] **Hermand, J.P.**, Continuous Acoustic Monitoring of Physiological and Environmental Processes in Seagrass Prairies with Focus on Photosynthesis, In *Acoustic Sensing Techniques for the Shallow Water Environment*, A. Caiti, N.R. Chapman, J.-P. Hermand, S.M. Jesus (eds.), Springer, pp. 183-196, 2006.

[22] **Crane, N.L., K. Lashkari**, Sound Production of Gray Whales, *Eschrichtius robustus*, along their Migration Route: a New Approach to Signal Analysis, *J. Acoustic. Soc. Am.*, 100(3), pp. 1,878-1,886, 1996.

[23] **Dahlheim, M.E.,** Bio-Acoustics of the Gray Whale (*Eschrichtius robustus*).*PhD Thesis*. Dept. Zoology, U. British Columbia, British Columbia, Canada, 1987.

ADVENT OF DEEP ARGO DATA & AN ATTEMPT AT ANALYZING THE DEEPER SOUND SPEED PROFILES FOR EXTRAPOLATION CORRECTIONS

Kashif Iqbal[a], Minghui Zhang[a], Shengchun Piao[a], He Ge[a]

[a]College of Underwater Acoustic Engineering, Harbin Engineering University, Harbin 150001, China; kashifjamshed607@hotmail.com; zhangminghui@hrbeu.edu.cn; piaoshengchun@hrbeu.edu.cn; heuhege@163.com

Minghui Zhang, College of Underwater Acoustic Engineering, Harbin Engineering University, Harbin 150001, China. Telephone No. 19845176629, Fax: 0451-82531753

Abstract: *Both R. Davis & D. Webb were able to develop Argo float technology during early 1990s. A profiling array comprising of 3300 such floats was proposed to cover the oceans globally in 1998 by the Argo's Science Team. The first Argo profiling float came into existence in the year 1999. By the year 2007, Argo had achieved its target of 3000 active floats covering the desired global ocean. The conventional depth for obtaining Argo data has been 0 - 2000 meters. As a giant leap forward, by the middle of 2014, a workshop named, "Deep Argo Implementation Workshop", was held in Hobart. In this conference, Johnson et al. proposed an array of 1228 floats providing coverage of 5° × 5° × 15-day cycles. Deployment of pilot arrays for covering particular regions has already been executed. Deep Ninja and Deep Arvor from Japan and France simultaneously cover depths of 0 - 4000, while Apex & Solo of Unites States are developed to cover 0 - 6000 meters. This study is focused on obtaining in-situ data from a couple of deep Argo buoys and then, compares their salinity, temperature, and sound speed's in-situ values with the extrapolated ones. Prior to availability of deep Argo, the data in depth was usually extrapolated for various parameter calculations. The literature presents numerous methods and examples for extrapolation of vertical profiles for salinity, temperature, and sound speed profiles. The measured temperature and salinity parameters with the pressure were converted to sound speed profile. The extrapolation was carried out using MATLAB's polyfit and polyval functions. The comparative analysis among in-situ data and the extrapolated one illustrates deviation in deeper vertical profiles especially after 2500 meters. The analysis results are presented in the form of graphs and marked accordingly for both in-situ and extrapolated curves. In addition, the study focuses on varying factors responsible for the typical anomalies especially in deeper oceans. The anomalies suggest that for deeper depth calculations, the real measured values present more accurate results instead of mere extrapolations.*

Keywords: *Argo profiling floats, temperature, salinity, sound speed profile, anomalies*

1. INTRODUCTION

Since 1999, Argo float's idea of measuring upper surface of ocean flourished, and by 2007, a targeted array of 3000 floats was accomplished & started covering the subsurface ocean. In the beginning, Argo floats were designed to collect ocean's salinity, temperature, and pressure data around the globe. Later on, various other sensors were included to measure the biogeochemical values around the ocean. To this day, over 1.6 million temperature/salinity profiles and trajectories have been acquired by this Argo program. Roughly, 90% of the profiles are available within a day of their collection. This in-situ Argo data is available online without cost and is capable of being used in research programs. On 11th of August 2014, New York Times famously quoted that, "That system, known as Argo, is one of the scientific triumphs of the age". Initially, the Argo floats were designed to dive deep to 2000 meters depth, but since mid-2014, a program for deploying deep Argo buoys was initiated. These deep Argo floats include Deep Ninja (Japan), Deep Arvor (France), Deep Solo (United States), and Deep Apex (United States) [1, 2, 3, 4]. Prior to availability of deep Argo, the data in depth was usually extrapolated for various parametric calculations [5, 6]. This study focuses on analyzing deep Argo data for salinity, temperature and sound speed profiles against the pressure. The analysis includes the measure values compared to the extrapolated ones for salinity, temperature, and sound speed profiles. Various deep Argo floats reaching the depths of 0 - 4000 meters with the help of deep sensors like SBE - 41 CTD, are selected for this particular analysis. These floats are detailed for their Argo number, cycle number, longitude, latitude, and dates accordingly. The study finally discusses the deviated results along with the reasons [4].

2. DEEP ARGO & ITS DATA UTILIZATION

As mentioned earlier, the conventional depth for obtaining Argo data has been 0 - 2000 meters. As a giant leap forward, by the middle of 2014, a workshop named, "Deep Argo Implementation Workshop", was held in Hobart. In this conference, Johnson et al. proposed an array of 1228 floats providing coverage of 5° × 5° × 15-day cycles. Deployments of pilot arrays for covering particular regions have already been executed. Deep Ninja and Deep Arvor from Japan and France simultaneously cover depths of 0 - 4000, while Apex & Solo of Unites States are developed to cover 0 - 6000 meters [7, 8]. This study is primarily focused on obtaining in-situ data from both NINJA D i.e. Float ID: WMO2902510 (Inactive) and Arvor D i.e. Float ID: WMO 3902132, and then compare its salinity, temperature, and sound speed profile's in-situ values with the vertically extrapolated profiles [9]. It is pertinent to mention here that extrapolation is carried out using MATLAB's polyfit and polyval functions after the conventional depth of 2000 meters [10]. In the following section, the study proceeds with the discussion of salinity, temperature and sound speed profile results for the above-mentioned deep Argo buoys.

3. COMPARATIVE STUDY FOR THE NINJA D (ID: WMO 2902510)

The NINJA D with ID: WMO2902510 (inactive), chosen for this study is currently inactive. The cycle of the float used for this study is 24th which commenced on 2014/03/02. The location of this particular float is illustrated in Fig. 1. This map is generated using the googleearth software [11]. This float covers the depth of ocean from 0 - 4000 meters. Similarly, Fig. 2 and Fig. 3 represent the salinity (degree celsius) and temperature (psu) profiles respectively for both in-situ and extrapolated values. The extrapolation is executed below the depth of 2000 meters for the entire comparative analysis. The sound speed profile is calculated by employing Mackenzie's equation has been employed. This equation is stated as [12]:

$$C = 1448.96 + 4.591T - 5.304 \times 10^{-2}T^2 + 2.374 \times 10^{-4}T^3 + 1.340 \times (S - 35) + 1.630 \times 10^{-2}D + 1.675 \times 10^{-7}D^2 - 1.025 \times 10^{-2}T(S - 35) - 7.139 \times 10^{-13}TD^3$$

where T = temperature in degrees Celsius, S = salinity in parts per thousand, and D = depth in meters.

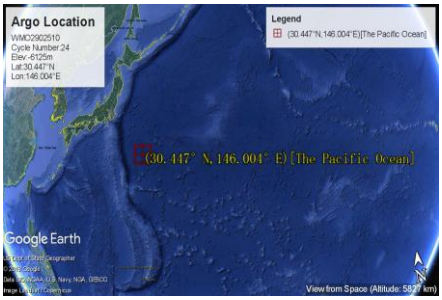


Fig.1: Location of the Argo float (Source: googleearth.com)

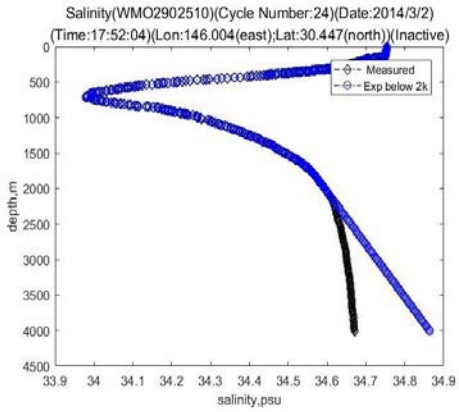


Fig.2: Salinity profile for both in-situ and extrapolated values

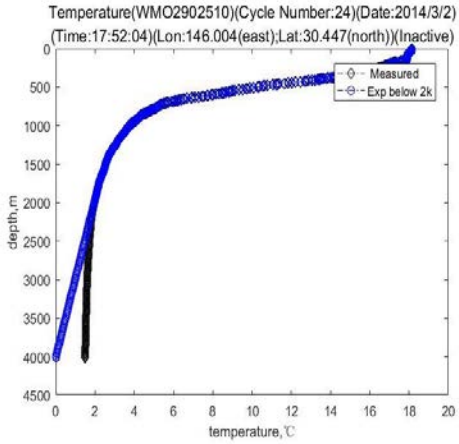


Fig.3: Temperature profile for both in-situ and extrapolated values

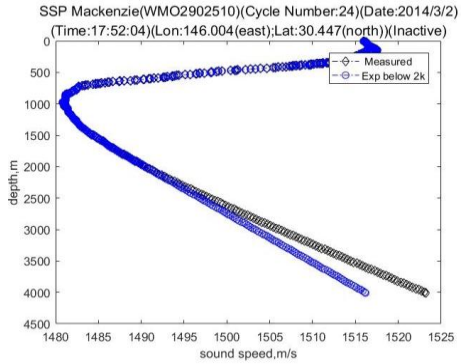


Fig.4: Sound speed profile for both in-situ and extrapolated values

The results shown in Figs. 2-4 are self-explanatory and detailed in the section 5. The extrapolated values for both the salinity and temperature profiles exhibit deviation from the

measured i.e. in-situ values. The deviation of these values contributes to the deviation of sound speed profile as well just below the 2000 meters.

4. FURTHER ANALYSIS WITH AN ARVOR D (FLOAT DEEP) (ID: WMO 3902132)

The Arvor D with ID: WMO 3902132 (operational) is chosen for further analysis of the CTD in the deeper oceans. This float is chosen to exhibit the similar results like NINJA D for salinity, temperature, and sound speed profile. The cycle chosen for this particular activity is 84. The data was recorded on 2019/03/08. In this case, the vertical extrapolation for salinity, temperature, and sound speed profiles is taken after the depth of 2000 meters. Fig. 5 displays the location of this particular float with the help of googleearth software. Salinity, temperature, and sound speed profiles are shown in Fig. 6, Fig. 7, and Fig. 8 respectively. As mentioned earlier, the sound speed profile is generated by using the Mackenzie equation.

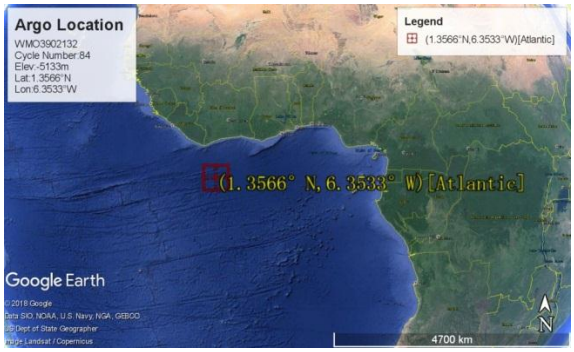


Fig.5: Location of the Argo float (Source: googleearth.com)

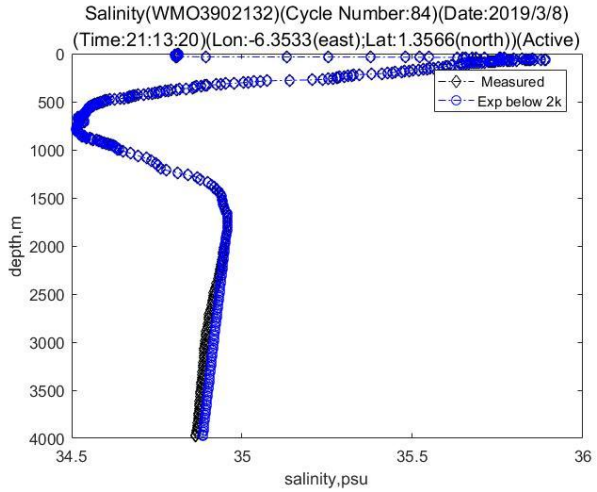


Fig.6: Salinity profile for both in-situ and extrapolated values

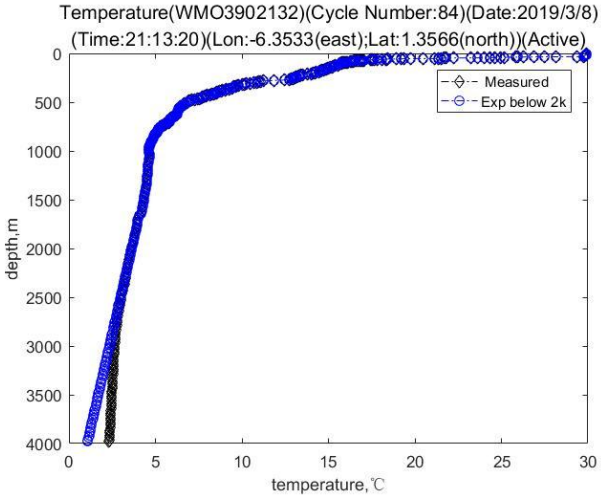


Fig.7: Temperature profile for both in-situ and extrapolated values

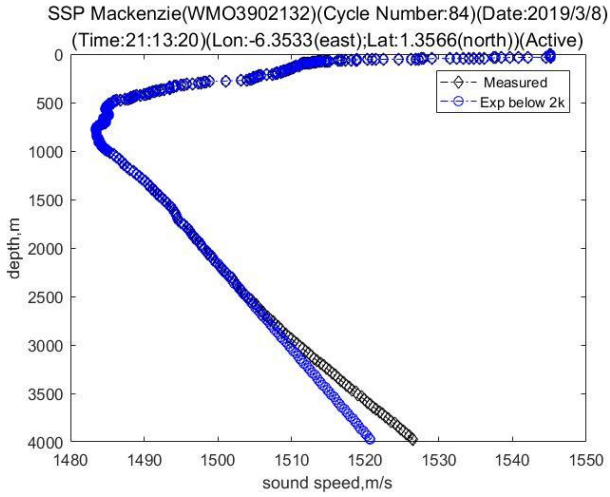


Fig.8: Sound speed profile for both in-situ and extrapolated values

5. DISCUSSION

The aforementioned discussion illustrates that the extrapolated value of the Core Argo Program below the depth of 2000 meters come out to be erroneous if compared with the in-situ values of the Deep Argo Program. In this regard, results from a Deep Ninja Argo float with ID: 2902510 are employed for observations and the float is in its 24th cycle. The outcomes illustrated in figures from 2 - 4 exhibit the obvious deviations from the measured in-situ values to the extrapolated ones especially below the depth of just below 2000 meters. This deviation for salinity in Fig. 2 is evident just below 2000 meters and becomes widely apart at the depth of 4000 meters with measured value lagging by 0.2 psu from the extrapolated value. Similarly, the temperature of the measured in-situ value exceeds roughly by 1.8 °C. This temperature difference has ultimately altered the in-situ value of sound speed profile to exceed by nearly 8 m/s than the extrapolated one as can be observed in Fig. 4. In the fourth section, the figures from 6 - 8 display the results for salinity, temperature, and sound speed profiles for both measured and extrapolated values in case of an Arvor D float with ID: 3902132. In Fig. 6, the measured value of salinity lags negligibly from the extrapolated value. The measured value of temperature starts deviating from the extrapolated value just below 2500 meters depth and ends by exceeding by roughly 1 °C at 4000 meters depth. The resulting sound speed profile for the measured value exceeds the extrapolated one by nearly 6 m/s. These obvious variations for the salinity, temperature, and the sound speed profile for both measured in-situ and extrapolated values suggest the alarming situation in case the real values are absent. Thus, the study strongly suggests the employment of measured data in case of precise calculations for the deeper oceans. The measured values have displayed obvious variations from the extrapolated values.

6. ACKNOWLEDGEMENTS

The author is especially thankful to Prof. Piao Shengchun & Mingzhang Hui for their valuable supervision and suggestions. In addition, the entire group has been thoroughly supportive for this particular study.

REFERENCES

1. **W John Gould**, "From Swallow floats to Argo - the development of neutrally buoyant floats," *Deep-Sea Research II 52, 529-543uthors, 2005.*
2. **Roemmich, D., G.C. Johnson, S. Riser, R. Davis, J. Gilson, W.B. Owens, S.L. Garzoli, C. Schmid, and M. Ignaszewski** , The Argo Program: Observing the Global Ocean with Profiling Floats, *Oceanography, Vol.22, No.2, June 2009*.
3. **Breck Owens**, The Argo Program - Present and Future, For the International Argo Steering Team, In *the Technical Conference of the Joint WMO/IOC Technical Commission for Oceanography and Marine Meterology (TECO JCOMM-5)*, Geneva, October 23, 2017.

4. **Dean Roemmich, Nathalie Zilberman, Philip Sutton,Russ Davis, John Gilson, Kyle Grindley, Carol Janzen, Gregory Johnson, Taiyo Kobayashi, Nordeen Larson, Serge Le Reste, Guillaume Maze, Robert Melvin, David Murphy, Ernest Petzrick, Stephen Riser, Jeff Sherman, Toshio Suga, Michihiko Tachikawa, Esmee van Wijk, Matthew Walkington, and Susan Wijffels**, "Development of the Deep Argo Program," *Ocean Surface Topography Science Team Meeting*, Lake Constance Germany, October 28 - 31, 2014.
5. **Shigeki Hosoda**, **Tsuyoshi Ohira**, and **Tomoaki Nakamura**, Report - A monthly mean dataset of global oceanic temperature and salinity derived from Argo float observations, JAMSTEC Rep. Res. Dev., Vol. 8, pp. 47-59, November 2008.
6. **Viktor Gouretski**, World Ocean Circulation Experiment - Argo Global Hydrographic Climatology, Ocean Sci., 14, pp. 1127-1146, 2018.
7. **Nathalie Zilberman** and **Guillaume Maze**, Report on the Deep Argo Implementation Workshop, Hobart, May 5-7th 2015 [http://www.argo.ucsd.edu/DAIW1report.pdf]
8. **Dean Roemmich, Nathalie Zilberman**, The Deep Argo Program: Broad-Scale Sampling of the Full Ocean Water Column, Scripps Institution of Oceanography, UCSD, La Jolla CA 92093-0230, U.S.A.
9. Data obtained from the websites given below:
   http://www.jcommops.org/board/wa/InspectPtfModule?ref=2902510 &
   http://www.jcommops.org/board/wa/InspectPtfModule?ref=2903212 respectively
10. **Ross L. Spencer, Michael Ware**, *Introduction to Matlab*, Department of Physics and Astronomy, Brigham Young University.
    [https://www.physics.byu.edu/courses/computational/phys330/matlab.pdf]
11. Data obtained from the website: www.googleearth.com
12. **Kenneth V. Mackenzie**, Nine-term Equation for Sound Speed in the Oceans, *Acoustical Society of America*, Vol. 70, No.3, pp. 807 - 812, September 1981.

Structured Session 2
Underwater acoustic calibration, testing, facilities and standards

Organiser(s): Robinson Stephen, Humphrey Victor, Linné Markus, Évora Victor

STANDARDS FOR PROJECT JOMOPANS: OCEAN NOISE MONITORING FOR THE NORTH SEA

Stephen Robinson, Lian Wang, Jake Ward.

National Physical Laboratory

Hampton Road, Teddington, TW11 0LW, UK. Email: stephen.robinson@npl.co.uk

Abstract:
At this moment, there are no international standards for monitoring ambient noise in the ocean. Such standards would require consensus on a number of topics: (i) terminology for describing the monitoring of underwater ambient noise; (ii) specification, performance requirements, calibration and deployment of the measurement equipment; (iii) analysis of the measured data obtained from monitoring. JOMOPANS is a project funded by the EU INTERREG programme with the aim of monitoring the ambient noise in the North Sea in response to the requirements of the Marine Strategy Framework Directive.
Within the project, the above activities are being standardized so that all partners use a common approach in order that data obtained within the project are comparable. This paper describes some of the standardization activities in the project, including the provision of protocols for describing the key practical activities within the project, and a benchmarking exercise to ensure that data analysis undertaken by the partners is mutually equivalent.

Keywords: *standards, ocean noise, monitoring*

1. INTRODUCTION

Project JOMOPANS is funded by the EU INTERREG programme. The aim of the project is to develop a framework for a fully operational joint monitoring programme for ambient noise in the North Sea. The outputs will be the tools necessary for managers, planners and other stakeholders to incorporate the effects of ambient noise in their assessment of the environmental status of the North Sea, and to evaluate measures to improve the environment.

Sounds are omnipresent in the underwater environment and can be produced by natural sources (waves, weather, and animals) and anthropogenic sources (shipping, construction, and geophysical surveying). International concern increasingly focusses on the potential negative effects of anthropogenic underwater noise on sensitive marine fauna. Sound sources, sound transmission, and the distributions of vulnerable species in the North Sea are all transnational questions which must be tackled transnationally, as specifically required by the Marine Strategy Framework Directive [1].

This project will deliver a combination of modelling and high quality measurements at sea for an operational joint monitoring programme for ambient noise in the North Sea. The use of consistent measurement standards and interpretation tools will enable marine managers, planners and other stakeholders internationally to identify, for the first time, where noise may adversely affect the North Sea. The project will explore the effectiveness of various options for reducing these environmental impacts through coordinated management measures across the North Sea basin. Figure 1 shows the location of the 14 JOMOPANS monitoring stations and the partners on the project.



Fig. 1: JOMOPANS monitoring stations (red dots) and project partners.

JOMOPANS has a duration of three years from January 2018 to December 2020. The project consortium has 11 partners from 7 countries. The project coordinator is Rijkswaterstaat in The Netherlands. Figure 2 shows the structure of the project and the relationship between the different work packages and activities.

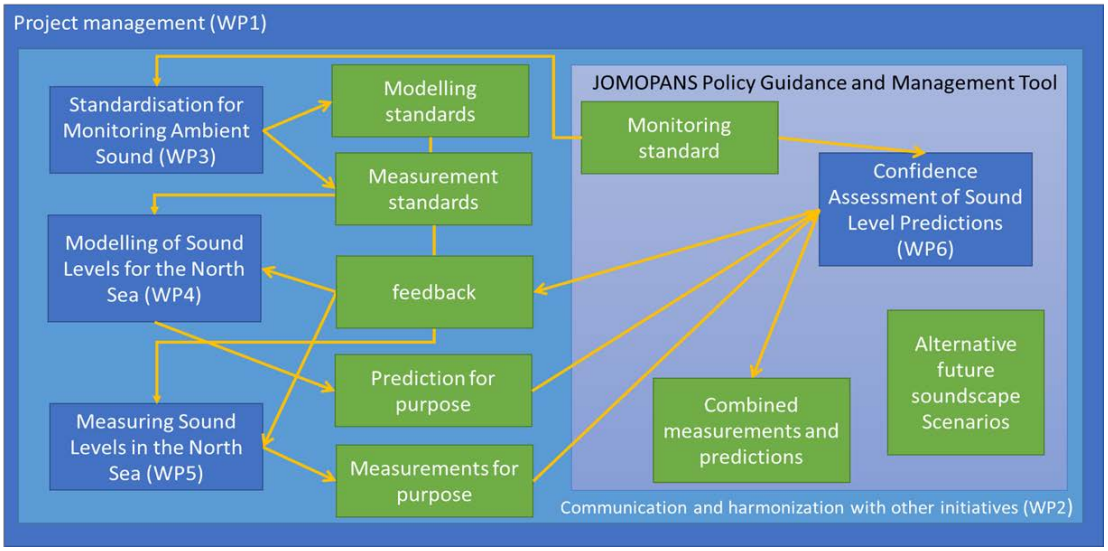


Fig. 2: Project structure for JOMOPANS

At this moment, there are no international standards for monitoring ambient noise in the ocean. In JOMOPANS, there is a need to standardize some activities so that all partners use a common approach and so that data obtained within the project are comparable. Therefore, we are developing standards within the project which address this need, and which will ultimately feed into the development of international standards. The work on standardization includes a number of topics:

- terminology for describing the monitoring of underwater ambient noise;
- performance requirements, calibration and deployment of the measurement equipment;
- analysis of the measured data obtained from monitoring.

The standardisation work in JOMOPANS also includes benchmarking of acoustic propagation modelling of underwater sound fields, but this work is not described in this paper.

2. TERMINOLOGY

There are a number of different metrics that may be used as measures of the sound pressure [2-6]. In the JOMOPANS project, the sound field metric chosen for estimation of the sound field is the sound pressure level (SPL). The SPL is calculated from the mean-square sound pressure described in ISO 18405 [2].

The temporal observation window and the temporal analysis window are both defined as being equal to 1 second [7]. The windows are not aggregated into longer analysis periods and the statistics of the ambient noise are calculated from the 1 second windows alone.

In JOMOPANS, the measured SPL values are filtered into 34 one-third octave bands (base 10) with centre frequencies in the range 10 Hz to 20 kHz [4]. In the JOMOPANS project, the base 10 calculation of one-third octave frequencies and bands (equivalent to one tenth decades) is the chosen definition and nomenclature. This is in accord with IEC 61260:1-2014 [4] and with the most common usage adopted throughout the field of acoustics.

An examination is made of the distribution of estimated SPL values averaged over 1 second and evaluated in the one-third octave bands described above. The statistical percentiles are calculated based on the above distribution of values [8].

Note that in the JOMOPANS project, the physical quantity being estimated is considered to be the ambient noise in the ocean; that is, all sound except sound associated with a specified signal and except acoustic self-noise. Note that all sound is to be measured and considered to be of interest (all sounds in the ocean are considered to be "signal"). Note that in some other ocean monitoring projects, the quantity being estimated is given the name "ambient sound".

3. EQUIPMENT PERFORMANCE, CALIBRATION AND DEPLOYMENT

This aspect of the standardisation falls into three categories

- Specification of required equipment performance
- Specification of calibration requirements for instrumentation
- Specification of deployment methodology

Regarding specification of required equipment performance, key equipment parameters to be specified include frequency range, dynamic range, sensitivity, directionality, sampling rate, filtering, system self-noise. Table 1 shows the agreed minimum equipment performance [9].

Regarding the calibration requirements for instrumentation, these include calibration methodology, traceability to international standards, specification of measurements required, frequency range, and uncertainty requirements [9]. Calibrations are completed on all devices before and after the deployments, with absolute calibrations obtained for any measurement hydrophone and recording system deployed for the study. Calibrations are ideally completed in the same (or as close as possible) mounting configuration and temperature/depth for which the hydrophone is likely to experience in the field. Field calibrations are conducted prior to deployment and post recovery to ensure there has been no major change in the hydrophones response over the course of the measurement. Recommended frequency range for calibrations should at minimum cover the frequencies of interest between 10 Hz and 20 kHz at least third octave centre frequencies. All calibrations must be traceable to internationally-recognised standards

Regarding the specification of deployment methodology, guidance is provided on recommended methodology for deployment, including rigging and anchoring [9]. Recommendations are also made for methods to mitigate the influence of parasitic signals caused by contaminating artefacts. In addition to the self-noise of the measuring system itself, the measured data may also be contaminated by signals originating from the platform or method of deployment. This is often called "platform noise" or "deployment noise". These parasitic signals are due to the deployment method for the hydrophone and recording system and its interaction with the surrounding environment (e.g. current, wave action, etc) and include such effects as cable strum, and flow noise, mechanical noise, etc.

Procedures are also recommended for quality assurance when retrieving and storing data. Recommendations are also made for measurement and recording of auxiliary data, for example, wind speed, water depth, air temperature, GPS location, seabed type, etc.

In JOMOPANS, some monitoring stations consist of autonomous recorders which are archival systems that are deployed for a fixed time duration (typically three or six months). However, a number of JOMOPANS monitoring stations are hardwired to the shore and provide continuous monitoring with 100% duty cycle.

Metric	Specification
Frequency range:	Nominally: 10 Hz – 20 kHz Note that to fully record the 34 third-octave bands in this frequency range requires measurement over the range 8.91 Hz to 22.39 kHz. Note: MSFD focus frequencies of interest are the 63 Hz and 125 Hz third-octave bands.
Dynamic range:	Minimum 16 bit (nominal dynamic range 96 dB), Preferably 24 bit (nominal dynamic range 144 dB) Note: actual dynamic range is from noise floor defined by system self-noise to the maximum measureable undistorted sound pressure
Sensitivity:	Ideally in the range: -165 to -185 dB re. 1 V/µPa
Frequency response	Ideally invariant with frequency (flat response) in the range 10 Hz to 20 kHz Note: see description of recorder performance when hydrophone is rigidly attached to body.
Directionality:	Omnidirectional to within +/- 1 dB up to 20 kHz azimuthal, and to within +/- 2 dB in vertical elevation Note: see description of recorder performance when hydrophone is rigidly attached to body
Sampling rate:	Minimum of 44 kHz Ideally at least 48 kHz (to capture upper band limit of 22.39 kHz for the 20 kHz third-octave band)
Filtering:	Any filter characteristics should be known and corrections applied (low pass and high pass filtering caused by instrumentation) Note: any low frequency roll-off in recorder performance due to high pass electronic filtering must be measured so that suitable corrections can be applied.
System self-noise:	Ideally, better than 64 dB re 1 μPa^2/Hz at 63 Hz; Ideally, better than 59 dB re 1 μPa^2/Hz at 125 Hz. Ideally, 6 dB below the lowest sound level. Note: the self-noise of some of legacy instrumentation used in the project (such as autonomous recorders) may not meet this specification.

Table 1: JOMOPANS agreed minimum equipment performance.

4. DATA ANALYSIS

Specifications have been defined for methods of calculating the key metrics from measurement data. Guidance provided on initial data processing includes removal of contaminated data, checks for clipping and distortion, checking for spurious signals. Guidance is also provided for software control and maintenance [10].

As a check on performance of software algorithms used by partners, benchmarked data sets were created for validation of analysis algorithms. The benchmarking exercise was carried out for project partners to compute one third octave band SPL levels from a common synthetic data set. The intention was to check how robust the guidance was and to compare the levels reported by partners following their own implementation of the processing.

Project partners were given two data files and instruction to compute the required metrics. The two files were generated with the same random seed and the two noise spectra were coloured white and pink (this description of the noise-types in the files was not given to participants at the time of circulating the simulated data). Partners returned the spectral levels

for each second of the two 100 second files individually and the results were compared, with sufficient agreement obtained between the partners' results.

5. SUMMARY AND CONCLUSION

Within JOMOPANS, standard procedures have been produced on (i) acoustic terminology; (ii) equipment performance, calibration and deployment, and (iii) processing of measurement data. In addition, a benchmarking exercise has been undertaken to enable partners to compare their data analysis software by processing the same sets of synthesized data of known characteristics.

The JOMOPANS standards will also be made available to the wider acoustical community. They will be submitted for discussion in standardisation committees to provide input to the drafting of international standards and the preparation of new work item proposals, for example within ISO.

JOMOPANS is also communicating with other relevant projects in Europe and across the world, like JONAS, QuietMed, UNAC-LOW, COMPASS, ECHO, Adeon and MarPAMM. This enables JOMOPANS to share valuable information on the approaches used and the lessons learned, and just as JOMOPANS builds on the original work of the BIAS project, these existing and future projects can build on work carried out within the JOMOPANS project.

Finally, during the JOMOPANS project underwater noise measurement data will be collected throughout 2019 at the 14 measurement stations. These measurements form a valuable data set which can be shared with experts around the world.

6. ACKNOWLEDGEMENTS

The work reported here for project JOMOPANS is funded by the EU INTERREG programme.

REFERENCES

[1] **Directive 2008/56/EC**, Establishing a framework for community action in the field of marine environmental policy (Marine Strategy Framework Directive), Official Journal of the European Union, 2008.

[2] **ISO 18405:2017** Underwater acoustics - Terminology, International Organization for Standardization (ISO, Geneva, Switzerland), 2017.

[3] **Robinson, S.P., Lepper, P. A.** and **Hazelwood, R.A**. *GPG 133. Good Practice Guide for Underwater Noise Measurement*. National Measurement Office, Marine Scotland, The Crown Estate, NPL Good Practice Guide No. 133, ISSN: 1368-6550, 2014.

[4] **IEC 60050-801:1994** International Electrotechnical Vocabulary: Acoustics and electroacoustics (International Electrotechnical Commission, Geneva), 1994.

[5] **IEC 1260-1:2014.** Electroacoustics — Octave-band and fractional-octave-band filters, Part 1: Specifications, International Electrotechnical Commission, Geneva, 2014.

[6] **Morfey, 2001**. Dictionary of Acoustics. Morfey, C.L. Academic Press, ISBN 0-12-506940-5, 2001.

[7] **Merchant, N. D., Farcas, A., Powell, C. F**. *Acoustic metric specification*. Report of the EU INTERREG Joint Monitoring Programme for Ambient Noise North Sea (JOMOPANS), 2018.

[8] **Wang, L**. and **Robinson, S. P**. *Standard for terminology*. Report of the EU INTERREG Joint Monitoring Programme for Ambient Noise North Sea (JOMOPANS), 2018.

[9] **Robinson, S. P., Wang L, Crawford, N**. *Standard procedure for equipment performance, calibration and deployment*, Report of the EU INTERREG Joint Monitoring Programme for Ambient Noise North Sea (JOMOPANS), 2018.

[10] **Wang, L, Ward, J, Robinson, S. P**. *Standard for Data Processing of Measured Data*. Report of the EU INTERREG Joint Monitoring Programme for Ambient Noise North Sea (JOMOPANS), 2019.

LOW FREQUENCY HYDROPHONE CALIBRATION WITH A LASER INTERFEROMETER

Jacob Ward and Stephen Robinson

National Physical Laboratory, United Kingdom

Jacob Ward
t: +44 (0)208 943 6363
jake.ward@npl.co.uk

National Physical Laboratory, Hampton Rd, Teddington, Middlesex, TW11 0LW, United Kingdom

Abstract: *This paper describes experimental work that aims to provide a new method for primary pressure calibration of hydrophones in the frequency range from 20 Hz to 250 Hz. A measurement setup with a laser interferometer has been used to realise the acoustic pascal in an enclosed chamber. An optically flat piston is driven harmonically in a chamber containing both a fluid and a hydrophone to be tested. The absolute displacement of the piston is determined by fringe counting on a Michaelson interferometer. The thermodynamic properties of the fluid are used to calculate the absolute acoustic pressure that the hydrophone is exposed to from the volume change in the chamber. An advantage of such primary calibration is its traceability to primary standards of length via the wavelength of laser light. Some provisional hydrophone calibration results are shown and a discussion provided on potential sources of uncertainty. This method offers a possible primary standard for the low frequency range where regulation mandates the monitoring of absolute noise levels in the ocean, and where many sound sources of concern emit the most of their energy.*

Keywords: *acoustic calibration, hydrophone sensitivity, pistonphone, low frequency, one third octave bands, ocean noise*

AIM

The aim of this experimental work is to provide a new primary acoustic pressure calibration standard at low frequency for hydrophones. The motivation is to provide traceability for noise recordings with a focus on evaluating the marine environment, particularly the impact of low frequency anthropogenic noise as identified in the Marine Strategy Framework Directive (MSFD)[1]. The MSFD identifies 63 and 125 Hz bands as a means to capture annual trends in noise[2]. Primary calibration and traceability will therefore be an important aspect of marine noise measurement in the future and is pursued in this paper. This will be particularly important where comparisons of underwater noise are to be made over several years or even decades.

METHOD

A pistonphone is an acoustic calibration device that generates pressure by driving a circular piston into a closed volume of fluid. Knowledge of the thermodynamic properties of the fluid in the chamber can be used to relate a change in volume to a change in pressure. The laser pistonphone uses a Michaelson interferometer to measure the displacement of the piston. The laser pistonphone is one of a number of low frequency hydrophone calibration techniques identified in the International Electrotechnical Commission standard for hydrophones[3].

The National Physical Laboratory (NPL) has established a method for absolute calibration of hydrophones using a laser pistonphone. This method of hydrophone calibration can in principle be applied from a few hertz to several hundred hertz [4, 5]. In this pistonphone, the sound pressure is generated in a small closed air-filled chamber by driving a piston with a toneburst signal. The acoustic pressure p in the chamber can be calculated from:

$$p = \frac{\gamma p_s \Delta V}{V}$$

where V is the volume of the chamber, ΔV is the volume change caused by displacement of the piston, p_s is the static pressure and γ is the ratio of specific heats for the fluid. In this case the fluid used is air, at approximately room temperature.

ΔV is calculated from the surface area of the circular piston and by counting fringes on a Michaelson interferometer as a means to obtain piston displacement. The surface of the piston is made optically flat to reflect the laser light.

The piston is driven into the chamber with a ten-cycle toneburst. The static pressure is taken as one standard atmosphere (101.325 kPa), however, barometric pressure could potentially be used to obtain a more accurate result at the time of the measurement. Unlike coupler reciprocity, this primary calibration method has its traceability to the primary standards of length via the wavelength of laser light.

RESULTS

This section describes measurement results for the calibration of a small hydrophone. A comparison is made between the original manufacturer's calibration at a single frequency and the range of calibration frequencies achieved in the test. The centre-frequencies of tonebursts were set to the (base 10) one-third octave intervals in the range from 20 to 500 Hz. The piston

displacement was observed through a small glass window in the chamber. Fig. 1 shows the interferometer set up with the laser path annotated with the chamber removed. Fig. 2 shows the front face of the piston and Fig. 3 shows the chamber fitted to the baffle with a socket for the hydrophone.

The photodiode signal from the interferometer was captured concurrently with the hydrophone signal on the same oscilloscope. A high sampling rate was needed to sample sufficiently the high bandwidth of the photodiode signal, while a significant amount of oscilloscope memory was needed to capture the full duration of the low frequency tonebursts. The shaker has low impedance at approximately 1.5Ω at 20 Hz. This leads to a minimal drive voltage needed for the piston to cross many fringes. Fig. 4 shows the photodiode fringe signal with the drive signal in continuous-wave. The drive signal is within 400 mV peak to peak at 300 Hz, which here generates 43 fringes of displacement on the photodiode signal.

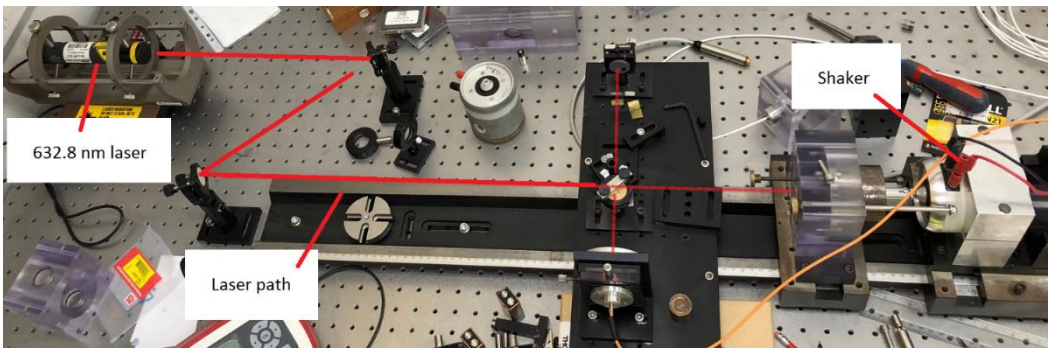


Fig. 1 Bench set up showing laser, laser path and shaker

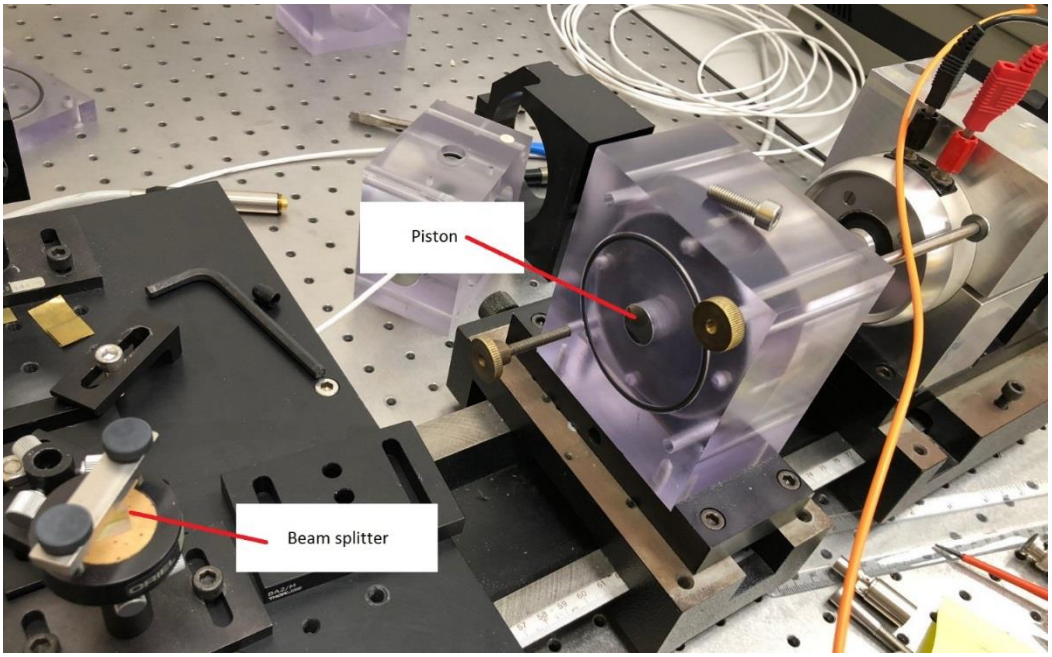


Fig. 2 Disassembled chamber showing front-face of the piston and beam splitter

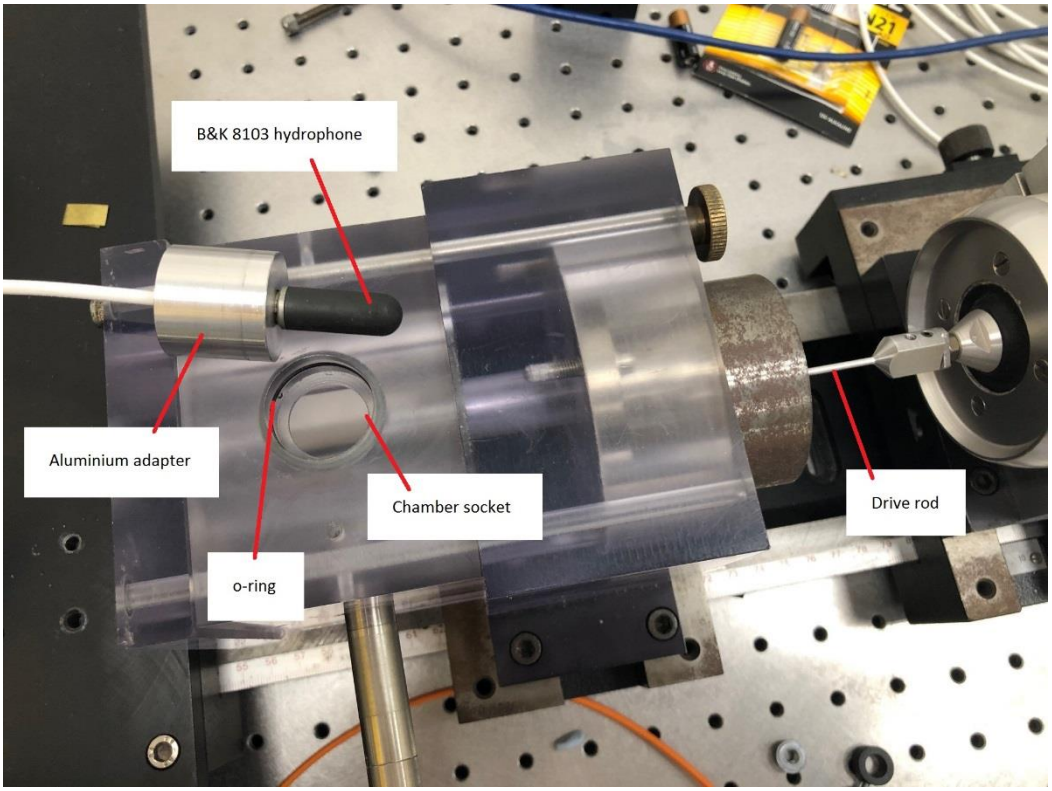


Fig. 3 Chamber showing hydrophone, fitting assembly and piston drive-rod

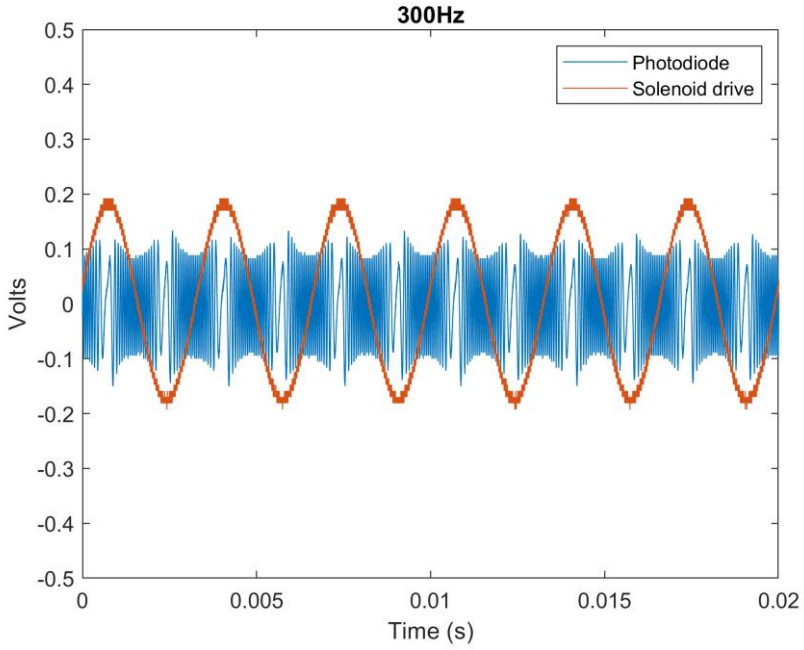


Fig. 4 Shaker drive voltage and interferometer signal in continuous-wave, showing the chirp-like nature of the photodiode signal

The hydrophone and photodiode signals are captured for a ten-cycle toneburst at 20 Hz. At low frequency the toneburst signal is replicated consistently on the hydrophone as seen in Fig. 5 and the photodiode registers many fringes. A spectrogram of the photodiode signal reveals the chirp-like nature of the signal in Fig. 6.

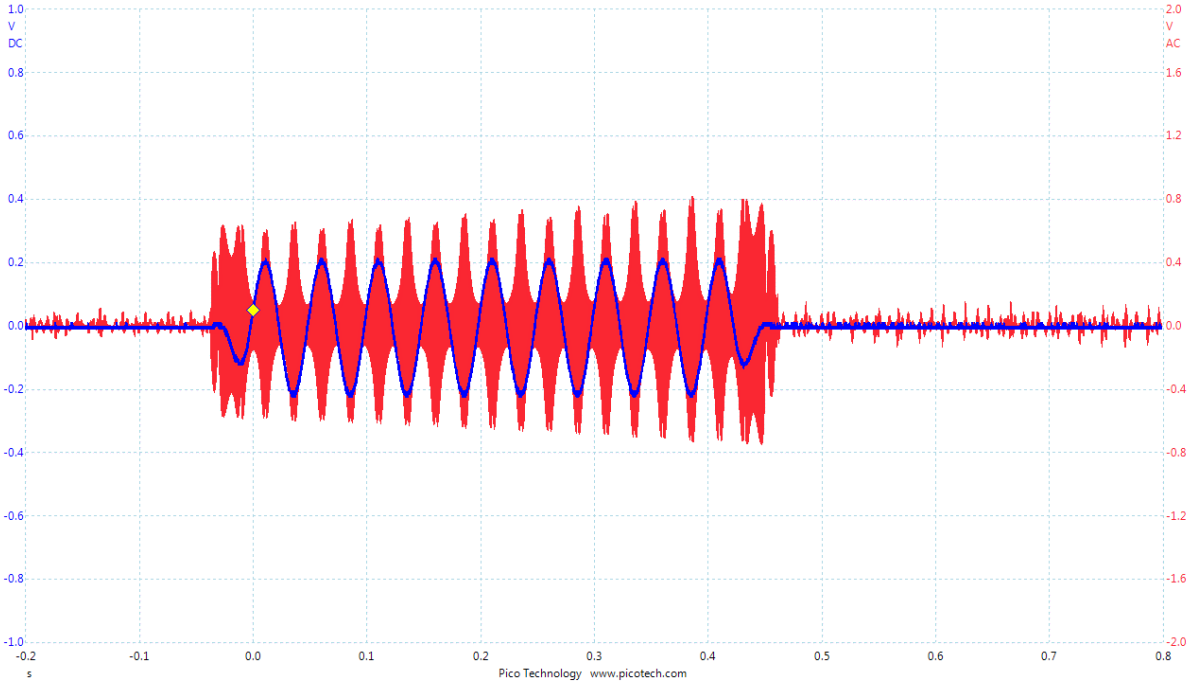


Fig. 5 Hydrophone (blue) and photodiode signal (red) for a ten-cycle 20 Hz drive signal

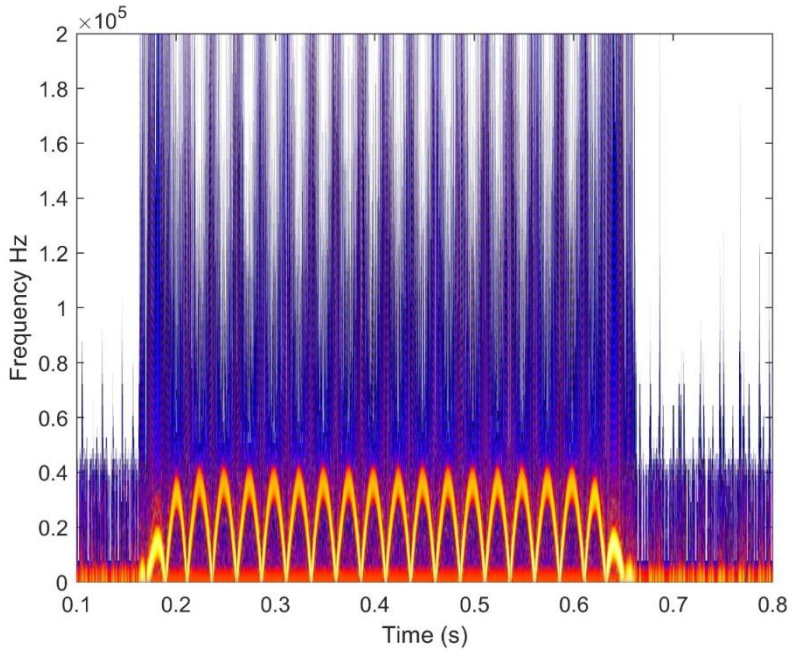


Fig. 6 Spectrogram of photodiode signal showing 40 kHz bandwidth required

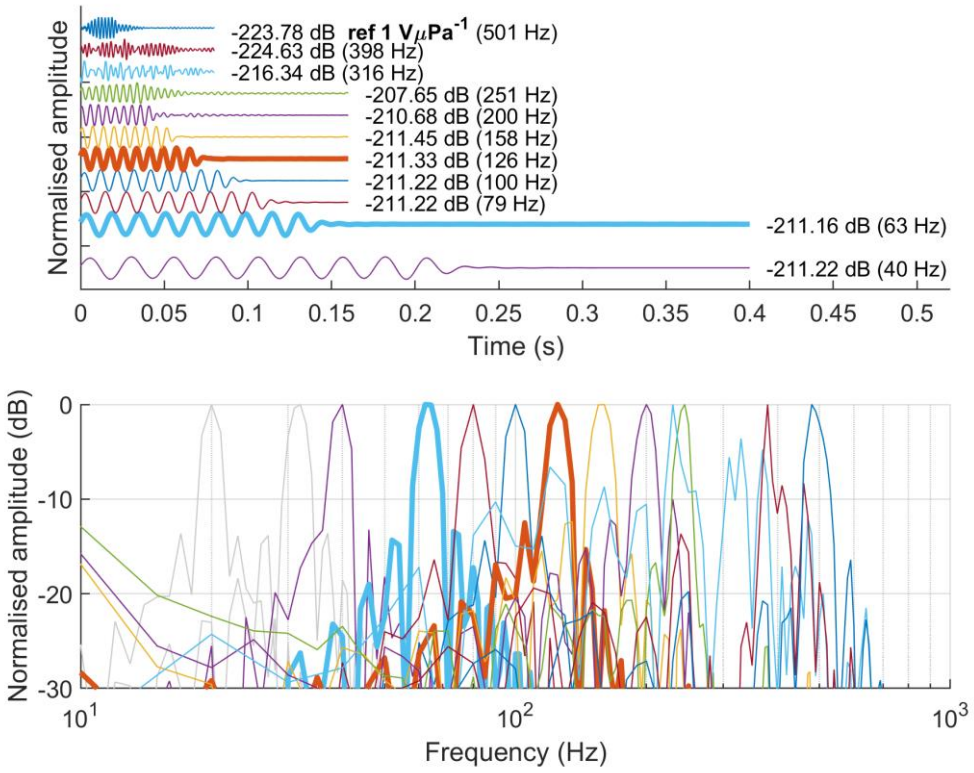


Fig. 7 Hydrophone signals and spectra. Principal MSFD frequencies shown in bold

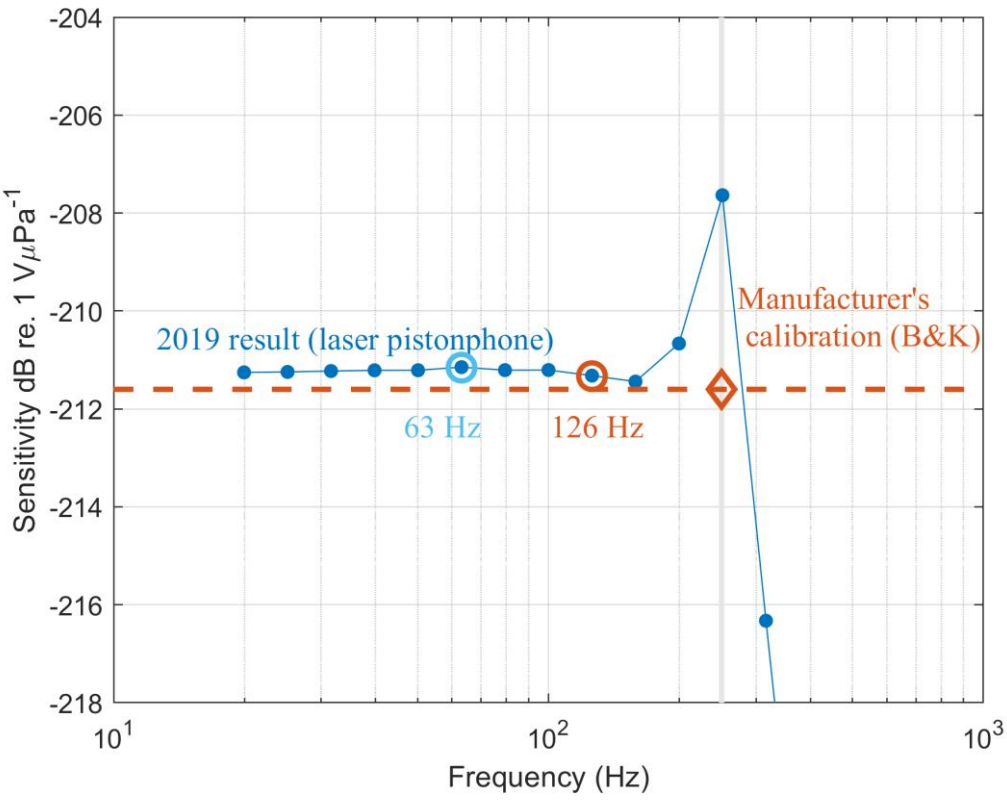


Fig. 8 Sensitivity compared with manufacturer's calibration at 250 Hz (type B&K 8103)

DISCUSSION

Fig. 7 (top) displays a sequence of hydrophone signals from tonebursts at different frequency. The corresponding hydrophone sensitivity is annotated on the graph in dB re. 1V/µPa. The pressure in the chamber is derived from both the laser interferometer and the open-circuit voltage signal on the hydrophone cable were used to calculate the sensitivity. As can be seen the toneburst is well replicated in the signals up to 158 Hz. The spectra for these time traces are given in Fig. 7 (bottom). Above 158 Hz the hydrophone measurement is affected by resonances in the chamber, the drive system and bench. The results are summarised in Fig. 8 and tabulated below. Table 1 indicates the reliable range of the measurement and highlights the 63 and 125 Hz frequencies in bold. These correspond to the bold lines in the signals and spectra plotted in Fig. 8. Opportunities identified to improve the measurement include updating the shaker to an actuator of higher blocking force and finding a means to adjust the volume of the chamber. Furthermore, an interferometer with sub-fringe resolution would be an advantage.

Frequency (Hz)	Sensitivity dB ref 1V/µPa
20.0	-211.3
25.1	-211.3
31.6	-211.2
39.8	-211.2
50.1	-211.2
63.1	**-211.2**
79.4	-211.2
100.0	-211.2
125.9	**-211.3**
158.5	-211.5
199.5	-210.7
251.2	-207.6
316.2	-216.3

Table 1 Measured hydrophone sensitivities with principal MSFD frequencies in **bold** and unreliable results in grey

SOURCES OF UNCERTAINTY

These laser pistonphone measurements rely on several physical measurements and assumptions. In these calculations it is assumed there is no heat conduction, that is to say that compression and rarefaction are adiabatic. It is also assumed that there is no leakage of air from the chamber around the piston. In practice both heat flow and air leakage would limit the lower bound in frequency. An approach to correcting for these effects can be found in detail in Barham and Goldsmith[4]. Contributors to uncertainty are listed below:

i. Atmospheric pressure (p_s)

ii. Ratio of specific heats (γ), taken as 1.4
iii. Diameter of the piston
iv. Optical wavelength
v. Integer fringe counting (and frequency)
vi. Photodiode signal to noise
vii. Hydrophone preamplifier gain
viii. Cavity volume (V)
ix. Distortion in the harmonic drive signal
x. Isothermal behaviour (heat flow in the chamber)
xi. Pressure leakage
xii. Vibration sensitivity
xiii. Voltage measurement uncertainty
xiv. Ambient temperature and humidity

CONCLUSION

The laser pistonphone is a valid and effective means for low frequency calibration of hydrophones. Through this work the technique has been adapted from an application of microphone calibration to hydrophones. The chamber used in these measurements has demonstrated the technique in the range from 20 to 158 Hz. This primary calibration technique is one suitable means to satisfy the requirement for traceability in the calibration of hydrophones and recorders used in monitoring annual trends in the 63 and 125 Hz bands, as identified in the MSFD Guidance[2].

ACKNOWLEDGEMENTS

The work described here was partly-funded by UNAC-LOW. UNAC-LOW is a EURAMET EMPIR project (project 15RPT02) aimed at an integrated, cost effective and internationally competitive measurement infrastructure for Europe. The work was also funded by the National Metrology Programme of the UK department of Business, Energy and Industrial Strategy.

REFERENCES

[1] **Directive 2008/56/EC**, Establishing a framework for community action in the field of marine environmental policy (Marine Strategy Framework Directive), Official Journal of the European Union, 2008.
[2] **Van der Graaf AJ, Ainslie MA, André M, Brensing K, Dalen J, Dekeling RPA, Robinson S, Tasker ML, Thomsen F, Werner S**, Guidance for 2012 reporting under the Marine Strategy Framework Directive, 5.3.3 Underwater Noise (8B03), 2012
[3] **IEC 60565-2006**, Underwater acoustics – Hydrophones – Calibration in the frequency range 0.01 Hz to 1 MHz, International Electrotechnical Commission, Geneva, Switzerland, 2006.
[4] **Barham, R.G and Goldsmith, M.J.**, The application of the NPL laser pistonphone to the international comparison of measurement microphones, Metrologia **44**, 210–6, 2007.
[5] **Wen He, Longbiao He, Fan Zhang, Zuochao Rong and Shushi Jia**, A dedicated pistonphone for absolute calibration of infrasound sensors at very low frequencies, Meas. Sci. Technol. **27**, 025018 (11pp), 2016.

METHOD FOR LF CALIBRATION IN CONFINED MEASUREMENT TANK

Per Abrahamsson, Óskar Ásgeirsson, Victor Borén, Bo Lövgren

Saab Dynamics, SE-581 88 Linköping, Sweden

Per Abrahamsson
Saab Dynamics
SE-581 88 Linköping, Sweden
Phone: +46 13 18 35 83
E-mail: per.abrahamsson@saabgroup.com

Abstract: Calibration of hydrophones and transducers is essential for measurements in the underwater domain. When measuring low frequency, below 4 kHz, transducers and hydrophones in a confined test tank problems occur due to the long wavelength. These problems occur mainly due to the multi-path that occurs in the tank. One way to eliminate this problem is to do the measurements in free-water where the risk of multi-path is reduced. However, a free-water measurement have other drawbacks that can be eliminated in controlled test environments such as a tank. In order to do the measurements in the controlled environment of a tank the impact of the tank has to be eliminated. In this paper a previously presented method is used together with some adaptations. The method is based on that the one can see the tank as a transfer function between the transducer and the hydrophone. If the transfer function can be estimated then the impact of the tank can be eliminated. To verify the method both free-water and tank measurements where performed. To be able to estimate suitable positions for both the transmitter and hydrophone a numerical wave propagation model was used. The result from the model was validated with a series of measurements to estimate the methods robustness against positioning errors.

Keywords: *Test-tank, Low frequency, Calibration, Measurement*

PROBLEM DESCRIPTION

To have calibrated and characterised equipment is an essential matter in the underwater domain. To get good measurements one should try to eliminate all external impacts on the measurement. For low frequency systems, in this paper low frequency is assumed to be frequencies below 8 kHz, this can be costly or difficult. This is due to the large wavelength of the system.

A measurement is performed either in a controlled environment of a test tank or from a ship. Ship measurements can be costly and the result can be degraded by unknown external factors. In tank measurements the test environments is known and may be controlled. However, test tanks often have a limited size, which can have a negative effect on the result for low frequencies.

The method tested in this paper is that the effect of the test tank is considered as a transfer function of the acoustic signal [1]. If the transfer function for a test object is known, a similar object can then be measured in the test tank.

METHOD

The method used to calculate the transmission sensitivity is based on

$$SL_i = L_{HT} - S_H + 20\log_{10}(R_i), \tag{1}$$

where SL_i is the source level, L_{HT} is the measured output from the receive hydrophone, S_H is the hydrophone sensitivity and R_i is the distance between the two objects. All terms except R_i are frequency dependent [1], [2].

Measurements are done both in a sea measurement and in the confined space of the test tank. The results SL_1 and SL_2 are then used to calculate the transfer function of the test tank, F:

$$F = SL_1 - SL_2. \tag{2}$$

The source level of a similar test object can then be calculated with:

$$SL = SL_{Measured} + F. \tag{3}$$

There are a number of error sources in this method:

- Time dependent path fluctuations in the sea measurement caused by altering wave patterns at the surface.
- Null-anomaly in the sea measurement caused by interference patterns.
- Position errors in the test tank. Due to the multi-path propagation in the test tank there is a complex interference pattern in the tank, which results in a high sensitivity for position errors in the method.
- Position errors in the sea measurement.

During the validation of the method, care where taken to reduce the external factors that can be observed in sea measurements.

NUMERICAL MODEL

In an attempt to eliminate the need for a sea measurement a numerical wave propagation model for the test tank environment was developed using a MATLAB toolbox [2]. The toolbox uses an optimized implicit method to solve the wave equation and uses a perfectly matched layer (PML) which absorbs the energy when it reaches the boundary of the computational domain. Waves in a heterogeneous medium where modelled using:

$$\frac{\partial \boldsymbol{u}}{\partial t} = -\frac{1}{\rho}\nabla p + \boldsymbol{S_F}, \tag{4}$$

$$\frac{\partial \rho}{\partial t} = -\rho_0 \nabla \cdot \boldsymbol{u} + S_M, \tag{5}$$

$$p = c_0^2 \rho. \tag{6}$$

Here $\boldsymbol{S_F}$ is the body force input to the system, N/kg or m/s^2. S_M is a mass source term and indicates how much mass per unit volume per second, kg/(m^{3}s), that is added to the system.

The PML is a thin absorbing layer, at the boundary of the domain, which uses a set of nonphysical equations to cause anisotropic absorption. The layer provides sufficient attenuation to prevent waves from being reflected back into the medium. The toolbox uses the Bergener's split-field formulation of the PML.

The source used in the simulation is a cylinder shaped transducer matching the physical test object. The transducer was set to produce an omni-directional sinus signal.

The computational grid was divided into two mediums, water and air. The set-up was so that the air was positioned around the water volume. Due to the large difference in acoustic impedance between the mediums causes only a small amount if the acoustic energy is transferred into the PML.

The mesh for the calculation were chosen as

$$f_s = \frac{c}{max(\Delta x, \Delta y, \Delta z)} \geq 2f, \tag{7}$$

where f is the frequency of interest. A too coarse mesh will result in an inaccurate result [3]. Since the frequency of interest for the conducted trials was between 1 and 4 kHz a mesh size of 0.05 m was chosen.

To get a stable solution a suitable time step has to be chosen. The Courant-Friedrichs-Lewy stability criterion was used to get an appropriate time step. The criteria states that the solution should travel faster than the wave propagation. This can be checked with

$$0 \leq \frac{c\Delta t}{min(\Delta x, \Delta y, \Delta z)} \leq CFL_{max}, \tag{8}$$

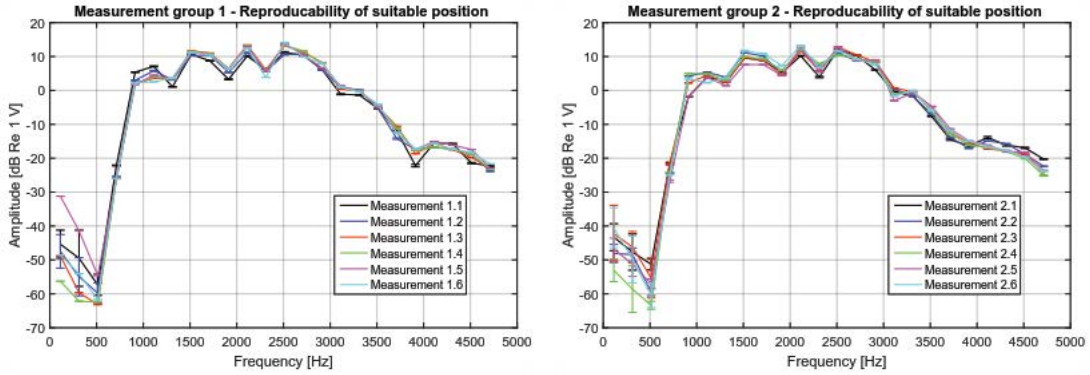
where CFL_{max} is the Courant number. To ensure stability the Courant number should be less than 0.5 for a three dimensional solution [4].

Applying the criteria in the experiment to equation (8) gives a Δt of 1.67 µs. These results now gives the set-up that enables the comparison between the numerical method and the measurements.

RESULT

To test the theory and the numerical method several measurements where done including sea measurements. The purpose of the measurements was to validate method and explore the stability of it.

To ensure the stability and repeatability of the method several measurements were done in the tank at different times, see Fig 1. The data shows that the method is repeatable and stable.



(a) Measurement group 1 (b) Measurement group 2

Fig. 1: Results from measurements performed at the chosen suitable location. Group 1 and 2 are measurements performed at different times.

A sensitivity comparison was also made for the positioning of the test object. The comparison was done in two steps. In the first step different positions in the test tank were used for the transmitter and receiver. Each measurement was repeated multiple times to test the sensitivity for that position. The trials showed that there was a difference in the repeatability between different positions. In the second step the most consistent position from step 1 was chosen and small variations in the position were made to see how this affected the result. Relatively large measurement differences, up to 5 dB rel. 1 V, were measured even with small changes.

Using the position from step 1 measurements were done to collect data and compare it to the sea measurements, see Fig 2. To enable comparison all data is normalized according to

$$SL_{Norm} = L_{HT} - S_H + 20\log_{10}(R) - SL_{Comp}, \tag{9}$$

where SL_{comp} is a factor that compensates for different level settings at sea and in the tank. The most obvious difference between the sea and tank measurements are the peaks at 1.6 kHz, 2.1 kHz and 2.5 kHz. These peaks come from the positioning in the test tank and move in frequency with the tested position which was observed in step 1 above.

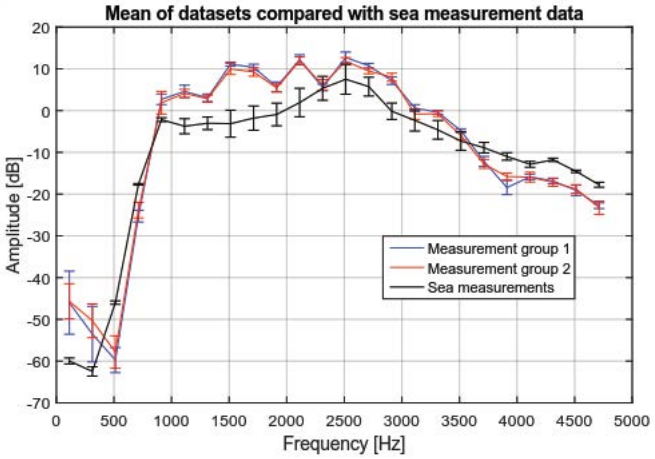


Fig. 2: Results from group 1 and 2 compared with sea measurement, normalized according to (9). [dB rel. 1 V]

A transfer function for the test tank could then be calculated from the data, see Fig. 3. This function could then be used to measure similar test objects.

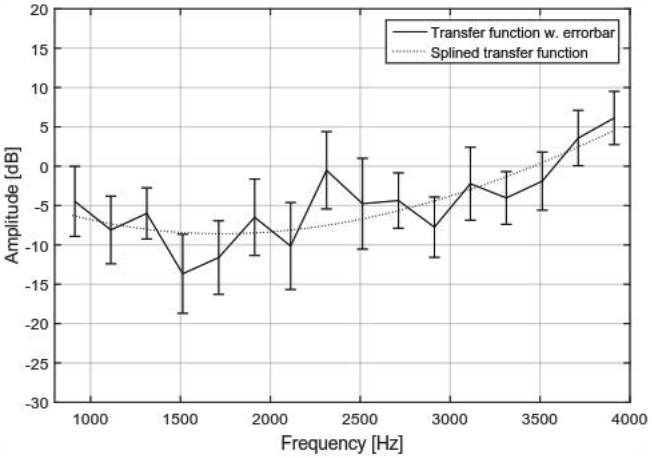


Fig. 3: Calculated transfer function. [dB rel. 1 V]

A transfer function was also calculated from the numerical method. The transfer functions are compared in Fig 4. As one can see, there are differences in the functions. Some causes of this that have been observed is the simplified model of the tank and that the numerical model only is a 2D model.

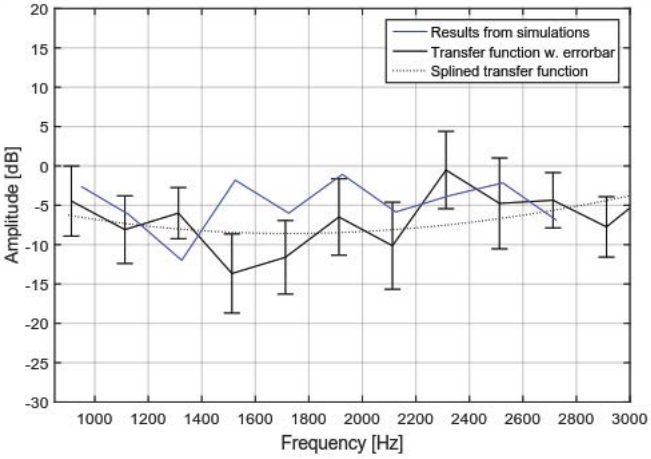


Fig. 4: Comparison between real results and the numerical method. [dB rel. 1 V]

DISCUSSION

The experiment shows that it is possible to use this method to measure the acoustic properties in a confined tank even for lower frequencies. However, the method requires care when choosing the placement of the test object and the measurement system. When using the method for a new object the placement of the object in the test tank has to be re-examined to get good quality in the measurement, see the sensitivity measurement above.

Due to the complex environment in the tank more consideration has to be taken to the geometry in the model to get to a level where the sea measurement can be excluded. The numeric calculation method must be enhanced with higher dimensions and a more detailed environment, especially mounting devices and tank structure, for it to replace the sea measurement.

Further work with other shape and frequencies equipment to further validate the method should be performed.

REFERENCES

[1] **Bo Lövgren**, Low Frequency Tank Calibration by Comparison. Presented at the inter.noise conference in Hamburg 2016

[2] **B. E. Treeby and B. T. Cox**, k-Wave: MATLAB toolbox for the simulation and re-construction of photoacoustic wave-fields. J. Biomed. Opt., vol. 15, no. 2, p. 021314,2010

[3] **National Instruments. Aliasing**, Accessed: 2017-03-07 from: http://zone.ni.com/reference/en-XX/help/370051V-01/cvi/libref/analysisconcepts/aliasing/

[4] **Peter J. Oliver**, Introduction to Partial Differential Equations. Springer, 2014. isbn: 9783319020893

NEAR-FIELD PARTICLE VELOCITY MEASUREMENT OF THE HIGH FREQUENCY PROJECTORS USING LASER VIBROMETRY METHOD

Shiquan Wang[a], Weiyin Wang[b], Yi Chen[c]

[a] Hangzhou Applied Acoustics Research Institute, Hangzhou, China,311400
[b] Hangzhou Applied Acoustics Research Institute, Hangzhou, China,311400
[c] Hangzhou Applied Acoustics Research Institute, Hangzhou, China,311400

Shiquan Wang, No.82, Guihuaxi Road, Fuyang District, Hangzhou, China, 311400

Abstract: *The near-field acoustic fields of a high frequency projector were investigated using the laser vibrometry method. An automatic scanning measurement system based on optical method was setup and introduced. The acoustic fields of the projectors were measured at the plane close to surface using a commercial laser vibrometer. The amplitude and phase distributions of particle velocity in the measurement plane were obtained. As a comparison, the acoustic pressure fields were also measured with a needle hydrophone at the same plane away from the surface of the projectors. The far-field directivities were then calculated with the near-field particle velocity data based on Rayleigh integrals (RI). The measured far-field directivities were compared to the calculated results. It showed that they were in good agreements. It is an effective way to measure the near-field particle velocity distributions and also a practical method to predict the far-field directivities of the projectors with the combination of the RI.*

Keywords: *Near-field measurement; particle velocity; laser vibrometry; far-field*

1. INTRODUCTION

The parameters of ultrasonic transducers, such as transmitting voltage response and directivity patterns were traditionally measured in the far field of the transducer. It became very difficult to perform the far-field measurement procedures for high frequency projectors with large aperture. The near-field measurement method was applied in the water tank with limited dimensions. A hydrophone or hydrophone array was usually used to measure the sound pressure in the near-field region of the projector. With scanning the hydrophone or array, the distribution of complex sound pressure of the projector can be mapped. The complex sound pressure data then were used to evaluate the far-field parameters and the elements vibration status of the projector.

There was a limitation for spatial resolution when using a hydrophone or array because of the finite sensitive elements size. The diffraction effects of a hydrophone or array might interfere with the sound field and then restricted the application of hydrophones especially for high frequency measurements. The quantity measured by a hydrophone was sound pressure. In order to obtain the particle velocity in the acoustic field, the differential of the complex pressure was required [1].

The optical method has been applied in the fields of underwater acoustic measurement since 1980s. With the development of optical techniques, many researchers have studied the measurement of underwater sound using optical methods. Higgins etc. [2] measured the amplitude and phase of ultrasonic transducers and reconstructed the sound field with angular spectrum method and subtraction to reference field method. NPL Robinson etc. [3] measured the sound field distributions of a 500 kHz transducer array using the optical reflective tomography method. HARRI Wang etc. [4,5] carried out an experiment to reconstruct the sound field of an ultrasonic transducer and evaluated the operating status of the array elements. As the laser beam can be focused into micro meter size, it has the advantages of high spatial resolution and no disturbance to the sound field. Furthermore, the measured quantity by the optical interferometry was the particle velocity or displacement, which can be directly used into Rayleigh integral formula and reconstruct the sound field. The optical method has great superiority to hydrophone in the measurement of sound field.

This paper introduced an automatic measurement system for underwater sound fields. The near field experiment was carried out to map the sound field of a high frequency projector. The amplitude and phase distributions of particle velocity were obtained using optical method in sound field. As a comparison, the amplitude and phase distributions of sound pressure were also measured with hydrophone scanning method. The far-field directivity patterns were calculated using RI with the particle velocity data measured in the near-field region. The calculated results were compared to the measured far-field directivity pattern.

2. MEASUREMENT PRINCIPLE AND SYSTEM SETUP

2.1. Measurement principle

A laser Doppler vibrometer is usually used to measure the velocity or displacement of a vibrating object in air. When it is used to measure the distribution of particle velocity in water, the scheme is shown in Fig.1. The projector is eradiating sound waves to the medium. A sound transparent reflective pellicle parallel to the surface of the projector is placed close to the projector. The pellicle vibrates in phase with the surrounding medium. The laser beam travels through the optical window and water to the pellicle where it is reflected to the optical

head of the vibrometer and the particle velocity is measured. With the laser and pellicle being fixed, the distribution of particle velocity can be measured by scanning the projector with the two-dimensional motion systems.

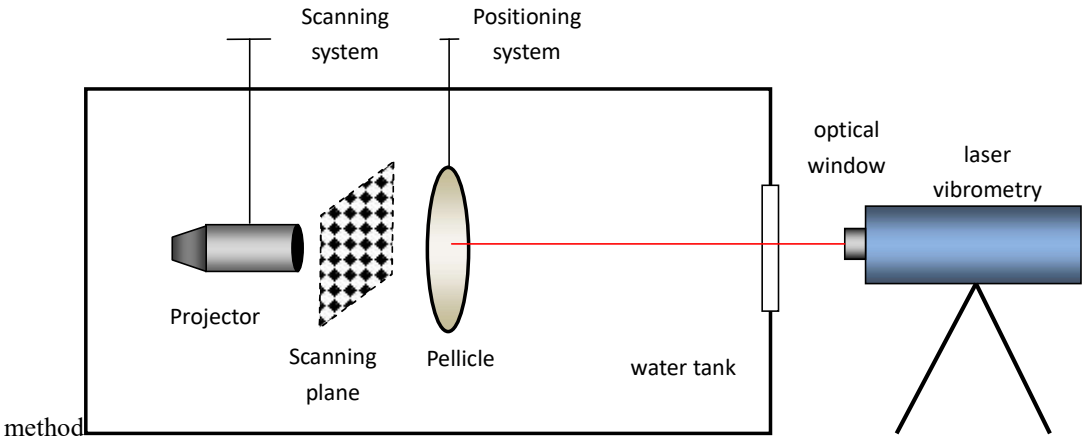


Fig.1 Scheme of measuring the distribution of particle velocity using optical method

The sound pressure at specified point P in the field can be calculated using the Rayleigh Integral when the particle velocity is known, as is shown in the coordinate system in Fig.2.

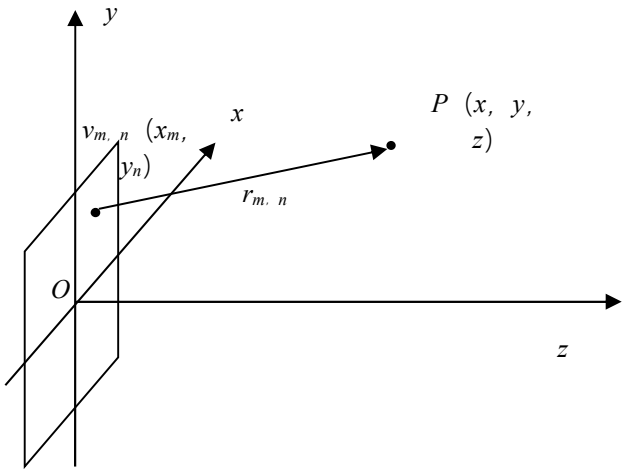


Fig.2. Calculation of far-field sound pressure using the measurement data

$$p(x,y,z)=\frac{j\rho ck}{2\pi}\sum_{m=1}^{M}\sum_{n=1}^{N}v_{m,n}\frac{e^{-jkr_{m,n}}}{r_{m,n}}\Delta x\Delta y \qquad (1)$$

where, $v_{m,n}$ is the particle velocity at the point (x_m, y_n) and m=1,2,⋯M; n=1, 2, ⋯N. M and N denotes the row and column t number. The distance from point (x_m, y_n) to point (x, y) is expressed in equation (2).

$$r_{m,n}=\sqrt{(x_m-x)^2+(y_n-y)^2+z^2} \qquad (2)$$

Where, $r_{m,n}$ is the distance from the point in the measurement plane to the point P. ρ is the density of the water, c is the sound speed and k is wave-number. Δx and Δy are the intervals in x and y direction in the measurement plane.

2.2. Measurement system

An automatic measurement system based on optical method was set up. The schematic diagram of the measurement system was shown in Fig.3.

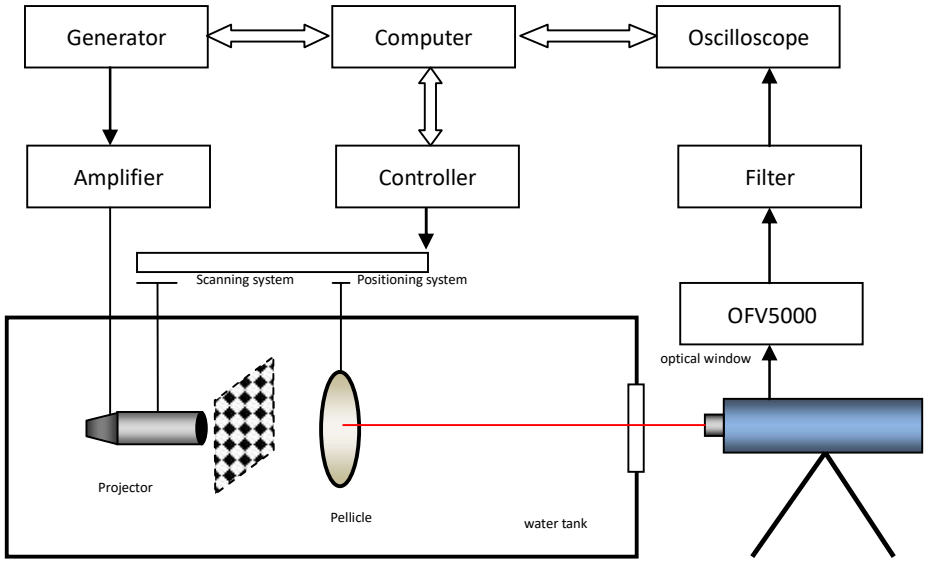


Fig.3. Schematic diagram of the sound field measurement system

The measurement system was composed of a generator, a power amplifier, a laser vibrometer, a filter, a digital oscilloscope, a set of motion systems, a water tank and a computer. The generator was Keysight 33612A and the amplifier was E&I 2200L. The laser vibrometer was OFV-505/5000 from the Polytec company. The projector was mounted to the positioning system and driven by the power amplifier to radiate sound to the medium. The pellicle was parallel to the surface of the projector and positioned in the acoustic field. The projector was scanned in a set plane with the positioning device driven by step motors. The laser beam was incident to the pellicle and the output of the laser vibrometer was conditioned by the filter and output to the digital oscilloscope. The computer was programmed to control the generator, the oscilloscope and the motion system. The measurement data was acquired and stored automatically.

3. MEASUREMENT AND CALCULATION RESULTS

The sound fields of a projector with a diameter of 25mm and a center frequency 500 kHz were mapped using the measurement systems. The distance from the measurement plane to the surface of the projector was about 5cm. The measurement plane covered the range of 40mm*40mm with the space interval of 1mm. The measured distributions of particle velocity at 500 kHz and 600 kHz were shown in Fig.4. and Fig.5.

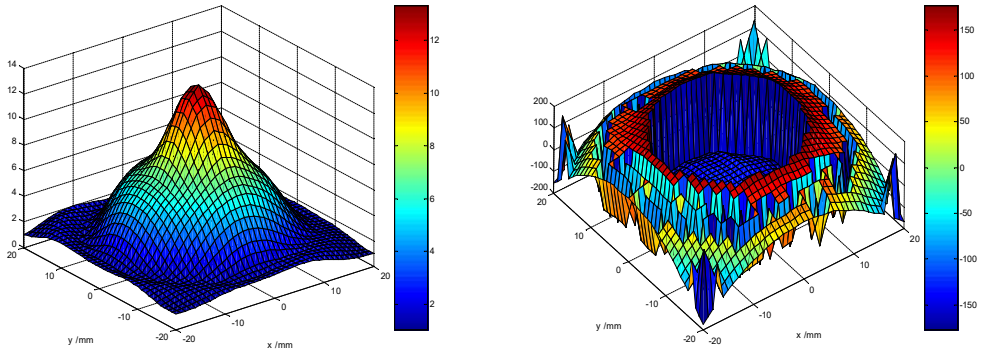


Fig.4 Amplitude and phase distributions of particle velocity at 500 kHz

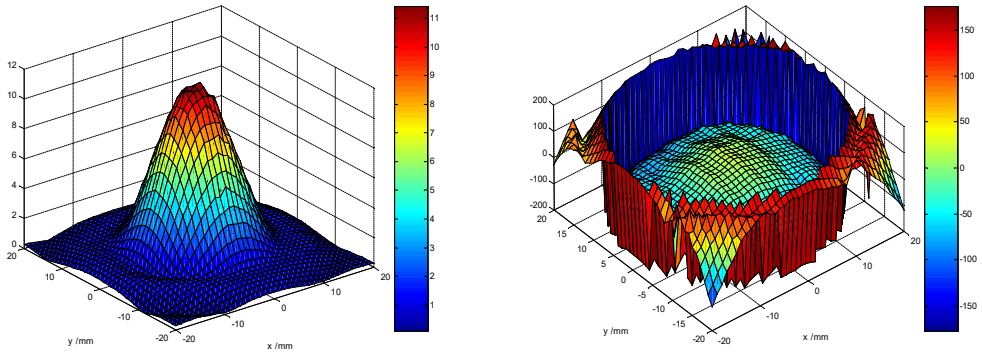


Fig.5. Amplitude and phase distributions of particle velocity at 600 kHz

For comparison, the sound pressure fields were measured using a needle hydrophone at the same measurement plane. The measurement results were shown in Fig.6. and Fig.7.

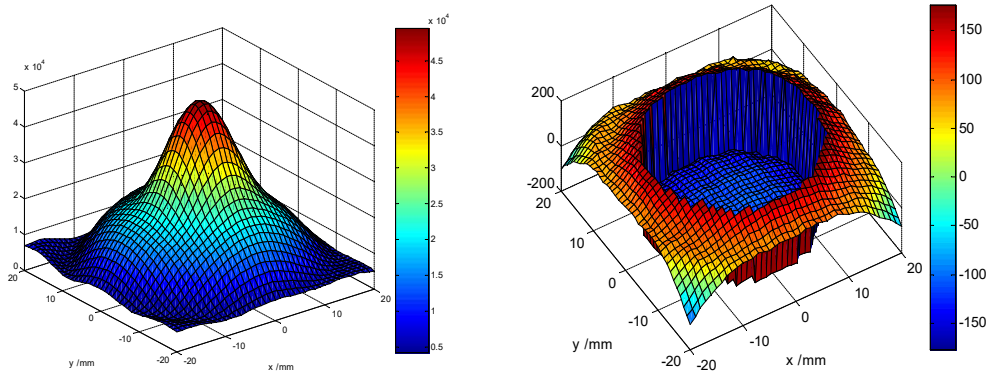


Fig.6 Amplitude and phase distributions of sound pressure at 500 kHz

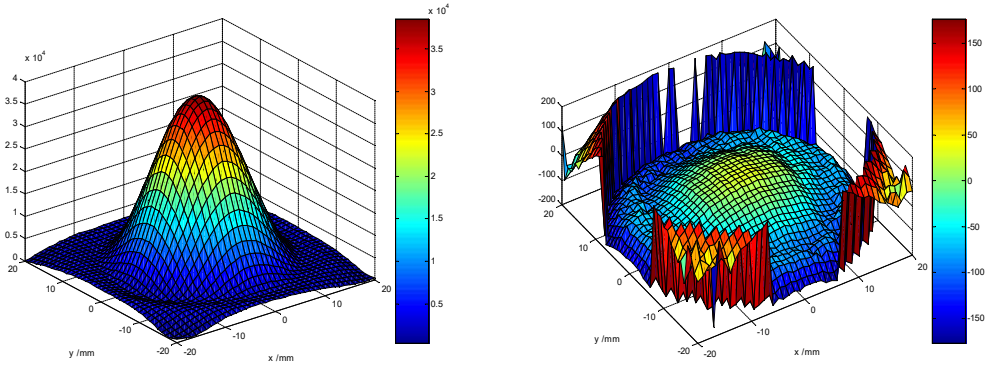


Fig.7 Amplitude and phase distributions of sound pressure at 600 kHz

The measured particle velocity was used to calculate the far-field directivities of the projector according to equation (1) and equation (2). The calculated directivity patterns then were compared with that measured in acoustic far-field as shown in Fig.8 and Fig.9.

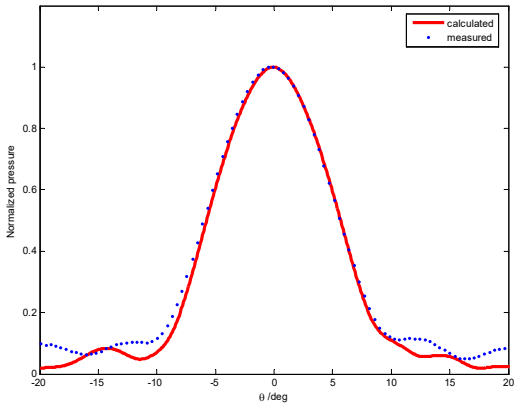


Fig.8 comparison of calculated and measured directivity patterns at 500 kHz

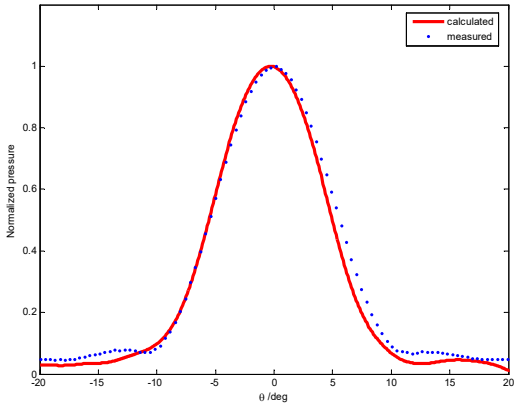


Fig.9 comparison of calculated and measured directivity patterns at 600 kHz

As were shown in Fig.8 and Fig.9., the directivity patterns calculated with the measured near-field particle velocity results were in good agreement with that measured in far-field. The maximal relative discrepancy of the -3dB beam width was not greater than 3%.

f (kHz)	calculated -3dB beam width (°)	measured -3dB beam width (°)	difference %
500	8.3	8.4	1.2
600	7.7	7.9	2.5

Table 1: Comparison of calculated and measured -3dB beam width

4. CONCLUSIONS

An automatic acoustic field measurement system was setup based on a commercial laser vibrometer. The distributions of particle velocity of high frequency projectors were mapped in the near-field region using optical method. The results were verified with the results of

hydrophone scanning method. Furthermore, the far-field directivity patterns were calculated with the particle velocity which can be directly used by RI. The comparisons of calculated and measured far-field directivity patterns showed very good agreement. It indicated that it was an effective way to measure the particle velocity field of a high frequency projector using laser vibrometry method. It could accurately predict the far-field parameters of high frequency projectors combined with RI.

5. ACKNOWLEDGEMENTS

This work was funded by National Key Research and Development Program of China （Grant No.2016YFF0200900）.

REFERENCES

[1] **Wang S Q**, Far-field performance prediction of high frequency projectors using secondary source array method, *Journal of Computational acoustics*, 25(2), 2017.

[2] **Higgins F P**, **Norton S J**, **Linzer M**. Optical interferometric visualization and computerized reconstruction of ultrasonic fields. *Journal of the Acoustical Society of America*, 68(4):1169-1176,1980.

[3] **Robinson S P**, **Theobald P D**, **Hayman G**, The use of optical techniques to map the acoustic field produced by high frequency sonar transducers. *Proceedings of the institute of Acoustics*, 28:726-734, 2006.

[4] **Wang S Q**, **Wang Y B**, The Application of Optical Interferometry in the Near-field Acoustic Holography Measurement of Ultrasonic Transducers, *ISAET2010*,2010.

[5] **Wang Y B**, **Wang S Q**, The application of laser reflective tomography in near-filed measurements of ultrasonic transducers, Chinese Journal of Acoustics, 33(3):257-266,2014.

PLANE/CYLINDRICAL WAVE SYNTHESIS IN A SMALL TANK APPLIED TO FAR-FIELD BEAM PATTERN MEASUREMENT OF A 300KHZ SONAR TRANSDUCER

Luigi Troiano

STO –CMRE ,Viale San Bartolomeo, 400, 19126 La Spezia (SP), Italy
Tel. : +39 0187 527 1
Fax: +39 0187 527 700
Email: luigi.troiano@cmre.nato.int

Abstract: *It is highly desirable to infer far-field behaviour of a radio antenna or SONAR transducer, from near-field measurements. This approach allows the measurements to be made in a small tank (or anechoic chamber), under controlled conditions at a fraction of the cost of the equivalent free-field procedure. One of the techniques available is to generate a plane wave in order to create far-field conditions at the transducer under test (TUT). The equipment required is often referred to as a Plane Wave Converter in the field of radio communications, or the Trott Array in underwater acoustics. In essence, the plane wave is synthesised by a 2-D array of point sources which, acting together, generate a plane wave according to the Huygens Wavelet principle. The 2-D array can be reduced to a line-array for a TUT with large aspect ratio, in which case a cylindrical wave is generated. A common criterion in the design of the array is that the Huygens element spacing should be less than four fifths of the wavelength. Applying this principle to the beam pattern measurement of the of a 300kHz SONAR transducer of length 108 wavelengths, would require an array at least 135 Huygens elements wide, in order to generate a uniform wave of the same dimensions. This would clearly require a significant investment, and is the reason that this method is usually applied at lower frequencies. An alternative implementation that is studied in this article, is to scan a single Huygens element mechanically. This allows the array to be composed of any number of elements. The spherical wavelets thus generated, when summed at the receiver, are equivalent to simultaneous transmission with multiple sources, and therefore indistinguishable from a plane (or cylindrical) wave. The transducer tested has a far-field distance of 58m, but the measurements presented were taken at only 67cm from the transducer (well in the near-field). The resulting horizontal beam pattern compares favourably with the calculated far-field pattern for a rectangular aperture.*

Keywords: *Plane wave, Cylindrical wave, Near-field, Beam pattern, Antenna, Transducer, Acoustic measurement, Superposition, Huygens*

1. INTRODUCTION

Ideally, measurement of transducer radiation patterns is carried out in the far-field. This is the region where spherical spreading occurs, with pressure falling off as the reciprocal of range and the beam pattern becoming independent of range from the transducer. A conservative estimate of the far-field distance is given by [1]:

$$r \geq L^2/\lambda \quad (1)$$

Where r is the far-field distance, L is the length of the transducer and λ is the wavelength.

The transducer under test (TUT) characterised in this article has a horizontal aperture of 108λ at 300kHz, which results in a far-field distance of approximately 58m. Even if such a facility were available, successful practical implementation would rely on a high degree of stability between transmitter and receiver due to the highly directional beam patterns which are a consequence of multi-wavelength apertures.

Alternative, near-field measurement techniques fall largely into two categories; the Helmholtz-Kirchhoff integral (DRL) and the Plane Wave Generation (PWG) methods [2].

In the PWG case, a plane wave is generated by an array of point sources, according to the classical Huygens wavelet concept. The plane wavefront, incident on the transducer to be tested allows measurement of the receivers' far-field characteristics. In the field of underwater acoustics these planar near-field calibration arrays are often referred to Trott arrays after their inventor [3]. Equivalent systems in the field of radio communications are referred to as plane wave converters (PWC) and are available commercially [4].

The generated wavefront can be represented by a summation of point sources (figure 1):

$$p(x_m, y_m, z_m) = \sum_{n=1}^{N} a_n \exp(-i\phi_n) \exp(-ikR_{mn})/R_{mn} \quad (2)$$

Where: $p(x_m, y_m, z_m)$ is the pressure at field point x_m, y_m, z_m , at range R_{mn} due to N point sources arranged on a plane, a_n and ϕ_n are the amplitude and phase weightings of the n^{th} source and k is the wavenumber (the time dependence term $\exp(i\omega t)$ has been omitted).

Ideally, the spacing of the point sources should be no greater than $0.8\,\lambda$ [2] in order to generate a uniform plane wave. This criterion can be difficult to achieve at short wavelengths, due to the expense and complexity that a large planar array with densely packed grid of sensors would imply. Furthermore, closely spaced elements ($<\lambda$) are more likely to suffer mutual coupling [1] thereby invalidating the isotropic point source approximation. For these reasons, the problem of how to optimise a_n and ϕ_n to provide an acceptable plane wave, over a specified volume for a minimum number of elements (N) has received much attention in the literature (for example [5]).

Scanning the point source mechanically obviates many of these issues, allowing parameterisation of the geometry of the planar array of point sources. Each position produces a series of spherical waves, which by the principle of superposition can be summed offline to produce the virtual plane wave.

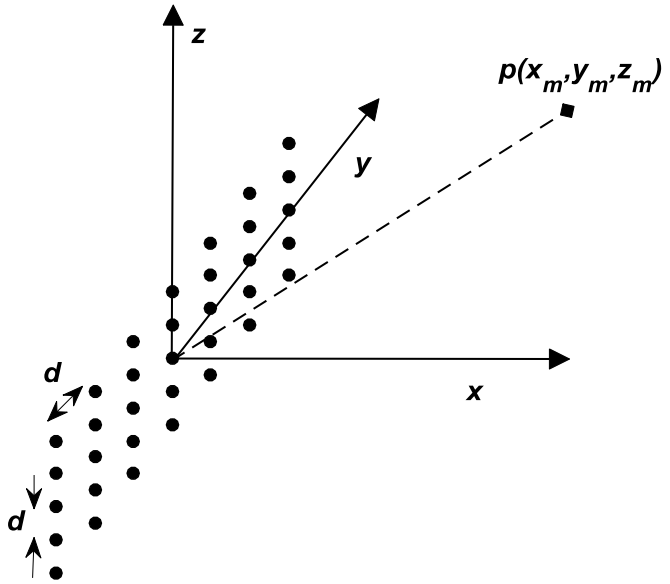


Fig.1: Geometry of the simulated plane wave showing N point sources spaced at d, arranged in a 2-dimensional grid

2. PLANE WAVE GENERATION METHOD APPLIED TO THE TRANSDUCER UNDER TEST

The TUT is a rectangular 300kHz SONAR receiver consisting of 16 elements with overall dimensions of 50mm x 533mm (approximately 10λ x 108λ). Ideally, in order to recreate far-field conditions, the face of the transducer should be insonfied by a uniform plane wave. Numerical evaluation of equation 2 at 300kHz using N = 51000 (340 columns x 150 rows), spacing d=2mm, at a range of 0.65m, Tukey amplitude shading and no phase shading is shown in figure 2. The predicted variation of sound pressure over the face of the transducer is ±0.5dB.

However, application of equation (1) to the relatively small vertical dimension of the TUT suggests that PWG can be replaced by a cylindrical wave generator (CWG), since the curvature of the field in the vertical direction will have no effect on the response of the TUT. This increases the speed of the measurement considerably since the plane array of point sources can be replaced by a line array.

3. SOUND FIELD PREDICTION

A plot of equation (2) for a single line of 340 point sources spaced at 2mm with no phase shading, with and without amplitude (a_n) shading is plotted in figure 3. The spacing used in the calculation (less that that required by 0.8 λ criterion) was chosen to extend the measurement range beyond 300kHz.

Choice of suitable amplitude shading window was based on uniformity of the generated field (in amplitude and phase) and also the scanned length required in order to insonify the TUT over

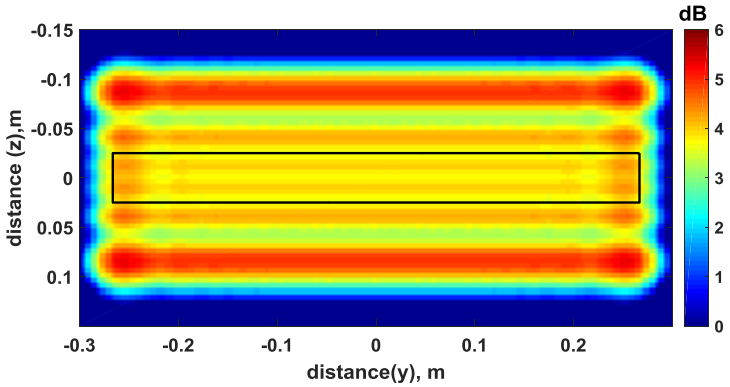


Fig.2: Vertical slice representing the predicted relative SPL at a range of 0.65m from the 2-D array of point sources. The rectangle indicates the outline of the TUT

its entire length. The 2dB variation between 500mm and 800mm range from the CWG is due to cylindrical spreading. Suitability of the Tukey shading was further assessed by calculating amplitude ratio and phase difference of the predicted field to that of an ideal plane wave (figure 4). Variation in amplitude along the line representing the TUT position is <1dB, whereas phase variation is approximately ± 2°.

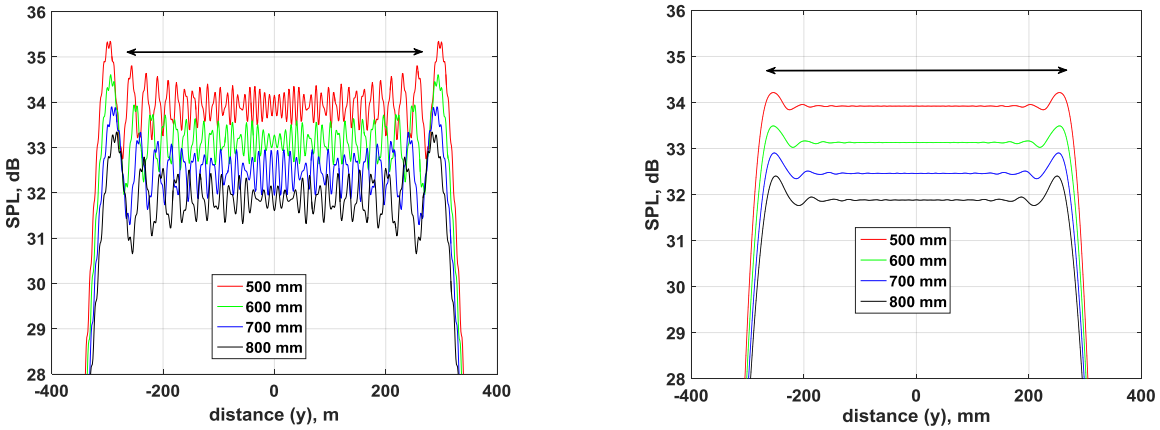


Fig.3: Equation 2 plotted for a single line of 340 point sources spaced at 2mm, for 4 different ranges: Left (no shading), Right (Tukey, 20%), The black arrow indicates the horizontal extent of the TUT

4. EXPERIMENTAL SETUP AND PROCESSING OF ACQUIRED DATA

The 'point' source used to implement the CWG was as a commercially available hydrophone/transducer (Reson TC4034), which at 300kHz is omnidirectional to within ±1.5dB.

The mechanical frame was made of commercially available 45x90mm cross section aluminium struts with transmitter side (scanning probe) and receiver side (TUT) bolted together for extra rigidity. The mechanical frame resulted in a source/TUT separation of around 0.68m.

The transmitted signal was a 200µs pulse centred on 300kHz. Measurements were taken at 340 positions in 2mm increments in the Y (horizontal) direction. For each position, the TUT's 16 channels were acquired, and beam pattern calculated by applying time delay beamforming to the data.

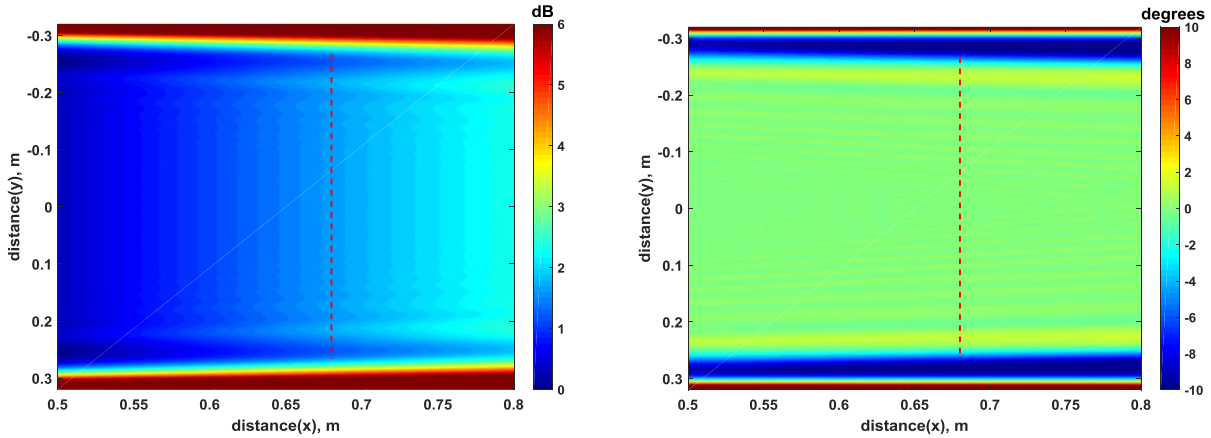


Fig. 4. Comparison of the generated cylindrical wave (Tukey shaded 340 point sources at 2mm spacing) with an ideal plane wave: Amplitude Ratio (Left) and Phase difference (Right). Position of the TUT is shown by the dotted line.

5. RESULTS

The beamformed measurements together with the analytic expression for a rectangular transducer [1] are plotted in figure 5. The main lobe of the analytic expression is followed to a good degree of accuracy by the measurements, and the predicted beam width of 0.47° is accurately determined. Positions of the sidelobes are also well reproduced, although the actual levels to a lesser extent. Depth of the nulls is also variable. Discrepancies can most probably be attributed to TUT element tolerances, TUT inter element couplings and positioning tolerances of the mechanically scanned point source.

6. CONCLUSIONS

Near-field measurement methods provide a practical alternative to far-field characterisation of SONAR transducers and RF antennas, as can be testified by the substantial number of publications on the topic, as well as availability of commercial equipment to perform these measurements.

However, the significant expense and complexity of near-field measurement arrays can act as a deterrent when evaluating other measurements options available. Replacement of the array with a mechanically scanned probe introduces many advantages; including equipment cost savings, increased spatial resolution and elimination of inter element couplings. Automation of the measurement process is straightforward and mitigates the disadvantage the longer measurement time required.

The measurement time can be reduced further by replacing the 2-D rectangular mechanical scan (producing a plane wave) to a linear scan (producing a cylindrical wave). This approximation is valid for transducers of high aspect ratio such as the unit characterised in this article.

Generation of a cylindrical wavefront allowed measurement of the beam width (0.47°) of a 300kHz SONAR transducer, 108λ in length in a small calibration tank, at a distance of only 67cm. The equivalent far-field measurement distance requirement would have been > 50m.

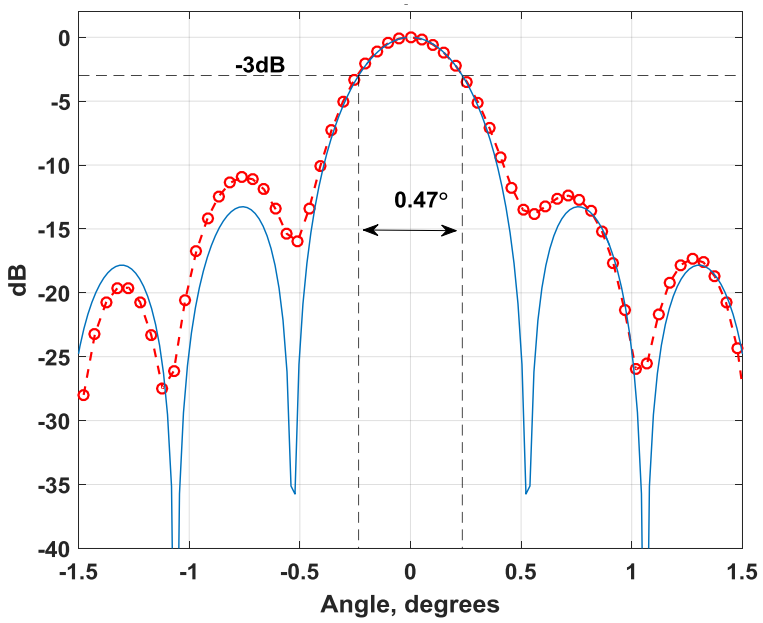


Fig. 5. TUT horizontal beam pattern at 300kHz: Beamformed results (red circles) plotted together with analytic expression for a rectangular transducer.

REFERENCES

1. C. H. Sherman, J.L. Butler, Transducers and Arrays for Underwater Sound, Springer, 2007
2. R.J. Bobber, Underwater Electroacoustic Measurements, Naval Research Laboratory, US Government Printing Office, Washington DC, 1970
3. W.J. Trott, Underwater Sound Transducer Calibration from Near Field Data, J. Acoust. Soc. Am., vol. 36, pp. 1557-1568, Aug. 1964.
4. R.C. Rowell, A Tankielun, Plane Wave Converter for 5G Massive MIMO Basestation Measurements, 12th European Conference on Antennas and Propagation, EuCAP 2018, London, United Kingdom.
5. O.M. Bucci, M.D. Migliore, G. Panariello, D. Pinchera, Plane-wave generators: Design Guidelines, Achievable Performances and Effective Synthesis, IEEE Transactions on Antennas and Propagation, vol. 61, no. 4, pp. 2005–2018, April 2013

PECULIARITIES OF FREE-FIELD CALIBRATION OF A VECTOR RECEIVER IN A REVERBERANT SOUND FIELD OF A WATER TANK

A. E. Isaev[a], A. N. Matveev[a]

[a]Mendeleevo, VNIIFTRI, Moscow region, Russia, 141570

A. E. Isaev. Mendeleevo, VNIIFTRI, Moscow region, Russia, 141570. Fax: +74956602539.
E-mail: isaev@vniiftri.ru

Abstract: *An experiment that was performed to confirm the possibility of free-field calibration of receiver of sound field vector quantity in a reverberant sound field of a water tank during radiation in a water tank continuous signal with a frequency-distributed power is described. The purpose of the experiment was to introduce reference distortions with known parameters into the projector direct wave and make sure that the distortion parameters measured by vector receiver in the reverberant field coincide with the predicted ones. The reference distortion was introduced by a sound wave reflected from the water-air interface. The proposed technique let experimentally establish the possibility to select in the reverberant sound field of water tank the vector quantity of projector direct wave in the frequency range overlapping the range of the tone-burst method and continued up to frequencies of standing sound wave chamber.*

Keywords: *Vector receiver of underwater sound, free-field calibration, continuous bandpass signal, reverberant sound field of water tank*

1. MOTIVATION

One of the disadvantages of the tone-burst method measurement is the distortion of the signal by the transient process. With decreasing frequency, the duration of the transient process increases, which limits the ability to calibrate underwater sound receiver at low frequencies.

The widespread in practice designs of the receiver of sound field vector quantity – vector receiver (VR) are created on the basis of the two-element receiver. The output signal of the VR is a superposition of signals from two spaced receiving elements. When VR receives a tone-burst impulse, output signals of each receiving element are distorted by transient process. This increases in time the distortions of the VR output signal. The suspension unit of VR also increases the duration of transient process.

Transient process distortion are not the only disadvantage of using the tone-burst method. VR is much larger than hydrophone in size. This forces us to increase the distance between projector and VR and leads to a decrease in the duration of the suitable for measurement part of the tone-burst impulse. Calibration of VR by the tone-burst method becomes problematic below 5-6 kHz.

The effect of sound scattering on the VR mount frame becomes significant, starting from 4-6 kHz. To represent the behavior of VR frequency response at higher frequencies, it is necessary to perform a calibration in small steps by frequency. At the same time, the labour intensity of such measurements by tone-burst method unacceptably increasing.

Due to the listed above reasons methods free from the indicated disadvantages of the tone-burst method are to be applied for VR calibration.

2. PROBLEM STATEMENT

Transient distortions can be avoided and detailed free-field frequency response can be obtained by methods based on processing the frequency dependence (FD) measured in a reverberant sound field at radiating in a water tank continuous signals with frequency-distributed power. These methods are used to calibrate the receiver of sound pressure – the scalar quantity of sound field. The ability to use these methods to calibrate the VR is not obvious.

In comparison with scalar quantities, the mechanism of vector quantities summation is more complicated. The phase of the VR output signal is determined not only by the delays of reflected waves in time, but also by the angles of their fall on the receiver. When calibrated using the tone-burst method, the VR oscillates collinearly to the propagation of projector direct wave. In the reverberant sound field, the form of VR oscillations becomes more complicated with the arrival of each reflected wave. As a result, the receiver moves along a complex 3-D trajectory, which is radically different from the trajectory when receiving a tone-burst impulse. Own oscillations of receiver suspensions can cause additional anisotropy of the VR.

This requires an experimental conformation of the possibility of free-field VR calibration in a reverberant sound field of water tank.

The gap in the frequency range not provided by other primary calibration methods prevents from such inspection. An accurate VR calibration in the sound field of a standing wave can be at frequencies not higher than 500 Hz, the tone-burst method can be applied starting from 6 kHz. The results of VR calibrating in the reverberant sound field of water tank in the range from 500 Hz to 6 kHz cannot be directly compared with the results of other primary methods.

This forces us to look for ways that are not based on a direct comparison of the results of measuring VR sensitivity.

3. EXPERIMENT

In the absence of the possibility to have the reference values of VR frequency response, an experiment was set up, the idea of which was to introduce into the measured frequency response "reference" distortions with known in advance parameters and to make sure that the distortion parameters measured in the reverberant sound field coincide with the predicted ones.

For example, if the projector direct wave is distorted by a single reflected wave, the frequency response will be distorted by interference oscillation, which is described by harmonic function. The amplitude, period and phase of the oscillations are directly determined by the geometrical parameters of the experiment and the reflection coefficient.

As a reflecting surface, the water-air interface (water surface of water tank) was chosen. Water-air interface has the following remarkable properties:

- sound reflection equals to 100% and does not depend on frequency;
- phase of the reflection coefficient is precisely known for both sound pressure and for sound particle oscillation velocity (further oscillating velocity) and sound pressure gradient, and does not depend on frequency;
- large sizes of the water tank provide for the negligible influence of edge effects on the parameters of reflected sound waves, starting at frequencies of hundreds hertz;
- ratio of the wavelength and the size of water tank allows you to use the laws and the ratios of geometric acoustics.

In the experiment, the receiver of oscillation velocity was used as VR. Projector and receiver were located in the water tank so that the first reflection was a reflection from the surface of the water. The chirp signals were radiated and the FD of transfer impedance (TI) of projector-receiver pair in the reverberant sound field of water tank was measured. Using the CMWA technique [1] the interference oscillations of FD due to the sound reflection from the water tank bottom and walls were suppressed, and oscillation FD caused by reflection from the water-air interface has been saved.

When a spherical sound wave falls on the water surface, the sound pressure at the water-air interface is zero, and the oscillation velocity of the medium particles is maximum. Consequently, at the media interface, the phases of sound pressure in the direct and reflected waves are opposite, and the phases of the oscillation velocity for both waves coincide. Due to the fact, when a sound wave is reflected, the direction of wave propagation vector is reversed, the phase of oscillation velocity and sound pressure in the reflected wave coincide with the accuracy up to the phase shift caused by the wave sphericity.

This situation occurs if the projector is located between the VR and the media interface (diagram B in Fig. 1). If the projector and the VR are changed positions (diagram A in Fig. 1), then the direct and reflected waves falling on the VR will propagate in the opposite directions and the phase of interference oscillation change to the opposite.

If instead of a VR, a hydrophone (sound pressure receiver) is used, then the interference oscillations will be identical for both locations. Fig. 2 shows the interference oscillation modules of the FD of projector-hydrophone pair TI when placing pair according to schemes A and B.

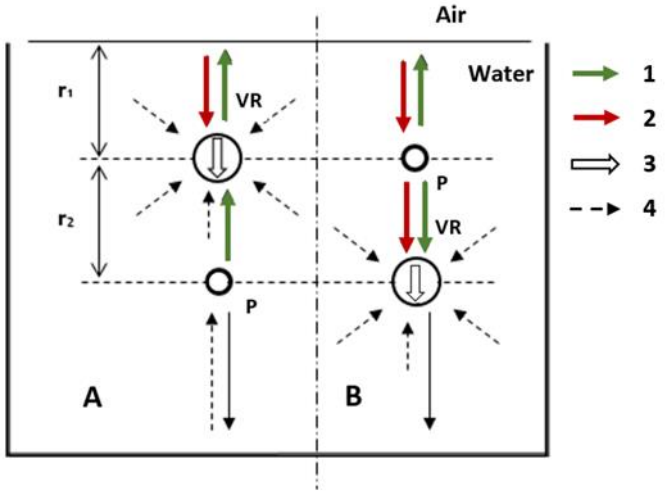


Fig.1: The location of the projector P, VR and the water-air interface: 1 - projector direct wave; 2 - wave reflected by the water-air interface; 3 - VR reference direction; 4 - waves reflected by the water tank boundaries. Direct and reflected waves fall on VR in opposite directions - A, in the reference direction - B.

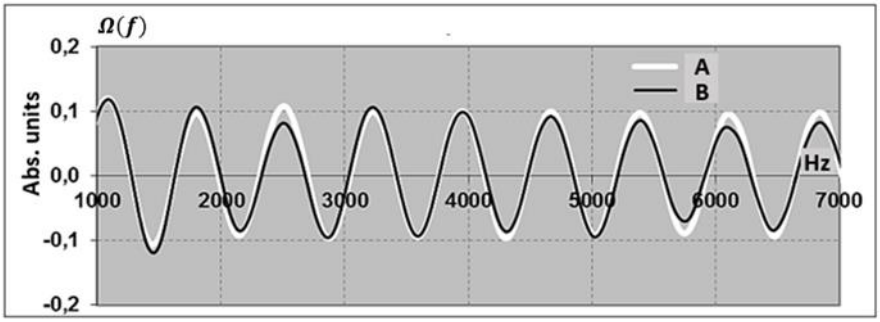


Fig.2: Interference oscillations of projector-hydrophone pair TI in experiment A and B.

The interference oscillations are almost identical, the amplitude is 0.096, the period is 724 Hz, and the phase π of oscillations is unambiguously determined by the geometrical parameters of the experiment and practically does not depend on the frequency properties of the projector and receiver.

Fig. 3 shows the frequency dependences of projector-VR pairs TI, when the pairs are placed according to diagrams A and B with the same geometrical parameters as in the experiments with the hydrophone.

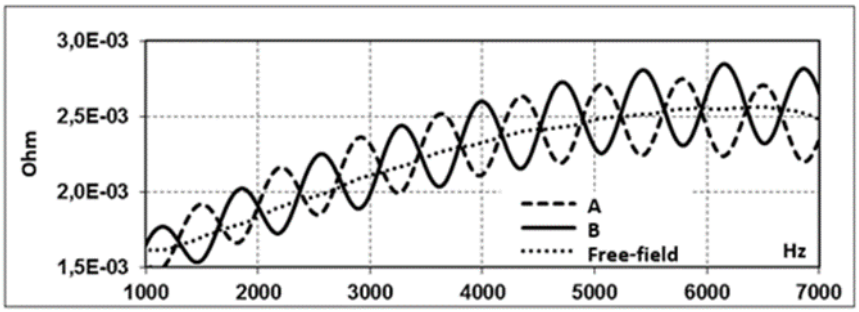


Fig.3: Frequency dependences of projector-VR pair TI module: free-field and distorted by reflection from the water surface in experiments A and B.

The difference in the behavior of interference oscillations in Fig. 2 and 3 illustrate the differences in the summation of scalar and vector values of the sound waves. When the

placement of projector-VR pair is changed from A to B, the amplitude and oscillation period remain unchanged, and the phase changes by π.When placed according to diagram B, the interference oscillations of projector-hydrophone and projector-VR pairs coincide (see Fig. 4).

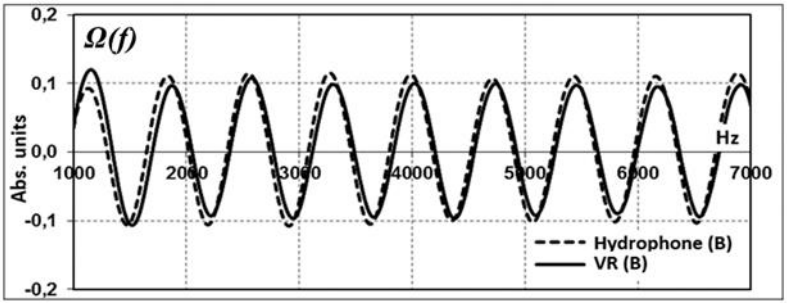


Fig.4: Interference oscillations of the projector-hydrophone and projector-VR pair TI module, placed according to diagram B.

Another confirmation of the correctness of the VR calibration in the reverberant sound field of water tank are phase-frequency dependencies of TI presented in Fig. 5 obtained when the VR is located according to diagrams A and B, and when the reference direction of VR is opposite to that shown in Figure 1 (dependences A* and B*).

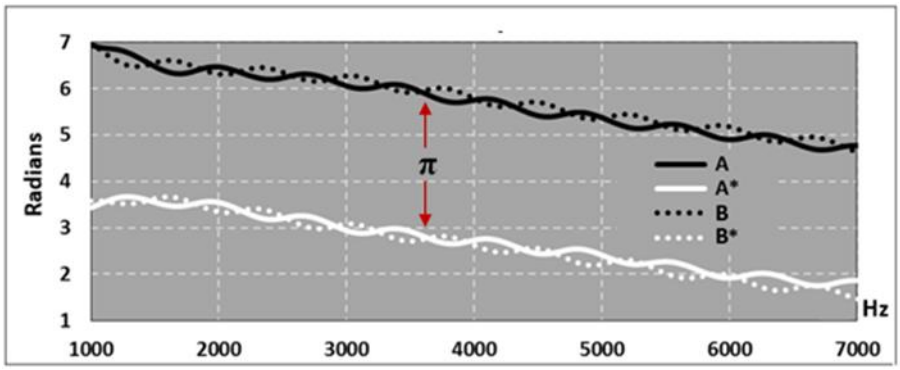


Fig.5: Phase frequency dependencies of projector-VR pair TI in experiments A and B, and when VR reference direction changing to opposite (A u B*).*

When the VR is oriented in opposite direction, the phase-frequency dependences retain their behavior, including the behavior of interference oscillations, but shift by π radian. The inflection points of the phase-frequency distortions correspond to the extremums of the interference oscillations of the TI module. The presented regularities correspond to the rules of summation the vectors of oscillatory velocity of direct and reflected from the water surface sound waves. For the receiver of scalar quantity – a hydrophone – the phase-frequency dependences are superimposed on one another with an accuracy determined by the directional properties of the receiver.

The independent method of indirect confirmation the accuracy of VR free-field calibration in the reverberant sound field of water tank was the measurement using VR of the sound pressure generated by the reference projector. The sensitivity of VR was determined using the CMWA technique [2]. The reference projector (reversible hydrophone) was calibrated by reciprocity method. The oscillatory velocity measured via VR was recalculated into the sound pressure, which was compared with the sound pressure created by the reference projector at the point of VR location. In the frequency range from 1000 Hz to 10000 Hz, the deviation of the sound pressure measured by the VR from that generated by the projector did not exceed 2.5%, which can be considered a good coincidence for calibration using the primary method.

4. CONCLUSIONS

The proposed technique, based on introducing a known distortion into the projector direct wave by a wave reflected from the water-air interface, made it possible to experimentally establish the ability to allocate the vector quantity of the projector direct wave in the reverberant sound field of water tank and apply a continuous band-pass signal for VR calibration at frequencies from 500 Hz to 10 kHz.

Using the CMWA technique allows to completely cover the frequency range of tone-burst method and expand the possibilities of free-field calibration to the frequencies of a standing sound wave chamber.

The results of performed experiment give grounds for using VR for free-field measurements of acoustic impedance of material sample, which allows, due to the VR directional properties, to reducing the influence of effects caused by diffraction of a sound wave at the edges of the sample.

REFERENCES

[1] **A. E. Isaev, A. N. Matveev**, Hydrophone free-field calibration at continuous radiation in non-anechoic water tank, *Acoustical Physics*, volume 55, pp. 762-770, 2009.

[2] **A. E. Isaev, A. N. Matveev, G. S. Nekrich and A. M. Polikarpov**, Complex calibration of a pressure gradient receiver using the reciprocity method procedure, *Acoustical Physics*, volume 60, pp. 45-51, 2014.

STUDY OF A TRUE FREE FIELD CALIBRATION METHOD OF AN ACCELEROMETER BASED VECTOR SENSOR FOR UNDERWATER USE

Markus Linné[a], Peter Sigray[a]

[a] FOI, Swedish Defence Research Agency, Gullfossgatan 6, 164 40 Kista, Sweden

Markus Linné, Swedish Defence Research Agency, FOI, Gullfossgatan 6, 164 40 Kista, Sweden. Fax: +46 8 5550 3869. Email: markus.linne@foi.se

Abstract: *Hearing is the main sensory organ for many marine species. Fish without swim bladder as well as Crustaceans and Cephalopods are known to be sensitive only to particle motion. Thus, sole measurement of acoustic pressure is not enough to assess the impact on marine species since particle motion cannot easily be derived from pressure. With the launch of the European Marine Strategy Framework Directive focus was directed to the low-frequency range where anthropogenic activities interfere with living conditions of marine animals. Most studies have been dealing with acoustic pressure but lately a shift towards particle motion has been observed, with the introduction of commercially available vector sensors. With this shift it will be necessary to develop calibration methods for particle motion. One alternative at hands is to perform calibration in-situ in free field conditions, provided that a stable, homogenous and large volume of water mass is available.*

Herein are the results from a three-axis calibration check of an accelerometer-based vector sensor presented. Prior to the calibration a reciprocal free-field calibration was done of a transducer which was used as a transmitter for the calibration of the vector sensor. The vector sensor was lowered to the same depth as the transmitter at 45 m depth with a horizontal separation distance of 25 m. Approximately 40 ms long continuous wave pulses in the frequency range of 400 Hz to 1200 Hz were used. Since the orientation of the vector sensor axis was unknown the resulting acceleration measurements from the three axes of the sensor were combined to give the total acceleration of the particle motion in the water. The calibration was repeated three times with varying incidence angles. The results were compared with the free field assumption of the acceleration of the particle motion resulting from the transducer.

Keywords: *Calibration, Vector Sensor*

1. INTRODUCTION

The vector sensor was developed for measurements of a large variety of applications with relatively high sound levels, for example measurement of energy produced by seismic airguns [1][2] and exposure experiments on cuttlefish [3]. These anthropogenic sources have in common that the majority of the energy is found below 1000 Hz.

The vector sensor was mainly optimized for the frequency band 0.5 Hz to 1000 Hz. The upper limit of the frequency band was limited by the size of the sensor. This broad frequency band makes calibrations of the sensor challenging. The classical way of calibrating underwater sensors is to use a time-gated tone burst of certain frequency and length and to measure the signals before the reverberation interferes with the direct field. Free field calibrations below 1000 Hz sets limits on which minimum water tank dimensions are usable. One solution is to use large water volumes like that of an ice-covered lake. The ice provides a stable platform to work from as well as reducing motional induced errors on the calibration results. It also makes it possible to measure horizontal distances with a relatively high precision. Thus, the vector sensor was calibrated in the lake Hornavan in Swedish Lapland in March 2018. The thickness of the ice was approximately 40 cm and the lake has a maximum depth of 200 m.

In order to calibrate the vector sensor, the sensor output was compared to the free field estimate of the acceleration field generated by a transducer, i.e. a comparison calibration technique is utilized in this study.

2. THE VECTOR SENSOR SYSTEM

The sensor of the system is a near neutrally buoyant (weakly positive) sphere with a diameter of 60.0±0.2 mm with a mass of 110±5 g. The sphere contains a three-axis accelerometer (PCB piezotronics model 356B18). The accelerometer is attached to a small aluminium support suspended to the sphere with screws and epoxy glue. The support has the additional function to provide the freedom to co-locate the mass at the buoyancy centre, see Fig.1. The sensitivity of the accelerometer is 1 V/g=-140 dB re 1 V/μm/s^2, g being the gravitational constant, with a flat sensitivity (±5%) in the frequency range of 0.5 Hz to 5.0 kHz. The noise floor at 100 Hz is approximately 1.2 μg/Hz$^{1/2}$ or 22 dB re 1 μm/s^2/Hz$^{1/2}$. The noise floor at 1000 Hz is approximately 0.4 μg/Hz$^{1/2}$ or 12 dB re 1 μm/s^2/Hz$^{1/2}$. The Vector Sensor system was custom built, based on the technique described in [4], the difference in this system being a smaller sphere and an autonomous recording system.



Fig. 1: The open sensing head of the vector sensor system showing its interior.

The sampling frequency of the data acquisition system was 14400 Hz, and the resolution of the Analog-to-Digital converter was true 21 bit. The recorded data were stored on a 32 Gb SD-card.

3. THE FREE FIELD MEASUREMENT SITE

Lake Hornavan is situated in the North of Sweden at the elevation of 425 m. The lake water is fresh with a little anthropogenic activities in the area.

The calibrations took place at two sites (see Table 1). The calibration of the vector sensor was conducted at site 1, and the transmitter, which had to be calibrated as well, was calibrated at both sites. The water temperature was logged at site 1 and site 2 using a Valeport Datalog X2. The temperature as a function of depth showed a monotonic increase from surface 0.65 degrees to the lake floor 3.6 degrees. The accuracy of the sound velocity meter was 0.06 m/s.

All the auxiliary instruments were kept in a measurement hut, which was heated to room temperature. The power for the data acquisition and signal generation units was generated using a portable power generator placed at a distance of approximately 100 m from the measurement hut. The generator was placed on top of vibration insulation materials in order to minimize sound leakage in to the water.

The weather during the calibration was stable, -15°C in the morning and -10°C at noon. The atmospheric temperature change did not affect the temperature of the water.

	Coordinates	Water depth [m]	Calibration depth [m]	Temperature at calibration depth [°C]	Sound velocity at calibration depth [m/s]
Site 1	N 66,194, E 17,664	90	45	3.3	1419.4
Site 2	N 66,183, E 17,774	45	20	2.6	1415.9

Table 1: Measurement sites.

4. CALIBRATION

The calibration was performed in two steps. In the first step, the Transmit Voltage Responses, TVR, was calibrated in a reciprocity scheme including two ITC-1007 and one ORT-1014. One of the ITC-1007 transducers was later used for the calibration of the vector sensor in the second step.

Step 1 was repeated eight times with the same transducers. The calibration was done in the frequency intervals 80 Hz - 20 kHz, 120 Hz – 5 kHz. 120 Hz – 10 kHz and 120 Hz- 20 kHz. At site 1, the distance between the three elements was 25 m. At site 2, the distance between the three elements was 20 m. The calibrations were conducted over a time period covering approximately two weeks. In Fig. 2 the TVR level is presented for frequencies up to 1.2 kHz. The presented TVR value is generated by taking the mean of all eight calibrations.

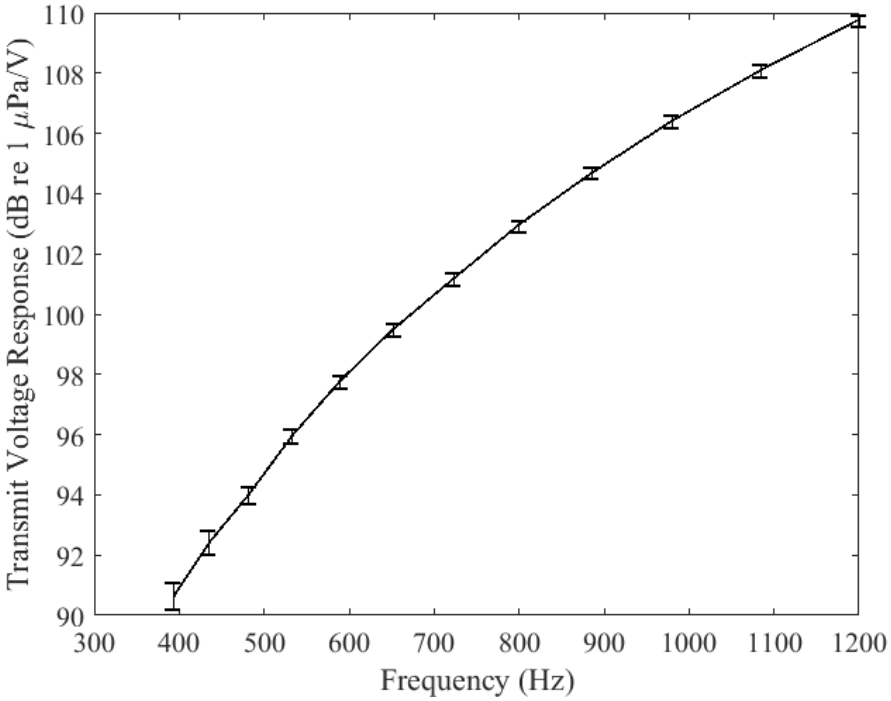


Fig. 2: The mean Transmit Voltage Response of the ITC-1007 used in the vector sensor calibration.

In step 2 the vector sensor was calibrated by using the newly calibrated ITC-1007 transducer. The vector sensor was placed at 25 m distance from the transducer. The deployment depth was 45 m, the same as for the transducer. The transducer generated 40 ms long tone bursts with discrete frequencies in the frequency range 392 Hz up to 1200 Hz. The following frequencies were used: 392 Hz, 434 Hz, 481 Hz, 532 Hz, 589 Hz, 652 Hz, 722 Hz, 799 Hz, 885 Hz, 979 Hz, 1084 Hz and 1200 Hz. Each tone was repeated ten times with a time separation of 1.5 s.

As a first step in the analysis the estimated acceleration was deduced using the TVR values generated in step 1, in combination with the measured voltages from the power amplifier to the transducer. The estimated acceleration, a_e, at the vector sensor was calculated using the following relations:

$$a_e = p \cdot w / Z, \text{ where } p = TVR \cdot v_o / d, \quad (1)$$

where p is the pressure generated by the transducer, w is the angular frequency of the generated wave, Z is the acoustic impedance in the water, V_o is the voltage generated by the power amplifier and d is the distance to the vector sensor. In this measurement the acoustic impedance was estimated to be 1419800 ± 60 Rayl.

The vector sensor output was compared to the generated acceleration levels. This analysis was done by measuring the peak-to-peak voltage of the signal from the recorded tone bursts. The measured voltages were scaled with the sensitivity, given by the accelerometer manufacturer, of –140 dB re 1 V/μm/s^2.

Since the orientation of the vector sensor axis was unknown the resulting acceleration measurements from the three axes of the sensor were combined to give the total acceleration of the obtained particle motion in the water. In Fig. 3 the estimated acceleration is shown with the measured acceleration from the vector sensor.

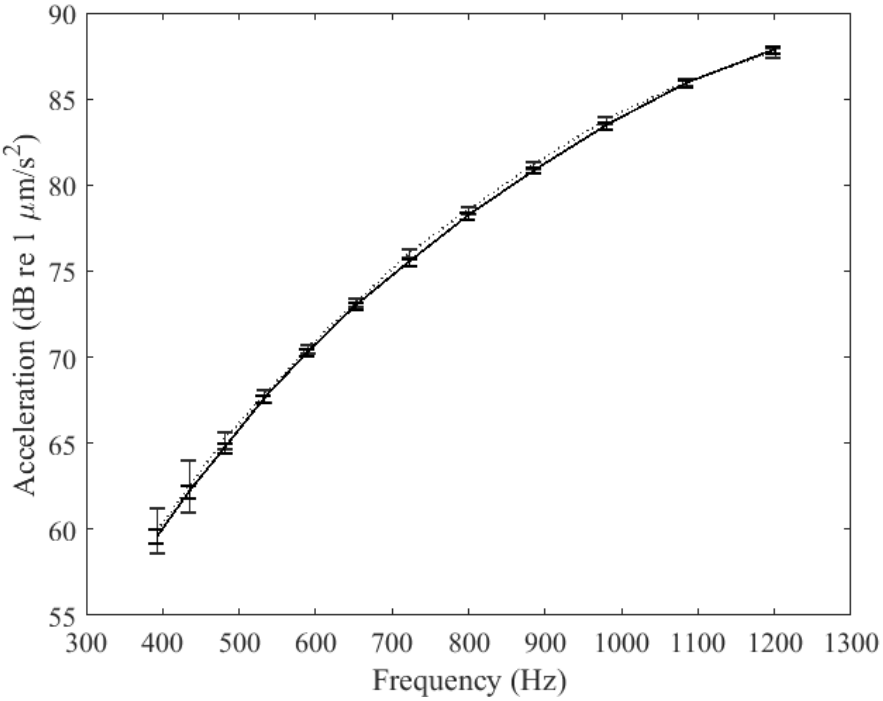


Fig. 3: The estimated acceleration using pressure and assuming that the free-field estimate is valid (solid line), and the measured acceleration (dotted line) using the output voltage from the accelerometer and manufacturer's sensitivity.

The solid line represents the estimated acceleration and the dotted line represents the measured acceleration. The calibration was repeated two times after rotating the vector sensor roughly 50-100 degrees between the measurements, supervised by using an underwater video camera. The measured accelerations were comparable to the one presented in Fig 3. Assuming that the relations and assumptions behind the estimated acceleration is correct, the sensitivity of the vector sensor can be rescaled according to:

$$M_e = M_m \cdot a_m / a_e \,, \tag{2}$$

where M_m is the sensitivity specified by the manufacturer, a_m is the measured acceleration and a_e the estimated acceleration. In Fig. 4, the resulting sensitivity for vector sensor is presented. This correction is advocated by the fact that the buoyance will change the sensitivity of the sensor [5].

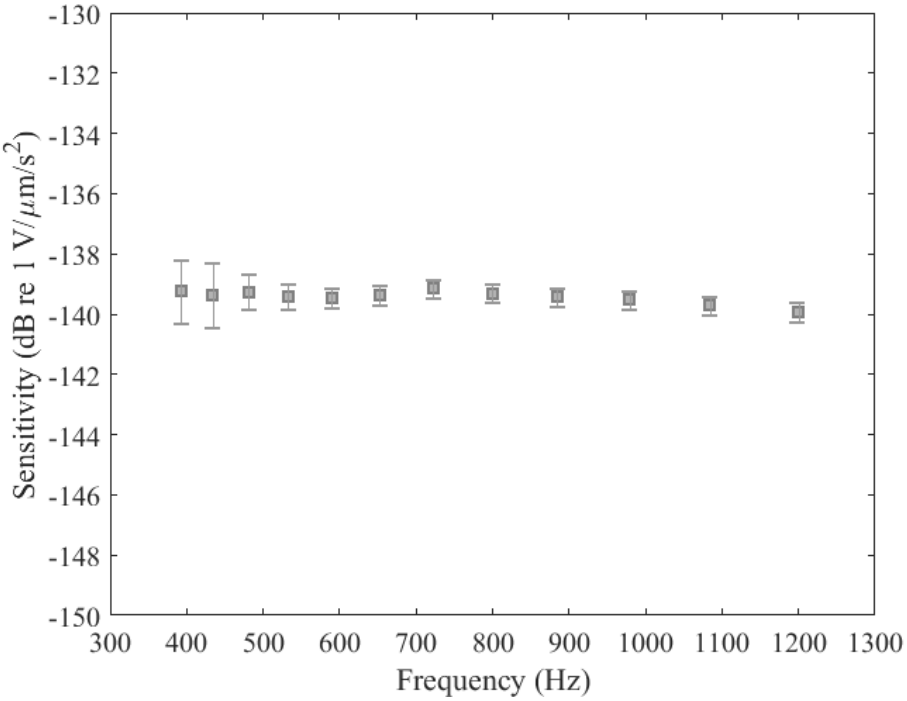


Fig. 4: The measured sensitivity of the particle motion sensor. The increase of the uncertainty for lower frequencies is explained by the decrease of SNR related to the transmitter and receiver.

5. SOURCES OF UNCERTAINTY

A number of sources contribute to the uncertainty in the estimated sensitivity. The uncertainties are listed and discussed briefly:

Transducer TVR uncertainty: The reciprocity calibration was done eight times. The repeated calibrations using the same frequency points gave a statistical spread, the standard deviation was evaluated and used as an uncertainty estimate. This uncertainty has its major impact at low frequencies where the signal to noise ratio was relatively low.

Vector sensor measurement uncertainty: The measurements were repeated 30 times for each frequency, when adding the three different impinging angles. The standard deviation was calculated for each frequency and this uncertainty has its major impact at frequencies close to 400 Hz where the signal to noise ratio was relatively low.

Distance: There is an uncertainty in the measurement of the distance between transmitter and receiver. Further, it occurs twice, both in the reciprocity calibration and in the vector sensor calibration. In the reciprocity scheme the uncertainty was estimated to 0.3 m or 0.11 dB. When conducting the vector sensor calibration this uncertainty was increased to 0.15 dB.

Directivity: The vector sensor was not oriented with the same side facing towards the ITC-1007 as was the case in the reciprocity calibration. It can be expected that there are small deviations from the omnidirectional response. According to the manufacturer of the ITC-1007 transducer there is a ±1 dB directional response at 10 kHz, however, this uncertainty is ±0.1 dB at 1 kHz.

Instrumentation: The resolution of both the vector sensor system and the reciprocity calibration instruments are 24 bit. The instrument accuracy, internal noise levels are <<0.1 dB. In this study a conservative uncertainty estimate of 0.1 dB is assumed for all the different instruments.

Thermal stabilization: The transducers used in the TVR calculation and the vector sensor were allowed to thermalize for at least three hours prior to the first measurements. No drift of electrical signals are observed over the course of measurements and these uncertainties are assumed to be hidden in the statistical variability in the measurements and thus covered by the two first entries in this list.

6. DISCUSSION

The measured acceleration was observed to be slightly higher than the estimated acceleration assuming free field conditions in the water volume. A positive buoyancy is known to amplify the amplitude of oscillations [5]. The mean density of the sensor head is 950± 50 kg/m^3, thus it is weakly positive. The resulting sensitivity for the vector sensor as presented in Fig. 4 indicates that there are no structural resonances apparent in the investigated frequency range. The sensitivity was offset by roughly +0.5 dB from the factory calibration, which is most probably explained by the positive buoyancy of the sensing head.

REFERENCES

[1] **Lise Doksaeter et al.**, Behavioural effects of seismic dose escalation exposure on captive mackerel (Scomber scombrus), *Rapport fra havsforskningen*, 34, 2017.
[2] **Jan G. Davidsen et al.**, Effects of sound exposure from a seismic airgun on heart rate, acceleration and depth use in free-swimming Atlantic cod and Saithe, *Conservation Physiology*, Volume 7, 2019.
[3] **Marta Solé et al.**, Offshore exposure experiments on cuttlefish indicate received sound pressure and particle motion levels associated with acoustic trauma, *Scientific Reports* ***7,*** Article number 45899, 2017.
[4] **Peter Sigray and Mathias Andersson**, Particle motion measured at an operational wind turbine in relation to hearing sensitivity in fish, *J. Acoust. Soc. Am.,* **130** (1), 200-207, 2011.
[5] **James A. McConnel**, Analysis of a compliantly suspended acoustic velocity sensor, *J. Acoust. Soc. Am*, **113** (3), 2003

STANDARD FACILITY FOR FREE-FIELD CALIBRATION OF HYDROPHONES AND VECTOR RECEIVERS IN THE REVERBERANT LABORATORY WATER TANK

A. N. Matveev[a], A. E. Isaev[a]

[a]Mendeleevo, VNIIFTRI, Moscow region, Russia, 141570

A. N. Matveev. Mendeleevo, VNIIFTRI, Moscow region, Russia, 141570.
Fax: +74956602539. E-mail: matveev@vniiftri.ru

Abstract: *The data on the standard facility for calibration of underwater sound receivers in the reverberant laboratory water tank are presented. The standard facility implements the measuring procedure of the reciprocity method in the free field of a spherical traveling sound wave using three transducers. A feature of the standard facility is the measuring by the absolute method the free-field sensitivity of hydrophones and receivers of vector quantity of underwater sound field. During measurements, the free-field conditions are provided by using the method of time gating of tone-bursts and the technique of complex moving weighted averaging. The results and uncertainty estimation of calibrations performed using the standard facility are shown.*

Keywords: *Vector receiver of underwater sound, free-field calibration, phase sensitivity, underwater acoustic standard facility*

1. INTRODUCTION

Sound field distortion caused by an underwater receiver placed in a small volume chamber increases with the frequency and at frequencies above 1 kHz leads to an unacceptably large measurement uncertainty. A similar problem exists for the hydrophone calibration. At frequencies above 1 kHz, hydrophone free-field calibrations are performed in a large test tank.

Most calibration facilities use a standardized measurement procedure of reciprocity method with three transducers, one of which is a reversible hydrophone *T*, the other is a projector *P*, and the third is a calibrated hydrophone *H*. Perform measurements of the free-field electrical transfer impedance of pairs *P*-*H*, *T*-*H*, *P*-*T*. The calibrated hydrophone free-field sensitivity is calculated by the formula:

$$M_H = \sqrt{\frac{2}{\rho \cdot f} \cdot \frac{Z_{PH} \cdot Z_{TH}}{Z_{PT}} \cdot \frac{r_{PH} \cdot r_{TH}}{r_{PT}}}, \quad (1)$$

where M_H is the hydrophone free-field receive sensitivity [V·Pa^{-1}], f is the frequency [Hz], ρ is the density of water [kg·m^{-3}], Z_{XX} is the free-field electrical transfer impedance of each transducer pair [Ohm], r_{XX} is the distance between projector and receiver for each transducer pair [m].

To eliminate the influence of sound reflections in the test tank and to measure the free-field transfer impedance in the presence of reverberation interference, various methods are used. The most accurate of these are the method of time gating of tone bursts and the technique of complex moving weighted averaging. When using time gating, the free-field hydrophone calibration can be performed at frequencies above 1 kHz. The reason for the limitation is insufficient resolution in the frequency of measurements by the tone-bursts method. When the technique of complex moving weighted averaging is used, the lower frequency of the calibration determines by the signal-to-noise ratio, which allows to extend the free-field hydrophone calibration range to 100 Hz [1].

For underwater acoustic measurements in addition to hydrophones – receivers of sound pressure (the scalar quantity), receivers of vector quantities of the sound field (vibrational velocity of water particles, sound pressure gradient) are getting more and more widespread. The first vector receivers (VR) were low frequency and their calibration was performed in the field of a standing sound wave of a small-volume chamber. The frequency range of modern VR is tens of kilohertz, which required to calibrate receivers at high frequencies. However, it is not possible to extend the frequency range of VR calibration in a small-volume chamber to frequencies above 1 kHz [2].

2. METHOD IMPLEMENTATION

Directly apply the reciprocity method for the VR calibration is not possible, because there is no reversible VR. Nevertheless, the formula of the reciprocity method can be used for the sensitivity of the VR determining. Note that the formula contains distance, receiver sensitivity, frequency. If we know the sound pressure at the point of VR location, the distance from the projector and frequency, we can calculate the value of vector quantities of the underwater sound field (vibrational velocity or sound pressure gradient). Thus, it becomes possible for the absolute calibration of the VR in the free field using the reciprocity method procedure.

In the field of a spherical sound wave, the vibrational velocity of water particles V and the gradient of sound pressure $grad(p)$ are related to the sound pressure p_{sph} by the following relations:

$$V = \frac{p_{sph}(r)}{\rho \cdot c} \cdot \frac{\sqrt{1 + k^2 \cdot r^2}}{k \cdot r}, \tag{2}$$

$$grad(p) = p_{sph}(r) \cdot \frac{\sqrt{1 + k^2 \cdot r^2}}{r}, \tag{3}$$

where $k = 2 \cdot \pi \cdot f \cdot c^{-1}$ is the wavenumber [rad·m^{-1}], c is the sound speed in water [m·s^{-1}].

The free-field sensitivity of VR to the desired vector quantity of the sound field can be determined using the formula:

$$M_{VR} = \sqrt{\frac{2}{\rho \cdot f} \cdot \frac{Z_{PR} \cdot Z_{TR}}{Z_{PT}} \cdot \frac{r_{PR} \cdot r_{TR}}{r_{PT}}} \cdot \sqrt{\frac{1}{\Theta(r_{PR}) \cdot \Theta(r_{TR})}}, \tag{4}$$

For the calibration of receiver of the vibrational velocity of water particles $\Theta(r)$ is:

$$\Theta(r) = \frac{1}{\rho \cdot c} \cdot \frac{\sqrt{1 + k^2 \cdot r^2}}{k \cdot r}, \tag{5}$$

and for the sound pressure gradient receiver calibration $\Theta(r)$ is:

$$\Theta(r) = \frac{\sqrt{1 + k^2 \cdot r^2}}{r}. \tag{6}$$

The difference between formula (4) for the sensitivity of the VR and formula (1) for the hydrophone sensitivity is the presence of a multiplier $\Theta(r)$ characterizing the relationship between the scalar and vector quantities of the sound field of a spherical wave.

The considered method makes it possible to perform an absolute calibration of the VR, using the reciprocity method. The peculiarity of the method consists in the fact that during vector receiver calibration a hydrophone (a scalar receiver) is used as a reversible transducer.

To reduce the dispersion of the measurement result due to the influence of noise interference, averaging is usually used. For example, averaging of the FFT estimations of received tone-burst signals reduces the dispersion, but gives a biased estimation and does not allow one to observe the envelope shape of the received signal. The feature of described facility that implements the proposed method is the synchronization of the radiating and receiving paths using one master signal generator. This ensures the invariance of the initial phase of the received signals and the possibility of synchronous accumulation of a series of signals. Synchronous accumulation allows to improve the signal-to-noise ratio while maintaining the received signal envelope, also it is used with radiation of tone-burst or chirp signals and allowed to apply the measurement algorithm, adaptive to the noise conditions.

The sensitivity of the underwater sound receiver is a complex value (the formulas (1) and (4) include complex values). Using a master generator enables measurement of the phase sensitivity characteristics. Phase responses more fully describe the properties of an

underwater sound receiver, which is very important for many problems solved using digital signal processing. Phase calibration is becoming more common and is already present in the IEC standard for hydrophone calibration [3].

For measurement of phase sensitivity, the transducers are arranged according to the Luker – van Buren scheme. To determine the correction for the shift of the acoustic center of the calibrated receiver, use the technique published by us earlier in [4]. To simplify the procedure for measuring the phase characteristics of the transfer impedance of a projector – receiver pair radiate supplemented quadrature signals [5]. The radiation of such signals allows to determine the instantaneous values of the phase and amplitude – the dependence of the phase and amplitude on time (on frequency during the radiation of chirp signals). This makes it possible to objectively estimate the distortion of a tone signal by transients and to obtain detailed amplitude and phase frequency dependencies when radiate chirp signals.

3. RESULTS

The correctness of the calibration results of the VR was checked by comparing the results obtained by various independent methods: calibration in the field of a standing wave of a small-volume chamber and free-field calibrations using the tone-burst method and CMWA technique. In fig. 1 shows the frequency dependence of the sensitivity of VR type of VHS56 to sound pressure in the frequency range from 500 Hz to 12.5 kHz.

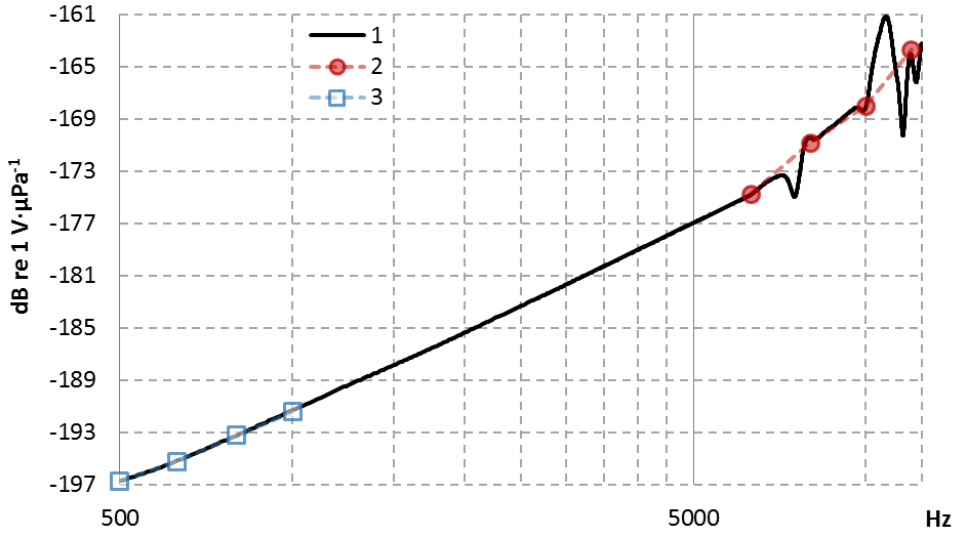


Fig. 1. Frequency dependence of receive sensitivity of VHS56 measured: in free field with tone-burst signals (1) and using CMWA technique (2), by pressure in the field of a standing wave of a small-volume chamber (3).

The presented data demonstrate a good agreement of the results obtained in various acoustic conditions. The differences do not exceed the uncertainty of calibrations estimated at 0.8 dB. Using the described method allowed us to obtain a continuous frequency dependence of sensitivity, including the range from 1 kHz to 6 kHz, not covered by other primary methods. Pay attention to the behavior of frequency dependencies at frequencies above 6 kHz. The data obtained by the tone-burst method lies close to the inclined straight line, while the continuous curve shows the presence of significant peaks and dips (oscillations), the range of which exceeds 6 dB. The reason for such typical oscillations of the frequency response is the scattering of sound on the VR mounting. This conclusion is based on the connection of the oscillation period with the distance to the source of sound scattering. The ability to establish

the presence of significant sources of scattering is impossible according to the dependences measured with a rare step, for example, at frequencies of a one-third octave.

4. CONCLUSION

The metrological characteristics of the standard facility were confirmed by comparisons of the results of calibrations of hydrophones – COOMET 531/RU/11 and vector receivers – COOMET 646/RU/14. The described calibration standard facility allows to:

- perform an absolute free-field calibration of the VR in the range up to the frequencies at which calibrations are performed in a small-volume chamber,
- reduce the uncertainty of the VR calibration to values close to the uncertainties of the calibration of the hydrophone.

Hydrophones and VR are usually used as a primary transducer integrated into various underwater acoustic measurement systems. The typical example of such system is an underwater sound recorder, which consists of a hydrophone, measuring and recording devices, and a power unit placed in a sealed container.

The developed method and facility are applicable for calibrating the primary transducers, and are based on processing their output analog signal. A recorder or other similar measuring device should be able to send a signal from the primary transducer to the input of the calibration facility. The measuring device should provide this opportunity in a submerged position. In order to take into account the influence of sound scattering on the body during calibration, the device must be completely under water, and continuous or very detailed frequency dependencies should be measured. This approach is standardized for sound level meters and provides the correctness of the calibration results and accounting the effect of sound scattering on its body.

REFERENCES

[1] **A. E. Isaev, A.S. Nikolaenko**, Laboratory free-field calibration of a hydroacoustic receiver at low frequencies, *Measurement Techniques*, volume 61 (1), pp. 72-78, 2018.

[2] **V. A. Gordienko, B. I. Goncharenko, S. S. Zadorozhnyi, M. V. Starkova**, Higher-frequency extension of the gauging ranges of vector receivers in the nonuniform field of measuring chambers, *Acoustical Physics*, volume 58 (5), pp. 571-574, 2012.

[3] IEC 60565(2006). Underwater Acoustics. Hydrophones. Calibration in the frequency range from 0.01 Hz to 1 MHz.

[4] **A. E. Isaev, A. N. Matveev, A. M. Polikarpov, N. G. Shcherblyuk**, Measurement of the sensitivity phase-frequency characteristics of hydrophones by the reciprocity method, *Measurement Techniques*, volume 56 (6), pp. 706-711, 2013.

[5] **A. E. Isaev**, Reducing the influence of a transition process in field calibration of hydrophones at low frequencies with the use of quadrature-added harmonic signals, *Measurement Techniques*, volume 53 (4), pp. 379-385, 2010.

CALIBRATION METHODS OF VECTOR RECEIVERS IN THE FREQUENCY RANGE 5 HZ TO 10 KHZ AND THEIR COMPARISON VERIFICATIONS

Yi Chen[a,b], A. E. Isaev[c], Guanghui Jia[a] and Teng Fei[a]

[a]Hangzhou Applied Acoustics Research Institute, 311400, China
[b]Department of Information Science & Electronic Engineering, Zhejiang University, 310027, China
[c]Russian National Research Institute for Physicotechnical and Radio Engineering Measurements, 141570, Russia

Yi Chen, Hangzhou Applied Acoustics Research Institute, Fuyang District, Hangzhou, Zhejiang Province 311400, China

Abstract: *A description of calibration methods of vector receivers in the frequency range 5 Hz to 10 kHz and comparison verifications are given here. At the low frequencies, the vertical and horizontal standing wave tube methods can be used for calibration of vector receivers. At the high frequencies, free-field reciprocity method and comparison method can be used for calibration. To verify the calibration methods, a pilot comparison calibration of vector receivers was performed between Hangzhou Applied Acoustics Research Institute (HAARI), China and Russian National Research Institute for Physicotechnical and Radio Engineering Measurements (VNIIFTRI). The vertical standing wave tube comparison method working in the frequency range 5 Hz to 400 Hz and free-field three-transducer spherical-wave reciprocity method working in the frequency range 500 Hz to 10 kHz were used for calibrating of three vector receivers VHS56, VHS90 and KGP-10. From the calibration results, the veracity of two calibration methods was proved effectively, no significant discrepancies were detected within these comparisons.*

Keywords: *Calibration method, vector receiver, comparison verification*

1. INTRODUCTION

Vector receivers are widely used in underwater acoustics area for their special capabilities on sensitivities and directivities. They are not only proportional sensitive to the sound pressure, but also to the sound pressure gradient and the particle velocity which are existed at the centres of these vector receivers in water. And there are three sensitivities for a vector receiver, and can be transformed between them [1].

Another special capability of vector receivers is that they have very strong directivities with their patterns of dipole type, and the directivities are independent of frequency within their working frequency bands. They can be measured in free-field and standing wave tube according to the different working frequencies and calibration methods.

The methods for calibrating vector receivers are always developing since the birth of vector receivers [2]-[6]. The free-field methods are usually used for calibrating vector receivers at the frequencies higher than 1 kHz, and standing wave tube method can be used for calibrating of vector receivers at low frequencies, generally low to 5 Hz.

In order to calibrate the sensitivity of vector receivers at low frequencies in laboratory water tank, special signal processing techniques such as CMWA shall be used to eliminate or decrease the sound waves which reflecting from the walls and water surface of the water tank [6]. The low calibration frequency when using this technique can usually be 250 Hz.

To verify the veracity of these calibration methods and prepare for drafting IEC International Standard on calibration methods of vector receivers, a pilot comparison calibration COOMET 646/RU/14 was performed in the frequency range 5 Hz to 10 kHz between Hangzhou Applied Acoustics Research Institute (HAARI, DI for Underwater Acoustics, China) and Russian National Research Institute for Physicotechnical and Radio Engineering Measurements (VNIIFTRI, DI CIPM MRA, Russia) from 2015 to 2018 [7].

Two vector receivers VHS56 and VHS90 which manufactured by HAARI and a vector receiver KGP-10 which manufactured by VNIIFTRI were used in the comparison as reference vector receivers, they were calibrated by HAARI and VNIIFTRI using their facilities independently. The consistency was proved by the calibration results, and no significant discrepancies were appeared within these comparisons.

2. CALIBRATION METHODS OF VECTOR RECEIVERS

2.1 Free-field calibration methods

There are two calibration methods which can be used in free-field for calibrating vector receivers [8]. One is free-field reciprocity method, which is an absolute calibration method, the other is free-field comparison method, which is a relative calibration method.

2.1.1 Free-field reciprocity method

The free-field reciprocity method used here is the free-field three-transducer spherical-wave reciprocity method which is often used for calibrating reference hydrophones. In this method, three transducers are applied, and at least one shall be reciprocal. The transducers shall be paired off in three measurement configurations, as shown in Fig.1. For each measurement configuration, the transducer pair shall be deployed in water separated by a known distance, d, with their axes aligned towards each other.

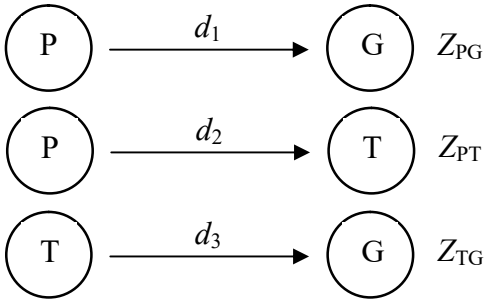


Fig. 1: Measurement configurations of free-field reciprocity method

The requirements for acoustic free-field conditions, far-field conditions and steady-state conditions shall be met for all configurations. In each case, using one transducer as a projector and the other as a hydrophone, the electrical transfer impedance can be determined at the calibration frequencies, and the free-field receiving sensitivity of vector receiver can be calculated from Equation (1)

$$M_{\mathrm{G}} = \sqrt{\frac{2}{\rho f}\frac{Z_{\mathrm{TG}}Z_{\mathrm{PG}}}{Z_{\mathrm{PT}}}\frac{d_{\mathrm{PG}}d_{\mathrm{TG}}}{d_{\mathrm{PT}}}}\sqrt{\frac{d_{\mathrm{PG}}d_{\mathrm{TG}}}{\sqrt{k^2d_{\mathrm{TG}}^2+1}\sqrt{k^2d_{\mathrm{PG}}^2+1}}} \tag{1}$$

Where, M_{G} is the pressure gradient sensitivity of vector receiver, f is the frequency, ρ is the density of water, Z_{PG}, Z_{TG} and Z_{PT} are electrical transfer impedances of projector and vector receiver, transducer and vector receiver, projector and transducer, d_{PG}, d_{TG} and d_{PT} are distances between projector and vector receiver, transducer and vector receiver, projector and transducer, k is the wavenumber.

2.1.2 Free-field comparison method

The comparison calibration of vector receiver in free-field can be accomplished by use of a reference hydrophone which had been previously calibrated by absolute calibration method. Since the uncertainty in calibration of the reference hydrophone will be inevitably introduced, free-field comparison method will have a higher uncertainty than the free-field reciprocity method.

When measuring, the sound field generated by an auxiliary projector in water is measured at a point in the acoustic far-field with the reference hydrophone. The vector receiver can measure the sound pressure at the same time or replace the reference hydrophone. The ratio of the open circuit voltages of such two transducers is equal to the ratio of their free-field sensitivities, and the free-field sound pressure receiving sensitivity of the vector receiver can be determined. Also, the directivity of vector receiver in free-field can also be determined by this method.

2.2 Standing wave tube calibration methods

There are also two kinds of calibration methods which can be used in standing wave tube for calibrating vector receivers. One is vertical standing wave tube method, the other is horizontal standing wave tube method, and the former is more widely used than the latter for its convenient installation and operation.

2.2.1 Vertical standing wave tube method

The calibration principle used in vertical standing wave tube is like vibrating column method. In this method, a vertical open-topped circular cavity which made of stainless steel is used as the standing wave tube. The tube is filled with water, and an auxiliary transducer is installed at the bottom of the tube as a projector to continuously transmitting the sound waves

vertically upwards. A schematic diagram of vertical standing wave tube calibration is shown in Fig.2.

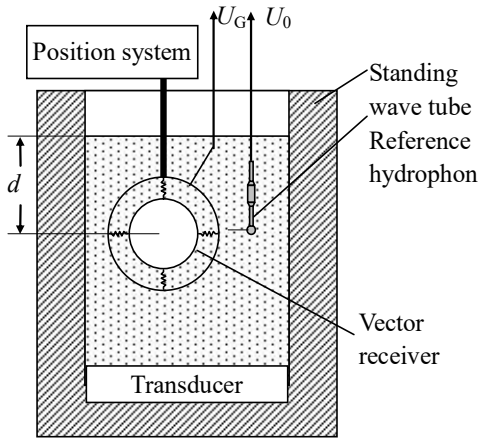


Fig. 2: Schematic diagram of vertical standing wave calibration

When measuring, the vector receiver and reference hydrophone were placed in the depth d and d_0 of the vertical standing wave tube, the open-circuit voltages U_G and U_0 of vector receiver and reference hydrophone were measured, and the sound pressure gradient sensitivity can be calculated from Equation (2).

$$M_G = \frac{U_G M_0}{kU_0} \frac{\sin kd_0}{\cos kd} \tag{2}$$

Where, M_G is sound pressure sensitivity of the reference hydrophone, k is the wavenumber.

Using this method, the directivity of vector receiver in standing wave tube can also be determined. If an accelerometer is used for determination of the sound pressure, it shall be an absolute calibration method, and the measurement uncertainty of this method can be lower than vertical standing wave tube comparison method.

2.2.2 Horizontal standing wave tube method

The measurement principle of the horizontal standing wave tube method is shown in Fig.3. The vector receiver is fixed in a rigid water-filled pipe closed at both ends, and the rigid pipe vibrates as a whole in horizontal direction, and the medium in the pipe moves like a small section of the standing wave.

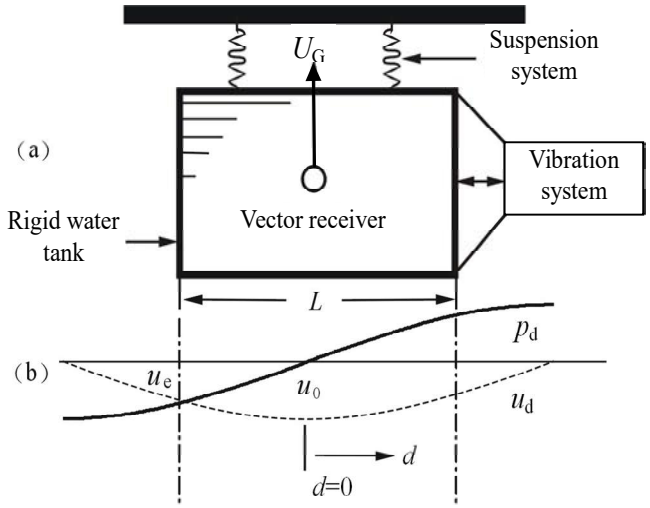


Fig. 3: Schematic diagram of horizontal standing wave tube calibration

The velocity sensitivity of vector receiver can be calculated from Equation (3).

$$M_{\mathrm{u}} = \frac{U_{\mathrm{G}} \cos(\frac{kL}{2})}{u} \tag{3}$$

Where, U_{G} is the open-circuit voltage of the vector receiver, L is the length of the tube, k is the wavenumber, and u is the vibration velocity of the pipe.

From the Fig.3, it can be seen that at the centre of the length of the standing wave tube, the sound pressure will be zero, and the vibration velocity and sound pressure gradient will be maximum. If the sound pressure gradient at the centre is measured, the pressure gradient sensitivity of vector receiver can also be calibrated.

3. COMPARISON CALIBRATION AND THEIR RESULT VERIFICATION

To verify the veracity of calibration methods of vector receiver, a pilot comparison calibration with its identifier number of COOMET/646/RU/14 beginning from 2015 was performed between HAARI, China and VNIIFTRI, Russia. Free-field three-transducer spherical-wave reciprocity method and vertical standing wave tube comparison method were used for this comparison, and the calibrations of vector receivers were carried from June to September, 2017 in Hangzhou, China and from April to July, 2018 in Moscow, Russia.

3.1 Vector receivers to be calibrated

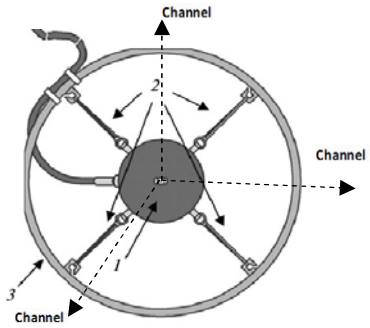
Three vector receivers were calibrated in this pilot comparison, each vector receiver is a three component sound particles velocity transducer, the detailed information of these vector receivers was listed in Table 1. They were calibrated at frequencies of 1/3 octave interval by different persons using different facilities and water tanks at different time and places.

Table 1: Detailed information of three vector receivers used in comparison

Type	Channels	Manufacturer	Frequency range [Hz]	Length of integral cable [m]	Diameter of transducer [mm]	Power supply [V]
KGP-10	X,Y,Z	VNIIFTRI	500–10000	6	53	±12 DC
VHS90	X,Y,Z	HAARI	5–4000	6	90	±12 DC
VHS56	X,Y,Z	HAARI	500–10000	6	56	±12 DC

3.2 Suspension of vector receiver when calibrating

The vector receiver to be calibrated was suspended into a ring which made of stainless steel through four rubber shock absorbers, and the vector receiver will be at the centre of the ring and in a zero buoyancy situation in water. The diagram of suspension of vector receiver when calibrating was shown in Fig. 4.



1 – three-component transducer in a spherical case, 2 – rubber shock absorbers, 3 – mounting ring

Fig. 4: Diagram of Suspension of vector receiver when calibrating

3.3 Calibration results and their comparisons

Three channels of three vector receivers were calibrated in the comparison, and the X channel calibration results of vector receivers VHS90 and VHS56 were given in Table 2 and Table 3. The comparison calibrations were carried in the frequency range 5 Hz to 10 kHz. At the frequencies from 5 Hz to 400 Hz, the vector receivers were calibrated by vertical standing wave tube comparison method. From 500 Hz to 10 kHz, free-field three-transducer spherical-wave reciprocity method was used for calibration.

Table 2: Calibration results of X channel of vector receiver VHS90

f [Hz]	M_{CN} [dB]	U_{CN} [dB]	M_{RU} [dB]	U_{RU} [dB]	f [Hz]	M_{CN} [dB]	U_{CN} [dB]	M_{RU} [dB]	U_{RU} [dB]
5	-224.2	1.0	-224.5	0.8	160	-195.4	1.0	-194.8	0.8
6.3	-222.5	1.0	-222.8	0.8	200	-193.3	1.0	-192.2	0.8
8	-220.5	1.0	-220.0	0.8	250	-191.4	1.0	-190.9	0.8
10	-218.9	1.0	-218.3	0.8	315	-189.4	1.0	-188.5	0.8
12.5	-217.2	1.0	-216.9	0.8	400	-186.5	1.0	-186.3	0.8
16	-215.1	1.0	-214.3	0.8	500	-184.8	0.7	-184.5	0.8
20	-213.2	1.0	-212.9	0.8	630	-182.7	0.7	-182.7	0.8
25	-211.0	1.0	-210.1	0.8	800	-181.0	0.7	-180.8	0.8
31.5	-209.8	1.0	-208.6	0.8	1000	-179.1	0.7	-178.9	0.8
40	-207.6	1.0	-207.0	0.8	1250	-177.2	0.7	-177.5	0.8
50	-205.4	1.0	-204.4	0.8	1600	-175.0	0.7	-175.3	0.8
63	-203.6	1.0	-202.7	0.8	2000	-173.1	0.7	-173.3	0.8
80	-201.2	1.0	-200.3	0.8	2500	-171.1	0.7	-171.2	0.8
100	-199.3	1.0	-198.4	0.8	3150	-168.8	0.7	-169.0	0.8
125	-197.2	1.0	-196.4	0.8	4000	-166.3	0.7	-166.6	0.8

Table 3: Calibration results of X channel of vector receiver VHS56

f [Hz]	M_{CN} [dB]	U_{CN} [dB]	M_{RU} [dB]	U_{RU} [dB]	f [Hz]	M_{CN} [dB]	U_{CN} [dB]	M_{RU} [dB]	U_{RU} [dB]
0.5	-196.6	0.7	-196.5	0.8	2.5	-183.2	0.7	-183.3	0.8
0.63	-194.8	0.7	-194.5	0.8	3.15	-181.2	0.7	-181.2	0.8
0.8	-192.9	0.7	-192.6	0.8	4	-179.1	0.7	-179.0	0.8
1	-191.2	0.7	-190.5	0.8	5	-176.9	0.7	-177.0	0.8
1.25	-189.2	0.7	-189.3	0.8	6.3	-174.8	0.7	-174.9	0.8
1.6	-187.0	0.7	-187.3	0.8	8	-171.2	0.7	-171.7	0.8

2	-185.3	0.7	-185.3	0.8	10	-168.5	0.7	-168.0	0.8

Where, M_{CN} and M_{RU} are sensitivity levels measured by HAARI and VNIIFTRI, U_{CN} and U_{RU} are expanded uncertainties declared by HAARI and VNIIFTRI [9].

The degrees of equivalence of X channel of vector receiver VHS90 and VHS56 are respectively presented graphically in Fig.5 and Fig.6 [10]. It can be seen that the calibration results of HAARI and VNIIFTRI are in good agreement, the equivalence of the results to the expanded uncertainties declared by HAARI and VNIIFTRI is not violated at any frequency points.

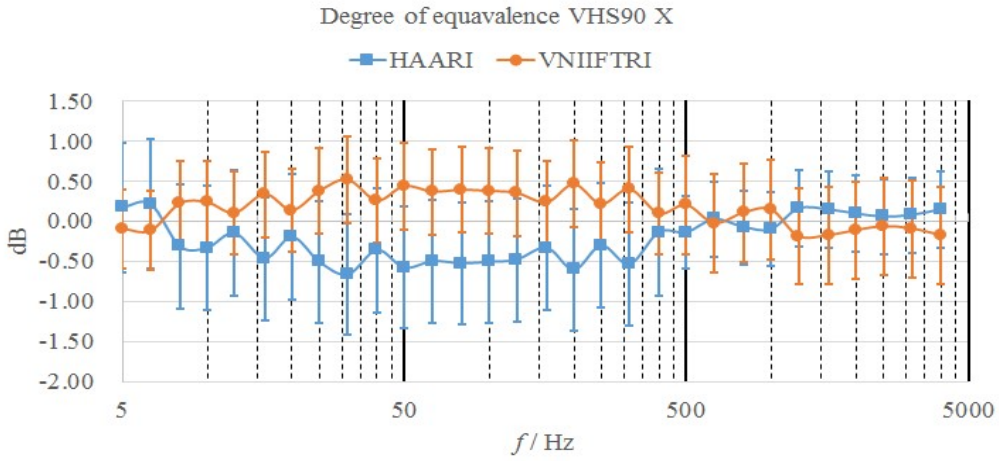


Fig. 5: Degrees of equivalence of X channel of vector receiver VHS90

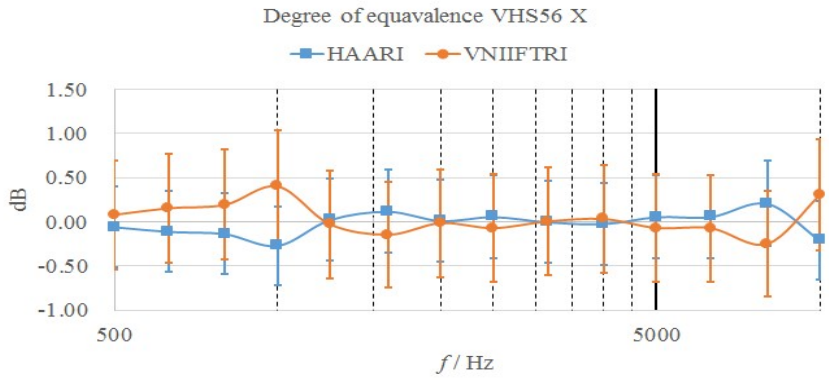


Fig. 6: Degrees of equivalence of X channel of vector receiver VHS56

4. CONCLUSION

The calibration methods of vector receivers and their comparison verifications are introduced here, and a pilot comparison COOMET/646/RU/14 was successfully performed between HAARI, China and VNIIFTRI, Russia.

From the calibration results, it can be seen that there is a good agreement between HAARI and VNIIFTRI, no significant discrepancies were detected within these comparisons. It effectively proves the veracity of free-field three-transducer spherical-wave reciprocity method and vertical standing wave tube comparison method, and the reliability of the calibration results. These works lay a good beginning for drafting an IEC International Standard on calibration methods of vector receivers.

REFERENCES

[1] **Chen Yi, Zhao Han, Yuan Wenjun**. *Measurements of underwater electroacoutic parameters*. Beijing: Ordnance Industry Publishing House, pp. 107-115, 2017. (In Chinese)

[2] **B. B. Bauer. L. A. Abbagnaro, J. Schumann**. Wide range calibration system for pressure gradient hydrophones [J]. *J. Acous. Soc. Am.*, 51(5), PT2, pp. 1717-1724, 1972.

[3] **V.E.Ivanov, V.A. Kirshov**. Calibration of acoustic vector receivers. *Measuring Technique*. 9, pp. 61-64, 1981

[4] **M. strasberg, F. Schloss**. Calibration of pressure gradient transducers in an oscillating liquid column. *J. Acous. Soc. Am.*, 54(2), pp.553,1973.

[5] **Mo Xiping, Wang Wenzhi, Zheng Shijie**. Calibration of hydrophone in a standing wave calibration system for dipole hydrophone. *Applied Acoustics*, 17(6), pp.158-160, 1998. (In Chinese)

[6] **A. E. Isaev, A. N. Matveev, G. S. Nekrich, A.M. Polikarpov**. Complex calibration of a pressure gradient receiver using the reciprocity method procedure. *Acoustical Physics*, 60(1), pp. 45-51, 2014.

[7] **A. E. Isaev, Chen Yi, A. N. Matveev, G. S. Nekrich, Fei Teng, Jia Guanghui**. Pilot comparisons of underwater sound particles oscillation velocity receiver calibrations in the frequency range from 5 Hz to 10 kHz (646/RU/14). *Measuring Technique*. To be published.

[8] IEC 60565:2016, *Underwater acoustics – Hydrophones – Calibration in the frequency range 0.01 Hz to 1MHz*. International Electrotechnical Commission, Geneva, Switzerland.

[9] JCGM 100:2008, *Evaluation of measurement data — Guide to the expression of uncertainty in measurement(GUM1995 with minor corrections)*

[10] **M. G. Cox**. The evaluation of key comparison data. *Metrologia*, 39, pp.589-595, 2002

MEASUREMENTS OF ACOUSTIC BACKSCATTERING FROM SYNTACTIC-FOAM SPHERES

Lian Sheng Wang and Stephen P. Robinson

National Physical Laboratory, Hampton Road, Teddington, TW11 0LW, UK

Lian.wang@npl.co.uk

Abstract: *Spherical targets were fabricated by machining syntactic foam samples from three products, HYTAC-W, HYTAC-WF, and HYTAC-XTL manufactured by CMT Materials, Inc. The compressional and shear wave speeds in the materials were determined by measurements. The nominal diameter of the spheres was 60 mm. Each sphere was held within its own minimum-knot bag woven of monofilament nylon and suspended in a laboratory tank during measurements in order to minimise the additional scattering effects.*

Acoustic backscattering was measured by ensonifying each sphere with a short-duration broadband signal generated with a monostatic transducer, spanning the respective frequency range 80-200 kHz. Measurements of backscattering by the syntactic foam spheres were accompanied by similar measurements made with a sphere made of tungsten carbide with 6% cobalt binder, with a diameter of 75 mm which has a known response in order to verify the measurements. Measured form functions are compared with model prediction using the acoustic properties measured previously in a separate study.

keywords: *syntactic foam; acoustic backscattering; standard calibration target*

1. INTRODUCTION

The standard-target method [1-5] is the most accurate, operationally convenient, rapid, and cost-effective method for calibrating active sonars, whether used for measurement or used for quantitative imaging.

Standard targets have been fabricated from diverse materials. For solid homogeneous elastic spheres, these materials have included, among others, electrolytic-grade copper [6], tungsten carbide with 6% cobalt binder [7], alternatively with nickel binder, steels [8], and an aluminum alloy [9]. For hollow elastic spheres, the shell materials have included aluminum [10-12] and alumina [13]. For fluid-filled focusing spheres, the shell materials have included steels [14-16]. Solid-layered spheres have also been fabricated for calibration purposes, witness those manufactured by Subsea Asset Location Technologies (SALT) Ltd., Portland, Dorset, UK. Other, non-spherical targets have also been fabricated.

The exemplified diversity of material types and sizes just for the spherical targets witnesses to needs. These include considerations of sonar transmit frequency and frequency band, constraints on target strength, transducer nearfield-farfield transition, ordinary operating

conditions at sea, and environmental conditions at the calibration site relative to those at the application site [17]. In every case, fabrication is a more or less complicated process that adds considerable value to the standard target, usually far in excess of the nominal cost of the material.

This study intends to determine the suitability of syntactic foam (SF) materials for use as a standard target as they are easy to machine and slightly buoyant. Three solid spheres were made of three syntactic foam materials with different mechanical and thermal properties. Three critical physical properties of each of three samples of syntactic foam were measured previously [18]. These were the mass density, compressional wave sound speed, and shear wave sound speed, assuming sample isotropy.

The goals of the present study are to measure the acoustic backscattering properties of three syntactic-foam spheres, and to compare the experimental results with the modelled results. Measurements in Acoustic Pressure Vessel with one of syntactic sphere will be reported in [19].

2. MEASUREMENT

Three product samples were provided by Engineered Syntactic Systems, CMT Materials, Inc., Attleboro, Massachusetts, USA. Each of these materials has other distinctive properties, for example, as quantified by thermal conductivity, thermal expansion coefficient, compressive strength, and flexural toughness, among other things.

They are HYTAC-W, HYTAC-WF and HYTAC-XTL, and referred to as W, WF and XTL hereafter. Their main physical characteristics are listed together with these measured physical properties: mass density, compressional wave speed, and shear wave speed, compressive strength Table 1. The wave speeds were measured at room temperature 20.5ºC. This assumes isotropy, which is plausible given the weakness of the observed anisotropy, less than 0.1% in two of the syntactic foams and perhaps as much as 2% in the third [18].

Three solid syntactic spheres with nominal diameters of 60 mm were fabricated from the bulk samples by machining. A precision sphere of tungsten carbide (WC) with 6% cobalt binder, with diameter 75 mm, was procured for comparative measurements. It is referred to as the WC sphere or WC75. Each sphere was bound in its own minimum-knot bag woven of monofilament nylon fishing line [4] to enable suspension.

The measurements of backscattering reported here were carried out in NPL's small open water tank (SOWT). The SOWT is 2.5 m x 1.5 m on the surface and 1.5 m deep. The measurements in SOWT were at a room temperature of 18.5°C.

Material	Density [kg/m^3]	Compressional wave speed [m/s]		Shear wave speed [m/s]		Attenuation [dB/λ]	
		measured	model	measured	model	compr-essional wave	shear wave
WC	14,900		6,853		4,171	0	0
W	716	2,110	2,118	1,121	1,100	0.2	0.9
WF	913	2,708	2,702	1,389	1,356	0.01	1.0
XTL	712	2,762	2,641	1,361	1,300	0.5	1.2

Table 1: *Physical properties of test spheres*

The experimental set-up to measure backscattering from the spherical targets is shown in Fig. 1. Short-pulse signals were used for the measurements in order to cover a large range in frequency. The transducer used provided good signal to noise ratio for the frequency band 80-200 kHz. All measurements were monostatic, with a single transducer used for both transmission and reception. The transmit signal consisted of a single cycle of a sinusoidal signal at 125 kHz generated by an Agilent 33220A signal generator coupled to a PA 400 (Precision Acoustics) power amplifier, thence a broadband transducer, the Reson TC-2130. This transducer is a piston type with a diameter of 50 mm.

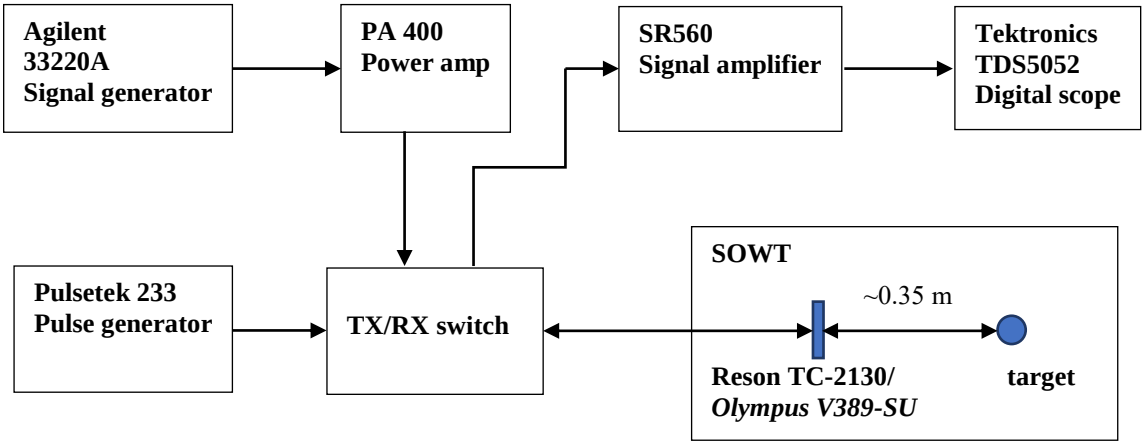


Fig. 2. Experimental set-up, where SOWT denotes the Small-Open-Water Tank

Because of the monostatic configuration with the transducer as both transmitter and receiver, a Pulsetek 233 pulse generator was used to control a TX/RX switch that short-circuited the input to the SR560 signal amplifier when the power amplifier was transmitting, and then connected it to the received signal from the transducer after a fixed time delay from the time of transmission. The received signals were filtered and amplified with the signal amplifier before being sent to the Tektronic TDS5052 digital scope to store the time waveforms of the measured signal for further processing. The signal waveforms were averaged typically 100 times in order to improve the signal-to-noise ratio.

Acoustic measurements were performed in SOWT on all three syntactic foam spheres. The water temperature was nearly constant at 18.5°C. Similar measurements were made with the 75-mm-diameter WC sphere, which has a known theoretical form function, for comparison purposes.

The acoustic results are expressed through a generalized form function, as in [5].

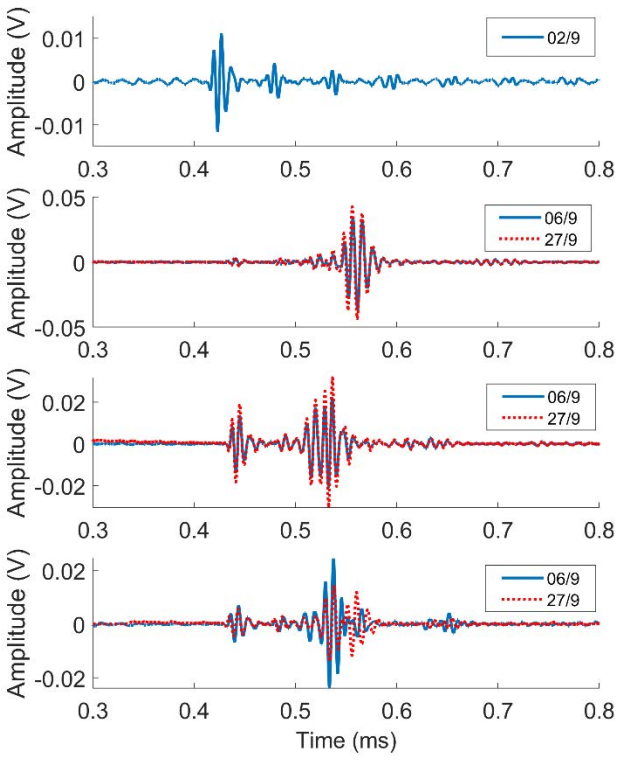


Fig. 1. Backscattering signal from target: WC, W, WF and XTL spheres from top to bottom plots

3. RESULTS AND DISCUSSION

Four spheres were ensonified in the frequency band 80-200 kHz using the TC2130 transducer in the SOWT. Echo waveforms are shown in Fig. 2 for WC75 and each of the three syntactic-foam spheres. These are duplicated for

measurements repeated on the SF spheres after 21-day immersion.

The expected periodical wave train of circumferential waves due to scattering by a sphere is observed with the WC75 sphere. The first echo in the wave train represents reflection from the front interface of the sphere. This echo is separated reasonably well from the second echo in the wave train. This first echo can be used as the incident wave at the target in the calculation of the form function [20]. There was only a single distinct and dominant echo from the W sphere. The width of the echo was greater than that of the first echo from the WC sphere, indicating a narrower frequency response for the W sphere. There were two echoes from the WF sphere, and the second one is higher than the first one. The first echo was almost a replica of the first echo by the WC75, while the second echo had a longer duration. There were three separate echoes from the XTL sphere, with much smaller first and third echoes in comparison with the second echo.

Measured form functions of the WC75 and the three SF spheres are shown in Fig. 3. The form function was also calculated by a model that is applicable to an elastic sphere with absorption [21] for comparison. The density and sound speeds of all the spheres are listed in Table 1 for the model. The agreement between the modelled and measured form functions is very good over most of the frequency band for the WC sphere. The modelled results are also in good agreement with measured results of W and WF spheres. However, there is much greater difference between the predicted and measured form functions for the XTL sphere, especially for the second measurement.

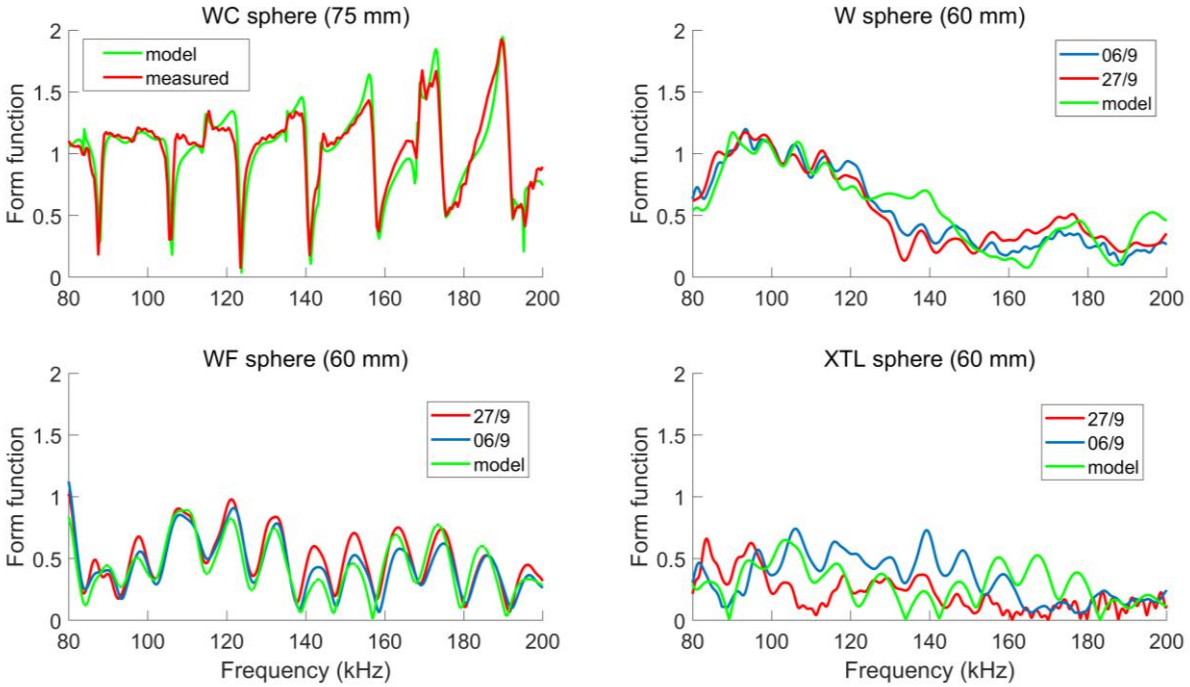


Fig. 3. Generalized backscattering form function of WC and three SF spheres

It was not unexpected that the backscattering from the three syntactic spheres was very different, because of the differences in their acoustic properties [18]. It is noticed that the W sphere shows a higher and relatively constant level of return over the frequency band 90-120 kHz than that at frequencies higher than 130 kHz. The relatively smaller bandwidth in the form function of the W sphere results in a longer pulse duration in the backscattered signal, as shown in Fig. 2. There are two dominant pulses in the reflected signal from the WF sphere in time domain, producing a periodical oscillation in its form function in the frequency domain as shown in bottom left plot of Fig. 3. The frequency span of the oscillation is about 10 kHz. The target echo is weakest from the XTL sphere in comparison with the echoes from the W and WF spheres.

Unlike metallic materials, the SF materials may be subject to water ingression while submerged. To examine the effects of water ingression into the materials, two measurements were carried out with a time span of 21 days, during which all three syntactic spheres remained submerged in water. There are reasonably good agreements among the measured data of the W and WF spheres over the time period. However, there are substantial changes between the two measurements of the XTL sphere both in time domain and in the frequency domain as shown in Fig. 3.

The acoustic scattering from an isotropic and homogenous spherical solid object depends only on its size, mass density, and sound speeds compared to the respective quantities of the immersion medium, namely water. This means that the bulk property of the XTL material changes with time of soaking as confirmed by the other tests [18]. It is likely that the sphere is still isotropic in its properties, but not homogenous, with presumed radial dependence. A surface layer with higher concentration of water was formed during the soaking, and the thickness of the layer should be a function of the soaking time. It can be seen that the form function from early measurement is closer to the predicted result as the effect of water ingression was less due to a short immersion time at the time of measurement, but there is little correlation between the second measurement and prediction because the prediction was only sensible with the initial acoustic properties before exposed to water. There was no or very little of water ingression into the W and WF spheres so that their backscattering responses remained reasonably constant.

4. SUMMARY

Experimental studies were performed to measure acoustic backscattering from three 60-mm-diameter spheres made of syntactic foams. Generalized form functions were determined over the frequency band 80-200 kHz.

The form functions from the three 60-mm-diameter syntactic-foam spheres are very different. The W and WF spheres are stronger targets than the XTL sphere. The W sphere showed little front interface echo, and it displayed a relatively flat response over the frequency band 90-120 kHz, while the WF sphere response was quasi-periodic, with period of order 10 kHz.

Both the W sphere and WF sphere showed stable backscattering strengths after long periods of immersion, while there were large changes with immersion time from the XTL sphere.

ACKNOWLEDGEMENTS

The authors are grateful to Kenneth G. Foote of WHOI who proposed the study. The following are thanked for sharing basic information on syntactic foams: Jim Teague of J. Teague Enterprises, LLC; Peter J. Fitzgerald and William J. Douglas, Global Dynamix; and Thomas J. Murray, Engineered Syntactic Systems, CMT Materials, Inc., who also generously provided the product samples that were measured in this study.

References

[1] K. G. Foote, H. P. Knudsen, G. Vestnes, D. N. MacLennan, and E. J. Simmonds, "Calibration of acoustic instruments for fish density estimation: a practical guide," *ICES Coop. Res. Rep.,* no. 144 (1987), 69 pp.

[2] K. G. Foote, D. Chu, T. R. Hammar, K. C. Baldwin, L. A. Mayer, L. C. Hufnagle, Jr., and J. M. Jech, "Protocols for calibrating multibeam sonar," *J. Acoust. Soc. Am.*, 117, 2013-2027 (2005)

[3] ANSI/ASA S1.20-2012, *American National Standard: Procedures for Calibration of Underwater Electroacoustic Transducers* (Acoustical Society of America, Melville, NY, 2012)

[4] D. A. Demer, L. Berger, M. Bernasconi, E. Bethke, K. Boswell, D. Chu, R. Domokos, A. Dunford, S. Fässler, S. Gauthier, L. T. Hufnagle, J. M. Jech, N. Bouffant, A. Lebourges-

Dhaussy, X. Lurton, G. J. Macaulay, Y. Perrot, T. Ryan S. Parker-Stetter, S. Stienessen, T. Weber, and N. Williamson, "Calibration of acoustic instruments," *ICES Coop. Res. Rep*., no. 326 (2015), 133 pp.
[5] K. G. Foote, "Standard-target calibration of active sonars used to measure scattering: Principles and illustrative protocols," IEEE J. Oceanic Eng., 43, 749-763 (2018); doi 10.1109/JOE.2017.2713538 [Date of Publication: 14 July 2017]
[6] K. G. Foote, "Optimizing copper spheres for precision calibration of hydroacoustic equipment," *J. Acoust. Soc. Am.*, 71, 742–747 (1982)
[7] K. G. Foote and D. N. MacLennan, "Comparison of copper and tungsten carbide calibration spheres," *J. Acoust. Soc. Am.*, 75, 612-616 (1984)
[8] Y. Miyanohana, K. Ishii, and M. Furusawa, "Spheres to calibrate echo sounders at any frequency," *Nippon Suisan Gakkaishi,* 59, 933-942 (1993)
[9] K. G. Foote, D. T. I. Francis, and P. R. Atkins, "Calibration sphere for low-frequency parametric sonars," *J. Acoust. Soc. Am.*, 121, 1482-1490 (2007)
[10] K. J. Diercks and R. Hickling, "Echoes from hollow aluminum spheres in water," *J. Acoust. Soc. Am.*, 41, 380-393 (1967)
[11] T. K. Stanton, D. Chu, J. M. Jech, and J. D. Irish, "A broadband echosounder for resonance classification of swimbladder-bearing fish," In: *Oceans 2007 MTS/IEEE Conference Proceedings*, 3 pp.; doi: 10.1109/OCEANSE.2007.4302346
[12] T. K. Stanton and D. Chu, "Calibration of broadband active acoustic systems using a single standard spherical target," *J. Acoust. Soc. Am.*, 124, 128-136 (2008)
[13] P. R. Atkins, D. T. I. Francis, and K. G. Foote, "Broadband ultrasonic target strengths of hollow ceramic flotation spheres," In: *Oceans 2007 IEEE Conference Proceedings*, 4 pp.; doi: 10.1109/OCEANSE.2007.4302487
[14] D. L. Folds and C. D. Loggins, "Target strength of liquid-filled spheres," *J. Acoust. Soc. Am.*, 73, 1147-1151 (1983)
[15] D. M. Deveau and A. P. Lyons, "Fluid-filled passive sonar calibration spheres: design, modelling, and measurement," *IEEE J. Ocean. Eng.*, 34, 93-100 (2009)
[16] D. M. Deveau and A. P. Lyons, "Corrections to 'Fluid-filled passive sonar calibration spheres: design, modelling, and measurement'," *IEEE J. Ocean. Eng.*, 34, 202 (2009)
[17] K. G. Foote, "Using a sonar in a different environment from that of its calibration: effects of changes in salinity and temperature," In: *Oceans 2018 MTS/IEEE Conference Proceedings*, 5 pp.; doi: 10.1109/OCEANS.2018.8604573
[18] L. Wang, K. G. Foote, P. D. Theobald, and S. P. Robinson, "Material properties of three syntactic foams," In: *Oceans 2017 MTS/IEEE Conference Proceedings*, 6 pp.; doi: 10.1109/OCEANSE.2017.8084739
[19] L. Wang, K. G. Foote and S. P. Robinson, "Acoustic backscattering spectra of three syntactic-foam spheres", IEEE Oceans 2019
[20] L. R. Dragonette, S. K. Numrich, and L. J. Frank, "Calibration technique for acoustic scattering measurements," J. Acoust. Soc. Am., 69, 1186–1189 (1981)
[21] Takahi Hasegawa, Yoshiko Kitagawa, and Yumiko Watanabe, "Sound reflection from an absorbing sphere," The Journal of the Acoustical Society of America 62, 1298 (1977); https://doi.org/10.1121/1.381629

ACOUSTC NOISE MEASUREMENTS OF VESSELS WITH ADAPTIVE CHANNEL EQUALISATION

Jens M Hovem, Hefeng Dong

Norwegian University of Science and Technology-NTNU, NO-7491 Trondheim, Norway

Jens M Hovem, Department of Electronic Systems, NTNU, NO-7491 Trondheim, Norway jens.hovem@ntnu.no

Abstract:

This paper reports on recent measurements and analysis of acoustic noise of fishing vessels. The measurements were conducted according to internationally accepted standards with a hydrophone close to the bottom and with the vessel following straight tracks of 1-2 km and passing the hydrophone at a distance of about 100 - 200 m distance. The measurements confirm that with a shallow source, as a surface vessel, the Lloyd's mirror effect, which is caused by interference between a direct arrival and a surface reflected arrival. A novel technique is presented for adaptive calibration for the Lloyd's mirror effects in noise measurement of noise from surface vessels. This technique uses a probe signal and signal processing combined with propagation modelling to estimate the actual underwater acoustic channel thereby reducing the distortion effects on the measured noise spectrum. The paper presents the concept and demonstrates the feasibility by using data from a recent sea trial.

Keywords: *Acoustic noise, channel estimation, Lloyd's mirror effects, fishery acoustics*

1. INTRODUCTION AND MOTIVATION

This contribution concerns measurement and characterization of underwater acoustic noise from vessels in general, but mainly from fishing vessels. The motivation for this work is that self-noise from fishing vessels may affect the catch rate. Equally important is to find the origins of the generated noise: whether the noise is coming from the propeller, the machinery or from vibration in the hull. The focus is on low frequencies since most of the commercial species of fish are sensing sound mainly at frequencies below 300 Hz.

2. NOISE MEASUREMENTS OF VESSELS

The standard way for noise measurement [1] is to let the vessel passing a fixed hydrophone on the bottom and the sailing tracks may extend to distance of about 1500 m of either side of the hydrophone position. Figure 1 shows one of the measured vessel and example of the sailing tracks. Figure 2 shows a 1200-second of one of the recordings and the highlighted 30-second section that is normally used and analysed in third octave bands, also displayed in the figure taken from [2].



Figure 1 Fishing vessel Kongsfjord (left) and sailing tracks during recordings (right).

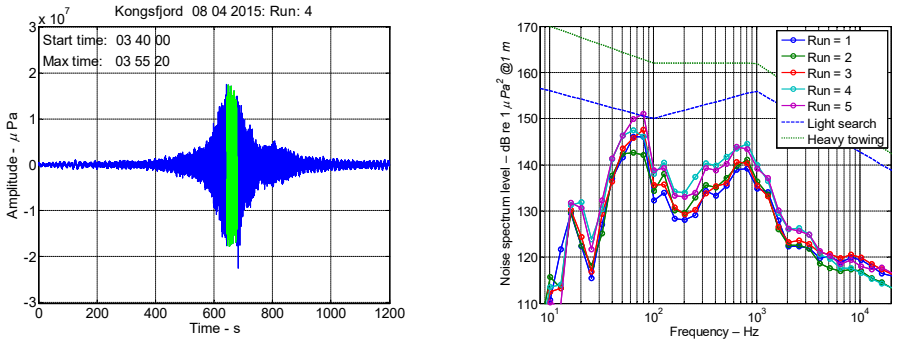


Figure 2.recorded signals of length 1200 second with the 30-second window (left) analysed in third octave bands (right).

Many species of fish can hear quite well, and this is also true for codfish having maximum hearing sensitivity in the frequency band of 30 Hz to 300 Hz as shown in Figure 3 (left) taken from [3, 4]. Since the project focusses on fishery acoustics, this band is subjected to high-resolution spectra analysis. The example in Figure 3 (right) shows the results of 1/24 octave analysis. It shows that the dominating noise is spectral lines in the frequency range of maximum sensitivity of cod. Many of these are caused from resonance of the outer plates of the hull, but some also come from multipaths propagation.

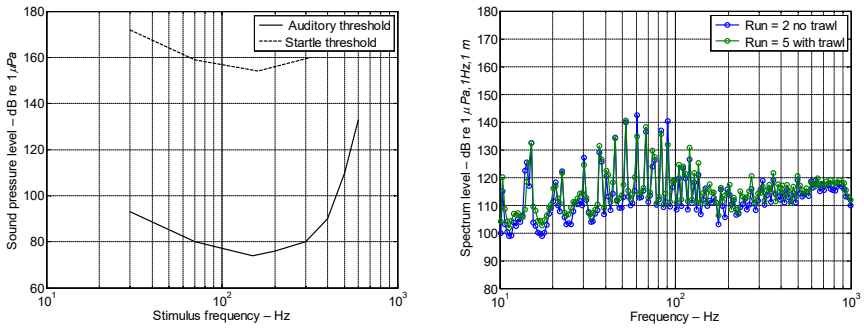


Figure 3 Auditory and startle threshold for Atlantic cod (left) and high resolution spectral analysis of noise in frequency band that the fish can hear (right).

2.1. Normalization and correcting for propagation effects

To correct for varying the distance between the vessels and hydrophone current practice is to assume geometric spreading of 20 log (r) or 18 log (r) [1]. This method for distance correction does not take account of varying oceanographic conditions and frequency dependency, which is demonstrated by Figure 4 showing calculated transmission loss in dB as function of range for some selected frequencies. The calculation shows the interference effect between a direct and a surface reflected under ideal conditions for a source depth of 5 m, receiver at the bottom at 140 m. Above the range of 100 m the transmission loss vary strongly with range and frequency. This variation is the Lloyd's mirror caused by interference between surface reflected and direct sounds. Normally the distances between vessel and measuring hydrophone is short, 100 to 200 m and the simple geometrical spreading are sufficient, but at longer distances this is not the case.

Figure 5 shows the measured level as function of position for some frequencies of interest for fishing. The dotted line represents level reduction of 40log(r), which is expected when the Lloyd's mirror effect is predominate. The measurements confirm that with a shallow source, as a surface vessel, the Lloyd's mirror effect is very important for the propagation of self-noise and therefore important for fishing. The implication of Figure 3 and 5 is that the fish is capable of hearing the vessel at a distance of 1000 m when the ambient noise from other natural or manmade sources is low. Note that this hearing range is considerably shorter than expected from using a level reduction of 20log(r).

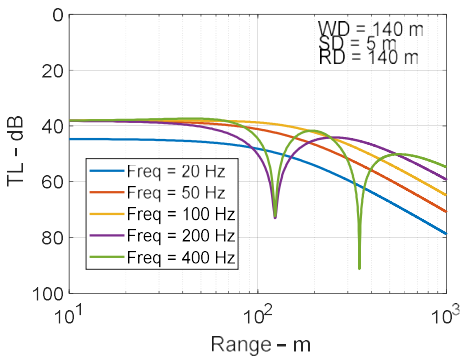


Figure 4 Transmission loss from a source at 5 me depth to a receiver at the bottom at 140 m as function of range and frequency

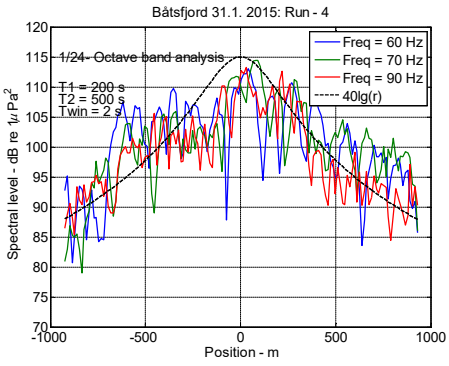


Figure 5 Measured levels in 1/24 octave bands as function of distance for selected frequencies.

3. ACOUSTIC CHANNEL ESTIMATION USING A PROBE SIGNAL

This section describes the method for acoustic channel estimation using a probe signal and matched field technique by correlating the received noise with a replica of the probe signal. The matched field output gives information of the acoustic channel impulse response. The vessel to be measured is towing an acoustic source at depth of a few meters and sending a probe signal at pre-set intervals. The probe signal should preferably be low level to avoid contaminating the noise measurement and low frequency to obtain channel estimates at frequency band of fish hearing according to Figure 3. These are conflicting requirements that cannot be satisfied at reasonable costs and size of transducer and towing gear. On the other hand, there are also relaxing arguments since the geometry is relatively simple. The noise source of the surface vessel is limited to a depth of a few meters and hydrophone is placed close to the bottom, which gives a simple multipath interference and Lloyd's mirror effects.

Figure 6 shows simulated results using the propagation program PlaneRay [5] of eigenrays from a transmitter at 7 m depth to a receiver 5 m above the bottom at a horizontal distance of 400 m. The sound reaches the receiver after two or more reflections from the surface or the bottom. Figure 7 shows two examples of impulse response to a receiver 5 m above the bottom. The first two arrivals arriving with a very short time separation are the direct and surface reflected paths, and the later are from rays with multiple reflections from surface and bottom. The amplitudes of these depends on the bottom composition, Figure 7 shows the cases of hard and soft bottoms.

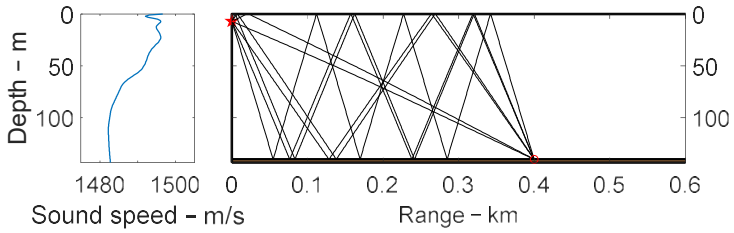


Figure 6 Eigen rays to a distance of 400 m to a receiver at 5 m above the bottom.

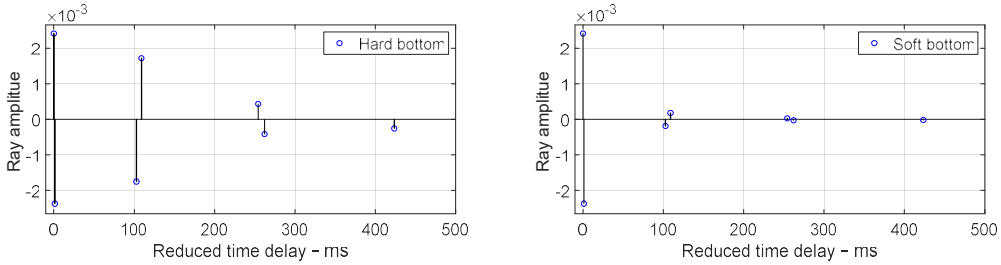


Figure 7 Impulse responses to a hydrophone at distance of 400 m received by a hydrophone 5 m above a hard bottom (left) and a soft bottom(right)

4. EXPERIMENTAL RESULTS

A sea trial was conducted in Trondheim fjord in September 2018 using the NTNU research vessel R/V Gunnerus. The main purpose was to test the concept of using a probe signal for automatic channel estimation, but also to measure the coherence of the direct arrivals compared with the surface reflected arrivals. The vessel moved at a speed of approximately 2 knots while towing a source (SonoTube 008/D13-DT from CTG) transmitting a one-second long linear FM sweep with nominal bandwidth from 7 kHz to 17 kHz and repeated every 10 second. The

processing gain of a FM sweep is 10 $\log_{10}$(TB) giving a potential processing gain about 40 dB but the actual processing may be lower. The time resolution is proportional to 1/*B*. The maximum time difference between the surface reflected and a direct arrival assuming a source depth of 7.5 m is 10 ms, but the difference reduces to zero at very large distances. The time resolution should be short enough to resolve the multipath structure and with this choice the time resolution of about 0.1 ms is sufficient for the purpose.

Figure 8 shows a section of 10 seconds duration of the received signal at a hydrophone near the bottom and the frequency spectrum of the same section. The selected section is marked with time of the record position determination using ship navigation log. As can be seen the probe signal dominates over the background noise and noise from the vessel. The frequency spectrum varies from a maximum of about 7 kHz dropping gradually to about 17 kHz as expected. The peaks outside this band is probably coming from the research vessel or from other manmade sources in the area. Important to observe that the levels in amplitudes in the two plots of Figure 8 are before the processing gain applies.

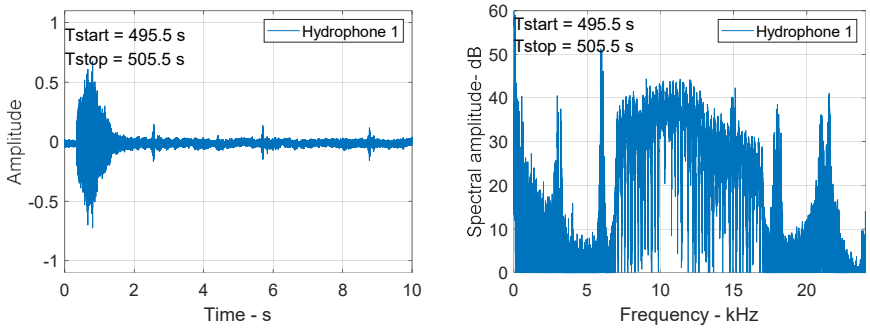


Figure 8. Selected window of 10 seconds and its frequency spectrum

For the matched filter processing a window of length 2 seconds at the beginning of the record is chosen and correlated with the FM sweep signal generated numerically and inputted to the source transducer. Figure 9 shows the cross-correlation between a section of length 2 ms of the received signal and a replica of the probe signal. The first two responses represent, respectively, the direct signal and the reflection from the surface. The rest of the response represents other reflections, but these are insignificant in comparison. Amplitudes of the plots are normalized such that with perfect correlation of one, but the actual value is about 0.4. The main reasons for the reduced amplitude is that the replica used in the correlation is the computer-generated signal input to the transducer and not the signal in the water.

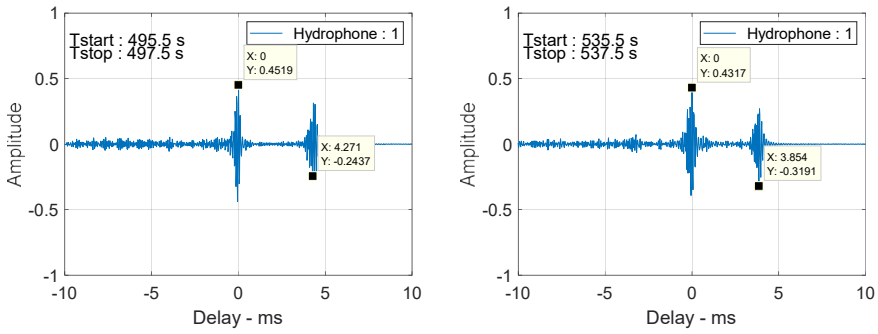


Figure 9 Matched filter output for a hydrophone 5 m above the bottom for two positions of the vessel separated in time of 40 seconds.

5. A SIMPLE CHANNEL MODEL

The simple channel assumes that the channel is two delta functions separated in time with dt and with amplitudes y_1 and y_2. Using the amplitude values found in the two cases in Figure 9 gives the result shown in Figure 10. The curves represent the correction to transmission loss due to the Lloyd's mirror effect in addition to geometric spreading loss. For low frequencies in the range of 10 Hz to 200 Hz the corrections are from -15 to 0 dB, for higher frequencies the corrections oscillate significantly. This agrees with the measured results in Figure 5 and confirms that the Lloyd's mirror effect is important for the hearing range of fish at low frequencies.

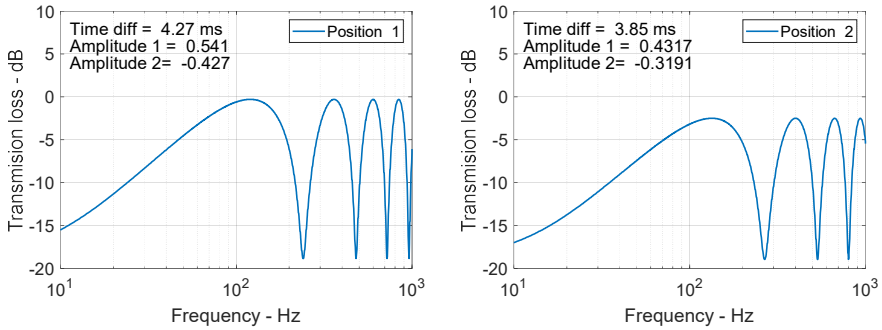


Figure 10 Correction in dB to the transmission loss caused by the Lloyd's mirror effect.

6. SUMMARY AND CONCLUSIONS

For measuring the self-noise of vessels, it is important to account for propagation effect of the propagation channel, which depends on the environmental conditions, the range depth and frequency in a way that is difficult or impossible to control. This paper has presented some preliminary works on using a probe signal and matched filtering for adaptive channel estimation in order to reduce the distortion effects on the measured noise spectrum. The paper presents the concept and demonstrates the feasibility by using data from a recent sea trial.

REFERENCES

[1]Rules for Classification of ships, Part 6 Chapter 2. Silent Class Notation, January 2010, DNV GL.

[2]Hovem, J. M., Sørheim , H., Haukebø, B., and Vågsholm, R. Measuerements and analysis of underwater acoustic noise of fishing vessels. OCEANS'15 MTS/IEEE ,Genova, May 18-21, 2015.

[3] Chapman, C. J. and A. D. Hawkins, (1973) A field study of hearing in the cod, Gadus morhua. L. J. Comp. Physiol., vol. 85: p. 147-167.

[4] Karlsen, H. E., W. Piddington, P. S. Enger, and O. Sand, *Infrasound initiates directional fast-start escape responses in juvenile roach Rutilus rutilus.* J. Exp. Biol., 2004. 2007(4185-4193).

[5] Hovem, Jens M.(2013) *Ray Trace Modeling of Underwater Sound Propagation,* in Marco G. Beghi (ed) "Modeling and Measurement Methods for Acoustic Waves and for Acoustic Microdevices", ISBN 978-953-51-1189-4, InTech - Open Access Publisher, Rijeka, Croatia.

Structured Session 3

Acoustic Monitoring of Ocean Environments and Processes: Biology, Ecology, Geophysics and Man-made activities

Organiser(s): Ratilal Purnima, Miksis-Olds Jennifer

Mechanoreceptors in Early Developmental Stages of the Pycnogonida

John A. Fornshell * [a]

[a] U.S. National Museum of Natural History

Department of Invertebrate Zoology
Smithsonian Institution
Washington, D.C.
USA

*Correspondence: johnfornshell@hotmail.com; Tel. (571) 426-2398

ABSTRACT Members of the phylum Arthropoda detect fluid flow and sound/particle vibrations using sensory organs called sensilla. These sensilla detect sound/particle vibrations in the boundary layer. In the present study, archived specimens from the United States National Museum of Natural History were examined in an effort to extend our knowledge of the presence of sensilla on the early post hatching developmental stages, first and second instars, of pycnogonids. In the work presented here we look at three families, four genera and ten species of early post hatching developmental stages of sea spiders. They are Family Ammotheidae, *Achelia cuneatis* Child, 1999*, Ammothea allopodes* Fry and Hedgpeth, 1969*,* Ammothea carolinensis Leach 1814, *Ammothea clausi* Pfeffer, 1889, *Ammothea striata* (Möbius, 1902)*,* Family Nymphonidae, *Nymphon grossipes* (Fabricius, 1780)*, N. australe* Hodgson, 1902*, N. charcoti* Bouvier, 1911*, N. Tenellum* (Sars, 1888) and Pycnogonidae, *Pentapycnon charcoti* Bouvier, 1910. Electron micrograph images of these species were used to identify and describe the sensilla present.

Most body organs such as mouthparts, the eye tubercle, appendages and spines are proportionally much smaller in the early post hatching developmental stages compared to their size in the adults, while the sensilla are comparable in size and shape to those found on the adults. In the first instar of *Pentapycnon charcoti* sensilla are present, but not in the adult. The sensilla have an external morphology homologous to the sensilla found on adult pycnogonids. The sensilla shaft lengths are tens of microns and two to seven in number. It is only possible to establish the presence of sound detecting sensilla. Their functionality remains to be established in future experimental work. Theoretical detection ranges of 1 to 100 m and 10 to 1 kHz are possible.

Key Words*: mechanoreceptors, Pycnogonida, Protonymphon, Sensilla*

Introduction

Members of the phylum Arthropoda detect sound energy using sense organs classed as mechanoreceptors on the surface cuticle of the animal. These same sense organs may also detect tactile signals and particle motion, fluid flow patterns and sound energy. The sensory inputs from these mechanoreceptors assist the animals in the detection of prey organisms, potential predators and mates [1-7]. Chemical sensory organs have also been described from the cuticle of arthropods [4 & 8]. These sensory sensilla termed filiform hairs in insects, trichobrothria in

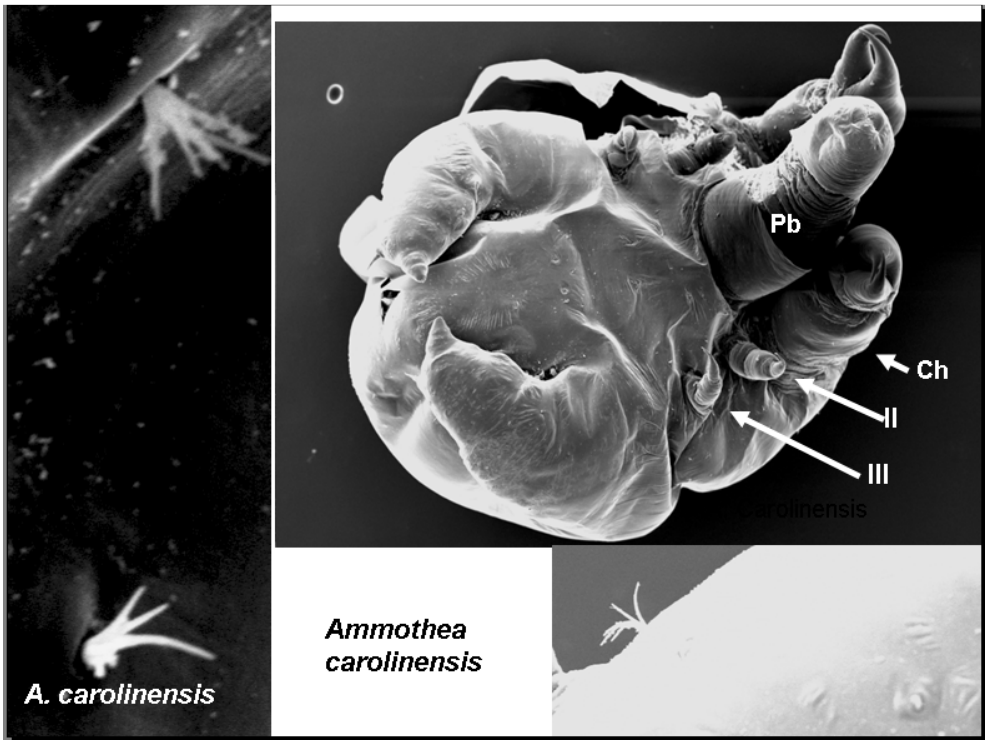


Fig. 1. The large image in the upper right is the 550 µm long second post hatching stage of *Ammothea carolinensis* Leach 1814 as seen in a ventral view. Pb= the proboscis; Ch= the cheliphore(s); II= the second larval appendage or larval palps; III= the third larval appendage or larval ovigerous appendage. The image on the left side shows two five (5) branched sensilla found on the cheliphores. The bottom right image is the same sensilla as seen from a side view.

arachnids and peg sensilla in crustaceans have been described in the scientific literature for over 130 years [8-12]. Sensory sensilla have been reported for the early developmental stages of two genera and four species of sea spiders [13 & 14].

Sea spider reproductive biology is unique among the invertebrates in several ways. Sexually mature male and female spiders release their gametes into the aquatic environment where

external fertilization occurs. The males then use special appendages called ovigerous appendages to collect the fertilized eggs, which are carried by the male until they hatch. If the newly hatched sea spiders receive any post hatching care it is provided by the male [15, 16 & 17]. There are six developmental patterns observed in the Pycnogonida [17 & 18]

Methodology

Archived specimens of pycnogonid early developmental stages from the collections of the National Museum of Natural History, Smithsonian Institution were used in this study. Larvae were recovered from the ovigers of adult male specimens. The specimens were critical point dried and coated with gold alloy for the scanning electron micrographs. A Phillips Electron

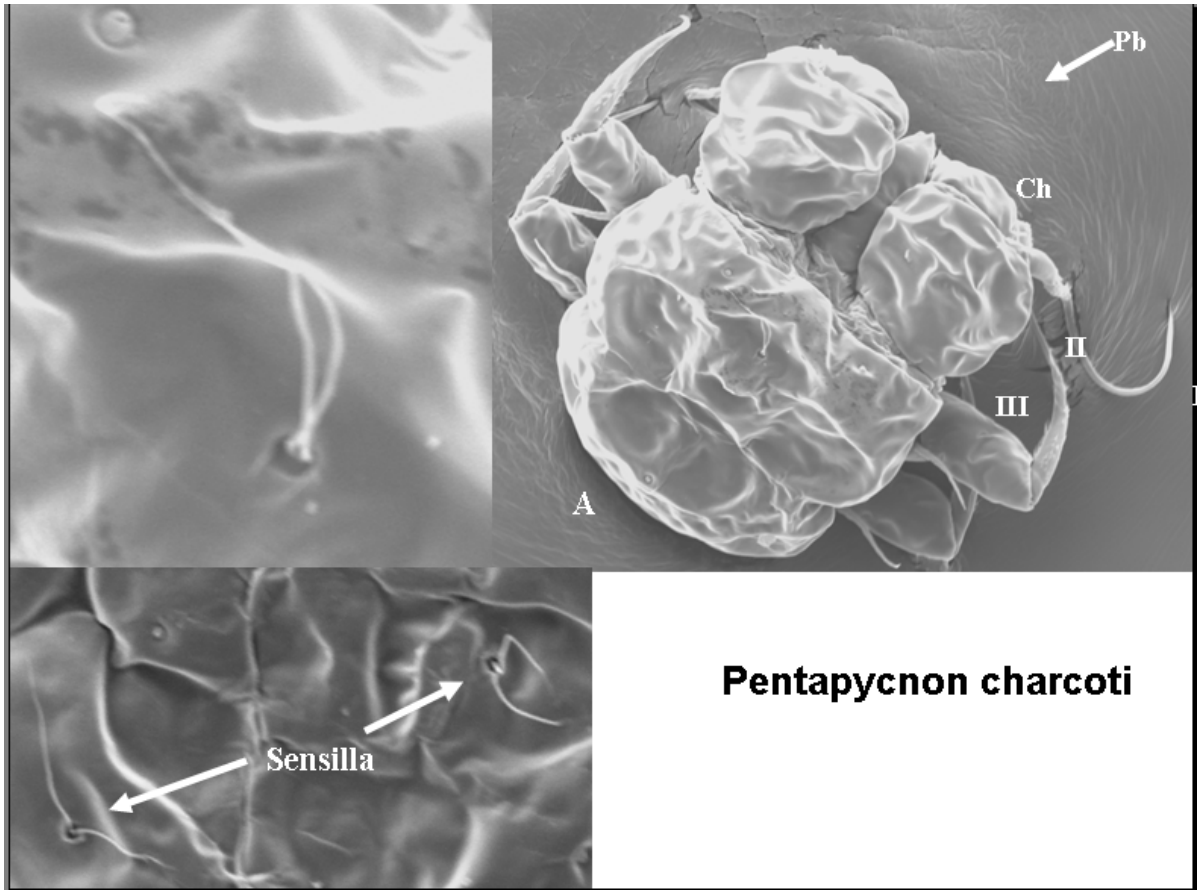


Fig. 2. Images A shows a dorsal view of the 141 µm long the first post hatching stage of *Pentapycnon charcoti*. Pb= the proboscis; Ch= cheliphore(s); II = Second larval appendages or larval palps; III= the third larval appendages or larval ovigerous appendages. The sensilla are found on the dorsal side of the body.

Microscope was used in this study. The length of the sensilla and diameter of the socket was measured on the electron micrographs. A total of 48 images of 25 specimens were analyzed in this study [18 & 19].

Results

The mechanoreceptors found on the early post hatching developmental stages of 10 species representing four genera and three families of sea spiders had socket diameters ranging from 1 µm to 8 µm; with shaft lengths ranging from 5 µm to 39 µm and 2 to 6 shafts (See Table 1).

Mechanoreceptors called sensilla were found on the cuticle of Family Ammotheidae, *Achelia cuneatis* Child, 1999*, Ammothea allopodes* Fry and Hedgpeth, 1969*, Ammothea carolinensis* Leach, 1814 (See Fig. 1), *Ammothea clausi* Pfeffer, 1889, *Ammothea striata* (Möbius, 1902), Family Nymphonidae, *Nymphon grossipes* (Fabricius, 1780)*, N. australe* Hodgson, 1902*, N. charcoti* Bouvier, 1911 (See Fig. 3)*, N. Tenellum* (Sars, 1888) and Pycnogonidae, *Pentapycnon charcoti* Bouvier, 1910 (See Fig. 2). The sensilla were located on the cheliphores (See Fig. 1-3) and dorsal surface) of the early post hatching stages of members of these three families, four genera and eight species.

The external form of the mechanoreceptors is the same as those described in adult sea spiders other chelicerates, crustaceans and insects [1-4, 8-13 & 22]. Electron micrographs showing the morphology of the early post hatching stages of sea spiders and their mechanoreceptors are provided in Figures 1-3.

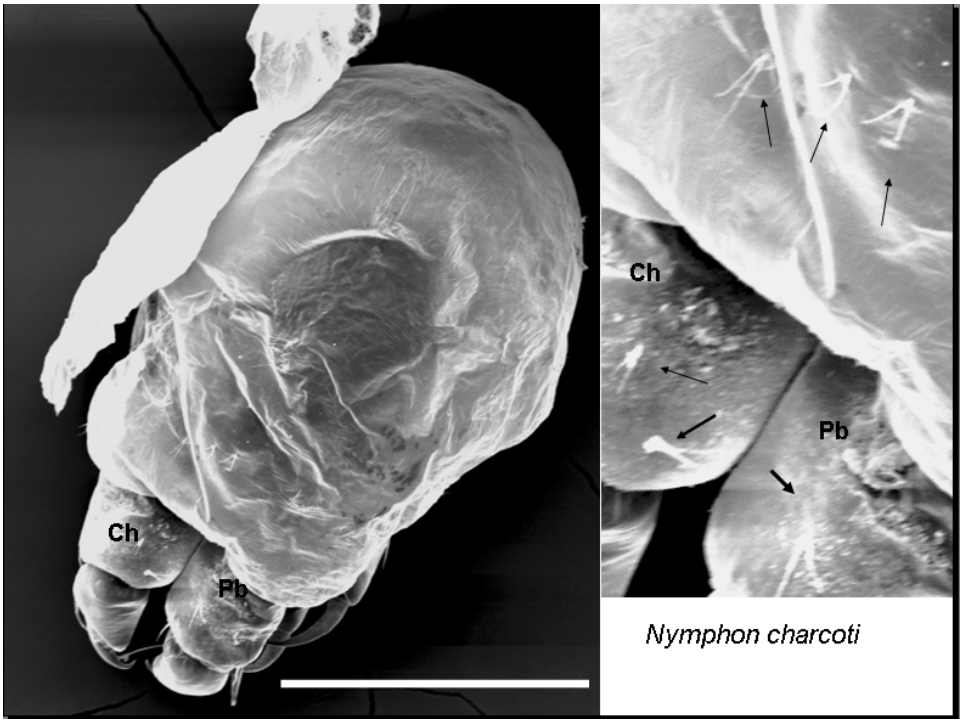


Fig. 3. *Nymphon charcoti* First post hatching stage on the left. Ch= cheliphore(s); Pb= proboscis. The scale bar is 200 µm. The arrows show the bifurcated sensilla on the dorsal side of the animal on the cheliphores and proboscis.

Discussion

The sensory organs on the early post hatching stages of sea spiders described in this study are of the fluid flow type described in the literature. They are composed of hair-like projections extending from a socket in the cuticle [9 & 10]. The hair-like shaft functions as a leaver responding to viscous forces in the water. The movements of the base end of the shaft stimulates

one or more neurons which, signals indicating the velocity, direction and acceleration of the water particles [7]. The sensing of fluid particle motion, that is, acoustic vibrations occurs in the boundary layer. The boundary layer in aquatic organisms is thinner than in air, on the order of 100 µm resulting in sensilla 10s of µm in length [20]. Homologous organs in crustaceans have been shown to detect sound frequencies between 10 Hz and 1 kHz. The detection ranges vary from approximately 1 m to 100 m [2 & 7]. Sea spiders have mechanoreceptors like those described above with sensilla attached to bi-polar neurons [10, 12 & 21]. The size and form of these sensilla are comparable to those found in adult specimens of sea spiders. Alexeeva et al. [14] have shown that the bifurcated sensilla of *Nymphon brevirostre* early post hatching stages have a bipolar neuron linked to the central nervous system. From this it may be inferred that at the time of hatching these sensory organs are in fact functional [21]. The functionality of these sensilla as mechanoreceptors is somewhat problematical due to the fact that at the time of hatching embryonic development is still incomplete [22].

Species	**Socket**	**Number of shafts**	**Shaft length**
Achelia cuneatis	3 µm	4	16 µm
Ammothea allopodes	1.0 µm	6	9 µm
Ammothea carolinensis	1.0 µm	5	8 µm
Ammothea clausi	4.0 µm	2	39 µm
Ammothea glacialis	8.0 µm	5	5.0 µm
Ammothea striata	3.6 µm	4	10 µm
Nymphon australe	5.0 µm	2	16 µm
Nymphon charcoti	4.0 µm	2	36 µm
Nymphon grossipes	2.6 µm	2	39 µm
Pentapycnon charcoti	2.0 µm	2	16 µm

Table 1. Showing the socket diameter, number of shafts and shaft length of mechanoreceptors found on early post hatching developmental stages of pycnogonids.

The developing body structures such as appendages and the other sense organs like the eyes are proportionally small in the early developing stages. The mechanoreceptors, by comparison, are formed in the size and shape found in the adults [20]. Whether such sensory sensilla are functional in detecting sound energy in the form of particle vibrations is not yet established.

Acknowledgements: I wish to thank Mr. Scott Whittaker of the National Museum of Natural History Imaging Laboratory for assistance with the electron microscope work. Also thanks are due to Mrs. Elvie T. Fornshell for editorial comments.

References

[1] **Trauntz, J., & Sandeman, D. C.** The detection of water born vibrations by sensory hairs On the chelae of the crayfish. Journal of Experimental Biology, **88**: 351-356, 1980.

[2] **Derby, C. D**. Structure and function of cuticular sensilla of the lobster *Homarus Americanus*. Journal of Crustacean Biology, **2** (1): 1-21, 1982.
[3] **Kiel, T. A.** Functional morphology of insect mechanoreceptors. Microscopy Research And Technique, **39** (6): 506-531, 1997.
[4] **Iwasaaki, M., Itoh, T. & Tominaga, Y.** VI Mechano-and Phonoreceptors. In: Atlas of Arthropod Sensory Receptors. Springer Press, 1999.
[5] **Barth, G. G.** Spider mechanoreceptors. Current Opinion in Neurobiology, **14**: 415-422, 2004.
[6] **Popper, A. R., Salmon, M. & Horch, K. W.** Acoustic detection and communication by Decapod crustaceans. Journal of Comparative Physiology, **187**: 83-89, 2001.
[7] **Casas, J. & Dangles, O**. Physical ecology of fluid flow sensing in arthropods. Annual Review of Entomology, 505-520, 2010.
[8] **Stock, J. H.** Experiments on food preference and chemical sense in Pycnogonida. In "Sea Spiders (Pycnogonida)". Zoological Journal of the Linnean Society of London, 63: 59 -74, 1978.
[9] **Dohrn, A.** Die Pantapoden des Golfes von Naples und der angrenzen Meeresabachunitte. In: Monographis der fauna und flora des Golfes von Naples, **Vol.** 3, pp.1-252. Wilhelm Englemann, Liepzig 1881.
[10] **Helfer, H. & Schlottke, E.** Pantapoda. In: Klassen und ordnungen des tierreichs (H. G. Bronns, ed.), **Vol.** 5 Abteilung 1 Buch 2, pp.1-314. Akademische Verlagsgesellschaft, Leipzig, 1935.
[11] **Brenneis, G.** Pycnogonida (Pantapoda). In: Structure and evolution of invertebrate nervous systems (A. Schmidt-Racsa, S. N. Harzsch, & G. Purschke, eds.) pp. 419-427, 2016.
[12] **Lehmannm, Heβ. M. & Meizer, R.** Sense organs in Pycnogonida: A review. Acta Zoologica, **Vol.** 98: 1-2, 2017.
[13] **Bogomolova, E. V.** Larvae of three sea spiders of the genus *Nymphon* (Arthropoda: Pycnogonida) from the White Sea. Invertebrate Zoology, **Vol.**33: 145-160, 2007.
[14] **Alexeeva, N., Bogomolova, E., Tamburg, Y. & Shunatova, N.** Oligomeric larvae of the pycnogonids revisited. Journal of Morphology, 278(9):1284-1304 (Arthropoda: Pycnogonida) from the White Sea. Invertebrate Zoology, 33 (3): 145-160, 2017.
[15] **King, P. E.** *Pycnogonids*. St Martens Press, 1973
[16] **Bain B. A.** Larval types and a summary of postembryonic development within the pycnogonids. Invertebrate Reproduction and Development, 43, 193-222, 2003.
[17] **Brenneis, G., Bogomolova E. V., Arango, C. P. & Krapp F.** From egg to "no-body": an overview and revision of developmental pathways in the ancient arthropod lineage Pycnogonida. Frontiers in Zoology, 14, 1-22, 2017.
[18] **Fornshell, J. A.** Larval stages of two deep-sea pycnogonids. Invertebrate Zoology, 12, 197–205, 2015.
[19] **Fornshell, J. A.** Larval stages *Nymphon charcoti* Bouvier 1911. Arthropods. (ISSN 2224-4255), 6, 1-7, 2017.
[20] **Rienstra, S.W. & Hirschberg, A.** *An Introduction to Acoustics*. Eindhoven University of Technology, 2016.
[21] **Fornshell, J. A. & Harlow, A. P.** Mechanoreceptors in pycnogonids (Arthropoda: Pycnogonida). Journal of Crustacean Biology, **Vol. 38** (3); 385-387, 2018.
[22] **Fornshell, J. A.** Early post hatching stages of *Nymphon australe*. . Arthropods. (ISSN 2224-4255), In Press.

Observations of the Sounds Produced by Swimming in the Spanish Lobster, *Scyllarides aequinoctialis* (Lund, 1793)

By

John A. Fornshell *[1]

[1.] U.S. National Museum of Natural History
Department of Invertebrate Zoology
Smithsonian Institution
Washington, D.C.
USA

*Correspondence: johnfornshell@hotmail.com; Tel. (571) 426-2398

ABSTRACT The objective of this research project was to study sound production by members of the Scyllaridae, slipper lobsters, specifically the Spanish Lobster *Scyllarides aequinoctialis* (Lund, 1793) when swimming at or near the surface. This is the first published record of swimming sounds produced by slipper lobsters. Analysis of recordings of swimming sounds produced by *S. aequinoctialis* in the laboratory indicates a peak of energy in the range of 100 Hz to 1.0 kHz with higher harmonics. The swimming sounds are co-incidental noise produced by slipper lobsters swimming near the surface. Such sounds may have significance for these animals.

Spiny lobsters and clawed lobsters produce sounds with a wide range of frequencies and amplitudes. Some of these sounds function as a means of communication with conspecifics. Others produce sounds to ward predators. Incidental sounds produced by feeding, walking or other biological processes may still be significant. Sensory organs that could detect particle motion at short ranges, millimeters to meters, are found on many decapod crustaceans.

Key Words: *Scyllarides aequinoctialis; of Scyllarides latus; bio-acoustics; noise;*

INTRODUCTION

The ability of spiny lobsters to produce sounds has been well established in the literature for over 134 years. The work of Parker [1] was the first to recognize the existence of two distinct groups of Palinuridae, spiny Lobsters, one producing sounds, the Stridentes, and the other lacking sound producing organs, the Silentes. George and Mann [2] reviewing the literature proposed a widely accepted evolutionary tree recognizing the two groups of spiny lobsters based on their sound production apparatus, termed Slip-stick, on the second antennae and carapace. The production of sounds in palinurid lobsters is a significant part of their anti-predator behavior [3]. Patek and Baio [4] greatly extended the work of Parker [1] and George and Mann [2] on Spiny lobster sound production. Reviewing the fossil record, Senter [5] concluded that stridulating insects first evolved in the Triassic and parallel evolution of stridulations occurred

multiple time in the Malacostraca. The existence of the primordia of sound producing organs on the phyllosoma larvae of some slipper lobster species indicates that the ability to produce sounds may have evolved at a very early stage in the evolution of the achelate lobsters [6].

There are no known examples of research establishing the ability to produce sound in the family Scyllaridae, slipper lobsters, however, Lavalli, and Spanier [7] offer anecdotal evidence, for sound production in *S. latus* Latreille, 1803, but state that there is no morphological evidence for sound producing organs like that in spiny lobsters. Spanier et al. and Spanier and Lavalli, [8 & 9], describe the swimming of the Mediterranean slipper lobster, *S. latus* in detail. They did not record any observations of sound production by swimming Nauen and Shadwick, [10] described the very similar swimming mechanics in the California spiny lobster *Panulirus interruptus* (Randall, 1840) providing more information on the actual energetics of the process, but again there is no mention of sound production in their study. In all of these descriptions of swimming achelate lobsters, the animals were not swimming at the surface as in our observations [9 & 10]. The objective of this research project was to study sound production by Scyllaridae, slipper lobsters, specifically *Scyllarides aequinoctialis* (Lund) when swimming at or near the surface.

MATERIALS AND METHODS

Live specimens of *S. aequinoctialis* were maintained in a 15 L aquarium at salinities between 34 $^{0}/_{00}$ and 36 $^{0}/_{00}$. Recordings of the sounds produced by were made in a shallow tank 50 cm X 80 cm with water depths of 15 to 20 cm. The recordings were made using a Cermic ER-M3 omnidirectional microphone with a diameter of 9.7 mm and length of 7.0 mm. The sensitivity of the microphone was – 58 dB to 3 dB. The frequency range was 0.10 to 16 kHz and the signal to noise ratio was 60 dB. A spectrogram of the background noise is shown in figure 1. The loudest noise is represented by red color with decreasing amplitudes represented by green, blue and violet. Only signals higher in intensity than the maximum background noise were considered to be produced by the swimming of the lobsters. The lobsters were not forced to swim, consequently the recording times varied with more than ten seconds elapsing before the animals began to swim. Both spectrograms and direct recordings of the sounds were produced.

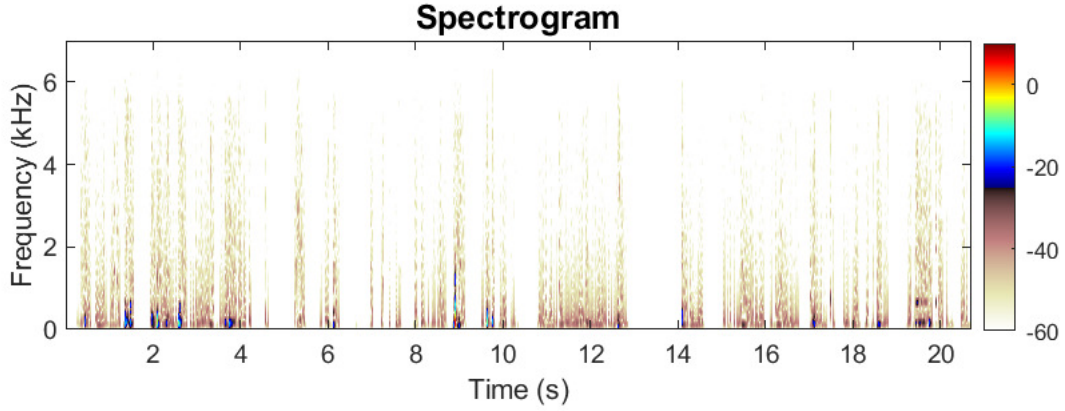


Figure 1. Background noise in the tank where all recording of the swimming animals were made. The residual noise may be due to small movements of the microphone.

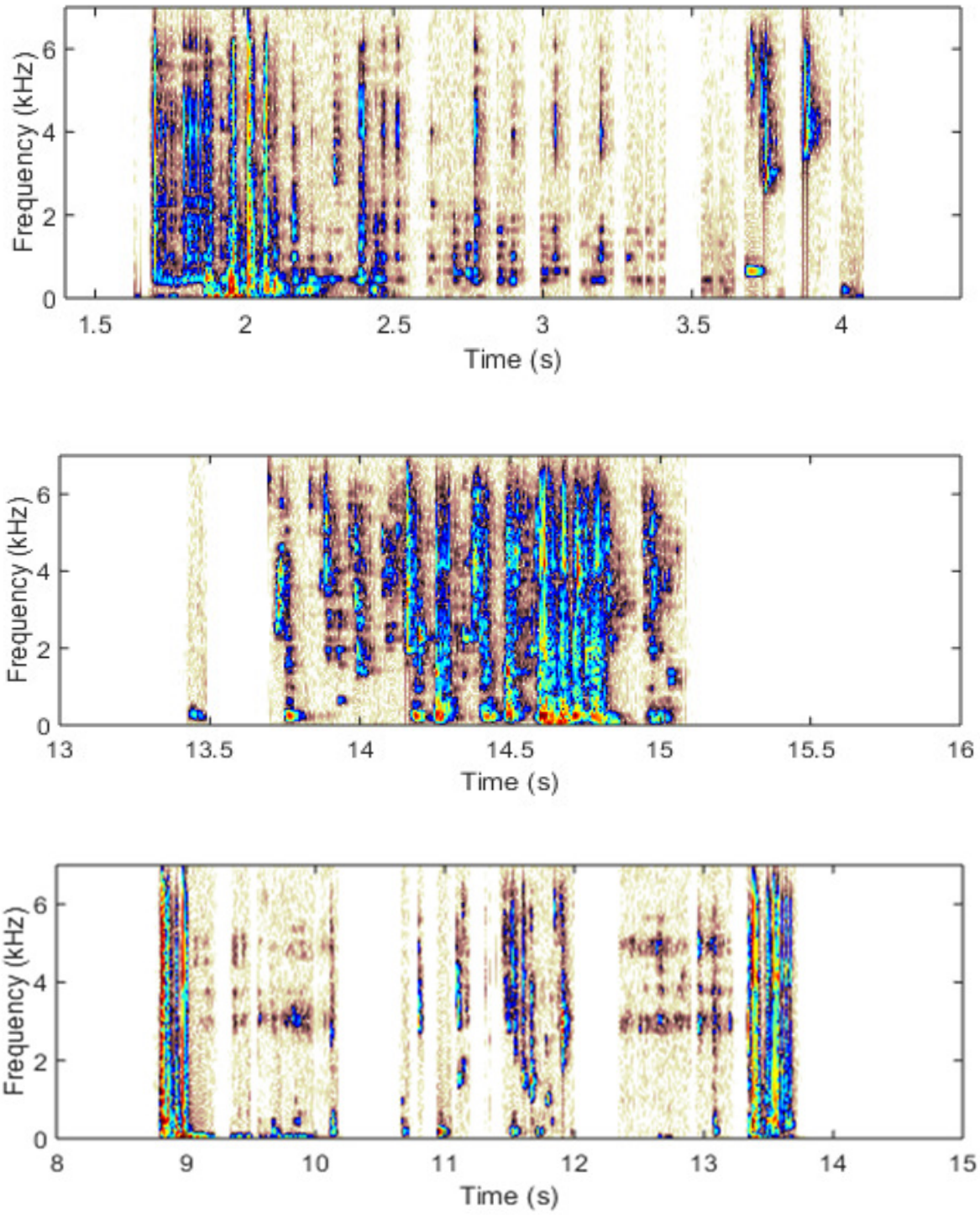


Figure 2. Three Spectrograms of sounds produced by *Scyllarides aequinoctialis* while swimming at the surface of a laboratory tank. The loudest sounds are produced by the impact of the uropods and telson on the water surface and the least intense by the pleopods. Only the period where the animals were actually swimming is shown.

RESULTS

Scyllarides aequinoctialis generates sounds when swimming at the surface between 100 Hz and 6 kHz with peak energy in the 100 Hz to 1.0 kHz range in most cases (see figure 2). This noise appears to be incidental to their swimming movements and not as a form of conspecific communication or an attempt to ward off a predator as is the case of spiny lobsters and clawed lobsters [3].

The swimming motion is typical of that described for both slipper lobsters and spiny lobsters [8 & 9]. That is *S. aequinoctialis* swims backwards by rapidly flexing the abdomen an average of seven times per second and using the uropods and telson as a paddle to exert force on the water. This swimming pattern is an escape mechanism used by decapod crustaceans used to avoid predators [8-10]. If this occurs at the surface, then the uropods and telson is in fact slapping the water surface to produce at least part of the recorded noise. The pleopods are also believed to produce part of the noise as they rub against each other. There are no stridulations on either the antennae, pleopods or uropods and telson like those found in spiny lobsters [1-4].

When swimming, the average pulse rate is seven (7) pulses per sec. and the range is from 2.5 pulses/sec. to 16 pulses/sec. The duration of the pulse is approximately 62.5 msec (Fig. 1).

DISCUSSION

The acoustic signals emitted by crustaceans span a broad range of frequencies. Low frequency rumblings (20–60 Hz) are produced by the mantis shrimp, *Hemisquilla californiensis*, [11] and the American lobsters (*Homarus americanus*) (87-261 Hz) [12] while ultrasonic signals (20-55 kHz) are emitted by the European spiny lobster, *Palinurus elephas* [13]. *Palinurus elephas* was also found to produce audible rasps in the 2-75 kHz range (15 kHz peak frequency) using a stridulating organ (plectrum) and rigid file. These sounds and undefined rasps occur following human manipulation and appear to be associated with anti-predator responses elicited by the introduction of an octopus [3]. Such findings suggest that crustacean noises function to startle potential predators or serve as a conspecific warning mechanism [14 & 15].

Many crustaceans produce sound as a part of their natural behavior. Coquereau et al [16] recorded the sounds produced by 11 species of crustaceans found in the North Eastern Atlantic Ocean identifying thirty-four distinct sounds in their study. In this study sounds produced by movement, such as walking, feeding, mandible rubbing, swimming and other non-identified behaviors, were detected.

Farre [17] provided the earliest account of sound detection in the crustaceans. Providing an early account of the structure of the sensilla on the cuticle of crustaceans. Farre [17] produced figures based on light microscope observations of the statocyst structure as well. Sound perception in aquatic crustaceans is accomplished by detecting particle motion, but not the pressure component of the sound energy [18 & 19]. The Norway lobster, *Nephrops norvegicus* (Linnaeus, 1758), for example, responds in a predictable way, postural responses, to close range (up to 90 mm) particle displacement vibrations with thresholds near 0.9μm in the frequency range of 20-189 Hz [20 & 21].

In insects, arachnids and crustaceans mechanoreceptor hairs serve as fluid flow sensors. These so-called filiform hairs in insects, trichobrothria in arachnids and flow sensilla in crustaceans are among the most sensitive sensory organs in the animal world. All fluid flow sensors have a similar design and represent hair-like structures. Suspended in a cuticular socket, the hair shaft functions as a lever, which responds to fluid viscus forces in the surrounding medium. The movement of the inner end of the hair shaft during deflection triggers one or several sensory neurons that transmit signals indicating the velocity, direction and acceleration of the flow to the central nervous system. To induce appropriate behavior. There is considerable variability in the number location and size of the sensory hairs in the three groups of arthropods [19-28]. Derby [25] found that the American lobster, *H. americanus,* has mechanoreceptors called Peg sensilla. These organs are found on the dactylus and propodus, Type I (70 µm long) and widely distributed on all segments of the walking legs, Type II (30 µm long). These organs may have a single hair-like projection or several, four, emanating from the cuticular socket. These sensilla are usually dually innervated permitting bidirectional sensitivity to flow sensitivity to water currents, pressure waves or tactile stimuli. Scyllarid lobsters, *S. aequinoctialis, S. latus,* and *S. nodifer* have chemosensory setae and mechanoreceptor setae on the second antennae which may function in the detection of sound energy by means of particle motion [22, 24-28].

Acknowledgements

The author wishes to acknowledge Alessandra Tesei for many very useful scientific discussions. Thanks are also due to Mrs. Elvie Fornshell for editorial comments.

Bibliography

[1] **Parker, J. J.** On the structure of the head in *Palinurus* with special reference to the classification of the genus, *Transactions of the New Zeeland Institute,* 16, pp. 297-307, 1884.

[2] **George, R. W. & Main, A. R.** The evolution of spiny lobsters (*Palinuridae*): A study of evolution in the marine environment, *Evolution* 21 (4), pp. 803-820, 1967**.**

[3] **Bouwma, P. E.** Aspects of Antipredation in *Panulirus argus* and *Panulirus guttatus*: Behavior, Morphology, and Ontogeny. *A Dissertation submitted to the Department of Biological Science,* 114 pages, 2006.

[4] **Patek, S. N. & Baio, J. E.** The acoustic mechanics of slip – slip friction in the California spiny lobster (*Panulirus interruptus). The Journal of Experimental Biology*, 210, pp. 3538 -3546, 2007.

[5] **Senter, P.** Voices of the past: a review of Paleozoic and Mesozoic animal sounds. *Historical Biology*, 20 (4), pp. 255–287, 2007.

[6] **Fornshell, J. A. & Tesei, A.** Observations of the sound producing organs in achelate lobster larvae. *Arthropods*, 6 (2), pp. 36-46, 2017.

[7] **Lavalli, K. L. & Spanier, E.** *The Biology* and *Fisheries of the Slipper Lobster,* CRC Press, 400 pages, 2007.

[8] **Spanier, K. L., Weihs, D., & Almog-Shtayer, G.** Swimming of the Mediterranean slipper lobster. *Journal of Experimental Biology and Ecology*, 145 (1), pp. 15-31, 1991.

[9] **Spanier, E. & Lavalli, K. L.** Natural history of Scyllarides latus (Crustacea: Decapoda): a Review of the contemporary biological knowledge of the Mediterranean slipper lobster.

Journal of Natural History, 32 (10-11), pp. 1769-1786, 2012.

[10] **Nauen, J. C. & Shadwick, R. E.** The dynamics and scaling of force production during the Tail-flip escape response of the California Spiny Lobster *Panulirus interruptus*. *The Journal of Experimental Biology,* 204, (Pt 10):pp. 1817–1830, 2001.

[11] **Staaterman, E. R., Clark, C. W., Gallagher, A. J., deVriess, M. S. Claverie, T. & Patek, S. N.** Rumbling in the benthos: acoustic ecology of the California mantis shrimp *Hemisquilla californiensis. Aquatic Biology*, 13, pp. 97–105, 2011.

[12] **Henninger, H. P. & Winsor H. Watson, III W. H.** Mechanisms underlying the production of carapace vibrations and associated waterborne sounds in the America lobster, *Homarus americanus.* The Journal of Experimental Biology 208, pp. 3421-3429, 2005.

[13] **Hill, P. S. & Oakley, T. H.** Comparative tests of evolutionary trade-offs in a palinurid Lobster acoustic system. *Evolution*, 57 (3), pp. 2082-2100, 2003.

[14] **Patek, S. N.** Spiny Lobsters stick and slip to make sound. *Nature*, 411, pp. 153, 2001.

[15] **Patek, S. N.** Squeaking with a sliding joint: mechanics of Experimental Biology and Ecology, motor control of sound production in palinurid lobsters. *Journal of Experimental Biology*, 205, pp. 2375-2385, 2002.

[16] **Coquereau, L, Grall, J., Clavier, J., Jolivet, A. & Chauvaud, L.** Acoustic behaviours of large crustaceans in NE Atlantic coastal habitats. *Aquatic Biology*, 25, pp. 151-163, 2016**.**

[17] **Farre, A.** On the Organ of Hearing in Crustacea. *Philosophical Transactions of the Royal Society of London* 133, pp. 233-244, 1843.

[18] **Popper, A. R., Salmon, M. & Horch, K. W.** Acoustic detection of Experimental Biology and Ecology, communication by Decapod crustaceans. *Journal of Comparative Physiology*, 187, pp. 83-89, 2001.

[19] **Breithaupt, T.** Sound perception in aquatic crustaceans. In: *The Crustacean Nervous System*, K. Weise (Editor) Springer-Verlag, pp. 348-358, 2002.

[20] **Ewing, A. W.** *Arthropod Bioacoustics.* Comstock Publishing Associates, 260 pages, 1989.

[21] **Hill, P. S.** *Vibrational Communication in Animals.* Harvard University Press, Cambridge Massachusetts, 261 pages, 2008.

[22] **Trantz, J. & Sandeman, D. C.** The detection of water born vibrations by the sensory hairs on the chelae of crayfish. *Journal of Experimental Biology*, 88, pp. 351-356, 1980.

[23] **Fletcher, N.** *Animal Bioacoustics.* Springer Handbook of Acoustics (Editor) Th. D. Rossing, pp. 473-489, 2007.

[24] **Casas, J. & Dangles, O.** Physical ecology of fluid flow sensing in arthropods. *Annual Review of Entomology*, pp. 505-520, 2010.

[25] **Derby, C. D.** Structure of Experimental Biology and Ecology, function of cuticular sensilla of the lobster *Homarus americanus*. *Journal of Crustacean Biology*, 2 (1), pp. 1-21, 1982.

[26] **Weisbaum, D. & Lavalli, K. L.** Morphology and distribution of antennular setae of scyllarid lobsters (*Scyllarides aequinoctialis, S. latus* & *S. notifer*). *Invertebrate Zoology*, 123, pp. 324-342, 2004.

[27] **Greenfield, M.D.** *Signals and Receivers.* Oxford University Press, New York, New York, 414 pages, 2002.

[28] **Iwasaki, M., Itoh, T. & Tominaga, Y.** Mechano and Phonoreceptors. In: *Atlas of Arthropod Sensory Receptors.* Springer Press. pp. 142-154, 1999.

ACOUSTIC CHARACTERIZATION OF AN ARTIFICIAL CO_2 SEEP USING SPLIT-BEAM ECHO SOUNDERS

Scott Loranger[a], Ann Elisabeth Albright Blomberg[b], Geir Pedersen[c], Ivar-Kristian Waarum[b] and Andreas Austeng[d]

[a] University of New Hampshire, 24 Colovos Road, Durham NH 03824.
[b] Norwegian Geotechnical Institute, Sognsveien 72, 0855 Oslo, Norway
[c] NORCE Norwegian Research Centre, P.O. Box 6031, Bergen 5892, Norway
[d]University of Oslo, POBox 1080 Blindern, NO-0316 Oslo, Norway

Scott Loranger, University of New Hampshire, 24 Colovos Road, Durham NH 03824. Ph: 1-603-862-3353. Email: sloranger@ccom.unh.edu

Abstract: *Geological carbon storage (GCS) has emerged as a promising method for reducing greenhouse gas emissions and achieving international climate goals. Currently, sub-seafloor GCS sites sequester about 1.8 MtCO_2/yr. Additional sites are under development and by 2050, there is potential for storage of ≈ 100 Mt CO_2/yr. For the expansion of sub-seafloor GCS to be successful, cost-efficient and effective leak monitoring systems must be available. The ACT4storage project is tasked with development of leak monitoring through the selection and use of available technologies. A part of the monitoring suite is the use of active acoustics to detect and quantify free CO_2 bubbles and droplets. An artificial seep device was created to simulate leaks of CO_2 bubbles. Leak simulations were quantified by two broadband split-beam echosounders (50-90 kHz and 250-450 kHz). The split-beam echosounders offer high sensitivity, broadband transmission and were calibrated to quantify flux from a leakage site. The split-beam echosounders show promise as cost-efficient and effective methods for the detection and quantification of free CO_2.*

Keywords: *Geological carbon storage, broadband, echo sounder, leak detection*

INTRODUCTION

Geological carbon storage (GCS) has emerged as a promising method for reducing greenhouse gas emissions[1]. GCS involves capturing CO_2 from industrial point sources (such as power plants) and injecting the CO_2 into geological storage sites. Potential sites include saline aquafers, coal seams, and oil and gas reservoirs. The overall goal of GCS is to return the CO_2 to long-term geological storage and to minimize the net flux of CO_2 to the atmosphere. Currently, there are three major GCS sites – the Sleipner and Snøhvit fields off the coast of Norway in the North Sea and Norwegian Sea respectively, as well as the pilot K12-B project offshore of the Netherlands [2]. The Sleipner field is the largest, accounting for ~ 1Mt/yr of CO_2 storage since 1996. As carbon capture and storage technology advances, there is the potential for much greater storage, including up to ~240 Gt of CO_2 in Europe alone [3], [4].

In order to assess the effectiveness of GCS, sequestration sites must be monitored for leaks of CO2. Current European Union regulations require that monitoring strategies cover the injection site, geological reservoir and surroundings[5]. Current monitoring practice includes a variety of technologies such as downhole monitoring, seismic surveying and environmental monitoring of the seabed and water column[6]–[8]. The ACT4storage (Acoustic and Chemical Technologies for environmental monitoring of geological carbon storage) project is tasked with evaluating available technologies GCS environmental monitoring of the seabed and water column to determine the most reliable, effective and cost efficient monitoring methods. As part of the ACT4Storage program, the use of acoustic instrumentation for the detection and quantification of CO_2 is currently being assessed. An artificial leak of CO_2 was generated in about 20 m water depth and broadband acoustic sensors used to detect and quantify the artificial seep.

The depth of the storage site is of especial importance in determining the appropriate frequency for leak monitoring. Below about 600 m CO_2 is in liquid form, and a higher frequency instrument would likely be needed in order to detect a leak. At small *ka*, where *k* is the acoustic wave number and *a* is the droplet radius, liquid droplets have a relatively low target strength (TS) [9], [10]. Target strength is the ratio of scattered intensity to incident intensity and is measure of the efficiency with which a target scatters sound. At higher *ka*, droplets are more efficient scatterers. To detect a leak at depths below 600 m, higher frequencies are likely necessary. This experiment used a high (333 kHz center frequency) and low (70 kHz center frequency) frequency echo sounder to evaluate the instruments likely to be used in either a gas or liquid CO_2 release scenario.

EXPERIMENTAL SETUP

Experiments were conducted at Horten inner harbor near Horten, Norway on October 15 and 19, 2018. The inner harbor is a sheltered environment with limited ocean currents, and low ambient noise levels. The experiment consisted of four seafloor-mounted frames; two chemical sensor frames, a CO_2 plume-generating frame and an acoustic sensor frame. The frames were deployed at depths between 16 m and 20 m. The acoustic sensor frame was 70 m (horizontally)

from the leak frame, with acoustic sensors oriented such that the beam at 70 m was just above the leak frame and below the water surface (Fig. 1).

Two split-beam echo sounders (SBES; Kongsberg Maritime ES70-7C and ES333-7CD – where 70 and 333 indicate the center frequency of the echo sounder) were mounted on the acoustic sensor frame. The SBESs were connected to Kongsberg wide band transceivers (EK80 WBT) to enable frequency modulated broadband (FM) transmission and reception. The echo sounders were calibrated according to the method described by Demer et al 2015 [11]. The SBESs transmitted simultaneous one-millisecond FM pulses from 45 kHz to 95 kHz and 280 kHz to 450 kHz. The ES70 was also run in narrowband (CW) mode to generate a one-millisecond narrow band pulse at the center frequency to compare the signal to noise ratio for FM and CW pulses.

The SBES have a two-way beamwidth of five degrees, resulting in a six m diameter beam at 70 m. The beam was oriented so that the deepest part of the beam was just above the top of the leak frame, and the 6 m beam covered depths from 15 to 9 m, in order to prevent interference from the sea surface and/or the leak frame.

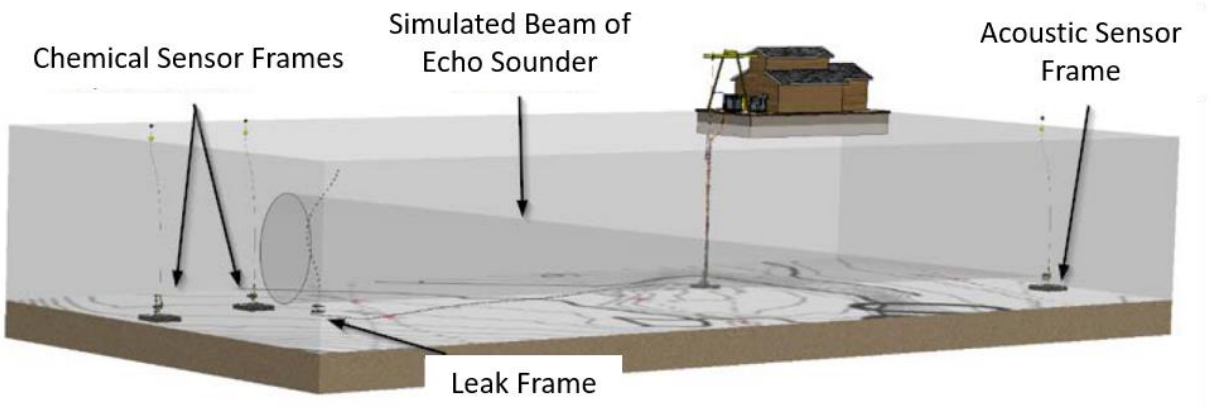


Fig. 1: Orientation of instrument frames. The horizontal distance from the acoustic sensor frame to the leak frame was 70 m.

The simulated CO_2 leak was generated by releasing CO_2 from pressurized bottles mounted on a surface barge anchored in the experiment site. The surface barge pumped CO_2 to the seafloor-mounted leak frame and released the CO_2 from a 3-mm orifice on the frame. A surface pressure regulator controlled the backing pressure applied by the CO_2 bottles to the leak generating system. A camera mounted on the leak frame monitored the orifice for the release of bubbles, and the backing pressure gradually increased until flow from the orifice began. For flows from 0.115 l/min to 1.15 l/min the minimum pressure (1.7 bars) required to generate flow out of the orifice in the leak frame was applied to the system. The pressure required to generate flow was assumed to be slightly greater than the hydrostatic pressure, indicating that the orifice was at a depth of slightly shallower than 17 m.

FLOW RATE

The flow meter had a maximum measureable flow rate of 1.15 l/min. Higher flows were generated by fully opening the flow meter so that it did not restrict flow. The pressure was then increased above 1.7 bars. The flow rate at higher pressures was determined by assuming that pressure was constant from the pressure regulator to the leak frame orifice, and therefore the density of CO_2 was constant. The Bernoulli equation was then used to determine that a change in pressure, ΔP, was proportional to the square root of a change in velocity, $\Delta \mathbf{U}$;

$$\Delta P \propto \sqrt{\Delta \boldsymbol{U}}. \quad (1)$$

For flows from 0.115 to 1.15 l/min, the pressure applied to the system for these flow rates was just high enough for gas to be expelled into the water column and the buoyant force was the dominant force driving the release of bubbles. For higher flows (1.15 l/min to 2.64 l/min), greater pressure was applied by the pressure regulator and that backing pressure was the dominant driving force. The result was two difference force balances at the orifice; the first was the buoyancy dominated forcing where droplets were released with an initial velocity near zero and the second regime is the backing pressure dominated forcing where droplets were expelled with an initial velocity greater than that of the buoyancy dominated forcing.

NOISE LEVEL

Both EK80s were able to detect the gas seep at 70 meters, regardless of flow rate.

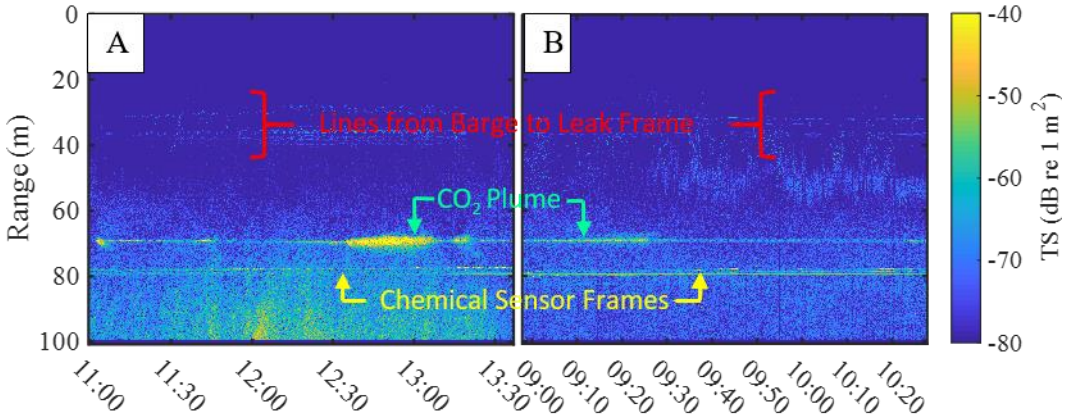


Fig. 2: Echograms from Oct 15, 2018 (A) and Oct 19, 2018 (B) for the ES70. The seep can be seen at 70 meters with intensity changes as the flow rate changes. The chemical sensor frames can be seen at around 80 meters, and returns from mooring ropes and the line connecting the leak frame to the barge are seen between 20 and 40 meters.

The noise level for each echo sounder was computed from the echograms in Fig 2 for ranges where no targets were in the acoustic beam (45 to 65 m). The average (computed in linear space) noise with no time variable gain (TVG) of all samples between 55 and 65 m was calculated for each ping, and then 100 pings were averaged together for both days the experiments to determine the distribution of noise level estimates (Fig 3). The median noise level for both days combined was -151 dB for the ES70 and -149 dB for the ES333.

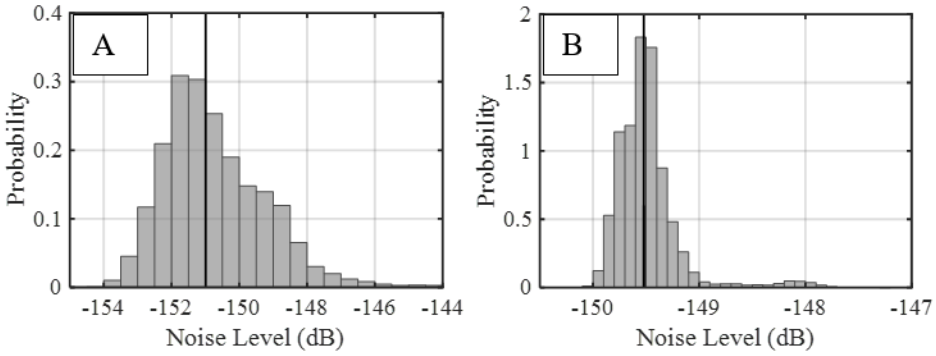


Fig 3. Sound pressure level measurements averaged from samples taken between 55 and 65 meters depth and averaged over 100 pings for the ES70 (A) and the ES 333 (B). The black line shows the median value for the distribution (-151 dB for the 70 kHz echosounder and -149 dB for the 333 kHz).

FLOW RATE AND TARGET STRENGTH

In order to determine the relationship between backscatter and flow rate, the TS of the plume was evaluated. TS is determined by the backscattering cross-sectional area, $\boldsymbol{\sigma_{bs,i}}$, of each target, $\boldsymbol{i}$, in the acoustic sample according to,

$$TS = 10\ log_{10}\left[\sum_{i=1}^{N} \sigma_{bs,i}\right], \quad (2)$$

where N is the total number of scatterers in the acoustic sample. If $\boldsymbol{\sigma_{bs,i}}$ is normally distributed then TS can be approximated from the average backscattering cross-sectional area $\bar{\sigma}$,

$$TS = 10\ log_{10}[N\ \bar{\sigma}]. \quad (3)$$

The target strength of the CO_2 plume generated by the leak frame as a function of flow rate was calculated by applying TVG (accounting for spherical spreading and absorption) and averaging (in linear space) the TS for all pings recorded during the time interval of a given flow rate (Fig. 4).

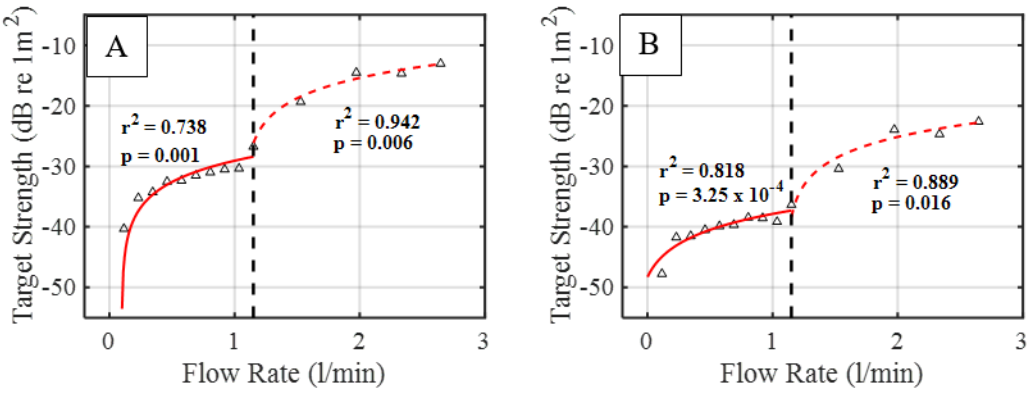


Fig 4: Average target strength as a function of the flow rate (black triangles) for the ES70 (A) and ES333 (B). The backscattering cross sectional area (linear component of TS) was linearly fit to flow rate for the two different forcing regimes: flow driven by the buoyance of the gas (solid red line) and flow driven by backing pressure (dashed red line).The dashed black line shows the division between the two forcing regimes.

The linear component of TS, ($N\overline{\sigma}$ in Eq. (3)) was fit to a line for the two different forcing regimes (buoyancy driven and backing pressure driven described above). The high correlation between TS and flow rate for the two forcing regimes indicates that $N\overline{\sigma}$ and flow rate are linearly related with the slope dependent on the forcing regime. It is likely that the size distribution (and therefore $\overline{\sigma}$) is constant within each forcing regime and that the number of targets, N, increases with increase in flow. If $\overline{\sigma}$, and therefore bubble size distribution, had changed within a forcing regime then the bubble size distribution and scaling factor N would both have to scale linearly with flow rate, which is an unlikely scenario. The difference in slope between the two flow regimes is likely due to a change in $\overline{\sigma}$. Bubbles formed in the pressure driven regime experience an initial velocity when exiting the orifice that is likely to result in increased fractioning of bubble, and a decrease in droplet size when compared to droplets in the buoyancy driven regime.

SIGNAL TO NOISE RATIO AND DETECTION RANGE

The signal to noise ratio (SNR) for the maximum flow rate (2.65 l / min) and the minimum flow rate (0.115 l/min) as a function of distance from the echo sounder was calculated in order to determine the detection limit for the extrema of flow scenarios in this experiment. The SNR as a function is equal to

$$\text{SNR} = 10\log_{10}\left(\frac{TS\, e^{-4\alpha r}}{r^4}\left(\frac{r}{70}\right)\right) - NL, \quad (4)$$

where α is the absorption coefficient in units of nepers / meter and r is the range and NL is the noise level in dB. The $r/70$ term accounts for the change in beam width due to a change in range relative to the range at with the TS was measured. Assuming that the bubbles within the beam of the echosounder are uniformly distributed in a vertical column in the water column, the horizontally oriented beam of the echo sounder will decrease in size as the instrument approaches the bubbles. Therefore, the number of bubbles (N) will decrease proportional decrease or increase in the beam "footprint" for ranges other than the range at which TS was measured (70 m). The limit to detection was set to a SNR of 10 dB. In FM mode the limit for detection for the maximum flow rate (2.64 l/min) was 598 meters and 176 meters for the ES70 and ES333 respectively (Fig 5). For the minimum flow rate (0.115 l/min), broadband detection was limited to within 399 meters and 86 meters of the ES70 and ES333 respectively.

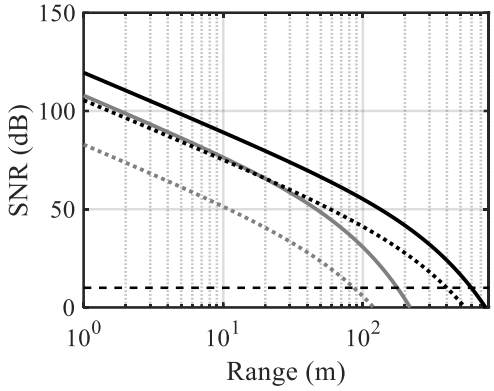


Fig. 5: The signal to noise ratio (SNR) as a function of range from the echo sounder for the maximum flow rate for the ES70 (solid black line) and ES333 (solid gray line) and the minimum flow rate for the ES70 (dashed black line) and ES333 (dashed gray line). The detection limit was set to 10 dB(horizontal dashed black line).

SNR of the seep was also determined for the ES70 in CW mode for the maximum leak rate of 2.65 liters / minute (Fig 6). The difference between the SNR in FM and CW mode was 25 dB, 5dB higher than the predicted increase in SNR for an matched filer FM pulse of 2 BT [12], [13], where B is the bandwidth and T is the pulse length.

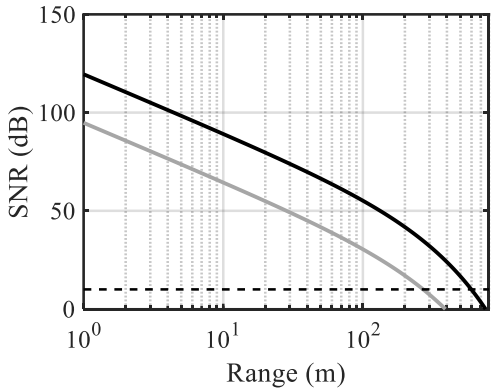


Fig. 6: The signal to noise ratio (SNR) as a function of range from the echo sounder for the maximum flow rate 2.6 liters / min for the ES70 in FM mode (solid black line) and the ES70 in CW mode (solid gray line) The detection limit was set to 10 dB (horizontal dashed black line).

CONCLUSIONS

The two broadband echo sounders were both capable of detecting the simulated seep for all flow rates. The TS of the seep in the ES333 was about 10 dB lower than that of the ES70. Bubble size appeared to be constant within each forcing regime; however, the size distribution appeared to change between forcing regimes, likely due to increased fractioning of bubbles due to the increased initial velocity in the pressure-forcing regime. The lower TS and increased attenuation of the higher frequency system resulted in significantly shorter detection ranges for the ES333 (176 m compared to 598 m for the ES70 at the highest flow rate). Operating the ES70 in FM (45

kHz to 95 kHz) mode resulted in an increased SNR of 25 dB relative to the same echo sounder in narrow band mode. The increased SNR was 5 dB higher than predicted.

While the ES70 had a higher SNR for the experiment conducted here, the appropriate frequency for monitoring GCS sites depends on the depth of the site. For sites below 600 m CO_2 will be in liquid form and higher frequencies are likely to be necessary.

The authors would like to acknowledge the ACT4storage Partners as well as the Norwegian Stat enterprise Gassnova for their support of this project.

REFERENCES

[1] IPCC, "Climate Change 2014: Synthesis Report. Contribution of Working Groups I, II and III to the Fifth Assessment Report of the Intergovernmental Panel on Climate Change," IPCC, Geneva, Switzerland, 2014.
[2] IEA Greenhouse Gas R&D Programme (IEA GHG), "Review of Offshore Monitoring for CCS Project," no. July, 2015.
[3] EU GeoCapacity, "Assessing European Capacity for Geological Storage of Carbon Dioxide," *D16 WP2 Storage Capacit.*, p. 170.
[4] IEA Greenhouse Gas R&D Programme (IEA GHG), "Assessment of sub sea ecosystem impacts," pp. 1–266, 2008.
[5] Directorate-General for Climate Action (European Commission), "Implementation of Directive 2009 / 31 / EC on the Geological Storage of Carbon Dioxide - Guidance Document 1: CO2 Storage Life Cycle Risk Management Framework," p. 54, 2009.
[6] S. Bourne, S. Crouch, and M. Smith, "A risk-based framework for measurement, monitoring and verification of the Quest CCS Project, Alberta, Canada," *Int. J. Greenh. Gas Control*, vol. 26, pp. 109–126, Jul. 2014.
[7] M. Dean and O. Tucker, "A risk-based framework for Measurement, Monitoring and Verification (MMV) of the Goldeneye storage complex for the Peterhead CCS project, UK," *Int. J. Greenh. Gas Control*, vol. 61, pp. 1–15, Jun. 2017.
[8] S. Hannis *et al.*, "Review of Offshore CO2 Storage Monitoring: Operational and Research Experiences of Meeting Regulatory and Technical Requirements," *Energy Procedia*, vol. 114, pp. 5967–5980, Jul. 2017.
[9] V. C. Anderson, "Sound Scattering from a Fluid Sphere," *J. Acoust. Soc. Am.*, vol. 22, no. 4, pp. 426–431, 1950.
[10] S. Loranger, C. Bassett, J. P. Cole, B. Boyle, and T. C. Weber, "Acoustically relevant properties of four crude oils at oceanographic temperatures and pressures," *J. Acoust. Soc. Am.*, vol. 144, no. 5, pp. 2926–2936, Nov. 2018.
[11] D. A. Demer *et al.*, "Calibration of acoustic instruments," *ICES Coop. Res. Rep.*, no. 326, 2015.
[12] D. Chu and T. K. Stanton, "Application of pulse compression techniques to broadband acoustic scattering by live individual zooplankton," *J. Acoust. Soc. Am.*, vol. 104, no. 1, pp. 39–55, Jun. 1998.
[13] G. L. Turin, "An Introduction to Matched Filters," *IRE Trans. Inf. Theory*, vol. IT-6, pp. 311–329, 1960.

DIVERSE ACOUSTIC MANIFESTATIONS OF SHALLOW GAS IN THE GDAŃSK BAY (SOUTHERN BALTIC SEA)

Damian Jaśniewicz[a], Jakub Idczak[b], Zygmunt Klusek[a], Aleksandra Brodecka-Goluch[b], Natalia Gorska[b], Jerzy Bolałek[b], Patryk Pezacki[b]

[a]Institute of Oceanology PAS, Powstancow Warszawy 55, 81-712 Sopot
[b]Institute of Oceanography, University of Gdańsk, Al. Marszałka Piłsudskiego 46, 81-378 Gdynia

Damian Jaśniewicz, Institute of Oceanology PAS, Powstancow Warszawy 55, 81-712 Sopot, Poland, e-mail: djasniewicz@iopan.pl

Abstract: *Continental shelves and sub-bottom layers of shallow seas are considered as the areas of main importance when it comes to global emission of methane from the marine environment. Due to relatively low solubility in water, methane can be often accumulated in shallow sediments as a gas. Presence of methane in shallow sediments is dependent on factors such as oxic/anoxic conditions, organic matter inflow and decomposition processes, which all are affected by recent intensification of climate changes. Non-invasive acoustic methods enable us to reveal various features of gas presence and distribution through distinct acoustic gas manifestations. This study is focused on assessing the extent of sediments saturated by gas (methane) in the Gdańsk Bay as well as identifying and analyzing the spatial variability of acoustic manifestations. Our approach was based on the combination of synthesis and digitization of various historical data obtained from literature, and analysis of new data from multi-device acoustic measurements (single and split-beam echosounders, multi-beam echosounder and side-scan sonar). Acoustic backscattering data from sub-bottom layers, sediment surface and water column were analyzed. In addition, verification of methane presence based on geochemical analyses of upper layers of sediments taken by core samplers were performed. The obtained results revealed that the total area of the Gdańsk Bay sea bottom sediments saturated by gaseous methane constitutes of about 380 km^2. Within the area of interest, at least three subareas of distinct gas presence features can be specified based only on acoustic data. Moreover, the results indicate strong spatial variation of gassy sediments as well as gas emission from seafloor characterized by distinct acoustic recordings.*

Keywords: *Shallow gas in sediments; acoustic imaging; single- and multi-beam echosounders; marine GIS*

1. INTRODUCTION

Sediments of shallow seas and continental shelves are the source of considerable amount of microbial methane (80% of the global oceanic production), mostly from the decomposition of organic matter [1]. Acoustic imagery evidence for methane presence in gaseous form in sediments of shallow seas is widely described in the literature [1]. Significant concentrations of methane in the organic-rich sediments of the Gdańsk Bay have been reported [2,3] since 1990s, and later verified by numerous acoustic and geochemical studies [3,4,5,6,7,8]. The main aim of this study is examination of the variability of acoustic manifestations of shallow gas (up to 10 m below sediment surface) in sediments of the area. For that reason, re-analysis of archival data together with recently collected acoustic data has been performed.

2. STUDY AREA

The investigations were carried out in the Gdańsk Bay (Fig.1) (Southern Baltic Sea), where the estuary of one of the biggest rivers in the region – the Vistula – is situated . High nutrient and organic matter loads from the river lead to the high primary production (225g $C \cdot m^{-2}y^{-1}$) [9]. Strong seasonal water stratification causes oxic depletion near the bottom, creating favorable conditions for methanogenesis through organic matter decomposition [9,10]. The bottom in the area of shallower waters of the Gdańsk Bay is covered by fine and medium-grain sands. Sediments graining gradually changes with the bottom depth, turning into better sorted and lower mean grain sizes clays and silts (Fig.1) [11,12]. The sedimentation rate varies from 1.0 to 3.9 $mm \cdot y^{-1}$, with higher values near the coast [13]. Significant concentrations of methane (6-8 $mmol \cdot dm^{-3}$) are widely present in sediments of the Gdansk Bay, at depths of 25-100 cm below sea floor (bsf) (Fig.1) [2,3].

3. MATERIAL AND METHODS

The historical data were collected based on various literature sources, such as local periodicals and reports with limited access, and unpublished archival data covering about 1000 km^2 of the area, which were subjected to digital processing, analyzed and mapped in the GIS environment (Fig.1). New data (2018-2019) have been collected using multifrequency hydroacoustic equipments in three subareas M1, M2, M3 of the Gdańsk Bay (Fig.1). The equipment consisted of: single-beam echosounder (12kHz) ODOM Echotrack MKIII, split-beam echosounders (38, 120, 333 kHz) Simrad EK80, multibeam echosounder (400 kHz) Reson SeaBat 7125 SV2 and side-scan sonar (300 & 900 kHz) Edge Tech Multi-Purpose Survey System 4200 with Ultra-Short Baseline (USBL) Easytrak Nexus 2690 Applied Acoustics. Calibration process of the echosounders and the measurements scheme were done accordingly to the general recommendations based on the hydrographic standards [14]. The analyzed informations included sub-bottom, sediment surface and water column backscattering data processed in: SonarWizz (side-scan sonar), Qinsy and Qimera software (multibeam) and furthermore in the MATLAB environment (single and split-beam). The analyses were conducted taking into account recognition of backscattering anomalies, in data from various acoustic devices, which pointed to gas presence in the study area.

4. RESULTS AND DISCUSSION

Gassy sediments in the Gdańsk Bay – summary of archival data

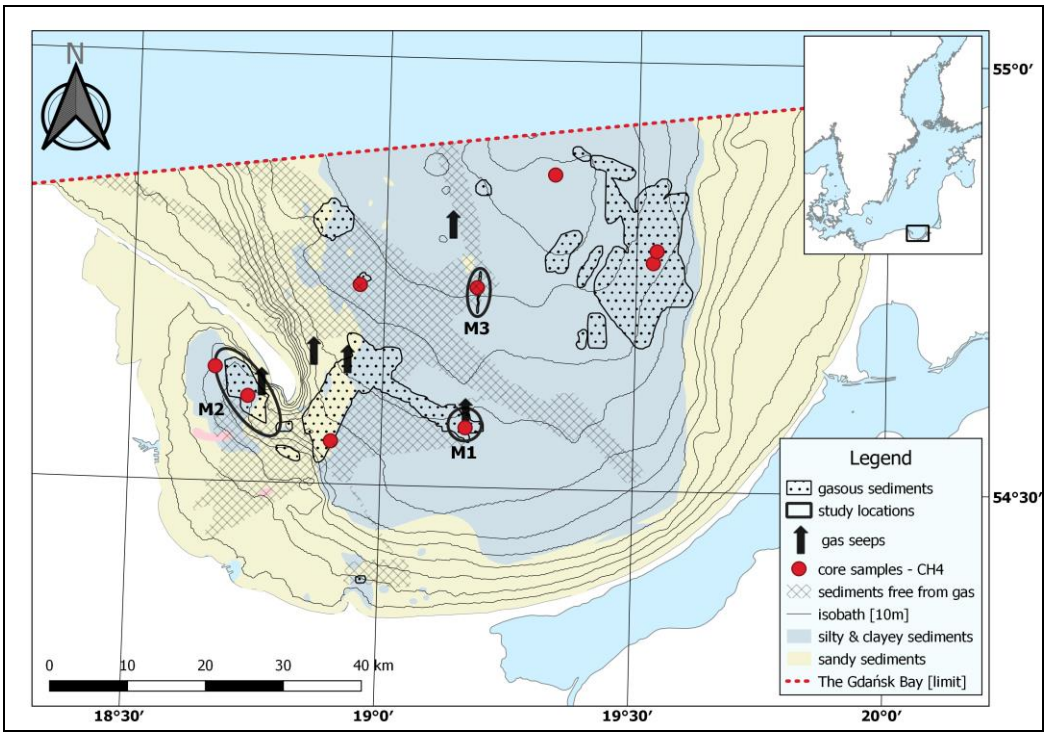


Fig. 1 Map of spatial distribution of gas saturated sediments and gas seeps in the Gdańsk Bay. Selected geochemical core sampling points are presented with red points. M1, M2 and M3 indicate study areas of our acoustic and geochemical measurements.

The summary of the key acoustic results concerning shallow gas distribution in the Gdańsk Bay is presented in Fig.1. The coverage by methane-saturated sediments in the Gdańsk Bay has been estimated acoustically and amounts to about 440 km^2. These sediments are marked on the map (Fig.1) as "gaseous sediments" [2,7,12,15,17]. The presence of acoustic anomalies in this area, associated with shallow gas presence, was confirmed by the geochemical studies [2,3,12].The dominant amount of results indicating gaseous methane presence in sediments, is associated with acoustic backscattering anomalies from sub-bottom layers of sediments. Most commonly recognized anomalies are: blanking in acoustic images echoes from sediments located beneath the upper boundary of gassy sediments (acoustic blanking), grainy blurry images due to many small reflections on gas intrusions (acoustic turbidity) and the enhancement of the sound reflection from the gas intrusions (layer enhancement) [2,3,7,12,15,16].

Within the Gdańsk Bay, numerous small surface pockmark structures connected with gas occurrence in sediments have been recognized [2,3,7,8,12]. Such structures create strong acoustic backscattering anomalies coupled with up to few meters of depression of sediment surface (Fig.2), which results from pockmark formation processes [3,7,8,17]. Such structures are most likely connected with gas migration from deeper layers of sediments, probably through formed gas chimneys [17,18]. Pockmarks in the area of the Gdańsk Bay vary in size and are up to 1 km^2. Their total estimated area is about 8.1 km^2. Pockmarks are usually found in clusters, typically get deeper in the bottom, up to 1-3 m, and have horizontal extension of

around 200 m [2,3,7,12,16]. Within the Gdańsk Bay, there are also structures classified as buried by semi-liquid sediments old pockmarks [3,7,16]. Few gas seeps from sediments were acousticaly observed in various regions of the Gdańsk Bay (Fig.1) [3,7,19].

Spatial variation of shallow gas manifestations in the Gdańsk Bay

The subarea M1 (Fig. 1) is part of a large gas-saturated sediment structure located in the western Gdańsk Bay [16]. It is characterized by medium-to-intense acoustic anomalies associated with the gas presence. The most profound sub-surface anomalies are: acoustic turbidity, layer enhancement and acoustic blanking (Fig.2a). Sub-bottom anomalies are highly irregular with the strongest expression in the central part (the pockmark with gas seeps). After surveying the M1 zone (2.4 x 2.3 km), the area with significant sub-bottom acoustic anomalies (Fig.1) was estimated to be 0.93 km^2. Bathymetric data combined with sub-bottom and side-scan sonar data indicated presence of the pockmark with a relatively significant extent 0.18 km^2. This pockmark is characterized by irregular shape, deviated from typical for pockmarks round geometry and surrounded by numerous smaller pockmarks [17,18]. The migration of small gas bubbles (gas seeps) from the pockmark was observed by single-beam echosounder. Such events have been previously reported in literature, which means continuous pockmark activity in this area [3,7,8,16].

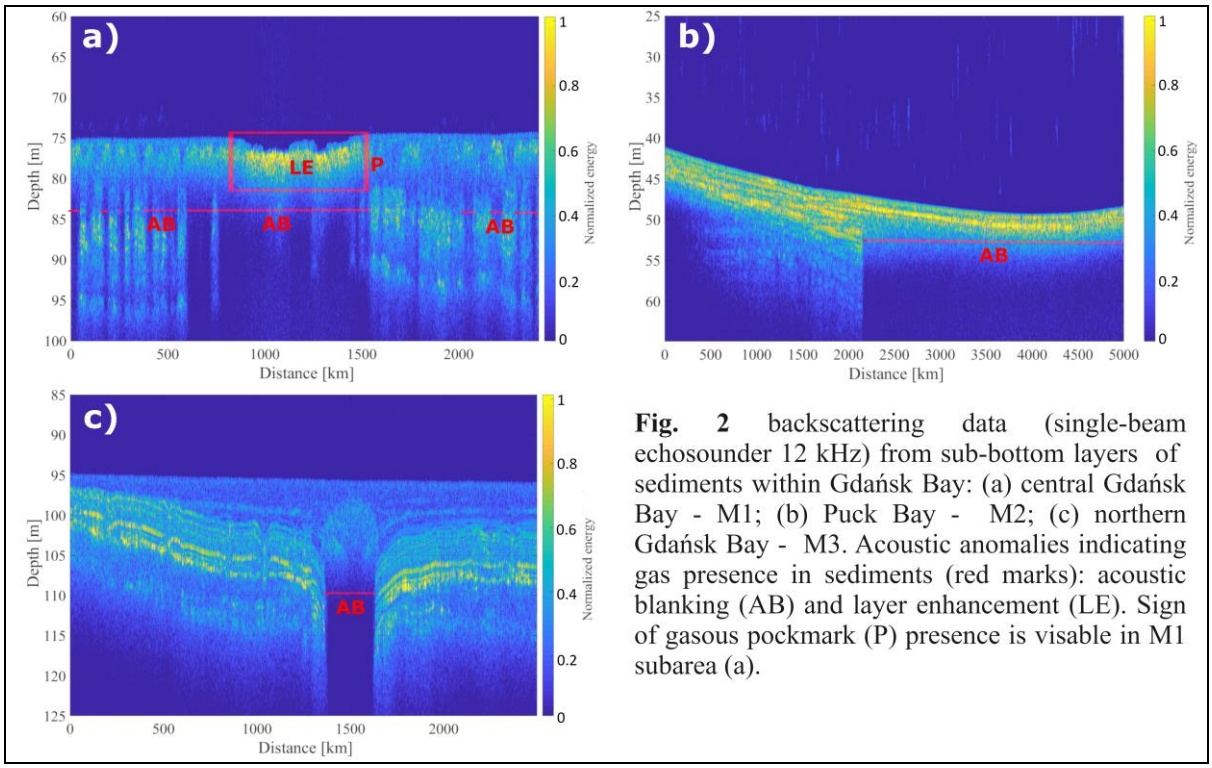


Fig. 2 backscattering data (single-beam echosounder 12 kHz) from sub-bottom layers of sediments within Gdańsk Bay: (a) central Gdańsk Bay - M1; (b) Puck Bay - M2; (c) northern Gdańsk Bay - M3. Acoustic anomalies indicating gas presence in sediments (red marks): acoustic blanking (AB) and layer enhancement (LE). Sign of gasous pockmark (P) presence is visable in M1 subarea (a).

The subarea M2 is located in the inner, shallower part of the Gdańsk Bay named as the Puck Bay, sheltered from the open sea by the Hel Peninsula (Fig.1). Gas-saturated sediments have been estimated to cover 20.44 km^2 of the surface, which is considerably more than the previously reported area [3]. It suggests increasing range of methanogenesis in sediments, Gassy sediments are characterized by extensive and homogenous area (2-4 km wide; and 9.75 km in length) of acoustic blanking and layer enhancement (Fig.2b). The transition zone from gas saturated sediments to sediments without gas is very rapid in this area and visible as sudden change of the depths of acoustic penetration (Fig.2b). It is difficult to recognize any surface geomorphological structures connected to gas presence in sediments of this subarea [15]. We observed unevenly distributed, appearing periodically gas seeps in this region. In echograms, the gas seeps were presented as strings of few vertically migrating (ascending)

bubbles in the water column and disappearing along the path of 20 m (about half of the water depth) [15]. It is interesting that during summer and autumn seasons when the bottom water temperature is rising, single streams of seeping gas with fine diameter are observed by echosounders over extended shallower areas.

The subarea M3 have the average depth of 95 m and relatively flat bottom covered by clay sediments. Within this area, unusual forms of acoustic backscattering anomalies are observed. The acoustic anomaly reported for M3 subarea is 5.7 km long and of 150-300 m wide with the total estimated area of 1.19 km^2. The echogram (Fig. 2c) shows narrow strong acoustic blanking, typical for this area, due to sound attenuation by gas. There are no enhancing reflections of acoustic energy from gas intrusions. Bending down the acoustic images of the most intense sub-bottom backscattering data are most likely caused by sound speed lessening in mixed environment gas [20]. Unusual shape of the structure may indicate the "deeper" origin of methane, which migrates from deeper gas reservoir through geological faults [17,18]. Using the available set of equipment, it was difficult to recognize any geomorphological structures connected to gas presence on the surface of sediments in M3 subarea. During measurement campaigns in this area, no gas seeps were observed.

5. SUMMARY

The objective of this study was to show the synthesis of various acoustic studies carried out in the Gdańsk Bay, based on historical and newly collected data with reference to acoustic manifestation of shallow gas in sediments, and examine their diversity. The estimation of spatial distribution indicates about 440 km^2 of gas-saturated sediments. Most common acoustic manifestations of gas presence are sub-bottom backscattering anomalies such as acoustic blanking, acoustic turbidity, layer enhancement and distortion of sediment layering. Various types of sub-bottom acoustic anomalies usually co-exist with each other and their intensity vary gradually within saturated sediments (Fig.2b). Some compliance of this rule is observed in the subarea M1, where strong spatial variations of gas manifestation within sediments with significant amount of methane are observed (the central Gdańsk Bay – Fig. 2a). Based on the acoustic data, the transition zone between the area with gas-saturated sediments and gas-free sediments is usually very narrow. Markedly different features of acoustic anomalies were observed between three surveyed areas: M1, M2, M3 (Fig. 2). Within the Gdańsk Bay, there are numerous pockmarks (however, constituting minority of gas manifestation) of various size, up to 1 km^2, with average 1-3 m depth and around 200 m size. The total area of pockmarks in the Gdańsk Bay is estimetad to be 8.1 km^2. There are reported and observed (M1, M2 locations) few gas seeps from sediments (Fig.1). The observed diversity of gas manifestations in sediments requires application of various acoustic methods and devices working in broad frequency range, in order to comprehensively describe physical and geomorphological characteristics of gaseous methane in shallow sediments of the Gdańsk Bay.

ACKNOWLEDGMENT

The study was supported by the Polish National Science Center project no. UMO-2016/21/B/ST10/02369 and was carried out in the frame of statutory projects of the Institute of Oceanology Polish Academy of Sciences in Sopot.

REFERENCES

[1] **Fleischer PT, Orsi H, Richardson MD, Anderson AL**, Distribution of free gas in marine sediments: A global overview, *Geo-Mar Lett* , vol.21, pp.103-122, 2001.

[2] **Pimenov NV, Ulyanova MO, Kanapatsky TA**, Veslopolova EF, Sigalevich PA, Sivkov VV, Microbial mediated methane and sulfur cycling in pockmark sediments of the Gdansk Basin, Baltic Sea. *Geo-Mar Lett*, vol.30(34), pp.439–448, 2010.

[3] **Brodecka A, Majewski P, Bolałek J, Klusek Z**, Geochemical and acoustic evidence for the occurrence of methane in sediments of the Polish sector of the southern Baltic Sea, *Oceanologia*, vol. 55(4), pp.951- 978, 2013.

[4] **Jankowska H**, The bottom deposits of Puck Bay, *Stud Mat Oceanogr* 64, pp.163–171, 1993 (in Polish).

[5] **Geodekyian AA, Trotsiuk VY, Blazhchishin AI**, Geoacoustic and Gasometric and Lithogeochemical, *Investigations in the Baltic Sea (in Russian) Moscow*, 1990.

[6] **Klusek Z, Matwiejew AL, Potapow AI, Sutin AM**, Observation of non-linear scattering of acoustical waves at sea sediments, *Acoustic Letters*, vol.18(11), pp.198-203, 1995.

[7] **Majewski P, Klusek Z**, Expressions of shallow gas in the Gdańsk Basin. *Zeszyty naukowe Akademii Marynarki Wojennej*, vol.4(187), pp.61-71, 2011.

[8] **Majewski P, Klusek Z**, Parameters of echo signals originated from a gas seepage site in the southern Baltic Sea, *Hydroacoustics*, vol.17, pp.143–150, 2014.

[9] **Witek Z, Ochocki S, Nakonieczny J, Podgórska B, Drgas A**, Primary production and decomposition of organic matter in the epipelagic zone of the Gulf of Gdańsk, an estuary of the Vistula, *ICES J. Mar. Sci*, vol.(56), pp.3-14, 1999.

[10] **Hansson M, Andersson L, Axe P**, Areal extent and volume of anoxia and hypoxia in the Baltic Sea 1960–2011, *Rep. Oceanography*, vol.42, 2011

[11] **PIG-PIB, Petrobaltic, Kronos, Geos, Geosfera (consortium)** *Prospective zones of occurence of hydrocarbon deposits (in Polish)*, In: Anolik P, Karczewska A (ed). Polish Geological Institute, Warsaw, part II, 2008 (in Polish).

[12] **Ulyanova M, Sivkov V, Kanapatskij T, Sigalevich P, Pimenov N**, Methane fluxes in the southeastern Baltic Sea, *Geo-Mar Lett*, vol. 32(5), pp.535-544, 2012.

[13] **Suplińska MM, Pietrzak-Flis Z**, Sedimentation rate and dating of bottom sediments in the Southern Baltic Sea region, *Nukleonika*, vol.53(2), pp.105–111, 2008.

[14] **International Hydrographic Organization, IHO** Standards for hydrographic surveys - Special Publication No.44, International Hydrographic Bureau, 2008.

[15] **Rudowski S, Szefler K, Fajfer G**, Gas in sediments of Puck Bay, *Geologia i geomorfologia pobrzeża południowego Bałtyku*, vol.8, pp.119–130, 2010, (in Polish).

[16] **Jaśniewicz D, Klusek Z, Brodecka-Goluch A, Bolałek J**, Acoustic investigations of shallow gas in the southern Baltic Sea (Polish Exclusive Economic Zone): a review. G*eo-Mar Lett*, vol.39 (1), pp.1–17, 2019.

[17] **Cathles LM, Sheng Su, Duofu Chen**, The physics of gas chimney and pockmark formation, with implications for assessment of seafloor hazards and gas sequestration, *Marine and Petroleum Geology*, vol.27, pp.82-91, 2010.

[18] **Dimitrov L, Woodside J,** Deep sea pockmark environments in the eastern Mediterranean. *Marine Geology*, vol.195, pp.63-276, 2003.

[19] **Orłowski A**, Acoustic Tracking Dynamic Phenomena in Marine Ecosystem, *Hydroacoustics*, vol.12, pp.167–180, 2009.

[20] **Wilkens RH, Richardson MD**, The influence of gas bubbles on sediment acoustic properties: in situ, laboratory, and theoretical results from Eckernförde Bay, Baltic sea, *Continental Shelf Research*, vol.18(14), pp.1859-1892, 1998.

ECOLOGICAL CATASTROPHE IN ARCTIC: AN ANOMALOUS GULF STREAM HEATING (TO 21°C) AND SHIFT (~200 KM) TO GREENLAND DUE TO OCEAN POLLUTION BY RAINBOW OIL FILM

Irina Bjørnø[1], Mikhail Grishin[2,3], Sergey Pershin[2]

[1] Russisk Kultur Mission I Danmark – RKMD www.rusmission.dk
[2] Moscow Institute of Physics and Technology (State University), 9 Institutskiy pereulok, Dolgoprudny, 141701 Russia
[3] Prokhorov General Physics Institute of RAS, 38 Vavilova street, Moscow, 119991 Russia
Жёлтым- оставить;

Irina Bjørnø (rusmission.dk@gmail.com)

Abstract: *An anomalous water heating – up to 21 ^{0}C – and ~200 km shift of the Gulf Stream to Greenland near New England coasts were observed in summer-fall of 2011. To explain this phenomenon a new physical mechanism is proposed and discussed. It is shown that the main consequence of the Deepwater Horizon (British Petroleum – BP) disaster in the Gulf of Mexico is oil rainbow slick or film formation over huge Gulf area of a hundred thousand square kilometers which has conserved the solar energy inside water and increased its temperature.*

We have shown that inertial "sliding" of Gulf Stream to Greenland as a result of strong drop of water viscosity in the vicinity of specific temperature 19-20°C which was observed in summer-fall 2011. Actually, at this temperature a several-fold reduction in sea water shear viscosity was observed earlier in turbulent flow.

We have suggested that water viscosity drop can be caused by thermally induced conversion of H_2O para/ortho spin isomers inside a turbulent vortex which formed during eastward turn of the Gulf Stream.

Keywords*: anomalous water heating due to rainbow oil film, shift of the Gulf Stream, thermally induced water viscosity reduction,ortho-H_2O and para- H_2O spin isomers, anthropogenic effect on global climate.*

Plain Language Summary: *An anomalous water heating – up to 21°C – and ~200 km northward shift of the Gulf Stream near New England coasts were observed in summer-fall of 2011. To explain this phenomenon a new physical mechanism is proposed and discussed. It is shown that water heating is a consequence of disaster in the Gulf of Mexico and of associated oil slick,*

which has led to oil rainbow film formation over the area of a hundred thousand square kilometers.

1 INTRODUCTION

In summer of 2011 the US fishermen have observed the ocean temperature in Gulf Stream surprisingly growth to 21°C and anomalous shift (~200 km) to Greenland in traverse of New England. Later, they have informed the scientists from Woods Hole Oceanographic Institution (WHOI) on this phenomenon that was never detected in the history of observations. The WHOI specialists have systematically measured ocean parameters like temperature and salinity depth profiles along some months till the end of December [1]. This data evolution is presented in Fig.1. It was established that the Gulf Stream shifted its path northward by over 200 km [1]. Anomalous heating of the ocean upper layer (up to ~8°C warmer than mean climatological value – 13-14°C on the 50 m depth) accompanied by a salinity growth could not be explained by any mechanisms known so far.

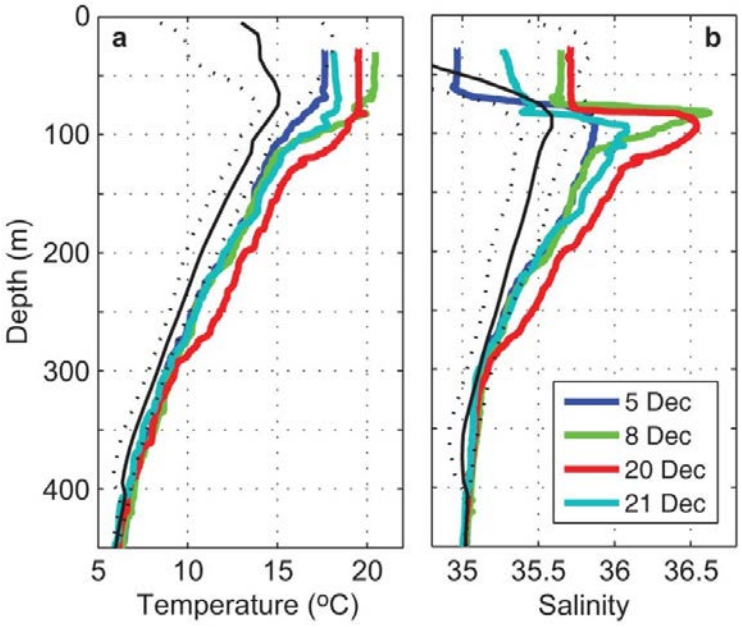


Fig. 1: Sea water temperature (a) and salinity (b) depth profiles measured near New England coasts (Reproduced from [1]). Black thin lines stand for mean climatological profiles and dotted lines represent standard deviation.

What could be the reason for the anomalous increase in temperature and, simultaneously, salinity of the Gulf Stream upper layer? Suggestions made in the work [1] and arguing that water warming could be due to warm tropical showers contradict the concurrent growth of salinity in the near-surface layer (Fig. 1) and stimulate the search for another physical mechanism [2] standing behind the ocean warming. For further examination of this phenomenon we will discuss the results of experimental studies on laser remote sensing of the rainbow oil film on water surface. The experiments were performed using a lidar based on a pulsed diode laser with an extremely low (comparable to solar) level of radiation with respect to energy density [3]. We have used the data

on *temperature induced water shear viscosity reduction* [4] and quantum differences between ortho-/para-H2O spin isomers [5,6] which correlates with two-state water model [7].

2 MATERIALS AND METHODS USED FOR INVESTIGATIONS

2.1 Lidar method for filed measurements of rainbow oil film

Figure 2 schematically shows shipborne lidar system used for oil slick sensing. In our lidar we have used a pulsed diode laser as an excitation source with an extremely low energy density (comparable to solar radiation level) without disturbing the oil slick during monitoring. The lidar beam was directed to oil slick (Figure 2, track II) and clean water surface (Figure 2, track I) at an angle about 30°.

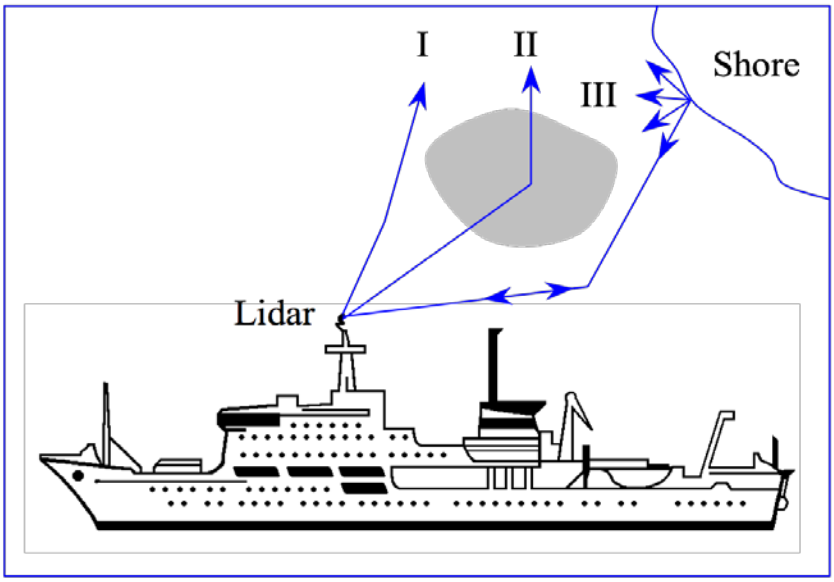


Fig. 2: Shipborne lidar sensing scheme. Tracks I-III correspond to laser beam pointed at clean water surface (I), oil silk (II) and shore objects (III).

Oil slick monitoring by this lidar showed an increase in the backscattering signal by a factor of 10 in comparison with a clean water surface. It should be mentioned that the presence of the oil slick has had a “smoothing-out” effect on the water surface, which can decrease the backscattering lidar return. In contrast, we have observed an increase.

Figure 3 shows the lidar sensing signals of oil slick (filled column) and water surface (hatched one), respectively. Intriguing that the oil slick backscattered lidar return is significantly stronger than one from water surface because, as it is well known, oil slick smoothens capillary waves on the surface.

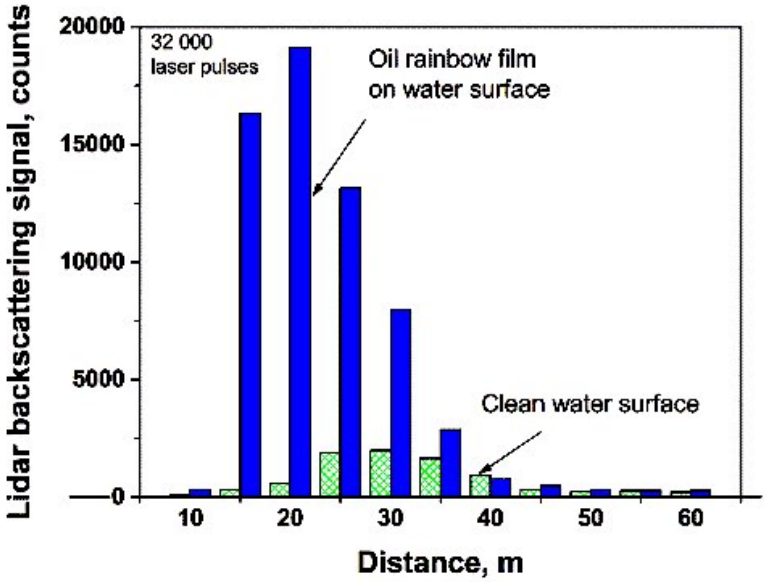


Fig. 3: Lidar backscattering signal from clean water surface (hatched columns) and oil rainbow film (filled ones).

One of the factors responsible for increasing the backscattering lidar return may be the process of H-bonded water clusters reconstruction in the subsurface layer in the vicinity of the oil slick layer. Reconstruction of the subsurface layer in water was observed earlier [8], when the polystyrene micro-balls were repulsed from the interface border into the water volume up to several microns thickness depth. So we have supposed that the oil slick can induce ice-like structure formation [8] in subsurface water layer. Further, the backscattering lidar return increased due to laser pulses interaction with this structured layer.



Fig. 4: A picture of an oil spill in Mexican Gulf, view from a helicopter. Photo from http://spill451.rssing.com/chan-5573071/all_p3.html.

It is known that clean sea water under calm conditions “transports” about 10% of solar energy in the visible range to over 100 m depth. Taking into account that the main part of solar radiation goes for heating of the 100-m thick water layer below the surface and only a small part (1–2%) is reflected according to Fresnel law. The structured water layer induced by oil slick on the water surface should be also kept in mind as it increases the scattering coefficient. So the subsurface layer several dozen meters of depth is heated more effectively in presence of the oil slick (Figure 1) than without one.

It should be noted that the oil slick, hydrocarbons (benzenes, kerosenes, etc.) and surface active substances (SASs) [9] also conserve the heat in water by actively blocking water evaporation. It is known (http://www.seapeace.ru/oceanology/atmosphere/31.html) that the value of water specific vaporization heat is 2450 kJ/kg. So, the water temperature is rising up when oil slick is present on water surface.

Actually [10], an oil slick on the water surface as anti-reflection film results in a growth of solar radiation transition into water and simultaneously reduces heat losses due to evaporation as in a classical greenhouse. Additionally, thick layers of oil spill (2-5 cm) also block evaporation, and at the same time effectively help to accumulate solar energy and transit it into water volume.

It is good to remember that around 200 tons of oil per day full filled the water of the Gulf of Mexico from the disaster day – on April 20, 2010. So, tens of thousands of square kilometers of Gulf of Mexico surface were covered by oil in form of “oil islands” by forming massive oil spots and rainbow film (Figure 4).

Finally, it is well known that the oil slick results in smoothing of small-scale gravity-capillary waves and roughness on the ocean surface. Figure 4 demonstrates how it worked in Gulf of Mexico after the disaster. It is physically clear that the surface smoothing immediately led to surface area decrease and, consequently, to a decrease in thermal energy up to ~20% [2, 10] due to evaporation losses.

It is clearly seen that small waves on the sea surface (at the bottom of Figure 4) are effectively smoothened by the oil film (upper part of the figure). The Gulf Stream temperature rising [1] (about 3% in comparison with the mean value in Figure 1, black thin lines) is equivalent to an additional power source comparable with dozens – or hundreds – of nuclear power plants. Remember that the solar constant is 1.3608 kW/m², which is 81.65 kJ/m² per minute. One can estimate the huge energy conserved in the Mexican Gulf by multiplying this value by time (months) and oil slick area (billions square meters).

This heat source was responsible for Gulf Stream water heating in Mexican Gulf area just after disaster, and then the one part of this additional heat energy was transported to the Arctic basin by the Gulf Stream. This undoubtedly is a catastrophe for the Arctic.

The other part of this additional heat energy was transformed into the tornadoes and typhoons energy over USA [11].

The question still remains, why the Gulf Stream shifted to the north after heating up to 21°C and then came back to the former path after water cooling back to 14-17°C [1]?

2.2 Laboratory results of water properties investigation near the specific point of 19°C

Let us now look at water rheological properties, which were studied in detail during past decades. In the physics of water [2, 5-7], the temperature around 19-20°C is known as the specific temperature point, i.e., the local extremum for water shear viscosity. Earlier [4] the

measurements of turbulent vortexes relaxation time have shown that shear viscosity decreases – by a factor of 6 – in the vicinity of water specific point temperature 20°C (see Figure 5, squares, plotted using the data of work [4]).

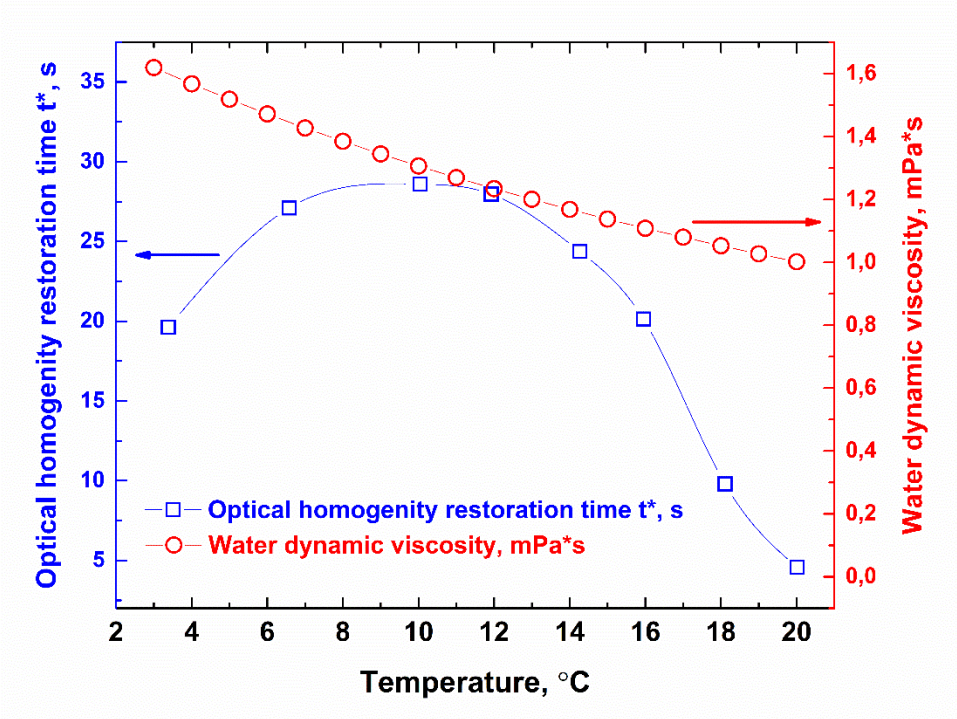


Fig. 5: Temperature dependences of saline water (0.08% NaCl) optical homogeneity restoration time after turbulent distortion (squares, left axis, reproduced from [4]) and of distilled water dynamic viscosity in laminar conditions (circles, right axis, data from [12])

Figure 5 shows that saline water shear viscosity substantially decreases (note that the time required for achieving the optical homogeneity of the turbulent vortexes is shortened in comparison with that in laminar flow – circles in Figure 5).

Thus, the Gulf Stream temperature in the vicinity of 19-21°C is **a key factor** for understanding the properties of water and its "sliding" maneuver. For the first time we pay attention to internal friction and water rheological properties during Gulf Stream turn towards the Europe. It is necessary to keep in mind that the geometry of peninsula coastline for Gulf Stream is similar to experimental configuration [4] with huge turbulent vortexes accompanied by the cavitation processes. Evidently, when sea water is heated up to 19-21°C, its viscosity drop down by factor of 6 (Figure 5, squares) due to turbulence and cavitation, rather than keeping approximately "constant" value (~20%) of laminar flow (Figure 5, circles) [12]. Therefore, such a drop in viscosity will lead to the shift in oceanic streams due to centrifugal force in areas where the Gulf Stream turns.

The physical origin of specific point temperatures, in particular 19°C (out of a few tens of others) in ice and water [5], is still unclear. We have suggested that these water anomalies and specific temperatures point existence are to be determined **by H_2O spin isomer quantum differences** [5,6]**.** Actually, rotational transitions in H_2O molecules and its spin conversion due to collisions induced by Brownian motion can change the ortho-/para ratio. It was found [5] that rotational transition energy $h\Omega_{mn}$ between the levels m and n of ortho- and para- H_2O isomers coincides with that of thermal motion kT_c in the vicinity of specific temperature point T_c:

$$kT_c = h\Omega_{mn} \quad (1)$$

where k and h are Boltzmann and Planck constants, correspondingly

Resonance collisions (1), as it was shown before [2, 5], result in rotational transitions which lead to excited (de-excited) state of ortho- or para-isomers (or both – in case of temperatures around 19°C). After transition induced by collisions to the upper (or lower) level, molecules create mixed quantum states (or quantum beats [13, 14], coupled with a close level of another H_2O isomer).

It is known [13, 14] that in mixed quantum states spin isomers undergo conversions (proton spin flip) in presence of a catalyst with a strong gradient magnetic field [5, 13–15]. In water, the most suitable catalyst is the triplet oxygen O_2 [15]. These are the reasons why the ortho-/para-conversion is more effective in turbulent water motion [2, 4], than in laminar – due to an effective H_2O molecule collisions in a gradient magnetic field in the vicinity of triplet oxygen O_2 [15].

It should be mentioned [2] that ortho-H_2O and para-H_2O spin isomers have significantly different quantum properties. Ortho-isomers have a magnetic moment and are visible in magnetic resonance imaging (MRI) and always are in rotational motion [5, 13-16]. In contrast, para-isomers have no magnetic moment (singlet states), and neither NMR nor MRI has been able to exploit the properties of the invisible singlet states [16]. So, a part of them does not rotate (proportionally to population of zero rotational level) at the room temperature in accordance to Boltzmann distribution. It is physically clear that these quantum differences are the reason for water existence as a two-liquid mixture with low and high density components [17] in dynamical equilibrium [7].

Further, the variation of an ortho-/para-isomer concentration ratio explains the ability of water molecules to form hydrogen-bonded complexes [18, 19]. Moreover, the ortho/para ratio may also be responsible for other properties of water [4, 13–17], especially in the vicinity of specific temperature points (in accordance with the equation (1)).

Actually, we have measured in our laboratory [18, 19] for the first time – as we know – that the ortho-/para- isomer concentration ratio in liquid water at room temperature is 1:1, which is non-equilibrium, i.e. it is overheated up to 270 K in terms of spin temperature [13-16]. This value is quite far from the well-known equilibrium ratio “3:1” in air [13-16]. Moreover, we have shown [19] experimentally, that the non-equilibrium state with ortho/para ratio ~1:1 increases twice – up to 2:1 – at 60°C.

3 MAIN RESULTS OF RESEARCH

A new physical mechanism of the Gulf Stream anomalous shift is proposed and discussed. We have proposed and proved that the Deepwater Horizon disaster in the Gulf of Mexico is the main reason for water heating due to oil slick in the form of rainbow film over the area of a hundred thousand square kilometers.

We have shown that the Gulf Stream shift (~200 km) to Greenland is an inertial “sliding” in the eastward turn maneuver (near Shelfbreak South of New England [1]) due to anomalous water heating to a specific temperature point (19-21°C) that occurred in the Gulf of Mexico. It was found that at this temperature a multiple-fold reduction in sea water shear viscosity takes place, which was observed earlier in turbulent flow [4].

We have suggested that water viscosity drop can be caused by thermally induced conversion of H2O para-/ortho-spin isomers inside a turbulent vortex which formed during the eastward turn of the Gulf Stream.

4 CONCLUSIONS

In the present paper we concluded that ecological catastrophe in Arctic has occurred: an anomalous Gulf Stream heating (to 21°C) and shift (~200 km) to Greenland due to ocean pollution by rainbow oil film as a sequence of Deepwater Horizon disaster in the Gulf of Mexico led to the Stream as a source of huge thermal power (~10^{15} W [20]) transportation closer to Greenland. Experts estimate [21] that about 20% of the ocean surface is now contaminated by products of the raw oil spill and by presence of oil rainbow film. So the lidar remote sensing techniques based on unmanned platforms together with satellite imaging allow us to estimate the scale of contamination by rainbow film and to make forecasts. The other key parameter, the ocean water temperature, can be measured by lidar remote sensing technique as we have recently shown in Svalbard (Norway) [22]. These data are quite important to calibrate the ocean temperature maps acquired from satellite images.

From the paper [23] it is clear that the Arctic region was relatively free from the rainbow oil film around ten years ago. However, the transportation of oil from Russian oil platforms (including platform "Prirazlomnaya") together with active oil tankers transport along the Northern Sea Route may lead to the Arctic water pollution by oil in the nearest future. Solution to this problem is to establish a reliable water surface monitoring system, which can be placed in ports and in the air, and should include new generation lidar systems [3, 22]. It can be a necessary step in keeping arctic water areas clean from pollution for the future use [24].

The 21st UN Conference on climate change (United Nations Framework Convention on Climate Change (COP-21)) and 11th meeting under the framework of Kyoto Protocol (CRP-11), which was held in France in December 2015, were aimed at signing and implementing an international agreement to maintain an increase in the average temperature of the planet below 2°C, which should be applicable for all countries [25]. Environmental catastrophes, such as the accident at the Deepwater Horizon oil platform in the Gulf of Mexico on April 20, 2010, can lead, as it is shown clearly in this paper, to local warming of the ocean by a factor of several times higher than 2°C, and can be the main reason for uncontrolled global processes, especially in the Arctic, which already heats up twice as fast as the entire globe.

REFERENCES

1. Gawarkiewicz, Glen G et al. (2012), Direct Interaction between the Gulf Stream and the Shelfbreak South of New England. *Scientific reports* 2.
2. Pershin, Sergey M. 2016. "Mechanism of an Anomalous Shift of the Gulf Stream in 2011 " Atmoshpheric and Ocean Optics 29(4): 331–338.
3. Pershin, Sergey M. 2001. "Oil Spill Detection by Portable Micropulse Eye-Safe Backscattering Diode Lidar." *Physics of Vibrations* 9(3): 192–96.
4. Stebnovskii, S V. 2004. "On the Shear Strength of Structured Water." *Technical Physics* 49(1): 19–21
5. Pershin, Sergey M. 2008. "Coincidence of Rotational Energy of H_2O Ortho-Para Molecules and Translation Energy near Specific Temperatures in Water and Ice." *Physics of Wave Phenomena* 16(1): 15–25.
6. Pershin, Sergey M. 2013. "Effect of Quantum Differences of Ortho and Para H2O Spin-Isomers on Water Properties: Biophysical Aspect." *Biophysics* 58(5): 723.

7. Russo, John et al. 2018. “Water-like anomalies as a function of tetrahedrality” www.pnas.org/cgi/doi/10.1073/pnas.1722339115

8. Pollack, Gerald H. (2013), The Fourth Phase of Water: Beyond Solid, Liquid, and Vapor. Seattle.

9. Rosen MJ & Kunjappu JT. (2012), *Surfactants and Interfacial Phenomena* (4th ed.). Hoboken, New Jersey: John Wiley & Sons. *ISBN 1–118–22902–9.Archived* from the original on 8 January 2017.

10. Petrichenko S. A., Pudov V. D., and Yaroshevich M. M. (1985), Method for indication of evaporation depressors on the water surface, *Vodn. Resur.* 12(6): 167–170.

11. S-Y Simon Wang, Lin Zhao, Jin-Ho Yoon4, Phil Klotzbach and Robert R Gillies, 30 April 2018, Environmental Research Letters, Volume 13, Number 5.

12. Cooper, J R, and R B Dooley. (2008), The International Association for the Properties of Water and Steam, Release on the IAPWS Formulation 2008 for the Viscosity of Ordinary Water Substance. *International Association for the Properties of Water and Steam*: 1–9. http://www.iapws.org/relguide/viscosity.html.

13. Buntkowsky, Gerd et al. (2008), Mechanisms of Dipolar Ortho/para–H2O Conversion in Ice. *Zeitschrift für Physikalische Chemie* 222(7): 1049–63.

14. Chapovsky, Pavel L. (2001), New Access to Very Weak Interactions in Molecules. *Journal of Physics B: Atomic, Molecular and Optical Physics* 34(6): 1123.

15. Michaut, Xavier, Anne–Marie Vasserot, and Luce Abouaf–Marguin. (2004), Temperature and Time Effects on the Rovibrational Structure of Fundamentals of H_2O Trapped in Solid Argon: Hindered Rotation and RTC Satellite. *Vibrational spectroscopy* 34(1): 83–93.

16. Mammoli, Daniele et al. 2015. “Challenges in preparing, preserving and detecting para-water in bulk: overcoming proton exchange and other hardles.” *Phys.Chem.Chem.Phys.*17: 26819.

17. Nilsson, Andreas, Pettersson, Lars G.M. 2015. “The structural origin of anomalous properties of water.” *Nature communications* 6(8998):…. DOI:10.1038/ncomms9998

18. Bunkin, Alexey F., Nurmatov Alisher A., and Pershin Sergey M. (2006), Coherent Four–Photon Spectroscopy of Low–Frequency Molecular Librations in a Liquid. *Physics–Uspekhi* 49(8): 855–861.

19. Pershin, Sergey M., and Bunkin Alexey F. (2009), Temperature Evolution of the Relative Concentration of the H_2O Ortho/Para Spin Isomers in Water Studied by Four–Photon Laser Spectroscopy. *Laser physics* 19(7): 1410–1414.

20. Shagaev, A. A. 2010. “A New Ice Age Is Coming? What Should We Do?” http://sciencereform.narod.ru/GolfstrimRu.html.

21. Pudov, V.D. (2007), Contamination of the World Ocean and the Greenhouse Effect. *Hydro–meteo security (Gidrometeobezopasnost’)* 4(1): 83–91.

22. Bunkin, Alexey F. et al. 2012. “Remote sensing of sea water and drifting ice in Svalbard fjords by compact Raman LIDAR.” *Applied Optics* 51(22): 5477-5485.

23. Maksakovskiy, V P. 2005. *Geographical Portrait of the World*.

24. International Arctic Summit Arctic 2018 SPb, contributions and abstracts, WEB: http://arcticas.ru/konfer.php

25. New UN Report Synthesizes National Climate Plans from 146 Countries, UNFCCC 30 October 2015, WEB: newsroom.unfccc.int/unfccc–newsroom/indc–synthesis–report–press–release/.

Structured Session 4

Towards Automatic Target Recognition. Detection, Classification and Modelling

Organiser(s): Groen Johannes, Jans Wolfgang, Pailhas Yan, Myers Vincent

WAVEFORM DESIGN FOR LOW FREQUENCY SYNTHETIC APERTURE SONAR

Yan Pailhas[a]

[a]NATO STO Centre for Maritime Research and Experimentation

Viale S. Bartolomeo 400, 19126 La Spezia, Italy
email: yan.pailhas@cmre.nato.int

Abstract: *Wideband sonars effectively utilise their bandwidth to provide high resolution in range. In most cases, wideband sonar waveforms are LFM (Linear Frequency Modulated) pulses or linear chirps. For a linear chirp, the instantaneous frequency varies linearly with time. The range resolution signal is obtained through pulse compression or matched filtering. It is well known that the resulting range resolution is inversely proportional to the bandwidth Δf, and that the gain after pulse compression is the product of the bandwidth Δf and the pulse duration τ. In this talk, we will study the case of Quadratic Frequency Modulated (QFM) pulses. We will first derive the matched filtered response of this particular pulse and show that the range resolution and the power gain is similar to the LFM case. However we will illustrate that QFM presents a non-constant energy distribution in frequency which can be utilised to compensate the transducer energy loss at the lower end of the spectra. QFM can then be used to normalise the overall pulse energy without loss in the SNR (Signal to Noise Ratio). We will also demonstrate that in the case of SAS (Synthetic Aperture Sonar) systems and in particular in the case of low frequency SAS, quadratic frequency modulated pulses provide more robustness toward navigation errors and that the resulting PSF (Point Spread Function) is less susceptible to blurring effects.*

Keywords: *LFSAS, Waveform design.*

1. INTRODUCTION

The pulse of choice for sonar or radar systems has often been the LFM (Linear Frequency Modulated) waveform, as it offers interesting characteristics in terms of range estimation and SNR (Signal-to-Noise Ratio) gain thanks to pulse compression. The use of high order PFM (Polynomial Frequency Modulated) waveforms with a non linear instantaneous frequency has also been of interest for the study of brown bat signals, frequency tracking algorithms [1], underwater communications [2] or image reconstruction algorithms for ISAR (Inverse Synthetic Aperture Radar) for targets with high manoeuvrability capabilities [3]. The PFMs ambiguity function has also been studied for SAR (Synthetic Aperture Radar) applications, PFM waveforms can provide a lower SNR threshold for target detection and better capability to discriminate multiple components signals [4]. As part of the HRLFSAS (High Resolution Low Frequency Synthetic Aperture Sonar) project [5], we investigate in this paper the use of PFM and in particular QFM (Quadratic Frequency Modulated) waveforms for low frequency systems. Low frequency ultra wideband systems can represent a great challenge in terms of engineering [6] as low frequencies require greater efforts to produce. We will show that QFM presents a non-uniform frequency spectra which can be utilised to increase the output energy at the lower end of the spectra.

2. POLYNOMIAL FREQUENCY MODULATED WAVEFORMS

2.1. LFM

In this paper, we are considering polynomial frequency modulated pulses $s(t)$ of the form

$$s(t) = A(t)\exp\left[2i\pi\left(f_1 t + \frac{t^k \Delta f}{k\tau^{k-1}}\right)\right], \tag{1}$$

for $t \in [0,\tau]$ and with $k \in \mathbb{N}^*$. In (1), Δf represents the bandwidth, f_1 the starting frequency, τ the pulse duration and $A(t)$ the windowing or weighting function. For $k = 2$, we obtain

$$s(t) = A(t)\exp\left[2i\pi\left(f_1 t + \frac{t^2 \Delta f}{2\tau}\right)\right], \tag{2}$$

which represents the classical formula for LFM (Linear Frequency Modulated) pulses. Range resolution is then obtained by cross-correlation between the received signal and the transmitted signal. The matched filter response $s_{MF}(t)$ is then given by

$$s_{MF}(t) = \int_{-\infty}^{+\infty} s^*(t)s(t'+t)dt'. \tag{3}$$

In radar, due to physical and electronic constraints, the windowing function $A(t)$ is most of the time a rectangular window. The analytical solution of (3) in that case is well known [7] and writes

$$s_{MF}(t) = \tau\frac{\sin[\pi t\Delta f(1-|t|/\tau)]}{\pi t\Delta f}\exp(2i\pi f_0 t), \tag{4}$$

where $f_0 = f_1 + \Delta f/2$ is the central frequency. For a Gaussian window with $A(t) = \exp\left[-\frac{(t-\tau/2)^2}{2\sigma^2}\right]$, the analytical solution to (3) also exists [8] and writes as

$$s_{MF}(t) = \sigma\sqrt{\pi}\exp\left[-\left(\frac{1}{4\sigma^2} + \frac{\pi^2\Delta f^2\sigma^2}{\tau^2}\right)t^2\right]\exp(2i\pi f_0 t). \tag{5}$$

2.2. QFM

Following the same notations as in section 2.1, a QFM pulse $s(t)$ corresponds to $k = 3$ in Eq. (1) and writes

$$s(t) = A(t)\exp\left[2i\pi\left(f_1 t + \frac{t^3\Delta f}{3\tau^2}\right)\right]. \tag{6}$$

Note that the instantaneous frequency corresponding to the time derivative of the phase $\varphi(t)$ of $s(t)$ divided by 2π is now a quadratic function as observed in Eq. (7).

$$\varphi'(t) = 2\pi(f_1 + \Delta f\tau^{-2}t^2) \tag{7}$$

The same Gaussian windowing function $A(t)$ as in 2.1 will be used for the derivation of $s_{MF}(t)$. Using (6) into (3) leads to

$$s_{MF}(t) = \exp\left(-\frac{\tau^2}{8\sigma^2}\right)s(t)\int_{-\infty}^{+\infty}\exp\left[-\left(\frac{1}{\sigma^2} - 2i\pi\frac{\Delta f}{\tau^2}t\right)t'^2 + \left(-\frac{t-\tau}{\sigma^2} + 2i\pi\frac{\Delta f}{\tau^2}t^2\right)t'\right]dt'. \tag{8}$$

Let

$$a = \frac{1}{\sigma^2} - 2i\pi\frac{\Delta f}{\tau^2}t \;\text{ and }\; b = -\frac{t-\tau}{\sigma^2} + 2i\pi\frac{\Delta f}{\tau^2}t^2. \tag{9}$$

The integral of the righthand side of (8) then becomes

$$\int_{-\infty}^{+\infty}\exp\left(-ax^2 + bx\right)dx = \sqrt{\frac{\pi}{a}}\exp\left(\frac{b^2}{4a}\right). \tag{10}$$

Note that the resolution of the complex Gaussian integral [9] is valid for all $a, b \in \mathbb{C}^*$. Let now define

$$\alpha = 2i\pi\frac{\Delta f}{\tau^2} \;\text{ and }\; \beta = \frac{1}{\alpha\sigma^2}. \tag{11}$$

It is interesting to note that $\alpha\beta = \frac{1}{\sigma^2}$. By combining (9) and (11), we arrive to

$$a = \alpha(\beta - t) \;\text{ and }\; b = \alpha(t^2 - \beta t + \beta\tau). \tag{12}$$

We can now derive the argument of the exponential function in (10) using a polynomial division

$$\frac{b^2}{4a} = \frac{\alpha}{4}\left[-t^3 + \beta(t-\tau)^2 - \beta\tau^2 + \frac{\beta^2\tau^2}{\beta - t}\right]. \tag{13}$$

Using the notations given by (13), the QFM pulse in (6) rewrites as

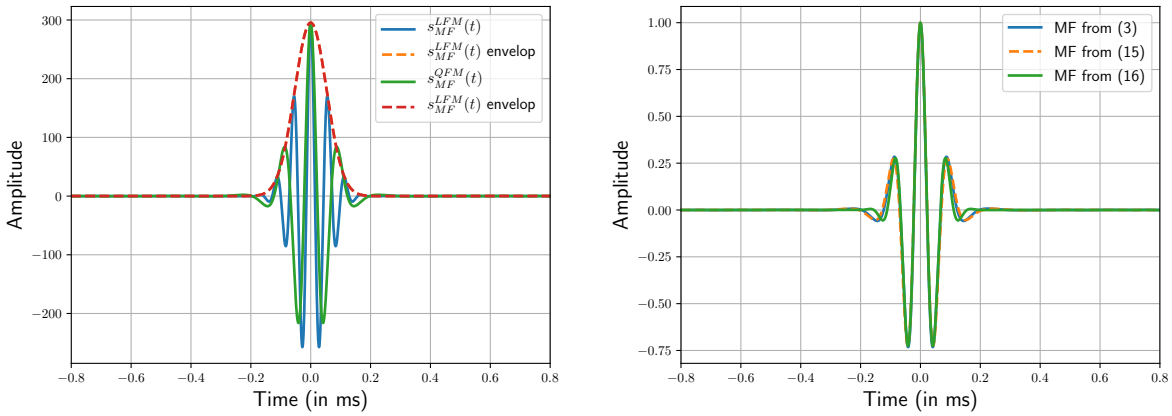
$$s(t) = \exp\left[-\frac{(t-\tau/2)^2}{2\sigma^2} + 2i\pi f_1 t + \frac{\alpha}{3}t^3\right]. \tag{14}$$

The exact analytical solution to (3) is then obtained by substituting (14) and (13) into (8):

$$s_{MF}(t) = \exp\left(-\frac{\tau^2}{8\sigma^2}\right)\exp\left[\frac{\alpha}{12}t^3 - \frac{t^2}{4\sigma^2} + \frac{\tau^2}{8\sigma^2} + 2i\pi f_1 t + \frac{\alpha}{4}\frac{\beta\tau^2}{1-t/\beta}\right]. \tag{15}$$

Eq. (15) gives the exact solution to (8), its direct physical interpretation however is rather complex due to the last fractional term. A more comprehensive result is given by performing a Taylor expansion at the second order on (15) which leads to

$$s_{MF}(t) \approx \sigma\sqrt{\pi}\exp\left[-\left(\frac{1}{4\sigma^2} + \frac{\pi^2\Delta f^2\sigma^2}{\tau^2}\right)t^2\right]\exp\left[2i\pi\left(f_1 + \frac{\Delta f}{4}\right)t + 2i\pi\frac{\Delta f}{12\tau^2}t^3\right]. \tag{16}$$

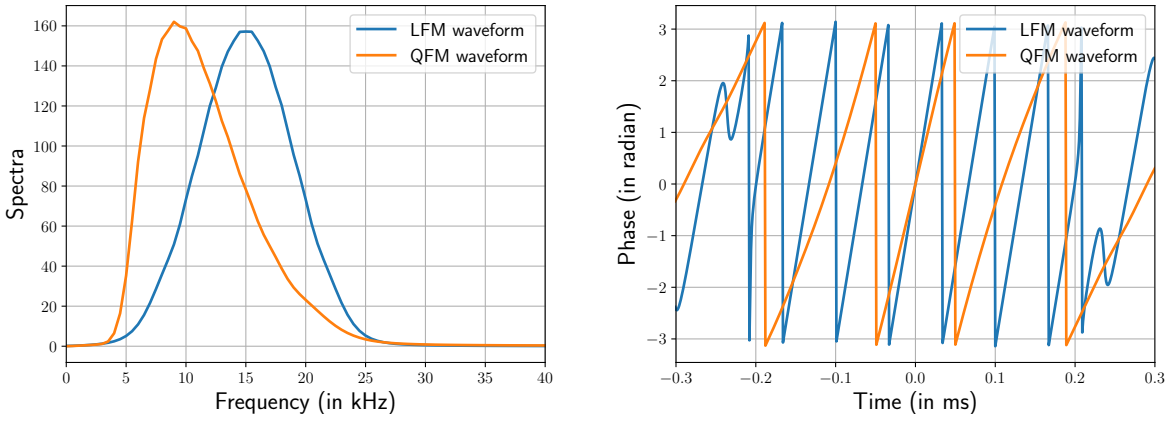


(a) (b)

Fig. 1: (a) *Matched filter responses of the LFM and the QFM with their respective envelopes.* (b) *Comparison between the matched filter responses of the QFM computed with the numerical method from* (3)*, the exact expression* (15) *and the approximation* (16)*.*

The comparison between the two matched filter responses (5) and (16) is particularly interesting. First, the amplification gain factor is identical and equals to $\sigma\sqrt{\pi}$ in both cases. Furthermore, the normalised amplitude envelope represented by the Gaussian term is also the same for both matched filter responses, meaning that range resolution as defined as the scatterer energy diffusion as in [8] is also identical for both waveforms. Thus, LFM and QFM Gaussian windowed waveforms provide through auto-correlation the same range resolution. The only difference between (5) and (16) lays in the phase of the function and is easily extracted from the last term in (16). Given that the width of $s_{MF}(t)$ is much smaller that the pulse duration τ, the cubic behaviour of the phase in (16) does not have a meaningful impact on the overall phase behaviour. At this point the only remaining difference lays in the apparent central frequency respectively $f_1 + \frac{\Delta f}{2}$ and $f_1 + \frac{\Delta f}{4}$ for the LFM and the QFM waveform. For a high frequency system such as the CMRE MUSCLE, $f_1 = 270$ kHz and $\Delta f = 60$ kHz. The central frequency after matched filtering will then be respectively 300 kHz and 285 kHz using a LFM and a QFM pulse. The 15 kHz difference at 300 kHz will not impact significantly the backscattered response nor the final sonar image. Considering now a low frequency system with $f_1 = 5$ kHz and $\Delta f = 20$ kHz. In that example, the central frequency of the QFM waveform will be lowered by a third of an octave compared to the LFM waveform, *i. e.* from 15 kHz down to 10 kHz.

For the next examples, the parameters for all waveforms (either LFM or QFM) are: $f_1 = 5$ kHz, $\Delta f = 20$ kHz, $\tau = 2$ ms and $\sigma = 4.10^{-4}$ s. In figure 1(a), we plotted the matched filter responses of a LFM and a QFM waveforms alongside their respective envelopes. As expected from the comparison between (5) and (16), both responses have the same maximum amplitude and the same envelope. The two envelopes actually superimpose perfectly. Figure 1(b) draws the matched filter response for a QFM pulse using the direct computation of the convolution as in (3), the exact analytical solution from (15) and the approximation response as written in (16). The figure shows that the approximation analytical solution (16) follows extremely closely the exact solution (15) with a small deviation in the sidelobes of the response which are not taken into account by the Taylor expansion at this order.



(a) (b)

Fig. 2: (a) *Spectra of the LFM and QFM matched filter responses.* (b) *Phase of the matched filter response of the LFM and QFM waveforms.*

Using the same pulse parameters, figure 2(a) plots the two spectra of the LFM and the QFM matched filter responses. As it has been highlighted previously, we observe a significant energy shift toward the lower frequency for the QFM response compared with the LFM response. A direct consequence of this energy shift can be spotted in figure 1(b) where the phase of the matched filter responses for the LFM and QFM pulses has been drawn. Note that the energy of both $s_{MF}(t)$ is concentrated in the time window $t \in$ [-0.2, 0.2] ms. Because the apparent central frequency of $s_{MF}^{QFM}(t)$ is significantly lower that the one of $s_{MF}^{LFM}(t)$ for low frequency systems, the phase variation is then significantly slower as seen in figure 2(b). In essence SAS processing consists in coherently summing matched filter echo responses. Decorrelation can come from imprecise estimation of the navigation (*i.e.* the precise localisation of the system when transmitting and receiving). A slower phase variation then provides more robustness to navigation errors.

3. CONCLUSIONS

In this paper, we derived the analytical formula for the matched filter response of a quadratic frequency modulated waveforms. For Gaussian windowed pulses and compared to LFM waveforms, QLMs offer the same amplitude gain and the same range resolution. The energy shift toward the lower frequencies however can represent an asset for low frequency systems as it

can concentrate the energy (and then offer a better SNR) on the lower part of the system's bandwidth. For SAS system, QLM waveforms also provide more robustness toward navigation errors.

ACKNOWLEDGEMENT

This work was performed under the Project SAC000905–High Resolution Low Frequency Synthetic Aperture Sonar (HRLFSAS) of the STO-CMRE Programme of Work, funded by the NATO Allied Command Transformation.

REFERENCES

[1] S. S. Abeysekera. Performance analysis of an autocorrelation based frequency tracker for LFM and QFM signals. In *2009 7th International Conference on Information, Communications and Signal Processing (ICICS)*, pages 1–5, Dec 2009.

[2] A. C. Pecci, C. Laot, and A. Bourre. Quadratic chirp modulation for underwater acoustic digital communications. In *OCEANS 2015 - Genova*, pages 1–7, May 2015.

[3] Y. Wang and Y. Jiang. Inverse synthetic aperture radar imaging of maneuvering target based on the product generalized cubic phase function. *IEEE Geoscience and Remote Sensing Letters*, 8(5):958–962, Sep. 2011.

[4] S. Barbarossa and V. Petrone. Analysis of polynomial-phase signals by the integrated generalized ambiguity function. *IEEE Transactions on Signal Processing*, 45(2):316–327, Feb 1997.

[5] Y. Pailhas, S. Fioravanti, and S. Dugelay. The high resolution low frequency synthetic aperture sonar (HR-LFSAS) project. In *SAR/SAS conference, Institute of Acoustics*, volume 40, pages 66–72, 2018.

[6] S. Fioravanti, F. Aglietti, A. Carta, A. Sapienza, and Y. Pailhas. Modular design of a 2D transmitting array for an advance low frequency synthetic aperture sonar. In *OCEANS 2019 - MTS/IEEE Marseille*, pages 1–6, Jun 2019.

[7] M. Cheney and B. Borden. *Fundamentals of Radar Imaging*. pp. 149. Society for Industrial and Applied Mathematics, Philadelphia, US, 2008.

[8] Y. Pailhas, Y. Petillot, and B. Mulgrew. Increasing circular synthetic aperture sonar resolution via adapted wave atoms deconvolution. *J. Acoust. Soc. Am.*, 141(4):2623–2632, 2017.

[9] A Zee. *Quantum Field Theory in a Nutshell*. pp. 576. Nutshell handbook. Princeton Univ. Press, Princeton, NJ, 2003.

CALIBRATION TARGET FOR ESTIMATION OF FREQUENCY DEPENDENCE IN SYNTHETIC APERTURE SONAR

Stig A V Synnes[a,b], Ole J Lorentzen[a]

[a] Norwegian Defence Research Establishment (FFI), PO Box 25, NO-2027 Kjeller, Norway.
[b] University of Oslo (UiO), Department of Informatics PO Box 1080, Blindern, N-0316 Oslo, Norway.

Contact author: Stig A V Synnes,
Norwegian Defence Research Establishment (FFI), PO Box 25, NO-2027 Kjeller, Norway.
E-mail: Stig-Asle.Synnes@ffi.no

Abstract: *Synthetic aperture sonar (SAS) can provide high resolution images of the seafloor backscatter. A current research topic is whether wider bandwidth and lower frequencies can support better discrimination of different materials. In principle, the frequency dependence of the backscatter can be estimated at high resolution over the image. We suggest a calibration target that can provide simultaneous ground truth on both strength and frequency dependence of the backscatter.*

We develop an extended target consisting of objects with different combinations of scattering strength and frequency dependence. In order to provide deterministic frequency dependencies, we use solid geometrical shapes in the form of spheres, cylinders/cones and corners as reflectors. The scattering strengths of these reflectors are functions of frequency to the power of 0, 1 and 2, respectively. These three frequency dependencies are combined with different scattering strengths by using replicas of different sizes. We try to limit the acoustic footprint of the targets to a point where possible, in order to support processing at the maximum SAS resolution. We mount the objects on a metal plate, and elaborate on the choice of material and thickness needed to provide the required acoustic properties at the frequencies under investigation.

Finally, we present SAS images of a prototype target measured both at and outside of the design frequency. The suggested calibration target should be well suited to validate algorithms extracting the frequency dependence, and their ability to isolate the frequency dependence from the scattering strength.

1. INTRODUCTION

Synthetic aperture sonar (SAS) has become a major success for seafloor surveillance, providing high resolution images with large area coverage. Its applications are wide and include, but is not limited to, naval mine hunting, searching for wrecks, mapping of dumped WWII conventional and chemical munitions, underwater archeology, pipeline inspection and mapping for oil rig decommissioning [1–3].

A current trend in SAS research is to investigate the added value of wider bandwidth and lower frequency, as these have the potential of supporting better discrimination of different materials, thereby improving the performance for many applications [4].

At FFI we have been developing an algorithm to extract the frequency dependence of the scattering at high resolution over a SAS image. When testing the algorithm, we observed that the estimated frequency dependence increases with the estimated scattering strength. The correlation was not expected and could indicate an error in the algorithm. We therefore are in need of a calibration and validation target, that contains different combinations of scattering strength and its frequency derivative.

In this paper we develop a SAS target that allows for validating methods and algorithms designed to extract the frequency dependence of the acoustic scattering, and to isolate frequency dependence from scattering strength.

2. METHOD

We suggest and develop a calibration target consisting of reflectors with different combinations of frequency dependence and scattering strength. It would be hard to find materials with the same scattering strength or frequency dependence over a wide frequency area. We therefore opt for using targets of simple geometrical shapes that provide different frequency dependencies. In order to support high resolution SAS, we also choose scatterers with a single point acoustic footprint where possible.

We choose to arrange the reflectors in a matrix pattern, such that row number reflects the intensity and the column number reflects the frequency dependence. Thus the calibration target can be used to validate estimation of both intensity and frequency dependence, in the presence of variations on the other.

We choose to mount the targets on top of a smooth metal plate, that is thick enough that the reflection off the seafloor is minimal. This will make it possible to isolate also weaker scatterers, in contrast to mounting the targets on a frame where they would be observed on top of the seafloor scattering.

2.1 Frequency Dependent Scattering with Geometrical Shapes

In order to provide deterministic frequency dependencies, we use solid geometrical shapes in the form of spheres, cylinders/cones and corners as reflectors. The scattering strength of geometrical shapes can be estimated directly from the geometry when the target dimensions are much larger than the wavelength. At wavelength λ the target cross section is $\sigma = 4\pi A^2/\lambda^2$, where A is the effective area (of a flat plate with the same scattering strength) and the scattering strength in dB re 1m follows as $TS = 10\log(\sigma/4\pi)$ [5, Sec 3.2].

We have examined the list of reflectors in [6] and focus on the few listed in Table 1. We observe that the scattering strength of these reflectors is a function of frequency to the power of 0, 1 and 2, depending on whether they are curved around two, one or no axes, respectively. Trihedrals provide single point acoustic footprint, as does the bicone when observed from its symmetry plane. The maximum scattering strengths for the shapes are listed in Table 1. For

simplicity of predicting the targets' scattering cross sections, we assume small grazing angles and choose targets of scattering strengths $0.01\,\mathrm{m}^2$, $0.1\,\mathrm{m}^2$ and $1.0\,\mathrm{m}^2$.

Mirrored Shape	**Scattering Cross Section**
Half Sphere	πr^2
Cylinder	$4\pi r h^2/\lambda$
Balancing Cone	$16\pi r^3/(9\lambda)$
Triangular Trihedral	$8\pi h^4/\lambda^2$

Table 1: Maximum scattering cross section σ for geometrical shapes mounted on a reflecting infinite plane and observed at low grazing angles. The arguments are target radius r and height h, and the acoustic wavelength λ. The frequency dependence follows from $\lambda = c/f$, with sound speed c and frequency f. The formulas were derived from [6, Chapter 6] and [7].

2.2 Plate Thickness

We would like the plate to provide a no-return area, masking the seafloor reflection, such that the object return is clean. This can be obtained by a low transmission through the plate for relevant seafloor grazing angles. For SAS, typical grazing angles are between 5 and 40 degrees.

Formulas for predicting the reflection and transmission off metal plates suspended in water are derived in [8]. For plates described through their dilational and shear wave speeds, along with density and thickness, sample predictions of reflection and transmission are showed in Fig. 1. For a given material, the prediction can be transferred to another sensing frequency

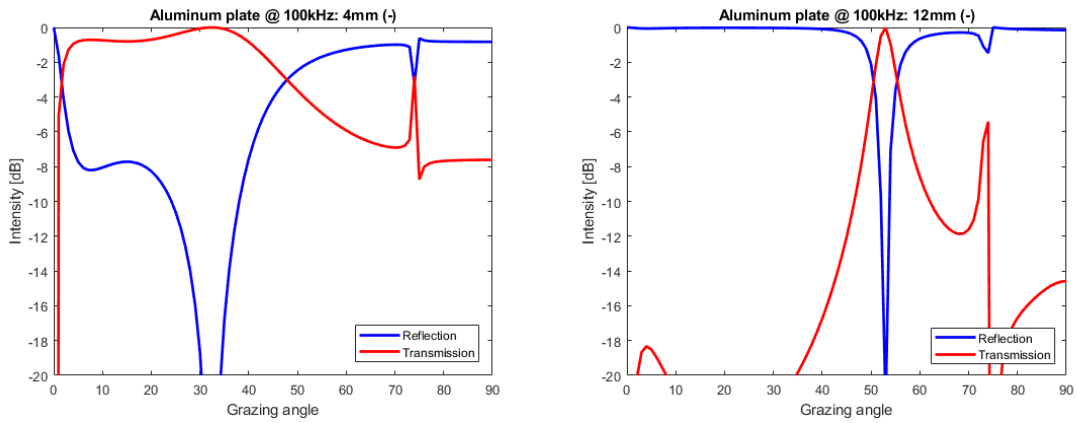


Fig. 1: Reflected and transmitted energy off 4 mm and 12 mm thick aluminum plates at 100 kHz, predicted from [8].

or plate thickness by keeping the product of frequency and thickness fixed. We find that for grazing angles below 30-40 degrees, aluminum plates provide *two-way transmission loss* at 100 kHz of around 2dB@4mm, 20dB@8mm, 40dB@12mm and 60dB@16mm plate thickness. For steel plates, the corresponding *two-way transmission loss* at 100 kHz is around 4dB@4mm, 20dB@6mm and 40dB@8mm. Steel has roughly three times the density of aluminum, with $7820\,\mathrm{kg/m}^3$ versus $2700\,\mathrm{kg/m}^3$.

If we have strong reflection off the plane at near normal incidence, the bicone target can be simplified by using a single standing cone, mirrored on the plate. In order to construct the

trihedral corner reflector from plates, we depend on strong scattering for any incident angle. We observe that both for aluminum and for stainless steel, the intensity loss for the reflected signal at 100 kHz is smaller than 1 dB from grazing angles above 60 degrees. There is, however, a strong intensity loss around 45-55 degrees for both materials and most plate thicknesses. As a result, corners made of metal plates will not provide the desired scattering strength.

3. EXPERIMENTAL RESULTS

We present SAS images of a prototype calibration target that was made before our knowledge on plate reflection and transmission was gathered. This target was first measured in the spring of 2017 during FFI's MAREX'17 marine robotics exercise, using the HISAS 1032 SAS of FFI's HUGIN-HUS autonomous underwater vehicle (AUV). The system was operated with 30 kHz bandwidth around 100 kHz. After examining the results and observing that the target was barely visible, we acquired the mentioned knowledge on plate reflection and transmission, and found that our prototype should work more as intended at higher frequencies. At the time, Kongsberg Maritime was developing their new HISAS 2040 SAS for operation from their new MUNIN AUV and from the Hydroid REMUS 600 AUV [9]. During the testing of their first MUNIN AUV around the summer of 2018, Kongsberg Maritime accepted to both deploy our target and record a few lines past it. The onboard HISAS 2040 system operated with 60 kHz bandwidth around 250 kHz. However, as the deployment of the plate was challenging, we only have recordings of the plate upside-down and standing-on-the-edge. Though these data cannot be used for calibration, they still prove useful for evaluating the design of the prototype calibration target and as benchmark for the theory as reported here.

3.1 Prototype Calibration Target

We present a photo of our prototype target in Fig. 2. Note that this target was made before the knowledge on plate reflection and transmission was acquired, based on the assumption that the mounting plate would allow only minimal transmission. The target measures 1.8 by 1.2 m, and the mounting plate is made of 4 mm aluminum. The distance between objects with the same scattering cross section is 0.6 m, and the distance between lines of different scattering cross section is 0.3 m. The solid shapes are made of aluminum, and the trihedral corner reflectors of 1.5 mm acid-resistant steel. On the far right corner, there is a 35 cm long cylinder holding an acoustic transponder used for positioning.



Fig. 2: Photo of the prototype target before deployment. Photo: Kongsberg Maritime.

3.2 Measurements at 100 kHz

In the 100 kHz SAS images, the plate appears transparent, but the edges normal to the line of sight can be made out. With the geometry of the plate known, also the transponder position can be discriminated, and at low grazing angles also some of the stronger scatterers. It was confirmed by optical images that the target plate rests on a flat seafloor with the targets facing up.

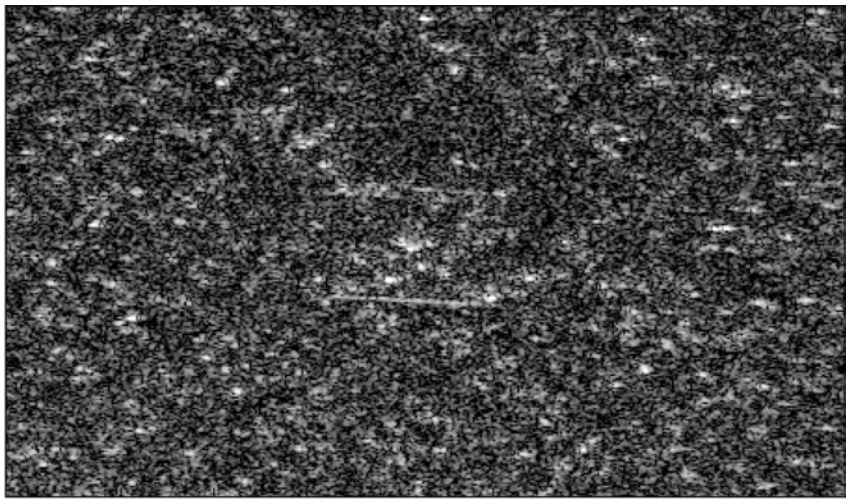


Fig. 3: SAS intensity image measured at 85-115 kHz with HISAS1032 from the HUGIN-HUS AUV. The image shows a 9 m x 5 m area covering plate and was recorded at 60 m distance and 10 m altitude.

3.3 Measurements at 250 kHz "upside-down"

The two SAS images of Fig. 4, recorded around 250 kHz from a HISAS 2040 on a MUNIN AUV, shows the target plate observed from two opposite directions. The images strongly indicate that the target plate is deployed upside-down, resting on the 35 cm long cylinder and the opposite short edge of the plate. The two SAS images shows the target plate observed from two opposite directions.

In the left image both the down-facing side of the plate with the reflectors and the seafloor beneath the plate are illuminated. The target intensities increase with the modeled target scattering strength. However, as the corner reflectors are illuminated normal to one of the cross-plates, a strong specular scattering occurs. Also, as the seafloor scattering is overlaid on the target scatterers, the weakest of the targets cannot be isolated from the background.

The right image shows the up-facing (rather smooth) back-side of the plate. The corner reflectors are clearly outlined, which is consistent with the fact that only these scatterers protrude through the plate. Some of the scatterers with low cross section are also more prominent than those of higher cross section, indicating that the target shapes closer to the edge could by partly insonified. We observe that there is a shadow beneath and behind the plate. The shadow is more filled-inn closer to the resting face of the plate.

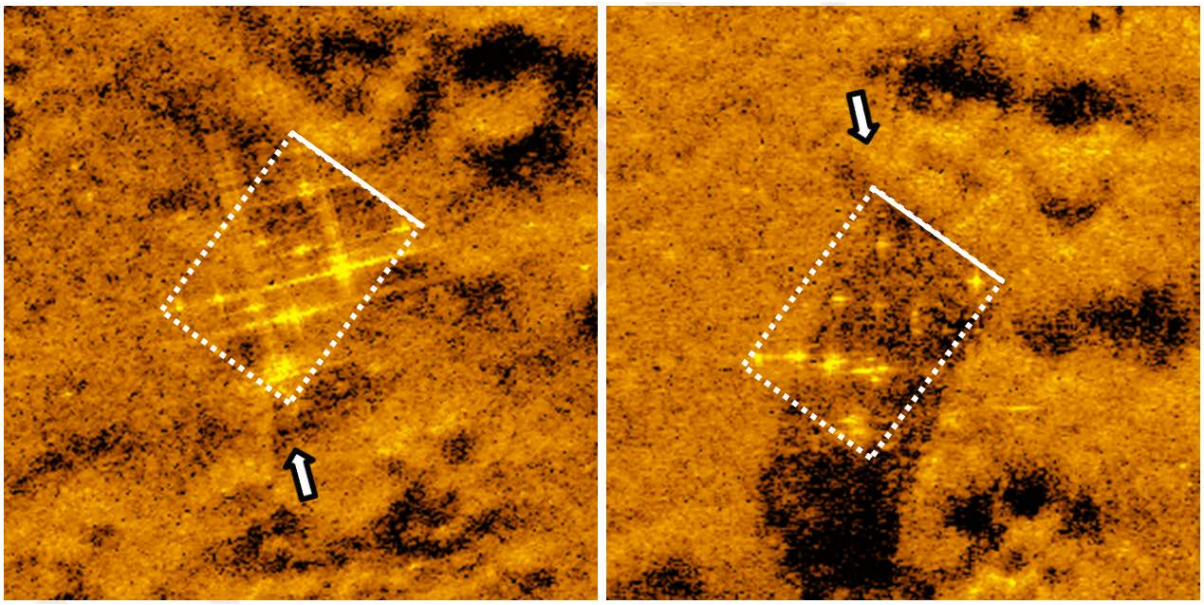


Fig. 4: SAS intensity images measured over 60 kHz around 250 kHz with HISAS 2040 from a MUNIN AUV. The two images are recorded from opposite directions at 33 m range and 4.5 m altitude, and the observation directions are indicated by white arrows. The plate appears to be resting upside-down, on a 35 cm long cylinder in the corner and on the opposite short edge of the plate. The outline of the plate is indicated by the white rectangle, and the solid line marks the edge resting on the bottom.

3.4 Measurements at 250 kHz "on-the-edge"

The two SAS images recorded around 250 kHz of Fig. 5 indicate that the target plate is deployed vertically, resting on the 35 cm long cylinder (holding an acoustic transponder) and its closest short edge of the plate. The two SAS images show the target plate observed from two opposite directions.

In the left image, the bottom side of the plate is illuminated at close to normal incidence. All the scattering is gathered on a short range-interval close to the resting face of the plate, and a high contrast shadow is observed behind the plate. (A junction between two images can be observed as an artefact on the left side of the scene.)

In the right image, the front side of the plate with reflectors is illuminated. Because of the vertical orientation of the plate, these are also gathered on a rather short range interval. Also here, a high contrast shadow is observed at some range behind the plate. However, at short range a seafloor is observed. This is in fact a mirror reflection of the seafloor in front of the plate, resulting from the top edge of the plate being closer to the sensor than the resting edge of the plate. Because of the opposite direction of observation, this patch resembles more a flipped cutout of the image with the opposite direction of observation.

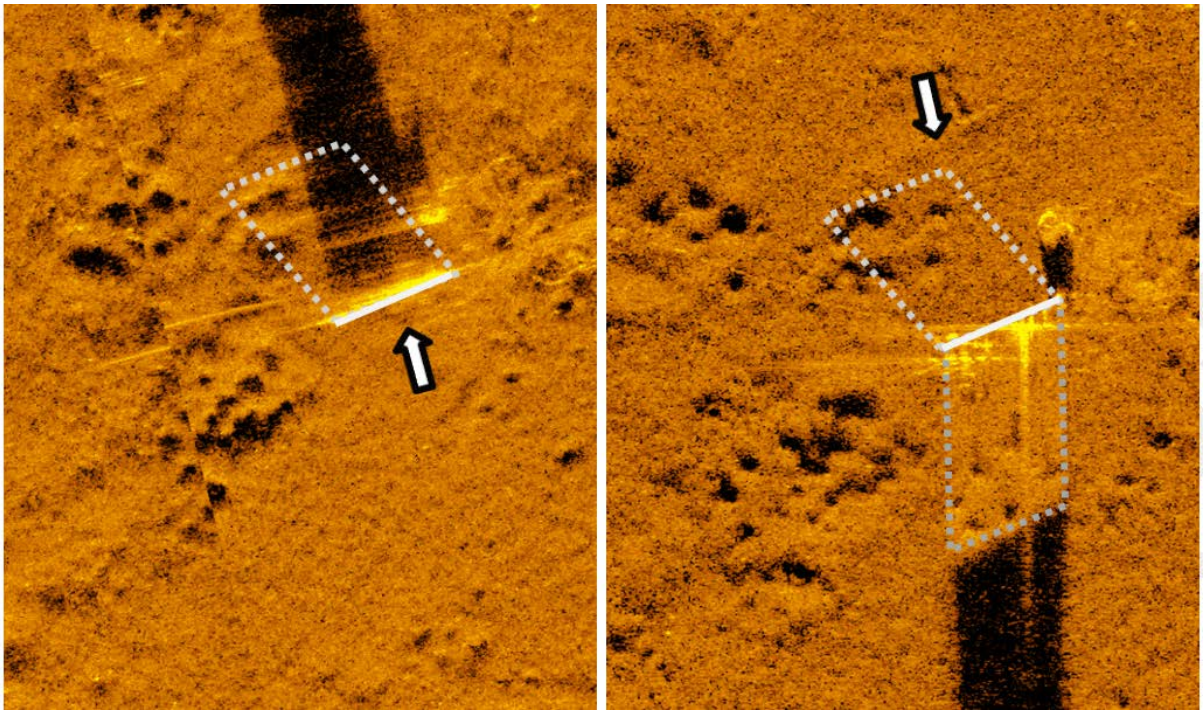


Fig. 5: SAS intensity images measured over 60 kHz around 250 kHz with HISAS 2040 from a MUNIN AUV. The two images are recorded from opposite directions at 33 m range and 5.0 m altitude, and the observation directions are indicated by white arrows. The plate appears to be resting vertically on a 35 cm long cylinder in the corner and on the closest short edge of the plate. The outline of the plate is indicated by the white trapezoid, and the solid line marks the edge resting on the bottom. The gray trapeze indicates an area filled-in by mirroring off the plate.

4. DISCUSSION AND ANALYSIS

Our measurements of the prototype target shows that its mounting plate is transparent at 100 kHz, and that the attached reflectors are hard to separate from the seafloor. Our initial assumption that the 4 mm aluminum plate would not support transmission at 5-40 degrees grazing angles around 100 kHz was clearly wrong. After gathering the theory on scattering off metal plates in Section 2.2, these predictions confirm that the plate should provide only 2 dB reduction of the seafloor scattering at this frequency. However, the reduction of the seafloor scattering should rapidly increase if switching to a higher frequency. At 250 kHz the reduction should be around 30 dB, and this is qualitatively confirmed in Section 3.3. The targets are also strong compared to the background at 250 kHz, in contrast to what we experienced at 100 kHz, where our observations are consistent with the sound being transmitted through the plate, rather than reflecting off it. For normal incidence the theory indicates strong reflection, and indeed, with the vertically oriented plate of Section 3.4, we observe both a good image of the seafloor reflected off the plate, and a deep shadow.

In general, our measurements are in line with the predicted scatterings off both the aluminum plate and the targets. The prototype target has been useful as a benchmark for the theoretical models, but a redesign is needed for its intended use at 100 kHz: First, the mounting plate must be replaced by a 12 mm aluminum plate or a 8 mm steel plate in order to provide 40 dB

reduction of the seafloor scattering. Next, the trihedral reflector should get a solid backside, in place of being constructed from metal plates, as metal plates are predicted to give strong transmission for the important 40-50 degrees incidence angle of looking directly into the corner.

5. CONCLUSION

With the suggested changes, our calibrated target should be well suited for independent validation of scattering strength and frequency dependence estimates at 100 kHz. The target can be adapted for other frequencies by scaling the plate thickness and target dimensions inversely to the applied scaling of frequency.

ACKNOWLEDGMENTS

The authors wish to thank Georgia Tech and in particular Daniel A Cook for directing us to the theory for transmission and reflection off elastic plates. The authors also wish to thank FFI's Prototype Workshop and in particular Pål Halvorsen for producing refined drawings and building the prototype target based on our hand sketch. The authors wish to thank Kongsberg Maritime and in particular Terje Halvorsen for recording data on our test target as they were finalizing the first HISAS 2040 SAS system on the new MUNIN AUV. And furthermore, the authors wish to thank all the participants of MAREX'17, including the RNoN who provided optical underwater images of the target with their HUGIN-MR AUV. And finally the authors wish to thank our colleagues Roy E Hansen, Torstein O Sæbø and Marc Geilhufe in FFI's SAS-team for ever enthusiastic and inspiring discussions.

REFERENCES

[1] Roy Edgar Hansen, Petter Lågstad, and Torstein Olsmo Sæbø. Search and monitoring of shipwreck and munitions dumpsites using HUGIN AUV with synthetic aperture sonar - technology study. Technical Report FFI-Rapport-19-00245, Norwegian Defence Research Establishment, 2019.

[2] Øyvind Ødegård, Roy E. Hansen, Hanumant Singh, and Thijs J. Maarleveld. Archaeological use of Synthetic Aperture Sonar on deepwater wreck sites in Skagerrak. *Journal of Archaeological Science*, 89:1–13, 2018.

[3] Arthur Ayres Neto, Geraldo Pinto Rodrigues, and Igor Drummond Alvarenga. Seabed Mapping with HISAS Sonar For Decommissioning Projects. *Sea Technology*, (September):15–18, 2017.

[4] Roy Edgar Hansen. Synthetic Aperture Sonar Technology Review. *Marine Technology Society Journal*, 47(5):117–127, 2013.

[5] Xavier Lurton. *An Introduction to Underwater Acoustics, Principles and Applications*. Springer, second edition, 2010.

[6] Philip G. Gallman. *Radar Reflectors for Cruising Sailboats*. Ulyssian Publications, 2005.

[7] Armin W. Doerry and Billy C. Brock. Radar cross section of triangular trihedral reflector with extended bottom plate. Technical Report SAND2009-2993, Sandia National Laboratories, 2009.

[8] Ralph Fiorito, Walter Madigosky, and Herbert Überall. Resonance theory of acoustic waves interacting with an elastic plate. *J. Acoust. Soc. Am.*, 66(6):1857–1866, 1979.

[9] *MUNIN AUV*, accessed April 11, 2019. https://www.kongsberg.com/maritime/products/marine-robotics/autonomous-underwater-vehicles/AUV-munin/.

2D & 3D, CENTRED & OFFSET, CIRCULAR SYNTHETIC APERTURE SONAR POINT SPREAD FUNCTION

Yan Pailhas[a]

[a]NATO STO Centre for Maritime Research and Experimentation

Viale S. Bartolomeo 400, 19126 La Spezia, Italy
email: yan.pailhas@cmre.nato.int

Abstract: *It has become clear over the last decade that target multiview brings significant improvement in terms of recognition rate and false alarm reduction. New acquisition and re-acquisition patterns have since emerged for autonomous missions to bring additional views of targets of interest. One of them is circular SAS (Synthetic Aperture Sonar) acquisition also known as CSAS (Circular SAS) which has proven to be very efficient both in terms of acquisition time and image resolution. However the theory of CSAS has not been fully investigated. In this talk, we study the problem of the CSAS PSF (Point Spread Function) which is the fundamental brick of the coherent image formation. We will first derive the analytical formula for the 2D centred CSAS PSF before extending the formula to any point in the full field of view (offset point). We will then derive the PSF for any point for a 3D configuration. Although the PSF is not constant in the CSAS image, we will show that it is possible to derive a uniformisation scheme of the PSF for any point in the field of view. We will also demonstrate that the proposed uniformisation increases the SNR (Signal-to-Noise Ratio) of the resulting CSAS image.*

Keywords: *CSAS, Point Spread Function.*

1. INTRODUCTION

With the increased resolution provided by SAS (Synthetic Aperture Sonar) systems, ATR (Automatic Target Recognition) algorithms have become more reliable [1–3] by drastically improving the detection rate and diminishing the false alarm rate. However, the false alarm rate has to be lowered further to an acceptable level for a fully autonomous MCM system. Target multiview reacquisition may offer to ATR algorithms additional information to properly classify an object of interest. Among the reacquisition patterns, circular SAS acquisition also known as CSAS is of great interest [4–6] and has not been fully investigated yet. The problem of the PSF (Point Spread Function) of such system in particular remains. In [7] , the authors proposed an analytical expression of the CSAS PSF for the central point. This paper describes the derivation of PSF analytical formulas for offset points, i.e. all the points in the full filed of view. It also tackles the problem of the PSF in the 3D case and proposes a normalisation scheme that increase CSAS image SNR (Signal-to-Noise Ratio).

2. CSAS CONFIGURATION

2.1. Geometrical configuration

Let **S** be a SAS system performing a circle $\mathcal{C}$ centred in **O** and with a radius R. Let now **O'** be a point within the full view area (*i.e.* insonified by **S** during the full circular revolution). **OO'** can be written as αR where $\alpha \in [0, \alpha_{\max}]$ with $\alpha_{\max} \leq 1$. When **S** is in A, it has travelled a distance of θR from it original position, and *sees* the point **O'** at an angle θ'. θ and θ' are linked through equations (1) and (2).

$$\theta' = h(\theta) = \mathrm{sgn}(\theta)\cos^{-1}\left(\frac{\cos\theta - \alpha}{\sqrt{1+\alpha^2-2\alpha\cos\theta}}\right) \text{ and} \tag{1}$$

$$\theta = h^{-1}(\theta') = \mathrm{sgn}(\theta')\cos^{-1}\left(\alpha\sin^2\theta' + \cos\theta'\sqrt{1-\alpha^2\sin^2\theta'}\right). \tag{2}$$

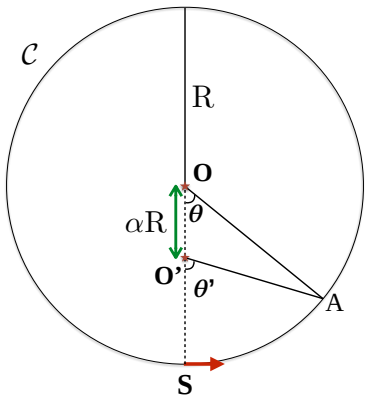


Fig. 1: (Color online) CSAS configuration and geometrical notations.

Figure 1 pictures the geometry and notations of the CSAS problem and the relationship between θ and θ'. Note that Eq. (2) and (1) are not linear. As a consequence, integrating along $\mathcal{C}$ is not uniform for **O'**. The PSF is then not uniform within the full view area.

2.2. CSAS parameters and centre point PSF

The CSAS centre point PSF has been analytically derived in [7]. We recall here some of the results needed for the calculation of the offset PSF. Let $p(t)$ be the transmitting pulse. Assuming a Gaussian weighted LFM (Linear Frequency Modulated) signal, $p(t)$ writes as

$$p(t) = \exp\left(-\frac{t^2}{2\sigma^2}\right)\exp\left[2i\pi\left(f_0+\frac{\Delta f}{2T}t\right)t\right]. \tag{3}$$

where T is the pulse duration, f_0 the central frequency and Δf the bandwidth. The matched filter response $p_{\mathrm{MF}}(t)$ of (3) is given by

$$p_{\mathrm{MF}}(t) = B(t)\, e^{2i\pi f_0 t},\ \text{where } B(t) = \sigma\sqrt{\pi}\exp\left[-\left(\frac{1}{4\sigma^2}+\pi^2\frac{\Delta f^2}{T^2}\sigma^2\right)t^2\right]. \tag{4}$$

We can see from (4) that the matched filter response $p_{\mathrm{MF}}(t)$ is only a low frequency envelope, $B(t)$, modulated by the central frequency f_0. The frequency content of $p_{\mathrm{MF}}(t)$ then comes from the frequency leakage caused by $B(t)$. The derivation of the point spread function I at the centre point $\mathbf{O}$ is obtained by integrating (4) along $\mathcal{C}$. Thanks to the problem symmetry, $I = I(r)$ is only function of r (distance to the centre $\mathbf{O}$), and can be analytically calculated:

$$I(r) = 2\pi B\left(\frac{2r}{c}\right)J_0(2kr), \tag{5}$$

where $k = 2\pi f_0/c$ is representing the wave number and $J_0(.)$ the Bessel function of the first kind of order 0. The 2D Fourier transform $\hat{I}(\rho)$ of (5) can also be calculated analytically in the special polar coordinates:

$$\hat{I}(\rho) = 4\pi^{5/2}a_0^2\sigma\exp\left[-2a_0^2(k^2+\pi^2\rho^2)\right]I_0(4\pi k a_0^2\rho) \tag{6}$$

where $a_0 = \frac{1}{\sqrt{2}}\frac{c\sigma T}{\sqrt{T^2+4\pi^2\Delta f^2\sigma^4}}$ and $I_0(.)$ represents the modified Bessel function of the first kind at the order 0. Eq. (6) can be well approximated:

$$\hat{I}(\rho) \approx \pi^2\sqrt{2}\frac{a_0\sigma}{k}\exp\left[-2a_0^2(k-\pi\rho)^2\right]. \tag{7}$$

We can see that, in the Fourier domain, the CSAS PSF is a Gaussian ring with a diameter of $2f_0/c$ and a variance of $1/\pi^2a_0^2$. Note that $\hat{I}(\rho) \in \mathbb{R}$

3. THE OFFSET POINT PSF PROBLEM

In coherent imaging, the PSF plays a central role in the understanding of the resolution problem. It is in essence the founding pillar of the image formation. The direct integration of (4) along $\mathcal{C}$ for any offset point to compute the generalised PSF within the full view area is not analytically trackable. This section extends the result given by (7) to offset points using a plane wave assumption. The justification of the plane wave assumption comes from the ratio between the expected radius of the PSF (in the order of few λ, where λ represents the wavelength) and the distance between the imaged point and the sensor (in the order of tens of metres). For example, assumming a PSF of 5λ radius and a ranging distance of 40m, the maximum error due to the plane wave assumption is less than $5.10^{-3}\lambda$, which represents more that one order of magnitude lower compared to the classic $\lambda/8$ needed for coherent processing.

3.1. Offset CSAS PSF

We saw in section 2.1 that the PSF is not uniform across the full imaging area. Let (x_0, y_0) the Cartesian coordinates of $\mathbf{O}'$. Under plane wave assumption, the CSAS PSF at $\mathbf{O}'$ can be written as

$$I(x,y) = \int_C B\left(2\frac{(x-x_0)\cos\theta' - (y-y_0)\sin\theta'}{c}\right)\exp\left[ik((x-x_0)\cos\theta' - (y-y_0)\sin\theta')\right]d\theta. \tag{8}$$

Let

$$\xi(x,y,\theta') = B\left(2\frac{(x-x_0)\cos\theta' - (y-y_0)\sin\theta'}{c}\right)\exp\left[ik((x-x_0)\cos\theta' - (y-y_0)\sin\theta')\right] \tag{9}$$

be the integrand of (8), and $(\alpha R, \theta_0)$ be the polar coordinates of $\mathbf{O}'$. The Fourier transform of (9) then writes as::

$$\hat{\xi}(\rho,\phi,\theta') = \pi\sqrt{2}a_0\sigma\exp\left[-2a_0^2(\pi\rho - k)^2\right]\exp(i\Phi)\delta(\phi+\theta'+\pi/2), \tag{10}$$

where $\Phi = 2\pi\rho\alpha R\cos(\theta_0 - \phi)$ is the offset phase shift. Note that the expression in (10) is perfectly intuitive: the Dirac function $\delta(.)$ came from the $\exp(.)$ expression in (9) and the Gaussian window from $B(.)$. Eq. (10) is in essence a slide in the k-space where only one angle contributes. It is important to note that $\{\hat{\psi}\}_{\theta'}$ is in essence a wavelet basis which reconstructs exactly the PSF given by (7). Variable manipulation in (8) leads to:

$$\mathrm{FFT}[I] = \hat{I}(\rho,\phi) = \int_{\theta=-\pi}^{+\pi}\hat{\xi}(\rho,\phi,\theta')d\theta = \int_{\theta'=-\pi}^{+\pi}\hat{\xi}(\rho,\phi,\theta')g(\theta')d\theta', \tag{11}$$

where

$$g(\theta') = \frac{\mathrm{d}h^{-1}(\theta')}{\mathrm{d}\theta'} = \frac{\sin\theta'\sqrt{1-\alpha^2\sin^2\theta'} + \frac{\alpha^2\cos^2\theta'\sin^2\theta'}{\sqrt{1-\alpha^2\sin^2\theta'}} - 2\alpha\cos\theta'\sin\theta'}{\sqrt{1-\left(\cos\theta'\sqrt{1-\alpha^2\sin^2\theta'} + \alpha\sin^2\theta'\right)^2}} \tag{12}$$

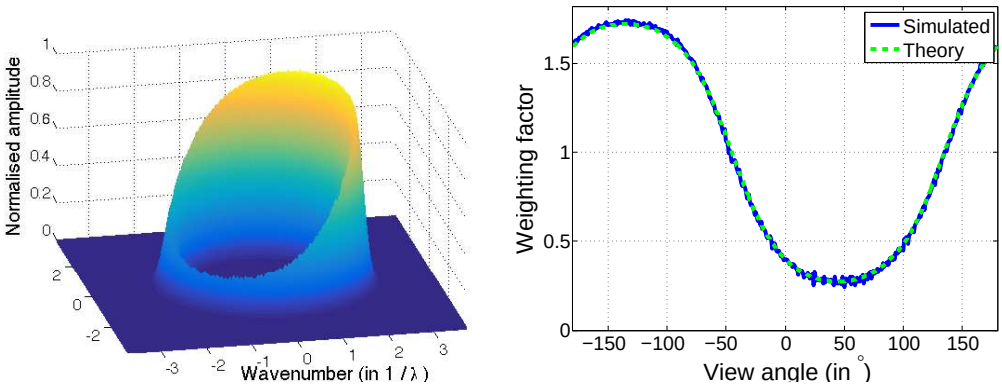
The first order of the MacLaurin series of (12) reduces to:

$$g(\theta') = 1 - \alpha\cos\theta' + O(\alpha^2). \tag{13}$$

Using finally (10) with (11) gives the general CSAS PSF:

$$\hat{I}(\rho,\phi) = \sqrt{2}\pi\sigma a_0\exp\left[-2a_0^2(\pi\rho - k)^2\right]\exp(i\Phi)\ g(\phi+\theta_0+\pi/2). \tag{14}$$

The two PSF expressions for an offset point given by (14) and for the central point only differ by the angular weighting factor $g(\phi+\theta_0+\pi/2)$. Figure 2(a) plots a 3D representation of the spectral CSAS PSF for an offset point with the parameters $\alpha = \frac{1}{\sqrt{2}}$ and $\theta_0 = 45°$ computed directly. As expected, the PSF in the Fourier domain is no longer symmetric and exhibits a strong angular dependency.



(a) (b)

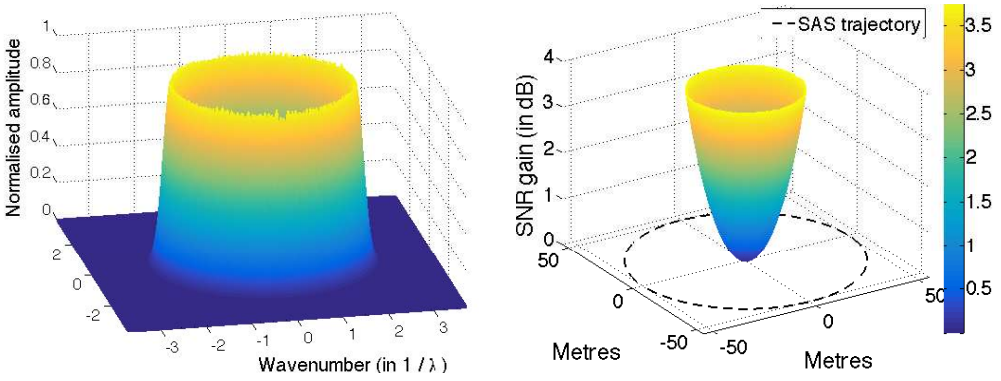
Fig. 2: (a) 3D plot of the normalised Fourier transform of an offset point. (b) Angular weighting factor for simulated data and the theoretical expression (14).

3.2. PSF normalisation

Figure 2(b) compares the angular weighting coefficient between the simulated data plotted in figure 2(a) and the theoretical value $g(.)$ from Eq. (12). Set apart the noise coming from the numerical simulation, the simulated and theoretical curves match extremely well. Now that the CSAS PSF for any point of the full view area has been fully characterised, and in particular the angular weighting dependency, it is possible to make the CSAS PSF uniform everywhere within the full view area by simply correcting the angular weighting factor. The discrete implementation of the angular compensation can be written as:

$$I(\mathbf{O}') = \sum_{n=1}^{N} \frac{1}{g(\theta_n - \theta_0)} s_{\mathrm{MF}}^{\theta_n}(t), \tag{15}$$

where N represents the total number of views obtained along the circular acquisition. Figure 3 plots the image spectra of the same offset point as figure 2(a) corrected using the proposed scheme (15). Note that the PSF is now symmetrical similarly to the central point PSF.



(a) (b)

Fig. 3: (a) 3D plot of the normalised Fourier transform of an offset point corrected using (15). *(b) SNR increase for the full field of view after PSF normalisation.*

The normalisation proposed by (15) also offers an unexpected advantage: by weighting more heavily the acquisitions where the SAS system is closer to the offset point, the uniformisation (15) increases the SNR (Signal-to-Noise Ratio). The SNR provided by the CSAS processing without normalisation can be written as:

$$\mathrm{SNR} \propto \int_{\theta=0}^{2\pi} \frac{\mathrm{d}\theta}{\mathbf{O}'\mathbf{A}^2(\theta)} = \frac{2\pi}{1-\alpha^2}. \tag{16}$$

By applying (15), the SNR can be calculated by performing a Taylor series decomposition and using the simplified expression (13) for the correction factor $g(.)$ and then becomes:

$$\mathrm{SNR}_{\mathrm{corr}} \propto \int_{\theta=0}^{2\pi} \frac{\mathrm{d}\theta}{g(\theta-\theta_0)\mathbf{O}'\mathbf{A}^2(\theta)} \approx \frac{9\pi}{4(1-\alpha^2)^{9/4}} - \frac{\pi}{4}. \tag{17}$$

The increase in SNR (expressed in dB) due to the proposed uniformisation is then approximately

$$\mathrm{SNR}_{\mathrm{inc}} \approx -30\log_{10}(1-\alpha^2). \tag{18}$$

Figure 3(b) shows the SNR increase depending on the location within the full field of view. It is interesting to note that the SNR gain can be significant (up to few dBs as shown in figure 3(b)). It is also worth mentioning that higher SNR is observed the further away from the central point.

4. THE 3D CENTRED & OFFSET POINT PSF PROBLEM

We first consider the 3D centred PSF problem. Let ψ be the grazing angle of the pulse. ψ is constant for the full revolution and can be computed with

$$\psi = \tan^{-1}\left(\frac{h}{R}\right) \tag{19}$$

where h is the high of the SAS system. We can derive $I(r)$ from Eq. (5) by writing:

$$I(r) = 2\pi B\left(\frac{2r}{c}\cos\psi\right) J_0(2kr\cos\psi). \tag{20}$$

For offset point, and similarly to the derivations of section 3, the PSF is not constant and not directly trackable. The expression of the 3D offset PSF can be found in the special domain using the plane wave assumption:

$$\hat{I}(\rho) = \frac{2\pi^{3/2}}{\cos^{3/2}\psi}\frac{\sigma a_0}{\sqrt{2k\rho}}\exp\left[-2a_0^2\left(\frac{\pi\rho}{\cos\psi}-k\right)^2\right] \tag{21}$$

where this time ψ is function of θ and reads as

$$\psi(\theta) = \tan^{-1}\left(\frac{h}{R(1-2\alpha\cos\theta+\alpha^2)^{1/2}}\right). \tag{22}$$

5. CONCLUSIONS

The analytical derivation of the PSF of 2D and 3D case, for central and offset points has been proposed. We showed that full coherent CSAS can be normalised such as the PSF becomes uniform for the full field of view.

ACKNOWLEDGEMENT

This work was performed under the Project SAC000905–High Resolution Low Frequency Synthetic Aperture Sonar (HRLFSAS) of the STO-CMRE Programme of Work, was funded by the NATO Allied Command Transformation.

REFERENCES

[1] Y. Pailhas, Y. Petillot, and C. Capus. High-resolution sonars: What resolution do we need for target recognition? *EURASIP J. Adv. Signal Process.*, 2010(1):205095, 2010.

[2] J. Sawas, Y. Petillot, and Y. Pailhas. Cascade of boosted classifiers for rapid detection of underwater objects. In *Proceedings of the European Conference on Underwater Acoustics*, pages 1507–1516. Institute of Acoustics, St Alban, UK, 2010.

[3] V. Myers and J. Fawcett. A template matching procedure for automatic target recognition in synthetic aperture sonar imagery. *IEEE Signal Process. Lett.*, 17(7):683–686, 2010.

[4] B. G. Ferguson and R. J. Wyber. Application of acoustic reflection tomography to sonar imaging. *J. Acoust. Soc. Am.*, 117(5):2915–2928, 2005.

[5] T. M. Marston, J. L. Kennedy, and P. L. Marston. Autofocusing circular synthetic aperture sonar imagery using phase corrections modeled as generalized cones. *J. Acoust. Soc. Am.*, 136(2):614–622, 2014.

[6] D. S. Plotnick, P. L. Marston, and T. M. Marston. Fast nearfield to farfield conversion algorithm for circular synthetic aperture sonar. *J. Acoust. Soc. Am.*, 136(2):EL61–EL66, 2014.

[7] Y. Pailhas, Y. Petillot, and B. Mulgrew. Increasing circular synthetic aperture sonar resolution via adapted wave atoms deconvolution. *J. Acoust. Soc. Am.*, 141(4):2623–2632, 2017.

IMPACT OF TEMPORAL DOPPLER ON CSAS IMAGERY

Herter Ulrich[a], Bonnett Blair[a], Schmaljohann Holger[b], Fickenscher Thomas[a]

[a] Helmut Schmidt University, Holstenhofweg 85, Hamburg, Germany
[b] Bundeswehr Technical Center for Ships and Naval Weapons, Maritime Technology and Research (WTD 71), Berliner Str. 115, 24340 Eckernförde, Germany

Herter Ulrich, Helmut Schmidt University, Holstenhofweg 85, Hamburg, Germany, fax: +49 (0)40 6541-2061, ulrich.herter@hsu-hh.de

Abstract: *Circular Synthetic Aperture Sonar (CSAS) coherently processes acoustic data acquired along a circular trajectory. One usual approximation applied is the stop-and-hop assumption (SHA) and, in particular, the assumption that the antennas are motionless during transmission and reception, i.e. the impact of temporal Doppler is ignored. However, in reality, for a particular ping half of the insonified area of a CSAS image centred around the point of rotation experiences pulse contraction while the other half experiences pulse dilatation. This phenomenon of temporal Doppler is incorporated into the simulation of raw data of point scatters for circular paths of a single transmitter multiple-receiver array. Results for images processed in time domain either with or without compensation of the temporal Doppler effect in the received signal are contrasted with each other. Comparative evaluation of the degradation is presented based on the shift and 6dB peak width of the point spread function (PSF) with the object locus, centre frequency, bandwidth, and pulse length as parameters. The errors caused by uncompensated temporal Doppler are compared with those caused by the SHA. Compensation of Doppler cell migration on CSAS data is presented and discussed.*

Keywords: *CSAS, temporal Doppler, Doppler distortion, Doppler compensation*

1. INTRODUCTION

Circular Synthetic Aperture Sonar (CSAS) provides higher resolution images as compared to strip-map SAS. This level of image quality makes the technique more vulnerable to imaging errors and approximations like the stop-and-hop assumption (SHA) or uncompensated temporal Doppler in the processing algorithms [1, 2]. Migrating the processing based on SHA to a model that incorporates the effect of platform motion – in the following called non-SH or without SHA – requires the compensation of geometric distortion due to range dependent platform motion between transmission and reception (in the following called intra-ping platform motion) and temporal Doppler distortion due to platform motion during transmission and reception. The impact of intra-ping platform motion on CSAS imagery has been investigated and a compensation algorithm proposed [3]. The impact of temporal Doppler will cause both, geometrical distortion and image defocus. For the case of circular apertures this will be subject of this paper. In essence the nature of both effects is the same; it is a time-domain compression or dilatation of the signal throughout the ping period. However, during the transmission and reception intervals of the pulse a Doppler frequency shift and a compression or dilatation of the envelope of the pulse is observed which – if uncompensated in the processing – will result in a shift of the peak of the matched filtered signal in conjunction with a loss of peak magnitude and a peak broadening.

For the case of linear trajectories the impact of temporal Doppler on SAS imagery has been studied in detail [4, 5]. The wideband ambiguity function for linear FM (LFM) and Hyperbolic FM (HFM) chirped pulse signals was developed based on the assumption that the Doppler-scale factor η is constant over the two-way travel time of the pulse. A detailed analysis of target migration in the range/cross-range plane due to the intra-ping motion of the platform is presented in [5]. Knowing the trajectory of the platform as well as the platform-to-target geometry, geometric distortion as well as temporal Doppler distortion can be corrected during processing. For a linear trajectory compensation of temporal Doppler distortion in the (ω, k_u)-domain [4] as well as in the time-domain [5] has been proposed. The use of Doppler compensation is desirable as any residual phase error due to uncompensated Doppler is likely to cause a bias in any autofocus algorithm. On the other hand, DPCA timing errors due to uncompensated Doppler are expected to be smaller than the residual phase centre errors after bulk phase centre correction [4].

In [3] the impact of SHA on CSAS imagery has been investigated by simulations. Data that have been collected from a moving platform were processed under the SHA. However, signal compression or dilatation due to temporal Doppler was not included in the simulated raw data. The shift of the peak and the degradation of the 6dB width of the point spread function (PSF) – compared to the case where the data have been collected under SHA – were analysed with the object locus, radius of mission, and platform speed as parameters. Unlike for linear trajectories in the case of circular trajectories not only a geometric distortion is apparent but also image blurring. Therefore, a compensation scheme for circular trajectories was presented to mitigate the impact of intra-ping platform motion when processing under SHA. It is certainly interesting to compare those findings with those where the temporal Doppler effect is incorporated into the process of data collection. In this paper we investigate the impact of uncompensated temporal Doppler for processing with SHA. The tangential shift and degradation of the 6dB width of the point spread function (PSF) due to the impact of temporal Doppler are analysed with the object locus, centre frequency, bandwidth, and pulse length as parameters. Furthermore, the results of [4] are transferred to a compensation scheme for

temporal Doppler distortion in the case of circular trajectories. Finally, the errors caused by uncompensated temporal Doppler are compared to those caused by the SHA.

2. MODELLING THE IMPACT OF TEMPORAL DOPPLER ON LFM SIGNALS

2.1. SYNTHETIC RAW DATA

A time-domain CSAS simulator for pulsed LFM signals is used to generate artificial raw data of point scatterers for circular paths of a single transmitter multiple-receiver array. The apertures of individual transducers are assumed to be of rectangular shape with their according theoretical beam patterns. The time-domain scaling due to the temporal Doppler effect is described by the Doppler scale-factor η with

$$\eta = \frac{c+v_{r,Rx}}{c-v_{r,Tx}} \tag{1}$$

where c is the speed of sound and $v_{r,Tx}$ and $v_{r,Rx}$ are the relative platform speeds in the direction of the scatterer seen from the locations of the transmitter at the time of the begin of the transmitted chirp and of the receiver at the time of the begin of the received chirp, defined positive for decreasing range ($\eta > 1$) and negative for increasing range ($\eta < 1$). The values of $v_{r,Tx}$ and $v_{r,Rx}$ and, thus, η are approximated as constant values for each ping-scatterer-receiver triplet. Ignoring the round-trip delay and amplitude scale factors the received echo $e(t)$ of the wideband transmit signal $p(t)$ distorted by the temporal Doppler effect is

$$e(t) = p(\eta t) \ . \tag{2}$$

For a LFM chirped pulse signal the distorted chirp has a new pulse length $T' = \eta T$, new carrier frequency $f_0' = \eta f_0$, new bandwidth $B' = \eta B$, and new chirp rate $K' = \eta^2 K$ (where the respective variables without a prime refer to the nominal transmitted pulse) [4, 5]. With the travel times calculated for each ping-scatterer-receiver triplet, the LFM signals are delayed, weighted individually for all receive (Rx) array elements by the transducer beam-patterns according to their respective aspect angles, and summed up over all scatterers. A navigation file with emulated navigation data is generated in addition.

2.2. PROCESSING AND TEMPORAL DOPPLER COMPENSATION

For each ping the echos are beam-formed accounting for the nominal carrier frequency f_0 using a time-domain (back-projection) near-field r-φ-beam-former in ground range plane with the approximation of rectangular shaped array patterns (cut off at 3dB points of the transducer beam patterns). Hereafter the beamformed data are downconverted to baseband (BB) using the nominal carrier frequency f_0 and are range compressed with optional Doppler compensation accounting for a beam angle θ dependant Doppler scale-factor η. The beam angle θ considered for the Doppler compensation refers to the centre of the phase centres of the physical aperture for the particular ping. Range compression is performed computational efficient in the temporal-frequency domain by a multiplication of the spectrum of the received signal with the conjugate complex spectrum of the temporal Doppler shifted pulsed chirp. The

Parameter	Symbol	Value
Receiver spacing	Δ	2.5 cm
Carrier frequency	f_0	50 kHz / 75 / 100 kHz
Horizontal opening angle, null-to-null	θ	90° / 60° / 45°
Bandwidth	B	30 kHz / 60 kHz
Pulse duration	T	10 ms / 20 ms
Sound speed	c	1500 ms^{-1}
Radius of trajectory	R	30 m
Radius of full view area	R_f	12.1 m / 8.2 m / 6.2 m
Puls repetition period (PRP)	T_{prp}	200 ms
Platform speed	v	1.5 ms^{-1}
Height over ground	h	10 m
Processing beamwidth	θ_b	45° / 30° / 22.5°
Image grid resolution	$\Delta x = \Delta y$	1.50 mm
Theoretical resolution at central point [6, 7]	Δx_{theo}	1.2 cm

Table 1: Simulation and processing parameters.

spectrum $S'(\omega)$ of a Doppler distorted signal can be evaluated from the spectrum $S(\omega)$ of the undistorted signal as follows:

$$S'(\omega) = \frac{1}{\sqrt{\eta}} S\left(\frac{f}{\eta} - (\eta - 1)f_0\right). \tag{3}$$

For computational efficiency the Doppler shift $\Delta f = (1 - \eta)f_0$ is applied to the matched data before interpolation on ground plane followed by an upconversion to passband (PB) accounting for the nominal carrier frequency f_0 and subsequent azimuth compression. To avoid aliasing effects, a resolution finer than the minimum theoretical resolution for the central point, based on the carrier frequency [6], was chosen for the image grid.

3. SIMULATION RESULTS

In this section, the temporal Doppler effect on CSAS imagery with an up-chirp LFM waveform is assessed. Table 1 provides an overview over the simulation and processing parameters. In particular the impact of carrier frequency and bandwidth as well as pulse length is considered. In order to separate the temporal Doppler effect from the impact of intra-ping platform motion we investigate a scenario where both, data collection and processing, are performed under SHA. As quality metrics, the maximum 6dB peak width of the PSF was chosen. This was performed by: 1. searching for local maxima, 2. refining the positions by fitting Gaussian curves in radial and azimuthal directions, 3. interpolating image data along 100 azimuthal directions with the peak position as origin, and 4. fitting Gaussian curves to the azimuthal data to determine the 6dB peak widths and find the maximum width over all azimuths.

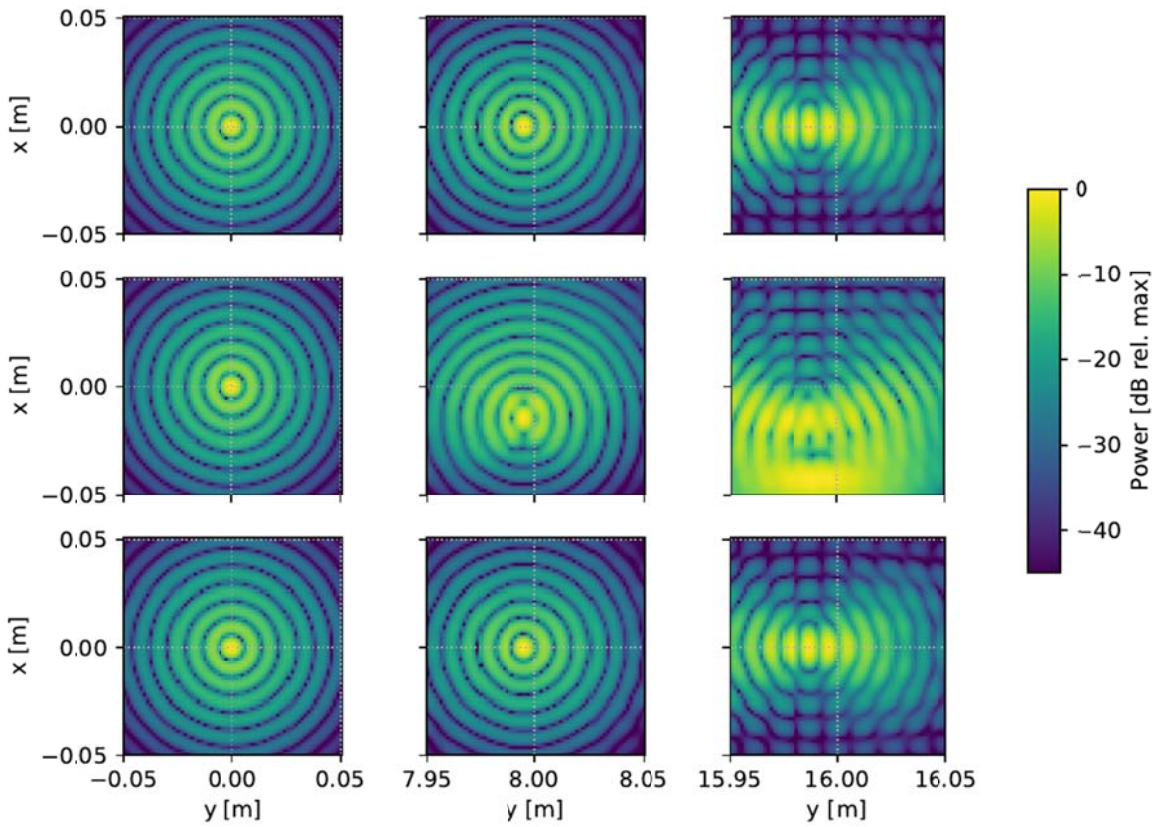


Fig. 1: PSF for three different locations at x_s = 0, and y_s = 5m, 10m, and 16m. Left and centre images are inside the full view area. Right column is outside full view area with apparent splitting of PSF into separate peaks. Top row: Ideal case, without temporal Doppler effect. Second row: with temporal Doppler effect in raw data. Third row: after processing with temporal Doppler compensation;
data simulated and processed under SHA for f_0 = 50 kHz, B = 30 kHz, and T = 10 ms. Slight offset in y-direction visible due to slant range beamforming.

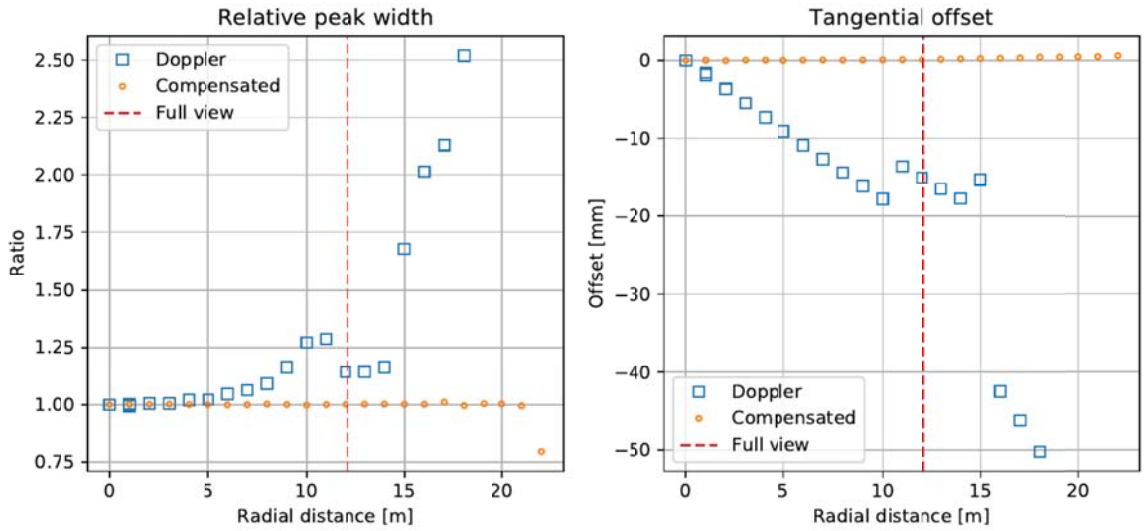


Fig. 2: Impact of temporal Doppler effect on PSF: (a) maximum 6dB peak width relative to the ideal case and (b) tangential offset vs. scatterer radial distance; data simulated and processed under SHA for f_0 = 50 kHz, B = 30 kHz, and T = 10 ms.

Figure 1 shows simulation results for the PSF at x_s = 0, and y_s = 5 m, 10 m, and 16 m, respectively (data simulated and processed under SHA for f_0 = 50 kHz, B = 30 kHz, and T = 10 ms). Left and centre cases are inside the full view area (fully insonified along complete trajectory around centerpoint at (0, 0)) whereas the right case is located outside the full view area with apparent splitting of the PSF into separate peaks. Top row: Ideal case, without temporal Doppler effect in raw data. Second row: with temporal Doppler effect in raw data and processing without temporal Doppler compensation. Third row: with temporal Doppler effect in raw data and processing with compensation for temporal Doppler effect. As expected, there is no impact of the temporal Doppler effect on the central point of the trajectory. There is an apparent increasing tangential shift of the PSF into the forward direction of the trajectory as well as an increasing blurring with rising distance to the central point. The sign of the tangential offset and, thus, its direction will change in case a down-chirp LFM waveform is used. Outside the full view area a quantitative evaluation of shift and blurring will become more and more difficult. However, when applying the compensation scheme for temporal Doppler as described above, the resulting PSF is retrieved almost perfectly even outside the full view area. No tangential offset or degradation of the peaks are visible. This will be analyzed in the following.

Figure 2 shows simulation results for the impact of the temporal Doppler effect on (a) the maximum 6 dB peak width of the PSF relative to the ideal case and (b) the tangential offset of the PSF into the forward direction of the trajectory vs. scatterer radial distance. At the edge of the full view area and outside of it our algorithm to determine the parameters width and shift of the peak of the PSF may fail to provide appropriate results due to the structure of the interference patterns visible in Fig. 1 right column. However, the compensation scheme is shown to be very successful to retrieve the original values for peak width and mitigates the shift almost perfectly even outside the full view area.

In a similar plot the variation with centre frequency, bandwidth, and pulse length is shown (Fig. 3). The impact of the center frequency on the relative 6 dB peak width of PSF is most obvious. This is for two reasons: The normalization relative to the 6 dB peak width in the ideal case without the impact of the temporal Doppler effect causes an increased resolution (decreased peak width) with rising carrier frequency and, secondly, the frequency dependence of the temporal Doppler effect itself. However, the latter one is less prominent as the half power beamwidth (HPBW) of the transducers is reducing with rising carrier frequency which will limit the maximum value of the Doppler shift $|1-\eta| \cdot f_0$. Fig. 4 depicts the two-way Doppler shift $|1-\eta| \cdot f_0$ versus transducer position (phase centre approximation) along the trajectory for a point scatterer at x_s = 10 m and y_s = 0 with parameter centre frequency f_0 = 50 kHz, 75 kHz, and 100 kHz, respectively. Those sub-apertures with a high relative radial velocity between transducer and scatterer along the trajectory (in our example for transducer positions around 70° and 290°) are blanked out for imaging due to the limited beamwidth for the higher frequency cases f_0 =75 kHz and f_0 =100 kHz. Thus, those cases give not rise to significantly higher Doppler shifts as compared to the case with f_0 = 50 kHz.

Finally, the errors caused by uncompensated temporal Doppler are compared to those caused by the SHA. Fig. 5(a) depicts the maximum 6dB peak width of PSF relative to the ideal case and Fig. 5(b) the tangential offset vs. scatterer radial distance for the two cases uncompensated SHA (ignoring temporal Doppler) and uncompensated temporal Doppler effect (SHA for data collection and processing). For the example considered (f_0 = 50 kHz, B = 30 kHz, and T = 10 ms), the blurring caused by uncompensated temporal Doppler is increasing significantly higher with rising scatterer radial distance than that caused by the impact of uncompensated SHA. The tangential offset is almost twice as high but of opposite direction.

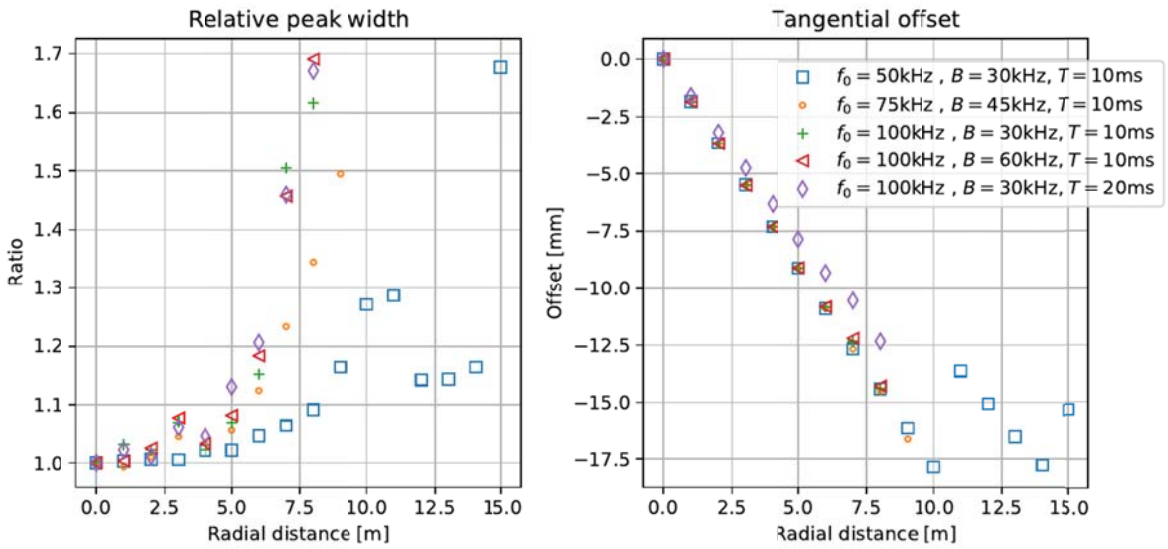


Fig. 3: Comparison of blurring and geometrical shift for various values of f_0, B, and T: (a) maximum 6dB peak width of PSF relative to the ideal case and (b) tangential offset vs. scatterer radial distance; data simulated and processed under SHA.

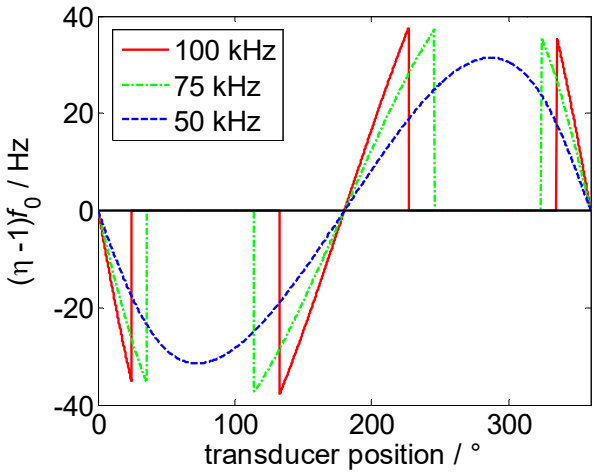


Fig. 4: Two-way Doppler shift $|1-\eta|\cdot f_0$ vs. transducer position along trajectory for point scatterer at x_s = 10 m and y_s = 0 with parameter centre frequency f_0 = 50 kHz ($\theta_b = 45°$), 75 kHz ($\theta_b = 30°$), and 100 kHz ($\theta_b = 22.5°$); transducer position rotating counterclockwise with origin at positive y-axis.

4. DISCUSSION AND CONCLUSION

Due to their high resolution CSAS systems suffer from Doppler time scaling effects. In particular higher speed, multiple receiver CSAS sonars should employ temporal Doppler compensation. The impact of uncompensated temporal Doppler for a LFM waveform and for time-domain processing with SHA was investigated by simulations. Broadening of the 6 dB peak width of the PSF relative to the case where the impact of the temporal Doppler effect was neglected is increasing significantly with rising carrier frequency. On the other hand there is no strong carrier frequency dependence of the temporal Doppler induced tangential shift of the maximum of the PSF. The blurring caused by uncompensated temporal Doppler is

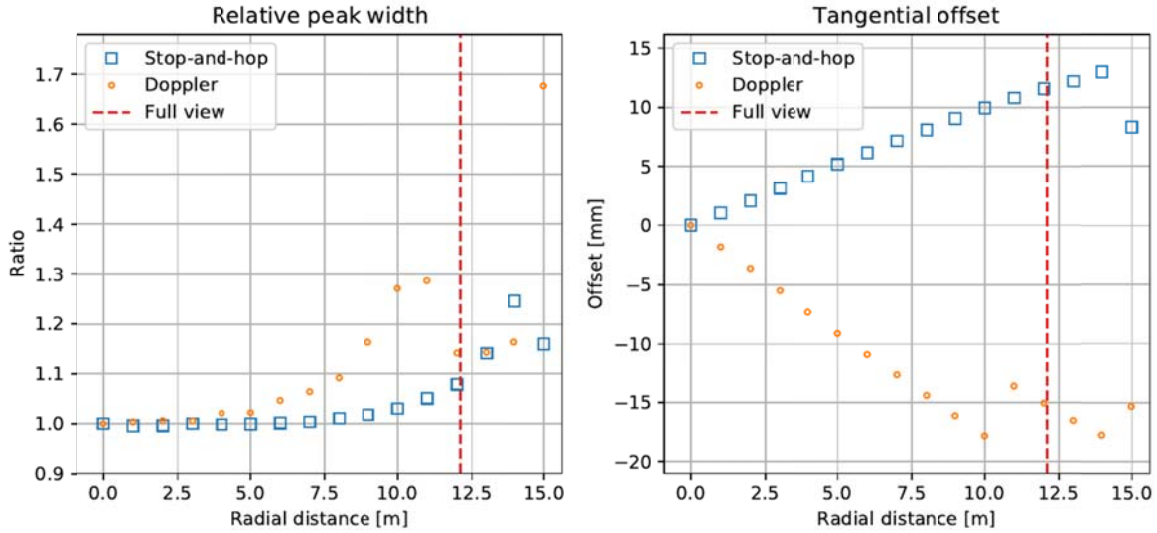


Fig. 5: Comparison of blurring and geometrical shift solely due to uncompensated SHA and solely due to uncompensated temporal Doppler effect: (a) maximum 6dB peak width of PSF relative to the ideal case and (b) tangential offset vs. scatterer radial distance; f_0 = 50 kHz, B = 30 kHz, and T = 10 ms.

increasing significantly higher with rising radial scatterer distance than the blurring caused by the impact of uncompensated SHA. The tangential offset is almost twice as high and in same direction when using a down-chirp waveform (opposite direction for up-chirp waveform). The computational efficient compensation scheme presented was proven to be very successful in removing the tangential offset (image distortion) as well as the blurring during reconstruction of the images. An investigation of the degradation caused by the impact of uncompensated temporal Doppler for the non-SH case (collection and processing) is underway.

ACKNOWLEDGEMENT

This work was supported by Wehrtechnische Dienststelle für Schiffe und Marinewaffen, Maritime Technologie und Forschung (WTD 71), Eckernförde, Germany.

REFERENCES

[1] **T. M. Marston and J. L. Kennedy**, Volumetric acoustic imaging via circular multipass aperture synthesis, *IEEE Journal of Oceanic Engineering*, vol. 41, pp. 852–867, Oct 2016.

[2] **H. Callow, R. Hansen, S. Synnes, and T. Sæbø**, Circular synthetic aperture sonar without a beacon, *Proc. Underwater Acoustic Measurements (UAM)*, 2009.

[3] **U.J. Herter, H. Schmaljohann, and T. Fickenscher**, Impact and limitations imposed by stop-and-hop approximation on CSAS imagery, *UACE 2017 Conference Proceedings*, pp. 561–567, 2017.

[4] **D. Hawkins, P. Gough**, Temporal Doppler effects in SAS, *Proceedings of the Institute of Acoustics*, Vol. 26, Pt. 5, 2004.

[5] **Y. Pailhas, S. Dugelay, and C. Capus**, Impact of temporal Doppler on synthetic aperture sonar imagery, *The Journal of the Acoustical Society of America*, vol. 143, pp. 318–329, 2018.

[6] **A. Ishimaru, T.-K. Chan, and Y. Kuga**, An imaging technique using confocal circular synthetic aperture radar, *IEEE Transactions on Geoscience and Remote Sensing*, vol. 36, pp. 1524–1530, 1998.

[7] **L. Kou, X. Wang, M. Zhu, J. Chong, and M. Xiang**, Resolution analysis of circular SAR with partial circular aperture measurements, *8th European Conference on Synthetic Aperture Radar*, pp. 1–4, June 2010.

THE ALGORITHM OF DETERMINATION OF COORDINATES OF UNDERWATER ACOUSTIC SOURCE USING THE CORRELATION FUNCTION OF THE SIGNAL

Andrei. I. Mashoshin

Concern CSRI Elektropribor, JSC
30, Malaya Posadskaya str., Saint Petersburg, 197046, Russia
fax: +78122323376; e-mail: aimashoshin@mail.ru

Abstract: *The purpose of the work is to study the algorithm that implements the method of coordinates (distance and depth) determination of the broadband signal source using the parameters of the interference maxima in the correlation function of the signal at the hydroacoustic antenna output. The algorithm takes into account a number of negative factors affecting the accuracy of the algorithm in real conditions. By means of simulation it is shown that developed algorithm potentially provides a high-precision signal source coordinates estimates in the conditions of the deep sea at sufficiently large distances. In the conditions of shallow water, as well as at short distances in the deep sea, the estimates of the coordinates using the developed algorithm are multivalued. The dependences of the accuracy of the coordinates estimation on the number of detected interference maxima in the correlation function, the signal-to-noise ratio at the antenna output and the accuracy of the sound speed vertical distribution measurement are studied.*

Key words: *underwater acoustics, multipath channel, correlation function, coordinates of the signal source.*

1. INTRODUCTION

One of the actual practical problems of underwater acoustics is determination of the submerged sound source coordinates in the passive mode of sonar operation. A large number of methods and algorithms are proposed to solve this problem.

One of these methods is based on the processing of a wide-band multi-path acoustic signal emitted by a submerged source. There are two types of this method. The first, called "Matched field processing (MFP)" [1-4], is based on the coherent addition of signal rays at the receiving antenna output taking into account the calculated signal ray structure at the antenna input for different variants of the source location in the "range – depth" space. The second type of this method [5] operates with the total multi-ray signal at the antenna output. Since the first type of the method imposes strict requirements on the vertical wave size of the receiving antenna and the magnitude of the signal-to-noise ratio (SNR), it is difficult to implement it in practice [4]. Taking this into account, the proposed article is devoted to the second type of the method, or rather to its variant, which is based on the comparison of the measured and calculated ray interference maxima (IM) in the correlation function (CF) of the received broadband signal [5-8].

The sense of the method under consideration is to find such position of the signal source (SS) in the "range–depth" space, for which the number and the location of calculated IMs are as close as possible to the number and location of IMs in the measured CF at the antenna output.

The fulfilled studies [7, 8] have shown that there are a number of factors that lead in specific cases to the large errors of the coordinate determination. These factors are:

1) the low coherence of rays in conditions, characterized by multiple signal reflections from the boundaries of the waveguide. As a result only few IMs are detected in CF or not detected at all;

2) the real ambiguity of the signal source coordinates determined by the considered method in a number of hydroacoustic conditions;

3) the low accuracy of the signal ray structure calculation due to inaccurate knowledge of hydroacoustic conditions parameters and their casual fluctuations.

The purpose of the work is to study the algorithm that implements the considered method in view of these factors.

2. THE ALGORITHM DESCRIPTION

The algorithm implementing the considered method has the following form

$$\left(R_{opt}, H_{opt}\right) = arg \quad \min_{R,H} \quad \sum_{k=1}^{K} \left| \hat{\tau}_k - T_{(i,j)_k}\left(R,H\right) \right|, \tag{1}$$

where R_{opt}, H_{opt} are the optimal estimates of the SS distance and depth; K is the number of IMs detected in the CF at the output of the receiving antenna; $\hat{\tau}_k$ is the abscissa (delay) estimate of the k-th IM, detected in the CF; $T_{(i,j)_k}\left(R,H\right)$ is function, linking the true SS coordinates R,H with the true value of the delay between i-th and j-th signal rays forming the k-th IM.

From the formula (1) it follows that the optimal SS coordinates estimates are those for which for each IM detected in the CF can be found a pair of signal rays emitted by SS, located in the point with R,H coordinates, the interference of which forms IM with delay in the CF, closed to the delay of the detected IM. It means that to implement considered method we must define the region in $[R,H]$ space and find in this region point satisfying the condition (1). And it is necessary to take into account the above-mentioned negative factors.

The analysis showed that it is not possible to completely eliminate the reasons that reduce the accuracy of the SS coordinates determination, but they can be minimized by applying some measures. Consider these measures.

1) It is experimentally established that the accuracy of the SS coordinates determination is higher the more IMs are found in the CF. Since the coherence coefficient of each pair of rays is a random variable, varying in time, the number of IMs, detected in the CF, calculated at different time intervals, can vary. Therefore, to obtain a sufficient number of IMs to solve the problem, it is advisable to combine IMs found at different time intervals.

To proof this hypothesis the Table 1 shows the values of IMs abscissa, detected in the 6 CF, calculated on the 10 sec interval each. From Table 1 it follows that the IM sets in CF, measured at the different time intervals, differ. The last line of the Table 1 contains all IMs, found in at least one CF.

CF number	IM abscissa, ms
1	7.5 19.3 42.0
2	6.9 71.8
3	7.0 49.4 79.3
4	6.8 49.5
5	7.6 41.9 49.3 71.9
6	7.4 6.8
1-6	6.9 7.5 19.3 42.0 49.4 71.8 79.3

Table 1: The values of IMs abscissa, detected in the 6 CF sequentially calculated on the 10 sec intervals

The Table 2 shows the results of the SS coordinates determination with the use of IMs detected in each CF and with the use of combined IMs. It should be noted that when using IMs from a single CF the result of the SS coordinates determination in all six cases was multi-valued. But in the case of the use of the combined IMs the result was single-valued, which shows the high accuracy of the SS coordinates determination.

CF number	Number of IMs, detected in CF	Distance estimate standard error, km	Depth estimate standard error, m
1	3	7,4	28
2	2	17,1	42
3	3	9,2	31
4	2	21,1	39
5	4	4,4	12
6	2	15,3	35
1-6	7	0,3	8

Table 2: The results of the SS coordinates determination

2) The influence of fluctuations of the ray parameters caused by fluctuations of the propagation channel can be reduced by trace analysis in time of the SS coordinates estimates.

Fig.1 shows 12 estimates of the SS coordinates (square blue markers) obtained in the experiment described above. Each estimate is obtained by applying the algorithm (1) using the combined IMs, found in six CF, sequentially measured at intervals of 10 seconds. The circle red marker indicates the true SS position.

From Fig.1 it follows that 10 estimates are located tight in the range from 45 to 51 km in distance and from 170 to 220 m in depth, and two estimates are far away. It is clear that the algorithmic elimination of such discharge estimates will not be difficult.

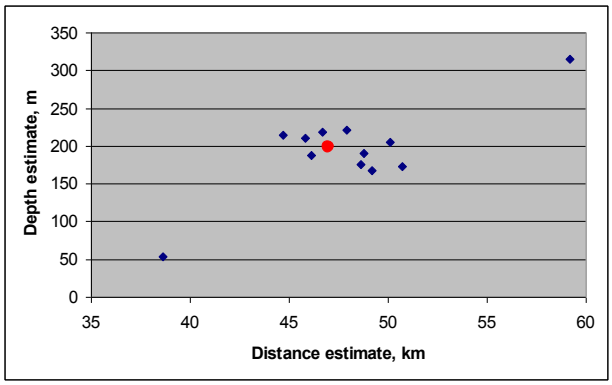


Fig.1: 12 estimates of the SS coordinates (square blue markers) and the true SS position (circle red marker)

3) Since the implementation of the algorithm (1) is based on the search of the expected points of the SS in the selected area in the space "range – depth", it is natural to assume that the uncertainty of the result will depend on the size of the this area: the smaller this area, the less uncertainty of the solution. In addition, narrowing the area reduces the time to solve the problem and the requirements to the calculator.

To determine the area of the solution, it is advisable to use one of the known SS coordinates determination methods, which give a less accurate but unambiguous result. Most simply it can be done by identifying the SS type and taking advantage of using appropriate probability density functions (PDF) of the SS depth and the signal intensity.

4) Taking in account the variability of hydroacoustic conditions in time, measurement of the environment parameters should be performed immediately before the implementation of the method.

3. THE ALGORITHM SIMULATION

The simulation was carried out in 2 steps. At the 1st step, the potential accuracy of the considered method was estimated under typical hydroacoustic conditions with precisely known parameters and with a large SNR at the antenna output. At the 2nd step, the influence of the different factors on the method accuracy was estimated.

Modeling was carried out for three types of signal propagation (Fig.2):

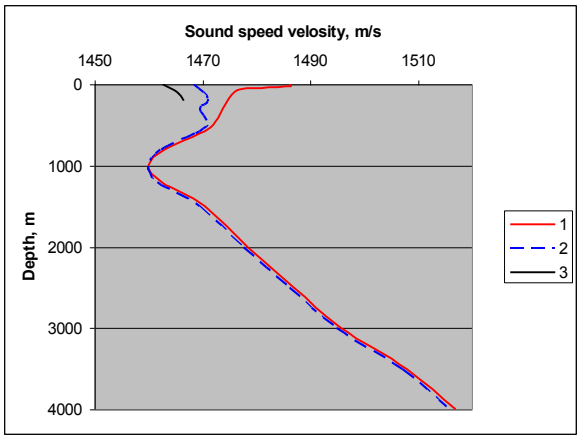


Fig.2: Types of the sound speed vertical distribution

1) the zone conditions. This type is the most favorable for the considered method, since the signal propagation in them is characterized by a small number of rays reaching the receiving antenna, and a small number of their reflections from the waveguide boundaries;

2) the conditions of continuous acoustic illumination (CAI) in the deep sea. This type is less favorable for the considered method, since the signal propagation in them is characterized by a large number of signal reflections from the sea surface, which leads to loss of signal rays coherence;

3) CAI in a shallow water. This type is even less favorable, since reflections from the bottom are added to the reflections from the sea surface, which leads to an even greater loss of signal rays coherence.

The results obtained at the 1st step of simulation are given in Table 3. The search of SS coordinates for all variants was carried out: on depth – in the range of 5-300 m; on distance – on the interval of ±30% from the true distance.

True SS coordinates		Area boundaries for solution search		SNR at antenna output, dB	Number of IMs in CF	SS coordinates estimations standard errors	
R, km	H, m	R, km	H, m			R, km	H, m
The zone conditions, receiving antenna depth 300 m							
a) near zone							
7	200	1-11	5-300	20	3	0,01	2
					3	0,02	10
					3	0,5	40
					3	0,3	100
b) 1st zone							
50	200	35-50	5-300	20	7	0,02	3
50	200	35-120	5-300	20	7	0,021	3
c) 2nd zone							
97	200	85-120	5-300	20	8	0,01	2
Continuous acoustic illumination in the deep sea, receiving antenna depth 300 m							
50	200	35-65	5-300	20	7	0,02	3
97	200	85-115	5-300	20	9	0,01	2
Continuous acoustic illumination in the shallow water, receiving antenna depth 50 m							
30	100	20-40	5-180	20	4	0,4	2
					4	9,8	3
					4	6,7	40
30	5	20-40	5-180	20	5	5,2	2
					5	4,4	5
					5	5,7	15
					5	6,3	55
					5	4,5	95
					5	3,8	115

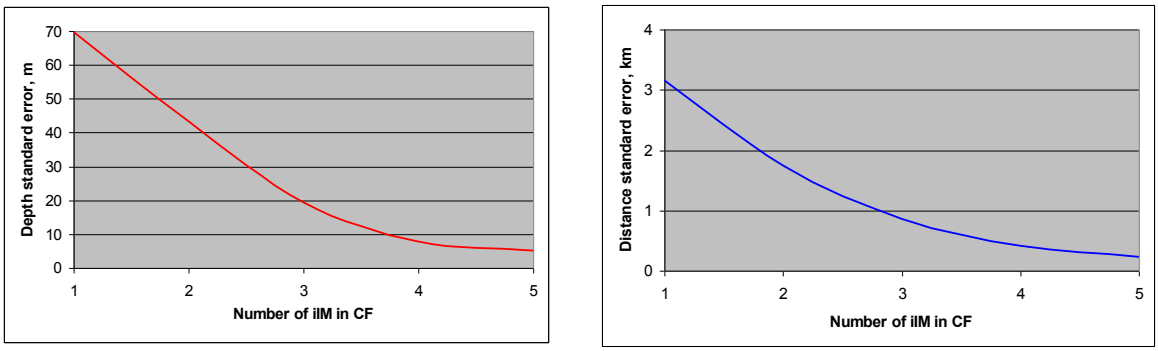
Table 3: The results obtained at the 1st step of simulation

The analysis of Table 3 leads to the following conclusions:

1) In the zone conditions, when SS is located in one of the far zones, as well as in the continuous acoustic illumination in the deep sea, the SS coordinates can potentially be determined unambiguously and with negligible errors. However, it should be noted that this conclusion is true if the number of IMs in CF is large enough (more than 3). At lower values, the solution of the problem becomes multi-valued and, as a result, the errors in the SS coordinates determination increase significantly (see Fig.3);

2) In the zone conditions, when SS is located in the near zone, as well as in a shallow water, the SS coordinates estimates are multi-valued with large standard deviation.

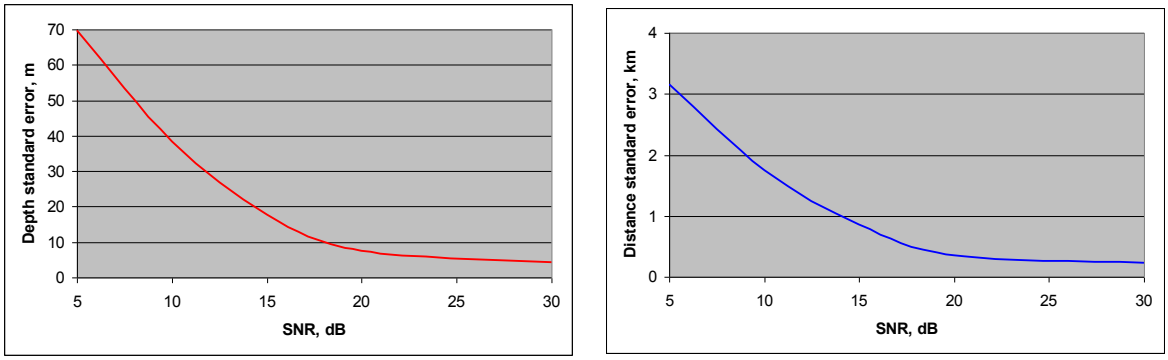
Thus, it can be concluded that the considered method is potentially applicable only in deep sea conditions and only at relatively large distances.



a) depth standard error *b) distance standard error*

Fig.3: The dependence of the SS coordinates estimates standard errors on the number of IM in CF

The results obtained at the 2nd step of simulation are given in Fig.4 and Fig.5. Fig.4 shows the dependence of the SS coordinates estimates standard errors on the SNR at antenna output when the SS locates in the 1st far zone in zone conditions. When the SNR less then 15 dB, the estimates become multi-valued and coordinate errors increase rapidly.



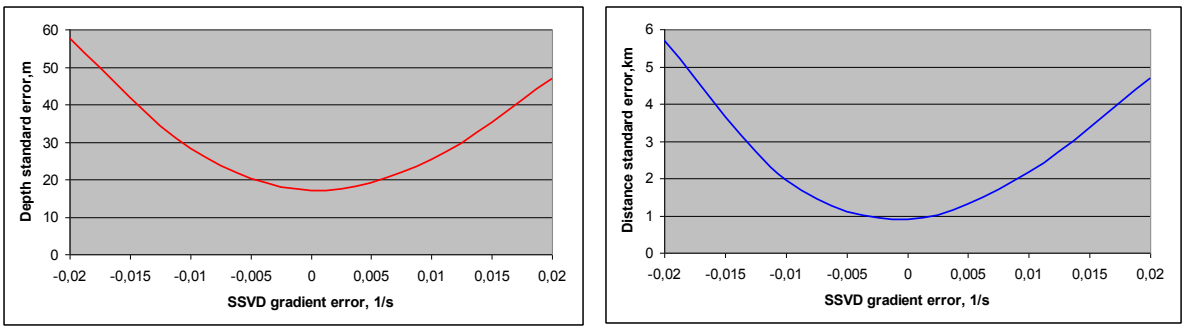
a) depth standard error *b) distance standard error*

Fig.4: The dependence of the SS coordinates estimates standard errors on the SNR at antenna output

Fig.5 demonstrates the dependence coordinates estimates standard errors on the sound speed vertical distribution (SSVD) errors for the SS, located in the 1st far zone. The true SSVD was distorted simultaneously in two ways:

– by use of sound speed and depth fluctuation errors with zero mean and RMS equal to 1 m/s and 1 m, respectively;

– by distort SSVD gradient in the interval from -0,02 to +0,02 1/s.



a) depth standard error *b) distance standard error*

Fig.5: The dependence of the SS coordinates estimates standard errors on the sound speed vertical distribution error

The consideration of Fig.5 shows:

1) if you make only the fluctuation errors (points on Fig.5, corresponding to zero abscissa) SS depth standard error increases up to 17 m and SS distance standard error increases up to 0,9 km;

2) in case of distortion of the true SSVD gradient in addition to the fluctuation errors the SS coordinates estimates standard errors increase significantly.

It follows a natural conclusion that for the application of this method in practice, the SSVD should be measured accurately.

4. CONCLUSION

An algorithm of the distance and depth of the broadband signal source (SS) determination is considered. The algorithm bases on the use the parameters of interference maxima (IM) in the correlation function (CF) of the signal at the output of the receiving hydroacoustic antenna. A number of algorithmic measures to partially overcome the negative factors affecting the accuracy of the algorithm when working in real conditions are proposed.

By means of simulation it is shown that developed algorithm potentially provides a high-precision SS coordinates estimates in the conditions of the deep sea at sufficiently large distances. In the conditions of shallow water, as well as at short distances in the deep sea, the estimates of the coordinates using the developed algorithm are multi-valued.

ACKNOWLEDGEMENTS

The work was supported by the Russian Foundation for basic research (projects 17-08-00666 and 19-08-00324).

REFERENCES

[1] **Bucker H.P.**, Use of calculated sound fields and matched field detection to locate sources in shallow water, *J. of the Acoustical Soc. of America*, vol. 59, No. 2, pp. 368 – 373, 1976.

[2] **Baggeroer A.B., Kuperman W.A., Schmidt H.** Matched field processing: Source localization in correlated noise as an optimum parameter estimation problem, *J. of the Acoustical Society of America*, vol. 83, pp. 571 – 587, 1988.

[3] **Baggeroer A.B., Kuperman W.A.** Matched Field Processing in Ocean Acoustics, in Acoustic Signal Processing for Ocean Exploration, edited by J.M.F. Moura and I.M.G. Loutrie, Kluwer Publishing, 1993.

[4] **Baggeroer A.B.** Why did applications of MFP fail, or did we not understand how to apply MFP? In *the 1st International Conference and Exhibition on Underwater Acoustics,* Corfu Island, Greece: Heraklion, pp. 41 – 49, 2013.

[5] **Hassab C.** Contact Localization and Motion Analysis in the Ocean Environment: a Perspective. *IEEE Journal of Oceanic Engineering*, vol. OE-8, No. 3, pp.136-147, 1983.

[6] **Mashoshin A.I.** Multipath Maximums in the Correlation Function of a Wideband Noise Signal Produced by a Sea Object: Noise Immunity of Their Extraction, *Acoustical Physics*, vol. 47, No. 6, pp. 727–732, 2001.

[7] Mashoshin A.I. Study of the Applicability Conditions of the Correlation Function of a Wideband Multipath Signal for Estimating Source Coordinates, *Acoustical Physics*, vol. 63, No. 3, pp. 331–337, 2017.

[8] Khil'ko A.I, Smirnov I.P., Mashonin A.I. Shafranyuk A.V. Study of the Coherence of Acoustic Fields of High-Frequency Noise Sources in a Randomly Inhomogeneous Ocean, *Acoustical Physics*, vol. 64, No. 2, pp. 215–224, 2018.

IMPROVED DEEP-LEARNING-BASED CLASSIFICATION OF MINE-LIKE CONTACTS IN SONAR IMAGES FROM AUTONOMOUS UNDERWATER VEHICLES

Abdesselam Bouzerdoum[a], Philip B. Chapple[b], Mark Dras[c], Yi Guo[d], Len Hamey[c], Tahereh Hassanzadeh[c], Thanh Hoang Le[a], Omid Mohamad Nezami[c], Mehmet Orgun[c], Son Lam Phung[a], Christian Ritz[a], Maryam Shahpasand[c]

[a] University of Wollongong, Wollongong, NSW, Australia
[b] Defence Science & Technology Group, Australia
[c] Macquarie University, Sydney, Australia
[d] Western Sydney University, Sydney, Australia

Abstract: *This paper describes recent work conducted by a team of researchers from three universities in partnership with defence researchers to investigate deep learning methods for automatic detection of mine-like objects from sidescan sonar images captured by autonomous underwater vehicles. While deep learning can produce state-of-the-art classification performances in several application domains, it often relies on a large amount of labelled training data, which is difficult to obtain in our application. To address this problem, we investigate the use of data augmentation, transfer learning, and compact neural networks. For data augmentation, approaches for increasing the size of the training data are investigated, including standard image processing and manual segmentation. For transfer learning, we use publicly available convolutional neural networks (CNNs) pre-trained on large image datasets, and replace later layers with classifiers trained on sonar image data. For compact neural networks, we train a custom small-sized CNN and also process only the region-of-interest in a sonar snapshot. The proposed techniques are evaluated on a data set consisting of three classes: mine-like objects, non mine-like objects, and false alarm objects. The experimental results indicate the feasibility of the proposed techniques, with a classification accuracy of 98.3%.*

Keywords: *Automatic target recognition, sonar image processing, mine-like object detection, convolutional neural network.*

1. INTRODUCTION

Automatic detection of mine-like objects from sidescan sonar images captured by autonomous underwater vehicles has been an active research topic [1-4]. Existing systems include a detection stage, which identifies regions-of-interest based on highlights, shadows and other image features [1, 3], followed by a classification stage to differentiate mine-like objects (MLOs), non mine-like objects (NMLOs), and false alarm objects (FAOs) (also known as false alarms [3]). However, accurate detection relies on optimising the algorithms using a large number of labelled data which are difficult and costly to collect. Furthermore, the available data may not cover the varying underwater environments where mines are found. Recently, researchers have investigated the use of deep learning for detection and classification of MLOs from sonar images [4-7]. In [7], a convolutional neural network (CNN) was used to classify snapshot images, produced by the first stage of the detection system, into three categories: MLO, NMLO and FAO. This CNN classifier is needed to improve the overall accuracy of the mine detection system.

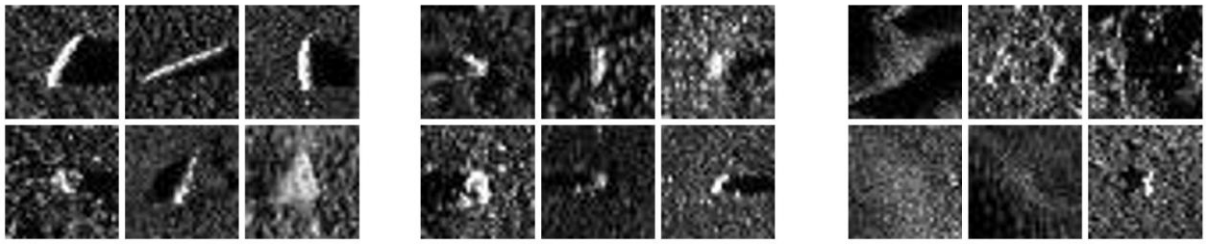
This paper describes several approaches to improve the performance of deep learning based techniques in underwater mine detection. First, we investigate data augmentation techniques to increase the size of the data set for training the CNN classifiers. Second, we explore the use of transfer learning, where the final layer of an existing pre-trained CNN is replaced by a more powerful classifier trained on the sonar data. Third, we design a compact CNN classifier to enhance the generalisation capability from limited training data. Lastly, we investigate the approach of using only the object-of-interest and shadow in classification.

The remaining of the paper is structured as follows. Section 2 of this paper provides an overview of the automatic target recognition system and sonar data collection. Section 3 presents four proposed techniques: data augmentation, transfer learning, designing a compact CNN, and processing only object-of-interest and shadow. Section 4 presents experimental methods and results of different classification methods. Section 5 provides the concluding remarks.

2. AUTOMATIC TARGET RECOGNITION AND SONAR DATA COLLECTION

Sonar data used in this project were collected by the DST Group over the last 10 years using several types of AUVs and sonar scanners: i) a REMUS 100 vehicle and a Marine Sonic Technology (MST) sonar operating at 900 kHz and 1800 kHz; ii) a Gavia vehicle and an MST sonar operating at 600 kHz and 1200 kHz; iii) a REMUS 600 vehicle and a Kraken AquaPix Interferometric Synthetic Aperture Sonar.

The existing SonarDetect software tool, developed by the DST Group for processing the sonar data captured by these AUVs, is described in [7]. This software tool displays sonar imagery alongside the navigation chart. It also indicates objects such as MLOs, NMLOs and FAOs that are automatically found in the image. These objects are detected using several image pre-processing steps that include mitigation of the surface return, detection of highlight and shadow, spatial filtering, clustering of pixels into regions according to size and shape criteria. These pre-processing steps have several parameters that need to be selected to maximise the detection of MLOs while minimising the detection of FAOs (e.g. irrelevant objects such as fish and rocks that should be excluded).



(a) MLO (b) NMLO (c) FAO

Fig. 1: Examples of sonar snapshots in the three categories.

For this study, the sonar images were acquired from a naval mine-shape recovery mission in Jervis Bay, Australia using the above AUVs [3]. The sonar images were processed by the SonarDetect tool to generate snapshots of size 501 × 501 pixels. For experiments, the snapshots were manually labelled by a defence analyst into three categories, MLO, NMLO and FAO. Examples of these snapshots are shown in Fig. 1. Table 1 presents a summary of the snapshots that are used in this study to investigate deep learning-based approaches for sonar snapshot classification.

Table 1: A summary of the sonar snapshots provided by the DST Group.

Category	MLO	NMLO	FAO
Number of snapshots	176	40	196

3. SONAR SNAPSHOT CLASSIFICATION METHODS

3.1. Convolutional Neural Network Classifier

The various methods in this paper are based on the convolutional neural network [8, 9]. Hence, we present here a brief description of the main layers in this architecture. A CNN typically consists of several blocks of convolutional layer, batch normalization layer, rectified linear unit, and pooling layer, followed by a block of fully-connected layer and softmax layer for classification.

- *A convolutional layer* extracts features from its two-dimensional (2-D) input using a convolution operator which preserves the spatial relationship between pixels. The output of a convolution layer is called a feature map, and is computed as the sum of convolutions of the 2-D input with a set of trainable kernels. An adjustable scalar bias is typically added to the sum. Formally, let Y_c^l be the *c*-th feature map in the *l*-th convolutional layer, and $K_{c,k}^l$ be the *k*-th convolutional kernel for the *c*-th input. The *k*-th output feature map is computed as

$$Y_k^{l+1} = f(\sum_{c=1}^{C} Y_c^l \otimes K_{c,k}^l + b_k^l), \quad (1)$$

  where $\otimes$ denotes the 2-D convolution operator, and f represents a non-linear activation function. Here, b_k^l is a scalar bias for the *k*-th output feature map.

- *A rectified linear unit* (ReLU) performs a nonlinear activation function to each element of its input. The ReLU function with a threshold of zero is defined as $f(x) = max(x; 0)$.
- *A batch normalization layer* is inserted between a convolutional layer and a ReLU layer to increase the stability of a neural network and accelerate network training [8]. This layer normalizes an output feature map by subtracting the mini-batch mean, and then dividing by

the mini-batch standard deviation. Effectively, this layer aims to provide inputs with a zero mean and unit variance for the subsequent layer in a neural network. Let $\boldsymbol{x} = \{x_1, x_2, \ldots, x_m\}$ be the activations over a mini-batch of m samples. The normalized activations $\hat{\boldsymbol{x}}$ are defined as

$$\hat{x}_i = \frac{x_i - \mu_B}{\sqrt{\sigma_B^2 + \varepsilon}}, \tag{2}$$

where $\mu_B = \frac{1}{m}\sum_{i=1}^{m} x_i$ is the mini-batch mean, and $\sigma_B^2 = \frac{1}{m}\sum_{i=1}^{m}(x_i - \mu_B)^2$ is the mini-batch variance. Here, ε is a pre-defined positive scalar, added for numerical stability. Furthermore, to improve training, this layer also shifts and scales the normalized activations as

$$\hat{y}_i = \gamma \hat{x}_i + \beta, \tag{3}$$

where γ and β are the trainable parameters.

- *A pooling layer* divides its 2-D input into smaller rectangular regions, and computes the maximum value (i.e. max-pooling) or average value (i.e. average-pooling) of each region. A pooling layer reduces the spatial dimension of the input and hence the computational complexity of the subsequent layers; it also helps extracting image representations that are more stable to variations in the inputs [9].

3.2. Data Augmentation Techniques

We investigate two approaches to data augmentation. The first approach applies simple image processing techniques on the sonar snapshots: reflections, scaling, shear, rotation and translation. These techniques are implemented as run-time randomised augmentations in Keras [10], so that each time a training image is used, a random combined augmentation is applied. We consider random rotations between [-10, +10] degrees, translations up to 10% of the image size, scaling by factor between [1, 1.5], and vertical and horizontal reflections. Among these techniques, only reflections and scaling are found to be useful in improving classification accuracy.

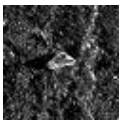
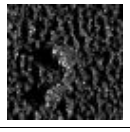
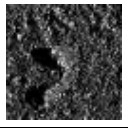
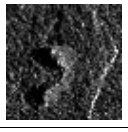
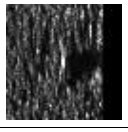
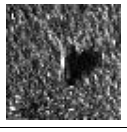
Class	*Original*	*Augment 1*	*Augment 2*	*Original*	*Augment 1*	*Augment 2*
MLO						
NMLO						

Fig. 2: Examples of snapshots and the corresponding augmented images.

The second approach uses masking to place objects on different backgrounds. To this end, the snapshots in the original data set are manually segmented to mark MLO and NMLO regions. Each marked region is then overlaid on random seabed backgrounds to generate additional training snapshots. During overlaying, the direction of the shadow cast by the object (left or

right) is matched to the shadow direction in the background image. Figure 2 shows examples of MLO and NMLO snapshots and the corresponding augmented images. Additional snapshots for the FAO class are generated by adjusting the pre-processing parameters of the SonarDetect tool.

3.3. Transfer Learning with SVM

For transfer learning, we consider several pre-trained CNN architectures including the VGG16 and VGG19. For each network, two approaches are investigated. The first approach replaces the last layers with a fully-connected layer, a softmax layer and a classification output layer. Then, the entire network is trained with snapshot images using a small learning rate. The second approach replaces the final layers of VGG with an support vector machine (SVM) classifier. That is, the SVM is used to classify the feature vector extracted by a pre-trained CNN. In our application, the second approach is found to be more effective than the first, so it is analyzed in more detail in this paper (Section 4).

3.4. Designing a Small-Sized CNN

Large CNNs (such as AlexNet, VGG16, VGG19, Inception) with millions of trainable parameters are prone to overfitting when training with limited data. To overcome this problem, we design a compact CNN with much fewer learnable weights.

The small-sized classifier is designed as a typical CNN comprising two convolutional blocks followed by a classification block, see Fig. 3. The kernel sizes used in the first and second convolutional layers are 5×5 and 3×3 pixels, respectively. The convolutional layers have a total of 33,782 trainable parameters. To stabilize the training, batch normalization layers are applied to the convolutional layers. A max-pooling layer of size 2×2 pixels with stride of 2 and no zero padding is employed after each convolutional unit for spatial dimensionality reduction.

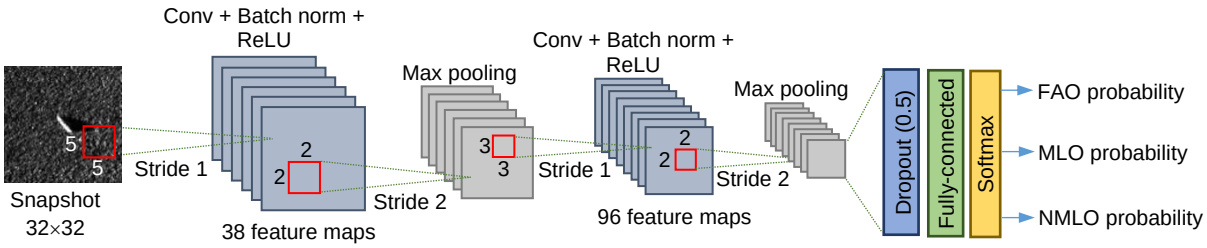


Fig. 3: A custom small-sized CNN for snapshot classification.

3.5. Classifying only Object-of-Interest and Shadow

The existing SonarDetect tool produces, after several pre-processing steps, each snapshot together with information (bounding box) about the object of interest and its shadow (OIS), which can be utilised for classification. We explore a dedicated CNN that considers only the OIS for three reasons. First, if appearance features of sonar snapshots are indeed significant for classification, then background distraction should be minimised. Second, by focusing only on the object of interest and its shadow, we can reduce the input size to the network, and consequently the network structure and the amount of required training data. Third, the dedicated CNN can be modified to perform object detection directly via window scanning on the full image.

In our approach, the tightest patches containing OIS from the snapshot images are extracted. Although the OIS vary in width and height, they are resized to a patch size of 27 × 58 pixels, which we find suitable for most of the snapshots. This resized patch is used as input to the dedicated CNN network, called ObjectNet. Figure 4 shows the extracted OIS of various sizes before rescaling.

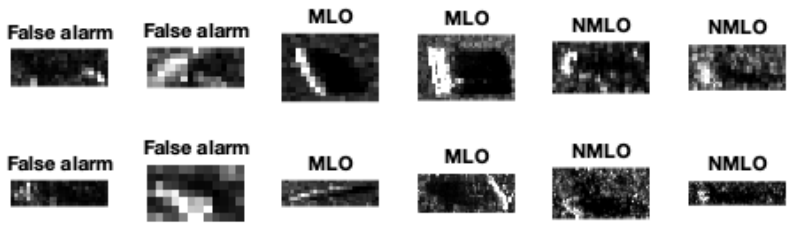


Fig. 4: Examples patches of objects of interest and shadows.



*Fig. 5: ObjectNet structure for OIS classification. The notation **conv_1,256@3×3** means the first convolutional layer has 256 feature maps produced using a kernel size of 3×3 pixels.*

The structure of the ObjectNet is shown in Fig. 5. It consists of a feature extraction block with 5 convolutional layers, ReLU layers, and max-pooling layers, followed by a classification block with a fully connected layer and a softmax layer. The max-pooling layers operate on non-overlapping local regions of size 2 × 2 pixels. Here, batch normalization is not used so that the network can be extended for object detection via window scanning. ObjectNet is trained with the stochastic gradient descent [9], using the augmented data created in Section 3.2. Several rounds of optimisation are performed with batch sizes varying from 50 to 800. For each batch size, the number of training epochs is 800. The best network found at each batch size is used as the initialised network for the next round of optimisation, which uses a larger batch size.

4. EXPERIMENTS AND RESULTS

4.1. Experimental Methods

The five-fold cross-validation technique is used to evaluate the different classification methods. The original snapshots in Table 1 are divided into five approximately equal partitions. For each fold, a partition is used for testing, and the remaining partitions are used for training. This step is performed five times for different choices of the test partition. The classification rates are averaged over the five folds to obtain the estimated classification rate (CR). For training, the data augmentation techniques described in Section 3.2 are applied to generate 11 additional snapshots for each MLO training snapshot, and 47 additional snapshots for each NMLO training snapshot.

The CR for each class and the overall CR are estimated through five-fold cross validation. We also report an additional classification measure: the *balanced* overall CR. As evident in Table 1, the snapshot data are unbalanced among the three classes. This is partially addressed through augmentation of the training data, but testing is still performed only on original snapshots. Therefore, the test data remain unbalanced, and the classification accuracy is biased toward the class with the highest number of test samples. The *balanced* overall CR measure addresses this problem by assigning a weight to each test sample so that all classes have an equal weighted number of test samples.

In this application, the end-user is also very interested in differentiating FAOs from the other two classes combined, MLOs and NMLOs. The main reason is that after an MLO *or* NMLO snapshot is detected, further processing can be performed, even by a human operator, to separate an MLO from an NMLO. Therefore, we also assess the performances of different classification methods for the two-class problem: MLO+ NMLO *versus* FAO.

4.2. Snapshot Classification Results

Table 2 presents the three-class classification results for each of the three deep learning approaches investigated in this study: i) transfer learning using a pre-trained VGG network and the SVM classifier (Section 3.3); ii) custom small-sized CNN (Section 3.4); iii) ObjectNet focusing on object of interest and shadow only (Section 3.5). For the transfer learning approach, the CR of the three-class classification is 76.2%, but this CR is affected by the imbalance in the dataset as the *balanced* CR is only 62.9%. For the custom small-sized CNN, the overall CR and the *balanced* overall CR are 98.3% and 98.7%, respectively. For the ObjectNet, the overall CR is 69.9%. The results indicate that a small-sized CNN can achieve quite high accuracy in sonar snapshot classification.

Table 2: Classification rates (%) produced by the transfer learning, the small-sized CNN, and the ObjectNet for the three-class problem.

Method	MLO	NMLO	FAO	Overall	Overall (balanced)
Transfer learning with SVM	84.7	25.0	79.0	76.2	62.9
Small-sized CNN	99.0	97.2	100	98.3	98.7
ObjectNet	82.4	65.0	59.7	69.9	69.0

Table 3: Classification rates (%) produced by transfer learning, the small-sized CNN and the ObjectNet for the two-class problem, MLO+NMLO versus FAO.

Method	MLO+NMLO	FAO	Overall	Overall (balanced)
Transfer learning with SVM	89.3	79.1	84.4	84.2
Small-sized CNN	99.0	98.2	98.5	98.6
ObjectNet	86.6	59.7	73.8	73.2

Table 3 presents the two-class classification results for each of the three deep learning approaches. For this two-class problem, there are 216 NMLO/MLO targets and 196 FAO targets, so the two classes have balanced data. Therefore, the overall CR and the balanced overall CR are quite similar. The overall CRs for the transfer learning VGG+SVM, the small-sized CNN, and the ObjectNet are 84.2%, 98.5%, and 69.9%, respectively.

5. CONCLUSION

This paper has described the application of deep learning to the classification of snapshots in sidescan sonar images collected by an AUV. To address the problem of limited training data and to improve the generalisation capability of the classifier, the paper explores the use of data augmentation, a small-sized network, and object-of-interest and shadow. The results indicate the feasibility of the proposed techniques, with a classification accuracy of 98.3%. Further work will combine the three proposed techniques and explore more advanced data augmentation methods.

REFERENCES

[1] G. J. Dobeck, J. C. Hyland, and L. Smedley, "Automated detection/classification of sea mines in sonar imagery," *Proc. SPIE 3079*, pp. 90-110, 1997.

[2] J.A. Fawcett, "Automatic target recognition methods for sidescan sonar images: The advances and the challenges," *Proc. Int. Conf. on Detection and Classification of Underwater Targets,* pp. 2-18, 2012.

[3] P. B. Chapple, "Unsupervised detection of mine-like objects in seabed imagery from autonomous underwater vehicles," *Proc. IEEE OCEANS Conf.,* pp. 1–6, 2009.

[4] D. P. Williams, "Underwater target classification in synthetic aperture sonar imagery using deep convolutional neural networks," *Proc. Int. Conf. Pattern Recognition,* pp. 2497–2502, 2016.

[5] P. Zhu, J. Isaacs, B. Fu, and S. Ferrari, "Deep learning feature extraction for target recognition and classification in underwater sonar images," *Proc. IEEE Annual Conf. Decision and Control*, pp. 2724–2731, 2017.

[6] K. Denos, M. Ravaut, A. Fagette, and H. Lim, "Deep learning applied to underwater mine warfare," *Proc. IEEE OCEANS Conf.*, pp. 1–7, 2017.

[7] P. B. Chapple, T. Dell, and D. Bongiorno, "Enhanced detection and classification of mine-like objects using situational awareness and deep learning," *Proc. Underwater Acoustics Conference and Exhibition (UACE)*, pp. 529-536, 2017.

[8] S. Ioffe and C. Szegedy, "Batch normalization: Accelerating deep network training by reducing internal covariate shift," *Proc. Int. Conf. on Int. Conf. Machine Learning*, pp. 448-456, 2015.

[9] Y. LeCun, Y. Bengio, and G. Hinton, "Deep learning," *Nature,* 521(7553), pp. 436-444, 2015.

[10] https://keras.io

ON THE BENEFIT OF MULTIPLE REPRESENTATIONS WITH CONVOLUTIONAL NEURAL NETWORKS FOR IMPROVED TARGET CLASSIFICATION USING SONAR DATA

David P. Williams[a], Ronan Hamon[a] & Isaac D. Gerg[b]

[a]NATO STO Centre for Maritime Research and Experimentation (CMRE), La Spezia, Italy
[b]Pennsylvania State University Applied Research Laboratory (PSU-ARL), State College, PA, USA

email: david.williams@cmre.nato.int

Abstract: ***The benefit of using multiple representations of data in the context of convolutional neural networks (CNNs) is demonstrated. We present three variations on this theme of multiple representations, in the form of (i) fundamentally different input data representations obtained from the same raw data, (ii) isometries of a given data representation, and (iii) intermediate representations arising from unique CNN architectures. Taken together, these variants can produce excellent classification performance while relying on orders of magnitude fewer free parameters than used in typical CNNs, thereby reducing training data requirements. The value of this multi-representation approach is demonstrated on a target classification task using real, measured sonar data collected at sea.***

Keywords: ***Convolutional neural networks (CNNs), multiple representations, classification, sonar.***

1. Introduction

Synthetic aperture sonar (SAS) [1] relies on the coherent processing of acoustic returns to produce high-resolution imagery of underwater environments that can be exploited for object classification and other tasks. But the richness of the *complex-valued* SAS data means there is potentially more exploitable information than what is apparent in the usual image domain. For example, the aspect-dependent nature of sonar returns off objects can be detected in the frequency domain [2], whereas the integration of this information to create (magnitude) imagery effectively obscures this key phenomenon. This insight motivates us to produce multiple data representations *that are fundamentally different in nature* – namely, a sonar magnitude image, phase image, and frequency spectrum – and use them jointly as inputs to a CNN to improve classification performance.

A standard CNN [3] is a sequence of convolutional layers, nonlinear activation functions, and pooling operations that collectively transform input data (*i.e.,* imagery) into a new representation space in which the classes are easily separable. But the alternative *input* data representations we propose could not be "uncovered" naturally by a CNN – *e.g.,* as intermediate-layer representations – because the relevant information is not *accessible* in the usual image domain. CNNs are a natural match for our multi-representation approach because they obviate the extraction of predefined features, which is challenging for difficult-to-interpret alternative data representations, such as sonar or radar *phase* imagery [4, 5].

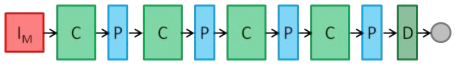
Some prior CNN-based research has focused on incorporating "multi-view" data from disparate sensor modalities [6–9], while other work has decomposed complex-valued data into two representations (*e.g.,* real and imaginary parts) [10, 11]. But our work is the first to derive and successfully exploit multiple input representations from the same raw sensor data. Our unification of the three multi-representation variants under a common theme, and our application to sonar data, are additional novel contributions.

The remainder of this paper is organized as follows. In Sec. 2, we present our multi-representation CNN framework and explain its benefits. Experimental results of the proposed approach on an object classification task using measured sonar data are shown in Sec. 3. Concluding remarks are made in Sec. 4.

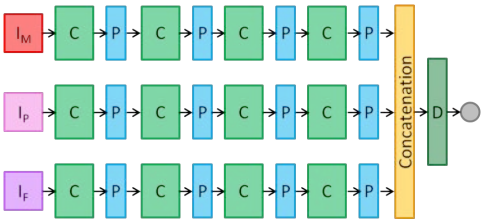
2. Multi-Representation Classification

2.1. CNN Design

We carefully design 4 CNN architectures, whose common schematic is shown in Fig. 1. The key design choice when using multiple *disparate* input representations is how and when to merge them within the CNN. Because the representations capture fundamentally different physics, it is important to *not* simply treat the different data representations as separate channels – as is done for three-channel RGB optical images – because the responses will destructively interfere after the first convolutional layer. Instead, the representations should be kept distinct until a late (*i.e.,* deep) stage of the CNN. Here we propose an elegantly simple solution that is extensible for various applications and types of data. Specifically, when multiple input representations (*viz.* sonar magnitude image, phase image, and frequency spectrum) are used, the respective data products from the CNN transformations are concatenated at the penultimate layer (*cf.* Fig. 1).



(a) Single-representation (M) CNN architecture



(b) Multi-representation (MPF) CNN architecture

Figure 1: Proposed CNN architectures for (a) single and (b) multiple representation inputs. *C*, *P*, and *D* denote convolution *blocks* (comprising one or more convolutional layers), pooling layers, and dense layers, respectively.

Table 1: CNN architecture details

CNN Label	Filter Sizes (Pixels Per Side)	Pooling Factors
A	[4] [3] [3] [4]	4, 4, 2, 4
B	[8] [6] [4] [5]	4, 4, 2, 2
C	[6 3] [6 3] [6 3] [6 3]	4, 2, 2, 4
D	[8 7 5] [8 7 5] [7 7 5] [8 7 5]	2, 2, 2, 2

More specific details about the architectures designed for this work are provided in Table 1. Each data input representation to the CNNs is assumed to be 267 pixels by 267 pixels. Each CNN contains 4 convolution blocks; each block contains a specific number of convolutional layers (equal to the number of rows in Table 1's filter-size column). Each filter is square, and only 4 filters are used in each convolutional layer. ReLU activations are used after each convolutional layer, while a sigmoid activation is used at the output. All pooling layers use average pooling (rather than max-pooling) because the former approach has been observed [12, 13] to better handle the speckle phenomenon that characterizes sonar imagery. The design of the architecture (and specifically the final pooling layer) ensures that the dense layer always contains 4 nodes per input data representation. The capacities of the CNNs are intentionally kept so low in order to scrutinize the classification power of small networks when faced with limited training data.

2.2. Data Processing

A large database of scene-level SAS images (each of which typically spans 50 m $\times$ 110 m of seafloor) was collected by CMRE's MUSCLE autonomous underwater vehicle (AUV) during 13 sea expeditions conducted between 2007 and 2017 in various geographical locations. The center frequency of the SAS is 300 kHz and the bandwidth is 60 kHz, providing centimeter-level resolution sonar imagery.

The data from each expedition varies greatly in terms of seafloor composition (*e.g.,* sand, mud, vegetation), clutter types and densities, target types, image quality, and environmental complexity. Data from the 8 oldest expeditions are treated as training data for learning the CNNs, while the data from the 5 most recent expeditions are used as *distinct* test sets (owing to their diverse characteristics). The Mondrian detection algorithm [14] is applied to the complex scene-level sonar images, with this resulting in a set of image "chips" of objects to be classified as targets (class 1) or clutter (class 0) by the CNNs. The target class corresponds to man-made objects (usually mimicking mine shapes) that were purposely deployed prior to the surveys. A summary of the data sets is shown in Table 2, where it can be seen that the number of target examples in the training set is extremely limited.

Table 2: Summary of sonar data sets

Data Set	Survey Years and Locations	Number of Clutter	Number of Targets
Training Data	2008–2013 Latvia; Italy; Spain	29280	2912
MAN2	2014 - Bonassola, Italy	14313	404
NSM1	2015 - Ostend, Belgium	6580	113
TJM1	2015 - Cartagena, Spain	1938	351
ONM1	2016 - Hyères, France	111	91
GAM1	2017 - Patras, Greece	157	75

Given a complex sonar image, $z = x + iy$, of an object, the frequency representation used as input to the multi-representation CNNs is $\mathbf{I}_F = \frac{1}{3}(\log_{10}|\mathcal{F}\{z\}| - 8)$, where $\mathcal{F}$ is the 2-d discrete Fourier transform (and the extra constants effect a normalization). The magnitude image representation is given by $\mathbf{I}_M = |z|$, and the phase image representation is the result of the two-argument arc-tangent function, $\mathbf{I}_P = \phi(y,x)$. Each magnitude image and phase image are further normalized so that the pixel values of each are in $[-1,1]$. Each data input representation to the CNNs is 267 pixels by 267 pixels; for the magnitude and phase images, this corresponds to a spatial extent of 4.005 m $\times$ 4.005 m. An example of these three input data representations for a target is shown in Fig. 2.

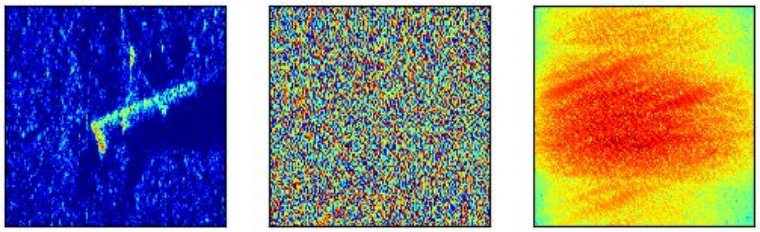


Figure 2: From left to right, a cylindrical target's three data representations: sonar magnitude image, phase image, and frequency spectrum. Strong normal-incidence returns from the cylinder face are visible (as linear features) in the latter.

2.3. CNN Training

CNN training was performed using the RMSprop optimizer with a learning rate of 0.001, in conjunction with a binary-cross-entropy loss function, until the loss on the training set con-

verged. A batch size of 64 was used, with equal numbers selected from each class to combat the severe class-imbalance of the training data. Importance sampling to bias toward choosing challenging training data – as quantified by the Mondrian detection score – was employed. Data augmentation was effected by applying minor random translations in the range and along-track directions, as well as along-track reflections, to each (complex) sonar image chip selected for the batch. No attempt was made to optimize the learning rate or batch size.

Using the architectures described in Sec. 2.1, we train 4 single-representation and 4 multi-representation CNNs, where the former set (denoted M) uses only the sonar magnitude image, while the latter set (denoted MPF) also uses the phase image and frequency spectrum as additional inputs.

3. Experimental Results

We conduct experiments to show the benefit to classification performance, measured in terms of the area under the curve (AUC), of using three multi-representation variants. Specifically, we compare (i) using a set of isometric inputs versus using only image-centered inputs with a CNN, (ii) using an ensemble of CNNs with unique architectures versus using only a single CNN, and (iii) using a set of alternative data representations versus using only sonar magnitude imagery as input to the CNN.

For the first case, demonstrating the value of multiple representations of sonar imagery resulting from isometries of each original input data example, we employ a set of 18 affine transformations that do not violate the physics of the sonar-object geometry. (These operations are performed on the raw complex-valued imagery.) This set is formed from the Cartesian product of range translations $i_{tx} = \{0, 0.25 \text{ m}, 0.50 \text{ m}\}$, along-track translations $i_{ty} = \{-0.25 \text{ m}, 0, 0.25 \text{ m}\}$, and along-track reflections $i_{ry} = \{0, 1\}$.

The classification performance of the 4 multi-representation CNNs on the 5 test data sets is shown in Table 3 for when the CNNs are evaluated using object-centered ($\oslash$) input images or the ensemble ($\mathcal{E}$) of 18 isometric inputs. (Bold values indicate the best performance achieved among methods within the table's double vertical lines, on a row-wise basis.) The use of multiple representations in the form of simple isometries clearly provides significant performance gains.

Also shown in the table is the result of using the ensemble of the 4 CNNs' predictions ($\mathcal{E}(\text{ABCD})$) as the final prediction for each test data point. This second form of multiple representations, exploiting the fact that the unique CNN architectures induce different intermediate representations, also consistently provides benefit over the individual CNNs.

And lastly, to demonstrate the value of employing multiple *input data* representations, Table 4 shows the performance of the single-representation CNNs (M) and the multi-representation CNNs (MPF). For comparison purposes, we also adapted the pre-trained VGG16 net [15] to our problem and (sonar magnitude) data; details of this transfer appear in [16]. The best VGG16 performance achieved (after considerable effort and parameter tuning) is shown in Table 4. The performance of the Mondrian detector, which makes predictions using a set of 5 features with fixed weights (and thus has no free parameters), is included as a baseline "shallow" classification approach.

Table 4 also shows the number of parameters of each method. The ensemble of our 8 CNNs generates predictions after training around 5×10^4 free parameters, which is only 0.3%

of the 1.47×10^7 parameters contained in the VGG16 net. The architecture of the VGG16 net is similar to ours, with alternating convolution blocks and pooling layers. One of the major differences is the number of filters in each convolutional layer; the VGG16 net uses between 64 and 512 filters in each convolutional layer, while our CNNs use only 4 filters in each layer. Despite the handicap of relying on orders of magnitude fewer free parameters, our limited-capacity CNNs collectively perform favorably to the VGG16 net, as can be seen in Table 4. Additionally, with our CNNs, training is more straightforward, free of extensive parameter tuning.

One valuable finding from the course of this work is that the individual branches of the multi-representation CNN should *not* be initialized with weights learned from training in isolation the analogous single-representation CNN. As can be seen in Fig. 3 (a) and (b), the filters that are learned for a single-representation CNN differ from those of the multi-representation CNN branch of the same data representation. We hypothesize that using the single-representation CNN to initialize, as was done in [16], causes training to get stuck in the equivalent loss-space minimum, thereby preventing gains (from the additional representations) from being realized.

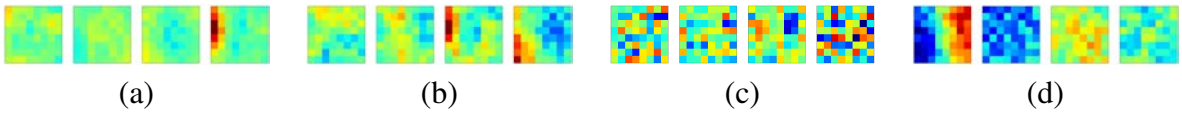
Finally, Fig. 4 shows the intermediate responses at each layer of CNN B in the single-representation and multi-representation forms. The drastically distinct responses arising from the disparate input data representations are obvious.

Table 3: AUC for multi-representation (MPF) CNNs using centered ($\oslash$) input images or an ensemble ($\mathcal{E}$) of isometric inputs

Test Data Set	CNN A		CNN B		CNN C		CNN D		$\mathcal{E}$(ABCD)	
	$\oslash$	$\mathcal{E}$	$\oslash$	$\mathcal{E}$	$\oslash$	$\mathcal{E}$	$\oslash$	$\mathcal{E}$	$\oslash$	$\mathcal{E}$
MAN2	0.958	**0.965**	0.969	**0.980**	0.975	**0.979**	0.978	**0.981**	**0.986**	**0.986**
NSM1	0.921	**0.935**	0.944	**0.963**	0.956	**0.975**	0.939	**0.952**	0.976	**0.980**
TJM1	0.985	**0.989**	0.993	**0.996**	0.994	**0.995**	0.993	**0.997**	0.997	**0.998**
ONM1	0.947	**0.962**	0.936	**0.957**	0.983	**0.991**	0.966	**0.985**	0.982	**0.987**
GAM1	0.975	**0.985**	0.992	**0.993**	**0.997**	**0.997**	**0.999**	**0.999**	**0.998**	**0.998**

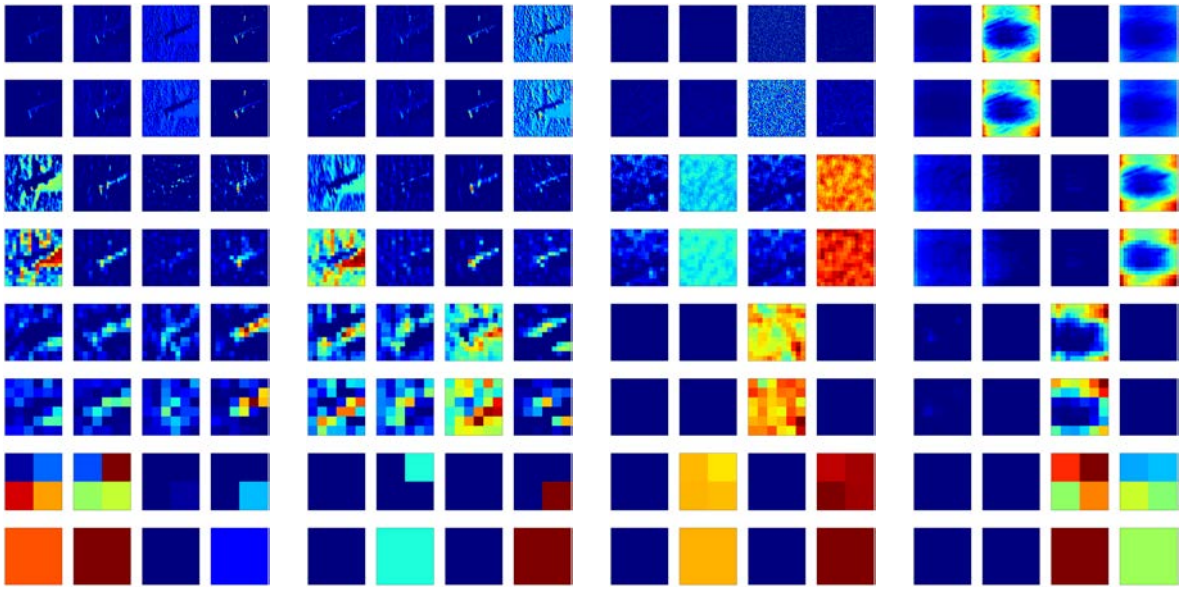
Table 4: AUC for single-representation (M) and multi-representation (MPF) CNNs and competing methods

Test Data Set	CNN A		CNN B		CNN C		CNN D		$\mathcal{E}$(ABCD)			VGG16	Mondrian
	(M)	(MPF)	(M)	(MPF)	(M)	(MPF)	(M)	(MPF)	(m)	(MPF)	(M, MPF)		
MAN2	0.964	**0.965**	0.979	**0.980**	**0.981**	0.979	0.955	**0.981**	0.984	0.986	**0.987**	0.986	0.928
NSM1	**0.935**	**0.935**	0.938	**0.963**	0.968	**0.975**	0.949	**0.952**	0.977	0.980	0.982	**0.983**	0.892
TJM1	0.985	**0.989**	0.995	**0.996**	**0.998**	0.995	0.993	**0.997**	0.998	0.998	**0.999**	0.996	0.955
ONM1	**0.978**	0.962	**0.987**	0.957	**0.991**	**0.991**	0.968	**0.985**	**0.992**	0.987	0.988	0.958	0.851
GAM1	**0.986**	0.985	0.988	**0.993**	0.994	**0.997**	0.990	**0.999**	**0.999**	0.998	0.998	0.997	0.978
Parameters	629	1885	1509	4525	2485	7453	7877	23629	12500	37492	49992	14715201	0



(a) (b) (c) (d)

Figure 3: For the single-representation CNN B using the magnitude image as input, (a) the first convolutional layer's filters. For the multi-representation CNN B, the first convolutional layer's filters for the (b) magnitude-image branch, (c) phase-image branch, and (d) frequency-spectrum branch. The filters of a given subfigure use the same colorscale; green corresponds to zero.



(a) (b) (c) (d)

Figure 4: Intermediate CNN layer responses for the data example in Fig. 2. For the single-representation CNN B using the magnitude image as input, (a) the responses after each layer. For the multi-representation CNN B, the responses after each layer, prior to concatenation, for the (b) magnitude-image branch, (c) phase-image branch, and (d) frequency-spectrum branch.

4. Conclusion

This work demonstrated the benefit of using three forms of multiple representations in the context of CNNs. Taken together, these variants can produce excellent classification performance while relying on orders of magnitude fewer free parameters. Thus, by exploiting alternative techniques that enable us to employ CNNs with limited capacity, we effectively reduce the amount of training data required. This result is valuable for remote-sensing applications, and in particular underwater target classification tasks, where the collection of data (at sea) is prohibitively costly.

REFERENCES

[1] M. Hayes and P. Gough. Broad-band Synthetic Aperture Sonar. *IEEE Journal of Oceanic Engineering*, 17(1):80–94, 1992.

[2] D. Plotnick and T. Marston. Utilization of Aspect Angle Information in Synthetic Aperture Images. *IEEE Trans. on Geoscience and Remote Sensing*, 56(9):5424–5432, 2018.

[3] Y. LeCun, Y. Bengio, and G. Hinton. Deep Learning. *Nature*, 521(7553):436, 2015.

[4] D. Williams. Exploiting Phase Information in Synthetic Aperture Sonar Images for Target Classification. In *Proceedings of the IEEE OCEANS*, pages 1–6, 2018.

[5] M. Alver, S. Atito, and M. Çetin. SAR ATR in the Phase History Domain Using Deep Convolutional Neural Networks. In *Image and Signal Processing for Remote Sensing XXIV*, volume 10789, pages 1078913–1 – 1078913–10, 2018.

[6] W. Wang, R. Arora, K. Livescu, and J. Bilmes. On Deep Multi-view Representation Learning. In *International Conference on Machine Learning*, pages 1083–1092, 2015.

[7] A. Wang, J. Lu, J. Cai, T. Cham, and G. Wang. Large-Margin Multi-modal Deep Learning for RGB-D Object Recognition. *IEEE Trans. on Multimedia*, 17(11):1887–1898, 2015.

[8] Y. Bin, Y. Yang, F. Shen, and X. Xu. Combining Multi-representation for Multimedia Event Detection Using Co-training. *Neurocomputing*, 217:11–18, 2016.

[9] J. Wagner, V. Fischer, M. Herman, and S. Behnke. Multispectral Pedestrian Detection Using Deep Fusion Convolutional Neural Networks. In *ESANN*, pages 509–514, 2016.

[10] J. Muth, S. Uhlich, N. Perraudin, T. Kemp, F. Cardinaux, and Y. Mitsufuji. Improving DNN-based Music Source Separation Using Phase Features. *arXiv preprint arXiv:1807.02710*, 2018.

[11] S. Riyaz, K. Sankhe, S. Ioannidis, and K. Chowdhury. Deep Learning Convolutional Neural Networks for Radio Identification. *IEEE Comms. Magazine*, 56(9):146–152, 2018.

[12] D. Williams. Underwater Target Classification in Synthetic Aperture Sonar Imagery Using Deep Convolutional Neural Networks. In *Proceedings of ICPR*, 2016.

[13] M. Emigh, B. Marchand, M. Cook, and J. Prater. Supervised Deep Learning Classification for Multi-band Synthetic Aperture Sonar. In *Proceedings of the 4th International Conference on SAS/SAR*, volume 40, pages 140–147, 2018.

[14] D. Williams. The Mondrian Detection Algorithm for Sonar Imagery. *IEEE Transactions on Geoscience and Remote Sensing*, 56(2):1091–1102, 2018.

[15] K. Simonyan and A. Zisserman. Very Deep Convolutional Networks for Large-Scale Image Recognition. *arXiv preprint arXiv:1409.1556*, 2014.

[16] I. Gerg and D. Williams. Additional Representations for Improving Synthetic Aperture Sonar Classification Using Convolutional Neural Networks. In *Proceedings of the 4th International Conference on SAS/SAR*, volume 40, pages 11–22, 2018.

ATR Performance for Target Clustering

José Melo[a], Samantha Dugelay[a]

[a]NATO STO Centre for Maritime Research and Experimentation (CMRE)
Viale San Bartolomeo 400, 19121 La Spezia
email:jose.melo@cmre.nato.int

Abstract: *The goal of Target Clustering algorithms is to cluster multiple detections of the same target, in a way that can minimize the uncertainty in their location. In order to do so, clustering algorithms usually build on data provided by an Automatic Target Recognition (ATR) software. In particular, they use information on the location of a given detection in a tile, together with an associated weight highlighting how likely a given ATR detection is to be originated from a target.*

In this article we will present an analysis and characterization of the performance of the ATR under use by the CMRE Autonomous Naval Mine Countermeasures (ANMCM) group, for constructive input to the target clustering algorithm. Motivations for this are two-fold. First, it has been observed that in some situations the ATR can fail to completely detect the target. On the other hand, the ATR can sometimes detect a target but assign it a low score which then, depending on the acceptance threshold, can cause the target to remain undetected. Therefore, the output of the ATR needs to be characterized. The analysis will build on experimental data, collected during past trials which cover different operational scenarios and environmental conditions, and curated by an expert.

Results from this analysis will enable to derive an empirically driven probability of detection, but also to statistically characterize the distribution of the ATR scores under different scenarios. It is expected that the obtained results will enable an accurate simulation of an (MCM) mission. Moreover, such results will provide a better link between ATR and clustering algorithm.

Keywords: *automatic target recognition, classification, target clustering*

1. Introduction

Target clustering algorithms use the output of an ATR in order to merge multiple detections of the same target into a single entity, or cluster. Ideally, the formed cluster will benefit from the multiple detections of the same target, by having a better estimate of the target's position. However, in some situations the ATR can fail completely to detect the target. On the other hand, the ATR can sometimes detect a target but assign it a low score which then, depending on the acceptance threshold, can cause a target to remain disregarded. In this article, the goal is to characterize the outputs of an ATR classification algorithm, that will then be used by a subsequent target clustering algorithm.

Figure 1 provides a schematic diagram of an ATR and its interface with target clustering algorithms. In the figure, the ATR obtains 13 detections of the 4 deployed targets, plus two false alarms. Each of the detections consists of an estimated location of the target (x_i, y_i), and an associated classification score, s_i. As illustrated, the target clustering algorithm combines these detections into an appropriate number of clusters. Due to the existence of navigation errors, multiple detections of the same target might present a different location for the same target. Therefore, the target clustering algorithm should also be able to cope with this aspect, providing a single estimate of the position of the target, but also an estimate of its uncertainty. The ATR software here considered consists of a detector [1] and a deep convolutional neural network (CNN) binary classifier [2]. The detector analyses each Synthetic Aperture Sonar (SAS) tile, and identifies possible existing targets. Subsequently, the classifier uses mugshots of those detections to discriminates targets (i.e., mines) from all types of clutter. The output of the ATR software then consists of all the detections and their associated scores.

The remainder of this paper is organized as follows. The next section focus on the experimental data of the different trials, and a review of the ground truth data. Then, Section 3 is devoted to analysing the ATR classification scores. Finally, Section 4, will present some conclusions and future developments.

2. Ground Truth analysis

It is known that some of the detections given by the ATR correspond to actual mine-like targets that have been purposely deployed in the seabed. However, there are also numerous detections which do not correspond to actual deployed targets, and are just an environmental feature, as for example existing rocks. Therefore, the first step on this analysis is to obtain the location of each of the deployed targets. For example, given a SAS tile, which detections given by the ATR correspond to actual targets, and which ones do not?

The data set here in analysis, comprising data collected in five different trials namely MANEX'14, TJMEX'15, NXMEX'15, ONMEX'16 and GAMEX'17, has been curated. This means that an expert in the field has reviewed the tiles and pinpointed the existing mine-like targets, which have been deployed purposely for the execution of the trials. These annotations consist of the pixel location of the centre of each these targets displayed on a given tile, and will be considered "ground truth". Conversely, "non ground truth" detections will be the term used for all the remaining detections.

All sonar data used in this work was collected at sea by MUSCLE, one of CMRE's

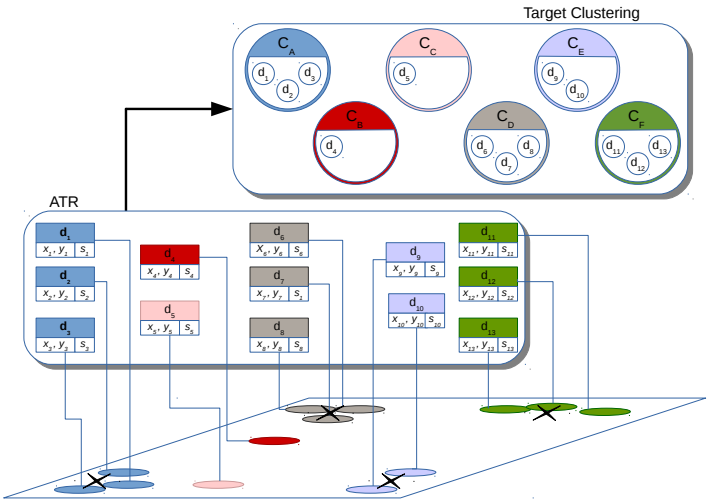


Figure 1: ATR and Target Clustering algorithms. The ATR algorithm provides 11 detections of existing targets, and false alarms. The Target Clustering algorithm merges the 13 detections into 6 different clusters, with the clusters C_A, C_D, C_E and C_F corresponding to the 4 existing targets, and C_B and C_C to the 2 false alarms.

Autonomous Underwater Vehicles (AUVs), which is equipped with a SAS system able to generate high-resolution centimetre level sonar imagery from the sea bottom. The entire data set is composed of a total of 162593 ATR detections, from which 1909 correspond to tiles that contain real targets, as given by ground truth information. Table 1 provides and overview of all the ATR detections data of each trial.

Trial	Detections	Target Observations
MANEX'14	23715	759
TJMEX'15	50420	534
NSMEX'15	65624	323
ONMEX'16	20974	138
GAMEX'17	2220	155

Table 1: Summary of the experimental data sets under analysis

2.1. Missed Detections

Having established the ground-truth, the next step is to assess how many of the targets have been detected or were missed by the ATR. For this, each tile is considered independently from the others. An empirically derived probability of detection, P_d, can then be calculated. Table 2 details the obtained results, categorized according to the respective trial. The column *"Observ."* refers to the number of independent observations of ground truth targets, while the column *"Missed"* refers to the number of times the ATR failed to detect them. The *"P_d"* columns refer to the empirically calculated probability of detection.

By reading Table 2, it can be seen that the probabilities of detection for NSMEX'15, TJMEX'15, and GAMEX'17 are very similar, and above 80%. On the other hand, the probabilities of detection for both MANEX'14 and ONMEX'16 are significantly lower. In

Trial	Day	Observ.	Missed	P_d	P_d
MANEX'14	1	52	52	0.00	0.43
	2	76	76	0.00	
	3	89	87	0.02	
	4	67	38	0.43	
	5	78	30	0.62	
	6	28	10	0.64	
	7	39	11	0.72	
	8	61	23	0.62	
	9	42	23	0.45	
	10	30	15	0.50	
	11	59	16	0.73	
	12	33	12	0.64	
	13	13	10	0.23	
	14	81	24	0.70	
	15	11	7	0.36	
NSMEX'15	1	110	19	0.83	0.82
	2	38	18	0.53	
	3	98	6	0.94	
	4	44	9	0.80	
	5	6	1	0.83	
	6	27	6	0.78	

Trial	Day	Observ.	Missed	P_d	P_d
TJMEX'15	1	73	7	0.90	0.85
	2	30	2	0.93	
	3	58	8	0.86	
	4	177	32	0.82	
	5	31	6	0.81	
	6	165	23	0.86	
ONMEX'16	1	9	5	0.44	0.59
	2	29	6	0.79	
	3	32	15	0.53	
	4	29	11	0.62	
	5	39	20	0.49	
GAMEX'17	1	2	0	1.00	0.88
	2	65	8	0.88	
	3	3	1	0.67	
	4	2	0	1.00	
	5	11	2	0.82	
	6	72	8	0.89	

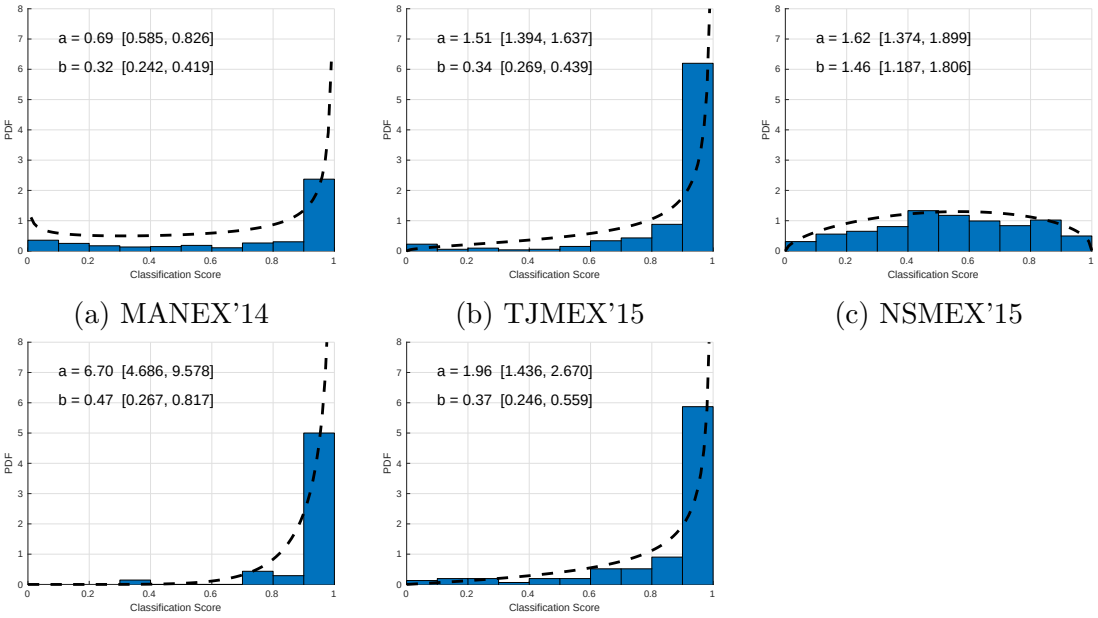
Table 2: Summary of the number of ground truth target observations and missed detections for the different trials

fact, for the MANEX'14 trial, the global P_d is of only 43%. However, it should be noted that the total P_d for MANEX'14 is affected by the extremely low values of P_d for the first 3 days of the trial, when almost none of the observed targets were detected. While it is difficult, at this time, to find a justification for the extraordinarily low probabilities of the detection for these first three days, it is safe to say that such performances are not typical. Therefore, disregarding the first three days, the overall probability of detection achieved during the entire MANEX'14 trial would be of around 60%, which is very similar with what has been achieved during the ONMEX'16 trial.

3. Classification Scores

The classification score provided by the ATR is in fact the output of aforementioned CNN classifier. This score then indicates the probability of a given detection belonging to the targets class. Figures 2 and 3 show the normalized histograms of the classifications scores for all the trials under analysis, where the number of bins was selected according to Sturge's rule. They display, respectively, scores histograms for the ground truth detections, and for all the remaining detections. Additionally, a Beta Distribution has also been fitted to the classification scores of each of the trials, with each of the plots also displaying the value for the a and b parameters of each fit, together with the respective confidence intervals.

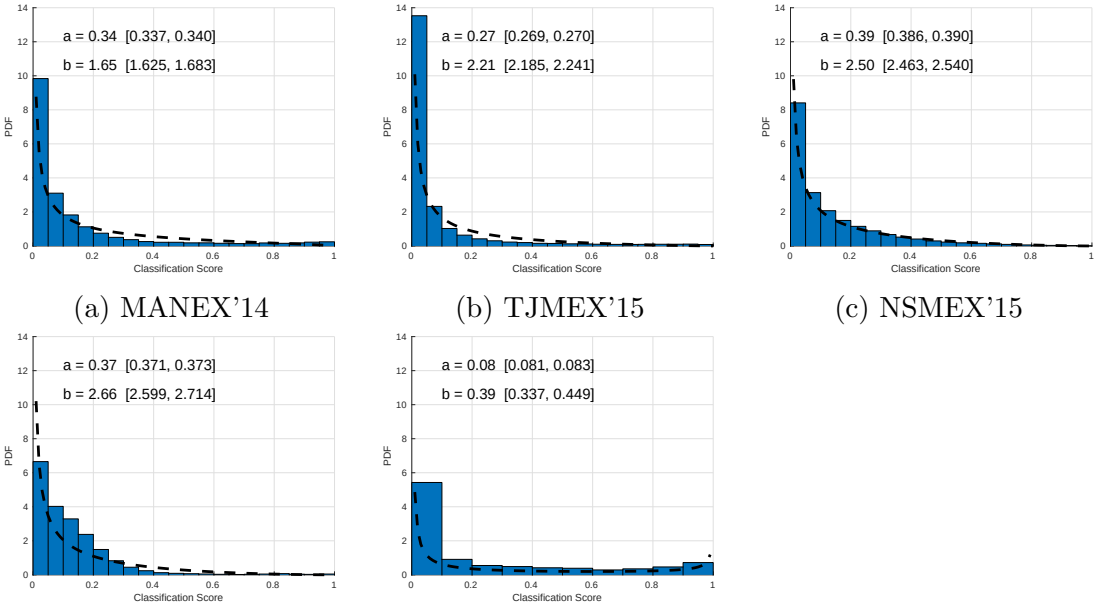
When comparing Figures 2 and 3, the main difference between them is the shape of histograms. While in Figure 2 the histograms corresponding to the different trials have a peak in the right most bin, for classification score values around 1, in Figure 3 the opposite happens, with peaks on the left most bin, in the vicinity of zero. The histograms also have an indication of the mode of the classification score, with a value of around 0.95 for the histograms in Figure 2, the ground truth detections, and a value of 0.05 for Figure 3. This is in fact the expected behaviour, which indicates that the ATR is performing



(a) MANEX'14 (b) TJMEX'15 (c) NSMEX'15

(d) ONMEX'16 (e) GAMEX'17

Figure 2: Normalized histogram of classification scores of ATR detections for ground truth targets



(a) MANEX'14 (b) TJMEX'15 (c) NSMEX'15

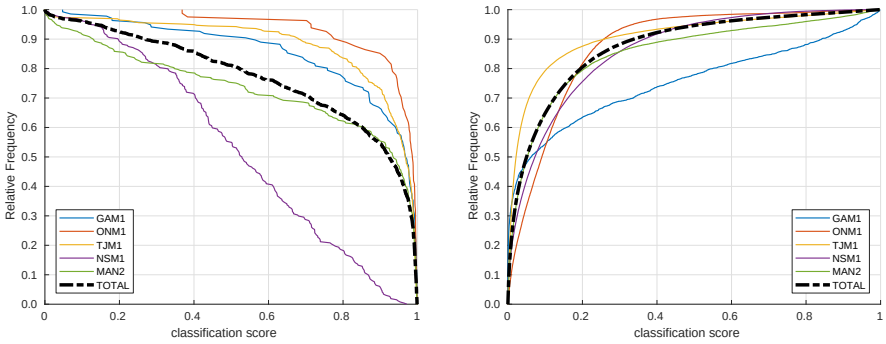
(d) ONMEX'16 (e) GAMEX'17

Figure 3: Normalized histogram of classification scores of ATR detections for non ground truth targets

well its classification phase. The only exception being Figure 2c, relative to the ground truth detections in the NSMEX'15 trial. In this particular case, the histogram of the ground truth targets detection scores is more evenly distributed among all the possible values for the classification score, with a value for the mode of 0.45. This derives from the fact that, for this particular trial, the ATR was attributing low classification scores to actual deployed mine-like targets. The explanation for this fact comes from the actual nature of the trial, performed in the North Sea, and where the existence of significant water currents was constantly affecting the missions performed by MUSCLE. As a result, the ability of the ATR in correctly classifying mine like targets was affected.

A similar analysis can be made for Figure 3, but in this case the distributions are more similar between each other. Even though the confidence intervals in this case are very narrow, all the plots are very identical, with the main difference being on the height of the peak at the left-hand side. The only exception to that is the plot relative to GAMEX'17, in Figure 3e, where the relative frequency of scores with higher scores is comparably larger than all the others.

Figure 4 presents a more aggregated view of the classification scores for both ground truth and non ground truth targets. Figure 4a presents the complementary cumulative distribution of the classification score for ground truth targets. This plot shows the percentage of the detections that have been assigned a score which is greater or equal than a certain value. For example, for the NSMEX'15 trial, it is possible to see that 100% of the detections have score above 0, 70% have a score above 0.4, and only around 20% of the detections have a score above 0.8. In that sense, it is very clear to see that ONMEX'16 is the trial on which the ATR performed better, with 80% of the detections with a score of roughly 0.8 or above. On the other end, there is NNSMEX'15, where only 5% of the ground truth targets with a classification score above 0.9. A curve for the ensemble of the four trials is also presented. Conversely, Figure 4b presents the cumulative distribution of the ATR classification scores for non ground truth targets. There it is possible to evaluate the percentage of such detections with a classification score below a certain value. For the case of GAMEX'17 trial, one can verify that only 65% of these detections have scores below 0.2, while 20% of them have classification scores above 0.55. It is also possible to see that in both TJMEX'15 and ONMEX'16 the ATR performed particularly well.



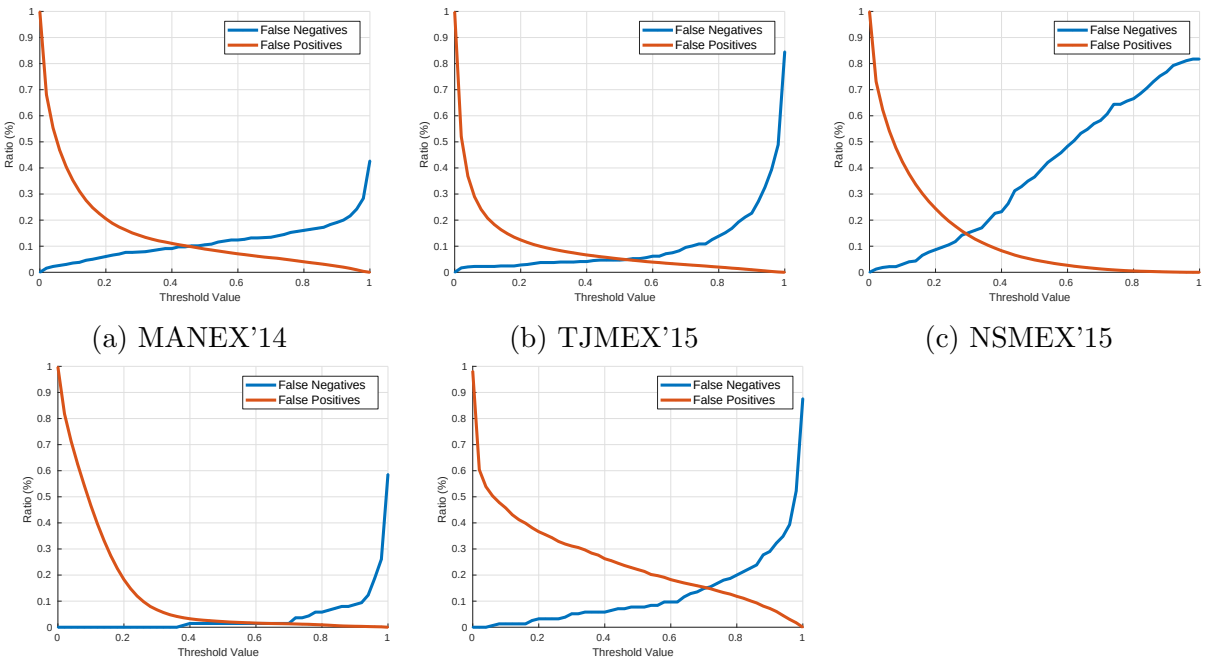
(a) (b)

Figure 4: Cumulative distributions of the classification scores: the complementary cumulative distribution of the classification scores for ground truth targets in 4a, and the cumulative distribution of the scores of non ground truth detections in 4b

3.1. False Positives and False Negatives

From the analysis above, it is possible to conclude that while the classification score gives a fair indication of how likely a given detection is originated from a mine like target, it does not provide an unambiguous indicator. The question that arises is then how to assess if a given detection corresponds to a target? The usual approach is to use a certain threshold level for the classification score to make that decision. Detections with a classification score below that threshold will be discarded, while detections with a score above the threshold will be considered the actual targets. That, however, has certain implications that should not be disregarded. For instance, ground truth target detections with low scores will be disregarded, constituting a false negative situation. Conversely, false positives, also commonly described as a false alarm situations, will arise for ATR detections which do not correspond to real targets. This situations can become particularly adverse when such detections have an associated score with a relatively high value. While it is clear that false positives and false negatives have inherently different costs, addressing this is outside of the scope of the work here presented.

It is clear that there exist two conflicting objectives regarding the false positives and false negatives. On one hand, the possibility of neglecting false negatives should be avoided, as it can result in devastating effects on an operational scenarios. Therefore, an eventual threshold level for the classification score should be set to an arbitrarily low level. However, setting such threshold level very low, will increase the number of false alarms dramatically. As a result, the burden required to process all the detections, in a timely fashion, can be unattainable. Moreover, this would negatively affect subsequent phases of unmanned MCM operations, such as target reacquisition and identification. In



(a) MANEX'14 (b) TJMEX'15 (c) NSMEX'15

(d) ONMEX'16 (e) GAMEX'17

Figure 5: Variation of the rate of False Positives and False Negatives with the classification score threshold

order to avoid this, then an eventual threshold acceptance level should be set arbitrarily high, so that the ratio of false positives is kept as low as possible. Figure 5 presents the plot for the rate of false positives and rate of false negatives for each one of the trials, with a varying threshold acceptance level. The mentioned conflicting objectives are evident.

A rather intuitive approach for that would be to choose a threshold value that would minimize both false positives and false negatives rate. Visually, this threshold level can be identified as the intersection point between both lines. This, of course, assumes that false positives and false negatives have a similar cost. Arguably, this might not be the case in operational scenarios as the cost of missing a real mine can be too high. Figure 5 also highlights another aspect of choosing a threshold level. By comparing the plots in Figures 5a to 5e, it is unequivocal that for the different trials, the false positives and false negatives lines intersect with different classification scores. While for NSNEX'15 this intersection occurs for a value of around 0.3, for GAMEX'17 this occurs for a value of around 0.7. These are the extreme cases, and for other trials this happens for intermediate values. This suggests that and adaptive threshold level should be used, that is dependent on operational and environmental conditions.

4. Conclusion and Outlook

This report presented an analysis performed to the output of the ATR. The motivation for this analysis is to obtain suitable characterization of the ATR output, under different operational environments, so that it can be used by a target clustering algorithm, which is an ongoing effort.

This analysis started with examining the missed detections and empirical probabilities of detection of the different trials. Taking into consideration the specifics of each trial, particularly the MANEX'14, results show that, roughly, the trials can be divided within two categories according to the empirical probabilities of detection: one with P_d of around 60%, and one with P_d of around 85%. Furthermore, the classification scores have been considered. It has been shown how the rate of false positives and the false negatives can be strongly influenced by the value of the chosen threshold level for the scores. A naive approach for choosing such threshold, on which both the rate of false positives and false negatives is minimized, highlighted the need for a more robust and adaptive way to select such threshold. Finally, the distribution of the classification scores has been approximated with a Beta distribution, that allowed to compare the similarities between data from all the trials.

REFERENCES

[1] David P. Williams. The mondrian detection algorithm for sonar imagery. *IEEE Transactions on Geoscience and Remote Sensing*, 56(2):1091–1102, Feb. 2018.

[2] David P. Williams. Demystifying deep convolutional neural networks for sonar image classification. In *Proceedings of the Underwater Acoustics Conference*, Skiathos, Greece, Sep. 2017.

MBES WATER COLUMN DATA PROCESSING FOR SMALL UNDERWATER TARGET RECOGNITION

Isabelle Quidu[a], Michel Legris[a]

[a] Lab-STICC UMR CNRS 6285, ENSTA Bretagne, 2 rue François Verny, 29806 Brest Cedex 9, France

isabelle.quidu@ensta-bretagne.fr
michel.legris@ensta-bretagne.fr

Abstract: *In the context of the mine warfare modernization plan, the French Ministry of Defense is studying the possibility of close object inspection by an autonomous underwater vehicle. To that end, the vehicle is equipped with a multibeam echosounder (MBES), and travels to within 10 meters of the object. With each narrow beam formed by the MBES, a sounding is measured by a detection algorithm that estimates the two-way propagation time between the sonar and the seabed. Unfortunately, manufacturer algorithms are designed for bathymetry estimation and suffer from two drawbacks for object recognition: first, multiple detections per beam are seldom available; second, too many false alarms arise in case of strong specular reflection. In order to achieve better recognition of small objects, in this paper we propose processing the water column data where the 3D shape of the object is visible. This huge volume of data needs to be reduced, however. Data are first enhanced by the use of the bitonic filter, which combines non-linear morphological and linear operators. Then, hysteresis thresholding is applied, allowing multiple detections, as well as false alarm mitigation. This technique is assessed on various data sets collected by the French Defense Procurement Agency (Direction Générale de l'Armement, Naval Techniques section) with three different MBES: R2Sonic2022 (700kHz), EM2040 (400kHz) and MB2250 (2.25MHz). Results show that the set of detected points allows us to complete the final step of recognition based on 3D shape matching.*

Keywords: *MBES water column data, target recognition*

1. INTRODUCTION

For the purpose of underwater mine warfare, the French Defense Procurement Agency, DGA TN (Direction Générale de l'Armement, Naval Techniques section), develops future MCM (Mine CounterMeasure) concepts. In order to mitigate human risks and to increase stealth, underwater mine warfare missions will mainly be achieved by AUVs (Autonomous Underwater Vehicles) deployed from a mothership or USV (Unmanned Surface Vehicle). A piece of these operational systems is the I-AUV or Identification-AUV, able to determine the type of mine. Common MCM procedures require identification to be performed either by divers, or by automated optical imaging. The main identification sensor is the camera but, except for specific optical imaging (like the *TileCam optical camera* in [1]), it is usually insufficient in turbid water. To gather additional information, the use of an acoustic system is proposed. This system is a multibeam echosounder (MBES) carried by the vehicle which travels to within 10 meters of the object. Usually, from each narrow beam formed by the MBES, a sounding is measured by a detection algorithm that estimates the two-way propagation time between the sonar and the seabed. Unfortunately, such manufacturer algorithms are designed for bathymetry estimation and generally provide a single detection per beam. By looking carefully at the water column data where the 3D shape of the object is visible, we sometimes notice that multiple echoes can be relevant per beam. This is even more noteworthy when specular reflection arises, together with sidelobes (due to the transmitter and/or the receiver arrays). In order to achieve better recognition of small objects, we propose in this paper to enhance the water column data (section 2) and to reduce this huge volume of data to a few relevant detections (section 3). Results will be obtained from three different MBES datasets (section 4). We will close with a comparison with the soundings obtained using the manufacturer's algorithm.

2. WATER COLUMN DATA ENHANCEMENT

In image processing, denoising while preserving edges (in terms of contrast and localization) is challenging because noise and edges are both high frequency components. Common methods include a preliminary step of detection of edges in order to only low-pass filter the areas with low gradient values. A famous example is the anisotropic filter [2]. However, the latter is not easy to set parameters for and, because of high gradient values, does not denoise nor connect pixels on the edges. Instead, we prefer the bitonic filter [3]. A bitonic sequence (defined in the context of sorting as an extension of monotonic) is one which increases monotonically (or not at all) to a peak, then decreases monotonically (or not at all), *i.e.* it has at most one local maxima or minima. Finally, noise is anything which is not bitonic over the given range. Notice that only the data rank matters, not the level. As such, a bitonic filter is based on rank filters with a small centile c, in order to preserve local maxima or minima, while rejecting unsignificant impulses. More precisely, a robust opening operation is used, with a small centile c rather than the usual minimum, and $(100 - c)$ instead of the usual maximum. A robust closing operation is similarly computed. In order to eliminate residual noise, a Gaussian filtering of the residue between the morphological (opening or closing) operation output and the original signal is performed (in image processing, this residue is known as the output of a top-hat filter). These two smoothed errors are used as weights to combine the previous opening and closing operators' outputs. This combination preserves mean signal values in the case of a noisy signal. The advantages of the bitonic filtering are twofold: a) contrast enhancement and b) denoising (impulsive as well as white Gaussian noises).

When dealing with 3D matrices, the practical implementation of the bitonic filter carries out 2D filtering channel by channel, which means ping by ping, in our case. Given the expected acoustic signature of the object returned by the MBES (*i.e.* edges of the object in the sonar image in polar coordinates), the structuring element that is used is a diamond whose size in pixels depends on the chosen degree of detail dm (in meters), and on the image resolution (in meters). The shape of the structuring element is a trade-off between the necessary neighborhood consideration for smoothing and the preservation of high frequency components of the edges (like corners). Following the filtering of the polar images, another filtering is performed beam by beam on "images" whose axes are the ping number axis and the range axis. This time, given the fact that data have already been filtered in range, the structuring element is set to only 3 pixels along this axis, while it is again set to a number of pixels tuned by the same chosen degree of detail along the ping number axis.

3. MULTIPLE DETECTION PER BEAM

After water column data enhancement, object edges are now denoised and enhanced. However, the volume of data is still too large for the final step of object recognition. The sonar image has to be processed so as to only keep a few detections per beam. Generally, these detections are automatically provided by the system. The systems used here compute a single detection or sounding, but the built-in algorithms are too sensitive to strong specular reflection, fish, or sidelobe effects (Fig.). This can lead to false alarms and to misrecognition. Unfortunately, these predictable physical effects cannot be removed easily from the image. For example, simply normalizing the polar image in order to mitigate the receiver sidelobe pattern also induces an unwanted enhancement of the transmitter sidelobe pattern in the transversal direction.

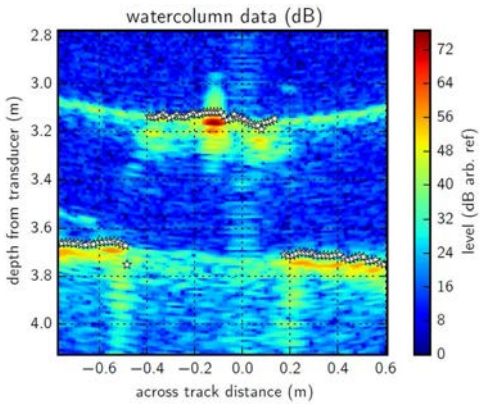


Fig. 1: Soundings measured by the R2Sonic 2020 MBES (700 kHz) on a sphere with strong specular reflection and sidelobes (sonar image in Cartesian coordinates).

In order to offer the possibility of multiple detections per beam with a reasonable false alarm rate, a 2D hysteresis thresholding is performed on each (previously enhanced) polar sonar image. This allows us to separate strong-highlight areas (over the upper threshold) from weak-highlight areas (over the lower threshold, and connected to at least one strong-highlight pixel). The trickiest part of this algorithm is the threshold adjustment. In our case, in order to have a fully automated procedure, the upper threshold is set as the proportion of pixels in the seafloor mask introduced below. This works in most cases, except in case of objects with very weak highlights. The lower threshold is a fraction k of the upper threshold. An example of hysteresis thresholding is showed in Fig. 2, on a polar sonar image where we can see the shape of a Manta mine.

The hysteresis principle is used here in order to suppress isolated weak highlights, as well as to mitigate sidelobe effects. However, this is still insufficient for sonar systems with

classical beamforming for which fairly large areas can be labelled as weak highlight after thresholding, and connected to a strong highlight. In order to discard them, we propose a post-procedure that consists in detecting the false weak areas, then to remove them from the ternary image obtained after hysteresis. The false weak area detection is achieved by using two masks: let us call “weak mask” (*resp.* “strong mask”) the binary image obtained by thresholding the enhanced image with the lower (*resp.* upper) threshold. These masks must first be pre-processed: a morphological smoothing of the weak mask is performed so as to remove or fill segments that do not contain at least np connected pixels along each beam; a morphological opening of the strong mask is performed with the cross-structuring element. The strong mask is then dilated with the same structuring element as for the bitonic filter. Finally, false weak-highlight pixels are pixels of the weak mask that are not marked by the dilated strong mask.

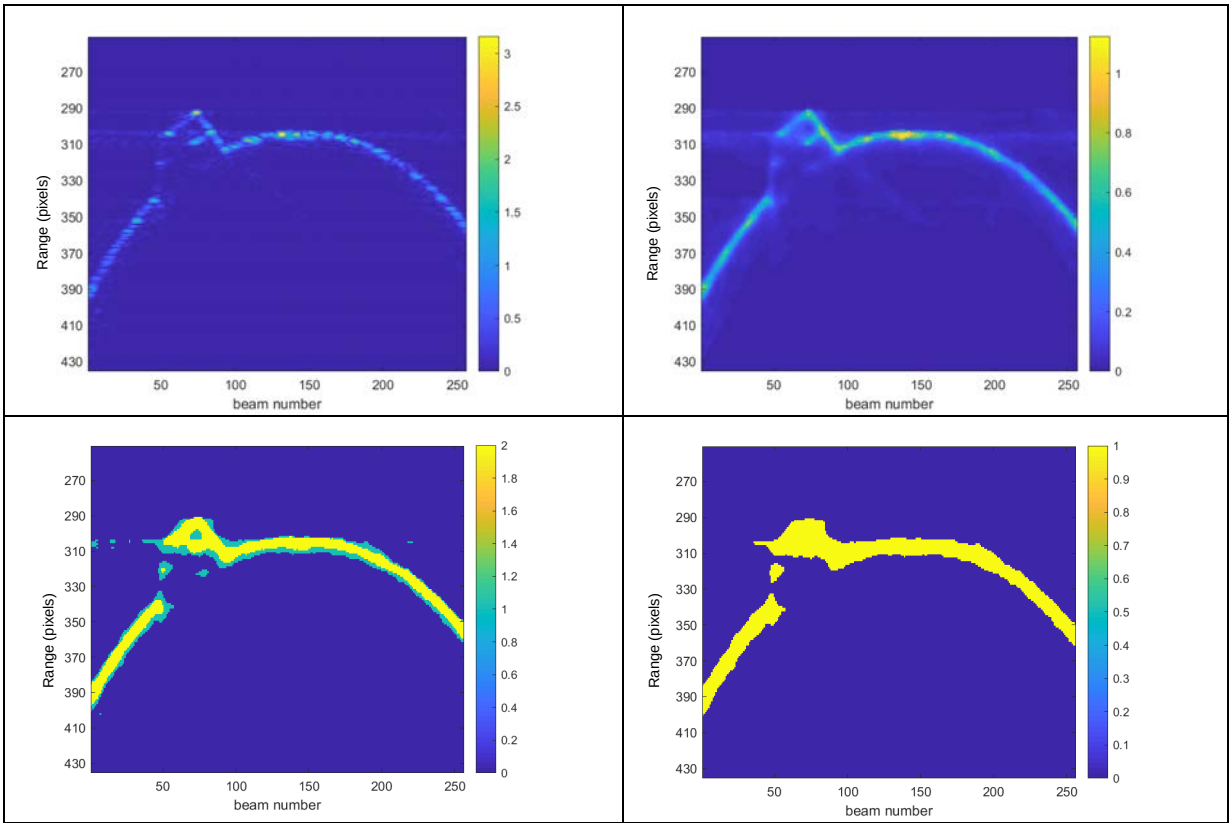


Fig. 2: EM2040 MBES (400kHz): polar image of a Manta mine (a); enhanced image (b); ternary image (c); hysteresis image (d)

The resulting image can now be processed with the following edge thinning procedure. Practically, the ternary image is processed column by column (or beam by beam). Each column vector is composed of values ranging from 0 (no edge) to 2 (strong-highlight pixel). A decision occurs on each pixel segment different from zero. In order to distinguish object detections from seabed detections, a seafloor mask is computed by averaging polar sonar images over the sequence and performing a thresholding at a centile that guaranties a full mask of the seafloor (that means, without hole for a given beam). If there is not a null intersection between this segment and the seafloor mask, the detected point is located at the mean index of the segment, and its value set to 0.5. In case of a null intersection, if the segment is composed of weak highlights, the detected point is located at the mean index of the segment, otherwise it is located at the index of the pixel of maximum value in the enhanced sonar image, and its value set to 1. An example of sidelobe effect mitigation and edge thinning is given on Fig. 3.

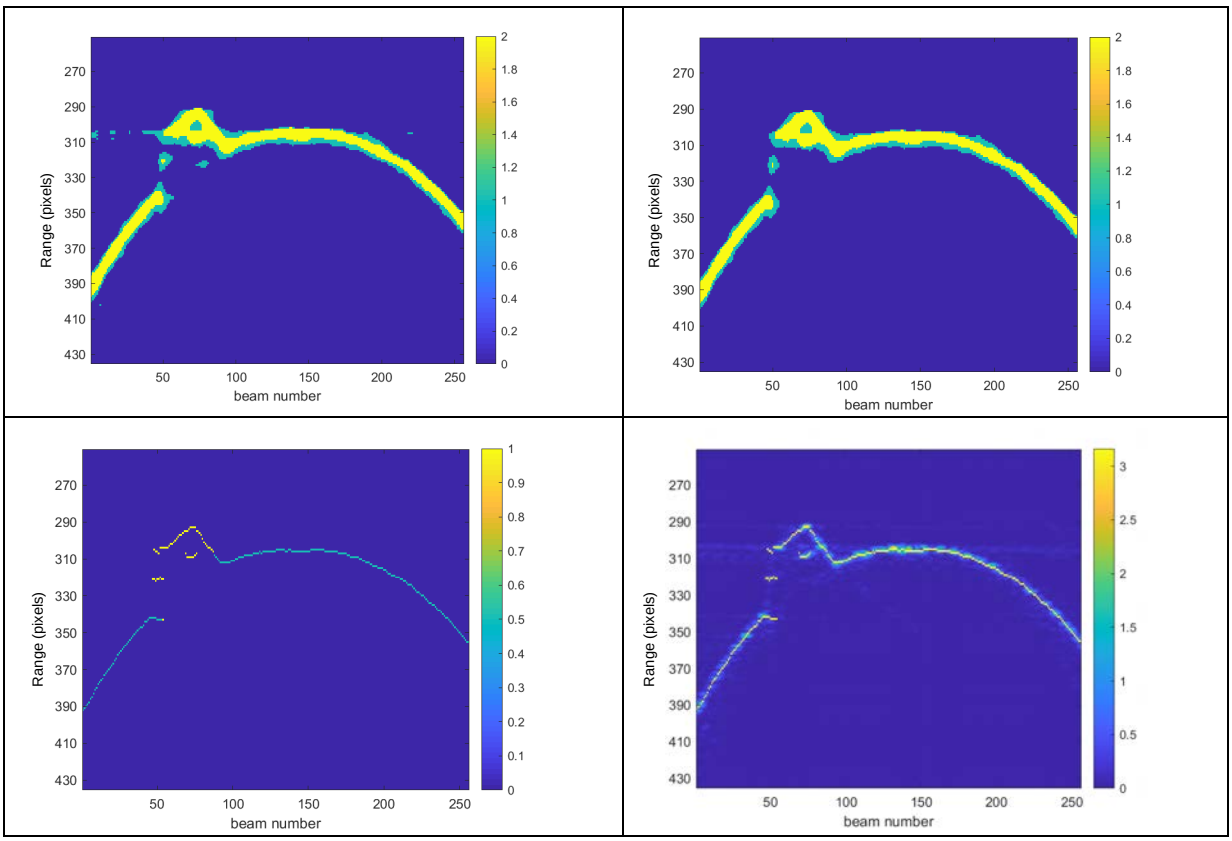


Fig. 3: EM2040 MBES (400kHz): ternary image (a); after post-processing (b); after edge thinning (c); superimposition of detections and polar image (d)

4. RESULTS

a) Dataset description

Since 2014, in preparation for this study, several MBES (specifications given in Table 1) were evaluated:

- BlueView MB2250-45 carried by the Daurade AUV and property of DGA TN (trials in 2014),
- R2Sonic 2022 rented by ENSTA Bretagne and mounted on a survey boat (trials in 2014),
- Kongsberg2040C lent by the National Hydrographic Service « SHOM » and mounted on a survey boat (trials in 2016)

An example of polar image obtained with each sensor is given Fig. 4.

b) Parameter setting

In the implementation of the bitonic filter, the diamond structuring element for morphological operations, with centile $c = 10\%$, is of size $l_i \times l_j$ and the rectangular window for Gaussian filtering is of size $2\sigma_i \times 2\sigma_j$ where $\sigma_x = \frac{l_x}{3}$, $x = i, j$. For each sensor, l_i (*resp.*

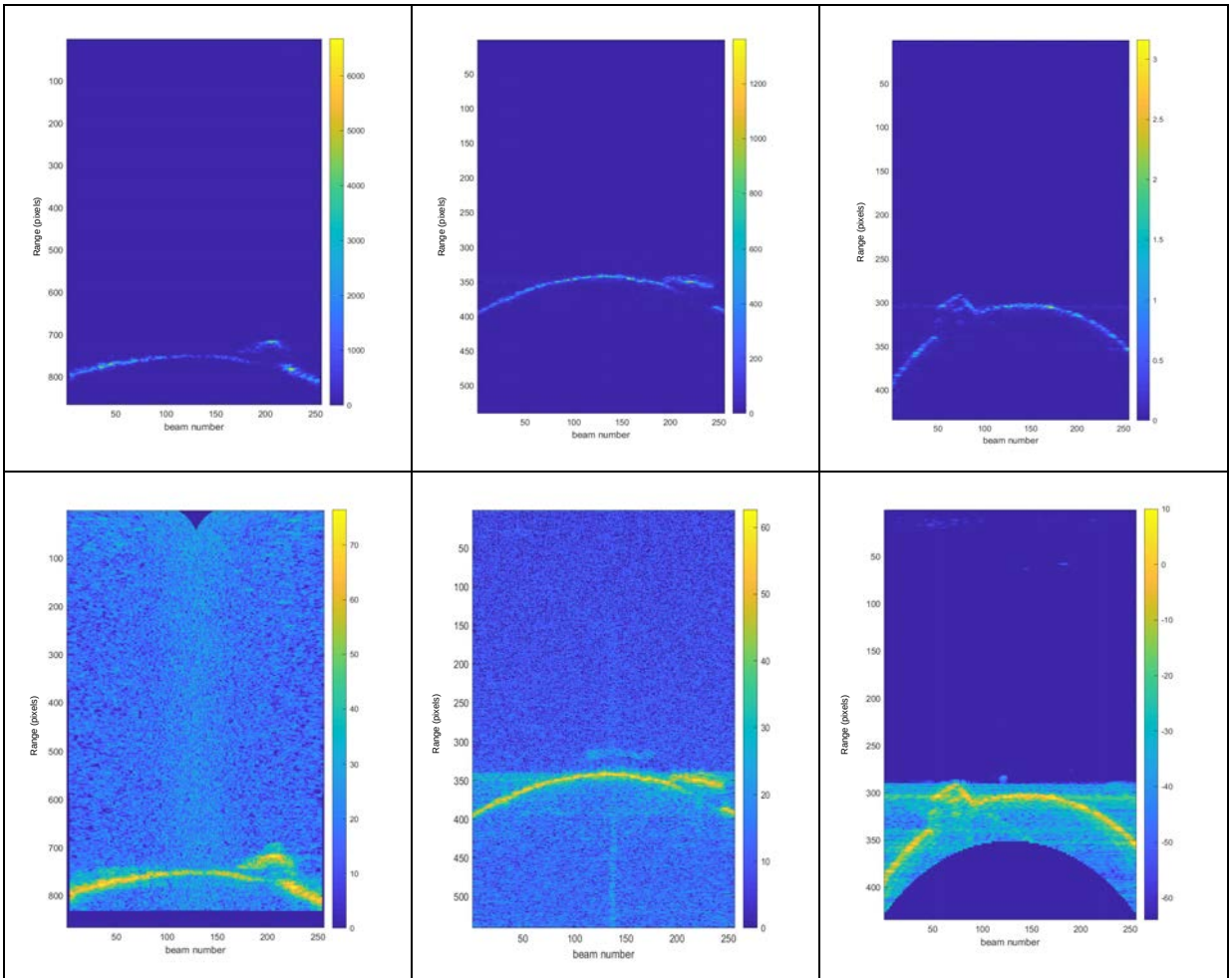
l_j) is fixed by considering the pixel size r_i (*resp.* r_j) at the shortest range to the seabed and the chosen degree of detail dm :

$$l_x = int\left(\frac{dm}{r_x}\right), \quad x = i, j \text{ where the } int(\ ) \text{ function gives back the closest integer.}$$

Whatever the sensor, $dm = 0.15m$.

	Frequency (kHz)	*Bandwidth (kHz)*	*Beamwidth*	*Swath sector*	*Range sampling rate (m)*	*Azimuth sampling rate*	*Distance travelled between pings (m)*
BlueView MB2250-45	2250	-	$1° \times 1°$	45°	0.006	0.16°	0.046
R2Sonic 2022	700	60	$0.6° \times 0.6°$	60°	0.011	0.23°	0.023
Kongsberg 2040C	400	60 max	$1° \times 1°$	60°	0.013	0.26°	0.019

Table 1: MBES specifications



BlueView 2250-45 (Rockan mine) Sonar altitude = 4.65m	R2Sonic 2022 (Rockan mine) Sonar altitude = 3.75m	Kongsberg 2040C (Manta mine) Sonar altitude = 4.0m

Fig. 4: Polar images from the different sensors (Up: linear scale; Down: dB scale)

Concerning the hysteresis thresholding, $k = 0.5$, except for MB2250 where $k = 0.6$, which leads to a higher value for the low threshold because of the high resolution of this sensor that can more easily induce false alarms. Morphological smoothing is performed with $np = 3$ pixels, except for MB2250, for which $np = 5$ pixels.

Last, Teledyne BlueView uses a blazed acoustic array to form and steer beams: the image is generated by time-frequency processing. Consequently, a given beam corresponds to a given frequency and then to a given resolution. Unfortunately, this impacts the backscattering level, which fluctuates along the beams. To avoid this, a preprocessing which consists in normalizing each row of the polar image is performed for this particular dataset. An example is given Fig. 5.

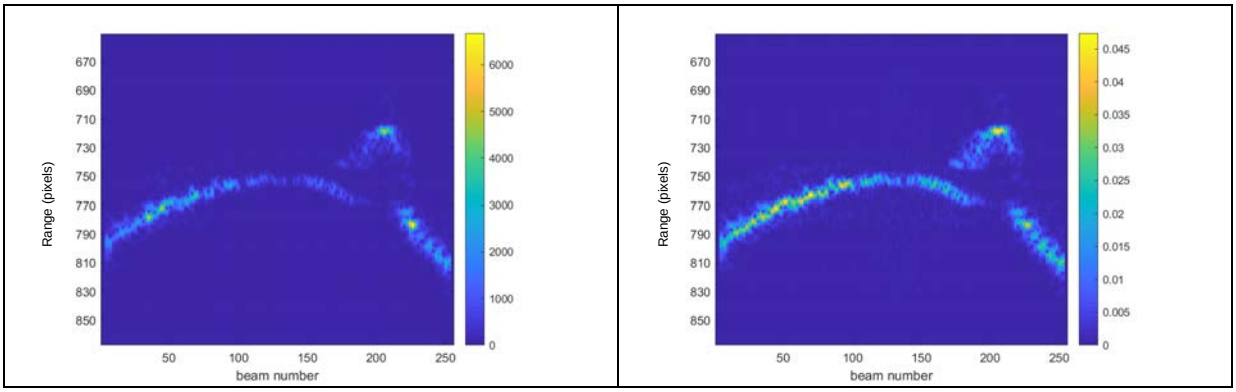


Fig. 5: MB2250 polar image normalization (left: without; right: with)

c) 3D detection views

As expected, compared to soundings measured by manufacturer detection algorithms, our algorithm perceives more details like multiple detections per beam and better describes objects which usually return strong specular reflection. An example is given in Fig. 6 for the MB2250 MBES with a cylinder.

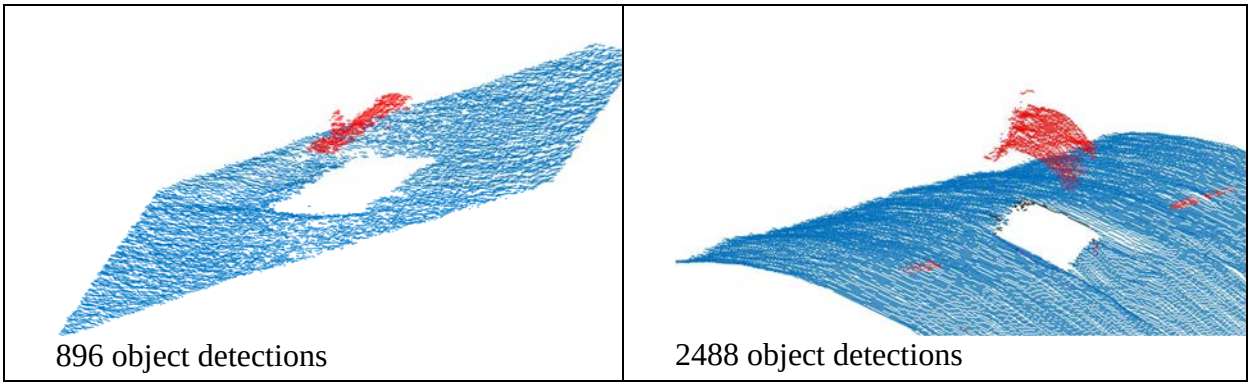


*Fig. 6: MB2250 MBES - Cylinder - Manufacturer detections (Left) compared to our detections (Right) - red (*resp. *blue): first object (*resp. *seafloor) detection per beam; magenta (*resp. *black): second object (*resp. *seafloor) detection per beam.*

The EM2040C MBES manufacturer detection algorithm performs generally better than ours but, again, multiple detections per beam can be useful to help recognizing the object and also, we notice that our algorithm can detect very small objects, as shown in Fig. 7.

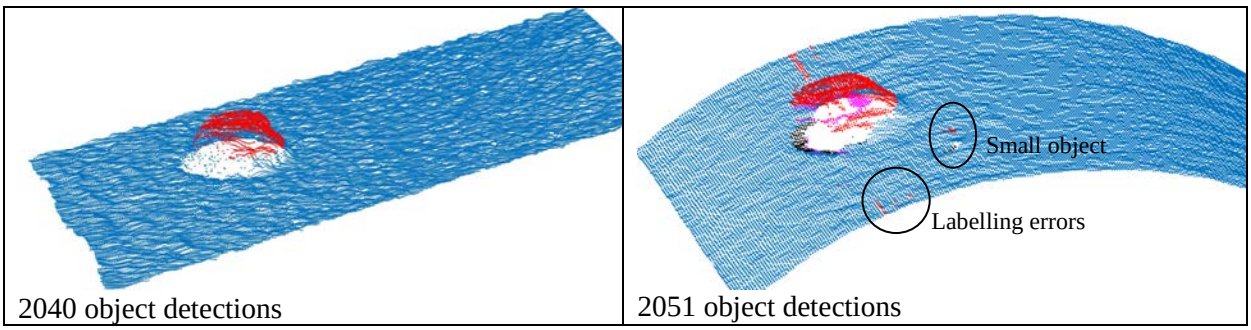


*Fig. 7: EM2040C MBES - Manta mine- Manufacturer detections (Left) compared to our detections (Right) - red (*resp. *blue): first object (*resp. *seafloor) detection per beam; magenta (*resp. *black): second object (*resp. *seafloor) detection per beam.*

5. CONCLUSION

In this paper, an algorithm has been proposed to enhance and then reduce the volume of data gathered by three different MBES. The first contribution is the introduction of the bitonic filter that has proven very successful in our context. The second contribution is the object contour detection by hysteresis thresholding together with morphological operations, followed by an edge thinning procedure. Results showed some improvements compared with other manufacturer algorithms: details can be recovered and multiple detections are available per beam. The next step is to find the best use of these results for recognizing objects for which a 3D model is available.

6. ACKNOWLEDGEMENTS

The authors would like to thank the Direction Générale de l'Armement/Techniques Navales for funding this study.

REFERENCES

[1] **T. R. Krogstad, M. S. Wiig and O. Midtgaard**, Autonomous object identification in mine countermeasure missions, In *OCEANS'11 MTS/IEEE KONA 2011*, 2011.

[2] **P. Perona and J. Malik,** Scale-space and edge detection using anisotropic diffusion, *IEEE Transactions on Pattern Analysis and Machine Intelligence*, 12(7), 629–639, July 1990.

[3] **G. Treece**, The bitonic filter: linear filtering in an edge-preserving morphological framework, *IEEE Transactions on Image Process*ing, vol. 25, no 11, pp. 5199-5211, 2016.

[4] **S. T. Bachelor, R. L. Thompson and J. L. Seawall**, Acoustic Imaging with Time-Frequency Beamforming, Blazed Arrays, and Other Array Designs, *US Patent* number US-4, 022,377, July 12, 2004.

ENVIRONMENTALLY ADAPTIVE AUTOMATIC DETECTION OF LINEAR SEAFLOOR FEATURES IN SIDESCAN SONAR IMAGERY: THE CASE OF TRAWL MARKS DETECTION

Charikleia Gournia[a], Elias Fakiris[a], Maria Geraga[a], David P. Williams[b], George Papatheodorou[a]

[a]Laboratory of Marine Geology and Physical Oceanography, Department of Geology, University of Patras, 26500 Rion, Greece.
[b]Centre for Maritime Research and Experimentation, NATO Science and Technology Organization, 19126 11 La Spezia, Italy.

Gournia Charikleia, math07041@upnet.gr; Fakiris Elias, fakiris@upatras.gr

Abstract: *This paper makes a detailed introduction to the design of a new automatic linear seafloor feature detection algorithm and its implementation on sidescan sonar (SSS) records, with its focus on trawl marks (TMs) detection. TMs are long linear scars on the seafloor, which are products of bottom trawl fishing. In image processing, detection of lines is a classical problem that seems to be more challenging on underwater acoustic imaging as the line segments are intermixed with wide-ranging environment backgrounds, and acoustic radiometric and geometric artifacts. Therefore, classic edge detection techniques based on the intensity gradient of the image do not yield reliable detection on SSS images. This proposed method integrates the characteristics of the linear features of interest in an environmentally adaptive procedure and is divided into three major steps. At the first step, preprocessing image techniques are applied to the original images. In the main stage, a spatial-domain filter is implemented through multi-scale rotated Haar-like features and integral images that measures the level of multiple oriented contrasts between adjacent areas. Seafloor characterization based on Anisotropy and Complexity calculations over the Haar-like filter's responses identifies three types of seafloor texture: complex (e.g. biogenic mounds, clutter), anisotropic (e.g. TMs, ripples), and plain (e.g. undisturbed sand). At the same step, another function over filter's responses produces a map that highlights the accurate locations where the candidate linear features prevail. The produced map is automatically binarized, morphologically processed and every linear image object is undergone properties measurement. The final linear features are selected according to a set of geometric and background textural feature criteria. In this study, is presented a set of assignment criteria that is tailored to the specific needs of TMs detection and is followed by TMs quantification that provides valuable measures for the estimation of bottom trawling impacts.*

Keywords: *automatic detection, sidescan sonar, trawl marks, Haar-like features, seafloor features, line detection*

1. INTRODUCTION

Seafloor features and objects detection are major interrelated areas of interest within the field of underwater acoustics. Along with the advancement of development in automatic seafloor feature detection, however, there is increasing concern over the type of underwater system and image processing method to be used. Sidescan sonar (SSS) system has established proven capabilities to identify seafloor types and detect seafloor features, despite the fact that its efficacy depends on operational limitations (e.g. position of the towfish). Linear and curvilinear seafloor features, whether natural or man-made, such as ripples, pipelines and trawl-marks (TMs) constitute an essential part of the description of the seafloor. The appearance of seafloor linear features on SSS imagery vary in their characteristics, e.g., geometric, gray-level values (intensity), density and surrounding area characteristics. In image processing, most common line detection techniques are based on edge detection. However, the high performance of edges on SSS imagery (e.g. stripe image noise, acoustic radiometric and geometric artifacts, boundaries of boulders or coral reefs) is having a serious effect on the accuracy of linear feature detection. This paper will focus on detecting TMs which are the result of the interaction of towed bottom fishing gears with the seafloor. Although the impacts of bottom trawl fishing have been the subject of intense debate within the environmental science community, a very small number of studies have been paid attention to automatic TMs detection. A major problem with this kind of concept is that the linear seafloor features are well visualized only if they are parallel to the axles of the insonified bottom strips (Fig. 1).

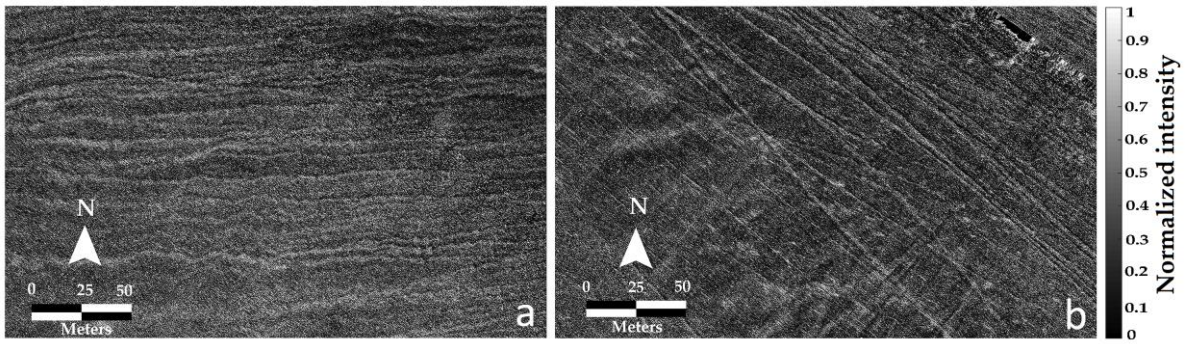


Fig.1: SSS images with high presence of trawl marks when the survey line is (a) almost perpendicular to the TMs direction, and (b) almost parallel to the TMs direction.

The methodological approach that is presented in this paper aims at detecting automatically linear seafloor features and is a mixed methodology based on linear edge detection, while suppressing texture elements of complex and featureless background. The study of Fakiris et al. [1] identifies several advantages of using seafloor texture information in underwater detection methods and achieves real time environmentally adaptive seafloor characterization through rotated Haar-like features and integral images. In the proposed method, we extend the aforementioned study in a useful way to produce linear edge maps utilizing a multi-scale version of rotated Haar-like features and appropriate calculations over their set of responses. The remainder of this paper is organized as follows. Section 2 will provide the scheme of the image processing techniques used in this work and establish criteria for identifying TMs. The experimental results of the approach on a real SSS mosaic are shown in Section 3 and are validated using corresponding analysis results of the SSS mosaic generated through a manual procedure that was proposed in the study of Patsourakis et al. [2]. Concluding remarks and a few thoughts for future work are made in Section 4.

2. IMAGE PROCESSING TECHNIQUES

In this section is presented a baseline overview of the image processing techniques used in this method (Fig. 2). Most of these techniques are widely used by the image processing and computer vision research communities. These were suitably applied in combination for the purpose of detecting candidate line segments in SSS images that possibly are parts of linear seafloor features of interest. The last subsection proposes a set of criteria that can be used to determine whether a line segment may most certainly be a TM.

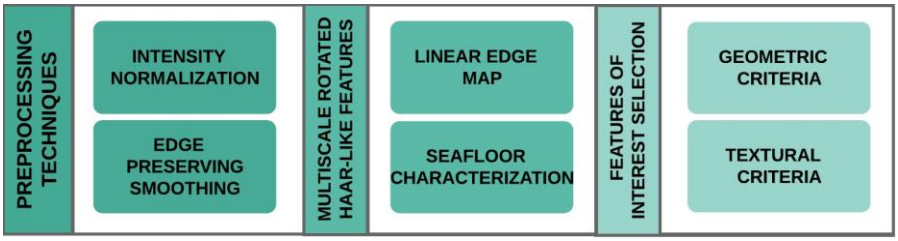


Fig. 2: The major stages of algorithm analysis and design.

2.1. Preprocessing techniques

A preprocessing stage occurs prior to the process of detecting seafloor features and identifying seafloor textures, in order to achieve efficient image restoration. Non uniform intensities and artificial shadow areas are noted in SSS images due to fluctuations of the backscattered energy. The first step of the algorithm utilizes the Homomorphic filtering, a popular technique in satellite and medical image processing for correcting non-uniform intensities and highlighting the desired image areas [3]. In the Homomorphic filtering process, the Fourier transform is used which provides access to the frequency domain. Following this, the Gaussian high-pass filter is applied to attenuate low frequency components which represent the gradual changes in the image intensities. Finally, non-uniform image intensity is normalized while the edges (high-frequency components) are maintained.

Once the Homomorphic filtering is applied, the output image is smoothed for the purpose of image noise reduction. We utilize Bilateral filtering with Gaussian kernels a non-linear filter which is synthesized by domain and range filtering [4]. To achieve edge preserving smoothing, the Bilateral filtering runs through the image pixel by pixel, replacing every pixel with a weighted average of the pixels that are close spatially and photometrically with it. Supposing that points are similar and nearby, Bilateral filtering allows the replacement of the centered point x with an average of the pixels in its vicinity. Inversely, if the pixels are not close, the Bilateral filtering bring neuter affects to the centered point x. To conclude, bilateral filtering smooths out the slight difference of neighboring pixels caused by noise, while sharp edges are preserved through the range component.

2.2. Multi-scale rotated Haar-like features

In the main stage of the algorithm, we use Haar-like features which consist of a white and a black rectangle enclosed in a template. Haar-like structure is represented as 0s and 1s in a geometrical order and the filter's response is calculated as the subtraction of the summation of the pixel values inside the two adjacent rectangles. Haar-like features have the advantage that

they can be calculated directly from an integral image, speeding significantly up data processing. Normal Haar-like features were developed by the authors of [5] and are broadly used but those are not rotation invariant. A number of researchers have presented rotated Haar-like features methods, including Fakiris et al. [1] that presented an extended set that covers twelve rotations (Fig. 3.b) and is capable of depicting features of almost any orientation. The rotated integral image, for a given integer rotation, is calculated by summing the pixels in the relevant aligned quadrant above the given pixel. For a more information-rich result, in this study we implement a multi-scale version of rotated Haar-like features. We utilize a sequence of rotated two-rectangle Haar-like features with common aspect ratio but whose widths respectively correspond on terms of an arithmetic progression. This subsections' filters are performed for each designed scale of the set of Haar-like features rotated at twelve directions that are capable of measuring the contrast between two adjacent oblong areas of the seafloor.

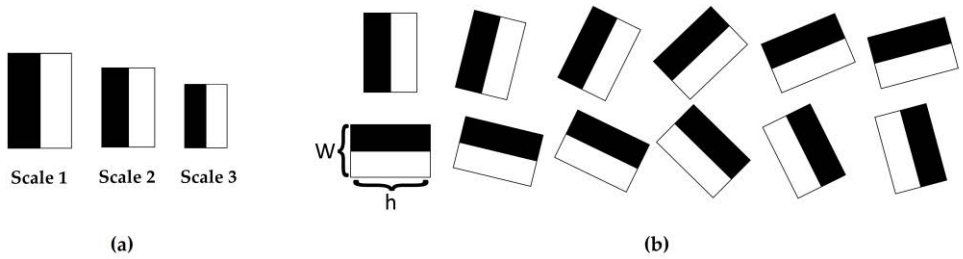


Fig 3: (a)The sequence of the two-rectangle Haar-like features with different scales and common aspect ratio (b)The Haar-like feature, rotated at twelve angles (revised from [1]*).*

2.3. Seafloor characterization

Texture can be described according to its two main characteristics: its contrast and orderliness, forming two groups of qualitative terms. Haar-like filtering can be used to quantify both contrast and orderliness, as a single feature that can assess the local variation of intensities but also highlight certain pre-specified structural geometries. Based upon the local averages of filter responses, two seafloor characterization measures have been estimated: Anisotropy and Complexity, that are described thoroughly in [1]. Anisotropy refers to the level of heterogeneity of filters' responses given for each direction [6] and therefore high values of Anisotropy indicates that at least one direction responses overrides the others. Complexity filter highlights the high-contrast areas where seafloor features are anarchical distributed with respect to their direction. The Anisotropy and Complexity threshold values discriminate the three types of texture: anisotropic (TMs, ripples), complex (biogenic mounds, clutter) and featureless (plain sand), were set manually by the human interpreter and pre-trained using a small part of the dataset.

2.4. Linear seafloor features detection

The second utility of multi-scale rotated Haar-like features concerns linear seafloor features detection (segmentation). Effort has been put to designing a new Haar-like filters with the use of the raw Haar-like filter's responses in order to scale down the analysis and achieve feature–level segmentation of sub-meter analysis. A function over the filter responses aims at enhancing the figure of the linear seafloor features. Linear edge enhancement filtering (LEE) works for each pixel of the image and is defined as:

$$(\mathrm{LEE}) = (\mathrm{MRF})^2 \quad (1)$$

where MRF (Maximum Response Filter) is the maximum contrast over all directions. For the binarization of the produced linear edge map, the Gaussian adaptive thresholding method is used, in which the threshold value is a weighted average of the pixel values in a manageable sized neighborhood (x,y) around pixel x.

For each scale of the rotated Haar-like features a binary image is produced with the extracted potential linear seafloor features. The binary images are combined with the logical operation "union" that synthesize a final binary image which contains each scale's extracted linear edges. All white connected pixels in the binary image are labelled as unique linear foreground objects and their properties are measured, such as their length and their orientation. Some lines intersect and their false orientation could lead to mistaken and incomplete analysis. Therefore, the intersected lines are split before the orientation of the identified image objects is computed. The splitting of the lines is achieved through logical and morphological operations by removing a small surrounding area around the junction points of the lines' skeletons.

Via the feature space we seek to substantiate which line structures correspond to linear seafloor features of interest. Final linear seafloor features selection is designed based on objects' geometric signature and the background environment features in the affected area. Following, this is a set of criteria that narrows the detected linear image objects down to those corresponding to TMs have been designed. The first geometric discrimination of the lines of interest is built upon their physical size. Lines with length more than 10m are kept for further analysis. Additionally, we excluded line segments that have orientation perpendicular plus-minus 5 degrees from the survey line. As for the textural criteria, objects in the image whose Anisotropy background values lie under the manually chosen threshold are excluded from analysis. Moreover, areas that are characterized by high complexity are deleted from the regions of interest.

3. EXPERIMENTAL RESULTS

3.1. Data acquisition and validation data set

The SSS data were collected in September 2006, on the western end of the Gulf of Patras (western Greece, Mediterranean Sea). The seafloor of the survey area is constituted by TMs, biogenic mounds and plain sand. The survey was conducted in a parallel-pass survey design to produce a SSS mosaic with 100% coverage of the seafloor with pixel size of 0.2 m. Six tracks were required (with a total length of 13.962 km) to cover an area of 2.98 km^2. Acoustic backscatter data of the seafloor were acquired with an EG&G 272TD sidescan towfish, connected to a top-side processor unit (EdgeTech 4200-P) and with the data acquisition software Discover (EdgeTech). The sonar towfish was towed at an average height of 45 m above the seafloor and was operated at a sound pulse frequency of 100 kHz. The swath range was set to 200 m and the ship speeds ranged between 3 and 4 knots.

The results of the application of the automatic TMs detection method in the SSS mosaic were evaluated using a dataset of manually extracted TMs. The results obtained by Patsourakis et al. [2] has preceded this, in which the same SSS mosaic were processed, and each individual TM was extracted manually, delineated and mapped on ArcGis software. The data results of the manually and automatically extracted TMs were undergone spatial analysis to derive their mean density, length and direction of TMs per 50x50m square area. For the purpose of statistical analysis and comparison between the manually and automatically quantified detected TMs, the blocks were classified into four classes according to the TMs' total length.

3.2. Results and discussion

Figs 4 through 6, below, show correspondingly the application of algorithm's main steps: preprocessing techniques, seafloor characterization through Anisotropy and Complexity definitions, and linear seafloor features detection.

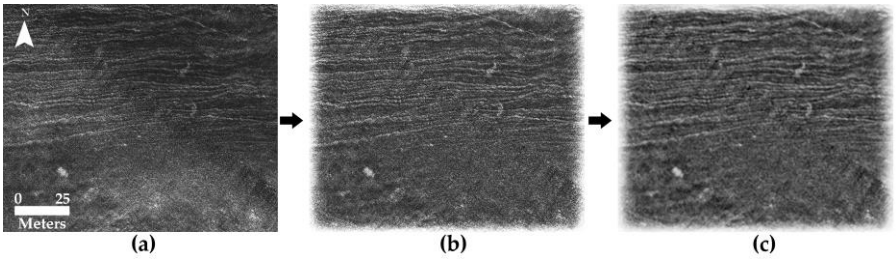


Fig 4: (a) The original SSS image, (b) the SSS image after application of Homomorphic filter and (c) after edge preserving filtering.

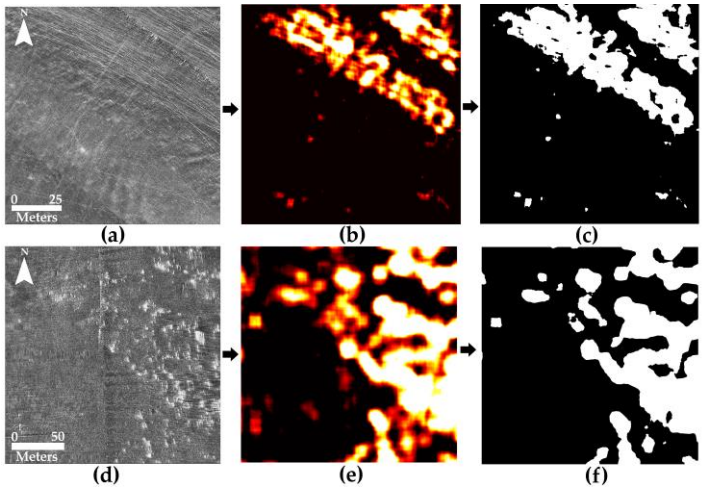


Fig 5: (a) SSS mosaic area with plain sand and TMs, (b) the Anisotropy map of up-left image, (c) fishing grounds segmentation, (d) SSS mosaic area with plain sand and biogenic mounds, (e) the Complexity map of low-left image, (f) biogenic mounds segmentation map.

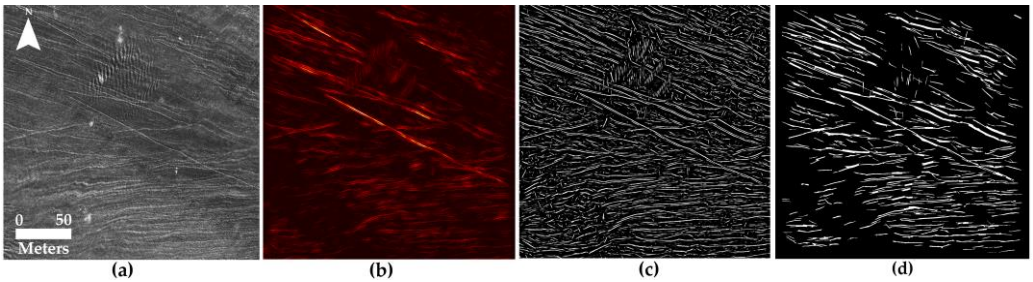


Fig 6: (a) The original SSS image depicting TMs of various orientations and contrasts, (b) the LEE filter over the preprocessed image, (c) linear edge segmentation map, (d) the final selected linear seafloor features.

The automatically detected TMs in SSS mosaic are shown in Fig.7.b. The Fig.8 visualize the fishing stress and the preferred axles of towing both for the automatic and manual TMs digitization cases, giving the means for visual comparison. Cross tabulation matrix (Fig 9.a) is

used to evaluate the one-to-one correspondence of the classes and the high concentration of scores in the diagonal indicates consistency and stable correlation between the corresponding classes of the two datasets. The Cohen's Kappa coefficient that evaluates the agreement between the corresponding class limits is equal to 0.65, indicating a substantial agreement of all class ranges that are used to classify the blocks of the manually and automatically derived TMs. Accuracy of automatic TMs detection method is also evaluated by comparing the two data sets that are defined by thresholds of the total TMs length used as binary classifiers. High accuracy values are in the diagonal of the accuracy vs threshold diagram (Fig 9.b), indicating highly accurate results as the total-length threshold increases (excluding more and more low TM density areas from the analysis). It is clear that TMs and other proud linear features (such as sand-ripples) are more difficult to be detected when they get perpendicular to the swath direction, where their contrast and shadow length decrease. Fig 9.c confirms the above hypothesis, showing an increased error per unit area as the deviation of the TM orientation from the survey-lines' equivalent gets higher. This finding is opposite to what one should expect, i.e. decreased ability of the system to detect TMs as the direction deviation gets higher, leading to increasing their underestimation. This paradox can be interpreted just in one way: what is expected to bias computer aided detections is also biasing human-interpretation.

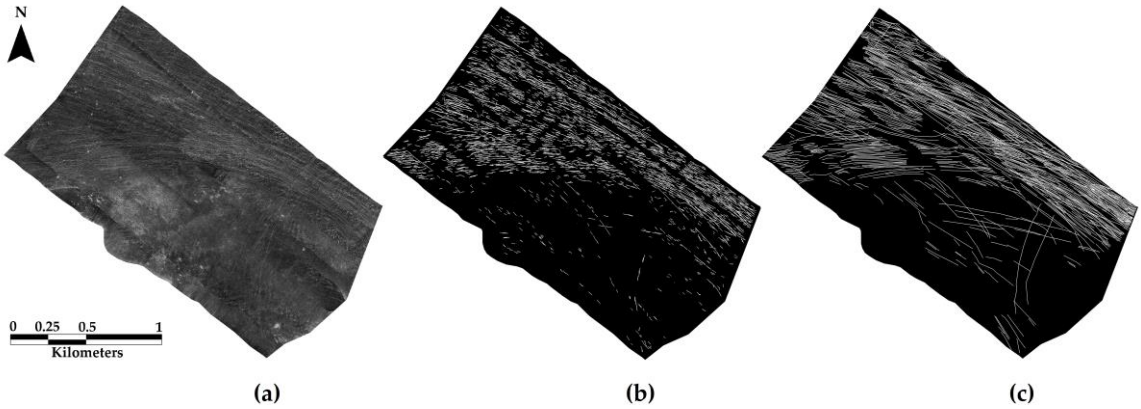


Fig 7: (a) The SSS mosaic of the study area, (b) a binary image showing the automatically extracted TMs and (b) an image depicting the manually digitized TMs (dataset from [2]*).*

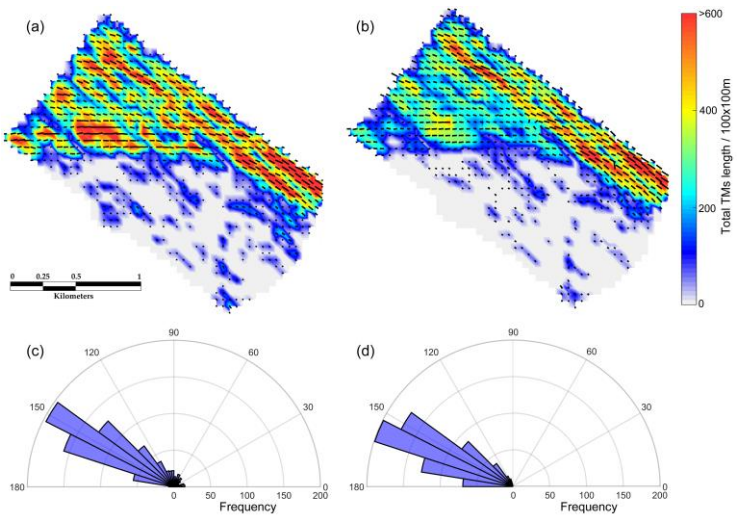


Fig 8: (a), (b) Quiver (vector) plots visualizing the mean length and orientation of the TMs within each analyzed block for the automatic and the manual TM detection cases respectively, overplayed to maps of the total length of TMs per 10.000 m^2 (100x100m block) unit area. (c), (d) Rose diagrams of the corresponding quiver plots.

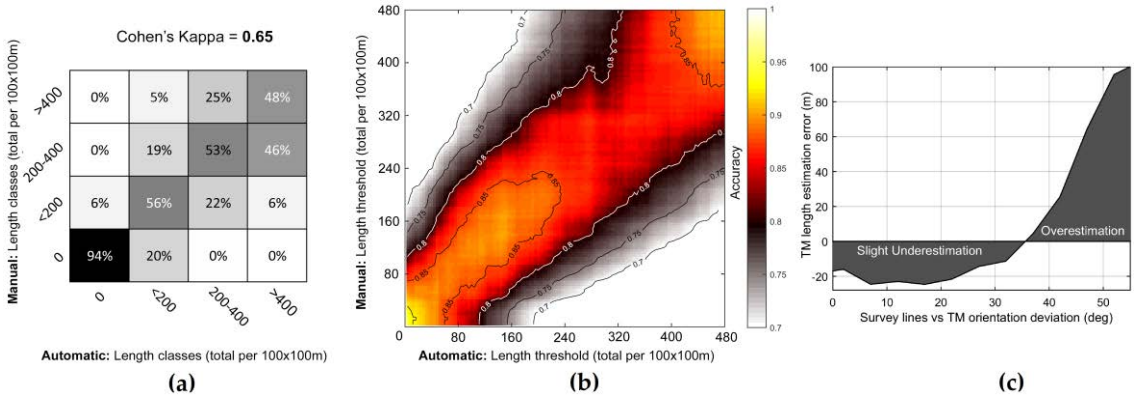


Fig 9: (a) The cross-tabulation matrix for the four-classes scenario and (b) accuracy versus TM length per unit area threshold and (c) the *total TM length error per 100x100m versus the deviation of TM orientation from the survey-line's equivalent.*

4. CONCLUSION

In this paper a new method was presented that achieves automatic detection and spatial quantification of linear seafloor features under challenging conditions of acoustic imaging when general-purpose SSS data are used. The algorithm was demonstrated on sidescan sonar images of board-scale and structural complex habitats, and detected successfully trawl-marks of great variability in orientations, intensities and contrasts. The preprocessing stage was a necessary step that gives at TMs a more discrete appearance in SSS image data while the information about the texture of the seafloor has a valuable impact on eliminating false alarms at the zones where TMs are absent. The exported data of this linear seafloor features detection when focusing on TMs could be used for rapid assessment of fishing impacts on the seafloor. A natural progression of this study is to implement some of its features in conjunction with machine learning principles through the use of extended sonar datasets of linear features.

REFERENCES

[1] **E. Fakiris, D. Williams, M. Couillard, and W. Fox**, "Sea-floor acoustic anisotropy and complexity assessment towards prediction of ATR performance," *Proc. Int. Conf. Exhib. Underw. Acoust.*, pp. 1277–1284, 2013.

[2] **M.-J. Patsourakis, E. Fakiris, and G. Papatheodorou**, "A method to estimate otter trawling effects on the seafloor morphology : A case study from Gulf of Patras , Greece .," in *13th Pan-Hellenic conference of the Greek ichthyologists.At: Lesvos - Greece.*, 2007.

[3] **S. Bazeille, I. Quidu, L. Jaulin, and M. Jean-Philippe**, "Automatic underwater image pre-processing.," in *CMM'06*, 2006.

[4] **C. Tomasi and R. Manduchi**, "Bilateral filtering for gray and color images," in *Sixth International Conference on Computer Vision (IEEE Cat. No.98CH36271)*, 1998, pp. 839–846.

[5] **P. Viola and M. Jones**, "Rapid object detection using a boosted cascade of simple features," *Proc. 2001 IEEE Comput. Soc. Conf. Comput. Vis. Pattern Recognition. CVPR 2001*, vol. 1, p. I-511-I-518, 2001.

[6] **D. P. Williams and E. Fakiris**, "Exploiting Environmental Information for Improved Underwater Target Classification in Sonar Imagery," *IEEE Trans. Geosci. Remote Sens.*, vol. 52, no. 10, pp. 6284–6297, 2014.

BAYESIAN SEAFLOOR CHARACTERIZATION FROM SAS IMAGERY

Bart Gips[a]

[a]*NATO Centre for Maritime Research and Experimentation (CMRE)*

Viale San Bartolomeo 400, La Spezia, Italy
email: Bart.Gips@cmre.nato.int

Abstract: *Synthetic aperture sonar (SAS) allows for high-resolution imagery of the seafloor with quality that approaches that of an optical camera. From these images a human can identify what type of seabed is in view (e.g. smooth sand, sand ripples, sea grass, rocks). Segmentation into different classes is useful in a setting where autonomous underwater vehicles (AUVs) are used, since information on the bottom type should be taken into account when controlling the behaviour of the AUV. In particular, we focus on mine countermeasures (MCM) applications, where AUVs are generally tasked with autonomously scanning the seabed for mine-like objects on the seafloor. In this scenario, characterizing the type of seafloor informs us about the difficulty the AUV will have when using an automatic target recognition (ATR) algorithm to find mine-like targets and as such this information can be used in a planning and performance evaluation context. Previous work has shown that seabed characterization is possible using through-the sensor features. In this work we focus on predicting the presence of different bottom types based on multifractal analysis of SAS images. Using a Bayesian framework, and a Gaussian process classification (GPC) algorithm, we not only predict the seabed type, but also provide an uncertainty estimate. Secondly, the GPC has the advantage that it will lead to predictions with high uncertainty if unknown data are encountered, i.e. when the SAS images contains features that are statistically different from the training dataset. We compare the GPC with a deterministic classification algorithm and highlight the advantageous and disadvantages compared to some of the methodology proposed in earlier work.*

Keywords: *Bottom type characterization, Gaussian process classification, Synthetic Aperture Sonar.*

1. INTRODUCTION

Sonar images contain a lot of information about the sea bed characteristics. This is especially true in the case of Synthetic aperture sonar (SAS), which allows for high-resolution imagery of the seafloor with almost photo-like quality. From these high-quality images, it is relatively easy to make out whether the seabed consists of sand ripples, is smooth, or is covered with sea grass or rocks.

Segmentation into different classes of sea floor is useful when controlling autonomous underwater vehicles (AUVs), since the bottom type is a possible important input for the autonomous control algorithms that affect the behaviour of the AUV. In mine countermeasures (MCM) applications in particular, AUVs are generally tasked with autonomously scanning the seabed for mine-like objects on the seafloor. This task varies in difficulty depending on the sea floor type. For example, the presence of vegetation such as posidonia will make it drastically more difficult to detect mine-like objects on the seabed, whereas sand ripples make it more difficult to detect targets when it is insonified from an angle perpendicular to the sand ripples, since the ripples create acoustic shadows that obscure targets. For this reason previous work has sought to automate sea bed characterization [10, 17, 3] with a specific focus on sand ripples in particular [5, 19]. In future work we aim to use the information on the bottom type in order to quantify the difficulty the AUV will have when using an automatic target recognition (ATR) algorithm that is designed to find mine-like targets. As such this information can be used in the context of planning and performance evaluation [7].

In this paper we use Gaussian processes prior in order to perform bottom type segmentation. Gaussian processes are a set of non-parametric Bayesian models [14]. As such this makes them more flexible than more commonly used parametric probabilistic models.

In the case of statistical models with a Gaussian likelihood function, as is the case in popular least square regression applications, Gaussian process priors are analytically tractable. However, in classification problems as in the context of bottom type characterization, the likelihood is no longer Gaussian. Therefore the resulting expressions contain intractable integrals that need to be evaluated numerically, e.g. by using Monte Carlo methods, or they can be approximated, e.g. by using a Laplace approximation, variational methods, or expectation propagation [13].

A secondary challenge comes in the form of scalability. In general, inference using Gaussian processes requires $O(N^3)$ computation, where N is the number of data points in the training set. A way to decrease this computational complexity comes in the form of sparse approximations. Generally this amounts to defining a set of *M induced* points, that are not necessarily a subset of the original data points [15]. These induced points do not have a corresponding target value (i.e. the class index in the case of classification), but instead they serve as "funnel" that attempts to catch and compress all information from the full original training dataset.

In this work, we use the induced points as variational parameters [8], in order to further reduce the computational demand. This allows us to use stochastic gradient descent to learn the model parameters, making it possible to use very large datasets to learn model parameters.

2. METHODS

Before we describe our Gaussian process-based classification model, we start by describing the more traditional multinomial logistic regression model. We will use it to contrast it with the more elaborate Gaussian process model.

2.1. Multi-class classification

Classification models generally work by transforming an input variable $\mathbf{x}_i$ into activation values $\mathbf{f}_i$. These activation values are then projected through a link function to project them onto the interval $[0,1]$ such that they can be interpreted as probabilities. For our logistic regression implementation, we use the softmax link function to translate an activation vector $\mathbf{f}_i = [f_i^1, f_i^2, \ldots, f_i^C]^T$ to the probability of class label $c \in \{1,2,\ldots,C\}$ [2]:

$$p(y_i = c|\mathbf{f}_i) = \exp(f_i^c)/\sum_{c'} \exp(f_i^{c'}) \tag{1}$$

where we use subscript i for indexing over data points, and superscript c for indexing over classes. In a traditional multi-class regression the activation vectors $\mathbf{f}_i$ are a linear combination of the feature values:

$$f_i^c = (\mathbf{w}^c)^T \mathbf{x}_i \tag{2}$$

We can then use Bayes' theorem to express the posterior over the model parameters $\mathbf{W}$:

$$p(\mathbf{W}|\mathbf{X}) = \frac{p(\mathbf{y}|\mathbf{f}_1, \mathbf{f}_2, \ldots, \mathbf{f}_N) p(\mathbf{W})}{p(\mathbf{y})}. \tag{3}$$

with $\mathbf{X} = \{\mathbf{x}_i\}_{i=1}^N$ being the input dataset, and $\mathbf{y} = [y_1, y_2, \ldots, y_N]$ the target values, i.e. class labels.

2.1.1 Gaussian processes for classification

Instead of using a linear combination of feature values $(\mathbf{w}^c)^T \mathbf{x}_i$, we can use a Gaussian process (GP) prior [14], i.e. where all activation values $\mathbf{f} = [\mathbf{f}_1, \mathbf{f}_2, \ldots, \mathbf{f}_N]$ are jointly Gaussian:

$$p(\mathbf{f}|\mathbf{X}) = \mathcal{N}(\mathbf{f}|\mathbf{0}, \mathbf{K}) \tag{4}$$

The activation values are now no longer an explicit function of the input $\mathbf{X}$, but are the result of an *a priori* unknown non-linear transformation of X ($\mathbb{R}^D \to \mathbb{R}^C$), where D is the dimensionality of the input data. Eq. (4) tells us how smooth we expect this transformation to be over the input domain through the covariance function. We use the squared exponential function to model the covariance of the feature values belonging to class c:

$$K_{ij}^c = K^c(\mathbf{x}_i, \mathbf{x}_j|\boldsymbol{\theta}) = \exp(-\frac{1}{2}\sum_{d=1}^{D} \theta_d^c (x_i^d - x_j^d)^2) \tag{5}$$

where K_{ij} are entries of matrix $\mathbf{K}$ in Eq. (4), and x_i^d is the d-th component of feature vector $\mathbf{x}_i$.

This leads to a posterior directly over the activation values $\mathbf{f}$, rather than model parameters:

$$p(\mathbf{f}|\mathbf{y}, \mathbf{X}) = \frac{p(\mathbf{y}|\mathbf{f}) p(\mathbf{f}|\mathbf{X})}{p(\mathbf{y}|\mathbf{X})}. \tag{6}$$

Prediction of activation values $\mathbf{f}_*$ belonging to a new data point $\mathbf{x}_*$ is performed by conditioning on the activation values of the reference dataset $\mathbf{f}$ and marginalizing over the posterior:

$$p(\mathbf{f}_*|\mathbf{y}, \mathbf{X}, \mathbf{x}_*) = \int p(\mathbf{f}_*|\mathbf{f}, \mathbf{x}_*) p(\mathbf{f}|\mathbf{y}, \mathbf{X}) \mathrm{d}\mathbf{f}. \tag{7}$$

Link function For the linear regression case, the softmax link function is attractive, since it is easy to differentiate with respect to the weight parameters $\mathbf{W}$. As in [11], we use the robust max function in the case of our GP classification:

$$p(y_i = c|\mathbf{f}_i) = \begin{cases} 1-\varepsilon & \text{if } c = \text{argmax}(\mathbf{f}_i), \\ \varepsilon/(C-1) & \text{otherwise.} \end{cases} \tag{8}$$

Sparse approximation In order to deal with with large datasets we introduce a pseudo data set of size $M < N$ [15] to find a sparse approximation to the full GP. This pseudo dataset $\bar{\mathbf{X}} = \{\bar{\mathbf{x}}_i\}_{i=1}^{M}$ has corresponding activation values $\bar{\mathbf{f}} = [\bar{\mathbf{f}}_1, \bar{\mathbf{f}}_2, \ldots, \bar{\mathbf{f}}_M]$.

This means we will perform inference on the pseudo activations $\bar{\mathbf{f}}$, i.e. we alter Eq. (6):

$$p(\bar{\mathbf{f}}|\mathbf{y}) = \frac{\int p(\mathbf{y}|\mathbf{f}) p(\mathbf{f}|\bar{\mathbf{f}}) \mathrm{d}\mathbf{f}\; p(\bar{\mathbf{f}}|\bar{\mathbf{X}})}{p(\mathbf{y})} \tag{9}$$

where $p(\mathbf{f}|\bar{\mathbf{f}})$ and $p(\bar{\mathbf{f}}|\bar{\mathbf{X}})$ follow our original GP prior (Eq. (4)). We use a variational approximation to this posterior, where the induced points are considered to be variational parameters as in [8].

Implementation For our control methodology of (linear) multinomial logistic regression, we use Newton's method to find the maximum a posteriori solution for weight parameters $\mathbf{W}$ in Eq. (3). The prior on the weight values is set to a univariate normal distribution with a mean of zero and a standard deviation of 10, i.e. $p(w_i^c) = \mathcal{N}(w_i^c|0, 10^2)$.

We implemented the variational multi-class GPC following the approach found in [8], using the GPflow python module [12]. We used a the robust max link function Eq. (8), with $\varepsilon = 10^{-3}$. The covariance functions were set to squared exponential (see Eq. (5)). Since we did not *a priori* expect different bottom type classes to have the same length scales in the space spanned by our predictors $\mathbf{x}_i$, we used class-specific hyper-parameters $\boldsymbol{\theta}_c$. These hyper-parameters were determined by maximization of the lower bound to the marginal likelihood (i.e. minimisation the variational free energy). The M pseudo inputs $\bar{\mathbf{X}}$ were initially selected at random from the training data set. Subsequently the variational free energy was minimized using the Adam method for stochastic optimisation [9].

2.2. Sonar Data

In total we had 254 SAS images in which a human had judged the sea bottom type by drawing polygons over the original image. The images were recorded of the coast of Bonassola, Italy by the SAS on board the CMRE MUSCLE AUV [1]. Subareas within each image were labelled by hand to belong to one of 5 classes: ripples, posidonia, posidonia on ripples, rocks, or smooth sand. These SAS images had a resolution of 2001 by 7333 pixels with a corresponding resolution of 0.025 and 0.015 m/pixel respectively in the along-track an across track direction.

Preprocessing Before extracting any features from a SAS image, the image was normalized in a manner similar to the method reported in [18]. Briefly, the modulus of the complex SAS image was log-transformed, after which the image was normalized row- and column-wise.

In order to facilitate data handling, we subsampled the images after the normalization step by a factor of 2 and 3 to achieve a more square resolution of 0.05 and 0.045 m/pixel.

For training and testing of our classification algorithms we extracted 500 samples at random from every SAS image to put in a training data set, and we extracted another 100 different random data points to use in a test set. In total, this initially resulted in a training set with 127000 data points and a test set containing 25400 points. To train the classification models in

an unbiased manner, the training set was further downsampled by randomly drawing without replacement where necessary such that every class had equal number of datapoints. This lead to a total of $4968 \times 5 = 24840$ points in the final training data set.

2.2.1 Predictive features

For either of our classification algorithms to function we need features to populate the vectors $\mathbf{x}_i$ (e.g. see Eq. (2)).

Ping-to-ping correlation The on-board processing of the SAS images on the MUSCLE provides us with a ping-to-ping correlation metric [4]. The ping echo time series were cut up into 10 time series of equal length centred on time samples corresponding to different ranges, giving us correlation coefficients for 10 different range bins. These values were then mapped to the image coordinates by averaging the correlation coefficients of all ping pairs that contributed to an image pixel.

Lacunarity Lacunarity has previously been shown to be a good metric for sea floor characterization in sonar imagery [17]. Lacunarity was estimated by a box counting method and is equal to the square of the coefficient of variation, i.e. the ratio between the sample variance and the squared mean.

Fractal dimensionality metrics We followed the procedure suggested in [3], and consider both the asymmetric and the directional fractional dimension, such that for every length scale we will have 4 metrics. We considered length scale ratios of $1:2$, $2:4$, and $4:8$ pixels, this lead us to a total of 12 different fractal dimension estimates. Finally we smoothed these estimates using a 50×50 pixel rectangular normalized filter kernel to reduce high-frequency noise. We assumed the relevant changes in these metrics to be the result of differences in bottom type, therefore the relevant changes should vary smoothly across the image and will not be present in high-frequency components.

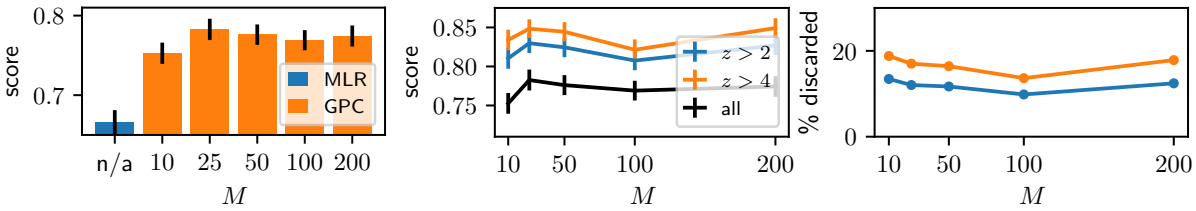
3. RESULTS

As mentioned in section 2.2, we used a training set consisting of 127000 data points and a test set of 25400 data points. We first applied the simpler multinomial logistic regression by calculating the maximum a posteriori estimate for the weight parameters based on the complete dataset. After having learned the weight parameters, we used them to predict the bottom type labels in our test set. To get an estimate on the standard error of the prediction performance we applied a bootstrapping procedure where we generated 1000 bootstrapped test datasets through resampling with replacement. The mean and standard deviation of the MLR prediction performance across these 1000 resampled test sets are shown with blue bars in Fig. 1.

Similarly we train the Gaussian process classifier (GPC) using different number of induced points M and predicted the class labels of the test set. The results are show with orange bars in Fig. 1. Note that all GP classifiers outperformed the MLR model on average as measured by the classifier accuracy scores in Fig. 1a, with $M = 25$ the best performing model among our tests, increasing the number of induced points beyond 25 seemingly lead to over-fitting.

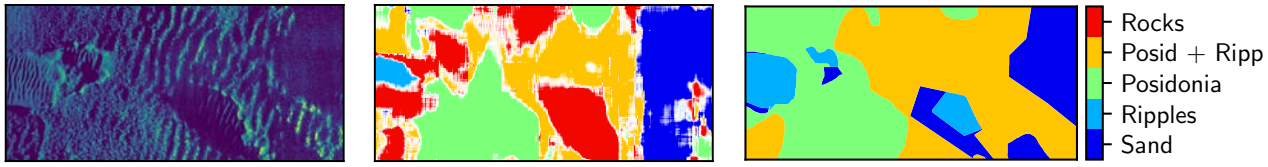
Note that classifying by chance would lead to a score of 20% and the classification accuracy of $> 66\%$ for the MLR model is well above that. This suggests that given the predictive features we use (section 2.2.1), the 5 bottom type classes are fairly separable using a linear model.

Our GPC models provide us with an uncertainty estimate on our predictions. To illustrate its usefulness, we repeated the accuracy analysis, but now we leave out predictions that are not



(a) (b) (c)

Fig. 1: (a) Prediction accuracy score (percentage correctly classified) for the MLR model (blue bar) and for the Gaussian process classifies using different number of induced points M (orange bars). (b) Prediction accuracy score as in 1a, with and without discarding samples for which prediction was uncertain. (c) Number of samples discarded to generate curves in (b). Bars and curves in (a) and (b) depict mean values across 1000 resampled test sets (bootstraps), error bars depict 5 times the standard deviation across these bootstrap distributions.



(a) (b) (c)

Fig. 2: (a) example SAS image. (b) GPC prediction using the model with $M = 25$, transparency level reflects uncertainty (z in Eq. (10)). (c) Manually labelled bottom types.

certain. To roughly quantify certainty of a prediction we calculate a "z-score" quantifying the statistical distance to the nearest alternative class:

$$z = \min_{k \neq i} \left[(\mu_i - \mu_k) / (\sqrt{\sigma_i^2 + \sigma_k^2}) \right] \tag{10}$$

where μ_k and σ_k^2 are the mean and variance of the predicted probability that the test point belongs to class k. We use index i to indicate the class with the most probability mass (i.e. $\mu_i > \mu_k,\ \forall k \neq i$). The higher the value of z, the more certain our prediction, with $z = 0$ when two or more "winning" classes are equally likely.

We performed two new analyses where we either discarded all test data for which $z \leq 2$ (blue curve), or $z \leq 4$ (orange curve). The results are shown in Fig. 1b, showing that indeed, the GPC model's predictions with lower uncertainty have higher accuracy, as seen by the accuracy increasing to approximately 85% when around 17% of the test points were discarded (Fig. 1c) for the cases of $M = 25$ and $M = 200$.

As an illustration, Fig. 2 shows a difficult example SAS image with manually segmented bottom types (Fig.2c), together with the most likely bottom type as predicted by the GPC model with $M = 25$ (Fig.2b). Note that the uncertainty is highest around the borders between bottom type classes, and that the "rocks" class seems overrepresented.

4. DISCUSSION

In this work, we applied Gaussian process classification to automated bottom type characterisation based on sonar imagery. Their non-parametric nature makes GP models able to perform well for data sets with non-linear class boundaries. The highest performance in simi-

lar classification problems is generally achieved by convolutional neural networks (CNN) [10]. The advantage of CNNs lies in the fact that they automate feature extraction and can find a non-linear transformation that separates the classes. However, their performance comes with a considerably higher computational cost, and since the final step in most classifier CNNs is a softmax function, they generally do not provide uncertainty estimates. In addition, an important feature of GPs that we have glossed over so far, is the fact that GP models do not work with a class boundary captured in model parameters (e.g. the weights in Eq. (2)), but with a covariance function that typically depends on the distance to the data points in the training set. This means that after learning, when we encounter a new data point that is not at all similar to our training data set (e.g. a new bottom type, or very noisy or distorted data), the GP will give a non-informative result. That is, the classes will be equally probable admitting maximum uncertainty, a feature neither the MLR model nor a sofmax-based CNN can exhibit. Even if an uncertainty estimate were introduced (e.g. by using the full posterior, rather than the maximum a posteriori estimate [2] of the MLR weights $\mathbf{W}$ in Eq. (3), or through dropout in the CNN [6]), uncertainty estimates on the class probabilities will go to zero far away from class boundaries, this could cause the classifier to yield a very confident false result for a new point far way from the training data set.

While the stochastic optimisation approach to learning the induced points $\bar{\mathbf{X}}$ and optimising the GP hyper-parameters allows us to deal with large datasets, it comes with considerably longer training times compared to other sparse methods that use the full (smaller) data set during every iteration. However, this training is still very feasible, training our GPC model with M=25 induced points took less than 30 minutes on a quad-core 3.6 GHz desktop computer. Besides, all the training can be done offline, since once these parameters have been optimized, prediction amounts to calculating the mean and variance of the activation value $\mathbf{f}_*$ in $O(CM^2)$ [8], where C is the number of classes, and $M \ll N$ is the number of inducing points. Note that since we are using a sparse approximation rather than a full Gaussian process, we are able to "compress" the 24840 training points to only 25 induced points, significantly decreasing the computational load for prediction. Assuming feature extraction can be done sufficiently fast, the GP model gives the opportunity for significantly faster inference than to a similar CNN approach. To improve the performance of GPC in the context of bottom type segmentation, more investigation in optimizing the set of predictive features is warranted, e.g. fractal dimensionality of different length scales can be considered. Since bottom types tend to vary smoothly across space, spatial covariance could be taken into account in our model, although care has to be taken such that the covariance will not go to zero as spatial distance increases. To achieve this, the spatial covariance can be modelled with its own covariance function, such that sonar-based and space-based covariance are additive. Altering the covariance function itself could also improve performance, e.g. adding a white noise term, and using a Matérn kernel [14] instead of the squared exponential function Eq. (5), as the latter is considered by some to be too smooth for modelling physical data [16]. Taken together, Gaussian process classification is a promising statistical method for bottom type characterisation based on sonar imagery.

ACKNOWLEDGEMENTS

The author would like to thank the CMRE's ANMCM team for labelling the training dataset, and Thibaud Berthomier in particular for creating the software tool that made this possible.

REFERENCES

[1] F. Baralli, M. Couillard, J. Ortiz, and D. G. Caldwell. Gpu-based real-time synthetic aperture sonar processing on-board autonomous underwater vehicles. In *OCEANS-Bergen, 2013 MTS/IEEE*, pages 1–8. IEEE, 2013.

[2] C. M. Bishop. *Pattern recognition and machine learning*. springer, 2006.

[3] D. Carmichael, L. Linnett, S. Clarke, and B. Calder. Seabed classification through multifractal analysis of sidescan sonar imagery. *IEE Proceedings-Radar, Sonar and Navigation*, 143(3):140–148, 1996.

[4] M. Couillard, J. Groen, and W. L. Fox. Performance assessment of the muscle synthetic aperture sonar. In *Proceedings of Meetings on Acoustics ECUA2012*, volume 17, page 070102. ASA, 2012.

[5] A. Crawford and A. Skarke. Automatic detection of sand ripple features in sidescan sonar imagery. In *2014 Oceans - St. John's*, pages 1–5, 2014.

[6] Y. Gal and Z. Ghahramani. Dropout as a bayesian approximation: Representing model uncertainty in deep learning. In *international conference on machine learning*, pages 1050–1059, 2016.

[7] B. Gips, C. Strode, and S. Dugelay. Residual risk maps for performance assessment of autonomous mine countermeasures using synthetic aperture sonar. volume 40, pages 47–56. Institute of Acoustics, 2018.

[8] J. Hensman, A. Matthews, and Z. Ghahramani. Scalable variational gaussian process classification. 2015.

[9] D. P. Kingma and J. Ba. Adam: A method for stochastic optimization. *arXiv preprint arXiv:1412.6980*, 2014.

[10] D. Kohntopp, B. Lehmann, D. Kraus, and A. Birk. Seafloor classification for mine countermeasures operations using synthetic aperture sonar images. In *OCEANS 2017-Aberdeen*, pages 1–5. IEEE, 2017.

[11] A. G. d. G. Matthews. *Scalable Gaussian process inference using variational methods*. PhD thesis, University of Cambridge, 2017.

[12] D. G. Matthews, G. Alexander, M. Van Der Wilk, T. Nickson, K. Fujii, A. Boukouvalas, P. León-Villagrá, Z. Ghahramani, and J. Hensman. Gpflow: A gaussian process library using tensorflow. *The Journal of Machine Learning Research*, 18(1):1299–1304, 2017.

[13] H. Nickisch and C. E. Rasmussen. Approximations for binary gaussian process classification. *Journal of Machine Learning Research*, 9(Oct):2035–2078, 2008.

[14] C. Rasmussen and C. Williams. *Gaussian Processes for Machine Learning*. the MIT Press, 2006.

[15] E. Snelson and Z. Ghahramani. Sparse gaussian processes using pseudo-inputs. In *Advances in neural information processing systems*, pages 1257–1264, 2006.

[16] M. L. Stein. *Interpolation of Spatial Data: Some Theory for Kriging*. Springer Science & Business Media, 1999.

[17] D. P. Williams. Fast unsupervised seafloor characterization in sonar imagery using lacunarity. *IEEE transactions on Geoscience and Remote Sensing*, 53(11):6022–6034, 2015.

[18] D. P. Williams. The mondrian detection algorithm for sonar imagery. *IEEE Transactions on Geoscience and Remote Sensing*, 56(2):1091–1102, Feb 2018.

[19] D. P. Williams and E. Coiras. On sand ripple detection in synthetic aperture sonar imagery. In *Acoustics Speech and Signal Processing (ICASSP), 2010 IEEE International Conference on*, pages 1074–1077. IEEE, 2010.

TARGET CLASSIFICATION USING MULTI-VIEW SYNTHETIC APERTURE SONAR IMAGERY

Benoît d'Alès de Corbet, David P. Williams and Samantha Dugelay

Science and Technology Organization - Centre for Maritime Research and Experimentation
La Spezia, SP, ITALY

Benoît d'Alès de Corbet, STO-CMRE, Viale San Bartolomeo 400, 19126 La Spezia, email: benoit.dales@cmre.nato.int

Abstract: *Synthetic Aperture Sonar (SAS) can be used commonly in many different underwater applications such as mine countermeasures, habitat mapping and archeology. It offers high resolution images over wide swath areas. A single-view SAS image however may lack critical information for an object classification task (a mine hidden by a rock for example, or a partial image). Instead, multi-view images of the same scene could provide much richer information. In this context, Thales developed a sonar capable of processing three views under different angles simultaneously. CMRE and Thales have teamed up to investigate deep learning applications for multi-view. This paper demonstrates the potential benefits of such a technology in the matter of target classification. The data used for this study are real SAS data collected at sea trials by the MUSCLE. The preliminary work compares different ways of classifying with Convolutional Neural Network (CNN) architectures. Transfer learning is also performed from pre-trained models.*

Keywords: *synthetic aperture sonar, multi-view, convolutional neural network, classification.*

1. INTRODUCTION

Synthetic Aperture Sonar (SAS) is commonly used in underwater applications such as mine countermeasures [1], habitat mapping [2] and archeology [3]. The principle is based on the coherent combination of successive pings synthesized in a large array. Compared to real aperture, the technique delivers a much higher resolution independent of range and frequency. Indeed, it is able to image the seabed with centimeter resolution up to hundreds of meters range. To perform, the sensor needs to move at a constant speed following a known path. In the context of mine countermeasures, a SAS payload is embedded on an Autonomous Underwater Vehicle (AUV). This sensor platform has the particularity of incorporating an Automatic Target Recognition (ATR) system [4]. During missions, large quantities of data are collected and processed in order to detect a Region of Interest (ROI) and classify it. In recent years, Convolutional Neural Network (CNN) has led to very good performance on sonar image classification [5]. However, this stage is largely dependent on the image quality and on the view-angle of the object. Indeed, if the latter is hidden behind a rock, it could mislead the process. Consequently, the ATR system adjusts the AUV's mission path to revisit potential target locations. The method is nevertheless time-consuming and uncertain.

A new approach is proposed by Thales [6]. They built a sonar able to simultaneously capture three high-resolution views under different angles. This system provides a new way of classifying mines. Rather than a single-view, the classification stage can exploit much richer information, either about the mine-like object or its environment. With the great expertise of the CMRE in ATR, Thales and the Centre have teamed up to explore the possibilities in the matter of target classification.

In the present study, Section 2 describes the multi-view classification process, from the proposed CNN model architectures to data processing. Section 3 provides the analysis of the results and Section 4 finally concludes the study.

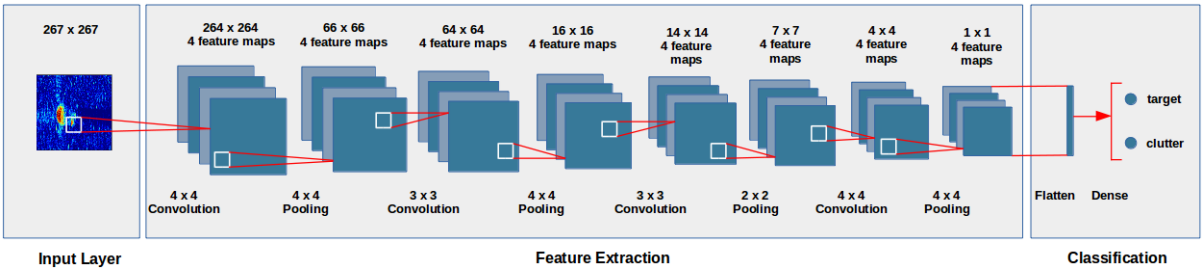
2. MULTI-VIEW CLASSIFICATION

2.1. Convolutional Neural Networks

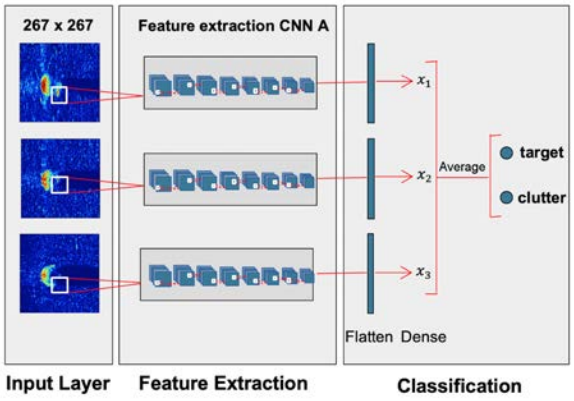
A CNN is a specific type of neural network which is specially used for image analysis. The CNN model architecture in Fig. 1a is used for the single-view classification (CNN A). It is taken from [7] where it has already proven its efficiency. It consists of a stack of convolutional and average pooling layers. On one hand, the convolutional layer applies a linear convolutional filter followed by a nonlinear activation function (ReLU). Thus, feature maps are generated from the input data. On the other hand, the pooling layer reduces the size of the image by only keeping the most important pixels. It distorts the image by losing the precise pixel positions. This helps to limit the risks of overfitting. After the feature extraction stage, the neural network finishes via a fully connected layer (also called dense layer). It combines all the specific characteristics detected by the previous layers and gives as result a binary prediction (i.e. clutter or target) with a sigmoid activation. This model serves as a basis for the building of our multi-view classifiers.

We propose two ways of classifying multi-view images. The first one consists in classifying each image independently with the previous model (CNN A). The resulting predictions are then averaged to give the final result. Let us call this model CNN B (*cf.* Fig. 1b).

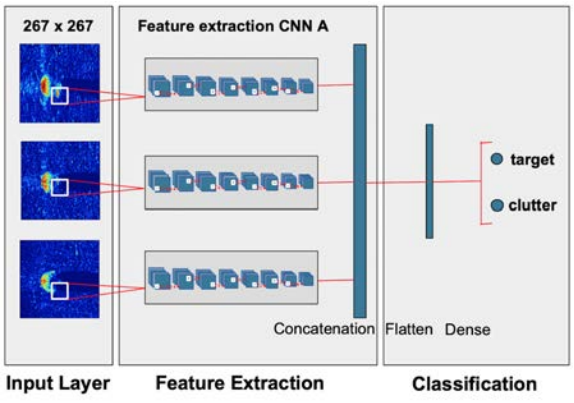
For the second one (*cf.* Fig. 1c), we have 3 inputs that follow the same feature extraction process on 3 independent branches. Then, the output branches are concatenated, just before the classification stage. Finally, the fully connected layer gives a prediction according to a sigmoid activation. Let us call this model CNN C.



(a) Single-view CNN architecture (CNN A)



(b) CNN architecture with averaged predictions (CNN B). x_1, x_2 and x_3 represent the prediction values of each image



(c) CNN architecture with the concatenation of the three branches (CNN C)

Fig. 1: CNN architectures

2.2. Datasets

Since 2007, CMRE has been conducting many sea trials. The Centre has collected a significant amount of SAS data with the SAS-equiped AUV called MUSCLE. We find there various seafloor compositions and mine-like objects with high-resolution imagery. The system has a center frequency of 300 kHz and a bandwidth of 60 kHz. It provides a resolution cell of 2.5 cm in the along-track dimension and 1.25 cm in the range dimension.

The training of the single-view CNN model in Fig. 1a is already performed with data from 8 expeditions conducted between 2008 and 2013 (*cf.* Table 1). Therefore, only weights resulting from the training are used. The data we have focuses on object detection from a specific trial conducted in 2014, in Italy. The detection process is achieved by the algorithm detailed in [8]. It delivers a rich database content such as muds, ripples, posidonias and various shapes of targets (symmetric and asymmetric). However, we do not use all the database. In order to build a multi-view dataset, only object detections with three different views are kept. It implies

that we are looking for the detections for which the AUV revisited the scene. The original dataset is consequently reduced. In addition, by grouping the three views together, the number of classifications is then divided by three. All images are labeled, either as clutter (class 0) or as target (class 1).

By building this multi-view dataset, we try to get closer to what the Thales sonar imagery could provide. However, we observe that the sonar from Thales processes SAS images under three fixed orientations. On our side, the angle view of the object is linked to the way the AUV revisits the scene. In order to deal with this important feature, we propose the following dataset (*cf.* Fig. 2). It consists in dividing the image wavenumber spectrum in three equal parts where each part corresponds to a view. The process is based on [9]. It allows to obtain three different orientations with a known deviation of a few degrees (approximately 5°). This generated dataset is denoted DS2.

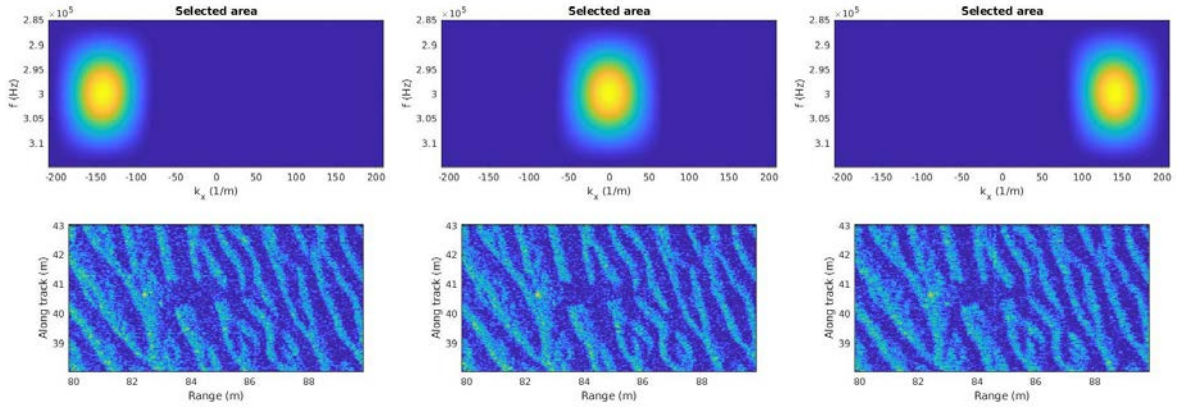


Fig. 2: Generated multi-view images

Table 1: SAS datasets

Sea trials	Type of dataset	Targets	Clutter
2008-2013 - Latvia, Italy, Spain	Single-view images	2912	29280
2014 - Italy	Multi-view images (DS1)	116×3	40×3
	Generated multi-view images (DS2)	348×3	120×3

Before input images are used by CNNs, a preprocessing stage is performed. The complex SAS images are first interpolated by converting pixels into squares covering 1.5 cm in each direction. Then, they are normalized so that pixel values fall between a fixed range, $[-1,1]$. The normalized image x'_{ij} is:

$$x'_{ij} = 2 \times \frac{\min\left(40,\ \max\left(0,\ x_{ij} - \frac{1}{N}\sum_{m,n} x_{mn}\right)\right)}{40} - 1, \tag{1}$$

where x_{ij} represent the unnormalized pixel values and N is the total number of pixels in the image.

Finally, the image is centered around the object highlight and cropped to an area of approximately 4.005 m $\times$ 4.005 m (corresponding to a size of 267 pixels $\times$ 267 pixels).

3. EXPERIMENTAL RESULTS

With these multi-view datasets (DS1 and DS2), we aim to experiment the benefits of the multi-view CNN architectures compare to the single-view CNN architecture. It is necessary for that to re-train CNN C, once with DS1 and once with DS2. The weights associated with the convolutional layers from the feature extraction stage in CNN A (*cf.* Fig. 1a) are kept for the three branches. After the concatenation of the independent branches, the parameters from the fully connected layer needs to be re-trained, according to both multi-view datasets (DS1 and DS2). Thus, we freeze weights from the feature extraction stage during the training. The other parameters are trained by minimizing the binary cross-entropy loss using back-propagation through RMSprop with a learning rate of 10^{-3}. One third of the respective datasets are used for the training. It represents a small amount of data but only 13 parameters have to be trained. Data augmentation is accomplished by randomly mixing the order of the input images in the 3 branches of the CNN model. To compare fairly the different datasets DS1 and DS2, the train-sets is based on the same original database imagery. The same applies for the test-sets.

In order to find out how accurate are the predictions, we use different performance metrics, such as precision, recall, F1-score and the Area Under the Curve (AUC). These measures are expressed below and the parameters are detailed in Table 2. As for the classification results, they are shown in Table 3.

Table 2: Definition of TP, FN, FP and TN

	Actual positive	Actual negative
Predicted positive	True Positive (TP)	False Positive (FP)
Predicted negative	False Negative (FN)	True Negative (TN)

On one hand, the precision metric is a ratio that shows us the correctly predicted targets to the total predicted targets. On the other hand, the recall metric is used as a ratio between the correctly predicted targets and the total true targets. Finally, F1-score is the harmonic mean of precision and recall.

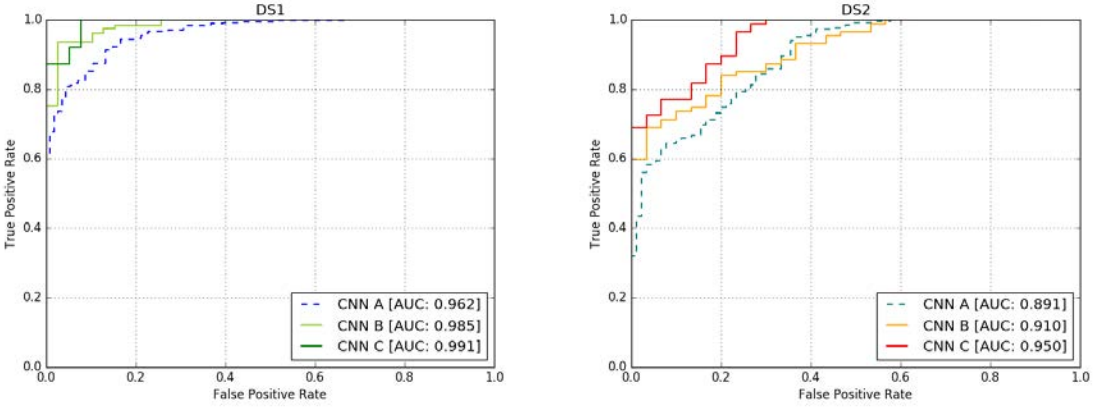
$$precision = \frac{TP}{TP+FP} \quad , \quad recall = \frac{TP}{TP+FN} \quad \text{and} \quad F_1 = 2 \times \frac{precision \times recall}{precision + recall}. \tag{2}$$

Table 3: Classification performance

Dataset	Model	Precision	Recall	F_1
DS1	CNN A	0.967	0.833	0.895
	CNN B	0.992	0.936	0.963
	CNN C	0.947	1	0.972
DS2	CNN A	0.919	0.736	0.817
	CNN B	0.942	0.747	0.833
	CNN C	0.95	0.874	0.91

Fig. 3 shows the Receiver Operating Characteristic (ROC) curves by plotting the probability of false alarm over the probability of detection, while threshold is varied. The calculated area under each curve is also indicated. With both datasets, CNN C delivers the most interesting

results. This can be explained by CNN B that does not take full advantages of the different object points of view. Because it averages predictions, it is not able to give more prominence to a specific image with valuable information. The drop in performance with the DS2 is justified because of its degraded resolution and because the feature extraction stage was pre-trained with orginal images. However, even with a small difference in orientation between images, the classification results of DS2 with CNN C demonstrated a much better performance than a single-view classification.



(a) CNNs performance with DS1 *(b) CNNs performance with DS2*

Fig. 3: Classification performance

4. CONCLUSION

In this preliminary work, we wanted to investigate the potential of multi-view SAS image classification. We described two ways to enhance SAS classifier performance. One independently classifies three images and averages the predictions. The other one fuses the data resulting from three independent feature extraction branches and delivers the prediction. We compared them with two types of multi-view dataset. The different classification tests showed very encouraging results. Fusing data at the end of the feature level demonstrated a significant gain in terms of performance. Indeed, it makes the best use of additional information given by the complementary views.

Future work will aim to enlarge our datasets by gathering more multi-view images. This would allow to reinforce the training of the last layer of CNN C. It could also allow to re-train the entire network for the generated dataset. Other types of CNN could also be explored and compared with those studied in this paper.

ACKNOWLEDGEMENT

This work was supported by the NATO STO Centre for Maritime Research and Experimentation (CMRE) and Thales. Data used in this paper were acquired by the CMRE with funding provided by the NATO's Allied Command Transformation (ACT). This manuscript has been approved for public release.

REFERENCES

[1] J. Groen, E. Coiras, J. Del Rio Vera, and B. Evans. Model-based sea mine classification with synthetic aperture sonar. *IET Radar, Sonar Navigation*, 4(1):62–73, February 2010.

[2] T. Thorsnes and L. R. Bjarnadóttir. Experiences from using autonomous underwater vehicles and synthetic aperture sonar for sediment and habitat mapping. *AGU Fall Meeting Abstracts*, 2017.

[3] Øyvind Ødegård, Roy E. Hansen, Hanumant Singh, and Thijs J. Maarleveld. Archaeological use of synthetic aperture sonar on deepwater wreck sites in skagerrak. *Journal of Archaeological Science*, 89:1 – 13, 2018.

[4] D. P. Williams, M. Couillard, and S. Dugelay. On human perception and automatic target recognition: Strategies for human-computer cooperation. In *2014 22nd International Conference on Pattern Recognition*, pages 4690–4695, August 2014.

[5] D. P. Williams. Underwater target classification in synthetic aperture sonar imagery using deep convolutional neural networks. In *2016 23rd International Conference on Pattern Recognition (ICPR)*, pages 2497–2502, December 2017.

[6] M. Chabah, N. Burlet, J.-P. Malkasse, G. Le Bihan, and B. Quellec. *SAMDIS: A New SAS Imaging System for AUV*, volume 6. Springer International Publishing, Cham, 2016.

[7] D. P. Williams, R. Hamon, and I. Gerg. On the benefit of multiple representations with convolutional neural networks for improved target classification using sonar data. In *Proceedings of the Underwater Acoustics Conference*, July 2019.

[8] D. P. Williams. Fast target detection in synthetic aperture sonar imagery: A new algorithm and large-scale performance analysis. *IEEE Journal of Oceanic Engineering*, 40(1):71–92, January 2015.

[9] D. P. Williams and A. J. Hunter. Multi-look processing of high-resolution sas data for improved target detection performance. In *2015 IEEE International Conference on Image Processing (ICIP)*, pages 153–157, September 2015.

THREATENING DEGREE ASSESSMENT METHOD OF SONAR TARGETS BASED ON MULTI-SOURCE INFORMATION FUSION

Bin Zhou[a,b], Xuejing Song[a,b], Qing Wang[a,b], Yuechao Chen[a,b]

[a]Science and Technology on Sonar Laboratory, Hangzhou, China
[b]Hangzhou Applied Acoustics Research Institute, Hangzhou, China

Bin Zhou
Pingfeng No.715, Liuxia Street, Xihu District, Hangzhou, Zhejiang Province, China
1986zhoubin@163.com

Abstract: *Multi-source information fusion can expand the detection range of a sonar system and improve the reliability and robustness of target recognition. To solve the problems of large transmission bandwidth, uncertain priori probability of target threatening degree discrimination, and inability to perform fusion processing within the framework of probability theory in the sonar target association using full spectrum feature information, a threatening degree assessment method for sonar targets based on multi-source information fusion is proposed in this paper. The method combines the target information output from low-frequency array, high-frequency array and non-acoustic sensor, to perform threatening degree assessment of low-frequency sonar target through multi-source information preprocessing, target track association, association information fusion and target classification. For target track association, an improved gray association algorithm is proposed, which can distinguish two different targets with the same track change trend but far away from each other. In the absence of a priori probability of threatening target discrimination, a multi-source information fusion method based on Dempster-Shafer evidence theory is proposed to solve the problem that probability theory cannot be effectively applied to information fusion processing, so as to eliminate non-threatening targets. Finally the Template matching technique is used to further improve the accuracy of target threatening degree assessment. The proposed method is verified by sea trial data of multi-source information, including low-frequency array data, high-frequency array data and automatic identification system(AIS) data. This work can meet the needs of low-frequency sonar target threatening degree assessment.*

Keywords: *sonar target detection, multi-source information fusion, threatening degree assessment method, Dempster-Shafer(D-S) evidence theory, template matching*

1. INTRODUCTION

Information fusion is a multi-level and multi-aspect processing procedure. It includes detection, correlation, combination and estimation of the multi-source data to improve the accuracy of state and identity estimation, and timely and complete evaluation of the importance of battlefield situation and threat[1-4]. In the field of sonar target detection, relative to single-array sonar, multi-dimensional (space, time) and multi-feature (frequency, electromagnetic) acoustic and non-acoustic sensor information fusion, can expand the detection range of sonar system, and improve the reliability and robustness of target recognition. The research of distributed and multi-base sonar detection technology is a hotspot in the field of sonar information fusion[5-6]. A single warship platform can also use the target information from different sonar arrays (bow array, flank array, towed line array, etc.) and non-acoustic systems (AIS, radar, magnetometer, etc.) installed on the platform for information fusion to evaluate the threatened targets. It can eliminate non-threatened targets and improve the efficiency of alert, and further improve the accuracy of target threatening degree assessment by combining Template matching technique. For the multi-source information fusion of single platform, the main processing flow includes: multi-source information pre-processing, target track correlation[8-9], and related information fusion. The existing processing methods have the following problems: (a) The pretreatment link lacks effective data collation and management methods for heterogeneous, sparse, granularity and other factors of multi-source information, (b) the amount of spectrum characteristic information required for target track association is too large to meet the engineering application conditions of real-time transmission[7], (c) The prior probability of threat target discrimination is uncertain, and it can't be fused under the framework of probability theory. [10-11], etc. Aiming at the above problems, this paper carries out relevant technical research, and forms a set of sonar target threat assessment method based on multi-source information fusion to meet the needs of low-frequency sonar target threatening degree assessment.

2. MULTI-SOURCE INFORMATION FUSION TECHNOLOGY BASED ON D-S EVIDENCE THEORY

The improved grey correlation method[12] is used to realize the correlation between the target of low-frequency array and the target of high-frequency and AIS target. Among AIS target, it is possible to find the corresponding associated low-frequency sonar target as a non-threatening target, and the probability of the non-threatening target can be roughly given by the correlation degree of the target. For example, when the target correlation degree is 1, the probability of judging a non-threatening target is also set to 1. The probability of judging a non-threatening target is not equal to 0, nor can it be simply set to 0.5 or any other parameter. This kind of uncertain estimation problem which can't give a prior probability can't be dealt with under the framework of probability theory. Aiming at this problem, this paper uses evidence theory to evaluate the non-threat degree. Evidence theory is a further extension of probability theory. It can map the hypothetical prior probability space to the hypothetical posterior probability space based on observation, overcome the disadvantage of requiring prior knowledge in the theory of absolute majority estimation, and use Dempster-Shafer synthesis formula to fuse multi-source information to obtain more accurate estimates.

The Multi-source information fusion method is validated by a sea trial data. The experiment lasts about 55 minutes. The multi-source input information includes the spatial energy spectrum of low-frequency array and high-frequency array and the target information of AIS. Firstly, the AIS target information is preprocessed and the final effective target data is

obtained as shown in Fig. 1. The horizontal axis is relative to the ship's azimuth (in the same azimuth coordinate system as the sonar output), and the vertical axis is time. There are 10 AIS targets, whose number has been marked in the figure. Then target tracking is carried out on the output space energy spectrum of low-frequency array and high-frequency array, and their target tracks are obtained, as shown in Fig. 2 (a), (b). Among them, there are 12 targets in low frequency array and 5 targets in high frequency array (including tugboat noise in this platform).

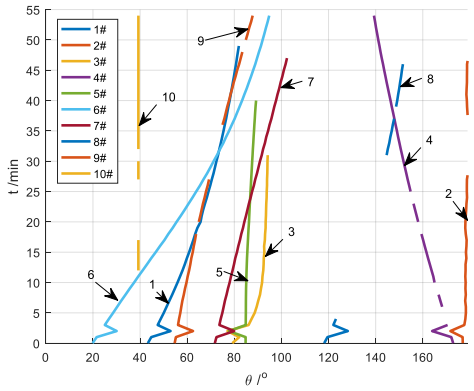
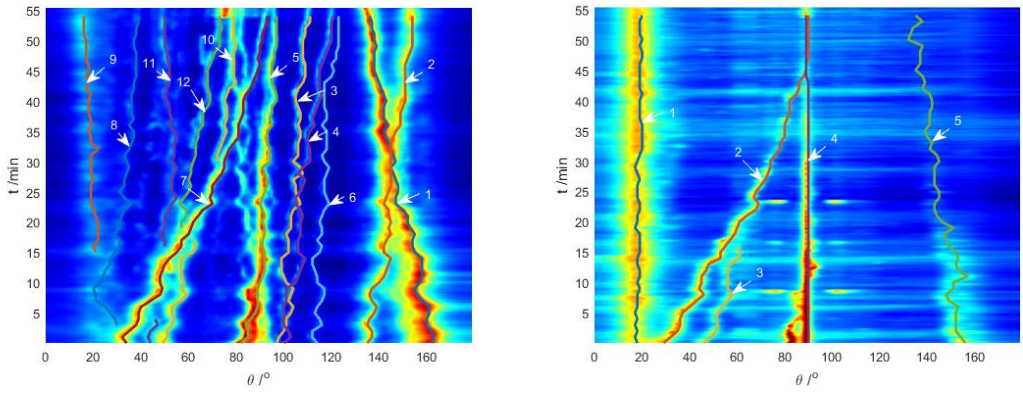


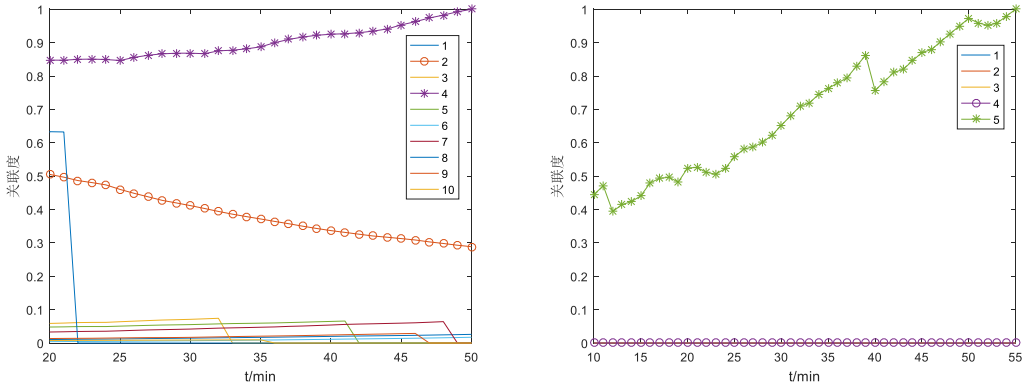
Fig.1: AIS target track.



（a） Low frequency sonar array *（b） High frequency sonar array*

Fig.2: Acoustical target track.

The improved grey correlation analysis method of target track is used to correlate the targets of low-frequency array and high-frequency array, and the targets of low-frequency array and AIS. Fig. 3 (a), (b) gives the normalized correlations of 1 # low-frequency array and all high-frequency array and AIS targets with time, respectively. It can be seen that 1 # target of low frequency array is strongly correlated with 4 # target of AIS and 5 # target of high frequency array.



(a) low frequency target and AIS targets (b) low frequency target and high frequency targets

Fig.3: Acoustical target track.

Then, multi-source information fusion technology based on D-S evidence theory is used to obtain the target non-threatening degree BPA value as shown in Table 1. Four non-threatening targets (5, 7, 9, 10) can be excluded. If all the low frequency targets are ranked according to the threatening degree, the 3#, 4#, 6#, 11#, 12# targets are in the forefront, so the subsequent target recognition can be mainly targeted at the 5 targets. Therefore, the non-threatening target is eliminated by the sonar target non-threatening degree assessment based on multi-source information fusion, which improves the alert efficiency.

Target Number	1#	2#	3#	4#	5#	6#	7#	8#	9#	10#	11#	12#
non-threatening degree	0.50	0.47	0	0	1	0	1	0.38	0.91	0.99	0	0

Table 1: List of non-threatening degree.

3. THREAT TARGET DISCRIMINATION TECHNOLOGY BASED ON TEMPLATE MATCHING

After eliminating non-threatening targets by multi-source information fusion method, the potential threatening targets are identified by Template matching technology. Firstly, input the beam-domain time-domain data of the tracking target, and accumulated a long time-domain signal, then analyzed the LOFAR spectrum. Then carried out Template matching by using the spectrum characteristics of threat targets in threat target template library. Finally, the evaluation results of target threat degree are given. Threat target discrimination technology processing flow based on Template matching is shown in Fig. 4.

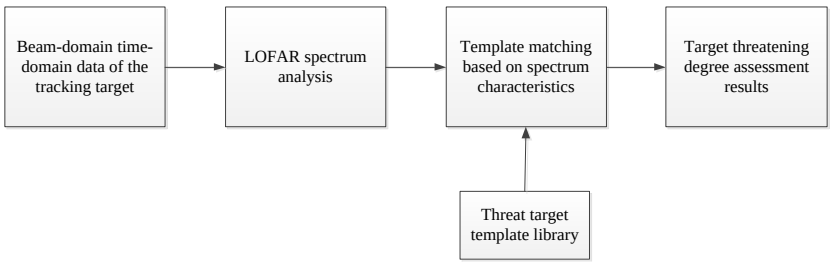


Fig.4: Flow chart of threat target discrimination technology based on template matching.

The results of the previous section of sea trial data processing are further analyzed to verify the threat target discrimination technology based on Template matching. Template matching is applied to the remaining targets after eliminating non-threatening targets. The target tracking single beam is divided into 150 samples, each sample for 0.3 minutes. The Template matching results are shown in Table 2. From the table, we can see that the low frequency target number 12 has the highest confidence. In fact, the 12# target in the sea trial is the simulated sound source of the threat target. The processing results are in accordance with the actual situation.

Target Number of low-frequency target	Total sample size	Distinguishing the number of threat targets	Distinguishing the Confidence of Threatened Targets
1	150	4	2.7%
2	150	0	0

3	150	0	0
4	150	10	6.7%
6	150	0	0
8	150	19	12.7%
11	150	24	16%
12	150	122	81.3%

Table 2: Results of Template matching.

4. CONCLUSIONS

In this paper, the target detected by low-frequency sonar array is taken as the target of threat elimination. Combining the target information output by high-frequency array and non-acoustic sensor, a threatening degree assessment method of sonar target based on multi-source information fusion is proposed. Using multi-source information fusion method based on Dempster-Shafer evidence theory, the credibility of non-threatening targets is given and non-threatening targets are eliminated. Combining with Template matching technology, potential threatening targets are identified to further improve the accuracy of target threat assessment. The method proposed in this paper is validated by sea trial data of low frequency array, high frequency array, AIS and other multi-source information. In this paper, the real-time processing of sea trial data has not been taken into account for the time being, so further related technical research will be carried out according to the actual engineering needs.

5. ACKNOWLEDGEMENTS

This study was founded by Young Elite Scientists Sponsorship Program by CAST(Grant No. 2017QNRC001) and the National Natural Science Foundation of China[Grant No. 61701450].

REFERENCES

[1] **Han Chongzhao, Zhu Hongyan, Duan Zhansheng**, *Multi-source Information Fusion*, Tsinghua University Press, 2010.
[2] **He You, Wang Guohong, Peng Yingyu, et al**, *Multisensor Information Fusion and Application* , Electronics industry Press, 2000.
[3] **Raffaele G, Parastoo A, Hassan G, et al,** Multi-sensor fusion in body sensor networks: state-of-the-art and research challenges, *Information Fusion*, 35, pp. 68-80, 2017.
[4] **Reda B, Didier C, Thanh-Long N, et al,** Multi-sensor information fusion: combination of fuzzy systems and evidence theory approaches in color recognition for the NAO humanoid robot, *Robotics and Autonomous Systems*, 100, pp. 302-316, 2018.
[5] **Sun Wei, Ge Yi-zhou, Yuan Yu-ting, et al,** Distributed Detection Fusion Used on Passive SonoBuoy, *Communication Countermeasures*, 35(3), pp. 23-27, 2016.
[6] **Lv Lin,** Multi-base sonar warfare in future anti-submarine warfare, *Electronic world*, 4, pp. 109-111, 2018.
[7] **Sergios Theodoridis, Konstantinos Koutroumbas,** *Pattern Recognition*, Academic Press, 2008.
[8] **Sun Qichen, Guo Weizhen, Yan Qianqian, et al,** A Multi-target Tracking Algorithm Based on Grey Relational Analysis, *Ludong University Journal*, 33(1), pp. 20-25, 2017.
[9] **Sun Wei, Shang Jintao, Zhu Kun,** A New Multi-targets Fusion Association Algorithms, *Acoustics and Electronic Engineering*, 123(3), pp. 1-3, 2016.

[10] **Wang Jie-gui, Luo Jing-qing,** Passive Tracking Based on Data Association with Information Fusion of Multi-Feature and Multi-Target, *Acta Electronica Sinica*, 32(6), pp. 1013-1016, 2004.

[11] **Kang Jian, Li Yi-bing, Lin Yun, et al,** Joint Probability Data Association Algorithm Based on Evidence Theory, *Systems Engineering and Electronics*, 35(8), pp. 1620- 1626, 2013.

[12] **Zhou Bin, Wangqing, Quan Hengheng,** Non-Threatening Degree Assessment Method of Sonar Targets Based on Multi-Source Information Fusion, *Journal of Unmanned Undersea Systems*, 26(5), pp. 439-443, 2018.

Structured Session 5
Underwater Communications and Networking

Organiser(s): Tsimenidis Charalampos, Mitchell Paul, Pelekanakis konstantinos

ROBUST DIGITAL SELF-INTERFERENCE CANCELLATION FOR FULL-DUPLEX UWA SYSTEMS: LAKE EXPERIMENTS

Lu Shen, Benjamin Henson, Yuriy Zakharov, Paul Mitchell

Department of Electronic Engineering, University of York, YO10 5DD, UK

Lu Shen, Department of Electronic Engineering, University of York, YO10 5DD, UK
Email: ls1215@york.ac.uk

Abstract: *Full-duplex (FD) underwater acoustic (UWA) communication has significant potential in increasing the capacity of acoustic links, but it suffers from severe self-interference (SI) caused by the near-end transmission. Existing SI cancellation techniques include analogue cancellation, digital cancellation and antenna beamforming. Among those techniques, the digital cancellation has the lowest complexity. However, the reported digital SI cancellation performance is limited. To improve performance, the non-linearity of the power amplifier (PA) should be taken into account. Here we use the digitized PA output as the reference signal for SI estimation to reduce the effect of the non-linear distortion. Such a system architecture allows us to use a low-complexity linear adaptive filter for SI cancellation. Specifically, we use the recursive least-squares (RLS) algorithm with dichotomous coordinate descent (DCD) iterations. This results in a low-complexity SI canceller. As observed from the experimental results with traditional single-branch digital canceller, the choice of the sampling time is crucial to the SI cancellation performance. In this paper, we present a robust digital SI cancellation scheme based on the RLS-DCD algorithm with the use of the PA output. To achieve robust SI cancellation performance, the PA output is oversampled to twice the symbol rate, de-multiplexed into two branches employing digital SI cancellation, and then combined based on the residual variance estimates in the two branches. The SI cancellation performance is investigated by conducting experiments in an indoor water tank and in a shallow lake. The tank experiments show that up to 66 dB of SI can be cancelled using the proposed scheme, which is high compared to existing FD designs. Meanwhile, up to 56 dB of SI is cancelled in the lake experiments. The difference in the SI cancellation performance is due to faster varying SI channels in the lake experiments. Both the water tank and lake experimental results show robust SI cancellation performance regardless of the choice of sampling time.*

Keywords: *Digital cancellation, full-duplex, field experiments, self-interference cancellation, underwater acoustic communication*

1. INTRODUCTION

Acoustic waves are the best candidate for long-range underwater communications [1]. However, the attenuation of acoustic waves is approximately proportional to the square of the frequency, which makes the available bandwidth for underwater acoustic (UWA) communications extremely limited [2] [3]. Furthermore, the usable frequency range of acoustic transducers and limited bandwidth (<1 kHz) for long-range communication (>1 km) impose additional constraints on the available frequency resources [2] [4]. To increase the capacity of acoustic links, we consider full-duplex (FD) UWA communications, when the transceiver simultaneously transmits and receives in the same frequency bandwidth. With FD operation, it is possible to increase the channel capacity [5] [6]. The major obstacle of FD communication is the strong self-interference (SI) introduced by the near-end transmission [7] [8] . For long-distance UWA communication with high transmission power, the SI can be millions of times stronger than the far-end desired signal.

Existing SI cancellation techniques for FD terrestrial radio communications include analogue cancellation, digital cancellation and antenna beamforming [8] [9] [10]. For terrestrial radio designs, a combination of analogue and digital cancellation is normally used to avoid saturation of the analogue-to-digital converter (ADC). For FD UWA systems, the low signal frequency allows the use of high resolution ADCs (e.g., 24 bits). In such a case, we intend to achieve a high level of SI cancellation in the digital domain. The major factor which affects the performance of digital cancellation is the non-linear distortion introduced by the power amplifier (PA). Existing designs [9] [10] deal with the PA non-linearity by using the Volterra series [11] and its extensions to model the nonlinear SI channel, which are of high complexity. We adopt a low-complexity digital canceller design by using the PA output as the reference signal [12]. In this case, a linear digital canceller can be sufficient, since the non-linear distortion introduced by the PA is incorporated in the reference signal. Specifically, the digital canceller is implemented using a low-complexity recursive least-squares (RLS) adaptive filter with dichotomous coordinate descent (DCD) iterations [13] [14].

From our investigation, another important issue which affects the performance of the digital canceller is the choice of the sampling time. When the sampling time is not properly chosen, the SI cancellation performance degrades significantly (see Fig. 2). To ensure robust cancellation performance, the PA output is sampled at two shifted sampling times. In that case, we obtain two time-shifted copies of the baseband PA output and these are used as the reference signal to perform digital cancellation on two branches independently. The two residual signals are then combined with weight coefficients, computed based on the residual variance estimates. The general idea of the combining scheme is to ensure that the combined residual signal is at the same level as in the branch with better cancellation performance.

The SI cancellation performance is investigated by conducting experiments in an indoor water tank and in a shallow lake. The tank experiments show that up to 66 dB of SI could be cancelled with the proposed digital canceller. Meanwhile, up to 56 dB of SI is cancelled in the lake experiments. The difference in the cancellation performance can be attributed to faster time-variation of the SI channel in the lake, which could be further improved by combining digital cancellation with other approaches, such as adaptive beamforming.

2. SYSTEM MODEL

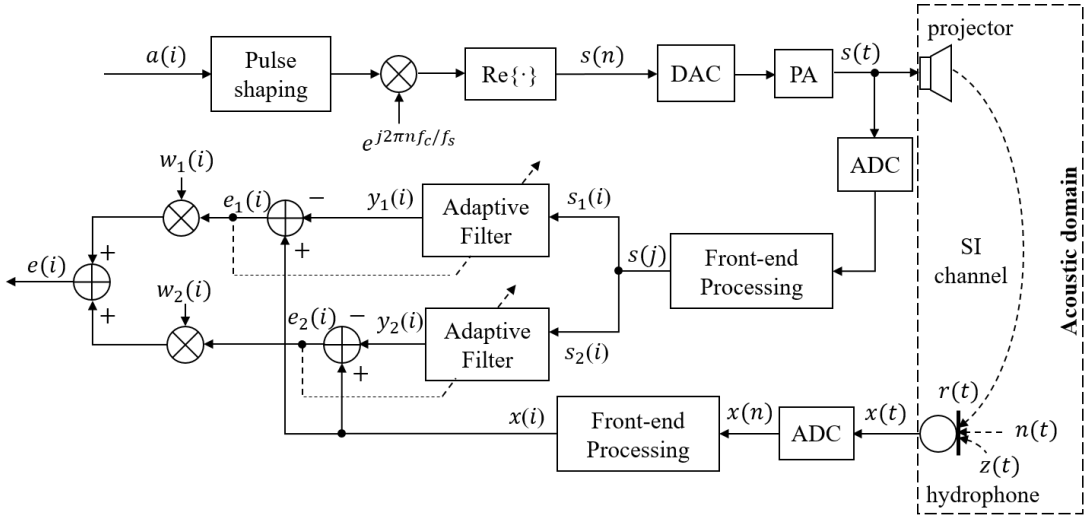


Fig.1: Block diagram of the FD UWA system. The sample index with sampling rate f_s, symbol rate f_d and $2f_d$ are denoted by n, i and j, respectively.

The block diagram of the FD UWA system with digital cancellation is shown in Fig. 1. We transmit a pseudo-random sequence of BPSK data symbols $a(i)$. The symbol rate is f_d. The BPSK data is up-sampled to a high sampling frequency f_s by a pulse-shaping filter, modulated to the carrier frequency f_c. The passband signal $s(n)$ is digital-to-analogue converted, amplified in a PA and emitted by an acoustic projector. The received signal $x(t)$ at the near-end hydrophone includes the SI signal $r(t)$, ambient noise $n(t)$ and far-end signal $z(t)$.

For SI channel estimation, we use the RLS-DCD adaptive filter, which is chosen for its low-complexity, fast convergence and numerical stability (see details in [13] [14]). The residual signal is computed by subtracting the adaptive filter output from the received signal. The adaptive filter works at the symbol rate to reduce the computational complexity and to avoid the ill-condition problem of the narrowband regressor [15].

We use the baseband equivalent received signal $x(i)$ as the desired signal for both adaptive filters. To obtain the baseband equivalent signal, the digitalized received signal $x(n)$ is demodulated to the baseband, low-pass filtered and decimated to f_d (in the front-end processing block). A pair of root-raised cosine (RRC) filters are used for pulse shaping and low-pass filtering.

From our observation, the sampling time is crucial for the SI cancellation performance. In Fig. 2, we show the mean-squared error (MSE) performance of a single branch with different choice of sampling time. We consider 4×96 different sampling time instants within 4 symbol intervals (4 ms), where each symbol contains 96 samples. It can be seen that the MSE performance is sensitive to the sampling time within one symbol duration. As high as 40 dB difference in the MSE performance can be observed. Similar phenomenon is also reported in [16] regarding the equalizer performance in a band-limited channel. To ensure robust MSE performance, the digitalized PA output $s(j)$ is oversampled to twice the symbol rate ($2f_d$). The digital samples of $s(j)$ are de-multiplexed into two branches. The signal $s_1(i)$ in the first branch contain odd samples, while $s_2(i)$ in the second branch contain even samples. $s_1(i)$ and $s_2(i)$ are used as the regressors of the two adaptive filters in the first and second branch, respectively. Note that the sampling delay shift between two branches is half a symbol duration. In that case, we can ensure that good cancellation performance can be achieved with at least one of the branches according to Fig. 2.

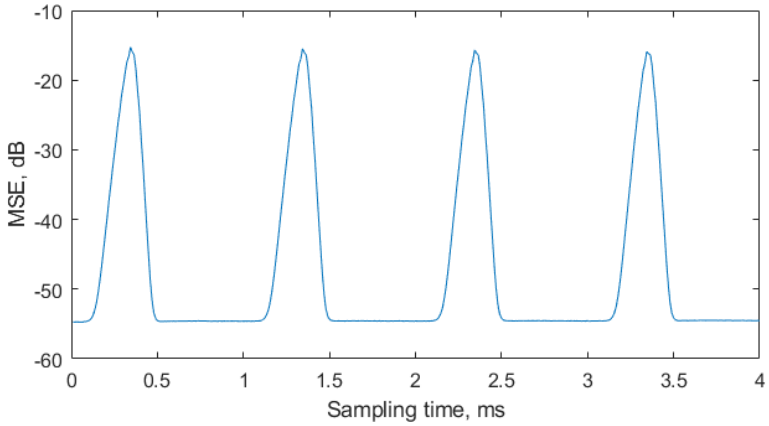


Fig.2: MSE performance with different sampling time using lake experimental data.

After digital cancellation, the residual signals $e_1(i)$ and $e_2(i)$ are combined with different weight coefficients which are computed based on the residual variance estimates in the two branches. The variance on the kth branch ($k = 1, 2$) at the ith time instant is estimated by:

$$\sigma_k^2(i) = \alpha\sigma_k^2(i-1) + (1-\alpha)|e_k(i)|^2, \tag{1}$$

where α is a forgetting factor. The weight coefficients $w_k(i)$ are then computed by:

$$w_k(i) = \frac{1}{\sigma_k^2(i)} \Big/ \left(\frac{1}{\sigma_1^2(i)} + \frac{1}{\sigma_2^2(i)}\right), \qquad k = 1, 2. \tag{2}$$

According to the combining scheme, a small weight coefficient is applied to the branch with high variance (residual signal power), and a large weight coefficient is applied to the branch with high level of SI cancellation. As the sum of the weights equals to one, the level of the received signal is not changed after combining. With this approach, robust SI cancellation performance can be achieved at any sampling time.

3. EXPERIMENTAL RESULTS

In this section, we investigate the SI cancellation performance in the water tank and lake experiments. The tank experiments are conducted in a 38cm×119cm×42cm indoor water tank. During the experiments, the projector [17] and hydrophone [18] are clamped by a retort stand, separated by 4cm and submerged underwater as shown in Fig. 3.



Fig.3: Configuration of the water tank experiments.

We transmit BPSK data with a sampling frequency of $f_s = 96$ kHz and a carrier frequency of $f_c = 12$ kHz. The frequency bandwidth is $F_d = 1$ kHz. The RRC filter we use has a roll-off factor of 0.2 and a filter length of 14 symbols duration (14 ms). A Hanning window is applied to the RRC filter taps to achieve higher attenuation at the passband. The transmitted signal length is 15 s, which includes 5 s of zero padding at the beginning of the signal. This silence period is used to measure the background noise level. Here we use the steady-state normalized MSE (NMSE) level as the indicator for the cancellation performance. The NMSE level at the kth branch ($k = 1, 2$) is computed by:

$$\text{NMSE}(i) = \frac{P_e}{P_x} = \frac{|e_k(i)|^2}{P_x}, \tag{3}$$

where $P_x = \sum_{i=0}^{N-1} |x(i)|^2 / N$ is the average power of the desired signal of the adaptive filter, N is the length of the desired signal, P_e is the instantaneous power of the residual signal $e_k(i)$. The NMSE level after combining is computed by:

$$\text{NMSE}(i) = \frac{P_{e_c}}{P_x} = \frac{|e(i)|^2}{P_x}, \tag{3}$$

where P_{e_c} is the instantaneous power of the combined residual signal $e(i)$. The steady-state NMSE is computed by averaging the NMSE over the last five seconds of the signal.

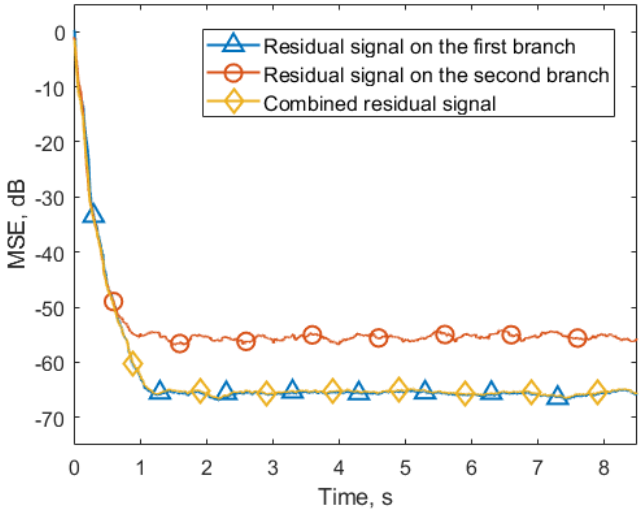


Fig. 4: Averaged NMSE performance in the tank experiment.

Fig. 4 shows the NMSE performance in the tank experiment. The NMSE curve is smoothed by averaging the instantaneous NMSE over a period of 0.3 s to provide a clearer view. The length of the adaptive filter is $L = 100$ (about 100 ms), which is long enough to capture the SI channel delay spread. The forgetting factor is $\lambda = 0.995$. The parameters of the DCD iterations are chosen as follows: the number of bits representing the impulse response $M_b = 16$, and the number of DCD updates $N_u = 4$. The forgetting factor used for the variance estimation is $\alpha = 0.95$. For the first branch, the steady-state NMSE is around -66 dB, while in the second branch the NMSE level is about 10 dB higher than in the first branch. As can be seen in Fig. 4, the NMSE level of the combined residual signal is approximately the same as that in the first branch after combining the signals in the two branches, showing the effectiveness of the combining scheme.

To evaluate the SI cancellation performance in a more practical scenario, lake experiments were conducted. The experimental site is shown in Fig. 5. In the lake experiments, the projector and the hydrophone are placed at a depth of 0.5 m, the distance between them is 3 cm (see Fig. 6).

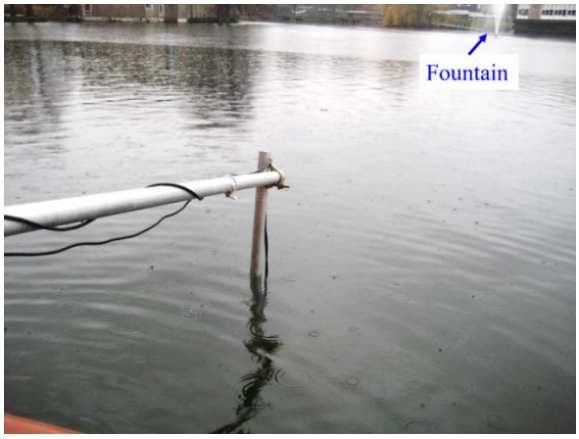


Fig. 5: Experimental site for the lake experiments.

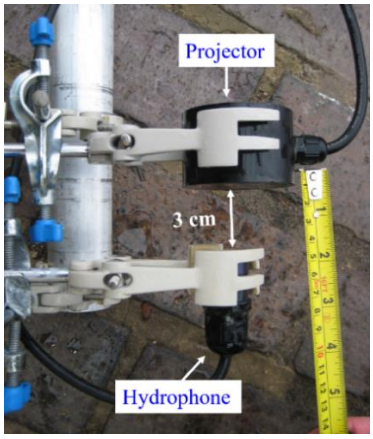


Fig. 6: Experimental setup

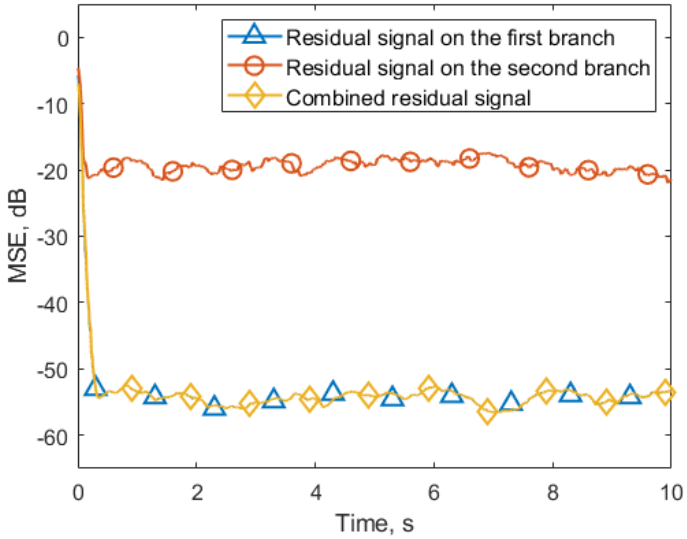


Fig. 7: Averaged NMSE performance in the lake experiment.

The NMSE performance in the lake experiment is shown in Fig. 7. The NMSE curve is smoothed by averaging the instantaneous NMSE over a period of 0.5 s. The averaging time window used here is longer compared to that of the tank experiment (0.3 s). This is due to the larger fluctuations in the MSE curve, which are caused by faster time-variation of the SI channel in the lake. We use an adaptive filter length of $L = 60$, and a forgetting factor $\lambda = 0.985$. As less number of reflections are received in the lake, a shorter filter length is used. For the DCD iterations, the number of bits representing the impulse response $M_b = 16$, and the number of DCD updates $N_u = 4$. The forgetting factor used for the residual variance estimate is $\alpha = 0.9$. It can be seen that the steady-state NMSE in the first branch is around -54 dB. For the second branch, the NMSE performance is significantly worse. After combining, the NMSE level of the combined residual signal is at the same level as that of the first (better) branch.

Note that for both the tank and lake experiments, the RLS-DCD algorithm achieves the same steady-state NMSE level as the classical RLS algorithm, but with significantly lower

complexity. The experimental results in the water tank and lake experiments demonstrate that robust and high level SI cancellation can be achieved with the proposed digital cancellation scheme regardless of the sampling time. The lower level of SI cancellation achieved in the lake experiments can be explained by faster SI channel variation in the lake experiments attributed by several environmental factors, including the time-varying lake surface. Another factor which limits the cancellation performance in the experiments could be the potential non-linear distortion introduced by the projector and the hydrophone, which is not being cancelled by the linear digital canceller [19].

4. CONCLUSION

In this paper, we investigate the SI cancellation performance of the proposed digital cancellation scheme in both water tank and lake experiments. The digital canceller is implemented using the low-complexity RLS-DCD adaptive filter with the PA output used as the reference signal for the SI channel estimation. The PA output is oversampled by two and de-multiplexed into two branches. The digital canceller is applied in each branch. The residual signals after digital cancellation are combined with different weights based on the residual variance estimate on two branches. This de-multiplexing and combining scheme is used to deal with the sensitivity of the SI cancellation performance to the sampling time. As demonstrated by the experimental results, effective and robust SI cancellation is achieved with the proposed digital cancellation scheme.

5. ACKNOWLEDGEMENTS

The work of B. Henson, Y. Zakharov and P. Mitchell was supported in part by the U.K. EPSRC through Grants EP/P017975/1 and EP/R003297/1.

REFERENCES

[1] **M. Stojanovic**, "Underwater acoustic communications," in *IEEE Electro International. Professional Program Proceeding*, 1995.

[2] **I. F. Akyildiz, D. Pompili and T. Melodia**, "Underwater acoustic sensor networks: Research challenges," *Ad Hoc Networks,* vol. 3, pp. 257-279, 2005.

[3] **T. H. Eggen, A. B. Baggeroer and J. C. Preisig**, "Communication over Doppler spread channels. Part I: Channel and receiver presentation," *IEEE Journal of Oceanic Engineering,* vol. 25, pp. 62-71, 2000.

[4] **M. Stojanovic and J. Preisig**, "Underwater acoustic communication channels: Propagation models and statistical characterization," *IEEE communications magazine,* vol. 47, pp. 84-89, 2009.

[5] **G. Qiao, S. Gan, S. Liu, L. Ma and Z. Sun**, "Digital Self-Interference Cancellation for Asynchronous In-Band Full-Duplex Underwater Acoustic Communication," *Sensors,* vol. 18, pp. 1700-1716, 2018.

[6] **G. Qiao, S. Liu, Z. Sun and F. Zhou**, "Full-duplex, multi-user and parameter reconfigurable underwater acoustic communication modem," in *MTS/IEEE Oceans*, 2013.

[7] **D. W. Bliss, P. A. Parker and A. R. Margetts**, "Simultaneous transmission and reception for improved wireless network performance," in *IEEE Workshop on Statistical Signal Processing*, 2007.

[8] **J. I. Choi, M. Jain, K. Srinivasan, P. Levis and S. Katti**, "Achieving single channel, Full duplex wireless communication," in *International Conference on Mobile Computing and Networking*, 2010.

[9] **D. Bharadia, E. McMilin and S. Katti**, "Full duplex radios," in *ACM SIGCOMM Computer Communication Review*, 2013.

[10] **D. Korpi, Y. S. Choi, T. Huusari, L. Anttila, S. Talwar and M. Valkama**, "Adaptive nonlinear digital self-interference cancellation for mobile inband full-duplex radio: Algorithms and RF measurements," in *IEEE Global Communications Conference*, 2015.

[11] **A. Zhu and T. J. Brazil**, "Behavioral modeling of RF power amplifiers based on pruned Volterra series," *IEEE Microwave and Wireless Components Letters,* vol. 14, pp. 563--565, 2004.

[12] **L. Shen, B. Henson, Y. Zakharov and P. Mitchell**, "Digital self-interference cancellation for underwater acoustic systems," *IEEE Transactions on Circuits and Systems II: Express Briefs,* 2019, In Press.

[13] **Y. V. Zakharov, G. P. White and J. Liu**, "Low-complexity RLS algorithms using dichotomous coordinate descent iterations," *IEEE Transactions on Signal Processing,* vol. 56, pp. 3150-3161, 2008.

[14] **J. Liu, Y. V. Zakharov and B. Weaver**, "Architecture and FPGA design of dichotomous coordinate descent algorithms," *IEEE Transactions on Circuits and Systems I: Regular Papers,* vol. 56, pp. 2425-2438, 2009.

[15] **S. S. Haykin**, Adaptive Filter Theory, Prentice Hall, 2002.

[16] **J. G. Proakis and M. Salehi**, Digital Communications, McGraw-Hill, 2008.

[17] "Low frequency underwater transducer," [Online]. Available: https://www.benthowave.com/products/BII-7530lowfrequencytransducer.html. [Accessed 29 March 2019].

[18] "Low Noise Broadband Hydrophone," [Online]. Available: https://www.benthowave.com/products/BII-7010Hydrophone.html. [Accessed 29 March 2019].

[19] **J. Butler and C. Sherman**, Transducers and Arrays for Underwater Sound, Springer International Publishing, 2016.

FULL-DUPLEX CHANNEL ANALYSIS FOR UNDERWATER ACOUSTIC COMMUNICATIONS

Cornelius Healy[a], Bilal Jebur[b], Charalampos Tsimenidis[a], Jeff Neasham[a], Jonathon Chambers[c]

[a] School of Engineering, Newcastle University, Newcastle upon Tyne, UK
[b] College of Electronics Engineering, Ninevah University, Mosul, Iraq
[c] Department of Engineering, University of Leicester, Leicester, UK

Cornelius Healy, School of Engineering, Newcastle University, Newcastle upon Tyne, UK, cornelius.healy@newcastle.ac.uk

Abstract: *The limited bandwidth available in underwater acoustic communication channels motivate the investigation of multiple access methods that maximize the capacity, such as full-duplex (FD) operation that can approximately double capacity. This paper presents characterization results of the self-interference (SI) channel from experimental data obtained by sea trials in the North Sea. Two scenarios are considered, i.e. hard and soft sea bottom with water column depths of 50 m. Initial results indicate that the delay spread of the local reverberation can extend up to 1.5 s before it reaches the noise floor level. This in turn has significant implications on the required hardware complexity of the SI mitigation methods based on adaptive filter echo cancellation, which will require tens of thousands of filter taps to deal with this delay spread range and prolonged training periods. Furthermore, the achievable range of the FD-based communication links will be affected by the levels of SI present in these channels, therefore, the results and channel modelling presented in this paper will be useful to FD modem designers.*

Keywords: *Underwater acoustic communication, In-band full-duplex communication, Acoustic measurements.*

INTRODUCTION

The potential to theoretically double the system throughput makes FD mode operation attractive in the severely impaired underwater acoustic channels. However, the close proximity of the concurrently active transducer and hydrophone will inevitably lead to large scale SI, relative to the desired distant signal. To realise a practical FD system, it will therefore be necessary to develop mitigation strategies to deal with the SI, both in the analog and digital domains. Development of these strategies will rely on accurate characterisation of the SI channel for real-world scenarios, to understand the behaviour and duration of the reverberations of the channel.

While FD communications has seen a great deal of interest in both wired and wireless radio frequency domains, significant work is still required on its application in underwater acoustic communications systems. The work in [1] presented early results on the feasibility of FD operation in underwater acoustic networking, with further developments on multi-user scenarios appearing in [2]. Hybrid SI interference suppression and cancellation techniques were considered in [3] for an OFDM system. In [4], an adaptive iterative scheme is proposed to deal with SI from the local channel along with inter-symbol interference. A recent work proposes novel MAC protocols for FD underwater acoustic networks [5]. Also recently published, the work in [6] considers the particular challenges of SI channel estimation in the FD underwater acoustic system and proposes a maximum likelihood based SI channel estimation algorithm with sparsity constraint. Most recently, the work in [7] proposes a digital-domain SI canceller which reconstructs the SI signal through use of the local transmit power amplifier (PA) output in a low-complexity adaptive filtering algorithm, improving the performance of the canceller by taking into account the nonlinearities introduced in the PA.

In this work, experimental measurements for the SI channel in a FD underwater acoustic communications system are presented. The characteristics of the channel are analysed and a simple model is proposed. This is key to understanding the challenges in developing techniques for a practical underwater acoustic system capable of FD operation. The rest of the paper is organised as follows: In Section 2, the details of the sea trial experiments are provided. Section 3 contains the channel measurements and related discussions, while Section 4 presents the proposed simplified channel model and demonstrates that it characterises the SI channel profile. Section 5 offers brief concluding remarks.

EXPERIMENTAL SETUP

Channel measurements were carried out in late August of 2018 in the North Sea at shallow water locations with depth approximately 50 m at two locations, with hard and soft sea bottoms. Fig. 1 provides the specification of the experiment, with the physical setup given in Fig. 1(a) outlining the channel geometry and defining a number of terms which will be used in later sections of the paper, and Fig. 1(b) provides the format of the transmitted signal used throughout the experiment, comprised of repeated Linear Frequency Modulated (LFM) chirp signals of increasing duration, followed by a number of pseudo-random binary sequences (PRSB) consisting of Binary Phase Shift Keying (BPSK) symbols modulated by m-Sequences of increasing chip length. The chirp signals had duration 0.1 s, 0.5 s and 1 s, respectively, while the PRSB signals used m-Sequences with chip length 2047, 4095 and 8191, respectively. The transmitted signals were separated by sufficiently large spacing to ensure that the reverberation effects of the channel could be observed.

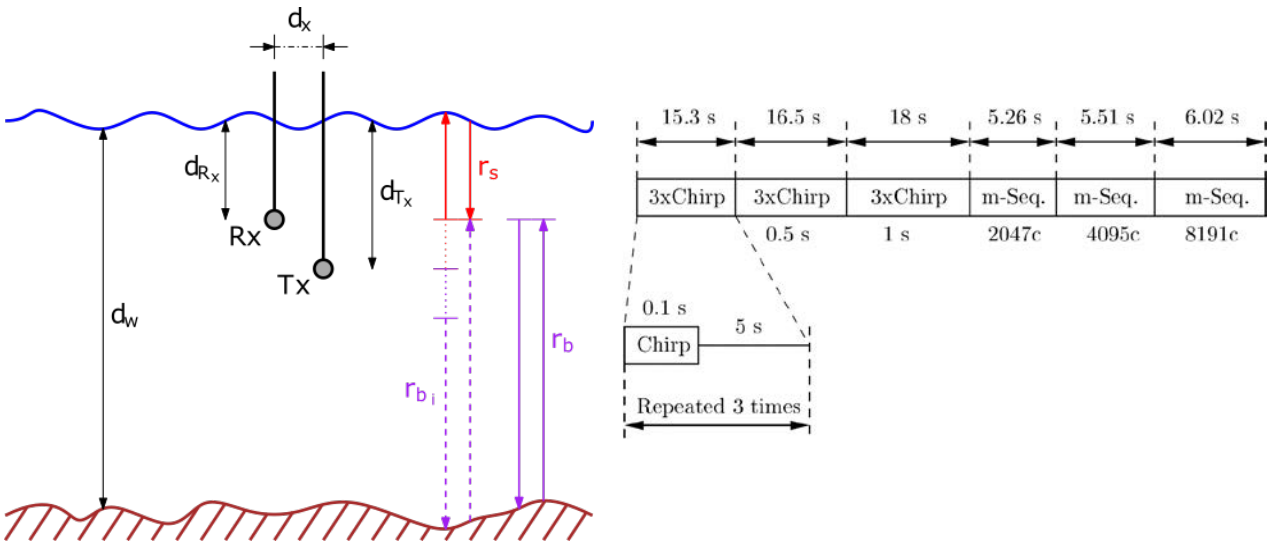


Fig. 1: Experimental setup (a) Channel geometry and (b) Signal format.

In the experiments, the receiver depth d_{Rx} was fixed for all measurements, while a number of different settings of transmitter depth d_{Tx} were taken. Two distinct settings of horizontal separation between transducer and hydrophone, d_x, were investigated, namely 0 m (no separation) and 1.2 m. As stated, the sea depth d_w was approximately 50 m throughout the experiment. For all measurements reported in this paper, the transducer and hydrophone were taken to be omni-directional, and no additional efforts were made to attenuate the signal between the transducer and hydrophone by means of absorbing material or baffle, so the presented measurements may be considered to constitute a worst-case scenario in terms of the SI reverberations. In future work the use of such physical SI suppression techniques will be considered.

Table 1 provides further details of the experimental parameters for the measurements presented in this work. Particularly notable are the transmitter depths for which the measurements were taken, and that during the experiment locations with both hard and soft sea bottom were encountered.

Parameter	Value
Centre Freq., BW	12 kHz, 8 kHz
Sampling Freq.	48 kHz
Source Level	170 dB
Signals	LFM Chirp / PRSB
R_x depth	5 m
T_x depth	6 m / 10 m / 15 m
Sea Bottom	Hard / Soft

Table 1: Experiment parameters.

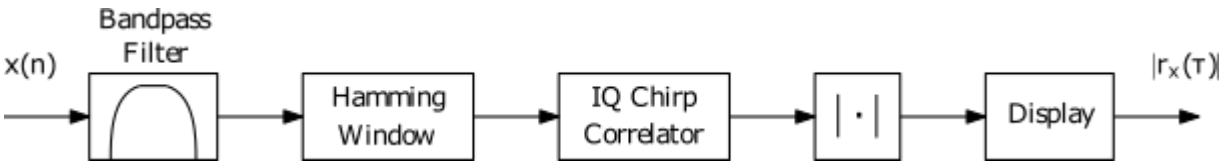


Fig. 2: Correlation processing chain on the measured SI signal.

CHANNEL MEASUREMENTS

In this section the measurements for the SI channel are presented, for a particular example of channel geometry and signal composition, as described in Fig. 1 and Table 1. In particular, the receiver depth was 5 m, transmitter depth 15 m, the sea bottom was soft and there was no separation between transmitter and receiver. The sea depth was approximately 52 m.

The correlation processing performed on the received SI signal from the channel is outlined in Fig. 2 for the LFM chirp signal. First, a band-pass filter is applied to the signal to remove observed noise contributions in the 18-20kHz range. Following this, a Hamming Window is applied to the signal, followed by the correlation operation and the magnitude of the output is used to produce the CIR plots shown in Fig. 3(a).

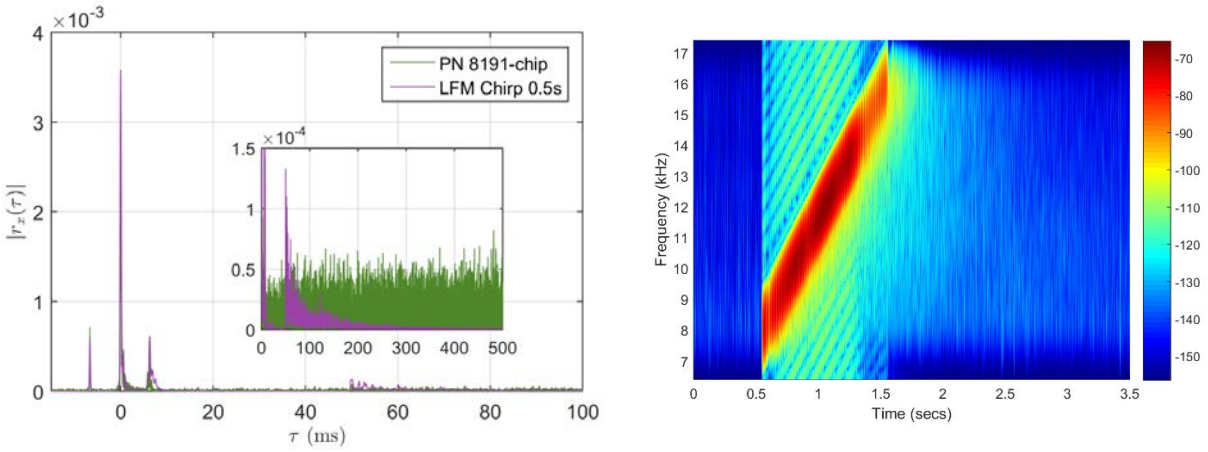


Fig. 3: Channel measurements (a) CIR for both chirp and PRBS and (b) Spectrogram.

In Fig. 3(a), two views of the produced CIRs are given. In the outer plot the shorter time scale view demonstrates the successful peaks corresponding to the direct path from transducer to hydrophone at zero delay, the first reflection from the sea surface after approximately 6.1 ms, and the first reflection from the sea bottom after approximately 50.2 ms. These values are consistent with the known geometry of the channel in Fig. 1(a) for speed of sound in water of approximately 1500 m/s. The outer plot demonstrates that both LFM chirp and PRBS signals can successfully extract these features from the signal. However, the larger time and smaller magnitude scale views shown in the inner plot demonstrate that the large side lobes of the m-Sequence autocorrelation obscure the finer details of the reverberation. Thus, for the following section, the LFM chirp signals will be the sole focus. A final note is needed on the peak which appears prior to the direct path peak. This peak is consistently observed throughout the recordings, and is believed to result from electromagnetic coupling. In Fig. 3(b), the spectrogram of a received signal for a 1 s LFM chirp is provided. This gives a clear visual demonstration of the long reverberations in the SI channel, which can be seen to extend well beyond one second. This will prove a significant challenge in implementing practical systems.

SIMPLE CHANNEL MODEL

In this section the simplified model for the SI channel is presented. Taking the well-known transmission loss model for acoustic waves in sea water, and accounting for non-ideal reflection losses at the sea bottom, a simple expression for the channel impulse response of the SI channel is proposed, and comparisons with the measured response of the channel demonstrate that the reverberations of the SI channel are characterised well.

Transmission and reflection loss for the SI channel may be expressed in terms of range r as

$$TRL(r) = TL(r) + n(r)\, RL\,, \tag{1}$$

where the transmission loss in sea water, *TL(r)*, is given by

$$TL(r) = A + \xi \log_{10}(r) + \alpha(f) r\,, \tag{2}$$

and the loss for each reflection from the sea bottom is

$$RL = 20 \log_{10}(\beta)\,, \tag{3}$$

where β is the reflection coefficient, and is taken here to be 0.96. The term $n(r)$ in (1) accounts for the number of sea bottom reflections undergone by the acoustic wave after it has propagated range r can be found according to

$$n(r) = k + \left\lfloor \frac{r}{2\, d_w} \right\rfloor, \tag{4}$$

where the operator $\lfloor\, x \,\rfloor$ denotes the largest integer smaller than x, and the term k is 0 for the acoustic waves which initially propagated in the upward direction, and 1 for those waves initially propagating downward.

From the geometry shown in Fig. 1, following the arrival of the acoustic wave taking the direct path from transducer to hydrophone, distinct arrivals occur for two sets of wave fronts, those initially propagating upwards and downwards, respectively. For the upward wave, in the notation of Fig. 1, arrivals will occur after the wave has travelled ranges

$$r = \{\, r_s\,, (r_s + r_b)\,, (2\, r_s + r_b)\,, 2(r_s + r_b)\,, (3\, r_s + 2\, r_b)\,, \ldots \}, \tag{5}$$

with each additional term occurring after an additional surface or bottom reflection. Likewise, for the initially downward propagating wave front, distinct arrivals after the direct path peak occur for ranges

$$\begin{aligned} r = \{\, & r_{b_i}\,, (r_{b_i} + r_s)\,, (r_{b_i} + r_s + r_b)\,, (r_{b_i} + 2\, r_s + r_b)\,, \\ & (r_{b_i} + 2\, r_s + 2\, r_b)\,, (r_{b_i} + 3\, r_s + 2\, r_b)\,, \ldots \}. \end{aligned} \tag{6}$$

The above equations, along with the frequency-dependent attenuation factor and related terms below comprise a simple model for the SI channel reverberations, assuming lossless reflection at the sea surface and in the absence of small-scale diffusion effects. Nevertheless, the comparison between this model and the measured channel CIR in Fig. 4 demonstrates that this simple model captures the large-scale behaviour of the reverberations quite well.

In (2), the term A combines the attenuation effects of transducer and hydrophone in the plane of transmission/reception, the term ξ is the spreading factor, $\xi = 15$ for practical spreading, and $\alpha(f)$ is the frequency-dependent attenuation factor for transmission in sea water, given by [8]

$$\alpha(f) = a f^2 + \frac{b f_0}{1 + \left(\frac{f_0}{f}\right)^2} + \frac{c f_1}{1 + \left(\frac{f_1}{f}\right)^2}, \tag{7}$$

$$a = 1.3 \times 10^{-7} + 2.1 \times 10^{-10} (T - 38)^2$$
$$b = 2S \times 10^{-5} \qquad c = 1.2 \times 10^{-4} \tag{8}$$
$$f_0 = 50 (T + 1) \qquad f_1 = 10 \frac{T - 4}{100}$$

The model described in (1)-(4) is presented in Fig. 4(a), which compares the transmission loss only case to that with both transmission and reflection losses. Fig. 4(b) demonstrates the fit achieved to the measured SI channel CIR, for the hard (HB) and soft (SB) sea bottom scenarios with transducer at 15 m and hydrophone at 5 m and no horizontal separation (d_x=0). The inner plot demonstrates that the transmission loss alone is sufficient in the short delay scale with the updated model of (1) not having a large effect. In the outer plot, the transmission loss only model deviates significantly at large delay for both scenarios. The proposed model better describes the observed CIR at the long delay range by taking into account the loss in reflection, with a very close match to the behaviour observed for the hard bottom, showing a small gap in the medium delay range for the soft bottom scenario.

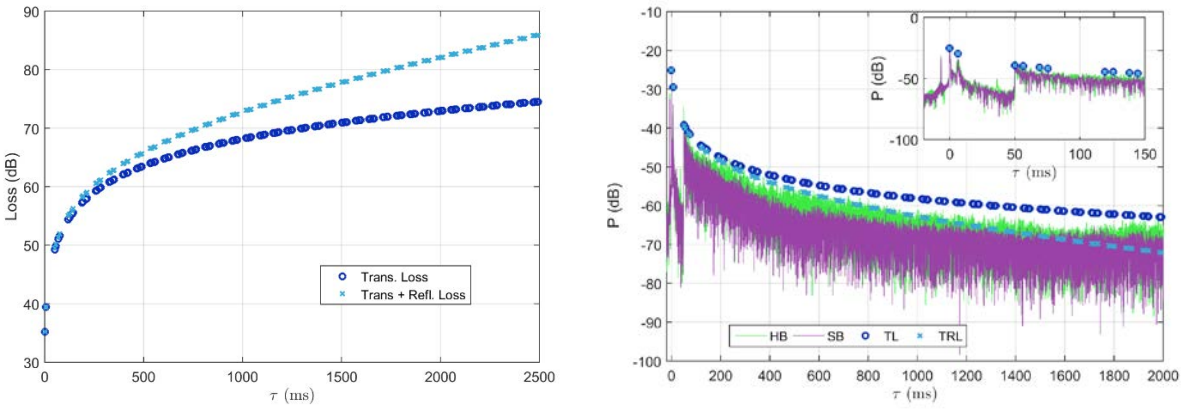


Fig. 4: Channel model (a) Transmission/reflection loss model and (b) Fit to the observed CIR.

CONCLUSIONS

In this paper the measurements for the SI channel in a FD system were presented for a number of shallow water scenarios. It was demonstrated through the use of CIRs and the received signal spectrogram that the reverberations in the SI channel persist for beyond 1 s in shallow water environments. A simple model was then introduced to characterise the taps of the SI channel CIR by taking into account sea water transmission loss and losses in reflection at the sea bottom. The model was demonstrated to accurately describe the behaviour of the SI

channel. The results presented will inform future work on development of SI suppression and cancellation techniques for practical systems.

ACKNOWLEDGEMENTS

This work was supported by the EPSRC under project EP/R002665/1, Full-Duplex for Underwater Acoustic Communications. The authors would like to thank the Research Council for this funding.

REFERENCES

[1] **G. G. Xie, J. H. Gibson, and K. Bektas**, Evaluating the feasibility of establishing full-duplex underwater acoustic channels, In *Proc. of the Third Annual Mediterranean Ad Hoc Networking Workshop*, 2004.
[2] **G. Qiao, S. Liu, Z. Sun, F. Zhou**, Full-duplex, multi-user and parameter reconfigurable underwater acoustic communication modem, In *OCEANS 2013 – San Diego*, 2013.
[3] **L. Li, A. Song, L. J. Cimini, X.-G. Xia and C.-C. Shen**, Interference cancellation in in-band full-duplex underwater acoustic systems, In *OCEANS 2015 - Washington*, 2015.
[4] **J. Tian, S. Yan, L. Xu and J. Xi**, A time-reversal based digital cancelation scheme for in-band full-duplex underwater acoustic systems, In *OCEANS 2016 - Shanghai*, 2016.
[5] **F. Qu, H. Yang, G. Yu and L. Yang**, In-band full-duplex communications for underwater acoustic networks, *IEEE Network*, volume (32), pp. 59-65, 2017.
[6] **G. Qiao, S. Gan, S. Liu and Q. Song**, Self-interference channel estimation algorithm based on maximum-likelihood estimator in in-band full-duplex underwater acoustic communication system, *IEEE Access*, volume (6), pp. 62324-62334, 2018.
[7] **L. Shen, B. Henson, Y. Zakharov and P. Mitchell**, Digital self-interference cancellation for full-duplex underwater acoustic systems, *IEEE Trans. Circuits and Systems II: Express Briefs*, pp. 1-1, 2019.
[8] **R. Coates**, Underwater acoustic systems, *Macmillan new electronic series, Macmillan, 1990.*

A Parallel Decoding Approach for Mitigating Near-Far Problems in Underwater Acoustic Communications Networks

Yuehai Zhou, Feng Tong, and Roee Diamant

***Abstract*—A limiting factor of communication networks is the so-called near-far effect, where transmissions from a node (near) close to a common receiver blocks transmissions of a farther node (far). Due to the high power attenuation in the underwater acoustic channel, near-far is common in underwater acoustic communication networks (UWANs), and the phenomena occurs even for a rate of 1/2 between the distances of the near and far nodes to the receiver. In this paper, we offer a novel interference cancellation (IC) approach for handling such interference by decoding the "near" signal and the "far" one in parallel, thereby improving detection for both signals. Simulation results show that, compared to the traditional decision feedback equalizer, our approach gains 12 dB in the output SNR of the jammed source and 4 dB in the output SNR of the jamming source.**

***Index Terms*—Underwater acoustic communications, near-far, interference cancellation, compresive sensing**

I. Introduction

With the boost of underwater acoustic communication (UAC) capabilities, multitude of applications started using this technologies. Among these, are settings involved multiple transmitting nodes such as for oceanographic data collection, communication between autonomous submerged vehicles, and group of scuba divers performing subsea maintenance [1]. A common challenge in these applications is how to deal with joint interferences from signals received simultaneously by a common receiver. Since the bandwidth in UAC is highly limited, the data rate is extremely low, and reception is mostly performed omni-diretional (i.e., no directivity is applied in reception), interfering signals cause collisions and loss of data.

In this paper, we focus on the so-called *near-far* problem, where colliding packets may be resolved for a source located close to the receiver, but for the farther node, the signal-to-interference ratio (SIR) is high. Here, the closer source is often called the *jamming* node while the farther node is called the *jammed* node. In UAC, due to the high dependency of the power attenuation in range both for propagation loss and absorption loss, the near-far problem exists even for range ratio of half between the jamming-receiver range and the jammed-receiver range.

While in some cases, near-far situations cause diversity and thus can be viewed as a network resource to assist network operations [2], [3], commonly, this phenomena is regarded as a source of interference that should be resolved either in the MAC layer or in the Physical layer of the communications stack. In the context of MAC scheduling, the near-far problem is viewed as a source for secondary conflicts [4], for which the network should avoid in the first place. The solution thus involves identifying a near-far scenario as part of the process of topology-discovery. In [5] near-far situations are identified by non-symmetric components in the network topology matrix, which basically mean that there is a jammed node in the network. In [6] near-far collisions are identified by the common receiver based on parts of the signals that do not collide. This approach is practical since, due to the long propagation delay in UAC, there is a very low chance for completely overlapping receptions. In [7] expected near-far collisions are identified prior to transmissions based on acoustic propagation models, assuming location knowledge of the nodes. Once a near-far is identified, the scheduling solution is altered by setting proper constraints for the selected transmission schedule such that the jamming and jammed nodes avoid transmitting together [8], or the near node is instructed to adjust its power to avoid the jamming altogether [9].

In the context of the Physical layer, near-far situations are solved through filtering. The most common is the noise-canceling filter, where the strong signal is first resolved and then removed from the received signal to allow the decoding of the jammed signal. To that end, a synthetic version of the resolved strong signal is used as a reference, which passes through a filter and is then subtracted from the received signal. The filter adapts by minimizing the output of the noise cancellation filter [10]. For UAC, in [11] this approach has been extended to direct the adaptive filter to identify only the strong signal, thereby reducing the effect on the jammed signal. Multiuser interference suppression has also been applied in the context of equalization, where interferences are treated as residuals from the channel estimation process [12], by iteratively resolving inter-block interferences [13], or by means of interference alignments [14]. In all these cases, the decoding is performed sequentially under the assumption that the jamming signal can be correctly resolved. While this be true in some cases, mostly the near-far situation is not conclusive, meaning that the jamming signal is also being interfered.

Different than current approaches that perform the interference cancellation (IC) sequentially, our approach performs the decoding on parallel. This not just offers benefit in terms of

Yuehai Zhou and Roee Diamant are with the Hatter Department of Marine Technology, University of Haifa, Haifa 3498838, Israel; Feng Tong is with the Key Laboratory of Underwater Acoustic Communication and Marine Information Technology of the Ministry of Education, Xiamen University, Xiamen, Fujian 361005, China.

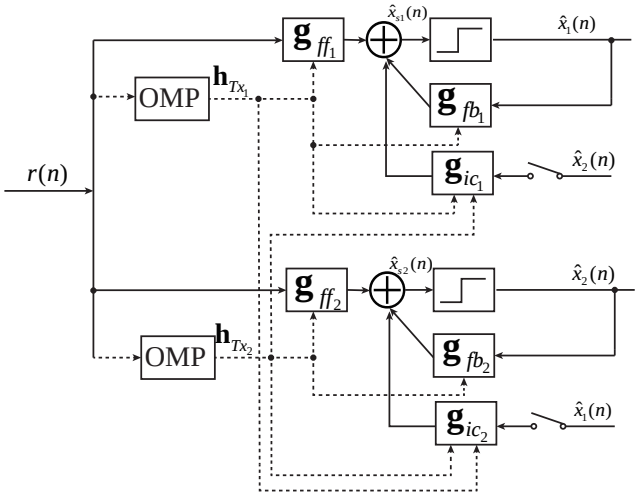


Fig. 1: The IC DFE scheme.

latency, but also allows better decoding of the near signal. Our method works by combining the IC operation within the decoding process of the two source-decoding branches in the framework of a decision feedback equalization (DFE). The IC operation exploits the spatial sparsity between the two near-receiver and far-receiver channels through a compressed sensing algorithm. Inside the source-decoding branch, this allows enhancing channel estimates with common delays, thus coming from the desired transmitter, and to suppress channel taps with different delays assumed coming from the other transmitter. In particular, the cancellation is performed in parallel to the feedback filter and by sharing the outputs of the feedback filter. The forward process adds positive channel taps to the support set of the equalizer, while the backward process removes those designated to the interference.

Our contribution is in the design of an IC-based approach for resolving the near-far problem for cases where the emissions of the near source are also affected by those of the far source. We analyze the performance of our algorithm in numerical simulations and demonstrate its practicality for a realistic sea environment in a designated sea experiment. Compared to the traditional DFE, the results show that our proposed method obtains higher output SNR.

II. The Joint IC method

We demonstrate our IC approach in the framework of a decision feedback equalizer (DFE). To facilitate simultaneous decoding of both the jammer and jammed signals, we execute two DFE branches in parallel. Yet, assuming the jammer-receiver and the jammed-receiver links are significantly different, each DFE is fed by its own channel estimator. For the later, we use the orthogonal matching pursuit (OMP) algorithm [15]. We use the OMP due to its compressed sensing application, which is specifically suitable for the case of two colliding signals that needs to be separated.

In essence, the IC operation is similar to the removal of residual channel estimation noises in the DFE scheme. Hence, as illustrated in Fig. 1, we operate the IC in parallel to the feedback filter of each DFE branch. Similar to the feedback filter, the IC draws its input from the symbol's hard decision. However, different than the feedback filter, this decision is taken from the second DFE branch. As a result, the IC is set to remove residuals of noises from the other channel. To that end, we note that such removal is possible only upon existence of an interference. In other words, only when there is in fact a hard decision output from the second DFE branch. We illustrate this operation in Fig. 1 by the switch at the entrance to the IC. This switch comes to combat the practical case of partial colliding between communication packets.

Much like the feedback filter, the IC is an adaptive filter. The IC filter is designed to mitigate interference from a different source. As such, referring to Fig. 1, the parameters of the filter are set by the estimated channel from the other DFE branch (the OMP block). Yet, since the IC for channel j is operated after the feed-forward filter of channel j, which in turn is set by the channel equalization for channel j, also channel j should be considered to set the parameters of IC i.

III. Simulation Results

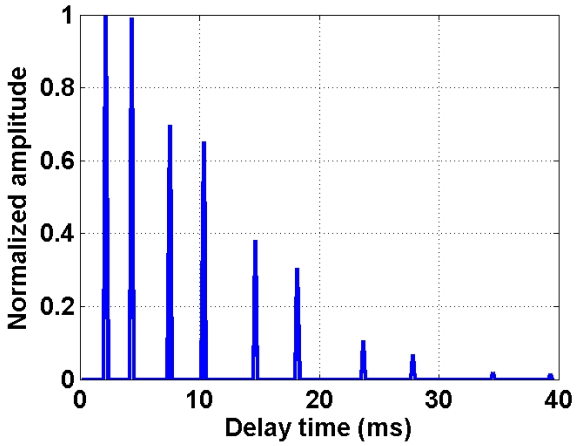
In this section, we describe results of our parallel IC approach in numerical simulation.

A. Setup

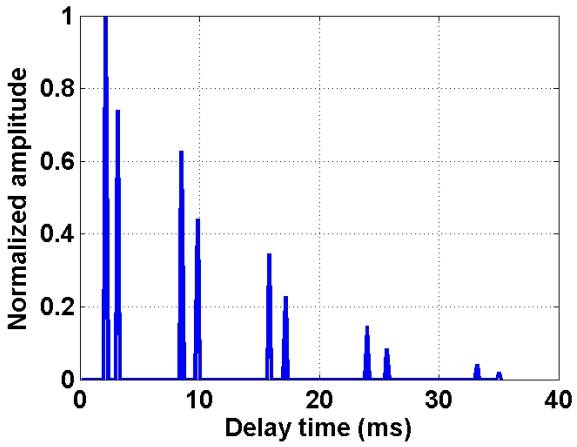
Our setup includes three nodes, a receiver array which contains four receiving elements and two transmitters. For each Monte-Carlo simulation run, the location of one of the transmitters is fixed at 1000 m from the receiver, while the location of the second transmitter is chosen uniformly randomly such that its range from the receiver is between 2000 m and 100 m. The depth of the 4 receiving elements is 4 m, 8 m, 12 m, and 16 m, respectively, the depth of the transmitters is fixed at 8 m. The two sources transmit equal packets of 134320 bits within the same frequency band and the same symbol rate at 6000 symbols/s. The packets are scheduled such that overlapping always occur.

To generate the propagation delay and channel impulse response for the jamming-receiver and jammed-receiver links, we use the Bellhop ray-tracing software package [16]. A flat ocean is assumed with a constant sound speed profile at 1500 m/s and a constant water depth of 20 m. For each location setup, the transmitted signals are convoluted with the corresponding channel, while for the latter we pick the 10 most dominant rays. An example for two such channels is shown in Fig. 2 for two transmitters located 1000 m and 500 m from the common receiver. In this example, the delay spread is roughly 40 ms, and a typical sparse nature is observed.

To benchmark our scheme, we use two channel estimation based decision feedback equalizers (DFE). The first, denoted as *DFE-IC*, removes interference, while the second, denoted as *DFE-NIC*, does not. In both cases, channel equalization



(a)



(b)

Fig. 2: Example of two simulated channels. Upper panel: 500 m range, 8 m depth. Lower panel: 1000 m range, 16 m depth.

is based on the OMP algorithm and a designated training sequence.

B. Results

To measure performance, we use the output signal-to-noise ratio (SNR) metric. The output SNR is measured at the input of the decision-making block and is defined by

$$\rho = \frac{\|\mathbf{x}\|_2^2}{\|\mathbf{x} - \bar{\mathbf{x}}\|_2^2} \,, \tag{1}$$

where $\boldsymbol{x}$ is the transmitted symbols, and $\bar{\boldsymbol{x}}$ is the soft output from the receiver. The range vs. output SNR is shown in Fig. 3 for the *fixed* node at 1000 m range and for the *varied* node. As expected, when the varied node is closer, it obtained higher output SNR since it experiences less interference from the fixed source. Similarly, high output SNR is measured for the signal obtained from the fixed transmitter when the varied transmitter is far. Comparing the DFE-IC and DFE-NIC schemes, we observe that higher output SNR is obtained by the former.

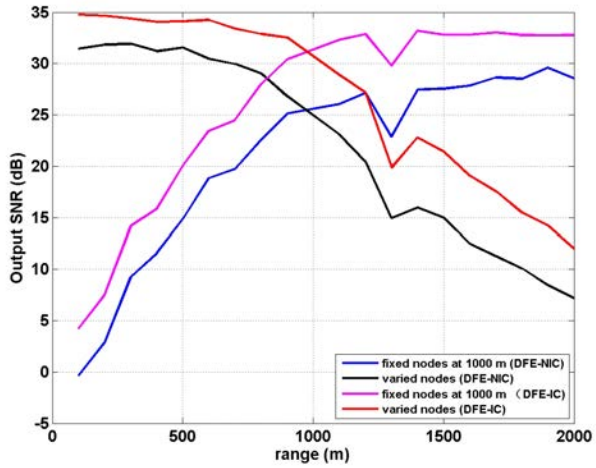


Fig. 3: Output SNR as a function of range of the varied source. SNR=30 dB.

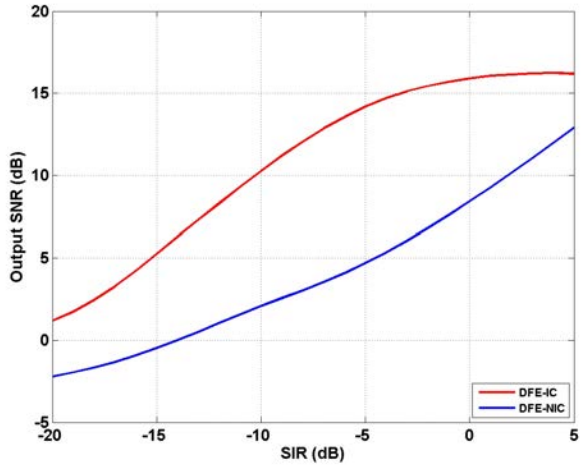


Fig. 4: SIR vs. Output SNR. SNR=30 dB.

Another measure of interest is the signal-to-interference ratio (SIR), defined by

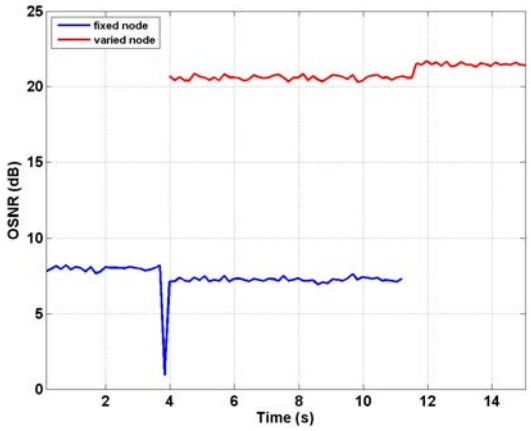
$$\rho = \frac{\|\boldsymbol{s}\|_2^2}{\|\boldsymbol{r}\|_2^2} \,, \tag{2}$$

where $\boldsymbol{s}$ is the desired signal, and $\boldsymbol{r}$ is the interfering signal. In Fig. 4, we show the SIR as a function of the output SNR in the training mode. Here, the signal from the transmitter at the 1000 m range is considered the desired signal, while the signal from the varied node, this time at 500 m from the receiver, is the interefering one. For a fair comparison, the two channels are normalized. We observe that output SNR increases with the SIR. This is because, the less interference the better the decoding process. In this respect, we observe a gap of 3 dB in favour of DFE-IC.

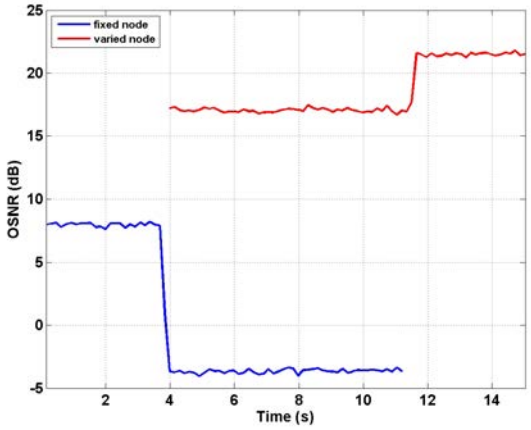
Another interesting performance exploration is the behaviour of the decoder for the practical case where the two signals do not collide perfectly. In this case, if the time of interference-free channel is identified well, a valid approach would be to operate DFE-IC at times when interference exists, and use DFE-NIC when the channel is interference-free. Adopting this approach, Fig. 5 shows the output SNR for the case where only signals from the fixed node arrive at the first 4 s of reception; collision occurs between time 4 s and 11.2 s; and then only signals from the varied node exist. The upper panel shows the results of the combine scheme, while the lower panel shows the results for only DFE-NIC. Looking at the results in Fig. 5b, we observe that when a collision occurs, the output SNR for DFE-NIC drops by roughly 13 dB for the jammed (far) source and by 5 dB for the jamming (near) source. However, in Fig. 5a, when IC is used, a reduction of only 1 dB is observed for the jammed and jamming sources. That is, the gain obtained is 12 dB for the jammed source, and 4 dB for the jamming source.

IV. Conclusions

In this paper, we considered the problem of near-far in the setting of an underwater acoustic communication sensor network, where packets from a near source collide with that of a far source. Different than common approaches that assume perfect decoding of the jamming signal and thus perform interference cancellation (IC) sequentially, our approach is based on a parallel decoding of the near and far signals. This approach holds the benefits of lower latency, but more importantly, as we showed in numerical simulations, higher output SNR is obtained both for the jammed signal and jamming signal. Further, we proposed a combined approach to perform non-IC when no interference exists, and IC when collisions occur. Our results showed a gain of 12 dB in the output SNR of the jammed source and 4 dB in the output SNR of the jamming source. Further work will exploit the channel differences between the near and far nodes for IC, and will prove the validity of our approach in a sea experiment.



(a)



(b)

Fig. 5: Output SNR as a function of time for the case of partial collision. Upper panel: use of a combination of DFE-IC and DFE-NIC. Lower panel: use of DFE-NIC only.

References

[1] Ian F. Akyildiz, Dario Pompili and Tommaso Melodia, "Underwater Acoustic Sensor Networks: Research Challenges," *Ad Hoc Networks (Elsevier)*, vol. 3, pp. 257–279, 2005.

[2] R. Diamant, P. Casari, F. Campagnaro, and M. Zorzi, "A handshake-based protocol exploiting the near-far effect in underwater acoustic networks," *IEEE Wireless Communications Letters*, vol. 5, no. 3, pp. 308–311, June 2016.

[3] ——, "Leveraging the nearfar effect for improved spatial-reuse scheduling in underwater acoustic networks," *IEEE Transactions on Wireless Communications*, vol. 16, no. 3, pp. 1480–1493, March 2017.

[4] M. Kodialam and T. Nandagopal, "Characterizing achievable rates in multi-hop wireless networks: the joint routing and scheduling problem," in *Proceedings of the 9th annual international conference on Mobile computing and networking*. ACM, 2003, pp. 42–54.

[5] R. Diamant and L. Lampe, "Spatial reuse time-division multiple access for broadcast ad hoc underwater acoustic communication networks," *IEEE Journal of Oceanic Engineering*, vol. 36, no. 2, pp. 172–185, April 2011.

[6] Y. Noh, U. Lee, S. Han, P. Wang, D. Torres, J. Kim, and M. Gerla, "DOTS: A propagation delay-aware opportunistic MAC protocol for mobile underwater networks," *IEEE Transactions on Mobile Computing*, vol. 13, no. 4, pp. 766–782, April 2014.

[7] B. Peleato and M. Stojanovic, "Distance aware collision avoidance protocol for ad-hoc underwater acoustic sensor networks," *IEEE Communications Letters*, vol. 11, no. 12, pp. 1025–1027, December 2007.

[8] R. Diamant, G. N. Shirazi, and L. Lampe, "Robust spatial reuse scheduling in underwater acoustic communication networks," *IEEE Journal of Oceanic Engineering*, vol. 39, no. 1, pp. 32–46, Jan 2014.

[9] D. Pompili, T. Melodia, and I. F. Akyildiz, "A CDMA-based medium access control for underwater acoustic sensor networks," *IEEE Transactions on Wireless Communications*, vol. 8, no. 4, pp. 1899–1909, April 2009.

[10] R. Chassaing and D. Reay, *Adaptive Filters*. Wiley-IEEE Press, 2008, pp. 319–353. [Online]. Available: http://ieeexplore.ieee.org/xpl/articleDetails.jsp?arnumber=5236581

[11] R. Diamant, "Robust interference cancellation of chirp and cw signals for underwater acoustics applications," *IEEE Access*, vol. 6, pp. 4405–4415, 2018.

[12] S. E. Cho, H. C. Song, and W. S. Hodgkiss, "Successive interference cancellation for underwater acoustic communications," *IEEE Journal of Oceanic Engineering*, vol. 36, no. 4, pp. 490–501, Oct 2011.

[13] Z. Wang, S. Zhou, J. Catipovic, and P. Willett, "Asynchronous multiuser reception for OFDM in underwater acoustic communications," *IEEE Transactions on Wireless Communications*, vol. 12, no. 3, pp. 1050–1061, March 2013.

[14] P. Pandey, M. Hajimirsadeghi, and D. Pompili, "Region of feasibility of

interference alignment in underwater sensor networks," *IEEE Journal of Oceanic Engineering*, vol. 39, no. 1, pp. 189–202, Jan 2014.

[15] Y. Zhou, A. Song, F. Tong, and R. Kastner, "Distributed compressed sensing based channel estimation for underwater acoustic multiband transmissions," *The Journal of the Acoustical Society of America*, vol. 143, no. 6, pp. 3985–3996, 2018.

[16] M. Porter *et al.*, "Bellhop code," Last time accessed: Nov. 2015. [Online]. Available: http://oalib.hlsresearch.com/Rays/index.html

Spread-spectrum Multi-carrier Communication in Interference-limited Acoustic Regimes

Zhengnan Li, *Graduate Student Member, IEEE,* and Milica Stojanovic, *Fellow, IEEE*
Northeastern University, Boston, MA, USA

***Abstract*—Interference-limited regimes occur in underwater acoustic communication scenarios for a variety of reasons: (i) ambient noise levels can be elevated in certain environments, (ii) intentional interference can be present in adversarial situations, (iii) the signal level can be reduced deliberately so as to achieve security, and (iv) multi-user interference can be present in networked systems. We focus here on signal detection in low SNR regimes using multi-carrier modulation in the form of orthogonal frequency division multiplexing (OFDM). We propose a transmission / detection method that integrates OFDM with direct-sequence spectrum spreading. Specifically, we capitalize on coupling the channel estimation / signal detection with structured coding to obtain an efficient receiver design. We consider both coherent and differentially coherent detection, and extend the detection principles to multi-channel receiver configurations. In addition, spread-spectrum OFDM detection is coupled with a custom-designed frequency synchronization techniques to counteract the motion-induced Doppler frequency shifting. Using experimental recordings from the Mobile Acoustic Communication Experiment (MACE'10), where signals were transmitted over a 3 km – 7 km shallow-water channel in the 10.5 kHz – 15.5 kHz band, with relative transmitter / receiver motion of up to 1.5 m/s, we study the system performance in terms of the mean squared error and symbol error rate in data detection. Varying the level of externally added noise, we show that the proposed methods provide excellent performance while maintaining simplicity needed for a practical implementation.**

***Index Terms*—Underwater acoustic communication, low SNR, interference, multi-user communication, OFDM, direct sequence spread spectrum, channel estimation, differentially coherent detection, Doppler effect, frequency synchronization.**

I. Introduction

We address the design of an underwater acoustic communication system capable of operating in noisy or interference-limited regimes. Such regimes occur in different situations, which can roughly be classified as having unintentional or intentional interference. While unintentional interference is created by environmental sources, intentional interference occurs in hostile environments or in multi-user systems where other users of the same network operate simultaneously in the same frequency band. Additionally, in systems that require low probability of intercept (LPI), signal level is deliberately reduced so as to hide the signal below the noise, thus making it inaudible to an unintended listener.

Communication in an interference-limited regime is typically established using spread spectrum methods, either of the frequency hopping (FH) or the direct sequence (DS) type. Both types have been extensively studied for use in terrestrial and satellite systems. A well known example is the 3G cellular standard based on DS code-division multiple access (CDMA). DS spread spectrum with single-carrier modulation has also been studied for underwater acoustic communications [1], where the major difference from terrestrial radio communications was found to be in the channel's time-variability that required re-thinking of the basic despreading operation, and resulted in the concept of chip-rate hypothesis-feedback equalization. Further studies of single-carrier DS acoustic systems included e.g. [2], [3] and [4], where the focus was on strategic design of the DS spreading process to alleviate the multiapth problem in low SNR regimes. A less conventional approach to covert underwater acoustic communications was taken in [5], where information signals were embedded into recorded dolphin sounds for subsequent transmission over an acoustic channel.

An alternative to single-carrier broadband modulation is the multi-carrier modulation, typically implemented in the form of orthogonal frequency division multiplexing (OFDM). The attendant signal processing issues that address equalization and motion-induced frequency shifting in an acoustic channel have been well understood at this point; see e.g. [8], [9], [10]. The major advantages of OFDM are bandwidth scalability and FFT-based signal processing; the latter leading to computationally-simple receiver architectures if the system is kept free of inter-carrier interference (ICI). In light of covert communications, the advantage of OFDM is in the fact that the signal waveforms exhibit Gaussian-like characteristics in the time domain, thus making them noise-like provided that the signal level is kept low.

Coupling of OFDM and DS spread spectrum has been investigated in the mainstream radio literature (e.g. [6]),but references specific to underwater acoustic communications remain scarce. A notable exception is [7], where a time-frequency spreading method was proposed and evaluated using experimental data. The method is based on a multi-band OFDM approach, where the total available bandwidth is divided into several subbands, and each subband devoted to one OFDM stream (e.g. 16 subbands with 256 carriers each). A coded signal is repeated (spread) over the subbands, as well as over blocks in time. Coherent detection is employed, with pilots allocated to each subband at an overhead rate of about 50%. Channel estimation utilizes a basis expansion method, while equalization and despreading are performed jointly. Good performance is obtained at the expense of computationally-heavy signal processing.

In this paper, we propose a method for DS OFDM, which aims for computationally efficient processing at the receiver. The method is suitable for both low SNR and multi-user

regimes, and allows for coherent, as well as differentially coherent detection. The latter is associated with very low computational complexity, as it does not require explicit channel estimation. The method capitalizes on DS spreading and interleaving across the carriers in a manner that allows for easy receive-side processing. We cast this method in a multi-channel receiver configuration (spatial diversity), and add frequency synchronization which operates jointly with data detection (equalization / despreading) using the principles described in [10]. To demonstrate the performance, we use experimental data recorded during the Mobile Acoustic Communications Experiment (MACE'10), adding varying amounts of noise to mimic the low SNR regime. Results are quite promising, showing satisfactory performance in sub-zero SNR conditions.

The rest of the paper is organized as follows. In Sec.II, we outline the basic principles of signal design and detection. Sec.III contains the results of experimental signal processing. We conclude in Sec.IV.

II. Signal Design and Detection

We consider an OFDM system with K carriers spanning bandwidth B. The carrier separation $\Delta f = B/K$ is chosen sufficiently narrow that the channel appears frequency-nonselective in each subband, yet wide enough that the channel remains approximately constant over each OFDM block of duration $T = 1/\Delta f$. In other words, we consider a properly designed OFDM system in which there is no ICI. The assumption of time-invariance does not include motion-induced frequency shifting, i.e. it refers to the channel after frequency synchronization. Additionally, the guard time between the blocks (cyclic prefix) is sufficiently long that multipath does not cause any inter-block interference.

With these notions, common to a conventional OFDM system design, the signals obtained after FFT demodulation can be modeled as

$$y_k = a_k H_k + z_k, k = 0, 1, \dots K-1 \tag{1}$$

where a_k is the symbol transmitted on the k-th carrier, $H_k = H(f_k)$ is the channel transfer function evaluated at the corresponding frequency $f_k = f_0 + k\Delta f$, and z_k is the noise. The noise is zero-mean, possibly uncorrelated across carriers.

The transmitted symbols a_k are obtained by coding (spreading) the original stream of information-bearing data symbols from a PSK (or QAM) alphabet. The length of the spreading sequence is chosen as $Q \geq BT_{mp}$, where T_{mp} is the multipath spread of the channel. This choice leads to a simple and elegant technique for channel estimation, as we will see later. Both K and Q are chosen as powers of 2 for ease of FFT processing. The spreading sequence can be a binary flip-coin random sequence, a maximum-length shift register sequence, or a custom-designed sequence such as Walsh-Hadamard, Gold or Kasami sequence. If noise protection only is sought on a point-to-point link, the choice of sequence is irrelevant. In multi-user applications, where interference is generated by other users of the same system, care has to be taken in assigning different sequences to different users.

The encoding process begins with mapping of each information-bearing data symbol onto a sequence of Q chips. With K carriers, $I = K/Q$ data symbols will form one OFDM block. Each symbol can have the same spreading code, or a different code, depending upon the desired level of security. So long as the code is known to the intended receiver, the conceptual system design does not change. Here, we will focus on using the same code for all the data symbols.

Denoting by d_i the $i-th$ data symbol, and by c_q the chips of the spreading sequence, the resulting sequence $d_0c_0, \dots d_0c_{Q-1}; d_1c_0, \dots d_1c_{Q-1}; \dots; d_{I-1}c_0, \dots d_{I-1}c_{Q-1}$ is interleaved. Interleaving is employed to ensure that a given data symbol is spread evenly across the carriers, thus providing frequency diversity and ease of channel estimation on the receiver side. Specifically, the interleaved sequence yields data-modulated chips $a_k,\ k = 0, \dots K$, where $a_{qI+i} = d_i c_q$ $(q = 0, \dots Q-1; i = 0, \dots I-1)$. The data-modulated chips are assigned to consecutive carriers and transmitted. At the receiver, FFT demodulation yields the noisy observations (1).

A. Signal Detection

FFT demodulation is followed by the first stage of despreading. The known spreading sequence c_q is used to counter-multiply the observations y_k, yielding a new set of observations

$$x_{qI+i} = c_q^* y_{qI+i} = d_i H_{qI+i} + c_q^* z_{qI+i} \tag{2}$$

The newly formed observations are now arranged into I separate vectors (each of length Q),

$$\mathbf{x}_i = d_i \mathbf{H}_i + \mathbf{z}_i \tag{3}$$

where $\mathbf{H}_i = [H_i\ H_{i+\mathtt{I}}\ H_{i+2\mathtt{I}} \dots]^T$ is the relevant channel vector, and $\mathbf{z}_i$ the corresponding noise.

As in any OFDM system, post-FFT signal processing capitalizes on the discrete Fourier transform (DFT) model, by which the K frequency-domain channel coefficients $\{H_k\}$ are related to a set of delay-domain coefficients $\{h_l\}$. Because the OFDM block duration is (much) longer than the multipath spread of the channel T_{mp}, the number of significant coefficients h_l is (much) smaller than K.

Grouping the frequency-domain channel coefficients into a $K \times 1$ vector $\mathbf{H}$, and the significant delay-domain coefficients into an $L \times 1$ vector $\mathbf{h}$, the DFT relationship is stated as

$$\mathbf{H} = \mathbf{F}\mathbf{h} \tag{4}$$

where the $K \times L$ tall matrix $\mathbf{F}$ contains the first L columns of a regular $K \times K$ DFT matrix with elements $e^{-j2\pi kl/K},\ k = 0, \dots K-1;\ l = 0, \dots L-1$.

Referring to the expression (3), we now have that

$$\mathbf{H}_i = \mathbf{F}_i \mathbf{h},\ i = 0, \dots I-1 \tag{5}$$

where $\mathbf{F}_i$ is a $Q \times L$ matrix obtained from $\mathbf{F}$ by taking every I-th row, starting with row i. Consequently, the signals $\mathbf{x}_i$ can be expressed as

$$\mathbf{x}_i = d_i \mathbf{F}_i \mathbf{h} + \mathbf{z}_i \tag{6}$$

Multiplying the above expression by the conjugate-transpose $\mathbf{F}_i'$, and recognizing that $\mathbf{F}_i'\mathbf{F}_i = Q\mathbf{I}$,[1] we arrive at a new set of signals

$$\mathbf{u}_i = \frac{1}{Q}\mathbf{F}_i'\mathbf{x}_i = d_i\mathbf{h} + \mathbf{w}_i \tag{7}$$

The signals $\mathbf{u}_i$ serve as a starting point for detecting the data symbols d_i, $i = 0, \ldots I-1$. Two facts are worth noting at this point: (1) each of the signals $\mathbf{u}_i$ carries information about the respective data symbol d_i, but depends on the *same* channel vector $\mathbf{h}$, and (2) if the noise vectors $\mathbf{z}_i$ are uncorrelated (which typically is the case), so are the noise vectors $\mathbf{w}_i$. In addition, it is worth pointing out that if $\mathbf{h}$ is sparse, i.e. has fewer than L significant coefficients, additional reduction in dimensionality can be performed at this stage.

The data detection problem can now be stated as follows: given the observations $\mathbf{u}_i$, determine the symbols d_i from a given alphabet (e.g. QPSK).

If the channel vector were known, optimal data detection would be performed by making a soft estimate $\hat{d}_i = \mathbf{h}'\mathbf{u}_i/||\mathbf{h}||^2$, and using it to make the decision $\tilde{d}_i = \text{dec } (\hat{d}_i)$. Additional channel coding, if applied, can be exploited at this point as well.

In practice, of course, the channel is not known, and an estimate $\hat{\mathbf{h}}$ has to be used instead of $\mathbf{h}$. Below, we propose two approaches for dealing with the unknown channel, one based on coherent detection using channel estimation, and the other based on differentially coherent detection.

1) Coherent detection: Assigning one of the data symbols as a pilot in an OFDM block, say d_0, the channel can be estimated as

$$\hat{\mathbf{h}} = \hat{\mathbf{h}}_0 = d_0^*\mathbf{u}_0 \tag{8}$$

This channel estimate can now be used to estimate the remaining data symbols as

$$\hat{d}_i = \hat{\mathbf{h}}'\mathbf{u}_i/||\hat{\mathbf{h}}||^2, \;\; i = 1, \ldots I-1 \tag{9}$$

Data detection follows through decision-making,

$$\tilde{d}_i = \text{dec } (\hat{d}_i) \tag{10}$$

While this is the basic principle of coherent detection, an alternative method can be used to improve the performance. Namely, after making the first tentative decision $\tilde{d}_1$, the corresponding channel estimate is formed as

$$\hat{\mathbf{h}}_1 = \tilde{d}_1^*\mathbf{u}_1 \tag{11}$$

This instant estimate is used to form a running average

$$\hat{\mathbf{h}} = \frac{1}{2}(\hat{\mathbf{h}}_0 + \hat{\mathbf{h}}_1) \tag{12}$$

which is set as the current channel estimate, and used to make the next symbol decision. The procedure continues until the last symbol decision has been made. With the final channel estimate $\mathbf{h}$, a fresh set of all symbol decisions is made according to (9), (10).

Note that the data estimation step (9) effectively accomplishes a second stage of despreading, whereby the multipath components are combined, i.e. their contributions are summed in a coherent manner. Refinements to the above procedure are also possible, including joint data detection and channel estimation, as well as the use of dedicated sparse channel estimation techniques. Coherent detection can further be improved by engaging a decision-directed mode of operation.

2) Differentially coherent detection: Our first stage of processing, which yields the signals $\mathbf{u}_i$ given by the expression (7), can be followed by differentially coherent detection, which eliminates the need for explicit channel estimation. Differentially coherent detection of OFDM signals has been analyzed within a standard (non-spread) system framework, showing excellent performance results in tests with real data [9], [10]. This fact serves as a motivation to investigate its use in the present DS OFDM setting.

Differentially coherent detection makes use of differential encoding performed at the transmitter, whereby the transmitted data symbols d_i are formed from the original information-bearing symbols b_i as $d_i = b_i d_{i-1}$. In doing so, the first data symbol d_0 is set to a known value, e.g. 1. Note that differential encoding is performed in the frequency domain (across carriers), not in the time domain.

Differentially coherent detection is now accomplished simply by forming the estimates

$$\hat{b}_i = \mathbf{u}_{i-1}'\mathbf{u}_i/||\mathbf{u}_{i-1}||^2 \tag{13}$$

and making the corresponding decisions $\tilde{b}_i = \text{dec } (\hat{b}_i)$.[2] The obvious advantage of differentially coherent detection is its simplicity of implementation. There is no need for explicit channel estimation, and all post-FFT processing is reduced to inner product operations.

The system architecture, including transmitter and the various approaches to detection, is illustrated in Fig.1.

B. Multi-channel processing

On the receiver side, extension to spatial diversity reception follows the principles of maximum-ratio combining (MRC) for coherent detection, or differential maximum-ratio combining (DMRC) for differentially coherent detection. Both extensions are straightforward.

Assuming M receiving elements, their FFT outputs $\mathbf{y}^m, m = 1, \ldots M$, are fed into M identical processors, which produce the observations

$$\mathbf{u}_i^m = d_i\mathbf{h}^m + \mathbf{z}_i^m \tag{14}$$

Assuming independent, identically distributed noise components, MRC yields the decision variables

$$\hat{d}_i = \frac{1}{\sum_{m=1}^{M}||\hat{\mathbf{h}}^m||^2}\hat{\mathbf{h}}^{m'}\mathbf{u}_i \tag{15}$$

[1] Recall that $Q \geq L$.

[2] Normalization can be omitted with PSK, both in coherent and differentially coherent detection.

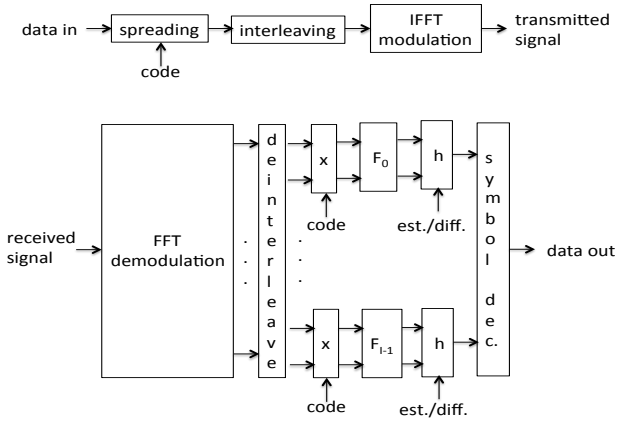


Fig. 1. Block diagram of the transmitter / receiver architecture. The length of the spreading code Q and the number of carriers K correspond to $I = K/Q$ data symbols comprising one OFDM block. Channel estimation can be performed explicitly, leading to coherent detection. Alternatively, differentially coherent detection can be used. In either case, frequency-domain channel equalization is represented by the blocks following the spreading code removal (total of I such blocks). This figure illustrates a single-input single-output system architecture, which serves as a basis for a multi-channel architecture.

Analogously, DMRC yields

$$\hat{b}_i = \frac{1}{\sum_{m=1}^{M} ||\mathbf{u}_{i-1}^m||^2} \mathbf{u}_{i-1}^{m'} \mathbf{u}_i \tag{16}$$

Again, normalizing the magnitude of the data estimate is significant only if any subsequent adaptive processing is driven by the data estimation error $e_i = \hat{d}_i - d_i$ (e.g., block-by-block adaptive channel estimation); otherwise, it can be omitted for PSK symbols.

C. Frequency offset compensation

So far, we have assumed that the channel is time-invariant over one OFDM block. This assumption is contingent upon accurate frequency synchronization. If the received signal contains a frequency offset, which typically is the case due to the Doppler effect, proper correction has to be made.

Denoting by $v_m(t)$ the m-th element's received signal down-shifted by the lowest carrier frequency f_0, and by $\hat{\beta}$ an estimate of the radial frequency shift, the post-FFT signal is given by

$$y_k^m = \int_T v_m(t) e^{-j\hat{\beta}t} e^{-j2\pi k \Delta f t} dt \tag{17}$$

If synchronization is accurate, the model (1) will hold, and our approach to data detection will be justified. Otherwise, a residual frequency shift will cause ICI, invalidating our model and disturbing the detection process. The data symbol estimate (15) will thus depend on the value $\hat{\beta}$, and so will the corresponding squared error

$$E_d(\hat{\beta}) = \sum_i |\hat{d}_k(\hat{\beta}) - \tilde{d}_k(\hat{\beta})|^2 \tag{18}$$

The same will be true for differential detection (16), where

$$E_b(\hat{\beta}) = \sum_i |\hat{b}_k(\hat{\beta}) - \tilde{b}_k(\hat{\beta})|^2 \tag{19}$$

Following the approach of [10], we calculate the squared error for a number of hypothesized values $\hat{\beta}$, and chose the best hypothesis as

$$\tilde{\beta} = \arg\min_{\hat{\beta}} E_d(\hat{\beta}) \tag{20}$$

The final symbol decisions are $\tilde{d}_i(\tilde{\beta})$. Identical procedure is used for differentially coherent detection.

Hypothesis testing can be used alone, or it can be augmented by a stochastic gradient approach for estimating the frequency offset in a closed-loop manner. The stochastic gradient approach provides additional accuracy and speeds up the computation. Description of this algorithm is lengthy; suffice it to say that it closely follows the approach of [10].

III. Experimental Results

The Mobile Acoustic Communications Experiment (MACE'10) was conducted in June 2010 off the coast of Martha's Vineyard island in the North Atlantic. A vertical array with 12 elements separated by 12 cm received the signals transmitted from a source moving to-and-from the receiver at a varying speed of up to 1.5 m/s. The system was deployed mid-column in about 100 m of water, while transmission distance varied between 3 km and 7 km. Acoustic signals were transmitted in the 10.5 kHz - 15.5 kHz band. A total of 52 transmissions were made over a period of 3.5 hours. Each transmission contained a suite of OFDM signals with varying number of carriers. The signal parameters are summarized in Table III.

TABLE I
Signal Parameters

bandwidth, B	5 kHz				
lowest carrier frequency, f_0	10.5 kHz				
guard time, T_g	16 ms				
number of carriers, K	128	256	512	1024	2048
OFDM blocks per frame	64	32	16	8	4
carrier spacing [Hz]	39.1	19.5	9.8	4.9	2.4
chip rate, $\frac{B}{1+BT_g/K}$ [kbps]	3.0	3.8	4.3	4.6	4.8

We present the results of QPSK data detection, measuring the performance in terms of the mean squared error (MSE) and symbol error rate (SER). The results shown here represent the average taken over the 52 transmissions.

In estimating the frequency offset, the range of hypothesized values $\hat{\beta}/2\pi$ is set to $\pm 3\Delta f$, with resolution $\Delta f/10$. A full search is performed only in the first OFDM block of a frame; from there on, the range of hypothesized values can be narrowed around the existing estimate, or stochastic gradient search can be used.

Fig.2 (top) shows the estimated MSE obtained after processing the MACE signals with varying number of carriers ranging from $K = 128$ to 2048. All $M = 12$ receiving elements are used for combining. Results are shown for coherent and differentially coherent detection, with varying processing gain Q. Unstructured, binary flip-coin spreading sequences are used. The MSE is calculated as the average over $I - 1$ data symbols in an OFDM block (the remaining symbol is the

pilot), and all blocks of the 52 transmissions. The performance clearly improves with the processing gain Q. The amount of improvement is generally about 3 dB for every doubling of Q; an occasional deviation at lower values of Q likely occurs because the assumption $Q \geq BT_{mp}$ is only partly satisfied. The MSE generally decreases as the number of carrier grows, but reaches a turning point at $K = 1024$ as the time-coherence assumption weakens. This trend has been observed previously as well [9], [10]. Coherent detection generally outperforms differential detection by about 6 dB-8 dB. This gain is a result of averaging the channel estimate over $I = K/Q$ symbols (and is again contingent upon the assumption $Q \geq BT_{mp}$ being satisfied).

Fig.2 (bottom) shows the estimated MSE vs. the number of receiving elements M. The number of carriers is $K = 1024$ in this example. The receiving elements are chosen among the 12 available as equally spaced whenever possible ($M = 2, 3, 4, 6$). As expected, the performance improves as the array size grows, but exhibits the effect of diminishing returns due to the finite aperture (the elements become more closely spaced as their number grows, thus introducing correlation). The strikingly good performance comes at the price of a Q-fold reduction in bit rate, $R_b = \frac{1}{Q} \cdot \frac{2B}{1+T_g B/K}$.

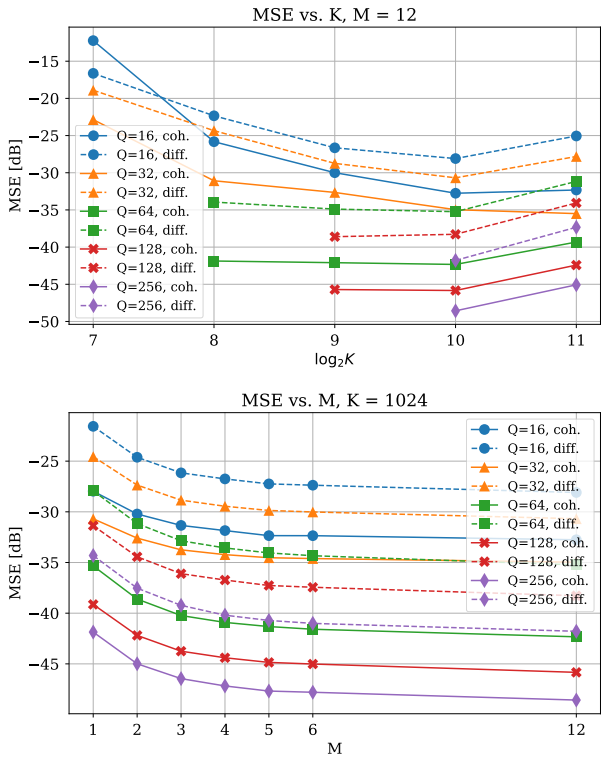


Fig. 2. Estimated mean squared error: average over 52 MACE transmissions.

Results of Fig.2 were obtained to calibrate the system with raw received signals that were not altered to contain more noise than they naturally did. To assess the system performance in low SNR conditions, noise was added artificially to the recorded signals. To do so, noise-only recordings were used to extract the noise statistics first. Specifically, the noise components z_k^m that contaminate the post-FFT observations (1) were modeled as zero-mean Gaussian, uncorrelated across the carriers (k), but correlated across the receiving elements (m). The spatial correlation matrix was estimated from the recordings, and used to generate samples of the spatially-colored noise from computer-generated independent Gaussian samples. The results are shown in Figs.3 and 4. As a benchmark, these results include the spatially-white noise case. The difference in performance observed with colored / white noise reinforces the need to have sufficient separation between the array elements.

Fig.3 shows the performance of coherent detection, while Fig.4 refers to differentially coherent detection. The symbol error rate refers to uncoded QPSK symbols; additional channel coding can of course be applied to further improve the SER. Both sets of results (coherent and differential) exhibit the same trend. The MSE "saturation" beyond 20 dB of SNR is an artifact of adding noise to an already noisy signals. Namely, the SNR value used to label the figures refers to the artificial noise only. As this noise vanishes, the actual SNR does not tend to zero, but instead remains at the level already present in the raw recorded signals. Coherent detection outperforms differential detection when $Q > 32$; however, one must note that differential detection still offers excellent performance, while its computational cost is minimal.

The results of Figs.3 and 4 can be used as a guideline for designing a multi-carrier system that needs to operate in low SNR. To do so, one would set a bar on the MSE, say -10 dB (this bar corresponds to a certain SER with or without channel coding), and look for those K, Q pairs that meet the bar. For example, if the system were to be deployed in the MACE environment, and required to operate at the SNR of -10 dB, we see that the processing gain needed with $K = 1024$ carriers is $Q = 64$ or more. Assuming a guard interval $T_g = Q/B$, the resulting bandwidth efficiency is $\frac{1}{Q} \cdot \frac{1}{1+Q/K}$ symbols per second per Hz of occupied bandwidth. With QPSK modulation, 1024 carriers, processing gain of 64 and 5 kHz of bandwidth, the resulting bit rate is 147 bps. Hopefully, an application that requires operation in -10 dB of SNR, will find this bit rate to be sufficient.

IV. Conclusion

We addressed the problem of acoustic signal detection in low SNR conditions by proposing a multi-carrier modulation method integrated with direct-sequence spectrum spreading. The method capitalizes on structured coding across the carriers, enabling a de-facto despreading operation to reveal the channel in the impulse response domain. Following this operation, either coherent or differentially coherent detection can be applied towards extracting the multipath gain. Detection is integrated with a custom-designed frequency offset estimation technique, which is necessary for a practical application to mobile acoustic systems.

Results of processing an experimental data set recorded over a mobile acoustic channel with externally added Gaussian noise clearly demonstrate successful operation in sub-zero SNR conditions. Such operation owes to three key factors: accurate frequency synchronization, multi-channel diversity

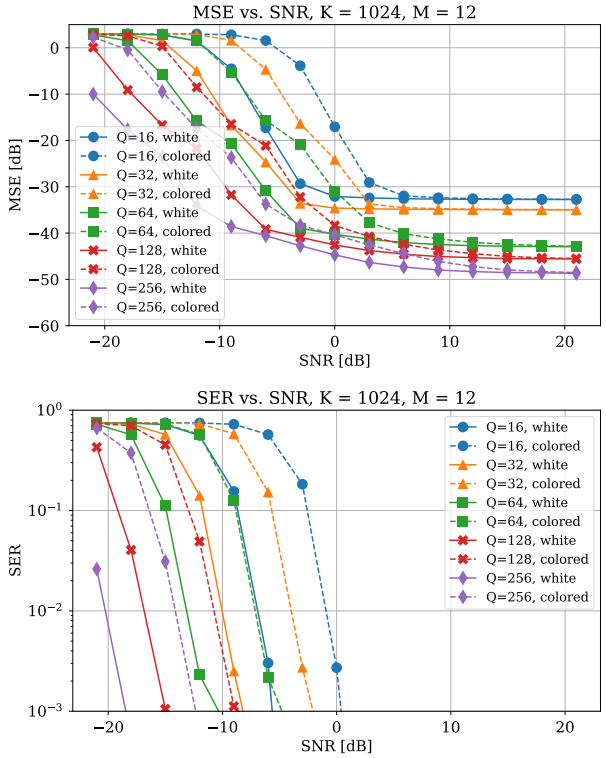


Fig. 3. Mean squared error and symbol error rate obtained with coherent detection. $K = 1024$ carriers, $M = 12$ receiving elements. The SNR refers to the artificially added noise (as artificial noise vanishes, natural noise remains, hence the MSE reaches a plateau).

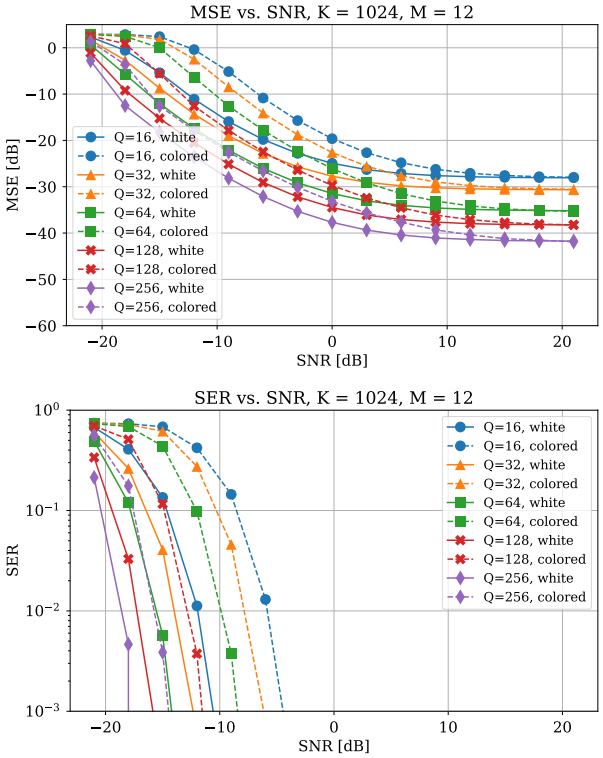


Fig. 4. Mean squared error and symbol error rate obtained with differentially coherent detection. $K = 1024$ carriers, $M = 12$ receiving elements. The SNR refers to the artificially added noise (as artificial noise vanishes, natural noise remains, hence the MSE reaches a plateau).

reception, and the proposed structure of despreading/multipath processing. While coherent detection outperforms differential detection, the latter nonetheless offers very good performance without explicit channel estimation, i.e. at a very low computational complexity.

Future research will focus on several aspects: (1) integration of super-resolution and sparse channel estimation methods into coherent detection, (2) time-adaptive receiver operation, and (3) multi-carrier CDMA networks. The latter is notably motivated by the present results, as multi-carrier multi-user interference exhibits Gaussian-like characteristics, for which the present system was shown to be well suited.

References

[1] M.Stojanovic and L.Freitag, "Multi-channel detection for wideband underwater acoustic CDMA communications," *IEEE J. Oceanic Eng.*, vol.31, No.3, July 2006, pp.685-695.

[2] C.He, J.Huang and Z.Ding, "A variable-rate spread-spectrum system for underwater acoustic communications," *IEEE J. Oceanic Eng.*, vol.34, No.4, Oct. 2009, pp.624-633.

[3] J.Ling, H.He, J.Li, W.Roberts and P.Stoica, "Covert underwater acoustic communications," *J. Acoust. Soc Am.*, vol.128, No.5, 2010, pp.2898-909.

[4] F.Qu, X.Qu, L.Yang and T.C.Yang, "Spread-spectrum method using multiple sequences for underwater acoustic communications," *IEEE J. Oceanic Eng.*, vol.43, No.4, Oct. 2018, pp.1215-1226.

[5] S. Liu, G. Qiao, and A. Ismail, ?Covert underwater acoustic communication using dolphin sounds,? *J. Acoust. Soc Am.*, vol.133, No.4, 2013, pp.300?306,

[6] D.Kalofonos, M.Stojanovic and J.Proakis, "Performance of Adaptive MC-CDMA Detectors in Rapidly Fading Rayleigh Channels," *IEEE Trans. Wireless Commun.*, vol.2, No.2, March 2003, pp.229-239.

[7] G G.Leus and P. van Walree, "Multiband OFDM for covert acoustic communications," *IEEE J. Select Areas Commun.*, vol.26, No.4, Dec. 2008, pp.1662-1673.

[8] C.Berger, S.Zhou, J.Preisig and P.Willet, "Sparse channel estimation for multi-carrier underwater acoustic communication: from subspace methods to compressed sensing," I*EEE Trans. Sig. Proc.*, vol.58, No.3, March 2010, pp. 1708-1721.

[9] Y.Aval and M.Stojanovic, "Differentially coherent multi-channel detection of Acoustic OFDM signals," *IEEE J. Oceanic Eng.*, vol.40, No.2, April 2015, pp.251-268.

[10] A.Tadayon and M.Stojanovic, "Low-complexity super-resolution frequency offset estimation for high data rate acoustic OFDM systems," *IEEE J. Oceanic Eng.*, Sept. 2018, DOI:10.1109/JOE.2018.2869657.

TOWARDS PHYSICAL LAYER CRYPTOGRAPHY FOR UNDERWATER ACOUSTIC NETWORKING

Konstantinos Pelekanakis, Camila M. G. Gussen, Roberto Petroccia and João Alves

Science and Technology Organization - Centre for Maritime Research and Experimentation, La Spezia, Italy.

Contact: Konstantinos Pelekanakis, 400 Viale San Bartolomeo, 19126 La Spezia (SP),
Tel: +390187527283, email: konstantinos.pelekanakis@cmre.nato.int

Abstract: *Two main approaches for securing a wireless link are symmetric encryption and public key encryption [1]. Both of these are applied to upper layers of the Open Systems Interconnection (OSI) stack. Underwater Acoustic Networks (UANs) typically have an ad-hoc structure and the use of public keys becomes not practical since there is no infrastructure that supports key management and authentication. Symmetric key strategies involve the distribution of new keys when new nodes join the network in the middle of a mission and this may not be desirable. In addition, if the current key is compromised, and is also used to share the future key, then secure communications is not possible anymore. Following the line of thought in radio communications, we investigate Physical Layer Security (PLS) for UANs. PLS leverages on the uncorrelated nature of multipath over space, and channel reciprocity to independently generate a cryptographic key between two authenticated nodes even if an eavesdropper is in their vicinity. In this initial study, we set up a network of two legitimate nodes and one eavesdropper in a shallow water environment in the Gulf of La Spezia, Italy, and we analyse thousands of channel-probe signals transmitted over different days and hours between the two legitimate nodes. We show that typical Channel Impulse Response (CIR) features, such as the* L_2/L_0 *norm, a smooth sparseness measure and the Root-Mean-Square (RMS) delay spread, can exploit reciprocity between the two legitimate nodes. However, when the eavesdropper is about a meter away from one of the legitimate nodes, then the smooth channel sparseness yields the best performance. With this feature, the probability of the legitimate nodes to independently generate the same key is three orders of magnitude higher than that of the eavesdropper.*

Keywords: *Underwater acoustic communications, underwater acoustic networks, physical layer security, cryptography.*

1. INTRODUCTION

Advances in both underwater acoustic communications and marine robotics enable the long-term deployment of networks of heterogeneous underwater assets [2],[3]. As these underwater networks are gaining momentum for future military and commercial applications, network security becomes critical, an issue that is manifested by the recent review papers [4]-[6].

The scenario of interest of this paper is shown in Fig. 1. Alice and Bob are two legitimate underwater assets that aim to establish secure acoustic communications in the presence of the passive adversary Eve. In traditional symmetric key cryptography, Alice and Bob use their pre-agreed keys prior to any encryption/decryption of their data. However, when new legitimate nodes without pre-agreed keys enter into the network, key management becomes an issue because Eve can infer the key if it is transmitted over an unsecure link. Various approaches have been proposed to share a common key in radio ad-hoc networks [7],[8] , however they are either based on some pre-shared secret or suffer from high communication overhead, which may not be practical in UANs.

Physical Layer Security (PLS) is a paradigm shift in symmetric cryptography and aims to generate keys dynamically based on channel propagation physics. It is built upon the theorem of reciprocity, which states that in a time-invariant waveguide the channels between Alice and Bob are equal. Furthermore, the channels observed by Eve are uncorrelated with those of Alice-Bob provided that Eve is a few wavelengths apart from them. Hence, Alice and Bob could use their channels as a common source of randomness to independently generate their keys while Eve cannot do better than a guessing-based exhaustive search for the key.

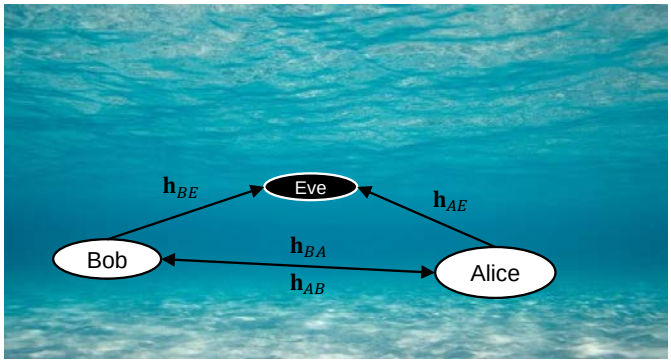


Fig. 1. Scenario of interest: two legitimate users, Alice and Bob, wish to establish secure communications in the presence of eavesdropper Eve. $\mathbf{h_{AB}}$, $\mathbf{h_{BA}}$, $\mathbf{h_{AE}}$, $\mathbf{h_{BE}}$, *respectively, denote the CIR between Alice to Bob, Bob to Alice, Alice to Eve, Bob to Eve.*

PLS has been extensively studied in radio communications ([9]-[11] and references therein). Typically, a key generation process includes four steps:

- **Channel Feature Extraction**: Alice sends a channel probe signal to Bob, and he estimates some pre-agreed channel parameters. Then Bob sends the same probe signal to Alice, and she also estimates the same channel parameters.
- **Quantization**: The estimated channel parameters of Alice and Bob are quantized and represented by a bit vector.
- **Reconciliation**: Bob and Alice compare their respective bit vectors. This procedure involves exchange of packets. The objective is to correct the differences between the vectors in order to derive a common cryptographic key.
- **Privacy Amplification**: The goal of this stage is to minimize the amount of information leaked to Eve in the reconciliation process.

In the underwater acoustics literature, only few studies of PLS are available [12]-[16]. In [12]-[13], the key generation is based on the reciprocity of the received signal strength (RSS)

between Alice and Bob. In [14], the amplitude of each sub-carrier of an Orthogonal Frequency-Division Multiplexing (OFDM) system is quantised in order to produce a crypto-key. In [15], a method based on distributed transmitters is proposed in order to minimize the signal strength at the eavesdropper. In [16], an algorithm for authenticating legitimate users by fusing statistics of channel parameters is proposed. However, the authors do not use the algorithm for crypto-key generation.

It is clear that there is great room for exploring PLS in the underwater domain. In this short paper, our focus is on extracting several new features from the multipath structure of the Bob-Alice link. The efficiency of our approach is tested based on an experimental setup of an Alice-Bob-Eve network in the Gulf of La Spezia, Italy. After offline processing thousands of probe signals, we show that the selected channel features exploit channel reciprocity. In addition, we compare their suitability for key generation under the scenario where Eve is very close to Alice.

Notation: vectors are represented in bold face with lowercase letters. The notation $\|\mathbf{x}\|_p$ denotes the p-norm (p≥1) of an n-tap vector $\mathbf{x}$ defined as $\|\mathbf{x}\|_p = (\sum_{i=0}^{n-1}|x_i|^p)^{1/p}$. The L_0 norm of $\mathbf{x}$, $\|\mathbf{x}\|_0$, is defined as the number of non-zero elements of $\mathbf{x}$.

2. CHANNEL FEATURES AND QUANTIZATION

The channel feature extraction is the first step for key generation. Since in the literature there is no consensus about an optimal feature for key generation purposes, our approach is to estimate the baseband channel impulse responses (CIRs) of the Alice-Bob links.

In general, the CIR, at time *n*, is represented by a complex-valued *L*-tap vector

$$\mathbf{h}(n) = [h_0(n)\ h_1(n)\ \dots h_{L-1}(n)]. \tag{1}$$

Moreover, each channel tap, $h_i(n)$, is associated with a fixed delay, τ_i, which is used to understand the time difference between two multipath components. For the three-node network in Fig. 1, the CIR between Alice-to-Bob, Bob-to-Alice, Alice-to-Eve, Bob-to-Eve, is $\mathbf{h_{AB}}(n)$, $\mathbf{h_{BA}}(n)$, $\mathbf{h_{AE}}(n)$, $\mathbf{h_{BE}}(n)$, respectively. Without limiting the generality of our results, the CIRs are estimated by matched filtering (or cross-correlating) the received signals with a known probe signal. After matched filtering, only the dominant taps are retained by normalising $\mathbf{h}(n)$ to 0 dB (i.e., the maximal element of $\mathbf{h}(n)$ is the unity) and substituting all taps whose amplitude fall below -25 dB with the zero value.

After the probe exchange, Alice and Bob compute the following four parameters/features:

1. Normalised L_2 norm: the L_2 norm of $\mathbf{h}(n)$ has the notion of power because it characterises channel fading and attenuation. A CIR with higher fading yields a smaller L_2 norm. Since $\mathbf{h}(n)$ is normalised to 0 dB, its theoretical maximal value is *L* and consequently the normalised L_2 norm is defined as:

$$\frac{1}{\sqrt{L}}\|\mathbf{h}(n)\|_2. \tag{2}$$

2. Normalised L_0 norm: The L_0 norm of $\mathbf{h}(n)$ characterises channel sparseness since a sparser CIR yields a lower L_0 norm. Due to the normalisation of $\mathbf{h}(n)$, the maximal value of $\|\mathbf{h}(n)\|_0$ is *L*. Hence, the normalised L_0 norm is given by

$$\frac{1}{L}\|\mathbf{h}(n)\|_0. \tag{3}$$

3. Channel sparseness: A different way to measure channel sparseness is given by

$$\beta = \frac{L}{L-\sqrt{L}}\left(1 - \frac{\|\mathbf{h}(n)\|_1}{\sqrt{L}\|\mathbf{h}(n)\|_2}\right) \tag{4}$$

For various degrees of sparseness, it can be shown that $0 \leq \beta \leq 1$, where sparser channels yield larger β.

4. RMS delay spread: The Root-Mean-Square (RMS) delay spread represents a measure of the multipath power delay spread (in seconds). In particular, it is the deviation of the multipath power about the average multipath delay. It is defined as:

$$\frac{\sqrt{\sum_{i=0}^{L-1}(\tau_i - \bar{\tau}(n))^2 |h_i(n)|^2}}{\|\mathbf{h}(n)\|_2} \tag{5}$$

where

$$\bar{\tau}(n) = \frac{\sum_{i=0}^{L-1} \tau_i |h_i(n)|^2}{\|\mathbf{h}(n)\|_2^2} \tag{6}$$

For almost all practical links, the RMS delay spread falls below one second [17].

After Alice and Bob compute their respective channel features, they must convert their measurements into a bit sequence. In this work, we test the following approach: each estimated feature, $x \in [0,1]$, is quantized and then multiplied by 2^{32} -1, i.e., the highest unsigned 32-bit integer. As a result, every quantized value is mapped onto the set of unsigned 32-bit integers. In the remainder of this paper, any 32-bit representation of a channel feature is called a *key*. Let $\boldsymbol{k}_A, \boldsymbol{k}_B$ denote the 32-bit key of a channel feature of Alice, Bob, respectively. To assess the feature suitability for key generation, we define the Bit Disagreement Rate (BDR),

$$BDR_{AB} = \frac{\|\boldsymbol{k}_A - \boldsymbol{k}_B\|_0}{N} \tag{7}$$

where $N = 32$ in our case and note that $BDR \in [0,1]$. Similarly, we define the BDRs between Alice-to-Eve and Bob-to-Eve.

3. EXPERIMENTAL RESULTS

Here, we analyse data acquired during the Littoral Acoustic Communications Experiment 2017 (LACE'17). The LACE'17 took place in the Gulf of La Spezia, Italy, in November 2017 and the experimental setup is shown in Fig. 2. A bi-directional link was established between two bottom mounted structures, M0 and M4 where M0 was placed close to the pier and M4 was at a range of 465 m. The bathymetry in the area was flat and the depth was about 11 m. Both M0 and M4 were equipped with projectors (sources) and hydrophones to emulate the scenario of Alice, Bob and Eve at different positions. For the purposes of this work, Alice is at M0 and her source and hydrophone is, respectively, 2,1 m and 1,8 m above the seabed. Bob is at M4 and his source and hydrophone is at the same altitude as Alice. Eve's hydrophone is at M0 and is located 1,2 m below Alice's hydrophone. Note that we address a particular challenging scenario since Eve and Alice are very close to each other. For instance, other researchers have considered Eve to be tens of meters [14] or kilometres [16] away from Alice and Bob.

The transmitted signal was a 1-sec-long up-sweep chirp (probe signal) followed by a 6-sec-long phase-modulated signal. The signal bandwidth was 8-12 kHz and it was exchanged between Alice and Bob every 10 seconds. A portion of the spectrograms of the received signals of Alice and Bob can be seen in Fig. 2. Note that Alice's received signal includes her own transmission (red intensity) followed by Bob's transmission (blue intensity) and this pattern continues every 10 seconds. Similarly, Bob's received signal includes Alice's transmission (blue intensity) followed by his own transmission (red intensity) and this pattern continues every 10 seconds. In total, Alice and Bob exchanged 3078 signals during the following four time slots (all times are in UTC):

1. 22/11/2017, 17:40:29 – 23/11/2017, 05:16:41
2. 23/11/2017, 16:46:29 – 23/11/2017, 20:26:28
3. 23/11/2017, 22:26:01 – 24/11/2017, 01:31:34
4. 24/11/2017, 02:40:07 – 24/11/2017, 04:37:51

To compare the BDRs of the proposed four features, Alice and Bob first estimate their respective CIRs based on the chirp signal. Assuming that Eve has knowledge of the signal processing chain of Alice and Bob, she estimates her CIR based on Bob's transmission with the aim to extract the same key. The Alice-to-Eve link is not processed because Alice's transmission saturated Eve's hydrophone during the experiment.

Fig. 3 shows all 3078 snapshots of the estimated $\mathbf{h_{AB}}(n)$, $\mathbf{h_{BA}}(n)$, and $\mathbf{h_{BE}}(n)$ during these four transmission intervals. The snapshots are stack in chronological order (y-axis) based on the signal transmissions. All CIRs are shown in a common delay axis (x-axis) whose maximal value is 70 ms. The zero delay corresponds to the line-of-sight (earliest arrival). Given that there is no mobility, the observed time variability is mainly due to the sea surface interaction with the transmitted signal. We can clearly see that $\mathbf{h_{AB}}(n)$ and $\mathbf{h_{BA}}(n)$ are highly correlated due to the principle of reciprocity while $\mathbf{h_{BE}}(n)$ exhibits low correlation with $\mathbf{h_{AB}}(n)$ and $\mathbf{h_{BA}}(n)$.

Fig. 4 shows the unquantised and quantised channel features for the Alice-to-Bob, Bob-to-Alice, Bob-to-Eve links. When quantised, all chosen features are equal most of the time between Alice and Bob. Yet, we note that after November 23rd, 12:00 pm, the measurements of Eve approach those of Alice and Bob, especially for the L_2/L_0 norm. This is due to the fact that environment is less in rich in multipath structure after that time (as can be seen in Fig. 3).

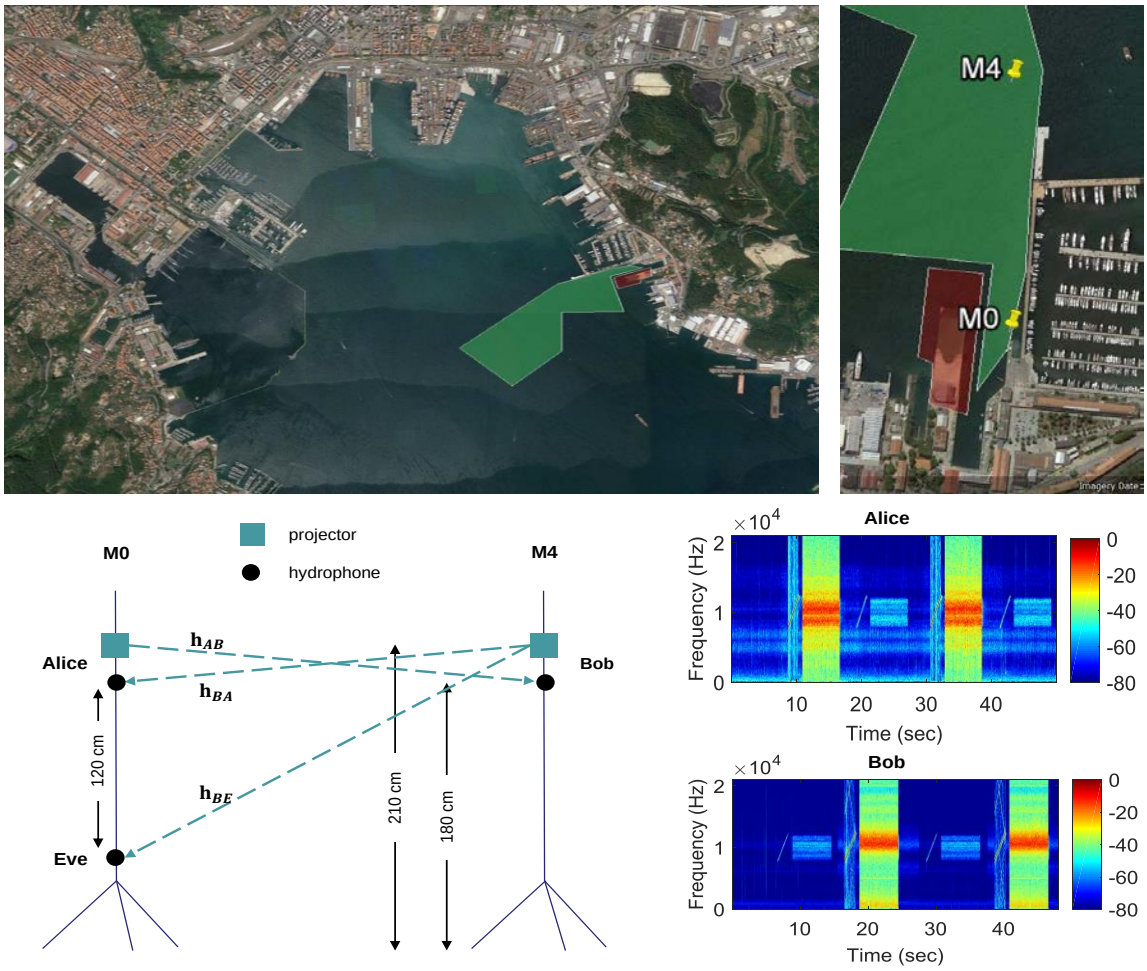


Fig. 2. Top left: experimental area in the Gulf of La Spezia. Top right: the location of the nodes M0 and M4 are with yellow marks. Bottom left: Positions of Alice, Bob and Eve on nodes M0 and M4. Bottom right: spectrograms of the received signals at the hydrophones of Alice and Bob. The colorbar represents the signal power in logarithmic scale.

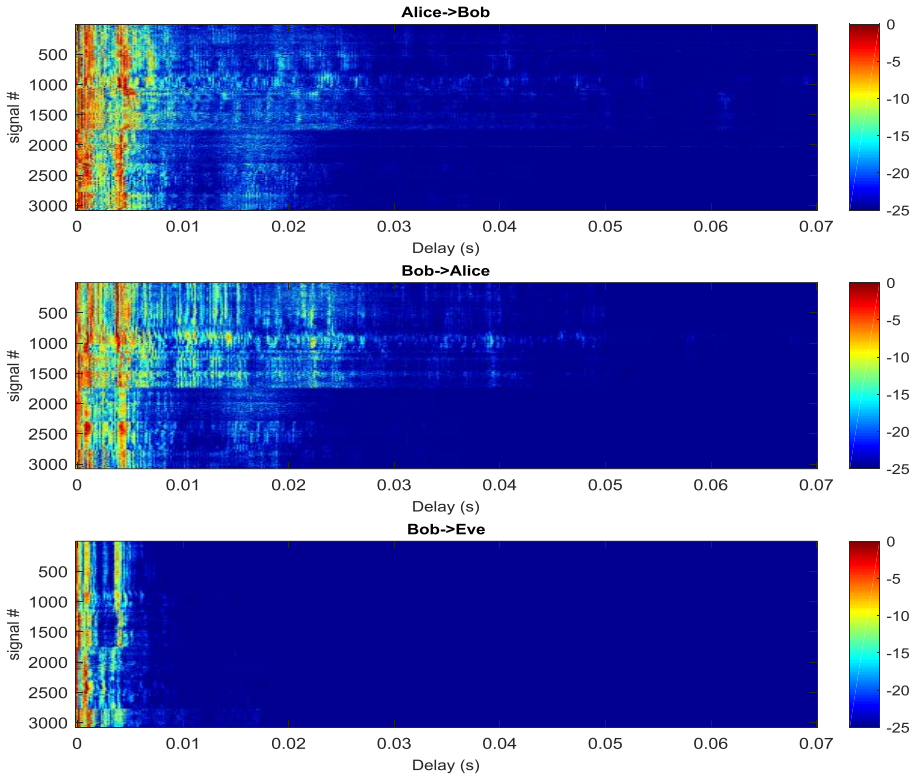


Fig. 3. Snapshots of the estimated CIRs of Alice-to-Bob, Bob-to-Alice and Bob-to-Eve links. The horizontal axis represents multipath delay, the vertical axis represents the signal probe number in transmission order. The colorbar represents the amplitude in logarithmic scale.

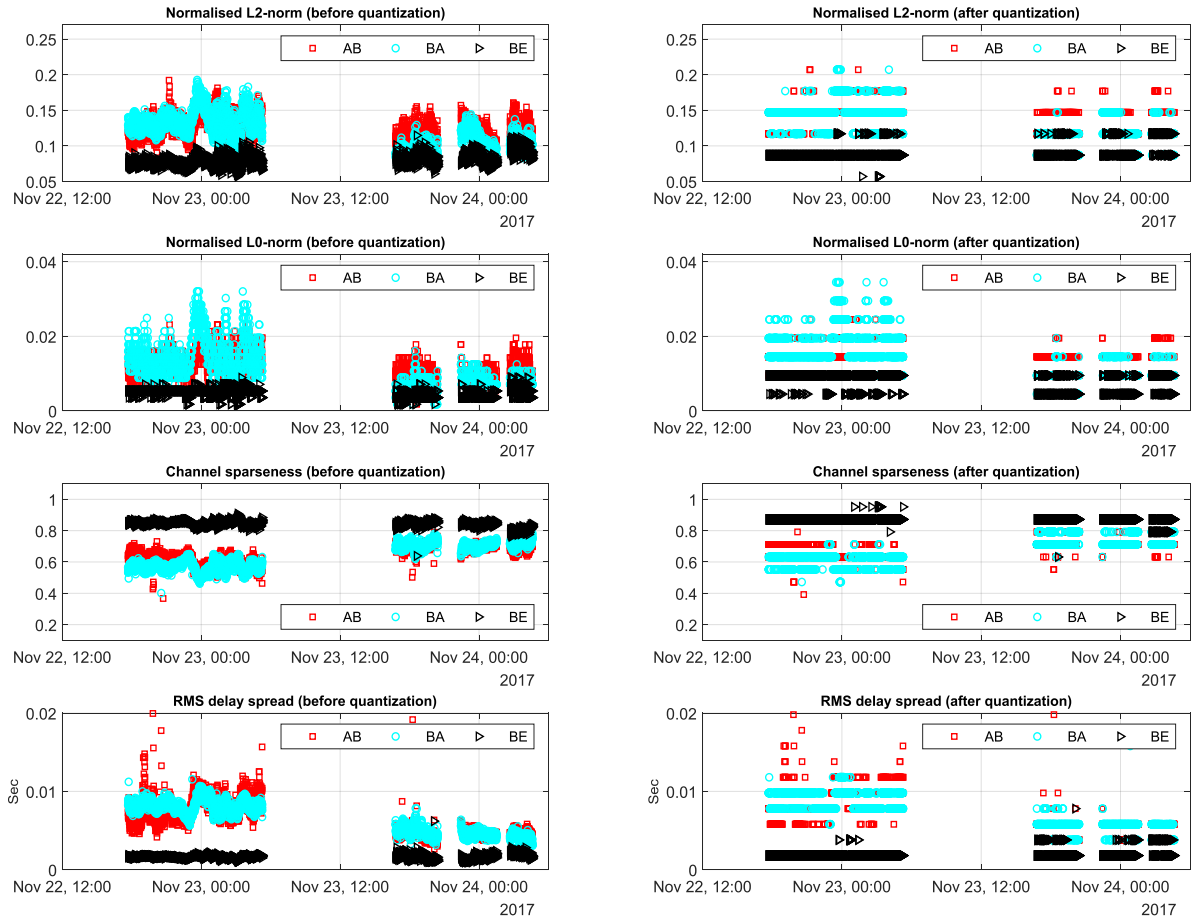


Fig. 4. The computed channel features unquantised (left) and quantised (right) for the Alice-to-Bob (AB), Bob-to-Alice (BA), Bob-to-Eve (BE) links.

Fig. 5 shows the computed BDR vs. time for all four features. Note that Eve's computed BDR for L_2/L_0 norm is similar to that of Alice-Bob after November 23rd, 12:00 pm. This result challenges the suitability of those parameters for this type of environment. Table 1 presents the BDR averaged over the entire experiment as well as the number of 32-bit key agreements per channel probe. Note that the channel sparseness, β, shows the smallest BDR ratio and so yields the best performance out of all proposed features. In addition, we see that Eve managed to get only one 32-bit key agreement out of 3078 probes when computing β. On the contrary, Alice got 1715 key agreements, which translates into three orders of magnitude higher probability to get the correct key than Eve.

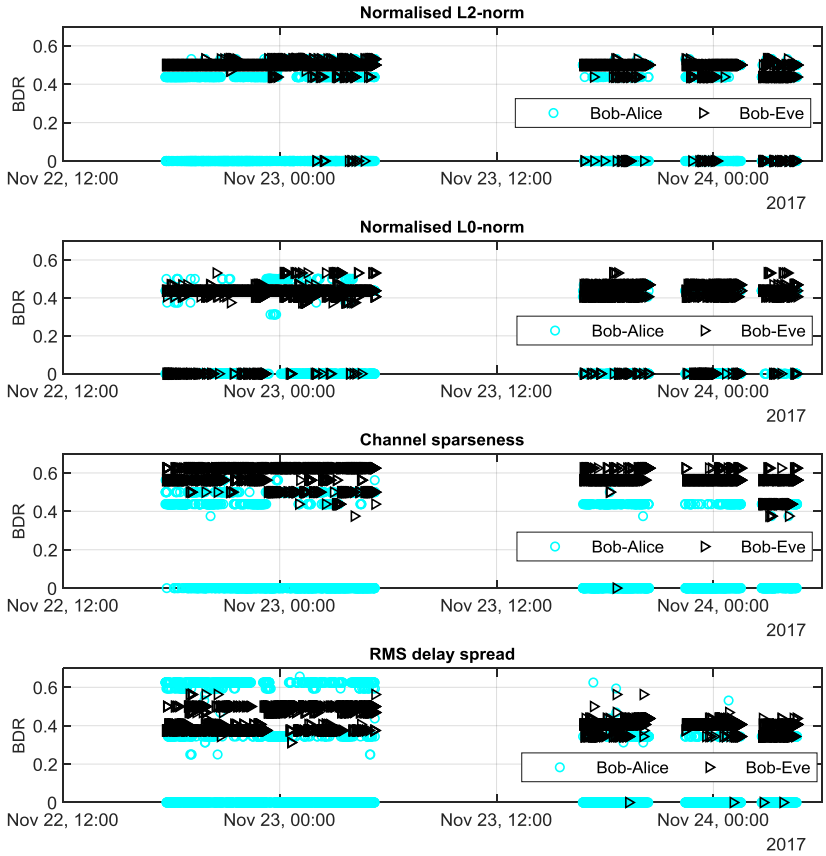


Fig. 5: BDR between Alice-Bob and Bob-Eve for normalised L_2 norm, normalised L_0 norm, channel sparseness, RMS delay spread.

Channel feature	$\overline{BDR}_{AB}$	$\overline{BDR}_{BE}$	$\frac{\overline{BDR}_{AB}}{\overline{BDR}_{BE}}$	# of key agreements Alice-Bob	prob. of key agreement Alice-Bob	# of key agreements Bob - Eve	prob. of key agreement Bob - Eve
Normalised L_2 norm	0.26	0.48	0.55	1333	0.43	106	0.034
Normalised L_0 norm	0.26	0.39	0.66	1268	0.41	339	0.110
Channel sparseness	0.20	0.58	0.35	1715	0.56	1	$3.2 \cdot 10^{-4}$
RMS delay spread	0.19	0.42	0.45	1890	0.61	4	$1.2 \cdot 10^{-3}$

Table 1: average BDR and number of 32-bit key agreements per channel probe between Alice-Bob and Bob-Eve.

4. CONCLUSION

In this work, we proposed four CIR features for symmetric key generation between two legitimate nodes, Alice and Bob. These were the L_2/L_0 norm, a smooth metric of channel sparseness and the RMS delay spread. After analysing a large set of channel probes transmitted

in a short-range, shallow water environment, we found that all features exhibited highly correlated values and so they are suitable for independent key generation between Alice and Bob. However, in the particularly challenging scenario where Eve is about a meter away from Alice, the smooth channel sparseness showed superior performance. In particular, we found that the probability of Alice-Bob key agreement was three orders of magnitude higher than that for Bob-Eve. Key reconciliation and privacy amplification will be pursued as a future work.

ACKNOWLEDGEMENTS

This work was supported by the NATO Allied Command Transformation (ACT) Future Solutions Branch under the Autonomous Security Network Programme and the Office of Naval Research Global under grant no N62909-17-1-2093

REFERENCES

[1] **J. Buchmann**, *Introduction to Cryptography*, Springer, New York, NY, 2004.
[2] **T. Melodia, H. Khulandjian, L.-C. Kuo, and E. Demirors**, *Advances in underwater acoustic networking,* in Mobile Ad Hoc Networking: Cutting Edge Directions, Hoboken, NJ, USA: Wiley, ch. 23, pp. 804-852, 2013.
[3] **G. Ferri *et al***., *Cooperative robotic networks for underwater surveillance: an overview*, IET Radar, Sonar & Navigation, vol. 11, no. 12, pp. 1740-1761, 2017.
[4] **M. Domingo**, *Securing underwater wireless communication networks*, IEEE Wireless Communications, vol. 18, no. 1, pp. 22–28, 2011.
[5] **G. Han, J. Jiang, N. Sun, and L. Shu**, *Secure communication for underwater acoustic sensor networks*, IEEE Communications Magazine, vol.53, no.8, pp.54-60, 2015.
[6] **C. Lal, R. Petroccia, K. Pelekanakis, M. Conti and J. Alves**, *Toward the Development of Secure Underwater Acoustic Networks*, IEEE Journal of Oceanic Engineering, vol. 42, no. 4, pp. 1075-1087, 2017.
[7] **M. A. Simplício et al**, *A survey on key management mechanisms for distributed wireless sensor networks*, Computer Networks, vol. 54, no. 15, pp. 2591–2612, 2010.
[8] **S. Seo, J. Won, S. Sultana and E. Bertino**, *Effective Key Management in Dynamic Wireless Sensor Networks*, IEEE Transactions on Information Forensics and Security, vol. 10, no. 2, pp. 371-383, 2015.
[9] **K. Ren, H. Su and Q. Wang**, *Secret key generation exploiting channel characteristics in wireless communications*, IEEE Wireless Communications, vol. 18, no. 4, pp. 6-12, 2011.
[10] **K. Zeng**, Physical layer key generation in wireless networks: challenges and opportunities, *IEEE Communications Magazine*, vol. 53, no. 6, pp. 33-39, 2015.
[11] **J. Zhang, T. Q. Duong, A. Marshall and R. Woods**, Key Generation From Wireless Channels: A Review, *IEEE Access*, vol. 4, pp. 614-626, 2016.
[12] **Y. Liu, J. Jing, and J. Yang**, *Secure underwater acoustic communication based on a robust key generation scheme*, in 9th International Conference on Signal Processing, pp. 1838-1841, 2008.
[13] **Y. Luo, L. Pu, Z. Peng, and Z. Shi**, *RSS-based secret key generation in underwater acoustic networks: advantages, challenges, and performance improvements*, IEEE Communications Magazine, vol. 54, no. 2, pp. 32–38, 2016.
[14] **Y. Huang, S. Zhou, Z. Shi, and L. Lai**, *Channel frequency response-based secret key generation in underwater acoustic systems*, IEEE Transactions on Wireless Communications, vol. 15, no. 9, pp. 5875–5888, 2016.

[15] **C. Wang and Z. Wang**, *Signal alignment for secure underwater coordinated multipoint transmissions*, IEEE Transactions on Signal Processing, vol. 64, no. 23, pp. 6360–6374, 2016.

[16] **R. Diamant, P. Casari, and S. Tomasin**, *Cooperative authentication in underwater acoustic sensor networks*, IEEE Transactions on Wireless Communications, vol. 18, no. 2, pp. 954–968, 2019.

[17] **P. A. van Walree**, Propagation and Scattering Effects in Underwater Acoustic Communication Channels, IEEE Journal of Oceanic Engineering, vol. 38, no. 4, pp. 614-631, 2013.

DATA COLLECTION IN SHALLOW FRESH WATER SCENARIOS WITH LOW-COST UNDERWATER ACOUSTIC MODEMS

Filippo Campagnaro[a], Fabian Steinmetz[b], Alberto Signori[a], Davide Zordan[a], Bernd-Christian Renner [b], Michele Zorzi[a]

[a]Department of Information Engineering, University of Padova,
via Gradenigo 6/B, 35131 Padova, Italy
[b] Research Group smartPORT, Hamburg University of Technology,
Am Schwarzenberg-Campus 1, 21073 Hamburg, Germany

Contact author: Filippo Campagnaro, Department of Information Engineering, University of Padova, via Gradenigo 6/B, 35131 Padova, Italy, email: campagn1@dei.unipd.it, telephone number: +39 049 827 7778.

Abstract: The Robotic Vessels as-a-Service (RoboVaaS) project intends to exploit the most advanced communication and marine vehicle technologies to revolutionise shipping and near-shore operations, offering on-demand and cost-effective robotic-aided services. In particular, the RoboVaaS vision includes a ship hull inspection service, a quay walls inspection service, an antigrounding service, and an environmental and bathymetry data collection service. In this paper, we present a study of the underwater environmental data collection service, performed by a low-cost autonomous vehicle equipped with a very low-cost acoustic modem and moving within a network of submerged acoustic sensor nodes. To this end, an underwater acoustic network composed by both static and moving nodes has been implemented and simulated with the DESERT Underwater Framework, where the performance of the smartPORT Acoustic Underwater Modem have been mapped in the form of lookup tables. The performance of the modem has been measured near the Port of Hamburg, where the RoboVaaS concept will be demonstrated with a real field evaluation.

Keywords: Underwater acoustic network simulations, DESERT Underwater, AHOI modem.

1 INTRODUCTION

Today, 90% of transported goods are waterborne [1]: the Robotic Vessels as-a-Service (RoboVaaS) project [2] intends to reorganize this sector by exploiting the most advanced communication technologies to interconnect unmanned vessels (UVs), such as autonomous surface vessels (ASVs), and autonomous underwater vehicles (AUVs). The main goal of this project is to offer on-demand robotic-aided services, requiring the capabilities of both Internet of Things (IoT) and Internet of Underwater Things (IoUT) [3,4] devices. The RoboVaas project

intends to identify those services, beneficial for near-shore maritime operations, that have a strong positive impact on automation and digitization. These include, among others, a data collection service with a wide range of applications, such as measuring environmental data with an underwater sensor network. In this paper we refer to this service, which requires the deployment of a low-cost underwater sensor network (UWSN). In this application, an AUV patrols the area and collects data from the UWSN, equipped with a low cost underwater acoustic modem, the smartPORT Acoustic Underwater Modem (AHOI) [5] (presented in Section 2). In order to retrieve the data from such network, we design a polling-based Medium Access Control (MAC) protocol (Section 3), tailored to the needs of an UWSN [6]. In Section 4, we evaluate the proposed solution via simulations based on field measurements, and, finally, in Section 5, we draw our concluding remarks.

2 SMARTPORT ACOUSTIC UNDERWATER MODEM

This section presents the smartPORT Acoustic Underwater Modem (AHOI) [5].

The AHOI modem is a small, low-power and low-cost acoustic underwater modem (see Fig. 1), developed to be integrated into micro AUVs or UWSNs. The modem consists of three stacked Printed Circuit Boards (PCB) with an overall size of 50x50x25 mm^3 and a component cost of about €200. The first PCB includes a CortexM4 microcontroller, power supply and external connections. In addition, the second PCB works as the receiver and involves amplifiers, a bandpass filter and an analog-to-digital converter. To receive acoustic signals with different signal strength, the amplifier gains are software adjustable (overall amplification between 40-96 dB). In the default setup, a software-based automatic gain control is used to adjust the amplifier gains. Finally, the third PCB is the transmission board including a digital-to-analog converter and a power amplifier. The power consumption in idle and receive mode is around 300 mW and 2.1 W during data transmission with highest amplification. For the acoustic signal reception and transmission, the AHOI modem uses an Aquarian Scientific AS-1 broadband measurement hydrophone with a price of about €400. In the case of the highest power amplifier level and a transmission in the 50-75 kHz range, the transmission source level is between 150-160 dBre1μPa^2@1m with an AS-1 hydrophone.



Fig. 1: AHOI acoustic underwater modem with hydrophone.

Signal processing is realized in software on the microcontroller, which allows a fast reconfiguration of frequency and coding setups. In the default setup, the modem uses an orthogonal binary frequency shift keying (BFSK) with 2.56 ms symbol duration and a 781.25 kHz frequency spacing. Each symbol consists of four superimposed sinusoidal waveforms. To counter frequency cancellations caused by multi-path propagation, each bit is repeated on three different carriers, and frequency hopping (FHSS) is applied to avoid inter-symbol interference. All in all, the modem has 25 kHz of bandwidth around a central frequency of 62.5 kHz. The default setup in combination with a Hamming coding leads to a net data rate of 260 bps (up to 4.7 kbps are feasible).

2.1 Modem's performance in very shallow water

A real-world evaluation was performed in a marina in southern Hamburg. The marina is located in a branch of the river Elbe, where depth ranges from 3.5 m to 7.5 m depending on the tide. The experiments were performed on Nov. 11, 2018. In total six AHOI modems were deployed on a jetty, one modem acted as the sender and the other five as the receivers. All hydrophones were submerged 1.5 m under the water surface and each modem was connected to a laptop to record the received packets.

During the evaluation, packets with different payload lengths were transmitted. In each setup the sender sent 200 packets with randomly generated payload. Table 1 contains the packet delivery rate (PDR) of the five receivers for 16, 32, and 96 bytes payloads. In this test, the node deployed 99 m far from the transmitter received more packets than the node at 24 m due to the effects of multipath and automatic gain control (the receiver at 99 m used a higher gain than the receiver at 24 m, as the latter had to employ a low gain to avoid saturation).

Size [Bytes]	*PDR@12 m*	*PDR@24 m*	*PDR@46 m*	*PDR@99 m*	*PDR@152 m*
16	96.5%	75.0%	89.5%	88.0%	84.5%
32	95.0%	70.0%	88.5%	99.0%	51.5%
96	77.0%	92.0%	83.0%	100.0%	n.a.

Table 1: Packet delivery rate achieved during the real-world evaluation in a marina in Hamburg.

2.2 Modem's reaction to shipping noise

The typical range of applications of UWSN include marinas, ports and rivers with high shipping activity. Each vessel produces acoustic noise, caused by propellers, machineries and other effects [7]. For this reason, in order to provide a stable communication link, the AHOI modem must be robust against vessel noise. The acoustic noise emitted by ships and vessels has highest power spectral density (PSD) below 10 kHz, which is smaller than the communication frequency range. In addition, the AHOI modem receiver involves a bandpass filter between 50 kHz and 75 kHz. Furthermore, a simulation was performed to prove the stability against vessel noise. The noise was generated offline and added to different recorded packets. A single AHOI modem was used to receive the signal, which was generated with an arbitrary signal generator (TiePie Handyscope HS5, 200 kHz sampling). The signal generator simulated the received hydrophone voltage for different PSDs. During the simulations a constant receiving sensitivity of -208 dBV re 1 µPa for frequencies up to 100 kHz was assumed. Fig. 2 shows the PSDs of received packets at the receiver side. At first, the packets were transmitted without additional vessel noise. In the following simulations, different noise profiles were added to the packets.

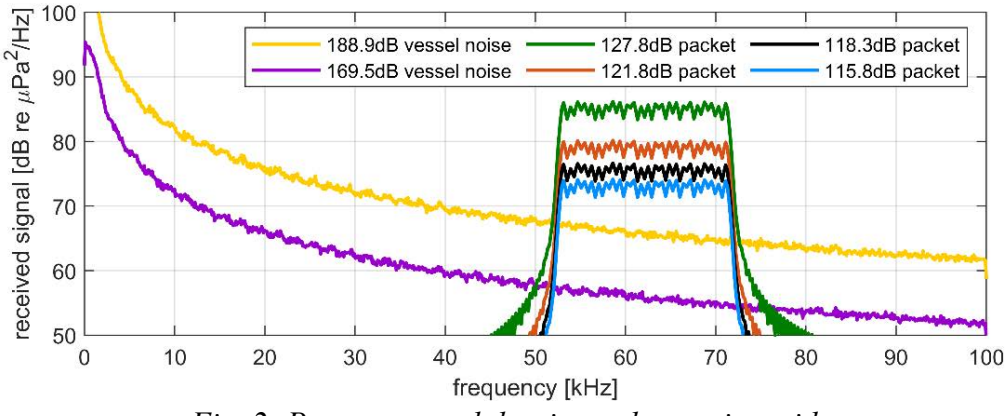


Fig. 2: Power spectral density at the receiver side.

The noise profiles were generated according to [7] and are shown in Fig. 2. For each combination of vessel noise level and communication signal strength, 100 packets (with 32 B payload) were transmitted. In all cases, the AHOI modem received all packets.

2.3 Modem's reaction to interference

In addition to the vessel noise discussed in Section 2.2, other underwater modems in a network could disturb the transmission. To evaluate the effect of packet interference and the resulting PDR, the described hardware setup in Section 2.2 was used. Instead of additional simulated vessel noise, a second recorded packet was added to the generator samples. All packets carried 32B payload and had a signal duration of 1.311 s, including the synchronization symbols. Fig. 2 displays PSDs of the different transmitted packets. Three different interference situations were simulated, for different degrees of overlap between the intended packet and the interfering packet, based on the time displacement between the two: (i) 0 s delay (100% overlap), (ii) 0.5 s delay (61.9% overlap), and (iii) 1 s delay (23.7% overlap). In addition, reception without any interference was also simulated (0% overlap). For each combination of communication signal strength and delay, 100 packets were transmitted.

The PDR has been measured by varying the interference component and its performance mapped in the simulator. Specifically, the Signal to interference Ratio (SIR) component has been calculated by employing the mean power model, computed as $SIR = Pr/(Pi \cdot ovr)$, where *Pr* is the power received by the signal carrying the data packet, *Pi* the power of the interfering signal and *ovr* the overlap percentage of the two signals, calculated as the portion of time the two signals are interfering divided by the total packet duration. The measurements are reported in Table 2.

Rx power [dB re μPa²@1m]	*Interf Rx power [dB re μPa²@1m]*	*Overlap*	*SIR [dB] (mean power)*	*PDR*	*average PDR*
127.8, 121.8, 118.3, 115.8	Same as Rx power	100.0%	0	0%	0.0%
121.8	127.8	23.7%	0.248	0%	0.0%
127.8, 121.8, 118.3, 115.8	Same as Rx power	61.9%	2.086	12%, 36%, 46%, 40%	33.5%
118.3	115.8	100%	≥2.5	100%	100%

Table 2: AHOI modem's reaction to interference.

In order to extend the measurements and model them in the simulator, we interpolated the samples by employing the Piecewise Cubic Hermite Interpolating Polynomial (PCHIP) with Matlab, obtaining the line depicted in Fig. 3.

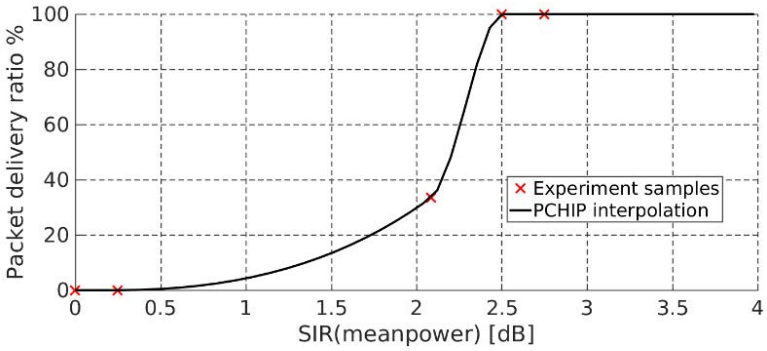


Fig. 3: Packet delivery ratio vs Signal to Interference Ratio, with PCHIP interpolation.

The AHOI modem performance figures have been included in the form of lookup-tables (LUTs). In particular, the PDR vs distance has been mapped to obtain the modem's behaviour in case of absence of interference. In addition, the PDR vs SIR LUT sampled by the PCHIP interpolation line presented in Fig. 3 has been included in the simulator, to obtain the penalty introduced by the interference. The resulting packet delivery ratio is approximated as $PDR = PDR(d) \cdot PDR(SIR)$, where $PDR(d)$ is the packet delivery ratio obtained at a distance d, while $PDR(SIR)$ is the packet delivery ratio obtained in ideal conditions with signal to interference ratio equals to SIR.

3 POLLING MAC PROTOCOL

Both [8] and [9] demonstrated that a polling-based MAC layer suits well underwater data-muling scenarios: in the uwpolling protocol [8], the AUV first triggers the channel and then waits for the static nodes to answer with a probe, that contains information on how much data the static node needs to transmit to the AUV. Before probing the channel, the static nodes wait for a back-off time randomly generated within a maximum interval *TbMax*. Then, the AUV sends a poll packet to assigns each static node the time interval within which that node can transmit its own data packets. In [9] the authors demonstrated that if the propagation delay is bigger than the packet duration and the distances from the AUV to the static nodes span a wide range, *TbMax* can be set to 0 to maximize the throughput, without increasing the probability of packet collisions. This result is not applicable in our scenario, where the packet duration can be bigger than the propagation delay, since many nodes are deployed within a range of 100 m, and the modem bit rate is 260 bps.

The protocol employed in our simulations is an enhanced version of uwpolling. In this protocol, the AUV first wakes up the surrounding nodes with a Trigger packet (*TrP*). Then each node *i* that received *TrP* and has data to transmit sends back a Probe packet (*PrP*) to the AUV containing the number of packets it needs to transmit ($P_{EXP,i}$). The transmission of *PrPs* is contention-based: each node waits for a random back-off period, up to a Maximum Backoff Time (*TbMax*), before transmitting its own *PrP*. After this first phase, the AUV selects the nodes to be polled in order, according to a fair policy: for each node *i* that successfully probed the channel, the AUV computes the weight $wgt_i = P_{EXP,i} / P_{RX,i}$, with $P_{RX,i}$ equal to the total number of packets received by the AUV from node *i* at that moment, and orders the nodes according to *wgt*. If no *PrP* has been received by the AUV within a Maximum Trigger Timeout (*MTT*) bigger than *TbMax* + *RTT*, or after the AUV finishes to poll all nodes of the list, the AUV transmits a new *TrP*.

The uwpolling protocol provides also the possibility to use a sink node different from the AUV, to which to upload the data collected by the AUV [10]. To use this feature with the AHOI modem, data compression techniques should be investigated in order to forward all the data collected from the AUV when the sink is in the range of the vehicle. This solution will be part of our future work.

4 SIMULATIONS

In Section 4.1 we describe the simulation settings and the simulation scenario, while in Section 4.2 we present the simulation results.

4.1 Simulation settings and scenario description

In our scenario the water conditions are the same as in the experiment presented in Section 2.1: the water column between 3 and 7 meters deep, and the nodes are deployed 1.5 meters below the sea surface. Each node is equipped with an AHOI modem with carrier frequency 65.2 kHz, bandwidth 25 kHz, payload data rate (computed as the packet size, in bits, divided by the total packet duration, including the preamble, in seconds) of 200 bps, and transmission power 156 dB re μPa^2@1m. The packet size is set to 256 bits, and each polled node transmits 5 data packets. The protocol is evaluated in different working conditions, where the AUV speed (v) is varied from 0.1 m/s to 4 m/s, and the node density (N), defined as the number of nodes within the coverage area of the AUV (circular area, with a radius of 110 meters), is varied from 3 to 30 nodes. A realization of the scenario with $N = 6$ is depicted in Fig. 4. The nodes position (blue dots) is set randomly, along the AUV path (red line). The AUV performs 7 laps of the same path, 1.6 km long, moving at a constant speed during each simulation run. The system is simulated with the DESERT Underwater framework.

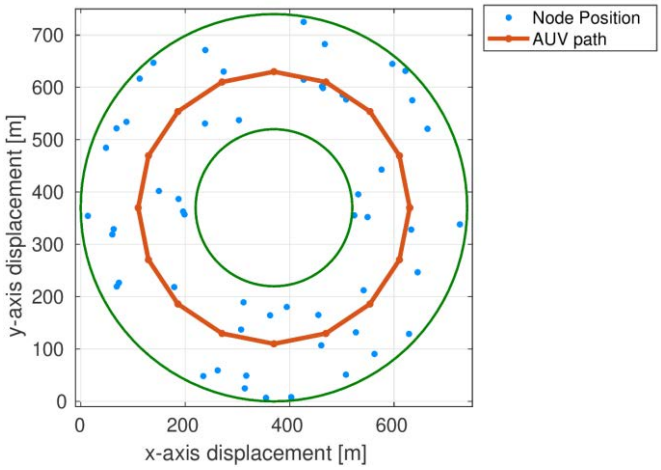


Fig. 4: Network scenario. The AUV path is described by the solid red line. The solid green lines define the area in which nodes are randomly placed

4.2 Simulation results

In this section we present the simulation results obtained by varying the node density and the AUV speed. The results are obtained averaging over 20 independent simulation runs. All the simulations are performed considering that each node always transmits 5 data packets when it is polled by the AUV. The analysed performance metrics are the throughput (*THR*) and Jain's Fairness Index (*JFI*), computed as

$$THR = \sum_{i}^{n} x(i) \cdot sz \cdot T^{-1}, \quad \text{and} \quad JFI = \left(\sum_{i}^{n} x(i) \right)^{2} \cdot \left(n \sum_{i}^{n} x(i)^{2} \right)^{-1}, \tag{1}$$

where *x(i)* is the number of packets received by the AUV from node *i*, *n* is the total number of nodes in the whole network, *sz* is the packet size, in bits, and *T* is the total simulation time, in seconds.

In Fig. 5 (a) the overall throughput of the network is reported as a function of the maximum backoff time *TbMax* for different values of the node density *N*. For $N = 6$, the throughput first increases as *TbMax* increases by reaching a maximum peak value of 58 bps for *TbMax* = *TbOp(6)*=8 s. With *TbMax* lower than 8 s the collision of probe packets at the AUV is very likely, thus many probe packets will not be received, and in turn a lower number of nodes will

be polled in the subsequent polling round. When *TbMax* is greater than 8 s the throughput starts to decrease as well, since some of the triggered nodes may get out of the transmission range of the AUV after waiting *TbMax* seconds. A similar behavior occurs also for $N = 3$ and $N = 10$, where *TbOp(3)* = 6 s and *TbOp*(10) = 14 s, respectively. For $N = 30$, *TbOp*(30) = 28 s, but the maximum throughput becomes 16% lower than with $N = 6$, because 28 s is enough to avoid collisions, but in that amount of time the AUV already moved 56 m away from the position in which it sent the trigger, leading to a large number of triggered nodes out of range.

With $N = 3$, $N = 6$ and $N = 10$, a *TbMax* = *TbOp(N)* provides a *JFI* of 0.89, 0.85 and 0.8, respectively, that is close to the maximum *JFI* reachable with those densities (Fig. 5 (b)). Therefore, in these cases the choice *TbMax* = *TbOp(N)* provides a good fairness as well. On the other hand, with $N = 30$, the AUV is not able to serve in a fair way all the nodes in the network, indeed the maximum *JFI* value obtained is equal to 0.58.

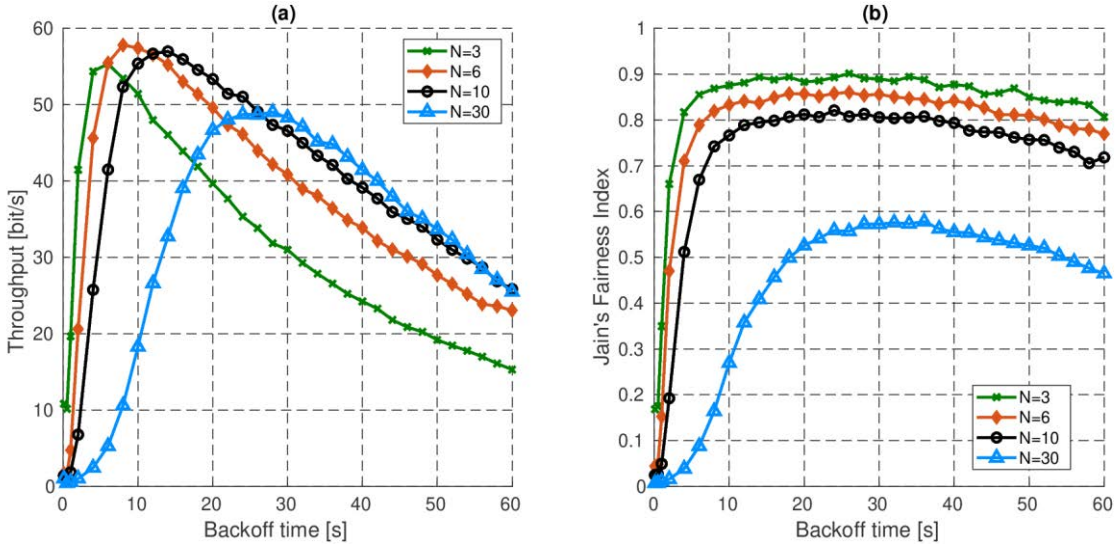


Fig. 5: Throughput of the network (a) and JFI (b) vs backoff time, for different values of the node density N.

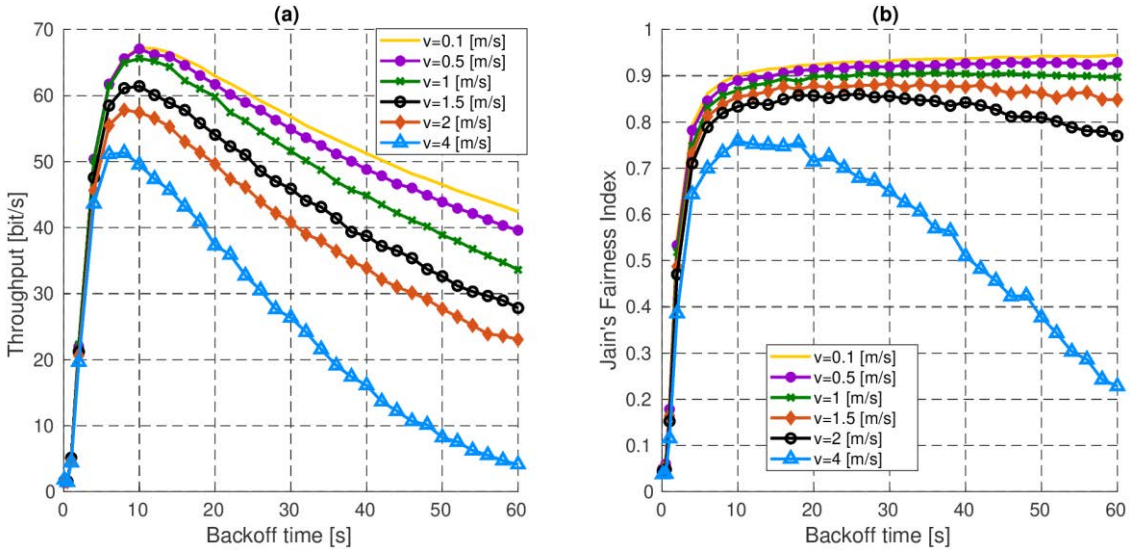


Fig. 6: Throughput of the network (a) and JFI (b) vs backoff time, for different values of the AUV speed v.

Fig. 6 (a) depicts the overall throughput of the network as a function of the maximum backoff time with $N = 6$, by varying the AUV speed *v* between 0.1 m/s and 4 m/s. The peak for

the overall throughput is reached, on average, around $TbMax = TbV = 10$ s, with small differences in the peak positions when varying the AUV speed. When *TbMax=TbV, JFI* is almost maximized for $v \leq 2$ m/s (see Fig. 6 (b)). On the other hand, with a speed of 4 m/s, the nodes are not served in a fair way because the AUV moves too fast, and many triggered nodes become out of range due to the new AUV position.

5 CONCLUSIONS

In this paper, we proved the feasibility of a data-muling application with the very low-cost AHOI modem, via simulations based on real field measurements. The proposed polling protocol ensures fairness to all nodes for AUV speeds up to 2 m/s. This encourages us tu pursue further developments, aimed at the optimization of the protocol and at the evaluation of the system in a real field test.

ACKNOWLEDGEMENTS

This work has been supported in part by the Italian Ministry of Education, University and Research (MIUR), the German Federal Ministry for Economic Affairs and Energy (BMWi, FKZ 03SX463C), and ERA-NET Cofound MarTERA (contract 728053).

REFERENCES

[1] Inernational Chamber of Shipping, “Key Facts,” Last time accessed: April 2019. [Online]. Available: http://www.ics-shipping.org/shipping-facts/key-facts

[2] RoboVaaS - Robotic Vessels as-a-Service, Last time accessed: April 2019. [Online]. Available: *https://www.martera.eu/projects/robovaas*,

[3] **R. Guida, E. Demirors, N. Dave, J. Rodowicz, and T. Melodia**, “An Acoustically Powered Battery-less Internet of Underwater Things Platform”, UComms, Lerici, Italy, 2018

[4] “SUNRISE: Building the internet of underwater things.” Last time accessed: May 2019. [Online]. Available: http://fp7-sunrise.eu/

[5] **C. Renner and A. J. Golkowski**, “Acoustic Modem for Micro AUVs: Design and Practical Evaluation,” in Proc. of the 11th ACM International Conf. on Underwater Networks & Systems (WUWNet), Shanghai, China, Oct. 2016

[6] **C. Audoly and E. Rizzuto,** “Ship underwater radiated noise patterns,” AQUO Project Consortium, final report R2.9, 06 2015.

[7] **F. Favaro, P. Casari, F. Guerra, and M. Zorzi**, “Data upload from a static underwater network to an AUV: Polling or random access?” in Proc. MTS/IEEE Oceans, Yeosu, Republic of Korea, May 2012.

[8] **W. Liu, J. Weaver, L. Weaver, T. Whelan, R. Bagrodia, P. A. Forero**, **and J. Chavez,** “Adaptive Polling for Underwater Data Collection Systems”, MTS/IEEE Oceans, Charleston, US, October 2018

[9] **J. Heidemann, M. Stojanovic, and M. Zorzi,** “Underwater sensor networks: applications, advances and challenges”, Phil. Trans. of the Royal Society 2012, vol. 370, no. 1958, pp 158-175

[10] **F. Campagnaro, D. Zordan, A. Signori, F. Favaro, and M. Zorzi**, “Underwater Acoustic Sensors Data Collection in the Robotic Vessel as-a-Service Project”, in Proc. MTS/IEEE Oceans, Marseille, France, June 2019

A MIMO Underwater Acoustic Transmitter Implementation with Space-Time Block Coding

Surinder Singh, Afolarin Egbewande, Anthony Chalmers,
Ryan Taylor, Jack de Gooyer and J.-F. Bousquet
Electrical and Computer Engineering
Dalhousie University
Halifax, Nova Scotia B3H 4R2
Email: s.singh@dal.ca

Abstract: *Underwater acoustic communication is sensitive to the environmental conditions. To optimize the link autonomously, a reconfigurable platform is highly desired. In this work, a multiple-input multiple output (MIMO) reprogrammable physical layer is implemented to enable a software defined modem (SDM). An Alamouti space-time block code is proposed to improve the reliability. The focus is on the the physical layer, and a platform is implemented to test the communication link reliability for a bit rate as high as 30 kbps, and for a range approaching two kilometers.*

Keywords: *software defined modem, reconfigurable transmitter, frequency shift keying, space-time block code, Alamouti code, diversity gain*

1 Introduction

Our society is confronted to global warming, and it has been recognized that monitoring and harnessing our ocean may help optimize resources that have been yet unavailable. To deploy remote infrastructure, the next generation underwater communications systems needs to have better quality, range, power and bandwidth efficiency, and be deployed in diverse environments.

Underwater acoustic transmission is inherently subject to channel distortion due to multipath and Doppler. Moreover, the channel characteristics can vary significantly as a function of the environmental conditions [1, 2].

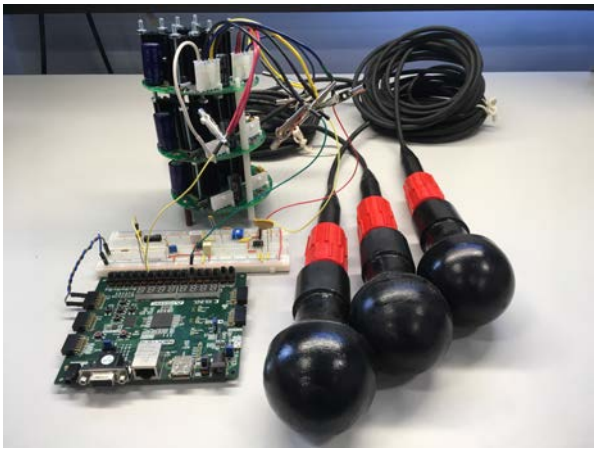
In this work, a software defined modem (SDM) is proposed to maintain a reliable high speed communication link in variable channel conditions. The SDM has been described previously for example in [3, 4]. Here, a fully custom design allows to test different modulation techniques, at a maximum bit rate of 30 kbps, and for a maximum range close to 2 km. Furthermore, to maintain reliability a space-time block code (STBC) is proposed to enable a multiple-input multiple-output (MIMO) communication link. While the communication reliability of the Alamouti STBC code is well understood when combined with coherent communication systems, in this work, we also show how to utilize the Alamouti code using continuous phase frequency shift keying (CPFSK), where the modulation index and alphabet of CPFSK is adjusted to accommodate different channel conditions [5, 6].

This paper is organized as follows: in Section 2, the structure of the prototyping hardware to test a communication link with a throughput as high as 30 kbps, (using 64-CPFSK) will be explained; then, in Section 3, the reconfigurable program on a field programmable gate array (FPGA) will be described; in Section 4, the expected performance of the STBC MIMO communication system will be evaluated coarsely; finally, in Section 5, the conclusion will be presented.

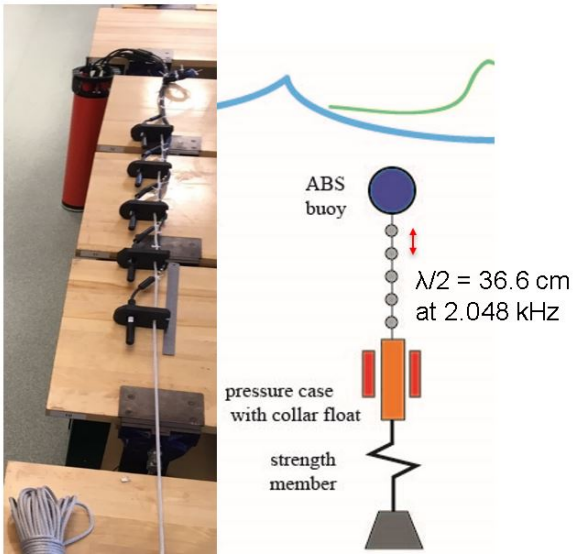
2 A Hardware Front-End to Enable High-Speed Transmission

In this section, the system characteristics for a MIMO testbed to enable a reconfigurable communication platform will be described. The objective is to implement a transmitter that is flexible and can test a variety of coded modulation techniques, and can also characterize the channel characteristics.

A custom prototyping platform is developed to test the performance of a variety of underwater communication techniques in different sea conditions that range up to a few kilometers. A 5-element vertical line array receiver shown in Figure 1b consists of wideband hydrophones with high-sensitivity, and can record data for several days. Real-time streaming of the acoustic data is also available at the receiver through a surface buoy equipped with a radio-frequency communication transceiver; that can enable a low-latency reverse link to enable the SDM.



(a) Transmitter hardware.



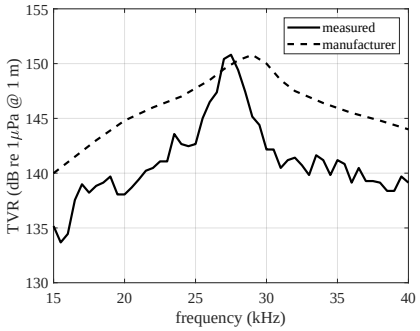
(b) Receiver.

Figure 1: The Communication System Hardware Platform.

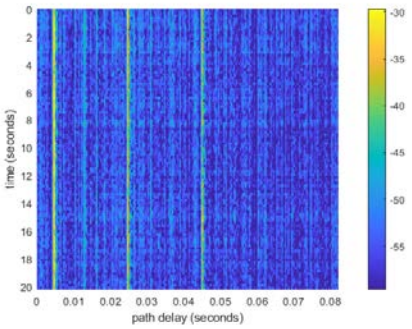
The transmitter shown in Figure 1a consists of three narrowband omnidirectional sound sources with a center frequency close to 28 kHz. The signal is amplified to a maximum of $V_{TX} = 25.4$ V_{RMS} using a linear power amplifier (PA) that is directly interfaced to the source. A 5-meter cable serves to deploy the sources from a pier or vessel, while keeping the electronics on the deck.

The transmit voltage response (TVR) of the sound source is verified as shown in Figure 2a. The testing was accomplished in a 1 m^3 tub, which limited the resolution of the calibration. Nonetheless, a coarse frequency response has been obtained. As can be observed, there is a degradation in the bandwidth of the transducer (the manufacturer bandwidth is over 5 kHz, while the measured bandwidth is closer to 2.5 kHz) and this is attributed to the poor match between the PA output and the transducer.

The maximum range of the system is estimated using a link budget. For this purpose, the underwater ambient noise P.S.D. is calculated using Urick's ambient noise model [7]. For low shipping activity, and wind speed on the order of 10 m/sec, the total P.S.D due to flow noise, shipping activity, surface noise, and thermal noise is estimated to be 67 dBm/Hz. As such, to achieve an SNR at the receiver equal to 10dB



(a) Measured Transmit Voltage Response.



(b) Channel impulse response as a function of time.

in bandwidth of 5 kHz, the minimum signal intensity level $\mathrm{SIL_R}$ at the receiver is $\mathrm{SIL_R} = (67 + 10\log(5000) + 10)$ which is equal to $\mathrm{SIL_R} = 113.9$ dBm re 1μPa.

Then, for a transmit power equal to $\mathrm{SIL_T} = 150.2 + 20\log_{10}(25.4)$, which equates to 178.3 dBm re 1μPa, it can found that the maximum transmission loss $\mathrm{TL_M}$ is 64.3 dB. This is obtained for a distance of approximately $10^{\mathrm{TL_M}/20} = 1600$ meters. Note that here the effect of absorption at 28 kHz is neglected. To increase the distance further, spread spectrum techniques can be applied at the expense of throughput.

The transmitter can be programmed to generate a variety of modulation schemes, including M-QAM, M-FSK, as well a linear frequency modulation (LFM). The probing sequence consists of a maximum length shift register pseudo-random noise (PRN) sequence. Optionally, the transmitter can be encoded using an error correction code to improve reliability. For easy experimentation at sea, the transmitter modem is configured using a graphical user interface.

An experiment was run in a 4-meter deep, 15-meter diameter seawater pool to confirm the ability of the prototyping system to extract the channel impulse response from multiple transmit elements. During the experiment, sequences were transmitted with and without waves at the surface. The three channel impulse responses with waves are shown in Figure 2b. Because the PRN sequences are delayed with respect to each other by 100 symbols, the three channels are separated by 20 msec. Given the PRN duration equal to 0.1 msec, this is acceptable for relatively benign sea multpath conditions. In the next section, the structure of the program on FPGA to enable the SDM will be described.

3 The Reconfigurable Modem

In this Section, the reconfigurable digital platform will be described. The underwater acoustic transmitter firmware is implemented on an Artix-7 FPGA from Xilinx. The transmitter performs encoding, modulation, and up-conversion of the binary source. The transmitter symbol rate R_s is fixed at 5 kBd to meet the bandwidth constraints of the piezoelectric sound source as specified by the manufacturer. The effective bit rate is equal to $R_b = R_s \log_2(M) R_c$, where M is the modulation index, and $R_c = k/n$ is the code rate.

Various parameters of the SDM saved in the FPGA control unit can be configured through the datapath. Specifically, a digital amplifier controls the amplitude of the signal produced by the digital processor, and the gain of the amplifier can be reconfigured by the user. The control unit can be configured to transmit different sequences of waveforms, that are optionally separated by guard intervals. To upconvert the signal, a sinusoid signal is generated using a direct digitized filter (DDS) that is configured using a phase increment, which defines the signal frequency.

To allow transmission from multiple elements simultaneously, the payload transmitted is encoded using a 1023-symbol long PRN with good auto-correlation properties. The 5-kBd modulated data is filtered using a cascade of a raised cosine filter as well as an interpolation filter that is sampled at 10 MHz, and the coefficients are defined to provide an excess bandwidth of 0.5. Before the signal is applied to the PDM, it is upconverted using a direct sequence synthesizer with a user-reconfigurable frequency. The FPGA processor is programmed to produce three independent modulated streams of information and that are multiplexed on each transducer.

In Fig. 3, a block diagram of the M-QAM modulator is shown. Usig M-QAM modulation, the binary sequence is encoded using (M) bits and for a fixed symbol rate R_s, the binary sequence clock rate is $R_b = R_s \log_2(M)$. The output of the modulator is de-multiplexed to represent the in-phase and quadrature values.

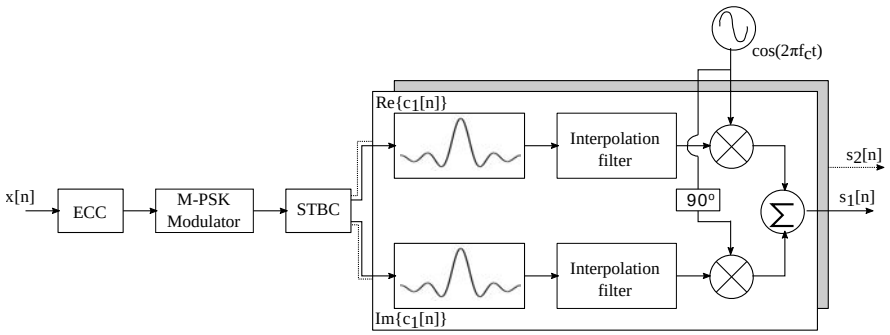


Figure 3: M-PSK transmitter block diagram

The root raised cosine (RRC) filter pulse shapes the data stream input to limit the signal bandwidth. The interpolation filter up-samples the RRC filter output, such that its sampling frequency matches the sampling frequency of the PDM.

To implement M-CPFSK, instead of implementing a modulator at baseband, in this program, the frequency of the DDS is controlled depending on the symbol to be transmitted. Since the DDS compiler is input a phase increment, this methodology ensures that continuous phase is respected.

Also, as an alternative modulation technique, the LFM has received recent interest to implement reliable underwater acoustic communication links (citations). As such, the DDS compiler is also configured to generate an LFM that sweeps over the symbol time T_{LFM} from a minimum frequency f_{min} to a maximum frequency f_{max}. The instantaneous frequency is fixed by continuously updating the phase at the sample rate.

To convert the digital signal to analog, a second order sigma/delta digital-to-analog converter (DAC) that produces a pulse density modulation output (PDM) is implemented on the fabric. The output of the PDM is applied to an analog 3rd order low-pass filter to recover the envelope of the signal. The filter is implemented using discrete components as shown in Figure 1a. In this work, the DAC clocking frequency is 10 MHz. The maximum signal to noise ratio (SNR) of the DAC output signal is approximately 58 dB, and as such represents a signal with an effective number of bits (ENOB) approximately equal to 8.

4 MIMO Performance

In this Section, the performance of the MIMO SDM performance will be assessed. In Section 4.1, the effect of channel impairments in the expected deployment environments

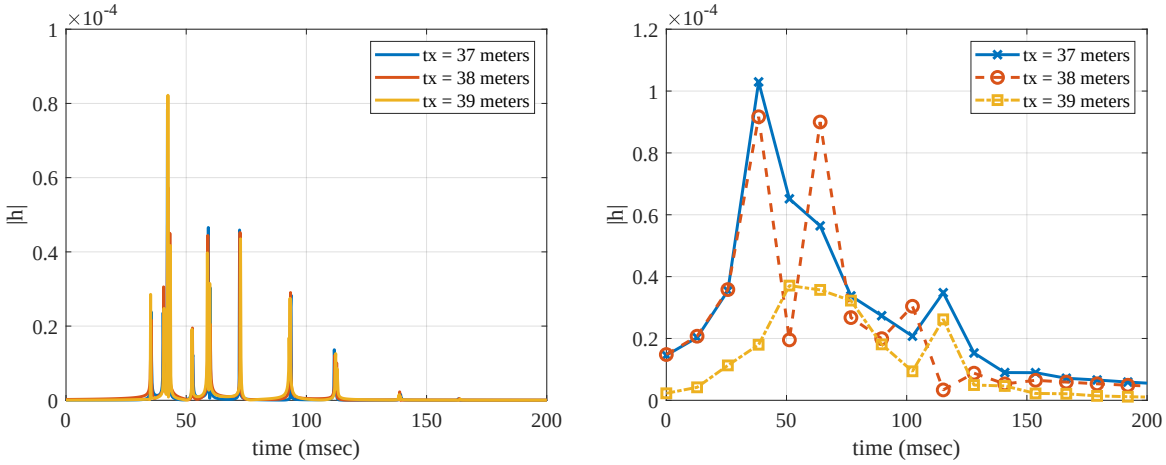
will be discussed. Then, the analysis a STBC performance using Alamouti with CPFSK will be presented in Section 4.2.

4.1 Effect of Doubly Spread Channel

In this section, how the channel impairments - mainly the multipath and the delay spread - impact the communication design is discussed.

To monitor commercial and governmental assets, underwater infrastructure is often deployed near the littoral and in sea ports. In these regions the communication channel is often shallow - below 100 meters - and reflections can occur from the different boundaries. Moreover, even when the equipment is fixed, sea surface motion as well as currents can induce motion in the channel. This effectively creates a Doppler shift on the different path arrivals. The combination of the multiple paths subject to mobility induces a Doppler spread, and the channel amplitude varies as a function of time and space. A database of common channel conditions is documented in [8]; however it can be expected that subtle changes can affect the performance significantly.

The Bellhop ray-tracing simulator can be used to predict the channel multipath profile, and provides a tuple $[c_p,\ t_p]$ of channel gain and delay for each $p \in P$. To model the effect of time variance, the channel gain c_p for each tap arrival with a reflection from the surface is multiplied by a phase shift θ_p that varies as a function of time. In this work, the phase θ_p is assumed to stay constant during the transmission of the frame, and can be extracted from a uniform distribution, assuming a rich scattering environment [9]. The rate of the phase change depends on the Doppler shift for each path.



(a) Sampled at 5 kBd.

(b) Sampled at 78 Bd.

Figure 4: Channel impulse response for 3x1 MISO

In Figure 4, a 3x1 multiple input single output (MISO) channel impulse response (CIR) for a distance between the transmitter equal to 1.6 km is shown, and sampled at two different symbol rates. It is assumed that the transmitter and receiver are deployed approximately in the middle of the water column. The 3 sound sources are at different depths and separated by 1 meter. In Figure 4a, the channel is extracted for a signal bandwidth of 5000 Hz, while in Figure 4b, the signal bandwidth is reduced to 78.1 Hz. As can be observed, the amplitude and profile of the channel are different for each sound source. As such, it can be expected that spatial diversity techniques will improve the performance. Note that for the signal bandwidth of 5000 Hz, the channel delay profile spans hundreds of symbols, and this will introduce excessive inter symbol interference, thus

deteriorating significantly the performance at the receiver. As such, it can expected that to maintain a reliable communication link, the signal bandwidth should be smaller than the nominal 5000 Hz. Effectively, the choice of symbol rate must take into consideration the delay spread.

It should also be noted that the Doppler spread also impacts the transmission rate. Using CPFSK modulation, the minimum frequency separation is equal to $\Delta f = R_s/2$ when the channel is time invariant. However, as was noted in [10], the Doppler spread introduces inter-carrier interference (ICI) and to mitigate ICI, the frequency separation Δf should be much greater than the Doppler spread D_S, i.e $\Delta f \gg D_S$. As a consequence, for a fixed total bandwidth B, the chosen symbol rate R_s may need to be limited by the Doppler spread.

4.2 Alamouti Coding combined with M-CPFSK

In this section, the benefit of an Alamouti STBC code using (M-CPFSK) will be demonstrated analytically. In a first instance, an analytical baseband model using continuous phase shift keying will be presented. Then, it will be augmented with the STBC

In conventional FSK, the signal is generated by shifting the carrier by an amount $m\Delta f, 1 \leq m \leq M$, to reflect the digital information that is being transmitted. As explained in [9], to avoid the use of signals having large spectral side lobes, the information-bearing signal frequency modulates a single carrier whose frequency is changed continuously. The resulting frequency modulated signal is phase-continuous, and hence, it is called *continuous-phase FSK* (CPFSK).

Using CPFSK, the phase $\phi(t; \boldsymbol{I})$ of the carrier can be expressed as [9]:

$$\phi(t; \boldsymbol{I}) = 2\pi \sum_{k=-\infty}^{n} I_k h_k q(t - kT), \qquad nT \leq t \leq (n+1)T \quad (1)$$

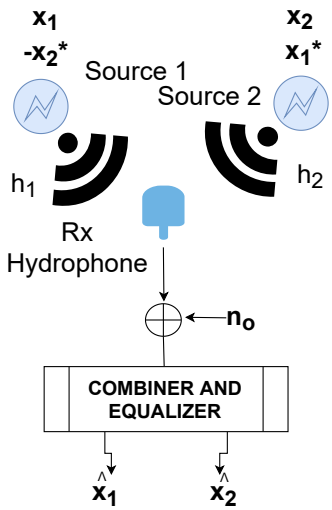


Figure 5: System Model

where I_k is the sequence of M-ary information symbols selected from the alphabets $\pm 1, \pm 3, \cdots, \pm(M-1)$ and where h_k is a sequence of modulation indices, and $q(t)$ is some normalized waveform shape, with symbol duration T. Then, the output of the modulator is a baseband representation of the modulated signal given by:

$$s(t) = \exp\left[j2\pi \sum_{k=0}^{n} I_k h_k q(t - kT)\right], \qquad nT \leq t \leq (n+1)T \quad (2)$$

In this work, the Alamouti STBC is chosen to implement spatial diversity at the transmitter. The Alamouti code does not require channel state information (CSI) at the transmitter. While the performance of the Alamouti STBC is implemented for a 2x1 MISO scenario, it can be generalized to two transmit antennas and M receive antennas to provide a diversity order of 2M.

Figure 5 shows the baseband representation of two transmitter sources and one receive hydrophone. At the transmitter the data frame is encoded, while at the receiver it is decoded to maximize reliability, and equalized to compensate for multipath distortion.

Let x_1 and x_2 be the modulated transmit symbols prior to the STBC encoder to be transmitted from Source #1 and Source #2 respectively. At the output of the STBC encoder, the signals are encoded on two consecutive time slots of duration T. In the first time slot t, they are unchanged, while during the next symbol period $-x_2^*$ is transmitted from Source #1, and x_1^* is transmitted from Source #2. This is summarized in Table 1.

Assuming a frequency flat channel, the channel amplitude from Source #1 and Source #2 are h_1 and h_2 respectively. Note that the channels are constant with time t and $t+T$, where T is the code duration duration. The received signals y_1 at time t and y_2 at time $t+T$ can then be expressed respectively as:

$$y_1 = h_1 x_1 + h_2 x_2 + n_1,$$
$$y_2 = -h_1 x_2^* + h_2 x_1^* + n_2,$$

where n_1 and n_2 are complex random variables representing the receiver noise and interference.

	Source 1	Source 2
time t	x_1	x_2
time t + T	$-x_2^*$	x_1^*

Table 1: Alamouti STBC - Two branch transmit diversity scheme

As shown in Figure 5, the two signals at the receiver can be combined as:

$$\hat{x}_1 = h_1^* y_1 + h_2 y_2^* + n_1,$$
$$\hat{x}_2 = h_2^* y_1 - h_1 y_2^* + n_2,$$

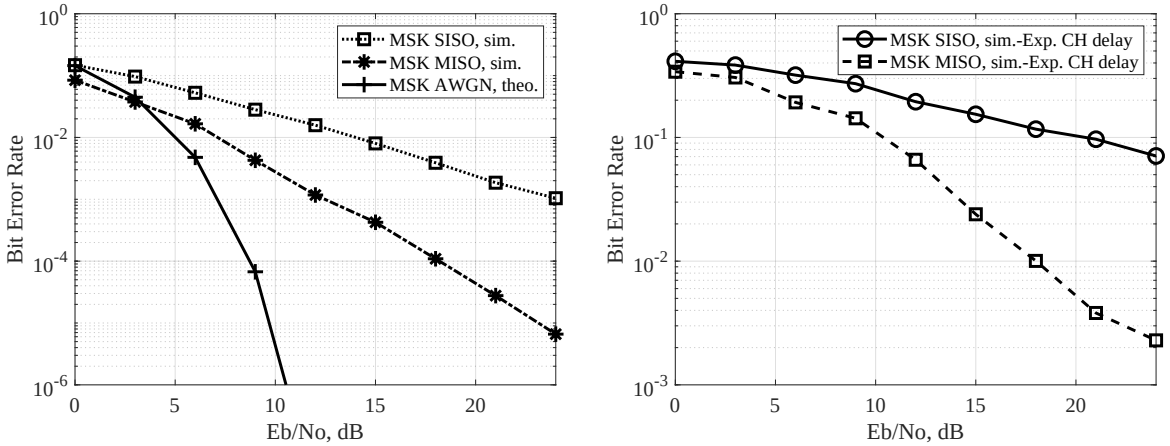
where $\hat{x}_1$ and $\hat{x}_2$ are estimates of x_1 and x_2. To recover the binary information, the sequence $\hat{x}_1$ of $\hat{x}_2$ is applied to the CPFSK demodulator.

In a multipath environment, the Alamouti decoder implementation can be enhanced with an equalizer, and in this work two recursive least square equalizers are implemented: the first minimizes the error between $\hat{x}_1$ and the transmit signal x_1, and the second minimizes the error between $\hat{x}_2$ and the transmit signal x_2, as suggested in [11].

In Figure 6, the simulated probability of bit error is shown as a function of SNR for different conditions. First, in Figure 6a, the MISO STBC is evaluated in flat fading conditions, assuming a Rayleigh fading channel. The diversity gain is clearly observed in comparison to a single-input single-output (SISO) scenario. For comparison purposes, the bit error rate in AWGN conditions is also shown. In Figure 6b, the performance of the STBC code, in multipath conditions is also evaluated. An exponentially decaying multipath profile is representative of the channel profile provided by the Bellhop simulator for a 78-bps symbol rate. The results demonstrate that the STBC also provides improvement in performance in multipath conditions. To further improve the performance, a MIMO STBC can be easily implemented with the prototyping system available. Error correction codes, such as Turbo codes can further improve the performance.

5 Conclusion

In this work, a reconfigurable transmitter with multiple sound sources has been described to implement a SDM. Due to the hardware front-end limitations, it is expected that the maximum throughput that can be achieved is approximately equal to 30 kbps,



(a) Flat fading conditions. (b) Multi-path - exponential channel delay

Figure 6: Probability of bit error for different conditions

and for a range of 1.6 km. The firmware implementation has been described, an the performance of a STBC has been assessed for different channel conditions. The use of multiple transmit elements does promise to provide diversity gain, and the future evaluation of the performance at sea will confirm the simulatin results.

References

[1] M. Siderius and M. B. Porter, "Modeling broadband ocean acoustic transmissions with time-varying sea surfaces," *J. Acoust. Soc. Am.*, vol. 124, pp. 137–150, 2008.

[2] P. Qarabaqi and M. Stojanovic, "Statistical characterization and computationally efficient modeling of a class of underwater acoustic communication channels," *IEEE J. Ocean. Eng.*, vol. 38, no. 4, pp. 701–717, Oct 2013.

[3] H. S. Dol et al., "Software-Defined Underwater Acoustic Modems: Historical Review and the NILUS Approach," *IEEE J. Ocean. Eng.*, vol. 42, no. 3, pp. 722–737, 2017.

[4] E. Demirors et al., "A High-Rate Software-Defined Underwater Acoustic Modem With Real-Time Adaptation Capabilities," *IEEE Access*, vol. 6, 2018.

[5] S. M. Alamouti, "A simple transmit diversity technique for wireless communications," *IEEE J. Select. Areas Comm.*, vol. 16, no. 8, pp. 1451–1458, Oct 1998.

[6] John B Anderson et al., *Digital phase modulation*, New York : Plenum Press, 1986.

[7] R.J. Urick, *Principles of Underwater Sound*, Peninsula Publishing, 2013.

[8] P. A. van Walree, F. Socheleau, R. Otnes, and T. Jenserud, "The Watermark Benchmark for Underwater Acoustic Modulation Schemes," *IEEE J. Ocean. Eng.*, vol. 42, no. 4, pp. 1007–1018, Oct 2017.

[9] Proakis, *Digital Communications 5th Edition*, McGraw Hill, 2007.

[10] A. Dobbin and J-F Bousquet, "Reliable Acoustic Link Using Non-coherent Turbo-coded Frequency Shift Keying," in *Proc. ACM WUWNET'17*, 2017, pp. 6:1–6:2.

[11] W. H. Gerstacker et al., "Equalization concepts for Alamouti's space-time block code," *IEEE Trans. Comm.*, vol. 52, no. 7, pp. 1178–1190, July 2004.

High-Data Rate Carrierless Impulsive Communications For Underwater Acoustic Networks

Emrecan Demirors, Deniz Unal, G. Enrico Santagati, Tommaso Melodia
Institute for the Wireless Internet of Things, Northeastern University, Boston, MA 02115, USA
Email: {edemirors, deniz, santagati, melodia}@ece.neu.edu

ABSTRACT

Underwater networks of wireless sensors deployed along the coast or in the deep water are the most promising solution for the development of underwater monitoring, exploration and surveillance applications. A key feature of underwater networks that can significantly enhance current monitoring applications, is the ability to support sufficiently high data rates that can accommodate real-time video information on an underwater communication link. Unfortunately, the intrinsic characteristic of the underwater propagation medium have made this objective extremely challenging. In this paper, we present the first physical layer transmission scheme for short-range and high-data rate ultrasonic underwater communications. The proposed solution, which we will refer to as Underwater UltraComm (U2C), is based on the idea of transmitting short information-bearing carrierless ultrasonic signals, e.g., pulses, following a pseudo-random adaptive time-hopping pattern with a superimposed rate-adaptive Reed-Solomon forward error correction (FEC) channel coding. We extensively evaluate the U2C performance through water tank experiments. Results show that U2C links can support point-to-point data rate up to 1.38 Mbps, and that by leveraging the flexibility of the adaptive time-hopping and adaptive channel coding techniques, one can trade between link throughput energy consumption.

KEYWORDS

Carrierless, Impulsive, High-Data Rate, Adaptive

1 INTRODUCTION

Underwater networks of wireless sensors deployed along the coast or in the deep water are the most promising solution for the development of underwater monitoring, exploration and surveillance applications. For example, a dense network of underwater sensors can enable environmental monitoring functionalities such as pollution levels monitoring, or prevention and recovery of catastrophic environmental disasters, e.g., oil spills form rigs or pipelines, or seabed dynamic tracking, e.g., monitoring of submarine volcano activities [1, 2]. A key feature of underwater networks that can significantly enhance current monitoring applications, is the ability to accommodate real-time video information on an underwater communication link. In fact, while today monitoring rely on the exchange of simple discrete information, e.g., water temperature, and particle concentration, among others, by introducing real-time streaming capability of non-static images between wireless underwater nodes one can completely revolutionize the whole underwater monitoring scenario.

To achieve this goal, underwater links are required to support sufficiently high data rate, compatible with the streaming rates of the transmitted video sequence. Unfortunately, the intrinsic characteristic of the underwater propagation medium have made this objective extremely challenging. Specifically, due to the physical properties of the propagation medium, underwater acoustic signals suffer from severe transmission loss, time-varying multipath propagation, Doppler spread, limited and distance-dependent bandwidth, and high propagation delays. These formidable challenges limit the available bandwidth, and therefore the achievable data rates in underwater acoustic communications. As a consequence, currently available underwater acoustic technology can support mostly point-to-point, low-data-rate, delay-tolerant applications. Most existing commercial point-to-point acoustic modems use signaling schemes that can achieve data rates lower than 35 kbit/s with a link distance of 1 km over horizontal links [3–6]. Most recently, a commercially available modem has been advertised to achieve data rates of 62.5 kbit/s over a horizontal underwater link of 300 m [7].

In this paper, we present the first physical layer transmission scheme for short-range and high-data rate ultrasonic underwater communications. The proposed solution, which we will refer to as Underwater UltraComm (U2C), is based on the idea of transmitting short information-bearing carrierless ultrasonic signals, e.g., pulses, following a pseudo-random adaptive time-hopping pattern with a superimposed rate-adaptive forward error correction (FEC) channel coding. Low duty cycle impulsive transmission and adapting channel coding combat the effects of multipath and scattering and provide a reasonable degree of robustness to multi-user interference. U2C operates at high frequency ranges of the acoustic spectrum, i.e., ultrasounds, and it is designed to enable multipath-resilient and high-data rate transmissions, up to several hundreds of kbps. However, the price we pay for

This work was supported by the National Science Foundation under Grant CNS-1503609 and Grant CNS-1726512.

these benefits is a higher acoustic attenuation, increasing with frequency, that limits the achievable distance ranges from few meters up to approximately 100 m. We evaluate extensively the U2C performance in real-scenario underwater experiments at the PHY layer, i.e., Bit Error Rate (BER). Results show that U2C links can support point-to-point data rate up to 1.38 Mbps, and that by leveraging the flexibility of the adaptive time-hopping and adaptive channel coding techniques, one can trade between link throughput and energy consumption, still satisfying application layer requirements.

The remainder of the paper is organized as follows. In Section 2, we discuss U2C PHY transmission scheme In Section 3, we extensively evaluate the performance of U2C through on-field experiments in a water test tank. Finally, in Section 4, we conclude the paper.

2 U2C: UNDERWATER ULTRACOMM

U2C is an impulse-radio inspired ultrasonic transmission technique based on the idea of transmitting short information-bearing carrierless ultrasonic pulses, following a pseudo-random adaptive time-hopping pattern with a superimposed an adaptive variable-rate FEC channel coding.

Underwater UltraComm (U2C) Transmission Scheme. Baseband pulsed transmissions enable high data rate, low-power communications, low-cost transceivers, and have been proposed for RF short-range, high data rate communications [8, 9], although with much shorter pulse durations (and consequently larger bandwidth) than achievable in ultrasonic communications. In ultrasonic communications domain, baseband pulsed transmissions are first used for intra-body communications and networks in very short distances(in the order of tens of cm), where the propagation medium has similar characteristics to the underwater propagation medium [10–12] .

The fine delay-resolution properties of pulsed transmission are well-suited for propagation in the channels strongly affected by multipath effect due to reflections and scattering. When replicas of pulses reflected or scattered are received with a differential delay at least equal to the pulse width, they do not overlap in time with the original pulse. Therefore, for pulse durations in the order of hundreds of nanoseconds [13], pulse overlaps in time are reduced and multiple propagation paths can be efficiently resolved and combined at the receiver to reduce the bit error rate. Finally, carefully designed interference mitigation techniques may enable MAC protocols that do not require mutual temporal exclusion between different transmitters. This is crucial in the ultrasonic transmission medium since the underwater propagation speed is about 1500 m/s and consequently the propagation delay is five orders of magnitude higher than in RF in-air channels (where the propagation speed is about

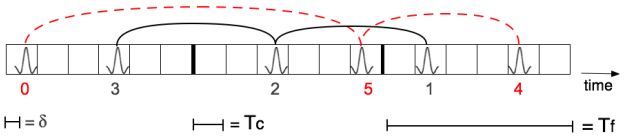


Figure 1: Two concurrent transmissions with $N_h = 6$, time-hopping sequences $\{3, 2, 1\}$ and $\{0, 5, 4\}$ and transmitted bit sequences $\{1, 1, 0\}$ and $\{1, 0, 0\}$.

$3 \cdot 10^8$ m/s) and carrier-sense-based medium access control protocols are ineffective [2].

Adaptive Time-Hopping. Consider, as in Fig. 1, a slotted timeline divided in slots of duration T_c, with slots organized in frames of duration $T_f = N_h T_c$, where N_h is the number of slots per frame. Each user transmits one pulse per frame in a slot determined by a pseudo-random *time-hopping sequence*. Information is carried through pulse position modulation (PPM), i.e., a '1' symbol is carried by a pulse delayed by a time δ with respect to the beginning of the slot, while a '-1' symbol begins with the slot. The resulting transmitted signal for a symbol d can be modeled as

$$s(t) = \sum_{j=0}^{N_s-1} p(t - c_j T_c - jT_f - d\delta) \tag{1}$$

where $p(t)$ is the pulse shape, $\{c_j\}$ is the time-hopping sequence with $0 \leq c_j \leq N_h - 1$, and δ is the PPM shift of a pulse representing a '1' chip. The resulting data rate, in pulses per second, is expressed as:

$$R(N_h) = \frac{1}{T_f} = \frac{1}{N_h T_c}. \tag{2}$$

For a given time-hopping frame length N_h, we define the average transmitted power as the total energy irradiated in the unit time:

$$\bar{P}_t(N_h) = \frac{E_p}{N_h T_c} \tag{3}$$

where E_p is the energy required for transmitting one pulse that is obtained as $P\,T_p$, with P the instantaneous transmission power and T_p the pulse duration. By regulating the time-hopping frame length N_h, i.e., the average inter-pulse time, a user can adapt its transmission rate, and as a consequence modify the average transmitted power.

Rate-Adaptive Channel Coding. Since a single pulse may collide with pulses transmitted by other users with a probability that depends on the frame size N_h, or alternative the pulse can be distorted by the time-varying channel condition, we superimpose a rate-adaptive forward error correction (FEC) channel coding technique that leverages the error correction capability of Reed-Solomon (RS) codes.

RS codes are linear, block error-correcting codes widely used in data storage and data transmission systems. A RS code can be denoted as $RS(s, n, k)$, with s is the symbol size in bits, n is the block length and k is the message length,

with $k < n$. The maximum block length depends on the symbol length as $n_{max} = 2^s - 1$. A RS encoder takes k s-bit information symbols and adds t *parity* symbols to make an n symbol block. Therefore, there are $t = n - k$ overhead symbols. On the other hand, a RS decoder is able to decode the received n-symbol block, and can correct up to $\frac{t}{2}$ data symbols that may contain potential errors due to the channel fluctuation or collisions with interfering pulses. The RS code rate can be defined as the ratio between the message length and the block length, i.e., $r_c = k/n$. The information rate, or the net rate, after the channel coding become:

$$R'(N_h, r_c) = R(N_h) r_c = \frac{r_c}{N_h T_c}. \tag{4}$$

Note that there is a tradeoff between robustness to channel fluctuation and multi-user interference (which increases with lower coding rate), and the information rate (which decreases with higher coding rate). For example, a $RS(8, 255, 192)$ encoder considers 8-bit symbols, and for every 191 information symbols gives as output a block of 255 symbols.The decoder can correct up to 32 symbols randomly located in the received block, independently of the number of bits wrong in each symbol (e.g., in the worst case scenario the bits in the 32 symbol can be all wrong). The resulting code rate is 3/4, thus the net rate after the channel coding is reduced of 1/4 with respect of the original information rate.

Signal to Interference-plus-Noise Ratio. We can express the signal to interference-plus-noise ratio (SINR) for impulsive transmissions at the receiver of link i as [8]

$$\mathrm{SINR}_i(\mathbf{N_h}, r_c) = \frac{1}{r_{c,i}} \frac{P_{r,i}\, N_{h,i} T_c}{\eta + \sigma^2 T_c \sum_{k=1}^{K} P_{r,k}}, \tag{5}$$

where $P_{r,i}$ is the average power per pulse period at the receiver of the i^{th} link, η represents background noise energy and σ^2 is an adimensional parameter depending on the shape of the transmitted pulse and the receiver correlator. Parameter K represents the number of pulses that interferers with link i in a time frame T_f, and $P_{r,k}$ is the average power of the interfering pulses measured at the receiver of the link i. The interfering pulses can belong either to co-located transmission links or to multipath component of the link itself, i.e., self-interference. In absence of interference, when no FEC coding and time-hopping is used, (5) give us what we defined SNR per pulse measured at the receiver, given by the ratio of the energy per pulse over the background noise energy

$$\mathrm{SNR}_p = \frac{P_{r,i}\, T_c}{\eta} \tag{6}$$

Note that increasing (or decreasing) the code rate of the link i, $r_{c,i}$, leads to an decrease (increase) in the SINR. This models the error correction effect of the FEC channel coding, i.e., the lower the code rate the higher the correction capabilities of the code. When the i^{th} link increases (decreases) its frame length, $N_{h,i}$, while the number of interfering pulse K remains constant, i.e., in condition of self-interference, the SINR increases (decreases). When the transmitting pulses belong to other co-located transmission links, the number of interfering pulses K scales with the frame length, thus increasing or decreasing the frame length does not affect the SINR.

Finally, no close forms of the BER as a function of the RS code rate and time-hopping frame length are available. However, intuitively, by increasing the code rate, i.e., reducing the code overhead, the BER may increases. By decreasing the time-hopping frame length, the BER may increase or remains constant. Thus, we can in general express BER as a non-strictly decreasing function on the SINR in (5).

3 PERFORMANCE EVALUATION

In this section, we evaluate the performance of the proposed transmission scheme in a water test tank through programmable Internet of Underwater Things (IoUT) platforms [14–18]. Specifically, we evaluate the performance of the U2C in terms of BER as a function of the code rate, time-hopping frame length, and the SNR per pulse in (6).

Testbed Architecture. To evaluate the performance of the U2C, as a first prototype, we built U2C combining both hardware and software programming to leverage the offered reconfiguration flexibilities on the USRP based platform [15, 17]. Specifically, the U2C signal processing is implemented in the ultrasonic software-defined node using a framework that combines (i) the GNU Radio software development toolkit and (ii) the open source Hardware Description Language (HDL) design for the FPGA embedded in the USRP. We interfaced each platform with a *standard immersion W-series ultrasonic transducers, Ultran WS37-5* [19]. The nominal bandwidth central frequency is about 5 MHz and the bandwidth at - 6 dB goes from 50% to 100% of the bandwidth central frequency, i.e., $2.5 - 5$ MHz. Furthermore, the standard immersion W-series is designed to operate in contact with water, and they come in a waterproof case with an UHF waterproof connector. To operate in fully underwater immersion, we use Olympus BCU-58W [20] waterproof cables with BNC to waterproof UHF connectors. The experiment setup consists of two IoUT platform prototypes communicating through water in an underwater tank. The distance between the two transducers is kept fixed to 1.83 m.

BER Vs SNR Per Pulse. In this experiment we evaluated the U2C PHY layer performance in terms of BER. To this purpose we transmit a sequence of 100000 packets each with

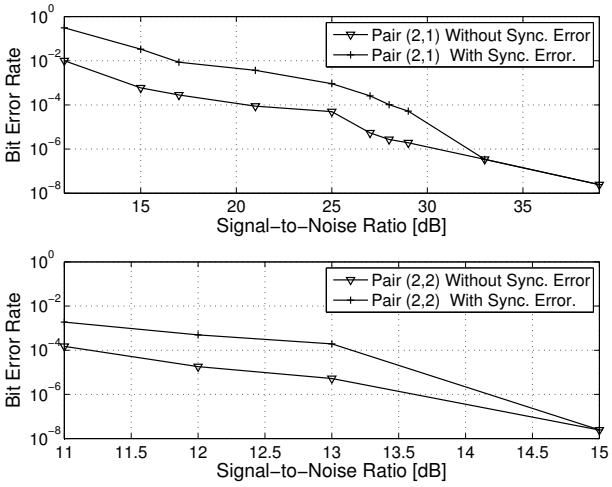


Figure 2: BER with and without synchronization error, as a function of the SNR measured at the receiver, for the pair (2,1) and (2,2).

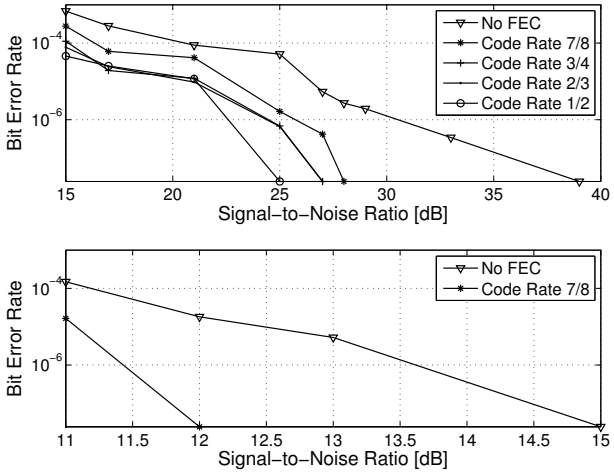


Figure 3: BER without synchronization error, as a function of the SNR measured at the receiver, for the pair (2,1) and (2,2), for different value of code rate.

256 bytes, i .e., approximately 20 Mbits of pseudorandom-generated raw data, and we vary different PHY layer parameters, e.g., SNR per pulse at the receiver, number of potential interfering pulses per time-hopping frame, FEC code rate and time-hopping frame length. At the receiver, the transmitted sequence is known, and the BER is calculated.

First, we evaluate the BER as a function of the SNR per pulse, defined in (6), measured at the receiver, in the absence of external interference. In order to vary the SNR per pulse at the receiver, we connect a variable-gain attenuator between the LFTX daughterboard and the power amplifier we vary the input power at the Tx transducer between 22 dBm and -17 dBm, to obtain values of SNR between 50 to 10 dB, respectively. In this experiments, we used pulses that has a duration of approximately 300 ns with a PPM shift of 60 ns, within a time-hopping slot of 360 ns. Moreover, we consider an over-imposed repetition code of length 2, i.e., each bit is sent represented by two pulses in two consecutive time-hopping frames. The raw transmission data rate, i.e., before FEC is applied, varies from about 1.38 Mbps to approximately 700 kbps. The information rate may vary according to the channel coding rate in use.

Figure 2 shows the BER performances as a function of the SNR per pulse measured at the receiver, assuming frame length of 2, without repetition code (top), i.e, pair (2,1), and with repetition code of length 2 (bottom), i.e., pair (2,2). Each plot reports the BER with and without considering errors due to packet synchronization failures. Finally, this results assume a channel coding rate equals to 1, i.e., no FEC is applied.

In Figure 3, we repeat the same experiments also varying the channel coding rates in {1, 7/8, 3/4, 2/3, 1/2}, for the pair (2,1) (top) and (2,2) bottom. Since the FEC works on the payload error only, the BER reported in this Figure does not consider errors due to packet synchronization failures, that however would be independent form the channel coding rate. The information rate varies from 1.38 Mbps to 700 kbps using the pair (2,1), and from 700 kbps to 350 kbps using the pair (2,2).

4 CONCLUSIONS

In this paper, we presented the first physical layer transmission scheme for short-range and high-data rate ultrasonic underwater communications. The proposed solution, which we referred to as Underwater UltraComm (U2C), is based on the idea of transmitting short information-bearing carrier-less ultrasonic pulses, following a pseudo-random adaptive time-hopping pattern with a superimposed rate-adaptive forward error correction (FEC) channel coding. We presented the design of the first prototype of a software defined underwater ultrasonic transceiver that implements U2C PHY transmission scheme through which we evaluate extensively the U2C performance in real-scenario underwater experiments at the PHY layer, i.e., Bit Error Rate (BER). Results shown that U2C links can support point-to-point data rate up to 1.38 Mbps, and that by leveraging the flexibility of the adaptive time-hopping and adaptive channel coding techniques, one can trade between link throughput and energy consumption.

REFERENCES

[1] J. Heidemann, M. Stojanovic, and M. Zorzi. Underwater sensor networks: applications, advances and challenges. *Philosophical Transactions of the Royal Society of London A: Mathematical, Physical and Engineering Sciences*, 370(1958):158–175, 2011.

[2] T. Melodia, H. Kulhandjian, L. Kuo, and E. Demirors. Advances in Underwater Acoustic Networking. In S. Basagni, M. Conti, S. Giordano, and I. Stojmenovic, editors, *Mobile Ad Hoc Networking: Cutting Edge Directions*, pages 804–852. John Wiley and Sons, Inc., Hoboken, NJ, second edition edition, 2013.

[3] DSPComm, AquaComm Underwater wireless modem, http://www.dspcomm.com/.

[4] AquaSent Acoustic Modem, http://www.aquasent.com.

[5] Teledyne Benthos Smart Products, http://teledynebenthos.com/.

[6] LinkQuest. http://www.link-quest.com/.

[7] EvoLogics Underwater Acoustic Modems, https://www.evologics.de.

[8] M. Z. Win and R. A. Scholtz. Ultra-wide bandwidth time-hopping spread-spectrum impulse radio for wireless multiple-access communications. *IEEE Trans. Communications*, 48:679–689, 2000.

[9] F. Cuomo, C. Martello, A. Baiocchi, and F. Capriotti. Radio Resource Sharing for Ad Hoc Networking with UWB. *IEEE Journal on Selected Areas in Communications*, 20(9), Dec. 2002.

[10] G. E. Santagati, T. Melodia, L. Galluccio, and S. Palazzo. Distributed MAC and Rate Adaptation for Ultrasonically Networked Implantable Sensors. In *Proc. of IEEE Conf. on Sensor, Mesh and Ad Hoc Communications and Networks (SECON)*, New Orleans, USA, June 2013.

[11] G.E. Santagati, T. Melodia, L. Galluccio, and S. Palazzo. Medium access control and rate adaptation for ultrasonic intra-body sensor networks. *IEEE/ACM Transactions on Networking*, 2015.

[12] G.E. Santagati and T. Melodia. Experimental evaluation of impulsive ultrasonic intra-body communications for implantable biomedical devices. *IEEE Transactions on Mobile Computing*, 16(2):367–380, 2016.

[13] E. Lacaze, S. Michau and P. Mauchamp. 20 MHz ultrasound array for medical imaging: from design to image evaluation. In *Ultrasonics Symposium*, October 2001.

[14] E. Demirors, B. G. Shankar, G.E. Santagati, and T. Melodia. SEANet: A Software-Defined Acoustic Networking Framework for Reconfigurable Underwater Networking. In *Proc. of ACM Intl. Conf. on Underwater Networks & Systems (WUWNet)*, October 2015.

[15] E. Demirors, G. Sklivanitis, T. Melodia, S. N. Batalama, and D. A. Pados. Software-defined underwater acoustic networks: toward a high-rate real-time reconfigurable modem. *IEEE Communications Magazine*, 53(11):64–71, November 2015.

[16] E. Demirors, J. Shi, R. Guida and T. Melodia. SEANet G2: A Toward a High-Data-Rate Software-Defined Underwater Acoustic Networking Platform. In *Proc. of ACM Intl. Conf. on Underwater Networks & Systems (WUWNet)*, Shanghai, China, October 2016.

[17] E. Demirors, G. Sklivanitis, G. E. Santagati, T. Melodia, and S. N. Batalama. A high-rate software-defined underwater acoustic modem with real-time adaptation capabilities. *IEEE Access*, 6:18602–18615, 2018.

[18] E. Demirors, J. Shi, A. Duong, N. Dave, R. Guida, B. Herrera, F. Pop, G. Chen, C. Cassella, S. Tadayon, M. Rinaldi, S. Basagni, M. Stojanovic and T. Melodia. The SEANet Project: Toward a Programmable Internet of Underwater Things. In *Proc. of IEEE Underwater Communications Conf. And Workshop (UComms)*, Lerici, Italy, August 2018.

[19] ULTRAN Group Transducers. http://www.ultrangroup.com/.

[20] Waterproof Transducer Cables, http://www.olympus-ims.com/en/ultrasonic-transducers/transducer-cables/.

ROUTING STRATEGIES FOR DUAL-HOP TDA-MAC: TRADE-OFF BETWEEN NETWORK THROUGHPUT AND RELIABILITY

Nils Morozs*, Paul D. Mitchell, Yuriy Zakharov

Department of Electronic Engineering, University of York, York YO10 5DD, UK

* Corresponding author: Nils Morozs, nils.morozs@york.ac.uk, +44 1904 322395

Abstract: *This paper investigates the use of underwater acoustic sensor networks (UASNs) for large scale monitoring of the ocean environment. The slow propagation of acoustic waves is a fundamental challenge in implementing reliable networking protocols due to the limited amount of control signalling that is achievable due to the long propagation delays in UASNs. Sequential Dual-Hop Transmit Delay Allocation MAC (SDH-TDA-MAC) is a Medium Access Control (MAC) protocol that mitigates these physical constraints by incorporating long propagation delays into the transmission schedules to provide high network throughput in dual-hop UASNs. In this paper, we take a cross-layer approach to designing a routing protocol tailored to SDH-TDA-MAC. We present and evaluate the minimum delay and fewest relays routing strategies with optional routing redundancy, to offer a trade-off between achieving high network throughput and reliable packet delivery.*

Keywords: *Medium Access Control, Routing, Sensor Network, Underwater Acoustic Network*

INTRODUCTION

The use of wireless sensor networks (WSNs) for remote monitoring of the ocean environment is becoming an increasingly popular research subject, owing to the modern developments in underwater acoustic modem technologies [1][2][3]. Acoustic waves are the preferred practical medium for underwater communications, since they exhibit significantly better propagation characteristics compared with electromagnetic and optical waves. However, acoustic communications are fundamentally limited by the low sound propagation speed and low usable frequency bandwidth [4]. These severe physical constraints necessitate the design of networking protocols dedicated to underwater acoustic sensor networks (UASNs).

Much of the well-established research on Medium Access Control (MAC) in UASNs focuses on Time Division Multiple Access (TDMA) based protocols that aim to schedule packet transmissions in a way that mitigates the negative effect of long propagation delays on the network performance, e.g. by exploiting large differences in propagation delays and/or topology sparsity for spatial reuse of the channel airtime [5][6]. For example, in [7] we proposed the Transmit

Delay Allocation MAC (TDA-MAC) protocol that leverages the knowledge of the propagation delays in a centralised UASN to achieve high throughput without clock synchronisation at the sensor nodes. In [8] we proposed Sequential Dual-Hop TDA-MAC (SDH-TDA-MAC), extending the TDA-MAC approach to dual-hop UASNs, which introduced the problem of routing, i.e. choosing which sensor nodes act as relays to optimise a particular performance objective, e.g. throughput, reliability, energy fairness etc.

Routing in WSNs is a well-established research field with many solutions available for different network architectures, and for specific performance objectives [9]. In this paper, we take a cross-layer approach to design routing strategies that are specifically tailored to dual-hop TDA-MAC applied to UASNs, i.e. a combined design of the MAC and the network layer. We believe that cross-layer protocol design is key for achieving efficient network operation under the severe constraints imposed by the long propagation delays in UASNs. The purpose of this paper is to provide an insight into the performance of several dual-hop routing strategies in the context of two performance metrics: network throughput and packet delivery ratio. The routing strategies presented in this paper incorporate both relay node selection to maximise the throughput, and routing redundancy to increase the network reliability, similar to flooding protocols [10] but designed specifically for dual-hop TDA-MAC [8].

The rest of the paper is organised as follows: Section 2 describes the SDH-TDA-MAC protocol; Section 3 presents details of several routing strategies for SDH-TDA-MAC; Section 4 evaluates the proposed routing strategies in simulation; finally, Section 5 concludes the paper.

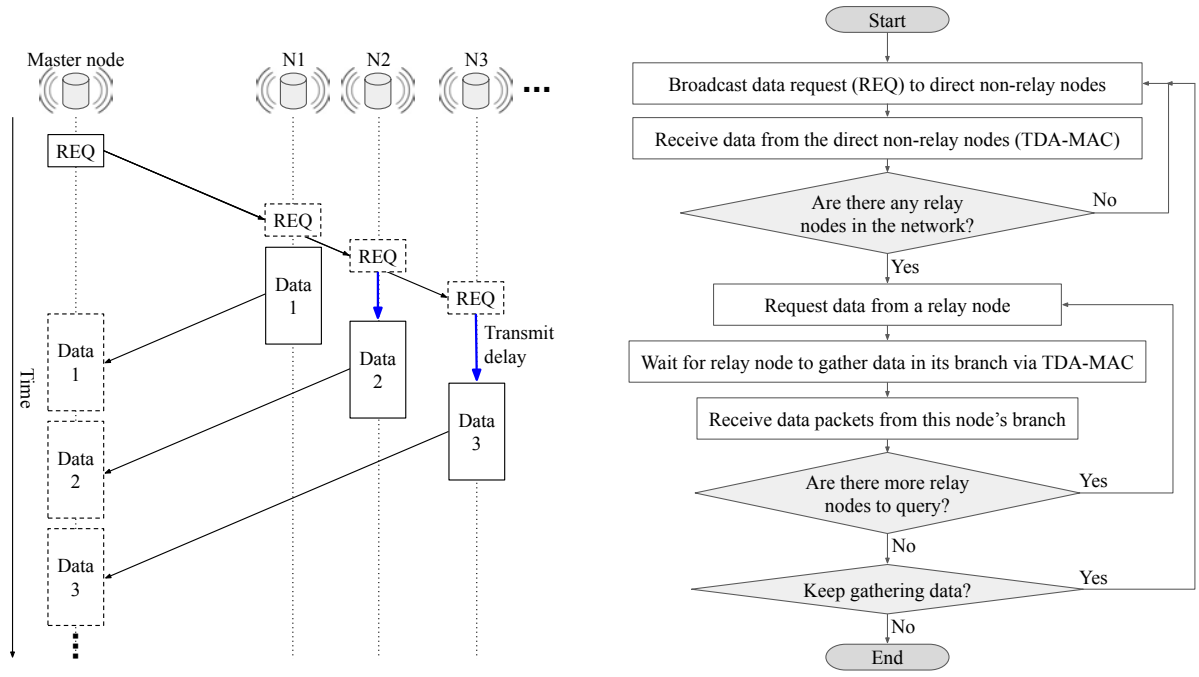
DUAL-HOP TDA-MAC

In [7], we proposed the TDA-MAC protocol for centralised scheduling of data transmissions from sensor nodes connected to a single gateway node. Its main advantage over other MAC protocols found in the literature is that it can achieve network throughputs close to the channel capacity without clock synchronisation at the sensor nodes. Therefore, it shows great potential as a practical solution for efficient data gathering in UASNs. A practical application of TDA-MAC was successfully demonstrated in sea trials with a small underwater sensor network in July 2018 in Fort William, UK [11]. Figure 1a shows an illustrative example of the packet flow in TDA-MAC. The gateway (master) node broadcasts a data request (REQ) packet that is received by every sensor node at a different time (due to the differences in propagation delays of the acoustic links). Each sensor node then waits for a specific (individually assigned) amount of time before transmitting their data packet back to the gateway node as shown in Figure 1a.

In [8], we extended the TDA-MAC protocol to dual-hop networks, i.e. where nodes that do not have a direct link with the gateway node are connected via another sensor node that acts as a relay. Figure 1b shows the flowchart of the SDH-TDA-MAC protocol. There, the single-hop TDA-MAC protocol depicted in Figure 1a is first used at the gateway node for all directly connected sensor nodes, and then at every relay node to gather data packets within their respective network branch sequentially. This approach was shown to achieve high network throughput by leveraging the many-to-one connections in dual-hop UASNs.

DUAL-HOP ROUTING STRATEGIES

In addition to scheduling, dual-hop TDA-MAC also needs to incorporate a routing procedure, i.e. choosing the dual-hop links between sensor nodes to deliver packets to the gateway node.



(a) TDA-MAC packet flow *(b) SDH-TDA-MAC protocol at the gateway node [8]*

Figure 1: Sequential Dual-Hop TDA-MAC (SDH-TDA-MAC) scheduling. The gateway node first uses TDA-MAC to gather data packets from directly connected non-relay sensor nodes. It then gathers data from every relay node sequentially, instructing it to gather data within its network branch using TDA-MAC.

In this section we present several routing strategies, expanding on our previous work in SDH-TDA-MAC in [8]. In particular, we investigate routing in terms of two key metrics: network goodput and robustness against link fading, typical in the underwater acoustic environment.

MINIMUM DELAY ROUTING

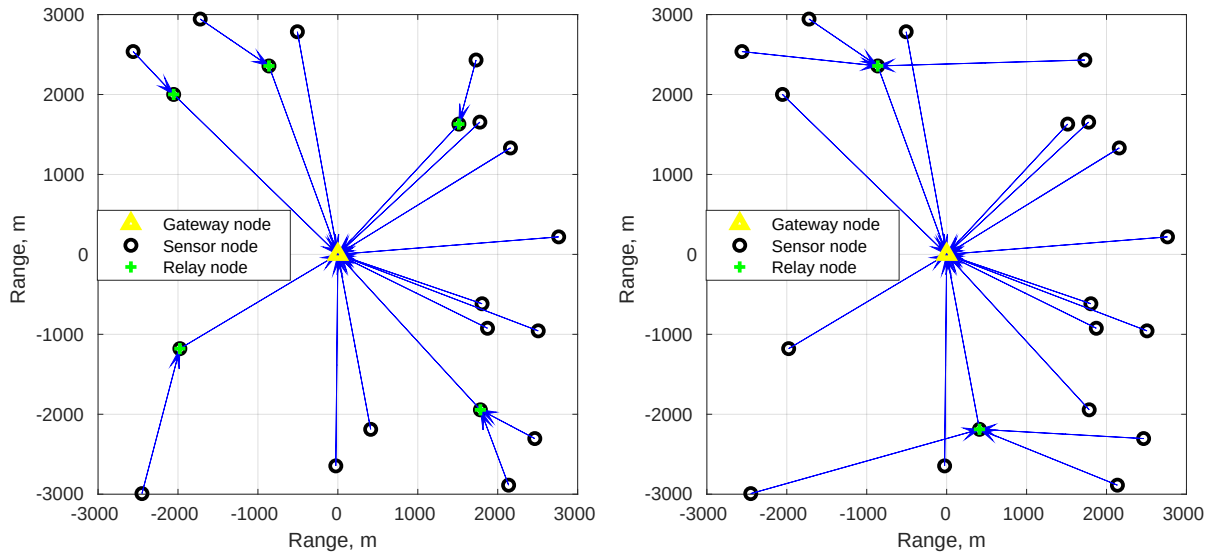
A simple and reliable approach to routing in WSNs is minimum delay routing. In most cases it is equivalent to shortest path routing, where a sensor node that requires a multi-hop route to the destination chooses the relay nodes by minimising the total propagation delay across all hops.

Let $\boldsymbol{C}$ and $\boldsymbol{T}_{\mathrm{p}}$ be $N \times N$ connectivity and propagation delay matrices respectively, established during the network discovery and setup stage, and then periodically updated based on received data packets, e.g. as described in [7]. This process is sufficient to maintain an accurate topology estimate of a quasi-stationary underwater sensor network. $N = 1 + N_{\mathrm{sn}}$ is the total number of nodes, including one gateway node and N_{sn} sensor nodes. $\boldsymbol{C}$ is a binary matrix, whose elements are $C[i, j] = 1$ if there is a link between nodes i and j, and $C[i, j] = 0$ otherwise. $T_{\mathrm{p}}[i, j]$ is the propagation delay from node i to node j.

We can identify the set of sensor nodes $M_{\text{dual-hop}}$, that do not have a direct link with the gateway node and, therefore, require a dual-hop connection, as follows:

$$M_{\text{dual-hop}} = \big\{ n \,|\, n \in [2, N],\, C[1, n] = 0 \big\} \tag{1}$$

For every sensor node i that requires a dual-hop connection, a relay node r_i is found that min-



(a) Minimum delay routing

(b) Fewest relays routing

Figure 2: Dual-hop routing strategies in a UASN comprising a surface gateway node and 20 sensor nodes at approximately 500 m depth with 3 km communication range.

imises the total propagation delay across two hops (sensor-relay and relay-gateway nodes):

$$\forall i \in M_{\text{dual-hop}},\ r_i = \underset{j \in [2,N]}{\operatorname{argmin}} \left\{ T_{\text{p}}[j,i] + T_{\text{p}}[1,j] \right\},\ \text{s.t. } C[1,j] = 1, C[j,i] = 1 \tag{2}$$

If there are no other sensor nodes that can serve as a relay, i.e. there is no node j that satisfies both $C[1,j] = 1$ and $C[j,i] = 1$ conditions, node i does not have dual-hop connectivity.

For an arbitrary multi-hop network, minimum delay routing can be achieved by the well-established Dijsktra's algorithm [12] which finds the shortest path tree topology, such as that shown in the 20-node example in Figure 2a. However, in the specific case of a dual-hop network topology, this process is significantly simpler, since an optimal relay node can be found by a single evaluation of (2) for every sensor node requiring a dual-hop connection.

Fewest Relays Routing

The disadvantage of the minimum delay routing approach is that it does not take into account the network throughput performance. The key feature of the SDH-TDA-MAC protocol described in Section 2 is the exploitation of many-to-one connections to achieve high throughput, whereas every relay branch of the network topology is processed sequentially, increasing the idle time caused by the dual-hop round trip delays and thus reducing the throughput.

Therefore, to maximise the throughput of the SDH-TDA-MAC protocol, the routing strategy should minimise the number of relay nodes, hereafter referred to as "fewest relays" routing. The aim of the routing algorithm is to find the smallest set of nodes M_{relays} such that:

$$\forall i \in M_{\text{dual-hop}},\ \exists j \in M_{\text{relays}},\ C[1,j] = 1, C[j,i] = 1, \tag{3}$$

i.e. the smallest subset of relay nodes that covers all sensor nodes requiring a dual-hop connection.

This is a set cover problem [13]. Every potential relay node j can be represented by a set of

nodes directly linked to it $M_C^j = \{i \,|\, C[j,i] = 1\}$. The optimal set of relay nodes $M_{\text{relays}} = \{a, b, ...\}$ is determined by finding the smallest collection of node sets $\mathcal{S} = \{M_C^a, M_C^b ...\}$ such that their union contains all nodes in $M_{\text{dual-hop}}$:

$$M_{\text{dual-hop}} \subseteq \bigcup_{M_C^j \in \mathcal{S}} M_C^j, \tag{4}$$

i.e. this is a problem of finding the set cover $\mathcal{S}$ of $M_{\text{dual-hop}}$ that uses the fewest sets M_C^j.

The set cover problem is NP-hard [13]; therefore, a computationally efficient method of finding the optimal set of relays M_{relays} does not exist. Instead, it can be found by a heuristic approximation algorithm that does not guarantee an optimal solution but efficiently finds good suboptimal solutions. Our implementation of such a heuristic algorithm is outside of the scope of this paper, but any existing general approximation algorithm for the set cover problem can be used to solve this problem, e.g. see [14], [15].

Figure 2b gives an example of the fewest relays routing solution found by our algorithm for the 20 node UASN. This routing strategy is more suitable for SDH-TDA-MAC, since there are only 3 sequential instances of TDA-MAC required to cover the whole network (1 gateway + 2 relays), compared with 6 TDA-MAC instances (1 gateway + 5 relays) using minimum delay routing shown in Figure 2a.

Routing Redundancy

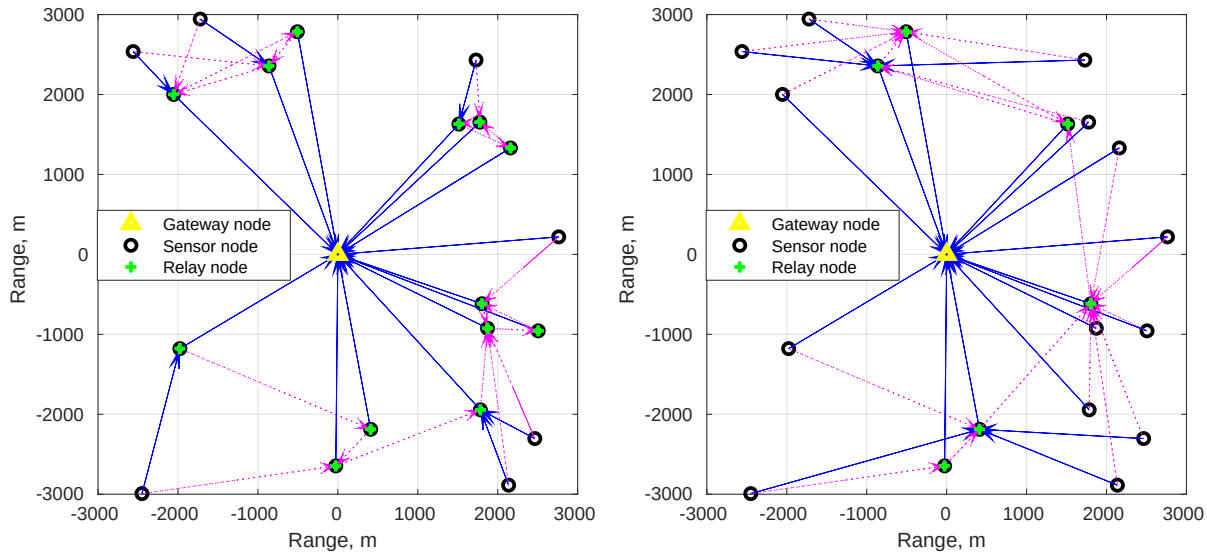
Although the fewest relays routing strategy increases the network throughput, it makes it less robust against random link fading typical for the underwater acoustic environment. For example, if a link between the gateway node and a relay node fails, e.g. due to signal path obstruction, excessive noise, interference, Doppler shift, multipath fading etc., all packets from this relay node's branch will be lost. To combat this issue, in [8] we proposed a routing diversity approach that is backward compatible with the SDH-TDA-MAC protocol, and where every node has multiple unique routes for its packets to reach the gateway node. Figure 3 shows an example of adding double redundancy to the two routing strategies from Figure 2. Every sensor node has two unique routes to the gateway, while the SDH-TDA-MAC protocol is identical to the original one described in Section 2.

The routing diversity approach, such as that shown in Figure 3 is implemented by repeating the routing procedure for every additional level of redundancy with extra constraints [8]:

- Every node (including directly connected nodes) must choose an extra destination different from the one already in use.
- Existing links cannot be used in reverse (i.e. if node j is a relay for node i, node i cannot be a relay for node j).

Simulation Results

This section presents the empirical evaluation results of the routing strategies discussed in this paper using an event-driven Matlab network simulator running the SDH-TDA-MAC protocol [8]. 100 sensor nodes are spread over a 6×6 km area at 470-490 m depth, similarly to the 20 node example shown in Figures 2 and 3. The gateway node is located at the centre of the coverage area at 10 m depth. The connection range is fixed at 2.5 km, which on average yields



(a) Minimum delay routing

(b) Minimum relay count routing

Figure 3: Dual-hop routing with double redundancy in a UASN comprising a surface gateway node and 20 sensor nodes at approx. 500 m depth with 3 km communication range. Every sensor node has two unique routes to send data to the gateway node.

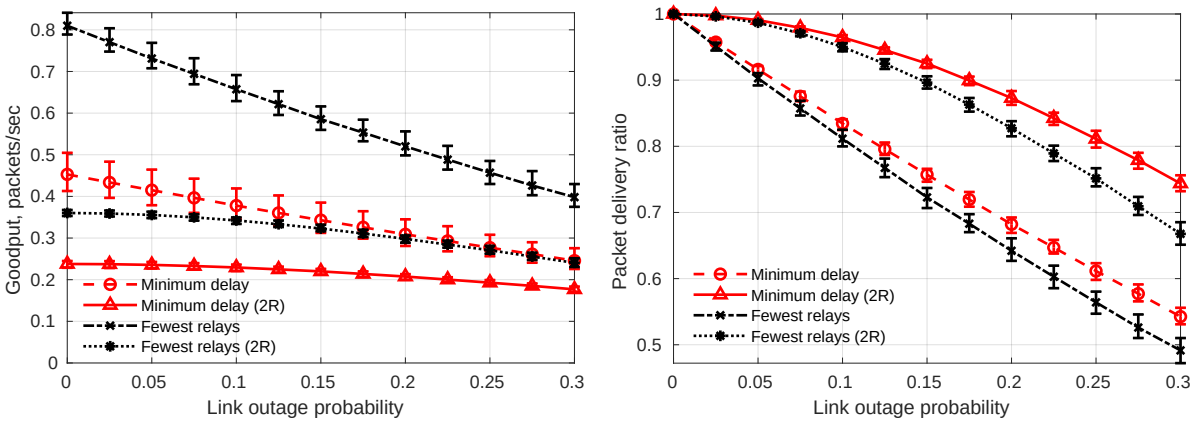
a 52/48% split among directly connected nodes and nodes connected via dual-hop links. All datapoints in the plots show an average of 50 simulations with different random seeds and node locations, with the error bars representing the 5th and 95th percentiles.

The network is simulated at a range of link outage probabilities to assess its robustness against random link fading. Link fading was modelled using a classical two-state Markov process [16] to approximate large-scale underwater acoustic link fading often observed in practice, where link outage may last for tens of seconds or minutes due to changes in the channel caused by node movement or external factors, such as noise. In the two-state Markov model both the duration of random link outage and the duration of normal link operation are exponentially distributed [17]. We fix the mean link outage duration at $\tau_{\text{outage}} = 30$ s, whereas the mean duration of the normal link operation is calculated as follows [17]:

$$\tau_{\text{normal}} = \frac{1 - p_{\text{outage}}}{p_{\text{outage}}} \tau_{\text{outage}} \tag{5}$$

where p_{outage} is the probability of link outage.

Figure 4 shows that the fewest relays routing strategy achieves a significant 79% increase in the network goodput (i.e. different data packets received at the gateway node) compared with minimum delay routing. However, it is less robust against random link fading compared with the latter that uses more relay nodes thus increasing the routing diversity. Introducing the double routing redundancy dramatically improves the network reliability, but at the cost of reducing the network goodput due to duplicate transmissions. For example, at 0.1 link outage probability the proportion of failed packet deliveries (one minus the packet delivery ratio) is reduced by a factor of 4, while the network goodput is reduced by 40% and 48% for minimum delay and fewest relays routing, respectively. This again shows that there is a trade-off between the network throughput and reliability. If maximising the network goodput is the primary concern, fewest relays routing with no redundancy is the best strategy, whereas if reliable packet delivery is more important than supporting high traffic loads, minimum delay routing with double redundancy is a far better strategy. The strategy that strikes a balance between the network



(a) Goodput at the gateway node *(b) Packet delivery ratio*

Figure 4: Trade-off between the network goodput and reliability achieved using the minimum delay and fewest relays routing strategies, with and without double redundancy (2R).

throughput and reliability is the fewest relays routing protocol with double redundancy, which combines the throughput maximising relay selection approach with routing redundancy for increased resilience against random link fading.

Another valuable metric to consider in future work on this topic is load balancing, i.e. designing routing strategies suitable for SDH-TDA-MAC that spread the transmission load more evenly among the sensor nodes, e.g. to maximise the network lifetime limited by the available battery energy at the underwater sensor nodes. For example, this could involve a dynamically changing network topology with different sensor nodes working as relays, based on the gateway node's knowledge of the channel state information received from the sensor nodes.

CONCLUSION

The routing strategies investigated in this paper provide new insights into the performance of the SDH-TDA-MAC protocol applied to UASNs with random link fading. Fewest relays routing maximises the network throughput, whereas minimum delay routing provides more robust packet delivery. Introducing the routing redundancy, where each sensor node has more than one unique path for its packet to reach the destination, dramatically increases the network reliability, but reduces the network goodput due to duplicate packet transmissions. Depending on the application-specific network criteria, e.g. high throughput vs reliable packet delivery, the routing strategies presented in this paper provide a range of options to achieve this trade-off.

ACKNOWLEDGEMENTS

This work was supported by the UK Engineering and Physical Sciences Research Council (EPSRC) through the USMART (EP/P017975/1) and Full-Duplex (EP/R003297/1) projects.

REFERENCES

[1] **H. S. Dol, P. Casari, T. van der Zwan, and R. Otnes.** Software-defined underwater acoustic modems: Historical review and the NILUS approach. *IEEE Journal of Oceanic Engineering*, 42(3):722–737, 2017.

[2] **B. Sherlock, J. A. Neasham, and C. C. Tsimenidis.** Spread-spectrum techniques for bio-friendly underwater acoustic communications. *IEEE Access*, 6:4506–4520, 2018.

[3] **Y. Zakharov, Y. Fei, P. Mitchell, N. Morozs, B. Henson, L. Shen, and T. Tozer.** Low-complexity UAC modem and data packet structure. In *Proceedings of Underwater Communications and Networking Conference (UComms'18)*, 2018.

[4] **J. Heidemann, M. Stojanovic, and M. Zorzi.** Underwater sensor networks: applications, advances and challenges. *Philosophical Transactions of the Royal Society of London A: Mathematical, Physical and Engineering Sciences*, 370(1958):158–175, 2012.

[5] **K. Kredo II, P. Djukic, and P. Mohapatra.** STUMP: Exploiting position diversity in the staggered TDMA underwater MAC protocol. In *Proceedings of IEEE INFOCOM*, 2009.

[6] **R. Diamant, G. N. Shirazi, and L. Lampe.** Robust spatial reuse scheduling in underwater acoustic communication networks. *IEEE J. Oceanic. Eng.*, 39(1):32–46, 2014.

[7] **N. Morozs, P.D. Mitchell, and Y. Zakharov.** TDA-MAC: TDMA without clock synchronization in underwater acoustic networks. *IEEE Access*, 6:1091–1108, 2018.

[8] **N. Morozs, P.D. Mitchell, and Y. Zakharov.** Dual-hop TDA-MAC with route diversity for robust data gathering in underwater acoustic sensor networks. Submitted to *IEEE J. Oceanic. Eng.*, 2019.

[9] **J. N. Al-Karaki and A. E. Kamal.** Routing techniques in wireless sensor networks: a survey. *IEEE Wireless Communications*, 11(6):6–28, 2004.

[10] **R. Otnes, J. Locke, A. Komulainen, S. Blouin, D. Clark, H. Austad, and J. Eastwood.** Dflood network protocol over commercial modems. In *Proceedings of the Underwater Communications and Networking Conference (UComms'18)*, 2018.

[11] **N. Morozs, et al.** Robust TDA-MAC for practical underwater sensor network deployment: Lessons from USMART sea trials. In *Proceedings of ACM WUWNet'18*, 2018.

[12] **E. W. Dijkstra.** A note on two problems in connexion with graphs. *Numerische Mathematik*, 1(1):269–271, 1959.

[13] **U. Feige.** A threshold of ln N for approximating set cover. *J. ACM*, 45(4):634–652, 1998.

[14] **D.S. Hochbaum.** Approximation algorithms for the set covering and vertex cover problems. *SIAM J. Comput.*, 11:555–556, 1980.

[15] **P. Slavík.** A tight analysis of the greedy algorithm for set cover. *Journal of Algorithms*, 25(2):237 – 254, 1997.

[16] **M. Zorzi, R. R. Rao, and L. B. Milstein.** On the accuracy of a first-order Markov model for data transmission on fading channels. In *Proceedings of the IEEE International Conference on Universal Personal Communications (ICUPC'95)*, pages 211–215, 1995.

[17] **E. N. Gilbert.** Capacity of a burst-noise channel. *The Bell System Technical Journal*, 39(5):1253–1265, 1960.

EXPLOITING SPATIAL DIVERSITY TO IMPROVE QOS-ENABLED UNDERWATER COMMUNICATIONS

K.C.H. Blom[a], H.S. Dol[a]

[a] TNO, Acoustics & Sonar department, The Hague, The Netherlands

Contact author: koen.blom@tno.nl, P.O. Box 96864, NL-2509JG The Hague

Abstract: *The bandwidth utilization of untethered underwater vehicles can be optimized by concurrently transmitting data with different Quality-of-Service (QoS) constraints, e.g., high-QoS telemetry data and low-QoS sensor data (such as a SONAR image) in a single transmission. The Multi-Stream Frequency-Repetition Spread Spectrum (MSFRSS) modulation has been developed to support such QoS-enabled underwater communications. This work evaluates MSFRSS performance in practical North Sea conditions. The unidirectional link between a RHIB and a bottom node is studied for single- and multi-hydrophone reception, and for different types of equalization. The potential performance increase for multi-hydrophone reception is illustrated by postprocessing of trial recordings.*

Keywords: *acoustic underwater communications, sea trial, Quality-of-Service levels*

1. INTRODUCTION

There is a growing interest in the use of untethered underwater vehicles to perform safe, sustainable and cost-effective underwater operations. For most applications, the bandwidth utilization of these vehicles can be maximized by concurrently transmitting data with configurable Quality-of-Service (QoS) constraints, e.g., high-QoS telemetry data and low-QoS compressed image snapshots in a single transmission. To support such QoS-enabled underwater communication, the Multi-Stream Frequency-Repetition Spread Spectrum (MSFRSS) modulation was introduced [1]. A short introduction to MSFRSS can be found in Section 2.

Previously, MSFRSS has been tested in a real-time demonstrator in a harbour and a fjord [2]. To evaluate the performance of MSFRSS in offshore conditions, a short North Sea trial was conducted on October 10th, 2018. During this trial, a series of communication and channel-sounding runs were executed to assess the unidirectional link between a RHIB and a bottom node. Details of this trial are discussed in Section 3.

Communication performance of the trial's unidirectional link was evaluated by postprocessing the bottom node recordings (for multiple receiver configurations). In contrast to earlier work, the exploitation of spatial diversity has now also been considered. The different receiver configurations are enumerated in Section 4, followed by their respective communication performances in Section 5.

Conclusions and recommendations are listed in Section 6.

2. MULTI-STREAM FREQUENCY-REPETITION SPREAD SPECTRUM

MSFRSS can be considered as a successor of Frequency-Repetition Spread Spectrum (FRSS) [3]. FRSS is a coherent multiband modulation where all subbands carry the same symbol sequence. This type of redundancy allows for joint equalization of these subbands at the receiver to exploit frequency diversity. In contrast to FRSS, MSFRSS modulates multiple sets of redundant subbands simultaneously. Each set of redundant subbands is called a stream, hence the name Multi-Stream Frequency-Repetition Spread Spectrum (MSFRSS).

To provide different QoS levels using MSFRSS, for each stream (i) its symbol constellation, (ii) its number of redundant subbands, (iii) its training configuration, and (iv) its code rate can be set. Details on the configuration used in the North Sea trial can be found below. An extensive description of MSFRSS, and its key transmitter/receiver operations are given in [2].

MSFRSS configuration

In the North Sea trial, high-QoS telemetry data and low-QoS compressed image snapshots were transmitted simultaneously (Section 3). The transmitted waveform covered a 30 kHz (half-power) bandwidth. This entire bandwidth was evenly divided over eight streams, each encompassing 3.75 kHz. One of these streams acted as high-QoS stream, holding six QPSK-modulated subbands, and the seven other streams were low-QoS streams, each holding three 8-PSK-modulated subbands. The configuration is visualized in Figure 1. For clarity, the depicted subband ordering is sequential. In reality, the distance between subbands is maximized using an objective function.

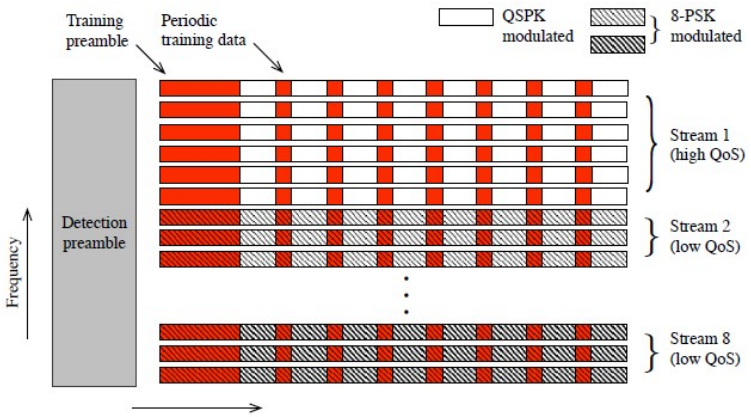


Figure 1: MSFRSS configuration used in the North Sea trial.

3. NORTH SEA TRIAL

To assess MSFRSS in offshore conditions, a NILUS bottom node [3] was deployed on the floor of the North Sea. An anchor was attached to the bottom node to prevent it from crabbing due to the current. Additionally, the node was tied to a surface buoy, for not having to depend on the acoustic release for recovery as this functionality was not 100% reliable in combination with the prototype MSFRSS implementation. The NILUS bottom node (Figure 2) was configured to continuously receive and record with all of its four hydrophones. The acoustic transmitter, broadcasting in the 17-47 kHz bandwidth, was deployed from the RHIB using the onboard crane (Figure 2).



Figure 2: The receiving NILUS bottom node (left) and the onboard crane used for deploying the transmitter (right).

The trial area was located approx. 10 km west of Scheveningen harbour, marked by the leftmost ellipse in Figure 3. The bathymetry in the trial area indicates that the local depths at low tide of the sandy seafloor in the trial area were between 16 and 22 m. During the trial day, on October 10th 2018, the actual depths as measured by the RHIB's echosounder during the bottom node deployments varied between 20 and 21 m, which was confirmed by the pressure sensor of the node. During these deployments, the air temperature was measured to vary between 14 and 15 °C. Wind speeds varied between 5 and 10 kn and there was no rain. The significant wave heights varied between 32 and 48 cm.

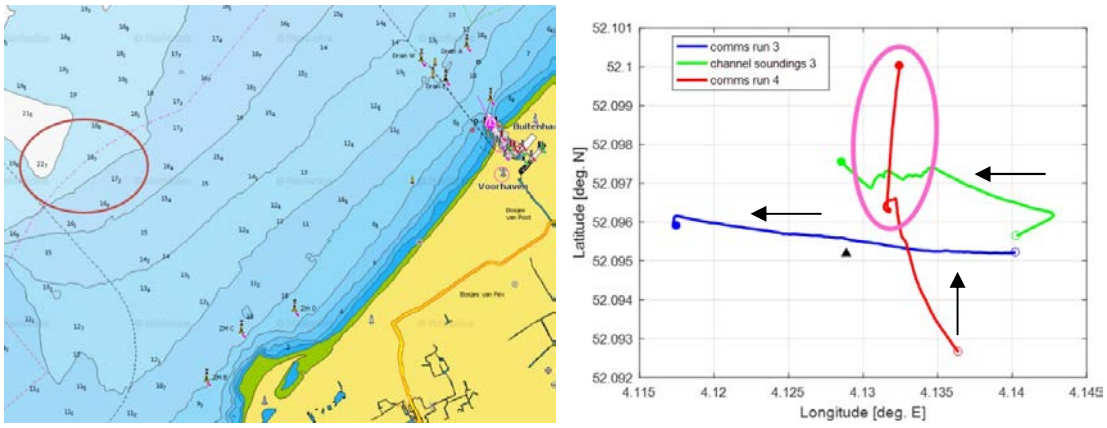


Figure 3: Bathymetry of the trial area (left); courtesy of Navionics. Tracks during the third deployment (right); the bottom node position is depicted by a triangle.

Deployment issues

There were three deployments of the bottom node in the trial area. Unfortunately, the bottom node had fallen on its side during every deployment, probably due to the connection to the surface buoy in combination with a sloping bottom and a strong surface current.

During the three deployments, in total three channel sounding experiments and four communication runs were executed. After on-board analysis of recordings from the first two deployments, the decision was made to stabilize the transmitter (near the end of the third deployment) by bringing in the crane. The latter decreased the Doppler induced by transmitter motion and improved communications results (Section 5). In this paper, only recordings from the third deployment are studied. The RHIB and bottom node positions during this deployment are depicted in Figure 3. Arrows indicate the direction of the RHIB's tracks.

Channel soundings

This section discusses channel soundings captured while sailing an in-bound track, i.e., the RHIB with transmitter was slowly moving towards the bottom node (Figure 3). The movement of the RHIB resulted in a negative Doppler velocity (assuming the sign convention that a positive velocity corresponds to an increasing range [4]). During this track, 16 series of of 4 pulse trains were transmitted and received, with each pulse train being a 10-s sequence of (Linear Frequency Modulated) LFM pulses of 32, 64, 128 and 256 ms. The 32-ms pulse train appeared to be the best fit for the delay-Doppler spread experienced in the channel.

Channel sounding results for the shortest and longest distance during the in-bound track of the RHIB are shown in Figure 4 and Figure 5, respectively. Herein, from left to right, the impulse response evolution, the spreading function, the Doppler spectrum and the power delay profile are shown.

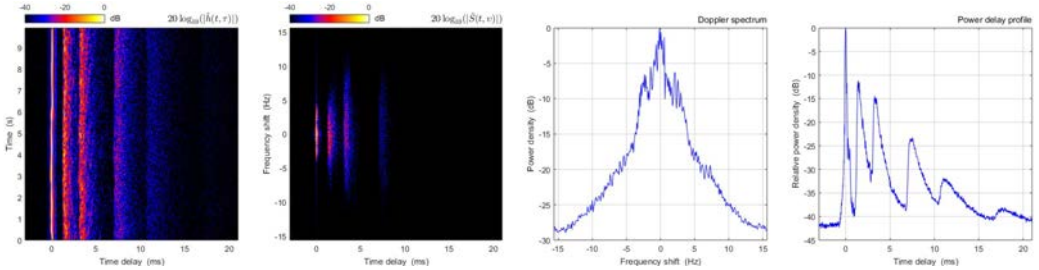


Figure 4: Channel sounding results at approx. 200 m distance.

There is a significant delay spread in both measurements. At 200 m distance, the first arrival is clearly the most powerful arrival. The channel sounding at 900 m seems to present evidence of non-minimum phase behaviour; due to the variation of the propagation speed while travelling through the water, the direct-path arrival arrives later than the reflected arrival.

Also, a relatively large Doppler spread can be recognized for both distances. As the receiver was stationary, this must have been because of (i) the transmitter moving heavily and (ii) reflections from a moving sea surface.

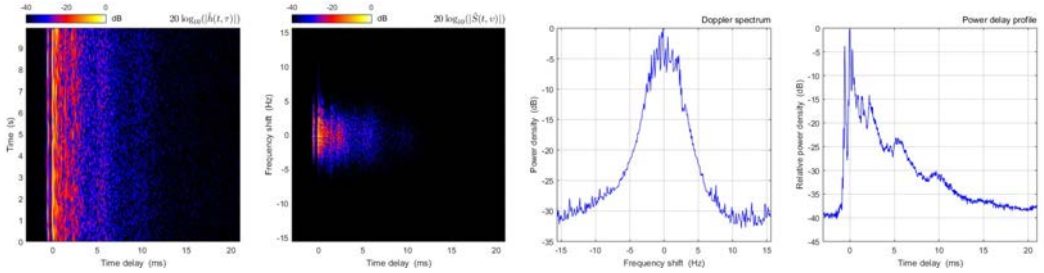


Figure 5: Channel sounding results at approx. 900 m distance.

Communication experiments

In each communication run, MSFRSS was employed to transmit image snapshots registered by an on-board webcam and telemetry data (GPS-NMEA strings) from the boat to the bottom node. Per MSFRSS transmission (Section 2) 96 bytes were reserved for the high-QoS payload (GPS-NMEA string) and 2.9 kB for the low-QoS payload (image data). The duration of each transmission was 4.35 s. The effective data rate of the QPSK/8-PSK configuration is 5630 bit/s.

4. RECEIVER CONFIGURATIONS

Compared to earlier experiments in Trondheim fjord [2], the channel conditions on the North Sea were more challenging. To deal with this offshore environment, instead of only using the top hydrophone channel of the NILUS' tetrahedron array, the MSFRSS receiver was extended to coherently combine all four hydrophone channels. Apart from exploiting spatial diversity, an option to switch the tap update algorithm between Least Mean Squares (LMS) or Recursive Least Squares (RLS) was also added.

Table 1 offers an overview of all receiver configurations and relevant parameters of the respective tap update methods. Herein, the subband equalizer length refers to the span of the feed forward filters per subband. The choice of the subband equalizer length, the LMS step-size parameter and the RLS forgetting factor are based on [2].

Configuration	*Subband eq. length*	*Parameters*	*Receive hydrophone(s)*
SISO-LMS	12.5 ms	0.3 (step-size par.)	top
SISO-RLS	12.5 ms	0.995 (forgetting factor)	top
SIMO-LMS	12.5 ms	0.3 (step-size par.)	all (4)
SIMO-RLS	12.5 ms	0.995 (forgetting factor)	all (4)

Table 1: MSFRSS receiver configurations

5. COMMUNICATION PERFORMANCE

This section focuses on the communication performance for single-hydrophone (SISO-LMS and SISO-RLS) and multi-hydrophone receiver processing (SIMO-LMS and SIMO-RLS).

SISO-LMS and SISO-RLS configuration

Initially, during the first half of the fourth communication run, very few correct (single-hydrophone) demodulations were obtained for the high-QoS payload and none for the low-QoS payload. As explained in Section 3, this was caused by the significant Doppler spread, being amplified by the RHIB's crane deploying the transmitter.

The situation improved significantly when bringing in the crane (Figure 2) and gently streaming the transmitter behind the boat. In Figure 3, the part of the track where receptions improved is indicated by the rightmost ellipse. Having the transmitter behind the boat, most of the high-QoS payloads could correctly be demodulated, but still none of the low-QoS payloads.

SIMO-LMS and SIMO-RLS configuration

After coherently combining all four hydrophone channels, both the demodulation of the low-QoS payloads and high-QoS improved significantly. In the SIMO-LMS receiver configuration, out of the 69 detections (of 76 transmissions; 91%), 64 high-QoS payloads (GPS-NMEA strings) were demodulated correctly (93%). These 64 GPS positions are visualized on top of the track recorded by the RHIB in Figure 6. Apparently, the GPS receiver in the transmit laptop had a coarser resolution than the RHIB's receiver. Assuming that the same source satellites were used, this difference must have been due to a lack of interpolation (e.g., by Kalman filtering) in the laptop's GPS receiver.

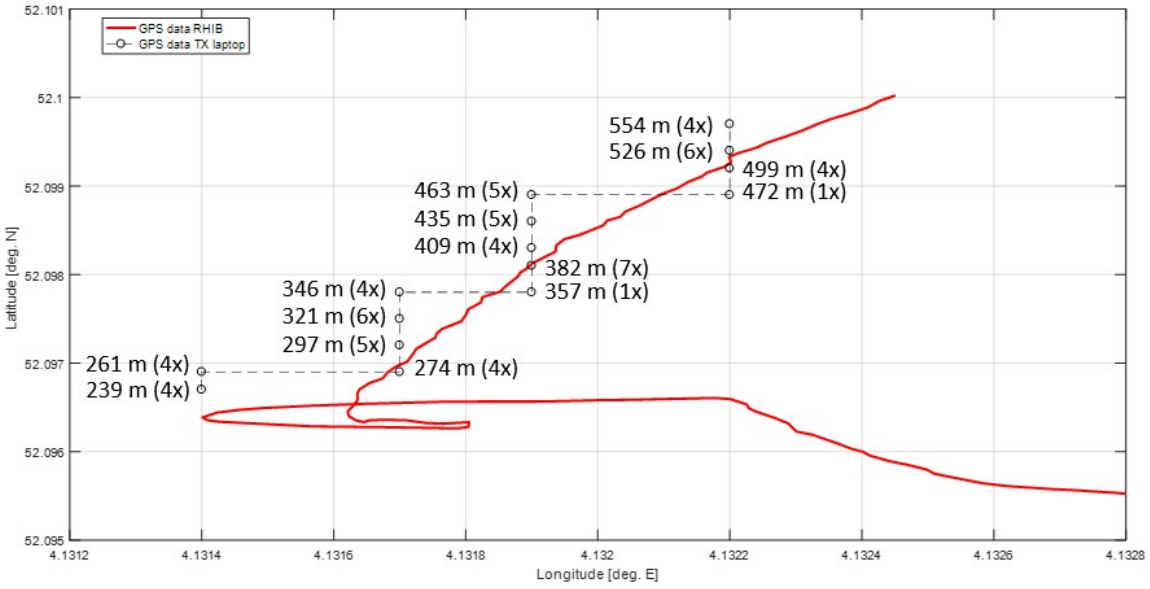


Figure 6: Demodulated GPS positions during the second half of the fourth comm. run.

Results for the demodulation of low-QoS payloads (images) for the multiple-hydrophone configurations are shown in Table 2. For these receptions, SIMO-RLS seems to perform slightly better than SIMO-LMS.

Configuration	*Partially correct image receptions*	*Fully correct image receptions*
SIMO-LMS	30 (43%)	5 (7%)
SIMO-RLS	34 (49%)	7 (10%)

Table 2: SIMO-LMS and SIMO-RLS performance for the low-QoS payload.

The output SNRs for demodulation of the high-QoS and the low-QoS payloads using both SIMO-LMS and SIMO-RLS are shown in Figure 7. In general, the output SNR is a good indicator for equalizer performance [5]. It appeared that, especially for the low-QoS payload, the SIMO-RLS receiver seems to outperform the SIMO-LMS receiver.

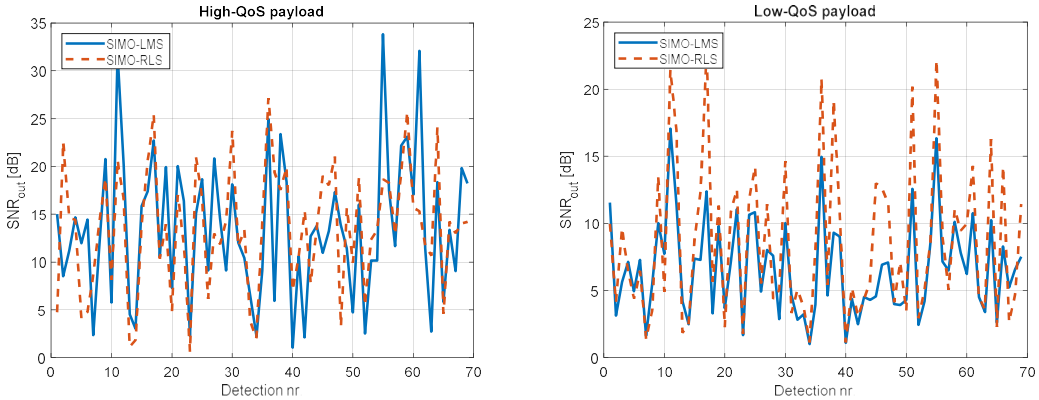


Figure 7: Output SNR comparison for the SIMO processing.

For three distances (321 m, 409 m, 499 m) the MSFRSS demodulation results are shown in Table 3. The respective number of bit errors for the different payloads were calculated using the reference transmissions available from the transmit laptop on the RHIB.

		
321 m, original image	SIMO-LMS: Bit errors high QoS = 0 / 768 Bit errors low QoS = 48 / 20125	SIMO-RLS: Bit errors high QoS = 0 / 768 Bit errors low QoS = 0 / 20125
		
409 m, original image	SIMO-LMS: Bit errors high QoS = 0 / 768 Bit errors low QoS = 43 / 20125	SIMO-RLS: Bit errors high QoS = 0 / 768 Bit errors low QoS = 0 / 20125

		
499 m, original image	SIMO-LMS: Bit errors high QoS = 0 / 768 Bit errors low QoS = 0 / 20125	SIMO-RLS: Bit errors high QoS = 0 / 768 Bit errors low QoS = 12 / 20125

Table 3: MSFRSS demodulation using the SIMO-LMS and SIMO-RLS configurations.

6. CONCLUSIONS

In this work, QoS-enabled underwater communication has been demonstrated for an unidirectional link between a RHIB and a bottom node under offshore conditions. To create QoS diversity, MSFRSS was employed. After stabilizing the RHIB's acoustic transmitter, to decrease the Doppler spread, most single-hydrophone receptions of the high-QoS payloads (GPS-NMEA strings) of the MSFRSS messages could be demodulated correctly.

Reception of the low-QoS payloads (images) required coherent combining of all four hydrophone channels that were available on the bottom node. When using coherent combining and RLS (SIMO-RLS) to determine the equalizer weight updates, approximately 10% of the low-QoS payloads were correctly received, and about 49% partially correct.

Although data rates were smaller than for an earlier demonstration in a fjord (5.5 kbit/s vs. 7.3 kbit/s) [2], the potential of multi-hydrophone reception for QoS-enabled underwater communications in offshore conditions has certainly been demonstrated.

ACKNOWLEDGEMENTS

The authors would like to thank Robert van den Bos, Mathieu Colin and Mark van Spellen for their help during the trial campaign.

REFERENCES

[1] **K.C.H. Blom, H.S. Dol and M.K. Prior**, Development of a wideband underwater acoustic modulation providing quality-of-service support, *MTS/IEEE OCEANS 2017, Anchorage (AK), USA*, pp. 1-4, 2017.

[2] **K.C.H. Blom and H.S. Dol**, QoS-enabled underwater acoustic communications, *MTS/IEEE OCEANS 2018, Charleston (SC), USA*, pp. 1-7, 2018.

[3] **H.S. Dol, M.E.G.D. Colin, P.A. van Walree and R. Otnes**, How smartphone industry made UComms easier: Moore's law goes underwater, *OCEANS 2015, Genova*

[4] **P.A. van Walree**, Channel sounding for acoustic communications: techniques and shallow-water examples, *Tech. Rep. FFI-rapport 7*, Norwegian Defence Research Establishment (FFI), 2011.

[5] **P.A. van Walree**, On the definition of receiver output SNR and the probability of bit error, *MTS/IEEE OCEANS 2013, Bergen*, 2013

ROBUST DIRECTION FINDING IN THE FLUCTUATING OCEANS BY COMPLEX L1-NORM PRINCIPAL COMPONENT ANALYSIS

George Sklivanitis[a], Gaultier Real[b] , Dimitris A. Pados[a]

[a]I-SENSE & Department of Computer and Electrical Engineering & Computer Science, Florida Atlantic University, Boca Raton, FL 33431, USA
[b]DGA Naval Systems, Toulon France 83137, France

George Sklivanitis, Florida Atlantic University, 777 Glades Road, Boca Raton, FL 33431, Phone: 561-297-1163, Fax: 561-297-2800, E-mail:gsklivanitis@fau.edu

Abstract: *We consider the problem of robust direction-of-arrival (DoA) estimation in dynamic ocean environments. Robust direction finding of underwater acoustic signals transmitted from known locations may enable accurate localization of a receiver node underwater, as well as enhance link communication rate by instructing the receiver to listen for transmissions from a specific direction. We propose to estimate the DoA of underwater acoustic signals via subspace methods, executed at a receiver array, that involve performing what is known as principal-component analysis (PCA) for finding the L2-norm principal vector subspace of the recorded signal snapshots. However, in practice coherence loss, which typically arises from dynamic wavefront fluctuations due to internal waves, scattering from the sea surface and/or bottom and other unknown environmental parameters, may result in recorded signal snapshots that may be corrupted by faulty measurements, leading to an inaccurate estimation of the DoA and source position. We propose to model the loss of coherence as multiplicative random noise applied to the measured acoustic signal. In such cases, L2-norm PCA methods suffer from significant performance degradation. Motivated by the resistance of novel L1-norm-derived subspaces against the impact of irregular, highly deviating points in reduced-dimensionality data approximations, we propose to employ L1-norm (absolute error) maximum-projection PCA of the antenna array measurements and evaluate the performance of a novel, outlier-resistant DoA estimation algorithm. Experimental assessment of the proposed DoA algorithm is conducted over underwater measurements acquired from an ultrasonic transmitter source (at 2.25MHz) operating in a controlled water tank environment that reproduces the effect of a fluctuating ocean. This experimental configuration allows to accurately reproduce the effects of spatial medium fluctuations on the propagated sound waves, in a fully reproducible and monitored fashion. The benchmark of the proposed DoA estimation algorithm on this experimental dataset represents a preliminary step before validating its performance on at-sea recorded data.*

Keywords: *Undersea localization, robust direction finding, complex L1-PCA*

1. INTRODUCTION

Fundamental to the success of underwater communications is robust localization and tracking to support position-aware data routing and autonomous vehicle navigation in the GPS-less oceanic environment. GPS-free localization schemes proposed for terrestrial radio networks involve intensive message exchanges, and therefore are not suitable for the low-bandwidth, high-latency undersea acoustic channel. For this reason, existing state-of-art approaches for undersea localization and tracking either consider expensive inertial sensors [1], geophysical-based [2], or acoustic communication techniques [3]. Inertial/dead reckoning techniques exhibit position error growth that is unbounded with traveled distance due to inertial sensor drifts. High cost and power consumption of quality inertial measurement sensors precludes their use in small, low-cost undersea vehicles. Geophysical-based techniques exhibit bounded position error, but they are challenged by the visual and acoustic range of cameras and sonar, that compromise accurate detection, identification, and classification of features extracted from corresponding imaging information. Acoustic-based localization techniques rely on angle or distance measurements between communicating nodes that are usually collected by received-signal-strength indicator (RSSI), time-of-arrival (ToA), time of flight (ToF), time-difference-of-arrival (TDoA), and angle-of-arrival (AoA) [4] methods. However, long propagation delays and the multipath nature of the undersea environment, especially in shallow water, results in significant errors and outliers in acoustic-based measurements. In this context, acoustic beacon ranging proposals in the literature have been seen to provide unreliable location estimates due to stringent time synchronization requirements and variable path loss. Similarly, acoustic localization based on multiple-signal-classification (MUSIC)-type and maximum-likelihood (ML) DoA estimation methods have their own limitations. MUSIC-type schemes are more efficient in terms of hardware and execution time requirements compared to their ML counterparts. However, they are limited in the case of loss of coherence (or correlation) due to ocean fluctuations such as internal waves or in the presence of multipath interference due to shallow water.

Conventional subspace-based DoA-estimation methods, such as the celebrated MUSIC [5], seek to exploit the inherent separability of the signal and noise subspaces. Therefore, they rely largely on the eigenstructure of the (estimated) received-signal correlation matrix, or the L2-norm-principal subspaces of the recorded snapshots, obtained usually by means of familiar singular-value-decomposition (SVD) [6] of the received data matrix. In unobstructed (normal) system operation, such methods are well known to afford high target-angle resolution, while, in Gaussian noise, offer unbiased and asymptotically consistent DoA estimates [7].

However, the coherence loss, which typically arises from dynamic ocean fluctuations and unknown environmental parameters may take the form of multiplicative colored random noise that is applied to the recorded measurements. In such cases, the performance of L2-subspace-based DoA estimation methods may be significantly degraded, due to corrupted signal snapshots that are represented in the receiver data matrix by points that lie far off the nominal-signal subspace. Squared-fitting-error minimizers [8] such as L2-principal subspaces are highly responsive to such outlier data points, thus L2-subspace-based DoA estimators are inevitably misled.

On the other hand, absolute-error minimizers place less emphasis on individual data-point divergence. More specifically, L1-PCA of real-valued data matrices has attracted extensive documented research since the mid-twentieth century [9] and even more so in the past decade. Work in [10] focused on L1-PCA in the form of residual error minimization. However, minimum error L1-PCA has to date no known solution for its general multiple component case. Work in [11] considered projection maximization L1-PCA where data projection is measured by means of the L1-norm, while the first exact solvers for L1-PCA of real valued

data are provided in [12], [13]. Simulation studies highlight the sturdy resistance of L1-derived subspaces against outlier-inflicted data corruption. Applications of the proposed algorithms include dimensionality reduction, image conditioning/restoration and direction finding. Lp-norm derived subspaces have been employed in [14] for robust MUSIC-like DoA estimation in impulsive noise environments. Recent work in [15] established theoretical and algorithmic foundations of L1-PCA for complex-valued data matrices.

In this paper, motivated by the resistance of L1-norm derived subspaces against outliers and/or impulsive noise data corruption, we propose to employ L1-norm (absolute-error) maximum-projection PCA on complex data measurements [15] from a hydrophone array and evaluate an outlier-resistant MUSIC-like DoA estimation algorithm on experimental data from a scaled water tank experiment [14]. The tank experiment aims to reproduce the effect of ocean fluctuations on the received pressure field. The coherence loss is mimicked by means of a random lens placed between an ultrasonic transmitter source (at 2.25 MHz) and the array of hydrophones. We assess the direction finding performance of complex L1-norm PCA algorithms [15] and compare to conventional MUSIC (L2) estimation methods by means of the standard root-mean square error (RMSE).

2. SYSTEM MODEL

We consider an underwater uniform linear array (ULA) of M elements. The length-M array response vector for a source impinging on the antenna array at an arbitrary direction of arrival $\theta \in (-\pi/2, \pi/2]$ is given by:

$$\mathbf{s}(\theta) \triangleq \left[1, e^{-j\frac{2\pi f_c d \sin(\theta)}{c}}, \ldots, e^{-j\frac{(D-1)2\pi f_c d \sin(\theta)}{c}}\right]^T \in \mathbb{C}^{M\times 1} \qquad (1)$$

where $(\cdot)^T$ denotes the transpose operator, f_c is the carrier frequency, c is the signal propagation speed underwater, and d is the fixed inter-element spacing of the array. Let θ be the direction of arrival of a monochromatic source that emits an acoustic signal at frequency f_c. The acoustic pressure field received at the antenna array is represented by its Discrete Fourier Transform (DFT). Thus, the n-th observation vector, for $n = 1, 2, \cdots, N$ is of the form:

$$\mathbf{y}_n = x_n(\theta)\mathbf{s}(\theta) + \mathbf{n}_n \in \mathbb{C}^{M\times 1} \qquad (2)$$

where $x_n(\theta) \in \mathbb{C}$ denotes the n-th snapshot of the source signal and $\boldsymbol{n}_n \in \mathbb{C}^M$ accounts for the additive zero-mean and white circularly-symmetric complex Gaussian noise vector at the n-th snapshot, with per-element variance σ^2, that is $\boldsymbol{n}_n \sim CN(0, \sigma^2 \boldsymbol{I}_M)$, where $\boldsymbol{I}_M$ is the identity matrix.

In order to model the loss of coherence along the antenna array, we introduce a random variable $\boldsymbol{\psi}_n \in \mathbb{C}^M$ such that:

$$\mathbf{y}_n = x_n(\theta)\mathbf{s}(\theta) \otimes \psi_n + \mathbf{n}_n \in \mathbb{C}^{M\times 1} \qquad (3)$$

where $\otimes$ denotes the hadamard product operator and $\boldsymbol{\psi}_n$ is assumed to account for the multiplicative zero-mean and complex normal distributed phase noise vector at the n-th snapshot with covariance matrix $\boldsymbol{\Sigma}_n$. Work in [18] has considered a similar model to statistically characterize particular regimes of fluctuation. In fact, such multiplicative complex noise is well-suited to model as additive phase noise. Considering the model in Eq. (3), we then assume that the loss of coherence is due to a perturbation of the phase wavefront. In order to facilitate the experimental setup, the covariance matrix $\boldsymbol{\Sigma}_n$ is assumed to remain constant in time, i.e., we consider only spatial fluctuations of the propagating medium.

3. SUBSPACE BASED DIRECTION OF ARRIVAL ESTIMATION

In regular system operation (i.e., when there are no spatial fluctuations) the one-dimensional principal subspace of the observed snapshots at the antenna array is the span of the steering vector $\boldsymbol{s}(\theta)$. Perfect knowledge of $\boldsymbol{s}(\theta)$ can lead to perfect knowledge of θ. In other words, for any $\theta \in (-\pi/2, \pi/2]$, $M - |\boldsymbol{s}^{\boldsymbol{H}}(\varphi)\boldsymbol{s}(\theta)| = 0$, if and only if $\theta = \varphi$. Unfortunately, perfect knowledge of $\boldsymbol{s}(\theta)$ is not possible with finite number of observations $\{\boldsymbol{y}_n\}_{n=1}^{N}$; $\boldsymbol{s}(\theta)$ can only be estimated from the received snapshots. In particular, the autocorrelation matrix of the complex valued observations is:

$$\mathbf{R}_y = \mathrm{E}\{\mathbf{y}_\mathrm{n}\mathbf{y}_\mathrm{n}^\mathrm{H}\} = \mathbf{s}(\theta)\mathbf{R}_\mathrm{x}\mathbf{s}^\mathrm{H}(\theta) + \sigma^2\mathrm{I}_\mathrm{M} \tag{4}$$

where $\boldsymbol{R}_x$ is the autocorrelation matrix of the source signal. Given the eigenvalue-decomposition (EVD) of $\boldsymbol{R}_y$:

$$\mathbf{R}_y \overset{\text{evd}}{=} \mathbf{U}\left(\boldsymbol{\Lambda} + \sigma^2\mathbf{I}_M\right)\mathbf{U}^H \tag{5}$$

where $\boldsymbol{\Lambda} = \boldsymbol{diag}[\lambda_1 \quad \cdots \quad \lambda_M]$ is the diagonal matrix containing the sorted eigenvalues $\lambda_1 \geq \lambda_2 \geq \cdots \geq \lambda_M$ and $\boldsymbol{U}$ is the corresponding $M \times M$ orthonormal eigenmatrix, the leftmost column of $\boldsymbol{U}_{:,\boldsymbol{1}}$ constitutes a complete orthonormal basis for the source signal subspace. Then the solution $\boldsymbol{q}_{opt} \in \mathbb{C}^M$ to the L2-principal subspace problem:

$$\underset{\mathbf{q}\in\mathbb{C}^M;\ \|\mathbf{q}\|_2=1}{\operatorname{argmax}} \ \mathrm{Tr}\left(\mathbf{q}^H\mathbf{R}_y\mathbf{q}\right) \tag{6}$$

coincides with $\boldsymbol{U}_{:,\boldsymbol{1}}$ and offers a complete characterization of the signal subspace. As a result, any $\theta \in (-\pi/2, \pi/2]$ can be optimally examined for source signal presence by:

$$\theta \in (-\pi/2, \pi/2] \Leftrightarrow (\mathbf{I}_M - \mathbf{q}_{\mathrm{opt}}\mathbf{q}_{\mathrm{opt}}^H)\mathbf{s}(\theta) = \mathbf{0}_M \tag{7}$$

In practice, perfect knowledge of $\boldsymbol{R}_y$ cannot be assumed, instead $\boldsymbol{R}_y$ may be sample average estimated over the N complex-valued snapshot vectors as $\boldsymbol{R}_y \triangleq \frac{1}{N}\sum_{n=1}^{N}\boldsymbol{y_n}\,\boldsymbol{y}_n^H$.

The maximization argument in Eq. (6) is accordingly calculated by $\frac{1}{N}Tr(\boldsymbol{q}^H\boldsymbol{Y}\boldsymbol{Y}^H\boldsymbol{q}) = \frac{1}{N}\|\boldsymbol{q}^H\boldsymbol{Y}\|_2^2$. Consequently, the solution to the problem in Eq. (6) is equivalent to the estimation of the L2 –principal subspace from a number of samples in $\mathbb{C}^M$ that is formulated as:

$$\mathbf{q}_{\mathrm{L2}} = \underset{\mathbf{q}\in\mathbb{C}^M;\ \|\mathbf{q}\|_2=1}{\operatorname{argmax}} \ \|\mathbf{q}^H\mathbf{Y}\|_2 \tag{8}$$

where $\boldsymbol{Y} \triangleq [\boldsymbol{y}_1 \quad \cdots \quad \boldsymbol{y}_N] \in \mathbb{C}^{M\times N}$ and $\|\cdot\|_{\boldsymbol{2}}$ denotes the L2-norm. The solution to Eq. (4) $\boldsymbol{q}_{L2}$ is the left singular vector of the complex-valued matrix $\boldsymbol{Y}$ that corresponds to its highest singular value. For fixed number of observation snapshots N and additive white Gaussian noise data corruption as described in Eq. (2), $\boldsymbol{q}_{L2}(N)$ is the maximum likelihood (ML) estimate of the true signal subspace $\boldsymbol{q}_{true} = \frac{\boldsymbol{s}(\theta)}{\sqrt{M}}$. As N increases to infinity, $\|\boldsymbol{q}_{L2}(N) - \boldsymbol{q}_{true}\|$ converges to zero in probability for every norm. In view of Eq. (7), the direction of

arrival for the source signal is estimated as the argument that corresponds to the highest peak of the power spectrum:

$$P_{L2}(\theta) = \|(\mathbf{I}_M - \mathbf{q}_{L2}\mathbf{q}_{L2}^H)\mathbf{s}(\theta)\|_2^{-1} \quad (9)$$

which is proved to be equivalent to the familiar MUltiple SIgnal Classification procedure (MUSIC) [5].

4. ROBUST DIRECTION FINDING WITH COMPLEX L1-PCA

We now steer our focus to the scenario of interest, where each snapshot is corrupted by multiplicative phase noise that emulates the loss of coherence in the receiver hydrophone array. Typically, the closer the antenna elements, the more correlated the acoustic pressure. On the other hand, two antenna elements that are far from each other may capture different signal perturbations. Consequently, the received signals should be less correlated. Considering that the coherence loss can be modelled as multiplicative random noise applied to the measured acoustic signal, then signal and noise subspaces are not separable by means of EVD operation any more. Another interesting observation is that, in a contaminated data record, the corrupted snapshots are expected to lie far away from the signal subspace snapshots. Importantly, as practitioners have long observed, squared-value expressions, such as L2-norm, put significant emphasis on extreme errors and render accordingly principal subspaces that are particularly sensitive to outlier-inflicted data corruption.

Recent studies in the field of L1-principal component analysis for complex-valued data [15] have demonstrated that L1-principal subspaces are far more resistant to sporadic contamination of data by outliers than L2-principal subspaces. Motivated by these observations, we propose to examine the direction finding performance of a DoA estimation algorithm that instead of $span(\boldsymbol{q}_{L2})$ uses the one-dimensional L1-principal subspace of the received complex-valued data matrix, defined by the span of :

$$\mathbf{q}_{\mathrm{L1}} = \underset{\mathbf{q}\in\mathbb{C}^M;\, \|\mathbf{q}\|_2=1}{\operatorname{argmax}} \|\mathbf{q}^H\mathbf{Y}\|_1 \quad (10)$$

where $\|\cdot\|_1$ denotes the L1-norm. Thereafter, the direction of arrival of the source signal of interest will be calculated in accordance to Eq. (9) as the argument that corresponds to the highest peak of the L1 principal subspace power spectrum that is defined as:

$$P_{\mathrm{L1}}(\theta) = \| \left(\mathbf{I}_M - \mathbf{q}_{L1}\mathbf{q}_{L1}^H\right) \mathbf{s}(\theta)\|_2^{-1} \quad (11)$$

By not placing squared emphasis on the magnitude of each point (as L2-PCA does) L1-PCA is far more resistant to outlying, peripheral data points. Recent studies have shown that when the processed data are not outlier corrupted the solutions of L1-PCA and L2-PCA describe a nearly identical subspace. Although L1-principal subspace finding in the form of Eq. (10) is not a new problem in the literature, the first exact/optimal solvers for real-valued data were provided in [12], [13]. Specifically, [13] proved that real-valued L1-principal component analysis can be converted into a combinatorial problem over antipodal binary variables (± 1) solvable with intrinsic complexity, polynomial in the data record size $\mathcal{O}(N^{\boldsymbol{rank}(Y)})$. In contrast to real-valued L1-PCA, complex L1-PCA –in the form of Eq. (10)- has no obvious connection to a combinatorial problem. Until recently, no finite-step algorithm (exponential or other) was known for providing an optimal solution to Eq. (10). Work in [15] has proved that Eq. (10) can be casted as an optimization problem over the set of unimodular vectors and provided two fast algorithms to solve Eq. (10) optimally.

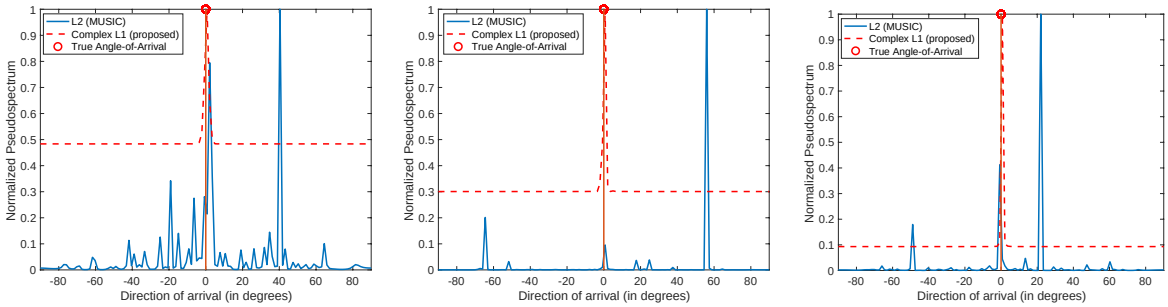


Fig.1: DoA estimation spectra P_{L1} and P_{L2} for unsaturated [US1, 17], partially saturated [PS1, 17], and fully saturated [FS1, 17] fluctuation categories in the experimental configuration (from left to right).

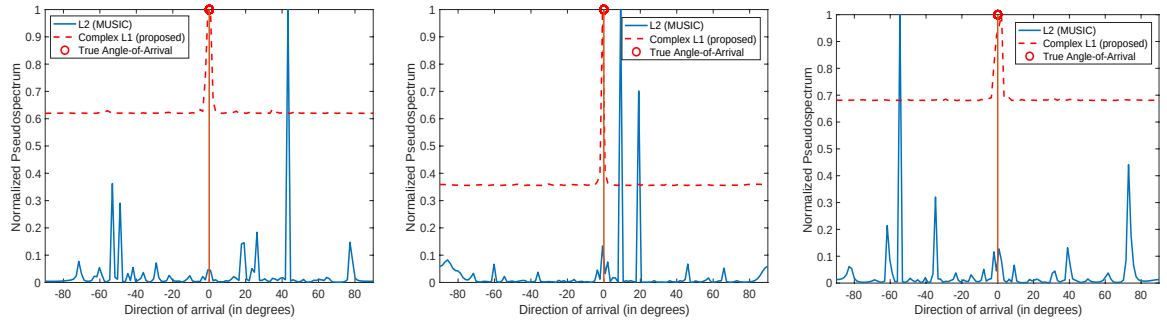


Fig.2: DoA estimation spectra P_{L1} and P_{L2} for unsaturated [US1, 17], partially saturated [PS1, 17], and fully saturated [FS1, 17] fluctuation categories in the P3DCOM configuration (from left to right).

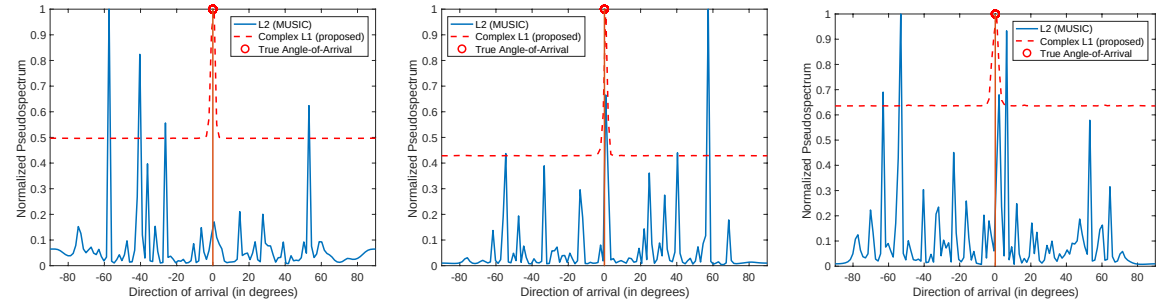


Fig.3: DoA estimation spectra P_{L1} and P_{L2} for unsaturated [US1, 17], partially saturated [PS1, 17], and fully saturated [FS1, 17] fluctuation categories in the P3DTEx configuration (from left to right).

5. EXPERIMENTAL RESULTS

We leverage direct complex L1-PCA introduced in [Algorithm 1, 15] to experimentally assess the direction finding performance of both L2-PCA and L1-PCA by carrying out DoA estimation over complex-valued measurements acquired from an ultrasonic transmitter source that operates in a controlled water tank environment. In particular, a moving hydrophone simulates a virtual array of hydrophones and measures the monochromatic continuous acoustic signal that is emitted from a fixed transducer [17]. We consider a CW chirp signal that is transmitted at $f_c = 2.25$ MHz with duration 22.2 μs, amplitude of 5 V, and wavelength $\lambda = 0.658$ mm. The signal is transmitted through a random faced acoustic lens that is used to to induce a spatially fluctuating sound pressure field [17]. Measurements are conducted in a 3m long, 1m wide and 1m deep, water tank filled with fresh water. The temperature was controlled by a probe continuously. The equipment was located in the middle of the tank depth and it was possible to ignore the influence of bottom and surface reflections. Automatic

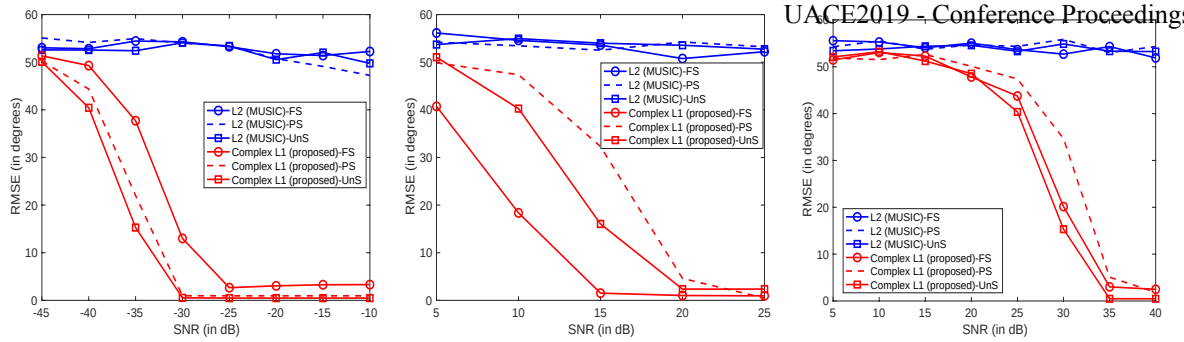


Fig.4: RMSE versus SNR for unsaturated [US1, 17], partially saturated [PS1, 17], and fully saturated [FS1, 17] fluctuation categories for experimental, PD3COM and PD3TEX configurations (from left to right).

displacements of the hydrophone on a vertical axis were used to simulate vertical arrays of $M = 64$ hydrophones, separated by a distance of 0.3 mm. More details and a diagram of the experimental setup can be found in [17].

Signal distortions from the random lens that is introduced between the transducer and the receiver array are classified into three categories: (i) unsaturated (UnS) i.e., the only observed perturbation arises from a single fluctuating path; (ii) partially saturated (PS) i.e., multipath correlation occur as well; (iii) fully saturated (FS) i.e., each multipath signal is subject to its own environmental fluctuation. Automatic displacements of the source and the receiver allowed us to acquire several realizations/snapshots of the same fluctuation category.

To obtain relevant comparisons between the configuration studied in a water tank and real scale oceanic cases, we use measurements from a dimensional analysis based on P3DTEx (for propagation in a 3D tank experiment configuration) and P3DCOM (for propagation in a 3D corresponding oceanic medium) software; both software tools are based on a 3D parabolic model). Oceanic configurations used in these models correspond to the propagation of acoustic waves in the mid-frequency band (1-15 kHz) over distances of the order 1-10 km. They correspond to short times of propagation compared with the daily period of medium fluctuations so that the studied phenomena are considered spatially but frozen in time.

Fig. 1 depicts the DoA estimation spectra P_{L1} and P_{L2} using L1-PCA [15] and L2-PCA methods, respectively, to estimate the angular position of the ultrasound source from experimental water tank measurements. Fig. 2 and Fig. 3 demonstrate the robustness of direct complex L1-CA versus conventional MUSIC (L2-PCA) method for DoA estimation using complex-valued measurements from P3DCOM and P3DTEx configurations, respectively. Parameters for the water tank experiment, the scaled tank experiment as well as the corresponding ocean configuration can be found in [17]. For the experiments above we consider a constant direction of arrival at $\theta = 0°$. Furthermore, we consider evaluation of the DoA spectra with $M = 64$ hydrophones and $N = 20$ snapshots for all the above configurations. The variance of the additive white noise for the experimental results reported in Fig. 1 is controlled by setting link signal-to-noise ratio (SNR) equal to -15dB. The link SNR for scaled tank and oceanic configurations using P3DCOM (Fig. 2) and P3DTEx (Fig. 3) software tools is fixed at 15dB.

Fig. 4 evaluates the average DoA estimation performance of the L2-PCA-based and L1-PCA-based methods for different SNR values by means of RMSE defined as $RMSE \triangleq \sqrt{\frac{1}{1000}\sum_{m=1}^{1000}|\theta - \hat{\theta}(m)|^2}$, where $\hat{\theta}(m)$ is the estimate of the true angle of arrival θ in the m-th experiment. At each iteration, we randomly select a DoA, and sample $N = 20$ corresponding snapshots (considering a stationary process scenario). The superiority of the proposed L1-PCA method over the conventional MUSIC (L2) method is demonstrated across a wide range of SNRs for all three fluctuation categories.

It is evident that the proposed direction finding method offers significant DoA estimation accuracy even when the recorded snapshots at the hydrophone array may be corrupted by outlying entries due to the dynamic spatial fluctuation of the propagation medium.

6. REFERENCES

[1] **G. T. Donovan**, Position error correction for an autonomous underwater vehicle navigation system (INS) using a particle filter, *IEEE Journal of Oceanic Engineering*, volume (37), pp. 431-445, 2012.

[2] **D. Ribas, P. Ridao, J. D. Tardos, J. Neira**, Underwater slam in man-made structured environments, *Journal of Field Robotics*, volume (25), pp. 898-921, 2008.

[3] **D. Thomson and S. Dosso**, AUV localization in an underwater acoustic positioning system, in *IEEE OCEANS - Bergen, 2013 MTS/IEEE*, pp. 1–6, 2013.

[4] **A. Savvides, C.-C. Han, M. B. Strivastava**, Dynamic fine-grained localization in ad-hoc networks of sensors, in *Proceedings of the 7th Annual International Conference on Mobile Computing and Networking*, pp. 166-179, 2001.

[5] **R. O. Schmidt**, Multiple emitter location and signal parameter estimation, *IEEE Transactions Antennas and Propagation*, volume (34), pp. 276-280, 1986.

[6] **G. H. Golub, C. F. Van Loan**, *Matrix Computations*, 3rd Ed. Baltimore, MD: The Johns Hopkins Univ. Press, 1996.

[7] **P. Stoica, A. Nehorai**, MUSIC, maximum likelihood, and CramerRao bound: further results and comparisons, *IEEE Transactions Acoustic Speech Signal Processing*, volume (38), pp. 2140-2150, 1990.

[8] **E. Candes, X. Li, Y. Ma, J. Wright**, Robust principal component analysis, *Journal of the ACM*, volume (58), 2011.

[9] **R. R. Singleton,** A method for minimizing the sum of absolute values of deviations, *Annual Math. Statist.*, volume (11), pp. 301-310, 1940.

[10] **N. Tsagkarakis, P. P. Markopoulos, D. A. Pados,** On the L1-norm approximation of a matrix by another of lower rank, in *Proceedings IEEE International Conference Machine Learning Applications*, Anaheim, CA, pp. 768-773, 2016.

[11] **N. Kwak,** Principal component analysis based on L1-norm maximization, *IEEE Transactions on Pattern Anal. and Mach. Intelligence*, volume (30), pp. 1672-1680, 2008.

[12] **P. P. Markopoulos, G. N. Karystinos, D. A. Pado**s, Optimal algorithms for L1-subspace signal processing, *IEEE Transactions Signal Processing*, 2013.

[13] **P. P. Markopoulos, G. N. Karystinos, D. A. Pados**, Some options for L1-subspace signal processing, in *Proc. 10th Int. Symposium on Wireless Communication Syst. (ISWCS)*, Ilmenau, Germany, pp. 1-5, 2013.

[14] **W.-J. Zeng, H. C. So, L. Huang**, Lp-MUSIC: Robust direction-of-arrival estimator for impulsive noise environments, *IEEE Transactions Signal Processing*, volume (61), pp. 4296-4308, 2013.

[15] **N. Tsagkarakis, P. P. Markopoulos, G. Sklivanitis, D. A. Pados,** L1-norm principal-component analysis of complex data, *IEEE Transactions on Signal Processing*, vol. 66, no. 12, pp. 3256-3267, 2018.

[16] **L. Yu, M. Zhang, C. Ding**, An efficient algorithm for L1-norm principal component analysis, in *Proc. IEEE Int. Conference on Acoustics, Speech, Signal Processing (ICASSP)*, Kyoto, Japan, pp. 1377-1380, 2012.

[17] **G. Real, D. Habault, X. Cristol, J. Sessarego, D. Fattaccioli,** An ultrasonic testbench for emulating the degradation of sonar performance in fluctuating media, in Acta Acustica united with Acustica, volume (103), pp. 6-16, 2017.

[18] **S. M. Flatte, R. Dashen, W. H. Munk, K. M. Watson, and F. Zachariasen**, Sound Transmission through a Fluctuating Ocean, Cambridge University Press, 2010.

THE INFLUENCE OF UPWELLING IN UNDERWATER COMMUNICATION OFF CABO FRIO ISLAND

Lussac P. Maia[a], Fábio C. Xavier[a], Jefferson Osowsky[a] ,Renato P. Vio[a], Sérgio M. Jesus[b]

[a]IEAPM, Brazilian Navy, Kioto st., 253, Arraial do Cabo, RJ, 28930-000, Brazil
[b]LARSyS, University of Algarve, Faro, PT8005-139, Portugal

Sea Studies Institute Admiral Paulo Moreira (IEAPM), Kioto st., 253, Arraial do Cabo, RJ, 28930-000, Brazil, Tel. +55 22 26229047, lussac.maia@marinha.mil.br
Laboratory of Robotics and Engineering Systems (LARSyS), University of Algarve, Gambelas Campus, Faro, PT 8005-139, Portugal, Tel. +351 289800949, sjesus@ualg.pt

Abstract: *This work aims at understanding the influence of upwelling in underwater acoustic communications as observed in a shallow water environment on the coast of Cabo Frio Island, Rio de Janeiro, Brazil, during the BIOCOM'19 experiment in January 14-18, 2019. This sea trial is part of the project "Building of signalling with bioacoustic noise characteristics for underwater communications" (BIOCOM) whose objective is to characterise biological acoustic signals and, based on such information, to transmit communication signals compatible with the characteristics of the studied bioacoustic signals. The scope of the experiment is to perform frequency modulated transmissions during 4 days from a source at 2.6m depth to a 4-hydrophones tetrahedron-like receiver array, located 1600m away in a range-dependent transect with depth between 3 and 22m. The deeper part of this transect is subject to sudden water column temperature change due to upwelling, therefore the study of its effect on communication performance is of interest for eventual adaptation and improvement. The project goal is to develop signalling technique that use the biological information of the soundscape to then establish communications with low signal to noise ratio in this environment, in an attempt of hiding, at some degree, the message in the noisy soundscape. A modulation scheme based on hyperbolic frequency swept chirps is used, aiming to increase detection capability at the receiver. The results indicate that upwelling can deteriorate the communications link due to the occurrence of severe refraction caused by the rise of cold water, that change significantly the water sound speed profile and potentially increase the number of bit errors. The present work indicates that the upwelling phenomenon significantly affects the acoustic channel and the underwater communication performance causing fluctuation of the signal level at the receiver. The development of techniques that efficiently compensate, or at least overcome the main effects of, the upwelling in shallow water acoustic propagation is still an open field of research.*

Keywords: *Underwater acoustic communications, upwelling, shallow water propagation*

1. INTRODUCTION

Upwelling is an oceanographic phenomenon that involves motion of cooler, dense water toward the sea surface, changing the water sound speed profile structure and ambient noise level [1]. The rise of nutrient-rich water stimulates reproduction of phytoplankton and high concentration of clorophila, causing increased biological activity [2,3]. A communication link can be potentially damaged by upwelling effects because the sound speed profile can be changed by cold water motion. Such motion can cause a mixture layer in the water column or also can induces the formation of waveguide duct with excessive energy interaction with the seabed and increased transmission loss. The upwelling phenomenon can occur in a shallow environment between source and receiver, potentially making message recovery to be significantly more challenging. Shallow water acoustic channels are characterized by time-frequency doubly dispersion, frequency selective attenuation, phase fluctuation and fading, features that make it difficult to achieve message recovery in underwater acoustic communications [4,5].

Underwater acoustic communications in shallow water requires the usage of a robust modulation scheme, capable to offer enough robustness against the above described channel distortions. The well-known uncoherent scheme Frequency Shift Keying (FSK) may be an attractive choice, in comparison to coherent schemes, because carrier frequency detection in underwater communications is easier than carrier phase detection. A disadvantage is the modest capacity of data throughput, which, however, can be tolerated in cases when high data rate is not a strong requirement. Furthermore, considering communications with low Signal to Noise Ratio (SNR), some action should be taken to improve signal detection and assure message recovery. In this sense, we propose in this work to test underwater communications applying a procedure that consists in substituting the frequency orthogonal tones from FSK by hyperbolic frequency swept chirps whose central frequencies are the same of the orthogonal tones, in a scheme hereafter named Hyperbolic Chirp Shift Keying (HCSK). It is expected to improve symbol detection capability with HCSK relying on the well-known good autocorrelation properties of frequency swept chirps in comparison to frequency tones, assuming that we use a matched filter based receiver. Also, the hyperbolic chirps are preferred to linear chirps because the former is more robust to Doppler effect [6].

The HCSK scheme was used in the BIOCOM'19 sea trial, employing signal frequency bandwdith empirically chosen, after observing the Cabo Frio Island soundscape during a three month period. Thus, an acoustic signature of that zone was statistically characterized before the experiment period, collecting data mainly of biological origin, and from this information the frequency band of communication was chosen to coincide with the noisiest part of the band, in an attempt of mixing messages in the environmental soundscape. Figure 1 shows the spectral characterization of a long term 89-days observation of the underwater environmental noise in the site where the experiment took place.

This paper presents results of the BIOCOM'19 experiment, occured off Cabo Frio Island, in Arraial do Cabo, Rio de Janeiro, Brazil, during January 14-18, 2019. Several HCSK modulated data set were transmitted in shallow water, from a source at 2.6m depth to a 4-hydrophones tetrahedron-like receiver array, located 1600m away in a range-dependent transect with 3 to 22m water depth. The transmissions analized in the present work were performed during the occurrence of upwelling, during the first three days, and during its absence in days January 17 and 18. Thus, we expect to achieve a fair comparison of communication results between these two scenarios.

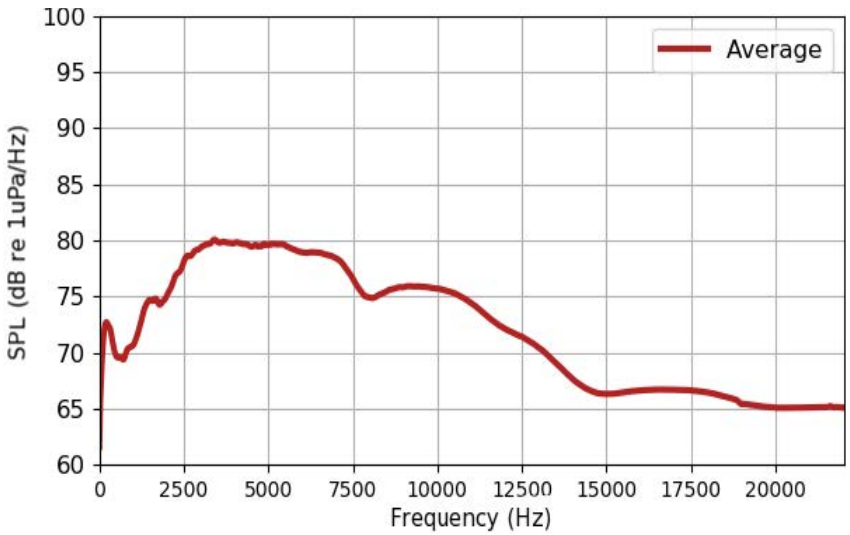


Fig.1: Soundscape observed during 89 days in the BIOCOM'19 experiment, forming an average characterization of an small underwater zone off the Cabo Frio island.

2. THEORETICAL BACKGROUND

Assume a M-FSK incoherent modulation, where the prefix M denotes the symbol map size. The method for generating this scheme is to gate M oscillators with the modulating signal:

$$x_m(t) = A\cos(2\pi f_m t + \theta_m); \quad m = 1,2,\ldots,M; \quad 0 \le t \le T_b \tag{1}$$

where the *m*-th carrier frequency is denoted f_m, the constant amplitude is *A* and the *m*-th carrier phase is θ_m, noting that the phases need not be the same in this uncoherent system. Furthermore, the frequencies f_m are chosen so that the signals $x_1(t)$ to $x_M(t)$ are orthogonal to each other over the time interval [0, T_b], as follows

$$\int_0^{T_b} x_m(t)\,x_n(t)\,dt = 0; \quad m = 1,2,\ldots,M; \quad n = 1,2,\ldots,M; \quad m \ne n \tag{2}$$

The proposed HCSK assumes that the set of orthogonal frequencies f_m are used respectively as the central frequencies of a set of hyperbolic frequency swept chirps, whose bandwith are two times the pulse bandwidth for better correlation results while also using large enough frequency guard intervals to avoid significant intercarrier interference. Thus, driven by the hyperbolic frequency swept chirp (HFM) definition [7], the M-HCSK signal is

$$s_m(t) = rect\left(\frac{t}{T_b}\right)\cos\left(\frac{2\pi}{k}\ln(1+k f_m t)\right) + \theta_m; \quad k = \frac{f_0 - f_{end}}{T_b f_0 f_{end}} \quad m = 1,2,\ldots,M; \quad 0 \le t \le T_b \tag{3}$$

where f_0 and f_{end} are respectively the starting and ending frequency of the HFM pulse.

The HCSK transmitted signal propagates through the shallow water channel that is assumed linear time-invariant since the transmission time is small enough and is contaminated by additive noise that has the non-flat power spectrum shown in Fig. 1, yielding the received signal. The received chirp symbols are then sequentially identified by a matched filter

detector that decides for maximizing the signal to noise ratio in reference to symbols contained in the symbol map.

3. THE ACOUSTIC PROPAGATION SCENARIO IN CABO FRIO ISLAND

The shallow water noisy channel in Cabo Frio Island can be represented by the impulse response of a LTI channel, assuming an invariant channel for the short time of few symbols (*e.g.*, ~50 miliseconds), as shown in Fig. 2, where pulse compression is used to capture the Channel Impulse Response (CIR) estimate. It was obtained by averaging the cross-correlation envelopes of eight chirp successively received with the emitted chirp, showing the channel main features.

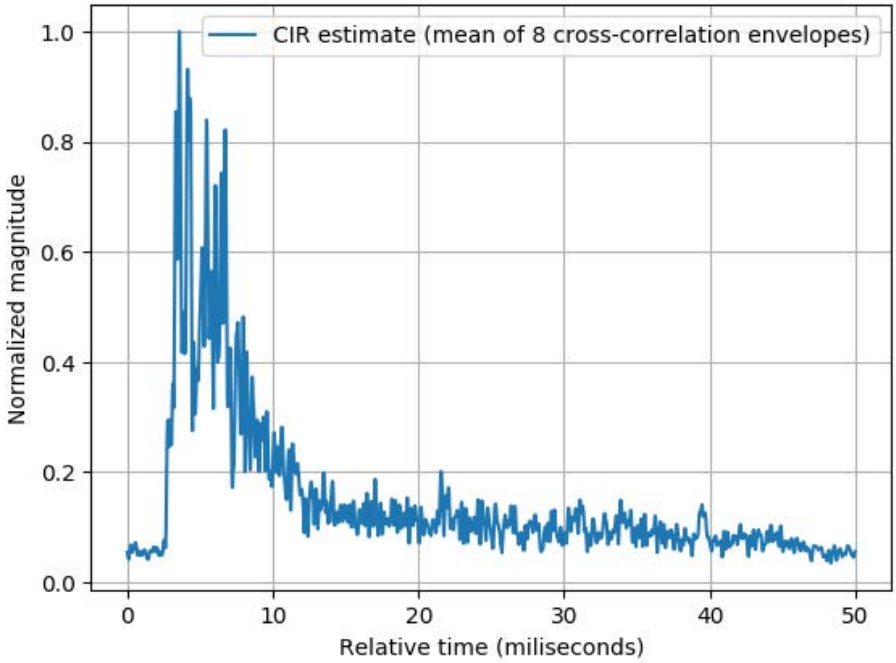


Fig.2: Channel Impulse Response (CIR) normalized estimate for the source-receiver transect of the BIOCOM'19 sea trial at time 10h20m on January 18, 2019.

Observing figure 2 we note that CIR delays spread significantly, indicating severe noise and multipath effect distortion along the whole CIR estimate.

The underwater communication transmissions were done in an environment where stratified water column occurs due to upwelling-driven cold water entering in the site of the experiment bellow the warm water. This stratification, a side effect of upwelling, occured on January 14-16, and was absent on January 17-18. Figure 3 shows the Sound Speed Profiles (SSP) recorded at afternoon of days 14 to 17, making it clear that there are a severe change in water sound speed for depths greater than 7 meters starting on January 17. In the first three days there are abrupt sound speed changes in the low part of the SSP profiles (decrease to about 1507 *m/s*), forming an acoustic propagation duct due to upwelling and this effect vanishes on the last day, presenting nearly isovelocity sound profile (with approximately 1530 *m/s*).

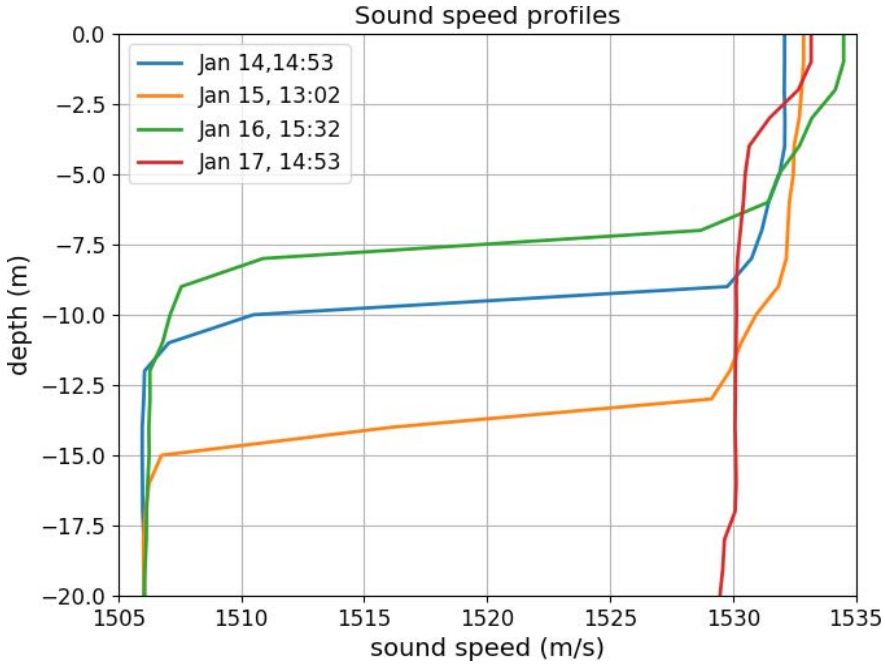


Fig.3: SSP at afternoon on January 14 (blue line), 15 (orange line), 16 (green line) and 17 (red line). Note the severe change of water sound speed occuring at depths greater than 7 meters before January 17. The acoustic duct that exists on the three ealier days vanished on the last day, presenting after 3 meters depth a nearly isovelocity sound profile.

In addition, in order to present a visualization of the acoustic propagation in the above scenarios of the BIOCOM'19 sea trial, a ray trace acoustic propagation model (Bellhop [8]) is used to compute the transmission loss in the scenario without upwelling effect (using isovelocity SSP with 1530 *m/s*), as shown in Fig. 4, and with upwelling effect (using the SSP of the day 15), as shown in Fig.5. The seabed is mainly formed by a sand half-space and its bathimetry is visualized by the upper limit of the blue part of plot in Fig 4. The source, a ITC-1001 omnidirecional transducer, is at 2.6 meters depth and the 4 hydrophones of the tetrahedron-like receiver array are at 7.5 meters depth (upper single hydrophone) and at 8.4 meters (three hydrophones at the bottom tips of the structure), with the tetrahedron edges separating each sensor being 0.9 meters. Eight carrier frequencies are distributed between 4520*Hz* and 12200*Hz* with separation of 960*Hz*, spreading the symbols in a noisy frequency band of the soundscape of the Cabo Frio Island shown in Fig. 1. The transmission loss simulation was done using the central frequency (8360*Hz*).

Observing the transmission loss figures it becomes clear that the energy level arriving on the receiver at the non-upwelling scenario (Fig. 4) is much better distributed, and probably higher due to increased bottom reflection, than the energy level arriving when in presence of upwelling (Fig. 5). In the latter, there is severe interaction with the seabed, indicating interference in terms of transmission loss. This effect is caused by the severe downward refraction in the SSP profile recorded in a zone influenced by the upwelling phenomenon off Cabo Frio Island.

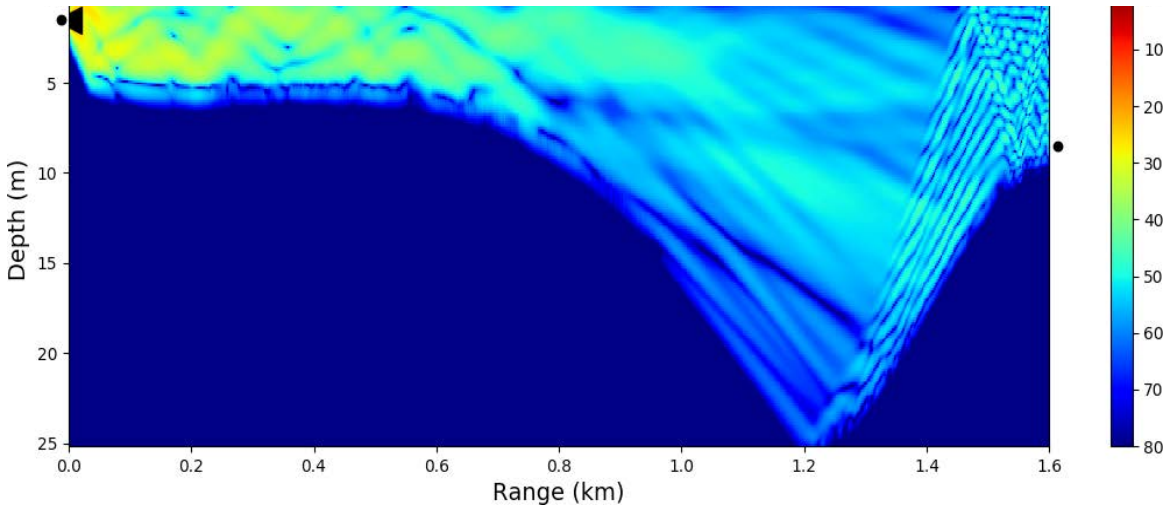


Fig.4: Transmission loss simulation at frequency 8360Hz with the environmental characteristics of the site of BIOCOM'19 sea trial using isovelocity sound speed profile.

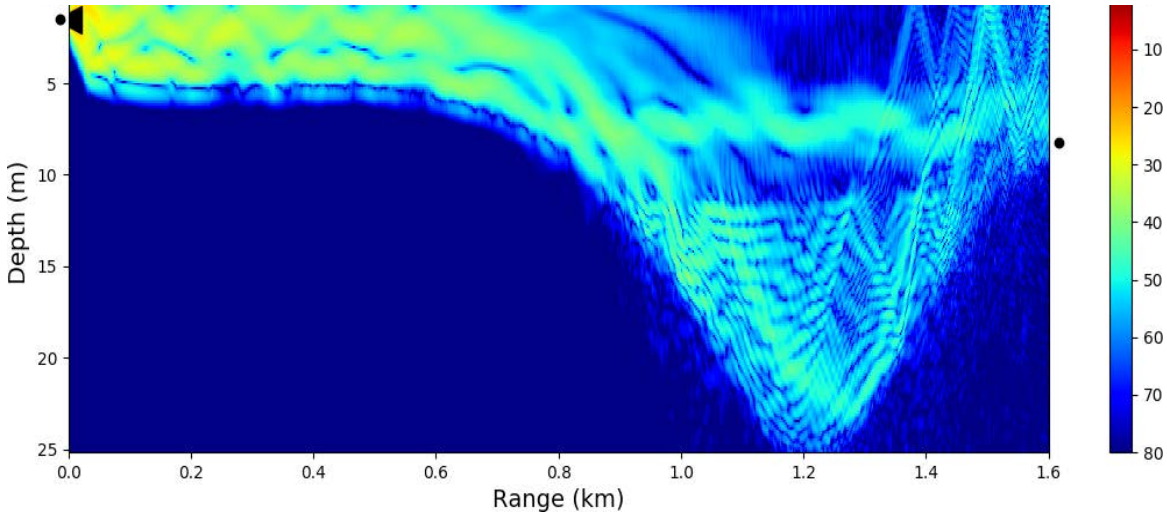


Fig.5: Transmission loss simulation at frequency 8360Hz with the environmental characteristics of the site of BIOCOM'19 sea trial using the sound speed profile captured on January 15, with severe downward refraction due to upwelling.

4. THE BIOCOM'19 SEA TRIAL RESULTS

The results are presented for the HCSK-modulated message transmitted repeatedly for 246 times during the days 15 and 18, and received at the 4-hydrophone array generating the total of 984 received messages by all channels together.

Figure 6 shows the Bit Error Rate (BER) of the processed messages received in each channel during the days 15 and 18 sequentially, where the result of each message (named as packet) is denoted by a blue star for data of day 15 and green star for day 18. This figure has the goal of presenting the performance variance of the results for all packets sequentially (blue/green stars) as well as their trend (red line) along those two days, in order to observe how the results are influenced by the SSP variations induced by upwelling. The vertical dashed line also marks the separation from one day to another. The red line is made by joining the points determined by the average of every 20 consecutive packets, thus representing a general trend of the results.

The upwelling effect is indirect in the BIOCOM'19 sea trial because the site of the experiment had entering of cold water through a passage between the Cabo Frio Island and the main land, causing SSP stratification with cold water bellow warm water. The strong stratification observed is not due to surface agitation but due to the sipping of cold water underneath the warmer water due to the combined effect of upwelling and tide. The stratified SSP versus nearly isovelocity SSP is the main cause of the variation between results from days 15 and 18.

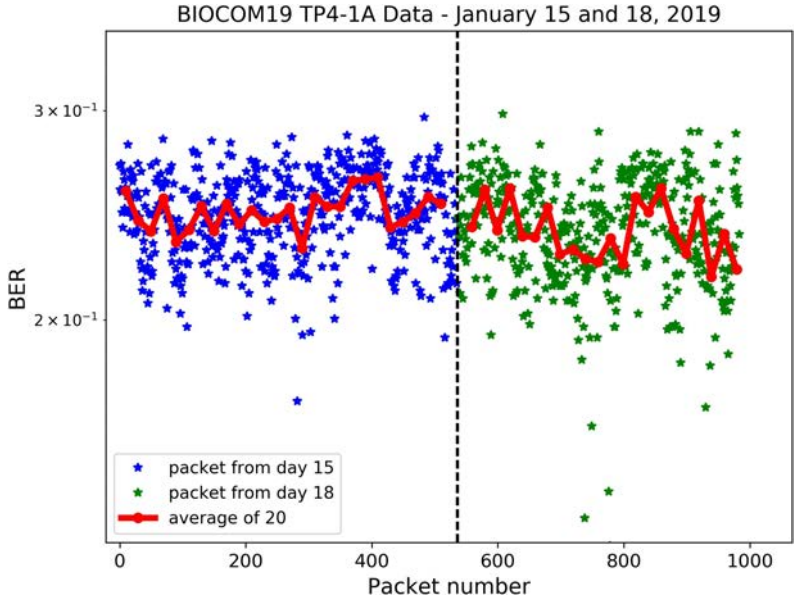


Fig.6: BER resullts of packets sequentialy received on January 15 (blue stars) and 18 (green stars). The vertical dashed line denotes the date change from one day to another. The red line is made by joining the points determined by the average of every 20 consecutive packets.

The data presented in this work have poor BER performance because of excessively low SNR in the receiver. Despite of that, these data is useful to analize communication degradation induced by the upwelling phenomenon observed in the experiment site. Figure 7 shows a comparison between the trend observed in the results obtained from data recorded on January 15, when the environment is under effect of upwelling, and the trend observed in the results obtained on January 18, without upwelling, also in terms of BER.

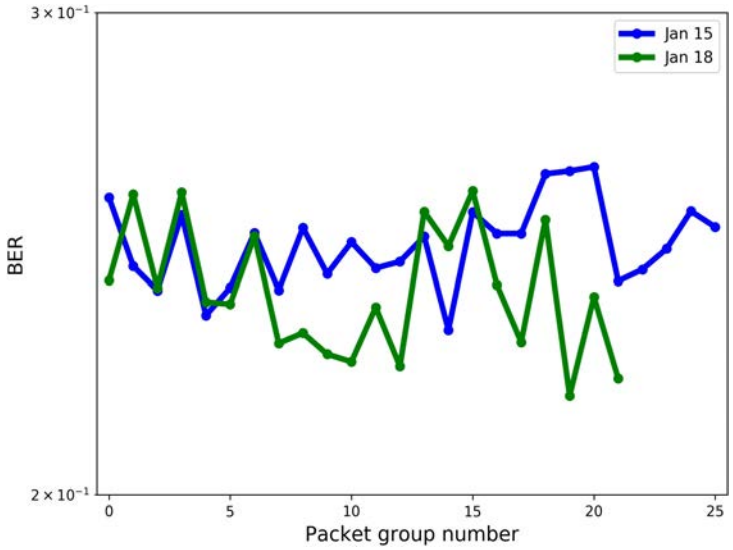


Fig.7: Average of each consecutive 20 packet results of data received on January 15 (with upwelling) and January 18 (without upwelling).

Results of figure 7 indicate that there are lost of communications performance for the data received in an environment under upwelling phenomenon, as expected, given the effects of the stratified SSP. This confirms that upwelling can significantly deteriorate an underwater acoustic comunication link, even using the HCSK modulation scheme in an atempt of reach robust detection in a shallow water noisy environment.

5. CONCLUSION

The performance of underwater acoustic communication systems is frequently affected by channel conditions. Variations in the underwater acoustic channel, such as those caused by upwelling phenomenon, can generate shadow zones due to high gradient of water density. Moreover, this gradient can improves the multipath effect in shallow water potentially making it worse for the intersymbol interference. The BIOCOM'19 results show this relationship between upwelling and bit error rate. The analyzed data indicated that there are a positive and linear relation, *i.e.*, the errors increase when upwelling is more severe. These results presented at very particular conditions encourage further studies in order to develop techniques to mitigate the upwelling effects in order to preserve acoustic communication links in shalow water.

6. ACKNOWLEDGEMENTS

The authors are grateful to the Brazilian Navy and to the *Conselho Nacional de Desenvolvimento Científico e Tecnológico* (CNPq)/*Ciências Sem Fronteiras* (Contract No. 401407/2014-4) for all the support given to BIOCOM Project. This work is also part of the effort developed for project 2DeepScape (contract MITEXPL/IRA/0070/2017) FCT program MIT-Portugal.

REFERENCES

[1] **Sarhan T.; Lafuente J.; Vargas, M.; Vargas J. and Plaza, F.;** Upwelling mechanisms in northwestern Alboran Sea, *Journal of Marine Systems*, volume (23), pp. 317-331, 1999.

[2] **Calado, L.; Rodríguez, O. C.; Codato, G. and Xavier, F. C.;** Upwelling regime off the Cabo Frio region in Brazil and impact on acoustic propagation, *The Journal of the Acoustical Society of America Express Letters*, volume 143 (3), pp. 174-180, 2018.

[3] **Valentin, J. L. and Coutinho, R.; Modelling maximum chlorophyll in the Cabo Frio (Brazil) upwelling: a preliminary approach, *Ecological Modelling*, volume 52, pp. 103-113, 1990.**

[4] **Stephanian, R. and Stojanovic, M.;** Underwater Acoustic Digital Signal Processing and Communication Systems, *Springer Science and Business Media New York*, 2002.

[5] **Maia, L. P.; Silva, A. and Jesus, S. M.;** Environmental Model-Based Time-Reversal Underwater Communications, *IEEE Access*, DOI 10.1109/ACCESS.2017.2724304, volume (6), pp. 10041-51, 2017.

[6] **Vio R. P.;** Improved UUV positioning using acoustic communications and a potential for real-time networking and collaboration, *PhD dissertation from the Naval Postgraduate School*, June 2017.

[7] **J. J. Kroszczynsky;** Pulse compression by means of linear-period modulation, *Proc. IEEE*, volume (57), n. 7, pp. 1260–1266, July 1969.

[8] **Porter, M. B.**, The Bellhop Manual and User's Guide. *Heat, Light and Sound Research, Inc.*, La Jolla, CA, USA, 2011.

AUV Tracking Using a Thruster Communication Link

Stephen Cronin*, Dr. Brian Butka**

**Embry-Riddle Aeronautical University, Daytona Beach, 32114 FL USA*
(email: cronins1@my.erau.edu)
***Embry-Riddle Aeronautical University, Daytona Beach, 32114 FL USA*
(email: butkab@erau.edu)

Abstract: *The acoustic noise produced by electric thrusters is commonly viewed as undesirable and efforts have been made to minimize this noise. Leveraging this noise, a frequency modulated PWM signal was used to create a uni-directional acoustic data link that does not require a separate acoustic transducer. The motor noise modulation system has demonstrated data transmission speeds of 250 bits/s. Building on this technology, this research investigates the ability to control the motor transmissions allowing other vehicles to localize their position in 3-dimensional space. Initial, calculations indicate that the system can localize the vehicle position to an accuracy of +/- 1% of the targets range. Possible applications of this technology include autonomous docking of underwater vehicles with surface vehicles and for the communication and control of swarms of underwater vehicles.*

Keywords: *Acoustic Communication, Localization, USBL*

Introduction

The use of ultra-short baseline arrays for localization is well established in underwater navigation. Current technologies leverage this technology along with robust bi-directional communication systems to accurately track the position of underwater assets. However, there is a focus as of late to build low cost or compact AUV systems to mitigate issues operating in high-risk or space constrained areas. The target vehicles in this on the size scale of a single sensor vehicle for missions (camera, water quality sensor, etc.) with an inertial measurement unit and compass for basic navigation. Extensions of this technology would enable swarms of these smaller vehicles each with individual motor sources communicating on small frequency bands.

This phase of research focuses on developing an acoustic communication link utilizing the switching frequency of a brushless electric motor, like those found in electric thrusters, as the basis for a frequency modulated data link [1], and a conventional hydrophone array as its receiver. This technology allows for the small vehicle to have a uni-directional data link to a hydrophone array.

Acoustic System

The localization system is based on four Teledyne Reson TC4013 hydrophones. They are arranged in a regular tetrahedron, with 1.8 cm sensor separation. This length was selected as it is less than half a wavelength of the highest frequency (40 kHz) used during testing. Each hydrophone signal is first passed through filtering and amplification hardware removing frequencies outside of the target band while amplifying the signals of interest. This is done in order to better align the

incoming data to the expected input of the data acquisition device. The data is then sampled at 500 kSamples/s/channel.

After sampling, the data is filtered digitally removing all but the target frequencies. The signals are then filtered to extract the wavefront of the arriving signal, the portion of the signal free of multipath, which impacts the calculation of signal phase and as such the localization of the source. A phase difference of arrival solution is then implemented to compute the location of the source using a numerical solver based on a 6-phase difference approach [2].

Localization Methodology

Localization of the target is accomplished with a by two separate measuements. The USBL provides bearing and inclination data to the source. Through the data link, the output of a depth sensor is periodically sent. This provides accurate depth data of the vehicle and as such grounds the location on a measurement external to the system. These two measurements can be combined to compute the 3-dimesional location of the vehicle.

Testing Methodology

To facilitate testing without a custom built AUV, a comparable acoustic source (Teledyne Benthos 365 Pinger) was mounted to a surrogate system, the SRS FUSION AUV. This system is outfitted with a host of navigation sensors, including a USBL, DVL, altimeter, and AHRS as well as a software stack allowing for planning missions that are repeatably reliably and repeatably followed [3]. This vehicles localization suite was used to provide a performance reference for localization accuracy. Figure 1 shows the comparison of pulses produced by the motor and pinger. As can be seen, both devices are capable of producing comparable sound pulses, in this case, a 4 ms pulse with multipath reflections trailing off after the arrival.

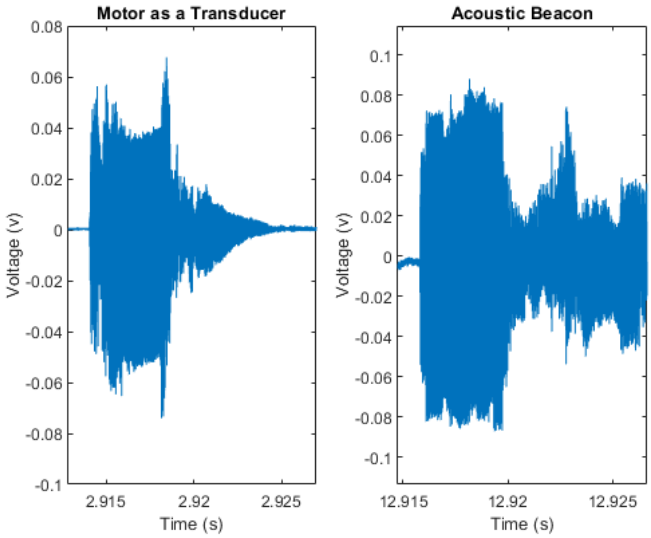


Figure 1: Comparison of Motor and Acoustic Beacon Sound Sources

Testing was conducted at Embry-Riddle Aeronautical University's pool. This allowed for controlled and repeatable testing free of external disturbances. The presence of solid walls raised

concerns regarding the impact of multipath on the received signals. However, the presence of multipath was determined to be an acceptable test condition as it is comparable to operations in littoral areas that small AUV systems are often deployed. To give the array a period of clean signals before the arrival of the multipath, the array was suspended approximately one meter away from the nearest wall and one meter below the surface of the water.

The specific test case run for this test was a static test where the vehicle was positioned at an off angle relative to the hydrophone array. Motion-based test were attempted with some successes, but due to space constraints, it was not feasible to create the desired motion vectors. To simulate the data link, depth data was streamed from the AUV. This data was time aligned to the ground truth data being used for reference and was of comparable accuracy when compared to common solutions for AUV's in the class of vehicles targeted.

Results

The presented test was conducted for a period of at least 60s. With a pinger update rate of once every 0.512s, this resulted in 128 samples. Figure 2 and Figure 3 show the measured bearing and inclination respectively to the ground truth data produced by the navigation suite on the SRS Fusion AUV. As can be seen, both measurements are centered around the ground truth data, with the inclination having slightly more noise than bearing. The characteristics of these measurements are tabulated in Table 1. Of note in this characterization is the zero-mean error. This allows for the application of navigational filters without violating their core assumptions.

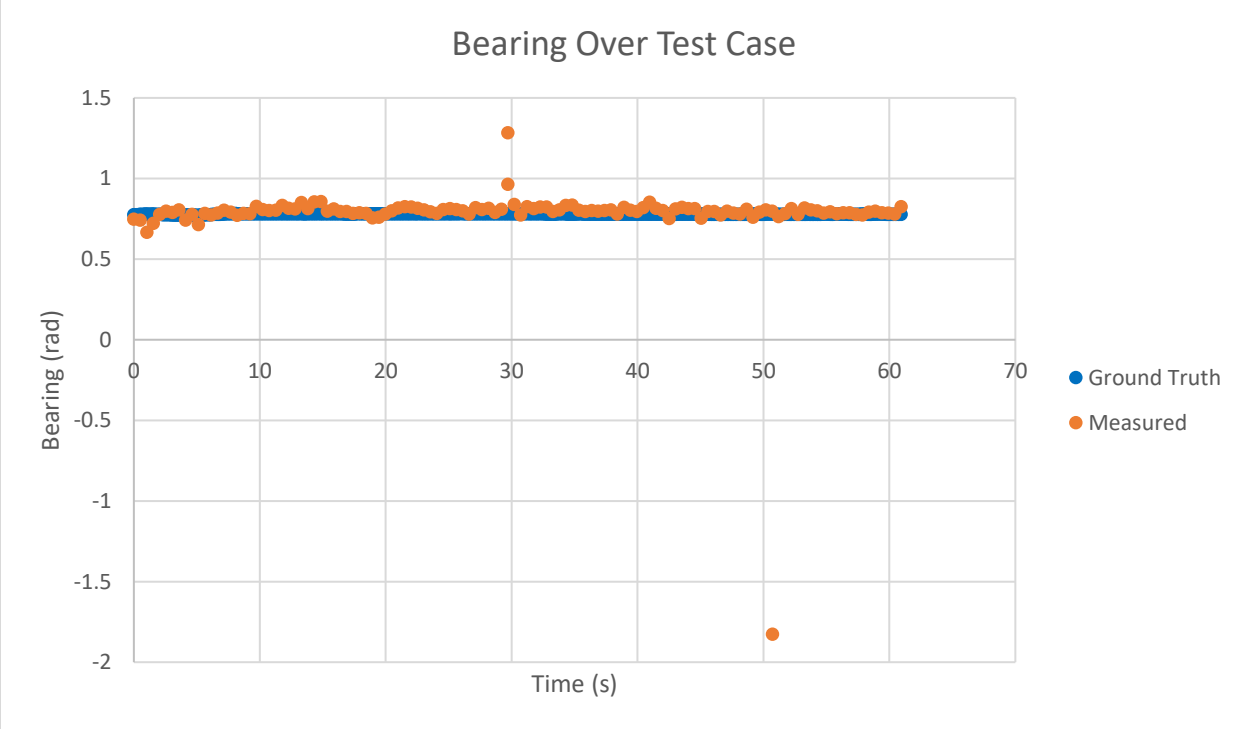


Figure 2: Bearing Measurement Comparison

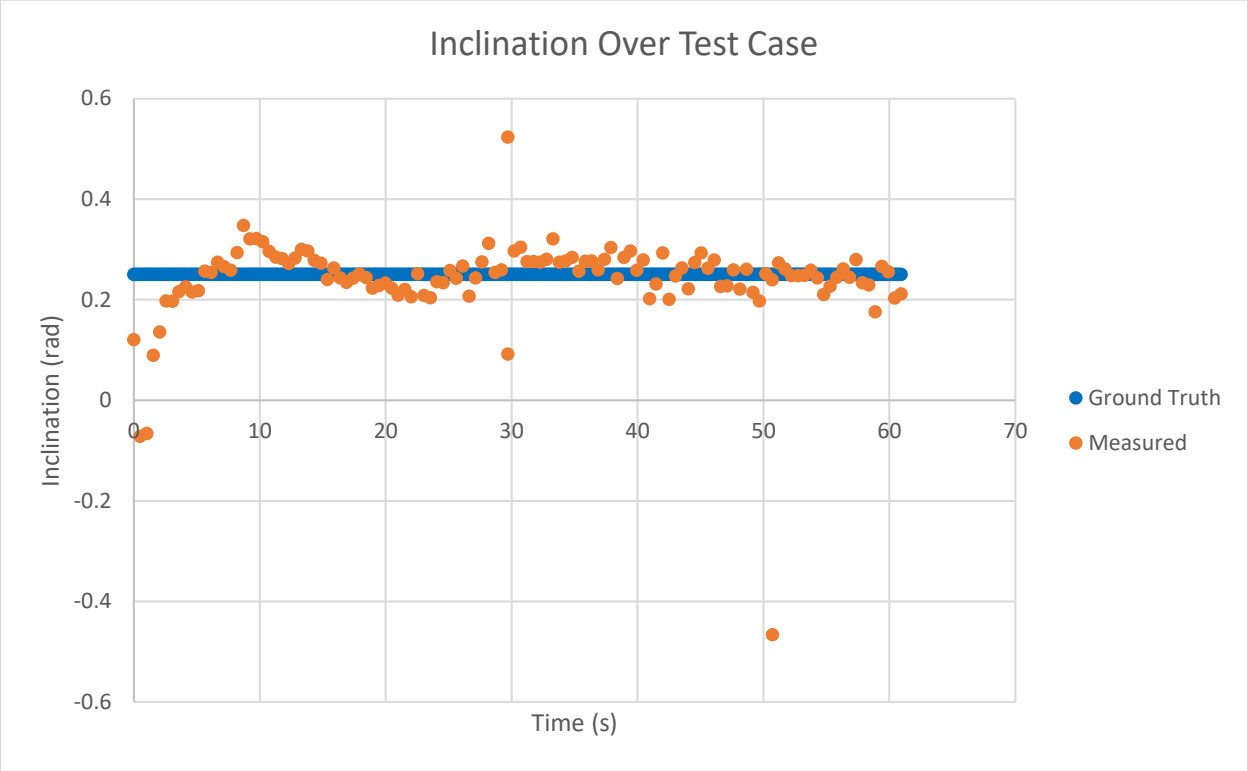


Figure 3: Inclination Measurement Comparison

Measurement	Mean Error (rad)	Variance (rad)	Std. Deviation (rad)
Bearing	~0	0.05284	0.2298
Inclination	~0	0.009247	0.09614

Table 1: Measurement Characteristics

An area of interest when analyzing this data is the presence of "pops" in the measurements. These "pops" are evident in their dramatic deviation from the correct value. When evaluating the overall accuracy of the localization of the source, it is useful to filter this data to better understand the underlying behavior. A moving average filter was applied to the measurement results. If a subsequent sample was beyond 0.4 radians of the average, it was removed from the set. In this case, 6 samples were removed, accounting for 4.68% of the data. In practice on a moving system, this boundary may need to be adjusted based on the update rate of the source or the speed of travel.

Using this measured data along with the transmitted depth data, the position of the vehicle can be mapped, and the accuracy of the localization evaluated. Figure 4 shows the XY plot of the computed locations, with Z data omitted from being shown as it was a measured value. The mean value of the location is shown with the green and orange marker for the measured and ground truth data respectively. From this data, the accuracy of the localization can be characterized using the average range error. In this case, the value was computed to be 1.18%, at the proposed performance goal set to be achieved in this work.

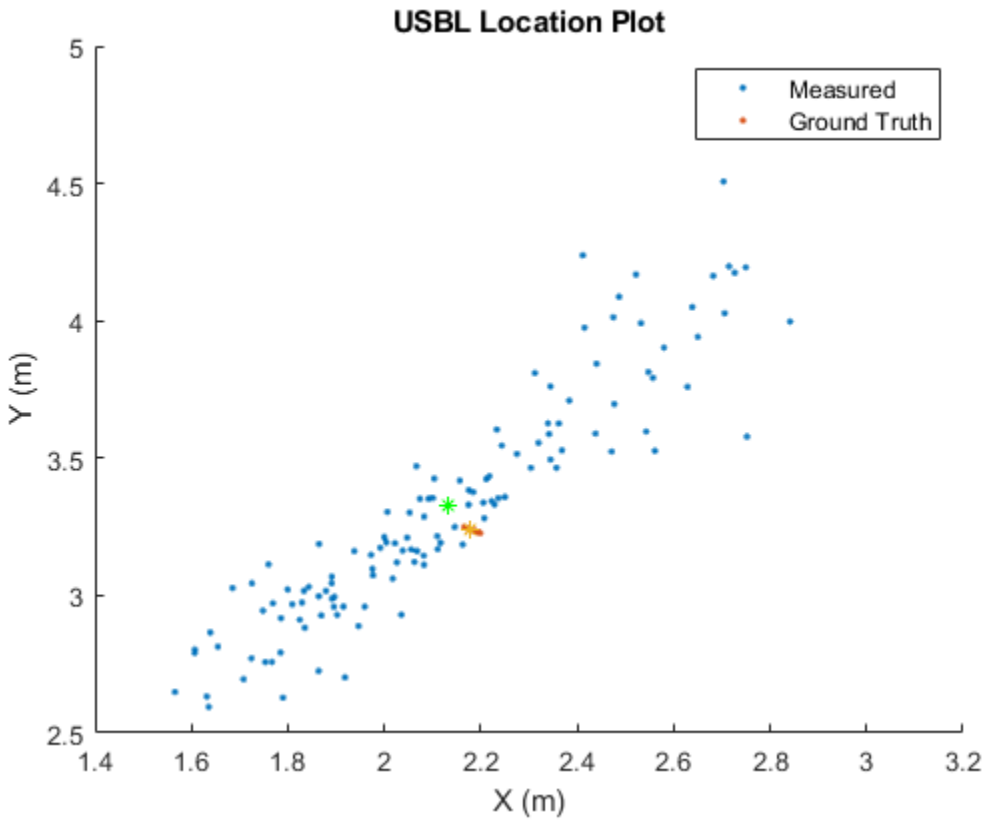


Figure 4: XY Plot of Position Data

Conclusions

The intended application of this technology is to enable tracking capabilities on simple low-cost AUV systems, which cannot support a discrete higher-fidelity navigation system due to cost or size. Building on the results of prior research, it was demonstrated that the system can accurately track the bearing to the vehicle while providing depth data through the data link. This work establishes foundational technologies to provide localization through a low-cost motor based communication system.

Future Work

The primary focus of future endeavors involves implementing this system on a small AUV to test a complete end-to-end implementation of the technology. Intermediate testing will involve a similar approach to the one outlined here, by mounting the communication system to a more instrumented platform or by conducting the testing with a motor mounted on a more capable system. In terms of the localization itself, considerations to further mitigate the impact of multipath should be taken to improve the accuracy of the source localization.

Acknowledgments

This research was performed with support from ONR grant ID: N0014-17-1-2492. The authors would also like to acknowledge the Robotics Association at Embry-Riddle for sharing their experience and their space.

References

1. Brian Butka, Stephen Cronin, Jefferson Romney, Using an Electric Thruster as an Acoustic Transducer, IFAC-PapersOnLine, Volume 51, Issue 29, 2018, Pages 372-377, ISSN 2405-8963, https://doi.org/10.1016/j.ifacol.2018.09.459.
2. J. A. Neasham, G. Goodfellow and R. Sharphouse, "Development of the “Seatrac” miniature acoustic modem and USBL positioning units for subsea robotics and diver applications," *OCEANS 2015 - Genova*, Genoa, 2015, pp. 1-8.
3. http://www.srsfusion.com/tech-specs

Structured Session 6
Underwater Noise - Modelling and Measurements

Organiser(s): Gavrilov Alexander, Skarsoulis Emmanuel, Taroudakis Michael

LOW FREQUENCY NOISE SOUTH OF AUSTRALIA FROM DISTANT SOURCES IN THE SOUTHERN OCEAN

Zhi Yong Zhang[a] and Alexander Gavrilov[b]

[a] Maritime Division, Defence Science and Technology Group, Edinburgh, SA 5111, Australia
[b] Centre for Marine Science & Technology, Curtin University, Perth, WA 6845, Australia

Yong Zhang: yong.zhang@dst.defence.gov.au

Abstract: *Multi-year ambient noise data recorded south of Australia show persistently high levels at low frequencies that could not be explained by shipping or local winds. The monthly median noise levels below 80 Hz are higher in Austral summer/autumn than in winter/spring. There are two possible sources of the persistently high noise at low frequencies and its seasonal variation: the strong westerly winds in the Southern Ocean and ice-related events (e.g., glacier and iceberg calving) in and near Antarctica. Examination of the wind and ice coverage in the Southern Ocean shows that the winds south of the Antarctic polar front are one of the major sources of the low frequency noise in austral summer. The retreat of the ice-edge in summer and autumn increases the open water surface area south of latitude 60° S. Although the winds over this area in summer are generally weaker than that north of latitude 60° S, the sea surface is not shielded by sea ice and hence exposed to wind waves that generate underwater noise ducted in the near-surface sound channel. Significant correlation was observed between the noise level below 80 Hz at the edge of the southern continental shelf in Australia and wind speed south of the Antarctic polar front in summer, whereas no correlation was found in winter. Ice breakup events also remain a likely source of seasonal variation of the low frequency noise observed south of Australia. The higher air and water temperatures near Antarctica in summer cause more frequent and intense calving of icebergs from ice-shelves and icebergs. Because the underwater sound channel is near the water surface in Antarctic waters, the noise energy from the ice events is efficiently coupled into the deep sound channel and ducted northwards with small losses, leading to a higher level of ambient noise at low frequencies and its seasonal variation.*

Keywords: *Ocean ambient noise, wind in southern ocean, seasonal variation, ice cracking.*

1. INTRODUCTION

As part of the Integrated Marine Observing System (IMOS) passive acoustic observatory program (http://imos.org.au/facilities/nationalmooringnetwork/acousticobservatories/), sea noise data were collected southwest of Kangaroo Island from December 2014 to October 2017 using autonomous recorders set on the seafloor at a water depth of about 170 m near the continental shelf-break off South Australia at the location shown in Figure 1. The recorders were programmed to make 300 s recordings every 900 s at a sampling frequency of 6 kHz.

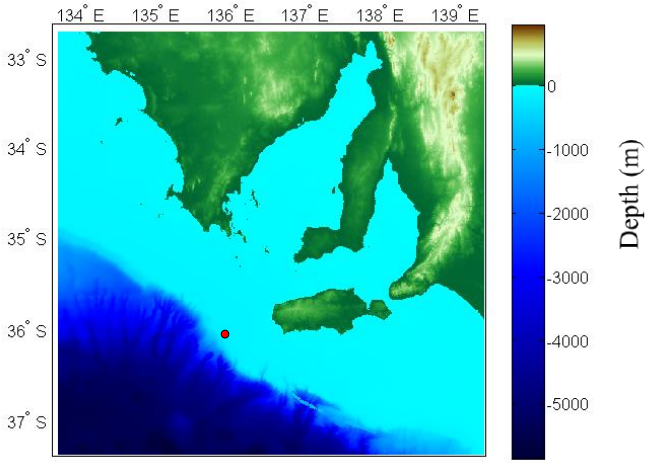


Fig. 1: Bathymetry around the site of sea noise data recording (the red dot).

We show that the ambient noise levels are persistently high which could not be explained by shipping or local winds, and reasonable explanations are that they originated from distant storms at high latitudes and ice breakup events near Antarctica. Oceanography in the Southern Ocean provides favourable conditions for such noises to propagate over long distances north, and the seasonal variation of the low frequency noise is consistent with the seasonal variation in the sea ice extent and ice breakup intensity in Antarctica.

2. LOW FREQUENCY NOISE

Figure 2 shows the Power Spectrum Density (PSD) levels of sea noise averaged in 1/3-octave bands at five different percentile values from aggregated monthly data in summer (February 2015, 2016, 2017) and winter (August 2014, 2015, 2016).

The peaks around 1.2 kHz are from evening and morning fish choruses. The peak around 20 Hz are from vocalisations of Antarctic blue and fin whales. At the higher frequencies, e.g., above 200 Hz, there are significant differences between the percentiles values. This is mainly due to the significant changes of the local wind conditions within a month.

The focus of this paper is the noise at the lower frequencies. Below 80 Hz the differences between the lower noise percentiles are small. This indicates that this noise is from persistent sources. We can rule out two obvious conventional noise sources: shipping and local winds.

According to Automatic Identification System (AIS) data from the Australian Maritime Safety Authority, shipping is not a significant contributor to the low frequency noise in this area.. Preliminary modelling shows that shipping-generated noise is much lower than that

shown in Fig.2. Examination of the noise recordings shows identifiable noise from shipping only on rare occasions.

Local winds can also be ruled out as the main source of the low frequency noise because: (1) to generate the low frequency noise levels shown in Fig.2, e.g., 80 dB re 1 $\mu Pa^2/Hz$ at 50 Hz, the local wind speeds need to be over 30 knots [1, 2], whereas the median wind speed in the region in February is about 15 knots [3]; (2) the local wind speeds vary significantly within a month, whereas the level of the low frequency noise varies little, as shown by the small difference between the 5 and 50 percentiles.

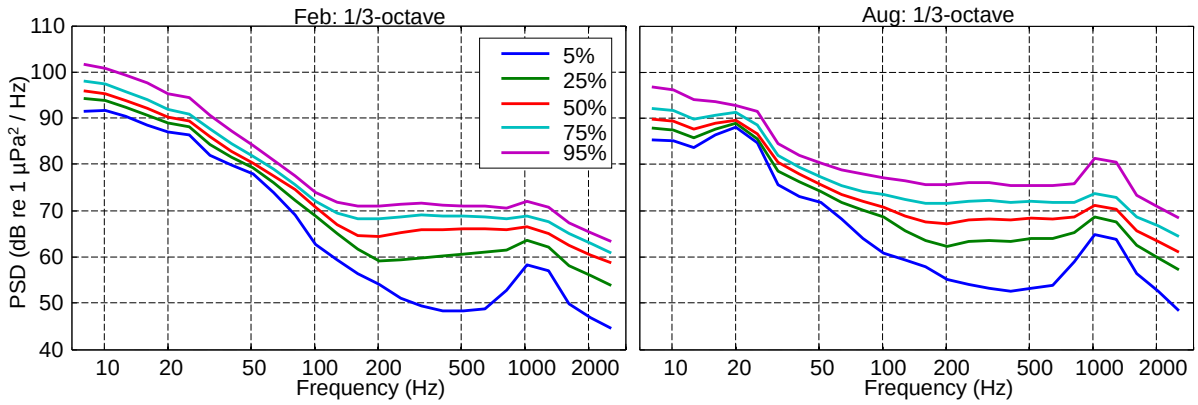


Fig. 2: PSD levels of sea noise averaged in 1/3-octave bands at five different percentiles from aggregated monthly data in February and August.

3. SEASONAL VARIATION OF THE LOW FREQUENCY NOISE

Figure 3 shows the variation of the noise level in 30 to 80 Hz band low-pass filtered with a median filter of one week length, which excludes the contribution of blue and fin whale sounds in the roughly 15-30 Hz band. It shows a seasonal variation pattern of being maximum in February-March and minimum from July to October. A similar seasonal pattern has also been observed in multi-year sea noise data collected at the HA01 station of the Comprehensive Nuclear-Test-Ban Treaty (CTBT) hydro-acoustic station southwest of Cape Leeuwin [4].

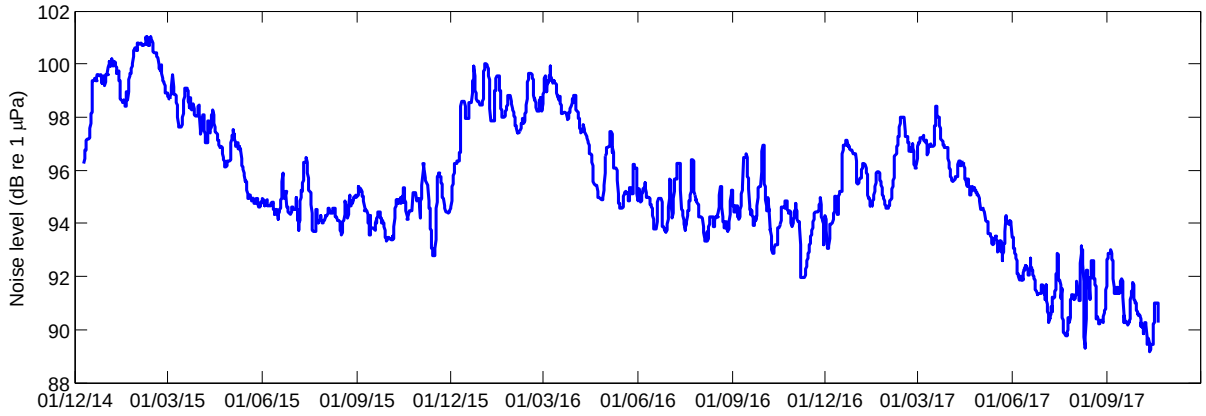


Figure 3: Weekly median underwater noise level averaged in the 30-80 Hz band from December 2014 to October 2017.

Analysis of ambient noise recorded at deep and shallow sites in the Great Australia Bight indicates that the low frequency noise is from the south [5].

We examine two possible explanations for the persistently high level noise at low frequencies and their seasonal variation: the strong westerly winds in the Southern Ocean and ice events (ice-shelf and iceberg calving) in Antarctica.

4. METEROLOGY AND OCEANOGRAPHY IN THE SOUTHERN OCEAN

The Southern Ocean off Antarctica has some meteorological and oceanographic features that are particularly relevant to the generation and propagation of underwater sound in the ocean. A prominent meteorological feature is the strong circumpolar westerly wind (known by sailors as the 'furious fifties'), which is caused by the combination of air being displaced from the Equator towards the South Pole, the Earth's rotation, and the scarcity of landmasses to serve as windbreaks (Fig.3).

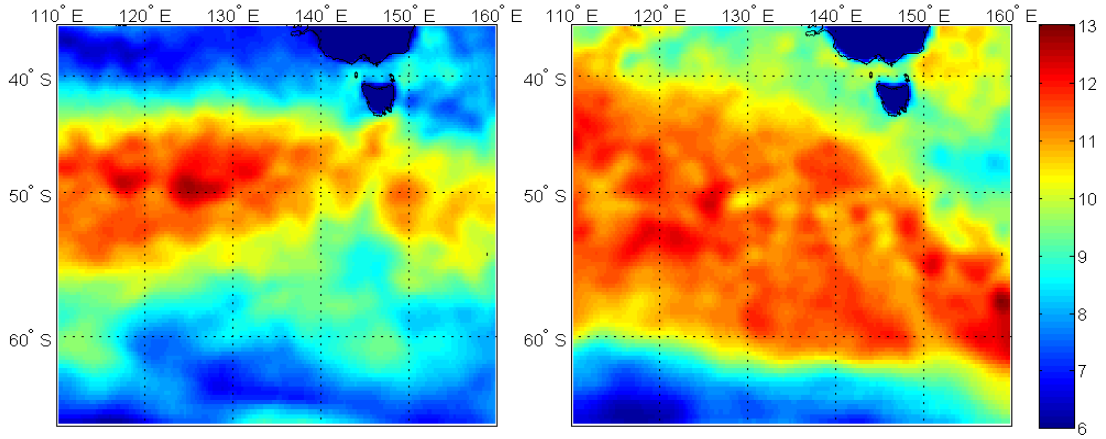


Fig.3: Monthly averaged wind speed (m/s) at 10 m above the sea surface in February and August 2017 (data from CCMPv2 database [3]).

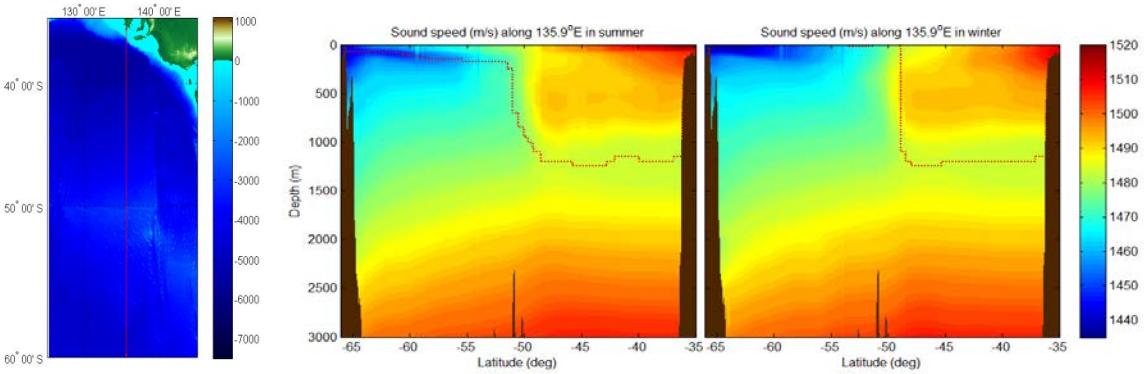


Fig. 4: Sound speeds along longitude 135.9°E computed from summer (middle panel) and winter (right panel) climatology of the World Ocean Atlas 2013. The red dashed lines show the minima of the vertical sound speed profiles (sound channel axis). The rapid sound speed variation between 50° S and 55° S agrees well with oceanographic studies of the Antarctic Circumpolar Current south of Australia, where at 136°E, the Sub-Antarctic Front and the Polar Front occur at about 50° S and 55° S respectively [6, 7].

A prominent oceanographic feature is the eastward Antarctic Circumpolar Current (ACC) driven by the strong westerly winds and the associated current fronts, where the cold, less saline Antarctic water meets the warmer, high-salinity waters to the north, leading to strong spatial variation in temperature, salinity, and hence sound speed. Across the ACC from the

north, the sound channel axis ascends from over 1000 m depth to the surface, with a more rapid transition in winter than in summer (Fig.4).

Ambient noise generated by strong winds and ice events, where the sound channel axis is near the surface, can efficiently couple with the deepening sound channel and be ducted northwards. Low frequency noise in the sound channel can propagate to great distances because of low surface and bottom interaction losses, low cylindrical spreading losses, and low absorption losses at low frequencies.

5. WINDS IN THE SOUTHERN OCEAN AS DISTANT SOURCES OF NOISE

It was suggested that strong winds in the Southern Ocean were the distant source of low-frequency noise at low-latitudes, and the noise levels were lower in winter because of greater sea-ice coverage which shields the sea surface from wind stress and prevents wind-generated noise [8]. Our observations partly confirm this hypothesis.

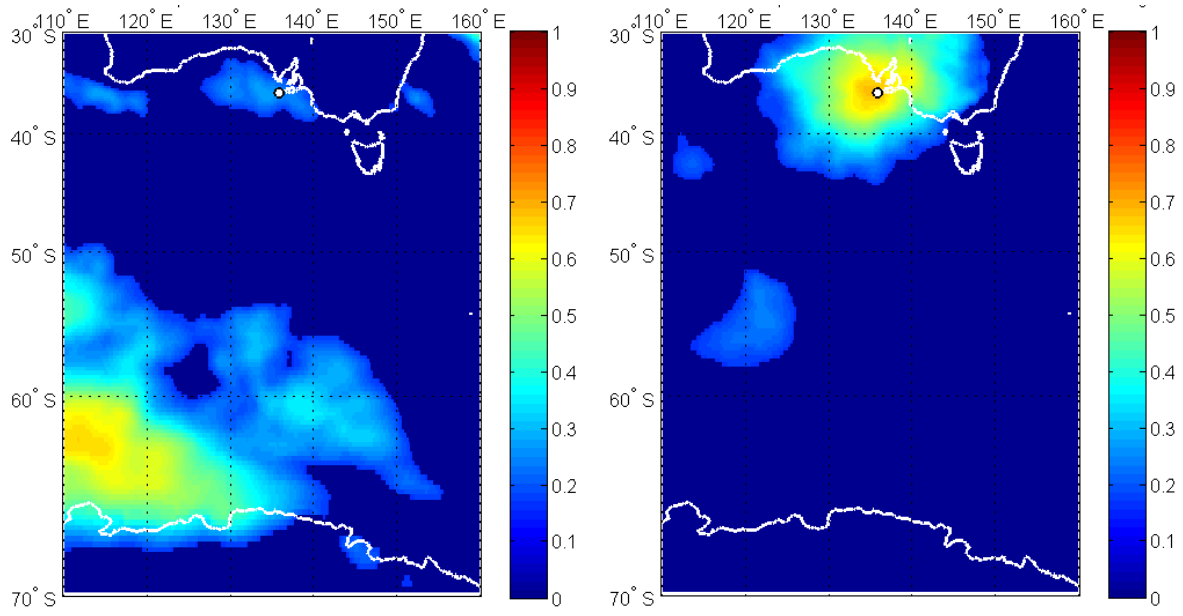


Fig. 5: Correlation between wind speed in the Southern Ocean off Australia and noise level of 50% percentile in a 30-50 Hz band recorded in Australia at the IMOS acoustic site (white dot) in austral summer (left panel) and winter (right panel).

Figure 5 shows the correlation of the wind speed in the Southern Ocean off Australia with the 50% percentile noise level measured in a 30-50 Hz band at the Kangaroo Island IMOS acoustic site in Austral summer and winter months. The low bound was set at 30 Hz to exclude the contribution of noise generated by blue and fin whale vocalisations. In summer, the correlation with the wind speed south of latitude 60°S is significant (nearly 0.7, p-value < 0.01), whereas it is very low (<0.3) for the wind around the IMOS site. In winter, the situation is opposite: the correlation is high (~0.7) at the IMOS site and negligible for the wind in the Southern Ocean south of latitude 45°S. At frequencies higher than ~100 Hz, the correlation of underwater noise levels with the local wind is dominating both in summer and in winter.

Although the wind speed is generally higher at latitudes north of 60°S, the noise from wind waves is not well coupled with the underwater sound channel. At higher latitudes, where noise sources at the sea surface are more strongly coupled with the sound channel, the

presence of the sea ice cover, which extends from Antarctica to about 60°S in winter and almost vanishes in summer, plays a determinant role in wind-noise generation and propagation by shielding the ocean from wind.

6. ICE EVENTS AS SOURCE OF NOISE IN THE SOUTHERN OCEAN

Various ice-related processes in Antarctica generate underwater noise of different waveforms and frequencies. Sea-ice related noise generating processes include ice floe collisions, thermal cracking and interactions with waves. Glacier/iceberg related processes include ice-quakes, calving events, grounding of icebergs, icebergs melting , etc.

Icebergs are known to generate several types of sounds: (1) long-lasting low frequency harmonic tremors, when icebergs shoal or collide with other icebergs [10, 11], which is surmised to be fluid-flow-induced vibrations inside the iceberg's tunnel/crevasse systems [12]; (2) broadband bursts associated with iceberg breakup (calving) in the open sea; and (3) continuous crackling/popping sound from iceberg melting.

Iceberg calving involves various stages: pre-cursor rumbles, ice fractures, impacts on the water and iceberg oscillations, each stage having different time and frequency characteristics [13, 14].

Melting icebergs and glaciers generates crackling/popping underwater noise as air bubbles entrapped in the ice under pressure are released explosively from the melting ice [15, 16]. Most of the noise energy from iceberg melting is above 1 kHz and thus it is unlikely to propagate over thousands of kilometres. However, we should note that the noise recorded (in May 2013) in a glacier fjord (Andvord Bay) in Antarctica was louder than that generated by sea state 6 in the open ocean, down to frequencies as low as 50 Hz [17].

Iceberg calving adds to the background ambient noise from iceberg melting, increasing the noise level and modifying the spectral characteristics over hourly to daily timescales [13, 14]. A large proportion of underwater sound signals were detected during austral summer when there was no sea ice, indicating calving events and drifting icebergs are the major contributors to the ambient noise [18].

Satellite remote sensing shows that there were more icebergs in Austral summer and their average size are also greater [19]. It was also found that the seasonal variation of ocean ambient noise level in the Southern Hemisphere is highly correlated with the volume of icebergs north of the sea-ice edge in the Southern Ocean [20], indicating that iceberg calving events are most likely one of the dominate sources of underwater noise in the Southern Hemisphere. Low frequency noise recorded in West Antarctica show that ice-quakes broadband, short duration signals emitted by fracturing of large free-floating icebergs, are prominent and the ice breakup activity peaks during austral summer and is minimum during winter. Iceberg grounding and rapid disintegration in summer releases significant acoustic energy. Background noise levels become lowest during austral winter, as the sea-ice cover suppresses wind and wave noise [21].

The question of the relative contribution of various noise sources to the low frequency noise observed south of Australia needs further investigation. Detailed analysis is beyond the scope of this paper. We make some qualitative comments in Concluding Remarks.

7. CONCLUDING REMARKS

The factors that should increase the low frequency noise level south of Australia in summer and decrease it in winter include:

- A much smaller sea ice coverage area in the Southern Oceans and hence much greater open water area for wind-generated noise south of the Polar front in summer;
- Warmer sea water in summer leading to more calving events from glaciers and icebergs;
- Winter sea ice trapping calved icebergs.

The factor that may decrease the low frequency underwater noise level off South Australia coast in summer versus winter is:

- In summer, there is a noticeably smaller surface area in the Southern Ocean where the sound channel axis reaches the surface, leading to less efficient coupling of the underwater noise energy from near-surface noise sources into the deep sound channel to the north.

Multi-year ambient noise data recorded south of Australia show persistently high levels at low frequencies that could not be explained by shipping noise or local winds. They are most likely due to distant sources. Wind waves at high latitudes in summer and ice-related events, especially ice calving are the most likely sources low-frequency underwater noise south of Australia coast and drivers of its seasonal variation.

8. ACKNOWLEDGEMENTS

CCMP Version-2.0 vector wind analyses are produced by Remote Sensing Systems. Data are available at www.remss.com. The authors acknowledge the financial support of the Maritime Division of the Defence Science and Technology Group.

REFERENCE

[1] Cato, D. (2012). A perspective on 30 years of progress in ambient noise: Source mechanisms and the characteristics of the sound field. In Advances in Ocean Acoustics, Zhou, J., Li, Z., Simmen, J., editors. *AIP Conference Proceedings*, pp 242 – 260, New York.

[2] Zhao, Z., E.A. D'Asaro, and J.A. Nystuen, 2014: The Sound of Tropical Cyclones. *J. Phys. Oceanogr.*, **44**, 2763–2778, https://doi.org/10.1175/JPO-D-14-0040.1.

[3] Wentz, F.J., J. Scott, R. Hoffman, M. Leidner, R. Atlas, J. Ardizzone, 2015: Remote Sensing Systems Cross-Calibrated Multi-Platform (CCMP) 6-hourly ocean vector wind analysis product on 0.25 deg grid, Version 2.0. Remote Sensing Systems, Santa Rosa, CA. Available online at www.remss.com/measurements/ccmp.

[4] Harris, P, Sotirakopoulos, K, Robinson, S, Wang, L, Livina, V. (2019), A statistical method for the evaluation of long term trends in underwater noise measurements, *J Acoust Soc Am.* 145(1):228. doi: 10.1121/1.5084040.

[5] McCauley, R., Cato, D., Duncan, A. (2016). Regional Variations and Trends in Ambient Noise: Examples from Australian Waters. In Arthur N. Popper and Anthony Hawkins (Eds.), *The Effects of Noise on Aquatic Life II*, (pp. 687-696). New York: Springer

[6] Sokolov, S. and S.R. Rintoul, 2007: Multiple Jets of the Antarctic Circumpolar Current South of Australia. *J. Phys. Oceanogr.*,**37**,1394–1412.

[7] Sokolov, S., and Rintoul, S. R. (2009), Circumpolar structure and distribution of the Antarctic Circumpolar Current fronts: 1. Mean circumpolar paths, *J. Geophys. Res.*, 114, C11018.

[8] Bannister, R. W. (1986). "Deep sound channel noise from high-latitude winds." *J. Acoust. Soc. Am.* 79(1): 41–48.
[9] Zuo, H., Balmaseda, M. A., Tietsche, S., Mogensen, K. and Mayer, M., The ECMWF operational ensemble reanalysis-analysis system for ocean and sea-ice: a description of the system and assessment, *Ocean Sci. Discuss.*, https://doi.org/10.5194/os-2018-154, in review, 2019.
[10] Chapp E., Bohnenstiehl D.R., Tolstoy M. Sound-channel observations of ice-generated tremor in the Indian Ocean, *Geochem. Geophys. Geosyst.* , 2005, vol. 6 pg. Q06003 doi:10.1029/2004GC000889
[11] Jacques Talandier, Olivier Hyvernaud, Dominique Reymond, Emile A. Okal, Hydroacoustic signals generated by parked and drifting icebergs in the Southern Indian and Pacific Oceans, *Geophysical Journal International*, Volume 165, Issue 3, June 2006, Pages 817–834, https://doi.org/10.1111/j.1365-246X.2006.02911.x
[12] Müller, Christian; Schlindwein, Vera; Eckstaller, Alfons; Miller, Heinz (2005): Singing Icebergs. *Science*, 310(5752), 1299, https://doi.org/10.1126/science.1117145
[13] Pettit, E. C. (2012), Passive underwater acoustic evolution of a calving event, *Ann. Glaciol.*, 53, 113–122, doi:10.3189/2012AoG60A137
[14] Glowacki, O., G. B. Deane, M. Moskalik, P. Blondel, J. Tegowski, and M. Blaszczyk (2015), Underwater acoustic signatures of glacier calving, *Geophys. Res. Lett.*, 42, doi:10.1002/2014GL062859.
[15] Urick, R. J. (1971). The noise of melting icebergs. *The Journal of the Acoustical Society of America*, 50(1B), 337–341. https://doi.org/10.1121/1.1912637
[16] Glowacki, O., Deane, G. B., & Moskalik, M.(2018). The intensity, directionality, and statistics of underwater noise from melting icebergs. *Geophysical Research Letters*, 45, 4105– 4113. https://doi.org/10.1029/2018GL077632
[17] Pettit, E. C., K. M. Lee, J. P. Brann, J. A. Nystuen, P. S. Wilson, and S. O'Neel (2015), Unusually loud ambient noise in tidewater glacier fjords: A signal of ice melt, *Geophys. Res. Lett.*, 42, 2309–2316, doi:10.1002/2014GL062950
[18] Gavrilov AN, Li B (2011) Location of ice noise sources in Antarctica, In: *Proceedings of 4th Underwater Acoustic Measurements conference*, 20–24 June, 2011, Kos, Greece
[19] Tournadre, J., N. Bouhier, F. Girard-Ardhuin, and F. Remy (2016), Antarctic icebergs distributions 1992–2014, *J. Geophys. Res. Oceans*, 121, 327–349,
[20] Matsumoto, H., D.W. R. Bohnenstiehl, J. Tournadre, R. P. Dziak, J. H. Haxel, T.-K. A. Lau, M. Fowler, and S. A. Salo (2014), Antarctic icebergs: A significant natural ocean sound source in the Southern Hemisphere, *Geochem. Geophys. Geosyst.*, 15, 3448–3458, doi:10.1002/2014GC005454.
[21] Dziak RP, Bohnenstiehl DR, Stafford KM, Matsumoto H, Park M, et al. (2015) Sources and Levels of Ambient Ocean Sound near the Antarctic Peninsula. *PLOS ONE* 10(4): e0123425. https://doi.org/10.1371/journal.pone.0123425

THE SOUNDSCAPE OF THE INNER IONIAN ARCHIPELAGO AS EVINCED THROUGH THE WEST PATRAIKOS GULF AMBIENT AND SEISMIC NOISE MONITORING PROJECT.

E. Fakiris[a*], D. Christodoulou[a], N. Georgiou[a], X. Dimas[a], G. Papatheodorou[a], Ph. Blondel[b], G. Mikoniatis[c], G. Zafiropoulos[c] and F. Symeonidis[c]

[a] Laboratory of Marine Geology and Physical Oceanography, Geology Dpt., University of Patras, Greece
[b] Department of Physics, University of Bath, UK
[c] HELLENIC PETROLEUM SA, Athens, Greece

* Elias Fakiris, fakiris@upatras.gr

Abstract: *Impacts of man-made acoustic noise on the marine environment are associated to the frequency and timing of any activity as well as the distribution and abundance of marine life. Offshore commercial operations, shipping activities, energy exploration and pile driving add noise to the already established ambient noise levels. Attention has been raised by the years to the topic of underwater noise and its effects on marine life, but the effects of underwater noise are not yet fully understood. As the adoption of the European Marine Directive (MSFD 2008/56/EC - Descriptor 11) has given great impulse to the research in this field, governments, companies and institutes are working to specify the background ambient noise levels. Those studies have formed the guidelines and have set the protocols for performing safer offshore operations, which are adopted by the major energy companies. Hellenic Petroleum S.A. has undertaken a Marine Seismic Survey in West Patraikos Gulf waters in Greece between January and February 2016, which was coupled with an intensive sound noise monitoring program. Acoustic data were collected around Marine Protected Areas of the Inner Ionian Archipelago during three monitoring phases: 1) the pre-start, 2) the concurrent and 3) the post-completion ones. Sound pressure levels (SPLs) were collected using drifting hydrophones deployed on a frequent schedule, spanning 1.5 months, collecting more than 130 hours of data. The ambient noise data gave insight into the footprints of the anthropogenic and biogenic factors on the soundscape of the Inner Ionian Archipelago. Most importantly, the recorded SPLs of the impulsive seismic and the continuous shipping noises were studied against the bearing and distance to the corresponding sound sources.*

Keywords: *ambient noise, seismic noise, ship noise, acoustic monitoring, Ionian sea*

1. INTRODUCTION

Hellenic Petroleum S.A. has undertaken a Marine Seismic Survey (MSS) in West Patraikos Gulf waters in Greece between January and February 2016. The MSS included acquisition of 3D seismic data from the Polar Empress R/V (Dolphin Geo). The purpose of this MSS was to better describe subsurface geology within the area and more accurately define potential prospective petroleum targets for exploration drilling. An Exclusion Zone of 750 m around the sound source, has been determined based on mathematical modelling, and monitored using the ACCOBAMS protocol [1], to ensure that noise levels were within the designated limits and to avoid adverse effects to marine mammals.

The effects of underwater noise on marine life are not yet fully understood. One reason for this is that only for a few species of mammals and fish, tests have been performed to identify hearing range and sensitivity and yet it is not sure how they react or what damage will be done to them. However, loud impulse noise and ambient (continuous) noise should be distinguished. The disturbance from shipping (from fishing, recreational and liner vessels) lies in particular in the fact that the noise input from these activities can be continuous and persistent in time. On the other hand, loud impulse sounds may instantly be more potentially harmful but they usually last for just some days (e.g. seismic surveys or pile driving). If the dedicated environmental protocols are followed, (e.g. soft start, exclusion zone etc. as in JNCC [2]) then the effects on marine life can be minimized. To accomplish this, the adoption of the European Marine Directive (MSFD 2008/56/EC - Descriptor 11) has given a great impulse to the research in this field and governments, companies and institutes have already performed a great amount of studies on the topic [3-6]. Those studies have set the protocols for safer offshore operations, adopted by the major energy companies. To ensure that the level of noise disturbance on the marine environment caused by offshore industrial and seismic survey operations is within the nominated limits, strict acoustic noise monitoring surveys are compulsory.

In the case of the MSS in West Patraikos Gulf waters, acoustic monitoring data have been recorded during three monitoring phases: 1) prestart, 2) seismic survey and 3) post completion so as to compare the soundscape before, during and after the seismic survey. Passive acoustic monitoring has been realized through spot measurements with drifting hydrophones [7] on a frequent schedule, which lasted for about 1.5 month, collecting more than 130 hours of raw underwater sound recordings from 4 pre-specified areas. Dense sound recordings were acquired and processed from as close to the seismic source to as far as possible away from it and sound pressure levels were estimated using all standardized metrics. It was verified that, in all cases, the seismic noise was well below the nominated limits. What was equally intriguing to investigate though, is the ambient noise monitoring data, as they were able to give greater insight into the footprints of the anthropogenic, mostly due to ship traffic, and biogenic factors on the local soundscape.

2. STUDY AREA

The zone where the 3D seismic survey took place in West Patraikos Gulf covers an area of 1892 km², with a mean and maximum sea depths of 158 m and 466 m respectively (Fig.1). It supports a diverse marine mammal fauna, including several species listed by IUCN as endangered or vulnerable. In addition, the survey area is in proximity to four Marine Protected Areas (MPAs), designated as Natura 2000 sites, that are almost completely surrounding it, thus making a strict seismic noise monitoring plan close to their boundaries essential. Four locations and specifically along the coasts of Ithaki, Atokos, Modi and Oxia

islands, were monitored using portable hydrophones, for all the phases of the project. Those locations are situated at the outer limits of the MPAs at the Northern extent of the survey area.

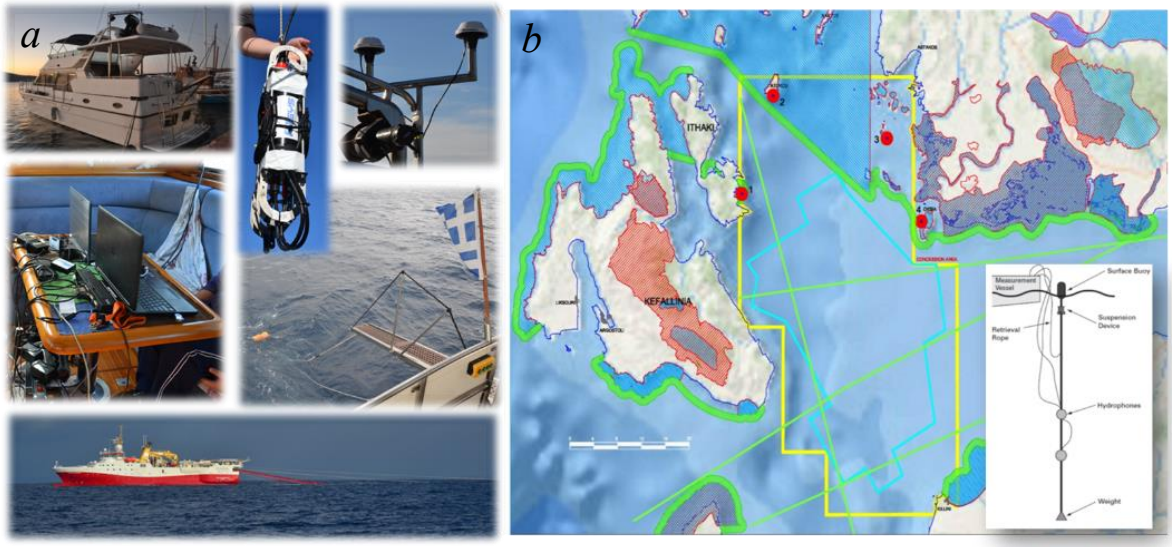


Fig.1: (a) Photographs from the monitoring and seismic vessels and the equipment used, (b) Map showing the seismic survey area (cyan polygon), the extents of the MPAs (green polygons) and the 4 locations (red dots) where spot acoustic measurements took place

3. MATERIALS AND METHODS

3.1. Equipment

Two pre-calibrated EA-SDA14 (RTsys) compact embedded recorders, able to connect to up to four hydrophones each were rented. Their broadband analog inputs allow over 500 kHz bandwidth with a dynamic range greater than 100 dB, guaranteeing efficient signal to noise ratios. Recorders came with 2 hydrophones each, a high sensitivity (170 dB dynamic range with 215 dB sensitivity) and a low sensitivity one (215 dB dynamic range with 170 dB sensitivity). Both channels were recorded at 24 bits, with a sampling frequency of 78,125 Hz. Using dual sensitivity hydrophones guaranteed that all dynamic ranges and amplitudes were successfully recorded without any signal clipping. All hydrophones were thoroughly calibrated by RTsys to be compatible with all international regulations. Apart from the recording units and hydrophones, the research vessel was also equipped with a Hemisphere VS101 GPS, to acquire accurate positioning data in real time.

3.2. Sound pressure level metrics

Noise sound pressure levels (SPLs) have been estimated regarding the zero to peak (SPLpeak), peak to peak (SPLp-p) and root mean square (SPLrms) definitions, as well as the sound exposure level (SEL), all integrated for 1s durations. All above SPL metrics have also been examined as a function of sound frequency components and specifically using a total 30 third-octave bands (from 16 to 20,000 Hz centre bands), according to the standard ANSI S1.6-1984 formula [8]. Finally, power spectrum densities (PSD) have been estimated using the Welch's method [9], being the power in the signal per 1 Hz unit frequency integrated over a duration of 30 s. To meet the above estimations in an automated fashion, a suite of MATLAB codes has been implemented to perform analysis and reporting of the acquired acoustic data.

3.3. Ambient noise monitoring

The ambient noise monitoring program was divided in two distinct stages, the pre-start and the post-end, each lasting for about 10 days of sound recordings. This was to compare any differences that might have occurred in the natural soundscape of the area before and after the 3D seismic survey. Realization of spot measurements, spanning wide spatiotemporal scales, has been decided to be the most cost effective and efficient approach for the acoustic monitoring survey. More precisely, instead of mooring several hydrophones at the monitoring stations for the full survey period, the monitoring research vessel changed locations between the specified station locations in a daily schedule, performing spot acoustic noise measurements. For each station the research vessel turned off the engines to avoid any mechanical acoustic noise and deployed the underwater recording unit at 20m water depth to uninterruptedly acquire sound data for 3 to 6 hours. In each deployment the vessel was left drifting in the winds and the sea currents, hardly stabilized by using a floating anchor. Whenever the vessel had drifted far from the intending position, correction movements were realized, the time and duration of which were noted in the logbook to be excluded from the post-survey analysis. More than 70 hours of raw data recordings have been acquired during the pre-start and post-end ambient noise monitoring stages.

3.4. Seismic noise monitoring

Spot measurement have also been realized for the needs of the seismic noise monitoring stage, which lasted 22 days. The recording schedule had been carefully planned in accordance to the prespecified survey-lines pattern of the seismic vessel, so that at the end of the seismic survey, dense acoustic noise monitoring data would have been acquired from as close as possible to the seismic source (900 m) to as far as possible away from it (60 km). During the seismic noise monitoring phase, the navigational data of the seismic vessel were sent to the acoustic data processing team in a daily fashion after a valid exchange data format had been agreed. Those data included time stamped positions of the seismic vessel, for time intervals that airgun shots occurred. More than 60 hours of raw seismic noise sound recordings have been acquired during the seismic noise monitoring stage. Transient sounds (pulses) were detected automatically for which their 90% pulse energy duration was estimated. A peak detector to the RMS smoothed signal was first applied to locate each airgun impulse and then the 5% - 95% rise time period of the cumulative squared signal was estimated. For this duration all sound pressure level metrics, as described in paragraph 3.2, have been estimated and analysed as a function of distance and bearing to the seismic source.

3.5. Monitoring the exclusion zone

Monitoring the exclusion (mitigation) zone around the seismic vessel (900m<d<3,000m) was a challenging task, both regarding the field-work planning as well as the data processing queue. The research vessel deployed the sound recorder at 20m depth, standing in positions agreed with the navigation team of the seismic vessel, as the latter was approaching executing its prearranged 3d seismic survey lines. Attention has been paid so that sound measurements were obtained from both the forward and broadside directions relative to the fore-aft axis of the air-guns. Each recording station lasted for about 30 to 40 minutes. A high pass filter over 50Hz was applied to the sound data to remove any self-noises. The navigational data of the seismic vessel were sent to the data processing team in a daily fashion. In order to study the attenuation of impulse (transient) sounds around the seismic source, the relative position of the monitoring vessel and each emitting airgun was estimated, putting the seismic sources at the centre and converting the Cartesian coordinates to polar.

4. RESULTS

4.1. Seismic noise

Spot measurements with drifting hydrophones, apart from being cost effective, were proven to be a very efficient means for seismic noise monitoring. They holded the advantage of retrieving acoustic data not only from an isolated position but also from a buffer around it, making the estimated SPLs more statistically representative. Following carefully planned recording agendas, in regard to the seismic vessel's prearranged daily survey-lines, spatially dense acoustic data were managed to be acquired. This practically replaces the need for moored hydrophones, minimizing at the same time the required equipment items, increasing the spatial coverage of the measurements as well as the flexibility of the monitoring team in terms of service capacity. Fig.2 presents the high spatial density of the seismic impulses that have been recorded from the Modia station, that lead to an almost continuous SPL vs distance graph (Fig.2b).

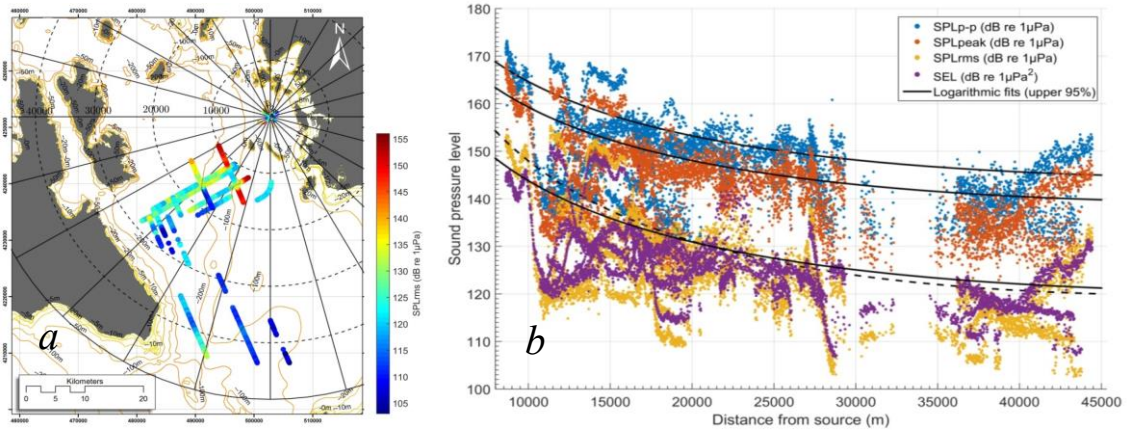


Fig. 2: a) Spatial density of recorded seismic pulses at Oxia station (center of the polar diagram) and b) impulse SPL vs distance to the seismic source.

It was clearly shown that the exclusion zone of 750 m around the seismic vessel adequate, as it received SPLs less than 200 db re 1µPa, far below the nominated limits for temporary or permanent hearing loss of marine mammals (Fig.3a). This result is in good agreement with the modelled by D'Apollonia transmission loss in the exclusion zone, which was used for the exclusion zone determination, and especially for the case of spherical spreading. The latter was a worst-case scenario, quite above the actual measurements (Fig.3b).

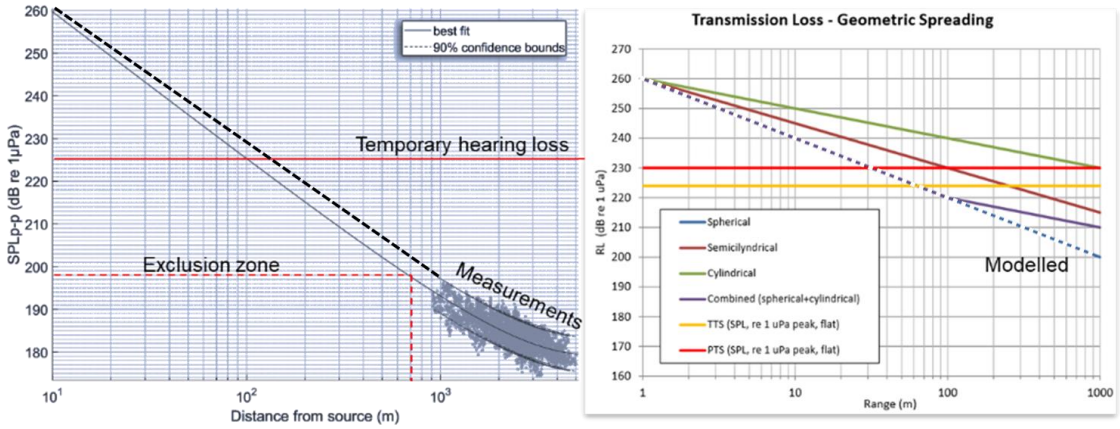


Fig.3: Measured and modelled verification of the exclusion zone. Dashed lines correspond to the modelled results for the case of spherical spreading, which suits well with the upper limits of the average measured SPLp-p in the area.

Apart from the core seismic noise monitoring results, some other intriguing findings were extracted from the collected seismic monitoring data. Those include the attenuation and frequency modulation of the seismic impulses in regard to their distance to the seismic source. Towards that, Fig.4a shows the spectrogram of the acoustic noise as the seismic vessel approached the recorder, exhibiting clear increase of both the mechanical noise of the vessel and the seismic impulse levels. Fig.4b shows the third- octave bands of each individually detected seismic impulse, with distance to the seismic vessel. The frequency modulation of the seismic impulses seems to be towards losing both its low but mostly its higher frequency components, which is also clear in their corresponding spectrograms.

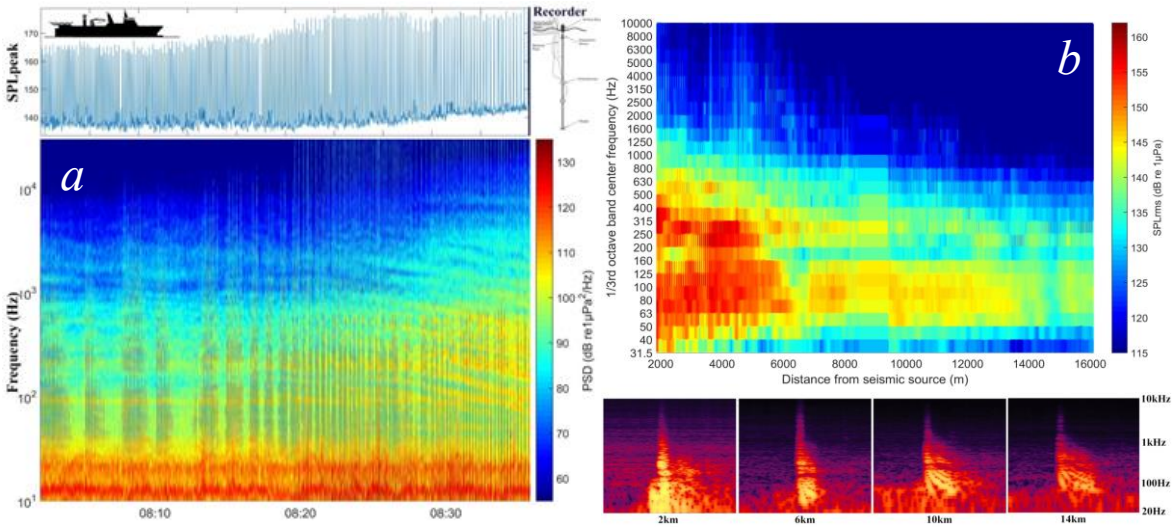


Fig.4: a) Spectrogram of the acoustic noise as the seismic vessel approaches the recorder and b) 1/3 octave bands of each individually detected seismic pulse with distance to the seismic vessel and corresponding spectrograms.

4.2. Anthropophony and Biophony of the ambient soundscape of Inner Ionian

The soundscape in West Patraikos was analysed during the ambient noise monitoring phases. It was realized that the anthropophony of the area is dominated by fishing but mostly liner passenger vessels, as well as sea-farm coastal noises. Fig.5 shows characteristic spectrograms of liner ships passing about 4 km and 6km away from Oxia station, increasing the ambient noise levels for 25dB and 10 dB respectively.

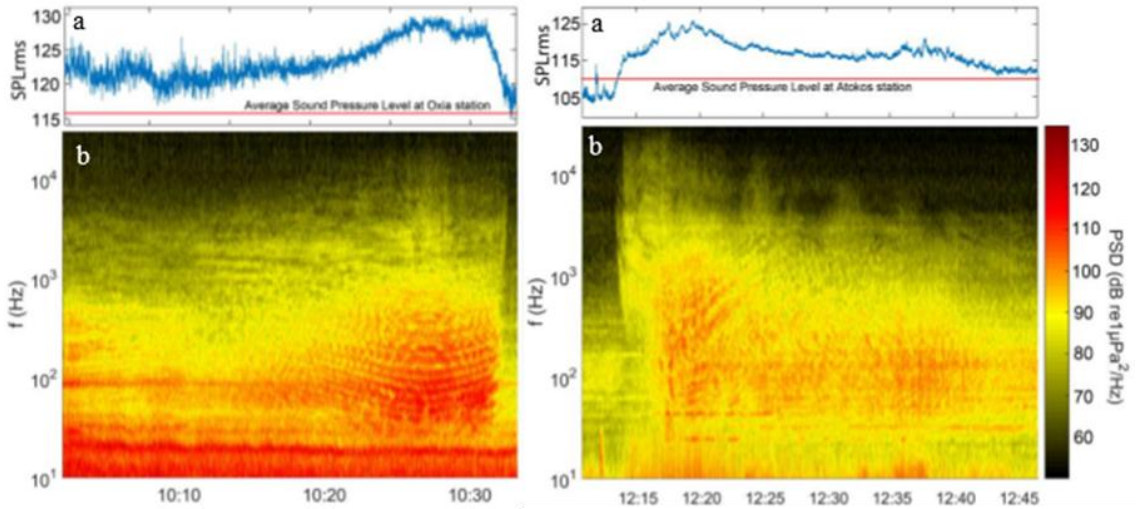


Fig.5: Spectrograms showing two instances of ship noise from two liners, one passing 4km away and another 6km away the recording unit.

Fig.6 provides a comparison of SPLrms between the ambient noise, the seismic activity (integrated over time unit or detected impulse) and the traffic in the same area, both in regard to 1/3 Octave bands and total SPL. It is clear that the traffic noise adds on average 20 dB to the ambient noise while the seismic activity adds about just 10 dB more (30dB). Integration per time unit (1s) over the full seismic activity period, resulted in 10 dB less than the traffic noise equivalent. It is also interesting that while seismic noise contributes greater in below 1kHz, maximum SPL_{rms} from ship traffic exhibits almost equal noise levels with the maximum seismic noises at frequencies higher than 1kHz.

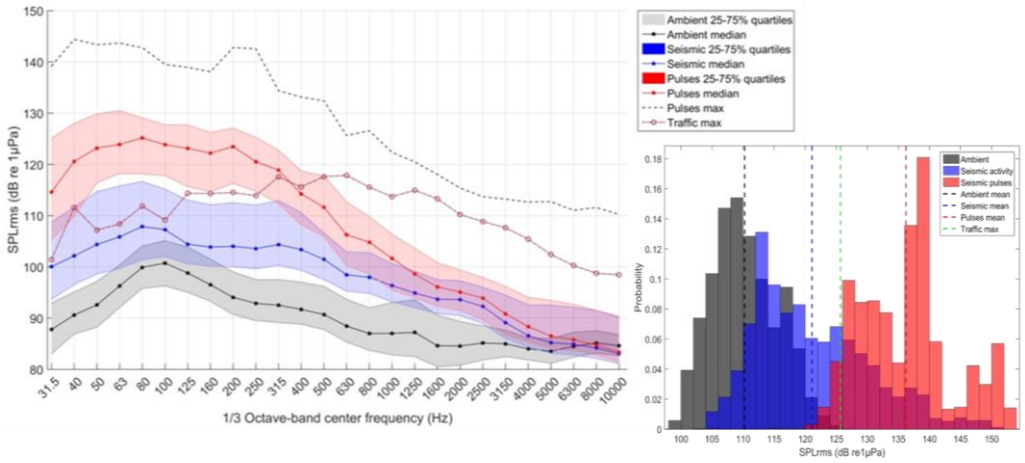


Fig.6: Comparison between the 1/3 octave-band SPLs (left) and the average SPLs (right) in the cases of seismic noise, seismic impulses, ship noise and ambient noise.

Biophony was a strong component of the soundscape in the area. Crustaceans produced characteristic click sounds (snapping shrimps), and dolphin whistles were recorded in a dozen of instances. Measuring benthic habitats through passive acoustics is a popular scientific topic nowadays [5,6] and drifting hydrophones could potentially greatly aid towards quantitative habitat mapping, as demonstrated in [7].

Eco-acoustic indices can offer the means for assessing the rate of biophony versus anthropophony in the marine soundscape. A popular index, the Normalized Difference Soundscape Index (NDSI) [10], seeks to "estimate the level of anthropogenic disturbance on the soundscape by computing the ratio of human-generated (anthrophony) to biological (biophony) acoustic components". NDSI varies between -1 and +1, where +1 indicates a signal containing no anthropophony. Here, the anthropophony frequency bands were defined as shipping (< 1 kHz) and sonar (> 10 kHz). A preliminary application of the aforementioned index at two instances of liner ship and seismic noise showed that they yielded a totally different NDSI pattern (Fig.7).

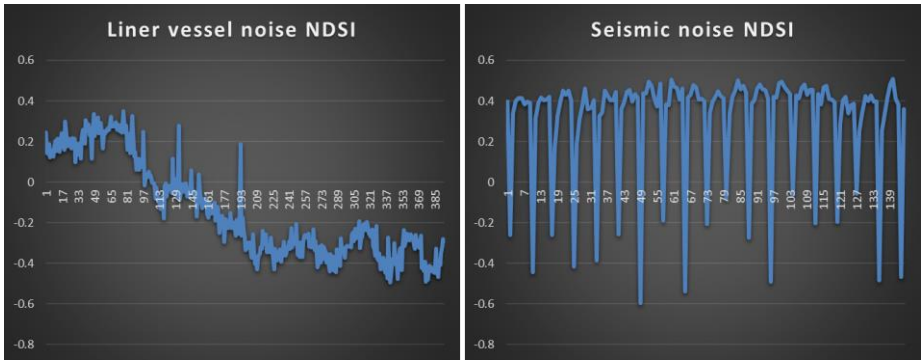


Fig.7: NDSI eco-acoustic index for two cases: Left: liner ship noise and right: seismic noise at the same station (Atokos). Recording duration was 5 min in both cases.

While ship noise produced a gradual degradation of the ecological status for the full duration of the ship passage, seismic noise (impulses) produced the same rate of degradation but with regular "jumps" from good to bad environmental status, following the airgun shooting rate pattern. Although ship noise exhibited lower mean NDSI than the seismic noise for the considered period, no safe assumptions can be made about the consequences of the one or the other type of anthropogenic noise on the marine environment.

5. CONCLUSIONS

The data collected, and the methods used for the seismic and ambient noise monitoring during the MSS in West Patraikos Gulf, were proved to be important both for investigating the induced seismic noises as well as other anthropogenic disturbances that dominate the soundscape of the area, such as ship noise. The seismic monitoring results showed a very good agreement between the modelled and the recorded SPLs in the exclusion zone. The seismic noise was proved to have always been lower than the nominated limits, especially outside the exclusion zone, but it was also realized that the ambient soundscape of west Patraikos Gulf experiences quite high and insisting anthropogenic disturbances due to sip noise. The diversity of anthropophony and biophony in West Patraikos, spanning from dolphin whistles and snapping shrimps, to "deafening" liner ships and sea farm noise was captured and eco-acoustic indices were showcased against their suitability for assessing anthropophony dominance in the marine soundscape.

REFERENCES

[1] **ACCOBAMS**, "Cetaceans of the Mediterranean and Black seas," *G. Notarbartolo di Sciara (Ed.), Cetaceans Mediterr. Black Seas state Knowl. Conserv. Strateg. A Rep. to ACCOBAMS Secr. Monaco, Febr. 2002*, p. Section 14, 7p. (2002).

[2] **JNCC**, "Guidelines for minimising the risk of injury to marine mammals from geophysical surveys, August (2017)

[3] **OSPAR**, "Assessment of the environmental impact of underwater noise 2009," *Comm. Rep.*, vol. Biodiversi, pp. 1–44, (2009)

[4] **N. D. Merchant**, **K. M. Fristrup, M. P. Johnson, P. L. Tyack, M. J. Witt, P. Blondel, and S. E. Parks**, "Measuring acoustic habitats," *Methods Ecol. Evol.*, **6**, no. 3, pp. 257–265, (2015).

[5] **P. Blondel and A. A. Z. Hatta**, "Acoustic Soundscapes and Biodiversity-Comparing Metrics, Seasons and Depths with Data from the NEPTUNE Ocean Observatory offshore British Columbia," in *UACE2017*, pp. 763–768. (2017)

[6] **D.M. Wisniewska, L.A. Kyhn, J.Tougaard, M. Simon, Y.T Lin, A. Newhall, K. Beedholm, J.F. Lynch** *"Propagation of airgun pulses in Baffin Bay 2012".* Scientific Report from Danish Centre for Environment and Energy (2014)

[7] **A. Lillis, F. Caruso, T. A. Mooney, J. Llopiz, D. Bohnenstiehl, and D. B. Eggleston**, "Drifting hydrophones as an ecologically meaningful approach to underwater soundscape measurement in coastal benthic habitats," *J. Ecoacoustics*, vol. 2, p. (2018).

[8] **ANSI S1.6** : 1984 *"Preferred frequencies and filter band center frequencies for acoustical measurements"* Acoust. Soc. Am., (1984)

[9] **Welch, P. D.** "The use of Fast Fourier Transform for the estimation of power spectra: A method based on time averaging over short, modified periodograms", IEEE Transactions on Audio and Electroacoustics, AU-15 (2), pp. 70–73 (1967)

[10] **Kasten, E.P**., **Gage, S.H., Fox, J. & Joo, W.** *"The remote environmental assessment laboratory's acoustic library: an archive for studying soundscape ecology.* Ecological Informatics, 12, 50-67. (2012)

UNDERWATER NOISE FROM WIND AT THE HIGH NORTH LOVE OCEAN OBSERVATORY

Lars Ødegaard[a] , Geir Pedersen[b] and Espen Johnsen[c]

[a]Norwegian Defence Research Establishment (FFI), Horten, Norway.
[b]NORCE Norwegian Research Centre, Bergen, Norway
[c]Institute of Marine Research (IMR), Bergen, Norway

Contact author's name and complete postal address:
Lars Ødegaard, FFI, PB 115, 3191 Horten, Norway.
Email: Lars-Alf.Odegaard@ffi.no

Abstract: *The Lofoten-Vesterålen (LoVe) Cabled Ocean Observatory is located in an oceanographic, ecological, and economical hotspot off the Northern Norwegian cost. The observatory is a national research infrastructure under development by a national consortium led by the Institute of Marine Research (IMR). The first observation node of the infrastructure was launched in September 2013 and is located at 258 m depth about 15 km offshore.*

Preliminary analyses [1] using hydrophone recordings from Node 1 indicate that wind generated noise at low frequencies is significantly higher at the LoVe Observatory than in the commonly used Wenz curve. A more thorough study of wind generated noise using larger datasets from the hydrophone at Node 1 is presented here.

Hydrophone data are summarized in percentile plots to describe the variation in underwater noise. Metadata on shipping from AIS (Automatic Identification System) and metadata on wind from the Norwegian metrological institute have been used to show how much of the variation in underwater noise that may be explained by wind. Our results show that the LoVe area is a quiet area suitable to study noise from wind, and our results confirms that the wind generated noise at low frequencies is significantly higher at the LoVe Observatory than in the Wenz curve.

Keywords: *Underwater noise, ambient noise, ocean soundscape, LoVe Ocean Observatory, wind, AIS, whale vocalization*

1. INTRODUCTION

The Wenz curve [2] is established as the main reference (Fig 7.5 in [3] and Fig 8.13 in [4]) for the ocean soundscape, but it is made for deep water. The soundscape in shallow water is site dependent [5] and still a topic for research [6]. Acoustic measurements from the Lofoten-Vesterålen (LoVe) observatory are in this paper used to investigate whether the Wenz curve is representative for the LoVe area as well.

2. THE LOVE OCEAN OBSERVATORY

The LoVe Ocean Observatory [7][8] is located at 258 m depth 15 km offshore of the Northern Norwegian coast. Node 1 was launched in September 2013 by Equinor, the Norwegian Institute of Marine Research (IMR) and Metas AS. Node 2, 3, 4, 5 and 7 will be launched in 2019 by a national consortium led by IMR. Node 6 may be installed in 2020. The expansion from 1 to 7 nodes is funded through the National Infrastructure for Research program.

The main objective of the infrastructure is to further develop the knowledge base of the physical, chemical, and biological environment in this ecologically important area. Each node will host a suite of oceanographic, biological and chemical sensors, including hydrophones which continuously monitor the marine soundscape. An analysis of the hydrophone data from Node 1 is presented here.

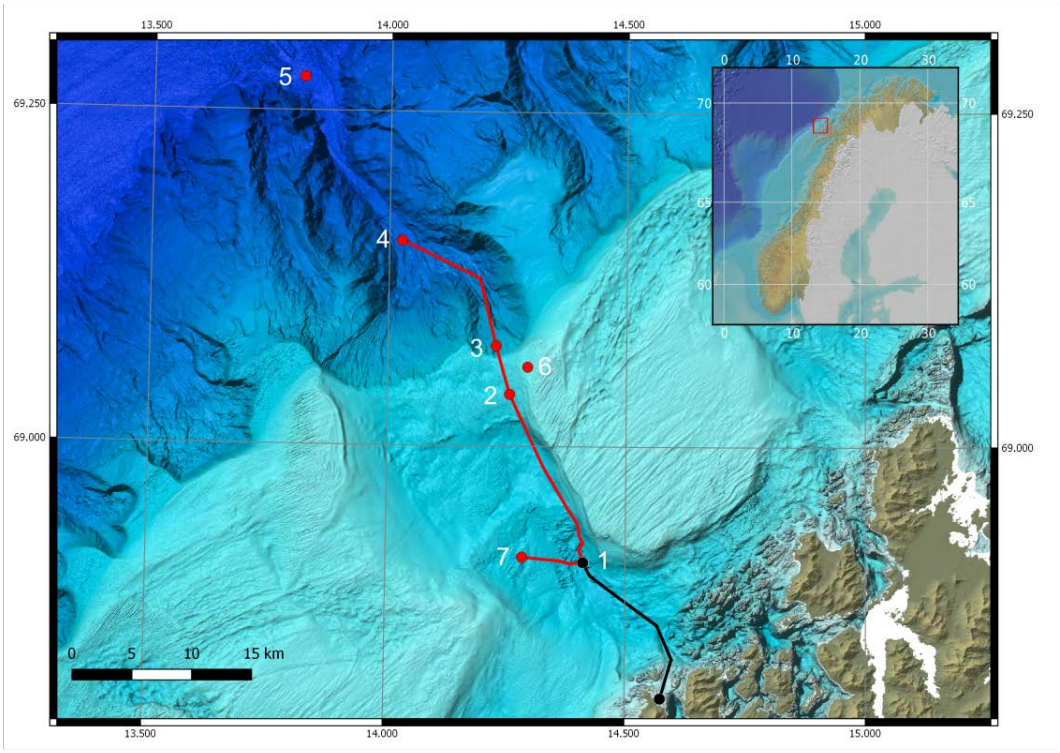


Fig.1: Localization of the LoVe Ocean Observatory and its underwater nodes.

3. METHOD

Underwater noise from wind is studied in samples with ship far from the hydrophone (Range > 30 km). The wind data used is from Nora10 (NOrwegian ReAnalysis with 10 km grid) [9][10] from the Norwegian Meteorological Institute. The wind data is a re-analysis of historical weather based on a model, but strongly constrained by available observations. An example of wind speed estimated at the LoVe Observatory is shown in Fig 2.

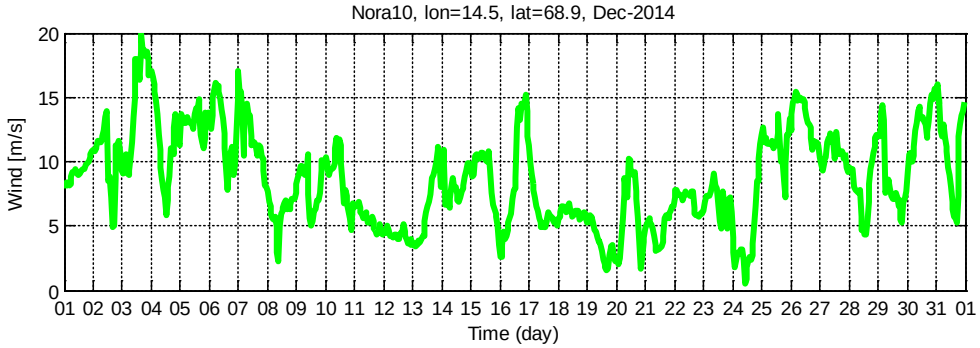


Fig.2: Wind at the LoVe Observatory (Nora10 data for Dec 2014)

AIS-information from Kystverket [11] on shipping around the LoVe Observatory has been used to find time periods without significant noise from shipping. The two first plots in Fig 3 show shipping information in two of the time periods used to study underwater noise from wind. Periods with AIS ship closer than 30 km from the hydrophone are removed in the study of ambient noise from wind.

The last plot in Fig 3 shows the shipping density in December 2014, which was the first complete month with high quality hydrophone data from the LoVe Observatory. The plot shows that the main traffic lane along Norway, i.e. the shipping lane for large ships as tankers and 200 m long cargo ship, has CPA (Closest Point of Approach) around 55 km from the LoVe Observatory, while a traffic lane for smaller Cargo ships has CPA close to the hydrophone.

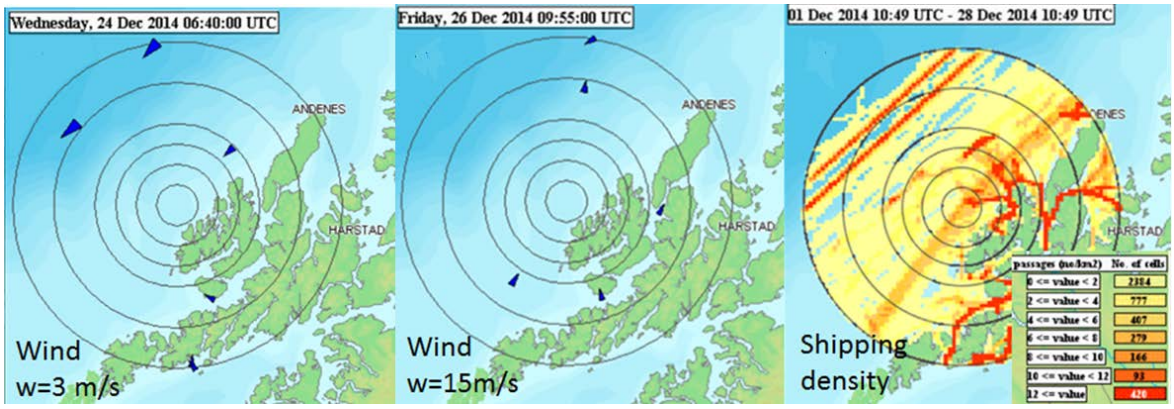


Fig.3: AIS plot from the LoVe (Lofoten Vesterålen) area. The LoVe-hydrophone is located at the center of the circles. The circles have radius of 10, 20, 30, 40, 60 and 80 km.

The hydrophone at the LoVe Observatory has recorded high quality data in the frequency band between 10 Hz and 16 kHz. The recordings at higher frequencies have not been used in this study, because they are disturbed by noise from the echosounders at the LoVe Observatory. The hydrophone data has first been processed as specified in the EU-project JOMOPANS [12], i.e. averaged over 1/3 octave frequency band and sampled every second. The results have then been resampled from 1s to 300s resolution by taking the median over 300 1s data to improve the estimates of the ambient noise from wind. The median is used to avoid or at least reduce the effect of biological and system noise transients.

Curves of ambient noise as function of frequency for a given wind speed are calculated as the median over all high quality samples in a month satisfying:

1. Wind within: Wind speed studied +/- 2.5 m/s
2. No ship (with AIS) closer than 30 km

The sensitivity of the hydrophone (SB35 ETH from Ocean Sonic) is -171 dB re 1 V/µPa with pre-amp [13]. This is an average value for all the frequencies and ± 3 dB must therefore be added to the spectrum levels reported here. The peak measured signal of the hydrophone is 175 dB re 1 µPa

4. RESULTS

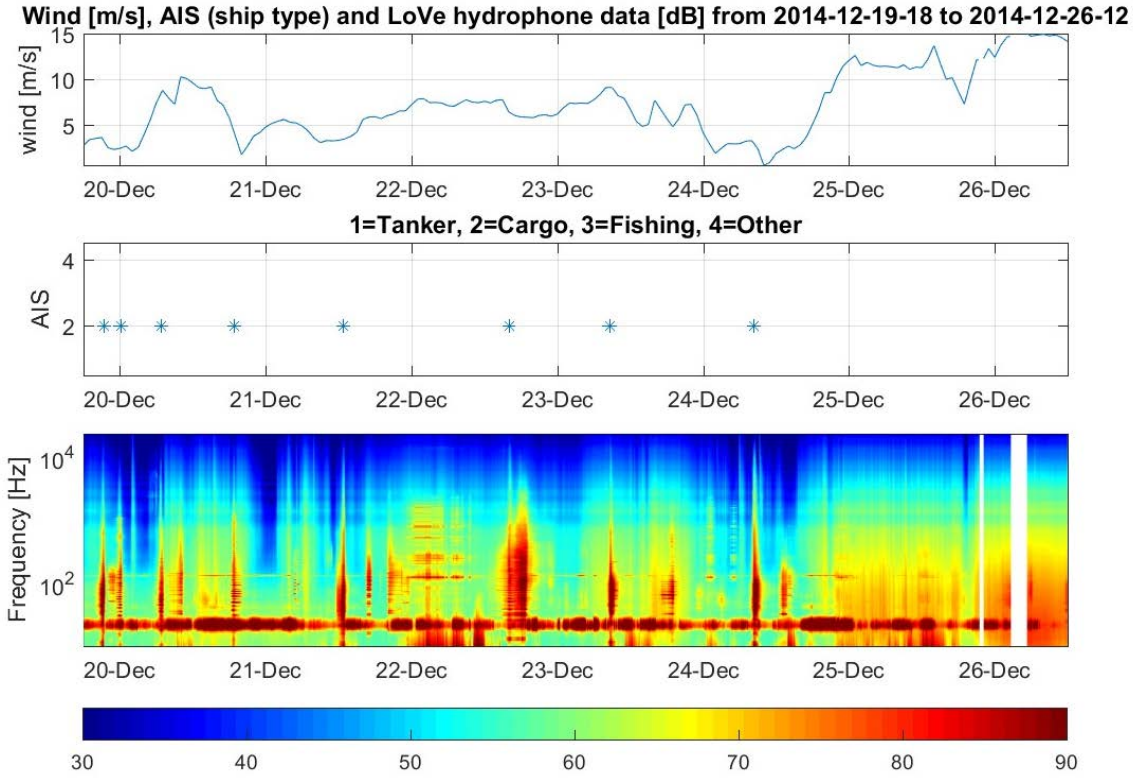


Fig.4: Underwater sound (lower), Shipping information from AIS (middle) and wind (upper) for a week in Dec 2014. Ship closer than 5 km to the LoVe Observatory is shown in the AIS plot. The frequency axis in the lower plot is logarithmic, and the color in dB re 1 µPa²/ Hz.

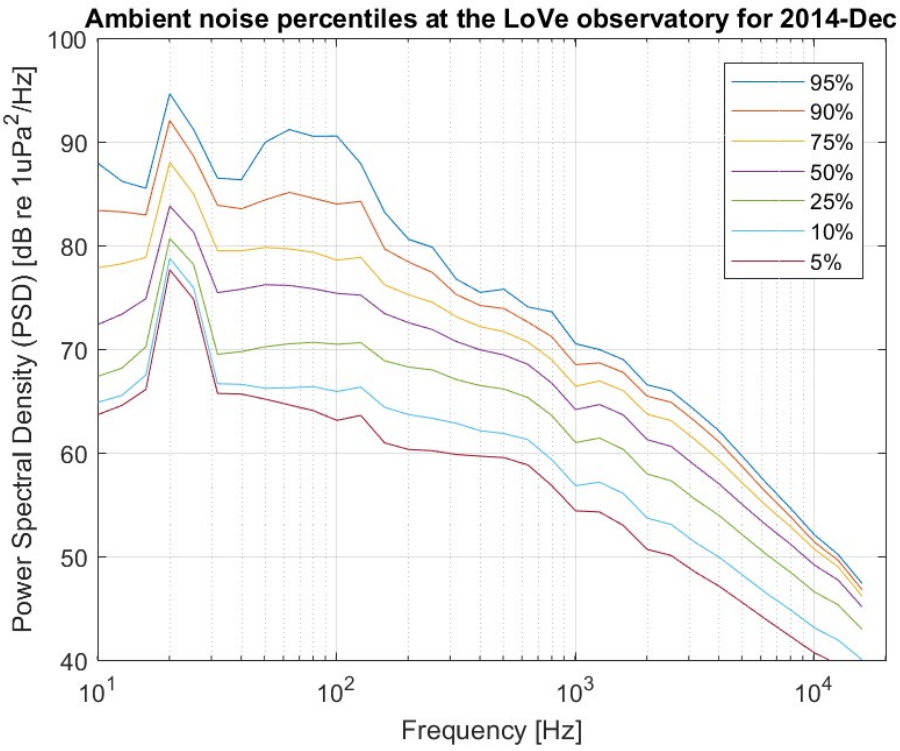


Fig.5: Percentile plots of underwater sound as function of frequency for December 2014.

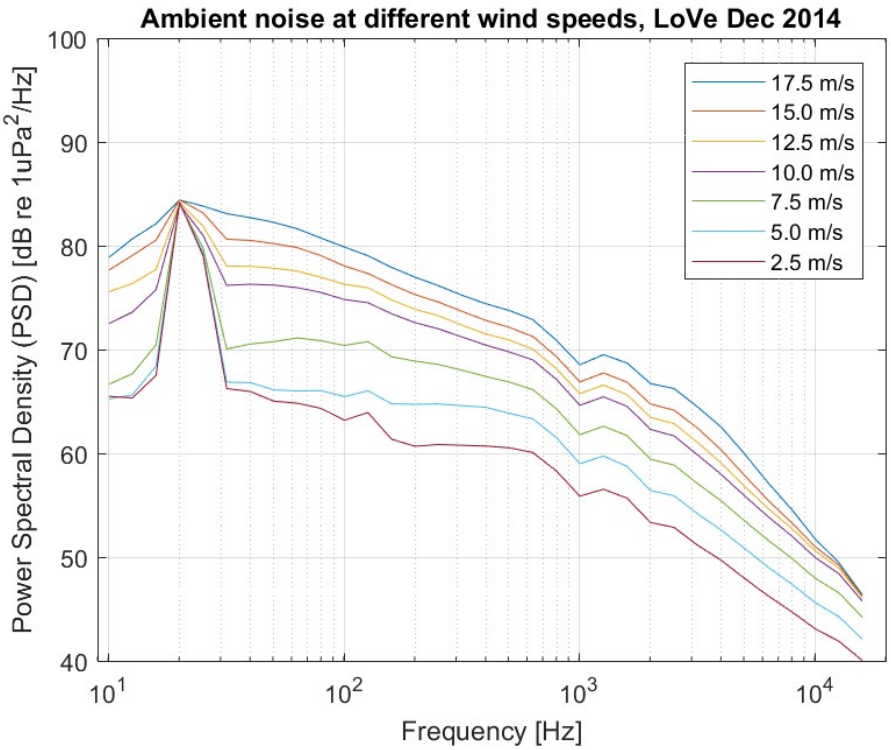


Fig.6: Underwater sound as function of frequency for different wind speeds.

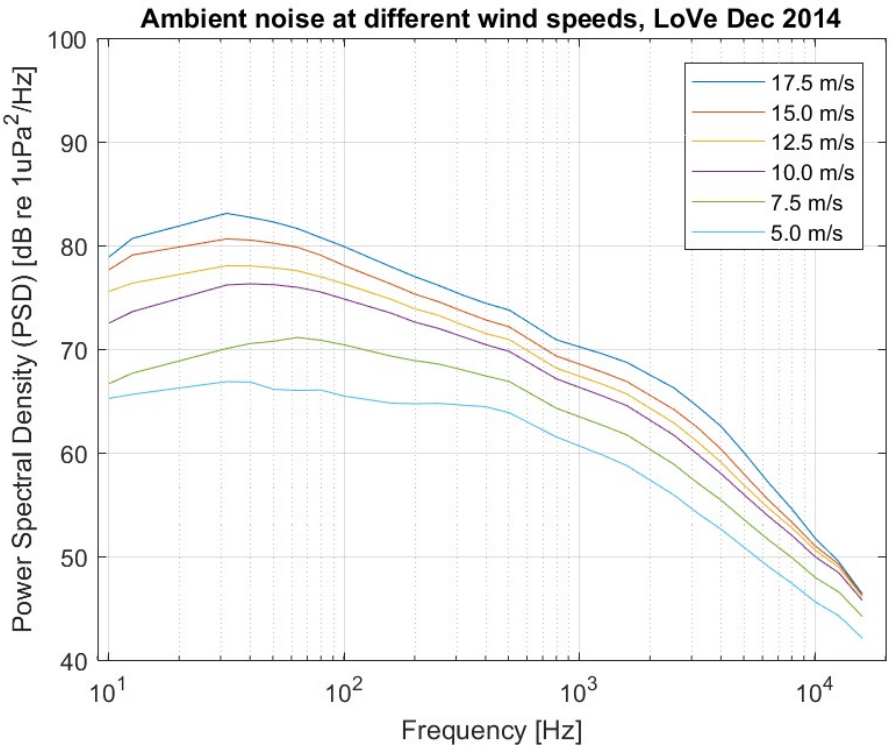


Fig 7: Underwater sound as function of frequency for different wind speeds after removing contributions from Fin whale and system resonances around 1000 Hz.

Fig 4 shows an example of the quality of the LoVe hydrophone data together with metadata on wind and shipping. A higher frequency resolution than 1/3 Octave frequency band has been used in this plot to better illustrate the quality of the data. The plots show that the ambient noise is correlated with wind, and the LoVe data is therefore useful for studying underwater noise from wind, but the plot also illustrate that periods with vessels close to the hydrophone must be removed in the wind study. More detailed plots confirm that periods with ship closer than 30 km to the hydrophone must be removed.

The variation in the ambient noise data recorded in December 2014 is summarized in a percentile plot in Fig 5, while the remaining variation after removing recordings with vessels close to the hydrophone are shown as a function of wind speed in Fig 6.

The Fin whale is known to vocalize around 20 Hz, and the strong peak between 17 and 28 Hz shown in Fig 5 and 6 is concluded to be Fin whale. The Fin whale frequencies are therefore removed in Fig 7. Some samples around 1000 Hz are also removed, because they are disturbed by system resonances.

5. DISCUSSION/ CONCLUSION

Fig 5 shows that the underwater noise is up to 27 dB higher in the 5% loudest periods compared to the 5% most quiet periods in December 2014, while Fig 6 shows that much of the variation in ambient noise may be explained by variation in wind speed. An increase in wind speed from 2.5 m/s to 17.5 m/s gives an increase in ambient noise of up to 17 dB.

The largest variation seen in the percentile plot in Fig 5 is between 50 and 100 Hz, which may be explained by shipping. Biological sounds are also significant. The Fin whale is known to vocalize at low frequencies, and the strong peak between 17 and 28 Hz shown in Fig 5 and 6 is concluded to be Fin whale. The Fin whale frequencies are therefore removed in Fig 7. Frequencies around 1000 Hz is removed as well, because they are disturbed by system resonances.

Fig 7 is concluded to be the final estimate of wind driven ambient noise at the LoVe observatory in December 2014. An interesting observation in Fig. 7 is that the ambient noise at high frequencies (20 kHz), do not increase with wind speed in the same way as for lower frequencies. The effect may be because of a layer with attenuating bubbles made by wind and waves.

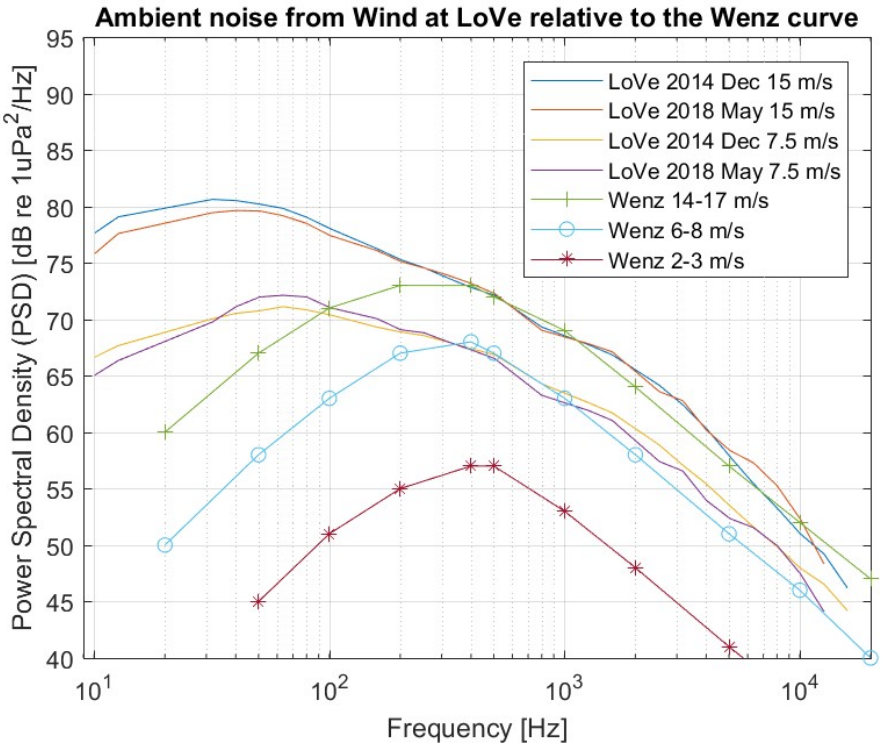


Fig 8: Underwater sound as function of wind at the LoVe Observatory compared to the deep water Wenz curve.

The main purpose of the work in this paper has been to compare the soundscape at the LoVe Observatory with the Wenz curve. The Wenz curve for 2-3 m/s, 6-8 m/s and 14-17 m/s wind is plotted in Fig 8. It is adapted from Fig 7.5 in [3] and based on Wenz's article from 1962 [2]. The LoVe wind curves plotted in Fig 8 are similar to the Wenz curve for frequencies higher than 400 Hz, but the LoVe wind curves show much higher ambient noise at frequencies below 400 Hz.

The results from the LoVe Observatory are more similar to measurements from shallow water [5], and we conclude that the data from the LoVe hydrophone at 258 m depth must be handled as shallow water data, not deep water data.

The results presented in Fig 4-7 shows data from December 2014 only, but the same calculations have been done for 1-27th May 2018 as well. Fig 8 shows that the ambient noise in December 2014 and May 2018 are almost equal for 7.5 m/s wind and 15 m/s wind, which indicate that the ambient noise from wind is independent of month.

The estimated curves for ambient noise at 2.5 m/s wind shows however a difference between the curves from December 2014 and May 2018. It is assumed that the ambient noise level at 2.5 m/s wind is so low that the samples are disturbed by shipping at larger distances than 30 km and biological sounds. The curve for 2.5 m/s wind in Fig 6 is therefore assumed to show too high ambient noise level and it is therefore removed from Fig 7 and 8. A more detailed and more manual study has to be done on the ambient noise curve for 2.5 m/s wind.

6. ACKNOWLEDGEMENTS

Thanks to Morten Køltzow at Norwegian Metrological Institute for making the Nora10 wind data available, and thanks to Petter Kvadsheim at FFI for help with understanding the biological sounds in the data.

REFERENCES

[1] **Ødegaard Lars**, *Ocean Soundscape Measurements at the LoVe Ocean Observatory*, UACE 2015, 3rd Underwater Acoustic Conference and Exhibition, pp 433-438, 2015

[2] **Wenz, G. M**., *Acoustic ambient noise* in *the ocean: Spectra and sources*, J. Acoust. Soc. Am, vol 30, pp 1936-1956, 1962.

[3] **Urick, R. J**., *Principles of underwater sound*, McGraw-Hill, 3rd edition, 1983.

[4] **Ainslie M. A**., *Principles of sonar performance modeling*, Springer, 2010.

[5] **Ingenito F. and S.N. Wolf**, *Site dependence of wind-dominated ambient noise in shallow water*, J. Acoust. Soc. Am, vol 85, pp 141-145, 1989.

[6] **Haxel J.H. , R.P. Dziak and H. Matsumoto**, *Observations of shallow water marine ambient sound: The low frequency underwater soundscape of the central Oregon coast*, J. Acoust. Soc. Am, vol 133, pp 2586-2596, 2013.

[7] **Godø, O.R., S. Johnsen and T. Torkelsen**, *The LoVe Ocean Observatory is in Operation,* Marine Technology Society Journal, vol 48, Nr 2, pp 24-30, March/ April 2014.

[8] https://love.equinor.com/

[9] **Reistad, M., Ø. Breivik, H. Haakenstad, O. J. Aarnes, B. R. Furevik, and J.-R. Bidlot**, *A high-resolution hindcast of wind and waves for the North Sea, the Norwegian Sea, and the Barents Sea*, J. Geophys. Res., Vol 116, C05019, 2011.

[10] **Furevik B.R. and H. Haakenstad**, *Near-surface marine wind profiles from rawinsonde and NORA 10 hindcast.* J. Geophys. Res., Vol 117, D23106, 2012.

[11] http://aisstat.kystverket.no/statistikk/

[12] EU project JOMOPANS; Joint Monitoring Programme for Ambient Noise North Sea; Standards on acoustic indicators and data processing: https://vb.northsearegion.eu/public/files/repository/20180925143035_Jomopans_Acoustic_indicator_report.pdf https://vb.northsearegion.eu/public/files/repository/20190329144007_Jomopans_WP3standardDataProcessing_v15.pdf

[13] **Metas AS,** *Technical Information LoVe Sensors installed.* https://love.equinor.com/Resources/LoVe%20Ocean%20Observatory%20Sensor%20System.pdf

MONITORNING OF ANTHROPOGENIC UNDERWATER NOISE IN THE VENICE LAGOON, ITALY

Jaroslaw Tegowski[a], Fantina Madricardo[b], Aleksandra Kruss[b], Jakub Zdroik[a], Lukasz Janowski[a]

[a]Institute of Oceanography, University of Gdansk, al. Marszalka Pilsudskiego 46, 81-378 Gdynia, Poland
[b]Istituto di Scienze Marine – CNR ISMAR, Arsenale - Tesa 104, Castello 2737/F, 30122 Venezia, Italy

Jaroslaw Tegowski, Institute of Oceanography, University of Gdansk, al. Marszalka Pilsudskiego 46, 81-378 Gdynia, Poland, fax: +48585236678, email: j.tegowski@ug.edu.pl

Abstract: *The Venice Lagoon and its major canals are an example of particularly high traffic of vessels from cargo and passenger ships to water busses (vaporetto) and fast recreational motorboats. In January and July 2018, we conducted underwater noise measurements in this area for three weeks in continous.We deployed near the island of Certosa in the San Nicolò channe at a depth of 4m a hydroacoustic buoy SM2M of the WildeLife Acoustics company, which recorded the ambient noise at the sampling frequency of 96 kHz. The maximum values of Averaged Noise Spectrum Level and Sound Pressure Level were in the frequency band between 500 Hz and 800 Hz corresponding to the underwater noise emitted by high-speed motor boats. For this frequency range, the average Sound Pressure Level was much higher than 110 dB re 1μPa^2. Recognition and quantification of noise events was carried out in the 1/3 octave frequency bands. In addition, wavelet analysis parameters of underwater noise were calculated as input data to the fuzzy logic clusters algorithm, which allowed for automatic detection of noise generated by ships and motor boats from underwater ambient noise.*

Keywords: *Anthropogenic underwater noise, Venice lagoon, nature conservation*

1. INTRODUCTION

Underwater noise levels of anthropogenic origin have been increasing in the seas and oceans since the end of the World War II [1]. It has a very negative impact on the life of marine organisms, disturbing their functioning and, in extreme cases, can lead to their death. Noise pollution is particularly noticeable in sea straits, along shipping routes as well as in areas with heavy traffic.

This problem is discussed in a number of important international documents, such as the Marine Strategy Framework Directive (MSFD). Monitoring projects have been developed to implement the recommendations of Descriptor 11 of the MSFD of the European Union.

The Lagoon of Venice (Fig.1) is an example of an area with a particularly high intensity of shipping traffic and a specific, limited shape of the maritime area. The lagoon with an area of 550 km^2 is located in the north-western part of the Adriatic Sea. It is very shallow with an average depth of approximately 1 m, but the deepest areas are more than 30 m deep [2]. Only 5% of the lagoon is deeper than 5 m while shallower areas, less than 2 m deep, cover about 75% of the lagoon. The lagoon consists of a complex system of navigation channels, tidal channels, intertidal mudflats and intertidal salt marshes [3]. The depth of the navigation channels ranges from 2 to 20 m.

Due to its structure, location and strong urbanisation, the lagoon is particularly vulnerable to the risks posed by the enormous intensity of boat and ship traffic [4]. The transport in the lagoon and the city of Venice is carried out by waterways, hence a large number of motor boats, water taxis, water busses (vaporettos) and speedboats travel along the navigational channels. In addition, cargo ships, ferries and cruise liners navigate the main channels. At the same time, Venice and its lagoon are a UNESCO World Cultural and Natural Heritage Site and requires particular efforts be protected from hazards.

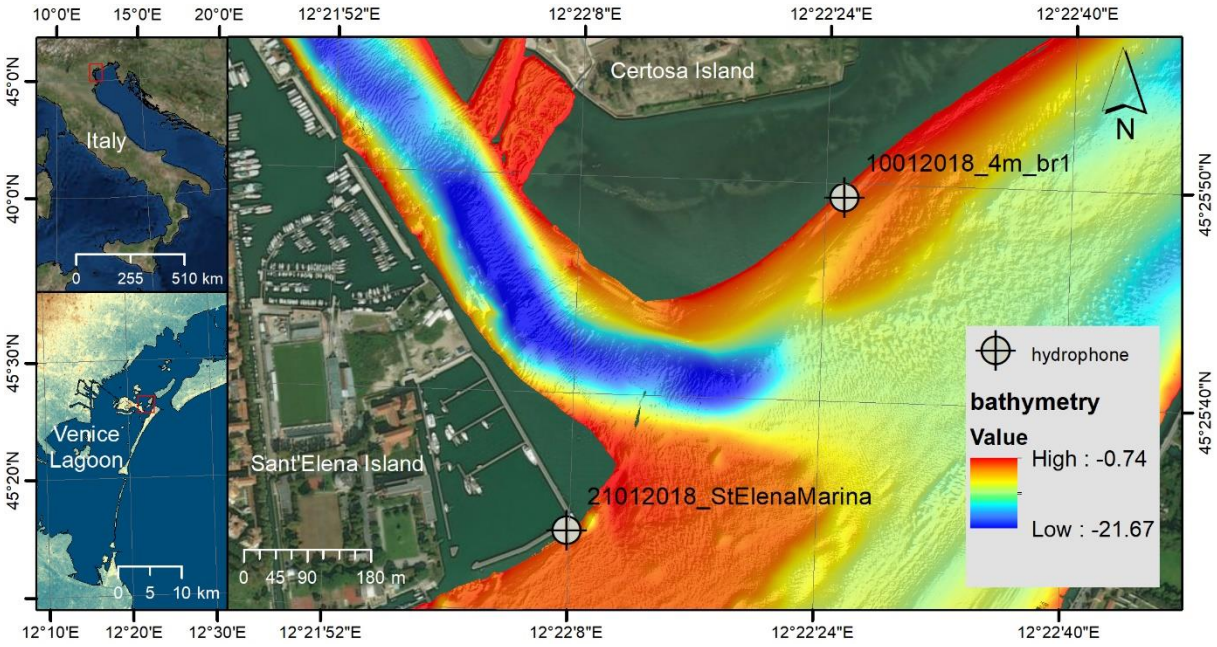


Fig.1: Fig.1: Map of the St. Nicola channel of the Venice Lagoon with localisation of hydroacoustic recorder deployment. Sources: Esri, DigitalGlobe, GeoEye, EarthStar Geographics, CNES/Airbus DS, USDA, USGS, AeroGRID, IGN, and the GIS User Community.

2. DATA ACQUISITION AND SIGNAL PROCESSING

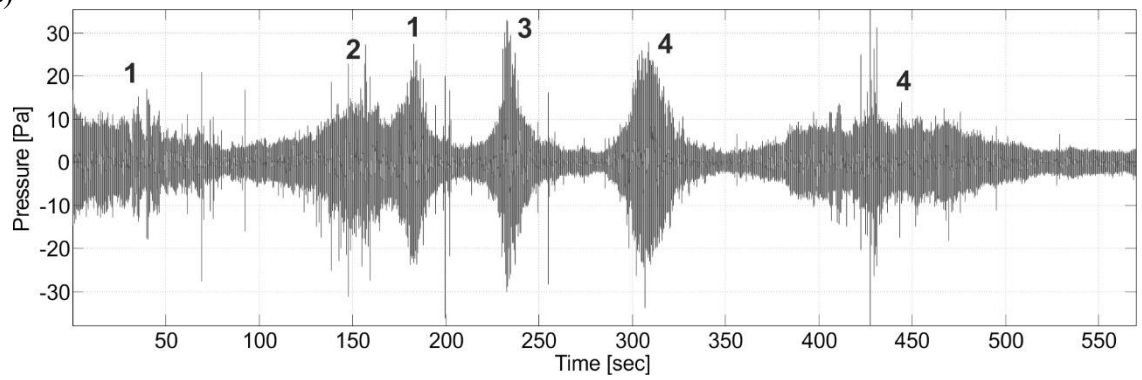
In 2018, we conducted a series of underwater noise measurements near the island of Certosa in the St. Nicola channel of the Venice Lagoon, placing a hydroacoustic buoy SM2M of the WildeLife Acoustics company at a depth of 4m (Fig.1). The hydrophone sensitivity was -165 dB re 1V/µPa and sampling rate of 96 kHz. Registration was conducted continuously in the periods from 19th to 30th of January and from 18th of July to 8th of August 2018.

Moreover, on January 21st, 2018, a HTI-96-Min hydrophone was immersed on the south east part of the Marina Santelena that lies on the island of Santa Elena opposite to the buoy deployment place. Underwater noise was recorded for one hour, synchronized with the video recording of passing vessels and motor boats to combine acoustic signatures with boat types that do not have the Automatic Identification System.

The Automatic Identification System (AIS) of vessel traffic information was used instead to identify bigger vessels traffic. However, it should be noted that most of the small motor boats and water trams operating in the lagoon are not equipped with AIS and could not be identified in this way.

The density of movement of vessels in the Venetian channels is very high, as evidenced by the exemplary and typical recording of underwater noise from the hydrophone submerged near Santa Elena place. During nine and a half minute registration, 6 vessels were observed, including 2 water busses, 1 motor boat, 1 speed boat and 2 water taxis (Fig.2.b)

a)



b)

1. water bus	2. motor boat	3.speed boat	4. water taxi

Fig.2: a) Example of 9 minutes and 30 seconds continuous underwater ambient noise registration at 21th of January 2018 at S. Elena location, b) Motor boat categories recorded during the measurement.

Figure 2.a) shows the changes in sound pressure at the recording location. Vessels sailed at different distances from the hydrophone and with different speeds, hence, similar vessels made noise at different sound pressure levels. Because of the high speed of some boats and their small distance to the acoustic logger, as well as the geometry of sound propagation, the level of hydroacoustic pressure was very high, reaching 30 Pa. Spectrograms of underwater noise were also calculated, showing that the underwater noise frequencies emitted by all boats observed in Figure 2 reached 48kHz. Recorded underwater sounds were filtered in 1/3 octave

in subsequent bands from 5 Hz to 40 kHz centre frequencies and sound pressure levels have been calculated for these bands.

For data collected in the San Nicolò channel, the following procedure of underwater noise classification and boats detection is proposed: for each registered 10 second signal portion sampled with 96 kHz, the 8 wavelet transformation parameters were computed. The continuous wavelet transformation of 10 second signal portions computed for the 7-channel dyadic decomposition (scale $a=2^j$, j=1,..,7) and 3rd-order Coiflet wavelet is the base for determination of wavelet energies:

$$E_{j,Coif3} = \int_0^{b_{max}} C^2(a,b)\mathrm{d}b, \tag{1}$$

where $C(a,b)$ are the wavelet transformation coefficients, $b_{\min}$ and $b_{\max}$ are boundary values of scale b (time). The additional wavelet transform parameter is the wavelet entropy h_{Coif3} defined as [5]:

$$h_{Coif3} = \sum_{j=1}^{7} E_{j,Coif3} \cdot \ln E_{j,Coif3}, \tag{2}$$

The above defined parameters formed 8-element vectors for each 10 second long part of the recorded signal. The vectors were the input to fuzzy c-means (FCM) segmentation procedure, which indicates main types of underwater noise registration as sounds coming from vessels, breaking surface waves and other underwater noise sources.

3. RESULTS

The averaged spectra of underwater noise recorded during measurements in the St. Nicola channel in winter and summer 2018 are shown in Figure 3. In the frequency range from 3 Hz to 48 kHz we observe differences in Noise Spectrum Levels between the two seasons.

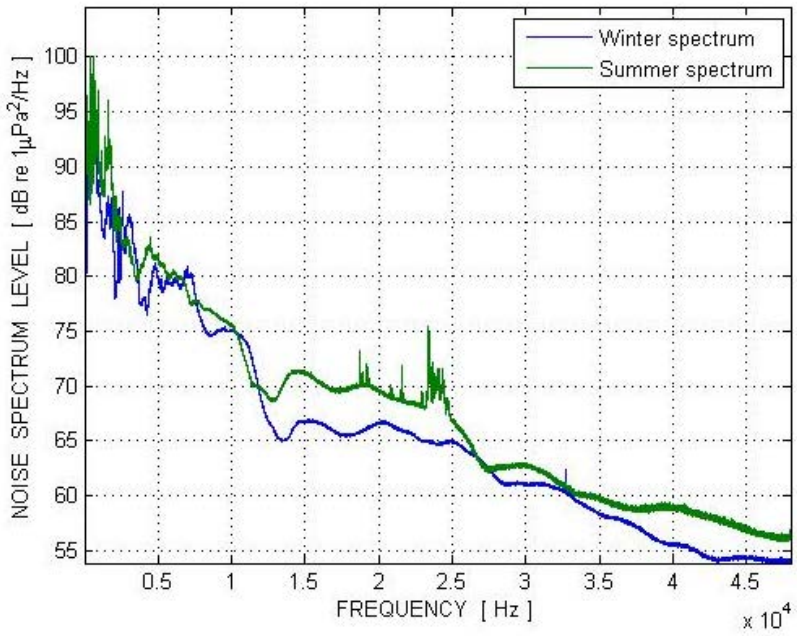


Fig.3: Underwater noise spectra recorded in winter and summer 2018 in the frequency range up to 48kHz.

For most of the analysed frequencies the level of underwater noise is much higher in summer than in winter. In the frequency range from about 18 kHz to about 25 kHz, jumps in the summer spectrum are visible, which can be caused by organisms living in the lagoon. Much more detailed picture of the spectra is shown in Figure 4, where the data from Figure 3 are shown for the range limited to 2 kHz. In this case we observe a high level of spectra for frequencies up to 200 Hz related to ship traffic. On the other hand, the higher spectral levels for the frequency range from 500 Hz to 800 Hz are demonstrably related to motor boats and water trams traffic.

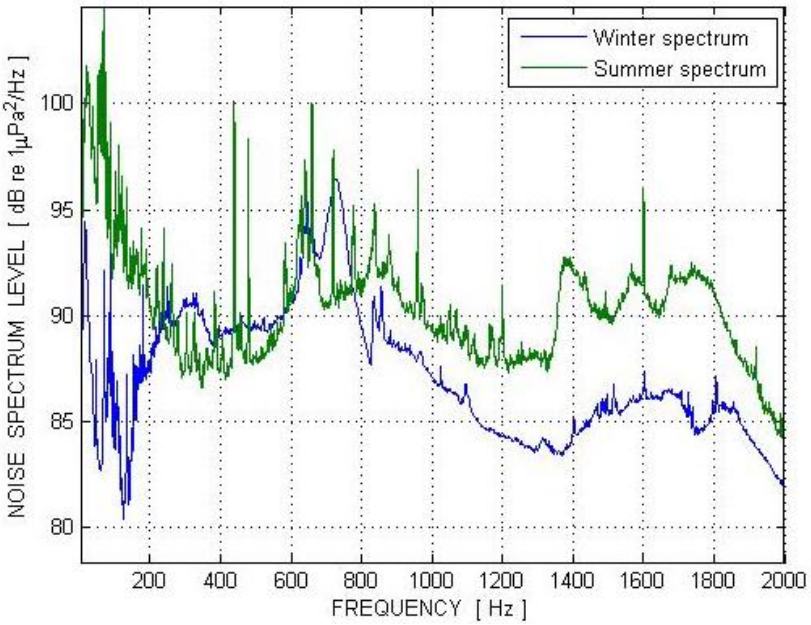


Fig.4: Underwater noise spectra recorded in winter and summer 2018 in the frequency range up to 2kHz.

Figure 5 shows averaged Sound Pressure Levels recorded in winter and summer 2018 in the 1/3 octave bands. The SPL measured in summer achieves a level exceeding 110 dB for the frequency range from a few Hz to approximately 125 Hz and excides 115 dB for 20 Hz to 80 Hz range. This is typical for the underwater noise generated by ships in motion. Also, for the frequency range around 800 Hz, the SPL exceeds 110 dB for both seasons.

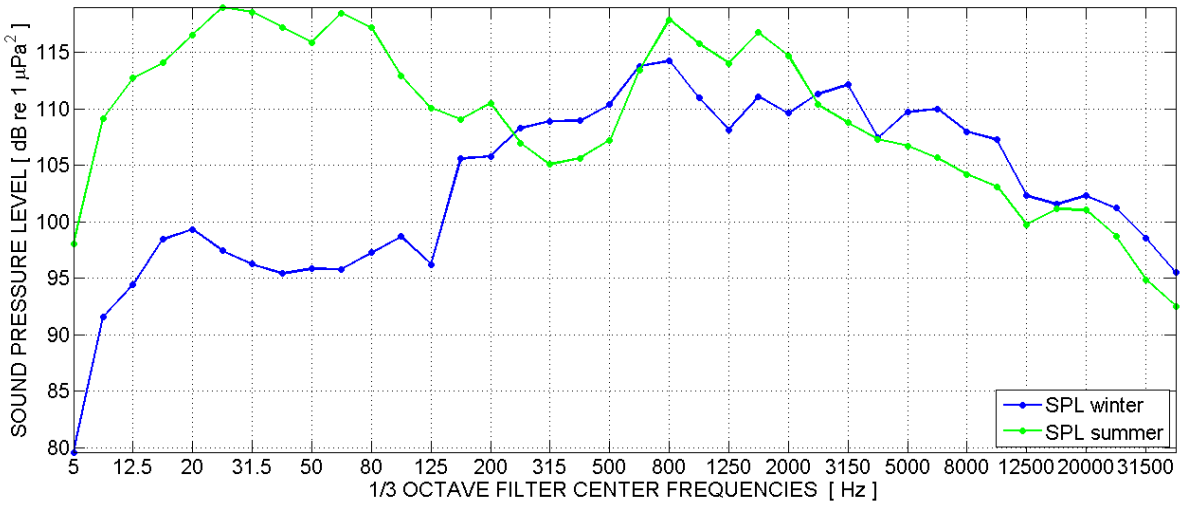


Fig.5: Sound Pressure Levels recorded in winter and summer 2018 in the 1/3 octave bands.

The noise classification result for the 24-hour noise record of January 20, 2018 is shown in Figure 6, which illustrates the spatial distribution of the values of wavelet energy $E_{5,Coif3}$ and wavelet entropy h_{coif3} with marked clusters corresponding to the noise generated by motor boats and ships. Each point in the graph shows a 10-second fragment of the noise signal, which was subject to wavelet analysis.

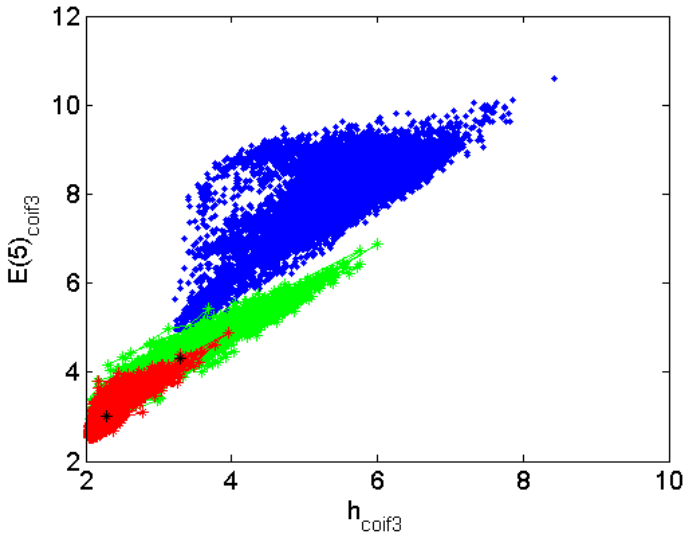


Fig.6: The spatial distribution of the values of wavelet energy $E_{5,coif3}$ and wavelet entropy h_{coif3} with marked clusters corresponding to the noise generated by motor boats - red dots, ships – green dots and other ambient noise – blue dots.

4. CONCLUSIONS

The preliminary results of underwater noise measurements in the Venice Lagoon channel indicate a large contribution to the anthropogenic noise field of motor boats often operating at high speed. A particularly high level of SPL was observed in the summer when boat traffic increases, noise exceeded 115 dB for frequency band of 500 Hz to 2000 Hz – high speed motor boats and from a 20 Hz to 80 Hz – ships. The underwater noise classification algorithm based on waveform transformation parameters as an input to the FCM procedure was also tested. The algorithm separated the noises coming from their main sources in the investigated channel.

The results presented here are preliminary to more extensive underwater noise research in the Venice lagoon, the knowledge of which is necessary for the proper protection of the environment against the acoustic pollution.

5. ACKNOWLEDGEMENTS

The authors would like to thank Giuliano Lorenzetti, Giorgia Manfé and Luca Zaggia for their help in the deployment and collection of the hydrophone. This work falls within the test activities preliminary to the Italy - Croatia Interreg Project SOUNDSCAPE started in January 2019.

REFERENCES

[1] **Bjørnø, L.** Man-made contributions to ambient noise in the seas. Alippi, A. and Cannelli, G.B. Proceedings of the Fourth European Conference on Underwater Acoustics 2, Rome, 543-548, 1998.

[2] **Umgiesser, G., Canu, D. M., Cucco, A. & Solidoro, C.**, A finite element model for the Venice Lagoon. Development, set up, calibration and validation. Journal of Marine Systems, Volume 51, pp. 123-145, 2004.

[3] **Molinaroli, E., Guerzoni S., Sarretta, A., Masiol M., Pistolato, M.** Thirty-year changes (1970-2000) in bathymetry and sediment texture recerded in the Lagoon of Venice sub-basins, Italy. Marine Geology, Volume 258, pp. 115-125, 2009.

[4] **Picciulin, M., Bolgan, M., Codarin A., Fiorin, R., Zucchetta, M., Malavasi, S.,** Passive acoustic monitoring of Sciaena umbra on rocky habitats in the Venetian littoral zone. Fisheries Research, Volume 145, pp. 76– 81, 2013.

[5] **Faghani, D., Sévrain A., Boisson H. C.**, Physical Eddy Recovery through Bi-Orthogonal Decomposition in an Acoustically Forced Plane Jet, Flow, Turbulence and Combustion, Volume 62, No. 1, pp. 69-88, 1999.

FEASIBILITY AND ACCURACY OF PREDICTION OF OCEAN NOISE ON A SHORT-TIME SCALE

Alexander Gavrilov[a], Robert McCauley[a], Zhi Yong Zhang[b]

[a] Centre for Marine Science & Technology, Curtin University, Perth, WA 6845, Australia
[b] Defence Science and Technology Group, Edinburgh, SA 5111, Australia

Alexander Gavrilov: a.gavrilov@curtin.edu.au

Abstract: *This study aims to examine the feasibility and accuracy of ocean ambient noise models to predict underwater noise spectra in a statistical way on a relatively short time scale from an hour to one day. The area around Perth Canyon west of Rottnest Island in Western Australia was chosen to verify a composite regional model of ocean noise. The model comprises components of physical origin, such as wind, sounds of great whales and fish choruses as biological components, and ship noise. Meteorological noise components are modelled using data from a weather station on Rottnest Island and models of wind driven underwater noise. Ship noise is modeled using Automatic Identification System data, including vessels' type, size, position and speed, typical acoustic signatures of a few most common ship types, such as tanker, cargo and passenger ships and some smaller vessels, and underwater sound transmission models. The regional model of noise from whale calls was built using data on seasonal variations in the presence of great whales in the area and spectra of their typical sounds. Fish noise and its diel and seasonal variations linked to the sunset and sunrise times were modelled using data of long-term underwater noise measurements made in the area. Modelling predictions were compared with ocean noise measurements conducted in this area for nearly 10 years within the Integrated Marine Observing System program. The comparison has demonstrated that the model is capable of predicting the 50% percentile spectrum levels of ocean noise in 1/3-octave bands within a few decibels on a daily basis.*

Keywords: *Ocean ambient noise, short time scale model, statistics of noise spectrum level*

1. INTRODUCTION

This modelling study aims to develop means for predict spectrum levels of ocean ambient noise in a statistical way on a relatively short-time scale from several hours to a few days, using (1) empirical models of wind and rain driven underwater noise, which assimilate meteorological data from the nearest weather station, weather forecasts or models, (2) models of seasonal and diel variations of noises from marine animals, e.g. fish and whales, typical for the area of interest and (3) a model of ship noise assimilating data from the Automated Information System (AIS) for marine traffic.

The area around Perth Canyon west of Rottnest Island was chosen to develop and validate the predictive model of ocean noise because (1) sea noise data have been collected in this area nearly continuously from 2009 as part of the Integrated Marine Observing System (IMOS, http://imos.org.au/facilities/nationalmooringnetwork/acousticobservatories/) and (2) meteorological data (wind speed and precipitation) are available from the Rottnest Island weather station, which is about 50 km away from the acoustic recording site (Fig. 1).

All sea noise recordings at the IMOS passive acoustic observation site (Fig. 1) were made using autonomous underwater sound recorders designed and built at the Centre for Marine Science and Technology (CMST), Curtin University, and set on the seafloor at a sea depth of about 430-450 m. The recorders were programmed to make 300 s to 500 s long recordings at a sampling frequency of 6 kHz repeated with 900 s intervals.

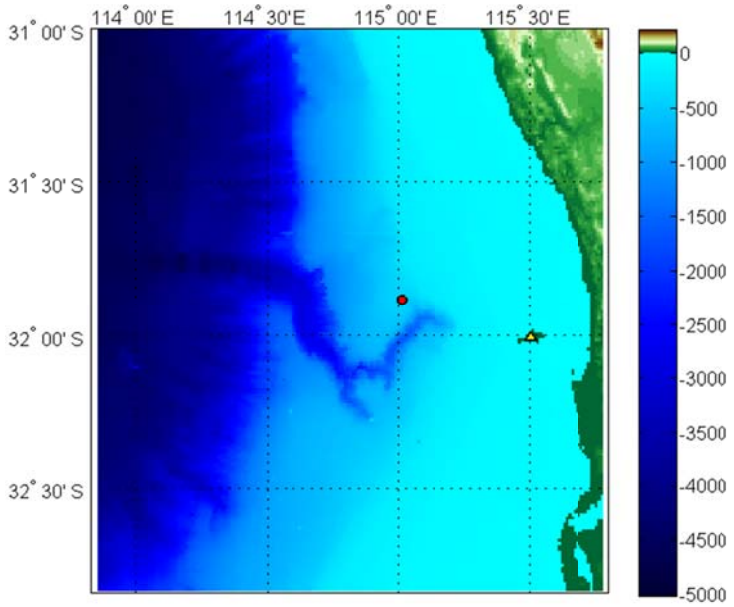


Fig. 1: Bathymetry around the Perth Canyon area. The red dot shows the location of the IMOS acoustic site and the yellow triangle indicates the location of the Rottnest Island weather station.

Section 2 of the paper presents a model of wind driven underwater noise. Underwater noise from rain was also modelled but not considered in this paper. Section 3 introduces models of noises of biological origin observed in the study area. In particular, the contribution of regular evening fish choruses and sounds from pygmy blue whales to the local underwater soundscape is modelled. The method to model underwater noise from vessels of various classes and speed cruising across the study area off Rottnest Island is considered in Section 4. Numerical predictions from a composite model of wind driven, biological and shipping underwater noises are compared with measurement data in Section 5.

2. WIND DRIVEN NOISE

The model of spectral levels of wind driven noise suggested by Doug Cato [1] was employed in the composite underwater noise prediction model. One IMOS dataset of underwater acoustic recording collected in 2016 was chosen to perform a more accurate analysis of the correlation between spectral levels of underwater noise and wind speed. The entire set was manually reviewed to localise time periods when sources of underwater noise other than wind and rain did not noticeably contribute to underwater noise spectra above 100 Hz. The Power Spectrum Density (PSD) levels of sea noise measured during those periods were selected for further analysis. As a result, the correlation coefficient of underwater noise level in a broad, 200 Hz – 3 kHz frequency band and wind speed has increased up to nearly 0.8 compared to approximately 0.55 obtained for all sea noise recordings in the dataset.

Then the selected noise spectra were clustered by the wind speed data measured at the same time at the weather station on Rottnest Island and falling within ranges of 5±2.5 knot (kt.), 10±2.5 kt., 20±2.5 kt. and 30±2.5 kt. As a result, approximately 2,000, 5,000 and 3,000 sea noise PSDs were found for the 5, 10 and 20-kt ranges respectively and about 400 for the 30-kt range. The mean 1/3-octave PSD levels and their standard deviation are shown for four wind speed ranges in the error-bar plot in the left panel of Fig. 2. As one can see, Cato's model accurately predicts the PSD levels at higher wind speeds of 20 to 30 kt. At lower wind speeds, the prediction is more or less accurate only above frequencies of about 100 Hz (10 kt.) and 200 Hz (5 kt.). Below those frequencies, the contribution of underwater noise of nondescript character, such as cumulative low-frequency noise from distant shipping and great whales, becomes significant compared to the wind driven noise.

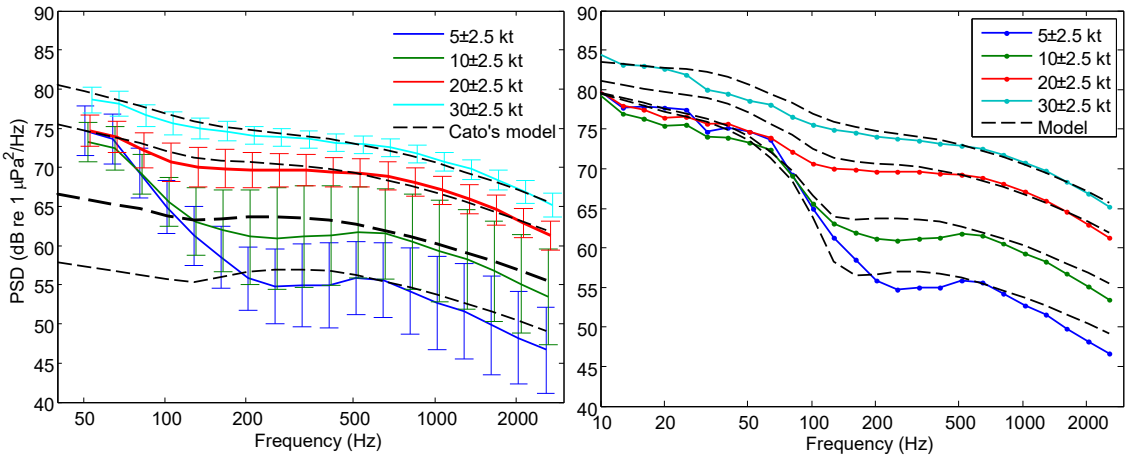


Fig. 2: (left panel) mean values and standard deviation of PSD levels of sea noise measured at the IMOS Perth Canyon site at four magnitude ranges of wind speed measured at the Rottnest Island weather station; (right panel) mean values of PSD levels and their predictions from the composite two-component model.

This nondescript low-frequency noise is persistent at any particular part of the ocean, although its spectral levels may gradually (seasonally and/or inter-annual) vary with time, e.g. due to changes in the ship traffic intensity. It is difficult to define the statistics of spectral levels of nondescript noise and its long-term changes in the nearly permanent presence of other sources of underwater noise. Therefore the spectrum level model of the nondescript noise was assumed to be such as it could approximate PSD of sea noise observed at lowest wind speeds. We assume that the resulting PSD of sea noise is:

$$S = S_B(f) + 10^{SL_C(f)/10}\,, \quad (1)$$

where $S_B(f)$ is PSD of the nondescript low-frequency noise and $SL_C(f)$ is the PSD level predicted by Cato's model for wind driven noise. A model of 1/3-octave spectrum level of nondescript noise was derived from the PSD of sea noise measured at the lowest wind speed.

The right panel of Fig. 2 demonstrates a comparison of the predictions from the model of spectrum level comprising nondescript and wind driven noise (10log(S) in Eq. 1) and the measured mean spectrum levels of sea noise in four different ranges of wind speed variation. The difference between the measured and modelled levels does not exceed 4 dB in any 1/3-octabe band. The composite two component noise model tends to overestimate the noise level below ~100 Hz at moderate wind speeds of about 20 kt., which is due to the contribution from the nondescript noise model.

3. NOISES OF BIOLOGICAL ORIGIN

Baleen whales of different species and fish are the major sources of underwater noise of biological origin observed in the Perth Canyon area. Toothed whales can also be found in this area, but their contribution to the local soundscape is minor.

Noticeable noise from fish sound is present in the ocean ambient noise in the study area only in the form of evening fish choruses which are produced by the same but as yet uncertain fish species in a frequency band of 2-3 kHz [2].

The baleen whales observed acoustically in the area are: pygmy blue whales (PBW) of the eastern Indian Ocean population, humpback whales, fin whales, Antarctic blue whales and an as yet unidentified whale producing the so-called "spot" call [3]. Noise from PBW sounds can be observed in sea noise data collected in this area from December to early July, dominating in ambient noise in a frequency band from about 17 Hz to 70 Hz from February to late-June. In the sea noise model presented in this report, only noise from PBW sounds is included, because it is most significant at low frequencies in the local underwater soundscape and lasts over a prolonged time period of more than six months.

It has been noticed that the start time of evening fish choruses is strongly linked to the sunset time. The start time of the fish chorus is around 1 hour after sunset (see Fig. 5 in [2]). The sound intensity of fish chorus varies slightly over time within each year, but the variation pattern is more or less consistent between different years, with the maximum intensity observed in May-June and the minimum intensity in September-October (Fig. 3). The duration of choruses and hence the variation of sound intensity within each chorus vary noticeably (see Fig. 8 [2]).

There are many factors that may affect the start time and duration of fish choruses, including the moon phase, which are considered in [2]. However, the yearly mean pattern of the variation of sound intensity during the chorus seems to be similar in different years (Fig. 3, right panel). This observation can be used in a simplified model of fish chorus noise present in the Perth Canyon area. The model suggested here is based on the following assumptions:

1) The chorus always starts 1 hour after sunset;
2) The pattern of sound intensity vs time in each chorus does not vary;
3) The intra-annual variation of chorus intensity is taken into consideration using monthly mean values measured in 2016.
4) The sound level and its variation are similar in two 1/3-octave bands with the central frequencies of about 2 kHz and 2.6 kHz.

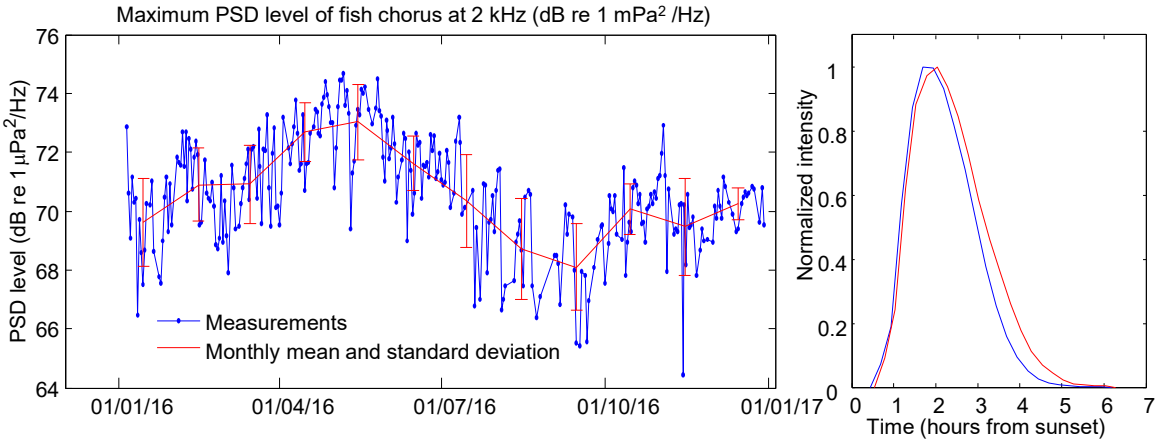


Fig. 3: (left panel) intra-annual variation of the PSD level of evening fish choruses in a 1/3-octave band around 2 kHz observed in 2016.The blue line and dots show daily mean levels and the red line and error bars show the monthly mean and standard deviation respectively. Correction for background noise was made using sea noise intensity measured in the same frequency bands right before each chorus; (right panel) normalised envelope of fish chorus intensity vs time since sunset averaged over sea noise recordings made in 2014 (blue) and 2016 (red).

PBWs produce stereotypic sounds in a series of themes forming a long lasting song [4]. Each theme may consist of three or two so-called units (or individual sounds). Unit 2 is always present in a theme. A theme consisting of only unit 2 was recently observed in PBWs songs, but it is relatively rare. The power density spectrum of units 2 and 3 is representative of all three units in 1/3-octave bands. This spectrum was chosen as a reference one for further modelling of PBW noise. The model of PBW noise and its variation over time is built using the following approach:

1) PBW calls were detected using an automatic detector of unit 2 [5] during the entire year of 2016. In addition to logging the detection time, the detector also measures the received RMS pressure of sound in each detected unit 2;
2) Assuming the relationship between the sound intensity of units 2 and 3 in each detected call to be similar to calls of different intensity of unit 2 received at different ranges from vocalising whales, the *PSD* of each detected call (n) was calculated using the following formula:

   $$PSD(n) = PSD_{ref} \cdot [P(n)/P_{ref}]^2,$$

   where PSD_{ref} is the PSD of the reference signal in linear units (µPa^2/Hz), $P(n)$ is the RMS pressure of detected call n and P_{ref} is the RMS pressure of unit 2 in the reference signal;
3) An average $\langle PSD(n) \rangle$ was calculated for each calendar day in 2016.

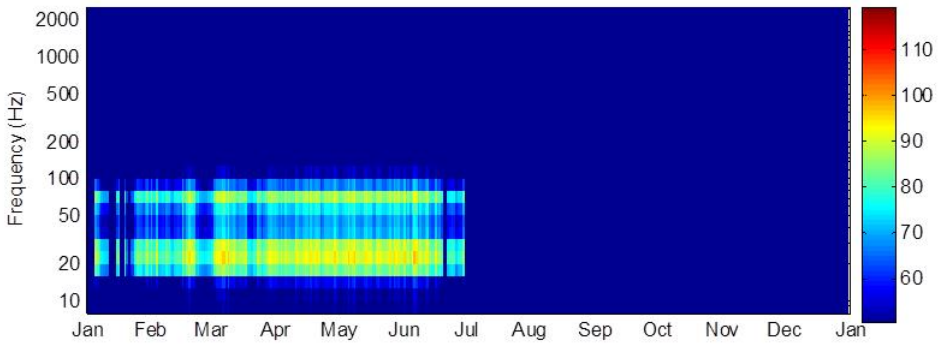


Fig. 4: Daily average 1/3- octave PSD levels of PBW sound in 2016, used as a PBW noise model for sea noise prediction.

The resulting model is shown in Fig. 4. It is important to notice that the model does not imply any contribution of PBW sounds to ocean ambient noise in December. This took place because no true detections of PBW sounds were made in December 2016; however, some datasets collected in the previous years showed the presence of PBW in the study area in December and even in late November.

4. SHIP NOISE

In the model presented here, ship noise and its spectra are predicted using the following approach:

1) AIS data for marine traffic in the Perth offshore area were acquired for a time period from August 2012 to October 2016. There were more than 110,000 records representing more than 9,000 different vessels found within a 50 km radius from the acoustic observation location.
2) The presence and intensity of ship noise in ocean noise data were associated with the presence of vessels in the AIS dataset. For selected ship passages, when noise from a single vessel dominated in a sea noise recording, the PSD of ship noise received at different ranges was calculated and corrected for the PSD of background noise measured in the absence of ships within the search area. The vessel ID (MMSI), type, length and speed were associated with the measured PSD. A total of 110 passages of ships at distances from about 1 km to 15 km were selected representing 95 different vessels: cargo ships of different length, including vehicle carriers; tanker ships of different length; passenger ships; various tugs; and search and rescue (SAR) vessels.
3) Sound transmission loss was numerically modelled in 1/3-octave frequency bands from 8 Hz to 2.6 kHz (central frequency). The modelling was carried out using a parabolic equation (PE) solution implemented in RAMGeo (http://cmst.curtin.edu.au/products/underwater/) with 8 Padé coefficients applied to more accurately model the transmission loss at short distances. The vertical sound speed profiles in the water column were calculated using the World Ocean Atlas 2013 yearly mean climatology data of water temperature and salinity (https://www.nodc.noaa.gov/OC5/woa13/). The seafloor was modelled as medium grain sand with the sound speed of 1770 m/s, density of 1850 kg/m^3 and attenuation of 0.47 dB/λ. The sound receiver was placed on the seafloor (sea depth of 436 m), as in the measurements. The sound source was placed at 5 m below the sea surface, which is a typical mean source depth for modelling sound emission from larger vessels. The sound propagation environment was assumed to be range and azimuth independent for simplicity.
4) The sound source PSD was calculated for each of 95 vessels selected in (2), using the PSD of received noise signals and the modelled transmission losses. Some ships had a number of sound source PSDs corresponding to different passages with different cruising speeds.
5) The ship noise prediction model firstly searches for vessels with the same type and similar length as those in the catalogue of 95 vessels with the estimated source PSD within the observation time period and the search radius of 25 km. If a vessel of the same type, similar length and speed is found, then its source PSD is used for forward sound transmission modelling and prediction of the received PSD of ship noise. If it is not present within the search time and distance frames, then a vessel of similar length and speed is chosen from the catalogue to carry out the forward sound transmission modelling using the AIS data on vessel's location.

5. COMPOSITE MODEL: COMPARISON WITH MEASUREMENT DATA

The composite model incorporates all modelled components in the same way as formulated in Eq. 1:

$$SL = 10log\left[SL_B(f) + 10^{SL_C(f,t)/10} + 10^{SL_R(f,t)/10} + 10^{SL_F(f,t)/10} + 10^{SL_{PBW}(f,t)/10} + 10^{SL_S(f,t)/10}\right]$$

where $SL_F(f,t)$ is the PSD level of fish chorus, $SL_{PBW}(f,t)$ is the PSD level of PBW noise and $SL_F(f,t)$ is the PSD level of ship noise predicted versus frequency f and time t.

An example of the composite noise model predictions compared to measurement results is shown in Fig. 5.

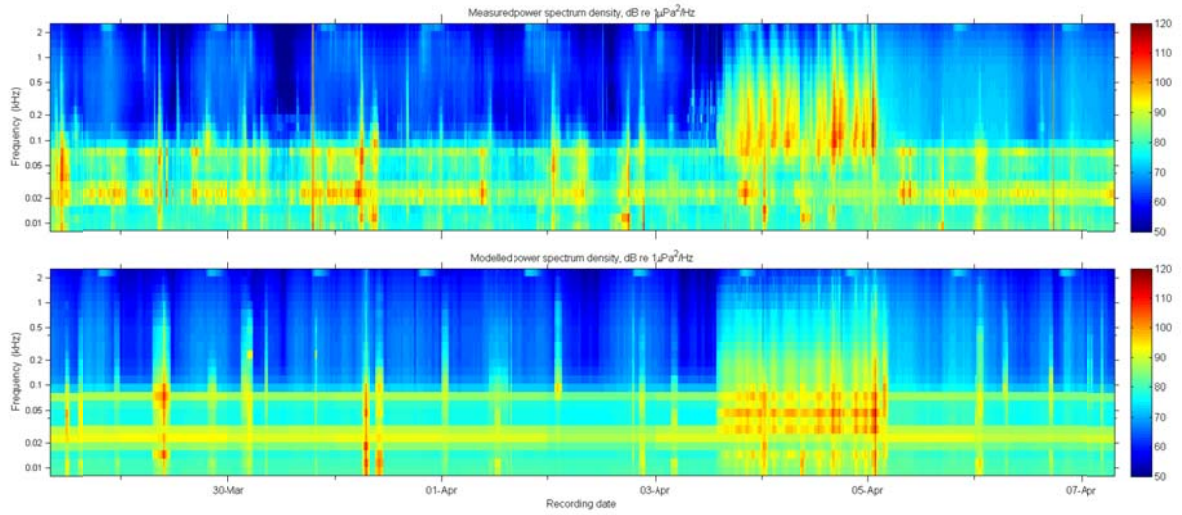


Fig. 5: Measured (top) and modelled (bottom) long-time (5 min) average spectrograms of sea noise in a 10-day period in March-April 2016

The agreement of the noise spectrum levels and their variation over time is reasonably good in general, except for minor discrepancies. For example, the spectra of the long lasting ship noise from the slowly moving vessels seen in Fig. 5 are somewhat different in the measured and modelled results. This is due to the use of another vessel of similar class and length in the model, which might have a different source spectrum. Also the model does not predict time periods of high intensity noise from PBW calls. This takes place because the PBW noise is modelled on a daily mean basis, so that any short-term presence of intense PBW sounds results in PBW noise of longer duration but lower intensity in the model.

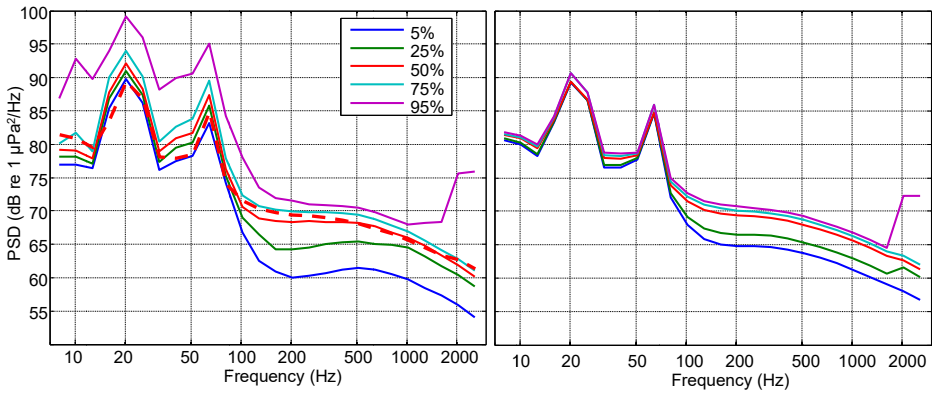


Fig. 6: Measured (left) and modelled (right) PSD levels of sea noise at five different percentile values for a 1-day time period in May 2014. The median values (50%) of the measured (solid red) and modelled (dashed red) PSD levels are compared in the left panel.

PSD levels of sea noise of different percentile values measured and modelled for one day in May 2014 are compared in Fig. 6. The median (50%) spectrum levels in measurement and modelling results differ from each other by less than 2 dB. At the highest percentile value of 95%, the difference is noticeably larger at frequencies below 100 Hz. This is because the model is based on daily average noise levels from PBW calls, whereas some measurements made every 15 min contained sounds of high intensity from calls produced by PBWs located nearby.

6. CONCLUSIONS

The composite model of underwater noise and its spectra developed for the Perth Canyon area west of Rottnest Island in Western Australia and presented in this paper includes noises generated by wind, fish choruses, blue whale sounds and noise from ship traffic. It demonstrates reasonably accurate predictions of spectral levels of sea noise in a frequency band from 8 Hz to 3 kHz, especially for a median percentile value of 50%. However, it requires further, more comprehensive testing using some other data sets of sea noise measurements in the study area to make more confident conclusions with respect to model performance.

Underwater noise from humpback whale songs needs to be included in the next generation of the model, as it contributes considerably into the local soundscape at frequencies from about 50 Hz to 700-800 Hz from mid-June to mid-October. This is the main challenge for the further development of the model, as the approach applied to the sounds from pygmy blue whales is not suitable for the noise from humpback whale songs. In contrast to the PBW calls, the sounds produced in humpback whale songs are much less stereotypic and, moreover, vary considerably over years. Hence, it is very difficult (and likely impossible) to suggest a universal automatic detector of humpback whale sounds.

7. ACKNOWLEDGEMENTS

The authors acknowledge the financial support of the Maritime Division of the Defence Science and Technology Group.

REFERENCE

[1] Cato, D.H., “Ambient sea noise in Australian waters”, in *Proceedings of the 5th International Congress on Sound and Vibration, International Institute of Acoustics and Vibration*, p. 2813 (1997).

[2] McCauley, R.D., Cato, D.H. “Evening choruses in the Perth Canyon and their potential link with Myctophidae fishes”, *J. Acoust. Soc. Am*. 130(6), pp. 3651-3660 (2016).

[3] Ward, R., Gavrilov, A.N. and McCauley, R.D., “Spot” call: A common sound from an unidentified great whale in Australian temperate waters”, *J. Acoust. Soc. Am.* 142(2), EL 231-236 (2017).

[4] Gavrilov A., McCauley R. Salgado-Kent C., Tripovich J., and Burton C., “Vocal characteristics of pygmy blue whales and their change over time”, *J. Acoust. Soc. Am*. 130(6), pp. 3651-3660 (2011).

[5] Gavrilov A.N. and McCauley R.D., “Acoustic detection and long-term monitoring of pygmy blue whales over the continental slope in southwest Australia”, *J. Acoust. Soc. Am*. 134(3), 2505-2513 (2013).

UNDERWATER ACOUSTIC RADIATION FROM PARTIALLY IMMERSED CYLINDRICAL SHELLS

Daher Diab, Fernand Leon, Farid Chati, Simon Marcellin, Dominique Décultot

Laboratoire Ondes et Milieux Complexes, LOMC UMR CNRS 6294, Normandie Université, Université Le Havre, 75 rue Bellot, 76600, Le Havre, France

Email: daher.diab@univ-lehavre.fr

Abstract: *The purpose of this work is to study the underwater acoustic radiation from a set of partially immersed cylindrical shells in water. First, the vibratory behavior of a stainless steel tube subject to an axial excitation on its emerged section is studied, numerically and experimentally; in the frequency range 20 kHz - 150 kHz. The identification of waves propagating along this tube is realized from a 2D finite element model developed using COMSOL Multiphysics code. The identified waves are the antisymmetric Lamb wave (A_0), the symmetric Lamb wave (S_0) and the Scholte Stoneley wave (A). A good agreement between numerical and experimental results is observed.*

The second part of this paper deals with the sound pressure radiated in water by partially immersed tubes. Two geometric configurations are studied: one tube or two tubes subject to axial excitation on the emerged tube section. In each case, a 3D finite element model is developed and implemented using COMSOL Multiphysics code. These ones enable us to determine the acoustic pressure (resonance spectra) radiated in water from each configuration in an azimuthal plane. In order to validate the numerical model, measurements have been realized in a large tank filled with water for the two distinct geometric configurations. The considered frequency band is between 10 kHz and 120 kHz. The resonance spectra show a good agreement between the numerical and experimental results.

Keywords: *Underwater acoustic radiation, partially immersed tubes, waves propagating in tube, finite element model, experimental measurements*

1. INTRODUCTION

The assessment of sound pressure generated by submerged structures is part of problems regarding underwater noise pollution. The growing number of offshore constructions related to energy generation by wind farms and the regulations on underwater noise pollution increase the importance of these studies [1-4]. Therefore, it becomes important to understand the physical mechanisms responsible for the radiation of a set of wind turbines towers. The object of this first work is the study of underwater acoustic radiation of vibrations of two tubes. This paper focuses on the acoustic radiation of two tubes of 38 mm in diameter. Experimentally, these tubes are immersed vertically in a large water tank (6mx4mx3m). The vibrations are emitted from a contact transducer generating a longitudinal wave on the emerged extremity of each tube. The studied frequency band is between 10 kHz and 120 kHz.

The acoustic radiation of a submerged structure is an important research field of underwater acoustic engineering. The study of the acoustic scattering by a single cylinder or tube excited perpendicular to its axis has been subject of theoretical [5-6] and experimental [7-8] works. The object of the present work is the study of underwater acoustic radiation from partially immersed tubes subject to an axial excitation.

2. IDENTIFICATION OF VIBRATION MODES

Beforehand, we identify the different wave types generated along one tube subject to an axial excitation. The stainless steel tube has the following geometrical and mechanical characteristics: 3 m of length, outer and inner radii of 19 mm and 17.5 mm respectively, density of 8027 kg/m^3, 212 GPa of Young's modulus, Poisson coefficient of 0.28, velocities of the longitudinal and transversal waves of 5823 m/s and 3210 m/s respectively.

2.1. Radial displacements of the tube

A 2D axisymmetric finite element model is developed using COMSOL Multiphysics code. This model allows to determine the radial displacements along the tube which is placed in air and then in water (Fig. 1).

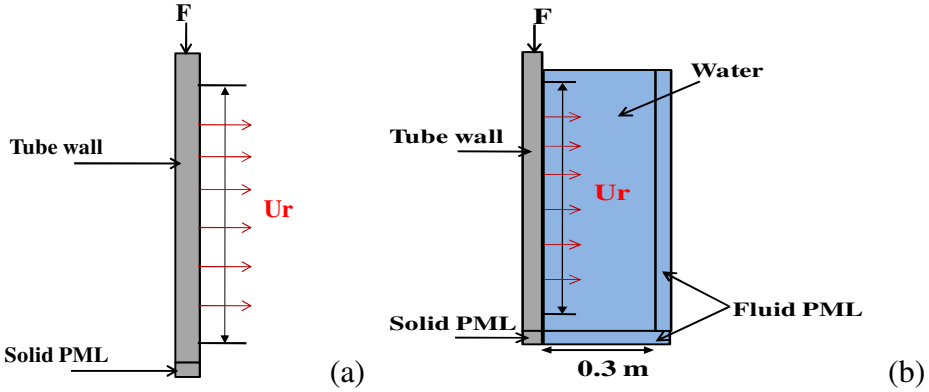


Fig.1: 2D axisymmetric model for the tube: (a) in air and (b) in water

A tube of length 1 m is used, and excited by a force F perpendicular to its top edge section. A Perfecty Matched Layer (PML) is defined to eliminate the reflected echoes from the end of the tube and the water boundaries. Studies are achieved in frequency domain between 20 kHz and 150 kHz and the radial displacement along the tube (0.6 m) is computed and recorded

with a space step of 0.2 mm. Then, a 1D spatial Fourier transform is applied on the radial displacement in order to plot the wave vector k versus frequency (Fig. 2) [9].

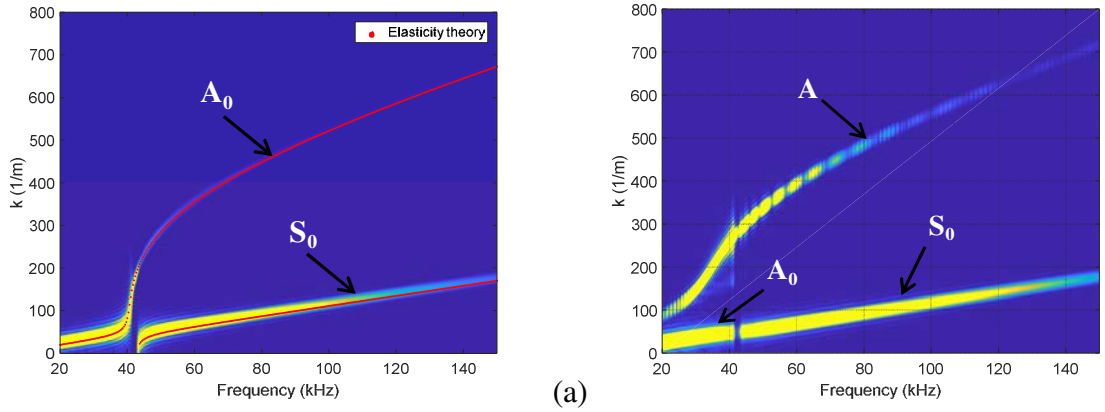


Fig. 2: Wave number dispersion curves of the tube: (a) in air and (b) in water

Fig. 2a shows the two waves generated in air denoted S_0 and A_0 which correspond to the fundamental mode (n = 0). S_0 is a compression wave named symmetric Lamb wave that appears at the ring frequency (45 kHz). At high frequency, its phase velocity tends to the plate velocity (5356 m/s). A_0 is a flexural wave named antisymmetric Lamb wave. At low frequency, the A_0 wave phase velocity tends to the bar velocity (5139 m/s), and tends to the Rayleigh wave velocity (2890 m/s) in higher frequency. These results are validated by analytical results from the theory of elasticity (red curve); a good agreement is obtained between the two cases.

When the cylindrical is immersed in water, the phase velocity of the flexural wave is modified and a new wave appears, the A wave or Scholte Stoneley wave (Fig. 2b). This wave radiates a weak energy in water and its phase velocity tends to the sound velocity in water.

2.2. Acoustic pressure radiated in water

From the 2D finite element model already presented, the sound pressure is determined vertically in the water along the tube length (0.4 m) (Fig 3a). Then, the numerical vibration modes radiating in water are determined by a 2D spatial Fourier transform applied on the pressure. For the experimental set-up (Fig 3b), the stainless steel tube is partially immersed in a large tank filled with water (6mx4mx3m) and excited by a fixed transducer (emitter) on the top edge section. An impulse measurement method is used in this experimental study [10], the emitter emits a short pulse with a broadband frequency.

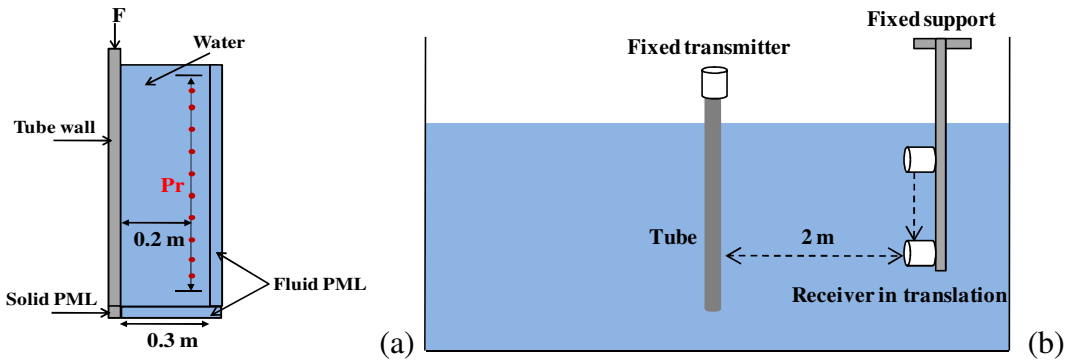


Fig. 3: Numerical model (a) and experimental set-up (b) of the acoustic pressure measurements

A second transducer achieves the measurement of the pressure radiated in water by the tube. These transducers are characterized by a central frequency of 100 kHz. The vertical displacement of the receiver enables us to record the time signals of the pressure radiated along the tube with a step of 1 mm. Then, the waves radiated in water are identified via a 2D Fourier transform of these signals. The experiment results are presented in Fig.4b. A good agreement is noted between the experimental (b) and numerical (a) results; The S_0 and A_0 waves are observed while the A wave does not radiate in water.

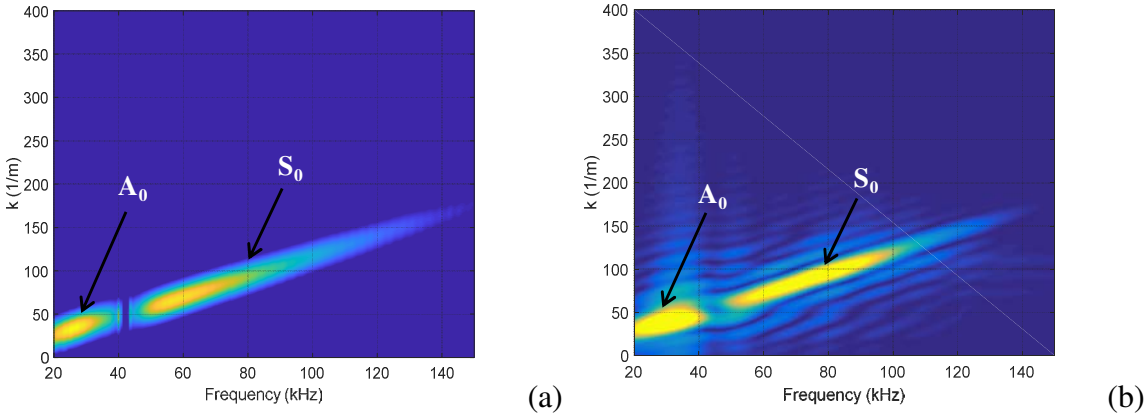


Fig. 4: Vibration modes radiating in water: (a) Numerical and (b) Experimental

3. RESONANCE SPECTRUM

3.1. One tube configuration

Fig. 5a shows the 3D geometry model of a partially immersed tube. This model is achieved using predefined multi-physics coupling for Acoustic-Solid Interaction in the case of a transient analysis. Fluid medium is defined by a water tube of radius 0.2 m and a length 0.5 m. A solid Perfectly Matched Layer having 10 mm of thickness is placed at the low extremity of the tube (tube length of 0.6 m). In this transient study, the fluid PML is not applicable. A mesh size of λ/4 is used on the tube and λ/3 in water for a frequency of 50 kHz. Then, a very short axial impulse force (F) is applied perpendicular to the total emerged tube section. The experimental set-up (Fig. 5b) is the one presented in §2.2; the immersion transducer rotates around the tube in an azimuthal plane perpendicular to the object axis.

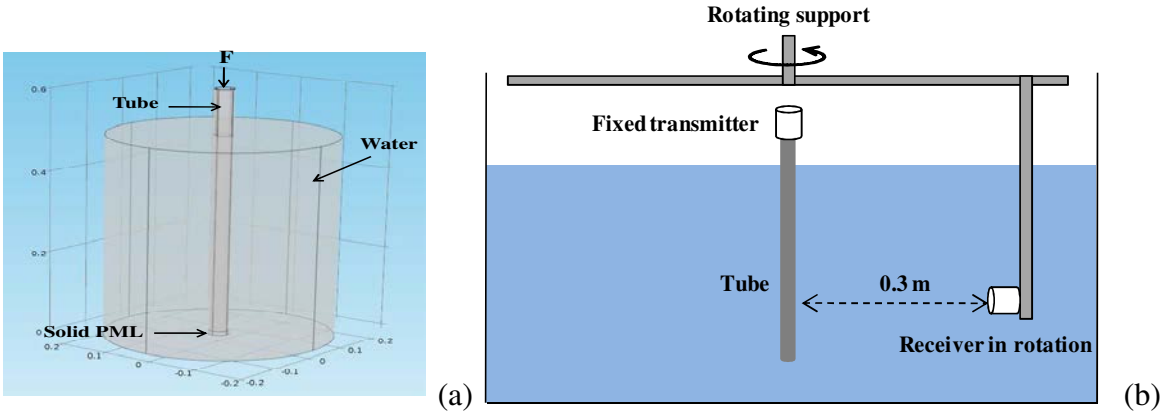


Fig. 5: 3D finite element model (a) and experimental set-up (b) of one tube configuration

Numerically and experimentally, the acoustic pressure has been calculated between 0 and 180° for an angular step of 1°. Then, the resonance spectra are obtained from a Fourier

transform of each time signal recorded at a given azimuthal angle. The high amplitudes appear in the form of two broad and yellow lines in Fig. 6a. The first around 20 kHz corresponds to an A_0 mode wave and the second around 60 kHz is a S_0 mode wave. At these frequencies, the magnitude varies few according to the angle; this is a breathing mode of the tube (n = 0). The experimental spectrum (Fig. 6b) shows a good agreement with the numerical results. The experimental characteristic frequencies are 25 kHz and 65 kHz. This agreement validates our 3D finite element model.

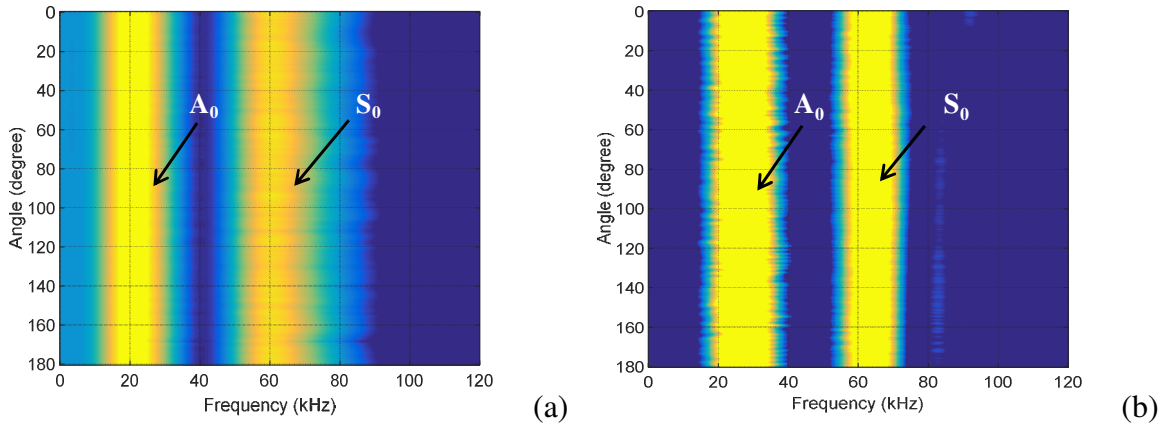


Fig. 6: Resonance spectrum of one tube configuration: (a) Numerical and (b) Experimental

3.2. Two tubes configuration

In the numerical model, the axes of these tubes are displaced forward and backward respectively by 2a relative to the central axis of rotation (Fig.7a). In this case, the distance between the axis of the tubes is d = 4a (a is the outer radius of the tube). A very short axial impulse F on the emerged tube sections excites these tubes. Experimentally (Fig.7b), a transducer excites the upper section of each tube. The signal applied to these transducers is identical.

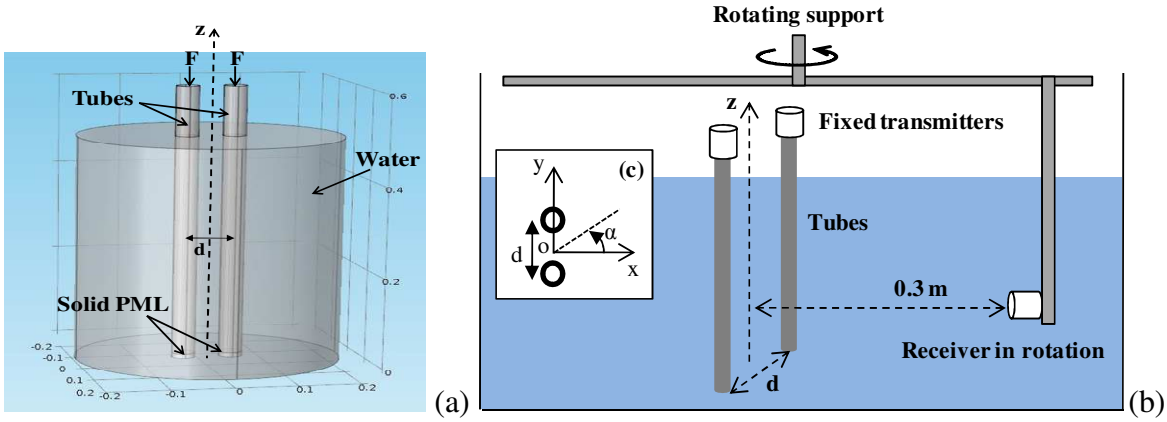


Fig. 7: 3D finite element model (a) and experimental set-up (b) of two tubes configuration, (c) Top view

A Fourier transform is applied on each time signal recorded at a given azimuthal angle α. The set of resonance spectra is assembled to obtain the figure 8. On Fig. 8a, the resonance frequencies are always around 20 kHz and 60 kHz by comparison with the one tube configuration (Fig. 6a). Nevertheless, regular spots appear according to the observation angle of the receiving transducer. The experimental results (Fig.8b) validate this numerical model; the resonance spectra are in good agreement with the numerical spectra.

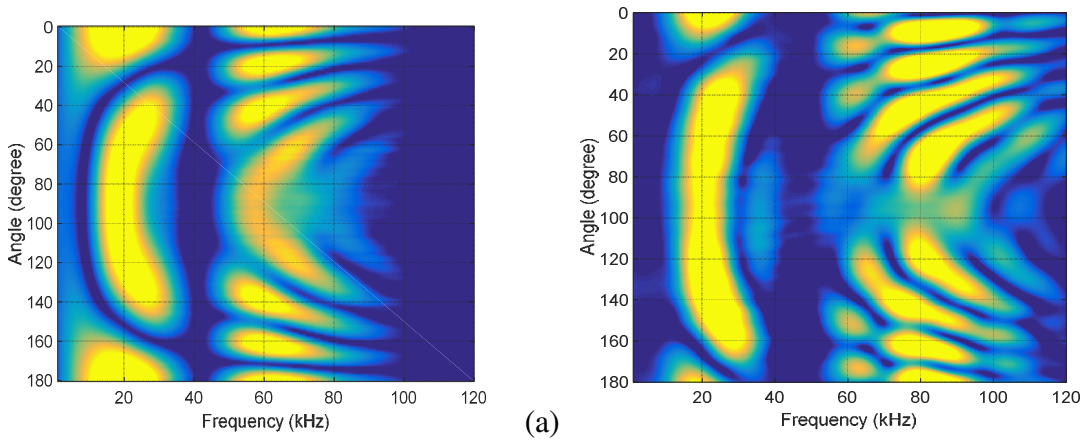


Fig. 8: Resonance spectrum of two tubes configuration: (a) Numerical and (b) Experimental

Fig. 9 shows the numerical resonance spectrum for three angles: 0°, 45° and 90°. As shown in Fig. 9b, at α = 0°, the two tubes configuration enables us to obtain a spectrum similar to that of one tube configuration (Fig. 9a). For this angle, the two tubes form two synchronous sources in phase. For α =45°, a doubling of resonance is obtained which is due to the path difference between the two radiated signals. Finally, at α = 90° we do not see the duplication of resonance. In this case, one tube is hidden by the other. The result is the spectrum of a single tube.

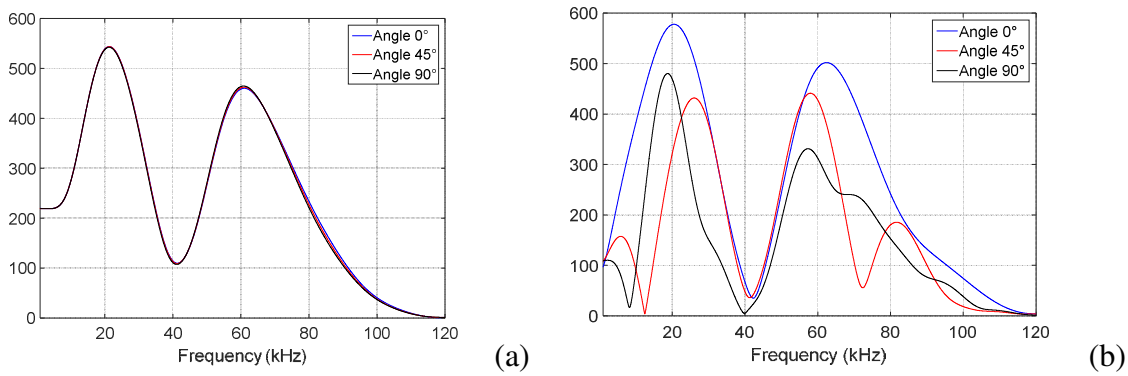


Fig. 9: Numerical resonance spectrum for three angles: one tube (a) and two tubes (b) configurations

4. CONCLUSION

In this work, firstly we presented a 2D finite element model and an experimental set-up used to identify the vibration modes of a stainless steel tube subject to an axial excitation. These studies are realized in air or in water. The identified waves are the antisymmetric Lamb wave (A_0), the symmetric Lamb wave (S_0) and the Scholte Stoneley wave (A).

Secondly, the acoustic pressure radiated in water by partially immersed tubes has been studied using two geometric configurations: one tube and two tubes. A 3D finite element model of partially submerged cylindrical shells is built for each configuration to predict the radiated sound pressure. Then, these numerical models are validated by measurements using two distinct geometric configurations. The resonance spectra show a good agreement between the numerical and experimental results.

5. ACKNOWLEDGEMENTS

This work is supported by Région Normandie.

REFERENCES

[1] **K. Betke, M. Schultz-von Glhan and R. Matuscheck**, "Underwater noise emissions from offshore wind turbines", *in CFA/DGA'04,* Strasbourg, *France*, pp. 591–592, 2004.
[2] **T. Neumann, J. Gabriel, W.-J. Gerash, K.-H. Elmer, M. Schultz-von Glhan and K. Betke**, "Standards for the assessment of acoustic emissions of offshore wind farms", *DEWI Mag.* 26, pp. 49–53, 2005.
[3] **C.A.F. De Jong and M. A. Ainslie**, "Underwater radiated noise due to the pilling for the Q7 offshore wind park", *in Acoustic'08 Paris Conference*, pp. 118–122, 2008.
[4] **H. Moller and C. S. Pedrersen**, "Low-frequency noise from large wind turbines", J. *Acoust. Soc. Am.* 129, pp. 3727-3244, 2011.
[5] **J. D. Murphy, E. D. Breitenbach and H. Überall**, "Resonance scattering of acoustic waves from cylindrical shells", *J. Acoust. Soc. Am.* pp. 64, 677-683, 1978.
[6] **J. W. Dickey and H. Überall**, "Acoustic high frequency scattering by elastic cylinders", *J. Acoust. Soc. Am.* 66, pp. 275-283, 1979.
[7] **W. G. Neubauer and L. R. Dragonette**, "Observation of waves radiated from circular cylinders caused by an incident pulse", *J. Acoust. Soc. Am.* 48, pp. 1135-1149, 1970.
[8] **F. Leon, F. Lecroq, D. Decultot and G. Maze**, "Scattering of an obliquely incident acoustic wave by an infinite hollow cylindrical shell", *J. Acoust. Soc. Am.* 91, pp. 1388, 1992.
[9] **F. Chati, F. Leon, M. El Moussaoui, A. Klauson and G. Maze**, "Longitudinal mode L(0,4) used for the determination of the deposit width on the wall of a pipe", *NDT&E International*, vol. 44 (2), p188-194, 2011.
[10] **P. Pareige, P. Rembert, J. L. Izbicki, G. Maze and J. Ripoche**, "Méthode impulsionnelle numérisée (MIN) pour l'isolement et l'identification des résonances de tubes immergées", *Phys. Lett. A*, vol. 135, p. 143‑146, 1988.

STRONG VARIATIONS OF THE ACOUSTIC NOISE SPECTRA ACCOMPANYING INTERNAL WAVE SOLITONS

Boris Katsnelson[a], Oleg A. Godin[b], Qianchu Zhang[a]

[a] L. Charney School of Marine Sciences, University of Haifa, Israel, 3498838 Haifa,
[b] Naval Postgraduate School, Monterey, CA, United States

Contact author: Oleg A. Godin, Physics Department, Naval Postgraduate School, 833 Dyer Road, Bldg. 232, Monterey, CA 93943, USA. Fax: 831-656-2834. Email: oagodin@nps.edu.

Abstract: *This paper investigates the nature of rapid, strong (20–40 dB), broadband variations of the acoustic noise intensity that were observed with moored hydrophones in the Shallow Water 2006 experiment. The experiment took place on the Atlantic shelf off New Jersey (USA) in an area with high levels of internal gravity wave activity. In particular, approximately twice a day trains of tidally generated nonlinear internal gravity waves (NLIW) propagated in the general upslope direction through the area, where a number of single hydrophone units (SHRUs), an L-shaped hydrophone array SHARK, and a number of thermistor chains were moored. Each NLIW train consisted of up to ten separate soliton-like features with peak isothermal displacement of 10–15 m. The thermistors provided 4-D sampling of the ocean variability, which allowed us to estimate the wavefronts, shape, and evolution of propagating NLIW trains and model NLIW activity at the hydrophone locations. For a number of NLIW events and for various hydrophones, we find a strong correlation between noise intensity spikes recorded by a hydrophone and NLIW-induced thermocline displacement at the hydrophone position. Noise intensity spikes tend to occur when the near-bottom current velocity is at maximum. Various possible physical mechanisms of the noise intermittency have been analyzed. Sediment saltation is identified as the most likely cause of the observed variations in the noise spectra.*

Keywords: *Nonlinear internal waves, noise, shallow water acoustics*

1. INTRODUCTION

Large-scale multi-institutional experiment Shallow Water 2006 (SW06) was carried out from June to September of 2006 on Atlantic shelf off the US East Coast [1]. It included a set of oceanographic equipment (thermistor strings, ADCPs, etc) and acoustic source and receiving systems. The area of experiment (New Jersey Atlantic shelf) is characterized by remarkable activity of internal waves. In particular, approximately twice per day trains of nonlinear internal waves (NLIW) consisting of up to ten separate peaks with the amplitudes of about 10–15 m and wave front parallel to the coastal line move toward the beach. During their motion trains of NLIW cross positions of five SHRUs, and L-shaped array (with horizontal and vertical parts, also referred to as HVLA), located about 5–8 km from each other along the line perpendicular to the coast as well as thermistor strings (Fig.1). The latter allow us to estimate the shape and evolution of trains while they are propagating. Using thermistor strings it is possible to find positions of wave fronts of NLIW during their propagation. The goal of this paper is to study the acoustic noise recorded by the SHRUs and HVLA in the presence and in the absence of NLIW

For this purpose, we studied the noise recorded during 5 events of NLIW propagation (on 17, 18, 19, and 22 of August 2006). All these trains were moving approximately toward the coast and contained a few separate peaks (solitons). As a representative example, events let's consider the event, which occurred on August 19. The corresponding diagram is shown in Fig.2.

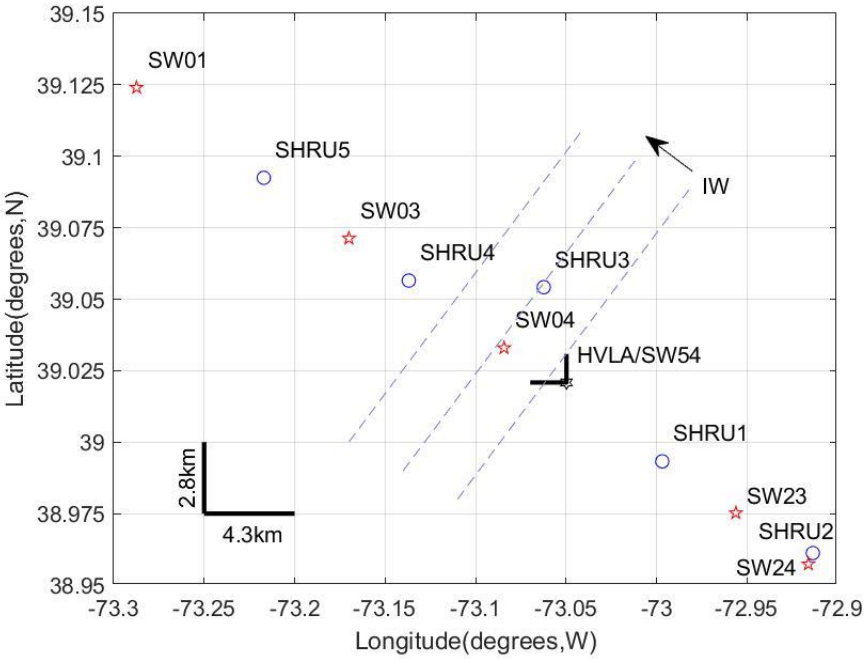


Fig.1. Layout of Shallow Water 2006 experiment

2. RESULTS AND DISCUSSION

In the Fig.3 the event of August 19 is shown in detail. Vertical axis corresponds to the line along positions of hydrophones, where locations of SHRUs and thermistor strings, (denoted as SW23, SW24, SW54, SW04, SW03 and SW01) are shown. Its total length between SW01 and SW24 is ~37 km. Horizontal axis is time, beginning approximately from moment of NLIW formation up to getting out of this train: since 6:00 till 21:00 GMT of 19 of August, time interval is ~ 15 hours. Next, in the Fig.3 for each thermistor's string line of temperature for the depth 40 m is shown by red color. We can see appearance of NLIW on the thermistor at some moment

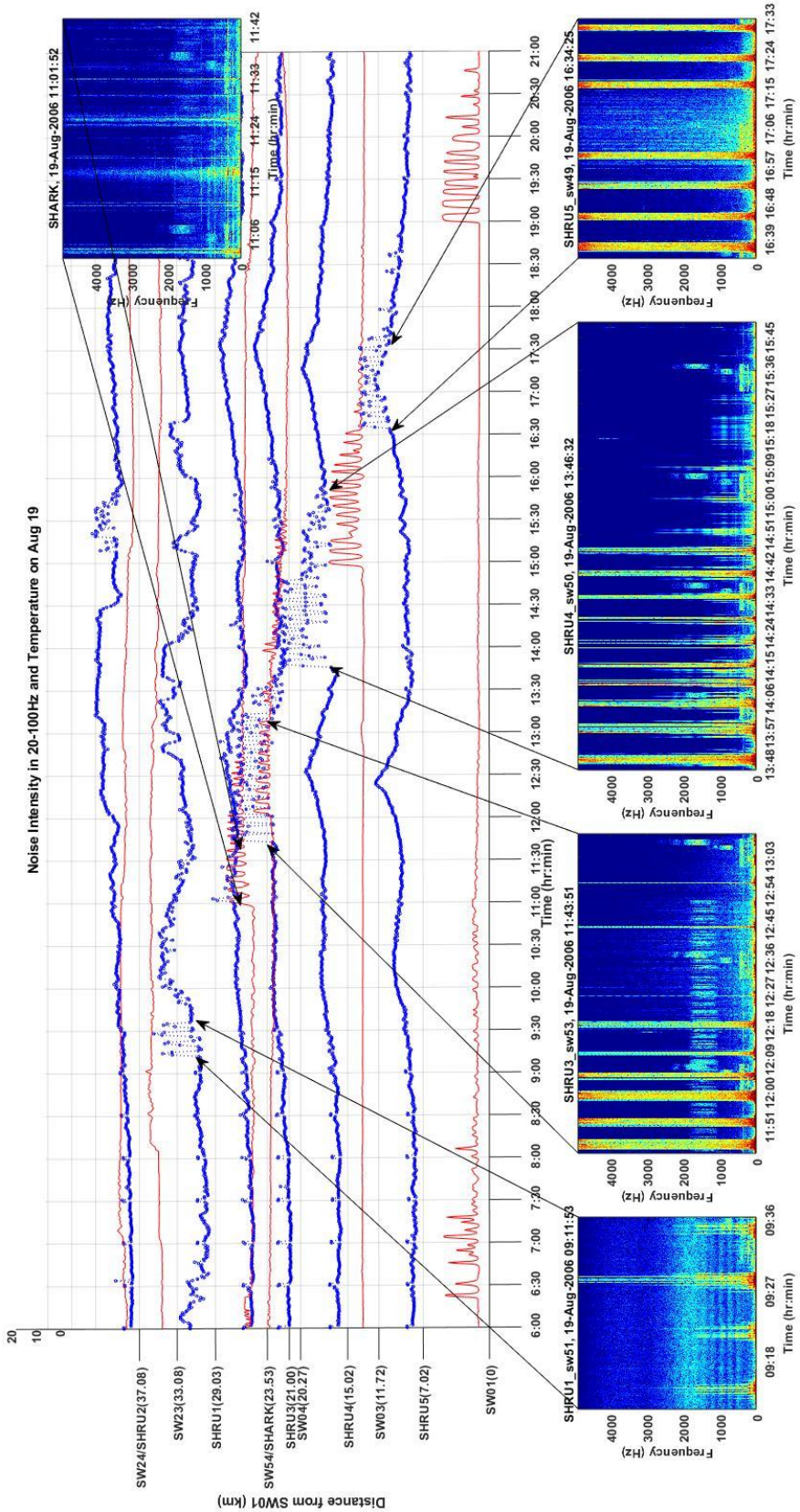


Fig.2. Spectrograms of noise and temperature records (in relative units) for different positions of NLIW 19th of August

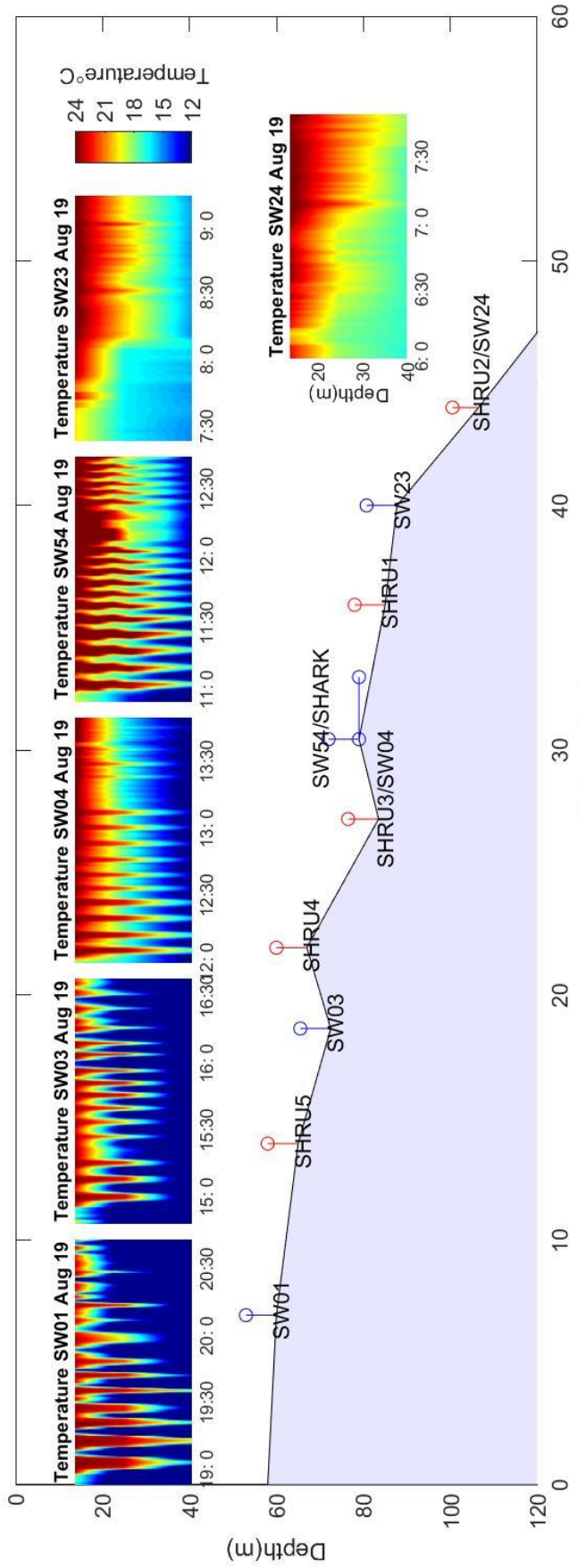


Fig.3. Evolution of NLIW train propagating toward the coast on 19th of August

of time. In accordance with commonly accepted theory, NLIWs are formed in the area between SW23 and SW54, where channel is sharply narrowing, and propagates further with evolving shape. In particular, using this diagram it is possible to estimate speed v of internal waves: distance between SW54 and SW01 is about 23500 m, time interval of NLIW passing by is about 8 h, so speed of NLIW is v~0.8 m/s. Blue lines denote noise amplitude on the corresponding SHRUs. In spite of positions of SHRUs being rather far from the thermistor strings, it is possible to estimate position of NLIW as a function of time, using their speed calculated above. After the corresponding simple estimations, it is seen that the increase of noise takes place when a train of NLIW is passing through the location of a corresponding SHRU. In Fig.2, spectrograms are also shown for the time intervals when NLIW passes through SHRUs and HVLA locations. Note that intensity of noise on the SHRUs is increasing while NLIW are moving toward the coast, in other words, noise intensity on SHRU5 is the biggest.

In Fig.3, the evolution of the NLIW shape is shown for the same time period of August 19. We can see that amplitude of NLIW remains approximately the same. However, the water depth is appreciably decreasing, and the hydrodynamic perturbation produced by NLIW is approaching bottom during its propagation. It means that for the big enough amplitude of the solitons the internal wave-induced currents near the bottom can be sizable. As a consequence, the boundary layer structure can be modified in the footprint of such waves [2, 3]. Therefore, the corresponding particles of sediment can generate significant noise as a result of collisions between them and with the seafloor [4].

It is interesting to note that analysis of spectra of noise, initiated by possible resuspension has carried out in [4], and one of the key features of this spectrum is a remarkable increase of power spectral density at frequencies above 10 kHz in contrast to typical noise spectrum, which decreases at high frequencies.

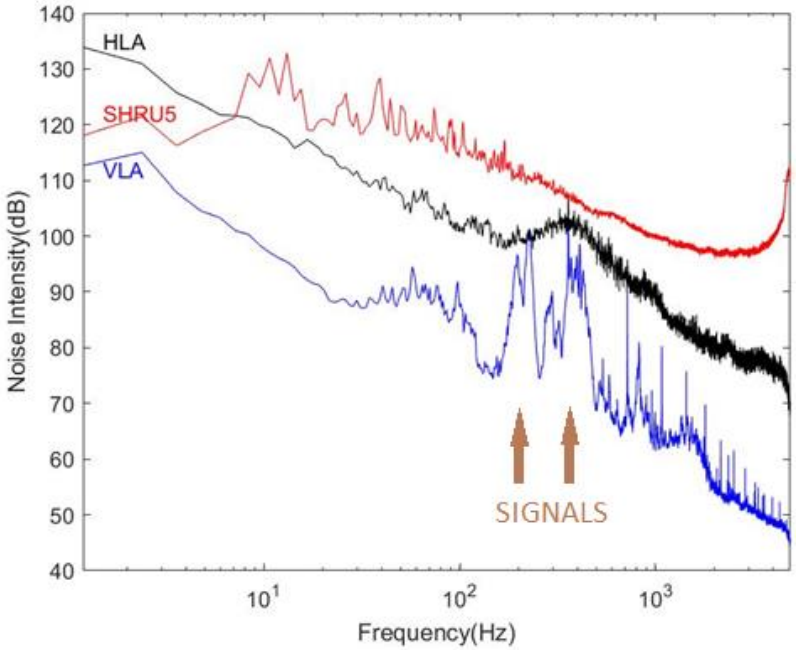


Fig.4. Power spectra of noise for different receivers. Arrows show manifestation of low-frequency sources in experiment

In Fig.4 three typical spectra presented for (i) one of the hydrophones of the HLA (the hydrophone is on the bottom), (ii) one of the hydrophones of the VLA (the hydrophone is approximately in the middle of the water column), and (iii) SHRU5. (For SHRU3 and 4 spectra are nearly the same as for SHRU5.). We can see that on HVLA, where influence of NLIW on bottom boundary layer seems rather week, noise spectra have decreasing frequency dependence. In contrast, the noise spectrum on SHRU5 as well as on SHRU3 and SHRU4, has a characteristic increase at high-frequencies. This is consistent with the above-mentioned possible manifestation of sediment resuspension [4].

Analysis of other events of NLIW propagation (on 17, 18 and 22 of August) confirms this hypothesis.

3. ACKNOWLEDGEMENTS

This work has been supported by NSF, grant OCE1657430, and BSF, grant 2016545.

REFERENCES

[1] **J. Lynch and D. J. Tang,** Overview of Shallow Water 2006 JASA-EL Special Issue Papers, *J. Acoust. Soc. Am.,*124 (3), pp. EL63–EL65, 2008.

[2] **M. Stastna and K. G. Lamb**, Sediment resuspension mechanisms associated with internal waves in coastal waters. *J. Geophys. Res.*, 113 (C10), C10016, 2008.

[3] **D. Bourgault, M. Morsilli, C. Richards, U. Neumeier, D. E. Kelley**, Sediment resuspension and nepheloid layers induced by long internal solitary waves shoaling orthogonally on uniform slopes, *Continental Shelf Res.,* 72, pp. 21–33, 2014.

[4] **T. Petrut, T. Geay, C. Gervaise, P. Belleudy, and S. Zanker**, Passive acoustic measurement of bedload grain size distribution using self-generated noise, *Hydrol. Earth Syst. Sci*., 22 (1), pp. 767–787, 2018.

NUMERICAL ANALYSIS OF PILE DRIVING DISTURBANCES INTO WATER AND SOIL FOR OFFSHORE WINDFARM CONSTRUCTIONS

Simon Marcellin[a], Farid Chati[a], Daher Diab[a], Dominique Décultot[a], Fernand Leon[a], Dominique Clorennec[b], Thomas Folegot[b]

[a]LOMC, UMR CNRS 6294, Université du Havre, 75 rue Bellot, 76600 Le Havre, France
[b]Quiet Oceans, 65 place Nicolas Copernic, 29280 Plouzané, France

simon.marcellin1@gmail.com

Abstract: *Underwater noise during offshore wind farm construction goes along with significant disturbances that potentially harm marine mammals in the vicinity. There is limited information on the scale of such disturbances, knowing that each implantation site is different from the other. Therefore, it has become important to lead upstream numerical analysis in order to predict pile driving effects and better understand the physical behavior of radiated acoustic waves. As part of the offshore wind farm project in the area of Dieppe-Le Tréport, in France, 11 monopile foundations were driven into the ground during May 2017, where the sedimentology is the same as the future offshore site. Acoustic measurements have been done to serve as a starting point for the development and calibration of a simple 2D finite element model (FEM) for future offshore implementation.*
With our 2D FEM model, we predicted and investigated sound pressure level and sound exposure level (SEL) in the water, as well as radial displacement in the different sedimentary layers. We showed that more than half of the radiation in the water comes directly from the seabed itself. We then investigated existing solutions for underwater noise reduction, like an air-bubble curtain or low acceleration pile driving. It showed good results on noise reduction, by lowering the SEL by 10 dB at only 50 meters away (upstream). This is significant information that should be considered when planning offshore pile driving and looking for noise reduction solutions.

Keywords: *Underwater noise, pile driving, modeling, offshore wind farm, sound exposure level*

1. INTRODUCTION

In the last decades, offshore wind industry and associated Offshore Wind Farms (OWF) has grown significantly, in connection with an increasing demand for renewable energy: since 1991 and the world's first OWF in Denmark, this industry has grown on average 52% each year [1]. This growth led to bigger constructions, larger wind turbines and stronger wind profiles [2]. However, offshore constructions may come along with significant disturbances that potentially harm marine mammals in the vicinity [3]–[6]. Therefore, underwater noise during OWF constructions, and specifically during pile driving, became a research topic on its own [7], in addition to existing studies on harmful human activities [8], [9].

Pile driving consist of delivering a series of vertical blows to the head of the pile with a hydraulic hammer in order to fixed it into the ground. There are many different pile driving formulas in use, limited models and therefore limited information on the scale of such disturbances because every implantation site is different from the other [10]. That's why it has become important to lead upstream numerical analysis on each site in order to predict pile driving effects on radiated acoustic waves.
First, the context of this study is described in section 2. Then the 2D-FEM approach of pile driving is presented in section 3. Next, the numerical results will be shown and discussed in section 4. Finally, the conclusions of the paper and perspective of the results are presented in section 5.

2. CONTEXT

As part of a new OWF project between Dieppe and Le Tréport in Normandy (France), a research project called RESPECT[1] gave rise to collaboration between our team and the *Quiet Oceans* Company. This project aims to:

- Validate a proper finite element model (FEM) of the pile driving operation.
- Deepen the knowledge of the acoustic wave propagation acquired during the former phase of the project.
- Leading investigations on new and existing noise reduction solutions.

In order to calibrate the FEM, experimental pressure measurements has been made by *Quiet Oceans* company into the ground [11]. The measurements have been realized during a pile driving operation where sedimentological ground properties are equivalent to the location of the future OWF. In this location, 11 piles of 30 meters long and 1.22 meters of diameter were first vibro-driven and then pile-driven up to 20 meters deep into the soil. Piles are 22.7 mm thick, made of 8000 kg/m^3 density steel with 200 GPa Young's modulus. These parameters will be used to simulate pile driving operation into the sea, in order to limit scaling problems, although the final dimensions of the pile will be larger.

[1] RESPECT: *Réduction des Empreintes Sonores des Parcs Eoliens en mer: Comprendre pour de nouvelles Technologies*; (Reduction of Sound Footprints of Offshore Wind Farms: Understanding for New Technologies).

3. FINITE ELEMENT MODEL

The measurement campaign allowed to collect data (pressure, applied force, dimensions) in order to set up and calibrate a numerical finite element model through the commercial software ANSYS Mechanical APDL™ [12].
Once calibrated and close enough to experimental results (among other, by using the right sedimentary attenuation parameters [13]–[15]), an extrapolation of this model has been made to a pile driving problem into the sea. A 5 meter water layer is added, above a 3 meter sand layer. Every parameter used in this simulation can be seen on ***Table 1***. Regarding the pile itself, the applied attenuation is 2 dB/λ [15].

Layers	h [m]	E [GPa]	α [dB/λ]	ρ [kg/m^3]	c_l [m/s]
Water	5	2.2	-	1000	1500
Sand	3	0.194	0.8	2000	1800
Marly chalk	5	1.5	0.6	2000	1060
Medium chalk	2	12.15	0.4	2500	2700
Compact chalk	7+	15.68	0.2	3000	2800

Table 1: Parameters of each layer used in our 2D-FEM model.

In order to better understand the radiation of the pile, the contribution of the seabed is separate from the entire contribution of the pile itself, which radiates in water as much as in soil. In our model, for a normal situation, every node in the water (FLUID29) has 3 degrees of freedom (DOFs) which is 2 displacements (UX, UY) and fluid pressure. In order to predict the seabed contribution only, the DOFs of each node is blocked in a vertical line, at one meter distance from the pile, knowing that there may be some reflections, but without considering it for the moment. The pressure is picked up along a further vertical line in the water, at 50 meters away, as it can be seen on the *Fig.1*.

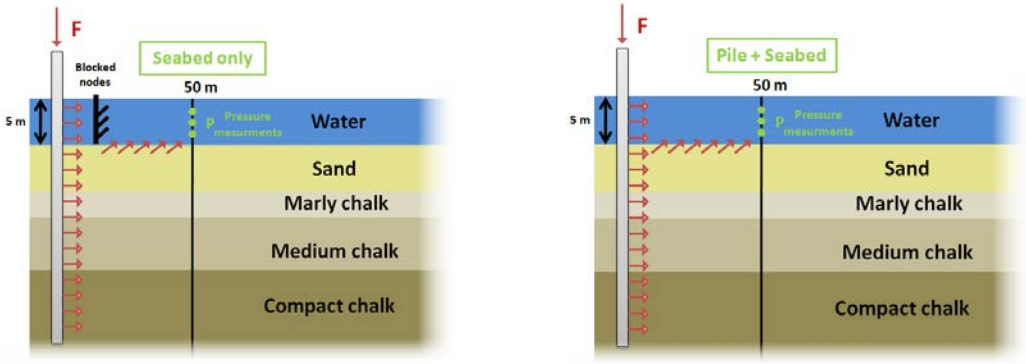


Fig.1: Measurement of the pressure at 50 meters by blocking the pile radiation in the water (left) and without blocking anything (right).

4. RESULTS AND DISCUTIONS

After separating the contribution, the pressure is calculated at 50 meters away from the pile, on a vertical line, over the entire depth of the water layer (5 meters), at the end of the pile driving operation. Then the SEL is plotted under both conditions, and results are discussed.

The effects of a noise reduction technique on the SEL with a low acceleration pile driving can be seen.

4.1. SEPARATION OF ACOUSTIC RADIATION

The calculated pressure at 50 meters at the end of the pile driving operation is plotted in the *Fig.2*. On the left graphic, the radiated sound pressure remains important even if the pile is not radiating into the water. In proportion, by a maximum amplitude ratio between both graphs, the seabed radiation is responsible for at least 50% of the pressure at 5 meters depth.

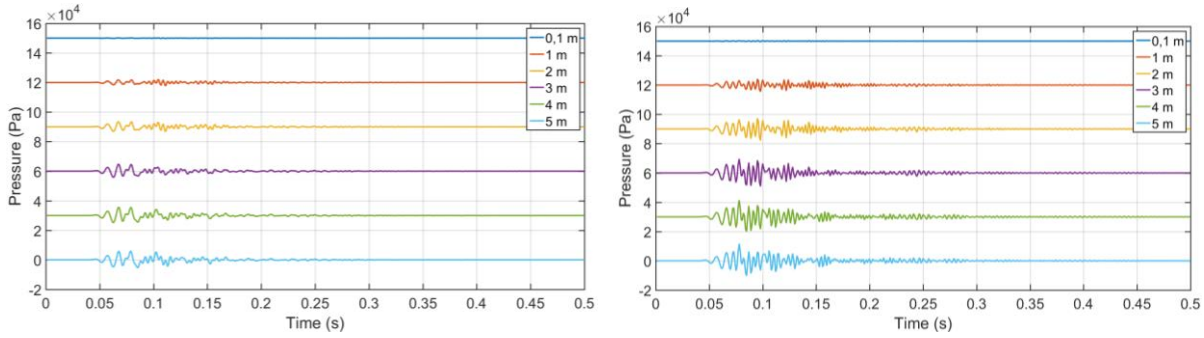


Fig.2: Sound pressure at 50 meters by blocking the pile radiation in the water (left) and without blocking anything (right).

The Sound Exposure Level (SEL) according to the depth is plotted on the *Fig.3*, and show the radiation from the seabed (red plot) being almost important as the entire SEL at 1 meter (blue plot), with a bigger contribution at 50 meters. This result suggests that long-range radiation should mainly relate to seabed radiation itself.

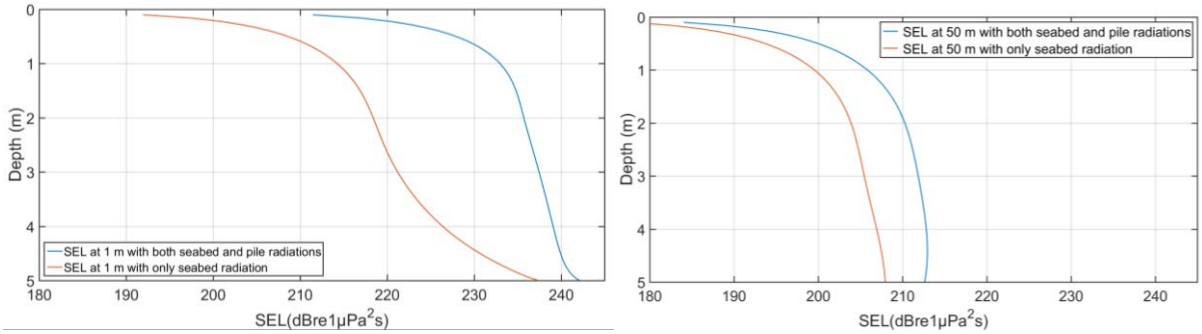


Fig.3: SEL at 1 meter (left) and 50 meters (right) by blocking the pile radiation in the water (red plot) and without blocking anything (blue plot).

This study shows that more than half of the radiation in the water comes directly from the seabed itself, which is significant information when studding noise reduction solutions. Hence, it could be noticed that an upstream noise reduction solution is more suitable than downstream technique. This is what is going to be shown in the next section.

4.2. NOISE REDUCTION SOLUTIONS

Classical and widely used noise reduction systems allowed between 10 and 14 dB (SEL) noise reduction, depending on the frequency range [16]–[19]. But those techniques only work as a downstream technique, and as we just have seen, the radiation of the pile in the water represents only a small part of the radiation. That is why upstream techniques could reduce

way more significantly the underwater noise during pile driving. One of them allowed a noise reduction between 4 and 25 dB (SEL), depending on the scale and the frequency range [20]–[22]. This technique has been applied in our model, by using the same hammer force, but spread over a period of 100 ms instead of the initial 10 ms. SEL results according to the depth are plotted in the *Fig.4*. This technique reduces by almost 11 dB (SEL) the underwater noise at only 50 meters away from the pile. This is significant information that should be considered when planning offshore pile driving and looking for noise reduction solutions.

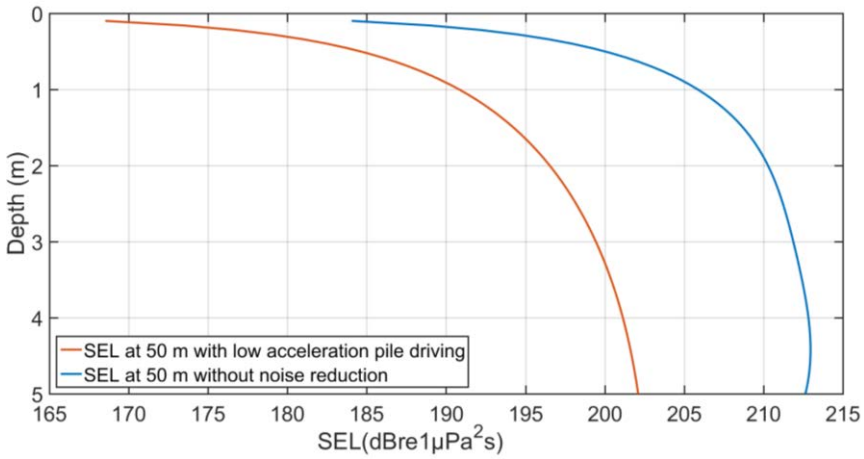


Fig.4: SEL at 50 meters from the pile using a soft pile driving (red plot) and without any noise reduction (blue plot).

5. CONCLUSIONS AND PERSPECTIVES

Our 2D-FEM model allowed us to easily separate radiation contributions and show that seabed itself is responsible of more than a half of the total radiation in water. Hence, reducing underwater noise should be better by lowering upstream signal, with optimized hammer for instance, than lowering downstream radiation, as downstream technique does. Existing upstream solution may offer a reduction of 11 dB (SEL) at 50 meters, which is not negligible.

In order to going further, it could be interesting to add friction in the model, losses in water, anisotropy and heterogeneities in the soil. It's also important to have a better knowledge of the stratigraphic distribution under the pile driving zone. Indeed, the thickness of a layer, specifically the first one, as a significant impact on the radiating wave's behavior into water.

ACKNOWLEDGMENTS

Financial support for RESPECT project was provided by EMDT (Eoliennes en Mer Dieppe Le Tréport).

REFERENCES

[1] **S. Rodrigues, C. Restrepo, E. Kontos, R. T. Pinto, and P. Bauer**, « Trends of offshore wind projects », *Renewable and Sustainable Energy Reviews*, vol. 49, p. 1114-1135, 2015.

[2] **R. Perveen, N. Kishor, and S. R. Mohanty**, « Off-shore wind farm development: Present status and challenges », *Renewable and Sustainable Energy Reviews*, vol. 29, p. 780-792, 2014.

[3] **O. S. Board and N. R. Council**, *Ocean noise and marine mammals*. National Academies Press, 2003.

[4] **H. Bailey, B. Senior, D. Simmons, J. Rusin, G. Picken, and P. M. Thompson**, « Assessing underwater noise levels during pile-driving at an offshore windfarm and its potential effects on marine mammals », *Marine Pollution Bulletin*, vol. 60, nº 6, p. 888-897, 2010.

[5] **B. L. Southall *et al.*,** « Marine mammal noise-exposure criteria: initial scientific recommendations », *Bioacoustics*, vol. 17, nº 1-3, p. 273-275, 2008.

[6] **D. Wilhelmsson, T. Malm, and M. C. Öhman**, « The influence of offshore windpower on demersal fish », *ICES Journal of Marine Science*, vol. 63, nº 5, p. 775-784, 2006.

[7] **P. G. Reinhall and P. H. Dahl**, « An investigation of underwater sound propagation from pile driving », Washington State Department of Transportation, Office of Research & Library …, 2011.

[8] **D. Ross,** *Mechanics of underwater noise*. Elsevier, 2013.

[9] **W. J. Richardson, C. R. Greene Jr, C. I. Malme, and D. H. Thomson**, *Marine mammals and noise*. Academic press, 2013.

[10] **E. A. Smith,** « Pile-driving analysis by the wave equation », *American Society of Civil Engineers Transactions*, 1962.

[11] **J. De Rosny, C. Prada-Julia, D. Clorennec, T. Folegot, G. Le Provost, and R. Chavanne**, « Mesure, analyse et simulation des ondes de compression engendrées lors d'un battage de pieux à terre. », CFA 2018 23-27 Avril, Le Havre, France, 1165-1166, 2018.

[12] **M. K. Thompson and J. M. Thompson,** *ANSYS mechanical APDL for finite element analysis*. Butterworth-Heinemann, 2017.

[13] **E. L. Hamilton**, « Sound velocity–density relations in sea-floor sediments and rocks », *The journal of the Acoustical Society of America*, vol. 63, nº 2, p. 366-377, 1978.

[14] **J.-X. Zhou, X.-Z. Zhang, and D. P. Knobles**, « Low-frequency geoacoustic model for the effective properties of sandy seabottoms », *The Journal of the Acoustical Society of America*, vol. 125, nº 5, p. 2847-2866, 2009.

[15] **F. B. Jensen, W. A. Kuperman, M. B. Porter, and H. Schmidt,** *Computational ocean acoustics*. Springer Science & Business Media, 2000.

[16] **B. Würsig, C. R. Greene Jr, and T. A. Jefferson**, « Development of an air bubble curtain to reduce underwater noise of percussive piling », *Marine environmental research*, vol. 49, nº 1, p. 79-93, 2000.

[17] **K. Lucke, P. A. Lepper, M.-A. Blanchet, and U. Siebert**, « The use of an air bubble curtain to reduce the received sound levels for harbor porpoises (Phocoena phocoena) », *The Journal of the Acoustical Society of America*, vol. 130, nº 5, p. 3406-3412, 2011.

[18] **R. Matuschek and K. Betke**, « Measurements of construction noise during pile driving of offshore research platforms and wind farms », in *Proc. NAG/DAGA Int. Conference on Acoustics*, 2009, p. 262-265.

[19] **P. Stein, H. Sychla, J. Gattermann, and J. Degenhardt,** « Hydro sound emissions during impact driving of monopiles using Hydro Sound Dampers and Big Bubble Curtain », *RAVE Offshore Wind R & D, Bremerhaven*, 2015.

[20] **S. Koschinski and K. Lüdemann**, « Quieting technologies for offshore pile driving », *Progress in Marine Conservation in Europe 2015*, p. 217, 2015.

[21] **J. S. Winkes and B. A. Genuit,** *The future of offshore pile driving: bigger, deeper, more silent*. EWEA Offshore, 2013.

[22] **T. Merck, S. Werner, S. Koschinski, and K. Lüdemann**, *OSPAR inventory of measures to mitigate the emission and environmental impact of underwater noise*. 2014.

Structured Session 7

Underwater Unexploded Ordnance (UXO) Detection and Remediation

Organiser(s): Jans Wolfgang, Richardson Mike

SERDP/ESTCP MUNITIONS RESPONSE PROGRAM: UNDERWATER REMEDIATION OF UNEXPLODED ORDNANCE (UXO)

Michael D. Richardson[a, b], Herbert H. Nelson[b], Kevin L. Williams[c], and Joseph Calantoni[d]

[a]Institute for Defense Analyses, Alexandria, VA, USA
[b]Strategic Environmental Research and Development Program, Alexandria, VA, USA
[c]Applied Physics Laboratory, University of Washington, Seattle, WA, USA
[d]Marine Geosciences Division, Naval Research Laboratory, Stennis Space Center, MS, USA

Michael D. Richardson, 326 Julia Street, Bay St. Louis, MS 39520, USA, mike.richardson@bellsouth.net

Abstract: *The US Department of Defense Strategic Environmental Research and Development Program (SERDP) and Environmental Security Technology Certification Program (ESTCP) Munitions Response program supports the development and demonstration of innovative technologies to characterize, remediate, and scientifically manage sites affected by military munitions, including unexploded ordnance (UXO) and discarded military munitions. Twenty year's work on terrestrial sites has resulted in a substantial decrease in remediation costs through the development of advanced geophysical sensors and signal-processing methodologies that allow detection and classification of buried UXO. The geophysical inversion of data from electromagnetic induction sensors allows separation of harmless subsurface scrap from dangerous buried UXO, thus reducing costs and improving the effectiveness of UXO remediation on the wide variety of contaminated Department of Defense sites. The Munitions Response program is now focused on reducing costs and improving effectiveness of UXO remediation in the underwater environment. The first stage of this effort was the development and evaluation of underwater sensors (acoustic, magnetic, electromagnetic, and optical) and platforms (remotely operated vehicle, autonomous underwater vehicle, towed, bottom crawler, and airborne) required to detect and classify UXO found in a variety of underwater sites. Field and laboratory studies of UXO behavior are being used to develop a probabilistic expert system model to predict burial, migration, and re-emergence of UXO in coastal, estuarine, freshwater, and riverine environments. Development of new technologies for physical removal or in situ remediation of UXO are also emphasized. The next step includes the development of standardized underwater UXO demonstration sites to test and evaluate the sensors and platforms that are designed to detect and classify underwater UXO. In this paper, we will summarize progress and provide a vision for cost-effective and efficient remediation of underwater UXO.*

Keywords: *munitions remediation, target classification, burial and migration*

1. INTRODUCTION

The Strategic Environmental Research and Development Program (SERDP) and the Environmental Security Technology Certification Program (ESTCP) are the Department of Defense's environmental research programs, harnessing the latest science and technology to improve environmental performance, reduce costs, and enhance and sustain mission capabilities at DoD facilities. Five programs areas (https://serdp-estcp.org/Program-Areas) support technologies (1) to improve energy efficiency, increase the use of renewable energy, and enhance water conservation on DoD installations; (2) to characterize, perform risk assessments, remediate, and manage contaminants in soil, sediments, and water; (3) to advance DoD's management of its natural and cultural resources; (4) to reduce, control, and understand the sources of waste and emissions in the manufacturing, maintenance, and use of weapons systems and platforms; and (5) that can characterize, remediate, and scientifically manage sites affected by military munitions on US lands and underwater.

Program support for UXO remediation (item 5) at terrestrial sites is nearing completion with the demonstration of advanced geophysical systems and signal-processing methodologies proved to detect and classify buried UXO. This allows separation of harmless subsurface scrap from dangerous buried UXO, reducing the number of costly UXO digs, thus improving the effectiveness of UXO remediation found on the wide variety of contaminated sites. The Munitions Response (MR) program has now turned its support to improving remediation of underwater UXO found in ponds, lakes, rivers, estuaries, and coastal areas out to depths of 30 meters. The main areas of this effort include development of systems to detect and classify UXO during wide-area assessment and detailed surveys, UXO recovery and disposal, munitions burial and mobility, and phenomenology associated with characteristics of munitions and site environmental conditions. These technologies are intended to support Defense Environmental Restoration Program remediation of sites contaminated by munitions which is conducted following the Comprehensive Environmental Response, Compensation, and Liability Act (CERCLA) process (Fig. 1). The US Army Corps of Engineers and the US Navy have identified over 450 formerly used and active underwater defense sites, totaling more than 10 million acres in US coastal and territorial waters, potentially contaminated with munitions (SERDP-ESTCP, 2010).

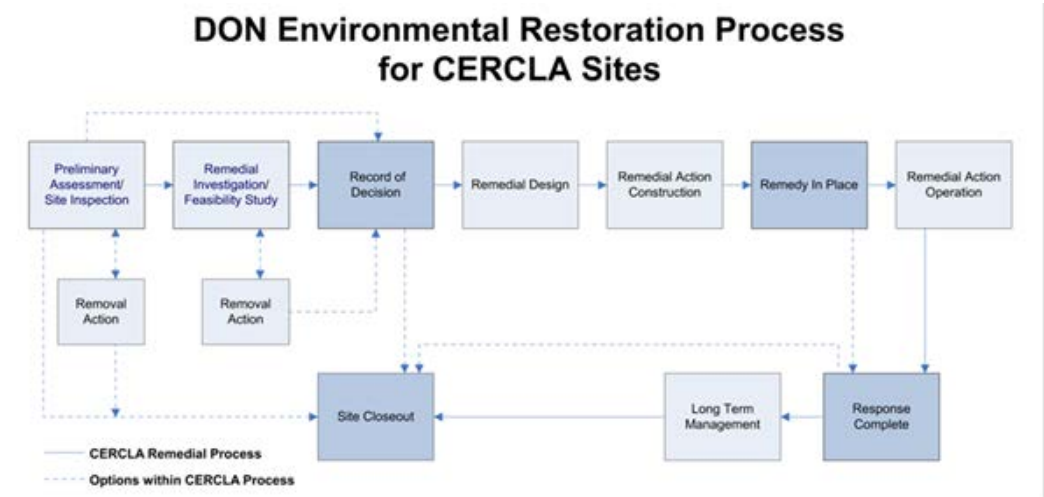


Figure 1 – Generic UXO restoration process covered under the Dept. of Navy (DON) Comprehensive Environmental Response, Compensation, and Liability Act (CERCLA).

2. SENSORS AND PLATFORMS

Given the wide variety of environments (coastal, estuarine, freshwater, and riverine), water depths and bottom types, munitions types, and hydrodynamic conditions, a single sensor modality or platform type is probably inadequate to accommodate requirements at all possible underwater remediation sites. A wide range of options for systems (sensors and platforms) to detect and classify UXO is therefore being investigated. Sensor modalities include high- and low-frequency acoustic sensors, various magnetic sensors, optical systems including LIDAR and traditional still and video camera systems, and cued and single-pass electromagnetic sensor combinations. Platforms include autonomous underwater vehicles (AUVs), remotely operated vehicles (ROVs), towed systems, surface systems, crawlers, and airborne platforms. Sensors including optical (LIDAR, still and video cameras) are limited to proud targets in clear waters. High-frequency acoustic sensors (side-scan and multibeam sonars) are primarily limited to proud targets without water clarity restrictions. Active electromagnetic induction (EMI) and passive magnetic sensors as well as lower frequency acoustic sensors can all be used to detect buried targets but with much different standoff or coverage rates. Towed or AUV platforms may be optimal for waters deeper than about 5 meters; bottom crawlers and surface and airborne platforms are most appropriate for shallow water. Given the maturity of optical and high-frequency imaging sensors to detect and classify proud targets, SERDP has concentrated support on magnetic, EMI, and lower frequency acoustic sensors designed to detect and classify buried targets.

2.1.1. Magnetic and EMI Sensors and Platforms

Both passive magnetic and active electromagnetic systems are being developed for the underwater environments. Potential magnetic and electromagnetic technologies include modified advanced systems proven for terrestrial UXO classification, systems developed for mine countermeasures (MCM) operations, and purpose-built systems specific for underwater UXO remediation. Magnetometers have greater standoff detection ranges (up to 5 meters) and are better suited for larger scale surveys; the shorter detection ranges (1–3 meters) for active electromagnetic systems restrict use to smaller areas (smaller coverage rates) or for cued classification.

Some of the magnetic systems developed or demonstrated under SERDP-ESTCP include towed magnetic arrays such as the Marine Towed Array (Kieswetter, MR-200324) and the Marine Gradient Array (Funk, MR-200808); hand-held diver-operated systems (Prouty, MR-2104); AUV-based laser scalar gradiometers (Angle, MR-201612); drone-based wide-area survey for hard-to-access very shallow underwater sites (Schultz, MR-19-5212); and commercially available AUV-based systems such as Geometrics G-880 total field magnetometer (Trembanis, MR-2730; Steigerwalt, MR-201002). Recent advances in magnetic sensors include miniaturization, improved sensitivity, lower power requirements, and lower cost. Platform magnetic interference and precise navigation and positioning continue to be technology issues.

The advanced EMI sensors and signal processing (inversions) developed for land-based UXO classification dominate the development of underwater EMI systems. The main logistical difficulties in using EMI technology in the marine environment include waterproofing all receiver and transmitter loops and electronics for a conductive environment, designing the optimal transmitter coils and receiver cubes configurations, and providing appropriate platform support and navigation and positioning for operation in a dynamic (e.g., wave and currents) and GPS-denied environment. The geophysical inversions (dipolar polarizations) of UXO electromagnetic responses seem unaffected by biofouling or corrosion (Steinhurst, MR-2500). Numerical (Billings, MR-2412; Shuditidze, MR-2728) and field

studies (Saville, MR-201313; Schultz, MR201233; Gasperikova, MR-2321; Bell, MR-2409) have demonstrated that the inversion and classification techniques (library matching, statistical classification methods) developed in the terrestrial setting are in principle adaptable to the underwater setting. The influence of eddy current response due to currents generated in the target and the galvanic coupling of currents through the body (the current channeling response) may affect the scattered field from a metallic target, but typically only at very early times and for large receiver-to-object offsets (Billings, MR19-1261). The effects of background subtraction from a highly variable seafloor (e.g., vertical gradients and horizontal variability) is still an ongoing research issue.

2.2.2 Acoustic Sensors and Platforms

Acoustics offer increased standoff distances relative to magnetic and EMI detection and classification systems. This in turn offers both increased area coverage and deployment-system safety advantages (by maintaining a larger altitude relative to the sediment), thus making acoustics an attractive technology. For munitions that are at least partly proud of the sediment, commercially available high-frequency systems such as multi-beam and side scan have the resolutions needed to detect and classify munitions. Detecting and classifying buried munitions, however, offers a larger challenge. The frequency dependence of the attenuation of sound in sediments motivates use of low frequencies while the resolutions important for classification drives the solution to high frequencies or large apertures. The solution being pursued by multiple SERDP researcher groups (Houston, MR-201714; Brown, MR-2545; Williams, MR18-5004; Sara, MR-2752) is to combine broadband, low-frequency acoustic systems with real cross-track and synthetic along-track processing. The along-track processing requires motion compensation to meet synthetic aperture sonar positioning requirements. Recent developments in motion compensation (Marston and Plotnick, 2015; Gao et al., 2014) have been shown to be successful under challenging conditions. Data from low-frequency, broadband systems allow us to examine munition response in a variety of two-dimensional spaces, for example, time-angle, wavenumber, frequency-angle, and *x*–*y* (image). Fig. 2 shows an example for a 2-foot-long, 1-foot-diameter aluminum cylinder from a SERDP-sponsored effort in the Gulf of Mexico (Kargl, MR-2231).

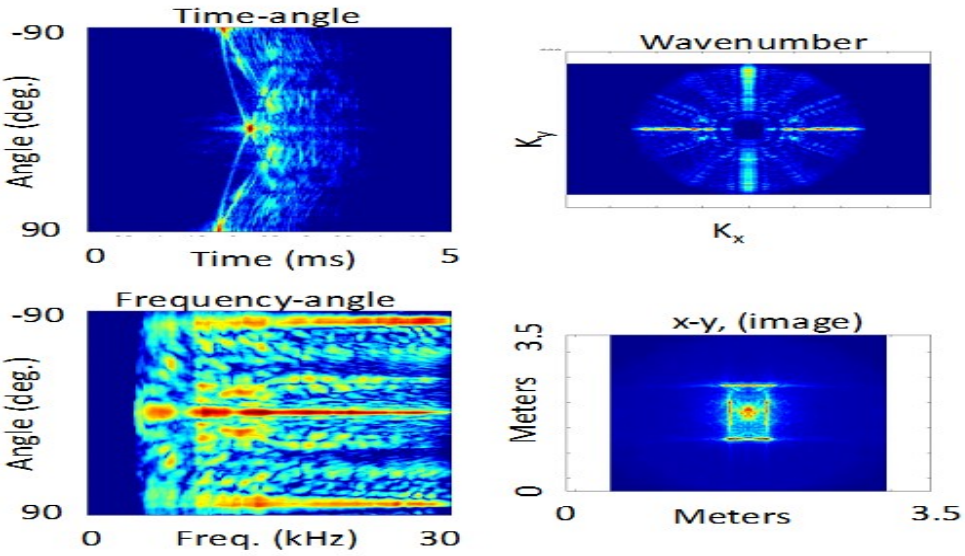


Figure 2. Possible two-dimensional spaces derivable from data acquired on a low-frequency, broadband system.

Different spaces in Fig. 2 offer easy access to different types of munitions information. From a classification standpoint, the ability to operate in a variety of spaces allows development of more discriminating feature sets. The maturity of these low-frequency sensors is to the point that ESTCP efforts to quantify their capabilities using ground-truthed test beds are now underway using three different deployment platforms. One effort (Houston, MR-201714) is fielding an AUV; the second, a surface-vessel-mounted system (Brown, MR-2545); and the third, a towbody mounted sensor suite (Williams, MR18-5005). In concert with these system developments, efforts aimed at developing test beds are in progress (Tomich, MR-2735; Khadr, MR-2736). Regardless of the system, an essential component is the ability to geolocate any object classified as a munition to a resolution sufficient for remediation. Fig. 1 is an example of the restoration process. Of particular importance in this process is the remedial investigation (RI) step. For RI, an area under the curve of 0.9 with as yet unspecified correct classification and false-alarm rates has been given as a starting point. Also for the RI, the goal is a geolocation uncertainty of less than 5 meters for munitions buried up to 0.5 meters in a sand sediment. The performance needed at the remedial action (RA) step will be significantly more stringent (e.g., geolocation to less than 1 meter and a false-negative rate of 0). SERDP and ESTCP researchers have previously used a variety of navigation and positioning methodologies, including high-quality inertial navigation modules onboard AUVs, real-time kinematic (RTK) GPS systems in concert with ultra-short-baseline and long-baseline systems for towbodies, and RTK GPS-only strategies for surface vessel deployments. These commercially available navigation sensors, in concert with the current generation geographic information system mapping technologies, should allow the geolocation requirements of the RI phase of remediation to be fulfilled. Efforts over the next few years will establish the limits of current strategies and their capability relative to RA requirements.

3. BURIAL AND MOBILITY MODELING OF MUNITIONS

Underwater environments represent areas where munitions are much more susceptible to mobility, burial, and re-exposure than terrestrial environments. A wide range of contaminated underwater environments exists, including rivers, lakes, estuaries, and coastal beaches. Each location has different wave and circulation patterns that drive sediment erosion and deposition, which are directly linked to burial, mobility, and re-exposure processes. Likewise, the bottom type can include soft clays or muds, sandy sediments, large cobbles, or coral reefs. Heterogeneous bottom types (or mixtures) are also prevalent, complicating models for burial and mobility. The wide range of boundary and forcing conditions that exist across underwater environments adds complexity to the problem. The need to assess and manage risk associated with each underwater site necessitates the development of robust predictive models. Predictive models require detailed observations for verification and validation. One of the goals of the burial and mobility modeling aspect of the SERDP MR program is to develop predictive models to quantify the behavior of the distribution of munitions contamination present at an underwater site. It is believed that these predictive models must be probabilistic in nature such that they not only make predictions, but also simultaneously estimate the uncertainty of the predictions.

Burial and mobility modeling of munitions in underwater environments will play an essential role in the management of contaminated sites from the initial wide-area assessment phase through any eventual remediation phase that may occur (Fig. 1). Consequently, the critical inputs for burial and mobility modeling must be determined. The inputs must be well characterized at each site, and due to the ephemeral nature of the environments, some inputs will require continuous monitoring such as meteorological and atmospheric forcing. We anticipate that site management will always begin by characterizing the necessary

environmental inputs for burial and mobility modeling, which in turn also overlap with the necessary inputs to assess sensor performance before deploying assets for detection and classification. The initial environmental characterization would be followed by site surveys to detect and classify munitions (i.e., quantify contamination). After initial mapping of munitions contamination is performed and UXO deemed hazards remediated, models for the meteorological and atmospheric forcing and probabilistic prediction of burial and mobility can be employed to determine if UXO not initially remediated could become be a hazard to the public because of re-emergence or mobility. If UXO is deeply buried and predicted to remain in place, a manage-in-place strategy of would appear to be the safest and least costly option. The chosen sequence of events will compose a concept for operations that will be focused on making predictions over the relatively short term, such as storm events and seasonal changes (intra-annual variability), as opposed to making predictions over multi-annual to multi-decadal time scales. The focus on predictions of intra-annual variability, starting with individual storm events, will provide a practical method for long-term site management.

The portfolio of projects funded by the SERDP MR program focused on burial and mobility modeling of munitions in the underwater environment ranges from the theoretical to the experimental. One category of projects is focused on the development of analytical and numerical models to predict the behavior of munitions in the natural environment. The portfolio represents a hierarchal approach that includes the effect of local processes by utilizing analytical models that predict scour burial processes (e.g., Friedrichs et al., 2016) and detailed numerical simulations (e.g., Rennie et al., 2017) that investigate the physics of liquefaction adjacent to munitions. Results from local models are combined with laboratory experiments for scour burial (e.g., Rennie, MR-2227) and the initiation of munitions mobility (e.g., Wu et al., 2019) in the development of an expert system based on Bayes theorem for predicting the statistics of phenomenology (Rennie, MR-2227), which is analogous to an existing expert system for mine burial (Rennie et al., 2007). The difficulty in implementing such an expert system lies in the inherit time dependence of the problem in which daily meteorology continually evolves the local hydrodynamics. Consequently, coupled Earth system models for predicting the local hydrodynamics are being utilized to drive the expert system (Palmsten, MR-2733).

Results from field experiments are necessary for verification and validation of the modeling systems for predicting munitions burial and mobility in underwater environments. Several ongoing and previous projects under the MR program portfolio have focused on gathering time-series observations of burial and mobility processes (e.g., Calantoni, MR-2320) through the development of technologies for determining the location and state of burial of munitions (e.g., Traykovski and Austin, MR-2319). In addition, high spatial and temporal resolution measurements of the relevant boundary layer processes (e.g., wave height and direction, current profiles, suspended sediment concentrations, and sediment erosion and deposition) have been recorded simultaneously while monitoring the burial and mobility of surrogate munitions. Unlike previous investigations that have provided before-and-after snapshots of munitions mobility (Wilson et al., MM-0417), more recent experiments have provided long time-series observations of munitions phenomenology.

The development of so-called smart surrogate munitions has provided a valuable tool to improve our understanding of munitions phenomenology. Smart surrogates contain embedded, self-logging sensors that allow monitoring of the state of munitions with high temporal resolution. A wide range of internal sensors has been placed inside of surrogate munitions, including miniature inertial motion units, Wi-Fi tags, shock sensors, photocells, pressure sensors, and data loggers (Puleo, MR-2503). While embedding sensors, care was taken to maintain the properties of size, shape, density, center of gravity, and moments of inertia of the munitions that the smart surrogates represent. The capability provided by smart surrogates becomes particularly significant in the harsh, shallow water environment of the

inner surf zone and swash zones of the beach. In these areas, foam on the water surface, along with intermittently high concentrations of bubbles and sediment in the water column, makes it exceedingly difficult to remotely sense the behavior of munitions using traditional optic and acoustic techniques.

4. REMEDIATION AND NEUTRALIZATION TECHNOLOGIES

Underwater munitions may require cost-effective, safe, and environmentally acceptable remediation techniques if leave-in-place options are unacceptable. Current practices employ divers for manual retrieval of targets, a dangerous and costly practice, or blow-in-place procedures, which produce shock-wave pressures and acoustic noise from bubble formation/collapse that are detrimental to marine life. SERDP-ESTCP has supported a variety of alternate neutralization procedures designed to be less dangerous and environmentally acceptable. These include the use of bubble currents to reduce the shock-wave and acoustic pressures generated from blow-in-place practices; covering UXO with geotextile bags to eliminate contact with the public and reduce the effects of potential detonations; robust underwater caisson-like structures to contain explosive impacts; development of blast-barge technology where munitions are brought to the surface and exploded in blast-restricting containers; dredging equipment modifications that detect and remove munitions from the dredged material; and designing robotic techniques to remove munitions from the seafloor, eliminating the need for divers.

More recent development of in situ methods to neutralize energetics contained in munitions includes using a high-pressure water jet to cut access holes into the body of the munition casing and wash out the internal explosive, which is then captured in bags for later analysis and disposal (Schmit, MR18-5116); development of an explosively generated plasma tool to cut holes in munitions via a plasma ablation process and generate high-temperature chemical decomposition that results in rapid deflagration of energetics without detonation (Douglas, MR-201611); and evaluation of an underwater electrochemical remediation system that uses an ablative chemical drilling method to drill access holes in munitions and electrochemical processes to transform nitro-containing explosives into stable compounds that can easily be removed (Jo, MR18-146). The long-term goal of these systems is to develop safe, cost-effective methods to remove or render inert the energetics from underwater UXO without leakage or detonation. But it has been shown that working in a dynamic underwater environment, especially using tethered ROV or independent AUV robotic platforms, is more difficult than operating in easily controlled laboratory settings.

5. STANDARDIZED UNDERWATER UXO DEMONSTRATION SITES

A workshop on the development of standardized underwater UXO demonstration sites ("test beds") was held during the SERDP and ESTCP 2018 Symposium (https://serdp-estcp.org/News-and-Events/Conferences-Workshops/Past-MR-Workshops/Underwater-UXO-Test-Bed-Workshop-Nov-2018). The objectives of this workshop were to establish the requirements, framework, protocols, responsibilities, and timelines for development of a series of sites that can be used to test, evaluate, and demonstrate acoustic, magnetic, EMI, and optical systems designed to detect and classify underwater UXO. Test-bed site locations will be based on a combination of environments representative of sites and munitions slated for near-term remediation (surrogate environments) and test-bed sites appropriate for systems and sensors that are ready for demonstration. Based on these criteria, a rather benign (easy) deeper area (5–20 meters) free of native UXO with both sandy and muddy sediments would provide the best location for the development of the initial test bed. That area should contain large football-field-sized areas with little spatial and temporal variation in sediment properties. Targets of interest should be easily buried and exhibit little or no mobility. Based on lessons

learned, a second location in shallow water (e.g., beach area) might provide a second test bed. Test beds in vegetative areas, at gravelly sites, and on coral habitats can follow as needed. The workshop report provides a list of environmental measurements (e.g., currents, waves, water column, bathymetry, meteorological, and sediment type, properties, and layering), numbers and types on munitions and clutter, and geo-positioning and orientation requirements for buried and proud targets of interest. Still to be determined are methods of emplacement of UXO and clutter, methods to determine location and orientation of UXO during demonstrations, and demonstration scoring requirements.

6. THE WAY FORWARD

The success of the terrestrial SERDP-ESTCP programs in reducing cost and improving the safety of UXO remediation via development of electromagnetic classification of UXO provides lofty goals for a similarity structured underwater program. Three technology improvements can greatly reduce costs and improve safety of underwater UXO remediation: development of probabilistic models to predict the behaviour (burial, migration and re-emergence) of UXO in the dynamic environment; improved UXO classification technologies, especially for buried UXO; and development of in situ methods to neutralize UXO without explosion or contaminating the environment with energetics or energetic residues. Significant developments in all three areas have been realized with ongoing SERDP-ESTCP–supported programs.

In addition to these three areas of technological advancement, technologies to measure and model environmental factors are being supported by SERDP. The behaviour of UXO depends on sediment type, water depth, and the dynamics of the overlying water column. Along with a knowledge of the types and spatial distribution of munitions, these environmental conditions provide the necessary inputs to predict UXO behaviour. Sediment and water column properties also provide important inputs to determine what types of platforms and sensors are most appropriate for UXO detection and classification in the wide range of contaminated underwater environments that require remediation.

7. REFERENCES

MR-xxxxx. These include references to summaries and reports from active (44) and completed (72) projects supported by the Munitions Response underwater programs which can be accessed on the SERDP-ESTCP website.

Friedrichs, C.T., Rennie, S.E, and A. Brandt (2016) Self-burial of objects on sandy beds by scour: A synthesis of observations, *Scour and Erosion – Harris, Whitehouse & Moxon (Eds.)*, Taylor and Francis Group, London, U.K., ISBN 978-1-138-02979-8.

Gao, Y., W. Yu, Y. Liu, R. Wang, C. Shi, (2014) Sharpness-based autofocusing for stripmap SAR using an adaptive-order polynomial model, *IEEE Geosciences and Remote Sensing Letters*, **11**, 1086-1090.

Marston, T.M. and D. S. Plotnick, (2015) Semiparametric Statistical Stripmap Synthetic Aperture Autofocusing, *IEEE Trans. on Geosc. and Remote Sensing*. **53**, 2086-2095.

Rennie, S.E, Brandt, A., and N. Plant (2007) A probabilistic expert system approach for sea mine burial prediction, *IEEE Journal of Oceanic Engineering*, **32**, 260-272.

Rennie, S.E, Brandt, A., and C.T. Friedrichs (2017), Initiation of motion and scour burial of objects underwater, *Ocean Engineering*, **131**, 282-294.

SERDP-ESTCP (2010). Munitions in the underwater environment: State of the science and knowledge. White paper, 16pps.

Wu, H., Zuniga Zamalloa, C.C., Landry, B.J., and M.H. Garcia (2019), Experimental comparison of initiation of motion for submerged objects resting on fixed permeable and impermeable beds, *Physical Review Fluids*, **4**, 013802.

FROM BASIC RESEARCH TO A PROTOTYPE TOWBODY PLATFORM: PROGRESS ON UNDERWATER UNEXPLODED ORDNANCE REMEDIATION

Kevin L. Williams, Steven G. Kargl, Aubrey L. Espana, Timothy Marston, Daniel S. Plotnick

Applied Physics Laboratory, University of Washington, 1013 NE 40th St., Seattle WA 98105-6698 USA

Steven G. Kargl, Applied Physics Laboratory, University of Washington, 1013 NE 40th St., Seattle WA 98105-6698 USA, FAX: 206-543-1300, kargl@uw.edu

Abstract: *Over the last decade, APL-UW has had an active basic research program to understand the physical mechanisms associated with the scattering of sound from objects near a water-sediment interface. Synthetic aperture sonar (SAS) data were collected during field measurements. A rail was deployed to the bottom, that allowed a mobile sonar tower to traverse an extended cross-range. Inert ordnance, scientific targets, and clutter objects were placed in the field of view. These data were used to validate high-fidelity models, which provided insight into various physical mechanisms observed in the data. Subsequently, the measured data, augmented by numerically simulated data, have been utilized in the development of detection and classification schemes. Our current effort is transitioning the knowledge gained in our basic research to an applied platform. The Multi-Sensor Towbody (MuST) is a prototype platform that integrates commercially available high-frequency side-scan (HF) and downward-looking, low-frequency (LF) sonars with our in-house signal processing package for detection, imaging and classification. The HF sonar provides high-resolution imagery of the water-sediment interface and any proud objects. The LF sonar offers detection depths of 1 to 2 meters (i.e., sand versus mud). This paper discusses the research that has led to design decisions for MuST. [Work supported SERDP, ESTCP, and ONR.]*

Keywords: *Multi-Sensor Towbody, Unexploded ordnance, Synthetic aperture sonar*

1. INTRODUCTION

The Applied Physics Laboratory at the University of Washington (APL-UW) has conducted basic research in the remediation of underwater unexploded ordnance (UXO) for nearly a decade. The primary focus has been the use of low-frequency (LF) synthetic aperture sonar (SAS) in the interrogation of objects near the water-sediment interface. This research included a two pronged approach of field experiments and numerical simulations to gain insight into the physical mechanisms that give rise to unique observable structure in data products derived from sonar data. Examples of data products are the coherent processing of the data to generate SAS images and conversion of data into acoustic colour (AC) templates (i.e., a coloured representation of absolute target strength as a function of frequency and aspect angle).

The transition of our basic research efforts to a prototype sonar platform is described in the remainders of the paper. Section 2 provides brief descriptions of the field experiments that provided data for model validation as well as training and testing data for approaches to the classification problem. Section 3 contains an overview of the numerical models that are used to gain insight into the underlying physical mechanism involved in the acoustic scattering from an object near a water-sediment interface. Signal processing is discussed in Sec. 4, where sonar data are converted to data products suitable for detection and classification schemes. The Multi-Sensor Towbody (MuST) is described in Sec. 5, and its current operational status is provided. Section 6 summarizes.

2. FIELD EXPERIMENTS

Our field experiments can be split into those conducted in a pristine fresh-water pond and those conducted at sea. Pond Experiment 2009 and 2010 (PONDEX09, PONDEX10) are well-controlled experiments where environmental influences (e.g., fish and fouling of objects) were absent. The at-sea field measurements are the Target and Reverberation Experiment 2013 (TREX13), Bay Experiment 2014 (BAYEX14), and the Clutter Experiment 2017 (CLUTTEREX17). These experiments are performed in open waters, and are subject to environmental factors (e.g., fish, shipping noise, weather events, etc.). The significance of each experiment is described below.

PONDEX09 and PONDEX10 were conducted in the test pond facility at the Naval Surface Warfare Center, Panama City Division. The pond is a chlorinated fresh-water pond offering a 17 m depth and medium-fine sand bottom (~1 m thick). A 21-m long rail was deployed, which gave a 19-m SAS aperture. Objects could be placed at 5 to 10 m horizontal ranges from the rail. Sonars were ~4 m above the water-sediment interface on a mobile tower, which moved at 5 cm/s. A sonar transmitted a linear-frequency-modulated (LFM) pulse every 0.5 s. The LFM pulses nominally covered the 1-4, 6-10, 12-28, 30-50, 60-100, and 110-190 kHz bands. PONDEX09 is the initial experiment where data were collected from an isolated UXO (~16-in length, 4-in diameter). Data were also collected from a solid 2:1 aluminum (AL) cylinder (i.e., 2-ft length, 1-ft dia.). The 2:1 AL cylinder has become a canonical reference target as its elastic response to an acoustic field is well understood. PONDEX09 provided proof-of-concept that LF SAS can address the underwater UXO remediation problem [1].

PONDEX10 expanded upon PONDEX09 in three important ways. First, a new sonar spanning the 1-30 kHz band replaced the LF sonars of PONDEX09; thereby increasing the amount of data collected by reducing the number of SAS data collection runs per object pose. Second, the number and types of objects were increased from the original UXO to include a 155-mm howitzer shell, 152-mm TP-T round, 82-mm finned mortar, solid AL and steel

replicas of the original UXO, two rocks of similar size (i.e., clutter), and the 2:1 AL cylinder. Third, six or more objects were placed in the field-of-view of the sonars. With multiple objects in a target field, techniques to isolate the scattering from a given object were required (see Sec. 4). Objects were again placed at 5 and 10 m horizontal ranges. Finally, a detailed description of PONDEX10 and the APL-UW rail-tower system is available in [1].

TREX13 represents a significant increase in the complexity of the experiment over that of the pond. First, this experiment was performed in the Gulf of Mexico south of Panama City, FL (~1 mile off shore). The sediment was a fairly flat medium-fine sand with a minor small-scale ripple field. Second, the rail was extended to a 42-m length with a usable 40-m SAS aperture. A 40×40 m^2 fixed grid was established in front of the rail. The SAS aperture allowed deployment of up to 30 objects in a target field with horizontal ranges from the rail of 5 to 40 m in 5 m increments. The primary frequency bands were 1-30, 30-50, and 110-190 kHz. With a water depth of ~17 m, maximum range of 40 m, and sonar height of ~4 m above the water-sediment interface, reflections from the air-water interface can be time-gated out of the data. Separation between adjacent objects was sufficiently large that multiple scattering can be ignored. Twenty-eight objects were available in TREX13 including 155-mm howitzer shells, 105-mm artillery shells with and without fins, the original UXO and its AL and steel replicas, the 2:1 AL cylinder, and a few clutter objects. Objects at the 5 m range were proud, partially buried, or fully buried. Objects at the 10 m range were either proud or partially buried. Objects were proud for all other ranges. Finally, the rail became an artificial reef in an otherwise flat underwater environment. Fish caused a significant increase in volume clutter.

BAYEX14 was conducted south of Panama City, FL in St. Andrew Bay, where the water is brackish with low visibility. The water depth was ~8 m, and the sediment consisted of a mud layer (15 to 30 cm thickness) over a sand subbottom. The 42-m length rail was again deployed with a 40×40 m^2 fixed grid. Horizontal ranges for object insertion coincided with those of TREX13. Objects from TREX13 were again used in BAYEX14. However, here, all objects were partially or fully embedded in the mud layer. For BAYEX14, two independent sonars simultaneously transmitted 1-30 and 110-190 kHz LFM pulses. The sonars were ~3.8 m above the subbottom (i.e., near mid water column). For the broad beamwidths of the sonars and horizontal ranges greater than a few water depths (e.g., > 20 m), reflections from the air-water interface cannot be neglected under calm conditions. Thus, environmental conditions of BAYEX14 presented a challenging increase in complexity.

CLUTTEREX17 returned to the site of TREX13. The 42-m long rail again was deployed, and simultaneous transmission of 1-30 and 110-190 kHz pulses were used during data collection. Here, the available objects increased to 68, where the inert UXO included 155-mm howitzer shells, 105-mm shells with and without fins, the 152-mm TP-T round, and the original UXO and its AL and steel replicas. Clutter objects included cement blocks, crab traps, lobster pots, boat anchors, small coolers, and rocks. In CLUTTEREX17, two types of experiments were conducted. First, 40×40 m^2 fixed grid was established, and targets were placed at locations similar to TREX13. Data were collected from targets only. Clutter objects then were inserted close to targets (i.e., typically < 1 m) and SAS data were recorded. Finally, targets were removed from the grid, and data were obtained for clutter objects only. The second type of experiment involved random target fields. Divers selected random objects and placed these object into a target field with random horizontal ranges and poses. Separation between adjacent objects in the initial target field was sufficient that the affect of one target on the acoustic target signature of another target was minimal. After data collection, divers were instructed to contract the target field where targets again have new random horizontal ranges and poses (i.e., target separation distances decrease). Contraction of the target field was repeated until the separation distance between neighbouring objects was ~1 m. Although the complexity of CLUTTEREX17 with respect to the environment is similar to that of TREX13, here an increase in complexity occurred due to the decreased separability of target acoustic signatures as the distance between targets is reduced.

3. NUMERICAL MODELS

Our experiments demonstrate that an acoustic response from an object depends on the environment and scattering geometry within that environment, so models must consider the target-in-the-environment. Two approaches to acoustic scattering from an object near the water-sediment interface have been pursued at APL-UW. These are the hybrid model and the target-in-the-environment response (TIER) model. Each is briefly described.

Many underwater UXO have cylindrical symmetry, which allows a decomposition of the full 3-D problem into a series of independent 2-D Fourier modal sub-problems. The hybrid model combines a 2-D finite-element (FE) model and a 3-D propagation model [1-3]. The 2-D FE model predicts the scattered pressure and derivatives on a discrete set of points closely surrounding an object. The pressure, derivatives, and an appropriate Green function are then used in a discrete form of the Helmholtz integral to propagate the scattered pressure to a distant receiver. The hybrid model is formulated in the frequency domain. As the hybrid model computes modal sub-problems, the modes of vibration of a target can be inspected. A superposition of the sub-problems, then allows one to obtain a complex-valued AC template. Thus, structure observed in an AC template can be directly attributed to an elastic response of the target in the environment.

Although advances in hardware and algorithms provide a reduction in the computational complexity of the hybrid model, it is still limited when large sets of data are required. The TIER model retains the high-fidelity of the hybrid model while providing a significant reduction in computation time. It combines an acoustic ray model for propagation and far-field scattering from an object in the free field (i.e., no boundaries) [4]. For the ray model, source and receiver are reflected through the boundaries of the waveguide to give a set of image sources and receivers. This effectively removes the boundaries and converts the scattering problem into a superposition of free-field scattering problems. Rays, associated with a source and its images, are scattered from an object. Scattered rays then propagate to the receiver and its images. Superposition of scattered rays yields the spectrum of the scattered pressure. Inverse Fourier transformation of the spectrum gives a time-domain signal (i.e., a sonar ping). The far-field scattered pressure has the form $p_s(\omega) = S(\boldsymbol{k}_i,\boldsymbol{k}_s,\omega)\exp(-i\omega t)/r$, where r is distance to a field point, the angular frequency is ω, and t is time. The scattering amplitude, $S(\boldsymbol{k}_i,\boldsymbol{k}_s,\omega)$, is a function of incident and scattered wave vectors $\boldsymbol{k}_i$ and $\boldsymbol{k}_s$ as well as ω. The scattering amplitude contains all of the information about an object (e.g., material properties) and the directionality of the scattered pressure. The hybrid model provided scattering amplitudes for the 2:1 and 3:1 AL cylinder, 155-mm howitzers, 105-mm artillery shells, AL and steel replicas of the original 4-in UXO, 2:1 open-ended AL pipe, and an oil drum. Comparisons to data and hybrid model results were used in the validation of the TIER model.

4. SIGNAL PROCESSING

Our signal processing steps include calibration, target isolation, and conversion of time-domain data to calibrated data products suitable for our classification schemes. Prior to an experiment, through-the-system calibrations of the sources, receivers, and electronics are performed. The calibration accounts for transmitter voltage response, receiver sensitivity, and characteristics of the electronic components (e.g., amplifier frequency response). Measured replicas of transmitted LFM pulses then are used during the pulse compression of the recorded data, where the system response is removed to give calibrated data. Target isolation and data products are then derived from the calibrated data as described in the following.

Although the rail provides a stable platform for the mobile tower to traverse, small-scale perturbations to straight-line motion occur. The small-scale motion causes a slight blurring in the SAS images, and affects HF SAS images more than LF images. A recent advancement in autofocusing of stripmap SAS images uses a collection of point-like glints and statistical metrics on contrast or sharpness to optimize for a phase correction [5]. This approach is applied to our HF data to obtain a phase correction. Simultaneous transmission of the LF and HF LFM pulses during BAYEX14 and CLUTTEREX17 allows for co-registration of LF and HF SAS images. Thus, HF phase correction can be applied to the LF SAS data.

Target isolation is performed by either synthetic aperture decomposition (SAD) [6] or holographic back-projection [7]. Both methods are essentially a spatial filtering of the data. The left panel in Fig. 1 shows an example of the isolated time signals after applying the SAD algorithm to data collected during TREX13 for a 2:1 AL cylinder. For SAD, an ω-k SAS algorithm converts the calibrated time-domain data into a complex-valued SAS image. A small region within the SAS image is preserved while all other parts are masked. Inverse SAS processing then converts the isolated portion of the SAS image back into the time-domain. With compensation for geometric spreading loss, the magnitude of the complex-valued SAS image is the absolute target strength (TS). The right panel is the full 360° AC template constructed from nine poses of the cylinder that span $-90° \leq \theta \leq 90°$.

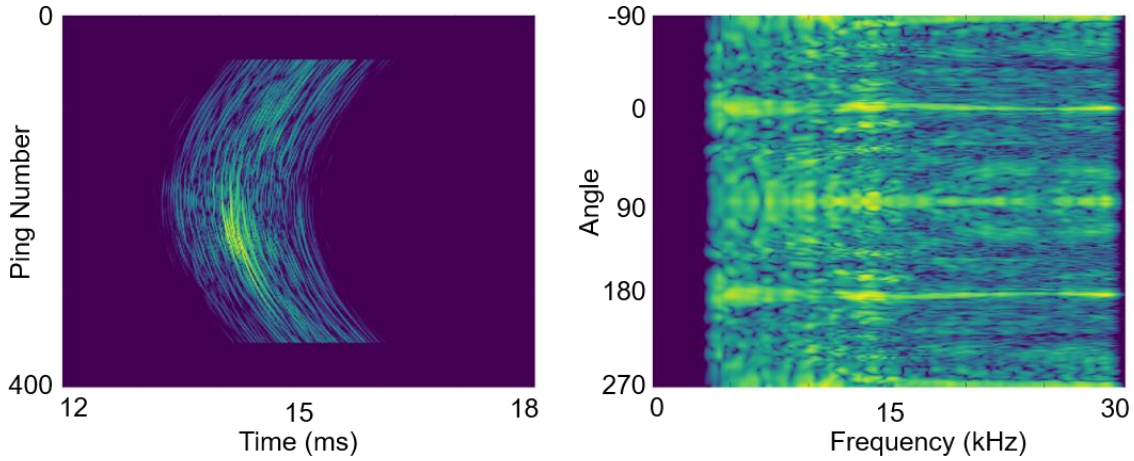


Fig. 1 Left: Time signature for scattering from a 2:1 AL cylinder. Right: Full AC template for the same cylinder. The data are from TREX13 with the cylinder at ~10 m range. The pings shown on the left correspond to approximately $-20° < \theta < 20°$ in the AC template.

The primary data products that we have used in our classification studies convert the time-domain data into AC templates. An AC template is the target strength as a function of target-centred aspect angle, θ, and frequency, f. For an axisymmetric target, an AC template spans $0° \leq \theta \leq 180°$ and $3 \leq f \leq 30$ kHz, where we typically have a 721×151 matrices. Three approaches have been developed. The first uses a template-matching scheme, based on cross-correlations of portions of AC templates (e.g., 40°×30 kHz or 81×151 matrix) and a relevance vector machine (RVM) classifier [8]. The second approach reduces the AC templates by an energy-based argument, where an AC template essentially is integrated over angular swaths and/or frequency bins [9]. Typically, this reduces the dimensionality of the data product from 81×151 to 1×18. The energy-based data products have been used with several classifiers available within MatLab™. The third approach trains a Gaussian mixture model (GMM) for each object, where individual angular values are randomly selected from its AC template (i.e., angular information within an AC template is lost) [10]. The GMM can be grouped to provide target vs non-target classification as well as be used in a multi-class situation to

distinguish one type of target from another (e.g., a 105-mm shell versus a 155-mm shell). Detailed discussion of the classification schemes is beyond this paper.

5. MULTI-SENSOR TOWBODY (MuST)

A limited-scope design study for an applied system was completed in 2016 [11], where it was determined that a towed platform was a cost-efficient option. The initial design includes both LF and HF sonars with additional electrical and communication capacity to support other sensors (e.g., magnetometers and optical devices). To reduce financial risk, the number of subsurface components is minimized such that the towboy control, signal generation, data collection, and data quality assessment are contained within a shipboard package. The left panel in Fig. 2 is an engineering design for the MuST displaying the LF source and receiver and the HF sonar. The right panel in Fig. 2 is a MacArtney Underwater Technology towbody, which was delivered to APL-UW in February 2019. The HF sonar is an EdgeTech 2205 side-scan sonar that can operate at 540 kHz and 1.6 MHz (giving sub-centimetre resolution for proud objects and sediment interface topology). The LF eBOSS sonar, also an EdgeTech product, is composed of one or more spherical radiators (5-35 kHz band width) and a 64-channel receiving array. Operationally, the eBOSS is a downward looking sonar, which offers ~1 m penetration into a sand sediment (~2 m for mud) for the detection of buried targets. Each channel of the receiving array is individually recorded. The shipboard package offers near real-time processing. It is anticipated that a 3-D image resolution of a 10×10×10 cm^3 voxel can be obtained with the eBOSS.

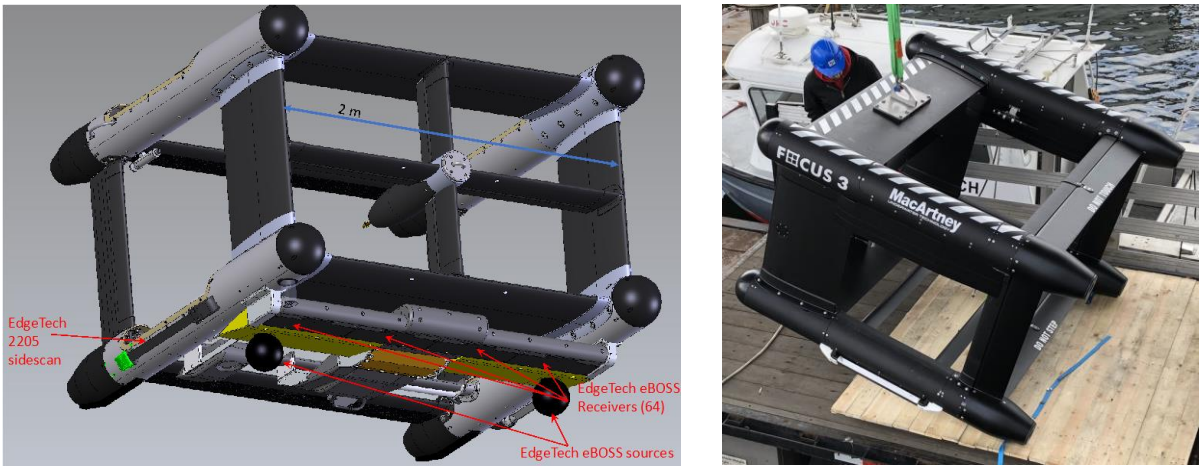


Fig. 2. Left: Engineering drawing of the MuST. Right: The MacArtney Focus 3 towbody. The LF omnidirectional sources and receivers comprise the EdgeTech eBOSS. The HF sonar is an EdgeTech 2205.

The MuST is designed to operate at a 5 m altitude above the water-sediment interface with a 100-200 m layout behind the ship. This altitude gives an ~19 m swath width for the eBOSS and ~30 m swath width for the HF side-scan sonar. Full coverage of an area of interest can be obtained with a mow-the-lawn survey and 15-m track spacing. An approximate area coverage rate of 0.1 km^2/hr is expected for a ship moving at 4 knots, where it is estimated that ~1 km^2 takes about 20 hr due to the necessary time for turning with a 200 m layout.

An initial wet test in Lake Washington and Puget Sound found that simple geo-location from reciprocal time-of-flight measurement and a 150 m layout gave ~3 m resolution with respect to absolute GPS geo-location. During the initial wet test, only the HF side-scan sonar was available. Data were collected for both the 540 kHz and 1.6 MHz frequencies. The eBOSS has been delivered to APL-UW and is currently undergoing calibration. A second test

is planned for Lake Washington in July 2019 where a single 2:1 AL cylinder will be deployed. Both LF and HF data are to be collected. The first test of MuST in an operational UXO remediation scenario is scheduled for September 2019 in Sequim Bay, WA. In this demonstration, two identical sets of objects will be deployed with one set placed in a sandy environment and one set placed in a muddy/silty environment. Each set will contain UXO (e.g., 155-mm howitzer), reference targets (e.g., 2:1 AL cylinder), and clutter objects (e.g., discarded scuba tanks).

6. SUMMARY

The transition of our basic research efforts into an applied platform to assist in UXO remediation is an on-going effort. The data collected from the five field experiments have been, and continue to be, used in validating two numerical models for target scattering. The numerical models then allow us to unravel the underlying target scattering physics by isolating mechanisms that lead to observable structure in data products derived from data. Both experimental data and simulated data were used in the training and testing of three approaches to classification. Each of these classification schemes have been integrated into software, which can be used for post mission analysis of a UXO remediation activity.

7. ACKNOWLEDGEMENTS

The research reported was jointly funded by the Strategic Environmental Research and Development Program (SERDP), the Environmental Security Technology Certification Program (ESTCP), and the Office of Naval Research (ONR). The experimental efforts were conducted in collaboration with the Naval Surface Warfare Center, Panama City Division. Both MacArtney and EdgeTech have been instrumental in overall MuST system definition and implementation.

REFERENCES

[1] **KL Williams, SG Kargl, EI Thorsos, DS Burnett, JL Lopes, M Zampolli, and PL Marston,** Acoustic scattering from a solid aluminum cylinder in contact with a sand sediment: Measurements, modeling, and interpretation, *J. Acoust. Soc. Am.*, 127, pp. 3356-3371, 2010.

[2] **M Zampolli, A Tesei, G Canepa, and OA Godin,** Computing the far field scattered or radiated by objects inside layered fluid media using approximate green's functions, *J. Acoust. Soc. Am.*, 123, pp. 4051-4058, 2008.

[3] **M Zampolli**, **AL España**, **KL Williams, SG Kargl, EI Thorsos, JL Lopes, JL Kennedy, and PL Marston**, Low- to mid-frequency scattering from elastic objects on a sand sea floor: simulation of frequency and aspect dependent structural echoes, *J. Comp. Acoust.*, 20, p. 1240007 (14 pp.), 2012, DOI: 10.1142/S0218396X12400073.

[4] **SG Kargl, AL Espana, KL Williams, JL Kennedy, JL Lopes**, Scattering from objects at a water sediment interface: Experiment, high-speed and high-fidelity models, and physical insight, *IEEE J. Ocean. Eng.*, 40, pp. 632-642, 2015.

[5] **TM Marston, DS Plotnick**, Semiparametric Statistical Stripmap Synthetic Aperture Autofocusing, *IEEE Trans. Geo. Remote Sensing.*, 53, pp. 2086-2095, 2015.

[6] **TM Marston, PL Marston, KL Williams**, Scattering resonances, filtering with reversible SAS processing, and applications of quantitative ray theory, In *Proc. 2010 OCEANS MTS/IEEE SEATTLE*, p. 9pp, 2010, DOI: 10.1109/OCEANS.2010.5664606.

[7] **DJ Zartman, DS Plotnick, TM Marston, PL Marston,** Quasi-holographic processing as an alternative to synthetic aperture sonar, *Proc. Mtgs on Acoust.,* 19, 5pp, 2013, DOI: 10.1121/1.4800881.

[8] **ME Tipping**, Sparse Bayesian Learning and the Relevance Vector Machine, *J. Mach. Learn. Res.*, 1, 211-244 (2001).

[9] **KL Williams, SG Kargl, AL España**, Use of time, space, frequency, and angle data products in understanding target-in-the-environment scattering physics, *J. Acoust. Soc. Am.*, 143, 1854, 2018.

[10] **CM Bishop**, Pattern Recognition and Machine Learning, (Springer, NY, 2006), Ch. 9. Sec. 2.

[11] **KL Williams**, Limited Scope Design Study for Multi-Sensor Tow Body, 2016, https://www.serdp-estcp.org/Program-Areas/Munitions-Response/Munitions-Underwater/MR-2501/MR-2501

ACOUSTIC-COLOR-BASED CONVOLUTIONAL NEURAL NETWORKS FOR UXO CLASSIFICATION WITH LOW-FREQUENCY SONAR

David P. Williams

NATO STO Centre for Maritime Research and Experimentation (CMRE), La Spezia, Italy
email: david.williams@cmre.nato.int

Abstract: ***In this work, we contribute a new target classification approach for low-frequency sonar data. More specifically, we illustrate the feasibility of using convolutional neural networks (CNNs) trained on acoustic-color data, a representation that expresses target strength as a function of object aspect and frequency. We show that it is possible, using only limited amounts of this sonar data, to design and train efficient networks with low capacity that avoid overfitting and generalize robustly, even to new objects not seen during training. We demonstrate this in the context of an unexploded ordnance (UXO) classification task using real, measured sonar data collected at sea.***

Keywords: ***Convolutional neural networks (CNNs), acoustic color, sonar, unexploded ordnance (UXO).***

1. Introduction

When an object is ensonified with low-frequency sonar, the response contains contributions resulting from geometric scattering as well as elastic effects due to the excitation of structural waves that are intimately linked to the material properties of the object [1]. Conventional wisdom maintains that these special phenomena should be valuable for underwater object classification tasks seeking to discriminate particular man-made targets of interest, such as unexploded ordnance (UXO), from other benign objects.

A popular display format that reveals these characteristic signatures is an acoustic-color plot, which is a two-dimensional representation showing target strength as a function of object aspect and frequency [2, 3]. Although angular and frequency dependent scattering clues are observable in this domain, the complicated wave phenomena involved in the process, and especially the complex interactions with the environment [4, 5], make data interpretation challenging.

Interesting investigations have begun isolating individual waves and effects for certain canonical objects [5, 6], but a comprehensive understanding and explanation of such data has not yet been attained. As a result, it has proven exceedingly difficult to define and extract robust acoustic-color-based features that can reliably discriminate objects. That is, manual feature-engineering for acoustic-color data remains an open problem. But it is for precisely this same reason that convolutional neural networks (CNNs) are a perfect match for acoustic-color "imagery." Because CNNs automatically learn the most useful bases in which to represent the data, the extraction of predefined features is obviated.

A standard CNN [7] is a sequence of convolutional layers, nonlinear activation functions, and pooling operations that collectively transform input data (*i.e.,* imagery) into a new representation space in which the classes are easily separable. This work demonstrates the feasibility of using CNNs, trained with only modest amounts of low-frequency acoustic-color data, for UXO classification. This is achieved by recognizing that a crucial quantity in determining the success of CNNs for classification tasks is not the amount of training data *per se*, but rather the relationship between training data and network capacity. As the capacity of a CNN – loosely speaking, the number of free trainable parameters in the model – grows, so too do the training data requirements. Therefore, when faced with extremely limited training data, it is imperative to constrain the CNN's capacity by designing small, efficient networks. In this work, we show that it is possible to design acoustic-color-based CNNs with low capacity that avoid overfitting and generalize robustly, even to new objects not seen during training.

Other studies have explored the use of high-frequency synthetic aperture sonar (SAS) image-based CNNs [8–11], but we are the first to successfully employ low-frequency *acoustic-color* data as input to a CNN. Prior work [12–14] that has attempted to use acoustic-color data for classification has relied on using features derived from template-matching and correlation-based methods. But these approaches have a fundamental shortcoming that make them scale impractically and generalize poorly. To wit, one will never possess data for the entire universe of clutter (*i.e.,* non-UXO) objects, and it is also not feasible to collect sufficient data that encompasses the full variability of the target class, given that the acoustic-color signatures will exhibit a strong dependence on object range, seafloor sediment properties, burial conditions, and UXO decay state. As a result, these correlation-reliant approaches can succeed only when data for a given test object – and collected in very similar conditions – is also present in the training set. For real-world UXO remediation, this assumption is unrealistic.

The remainder of this paper is organized as follows. In Sec. 2, we present our acoustic-color-based CNN framework. Experimental results of the proposed approach on an object classification task using measured sonar data are shown in Sec. 3. Concluding remarks are made in Sec. 4.

2. Acoustic-Color-Based CNN

2.1. CNN Data-Preparation

Low-frequency sonar data were collected on various UXO and non-UXO objects during the Target and Reverberation Experiment 2013 (TREX13) in the Gulf of Mexico using a rail system [15]. More specifically, data were collected over the frequency band 3-30 kHz for 27 unique objects at ranges 10-40 m on a sandy seafloor.

Each individual data-collection run provided along-track-versus-time scattering data over only a certain aspect (*i.e.,* orientation) span, so multiple runs were executed. For a given object, the raw sonar data was transformed and the results then stitched together [12] to form a full 360° acoustic-color data product expressing target strength as a function of object aspect and frequency. This data has a discretization of 0.5° in aspect and 100 Hz in frequency, meaning a full acoustic-color plot is an "image" – in the general sense of values organized as a two-dimensional array – of size 720 pixels $\times$ 271 pixels. A total of 90 such acoustic-color plots were produced, 54 corresponding to UXO objects (11 unique objects at various ranges) and 36 corresponding to non-UXO objects (16 unique objects at various ranges).

We divide this data into disjoint training and test sets *by object type*, meaning data for a given object exists either only in the training set (13 objects) or only in the test set (14 objects). *This separation is vital because it will allow for true generalization ability of the CNNs to be assessed properly,* a shortcoming of earlier acoustic-color-based classification experiments.

The set of UXO objects in the training set (using the TREX13 nomenclature [12]) include: 155 mm howitzer without collar, 152 mm TP-T, aluminum UXO replica, bullet #1, finned shell #1. The set of non-UXO objects in the training set include: DEU trainer; rock; 55-gallon drum, water-filled with fixture; scuba tank, water-filled, without stem; 2:1 aspect telephone pole section; 2′ aluminum pipe; solid aluminum cylinder with notch; hollow aluminum cylinder with notch. The objects in the test set are listed later in Table 4. Based on the data division imposed, 47 acoustic-color plots (29 UXO, 18 non-UXO) comprise the training set, and 43 acoustic-color plots (25 UXO, 18 non-UXO) comprise the test set. It is worth reiterating that the objects available for training are distinct from those reserved for testing.

To maximize the amount of data for CNN training, each acoustic-color plot is converted into 720 unique (but highly correlated) images in which each image spans the full frequency band. The aspect span of each image is $[\theta_c - \theta/2, \theta_c + \theta/2]$, so each image is of size $(2\theta + 1) \times 271$, and the images are distinguished by the center aspect θ_c. We construct distinct data sets for $\theta = \{10^\circ, 30^\circ, 40^\circ, 90^\circ\}$ so that the impact of data aspect span on CNN performance can be analyzed. Each data set is then further augmented by a factor of 2 by reversing the order of the data aspects (*i.e.,* vertically flipping the acoustic-color data), which is physically justified given the data-collection geometry. The effect of all of the above data augmentation was that the original 90 acoustic-color plots were transformed into a training set of 67680 images and a test set of 61920 images; the images are unique but many contain highly redundant information. (This is another reason it is imperative to create the training/test division by *object*

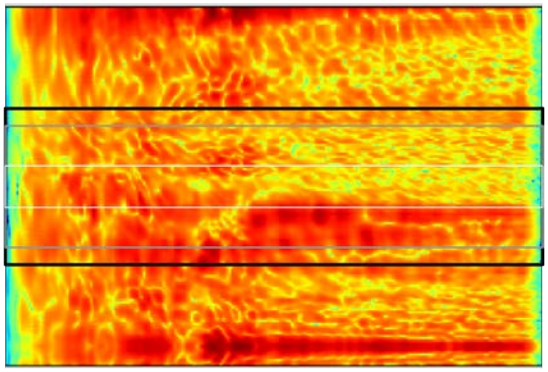


Figure 1: Example input data to the CNNs of a 3′ aluminum cylinder (object 7), centered about an aspect of 229° at a range of 30 m, when the data spans 90° (entire image), 40° (delineated by the black box), 30° (gray box), and 10° (white box). The x-axis corresponds to frequency, from 3 kHz to 30 kHz; the y-axis indicates aspect.

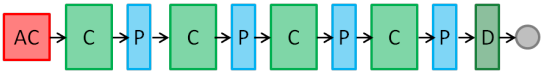


Figure 2: General CNN architecture for acoustic-color data inputs. *C*, *P*, and *D* denote convolution *blocks* (comprising one or more convolutional layers), pooling layers, and dense layers, respectively. (The specific architecture shown, with 4 convolution blocks, corresponds to CNNs G-I.)

type.) Example input data to the CNNs for different θ are shown in Fig. 1.

2.2. CNN Design

We carefully design 9 CNN architectures, whose common high-level schematic is shown in Fig. 2. Each CNN contains between 2 and 4 convolution blocks; each block contains an identical number of convolutional layers (between 1 and 3, depending on CNN). Only 4 filters are used in each convolutional layer. ReLU activations are used after each convolutional layer, while a sigmoid activation is used at the output. All pooling layers use average pooling; with an eye toward generalizability and limiting the number of free parameters, aggressive (*i.e.,* large) pooling factors – as high as 8 – are employed. The filter sizes vary for each CNN, but are typically on the order of a few pixels in each dimension. The number of nodes contained in the dense layer is either 12 (CNNs A-C) or 4 (CNNs D-I). Space constraints prevent us from giving more specific details (*e.g.,* filter sizes and pooling factors) about each CNN.

A CNN is designed for specific input-data dimensions (*i.e.,* number of rows and columns of pixels). When dealing with the acoustic-color data, however, the size of the input data will vary as a function of the aspect span considered. Specifically, the size of the input image will be $(2\theta + 1) \times 271$ for data spanning θ aspect degrees. Rather than re-sizing the imagery (*e.g.,* via interpolation) to the largest aspect span considered, which could introduce artifacts and would increase computational effort during training, we instead design a unique CNN architecture for each input-data aspect span considered.

Nevertheless, the CNN architectures are designed to be as similar as possible for different θ. For a given CNN architecture, the same column-wise filter sizes and pooling factors are used regardless of θ (since this dimension is not affected by θ). The row-wise pooling factors for a

given CNN are generally kept identical across different θ, while the row-wise filter sizes scale roughly linearly with θ.

For input data spanning $\theta = [10^\circ, 30^\circ, 40^\circ, 90^\circ]$, the mean number of free parameters of the 9 CNNs are $n = [665, 1406, 1833, 3795]$. This should be contrasted with popular (optical-image) CNNs commonly used "off-the-shelf" that each contain more than 10^6 parameters. (The sensing modality and image properties of acoustic-color data are so fundamentally different from optical photographs that transfer is not a feasible approach.)

The capacities of our CNNs are intentionally kept so low in order to scrutinize the feasibility of using CNNs when faced with modest amounts of training data. That is, we purposely constrain the networks in an attempt to force them to learn robust filters that will generalize across object class and operating conditions.

2.3. CNN Training

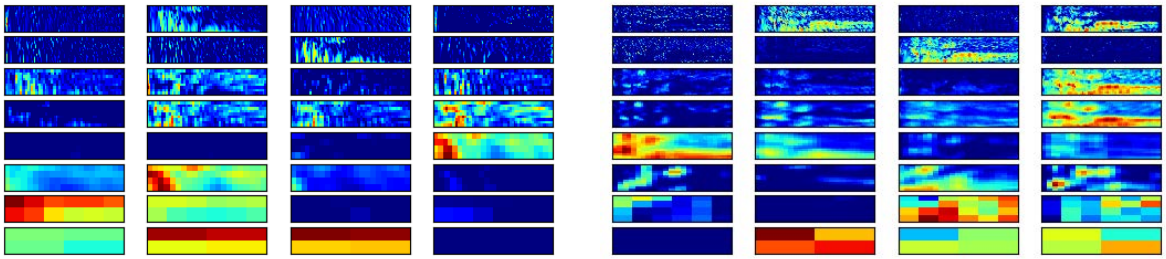
Each raw acoustic-color "image," $\mathbf{A}$, was normalized as $\mathbf{A}' = (\mathbf{A} - 80)/50$ to scale the pixel values approximately into the range $[-1, 1]$. CNN training was performed using the RMSprop optimizer with a learning rate of 0.001, in conjunction with a binary-cross-entropy loss function, until the loss on the training set converged. A batch size of 128 was used, with equal numbers selected from each class. No attempt was made to optimize the learning rate or batch size. The final prediction for a test image was taken as the ensemble (mean) of the predictions on the standard and aspect-reversed input data.

3. Experimental Results

Experiments were conducted to assess the feasibility of employing CNNs with acoustic-color sonar data for discriminating UXO from non-UXO when possessing extremely limited training data. Classification performance is measured in terms of the area under the curve (AUC). Because an auxiliary goal of this work is to enable better understanding of the factors impacting classification success, we also examine performance as a function of various conditions.

Table 1 presents the performance of the 9 CNN architectures for input data sizes of $\theta = \{10^\circ, 30^\circ, 40^\circ, 90^\circ\}$. Performance as a function of object range, object center-aspect, and object type is shown in Tables 2, 3, and 4, respectively. For the latter, the AUC values correspond to the binary-classification task of discriminating one given object from all objects in the opposite class (the first eight objects in the table belong to the non-UXO class). There are numerous interesting findings from these results.

One of the most remarkable results from Table 1 is that CNN G when using only 10° input data was actually the single most powerful classifier. (It may be germane to note that the beamwidth of dolphin biosonar has been measured to be 10° [16].) The architectures corresponding to CNNs B, D, and G appeared to be the most robust, reliably providing decent performance across different input data aspects. But importantly, employing the ensemble of 9 CNNs consistently improved performance. This valuable result implies that one need not select a single best CNN architecture, but rather that drawing from the unique representations of the individual networks collectively provides superior classification performance. The improvement with larger input data aspect spans is also evident when using the ensemble.



(a) 10° input data (b) 40° input data

Figure 3: For the data from Fig. 1, the intermediate responses after each convolutional layer (layer-wise by row) of CNN H.

Table 2 shows that classification performance of objects at short range (*e.g.,* 10-20 m) improves dramatically as wider aspect span data is available. This finding has useful implications for data-collection strategies.

In Table 3, it can be seen that objects interrogated at certain sets of aspects, namely $[-60°, 0°)$ and $[180°, 240°)$, which are just off-broadside, become classified much more accurately as the aspect span of data increases. It is possible that more prominent elastic effects are present at those aspects. Slightly off-endfire aspects, namely $[-90°, -60°)$ and $[240°, 270°)$, appear to contain the most discriminatory information even over short aspect spans. Interestingly, these aspects comport with the sensing strategy of marine mammals [17, 18].

Table 4 reveals that the $3'$ aluminum cylinder (object 7) was easily discriminated from the UXO targets with only 10° aspect data, whereas classifying the $2'$ aluminum cylinder (object 17) was challenging. This particular finding suggests that object length information is present even in small spans of aspect. By examining the intermediate responses of the 10° aspect CNNs for the $3'$ aluminum cylinder, one can hopefully discover and isolate interpretable, physics-based clues that will lead to increased understanding of the low-frequency phenomenology. For example, for the cylinder data of Fig. 1, it can be seen via the intermediate-layer CNN responses in Fig. 3 (a) that a certain (lower) frequency band appears to contain the discriminatory information that is keyed on to enable the correct classification of the non-UXO object. Comparing Fig. 3 (a) and (b), it is also evident that different features are being leveraged depending on the aspect data provided as input to the CNN.

4. Conclusion

The feasibility of using CNNs trained on low-frequency sonar acoustic-color data was demonstrated. It was shown that powerful classifiers could be constructed even from limited training data if the network capacity is intentionally constrained. To perform an honest assessment of algorithm generalizability, we invoked a proper, realistic split of data in which the objects in the training set and test set were disjoint. Future work will attempt to link the discriminatory features isolated in intermediate representations of the CNNs with physics-based phenomena. A preliminary analysis of performance revealed potential clues to pursue.

Table 1: AUC for CNNs of the given input data size

	Input Data			
	10°	30°	40°	90°
CNN A	0.7302	0.7503	0.7975	0.7063
CNN B	0.8491	0.8485	0.8007	0.8091
CNN C	0.7826	0.7510	0.7987	0.6273
CNN D	0.8189	0.8615	0.8321	0.8172
CNN E	0.7775	0.8159	0.8005	0.8002
CNN F	0.8496	0.7813	0.7353	0.8227
CNN G	0.8886	0.8128	0.8037	0.8633
CNN H	0.8085	0.7931	0.8395	0.6561
CNN I	0.7620	0.8287	0.7354	0.8313
$\mathcal{E}$(A-I)	0.8534	0.8754	0.8985	0.9198

Table 2: AUC for ensemble of 9 CNNs of the given input data size, as a function of object range

	Input Data			
Range	10°	30°	40°	90°
[10 m, 15 m)	0.5739	0.5949	0.5573	0.7595
[15 m, 20 m)	0.6859	0.8058	0.7809	0.8290
[20 m, 25 m)	0.9187	0.8874	0.8914	0.9500
[25 m, 30 m)	0.7914	0.8388	0.8871	0.9292
[30 m, 35 m)	0.8863	0.9000	0.9678	0.9877
[35 m, 40 m)	0.9984	0.9988	1.0000	1.0000

Table 3: AUC for ensemble of 9 CNNs of the given input data size, as a function of object center-aspect (0° is broadside)

Center	Input Data			
Aspect	10°	30°	40°	90°
$[-90°, -60°)$	0.9237	0.9263	0.9428	0.9197
$[-60°, -30°)$	0.8155	0.8634	0.8941	0.9271
$[-30°, 0°)$	0.8431	0.9010	0.9007	0.9680
$[0°, 30°)$	0.8835	0.8950	0.9518	0.9400
$[30°, 60°)$	0.8013	0.8180	0.8515	0.8637
$[60°, 90°)$	0.8585	0.8674	0.8502	0.8964
$[90°, 120°)$	0.8589	0.8691	0.8517	0.8962
$[120°, 150°)$	0.8015	0.8183	0.8500	0.8639
$[150°, 180°)$	0.8828	0.8925	0.9511	0.9383
$[180°, 210°)$	0.8448	0.9030	0.9024	0.9682
$[210°, 240°)$	0.8145	0.8622	0.8935	0.9273
$[240°, 270°)$	0.9222	0.9255	0.9427	0.9201

Table 4: AUC (object vs. opposite class) for ensemble of 9 CNNs of the given input data size, as a function of object type

	Input Data			
Object Index – Description	10°	30°	40°	90°
5 – 5:1 aspect telephone pole section	0.865	0.895	0.920	0.940
6 – 55-gallon drum, water-filled	0.993	0.996	0.999	0.995
7 – 3′ aluminum cylinder	0.990	0.997	0.998	0.986
10 – panel target	0.779	0.791	0.896	0.925
14 – scuba tank, water-filled, w/ stem	0.741	0.842	0.881	0.939
17 – 2′ aluminum cylinder	0.550	0.535	0.534	0.686
18 – cement block	0.787	0.882	0.795	0.839
19 – tire	0.920	0.778	0.766	0.678
8 – 155 mm howitzer w/o collar	0.781	0.826	0.865	0.924
12 – 81 mm mortar	0.851	0.815	0.825	0.888
21 – steel UXO replica	0.881	0.900	0.910	0.916
22 – original material UXO	0.873	0.876	0.888	0.905
28 – 155 mm howitzer w/ collar	0.834	0.878	0.920	0.901
29 – bullet #2	0.924	0.942	0.967	0.979

5. Acknowledgments

The author thanks Kevin Williams at the University of Washington Applied Physics Laboratory for providing the TREX13 data. This work was supported by the Strategic Environmental Research and Development Program (SERDP).

REFERENCES

[1] D. Plotnick and T. Marston. Utilization of aspect angle information in synthetic aperture images. *IEEE Transactions on Geoscience and Remote Sensing*, 56(9):5424–5432, 2018.

[2] S. Kargl, K. Williams, T. Marston, J. Kennedy, and J. Lopes. Acoustic response of unexploded ordnance (UXO) and cylindrical targets. In *Proc. IEEE OCEANS*, pages 1–5, 2010.

[3] D. Plotnick, P. Marston, K. Williams, and A. España. High frequency backscattering by a solid cylinder with axis tilted relative to a nearby horizontal surface. *The Journal of the Acoustical Society of America*, 137(1):470–480, 2015.

[4] K. Williams, S. Kargl, and A. España. TREX13 target experiments and case study: Comparison of aluminum cylinder data to combined finite element/physical acoustics modeling. *The Journal of the Acoustical Society of America*, 136(4):2111–2111, 2014.

[5] S. Kargl, A. España, K. Williams, J. Kennedy, and J. Lopes. Scattering from objects at a water-sediment interface: Experiment, high-speed and high-fidelity models, and physical insight. *IEEE Journal of Oceanic Engineering*, 40(3):632–642, 2015.

[6] A. España, K. Williams, D. Plotnick, and P. Marston. Acoustic scattering from a water-filled cylindrical shell: Measurements, modeling, and interpretation. *The Journal of the Acoustical Society of America*, 136(1):109–121, 2014.

[7] Y. LeCun, Y. Bengio, and G. Hinton. Deep learning. *Nature*, 521(7553):436, 2015.

[8] D. Williams. Underwater target classification in synthetic aperture sonar imagery using deep convolutional neural networks. In *Proceedings of ICPR*, 2016.

[9] D. Williams. Demystifying deep convolutional neural networks for sonar image classification. In *Proceedings of the Underwater Acoustics Conference*, 2017.

[10] M. Emigh, B. Marchand, M. Cook, and J. Prater. Supervised deep learning classification for multi-band synthetic aperture sonar. In *Proc. SAS/SAR*, volume 40, pages 140–147, 2018.

[11] N. Warakagoda and Ø. Midtgaard. Transfer-learning with deep neural networks for mine recognition in sonar images. In *Proc. SAS/SAR*, volume 40, pages 115–122, 2018.

[12] S. Kargl. Acoustic response of underwater munitions near a sediment interface: Measurement model comparisons and classification schemes. Technical report, SERDP Project MR-2231, April 2015.

[13] M. Azimi-Sadjadi. Multichannel detection and acoustic color-based classification of underwater UXO in sonar. Technical report, SERDP Project MR-2416, Sept. 2015.

[14] J. Hall, M. Azimi-Sadjadi, and S. Kargl. Underwater UXO classification using matched subspace classifier with synthetic sparse dictionaries. *Proc. IEEE OCEANS*, pages 1–9, 2016.

[15] K. Williams, S. Kargl, E. Thorsos, D. Burnett, J. Lopes, M. Zampolli, and P. Marston. Acoustic scattering from a solid aluminum cylinder in contact with a sand sediment: Measurements, modeling, and interpretation. *The Journal of the Acoustical Society of America*, 127(6):3356–3371, 2010.

[16] W. Au. *The sonar of dolphins*. Springer Science & Business Media, 2012.

[17] W. Evans and B. Powell. Discrimination of different metallic plates by an echolocating delphinid. In *Animal Sonar Systems: Biology and Bionics*, volume 78, pages 363–382, 1967.

[18] P. Moore, S. Martin, and L. Dankiewicz. Investigation of off-axis detection and classification in bottlenosed dolphins. In *Proc. IEEE OCEANS*, volume 1, pages 316–319, 2003.

COMPARISON OF SYNTHETIC APERTURE SONAR IMAGES AND OPTICAL IMAGES OF UXOS FROM THE SKAGERRAK CHEMICAL MUNITIONS DUMPSITE

Roy Edgar Hansen, Marc Geilhufe, Erik Makino Bakken, Torstein Olsmo Sæbø

Norwegian Defence Research Establishment (FFI), P O Box 25, NO-2027 Kjeller, Norway

Contact author: Roy Edgar Hansen
Norwegian Defence Research Establishment (FFI) P O Box 25, NO-2027 Kjeller, Norway
Fax: +47 63 80 75 09, E-mail: Roy-Edgar.Hansen@ffi.no

Abstract: *After World War II chemical munitions were loaded onto large ships and sunk in the Skagerrak Strait in the Norwegian trench, in deep waters between Norway and Denmark. In collaboration with the Norwegian Coastal Administration, Norwegian Defence Research Establishment (FFI) conducted two separate missions in 2015 and 2016, where around 450 square kilometers were mapped using a HUGIN autonomous underwater vehicle (AUV) equipped with a HISAS interferometric synthetic aperture sonar (SAS). 54 wrecks were found, and 36 of these are believed to be part of the chemical munitions dumpsite. Many shipwrecks have suffered severe damage, and their cargo is spread out around the shipwrecks. In January 2019, FFI revisited the Skagerrak dumpsite for additional data collection using the HUGIN AUV with SAS and an optical camera. Multiple wrecks were revisited, and SAS images and optical images of unexploded ordnances (UXO) were gathered. In this paper, we compare SAS images with optical images of UXOs. We assess the retrievable information present in high resolution large area coverage rate SAS images by comparing separate objects and their conditions as seen with optical camera.*

Keywords: *Synthetic aperture sonar, Optical Imaging, Unexploded Ordnance*

1. INTRODUCTION

After World War II, a substantial amount of chemical munitions were loaded onto large ships and sunk in the Skagerrak Strait in the Norwegian trench, in deep waters between Norway and Denmark [1]. In collaboration with the Norwegian Coastal Administration, Norwegian Defence Research Establishment (FFI) conducted two separate missions in 2015 and 2016, using FFI's HUGIN autonomous underwater vehicle (AUV) equipped with the HISAS interferometric synthetic aperture sonar (SAS) [2, 3]. This was a continuation of cruises done in 1989, 2002 (without AUV) [4], and 2009 (with AUV but without SAS) [5, 6]. The main goal of the 2015-2016 mission was to search the largest possible area with SAS, find the ship wrecks, judge their conditions, as well as to search for objects, debris, and UXOs. Approximately 450 km^2 were mapped in 4 cm$\times$4 cm resolution, and 54 wrecks were found, 36 of these are believed to be part of the chemical munitions dumpsite. An indication of the wreck locations is shown in Fig. 1. The boxes indicate the recommended no fish zone as of 1947, 1990, and 2018. The zone was substantially expanded after the 2015-2016 HUGIN missions due to the newly discovered wrecks found using AUV with SAS. More details about the missions and the technology can be found in [7].

In January 2019, FFI revisited the Skagerrak dumpsite for additional data collection using the HUGIN AUV with SAS and an optical camera. Multiple wrecks were revisited, and SAS images and optical images of unexploded ordnances (UXO) were gathered.

In this paper, we compare SAS images with optical images of UXOs. We assess the retrievable information present in high resolution large area coverage rate SAS images by comparing separate objects and their conditions as seen with optical camera.

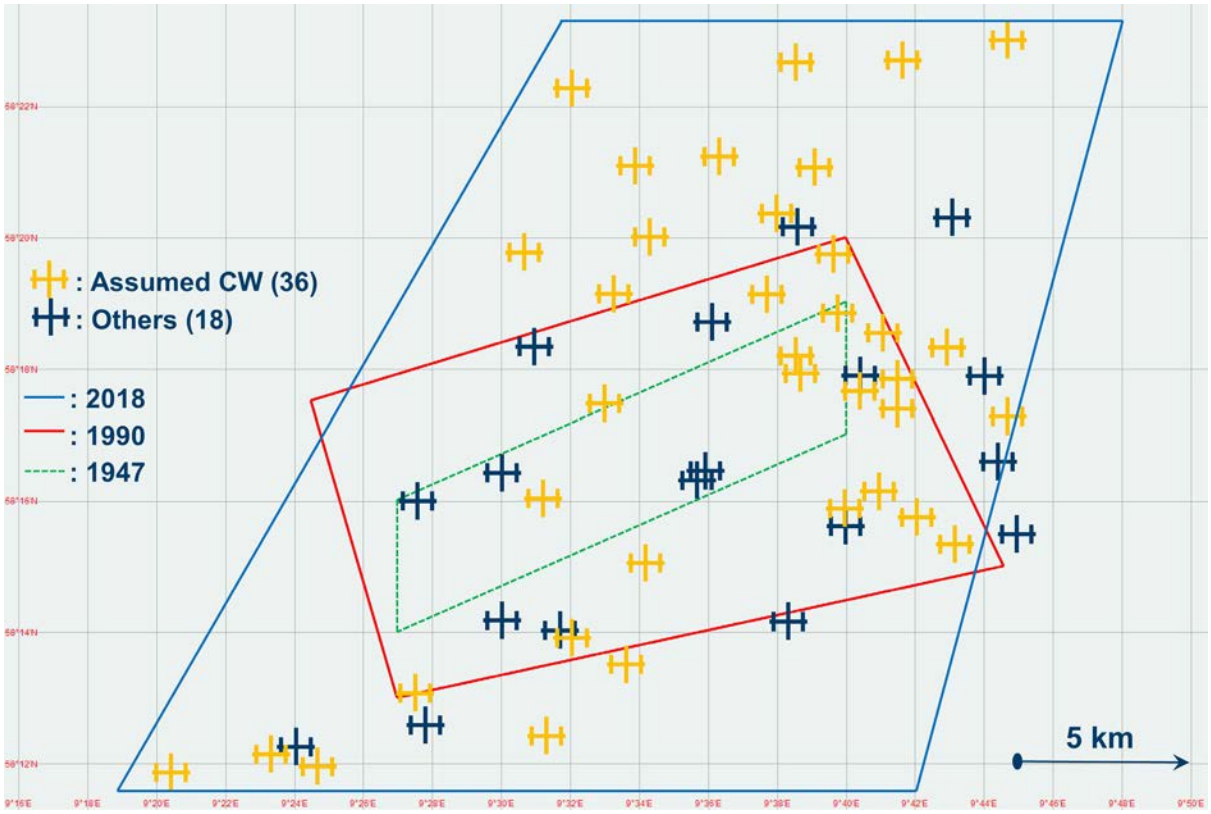


Fig. 1: Wreck positions in the Skagerrak dumpsite.

2. HUGIN AUV AND ITS SENSORS

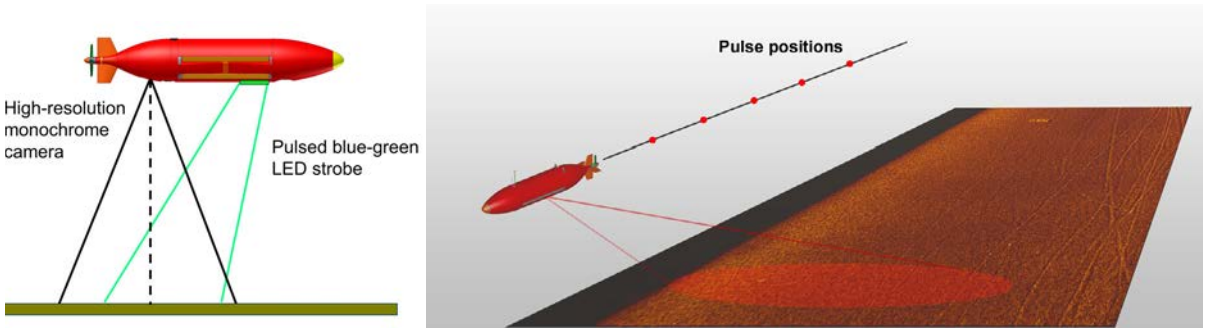


Fig. 2: Sensor geometry for the optical camera (left) and the SAS (right) on HUGIN AUV

The HUGIN AUV is a medium sized autonomous underwater vehicle developed by Kongsberg Maritime and FFI [8]. A typical operation is that the vehicle dives to the operational depth close to the seabed, and images or maps the seabed when running in a lawnmower pattern or in a dedicated pattern. The vehicle can be equipped with high performance imaging and mapping sensors such as the HISAS interferometric SAS, the EM2040 multibeam echosounder, flash based optical camera, and laser 3D profiler. Other sensors commonly used are subbottom profiler, magnetometer, turbidity sensor, CTD, and chemical sniffers. In this work, we only consider the optical camera and the SAS system.

2.1 Camera

FFIs HUGIN AUV is equipped with a TileCam optical camera and a synchronized pulsed LED strobe. The camera and strobe are mounted with maximal distance from each other (see Fig. 2) to reduce backscattering. The typical range (vehicle altitude) is between 3 m and 10 m, dependent on the water clarity. The swath width is approximately equivalent to the altitude. For a vehicle operating at 2 m/s and 5 m altitude, the area coverage becomes 10 m^2/s. TileCam has earlier been used for several missions [9, 10], but this is the first time we are using it for UXOs.

Each image has varying illumination with typically more light in the middle and less around the edges. In order to make the transition between the images in the mosaic smoother, the illumination is evened out with a height dependent model, similarly to what is done in [11]. The image quality also varies throughout the image, and is worse where there is little light or a large amount of backscattering. The seam between the images is optimized such that the higher quality image is used for each part of the mosaic. A mosaic based on 10 individual images showing several UXOs can be seen in Fig. 3.

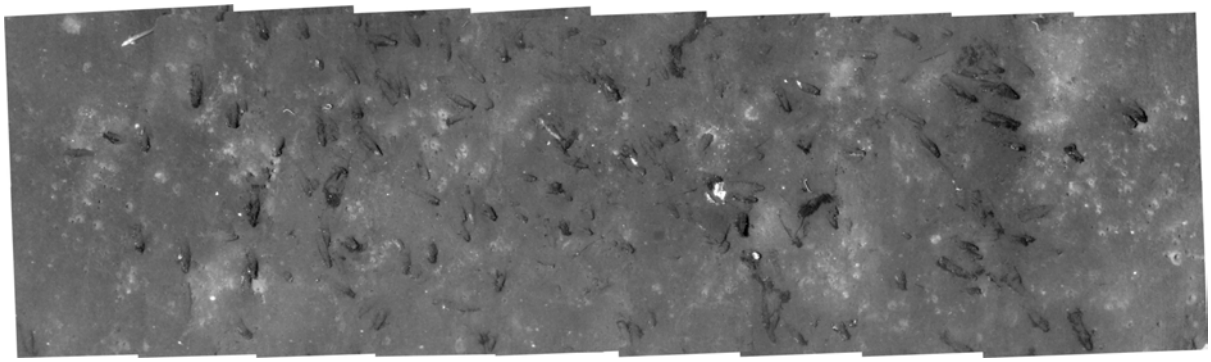


Fig. 3: Camera mosaic of 10 images of an area of ~6 m×20 m with high density of UXOs.

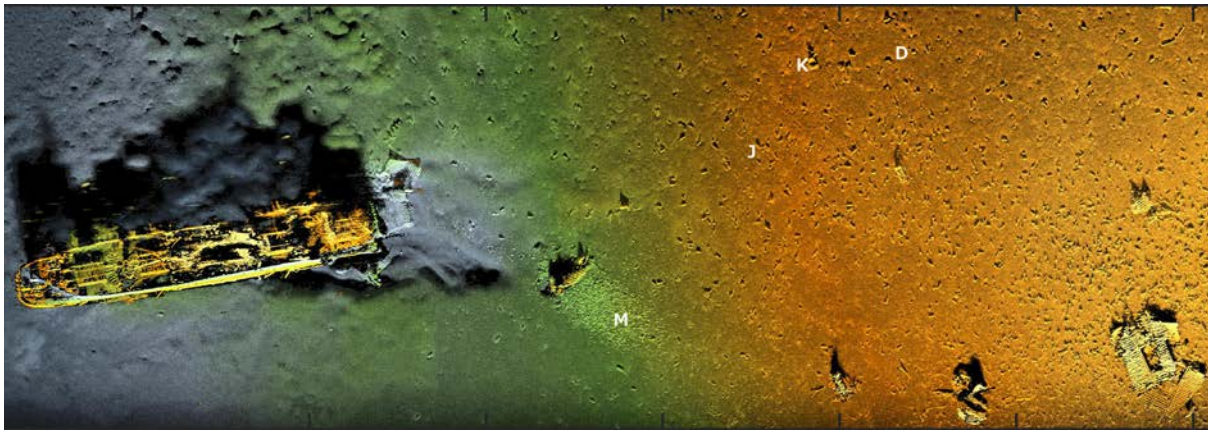


Fig. 4: SAS image fusioned with SAS bathymetry of wreck 13. The image size is 330 m×120 m, and the depth variation is 10 m in the color mapping. We have marked the positions of area M (Fig. 3), J (Fig. 5), D (Fig. 6, upper row) and K (Fig. 7). E and F (Fig. 6, middle and bottom row) are not covered in this image.

2.2 SAS

SAS is a sonar imaging technology that allows for high resolution and large area coverage rate at the same time [12]. The basic principle is based on coherent combination of sonar data from multiple pings when moving in order to improve along-track resolution (see Fig. 2). The HISAS 1032 has a theoretical resolution of around 3 cm×3 cm, and an instantaneous area coverage rate of approximately $400\,\mathrm{m}^2/\mathrm{s}$. Note that the area coverage rate is reduced if the SAS sensor is used as the gap-filler (covering the blind-zone for the SAS itself). See [2, 13] for details. Fig. 4 shows an example SAS image fusioned with SAS bathymetry from the Skagerrak dumpsite. The SAS image is despeckled using a multitaper despeckler [14]. The image shows wreck 13 where parts of the cargo is spread over a large area surrounding the wreck. This area forms the basis of our study in this manuscript.

3. COMPARISON OF CAMERA AND SAS

FFI performed a new HUGIN AUV survey of the Skagerrak dumpsite in January 2019 revisiting chosen wreckages. For the first time, we have gathered information of UXO on the Skagerrak site with HUGIN's optical camera. Each UXO or other wreckage part covered in the camera swath is also covered multiple times by SAS data, in up to four different orthogonal directions and at varying ranges. This makes it possible to co-register optical and sonar data for visual comparison purposes, see Figs. 5 – 7. All SAS images in this section is processed using the product version of the SAS processor, where we have selected to use backprojection for spot images, autofocus based on Phase Gradient Autofocus (PGA) [15], and despeckling using a median filter.

Fig. 5 shows three UXOs of approximate size 1.6 m×0.4 m that are cleary damaged and torn into pieces. From the optical images it is not unlikely to expect that their chemical munition is discharged into the water, though this would need to be evaluted with e.g. core sampling. The UXOs are well visible in the three displayed SAS images independent of look angle. However, from the SAS images it is only possible to determine the general object shape, not the UXO's integrity. SAS is well suited for covering large areas with high resolution, while an optical camera is better suited for a more detailed look at single object for identification purposes.

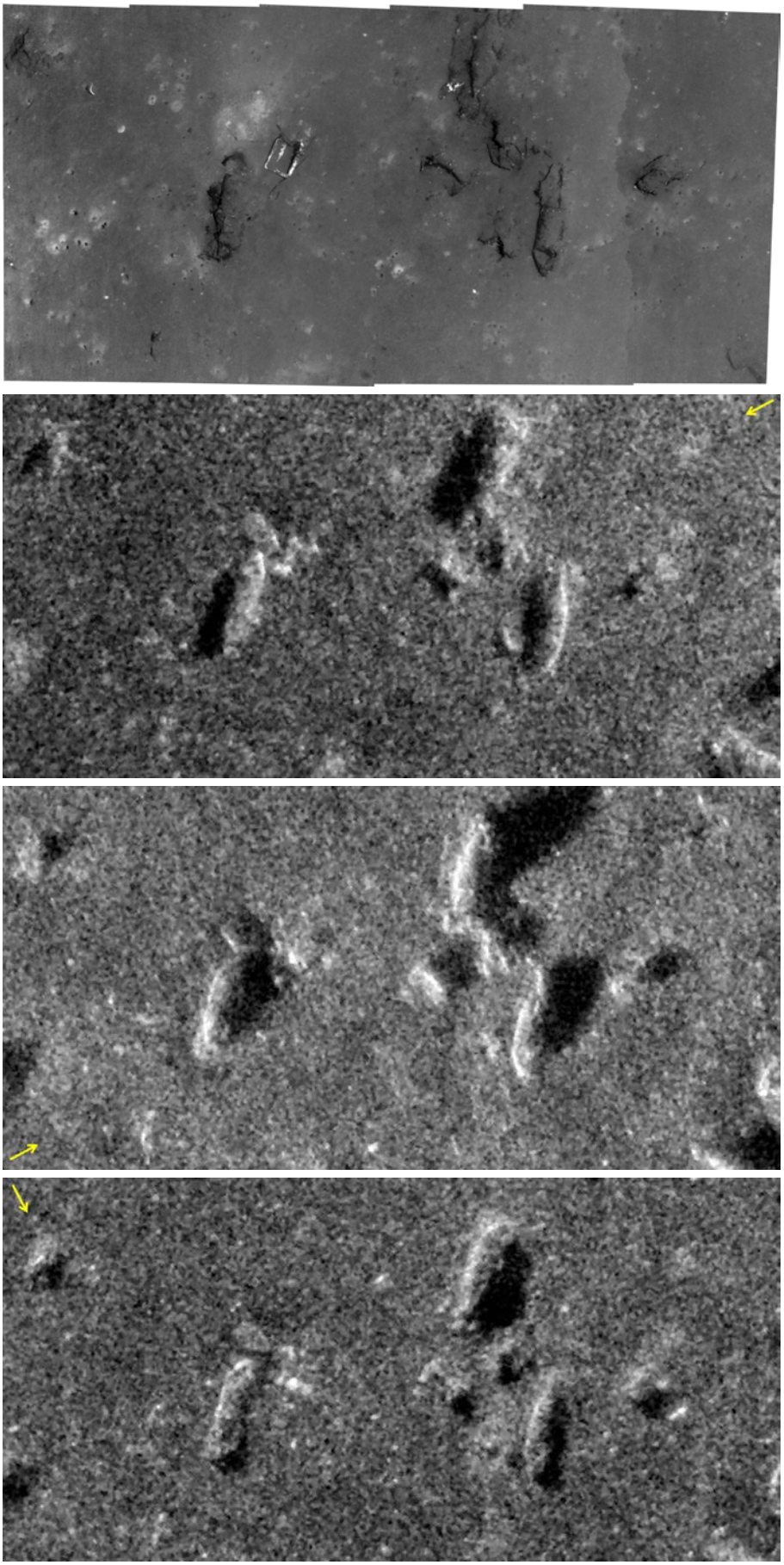


Fig. 5: Camera mosaic of six optical images covering ~6 m×12 m (top) compared with SAS images taken at ranges 70 m (second from the top), 111 m (second from the bottom) and 63 m (bottom). The yellow arrow in each SAS image indicates the sonar look direction.

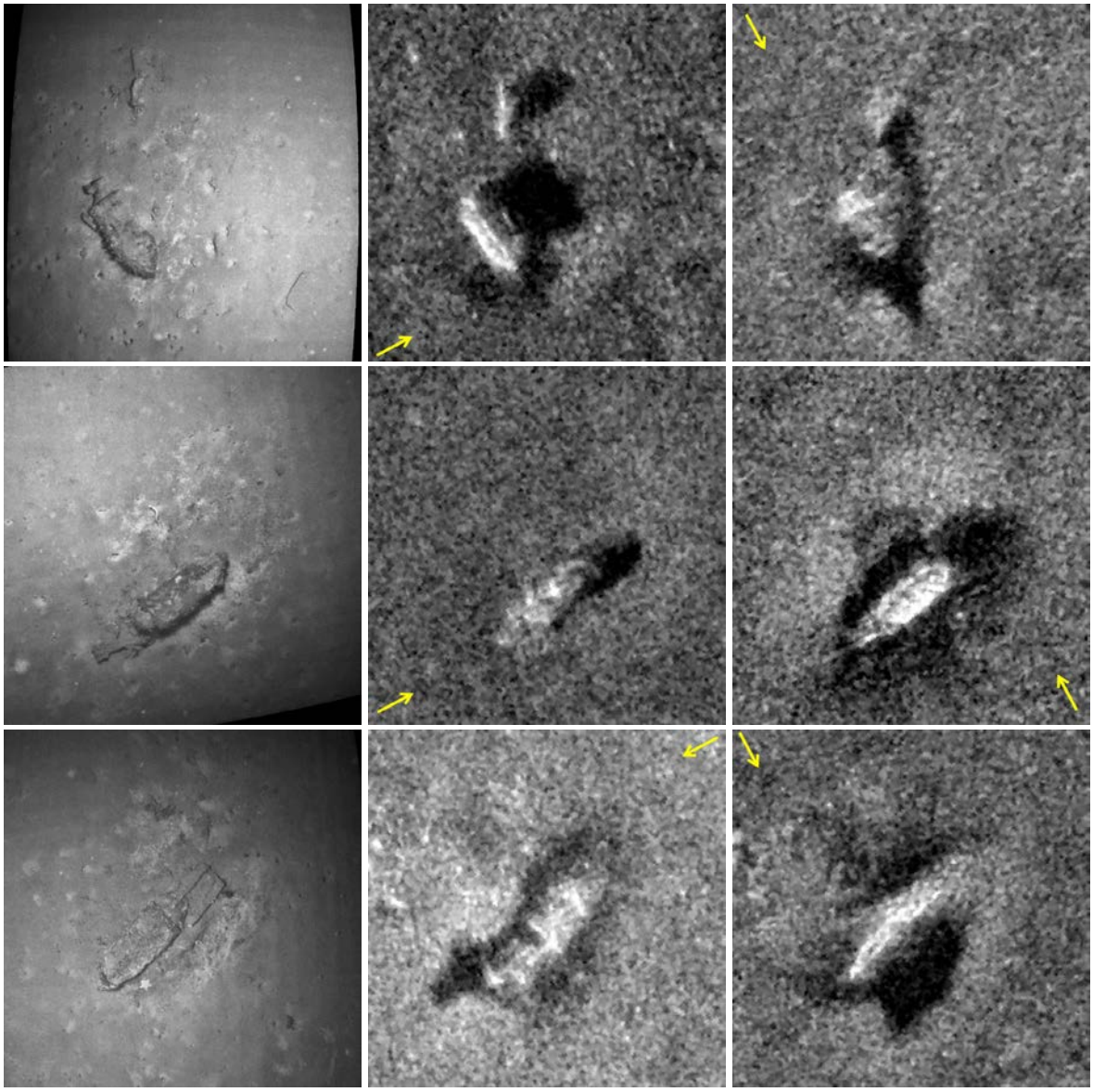


Fig. 6: Camera images (left) compared with two SAS images for each scene taken at ranges 140 m, 107 m (top row), 50 m, 128 m (middle) and 121 m, 115 m (bottom). The sonar look angle is indicated by the yellow arrow in each SAS image. UXO sizes vary from ~1.2 m× 0.45 m (top) to 1.65 m×0.4 m (middle and bottom).

Three further UXOs are visible in Fig. 6. They seem more intact than those in Fig. 5, however not undamaged either. The upper row object is around 40 cm shorter than the two others, which could be an indication that some part of the tail section is missing.

Operating an AUV with an optical camera is somewhat more risky than with SAS, as the typical AUV height for good optical images is around 5 m, while we usually perform SAS surveys at 20–25 m altitude. The risk of low altitude is that the AUV crashes into an object or the seafloor, especially if there is lots of terrain (which was not the case in our example), or that it gets stuck in e.g. fishing trawl. In Fig. 7, the optical image indicates that there is trawl in the upper right part of this unknown man-made wreckage object.

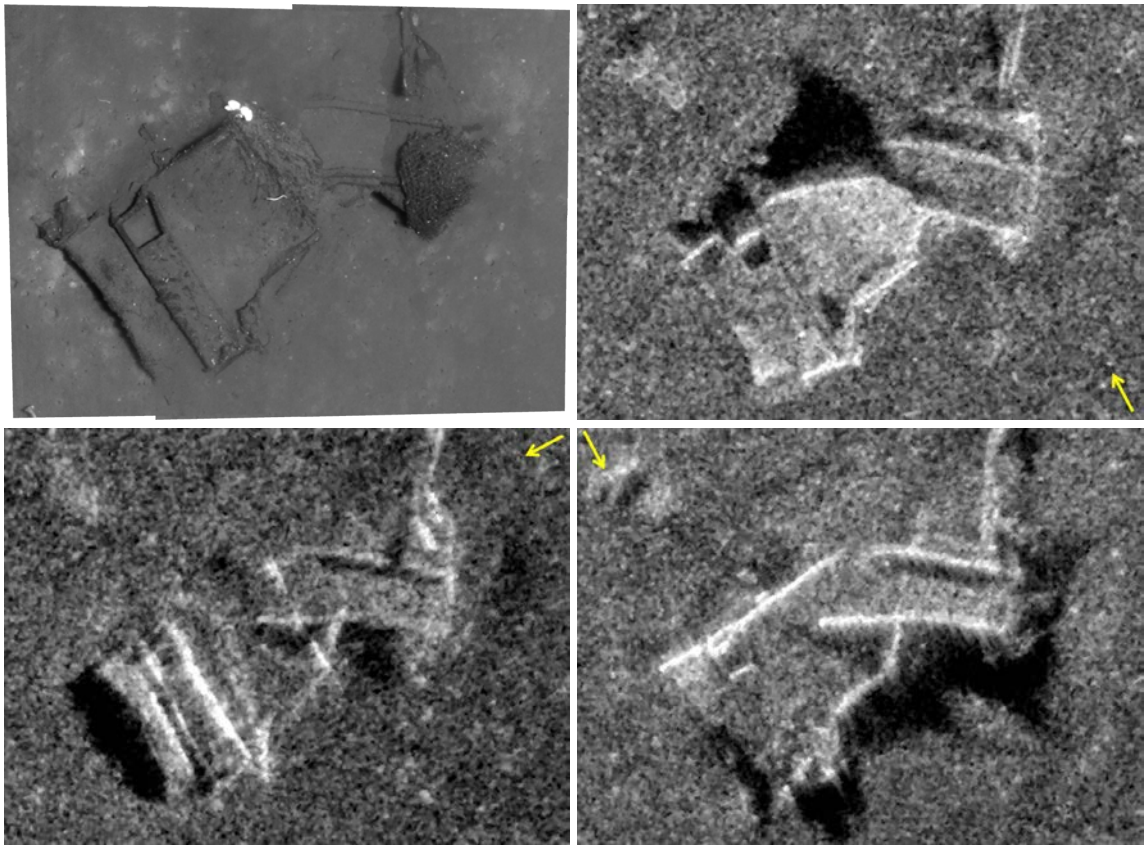


Fig. 7: Camera mosaic covering ~6 m×8 m (top left) compared with three SAS images at ranges 41 m (top right), 44 m (bottom left) and 79 m (bottom right). The look sonar angle is indicated by a yellow arrow.

In Fig. 7 we show a larger object, which is not a UXO, but potentially a part of the ship wreckage partly buried into the seafloor. Here we clearly see strong specular reflections that vary with the sonar look angle. Each SAS image thus contributes with different information, though the general object shape is evident in any of the SAS images.

4. SUMMARY

In this paper, we have examined the suitability of SAS and optical imagery for finding and judging the conditions of UXOs in the Skagerrak chemical munitions dumpsite. SAS is well suited for searching after small and large objects over large areas. This includes detection and classification of objects. As we have found here in our small study, SAS is less suitable for judging the conditions of UXOs. The optical camera is well suited for identification and judging of the conditions of individual UXOs. Camera is less suited for searching over large areas due to the limited area coverage rate. It is also of limited use when operated from HUGIN type AUVs in mapping and imaging large structures such as ship wrecks. This is due to the limited range in water. In such cases, a high frequency multibeam echosounder may be a good choice.

In our experience, the SAS and a flash based optical camera on an AUV is a very powerful combination. This allows for searching over large areas for detection and localization of UXOs with SAS, and identification and judging of the conditions with the camera.

ACKNOWLEDGEMENTS

The authors thank the Norwegian Coastal Administration for making the 2015 and 2016 data available. The authors also thank the crew onboard FFI's research vessel H.U. Sverdrup II, and the HUGIN AUV operators for collecting the data. Finally the authors thank Stig Synnes, Ole Lorentzen, Øivind Midtgaard, and Petter Lågstad for fruitful discussions.

REFERENCES

[1] H. L. Arison III. *European Disposal Operations: The Sea Disposal of Chemical Weapons*. H. Lindsey Arison III, 2013.

[2] R. E. Hansen, T. O. Sæbø, O. J. Lorentzen, and S. A. V. Synnes. Mapping unexploded ordnance (UXO) using interferometric synthetic aperture sonar. In *Proceedings of the 4th Underwater Acoustic Conference and Exibition*, Skiathos, Greece, September 2017.

[3] T. O. Sæbø, R. E. Hansen, and O. J. Lorentzen. Using an Interferometric Synthetic Aperture Sonar to Inspect the Skagerrak World War II Chemical Munitions Dump Site. In *Proceedings of Oceans 2015 MTS/IEEE*, Washington DC, USA, October 2015.

[4] J. Tørnes, Ø. A. Voie, M. Ljønes, Aa. M. Opstad, L. H. Bjerkeseth, and F. Hussein. Investigation and Risk Assessment of Ships Loaded with Chemical Ammunition Scuttled in Skagerrak. FFI-rapport 2002/04951, Norwegian Defence Research Establishment, 2002.

[5] C. M. Hansen, P. E. Hagen, P. A. Lågstad, and J. A. Tørnes. Case Study: Skagerrak Wrecks and Measures to Reduce the Environmental Risk. *Marine Technology Society Journal*, 43(4):100–104, Fall 2009.

[6] J. A. Tørnes, Ø. A. Voie, E. Mariussen, and P. Lågstad. Chemical warfare munitions dumped outside the Norwegian coast after World War II - what is dumped and what effect does this have on marine organisms. FFI-rapport 2015/00925 (In Norwegian), Norwegian Defence Research Establishment, 2015.

[7] R. E. Hansen, P. Lågstad, and T. O. Sæbø. Search and monitoring of shipwreck and munitions dumpsites using HUGIN AUV with synthetic aperture sonar – technology study. FFI-rapport 19/00245, Norwegian Defence Research Establishment, 2019.

[8] Kongsberg Maritime. Autonomous Underwater Vehicle, HUGIN, 2019 [Online; accessed 04-May-2019]. `https://www.kongsberg.com/maritime/products/marine-robotics/autonomous-underwater-vehicles/AUV-hugin`.

[9] Ø. Midtgaard, R. E. Hansen, T. O. Sæbø, V. Myers, J. R. Dubberley, and I. Quidu. Change Detection Using Synthetic Aperture Sonar: Preliminary Results from the Larvik Trial. In *Proceedings of Oceans 2011 MTS/IEEE*, Kona, HI, USA, September 2011.

[10] T. R. Krogstad and M. S. Wiig. Autonomous survey and identification planning for AUV MCM operations. In *Proceedings of Undersea Defence Technology 2014*, London, UK, June 2014.

[11] R. P. Gutiérrez. *Image Blending Techniques and their Application in Underwater Mosaicing*. PhD thesis, Universitat de Girona.

[12] R. E. Hansen. Introduction to Synthetic Aperture Sonar. In N. Z. Kolev, editor, *Sonar Systems*, chapter 1, pages 3–28. Intech, September 2011.

[13] P. E. Hagen and R. E. Hansen. Area coverage rate for Synthetic Aperture Sonars. In *Proceedings of Oceans '07 Europe*, Aberdeen, Scotland, June 2007.

[14] A. Austeng, H. J. Callow, Y. Larsen, and R. E. Hansen. Speckle Reduction in Synthetic Aperture Sonar Images Using Thomson's Multitaper Approach. In *Proceedings of the 1st Underwater Acoustic Conference*, Corfu, Greece, June 2013.

[15] H. J. Callow. *Signal Processing for Synthetic Aperture Sonar Image Enhancement*. PhD thesis, University of Canterbury, Christchurch, New Zealand, 2003.

TEST OF A SUBMARINE TRANSIENT ELECTROMAGNETIC SENSOR FOR UXO CLASSIFICATION BY REMOTELY OPERATED VEHICLES (SUBTEM-ROV)

Tobias Kulgemeyer[1], Michael Schwartz[1], Stephen D. Billings[2,3]

[1]Boskalis Hirdes – Heinrich Hirdes EOD Services GmbH, Am Festungsgraben 10, 21079 Hamburg, Germany
[2]Gap Explosive Ordnance Detection Pty. Ltd., West End, Queensland, Australia;
[3]Black Tusk Geophysics Inc., Vancouver, BC, Canada

Contact author: Tobias Kulgemeyer, e-mail: tobias.kulgemeyer@boskalis.com

Abstract: *A multi-component submarine transient electromagnetic sensor for the detection of unexploded ordnance with a remotely operated vehicle has been developed. This system (SubTEM-ROV) is the latest iteration of an ongoing line of development for the commercial application of advanced EM sensors in the marine realm. It allows to evaluate the geometry of targets and subsequently to classify them as potential UXO based on their characteristic electromagnetic polarizability. The system is presented here along with results of a test survey and comparison to conventional methods. Prior to conducting the survey, the capability of the SubTEM-ROV to distinguish objects of different sizes and geometry was demonstrated during a surrogate item trial (SIT). During the SIT, data were gathered over three items (dummy depth charge, steel tube, steel plate). Measured data were then inverted to determine the three-dimensional polarizabilities of the objects. Based on the inversion results, the items could be clearly distinguished in different orientations and standoffs. The test survey took place across a 50 m x 50 m area close to the island of Minsener Oog in the southern German Bight. This area is part of a region heavily polluted by UXO and other forms of debris. Anomalies indicating the presence of metallic objects have been picked and the data inverted to separate potential UXO from harmless debris. The results are compared to those of a previous single-component EM survey. This test highlights the strengths of the new system and demonstrates the value of a multi-component EM sensor for operations in a site polluted by both UXO and non-hazardous scrap.*

Keywords: *transient electromagnetic sensor, TEM, unexploded ordnance detection, UXO, marine unexploded ordnance, ROV sensor*

1. INTRODUCTION

Unexploded ordnance (UXO), originating primarily from World War II, pose a persistent challenge for offshore constructions in the North and Baltic Sea. The state of the art for UXO detection is multi-component transient electromagnetic (TEM) induction with subsequent inversion for the electromagnetic polarizability (Beran et al., 2011; Billings & Beran, 2017). This parameter relates the dipole vector components of a (secondary) magnetic field created in a target by induced eddy currents to the magnitude of the inducing uniform step-off (primary) field of the transmitter coil. As the induced eddy currents decay over time, the polarizability is given as three time-dependent curves along the principal axes of the target. Polarizability is an intrinsic property of a body which depends on its electromagnetic properties and geometry, but not on the orientation to the sensor. This method has been successfully used on land during the last decade for the identification of buried bodies (Prouty et al., 2011), but has only recently been transitioned to the marine environment (Shubitidze et al. 2008; Song et al., 2016).
In 2015, Boskalis Hirdes commissioned Gap Explosive Ordnance Detection (GapEOD) and Black Tusk Geophysics (BTG) with the development of a commercial multi-component TEM sensor with UXO specific inversion capabilities for marine environments. The first version of this instrument (SubTEM) was installed on a towed platform, while the second version that is the subject of this paper was developed for use by a remotely operated vehicle (SubTEM-ROV). The functionality of this instrument is demonstrated with two tests: First, the ability of the instrument to accurately identify objects of differing geometry is shown during a surrogate item trial (SIT) by comparing the inverted polarizability of three known, isolated objects. Then, results of two surveys in a UXO contaminated area in the southern German Bight, close to the island of Minsener Oog, are compared. Parts of this area were investigated in May 2018 using the Teledyne TSS-440, a single-component TEM pipe tracker that has seen wide-spread usage. In November 2018, a 50 m x 50 m box within the greater area, was re-surveyed with SubTEM-ROV.

2. INSTRUMENTS AND SURVEY

Both sensor arrays were attached to the same Schilling HD W-ROV, operated by pilots on board the Boskalis vessel *Smit Kamara*. Sensor positioning was provided by a Sonardyne USBL system, and altitude measured with a Tritech PA500 altimeter.

SubTEM-ROV
The sensor array consists of five horizontal 1.8 m x 1.8 m transmitter (Tx) coils in two rows of three, resp. two, coils, and 19 three-component (x, y, z) receiver (Rx) cubes arranged in a regular pattern across the array (Figure 1). Tx currents are set to achieve 300 Amp turns. Rx voltages are normalized by the coil area and the Tx current and given in values of nT/s/A.
Before surveying the area of interest, the responses of three test items (steel tube, dummy depth charge and steel plate) were evaluated. For this test, the items were placed in a line on the seafloor with 5 m distance between them; if applicable, the long axis of the item was oriented parallel to this line. The sensor was first moved along the line four times with variable altitude of 1 m, 1.5 m, 2 m and 2.5 m. After that, the test was repeated across the steel tube and the dummy depth charge on lines perpendicular to the first (as the steel plate is horizontally isometric, it was not measured again).

The subsequent field survey with SubTEM consists of 12 profiles oriented roughly east to west with a nominal height above ground of 1 m at 0.3 kn. The raw data were leveled, and the background response subtracted by applying a running mean filter. The inversion algorithm makes use of responses recorded between ca. 100 and 10,000 µs after Tx shutdown.



Figure 1: SubTEM-ROV deployment

Teledyne TSS-440

The Teledyne TSS-440 consists of three 1 m x 0.94 m coils which function both as transmitter and receiver. Tx currents are limited to 20 A. Rx voltages are given directly in values of µV. The TSS-440 survey consists of 25 parallel profiles with a nominal height above ground of 0.5 m at a speed of 0.4 kn. Raw data were processed by applying positional filters to de-spike recorded USBL coordinates of each coil and reject all data measured higher than 0.65 m altitude above ground. EM data were likewise de-spiked, and the average background response subtracted. The TSS-440 provides two values for each measurement, one for the early time and one for the "standard" response (300 µs to 400 µs after Tx shutdown). The latter one was used for evaluation.

3. RESULTS AND DISCUSSION

Results of the SIT are shown in Figure 2. The steel tube exhibits a polarizability pattern typical of a ferromagnetic cylindrical object, with one relatively high value along its long axis and two lower values associated with the short axes. The dummy depth charge has a more compact build and more complex internal structure, which results in approximately equal polarizabilities along all three axes. Finally, the signature of the steel plate consists of two relatively high polarizabilities along the horizontal and a smaller one along the vertical axis. These results are consistent regardless of the orientation of the target.

Reference curves like these, taken from actual UXO, can also be stored in a library and used for an automatic matching and classification routine.

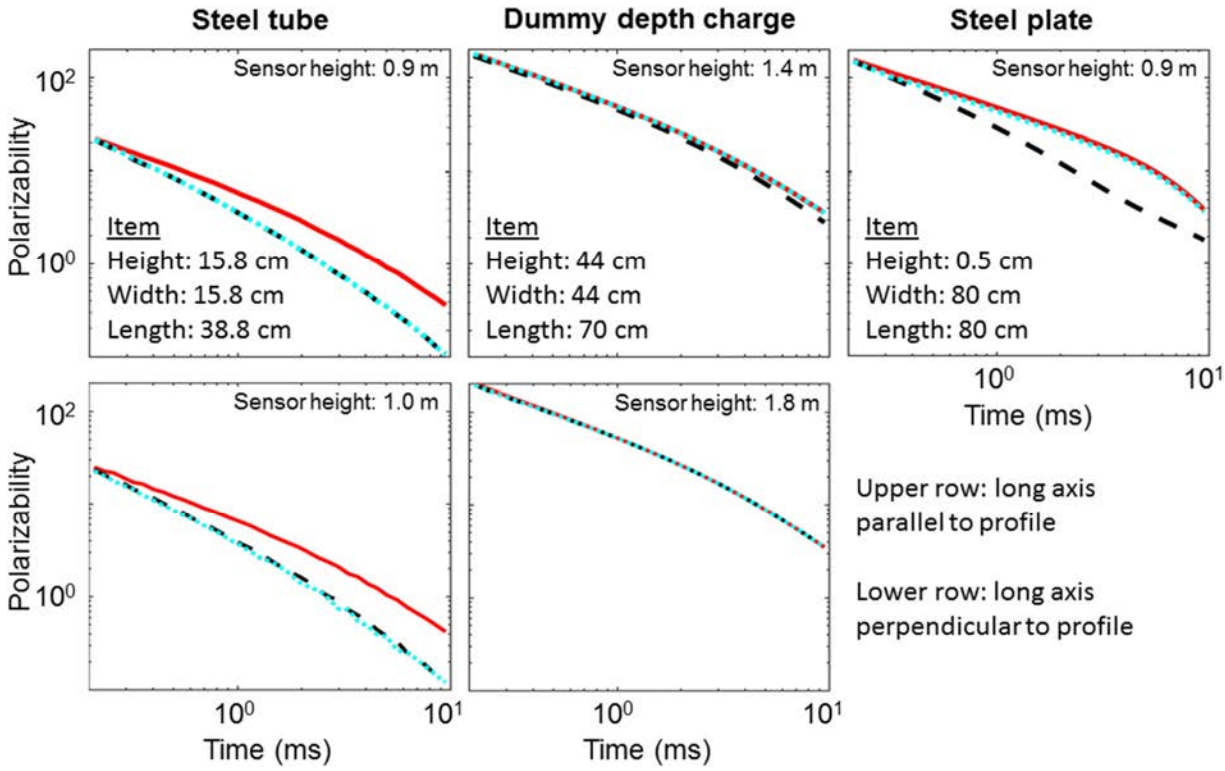


Figure 2: Examples of the inverted polarizabilities along the primary axes of the three test items.

The results of the test survey are shown in Figure 3. The processed TSS-440 data have a base noise level of about +/- 20 µV; it is usual practice to consider positive anomalies larger than twice the noise level as valid targets. In total, 16 suspicious anomalies were identified. One of these was cleared as part of sampling campaign to assess the regional UXO contamination in June 2018. The excavation revealed metal debris, which was identified as remnants of a ground mine.

During the SubTEM-ROV survey, 14 relevant anomalies were detected. The direct comparison shows that while most of the larger anomalies are stationary – as would be expected for a deeply buried object – some of the smaller anomalies detected in May did not appear again in November. Likewise, a number of new small-scale anomalies were detected with SubTEM-ROV, that did not appear during the TSS-440 survey. A part of these could be explained by the performance of the two systems, e.g. differences in the data acquisition, the higher detection range provided by the larger SubTEM-ROV transmitters and the greater spatial resolution achieved by the higher number of receivers. However, the area also has a highly dynamic tide-induced seafloor morphology, and small surficial debris can easily be transported with the currents.

Upon closer analysis, only one of the 14 anomalies detected with SubTEM-ROV displays a polarizability that can be associated with an intact, cylindrical UXO. All other objects appear to be either plate-like or random in their geometry; examples with best matches from the currently implemented UXO library are shown in Figure 4. In an actual UXO disposal campaign, this kind of information would drastically reduce time and cost requirements. In addition, remote classification by matching measured responses to an extensive library of known ordnances would allow for a better risk assessment before an excavation. The adaption of this technology to an ROV provides a high degree of flexibility in the operations, as the survey of a small area and excavation of potential UXO can be done in a single dive. A drawback of using an ROV would be the

relatively small sensor footprint and the requirement of a suitable support vessel, trading high data quality and discrimination capability for the ability to survey large areas in short times and at low operational costs. Overall, the performance of SubTEM-ROV is excellent.

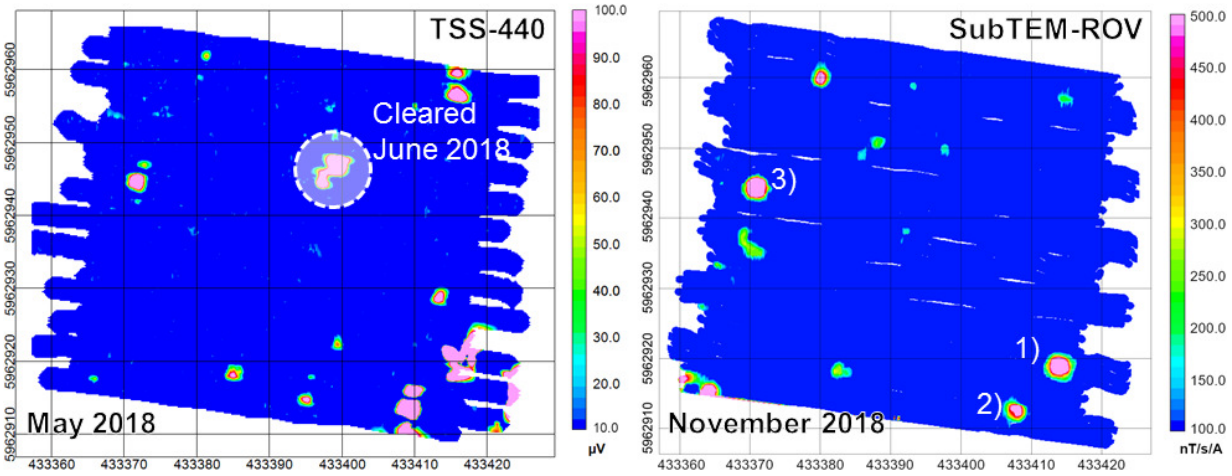


Figure 3: Comparison of the TSS-440 and SubTEM-ROV surveys. TSS data are recorded within the 300 µs to 400 µs time gate, SubTEM data show the 100 µs to 1000 µs time gate of the vertical field components in a monostatic Tx/Rx selection. One anomaly was cleared before the SubTEM survey took place; all other TSS anomalies would be considered valid targets. Closer analysis of SubTEM data reveals only one potential UXO (No. 2, see Figure 4).

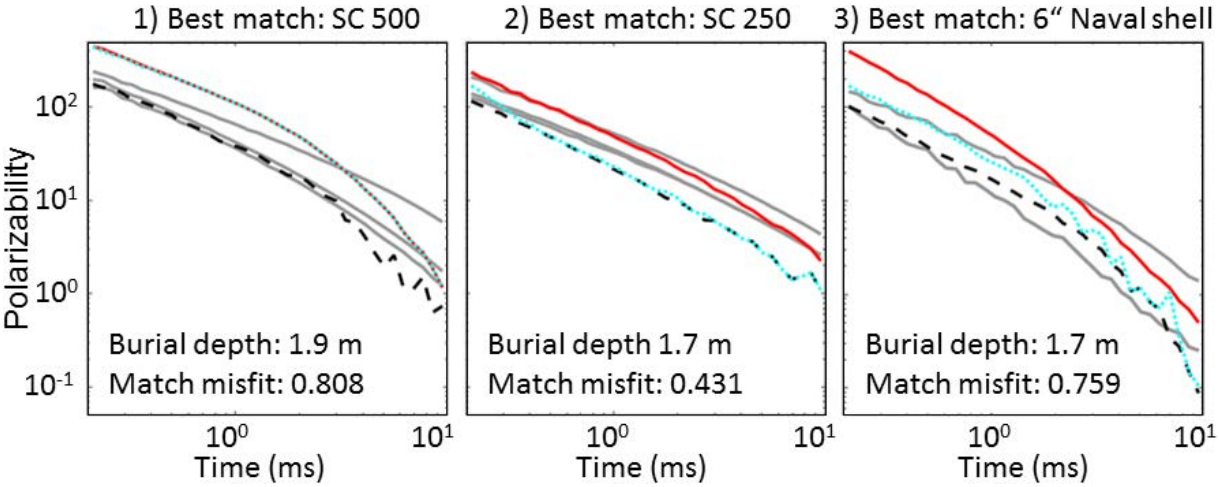


Figure 4: Examples of inverted polarizabilities and best matching library item for 3 anomalies. None of the items are a close match to the currently available UXO library. No. 1 appears to be plate-like, No. 2 cylindrical (UXO-like), No. 3 irregularly shaped.

ACKNOWLEDGMENTS

The TSS-440 survey was conducted for the Wasserstraßen- und Schifffahrtsamt (WSA) Wilhelmshaven; we also thank the WSA for later allowing access to the test area for the SubTEM-ROV survey. Development of SubTEM-ROV was financed by the Heinrich Hirdes EOD Services GmbH of Boskalis Hirdes, a subsidiary of Royal Boskalis Westminster N.V.

REFERENCES

[1] Beran, L., Billings, S.D., Oldenburg, D.W., Robust Inversion of Time-domain Electromagnetic Data: Application to Unexploded Ordnance Discrimination, *Journal of Environmental and Engineering Geophysics*, 16 (3): 127-141, 2011

[2] Billings, S.D., Beran, L., Optimizing electromagnetic sensors for unexploded ordnance detection, *Geophysics*, 82 (3): EN25-EN31, 2017

[3] Prouty, M., George, D.C., Snyder, D.D., Metalmapper: A multisensory TEM system for UXO detection and classification, *ESTCP Project MR-200603: Technical report*, 110 pp., 2011

[4] Shubitidze, F., Barrowes, B., Shamatava, I., Fernández, J.P., O'Neill, K., Underwater UXO Detection and Discrimination: Understanding EMI Scattering Phenomena in a Conducting Environment, *Proceedings of SPIE*, 6953, 2008

[5] Song, L., Billings, S.D., Pasion, L.R., Oldenburg, D.W., Transient Electromagnetic Scattering of a Metallic Object Buried in Underwater Sediments, *IEEE Transactions on Geoscience and Remote Sensing*, 54 (2): 1091-1102; 2016

MOBILISATION OF UXO, CAUSED BY HYDRODYNAMICS

Peter Menzel[a], Anja Drews[b], Christoph Otto[a], Clemens Schütt[a]

[a]University of Rostock, Chair of Ocean Engineering, Albert-Einstein-Str. 2, 18059 Rostock, Germany
[b]TenneT TSO GmbH, Eisenbahnlängsweg 2a, 31275 Lehrte, Germany

Dr. Peter Menzel, University of Rostock, Chair of Ocean Engineering, Albert-Einstein-Str. 2, 18059 Rostock, Germany, email: peter.menzel@uni-rostock.de

Abstract: *Offshore construction works are increasing permanently. Especially since offshore wind energy is developing very rapidly, the presence of UXO on the seafloor is an issue for any type of construction works offshore. Expensive and time-consuming UXO campaigns are done to locate, identify, and remove these objects. The release of a site for construction documented in a sign-off certificate is then often given for a limited time assuming potential UXO migration on the seafloor caused by hydrodynamic loads. As a consequence, UXO measures have to be repeated after the expiring of the sign-off certificate. This problem affects subsea cable installation, the installation of offshore pipelines, offshore mining activities, offshore construction works and activities of authorities and navies.*
A model for current- and wave-induced mobilisation of objects on a sandy sea floor, based on the Morison equation, is presented.

Keywords: *UXO, modelling, hydrodynamics*

INTRODUCTION

During the World Wars and afterwards, huge amounts of Ammunition was dumped into the Oceans, especially into the North Sea. Since this time, these Unexploded Ordnance Objects (UXO) were and are exposed to a large variety of physical and chemical processes. Due to currents and waves, the surrounding seabed can be mobilised which can cause scour around the objects and may lead to partial self-burial as described in [1] [2] and [3]. According to [1] and [4] the burial depth, caused by this effect is limited to about 80% of the Object diameter D. Thus, these objects are still exposed to the fluid by about 20% of their diameter. Effects like moving ripples, megaripples, sand waves and dunes as well as an overall change of the slope of the seabed may cause complete burial of such objects. These effects will be neglected for this study of single physical effects. The seabed is assumed to consist of homogeneous fine sand.

Before offshore construction works, these objects have to be detected, identified and cleared to establish a safe working environment. Especially for the installation of Offshore windfarms and their grid connections, large areas have to be investigated. Due to the weather situation, these UXO-campaigns commonly start in early spring in the North Sea, which allows the installation works to be done in the following spring. As the UXO-clearance is often given for a limited time due to the assumption that UXO can migrate, the UXO-measures might have to be revised before the installation works are finished and before repair operations. To improve this practice to a weather based clearance model, a better understanding of the mobilisation of UXO due to currents and waves is needed.

An advanced approach on the mobilisation of UXO is published by [5] within the Strategic Environmental Research and Development program (SERDP) of the US Navy. This approach uses the approach of Shields [6] and the hydrodynamic loads on artillery munition. Especially their experimental work is very considerable.

An approach for the current induced mobilisation of UXO, based on the Reynolds Number and a dimensionless Moment Factor was presented in [7]. This general prediction model can be used for small and large-scale objects of different shape. From this, the critical bottom near current velocity U_{cit}, which is needed to mobilise an object on the seafloor is given as

$$U_{crit} = \sqrt[b]{\frac{\rho_w g D_{avg} V_{obj}(\rho_{obj} - \rho_w)}{2a\mu^2 L}} \cdot \frac{\mu}{\rho_w (1 - z_b^*) D_{avg}} \tag{1}$$

with density of the water ρ_w, and the object ρ_{obj}, the gravitational acceleration g, the dynamic viscosity μ, the averaged diameter of the object D_{avg}, its length L and its volume V_{obj}. The burial depth z_b^* describes the fraction of the object's diameter that is buried. The parameters $a = 0.2315$ and $b = 2.1137$ are found by statistics and published in [7].

METHODS

The following analysis are applied to typical UXO, found in the North Sea. These are for example the British 250lb General Purpose bomb and the German Mine Type GY. Drawings of these objects are shown in fig. 1. The German Mine Type GY is assumed completely flooded as consequence of corrosion. The absolute mass of the British 250lb General Purpose Bomb is assumed to be $m = 112\ kg$, whereas the flooded absolute mass of the German Mine Type GY is approximated to be $m = 630{,}5\ kg$.

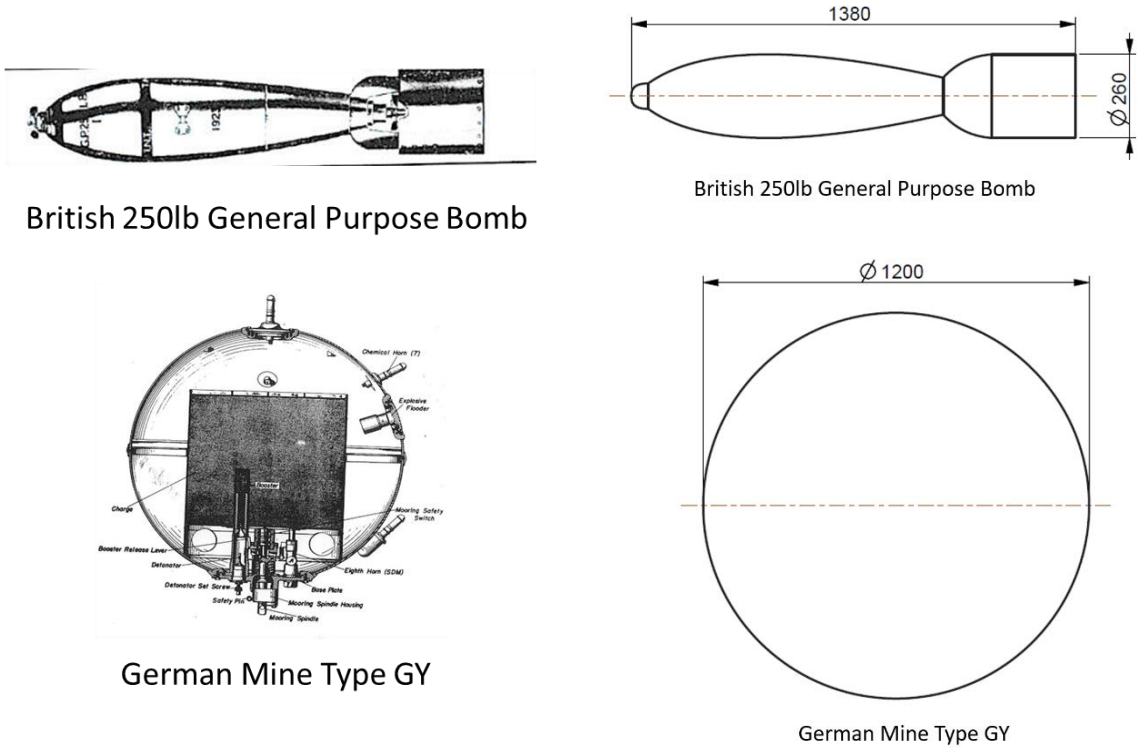


Fig. 1: Drawings of the axial symmetric objects and their simplified models.

Besides the current-induced scour, burial and mobilisation, the wave-induced actions are much more common in offshore regions. Even if the water depths are more than $h = 40\ m$, the sediment and the objects may be influenced by waves as the wavelengths can be much longer than $\lambda = 80\ m$. The loads on a cylindrical object in a symmetrical wave-induced scour pattern are shown in fig. 2. Here the seabed elevation is approximated to be sinusoidal with a maximum slope of $\alpha = 36°$, which has been found for fine sand in laboratory experiments. The absolute burial depth is given by z_b.

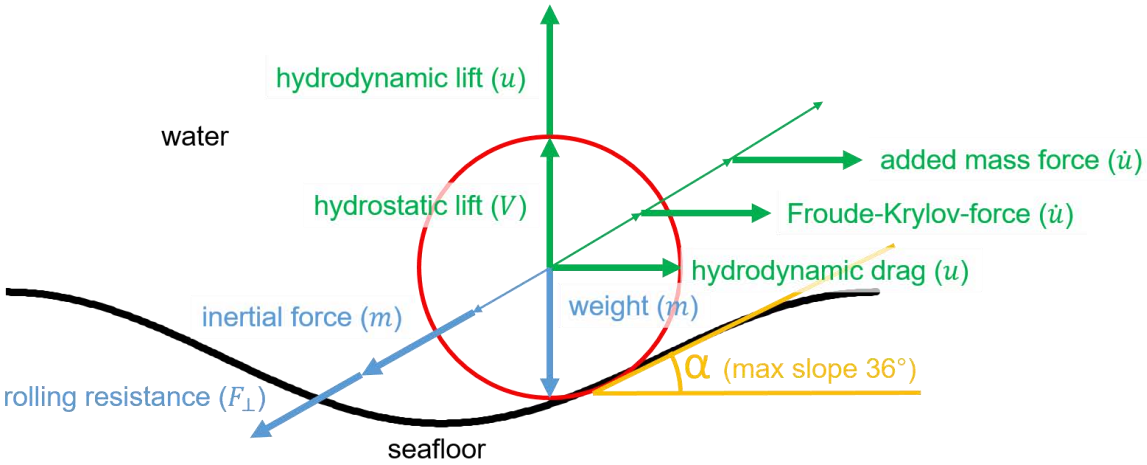


Fig. 2: Loads on a cylindrical object in a symmetrical scour trough in waves.

An equation for the dynamic loads on a moving body in an oscillatory flow was published by [8] and later was called the Morison equation. For the horizontal load, the Morison equation can be written as

$$m\dot{u}_{obj} = \rho V_{obj}\dot{u} + \rho c_a V_{obj}(\dot{u} - \dot{u}_{obj}) + \frac{\rho}{2}(u - u_{obj})|u - u_{obj}|c_d A_{obj} \tag{2}$$

with m being the mass of the object and A_{obj} the cross section of the object, u and $\dot{u}$ the velocity and acceleration of the water, u_{obj} and $\dot{u}_{obj}$ the velocity and acceleration of the object, ρ the density of the water, c_a the added mass coefficient and c_d being the drag coefficient. The first term on the right side of the equation is called the Froude-Krylov force, which is induced by the horizontal pressure gradient due to surface waves. The second term is the hydrodynamic mass force, which can be interpreted to be caused by the energy that is needed to build up the boundary layer at the walls of the object during the relative acceleration of the fluid. The third term is the already known hydrodynamic drag, which is caused by the wall shear stress at the objects surface and the flow-induced pressure difference between the front and the wake of the object. In practice, the hydrodynamic mass can be written on the left side

$$(m + \rho c_a V_{obj})\dot{u}_{obj} = \rho V_{obj}\dot{u}(1 + c_a) + \frac{\rho}{2}(u - u_{obj})|u - u_{obj}|c_d A_{obj}. \tag{3}$$

The vertical loads on the object will be handled separately as they result in a horizontal force due to the slope of the seafloor. Thus, the horizontal force

$$F_x = cos\,\alpha\, F_{\parallel} = cos\,\alpha\, sin\,\alpha\,(F_g - F_b - F_l) \tag{4}$$

has to be derived in dependency of the instantaneous angle α like shown in fig. 3a.

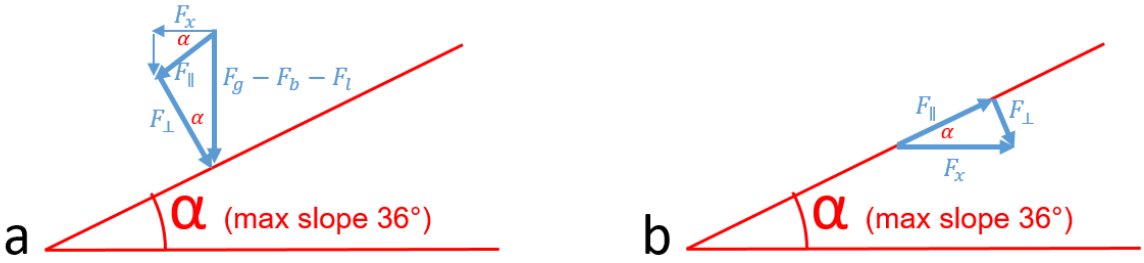


Fig. 3: Downhill-slope force (a) and friction force (b).

Inserting the weight F_g, the hydrostatic buoyancy F_b and the hydrodynamic lift F_l, eq. (4) develops as

$$F_g - F_b - F_l = (m - \rho V_{obj})g - \frac{\rho}{2}(u - u_{obj})|u - u_{obj}|c_l A_{obj} \tag{5}$$

and eq. (3) can be written as

$$\begin{aligned}(m + \rho c_a V_{obj})\dot{u}_{obj} &= \rho V_{obj}\dot{u}(1 + c_a) + \frac{\rho}{2}(u - u_{obj})|u - u_{obj}|c_d A_{obj} \\ &+ cos\,\alpha\, sin\,\alpha\left\{(m - \rho V_{obj})g - \frac{\rho}{2}(u - u_{obj})|u - u_{obj}|c_l A_{obj}\right\}.\end{aligned} \tag{6}$$

From these horizontal loads, the force component perpendicular to the surface can be derived as

$$F_{\perp} = F_x \sin\alpha, \tag{7}$$

which is shown in fig. 3b. The rolling resistance, which is parallel to the surface, then can be calculated from

$$F_{r\parallel} = c_r F_x \sin\alpha \tag{8}$$

and the horizontal component is defined as

$$F_{rx} = c_r F_x \sin\alpha \cos\alpha. \tag{9}$$

Inserting eq. (9) into eq. (6) in which the horizontal force is written on the right side, the final equation can be written as

$$\begin{aligned}\dot{u}_{obj} = [1 + c_r \sin\alpha \cos\alpha]\Big[&\rho V_{obj}\dot{u}(1 + c_a) + \frac{\rho}{2}(u - u_{obj})|u - u_{obj}|c_d A_{obj} \\ &+ \cos\alpha \sin\alpha \left\{(m - \rho V_{obj})g - \frac{\rho}{2}(u - u_{obj})|u - u_{obj}|c_l A_{obj}\right\}\Big] \\ &\cdot (m + \rho c_a V_{obj})^{-1}.\end{aligned} \tag{10}$$

Inserting the wave-induced velocity and acceleration of the water, which e.g. can be derived from several wave theories, the instantaneous horizontal component of the acceleration of the object can derived. Adding the vertical force-components, the full acceleration of the object is dissolved. This is used to simulate the velocity and to integrate the position of the object. This simulation is used to decide whether the object is moved out of the scour hole or not. By simulating this for different burial depths, water depths, wavelengths and wave heights H, the critical parameters can be found.

RESULTS

The critical conditions for the two objects of interest in waves are shown in fig. 3 and fig. 4. The graphs show the critical wavelength and wave height for different water depths (numbers on the graphs) at a burial depth of $z_b/D = 0.5$. The left limit of the graphs is given by the steepness of the wave slope representing the critical condition for wave braking.

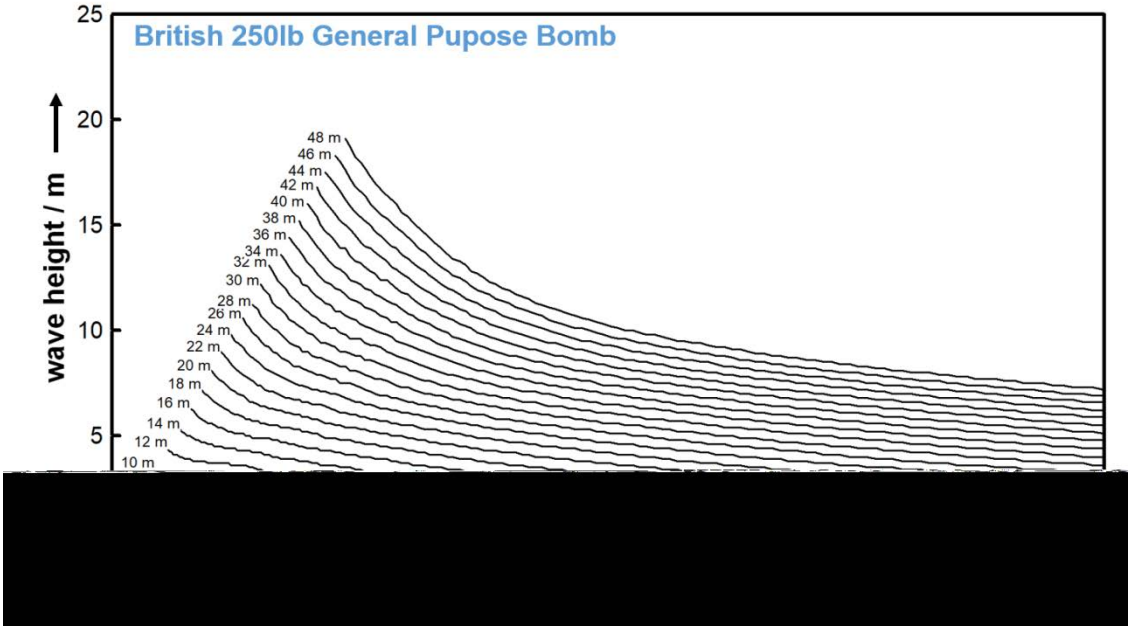


Fig. 3: Critical Conditions for the British 250lb General Purpose Bomb.

It is obvious, that the critical wave heights for typical wavelength in a storm (wave periode $T \approx 10s, \lambda = 156\,m$) are larger than $H = 15m$ (for $h > 40m$) for the British 250lb General Purpose Bomb. It is also obvious that the more spherical German Mine Type GY is more mobile in waves than the British 250lb General Purpose Bomb. From these plots both objects are expected to stay immobile for water depths of $h > 20m$ and during "normal" sea state conditions.

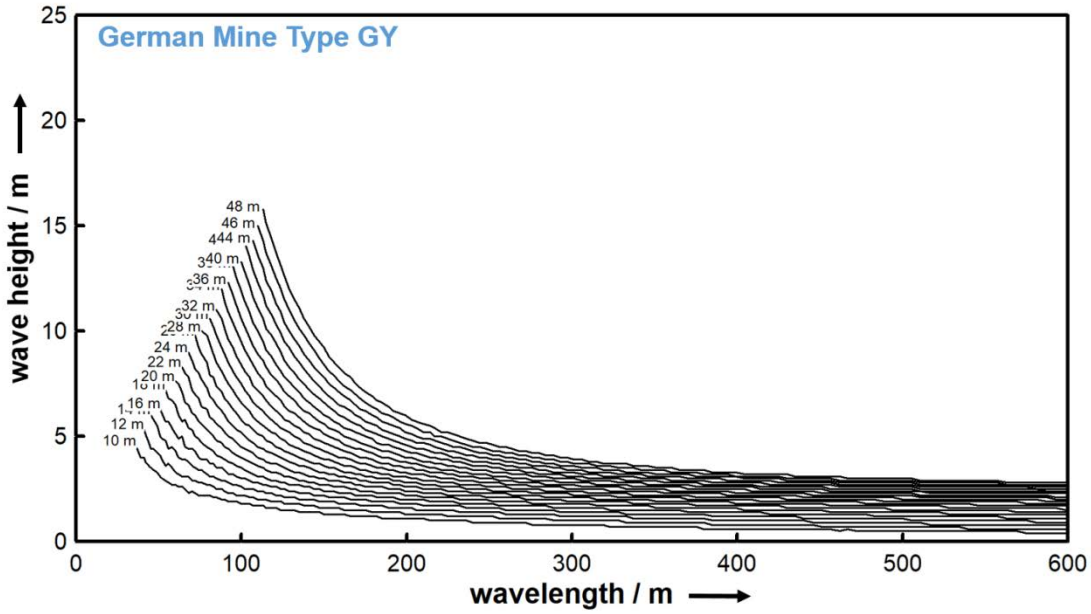


Fig. 4: Critical Conditions for the German Mine Type GY.

SUMMARY AND DISCUSSION

Using eq. (10), the mobilisation of objects on the seafloor by the loads, generated from the orbital velocity and acceleration of surface waves can be simulated by integration of the position offset. The current induced mobilisation was already described in [7]. Using the approach from [7] for the current induced mobilisation, the critical moment on the object M_{DL}, induced by the

hydrodynamic lift and drag with regard to the resetting moment, induced by the relative mass of the object is plotted against the Reynolds number Re in fig. 5 (right). The equilibrium $M_{DL} = M_0$ represents the situation, where an object is mobilised by the incident flow. The corresponding Reynolds number is proportional to the critical current velocity. The critical Reynolds number for the British 250lb General Purpose Bomb is found to be lower than the critical Reynolds number for the German Mine Type GY in fig. 5 (right). From this, slim objects are assumed to be more mobile than more stout objects in constant currents.

On the other hand, the wave-induced mobilisation of the same objects is plotted in fig. 5 (left). Obviously the critical waves for the mobilisation of the German Mine Type GY are significant smaller than the critical waves that are necessary to mobilise the British 250lb General Purpose Bomb. Comparing both results, it can be concluded that slim objects are more sensitive to currents whereas thick bodies are more sensitive to waves, with regard to their mobilisation.

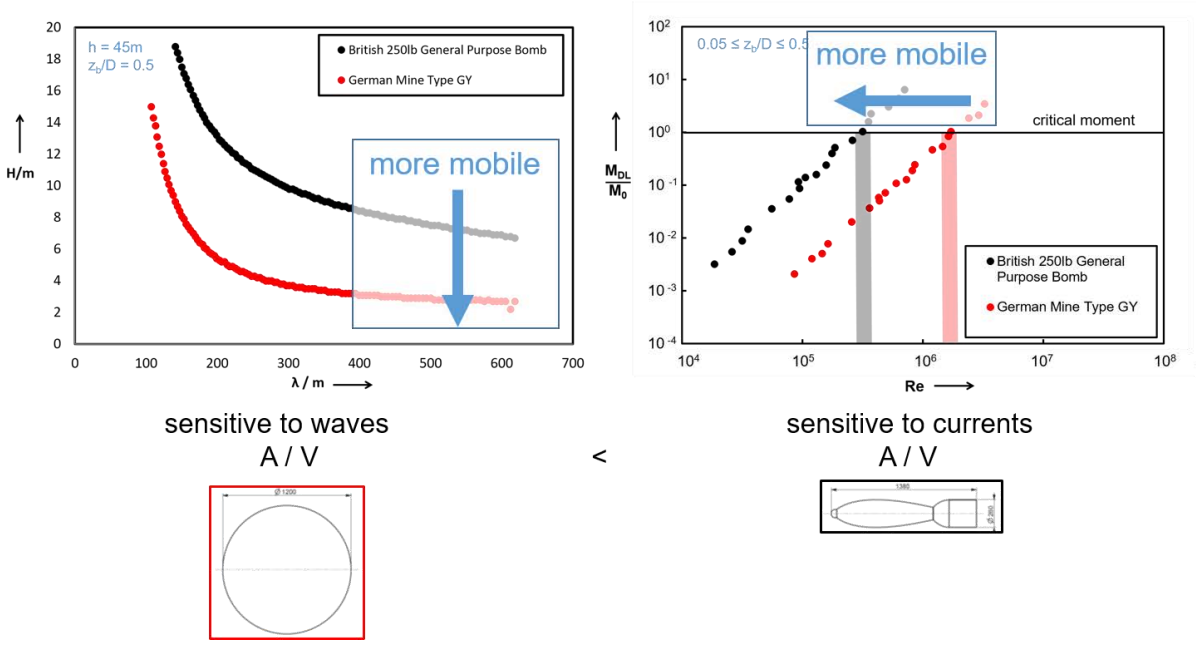


Fig. 5: Comparison of the wave- and current-induced mobilisation.

This behaviour becomes, regarding eq. (2). Here the current-induced loads relate to the cross section of the objects. In contrast to this, the acceleration-induced loads relate to the volume of the objects. In constant currents, the acceleration is zero. Thus, the loads relate to the cross section of the object. In wave conditions, the acceleration of the water particles is omnipresent and thus, the loads strongly relate to the volume of the object. As the ratio of the objects cross section to its volume is larger for slim objects than for an ideal sphere, the slim object is more sensible to constant currents whereas the sphere is more sensible to oscillating currents due to waves.

As a consequence of this, slim objects like the British 250lb General Purpose Bomb tend to be more mobile in protected areas, dominated by tidal currents. Spherical objects as sunken buoyant mines are tend to be more mobile in coastal regions, dominated by waves.

ACKNOWLEDGEMENTS

This Project was funded by the TenneT TSO GmbH and the Bundesrepublik Deutschland, represented by the Bundeswehr Technical Centre for Ships and Naval Weapons, Naval Technology and Research (WTD 71) in Eckernförde. The authors like to thank for the financial support.

REFERENCES

[1] Whitehouse, R., (1998). *Scour at marine structures - A manual for practical applications.* London: Thomas Telford.

[2] Wilkens, R.H. & Richardson, M.D., (2007). *Mine Burial Prediction: A Short History and Introduction.* IEEE Journal of Oceanic Engineering, January. pp.3-9.

[3] Jenkins, S.A., Inman, D.L., Richardson, M.D., Wever, T.F. & Wasyl, J., (2007). *Scour and Burial Mechanics of Objects in the Nearshore.* IEEE Journal of Oceanic Engineering, January. pp.78-90.

[4] Menzel, P.; Rückborn, T.; Leder, A.; *Flow and scour around cylindrical objects in laboratory experiments*; OCEANS - Bergen, 2013 MTS/IEEE , vol., no., pp.1,8, 10-14 June 2013, doi: 10.1109/OCEANS-Bergen.2013.6607970

[5] Rennie, S.E., Brandt, A. & Friedrichs, C.T., (2017*). Initiation of motion and scour burial of objects underwater.* Ocean Engineering 131 (2017) 282-294, February.

[6] Shields, A., (1936). Anwendung der Ähnlichkeitsmechanik und der Turbulenzforschung auf die Geschiebebewegung. *Mitteilung der Preußischen Versuchsanstalt für Wasserbau und Schiffbau*.

[7] Menzel, P.; Schütt, C.; Wranik, H.; Paschen, M.; Drews, A.; *Towards a general prediction-model for the current-induced mobilisation of objects on the sea floor*; Ocean Engineering, Volume 164, 2018, Pages 160-167, ISSN 0029-8018, https://doi.org/10.1016/j.oceaneng.2018.06.047.

[8] Morison, J.R., O'Brien, M.P., Johnson, S.A. & Schaaf, S.A., (1950). *The force exerted by surface waves on piles.* Petroleum Transactions AIME Vol.189, pp.149-54.

Structured Session 8
Comprehensive nuclear test-ban treaty monitoring

Organiser(s): Haralabus George, Zampolli Mario, Nielsen Peter

EFFICIENT MODELING OF 3D ACOUSTIC PATHS TO IMPROVE SOURCE TRIANGULATION

David R. Dall'Osto

Applied Physics Laboratory, University of Washington
1013 NE 40th Street Seattle, Washington 98103 USA

email: dallosto@uw.edu
fax: (206) 543 - 6785

Abstract: *Hydroacoustic signals recorded on the International Monitoring System (IMS) network have proven their capability to identify the origin of intense sound sources. A recent example is the detections CTBTO used to identify the search area where the lost Argentine submarine ARA San Juan was found. To triangulate a source, isochrones or surfaces of equal travel time are propagated from each station using a global model of ocean sound speed. With detections on two stations, the intersection of these isochrones form a line, which reduces to point when time of occurrence is known. With detections on 3 stations, isochrones intersect at the source origin and establish a time of occurrence, noting that confidence is limited by accuracy of the propagation model. Finding a detection on three stations however is not always possible, and as such azimuthal information garnered from coherent processing of the hydrophone triads that make up each IMS station provide another means to bound the triangulation. Furthermore, when additional arrivals distributed in azimuth can be associated with a particular source, e.g. delayed arrivals having a common spectral feature, these 3-dimensional paths can be modelled to establish additional isochrones. This serves as an addition of "virtual" stations to improve triangulation, and is demonstrated using the bathymetrically refracted 3D features observed in the signal of the ARA San Juan. Spectral and cepstral features allow for unambiguous association of the 3D arrivals recorded HA10-Ascension and HA04-Crozet. This study concludes with an assessment of the accuracy, limitations and efficiency of 3D modelling techniques based on hybrid of rays, acoustic modes and the parabolic equation.*

Keywords: *3D acoustics, normal modes, long-range propagation*

1. INTRODUCTION

On November 15th, 2017 an intense sonic impulse was recorded by two Comprehensive Nuclear Test Ban Treaty (CTBTO) hydroacoustic stations. This sound was generated by the catastrophic failure of *ARA San Juan* (a submarine) hull as it sank to the bottom of the ocean.[1] This intense signal propagated 6000 km to Ascension Island (HA10) and 8000 km to the Crozet Islands (HA04). The signal contains a wealth of information relating to the origin of the sound as well as oceanography.

Echoes of intense impulses produce a long duration coda, which in the case of a nuclear detonation lasts for hours.[2] The coda of the *San Juan* impulse observed at the Mid-Atlantic station was detectable for over 15 minutes, and consisted of delayed arrivals from multiple directions.[3] These 3D arrivals were sound energy redirected, i.e. refracted, by ocean topography (bathymetry).[4] This focused study develops an acoustic propagation model to reliably reproduce three-dimensional (3D) features (an example is the dotted line in Fig. 1).

This paper is organized as follows: first, a forward model reproduces characteristics of the observed signal dispersion. This forward model provides important information relating to modal arrival times needed for triangulation. Next, timing of distinct modal arrivals is modelled with adiabatic mode theory, and a piecewise approach efficiently reconstructs the energy path of 3D arrivals. The paper concludes with triangulating *San Juan* based on three arrivals (those shown in Fig. 1).

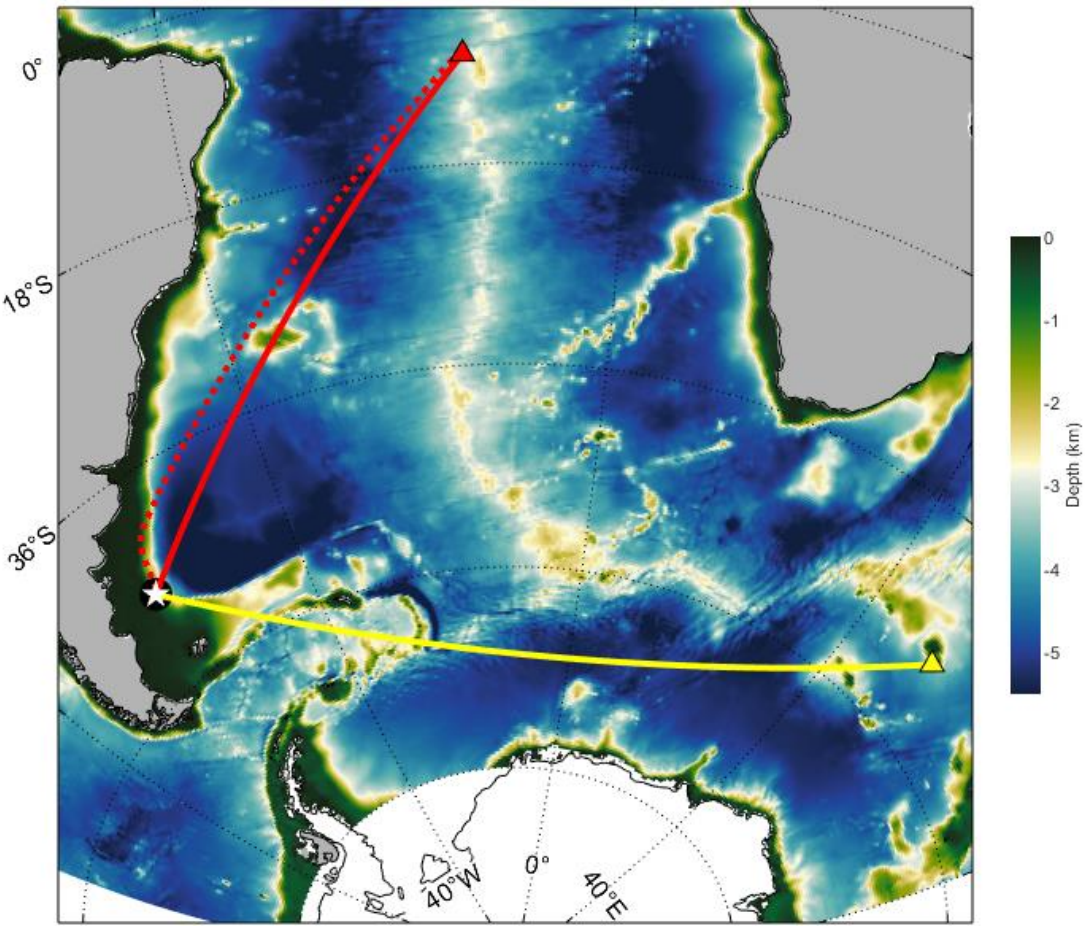


Fig. 1: Acoustics paths to H10N (red) and H04S (yellow) used for triangulation.

2. FORWARD MODELING PROPAGATION (FEATURE IDENTIFICATION)

Modelling propagation paths at megameter scale requires some careful considerations. Boundary interactions and interplay with oceanography are fundamental aspects of long-range sound propagation. This vertically confinement, or trapping of sound energy makes long range acoustic detection possible. Sound trapping by boundaries, the characteristic defining shallow water propagation, is efficient when wavefronts of the incident field propagate at a low (horizontal) grazing angle. For bottom reflections, sound is nearly perfectly reflected at grazing angles less than the critical angle, $\Theta_c = \cos^{-1}(n)$ where n is the ratio of sound speed (index of refraction) across the interface. Propagation can be approximated by a set of discrete trapped modes populating propagation angles from horizontal to Θ_c. As frequency increases so does the number of modes, and the mode-1 propagation angle migrates closer to horizontal.

In the deep ocean, very little sound energy propagates to the sea floor due to a gradient in sound speed caused by increasing pressure (roughly an increase of 10 m/s per km depth). This turning of energy is more efficient than a boundary reflection, as scattering from surface roughness is avoided. In addition to upward refraction, downward refraction by temperature gradients in the upper ocean form a true sound speed duct known as the Sound Fixing and Ranging (SOFAR) channel.[3] In avoiding scattering from the sea surface and sea floor, sound in the SOFAR channel propagates great distances.

The most basic model of a propagation path in latitude and longitude is the shortest path on the surface of the Earth. These geodesics are defined here on the World Geodetic System (WGS84). Although providing a reasonable representation of the sound energy path, prediction of the arrival time also depends on the meandering depth of the sound energy. This aspect elongates the propagation path, but as speed of sound also changes with depth, dispersion in mode arrivals is geospatially dependent. The depth dependent speed of sound (sound speed profile) along the geodesic from [45.9402° S, 59.8101° W] to the two CTBTO hydroacoustic stations are shown in Fig 2; observe the SOFAR channel at HA10 (top).

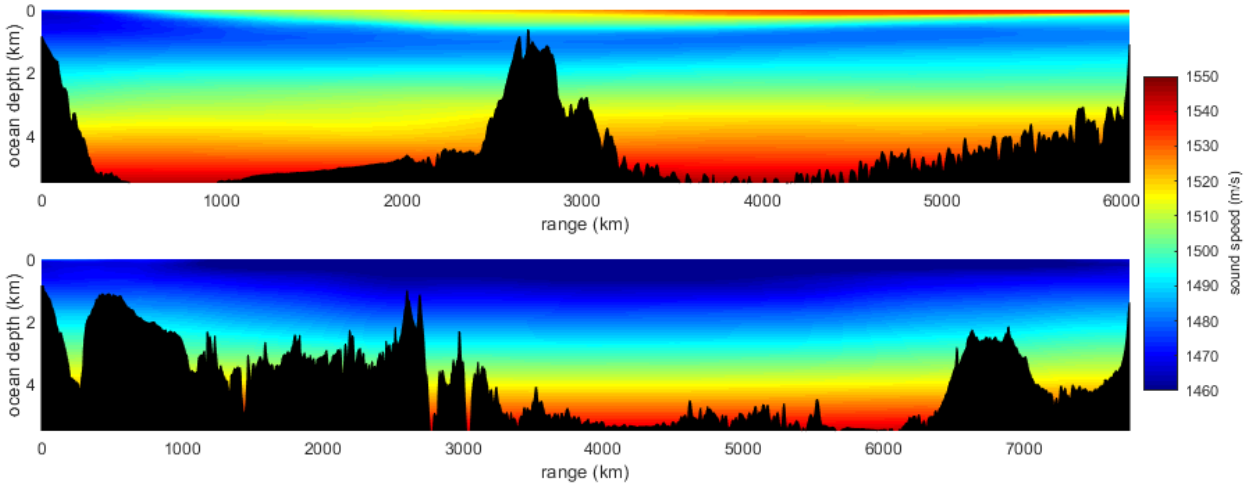


Fig. 2: Sound speed profiles along the propagation path to HA10 (top) and HA04 (bottom). Data tabulated from the World Ocean Atlas.

A two dimensional propagation model (along a geodesic and depth) provides valuable insight into the time frequency characteristics of the direct energy path. Propagation models cast in a Cartesian coordinate system must implement an Earth flattening transformation to account for path shortening in depth for a given arc length. This applies to both sound speed and ocean depth, which are multiplied by the ratio R / (R – D), where R is the radius of Earth, and D is depth.

Figure 3 shows a model of the direct field at HA10 and HA04, based on the numerical PE solver RAM-PE.[5] The time series are a Fourier synthesis of 601 discrete frequencies, with time-frequency characteristics showing a dispersed signal similar to those observed in the data (see Fig. 4). A matched field comparison can provide a precise estimate of the source range (and time); however it is worth noting the computation time to produce Fig. 3 was nearly 24-hrs. Although at long ranges such numerical methods are slow, the full wave-representation maintains a high degree of accuracy.

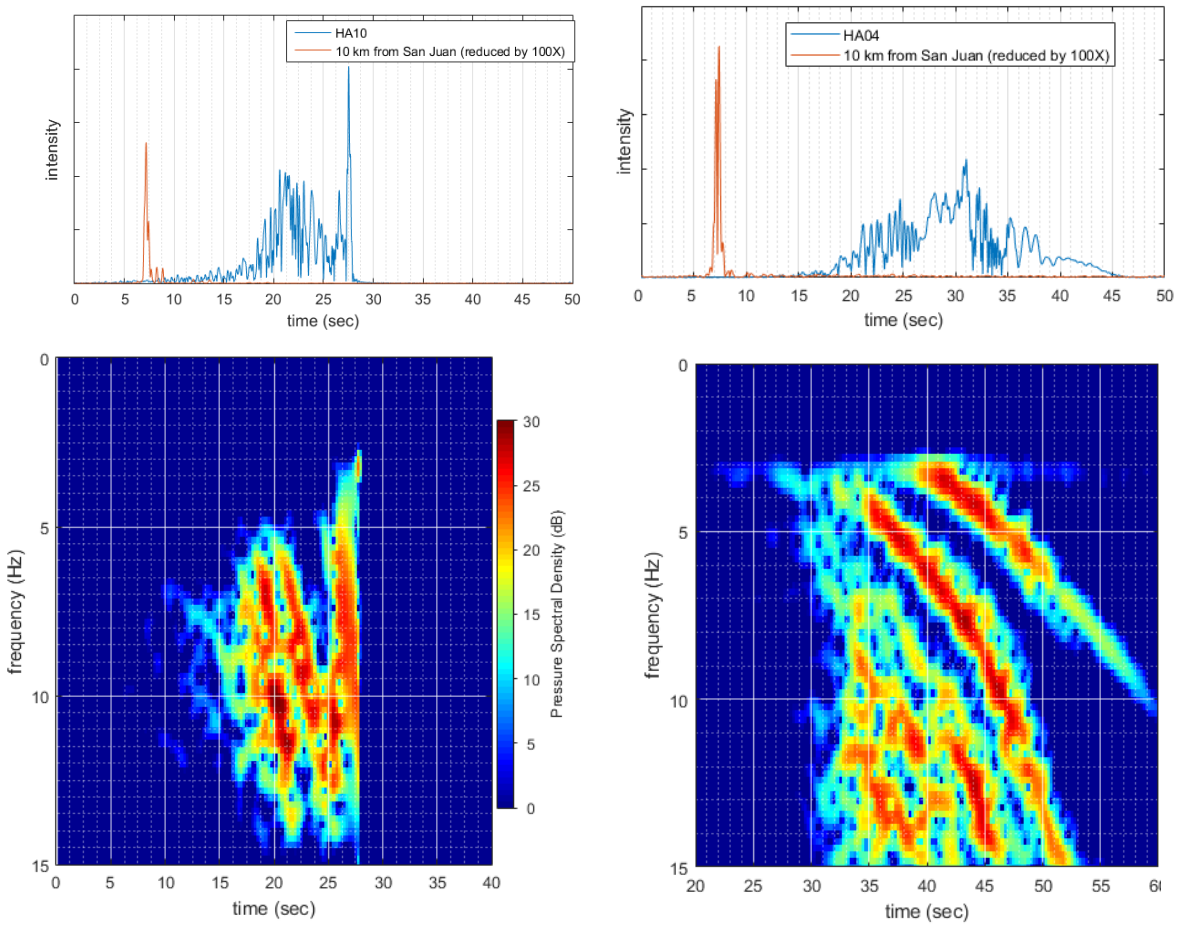


Fig. 3: [*left*] *Synthesized impulse pressure as received 10 km from the San Juan location and HA10, and [right] at 10 km and HA04. Vertical axis is intensity on a linear scale, and level at 10 km is divided by 100. Lower time-frequency plots are the corresponding he pressure spectral density at HA10 and HA04 (decibel units).*

An alternative and computationally fast model of propagation is based on adiabatic mode theory (adiabatic implies no energy is exchanged between modes). The dispersion characteristics of the *San Juan* impulse at the CTBTO stations show distinct mode arrivals. A difference in dispersion at the two stations is striking, and it is due to the different oceanography along each path (discussed in the next paragraph). Correct identification of modal arrival times is essential for triangulation through back-propagating of detected arrivals. Arrival times depend on group velocity, and an estimate of arrival time (T_n) for the n^{th} mode is given by,

$$T_n = L\frac{d\bar{k}_n}{d\omega} \tag{1}$$

where L is the distance along the geodesic connecting source and receiver, ω is frequency times 2π, k_n is the horizontal wavenumber of the n^{th} mode and the overbar indicates an average value over the propagation path.

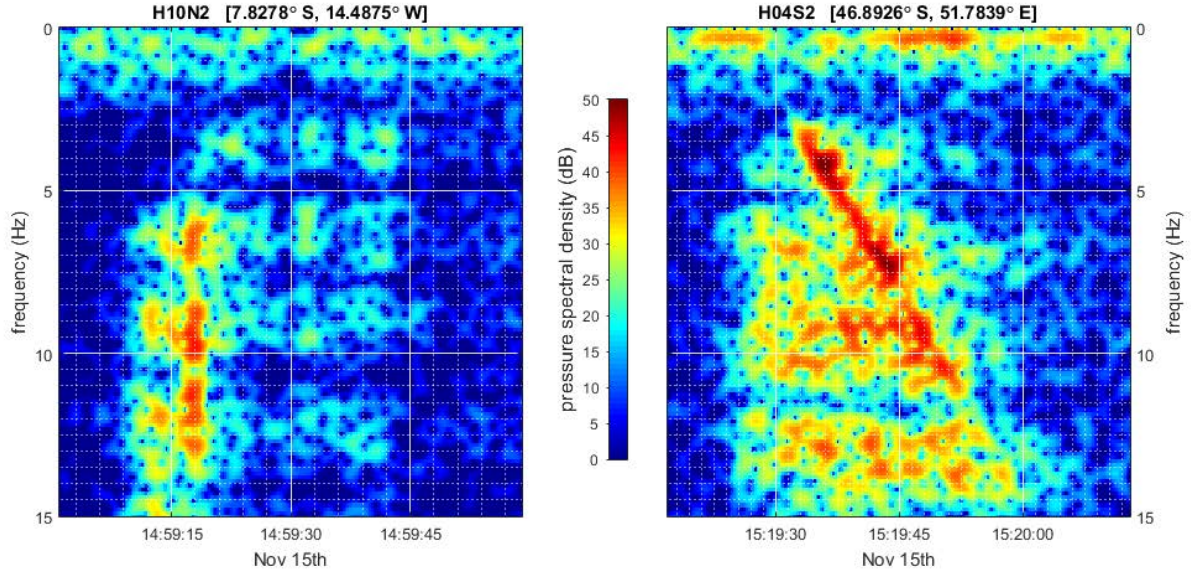


Fig. 4: Time-frequency plot of recorded direct arrival at H10N2 (left) and H04S2 (right)

Propagation to HA10 is primarily within the SOFAR channel, and mode-1 group velocity is effectively frequency independent from 5-15 Hz. Propagation to HA04 is within a surface duct, i.e. reflected from the sea surface and refracted by the deep ocean. Due to the increase in mode number with frequency, mode-1 is pushed closer to horizontal causing its group velocity to slow down linearly with increasing frequency. Group velocity ($d\omega/dk_n$), phase velocity and horizontal wavenumber can be readily calculated via a mode finding routine. With Eq. (1) and mode properties ascertained from the normal mode program KRAKEN [6], and frequency dependence of T_n reproduce the characteristic or mode-1 dispersion. At HA10, the mode-1 arrival is frequency independent, and at HA04 the mode-1 arrival exhibits a 2.5 second delay per Hz [see Fig. 4]. This also confirmed the peak arrival at 10 Hz corresponds to mode-1, and the delay of mode-1 from the onset of signal detection at both stations.

3. PIECEWISE MODELLING OF AZIMUTHALLY REFRACTED ARRIVALS

The 2D model lacks information about the signal coda after the direct arrival (about 30 seconds). The later part of the coda consists of bathymetrically refracted arrivals, and contains valuable information for triangulating sources. To elaborate on this, let us consider the first (and loudest) 3D arrival observed in the HA10 recording. This sound arrives roughly 90 seconds after the first detection, having travelled further to the continental slope where refraction occurred (see dotted red line in Fig. 1).

To model refracted arrivals, horizontal dependence of the adiabatic mode description is modified from a single radial coordinate to two horizontal coordinates (easting and northing). Depth dependence is maintained by the phase and group velocity description of the mode. What drives refraction are gradients in mode phase speed, and thus azimuthal coupling can be modelled with standard 2D ray tracing or PE methods where phase speed is the surrogate for speed of sound.

What we gain with the PE comes at great computational expense. This inherently narrowband simulation method requires a Fourier synthesis to reproduce a timeseries. Note again the long computation time to produce Fig 3, nearly 24-hr for 601 discrete frequency PE simulations. However, narrowband simulations can still be used to identify the path of sound energy. Energy flux streamlines depict the path of energy and are formed by marching in the direction intensity, and divergence of two neighbouring streamlines corresponds to intensity (less energy lost to heat or transmission into the sediment). In free-space, i.e. a uniform medium with no boundaries, streamlines and rays are identical, excepting in the nearfield of complicated sources.[7]

In deep water, low-frequency sound (10 Hz) follows geodesics. Shoaling of sound energy at the continental shelf can be modelled with ray tracing techniques. Ideally the ray connecting a source and receiver is in the direction of the detected energy. However, due to scattering from a realistic bathymetry, finding of such rays is not always possible. To overcome this, a PE solution with a beam starting field is implemented to construct refracted streamlines. The PE embodies the complete dynamics of the refraction process, and by using a beamed source the refracted field is isolated from the direct field [see Fig. 5].

Efficient modelling of 3D arrivals makes use of PE only for the portion of propagation into shallows (the water depth where refraction takes place, which also depends on frequency). The streamline description allows for initiation and then continuation of streamlines with rays (geodesics at 10 Hz) if they propagating into deeper water. Figure 5 shows the continuation of 10 Hz mode-1 with an intensity beam, representing the back propagated energy from H10N2; a clear path exists to the *San Juan* location (star). Of curiosity is a hint of an additional 'whispering gallery' path that follows contours of the continental slope. The region where PE computation of the refracted path is needed is roughly 100 km x100 km, which takes less than a minute to compute.

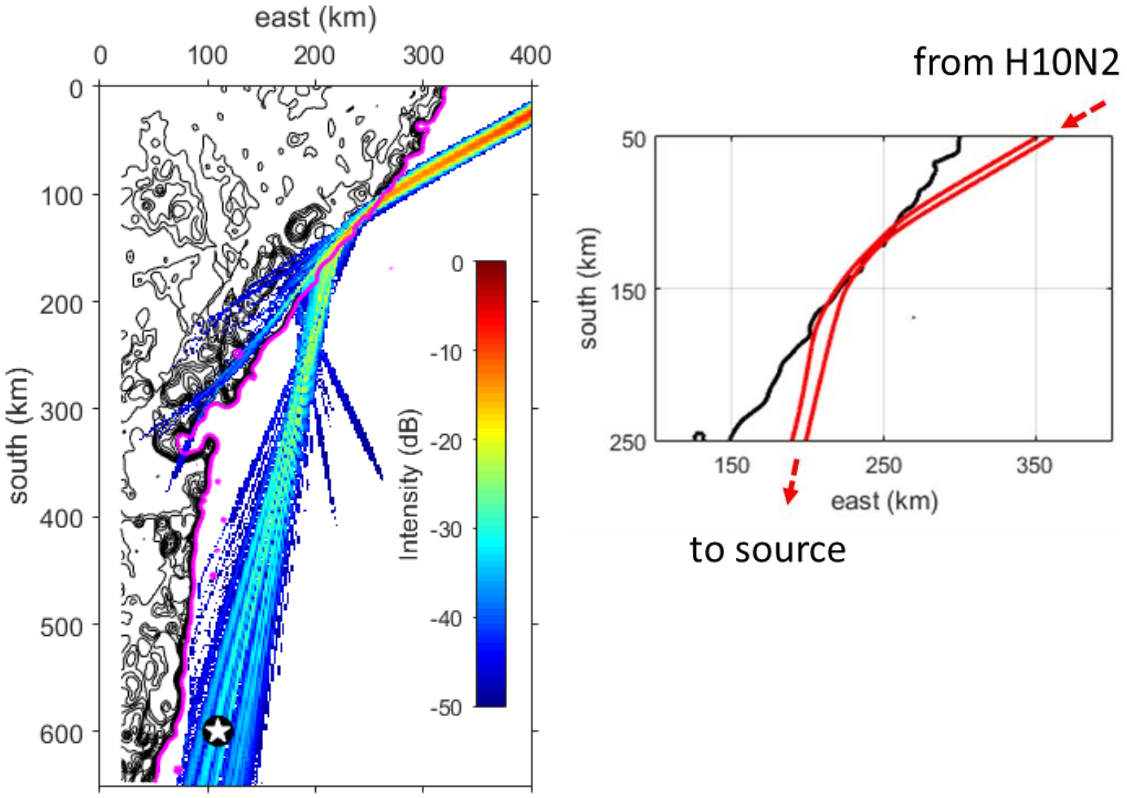


Fig. 5: [Left] Intensity beam of mode-1 at 10 Hz depicting horizontal refraction and energy path to the San Juan (star). The input beam direction is a continuation of the geodesic launched from H10N at bearing 221.3°, and the magenta line indicate the 300 m depth contour where bathymetric refraction come into play. [Right] Streamline tube built from the PE simulation, input heading 241° and output heading is 193°.

4. TRIANGULATION OF THE ARA SAN JUAN

With the 3 energy paths shown in Fig. 1 established, two paths to HA10 (Ascension) and one to HA04 (Crozet), the timing of the mode-1 arrival is calculated via Eq. 1. Since mode-1 is characterized by the peak energy arrival at 10 Hz, arrival times are extract from the data. Table 1 outlines the extracted arrival time estimates for mode-1 at 10 Hz used for triangulation. Source triangulation is at the intersection of three isochrones, or the surfaces of equal travel time that are perpendicular to propagation paths. Fig. 6 shows the intersection of the three isochrones, occuring near the location of the *San Juan* (star). With the model parameters, this estimates a source time 13:51:18 UTC.

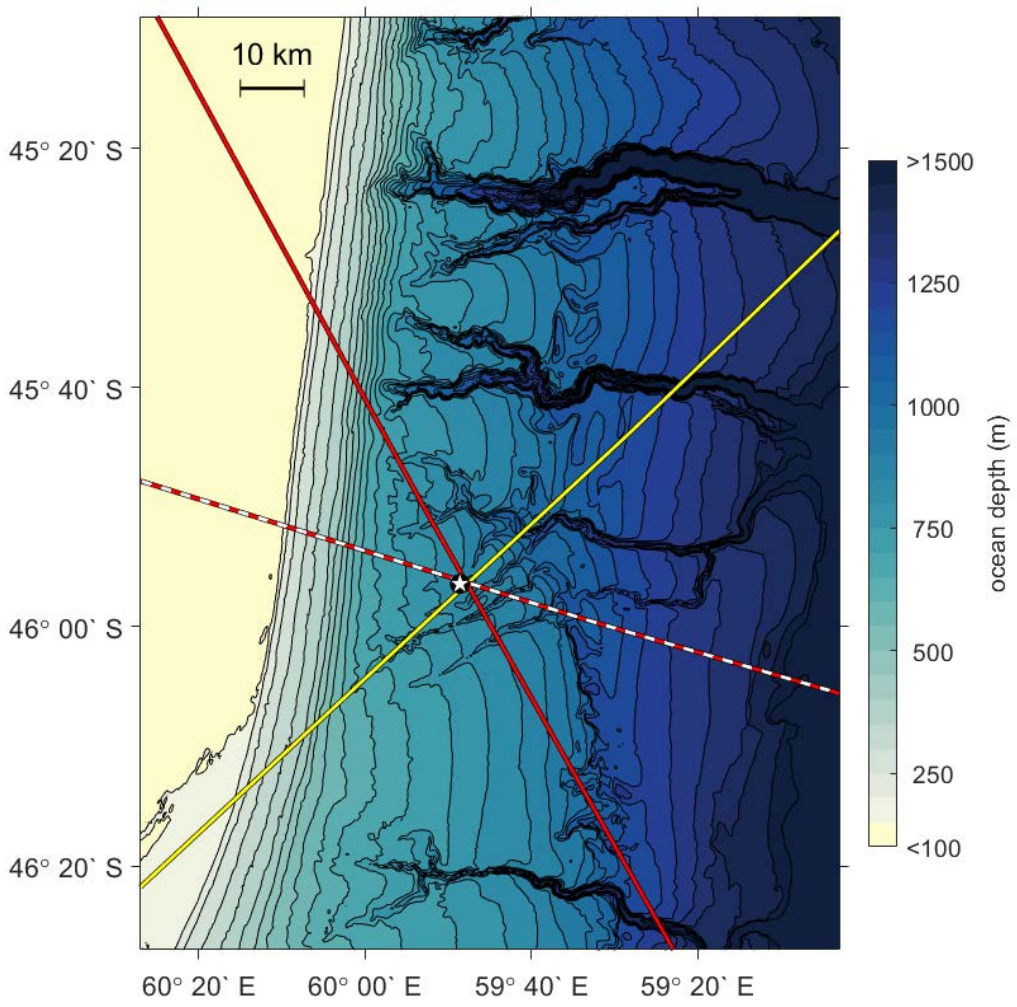


Fig. 6: Triangulation result giving a source time of 13:51:18.

MODE 1 ARRIVAL TIME	NOV 15TH	DEC 1ST
H10N2	14:59:15	21:12:06
H10S2	14:58:04	21:10:51
H04S2	15:19:44	21:33:00
REFRACTED ARRIVAL TIME		
H10N2	15:00:29	21:13:24
H10S2	14:59:23	21:12:15

Table 1: Timing of mode-1 arrivals at 10 Hz used in triangulation

5. SUMMARY AND DISCUSSION

The intense impulsive sound emitted from the submarine, *ARA San Juan*, produced a number of bathymetrically refracted arrivals. A refracted arrival observed at the Ascension Island CTBTO hydroacoustic station was modelled and used to triangulate the sound source from the detections. The energy path of this refracted arrival was reproduced through back-propagating an energy streamline by a piecewise model based on adiabatic modes. By design, azimuthal dependence of streamlines are only calculated with a computationally expensive PE where refraction occurs (at 10 Hz this is in water depth less than 300 m).

Although only one 3D path is detailed here, this technique can be applied to model additional 3D arrivals in the arrival coda and reduce uncertainty in triangulation. The beamed sources with a PE computation addresses complicated propagation the continental slope, but also applies to modelling the modulation of direct propagation around seamounts. Furthermore, this beamed energy technique can build a transfer function to account for refraction (i.e. change in propagation direction) caused by bathymetry surrounding the CTBTO stations.

6. ACKNOWLEDGEMENTS

This work was supported by the Office of Naval Research (ONR), Ocean Acoustic Program (322OA). The author would like to thank Brian Dushaw for our recent discussions, and willingness to share his expertise in ocean tomography.

REFERENCES

[1] **Villán, José Luis**, The Tragic Loss of ARA San Juan, *Proceedings of the U.S. Naval Institute*, Vol. 45, pp. 1393, 2019.

[2] **Dushaw, Brian D.,** WIGWAM Reverberation Revisited, *Bulletin of the Seismological Society of America*, vol. 105, pp. 2242-2249, 2015.

[3] **Nielsen P., M. Zampolli, R. Le Bras, P. Mialle, P. Bittner, A. Poplavskiy, M. Rozhkov, G. Haralabus, E. Tomuta, R. Bell, and P. Grenard**, ”Analysis of hydroacoustic and seismic signals originating from a source in the vicinity of the last known location of the Argentinian submarine ARA San Juan,” *European Geosciences Union General Assembly*, Vol. 20, EGU 2018-18559, 2018.

[4] **Munk, W.H., and F. Zachariasen,** Refraction of sound by islands and seamounts, *J. Atmos. Ocean. Tech.,* vol. 8, pp. 554–574, 1991.

[5] **Collins, Michael,** A Split-Step Padé Solution for the Parabolic Equation Method, *Journal of the Acoustical Society of America,* vol. 93, pp. 1736-1742, 1993.

[6] **Porter, M. B. and E. L. Reiss,** “A numerical method for ocean acoustic normal modes,” *J. Acoust. Soc. Am.* 76, pp. 244-252, 1984.

[7] **Heyser, Richard C.,** Instantaneous intensity, *Proceedings of the 81st Convention of the Audio Engineering Society* , Preprint 2399 (1986).

FLUCTUATION DRIVERS AND VARIABILITY OF VERY LOW FREQUENCY LONG TERM OCEAN AMBIENT NOISE

Anthony I. Eller[a], David L. Bradley[b]

[a] Applied Ocean Sciences, 11006 Clara Barton Drive, Fairfax Station, VA 22039, USA
[b] University of New Hampshire, Durham, NH 03824, USA.

Anthony Eller, Applied Ocean Sciences,11006 Clara Barton Drive, Fairfax Station, VA 22039, USA , anthony.eller@appliedoceansciences.com

Abstract: *Long term ocean acoustic noise data from widely separated measurement sites, spanning periods of up to 15 years, have been made available for analysis by the Comprehensive Test Ban Treaty Organization (CTBTO). Raw noise data, sampled at a rate of 250 Hz, were Fourier Transformed in 10-sec segments to provide noise spectra with a resolution of 0.1 Hz over long periods of time. Low-frequency spectrum level time series data were examined for two purposes: (1) to identify long term statistical trends that might signal changes in climate, and (2) to identify natural or man-induced processes that drive observed fluctuations in noise spectral level. Noise levels in the 1 – 5 Hz part of the spectrum are thought to be relatively free of noise from shipping and marine life. As such, noise fluctuations in this band tend to be driven by natural processes, such as weather, natural seismic activity and sun and moon positions. The statistical behavior of noise at these low frequencies has unique properties, which may provide the opportunity to confidently isolate specific noise forcing functions, allowing interpretation of the time change of oceanic sea noise.*

Keywords: *ambient noise, noise fluctuations*

1. INTRODUCTION

Long term ocean acoustic noise data from three widely separated measurement sites, spanning periods of up to 15 years, have been made available for analysis by the Comprehensive Test Ban Treaty Organization (CTBTO). Analysis results presented here pertain to the site near Wake Island in the Western Pacific Ocean. Raw noise data, sampled at a rate of 250 Hz, were Fourier Transformed in 10-sec segments to provide noise spectra with a resolution of 0.1 Hz over long periods of time. Low-frequency spectrum level time series data were examined for two purposes: (1) to identify long term statistical trends that might signal changes in climate, and (2) to identify natural or man-induced processes that drive observed fluctuations in noise spectral level.

Noise levels in the band from 1 to 5 Hz, which are the focus of the present paper, are thought to be relatively free of noise from shipping and marine life. As such, noise fluctuations in this band tend to be driven by natural processes, such as weather, natural seismic activity and sun and moon positions. The statistical behavior of noise at these low frequencies has unique properties, which may provide the opportunity to confidently isolate specific noise forcing functions, allowing interpretation of the time change of oceanic sea noise.

2. TIME SERIES FOR 1-HZ SPECTRUM LEVEL

Figure 1 presents a roughly 10-year-long time series for the 1-Hz ambient noise spectrum level near Wake Island in dB re $1\mu Pa^2/Hz$. There are obvious issues with the data, mainly the time gaps where data could not be extracted from the hard drive using existing software and the spikes seen in year 2013 and later. The statistics presented within the figure are based only on the actual data. It is expected that the issue with the gaps will be resolved later, but for the temporal statistics discussed later, the missing values were replaced by the overall mean noise level. Several data values showed NaN (not-a-number). These were replaced by the average spectral level in order to do the subsequent analysis.

Possibly the two most obvious features of the black band representing the data are its height – standard deviation of 6.84 dB – and its general steadiness over the 10-year span. The dashed line is a linear regression curve computed to show growth or decline of noise level. The result is an increase of about 1 dB/decade. Regression trends were computed also for individual years, and significant rates of increase or decrease were found, but these all even out over the full ten- year period. A lesson to note here is that one should not look for meaningful long-term trends in single year data.

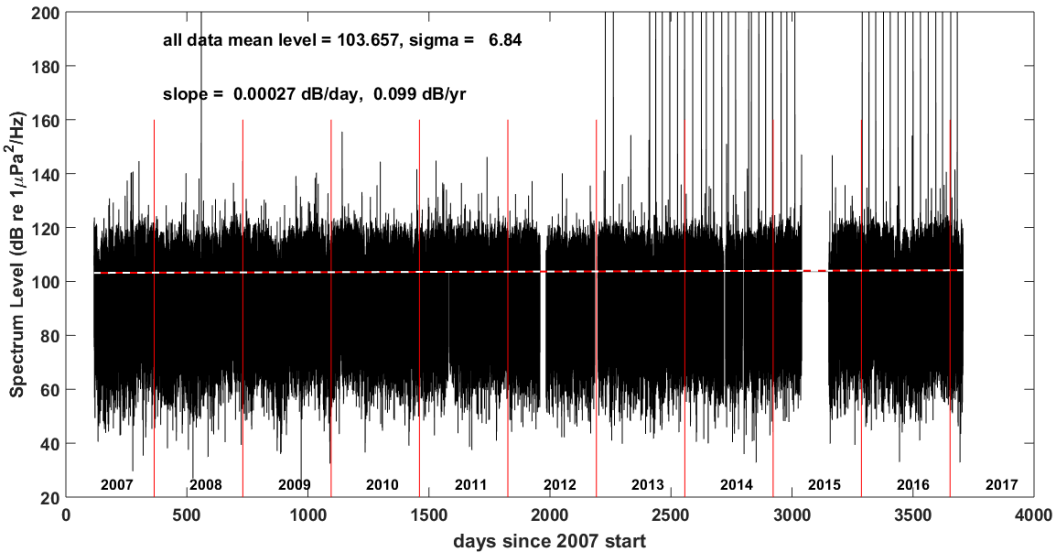


Figure 1. Time series of spectrum level for 1-Hz tonal.

3. ANALYSIS OF TIME SERIES FLUCUATIONS

The fluctuations in the noise spectrum level, as plotted in Figure 1, are investigated through the computation and display of three analysis products; (1) power spectral density of the time series, (2) the logarithmic spectrum, or distribution of variance, and (3) the coherence of the time series as a function of time shift. The power spectral density for the 1-Hz level time data in Figure 1, computed by taking the Discrete Fourier Transform of the time series, is presented in log-log format in Figure 2. Note here that the unit of frequency used in describing the fluctuations is a cycle per hour (cph).

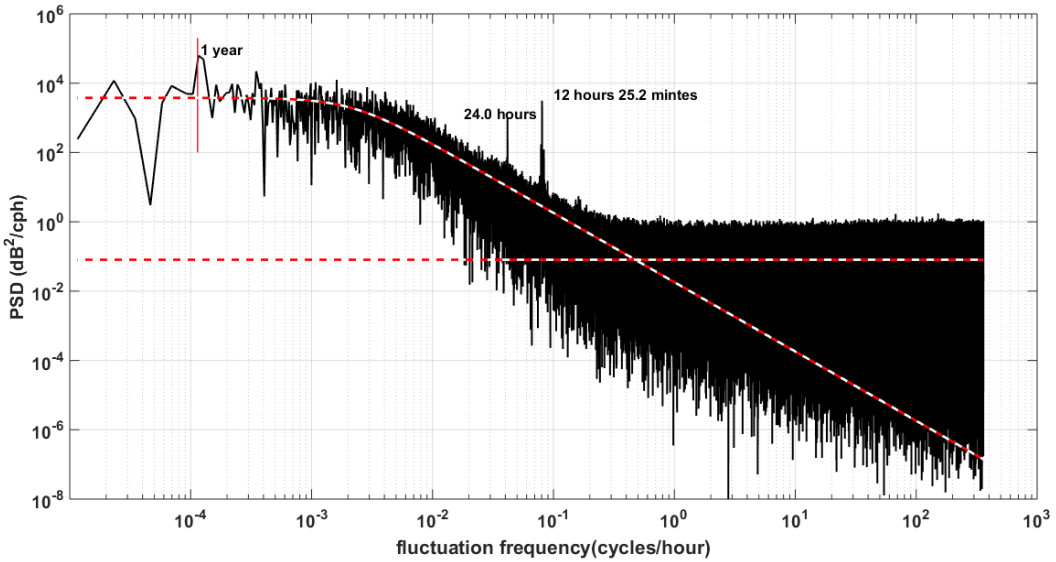


Figure 2. Power spectral density of fluctuation in 1-Hz noise level.

Two general processes are indicated in this figure. The first process, shown on the left side of the figure, is indicated by the generally flat region at low frequencies up to about 0.004 cycles per hour (cph), followed by a decay rate of about $1/f^2$ or -2 on the log-log plot. The

presence of a flat section followed by a slope of -2 is characteristic of a first-order stochastic Markov process. The theoretical expression for the spectral density Φ of a first-order process is [1]

$$\Phi = 2V\tau / (1 + (2\pi f\tau)^2) \quad (1)$$

where τ is the coherence time of the process and V is its variance. The coherence time is estimated from the coherence function in Figure 4 and, for this case, is estimated to be 72.7 hours, or about 3 days, and the variance associated with this process, from Figure 3, is 13.03. The upper dashed line in Figure 2 has a slope of -2, corresponding to $1/f^2$ and provides confirmation that the fluctuations come from a first-order stochastic process.

A second process is indicated by the flat region at fluctuation frequencies above about 0.2 cph. The flat section to the right of about 0.2 cph suggests the presence of a second stochastic process that does not begin a downward slope until fluctuation frequencies above the upper frequency limit in this analysis, which is 360 cph. The power spectral density in this second flat region is given by

$$\Phi = V / f_{max} , \quad 2)$$

where V in this case is the variance associated with this second process, which is 29.17. The resulting spectral density is 0.0806 dB^2/cph and is indicated by the horizontal dashed line in Figure 2..

The second set of features consists of the three spectral lines indicated in the figure. These correspond, as labeled, to periods of 12 hours 25 minutes (the tidal cycle), 24 hours, and one year.

Figure 3 provides an alternate way to view the spectrum of the fluctuations. In this presentation the spectrum is presented in proportional bins – tenth decade – instead of in uniform frequency bins. In addition the information is presented in terms of period along the abscissa, rather than frequency. Each bar represents the variance contribution in a one-tenth-decade bin, and the total variance is the sum of the contributions from all bins. These results are based on the data in Figure 1. The quantity presented here is known by some as the logarithmic spectral density.

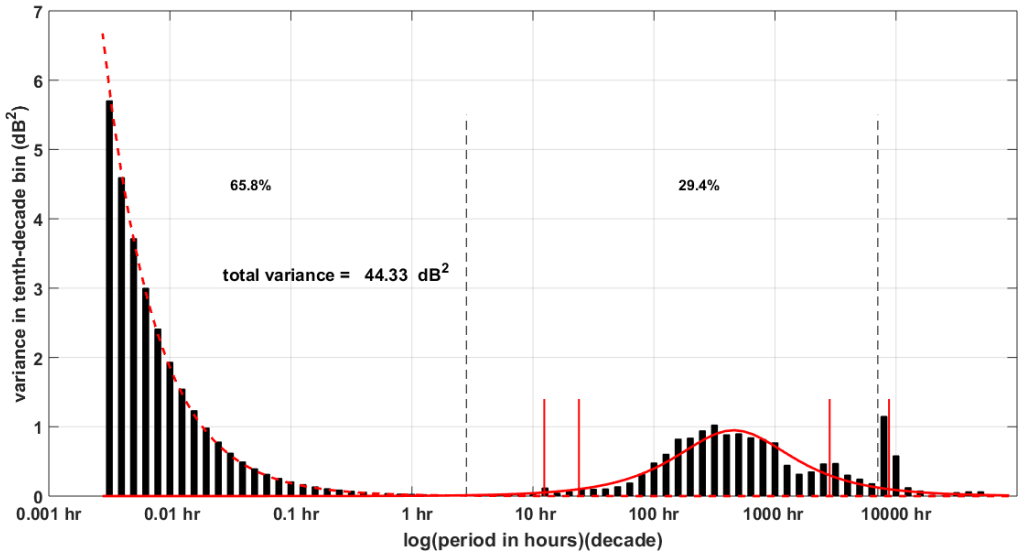


Figure 3. Distribution of fluctuation variance for 1-Hz tonal over 10 years.

What is notable here is the near total absence of variability for fluctuation periods in the range ½ to 20 hours, thus separating the character of the variability into three contributing sections: first is the very short term process that extends in the figure to periods up to about 3 cph and accounts for approximately 66% of the total variance (found by adding the variance contributions in the left hand section), second is the appearance of one or possibly two partly overlapping stochastic processes apparent from about 3 to 8000 cph and which together account approximately for an additional 30% of the variance, and lastly an annual variation that is interpreted as a cyclical process driven by the annual solar cycle and not as a stochastic process. The primary peak in the middle section occurs at 316 hours or about 13 days, and the secondary peak at about 118 days.

The two theoretical curves for the logarithmic spectral density are given by

$$\text{Logarithmic spectral density} = \text{power spectral density} * \text{frequency} * 2.3, \quad (3)$$

where the power spectral density is given by either of Equations 1 or 2, and the factor 2.3 enters because the data are presented using logarithms to base 10 rather than natural logarithms.

Figure 4 shows the coherence function for the 1-Hz time series in Figure 1 for time shifts from zero to 150 hours. The coherence function is normalized to unity for zero time shift. This figure, again, indicates the presence of at least two temporal fluctuation processes. First is the delta-function-like behaviour at time shift near zero. The coherence drops from unity almost immediately to a value of about 0.35, indicating a coherence time less than the time step size of 5 s. Following this drop the coherence drops roughly exponentially, consistent with a first-order process. A straight-line regression curve was fitted to the natural log of the coherence function against time, and the slope of this line was then used to provide an estimate of the coherence time of about 72.7 hours. The coherence time commonly is taken as the time for the coherence function to drop below 1/e of its initial value. The two dashed lines in Figure 4 are the 1/e lines for each of the two processes.

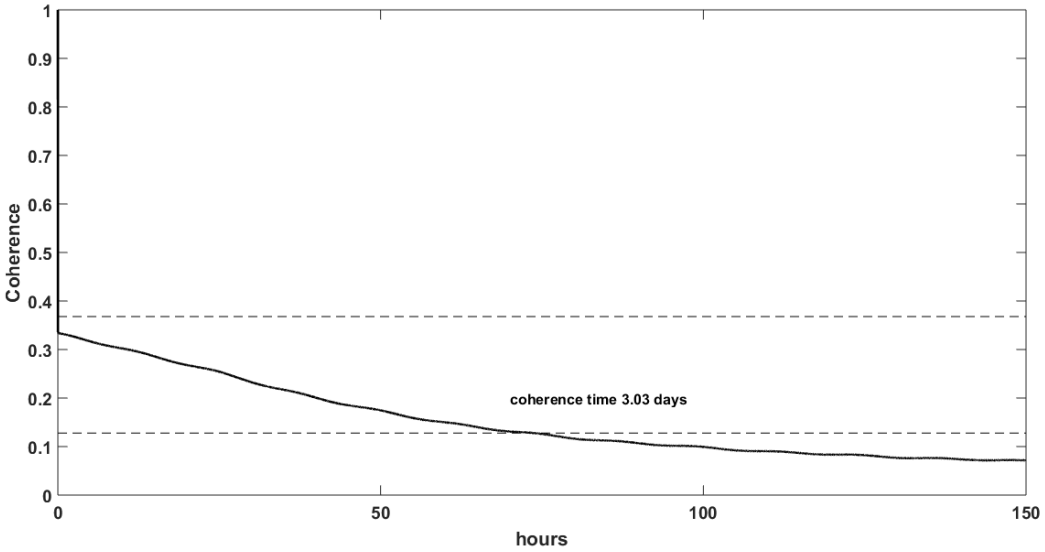


Figure 4. Coherence function for fluctuations of 1-Hz tonal.

In summary, fluctuations in the 1-Hz signal appear to be related primarily to three, possibly four principal causes: short-period fluctuations at the left of Figure 3 are likely caused by phase interference, a mid-range stochastic process centred about 13 days or 2 weeks and likely related to wind speeds, a weaker longer-period stochastic process of unknown cause centred

around about 4 months, and finally an annual variation. Bradley and Nichols [2] report strong correlation between wind speeds near Wake Is. and the 1-Hz noise level.

Results at 3 and 5 Hz are, in a general sense, like those at 1 Hz but with some substantial differences in how the variance is distributed over fluctuation period. The distributions of variance are shown in Figure 5 for these three frequencies. One notices especially the growth at 3 and 5 Hz of substantial variability at periods of around 10 to 20 minutes, and the relative lack of variability in the 2-week time frame. The goal now is to unravel the extent to which the variability is caused primarily by changes in the strength or number of sound sources or changes in propagation losses.

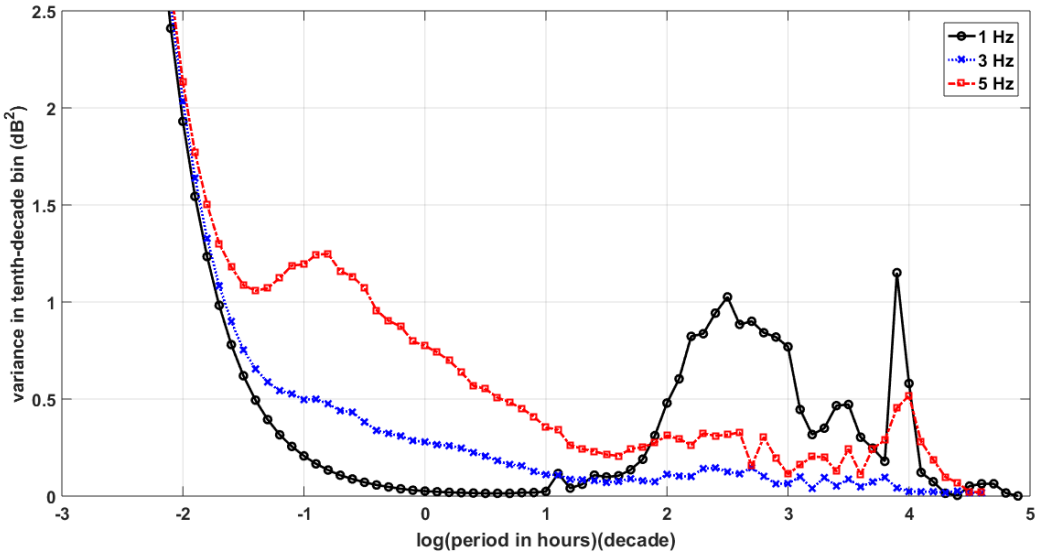


Figure 5. Comparison of fluctuation variance for tonals of three frequencies.

REFERENCES

[1] **Arthur Gelb**, editor, *Applied Optimal Estimation*, The Analytical Science Corporation, p. 44, 1974, Tenth printing, MIT Press, 1988.

[2] **David L. Bradley** and **Stephen M. Nichols**, Worldwide Low-Frequency Ambient Noise, *Acoustics Today*, 11, pp.20-26, 2015.

EVALUATION OF LONG-TERM TRENDS IN DEEP-OCEAN NOISE IN THE SOUTHERN OCEAN USING CTBTO HYDROACOUSTIC DATA

Stephen Robinson, Peter Harris, Lian Wang, Valerie Livina and Sei-Him Cheong
National Physical Laboratory, United Kingdom

Stephen Robinson
t: +44 (0)208 943 7152; stephen.robinson@npl.co.uk

National Physical Laboratory, Hampton Rd, Teddington, Middlesex, TW11 0LW, UK.

Abstract: *The variation in the ambient sound levels in the deep ocean has been the subject of a number of recent studies, with particular interest in the identification of long term trends. This paper describes a statistical method for performing long term trend analysis and uncertainty evaluation of the estimated trends from deep-ocean noise data. The measured data used here originate from the Southern Ocean and span up to a maximum of 15 years, from 2003 to 2018. The data were obtained from the hydro-acoustic monitoring stations of the CTBTO. The analysis method uses a flexible discrete model that incorporates terms that capture seasonal variations in the data together with a moving-average statistical model to describe the serial correlation of residual deviations, with uncertainties validated using bootstrap resampling. The main features of the approach used include (a) using a model that includes terms to represent explicitly seasonal behaviour, (b) using daily aggregation intervals derived from 1 minute SPL averages, and (c) applying a non-parametric approach to validate the uncertainties of trend estimates that avoids the need to make an assumption about that distribution of those differences. The trend analysis is applied to time series representing monthly and daily aggregated statistical levels for five frequency bands to obtain estimates for the change in sound pressure level with associated coverage intervals. Statistically significant reductions in SPL are observed for all statistical percentiles for the different frequency bands as a result of negative trends in the examined time series. Strong seasonal variation is also observed, with a high degree of correlation with climatic factors such as sea surface temperature, Antarctic ice coverage and wind speed.*

Keywords: *ocean ambient noise; statistical trends, CTBTO monitoring*

BACKGROUND

Measurements of underwater ambient noise have been carried out since at least the 1960s [1]. Most of the studies demonstrating an increase in the levels of low frequency sound in the deep-ocean have been undertaken in the Pacific Ocean [2-4]. In part, the observed increasing trend has been attributed to increases in noise produced by shipping [5,6], but it is recognised that there is a variety of sound man-made and natural sources which contribute to the ambient sound field at frequencies below 100 Hz, including ice breaking [7,8]. The paucity of available data over the last 50 years has meant that attempts to determine trends have often been based on very few data points and relied on simple statistical techniques such as straight-line fits but in more recent studies covering the last 15 years, use has been made of much richer data sets where continuous monitoring has been undertaken [9-12].

This paper describes a statistical method for performing long term trend analysis and uncertainty evaluation of the estimated trends [13]. The method uses a flexible discrete model that incorporates terms capturing seasonal variations in the data together with a moving-average statistical model to describe the serial correlation of residual deviations, with uncertainties validated using bootstrap resampling. The measured data used in this study were obtained from the hydroacoustic stations of the Preparatory Commission for the Comprehensive Nuclear Test Ban Treaty Organization (CTBTO).

DATA PROCESSING

Each CTBTO hydroacoustic station consists of three hydrophones separated by approximately two kilometres that are typically placed in the deep ocean sound channel where the vertical sound speed profile exhibits a minimum. Although relatively sparse, the underwater network's design is such that it allows very good spatial coverage of the world's oceans by taking advantage of the physical principles governing the propagation of sound in water. The sampling frequency for the CTBTO sound pressure recordings is 250 Hz to provide information at acoustic frequencies up to 105 Hz. The selected bit depth of 24 bits yields a maximum possible dynamic range of approximately 144 dB.

The data analysed in this study come from the three hydrophones of CTBTO's Cape Leeuwin (H01W) station located off the south west shore of Australia at a depth of about 1 km. For this study, recordings over 14 years, from January 1, 2003 to January 1, 2017, were examined. The data during this period was essentially complete with the total number of days of no data availability being approximately 2.5% of the overall duration of the recordings.

During the processing, the raw data were extracted, and the scaling factors were used to transform the data from A/D counts (outputs of the Analogue to Digital converter relative to the maximum range of the converter) to values of sound pressure. The scaled data were filtered using the inverse frequency responses of the hydrophone channels in order to eliminate artefacts introduced by the recording equipment and to obtain the true frequency content of the recorded signals. The filtered signals were then windowed into 1 minute long rectangular windows, and the data in each window were then filtered in the following five frequency bands to allow multiband analysis: 5–105 Hz (hereafter referred to as broadband), 10–30 Hz, 40–60 Hz, 56–70 Hz, and 85–105 Hz. The mean-squared sound pressure within each frequency band was calculated for each data window, and the resulting values were expressed as sound pressure levels (SPLs) in units of dB re 1 μPa^2. Though the choice of frequency bands is somewhat arbitrary, dividing the data into frequency sub-ranges does enable investigation of how the trends might vary with frequency, and the bands chosen match those used in several other studies of CTBTO noise data, thus enabling a degree of comparability [9].

The 1 minute averaged SPL values were aggregated to give daily, monthly, and annual average and percentile levels for the SPL distributions. The percentiles computed were the 1st, 10th, 50th, 90th, and 99th, hereafter referred to as P_1, P_{10}, P_{50}, P_{90}, and P_{99}. Use of percentiles allows thorough examination of various features of the time series associated with different aspects of the acoustic environment. The last step of the data reduction process was the removal of outliers from the aggregated time series. For this study, outliers were considered to be SPL values at least 20 dB greater than the arithmetic mean of the entire time series, but for this particular dataset, there was only a small number of such anomalously-high observations for each time series (most likely caused by electrical issues) so their removal was considered to have negligible impact on the analysis. An example of the resulting daily aggregated time series for the six statistical levels derived from the broadband values measured by hydrophone H01W1 is shown in Fig. 1. In the figure, the strong annual oscillations are clearly visible in all aggregated statistical levels.

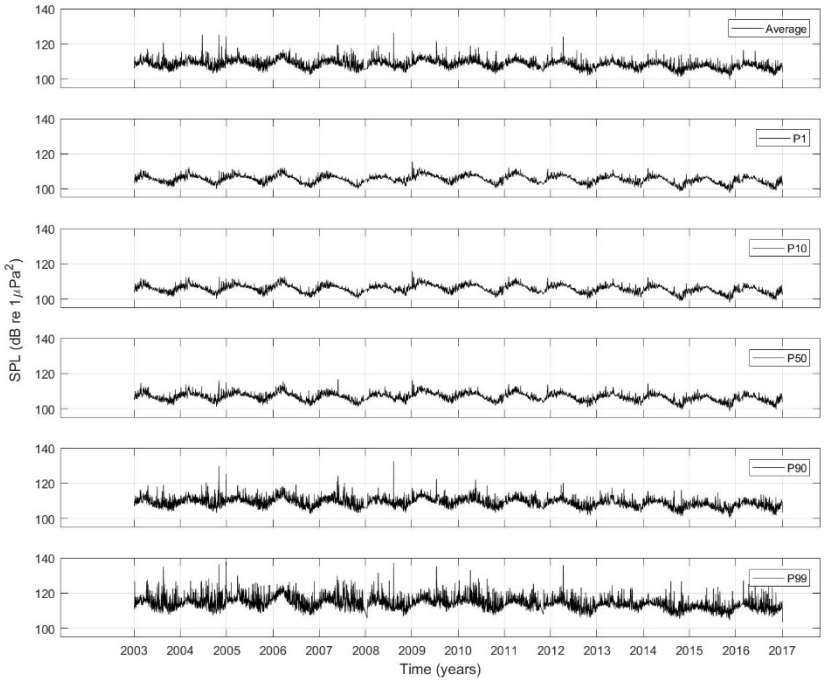


Fig. 1: Daily aggregated broadband SPL values for hydrophone H01W1 showing, from top to bottom, average, P_1, P_{10}, P_{50}, P_{90}, and P_{99} statistical levels.

ANALYSIS METHOD

The analysis method uses a flexible discrete model that incorporates terms that capture seasonal variations in the data together with a moving-average statistical model to describe the serial correlation of residual deviations, with uncertainties validated using bootstrap resampling. The main features of the approach used include (a) using a model that includes terms to represent explicitly seasonal behaviour, (b) using daily aggregation intervals derived from 1 minute SPL averages, and (c) applying a non-parametric approach to validate the uncertainties of trend estimates that avoids the need to make an assumption about that distribution of those differences.

Let $y_{i,j}, j = 1, \dots, n, i = 1, \dots, N$, denote the value of SPL at time $t_{i,j}$ corresponding to a chosen percentile (for example, P_1, P_{10}, P_{50}, P_{90} or P_{99}) of the distribution of SPLs for a chosen aggregation period (for example, daily, monthly or yearly). Here, n is the number of

aggregation periods in a year and N is the number of years over which data are recorded. The data are modelled as:

$$y_{i,j} = at_{i,j} + s_j + e_k,\ k = (i-1)n + j,\ j = 1, \dots, n,\ i = 1, \dots, N, \quad (1)$$

where

$$e_k = \varepsilon_k + \theta_1 \varepsilon_{k-1} + \theta_2 \varepsilon_{k-2} + \cdots + \theta_q \varepsilon_{k-q}. \quad (2)$$

The parameter a describes the long-term trend and the terms $s_j, j = 1, \dots, n$, are used to represent seasonal behaviour as departures from a long-term trend that are reproducible from year to year. A moving-average (MA) model of order q is used to account for possible serial correlation of the data-model differences e_k in which the ε_k are assumed to be random draws made independently from a normal distribution with expectation zero and variance, σ^2.

Estimates of the parameters $a, s_1, \dots, s_n$ of the seasonal regression model, of the parameters $\theta_1, \dots, \theta_q$ of the MA model and of the variance σ^2 are obtained by maximum-likelihood estimation. To select the order q of the MA model the estimation problem is solved for a sequence of models of increasing order, and selecting the value of q that minimises a measure of the quality of fit, such as the Bayesian Information Criterion. The uncertainty of the estimate of the trend a is calculated from a first-order sensitivity analysis of the maximum-likelihood estimator, and depends on the estimate of σ and the values of the derivatives of the model function with respect to the parameter estimates. A method of bootstrap resampling has been used to validate the calculated uncertainties.

A motivation for the model, and a comparison of its performance against simpler models (for example, without the MA model and without the seasonal terms), is given in Harris *et al*, 2019 [13].

RESULTS

Figure 2 illustrates a seasonal model fitted to the monthly aggregated data using a moving-average statistical model as well as the time series of the standardised residual deviations that estimate ε_k/σ. An analysis of these results show that there is no statistically significant serial correlation of the standardised residual deviations and that they can be considered as random draws made independently from a normal distribution.

Using daily aggregation of the SPL values, Figure 3 shows the results of the regression analysis using a seasonal model with a moving-average statistical model aggregated over the three hydrophones and for the six statistical metrics and each of the five frequency bands [13]. The aggregated trend estimates present some interesting characteristics. Perhaps the clearest observation is that the estimates for all metrics and all frequency bands show statistically significant SPL decrease corresponding to negative long term trends in the time series of the statistical noise levels, with the 85–105 Hz and 40–60 Hz frequency bands showing the slowest and fastest decrease with time, respectively. Another observation is that broadband trend estimates are very similar to the estimates for the lower end of the spectrum, indicating that the trends are dominated by the lower frequencies in the distribution of the spectral energy. Additionally, it is interesting that the distributions of the trend estimates for the different percentiles within each frequency band appear to be remarkably similar, with estimates for the lower percentiles indicating a negative trend that is smaller in absolute value than for higher percentiles. This indicates that apart from the overall reduction in SPL with time, the dynamic range of the recorded sound pressure decreases with time.

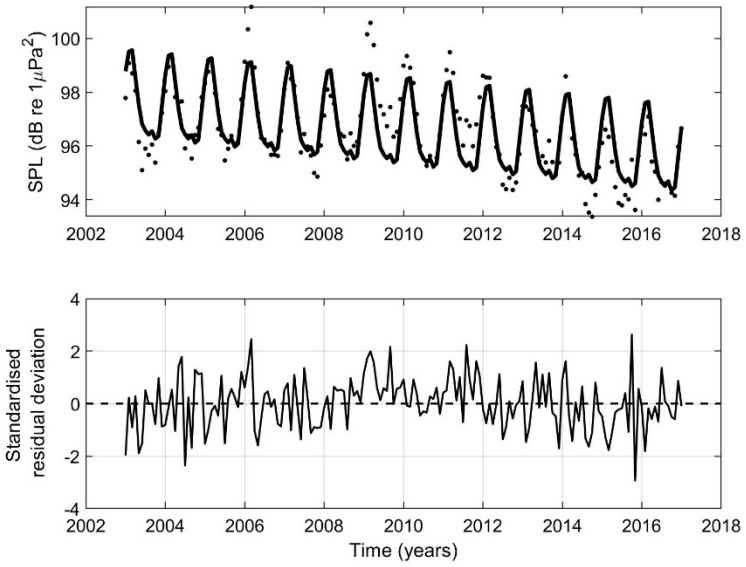


Fig. 2: Monthly aggregated P_{50} values for the 40-60 Hz frequency band from hydrophone H01W1 with fitted straight-line model including seasonal terms and a moving-average statistical model. The standardised residual deviations are also shown.

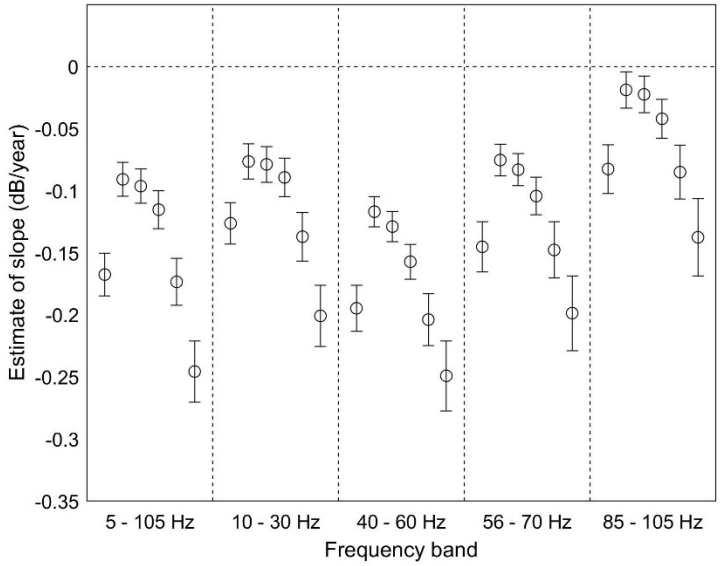


Fig.3: For daily aggregated data and each frequency band and each statistical level, estimates of the slope with associated 95 % coverage intervals obtained by aggregating the results for the three hydrophones. For each frequency band, results are presented for (left to right), average, P_1, P_{10}, P_{50}, P_{90} and P_{99} statistical levels.

These results are in accord with some of the outcomes from some recent studies performed on noise data from different locations [4, 9, 12], they contradict the understanding that noise in the oceans is in general increasing due to increasing human offshore activity. Shipping traffic, in particular, is believed to be one of the main man-made contributors to low-frequency ocean noise and it has been posited that a correlation should exist between trends in the international fleet size and ocean noise levels [6]. According to "Review of Maritime Transport 2016" issued by the United Nations [14], the trend in the international seaborne trade expressed in tonne-miles per year appears to monotonically increase from the mid-1980s until 2016 with only a

small anomaly observed in 2009 because of the Great Recession. There is no evidence that the local volume of ship traffic in the region is decreasing, though no detailed information on ship movements derived from maritime Automated Identification System is available over the required time period to inform the work described here.

Another possible explanation is that there is a downward drift in the sensitivity of the hydrophones, but such a drift would have to affect all three hydrophones equally, and results of studies of the long-term stability of the CTBTO hydroacoustic stations suggest that this is an unlikely explanation, though hard to eliminate [15]. In addition to anthropogenic factors, there are also natural influences which could potentially be responsible for both the seasonal variation and long-term trends. Surface winds generate waves which are sources of sound on the ocean surface, and the sea surface temperature can influence the proportion of sound energy from surface sources which reaches the deep-ocean sound channel. In the latter case, the temperature-induced changes to the sound speed profile alter the propagation of sound due to refraction, a process sometimes called the "afternoon effect" [16.17]. Considering the location of Cape Leeuwin, the effect of low frequency noise generated by Antarctic ice breaking is also a possible influence, ice calving being known to be a source of low frequency sound and to influence the sound scape in the Southern ocean [7, 8].

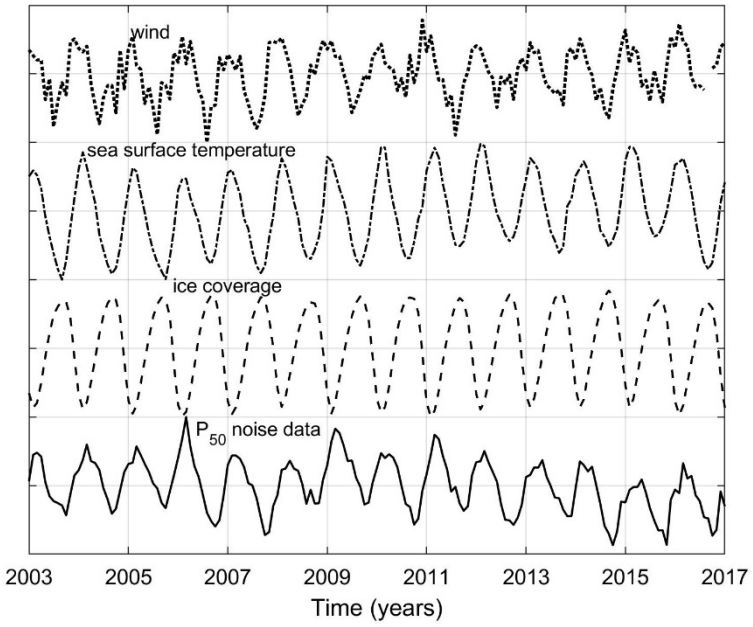


Fig. 4: Comparison (from bottom to top) of daily aggregated P_{50} values, Antarctic ice volume, sea surface temperature and wind speed. The time series for each effect is shifted to have the same mean, scaled to have the same amplitude, and then displayed with a different vertical offset.

To examine these effects, data for wind speed, sea surface temperature and ice coverage was obtained from public databases [18-20] and the data were examined for correlations with the acoustic noise data (see Figure 4). Data for wind speed shows only modest correlation, but there is strong correlation with sea surface temperature, and an even stronger correlation with Antarctic ice volume. This provides some empirical evidence that climatic factors such as ice coverage and sea surface temperature are influencing deep-ocean noise levels at seasonal timescales, and suggests the possibility that long-term gradual changes in these factors influence the noise trends over longer timescales.

CONCLUSION

The analysis demonstrated that it is possible to determine statistically significant trends in deep-ocean noise data over periods exceeding a decade. The results showed that statistically significant reductions in SPL are observed for all statistical percentiles for the different frequency bands as a result of negative trends in the examined time series for Cape Leeuwin. At this point, given the complexity of the acoustic environment and the fact that this is a purely observational study, it is difficult to be confident about the causes of the observed trends, which may be due to changes in anthropogenic sources, but could also be influenced by environmental factors such as seasonal and long-term variations in ice breaking noise and sea surface temperature.

ACKNOWLEDGEMENTS

The work described here was funded by the National Metrology Programme of the UK Department of Business, Energy and Industrial Strategy. The data was provided by the CTBTO, and the specialists at the virtual Data Exploitation Centre (vDEC) are gratefully acknowledged by the authors. The views expressed in the paper are those of the authors and do not necessarily represent those of the CTBTO.

REFERENCES

[1] **G. M. Wenz**, Acoustic ambient noise in the ocean: Spectra and sources *J. Acoust. Soc. Am*. 34 (12), pp. 1936–1956, 1962.

[2] **R. K. Andrew, B. M. Howe,** and **J. A. Mercer**. Long-time trends in ship traffic noise for four sites off the North American West Coast. *J. Acoust. Soc. Am*. 129 (2), pp.642–651, 2011.

[3] **M. A. McDonald, J. A. Hildebrand,** and **S. M. Wiggins**. Increases in deep ocean ambient noise in the Northeast Pacific west of San Nicolas Island, California. *J. Acoust. Soc. Am*. 120 (2), pp. 711–718, 2006.

[4] **N. R. Chapman** and **A. Price**. Low frequency deep ocean ambient noise trends in the Northeast Pacific Ocean. *J. Acoust. Soc. Am*. 129 (5), pp. EL161–EL165, 2011.

[5] **M. F. McKenna, S. L. Katz, S. M. Wiggins, D. Ross,** and **J. A. Hildebrand**. A quieting ocean: Unintended consequence of a fluctuating economy. *J. Acoust. Soc. Am*. 132, pp. EL169–EL175, 2012.

[6] **G. V. Frisk**. Noiseonomics: The relationship between ambient noise levels in the sea and global economic trends," *Sci. Rep*. 2, pp. 437, 2012.

[7] **W. S. D. Wilcock, K. M. Stafford, R. K. Andrew**, and **R. I. Odom**. Sounds in the ocean at 1–100 Hz. *Ann. Rev. Mar. Sci*. 6, pp. 117–140, 2014.

[8] **H. Matsumoto, D. W. R. Bohnenstiehl, J. Tournadre, R. P. Dziak, J. H. Haxel, T.-K. A. Lau, M. Fowler**, and **S. A. Salo**. Antarctic icebergs: A significant natural ocean sound source in the Southern Hemisphere. *Geochem. Geophys. Geosyst*. 15, pp. 3448–3458 2014.

[9] **J.-L. Miksis-Olds, D. L. Bradley**, and **X. M. Niu**. Decadal trends in Indian Ocean ambient sound. *J. Acoust. Soc. Am*. 134 (5), pp. 3464–3475, 2013.

[10] **M. van der Schaar, M. A. Ainslie, S. P. Robinson, M. K. Prior**, and **M. André**. Changes in 63 Hz third-octave band sound levels over 42 months recorded at four deep-ocean observatories. *J. Mar. Syst*. 130, pp. 4–11, 2014.

[11] **J. L. Miksis-Olds** and **S. M. Nichols**. Is low frequency ocean sound increasing globally? *J. Acoust. Soc. Am*. 139 (1), pp. 501–511, 2016.

[12] **V. N. Livina, A. Brouwer, P. M. Harris, L. Wang, K. Sotirakopoulos**, and **S. P. Robinson**. Tipping point analysis of ocean acoustic noise. *Nonlinear Process. Geophys*. 25, pp. 89–97, 2018.

[13] **P. M. Harris, K. Sotirakopoulos, S. P Robinson, L. S Wang** and **V. N Livina**. A statistical method for the evaluation of long term trends in underwater noise measurements, *J. Acoust. Soc. Am*. 145 (1), pp. 228-242, 2019.

[14] **United Nations**. Review of Maritime Transport 2016. *United Nations Conference On Trade and Development*, the Hague, the Netherlands, 2016.

[15] **L. Wang** and **S. P. Robinson**. Study of baseline calibrations for CTBTO hydroacoustic hydrophone stations. *Proceedings of the 1st International Conference and Exhibition on Underwater Acoustics,* UACE 2013, Corfu, Greece, pp. 765–774, 2013.

[16] **M. A. Ainslie**. Potential causes of increasing low frequency ocean noise levels. *Proc. Meet. Acoust.* 12, 070004, 2011.

[17] **M. A. Ainslie**. Periodic changes in ambient noise: Possible causes and implications for long term prediction. *Proceedings of the 1st International Conference and Exhibition on Underwater Acoustics, UACE 2013*, Corfu, Greece, pp. 665–662, 2013.

[18] **NOAA**, "Blended sea winds," https://www.ncdc.noaa.gov/data-access/marineocean-data/blended-global/blended-sea-winds (Last viewed 1 June 2018).

[19] **NCAR/UCAR**, "NCEP version 2.0 Global SST and NCDC version 4.0 extended reconstructed SST analyses," http://rda.ucar.edu/datasets/ ds277.0/ (Last viewed 1 June 2018).

[20] **NSIDC**, "National Snow & Ice Data Center," http://nsidc.org/ (Last viewed 1 June 2018).

Structured Session 9
Acoustics in polar environments

Organiser(s): Tegowski Jaroslaw

INTERNATIONAL QUIET OCEAN EXPERIMENT – ARCTIC ACOUSTIC ENVIRONMENTS

Philippe Blondel[a], Hanne Sagen[b], Marie-Noëlle Houssais[c], Peter Mikhalevsky[d], Jukka Pajala[e], Roberto Racca[f], Jaroslaw Tegowski[g], Karolin Thomisch[h], Jakob Tougaard[i], Ed Urban[j], Alexander Vedenev[k]

[a]University of Bath; Bath, United Kingdom
[b]Nansen Environmental and Remote Sensing Center; Bergen, Norway
[c]University Pierre and Marie Curie; Paris, France
[d]Leidos Inc.; Arlington, VA., USA
[e]Finnish Environmental Institute; Helsinki, Finland
[f]JASCO Applied Sciences (Canada) Ltd.; Victoria, B.C., Canada
[g]University of Gdansk; Gdansk, Poland
[h]Alfred Wegener Institute; Bremerhaven, Germany
[i]Aarhus University; Aarhus, Denmark
[j]Scientific Committee on Oceanic Research, University of Delaware; Newark, DE, USA
[k]Shirshov Institute of Oceanology; Moscow, Russia

Philippe Blondel, University of Bath, Bath BA2 7AY, UK; P.Blondel@bath.ac.uk

Abstract: *High-latitude regions like the Arctic Ocean are becoming increasingly important as global warming makes them more accessible, raising economic and political interests. Sea ice reduction is facilitating resource exploration, marine transport and other activities. Warming waters and changing sea ice conditions lead to shifts in ecosystems. Resource exploitation will grow in the coming decades, offering new opportunities but also new challenges to these fragile environments and their biodiversity. The natural and anthropogenic changes in this region will change the characteristics of soundscapes. To measure and assess them at a variety of spatial and temporal scales, the International Quiet Ocean Experiment created in 2017 a working group on Arctic Acoustic Environments. First activities focus on synthesising state-of-the-art knowledge of Arctic sounds—past, present and future. WG activities were presented at the Arctic Observing Summit 2018 and its recommendations adopted at the 2nd Arctic Science Ministerial. We are linking with indigenous communities and other stakeholders to address emerging trends, plan where/when to conduct optimal acoustic surveys, and prioritise metrics. We present the plans and first actions of this IQOE WG.*

Keywords: *Arctic acoustics, ambient noise, International Quiet Ocean Experiment (IQOE)*

1. ARCTIC ACOUSTIC ENVIRONMENTS

Arctic regions are directly and visibly affected by climate change, and they are expected to see major transformations over the coming decades [1]. For example, the extent of sea ice has decreased at a rate of -0.78×10^6 km^2 (6.15%) per decade over the period 1993 – 2016, and the volume of sea ice has decreased at a rate of 15.4% per decade, increasing freshwater content of the Arctic Ocean [2]. Warming extends deep: models using surface data (satellite and *in situ* measurements) conclude there were changes of $+(0.6 \pm 0.1)$ W/m^2 in the upper ocean (0–700 m) during the same period [3]. Fig. 1 shows how these important changes correlate and how they affect other parameters (e.g., increasing wind velocities over the entire Arctic region). Recent, important changes in exchanges between the Atlantic Water and the Arctic Ocean [4] are further influencing sea-ice cover, in particular in the Barents Sea and near Svalbard. Since 1993, this contributed 15% of the total contributions to sea level rise [1].

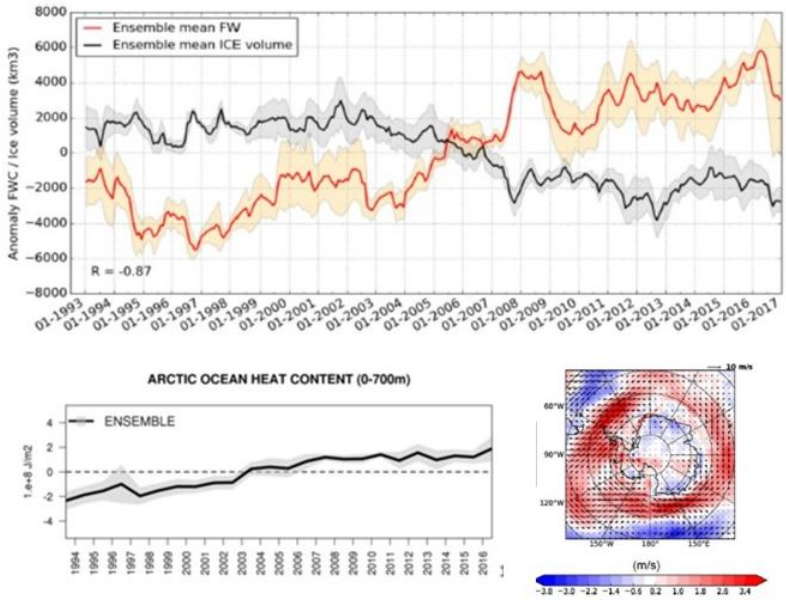


Fig.1: Arctic changes, 1993-2016, derived from models and in situ observations. Top: Freshwater content (red) and sea ice volume (black) in areas above ocean depths of more than 500 m [8]. Bottom left: basin-average temperatures over the upper 700 m [3]. Bottom right: average wind speeds (colours) and wind velocities (black arrows) [2].

Decreases in glaciers and ice caps contributed another 28% to sea level rise [1, 5]. These changes are expected to increase substantially to the end of this century [6]. Submarine melting and calving of tidewater glaciers represent a significant source of cold freshwater, increasing the variability of temperature and salinity in the water column of glacial bays and fjords [7]. Changes in the timings and lengths of seasons, along with warmer waters, are also changing the distributions and quantities of different marine species, with “detrimental effects on many organisms including migratory birds, mammals and higher predators” [1], making them more vulnerable. Impacts on human communities in the Arctic, although mixed, will particularly affect infrastructures and traditional indigenous ways of life [1].

These changes are projected to accelerate in the 21st century [1] and changes in underwater soundscapes will become more pronounced. Large-scale acoustic propagation is particularly sensitive to changes in water temperatures and sea ice properties (e.g., [9]) and changes in under-ice ambient sound are already noticeable in some regions (e.g., [10]). Increased winds

and changes in ice types, areas and volumes will also affect both natural sound generation and sound propagation at larger spatial scales. Acoustic impacts of melting tidewater glaciers [11] and freshwater ice [12, 13] will be more frequent [14] and Arctic Ocean areas will potentially become louder. These changes will also affect marine animals dependent on sound [15].

The Arctic Ocean and surrounding regions host important natural resources, resulting in growing economic and political interests, and transforming a pristine wilderness into a "useful" region. Under-ice soundscapes already combine noises from marine natural background noise and mammal vocalisations, but also noise from ship cavitation (from ice-breaking) and seismic airguns (sometimes audible more than 800 km away) [16-19]. Sea ice reduction will facilitate navigation, resource exploration and exploitation, and associated offshore activities. Noise levels are therefore expected to increase in the coming years.

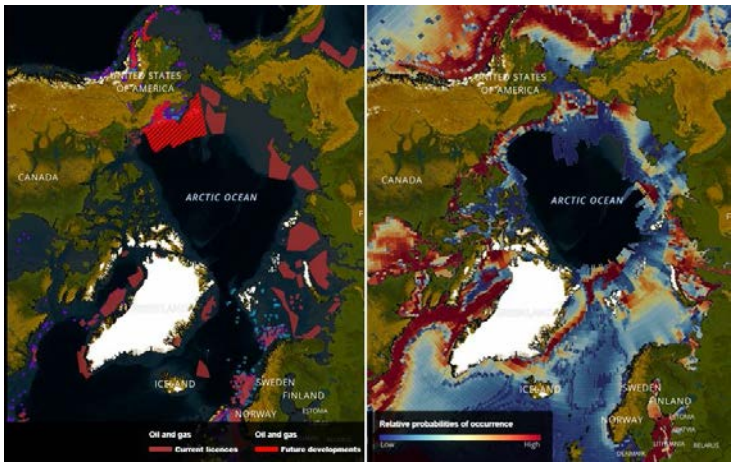


Fig.2: The "useful" Arctic. Current and future activities related to oil and gas (left) and fisheries potential (right). Both baseline maps adapted from wwfarcticmaps.org.

Recent assessments of mineral resources in the Arctic [20] concluded that it contains about 30% of the world's undiscovered gas and 13% of the world's undiscovered oil, mostly offshore under less than 500 meters of water (Fig. 2, left). Natural gas reservoirs are largely concentrated in Russia, and some deposits in Norwegian waters (e.g., Johan Castberg field, Barents Sea) have recently been approved for exploitation. Seismic exploration (using airguns) will be supplemented with offshore construction and drilling, with significant acoustic impacts (e.g., [21]). The Barents Sea is also the most important fishery area in Europe, and because of global warming there is a large potential for increased exploitation of living marine resources in the Arctic seas (Fig. 2, right). A 16-year ban on commercial fishing in the high seas portion of the Central Arctic Ocean was endorsed in 2018, although there are questions about its enforceability (especially in international waters) and long-term sustainability as pressures from declining fisheries in the rest of the world will intensify, and there are no restrictions on fishing in other areas of the Arctic. The retreat of sea ice also leads to increases in shipping, with more traffic along the Northern Sea Route (Fig. 3, left). Russia aims to open the Bering Strait for large tankers, and China is planning to expand its One Belt One Road Initiative to include Arctic routes. The Arctic Transportation Accessibility Model [22] uses different IPCC representative concentration pathways (RCPs) for radiative forcing. By 2050, the RCP 4.5 medium-low projection leads to predictions of expanded navigability for common open-water ships crossing the Arctic along the Northern Sea Route, robust new routes for moderately ice-strengthened ships over the North Pole, and new routes through the Northwest Passage for both classes (Fig. 3, right). Increased tourism will increase sound levels at low frequencies (e.g., the 63 Hz and 125 Hz used by the European Marine Strategy Framework Directive for shipping (MSFD, 2014)) and at higher frequencies (e.g., [17]).

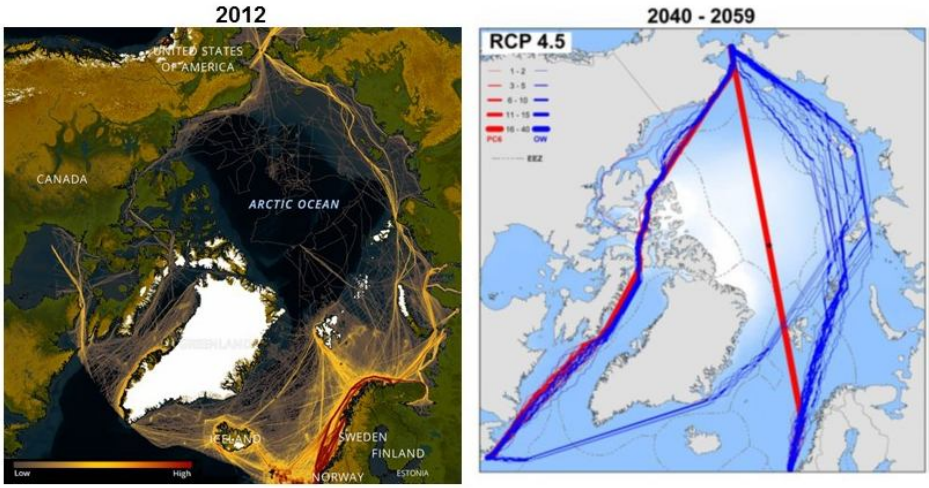


Fig.3: Changes in Arctic shipping. Left: current traffic, based on AIS recordings (from wwwfarcticmaps.org). Right: new routes [22] in red (polar vessels) and blue (other vessels).

2. THE INTERNATIONAL QUIET OCEAN EXPERIMENT

Several actors—academic, governmental and commercial—are already collecting passive acoustic data in the many marine environments encompassing the Arctic region, but the different activities are not coordinated, and communication is not very developed. It is therefore imperative to increase collaboration in the Arctic in order to obtain a better knowledge of current noise status and more coordinated observing programs in this harsh environment. This is the goal of the *International Quiet Ocean Experiment*. Its Science Plan was reviewed and approved by the Scientific Committee on Oceanic Research (SCOR) and the Partnership for Observation of the Global Ocean (POGO). In late 2017, IQOE established the Working Group on *Arctic Acoustic Environments* (www.iqoe.org/groups/arctic). This builds on previous efforts, e.g., Oceanoise'2015 and Oceanoise'2017 [23]. We aim to produce acoustic baselines against which future changes can be compared, and sustainable management practices considered and benchmarked. Our objectives are to:

- Identify locations of existing acoustic receivers in the Arctic Ocean
- Identify potential sources of historic acoustic data from the Arctic Ocean
- Inform IQOE Data Management & Standardization WGs of past/current data sources
- Compile existing acoustic data to determine whether time series showing evolution and future trends of relevant acoustic metrics can be created
- Create a synthesis of research papers and state-of-the-art knowledge on the effects of sound on organisms in the Arctic Ocean
- Identify data/research conducted on the effects of permafrost and gas-saturated sediments on Arctic Ocean soundscapes
- Identify an ideal receiver array (location, number of receivers, types of receivers) to observe the baseline acoustic environment for the Arctic Ocean
- Identify ongoing and planned experiments with passive acoustics planned or possible
- Conduct and support endorsement processes with the Arctic Council

3. ARCTIC ACOUSTIC ENVIRONMENTS – FIRST ACTIVTIES

The Working Group on "Arctic Acoustic Environments" comprises all authors of the present article, spanning 10 countries and a wide range of Arctic field work and research activities. Its first e-meeting took place in November 2017, and a co-chair meeting was organised in February 2018, with further *ad hoc* meetings at conferences. WG plans were presented at the Arctic Observing Summit AOS-2018. The IQOE WG's goals and activities were endorsed by the Arctic Observing Summit, and WG members participated in the Summit's themes of "Need for the Observing System", "Implementation and Optimisation" and "Leveraging Observing Systems and Networks". The AOS-2018 recommendations were taken aboard at the 2nd Arctic Science Ministerial in October 2018 attended by the science ministers of 26 Arctic-concerned nations and the representatives of six Arctic indigenous peoples' organizations. The final report [24] concluded in particular:

- *"We recommend exploring the possible call of a forum of Arctic science funders to discuss strategies for supporting the research that is necessary to achieve the goals agreed at this Ministerial meeting";*
- *"There is a need to enhance reciprocal collaboration and coordination of efforts on Arctic observations of all types, spanning from community-based observatories to high-tech autonomous systems, and increase their spatial and temporal coverage".*

Subsequent WG activities (e.g., [25]) led to the first full meeting in January 2019 in Paris (France). Compilation of existing and past research is supporting (and supported by) the Aquatic Acoustic Archive Literature Library (iqoe.org/library). We are building links with other existing initiatives, from European consortium research like INTAROS (www.intaros.eu) to organisations like the Arctic Council (arctic-council.org), the working group on Protection of the Arctic Marine Environment (PAME: www.pame.is) and the Arctic Monitoring and Assessment Program. We are reaching out to policy-makers at national and international levels. Our ultimate goal is to create awareness of acoustic environments and get the topic on funding agencies research agenda. Finally, we are actively supporting worldwide efforts to build an integrated Arctic Ocean observatory system, or system of systems.

4. ACKNOWLEDGEMENTS

The logistical and financial support of IQOE is gratefully acknowledged.

REFERENCES

[1] **IPCC**, *Climate Change 2007: Synthesis Report*, Cambridge U. Press, pp. 52, 2007.
[2] **H. Zuo, et al.,** Extreme Sea-Ice Conditions, In *Copernicus Marine Service Ocean State Report, Issue 2, J. Operational Oceanography*, 11:sup1, s120–s123, 2018.
[3] **K. von Schuckmann et al.,** Ocean Heat Content. In: *Copernicus Marine Service Ocean State Report, Issue 2, J. Operational Oceanography*, 11:sup1, s40–s45, 2018.
[4] **V. Lien, R.P. Raj**, North Atlantic – Arctic exchanges, In: *Copernicus Marine Service Ocean State Report, Issue 2, J. Operational Oceanography*, 11:sup1, s88–s91, 2018.
[5] **A.S. Gardner, et al.,** A Reconciled Estimate of Glacier Contributions to Sea Level Rise: 2003–2009, *Science*, 340 (6134), pp. 852–857, 2013.

[6] **M. F. Meier et al.,** Glaciers Dominate Eustatic Sea-Level Rise in the 21st Century, *Science*, 317 (5841), pp. 1064–1067, 2007.
[7] **F. Straneo et al.,** Impact of Fjord Dynamics and Glacial Runoff on the Circulation near Helheim Glacier, *Nat. Geosci.*, 4, 322–327, 2011.
[8] **G. Garric et al.,** Arctic Ocean Freshwater Content, In *Copernicus Marine Service Ocean State Report, Issue 2, J. Operational Oceanography*, 11:sup1, s70–s72, 2018.
[9] **H. Sagen, P. Worcester,** Capabilities and Challenges of Ocean Acoustic Tomography in Fram Strait, *J. Acoust. Soc. Am.*, 140 (4), pp. 3134-3134, 2016.
[10] **R. Chen, A. Poulsen, H. Schmidt,** Spectral, Spatial and Temporal Characteristics of Underwater Ambient Noise in the Beaufort Sea in 1994 and 2016, *J. Acoust. Soc. Am.*, 145 (2), pp. 605-614, 2019.
[11] **O. Glowacki, et al.**, Underwater Acoustic Signatures of Glacier Calving, *Geophys. Res. Lett.*, 42, 804–812, 2015.
[12] **J. Tegowski, G.B. Deane, A. Lisimenka, Ph. Blondel**, Spectral and Statistical Analyses of Ambient Noise in Spitsbergen Fjords and Identification of Glacier Calving Events, in *Proceedings ECUA-2012)*, Edinburgh, Scotland, pp. 1667–1672, 2012.
[13] **Ph. Blondel, J. Tegowski, G.B. Deane**, Laboratory Analyses of Transient Ice Cracking in Growlers, in *Proceedings of the 1st International Conference and Exhibition on Underwater Acoustics*, Corfu, Greece, pp. 1253–1260, 2013.
[14] **T. Jacob, J. Wahr, W.T. Pfeffer, S. Swenson,** Recent Contributions of Glaciers and Ice Caps to Sea Level Rise, *Nature*, 482, 514–518, 2012.
[15] **I.C. Van Opzeeland, J.L. Miksis-Olds,** Acoustic Ecology of Pinnipeds in Polar Habitats, in *Aquatic Animals*, D.L. Eder (ed.), p.1-52, Nova Science Publishers, 2012
[16] **J.A. Hildebrand,** Anthropogenic and Natural Sources of Ambient Noise in the Ocean, *Marine Ecology Progress Series*, 395, pp. 5-20, 2009.
[17] **K. Stafford,** Anthropogenic Sound and Marine Mammals in the Arctic: Increases in Man-Made Noises Pose New Challenges", *The Pew Charitable Trust*, 20 pp., 2013.
[18] **S.B. Blackwell et al.,** Effects of Airgun Sounds on Bowhead Whale Calling Rates: Evidence for Two Behavioral Thresholds, *PLOS One*, 10(6), 2015.
[19] **F. Geyer et al.,** Identification and Quantification of Soundscape Components in the Marginal Ice Zone, *J. Acoust. Soc. Am.*, 139(4), pp. 1873-1885, 2016.
[20] **D.L. Gautier et al.**, Assessment of Undiscovered Oil and Gas in the Arctic, *Science*, 324 (5931), pp. 1175-1179, 2009.
[21] **A. Farcas, P.M. Thompson, N.D. Merchant,** Underwater Noise Modelling for Environmental Impact Assessment, *Env. Impact Assess. Review*, 57, pp. 114-122, 2016
[22] **L.C. Smith, S.R. Stephenson,** New Trans-Arctic Shipping Routes Navigable by Mid-Century, *PNAS*, 110 (13), pp. E1191-E1195, 2013.
[23] **Ph. Blondel et al.,** Report of the Polar Session, In *Oceanoise2015*, Vilanova i la Geltrú, Spain, (M. André, P. Sigray, eds.), 2015**.**
[24] **ASM-2**. Co-operation in Arctic Science – Challenges and Joint Actions, *Report of the 2nd Arctic Science Ministerial*, 25-26 October 2018, Berlin, Germany, 152 pp., 2018
[25] **Ph. Blondel, H. Sagen,** Monitoring the Arctic Acoustic Environments with the International Quiet Ocean Experiment, *J. Acoust. Soc. Am.*, 144 (3), p. 1696, 2018

LONG-RANGE SOUND PROPAGATION IN THE CANADA BASIN

Timothy F. Duda, Weifeng Gordon Zhang, Ying-Tsong Lin and Arthur E. Newhall

Woods Hole Oceanographic Institution, Woods Hole, MA, USA

Contact author Timothy Duda, WHOI AOPE Dept., Woods Hole, MA 02543, USA, v: 1-508 289 2495, tduda@whoi.edu

Abstract: *The existence of a sound duct created by the presence of waters of Pacific origin in the Canada Basin and Beaufort Gyre allows sound to travel great distances with little attenuation. However, the water mass layering that creates the duct varies in time and space, and the ducting effect also varies. Output from a surface-forced hydrodynamic model of the region is analyzed to learn about the formation and flow of the water masses, and about eddies and filaments that strengthen and weaken the duct. The model results are then used for broadband two-dimensional parabolic equation modeling of sound to learn about seasonal variation of propagation in the region, as well as statistics of propagation variability.*

Keywords: *Ocean dynamical modeling, Beaufort Gyre, Pacific Summer Water, sound channel*

1. INTRODUCTION

The Beaufort Gyre lies north of Alaska in the southern portion of the Canada Basin of the Arctic Ocean. The anticyclonic (clockwise) gyre structure arises from atmospheric forcing [1], and impacts the flow throughout the region of relatively fresh water inputs with Bering Strait origin. Observations show that a layer of warm and fresh Pacific Summer Water (PSW) can lie above a very persistent layer of cold fresh Pacific Winter Water (PWW), which in turn overlies salty Atlantic Water. This creates a PWW duct with a sound velocity minimum, lying at 75 to 250 m depth. A recent article presents a discussion of propagation in this duct [2]. Fig. 1 shows the duct structure in a transect with seven deep CTD stations by the Canada Institute of Ocean Sciences in 2017 [3]. Below 350 m depth sound speed increases, which means that all sound is surface interacting unless it is confined to the PWW duct.

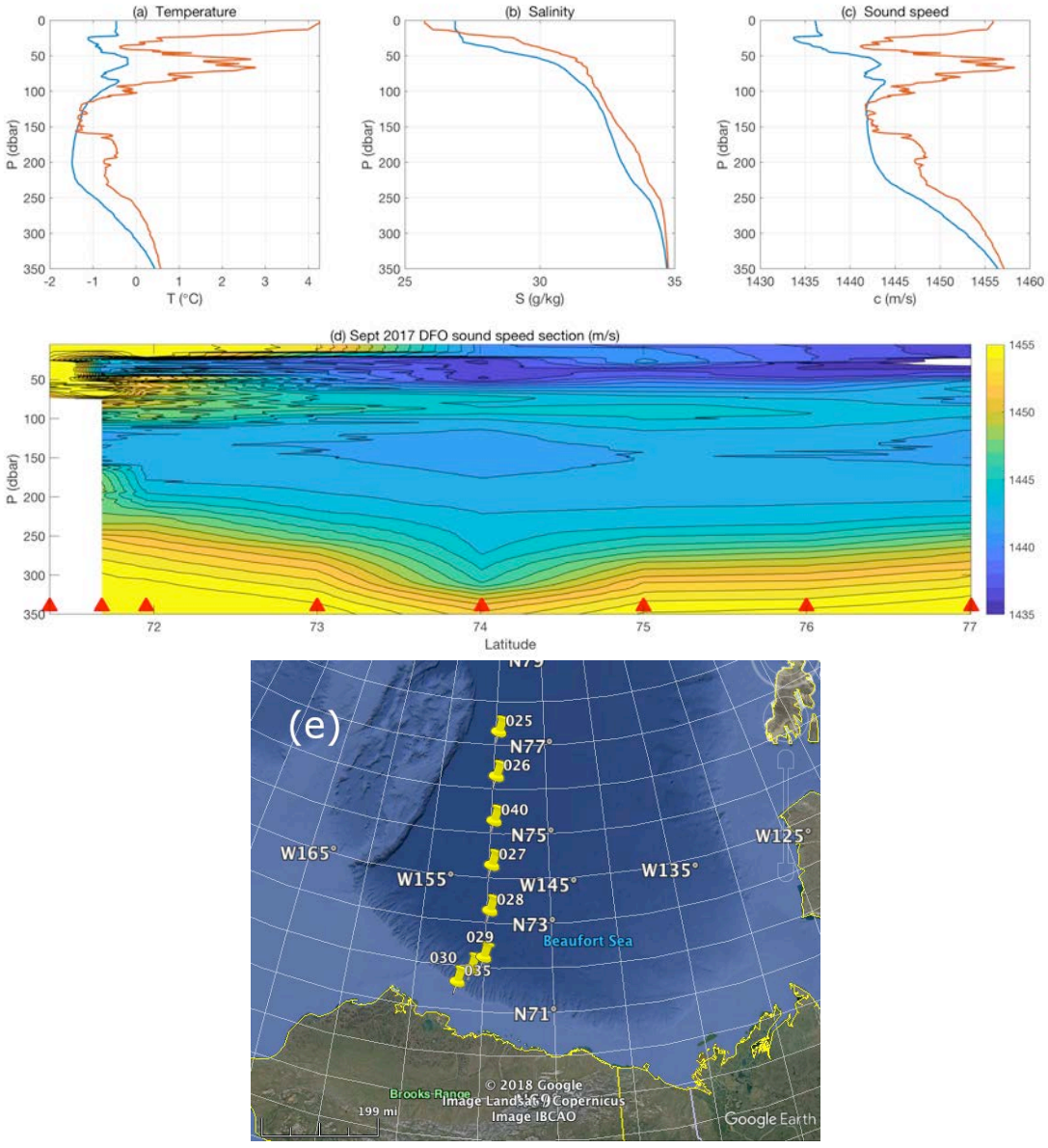


Fig 1: The Pacific Winter Water sound duct is shown. The top three panels show data from northern station 25 and southernmost deep station 30: (a) shows temperature, (b) shows salinity, and (c) shows sound speed. The center panel (d) shows sound speed in transect with 0.5 m/s contour interval. The lower panel (e) shows the station locations in the Canada Basin.

The duct is capped with warmer water in the south and is “stronger”, while it is weaker at the north. It appears to be continuous with this sparse sampling. In the northern five stations the sound speed minimum is near 1442 m/s and the duct top value is between 1444 and 1446.

In the next section, we present hydrodynamic model simulations for the area which show that the duct may be discontinuous. Evidence of duct discontinuity was found in the Canada Basin Acoustic Propagation Experiment (CANAPE) of Oct 2016 - Aug 2017, when sound propagating in the duct over hundreds of km in fixed paths showed time variability. In Section 3, acoustic propagation simulations made using the simulated duct conditions show potential effects of horizontal variations of the duct on long-range 200-Hz sound propagation.

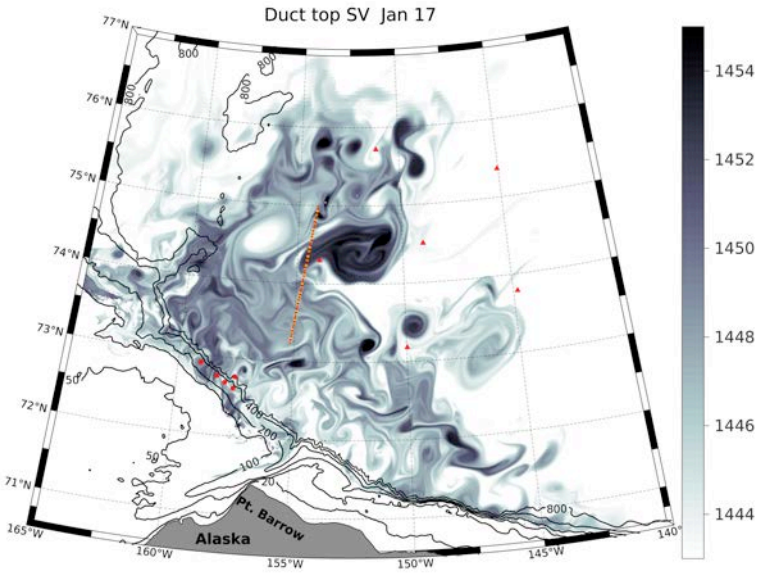


Fig 2: Modeled sound velocity (m/s) at the top of the PWW duct is shown for the Beaufort Gyre portion of the model. The color white is used where no duct is detected. Dark tint indicates very warm PSW and a substantial duct. The PWW layer and the Atlantic layer are relativly uniform, so the depicted duct-top sound velocity governs sound trapping. Also shown are a 200-km acoustic model track and CANAPE mooring stations.

2. REGIONAL OCEAN MODEL

To study the upper ocean conditions in the region, a high-resolution simulation was performed with the MITgcm primitive equation model. The model setup was patterned after that of Spall et al. [1], with some important changes. First, the horizontal resolution in the new model was much finer, with spacing of 500 m in much of the region. Next, the surface forcing was done using daily averages, updating each day, replacing monthly average forcing updated each month. The purpose of this is to widen the dynamic range of temporal response, which will produce an entirely different flow structure. The model was initialized with climatic PCHG3.0 climatological conditions that do not include much PSW and essentially no duct. The model is run with 2016 forcing (1 Jan to 31 Dec) that is repeated for three years. After a 720-day spin up, 375 days of model state were saved for analysis.

Fig. 2 shows the sound velocity at the duct top on day 748 of the run (Jan. 17). The dark areas show where two summers of PSW introduction into the area have built a duct. The PSW enters from the coastal current flowing eastward along the north shore of Alaska, then moves clockwise around the gyre. The western part of the Beaufort Gyre (west of 155W) contains a largely uninterrupted duct. Between 150 and 155 W, that filaments of colder water at the

density of the PSW disrupt the duct continuity. East of 150 W PSW is scarce and there will only be sound ducting in isolated patches.

The sound speed in the density layers above the PWW duct core is the primary variation in the ducting geometry in the model results, but there are other variations. Fig. 3 shows the duct sound speed versus density along one transect (a southward continuation of the 200-km track of Fig. 2). The warm upper duct boundary PSW layer lies at potential density 26.1 to 26.3 kg/m^3. The sound-speed $c(x,z,t)$ structure below the PWW duct is relatively uniform. The duct center, with minimum sound speed with respect to depth or density, is near 26.8, and has sound speed variations (temperature and salinity variations). Fig. 3c shows that salinity controls density at these temperatures, so that temperature is somewhat passive dynamically in the gyre, and that sometimes there is little or no signature of warm PSW which determines the existence of the duct. The intrusion of PSW and the stirring of PSW along isopycnals are processes that respond to density patterns created by surface forced circulation.

Fig. 4 shows the April 11 duct $c(x,z)$ more conventionally. In addition, the duct parameter $P=\Delta c\Delta z$ is plotted, where Δc is c at the duct top minus c at its minimum in the duct, and Δz is the height of the duct between the depths where c is maximum above the duct and where c rises again, below the duct, to that maximum value. Fig. 4 also shows variability of $P(x,t)$ along this line, and the cumulative distribution of log$P$ scaled against a normal distribution. The plot indicates that the duct is present about 70% of the time. Analysis shows that the correlation length scale of P is 26.5 km, and the length scale for duct-top c is 30 km.

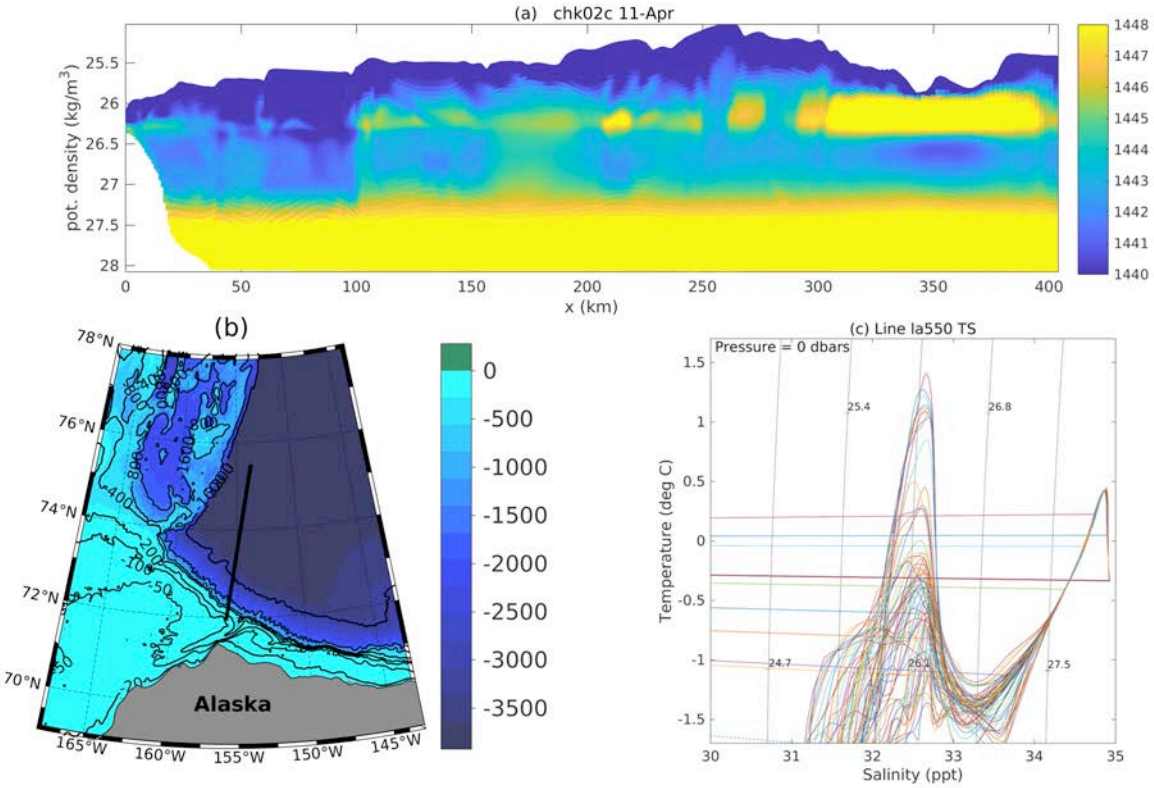


Fig. 3: (a) The sound velocity is plotted versus potential density re 0 dbar and distance along a line (550) of the MITgcm model grid. Range zero is at the south. Speed above 1448 m/s is color saturated. (b) The bathymetry of the area and the postion of line 550 are drawn. (c) The TS properties of a sequence of profiles are shown. Selected potential density contours are drawn. In (a), note that the duct upper cap (sound-speed maximum) is absent at 90 km. The sound-speed minimum in the duct is variable.

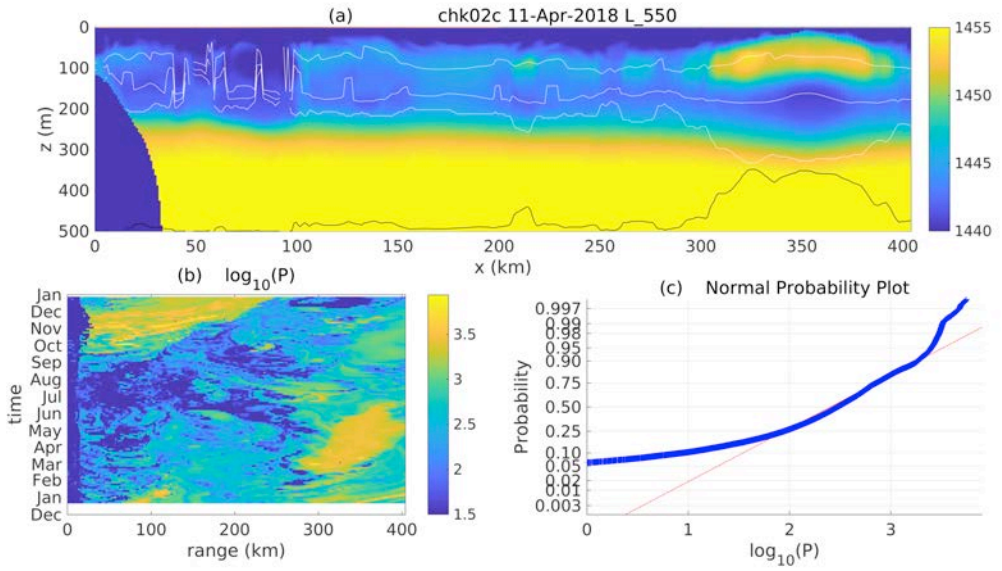


Fig. 4: (a) The sound speed in the duct of April (Fig. 3a) is plotted vs depth and distance. At the bottom, the duct parameter P(x) is plotted, multiplied -0.05 to fit onto the plot, with P=0 at 500 m depth (i.e. P=2000 would be at 400). (b) $Log_{10}(P(x,t))$ on the same transect is plotted for 375 days. (c) A probability plot of the cumulative distribution of $log_{10}(P)$ shows lognornal behavior from P=100 to P=2000. A weak duct would have P=(150 m)(1 m/s)=150, so the plot shows that 30% of the samples show no duct (P < 150).

3. SOUND PROPAGATION MODELING

Sound propagation modeling at 200 Hz was done with a parabolic equation (PE) technique that we have already applied to this area [2]. Most simulations have the source in the duct at 173-m depth, the same as used in CANAPE for sources moored in deep water. Initial results show that the sound in the duct is weakly affected by ice cover. When present, the ice strongly attenuates all other (not PWW ducted) sound. The effects of rough-underside ice on sound are approximately incorporated into the PE method using the equivalent fluid half-space complex-density method [4]. The half space approximation means that reflections from the surface are disregarded. The important interference effect that will occur with a uniform thickness ice layer will not be included, but with rough ice the disregarded interference will be random, so neglecting the surface boundary in that case should have relatively less error in the modeled ice reflectivity. The minimum nominal reflections coefficient of the ice lower surface is about 0.25 at 30° grazing angle.

Fig. 5 shows modeled sound in the duct versus range for a “broken duct” where a section of the PSW layer has a section that is too cold to form an effective duct. The function $\Psi(x, z)$ from the cylindrically symmetric PE is shown [5], which does not account for cylindrical spreading. The modeling was done with ice that has small background roughness plus ice keels. One of the primary results here is that ducted sound is converted to surface interacting sound when the layer at density 26.2 is not warm enough to create a duct (i.e. lacks sufficient PSW water). With no ice cover, the sound levels far from source may not be affected by this, but the sound energy may be reduced with ice above due to poor reflection, or to reflection to high angle from tilted ice, which will send sound into the seabed. All of these effects have been seen in our numerous simulations with variable ice and duct properties.

CANAPE data show surface interacting ~200-Hz sound to gradually lose intensity 220-km from a source at a rate of about 10 dB/month after ice appears in November. On the other

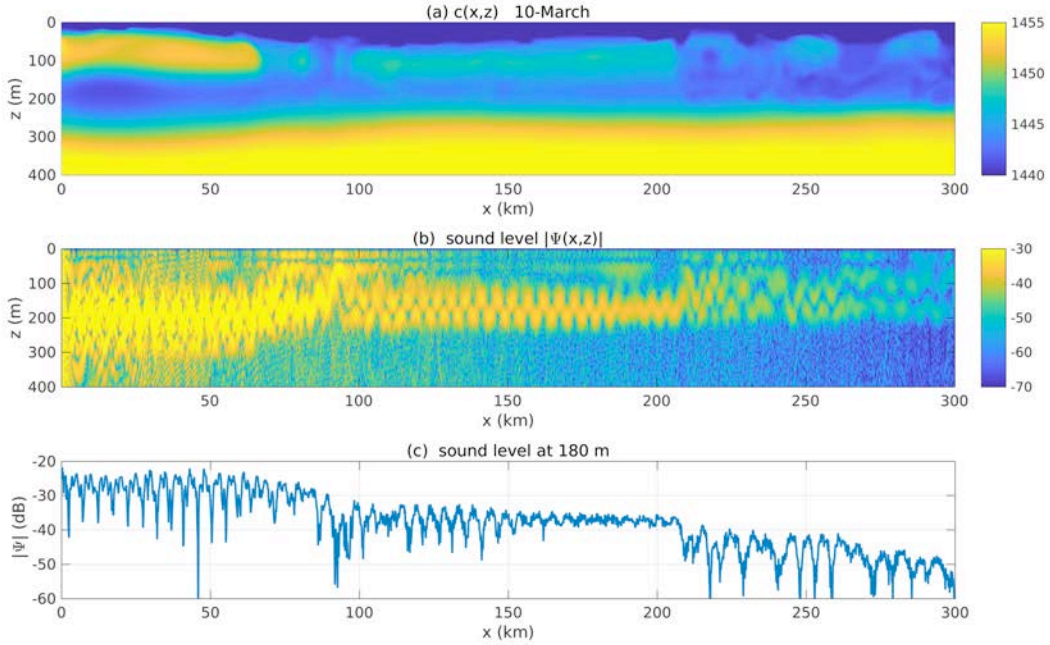


Fig. 5: (a) Sound speed in the upper layers is shown. Breaks in the PSW layer that affect sound trapping occur at x equals 85, 207 and 261 km. (b) Sound field intensity $|\Psi(x, z)|$ re 0 dB source is plotted. High intensity is color saturated. (c) Intensity at 180 m depth in the duct.

hand, identified ducted sound retains its energy until March, with a few brief interruptions, then it loses 45 dB in less than a month. To determine whether ice cover could reduce the level of ducted sound, range-independent simulations were performed with two ducts, weak and strong (Fig. 6) taken from the MITgcm output, and many ice conditions. Selected results are shown in Table 1. No simulations showed attenuation of the ducted sound equal to what was seen in the field. The surface-interacting sound was highly attenuated by the ice, as expected (not shown). For the simulations, ice was given a background roughness with Gaussian height distribution ranging from 0 to 4 m rms, with horizontal scales restricted from 4 m to 100 m wavelength. Some simulations had a synthesized set of ice keels added to flat surface with a very small roughness. The keel geometry followed statistics measured in the area at the time of CANAPE by the Beaufort Gyre Exploration Project [6] with upward looking ice sonars. The keel height distribution was near exponential, the half-width to depth ratio was 4.85 [7], and there were 4.1 keels per km. Keels deeper than 8 m numbered about one per 2 km.

Waveguide model	*400-km ducted TL, dB, cyl. spread. removed*
No ice	34
R-indep strong duct, flat ice	35
R-indep strong duct, rough ice	35
R-indep weak duct, flat ice	37.5
R-indep weak duct, keel model 1 ice	40
R-indep weak duct, rough ice	52

Table 1: Transmission loss (TL) for range-independent modeling of ducted 200-Hz sound. The effect of the ice cover on ducted sound at 400 km is a maximum of 18 dB loss. Cylindrical spreading loss is not included (10 $\log_{10}$ 40 km, 56 dB). Fig. 6 shows the ducts. Ducted sound level is computed with a 30-km long, 100-200 m depth incoherent average. The rough ice case is unrealistic and its attenuation exceeds that of keels.

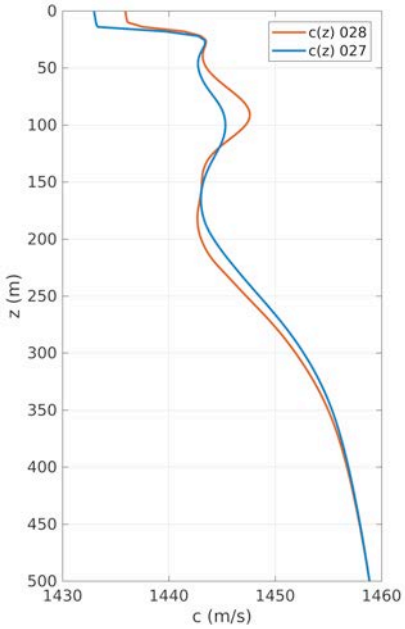


Fig. 6: Sound-speed profiles for range-independent weak duct (027) and strong duct (028) propagation modeling. See Table 1.

Finally, simulations were performed with range-dependent duct conditions taken from the hydrodynamic model. Result from two full-year, 400-km simulations are shown in Fig. 7, along the same north-to-south track used in the other simulations. The simulations have the same ice year-round (artificially), with one having the same ice keel statistics as used in the range-independent study (Table 1), and the other having scaled-down keel heights. Up to 35 dB of sound level reduction is seen as the PSW layer changes over the winter and spring.

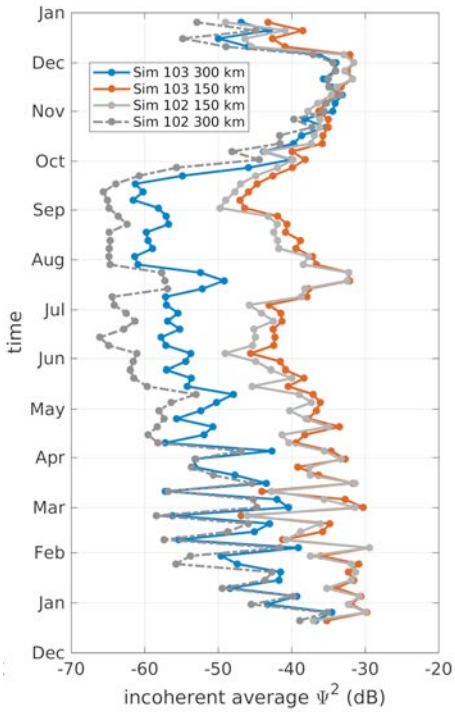


Fig 7: Sound level over one-year of simulations with keel ice above the time-dependent range-dependent conditions taken from the regional model. The track line is shown in Fig. 3b. The 200 Hz source is at 173 m depth at the north end.

4. SUMMARY

Sound propagation in the Beaufort Sea has been modeled using conditions taken from a surface-forced regional hydrodynamic model of the region. The propagation model includes a method to simulate the attenuating effects of ice. The field-observed effect that motivates this work is the reduction of sound trapped in the Pacific Winter Water sound duct. In the model, the duct has intermittent gaps that causes sound to escape from the duct and interact with the surface, resulting in up to ~35 dB reduction of sound intensity relative to an intact duct situation. Range-independent modeling was used to show that sound in an uninterrupted duct can also suffer loss from ice, but the loss only exceeds 10 dB for unrealistically rough ice. The results imply the 45 dB attenuation observed in the experiment requires the duct to be interrupted; ice loss alone is not of this magnitude. The broken-duct effect is insensitive to the detailed nature of the ice scattering and loss mechanisms. On the other hand, effects of ice on unducted sound may be more sensitive to the ice attenuation because that is the primary cause of time-dependent attenuation.

5. ACKNOWLEDGEMENTS

This work was funded by the US Office of Naval Research Ocean Acoustics Program. The regional model was run at a US Department of Defense High Performance Computing Facility, computing access was arranged through ONR. The Beaufort Gyre water-column data data were collected and made available by the Beaufort Gyre Exploration Program based at the Woods Hole Oceanographic Institution (https://www.whoi.edu/beaufortgyre) in collaboration with researchers from Fisheries and Oceans Canada at the Institute of Ocean Sciences. The parabolic model code was adapted from a Matlab version of the acoustic code RAM. The Matlab version is from M. Dzieciuch of UCSD.

REFERENCES

[1] **Spall, M. A., R. S. Pickart, M. Li, M. Itoh, P. Lin, T. Kikuchi, and Y. Qi, Y.,** Transport of Pacific Water into the Canada Basin and the formation of the Chukchi Slope Current, *J. Geophys. Res.,* volume 123, pp. 7453-7471, 2018.

[2] **Duda, T. F.,** Acoustic signal and noise changes in the Beaufort Sea Pacific Water duct under anticipated future acidification of Arctic Ocean waters, *J. Acoust. Soc. Am.,* volume 142, pp. 1926-1933, 2017.

[3] **Beaufort Gyre Exploration Project,** CTD and Geochemistry Data, 2017, https://www.whoi.edu/website/beaufortgyre/data

[4] **Zhang, Z. Y. and C. T. Tindle,** Improved equivalent fluid approximations for a low shear speed ocean bottom, *J. Acoust. Soc. Am.,* volume 98, pp. 3391-3396, 1995.

[5] **Jensen, F. B., W. A. Kuperman, M. B. Porter and H. Schmidt,** *Computational Ocean Acoustics,* 2nd Edition, Springer, 2011. (Chapter 6)

[6] **Beaufort Gyre Exploration Project**, https://www.whoi.edu/website/beaufortgyre/home

[7] **Kuuliala, L., P. Kujala, M. Suominen, and J. Montewka,** Estimating operability of ships in ridged ice fields, *Cold Regions Science and Technology*, volume 135, pp. 51-61. 2017.

SOUNDSCAPE CONTRIBUTIONS OF GLACIER ICE BLOCKS – INSIGHTS FROM LABORATORY MEASUREMENTS

Philippe Blondel[a], Jaroslaw Tęgowski [b], Grant Deane[c]

[a]University of Bath; Bath (United Kingdom)
[b]University of Gdanks; Gdansk (Poland)
[b] Scripps Institution of Oceanography, La Jolla (USA)

Philippe Blondel; Department of Physics, University of Bath, Bath BA2 7AY, UK;
P.Blondel@bath.ac.uk

Abstract: *Acoustic measurements in Arctic fjords and next to marine-terminating glaciers show important contributions from glacier melting, and individual icebergs or growlers. As they melt, they release high-pressure gases and produce sounds at medium to high frequencies. Associated to fields of hundreds or thousands of melting growlers and ice blocks, they add significantly to the soundscape. A summer 2009 survey of Murchison Fjord and Hornsund Fjord (Svalbard) by Tegowski et al. (2010) show these contributions can, even in extremely calm weather (Sea State 0), be as loud as Sea State 4. To isolate individual contributions, a series of laboratory experiments have been conducted, using growlers of different sizes and freshness. In 2012, growlers collected in Svalbard and stored on R/V Horyzont II were measured a few months later in an anechoic tank at the Technical University of Gdansk in a variety of configurations, individually and in groups of colliding and scraping icebergs. A field survey in Svalbard, in summer 2014, was used to collect another series of growlers of different sizes, aspects (e.g. bubble contents, ice colours) and morphologies (from rough to rounder and partially melted). After collection, they were immediately measured in an ad hoc tank at the Polish Polar Station, until full melting of each growler. Both sets of experiments used similar setups, with high-sensitivity broadband hydrophones and high-frequency data acquisition (96-kHz sampling rates). The acoustic pressures and energies radiated over the lifetime of the growlers were measured by 0.1-second segments. Relative levels of individual transients and evolution over the lifetimes of the individual growlers, in different configurations and with different melting rates, have been measured. These two sets of measurements can then be related to large fields of melting ice blocks, and compared to field measurements, quantifying the soundscape contributions at different frequency bands, and offering insights into ice dynamics and local conditions.*

Keywords: *polar acoustics, ambient noise, Svalbard, tank experiments, glacier ice, growlers, transient emissions*

1. SOUNDCAPE CONTRIBUTIONS OF GLACIER ICE

The Arctic Ocean and surrounding regions are becoming increasingly important as global warming makes them more accessible, raising economic and political interests. Current and future changes, natural and anthropogenic, will affect the characteristics of Arctic soundscapes. The International Quiet Ocean Experiment (iqoe.org) and its working group on "Arctic acoustic environments" [1] are working toward establishing baseline soundscapes for different regions. Low-frequency acoustics of sea ice is well understood [2], for example from past programmes like SHEBA (*Surface Heat Budget of the Arctic Ocean*, www.esrl.noaa.gov/psd/arctic/sheba/) and current, multidisciplinary and large-scale activities like INTAROS (*Integrated Arctic Observing* System, www.intaros.eu). But there are still many questions about the acoustic contributions of freshwater ice, from melting glaciers and from icebergs. How their broadband acoustic emissions can be used to monitor calving has been well studied by [3-5] *inter alia*. The acoustic contributions from smaller ice blocks, from growlers to ice floes, are less well understood, but they are important to better understand ice melting processes, soundscape evolutions with time and with local environmental conditions, and contributions to air-ocean boundary transfers.

Measurements by [6], made in summer 2007 along Kongsfjord in Svalbard, clearly distinguished the higher-frequency acoustic signatures of small icebergs (up to 48 kHz) from other environmental processes, down to < 10 Hz (Fig. 1, left). More extensive surveys [7] measured broadband ambient noise (20 Hz – 24 kHz) in Hornsund and Murchison fjord in Svalbard during the summer of 2009 (Fig. 1, right). Statistical analyses of the probability density distribution of noise showed it was not normally distributed between 20 Hz–1 kHz, and could be explained by few, loud sources. Conversely, the noise above 2.5 kHz was normally distributed and consistent with a large number of distributed and superposed sources [7-8]. Similar observations in Hornsund in summer 2013 [4], associated with directional measurements, further confirmed these observations.

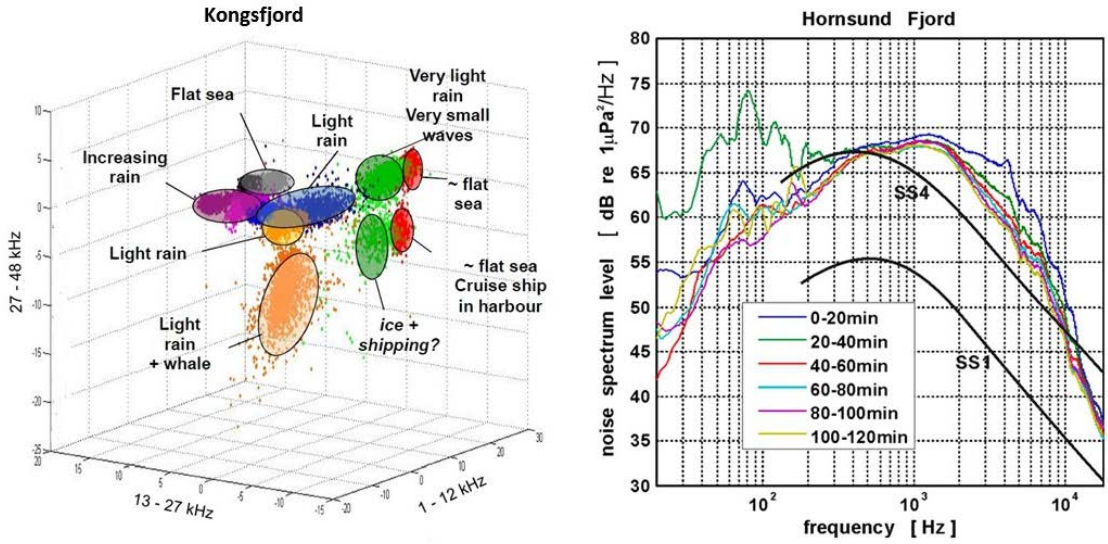


Fig.1: Left: Principal Component Analysis of broadband ambient noise measured in Kongsfjord (2009) identify different processes, each associated to specific frequency bands [6], Right: broadband measurements in other fjords show melting ice in calm seas can be as loud as Sea State 4 [7], with clear contributions above 1 kHz.

Freshwater glacier ice contains many air bubbles, formed as the snow compacted and pressurised over time. Their pressures can reach 2MPa [9], and the release of gas as the ice

melts can be a noisy process. It is referred to as “Seltzer ice” by submariners (Wadhams, personal communication) and was first measured by [10]. Detailed experimental measurements of gas bubbles and comparison of acoustic signatures with high-speed photography and mathematical models have been published [11-12]. The work presented here is focusing on the long-term acoustic contributions of individual ice blocks throughout their melting. To study them in isolation from other processes (e.g. wind, waves, other ice blocks in the vicinity), we use tank measurements of single blocks, or in small groups. Logistical constraints in the collection of ice blocks in the field and tank sizes mean these studies are restricted to sub-metric sizes, called “growlers” [13]. Section 2 extends analyses by [14] of growlers in an anechoic tank, and Section 3 presents studies of freshly-collected growlers at a field station. The main observations will be synthesised in Section 4.

2. ANECHOIC TANK MEASUREMENTS OF GROWLERS

To understand the high-frequency contributions of individual growlers, ice blocks similar to those observed in the field in summer 2009 [7] were harvested by the same field team, in the same part of Hornsund Fjord, in summer 2012. The growlers were kept in cold chambers on board R/V *Horyzont II* and at the Institute of Oceanology, Polish Academy of Science in Gdansk, until the time of the experiments. Typical growlers are around 20-40 cm wide, and they show numerous gas inclusions, most often small (< 3-mm width). The melting, cracking and general interaction of these growlers with their immediate environment were investigated acoustically in an anechoic water tank at the Technical University of Gdansk.

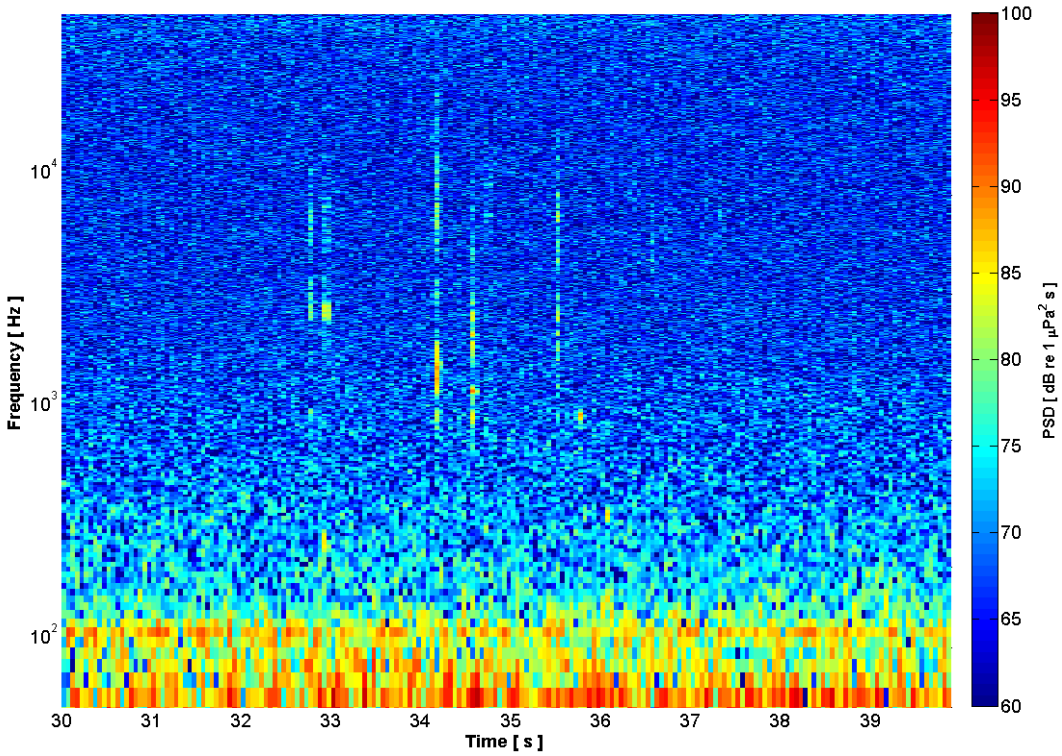


Fig.2: Typical spectrogram extract of a melting growler, showing strong transient events with high frequencies (> 1 kHz) and very short durations (< 0.1 second) [14].

Measurements with several hydrophones included a Brüel and Kjaer omnidirectional B&K-8103 hydrophone (effective bandwidth 0.1 Hz to 180 kHz, receiving sensitivity –211dB re 1V/µPa), plugged into a 1:1-gain signal preconditioner and connected to a B&K Heterodyne Signal Amplifier type 2010, with a 30-dB gain. Received voltages were sampled

at 96 kS/s and 24-bit resolution, using a USB-4431 data acquisition card from National Instruments. The files were in LabVIEW's proprietary format TDMS, then converted to CSV (Comma-Separated Values) and 24-bit WAV files. Still photography and video were used to further document these experiments, fully detailed in [14].

All growlers (initially at sub-freezing temperatures) were measured until full melting, often lasting several hours. This process was characterised with very short acoustic emissions, audible over a range of frequencies, defined as "transients" and visually associated to escaping bubbles [14]. Typical spectrograms (Fig. 2) show constant background noise below 100 Hz, associated to the melting process, and very short emissions with high-frequency signatures extending to 40 kHz. Using analysis windows of 0.08 s (2^{13} samples at the sampling frequency used), these transients are defined on the basis of their Sound Pressure Level (SPL) being significantly larger than the surrounding 10-second segments. Frequency distributions were compared for segments with and without transients (Fig. 3). In this particular example, they showed broad peaks at 500 – 700 Hz, 800 – 900 Hz. Above 1 kHz, the segments with no transients are undistinguishable from the background noise, but those with transients show sharp peaks at 1 – 2 kHz, 2.5 kHz, up to 10 kHz.

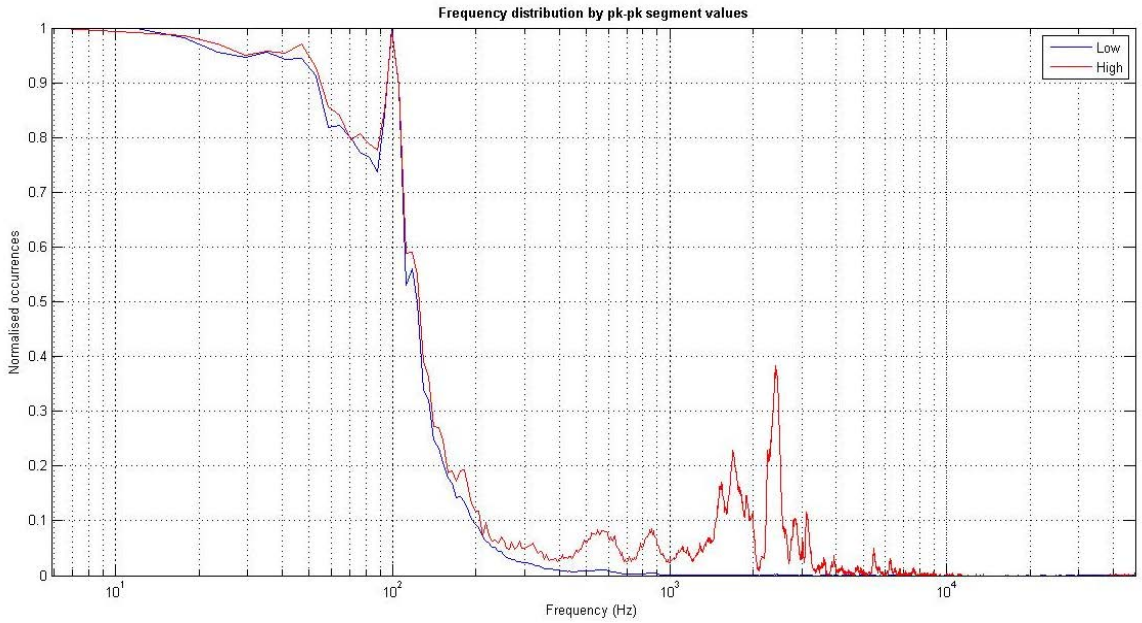


Fig.3: Compared frequency distributions of background segments (blue) and high-SPL transients (red) for the full melting of one single growler. See text for details. From [14].

How do acoustic emissions evolve as a single growler melts? As there will be less ice volume, they should obviously decrease in numbers and in intensities, but the increasing exposure of more gas bubbles might lead to more frequent emissions. As they melt, the shape of growlers will change their centre of gravity and they will capsize, each time with a different energy (based on the shape of the growler at that stage, and on its volume), adding acoustic contributions at lower frequencies. Broadband measurements to full melting (Fig. 4) show RMS mean and percentile probability densities of the same growler, with clear contributions at higher frequencies (> 1 kHz). Measurements over all 0.1-second segments, with a 50% overlap, were arbitrarily separated between third-octave bands below 1 kHz and above: the higher frequencies are in average 8 – 9 dB louder, with frequent peaks up to 14 dB for some of these 0.1-second segments (meaning short, loud sounds with higher frequencies).

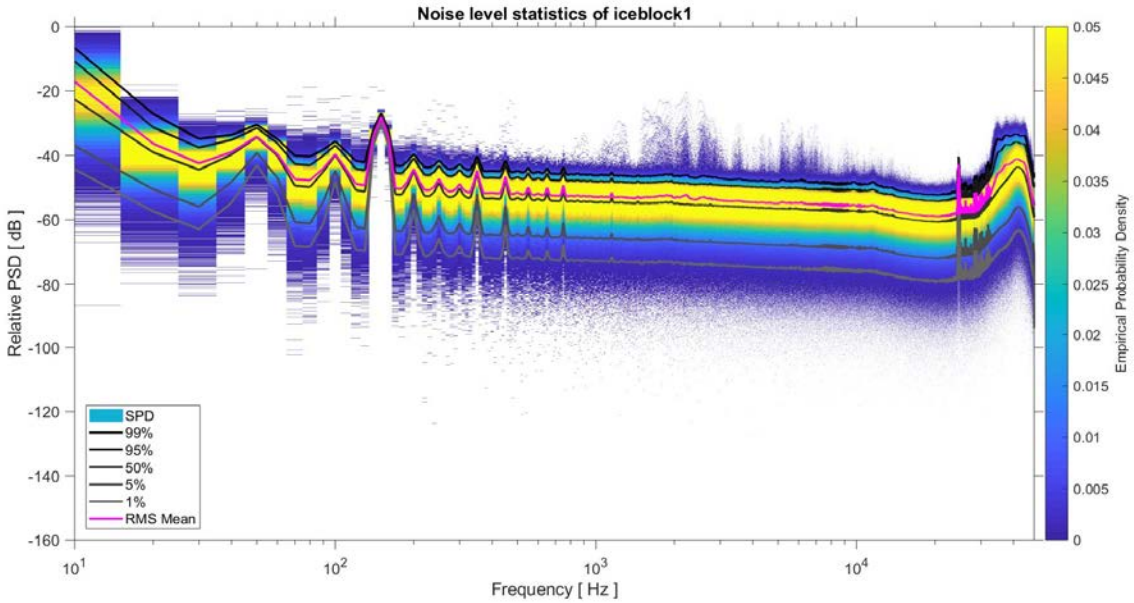


Fig.4: Probability Spectral Density for a fully melting growler, calculated with PAMGuide [15] over 0.1-s segments, overlapping by 50%, with strong high-frequency contributions.

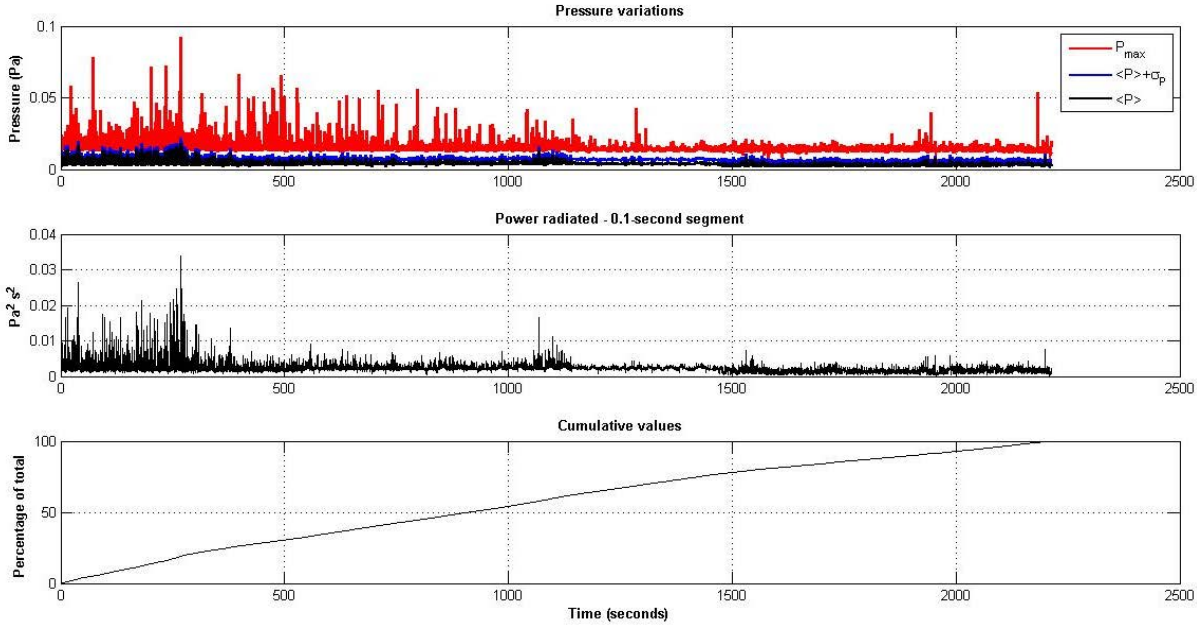


Fig.5: Variations in pressure (mean pressure within each 0.1-second segment, mean pressure and standard deviation and maximum instantaneous pressure recorded within the segment) and acoustic power radiated for the full melting of a single growler.

Broadband pressures from the moment the growlers were put in the water to their full melting show regular variations, decreasing in amplitudes and frequencies of occurrence as melting progresses (Fig. 5). Fig. 5 (top) shows the mean pressure within each 0.1-second segment (in black), its variation with the local standard deviation (in blue), and the maximum instantaneous pressures (red). Fig 5 (middle) shows the power radiated within each 0.1-segment segment, and its cumulative variation (Fig. 5, bottom). The power radiated is more important at the onset of melting and steadily increases to full melting. Similar results are seen for the other growlers analysed in this series of experiments.

3. TANK MEASUREMENTS OF FRESH GROWLERS

The measurements presented in Section 2 were supplemented in summer 2014 with the direct measurement of fresh growlers collected in Hornsund Fjord, Svalbard. Field conditions varied from day to day, with recent glacier melting episodes producing large numbers of growlers (Fig. 6, left). These growlers come in all shapes and sizes. The ones selected for analyses (Fig. 6, right) were of similar sizes (approx. 30 cm wide, 25 cm high and 20 cm long), with surface temperatures of –2°C. They exhibited different bubble densities, estimated visually, and different colours (i.e. different origins within the original glacier). Bubbles sizes close to the surface of each growler varied between a few millimetres and below, with irregular shapes. All growler samples were measured to full melting in cold water (external temperature), in a small tank at the field station nearby, within 20 minutes of collection.

Acoustic measurements were conducted again with a B&K 8103 hydrophone. Signals were amplified with a Parnell precision amplifier, using a constant 80-dB gain and bandpass filtering from 100 Hz to 100 kHz. The signals were sampled at 96 kHz with 24-bit precision, using a NI-USB 4431 card controlled with LabVIEW. Later processing was done with Matlab. Concurrent video was usually limited to the most intense melting (within the first 30 minutes), due to HD card size, and it was complemented with log of visual observations. Melting times varied significantly, typically up to 2 hours, and was not correlated with their volumes. They were determined visually and acoustically (no change in ambient noise). A dozen growlers and smaller ice blocks were analysed, and the background noise was small enough not to be an issue. A batch of similar growlers (same sizes, same apparent bubble densities) were set apart to measure the influence of warmer waters (i.e. faster melting).

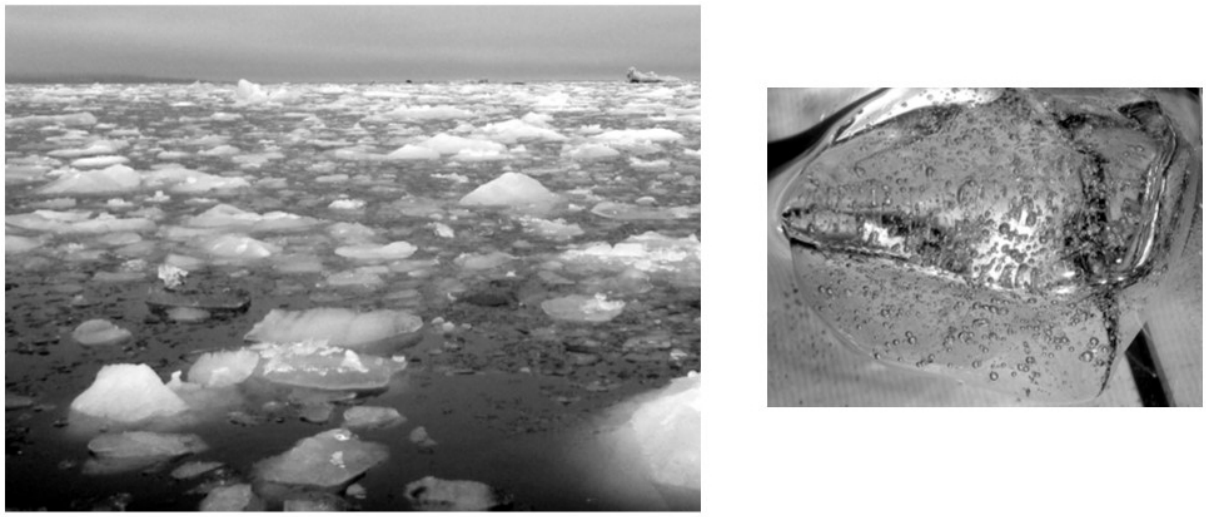


Fig.6. Left: field conditions in Hornsund, on a particular day. Growlers come in all shapes and sizes. Right: growler analysed in Fig. 7. Both images were contrast-enhanced to better show relevant features.

Pressure variations and total acoustic power radiated were again measured in 0.1-second segments for each growler (Fig. 7). The amplitudes and the total power radiated by the time of full melting varied with apparent bubble densities, but still within the same order of magnitude. 90% of this total power was radiated between 55% and 90% of the normalised melting times, with no discernible trend between types of growlers. The total acoustic power radiated between the time a fresh ice block was put in the tank and the time it had totally melted was exponentially correlated with the time to full melting.

There are many loud transients (Fig. 7) and similar analyses to Section 2 were conducted. They cannot be presented fully here, but one key result is how much they contribute to the soundscapes. They were conservatively defined here as segments contributing more than 3 σ of the mean acoustic energy radiated. Although few in number (0.1-0.3% of all 0.1-s segments), these loud transients contribute 10% – 56% of the total acoustic energy radiated by each growler before full melting. They decrease steadily in numbers until melting is 50% complete, and near-final melting (90% of total time) sees a sudden increase in loud transients.

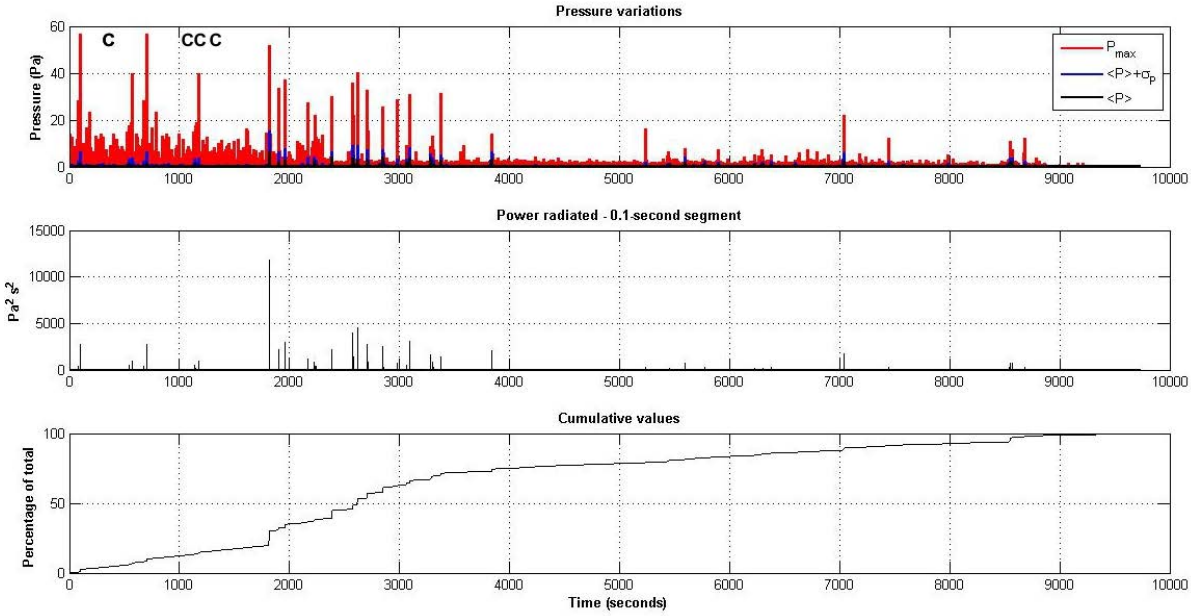


Fig.4: Acoustic emissions from a fresh growler until total melting ("C" indicates capsizing events recorded on video, available for the first 1,800 seconds).

4. DISCUSSION - CONCLUSIONS

Field measurements [6-8,11] show contributions of glacier ice and ice blocks (from floes to growlers to icebergs) include significant high-frequency components, above 1 kHz and up to 30 kHz. To better constrain the relative importance of individual growlers, we have measured their total melting in controlled conditions. Section 2 used growlers collected in a fjord, stored in cold conditions and measured in an anechoic tank several months later. Section 3 used growlers collected in the same fjord, and measured immediately afterwards in a standard tank. Growlers were selected with similar sizes but with variations in colours (i.e. originating depths within the glacier, and therefore bubble pressures) and in apparent bubble densities (as seen from the surface of the growlers).

Both series of experiments confirm the large amount of acoustic transients, with Sound Pressure Levels larger than the baseline, lasting < 0.1 second and with high-frequency components. These transients occur 0.1 – 0.3% of the time to full melting, but contribute up to 56% of the total energy radiated by each growler. They decrease steadily until melting is 50% complete, and reoccur in larger numbers in the final stages of melting.

Detailed analyses of the frequency content of each transient, and how it varies with stages of melting and the nature of the growler (volume, colour, bubble density) is on-going. They will be supplemented with other studies of how bubble pressures and shapes affect the acoustic signatures of the bubbles. These results will help quantify the contributions of growlers and fields of growlers to the changing Arctic soundscapes.

5. ACKNOWLEDGEMENTS

The measurements presented in Section 2 (PB, JT) were conducted at TU Gdansk in the laboratory of Dr W. Lis. The measurements presented in Section 3 used growlers collected in field surveys (PB, JT, GD), with funding from the Polish Science Foundation. The hospitality and technical help of staff at the Polish Polar Station (Hornsund) is gratefully acknowledged.

REFERENCES

[1] **Blondel, Ph. H. Sagen, M.-N. Houssais, P. Mikhalevsky, J. Pajala, R. Racca, J. Tegowski, K. Thomisch, J. Tougaard, E. Urban, A. Vedenev**, International Quiet Ocean Experiment – Arctic Acoustic Environments, *Proc. UACE-2019* (this volume), 2019.

[2] **Diachok, O.I., R.S. Winokur**, Spatial variability of underwater ambient noise at the Arctic ice-water boundary, *J. Acoust. Soc. Am.*, 55 (4), pp. 750-753, 1974.

[3] **Pettit, E.C.**, Passive underwater acoustic evolution of a calving event, *Annals of Glaciology*, 53(6), pp. 113-122, 2012.

[4] **Deane, G.B., O. Glowacki, J. Tegowski, M. Moskalik, Ph. Blondel**; Directionality of the ambient noise field in an Arctic, glacial bay, *J. Acoust. Soc. Am.*, 136, EL350, 2014.

[5] **Glowacki, O., G.B. Deane, M. Moskalik, J. Tegowski, Ph. Blondel**; Two-element acoustic array gives insight into ice-ocean interactions in Hornsund Fjord, Spitsbergen, *Polish Polar Research*, 36(4), p. 355-367, 2015.

[6] **M. Keogh, Ph. Blondel**, Underwater monitoring of polar weather: Arctic field measurements and tank experiments, In *Third Conference on Underwater Acoustic Measurements: Technologies and Results*, Heraklion, Crete, Greece, 8 pp., 2009.

[7] **Tegowski, J. G.B. Deane, A. Lisimenka, Ph. Blondel**; Underwater ambient noise of glaciers in Svalbard as indicator of dynamic processes in the Arctic, In *Proc. Inst. Acoustics*, 33(5), 3 pp., 2011.

[8] **Tegowski, J., G.B. Deane, A. Lisimenka, Ph. Blondel**, Spectral and statistical analyses of ambient noise, *POMA*, 17, 070079, 7 pp., 2013.

[9] **Scholander, P. F., D. C. Nutt**, Bubble pressure in Greenland iceberg, *Journal of Glaciology*, 3(28), pp. 671-678, 1960

[10] **Urick, R.J.**, Noise of melting icebergs, *J. Acoust. Soc. Am.*, 50(1), pp. 337-341, 1971.

[11] **Tegowski, J., G. Deane, Ph. Blondel, O. Glowacki, M. Moskalik,** An acoustical study of gas bubbles escaping from melting growlers, 6 pp., In *Proc. Underwater Acoustics Conference UAC-2014*, 2014.

[12] **Deane, G., J. Tegowski, Ph. Blondel**, A model for the sound generated by the explosive release of gas from melting glacier ice, In *Proc. Underwater Acoustics Conference and Exhibition (UACE) 2017*, 8 pp., 2017

[13] **Wadhams, P.**, *Ice in the ocean*, Gordon & Breach Science Pub., 364 pp., 2000

[14] **Blondel, Ph., M. Collins, J. Tegowski, G.B. Deane**, Transient events in underwater noise from ice floes – Field and laboratory experiments, In *European Conference in Underwater Acoustics (ECUA)*, Edinburgh, UK, 2012

[15] **Merchant, N.D., K.M. Fristrup, M.P. Johnson, P.L. Tyack, M.J. Witt, Ph. Blondel, S.E. Parks**; "Measuring acoustic habitats", *Methods in Ecology and Evolution*, 6(3):25-265, 2015.

A STUDY ON THE YEARLONG RECORD OF SOUND PROPAGATION FROM THE CANADA BASIN TO THE CHUKCHI SHELF MEASURED ON A HORIZONTAL LINE ARRAY

Megan S. Ballard[a], Mohsen Badiey[b], Jason D. Sagers[a], John A. Colosi[c], Altan Turgut[d], Sean Pecknold[e], Ying-Tsong Lin[f], Andrey Proshutinsky[f], Richard Krishfield[f], Peter F. Worcester[g], and Matthew A. Dzieciuch[g]

[a]Appl. Res. Labs., Univ. of Texas at Austin, Austin, TX, USA
[b]University of Delaware, Newark, DE, 19716, USA
[c]Naval Postgrad. School, Monterey, CA, USA USA
[d]U.S. Naval Research Laboratory, Washington, DC, USA
[e]Defence Research and Development Canada, Dartmouth, Nova Scotia, Canada
[f]Woods Hole Oceanographic Institution, Woods Hole, MA, USA
[g]Scripps Institution of Oceanography, University of California at San Diego USA

Abstract: *The Pacific Arctic Region has experienced decadal changes in atmospheric conditions, seasonal sea-ice coverage, and thermohaline structure. From September 2016 to October 2017, the Canada Basin Acoustic Propagation Experiment (CANAPE) was conducted to observe the changing soundscape and to explore the use of acoustic remote sensing techniques in the transitioning Arctic. During the experiment, low-frequency signals from five tomographic sources located in the Canada Basin were recorded by an array of hydrophones with both horizontal and vertical apertures located on the Chukchi Shelf at the 150 m isobath. The propagation distances ranged from 240 km to 520 km, and the propagation conditions changed from persistently ducted in the basin to seasonally upward refracting on the continental shelf. An analysis of the received level from the tomography sources revealed a spatial dependence in the onset of the seasonal increase in transmission loss, which was correlated with the locations of the sources in the basin. This observation led to the hypothesis that the water advected from Barrow Canyon westward over the continental slope by the Chukchi slope current contributes to the temporal and spatial dependence observed in the acoustic record. The water column properties and ice draft were measured by oceanographic sensors on the basin tomography moorings and by six vertical arrays of oceanographic moorings on the continental shelf to characterize the temporal and spatial variability of the environment. This talk examines the range-dependent measurements and seeks to explain the observed variability in the received signals through propagation modeling.*
© Her Majesty the Queen in Right of Canada, Department of National Defence, and authors 2019.

Keywords: *Arctic Oceanography, Sea Ice, Beaufort Gyre, Chukchi Shelf*

1. INTRODUCTION

The Pacific Arctic Region has experienced decadal changes in atmospheric conditions, seasonal sea-ice coverage, and thermohaline structure. Sea-ice losses in the northern Chukchi and Beaufort Seas during the summer melt season have resulted in an increase in the ice-free ocean area of 70% compared to the climatological mean [1]. Furthermore, a doubling in Beaufort Gyre halocline heat content has been observed over the past three decades [2]. Both of these changes have implications for acoustic propagation: sound incurs less surface loss from open water than from the rough ice interface, and it is more efficiently channeled by warmer water in the upper halocline which forms the top boundary of an acoustic duct.

The Canada Basin Acoustic Propagation Experiment (CANAPE) was conducted over a yearlong period beginning in September 2016. The experiment objectives were to understand the changing soundscape and to explore the use of acoustic signals as a remote sensing tool in the transitioning Arctic. During the experiment, low-frequency signals from five Scripps Institution of Oceanography (SIO) tomographic sources located in the Canada Basin were recorded by the Applied Research Laboratories at the University of Texas at Austin (ARL:UT) PErsistent aCoustic Observation System (PECOS) array of hydrophones located on the Chukchi Shelf. The locations of the SIO sources and the PECOS array are shown in Fig. 1.

To support the acoustic propagation experiment, environmental measurements were made in the Canada Basin and on the Chukchi Shelf. The locations of environmental measurements are indicated by triangles in Fig. 1. Water temperature and salinity were measured in the basin by the SIO deep vertical line array (DVLA) and on the shelf by the University of Delaware (UDel) array of oceanographic moorings (OM). An additional set of oceanographic measurements in the basin were obtained by the Beaufort Gyre Exploration Project (BGEP) [3,4]. Collectively, these data indicate that the range-dependent propagation conditions change from predominately ducted in the basin to seasonally upward refracting on the continental shelf. Ice draft was measured in both locations by Upward Looking Sonars (ULS). In the basin, each of the SIO tomography moorings included an ULS, and on the shelf, ice draft was measured by the Naval Research Laboratory (NRL) ULS. This paper examines the temporal changes of the

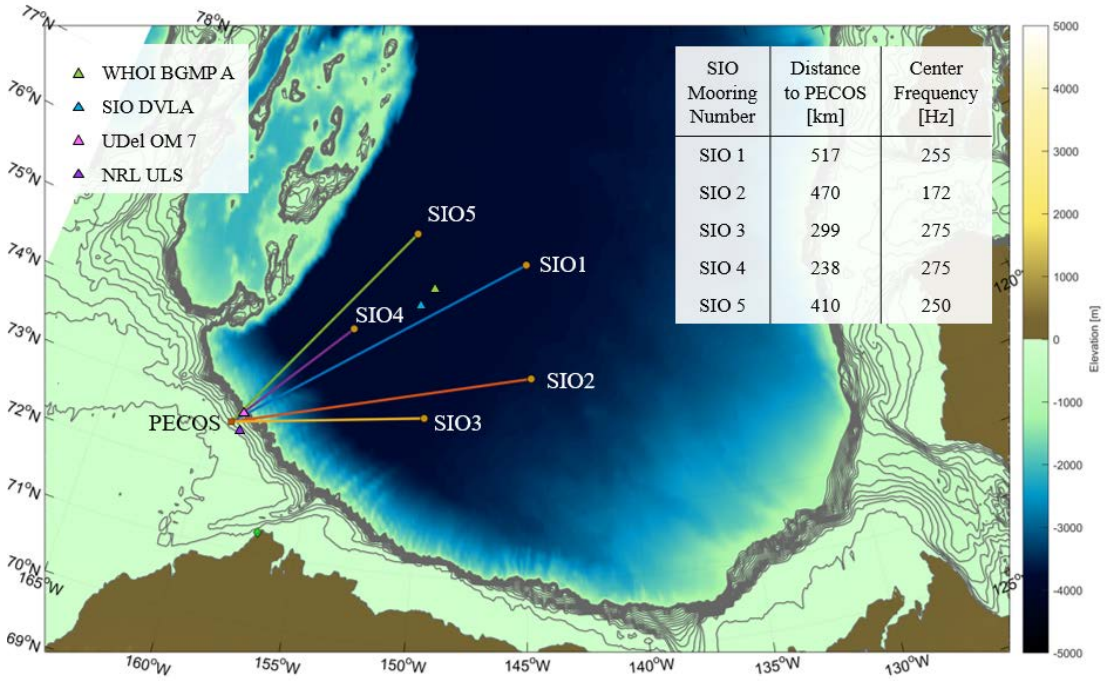


Fig.1: Map of CANAPE, including the locations of acoustic sources (circles), receiver (square), and environmental measurements (triangles). The propagation paths from the SIO sources in the basin to the PECOS receiver array on the shelf are illustrated by the colored lines.

range-dependent measurements and explains the observed variability in the received level (RL) of the acoustic signals through propagation modeling.

2. ACOUSTIC MEASUREMENTS

The SIO tomography sources in the Canada Basin broadcast 135 s-long linear frequency modulated (LFM) signals. The sources were scheduled to broadcast sequentially at 6 min. intervals once every four hours. The signals had 100 Hz bandwidth, and the center frequencies are listed in the embedded table in Fig. 1. The sources were deployed at a nominal depth of 175 m, so that they were located in the sound speed duct.

The signals were measured by the horizontal line array (HLA) and recorded by PECOS. The 34-element HLA was designed as a 220 m-long center-tapered array, and the data were recorded at a sampling rate of 8192 Hz. The measured signals were pulse compressed and conventional frequency-domain beamforming was applied using 0.5 s integration time with 75% overlap. The transmission loss (TL) for each reception was determined by subtracting the peak RL (calculated from the pulse-compressed beamformed time series) from the known source level (SL). Relative TL was calculated by normalizing TL throughout the year such that the average TL during the open-water condition in August was equal to zero.

Relative TL from all five SIO tomography sources is shown in Fig. 2. Receptions from all five moorings display the seasonal increase in TL during the fall and winter, and a decrease in TL in the summer. However, the onset of the increase/decrease in TL appears correlated with position. Receptions from the most eastern moorings experience the change in propagation conditions more than a month before the receptions from the western most moorings. Additionally, the rate of decrease in TL appears faster for the western moorings. For receptions from all sources, TL temporarily decreases for periods between April and June. There are also periods for which the ambient noise level exceeded the RL; relative TL is not reported for these periods.

3. ENVIRONMENTAL MEASUREMENTS

The top panel of Fig. 3 shows the daily mean ice draft measured by the ULS in the basin and on the shelf. The ULS measurements were made on all five SIO source moorings, but are missing for periods when currents on the mooring line pulled the ULS away from the ice canopy. The NRL ULS on the shelf stopped recording in the beginning of February. For all

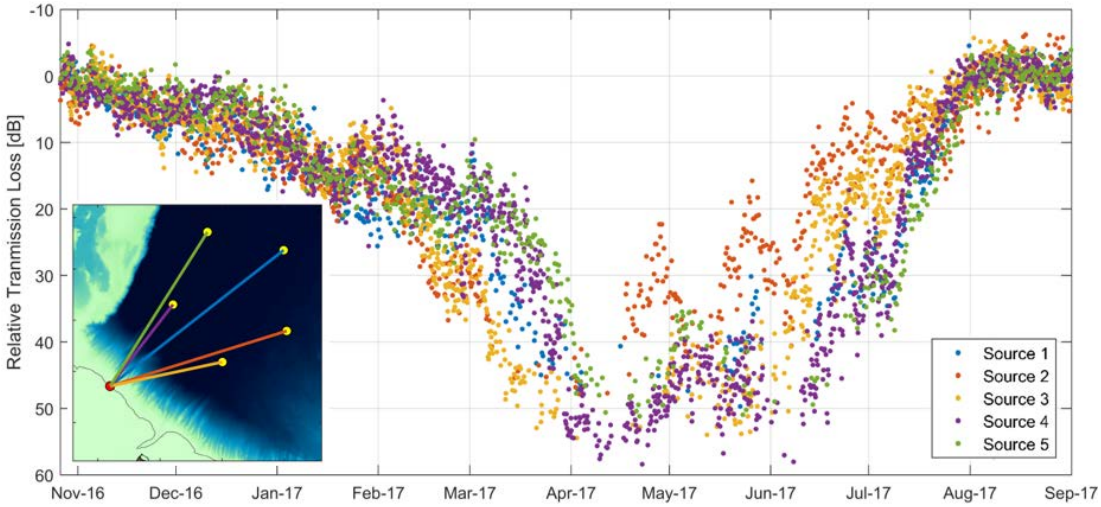


Fig.2: Relative TL of receptions from the SIO tomography sources recorded on PECOS. The inset map shows the acoustic paths from the SIO moorings to the PECOS array.

moorings, a gradual increase in ice thickness is observed between November and April, at which time the ice reaches its maximum daily mean thickness of 1.5 m to 2 m. After mid-June, the ice begins to melt, and the mean ice draft rapidly decreases.

The lower panel of Fig. 3 shows seawater temperature representative of the water masses in the halocline that form the sound speed duct. The Pacific summer water (PSW), which forms the upper boundary of the acoustic duct, is warmer and less saline and consequently overlies the cooler Pacific winter water (PWW), which forms the sound speed minimum in the duct. For each of the three measurement locations shown in Fig. 3, the temperature of the PSW was calculated as the maximum temperature in the upper 150 m of the water column, and the PWW was calculated as the minimum temperature between 100 and 200 m depth.

Within the Beaufort Gyre, the temperatures of the PSW and PWW were relatively constant over the yearlong measurement period. The PSW is consistently warmer than -0.5ºC; the anomalous values in early May in the DVLA measurements are caused by movement of the mooring line that pulled the sensors below the depth of the PSW layer. The observed variability in the PSW in the Canada Basin is due to in situ mixing and changes in source-water properties. The PWW shows even less variability with persistent temperatures around -1.5 ºC. These data indicate the ducted sound propagation conditions are present in the Beaufort Gyre throughout the yearlong measurement period.

In contrast, the temperatures measured on the shelf show considerably more seasonal variability. On the Chukchi Shelf, it is typical to further subdivide the Pacific water masses into a greater number of categories depending on their temperature and salinity [5-8]. The present analysis does not make this discrimination, as the larger focus of this study is on determining the presence of an acoustic duct. As shown in the lower panel of Fig. 3, the maximum temperature in the upper 150 m measured by UDel OM 7 exceeds 1ºC for the open water period in summer as well as in the fall and early winter. Beginning in January, the maximum temperature begins to decrease, with the most dramatic decrease in temperature occurring in February and March. The maximum temperature on the shelf remains lower than the temperature of the PSW in the basin until the breakup of the ice cover in early July. Similarly, more variability is observed in the minimum sound speed on the slope compared to the PWW



Fig.3: Top panel: Daily mean ice draft calculated from measurements of ULS on each of the SIO moorings in the basin and the NRL mooring the shelf. Bottom panel: Temperature of the upper boundary of the acoustic duct in the basin and on the shelf.

in the basin. These measurements indicate the acoustic duct is present on the Chukchi Shelf in the summer and fall, but weakens and/or dissipates in the winter and spring. The influx of colder water in the upper 150 m observed in the UDel OM 7 measurements is believed to be transported by the Chukchi slope current. The Chukchi slope current transports Pacific-origin water westward over the continental slope [5]. The volume of water transported and speed of its flow change throughout the course of the year [6-8].

Comparison of the relative TL to the environmental measurements reveals some potential relationships between the data sets. For example, the increase in TL that occurs in February and March appears correlated with the decrease in the maximum temperature on the shelf. The decrease in relative TL between mid-June and August appears correlated with the melting ice cover as indicated by the decrease in the daily mean ice draft. Although these observations may lend some understanding into the environmental effects on TL, the true propagation conditions are simultaneously influenced by both the presence of the ice cover, which causes increased loss due to surface scattering, and the water column properties, which can insulate the acoustic field from surface loss when the sound speed profile is downward refracting. To investigate the interrelationship between these effects, acoustic propagation modeling was carried out using the environmental measurements.

4. ACOUSTIC PROPAGATION MODELING

Transmission loss from the SIO sources in the basin to the PECOS array on the shelf was modeled using the ray model BELLHOP [9]. The ray theory is an approximate solution to the wave equation, and this modeling approach was chosen for its efficiency. In this application, there are inaccuracies related to the frequency-dependent extent to which sound is trapped in the sound speed duct. The ray solution includes rays that are fully trapped within the duct that do not incur surface loss. However, the low-frequency SIO source signals are not fully trapped in the duct, and accumulate loss as they propagate through the Beaufort Sea. Additionally, the environmental measurements between deep and shallow water sites are sparse and temporally and spatially under-sampled. Despite these shortcomings, the model reproduces the seasonal changes in TL studied in this paper.

Surface loss was calculated using an empirical model derived from historical data based loosely on Ref. 10. The only inputs to the model are the root-mean-square value of the ice draft σ, which was calculated from the ULS on the SIO moorings, and the center frequency of the source signals. By ony using ULS data from the source location, constant ice draft statistics are assumed over the entire propagation path. The reflection coefficient R in dB is calculated by

$$\begin{aligned} R(\sigma, f) &= 0.00190 f (2\sigma)^{1.5} && f \leq 403(2\sigma)^{-0.5} \\ R(\sigma, f) &= 0.541(2\sigma)^{1.5} && f > 403(2\sigma)^{-0.5}\,. \end{aligned} \tag{1}$$

This surface loss model does not account for dependence on sea ice thickness, properties, spatial correlation length of the roughness, and other characteristics that are important in determining the reflection coefficient. To account for variable sea ice coverage over the acoustic propagation path, the sea ice concentration was taken into account using the MASIE-AMSR2 (MASAM2) database [11]. For seasonal periods of ice growth in October and November and ice melt in June and July, the reflection coefficient calculated from Eq. (1) was weighted by the range-dependent ice concentration along the propagation path.

For each eight-hour period of the yearlong experiment, the range- and depth-dependent water-column sound-speed field was constructed using measurements from the BGEP and the UDel OM array. The two-dimensional sound-speed field was divided into four domains which were each informed by different data sets or interpolation schemes. An example of the water-column sound-speed field for April 1, 2017 with the different domains labeled is shown in

Fig. 4. The boundary between the regime of ducted propagation in the basin and seasonally upward refracting propagation in the slope was defined to be 100 km offshore [5].

The first domain is characterized by ducted sound propagation and is made up of data measured by BGEP Mooring A. Range-dependent sound-speed profiles were derived from the temporal measurements by advecting the measured profile in space using the average Beaufort Gyre speed of 0.02 m/s. The sound speed in the second domain was constructed using the temporally relevant measurement from each of the UDel OM. The locations of the UDel OM are indicated by the white triangles above the plot. The third domain is defined as the upper 140 m of the water column offshore of the UDel OM array. Within domains two and three, the sound speed profile is expected to show strong seasonal dependence influenced by the water masses advected by the slope current. Since no direct measurements were made within region three, the water column properties were extrapolated from the northernmost mooring of the UDel OM array. For the five locations marked by the black triangles in Fig. 4, the median sound speed for a 24-hour period immediately following the signal transmission was used. To simulate range-dependence within this region, the sound speed profile for each marker location was calculated from different interleaving 5-hour blocks with the 24-hour period. A 2D interpolation was used for the fourth domain to accommodate the change in the depth of the Atlantic water layer between the measurements in basin and on the shelf. Finally, all the profiles were interpolated onto a 1 km grid for use in BELLHOP.

To account for the advection of PWW by the Chukchi slope current, the water-column properties making up domains two and three were temporally shifted to account for the lag in the seasonal increase in TL. Recalling the experiment geometry in Fig. 1, the propagation paths are spread over the slope so that water from the westward flowing slope current reaches the propagation path from SIO 3 first, followed by the paths from SIO 2, SIO1, SIO 4, and SIO 5. The estimates for the lag times were obtained from an examination of the increase in the relative TL during February and March shown in Fig. 2. For the propagation path from SIO 1 to PECOS, which is perpendicular to the shelf break, no temporal shift was applied. For the propagation paths from SIO 2 and SIO 3, which are located to the east of the SIO 1 propagation path, temporal shifts of -16 days and -23 days were applied. For the propagation paths from SIO 4 and SIO 5, which are located to the west of the SIO propagation path, temporal shifts of 6 days and 12 days were applied. The application of a uniform temporal shift to the 2D sound speed field is a coarse approximation of the advection of water by the slope current. A more accurate representation would account for the orientation of the propagation paths oblique to the shelf break as well as the seasonal variation in the speed of the current.

The BELLHOP model produces a set of arrivals, each described by a complex amplitude and travel time. The time-domain representation for the received waveform was calculated through application of the convolution theorem [12]. A short-time Fourier transform with 0.5 s time

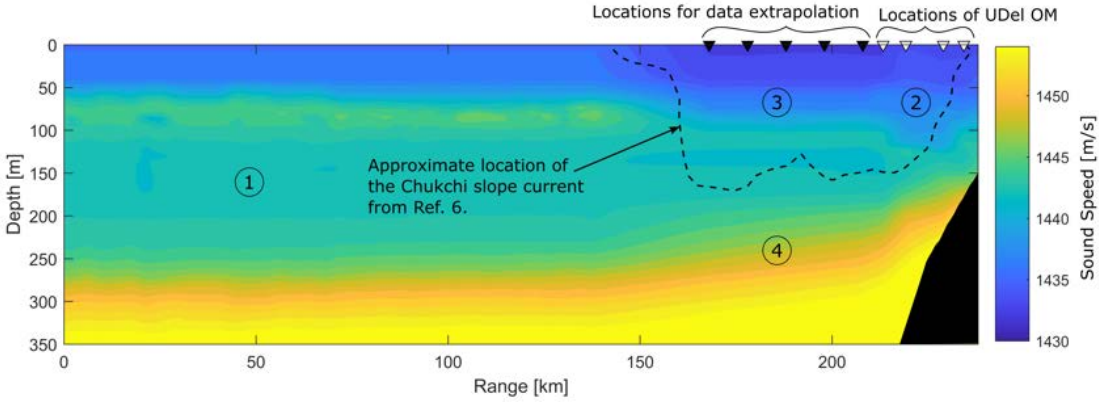


Fig. 4: Water-column sound-speed field constructed for April 1, 2017. The numbered markers represent regions informed by different data sets and/or interpolations.

window and 75% overlap was applied to the calculated time series for comparison with the measured data, which were beamformed in the frequency domain using 0.5 s integration time.

A comparison of the measured and modeled peak RL is shown in Fig. 5. Two calculations of the modeled RL are shown: one that accounts advection of the PWW by the slope current using the temporal shifts described above, and another that neglects the temporal shifts. For both calculations, there are times throughout the year when the model overestimates/ underestimates TL. The discrepancies between measured and modeled RL can be attributed to both approximations in the environmental model and the acoustic propagation model. There are also distinct periods where the modeled RL is lower than the 20 dB limit of the plot (i.e., mid-Feb. to mid-Apr. for SIO 2, and late Mar. to late Apr. for SIO 4). These periods correspond to times when currents pulled the mooring cable down so that the source was no longer in the sound speed duct.

For propagation from SIO 1 to PECOS, no temporal shift was applied for either modeled case since the propagation path is perpendicular to the shelf break. Comparision with the measured data shows good agreement in both the timing and magnitude of the seasonal increase and decrease in TL. For SIO 2 and SIO 4, the depth of the source influences the increase in TL in February and March, and the effects of the advection by the slope current cannot be readily observed. Comparisons of the two calculations of RL with the measured data for SIO 3 and SIO 5 most clearly show the impact of the advection of PWW over the slope. For SIO 3, calculation that neglects the temporal shift, the seasonal increase in TL occurs approximately three weeks late, and for SIO 5, it occurs almost two weeks early. Conversely, the solutions that include the temporal shifts agree with the measured data. These results support the hypothesis that the increase in TL February and March is caused by the advection of cold water by the slope current, which produces an upward refracting sound speed profile over the shelf.

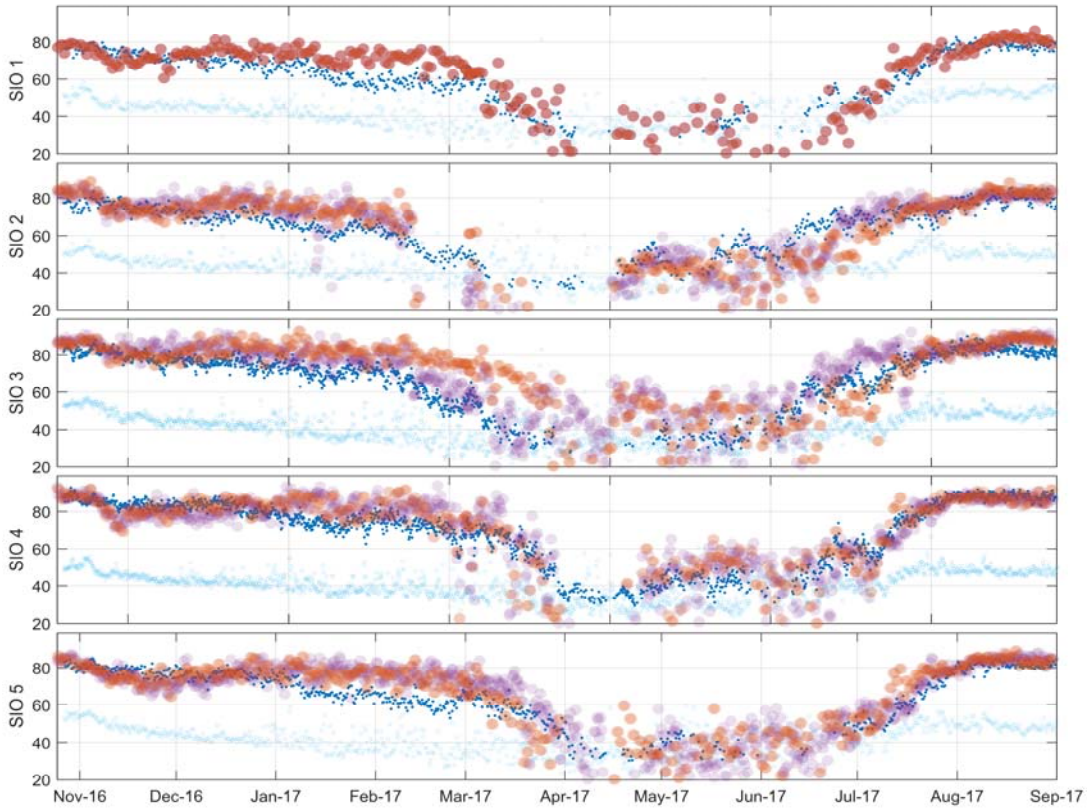


Fig.5: Peak RL for the measured and modeled signals from the five SIO moorings to the PECOS array. The measured RL (dark blue dots), and the measured background noise (light blue dots). The modeled RL are shown by the including the temporal shift to account for advection of water by the Chukchi slope current (purple dots) and neglecting the temporal shift (orange dots).

5. CONCLUSIONS

The measurements of long-range acoustic propagation from the Canada Basin to the Chukchi Shelf show a seasonal pattern of TL believed to be related to the outflow of the Chukchi slope current and the ice cover. The increase in TL in the winter was hypothesized to be caused by the advection of cold water by the Chukchi slope current westward, which resulted in an upward refracting sound speed profile leading to increased surface loss over this portion of the propagation path. The decrease in TL in the summer was associated with breakup of the ice cover, which exposed the eastern mooring locations to open water conditions first. These interpretations were supported by results from a ray-based acoustic propagation model that provided good agreement in both the timing and magnitude of the seasonal changes in TL. However, the modeling involved a number of assumptions, including extrapolation of the oceanographic data and simplified modeling of the surface loss from the ice cover. A physics based, coupled ice-ocean model of this region can improve reconstruction of time and range dependent environmental input parameters.

6. ACKNOWLEDGEMENTS

This work was sponsored by the Office of Naval Research under Grant Numbers N00014-15-1-2144, N00014-15-1-2119, N00014-15-1-2017, N00014-15-1-2068, N00014-15-1-2110, and N00014-15-1-2898.

REFERENCES

[1] K. R. Wood, N. A. Bond, S. L. Danielson, J. E. Overland, S. A. Salo, P. J. Stabeno, and J. Whitefield, “A decade of environmental change in the pacific arctic region,” Prog Oceanogr. 136, 12–31, 2015.
[2] M. L. Timmermans, J. Toole, R. Krishfield, “Warming of the interior Arctic Ocean linked to sea ice losses at the basin margins,” Sci. Adv., 2018.
[3] http://www.whoi.edu/beaufortgyre
[4] R. A. Krishfield, A. Proshutinsky, K. Tateyama, W. J. Williams, E. C. Carmack, F. A.McLaughlin, and M. L. Timmermans, “Deterioration of perennial sea ice in the beaufort gyre from 2003 to 2012 and its impact on the oceanic freshwater cycle,” J. Geophys. Res. Oceans 119, 1271–1305, 2014.
[5] W. B. Corlett and R. S. Pickart, “The Chukchi slope current,” Prog Oceanogr. 153, 2017.
[6] M. A. Spall, R. S. Pickart, M. Li, M. Itoh, P. Lin, T. Kikuchi, and Y. Qi, “Transport of PacificWater Into the Canada Basin and the Formation of the Chukchi Slope Current,” J. Geophys. Res. Oceans, 2018.
[7] P. Stabeno, N. Kachel, C. Ladd, and R. Woodgate, “Flow Patterns in the Eastern Chukchi Sea: 2010–2015,” J. Geophys. Res. Oceans, 2018.
[8] M. Li, R. S. Pickart, M. A. Spall, T. J. Weingartner, P. Lin, G.W.K. Moore, and Y. Qi, “Circulation of the Chukchi Sea shelfbreak and slope from moored timeseries,” Prog Oceanogr. 172, 14–33, 2019.
[9] M. B. Porter and H. P. Bucker, “Gaussian beam tracing for computing ocean acoustic fields,” J. Acoust. Soc. Am. 82, 1349–1359, 1987.
[10] D. F. Gordon and H. P. Bucker, “Arctic acoustic propagation model with ice scattering,” Technical Report 985, Naval Ocean Systems Center, San Degio CA 92152, 1984.
[11] F. Fetterer, J. S. Stewart, and W. Meier, “MASAM2: Daily 4 km Arctic Sea Ice Concentration, Version 1,” (2015), updated daily.
[12] M. Siderius, M. B. Porter, P. Hursky, V. McDonald, and the KauaiEx Group, “Effects of ocean thermocline variability on noncoherent underwater acoustic Communications,” J. Acoust. Soc. Am., 121, 1895–1908, 2007.

Structured Session 10

Design of new experimental facilities to address future problems in underwater acoustics

Organiser(s): Sessarego Jean-Pierre, Fattaccioli Dominique, Real Gaultier

A BRIEF FIVE-YEAR PROGRESS REPORT ON THE DGA "ALMA" PROJECT: SCIENTIFIC PROGRAM AND PROJECTS, AT-SEA CAMPAIGNS AND DATA COLLECTED, SYSTEM EVOLUTIONS AND IMPROVEMENTS.

Dominique Fattaccioli, Gaultier Real

DGA Naval Systems, avenue de la Tour Royale, BP 40915, 83050 Toulon cedex, France.

dominique.fattaccioli@intradef.gouv.fr
gaultier.real@intradef.gouv.fr

Abstract: *ALMA (Acoustic Laboratory for Marine Applications) is a deployable and autonomous acoustic system, with passive and active sub-systems, designed in 2012 by DGA Naval Systems. The objective of the ALMA project is to anticipate and explore new scientific and technical topics for Naval Programs in Underwater Warfare, in order to contribute to the risk reduction on new technical challenges and to improve the mastering of sonar performance in highly variable and fluctuating environments (especially in coastal waters or shallow waters).*
The main scientific and technical objective of the ALMA project is to increase the scientific knowledge of the impact of the environment and of its variability at different temporal and spatial scales, on the acoustic propagation and on the signal processing in the sonar domain.
Related to this objective the ALMA approach is to mobilize and to federate the academic and industrial communities on new issues and challenges in Underwater Acoustics by : (1) collecting high quality and unclassified real data (acoustic and environmental data) which may be shared with the scientific community, and (2) by conducting actions with the S&T DGA support tools (Defence and Dual research programs).
In this paper, the authors present a brief progress report on the ALMA project since the first at-sea deployment of the first version of the system in 2014. This five-year progress report is presented in three axes of complementary actions : (1) the scientific program and the related scientific projects, (2) the five at-sea campaigns (one per year) and the associated acoustic and environmental data collected, and (3) the successive evolutions and improvements of the ALMA system, related to the scientific projects.

Keywords: *underwater acoustics, deployable acoustic system*

1. INTRODUCTION

The interest in the acoustic monitoring of the underwater environment at different temporal and spatial scales, especially in coastal waters and shallow waters, is in a continuous increasing since many years, either in the civilian community than in the defence community.

In the civilian domain, this interest is mainly due to environmental preoccupations linked with, for example, the monitoring of ambient noise and the quantification of effects of the anthropogenic noise on marine life, species counting and, more generally with ecological objectives such as the global warming monitoring.

In the defence community, the continuous increase in the sonar capabilities and performance makes those systems more and more sensitive to the environment and to its variability and fluctuation at different temporal and spatial scales, and makes them often working at the limits (and beyond) of the underwater acoustics state of the art. The mastering and the optimization of sonar performance in all environmental typologies, which is a constant objective of the underwater warfare domain, thus requires to continuously increase the scientific knowledge of the impact of the environment and of its variability on the acoustic propagation and on the sonar signal processing, especially in harsh environments such as coastal and shallow waters.

In this context, DGA Naval Systems designed in 2012 a deployable and autonomous acoustic system named ALMA (Acoustic Laboratory for Marine Applications). In this paper, we present a brief progress report on the ALMA project since the first at-sea deployment of the first version of the system in 2014. This five-year progress report is presented in three axes of complementary actions : (1) the scientific program and the related scientific projects, (2) the five at-sea campaigns (one per year) and the associated acoustic and environmental data collected, and (3) the successive evolutions and improvements of the ALMA system, related to the scientific projects.

2. ALMA: OBJECTIVES AND APPROACH

The objective of the ALMA project is to anticipate and to explore new scientific and technical topics for Naval Programs in Underwater Warfare, in order to contribute to the risk reduction on new technical challenges and to improve the mastering and the optimization of sonar performance in all environmental typologies.

The approach of the ALMA project is to federate and to engage both academic and industrial communities on new issues and challenges in underwater acoustics

- by collecting high quality acoustic and environmental data. The data collected are representative of operational sonar scientific issues and are unclassified in order to be shared with the whole community of underwater acoustics, especially with the scientific community.
- through the DGA S&T support tools: Defence and Dual research programs with research laboratories (through PhDs, Post-Docs, basic research programs), with innovative SMEs (through basic and advanced research programs) and with large industrial groups (through advanced research programs). The S&T scope goes from TRL 1 to TRL 7-8, from basic research to advanced research and technology demonstrators.
- by encouraging joint efforts between academic and industrial partners.
- by promoting ALMA as a testbed for new technologies.

3. ALMA: SCIENTIFIC PROGRAM

The main lines of the scientific program of the ALMA project have the objective to address the main issues in the detection, localization and classification processes for current and future sonar systems in a context of low and very low signal to noise ratio, which is the natural environment of sonars.

The main technical topics of interest are:

- ✓ The noise gain improvement, through the array gain optimization and the traffic noise rejection.
- ✓ The signal degradation reduction (degradation mainly due to environmental fluctuations).
- ✓ The source depth discrimination: surface-submerged sources discrimination.
- ✓ The sonar performance optimization and control.

The following (non-exhaustive) main scientific topics can be derived from the previous main technical topics:

- ✓ The spatio-temporal coherence of ambient noise.
- ✓ The effects of environmental fluctuations on sonar processing.
- ✓ The corrective signal processing to the loss of signal coherence, leading to the concept of environmentally adaptive sonar.
- ✓ The inverse problems, such as 3D localisation and the environment characterization.
- ✓ The sonar processing adapted to (very) low SNR, and to non-stationary noise.

4. ALMA: THE SYSTEM

Under the design and the technical specifications by DGA Naval Systems in 2012, ALMA was developed and realized in 2013-2014 by the ALSEAMAR and CeSigma companies with the support of COMEX for at-sea operations. Since the qualification at-sea of the first version on October 2014 [1], ALMA is in a continuous upgrade and evolution thanks to the high degree of modularity of the system, allowing to address a large scientific program.

The ALMA system is based on a modular, evolutionary and efficient passive acoustic array, itself based on a "basic unit" which is a 2.70m long rigid "arm", with 16 hydrophones (with an adjustable spacing between 3 cm and 15 cm) and a watertight case for data digitization (cf. Fig. 4.1). Since 2016, the passive array is composed with eight "arms", for 128 hydrophones.



Fig. 4.1: ALMA modular acoustic arms: 8 rigid acoustic "arms", each composed with 16 hydrophones with an adjustable spacing between 3 cm and 15 cm.

The high degree of modularity of the system allows several array geometry configurations: linear, plane, volumic (cf. Fig. 4.2).

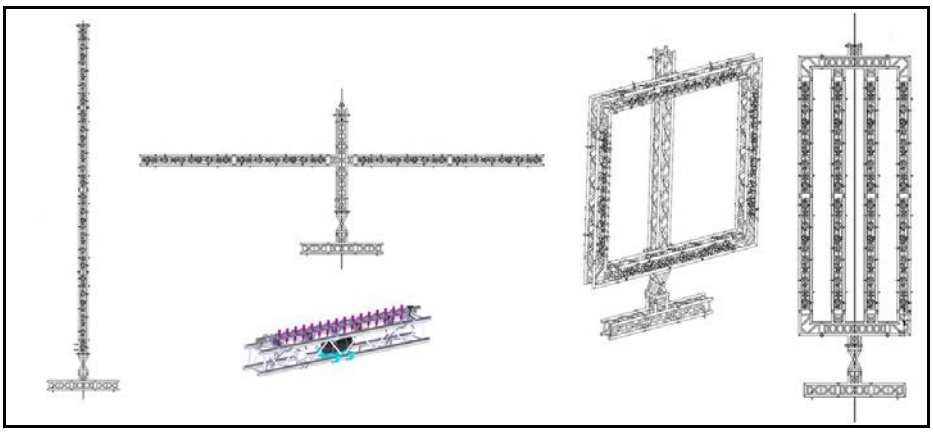


Fig. 4.2: some examples of array geometries allowed by the modular structure of the ALMA passive array.

The main characteristics for the passive array are:

- ✓ High quality acoustic measurements, with a noise level less than sea state 0 up to 20 kHz,
- ✓ Adjustable sampling frequency from 7.5 kHz to 48 kHz,
- ✓ Minimum specific technological developments (COTS),
- ✓ Thermistor string on the passive acoustic array,
- ✓ 3D positioning sensors for continuous array orientation monitoring

The complete ALMA system is composed of two separated components with their dedicated anchoring and acoustic systems: a passive sub-system and an active sub-system (cf. Fig. 4.3 for an "artist rendering" of the system).

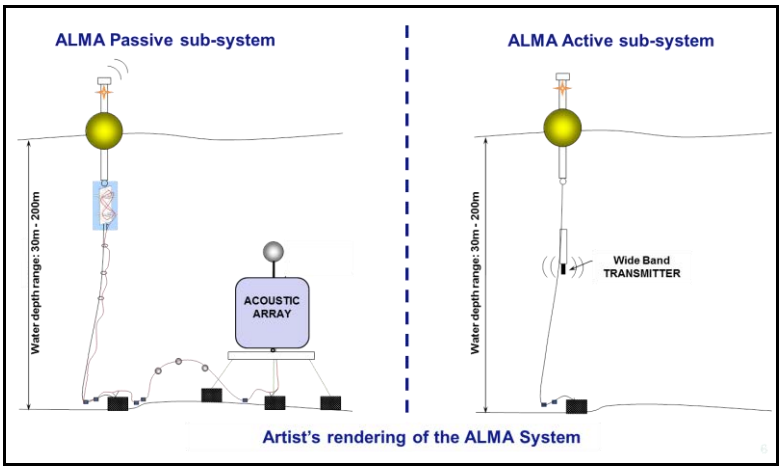


Fig. 4.3: "Artist rendering" of the ALMA system composed of passive and active sub-systems.

- ✓ <u>Passive sub-system:</u>

  - Passive acoustic array (described previously)
  - Deployment configurations:

- From a surface ship (2018 campaign)
- Anchored in shallow and coastal waters (water depth less than 200m)

- Surface buoy (cf. Fig. 4.4) for:

  - Energy storage (10kWh) for 80hrs autonomy in continuous measurement
  - Link to passive acoustic array via electro-optical cable (550m)
  - Data storage: extractible 2TB HD
  - Remote control and programing via long range WiFi

✓ Active sub-system:

- 2 autonomous wideband acoustic pingers (cf. Fig. 4.5)

  - 1 - 14 kHz frequency band
  - Adjustable source level up to 160 dB ref µPa@1m.
  - 24hours autonomy in continuous transmission with source level of 160 dB ref µPa@1m.
  - Transmitted signal programming through .wav files

The ALMA design and deployment process ensure a minimum impact on the environment during the at-sea trials: low acoustic levels transmitted, and nothing left on the seafloor, making ALMA an "environment-friendly" system.



Fig. 4.4: surface buoy for the ALMA passive component: energy and data storage, link to Acoustic Array via electro-optical cable communication link by long range WIFI.

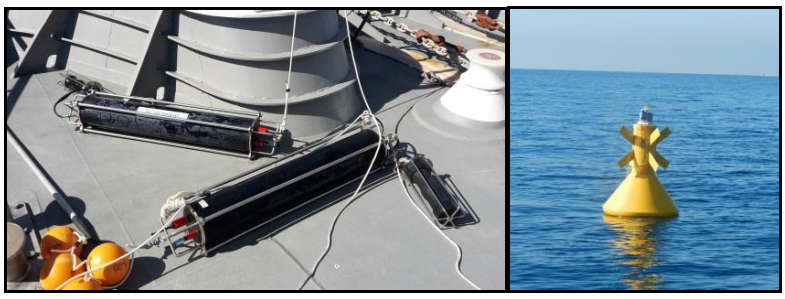


Fig. 4.5: omnidirectional wideband transmitter (realized by ALSEAMAR) and its mooring surface buoy.

5. ALMA: THE CAMPAIGNS

Since the qualification of the first version of the system in 2014, five at-sea campaigns were conducted with the ALMA system:

- ✓ on the continental shelves of Corsica (Alistro 2014, Campoloro 2016, and Saint-Florent 2017) and of Provence (La Ciotat 2015) (cf. Fig. 5.1),
- ✓ in coastal and deep water environments of Mediterranean sea and Atlantic ocean in 2018 (cf. Fig. 5.2).

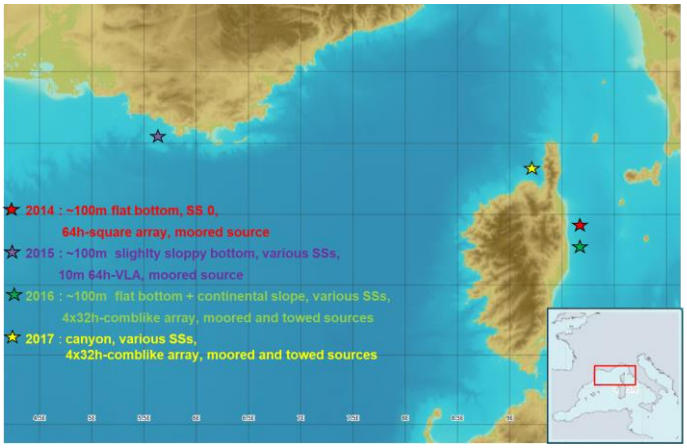


Fig. 5.1: Mediterranean Sea areas for the 2014, 2015, 2016 and 2017 ALMA at-sea campaigns.

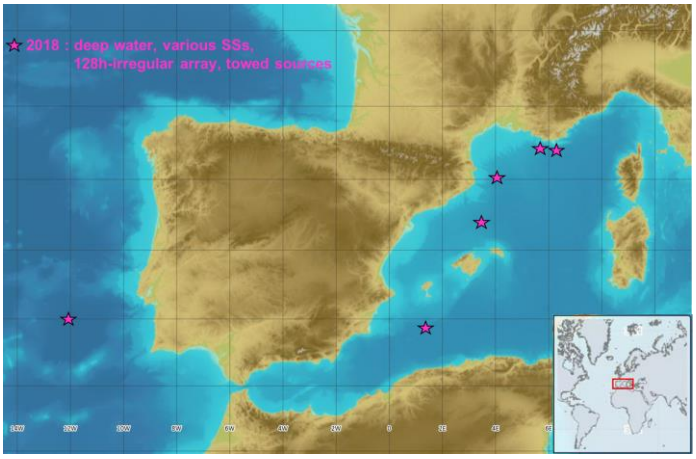


Fig. 5.2: Mediterranean Sea and Atlantic Ocean coastal and deep-water areas for the 2018 ALMA at-sea campaign.

Each of these five campaigns allowed: (1) to validate the evolutions of the system, and (2) to gather high quality data, acoustical and environmental, in various environmental conditions and for different geometries and capabilities of the passive array (cf. Fig. 5.3 and Fig. 5.4).

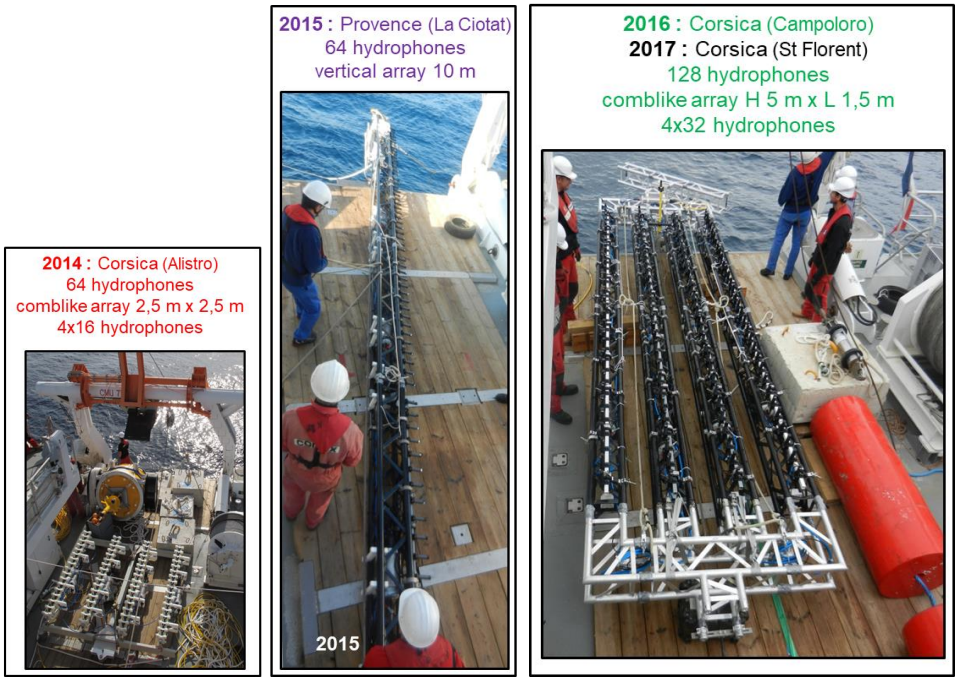


Fig. 5.3: ALMA Passive Array configurations for the 2014, 2015, 2016 and 2017 at-sea campaigns.

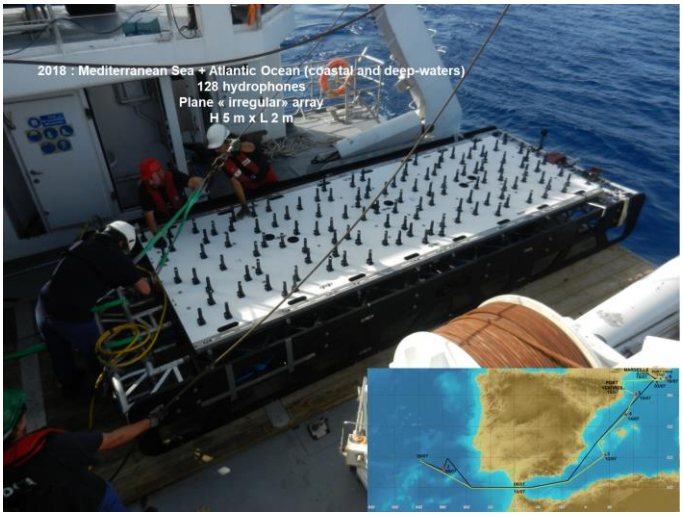
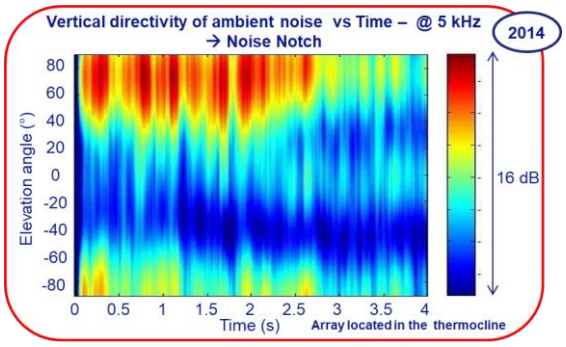


Fig. 5.4: ALMA Passive Array configuration for 2018 at-sea campaign.

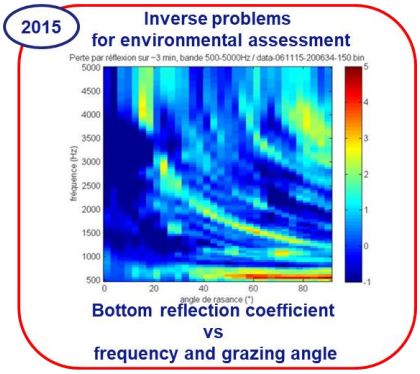
6. ALMA: SOME RESULTS

The aim of this paper is not to give an exhaustive view of all the scientific works and of the associated results obtained. The published results are given in reference of this paper (see Ref. [2] to [11]), in particular the results [9][10][11] which are presented in UACE 2019 jointly with this paper. We focus here on some results, which show the diversity of the data collected during five years of the ALMA project and the large spectrum of scientific works done from these data.

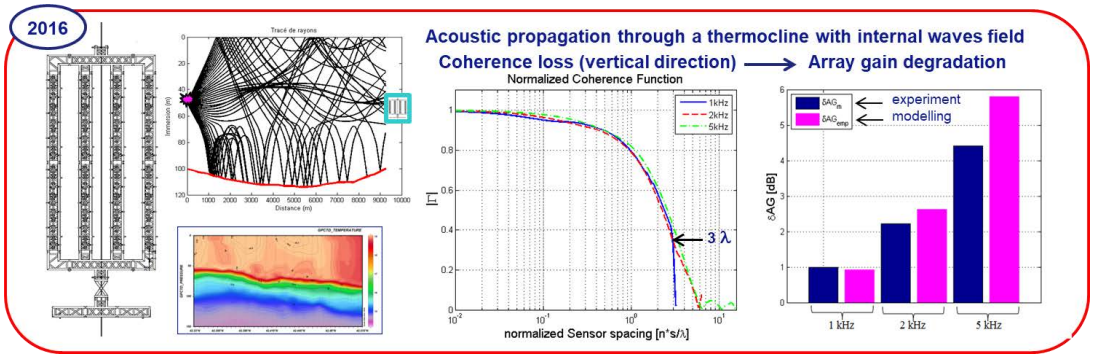
✓ Vertical directivity of ambient noise (from ALMA 2014 campaign):



✓ Inverse problems for environmental assessment (from ALMA 2015 campaign):



✓ Acoustic propagation through a thermocline with internal waves field (from ALMA 2016 campaign):



7. ALMA: OVERVIEW AND PERSPECTIVES

Some numbers can resume the technical investment and the diversity of the data collected during five years of the ALMA project: 5 at-sea campaigns, 50 days at sea, 10 different measurement areas, 4 different array configurations, 300 hours of acoustic data, 20 TB of data. The data collected allowed carrying out more than 15 S&T projects supported by DGA. Under the leadership of DGA Naval Systems, an « ALMA community » has emerged, composed with scientific Labs, innovative SMEs, large industrial groups and State agencies. Through data sharing and scientific exchanges between French and foreign state organizations, laboratories or industrial partners, the « ALMA community » can be opened to international cooperation.

After five years of exploitation and of technical evolutions, the ALMA system demonstrated its capabilities to fulfill the technical and scientific objectives dedicated to it:

- ✓ a high level of modularity, capability of evolution and of acoustical measurements
- ✓ a scientific acoustic system able to address the main current and future issues of operational sonar systems (in particular the de-coherence effects).
- ✓ a very useful tool for sharing real data and "real life sonar issues" with the scientific community, contributing to the improvement of the scientific knowledge in underwater acoustics, especially for coastal and shallow waters.
- ✓ a "TRL accelerator", by federating the underwater acoustics community (laboratories and companies) on joint projects.

ALMA is currently undergoing some evolutions towards higher sampling frequency and more sensors, allowing increasing the ALMA frequency domain to higher frequencies. At the same time, reflections are carried out on a future VLF capability for the ALMA system.

REFERENCES

[1] Fattaccioli D., ALMA: a new experimental acoustic system to explore coastal waters, In UACE 2015 Proceedings, 2015.

[2] Fattaccioli D. and Real G., The DGA "ALMA" Project: an overview of the recent improvements of the system capabilities and of the at-sea campaign ALMA-2016. In UACE 2017 Proceedings, 2017.

[3] Cristol X., Real G., Fattaccioli D. and Chalindar B., ALMA 2014: Observations of multiple scattering from random inhomogeneities transported by a mean flow, In UACE 2017 Proceedings, 2017.

[4] Real G. and Fattaccioli D., Acoustic coherence in a fluctuating ocean: analysis of the 2016 ALMA campaign, In UACE 2017 Proceedings, 2017.

[5] Bennaceur I., Cristol X., Docquois R. and de Pampelone F.R., Target Localization in Depth and Range from Passive Sonar, In OCEANS 2018 MTS/IEEE Charleston (pp. 1-9) IEEE, 2018 October.

[6] Real G. and Fattaccioli D., Acoustic Laboratory for Marine Applications: Overview of the ALMA system and data analysis, In OCEANS 2018 MTS/IEEE Charleston (pp. 1-7) IEEE, 2018 October.

[7] Magalhaes P. E., Cristol X., Ioana C., Fattaccioli D. and Mars J., ALMA 2015: Sea Trial of an Underwater Target Localization Technique Using Hausdorff Distance, In 2018 OCEANS-MTS/IEEE Kobe Techno-Oceans (OTO) (pp. 1-6). IEEE, 2018 May.

[8] Dumaz, L., Garnier, J., & Lepoultier, G., Acoustic and geoacoustic inverse problems in randomly perturbed shallow-water environments, arXiv preprint arXiv:1812.10141, 2018.

[9] Bennaceur I., Cristol X., Chalindar B., Real G. and Fattaccioli D., ALMA 2015: Study and modeling of the impulse response vertical de-coherence of a fluctuating shallow channel, to be presented in UACE 2019.

[10] Beaumont G., Drémeau A., Fablet R., Le Courtois F. and Real G., At-sea experimental evaluation of the infuence of environmental fluctuations on the acoustic coherence radius, to be presented in UACE 2019.

[11] Real G. and Fattaccioli D., Sound waves propagating in fluctuating media: experimental analysis using ALMA data, to be presented in UACE 2019.

AT-SEA EXPERIMENTAL EVALUATION OF THE INFLUENCE OF ENVIRONMENTAL FLUCTUATIONS ON THE ACOUSTIC COHERENCE RADIUS

Guillaume Beaumont[a], Angélique Drémeau[a], Ronan Fablet[b], Gaultier Real[c], Florent le Courtois[d]

[a]ENSTA Bretagne, Lab-STICC UMR 6285, CNRS, 2 Rue François Verny, 29200 BREST, FRANCE
[b]IMT Atlantique, Lab-STICC UMR 6285, CNRS, 655 Avenue du Technopôle, 29280 PLOUZANE, FRANCE
[c]DGA Naval Systems, Avenue de la Tour Royale, BP 40915, 83050 TOULON cedex, FRANCE
[d]SHOM, 13 Rue de Châtellier, 29200 Brest, FRANCE

guillaume.beaumont@ensta-bretagne.org

Abstract: *Sound propagation in a fluctuating medium can be impacted by local space and time variation of the celerity. In the ocean, this environmental variability is mainly due to internal waves, tides or gyres and is well studied by oceanographers. More specifically, major research tackles the issue of characterizing the impact of these internal waves on a measured signal [1, 2, 3] propagated throughout the perturbed medium. One important quantity defined in this literature is the "coherence radius": a metric that evaluates the distance between two sensors on which the received signals can be considered as correlated. It can be related to the level of spatial fluctuations under a high frequency approximation. Hence, integrated as prior knowledge on the propagating medium, the coherence radius can be very useful to determine the degree of corruption of a measured signal for typical inverse problems in underwater acoustics, such as tomography and source localization. In this work, we present different results from the analysis of the ALMA 2017 measurement campaign. ALMA (for Acoustic Laboratory for Marine Applications) is an autonomous acoustic observatory designed by DGA Naval Systems in 2012 and deployed in 2017 in the Saint-Florent Gulf, in the Western Mediterranean Sea. We specifically aim at assessing the intensity of environmental and acoustic fluctuations on sound waves propagated from a known source to a set of vertical line arrays and at comparing it to the theoretical predictions. Results suggest a strong relationship between the coherence radius and temperature fluctuations as well as other phenomena such as tides or water-mixing areas. Given hypotheses made about the influence of fluctuations on the radius of coherence, we further discuss future experimental settings to validate or discard these hypotheses.*

Keywords: *At-sea experiments, Internal Waves, Wave coherence, Fluctuating medium*

1. INTRODUCTION

Wave propagation through random media has been a raising topic of interest in the past few years. Common to many applications (e.g. aerial acoustics, RADAR, SONAR), the aim is to characterize the impact of a randomly fluctuating medium on a measured signal. This knowledge is essential to perform robust and reliable signal processing such as direction-of-arrival (DOA) estimations or to mitigate the degradation of the array gain [3].

In order to to relate the environmental fluctuations to the propagation of sound waves, several formulations of ‘‘stochastic ocean’’ fluctuations were formulated in [1] and more recently [2], both corroborated by in-situ measurements. In this paper, we focus on a high-frequency formulation, leading to the definition of a particular quantity called ‘‘coherence radius’’ related to the mean size of the fluctuations in the medium.

In the interest of measuring and characterizing ocean variability, DGA Naval Systems conducted the design of a modulable underwater acoustic observatory, named ALMA (for Acoustic Laboratory for Marine Applications) [4]. Since 2014, the ALMA system is deployed each year and acquire data for this purpose [5]. In this paper, we focus on phases of the 2017 campaign and analyse the variability of quantities such as the coherence radius compared to the measurable variations of the propagation medium.

2. FOCUS ON THE 2017 ALMA CAMPAIGN

The 2017 experiment took place in the Gulf of Saint-Florent (Corsica) from the 3rd to the 13th of October. Here we focus on the phases involving the Passive Antenna (PA) and two emitters (S1&S2).

Two omnidirectional wideband pingers denoted S1 and S2 transmitted a controlled sequence. Every 3 minutes, both S1 and S2 emit the same sequence (see [5]) .A 100 Hz positive frequency shift was applied to S2 for source separation purpose. The sequence is composed of 5 different signals : a Ricker pulse, a chirp, tone signals (from 1 to 13 kHz), multitonal signal and a white noise. The aim of such a sequence is to measure the impact of the corruption of the signal due to its propagation regarding the frequency of the signal.

These sources are immersed at different depths, 170 meters for S1 and 130 meters for S2 at the beginning of the campaign then at 50 meters depth.

The seabed follows a canyon topography, that implies great depth variations between the sources and the antenna (16 kilometers distants) and strong interaction between the variations of the seabed and the propagation medium.

Antenna

The previous ALMA experiments introduced different usable array geometries. For this campaign, the geometry chosen is an vertical antenna composed with 32 uniform linear subantennas with a 15 cm sensor spacing [4] anchored at a depth of 140 meters. The antenna measures continuously during the phases involving the S1 & S2 emissions.

In-situ measurements of the variability: thermistor chain

In order to measure the variability of the propagation medium, a thermistor chain is deployed and continuously records the temperature variations during the campaign. The thermistor chain is composed of 24 sensors on a 150 m array.

3. COHERENCE RADIUS OF THE SIGNAL

Characterizing the impact of stochastic fluctuations of the propagation medium on a measured signal is a challenging problem in underwater acoustics. Works initiated in [1] and pursued in [2] aim to define statistical properties of the signal perturbations. One of them relies on a high-frequency approximation of the emitted signal. Considering rays propagating along a perturbed path, this approximation assumes a Gaussian spread of micro-multipaths around a main ‘‘eingenray’’.

Asymptotically, this leads to the so-called "simplified theory" (see [1]) which defines the theoretical value of the mutual coherence function (i.e. the normalized correlation function) between the *n*-th and the *m*-th sensors of an ULA:

$$|\Gamma_{mn}| = \exp\left(-\frac{1}{2}\frac{((m-n)\delta)^2}{R_c^2}\right) \qquad (1)$$

with δ the sensor spacing and R_c the coherence radius. In the literature [1,2], m and n the sensor indexes, R_c is a function of the mean perturbation of the propagation medium, the fluctuation spectrum and the frequency of the measured signal. A knowledge of this quantity allows us to put some hypotheses about the strength of the fluctuations and can be favorably exploited as prior information in DOA estimation schemes (see e.g. [6]).

To recover R_c, we confront (1) to an empirical estimation of the mutual coherence between the signals measured at the *n*-th and the *m*-th sensors (resp. Y_n and Y_m), such as :

$$|\hat{\Gamma}_{mn}| = \left|\left\langle \frac{Y_n Y_m}{|Y_n||Y_m|}\right\rangle_{Ns}\right| \qquad (2)$$

Where N_s is the number of snapshots. With N_s large enough, we are able to identify the quantity R_c from $|\hat{\Gamma}_{mn}|$ and observe the variations of this distance over time. For this calculation, we will consider Ns as the total number of detected samples at a given frequency at a given measurement phase.

4. COHERENCE RADIUS ESTIMATION

In this section, we will analyze the results of the 5th phase of the 2017 ALMA campaign. This phase started the 9th of October with a continuous emission of S1 and S2 had a duration of 3 hours and 40 minutes.

To process this phase, we identified the coherence radius using equations (1)-(2) for the multi-tonal sequences emitted by the sources. The interest of these signal lies in the fact that by filtering the signal at a given frequency we can observe the variations of the received signal at different frequencies subject to the same fluctuations.

Figure 1 represents the mutual coherence function for the lowest frequencies emitted by S1, as a function of the distance between two sensors (namely, as a function of $\delta_z = (m-n)\delta$, with (m, n) indices of two different sensors).

We observe here a decrease of the coherence radius with the frequency, confirming the theoretical model defined by [1,2].

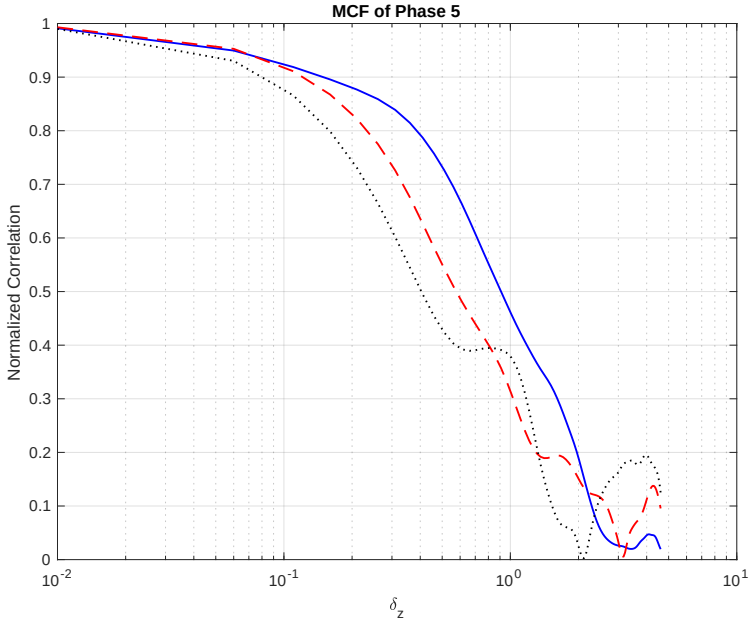


Figure 1: Mutual coherence function for 1kHz (in blue solid line), 2kHz (in red dashed line) and 5kHz (in black dotted line). We observe the decrease of the correlation distance with an increase of the frequency.

A time varying radius of coherence

For this phase, another interesting result is the evolution of the coherence radius. Its periodicity is indeed synchronized with the semi-diurnal tide. Figure 3 presents the tide chart of Centuri near the experiment area.

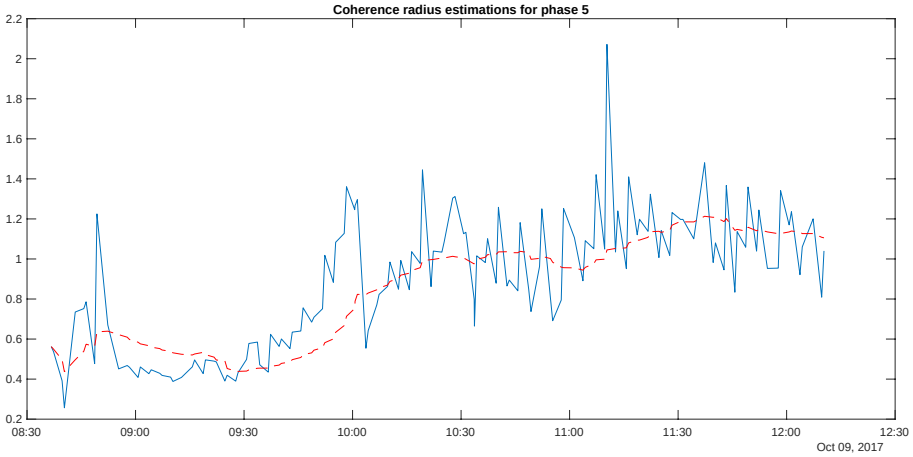


Figure 2: Evolution of the estimated coherence radius during the phase 5 for 1 kHz. The continuous line represent the coherence radius estimation while the dashed line represent its moving average.

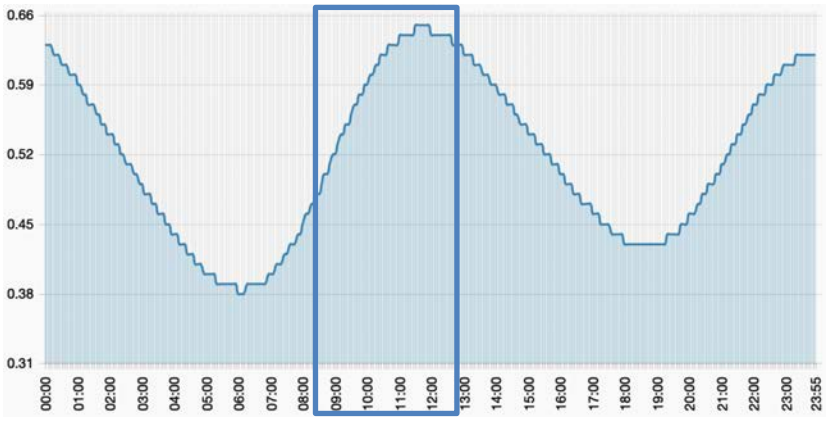


Figure 3 : Evolution of the tide at Centuri in the 9th of October, with a highlight on the tide for the 5-th phase (source maree.shom.fr).

Confronting figures 2 and 3 tends to underline the dependency of the coherence radius on a phenomenon essentially driven by a semi-diurnal tide component. However, this observation does not explain the entire behavior of the evolution of the coherence radius. Other low frequency phenomena and a high frequency noise seem indeed to be involved. In the next subsection, we try to highlight the presence of other internal waves as major contributors to the variations of R_c.

In-situ measurement of internal waves

Internal waves, as the result of circulation of fluids exited by gravity waves, provoke turbulent mixing. Observing and quantifying them can thus be done by measuring the thermal mixing through the thermistor chain.

The bottom sub-figure of Figure 4 is the power density spectrum of the temperature measurement for the entire campaign on the last sensor (i.e. the deepest sensor of the chain). We can observe an important quantity of energy related to high-frequency phenomena which can be related to waves and bathymetry-induced mixing. Moreover, some low-frequency peaks correspond to diurnal (M2, S2 & N2) gravity waves. These results highlight the presence of gravity-induced internal waves in the experiment. According to the Munk classification of internal waves [7], the PSD (for Power Density Spectrum) of the temperature measurements allows us to identify the presence of long-period waves and infra-gravity waves in the environment.

5. ANALYSIS OF LONGER PHASES

In order to find a true relationship between the variations of the coherence radius and the measured fluctuations of the propagation medium, more phases of the ALMA campaign have been analyzed. Due to the long period of the signals of interest, longer phases were evaluated.

The following phases are the 12th, 13th and 14th phases, with durations of 12 hours approximatively for each phase. We expect to observe a periodic variability of the coherence radius with a higher precision than in our previous study.

Because they are contiguous, an analysis of both phases can be done by visualizing the PDS of the coherence radius regarding the PDS of temperature variations.

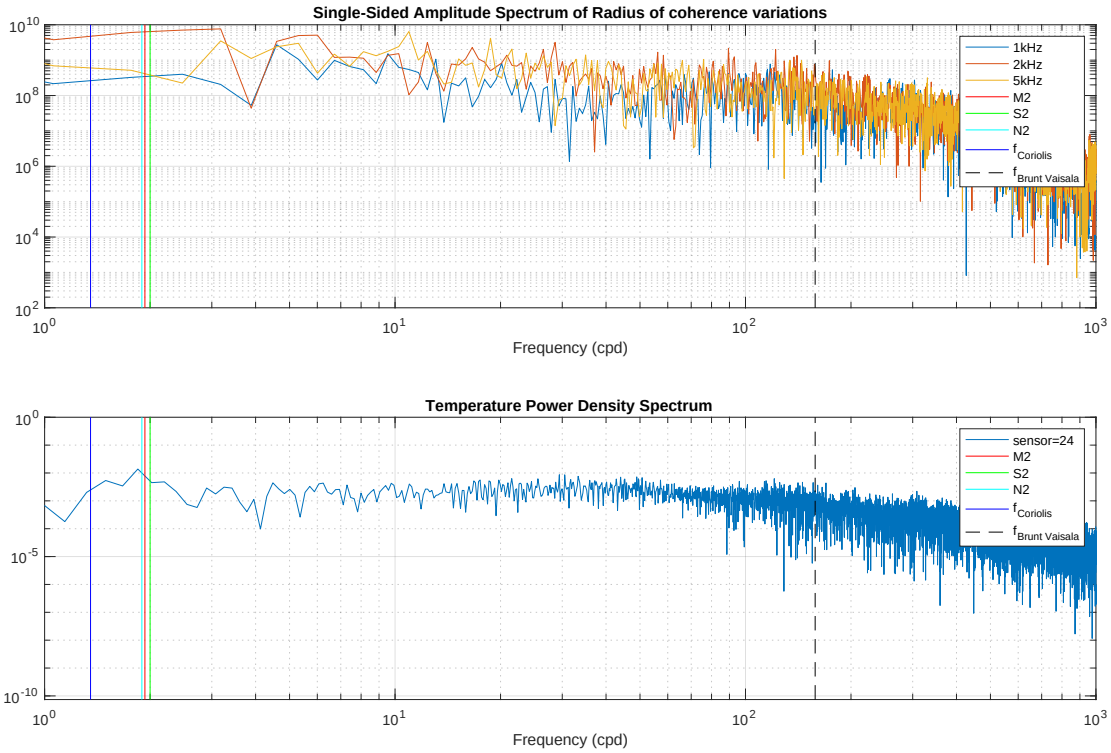


Figure 4: Comparison of the variation spectrum of the coherence radius for the 3 lowest frequencies of the ALMA sequence (top) and the temperature measured by the thermistor chain (bottom).

Figure 4 highlights similarities between the spectrum of temperature variations and the spectrum of coherence radius variations. Indeed, especially at low frequencies, the trend of the coherence radius variations follows the temperature spectrum. Moreover, we can notice similar lobes in the spectrum in the low frequencies domain of Figure 4 (more precisely the local maximum at 5 and 10 cpd and local minimum at 4 cpd) showing a possible measurability of the internal wave spectrum using the coherence radius estimation. However, the temporal resolution of the measurement (driven by the sequences emitted by S1 and S2) does not allow us to draw any strong conclusion on the impact of the temperature variations on the coherence of a measured signal.

6. CONCLUSION

Useful for antenna processing application like array gain compensation or adaptative processing for DOA estimation, the estimation of the radius of coherence of the signal is a complex issue due to the fact that this quantity varies with the propagation environnement.

In this work, we have observed with long-duration measurements a strong correlation of the spectrum of the variations of temperatures in the water column and the variations of the

coherence radius spectrum. More generally, we have provided elements to identify measurable quantities influencing these variations. Such elements are of interest to proceed to a rapid assessment of the fluctuations of the environment and the coherence radius. They can then be used as reliable prior information for signal processing tools.

REFERENCES

1. **Dashen, R., Flatté, S. M., Munk, W. H., Watson, K. M and Zachariasen, F.**, *"Sound transmission through a fluctuating ocean"*, Cambridge University Press, 2010.
2. **Colosi, J. A.**, *"Sound Propagation through the Stochastic Ocean"*, Cambridge University Press, 2016.
3. **Real, G., Cristol, X., Sessarego, J.-P. and Fattaccioli, D., "**Propagation of acoustic waves through a spatially fluctuating medium: theoretical study of the physical phenomena''**,** *2nd International Conference and Exhibition on Underwater Acoustics*, 2014.
4. **Fattaccioli, D. and Real, G. ,**"The DGA "ALMA" Project: an overview of the recent improvements of the system capabilities and of the at-sea campaign ALMA-2016'', *International Underwater Acoustic Conference and Exhibition, Skiathos, Greece*, pp. 1-6, 2017.
5. **Real, G., Fattaciolli, D.,** "Acoustic coherence in a fluctuating ocean: analysis of the 2016 ALMA campaign'', 4*th International Conference and Exhibition on Underwater Acoustics*, 2017.
6. **Beaumont, G, Fablet, R. and Drémeau, A. ,**"An Approximate Message Passing approach for DOA estimation in phase noisy environments'', *International Conference on Latent Variable Analysis and Signal Separation (LVA/ICA)*, Guilford, UK, 2018.
7. **Munk, W. H.,** "Origin and generation of waves". *Proceedings 1st International Conference on Coastal Engineering*, Long Beach, California. ASCE, pp. 1–4, 1950.

ALMA 2015 : STUDY AND MODELING OF THE IMPULSE RESPONSE VERTICAL DE-COHERENCE IN A FLUCTUATING SHALLOW CHANNEL

Iannis Bennaceur[a], Xavier Cristol[a], Bruno Chalindar[a]
Gaultier Real[b], Dominique Fattaccioli[b]

[a]THALES Defense Mission Systems France
[b]DGA Naval Systems

525 route des Dolines, 06560 Valbonne FRANCE.
iannis.bennaceur@fr.thalesgroup.com

Abstract: *Before reception by a sonar array, acoustic signals of interest are strongly altered during propagation through the unstationary inhomogenous random sea. Some configurations, like shallow waters, are particularly impacted by strong stochastic fluctuations of the sea features and much work is still needed to understand, model and mitigate the effects of random acoustic propagation on the sonar performance.*
Acoustic propagation in shallow water is investigated using signals collected by the "ALMA" (Acoustic Laboratory for Marine Applications) system deployed in 2015 by DGA Naval Systems, in the Mediterranean Sea. The 2015 instrument configuration combined an acoustic source transmitting different types of wide- and narrow-band pulses over the 2 to 11 kHz band, and a 10 meter high receiving vertical array of 64 hydrophones. The main topic of this article is the experimental study of the vertical loss of coherence of the received signals, which would have an impact on sonar performance. The first step of the work was to evaluate the impulse response and a vertical coherence characteristic length using the pulses propagated through the stochastic fluctuating channel in a relatively calm-sea configuration. Then, the observed impulse responses and the coherence scales are simulated with the in-house stochastic numeric tool NARCISSUS and compared to the experimental measurements.

Keywords: *Underwater acoustic modelling, vertical coherence, shallow-water acoustic propagation*

1. INTRODUCTION

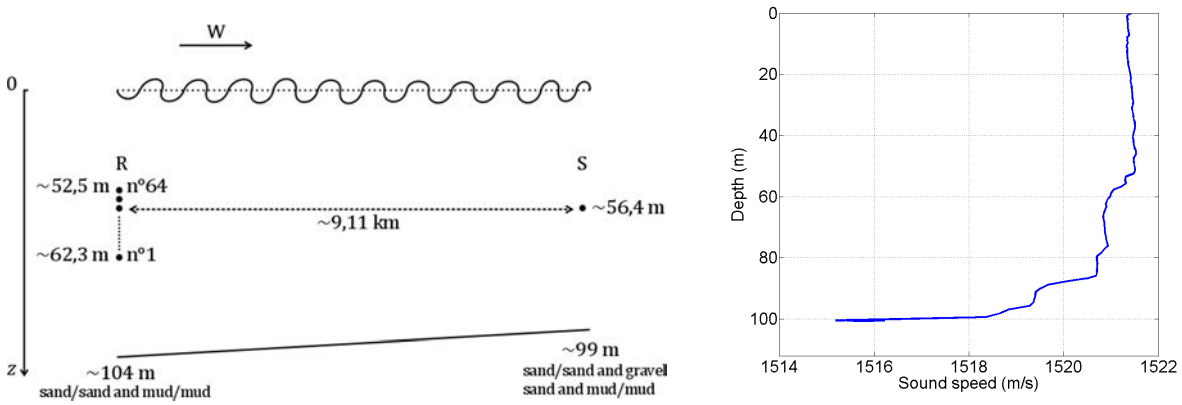
There is some confusion around the use of the word "*coherence*" in physics of waves and radiation. This term appears in at least three interconnected semantic fields. Firstly, the "historical" use, arising from the early XIX° century optics, applies to the capability of waves, radiating sources or experimental devices to produce observable interference effects (fringes, beatings). Secondly, in a "statistical" sense, "*coherence*" or "*coherence function*" may stand as synonyms to the "cross-correlation" of a wave field in phase and amplitude, *i.e.* the expectation of the product of the complex wave amplitudes taken at two locations, two times, or two frequencies, and considered as a function of the lag in location, time or frequency. In a third "cognitive" definition, "*coherence*" refers to the possibility for an intelligent agent to predict the state of a physical system at some arbitrary time or location, from the preliminary knowledge of its state at a first time or location; this prediction must rely on a practically tractable, deterministic model, involving not too high a number of degrees of liberty. In the LF and HF sonar or radar fields, "coherent processing" generally assumes a predicting model, according to which delayed versions of the same waveform are observed at different locations along wave-fronts with simple geometries (plane, spherical), at least over the span of an array.

According to these three definitions, the *lack* or *loss of coherence*, or *de-coherence*, or *partial coherence*, may refer to three different, but mutually related phenomena: 1) the smoothing, instability or disappearance of interferences; 2) a cross-correlation function featuring significant non-zero values only over a narrow domain; 3) an inadequate prediction model of the variations of the considered physical system, 'inadequate' meaning that a correct model should be either stochastic, or deterministic with a very high, virtually infinite number of degrees of liberty. We will explore the last two conceptions of de-coherence for sonar applications and the capability to model them numerically, using data from the 2015 ALMA experiment,

"ALMA" (Acoustic Laboratory for Marine Applications) is a deployable and autonomous acoustic and environmental system, with passive and active sub-systems; it was designed by the French Defence Procurement Agency to address the main topics of underwater acoustics by gathering real environmental and acoustical data for developing and validating advanced signal processing algorithms and acoustic models [1]. From 2014 to 2018, five large scale campaigns were conducted in the Mediterranean Sea and the Atlantic Ocean, evoked in various publications ([2], [3], [4]). In this paper, we use some of the data collected during the 2015 ALMA campaign to investigate the vertical de-coherence of the acoustic field after propagation through a randomly fluctuating shallow channel.

2. THE "ALMA 2015" EXPERIMENTAL CONFIGURATION

The 2015 ALMA campaign was conducted from the 5th to the 10th of November 2015 in a shallow Mediterranean environment, over a 100m-deep, gently sloping, sandy-gravely continental shelf, near the French harbor of Toulon. The acoustic system consisted in a moored active source and a moored vertical 10-meter high array of 64 hydrophones, separated by 9.11 km and immersed at approximately 56 m (see *Fig.1(a)*). The source transmitted, among others waveforms, 1-second long continuous waves (CW) at the frequencies 2, 5, 7 and 11 kHz and 2-seconds long linear frequency modulated (LFM) pulses over the 4-6 kHz band. During 20 hours, 415 pings were emitted, including 2 CW for each frequency and 2 LFM transmissions, every 3 minutes. The sound-speed profile measured close to the source, on the 6th of November, is almost iso-thermal over the first 50 m, and suddenly decreases quite sharply and irregularly down to the seabed (see *Fig.1(b)*).



(a) *(b)*

Fig.1: (a) Experimental ALMA 2015 configuration. (b) Sound-speed profile near the source.

We have firstly observed a particularly favorable period of 5 hours (~100 pings), during the night, over which the signal-to-noise ratio was high: a smooth well-aroused swell, corresponding to a sea-state 1.5-2, coinciding with a low wind velocity, resulted in a very low noise level (less than equivalent to sea-state 1). After sunrise, the rest of the experiment was unfortunately corrupted by intense bursts in sea-noise, due to the diurnal near shipping and to higher wind velocities.

3. PRELIMINARY ANALYSIS OF THE CHANNEL IMPULSE RESPONSE

In this section, we present a first investigation of the structure of the Impulse Response (IR) of the channel over all receivers of the array, estimated from 4-to-6kHz LFM pulses as the output from the matched filtering; this estimated IR is then compared to the IR simulated with an in-house stochastic numerical tool named NARCISSUS.

The three grey mappings of *Fig.2* display the level of the estimated IR issued from the pings 40, 137 and 143, as a function of the hydrophone depth (vertical axis) and of the time delay (horizontal axis). The ping 40 was emitted when the sea was calm, the 137 when it was slight and the 143 when it was moderate. The reference time delay 0 ms is taken at the time for which the vertically averaged impulse response is maximum. The IR associated with the ping 40 presents a first highly energetic arrival (A_1), followed by a 10-second highly fluctuating cluster (B), and some more later arrivals (A_2 at 20 ms and A_3 at 27 ms), less energetic than A_1 and slightly tilted. When the sea-surface roughness grows (pings 137 and 143), the most energetic arrival may not be the first one. Moreover, the levels of late arrivals decrease for the benefit of scattered 'reverberated' energy, filling the time intervals between late arrivals (especially for the ping 143).

For our comparison with the modelled IR, we have computed an averaged IR response over 30 pings emitted when the sea was calm (sea-state of 1.5) and the noise level particularly low. Due to the verticality of the late arrivals, averaging was performed first over the receiver depth, and then over the pings. The resulting averaged IR is displayed by the dark line of *Fig.4*, along with a measure of the dispersion over the pings (± standard deviation).

We have otherwise simulated the impulse response of the channel using NARCISSUS which computes, with a Monte-Carlo technic, the sea-surface and bottom scattering of an acoustic field emitted at more than about 500 Hz. The acoustic kernel, that described acoustic scattering from surface roughness, is evaluated using the "integral small-slope approximation" (or "Meecham-Lysanov approach", see [5], pp. 191-194); the surface height fluctuations are computed with the JONSWAP model ([6],[7]) and we use the Beckmann

approximation to model the scattered field spectrum. The seabed is inhomogeneously composed of sand, mud and gravel, which we described by a median porosity of 55% and a roughness of 0.15 m. When the surface roughness (standard deviation of height) is set to 0.094 m, well-fitting to the sea-state 1.5, a good agreement between the averaged measured IR and the simulated one is obtained, as demonstrated by Fig.3.

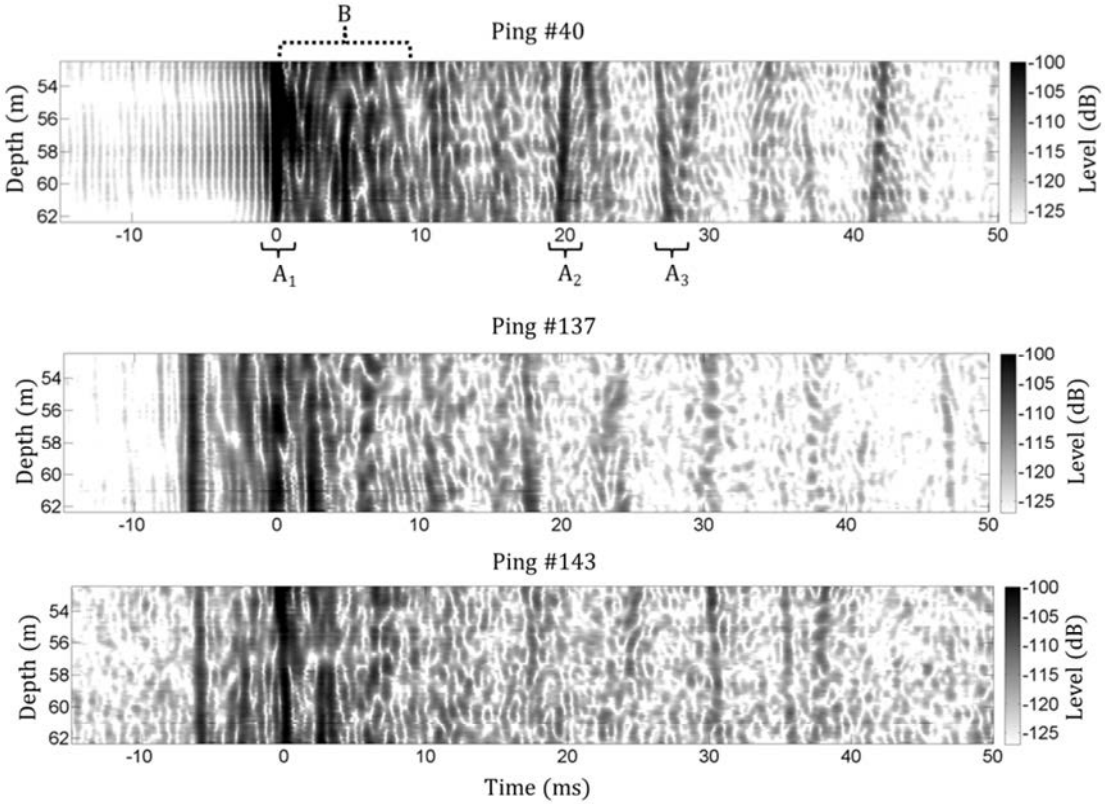


Fig.2: Impulse response of the channel under LFM pulses at the output of the matched filter emitted at the ping 40, 137and 143.

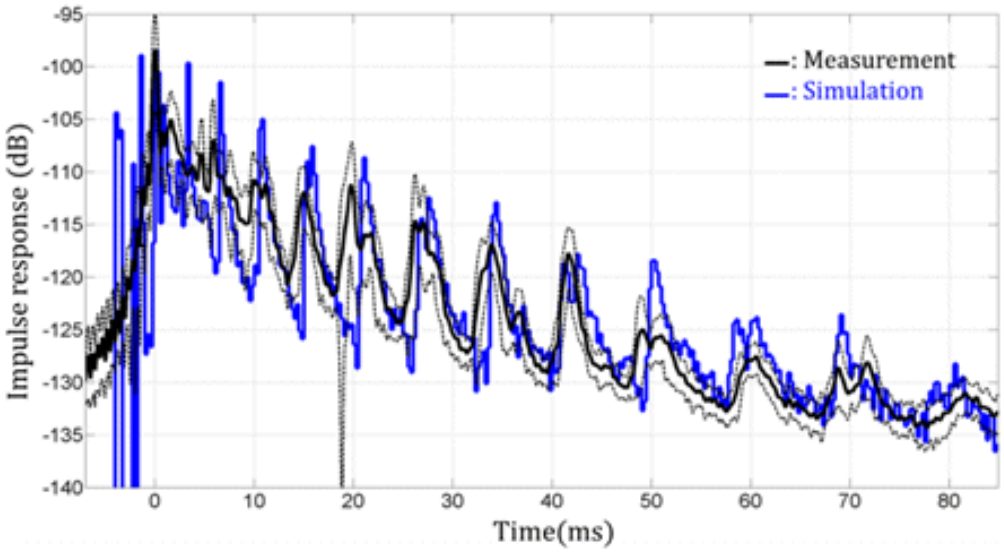
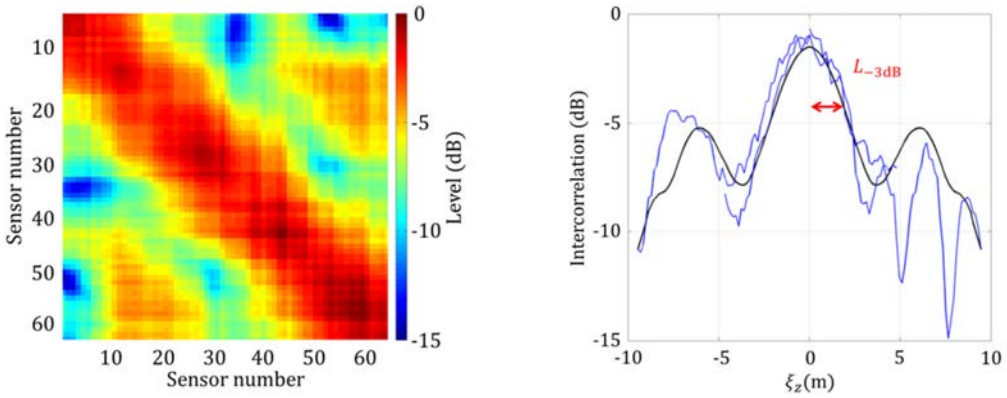


Fig.3: Averaged measured IR: (---) and the simulated with NARCISSUS: (---).

4. OBSERVATION AND PREDICTION OF VERTICAL COHERENCE

4.1. Coherence for CW pulses

In the "statistical" meaning of coherence, we investigate the cross-correlation of the acoustic pressure between all pairs of receivers for the CW pulses. A processing for measuring a typical vertical coherence scale is the following one: firstly, we get the maximum value of the matched filter output for each hydrophone and each pulse; secondly, we compute the cross-correlation matrix averaged over the 200 harmonic pulses emitted during the calm sea period (we get *Fig.5(a)* for $f = 2$ kHz); finally, we average the cross-correlation matrix over the receivers after having re-centred the matrix around its diagonal (see *Fig.5(b)*). We then define the –3dB vertical coherence length $L_{-3\mathrm{dB}}$ as the length corresponding to a decrease of 3dB from the maximum of the averaged cross-correlation coefficient.



(a) *(b)*

Fig.4: (a) Averaged cross-correlation matrix over the 200 pulses of the CW at 2 kHz. (b) Averaged cross-correlation matrix at sensors 1, 34 and 64: (---) and cross-correlation coefficient issued from an average over the hydrophones: (---).

The values of $L_{-3\mathrm{dB}}$ for $f = 2$ kHz, 5 kHz, 7 kHz, and 11 kHz are 2 m, 1.16 m, 0.88 m, and 0.6 m respectively. Plotted against the normalized length ξ_z/λ (where λ stands for the emitted wavelength), the four cross-correlation functions roughly coincide (*Fig.5*); the vertical coherence length is then close to proportional to λ as could be expected. We find $L_{-3\mathrm{dB}} \approx 4\lambda$.

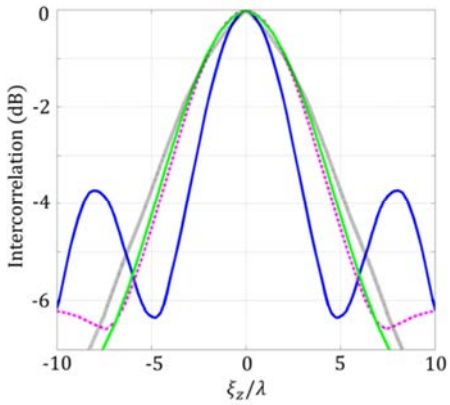


Fig.5: Averaged cross-correlation over the hydrophones against the normalized length ξ_z/λ computed for $f = 2$: (—), 5: (-- --), 7: (—) and 11 kHz: (· · ·).

4.2. Coherence for the individualized arrivals for the LFM pulses

The vertical coherence of the channel's IR according to the "cognitive" meaning may be investigated by using the matched filter outputs computed upon the LFM pulses. The acoustics arrivals occur in two different groups, as observed in section 3: well-separated individualized arrivals, and an early fluctuating cluster. In this study, we try to evaluate the vertical coherence length of both groups and compare it to the coherence length predicted by the numerical model NARCISSUS. We start with the late, strongly individualized arrivals.

After reflection at the random rough sea-surface, wave-fronts have no more simple shapes, but feature complex random undulations around those simple shapes; the description of those stochastic oscillations would require a virtually infinite number of degrees of freedom, and defies deterministic description; the loss of coherence impacting a processing like beamforming is due to the ignorance of those unknown descriptive parameters. The coherence of an arrival has then to be evaluated like in section 3, but around a simple trend most fitted with the descriptive parameters that are taken in consideration: for instance, the two independent parameters that determine a straight line, valid for describing a "mean" wave-front over a short array length.

The processing for quantifying the vertical coherence length of the late arrivals is then as follows. We interpolate the impulse response over a set of variable incidence straight lines around the forthright arrival (yellow lines on *Fig.6*) and we get the line for which the IR level, averaged upon the immersion, is the highest (red line *Fig.6*). This gives us the matched filter outputs for each hydrophone, each pulse and each arrival. To evaluate $L_{-3\mathrm{dB}}$, we then follow the same method as the one described previously for CW pulses.

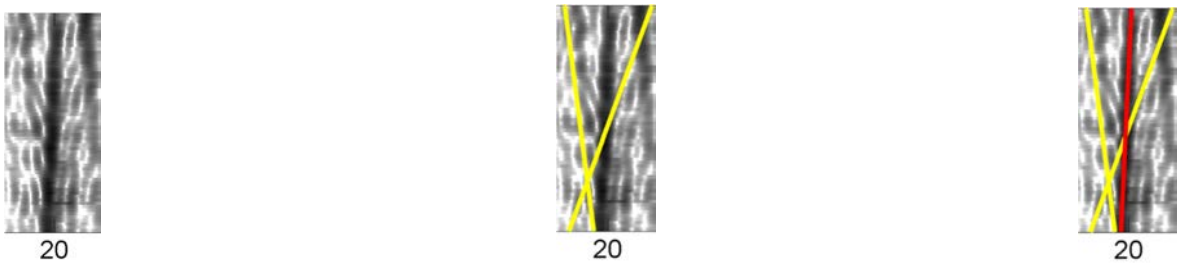
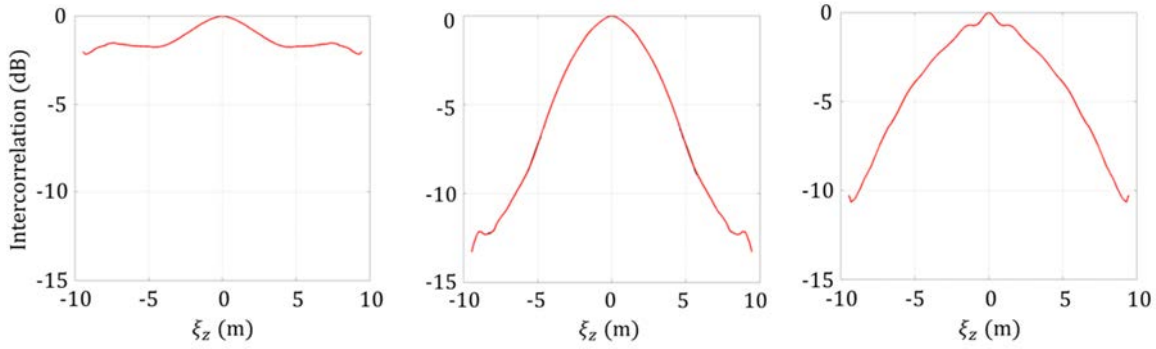


Fig.6: Sketch of the method to evaluate the vertical coherence length of forthright arrivals.

The three plots of *Fig.7* display the cross-correlation functions of arrivals A_1, A_2 and A_3. For the most energetic arrival A_1, the cross-correlation decrease does not exceed 3dB along the 10-meter high array. For the later arrivals A_2 and A_3, a decrease of 3dB occurs at shorter lags, about 3 m and 4.05 m respectively.



(a) *(b)* *(c)*

Fig.7: Cross-correlation coefficient matrix of the arrivals (a): A_1, (b): A_2 and (c): A_3.

With NARCISSUS, we are able to compute the vertical coherence scale L_N, defined as the half-width of the second-order moment of the probability density function of the impulse response, which is not exactly equal to $0.5\,L_{-3\mathrm{dB}}$. However, it is still interesting to see if NARCISSUS is able to predict the rise of the vertical coherence of the pressure field when a forthright arrival reaches the array. On *Fig.8*, we observe a strong increase of L_N around the delay 27 ms that reaches 2 m, corresponding to the arrival A_3. Such observation would indicate that $L_{-3\mathrm{dB}} \approx 2\,L_N$. We also guess a slight increase between 17 and 20 ms that could correspond to A_2. Here we see that NARCISSUS is an appropriate tool to predict the variation of vertical coherence scale.

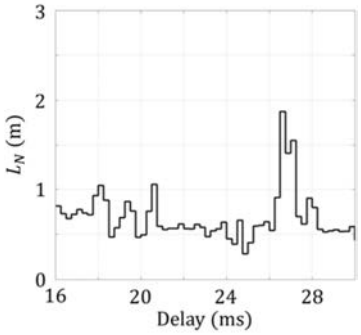


Fig.8: Vertical coherence length issued from NARCISSUS.

4.3. Coherence for the early fluctuating cluster for the LFM pulses

Measuring the vertical coherence length of the fluctuating cluster B is not an easy task, since there are no stable, individualized arrivals that can be easily isolated. Our method here is to sub-divide the impulse response into 0.25 ms wide time-cells (white dot on *Fig.9*) and to apply the same procedure as the one used for the individualized arrivals for each time-cell. We limit to less than 10° the module of the incident angle α of the mean straight line used for the interpolation (*Fig.9*). This processing results in $L_{-3\mathrm{dB}}$ and α according to the delay associated with each cell.

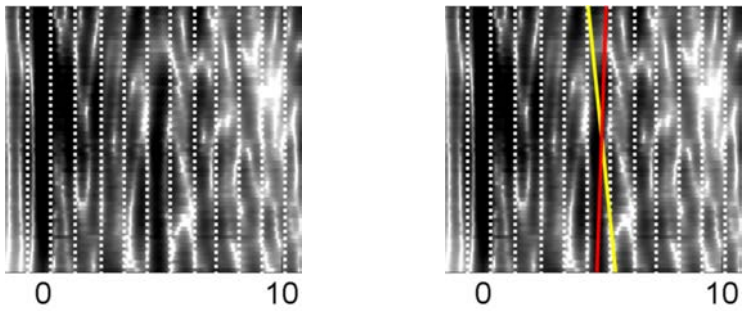
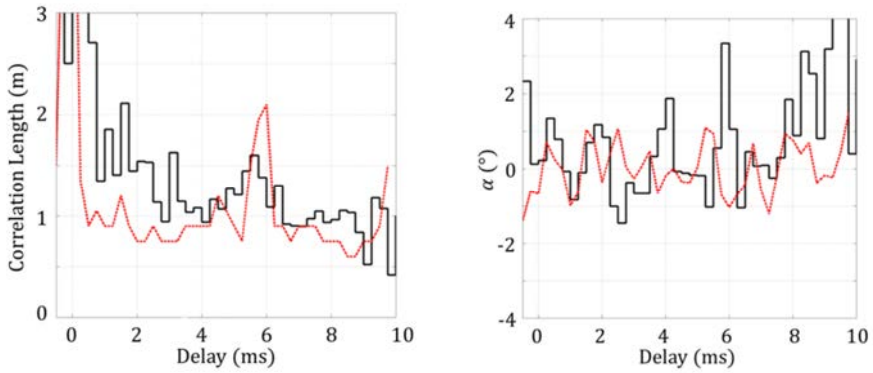


Fig.9: Sketch of the method to evaluate the vertical coherence length of the fluctuating cluster.

We plot these two quantities on *Fig.10*, along with the coherence scale L_N and the incidence angle issued from NARCISSUS. We see that both our evaluation method and NARCISSUS predict a very strong vertical coherence for the time 0 ms corresponding to the most energetic arrival A_1. Moreover, both approaches reveal an increase of the vertical coherence length around 5.5 ms, which probably corresponds to the arrival visible on *Fig.9*. Furthermore, our evaluation method does not seem relevant to correctly evaluate the incidence angle.



(a) *(b)*

Fig.10: (a) Vertical coherence length and (b) incidence angle of the fluctuating cluster against time measured: (- -) and issued from NARCISSUS: (---).

5. CONCLUSION

In this paper, we studied the vertical de-coherence of wide and narrow-band pulses over the 2 to 11 kHz band that propagated through a fluctuating shallow channel over 9 km. Environmental data collected on the experiment site allowed a relevant estimation of the channel characteristics, in particular the roughness of the sea-surface and the roughness and porosity of the seabed. Then, we observed the measured impulse response depending on the sea-state and we noticed two distinct features; quasi-vertical individualized arrivals and a strongly fluctuating cluster. In the meantime, we have successfully simulated the impulse response using the stochastic numerical tool NARCISSUS using the channel characteristics. Finally, we have estimated the vertical coherence lengths of the CW pulses and of the LFM pulses features. These were compared quite favourably to the coherence scales issued from NARCISSUS.

6. REFERENCES

[1] **Fattaccioli D., Real G.**, The DGA "ALMA" project: an overview of the recent improvements of the system capabilities and of the at-sea campaign ALMA-2016, In *UACE Proceedings*, 2017.

[2] **Cristol X., Real G., Fattaccioli D., Chalindar B.**, ALMA 2014: Observations of Multiple Sound Scattering from Random Inhomogeneities Transported by a mean flow, In *UACE Proceedings*, 2017.

[3] **Bennaceur I., Cristol X., Docquois R., De Pampelone F-R.**, Target Localization in Depth and Range from Passive Sonar, In *Ocean*, 2018.

[4] **Real G., Fattaccioli D., Bennaceur I., Cristol X.**, ALMA, a tool to study sound propagation in fluctuating oceans: latest evolutions and analyses, In preparation for *Ocean*, 2019.

[5] **Voronovitch A. G.**, *Wave scattering from Rough Surfaces*, Berlin: Springer-Verlag, 1994.

[6] **Hasselmann K., Ross D. B., Müller P., Sell W.**, A parametric Wave Prediction Model, *Journal of Physical Oceanography*, volume (6), pp. 200-228, 1976.

[7] **Carter D. T. J.**, Predictions of Wave Height and Period for a Constant Wind Velocity using JONSWAP Results, *Oceanic Eng.*, volume (9), pp. 17-33, 1982.

SOUND WAVES PROPAGATING IN FLUCTUATING MEDIA: EXPERIMENTAL ANALYSIS USING *ALMA* DATA.

Gaultier Real[a], Dominique Fattaccioli[a]

[a]DGA Techniques Navales, avenue de la Tour Royale, 83050 Toulon
gaultier.real@intradef.gouv.fr

Abstract: *The ALMA – Acoustic Laboratory for Marine Applications- system has been the object of several publications and presentations within the past few years. In this paper, the authors focus on a joint environmental and acoustic analysis: during the 2016 campaign, where a 128-hydrophones comblike array was deployed approximately 9km away from an active acoustic source in shallow waters, temperature fluctuations were recorded by a thermistor string deployed in the vicinity of the passive acoustic array. These fluctuations translate into variations of the local sound speed profile. A study of the relative changes in the sound speed profile shows a strong periodicity of these variations, henceforth supposedly related to linear internal waves. The impact of these environmental fluctuations on the sound waves propagated throughout this medium is measured by calculating the acoustic intensity and the normalized acoustic intensity distribution. A strong discrimination can be observed between the various configurations, in very good agreement with what can be found in the literature.*

Keywords: *coherence, fluctuations, acoustic intensity, saturation.*

1. INTRODUCTION

This paper addresses the topic of sound waves propagating in a fluctuating ocean. The increase in the dimensions and frequency band of interest in order to adapt to the increasing stealth of the threats lead to a stronger sensitivity of the sonar systems to the environmental fluctuations [1-3]. To tackle this issue, a better understanding of the propagation of acoustic waves in randomly fluctuating media is needed. While an exhaustive literature on the topic is available [4-6], some progress to design robust corrective signal processing techniques allowing to compensate for the degradation of the array gain due to the medium fluctuations are still required.

The ALMA system was designed in 2012 by DGA Naval Systems to gather underwater acoustic data representative of the real-life of sonar systems and share them with the scientific community [7-8]. By recording acoustic data propagated in shallow and coastal waters, where water mixing processes are likely to happen, it is possible to study the phenomena associated with the propagation of sound waves in challenging environments and how that process affects the sonar systems performance (detection, localization, …). A companion paper focuses on the latest evolutions and upgrades of the ALMA system [9].

We propose, in this paper, to continue the study carried out in [10-11]: we apply a classification scheme based on the probability density function (pdf) of the normalized acoustic intensity. This scheme is validated on data acquired during the 2016 ALMA campaign, where fluctuations of the local temperature profile were recorded by a thermistor string. Section II provides a reminder of the acoustic experiment, while section III focuses on the various normalized intensity found in the literature and how they are linked to the theory of regimes of propagation. Section IV provides the experimental results associated with this analysis.

2. THE 2016 ALMA EXPERIMENT

The experiment was located in the Western Mediterranean Sea, on eastern coast of the island of Corsica, 5 km away from the shore of Alistro. On the receiving end, a comblike, 4x32-hydrophones passive array was deployed, along with its power supply and data recording buoy. The passive array is displayed in Figure 2. About a mile east from the passive array, a thermistor string was deployed. The length of the thermistor string was 150m, allowing to sample every 6.25 m the water temperature across the water depth. The acoustic pinger was moored 9 km south from the passive array at a 50m depth (see Figure 1). The locations and depth of those elements are available in [11].

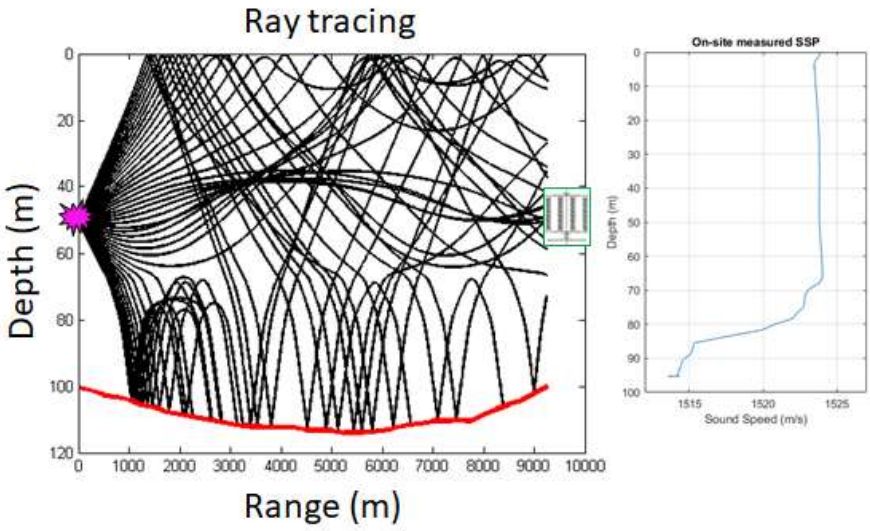


Figure 1. *ALMA 2016 Experiment Area*

The passive array was arranged as follows: 4 vertical arrays of 32 hydrophones (acoustic sampling $\Delta h = 0.15\,m$, total acoustic height $H_a = 4.8m$) horizontally spaced by $\Delta S = 0.5m$). The overall dimensions of the array is $L = 2m \times H = 5m$.



Figure 2. *Passive Array Arrangement (left) - ALSEAMAR's SG01 Acoustic Pinger (right)*

The signal emitted was a sequence consisting of broadband pulses, frequency modulated signals, continuous waves (CW) and white noise, in the frequency range 1-13 kHz. The total duration of this sequence was $T_{seq} = 59s$, with a repetition rate of $T_r = 60s$ (see [11] for more details).

The thermistor string recorded temperature fluctuations throughout the entire duration of the campaign. It was therefore possible to identify specific time periods in which strong temperature fluctuations were observed. After translation of the temperature data into relative sound speed changes data, Figure 3 displays two time windows of interest: a relatively stable phase (left), where solely slight changes in the relative sound speed temporal evolution are notices; and a perturbed time series, where oscillations are noticed (right). The identification of these two time windows will allow to relate those environmental fluctuations to the acoustic observations. Note the appearance of a turbulence layer around 50m depth, fluctuating at very high frequency during the two phases.

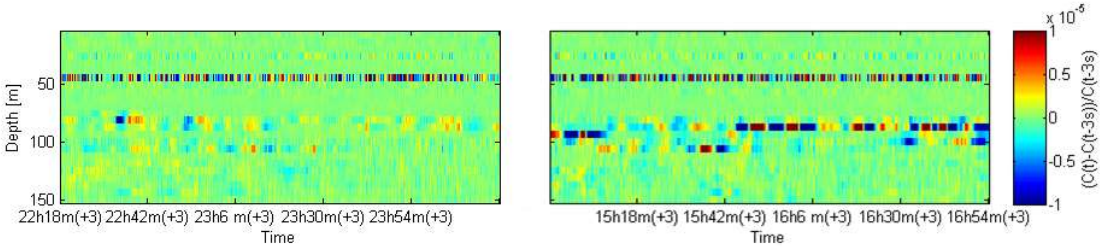


Figure 3. *Unperturbed (left) and perturbed time periods during vertical relative sound speed variations profile.*

3. PDF OF THE NORMALIZED ACOUSTIC INTENSITY

It was shown in the literature that classifying experimental configurations involving propagation of waves in fluctuating media into regimes of fluctuations was extremely helpful. Indeed, depending on parameters such as the range of propagation, the relative amplitude of sound speed fluctuations, its two-dimensional correlation lengths, and the frequency of the signal of interest, one can attribute a specific regime of saturation, according to [5].

The behaviour of the normalized acoustic intensity I/I_0 strongly depends on the observed regime of fluctuation [12]. It can therefore theoretically constitute a way to characterize a given experimental configuration, using passive acoustics only

The statistics of this quantity are used to perform this analysis, namely the pdf of the normalized acoustic intensity. In the fully saturated regime, where phase and amplitude fluctuations of the acoustic signals are noticed, inducing a strong degradation of sonar performance, the pdf of I/I_0 is known to follow an exponential distribution of the form:

$$D_1(I/I_0) = I/I_0\, e^{-I/I_0}.$$

In [13], the authors introduce an alternative distribution, called Modulated Exponential, where a factor depending on the scintillation index $SI = \frac{I_0^2}{\langle I \rangle^2} - 1$ appears:

$$D_2(I/I_0) = e^{-I/I_0}\left[1 + \frac{SI-1}{4}\left(\frac{I^2}{I_0^2} - \frac{4I}{I_0} + 2\right)\right].$$

Finally, in the unsaturated regime, where sole phase fluctuations are likely to happen, the pdf of normalized intensity supposedly follows a log-normal law:

$$D_3(I/I_0) = \frac{1}{\sqrt{2\pi} I\sigma}\, e^{-\left[\frac{\left(ln\left(\frac{I}{m}\right)+\frac{\sigma}{2}\right)^2}{2\sigma^2}\right]}.$$

4. EXPERIMENTAL RESULTS

We hereby calculate the pdf of normalized intensity on the 1 kHz CW emitted by the active pinger as part of the global emission sequence. The duration of the signal of interest is 2s. The intensity if then calculated and normalized on 5 hydrophones taken at the geometrical center of the first Vertical Line Array (VLA). The two time-windows described in Section 2 are considered (unperturbed and perturbed media).

Figure 4 displays the time series of normalized intensity in both cases:

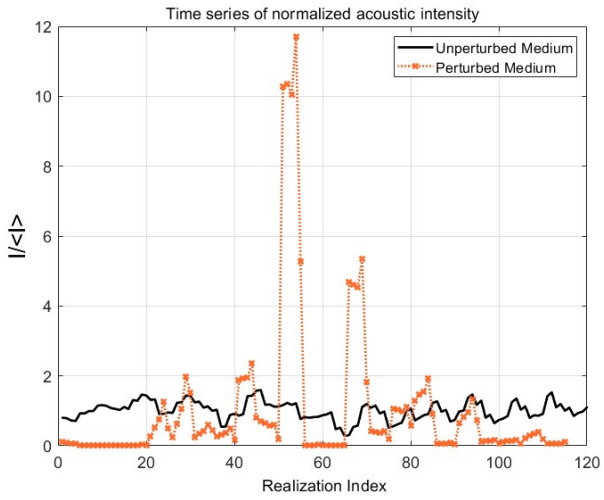


Figure 4. *Time series of the normalized acoustic intensity - Unperturbed (solid line) and perturbed (dotted crosses) time periods.*

Figure 5 displays the calculated pdf of normalized intensity, as well as the theoretical pdf expressed in Section 3. As expected, the perturbed case fits nicely with the ME distribution, while the log-normal distribution fits the unperturbed case.

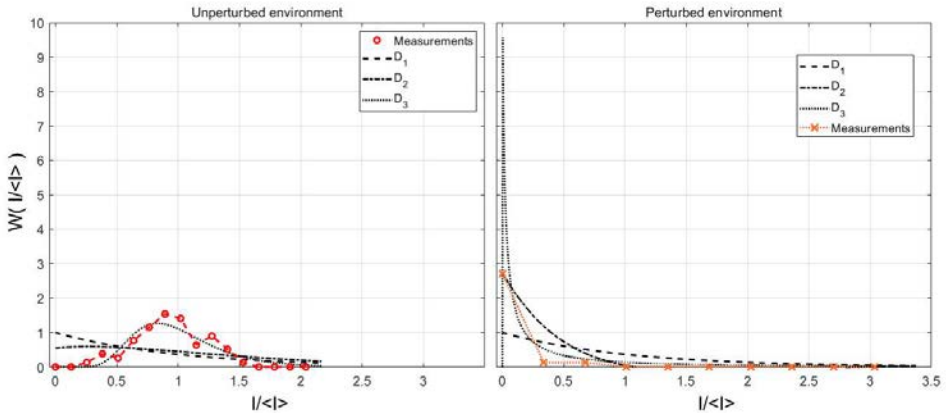


Figure 4. *Pdf of normalized intensity: comparison between theoretical distributions and measurements - Unperturbed (left) and perturbed (right) time periods.*

CONCLUSION

In this paper, we demonstrated the capability to associate specific experimental configurations or time periods of a given setup with regimes of fluctuations. The association was performed using the probability density function of the normalized received acoustic intensity. It was indeed shown that, in presence of strong fluctuations (i.e. in the fully saturated regime), an exponential decrease of the normalized intensity pdf was observed. On the contrary, when slight fluctuations are observed, a log-normal distribution is a better fit for this quantity.

Our interpretation of this result is that it could constitute a first step in a global processing scheme allowing to first identify the regime of saturation involved in order to, in a second time, select the appropriate algorithm to process the data and guarantee the maximum sonar performance.

REFERENCES

[1] **Dashen, R., Munk, W. H., & Watson, K. M.** (2010). *Sound transmission through a fluctuating ocean*. Cambridge University Press.

[2] **Real, G., Cristol, X., Habault, D., Sessarego, J. P., & Fattaccioli, D.** (2015). Influence of de-coherence effects on sonar array gain: scaled experiment, simulations and simplified theory comparison, *Proceedings of the 3rd Underwater Acoustic Conference and Exhibition*, Chania, Greece, pp. 1-6, 2015.

[3] **Real, G., Cristol, X., Habault, D. & Fattaccioli, D.** Mitigation of decoherence effects in passive sonar : application to a scaled experiment, *Proceedings of the Acoustic and Environmental Variability, Fluctuations and Coherence Workshop,* Cambridge, UK, pp. 1-8; 2016.

[4] **Lynch, J. F., Lin, Y. T., Duda, T. F., & Newhall, A. E.** (2010). Acoustic ducting, reflection, refraction, and dispersion by curved nonlinear internal waves in shallow water. *IEEE Journal of Oceanic Engineering*, *35*(1), 12-27.

[5] **Colosi, J. A.** (2016). *Sound Propagation through the Stochastic Ocean*. Cambridge University Press.

[6] **Duda, T. F., Flatté, S. M., Colosi, J. A., Cornuelle, B. D., Hildebrand, J. A., Hodgkiss Jr, W. S., ... & Spindel, R. C.** (1992). Measured wave-front fluctuations in 1000-km pulse propagation in the Pacific Ocean. *The Journal of the Acoustical Society of America*, 92(2), 939-955.

[7] **Fattaccioli, D.** Alma: a new experimental acoustic system to explore coastal waters, *Proceedings of the 3rd Underwater Acoustic Conference and Exhibition*, Chania, Greece, pp. 1-6, 2015.

[8] **Fattaccioli, D. and Real, G.** The DGA "ALMA" Project: an overview of the recent improvements of the system capabilities and of the at-sea campaign ALMA-2016, *Proceedings of the 4th Underwater Acoustic Conference and Exhibition*, Skiathos, Greece, pp. 1-6, 2017.

[9] **Fattaccioli, D. and Real, G.** A brief five-year progress report on the DGA "ALMA" project: scientific program and projects, at-sea campaigns and data collected, system evolutions and improvements, *Proceedings of the 5th Underwater Acoustic Conference and Exhibition, Knossos, Greece, pp. 1-9, 2019*.

[10] **Real, G., & Fattaccioli, D.** (2018, October). Acoustic Laboratory for Marine Applications: Overview of the ALMA system and data analysis. In *OCEANS 2018 MTS/IEEE Charleston (pp. 1-7). IEEE*

[11] **Real, G., & Fattaccioli, D.** (2017). Acoustic coherence in a fluctuating ocean: analysis of the 2016 ALMA campaign. *In UACE 2017 Proceedings*.

[12] **Blanc-Benon, P., & Juvé, D.** (1993). Intensity fluctuations of spherical acoustic waves propagating through thermal turbulence. *Waves in random media, 3(2), 71-83*.

[13] **Colosi, J. A., Tappert, F., & Dzieciuch, M.** (2001). Further analysis of intensity fluctuations from a 3252-km acoustic propagation experiment in the eastern North Pacific Ocean. *The Journal of the Acoustical Society of America, 110(1), 163-169*.

HOLOGRAPHIC ARRAY FOR DETERMINING STRUCTURAL ACOUSTIC PROPERTIES

Jit Sarkar[a], Sandrine T. Rakotonarivo[a,b] , Simone Sternini[a], Alexis Bottero[a], Earl G. Williams[c], Jeffrey Dwayne Tippmann[a,d], and William A. Kuperman[a]

[a] Scripps Institution of Oceanography, University of California, San Diego, 9500 Gilman Drive, La Jolla, California 92093-0238,
[b]Aix Marseille Univ, CNRS, Centrale Marseille, LMA UMR 7031, Marseille, France
[c]Naval Research Laboratory, Acoustics Division, Washington, DC 20375, USA
[d]Los Alamos National Laboratory, Intelligence and Space Research Division, P.O. Box 1663, Los Alamos, New Mexico 87545, USA

Contact author: William A. Kuperman
Scripps Institution of Oceanography, University of California, San Diego,
9500 Gilman Drive, La Jolla, California 92093-0238
wkuperman@ucsd.edu

Abstract: *It has already been shown that the scattering properties of an arbitrary object in an external medium can be determined by three quantities: The structural impedance matrix, Z_s, the input impedance matrix Z_i, and the radiation impedance matrix, Z_r. Only Z_s is dependent on the specific, possibly unknown and complicated internal structure of the object; the other two are only dependent on the surface shape of the object and the external medium so they can be routinely computed. We have constructed a laboratory facility to measure the structural impedance of an object by placing it in an external, diffuse noise field. The measurements are made using an array of a double layer of MEMS microphones placed in the near field of the object; the array is embedded in a skeletal structure which surrounds the object. This array structure is programmatically generated from a 3D scan of the object, and constructed using a large 3D printer. Cross correlating the MEMS acoustic data together with holographic signal processing yields the structural impedance, with the large matrix-matrix calculations being accelerated on a GPU computing platform. These results combined with the other computed impedances provides the scattering properties of the object when placed (loaded) in an external medium. The details of the experimental setup are explained and preliminary results are presented.*

Keywords: *Structural Acoustic , Holographic Array, Impedance Matrix, MEMS microphone array*

INTRODUCTION

We have developed a method based on earlier work of Bobrovnitskii [1] to measure the in vacuo structural impedance (or admittance) matrix of a complex object by placing it in a random noise field and correlating pressures and velocities on its surface [2]. The importance of this procedure is that once the structural impedance matrix of an object is known, it can be combined with easily computable interior and exterior (radiation) impedances [1] that only depend on the object shape and the external medium. Furthermore, these impedances can be easily modified to determine the scattering properties of the object arbitrarily oriented in any medium [3–5], as opposed to intensive numerical modeling and/or exhaustive scattering experiments involved with measurements *in situ*. The components of the total theory [1,2] are illustrated in Fig.1 for which only Z_s need to be measured while the other two impedances are readily computed.

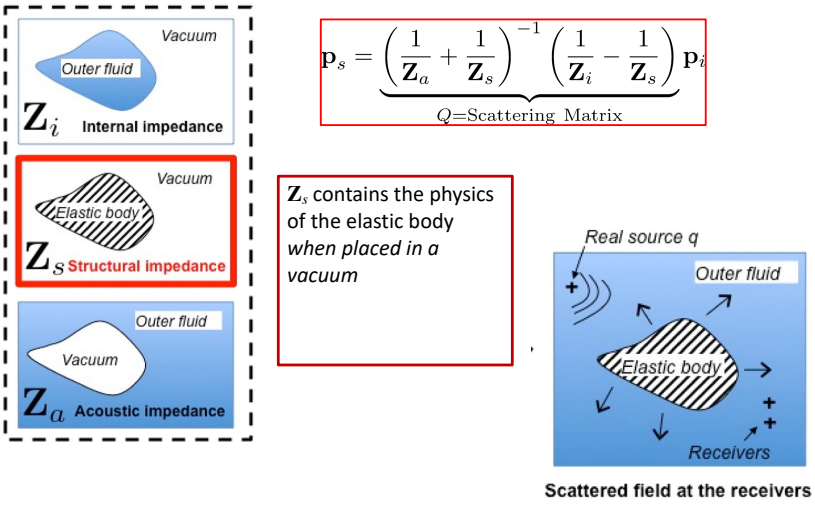


Figure 1: The scattered field is derived from three impedances

An experiment on an air-filled, thick spherical shell was carried out to demonstrate the measurement of the in vacuo structural admittance [6] using a small set of surface mounted accelerometers and microphones with remotely placed loudspeakers for excitation.

We are now constructing a laboratory facility which combines dual surface Nearfield Acoustical Holography (NAH) [7,8], Equivalent Source Method (ESM) [3,9] with Field Separation Techniques (FST) [10,11] for measuring the structural impedance of an object by placing it in an external, diffuse noise field. The measurements are made using an array of a double layer of Micro-Electro-Mechanical Systems (MEMS) microphones placed in the near field of the object; the array is embedded in a skeletal structure which surrounds the object. This array structure is programmatically generated from a 3D scan of the object, and constructed using a large 3D printer. Cross correlating the MEMS acoustic data together with holographic signal processing yields the structural impedance, with the large matrix-matrix calculations being accelerated on a Graphical Processing Unit (GPU) computing platform. These results combined with the other computed impedances (internal and acoustic) provide the scattering properties of the object when placed (loaded) in an external medium. The details of the experimental setup are explained and preliminary results are presented.

2. BACKGROUND THEORY FOR MEASUREMENT

The structural impedance is the ratio of the force and normal velocity at the surface of the object and as derived in [1,2] can be written in terms of matrices of the correlations of the surface pressures between (N) points on the surface and correlation of pressures and normal velocities between the same points on the surface as shown in Fig. 2, where p and v are vectors whose elements are the frequency domain pressures and normal velocities and the brackets denote an ensemble average over many (L) noise realizations.

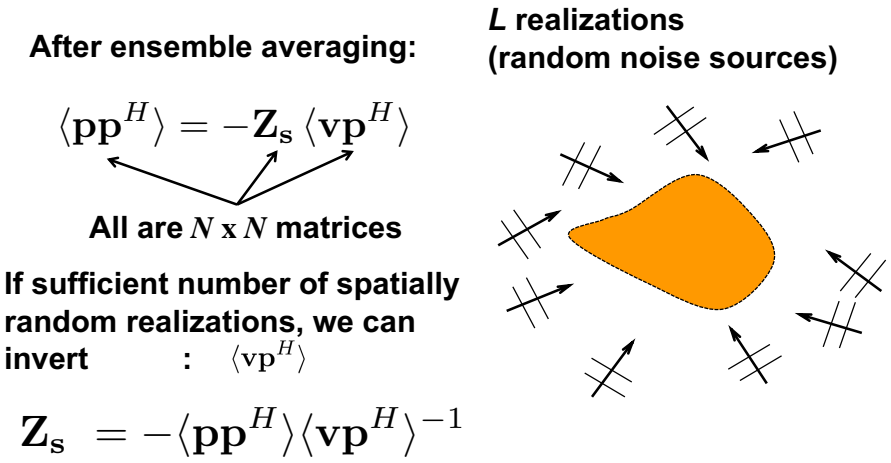


Figure 2: The structural impedance is derived from correlating surface pressures and normal velocities.

Our earlier measurements were of a spherical shell, such that its symmetry allowed using only a limited number of sensors on the surface [6]. An arbitrary shaped object required more intensive sensing so that a large number of sensors attached to the surface become problematic. To overcome this impediment, we employ NAH that utilizes sensors arranged on two concentric surfaces a small distance from the object [12] and then translate these measurements to surface pressure and normal velocity on the surface using FST together with ESM and subsequently implementing the process of Fig. 2 from which the scattered field can be obtained as per Fig. 1.

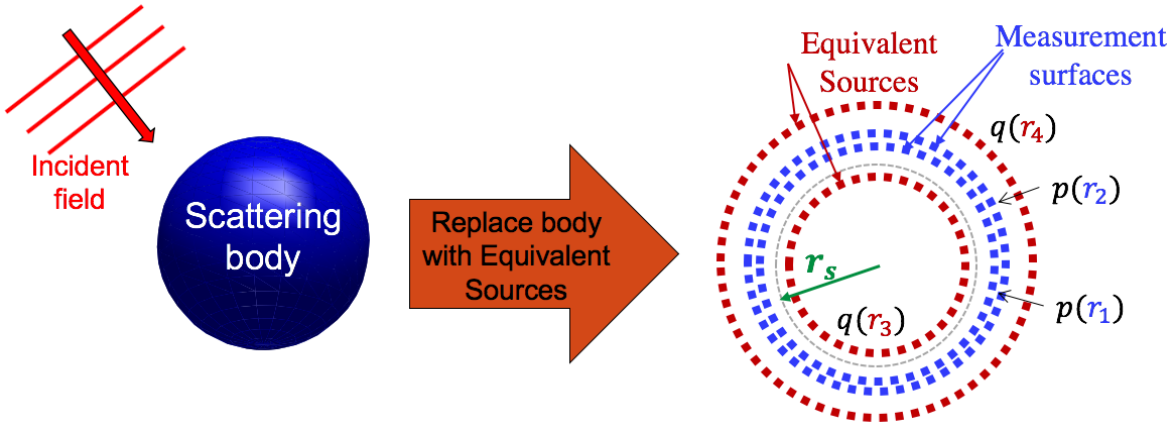


Figure 3: Combining ESM with FST: Data from two measurement layers of sensors, p(r1) and p(r2), are used to construct two equivalent source arrays such that the q(r3) sources and q(r4) sources respectively separate scattered and incident fields which can then be propagated to the surface, r_s, of the object.

Referring to Fig. 3. the two layers of sensors, $\mathbf{p}(\mathbf{r}_1)$ and $\mathbf{p}(\mathbf{r}_2)$, allow separation of incoming and scattered fields creating synthetic, surrogate source arrays (ESM) inside, $\mathbf{q}(\mathbf{r}_3)$, and outside, $\mathbf{q}(\mathbf{r}_4)$, the surface such that the scattered field is determined by the former and the incoming by the latter [10,11]. With that field separation, NAH can then determine the pressure and velocity at the object surface, $\mathbf{r}_s$. Free field Green's functions are used between the real sensors and equivalent source locations.

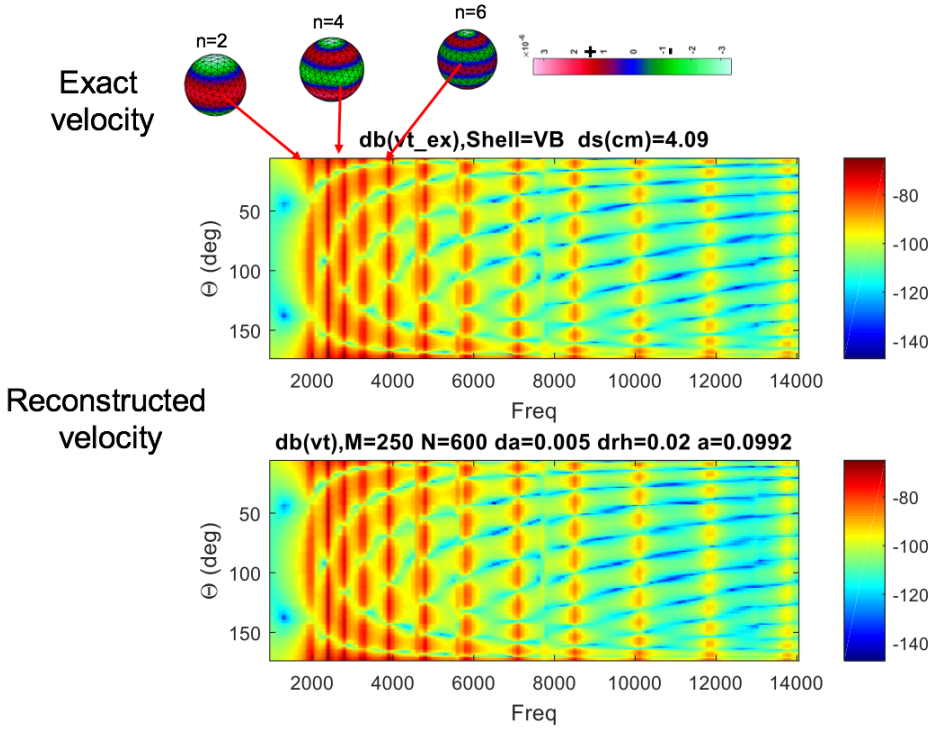


Figure 4: Comparison of a data analysis procedure based on the methodology of Figure 3 with an exact solution.

An example of the accuracy of the method is shown in Fig. 4 which compares a simulation involving the steps outlined in Fig. 3 for two layers of 250 pressure sensors separated by .5 cm with the inner layer being 2.0 cm from the sphere and 600 "Equivalent Sources" with an analytic result from which some of the shell modes are also shown.

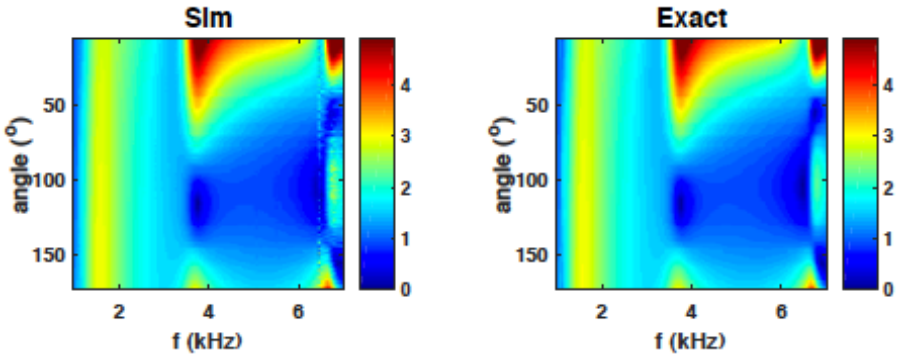


Figure 5: Comparison of Monte Carlo simulation of the holographic array processing with an analytic solution for scattering of a plane wave incident on a spherical shell.

Figure 5 then shows a comparison of a scattered field result in a water medium for a specific incident angle obtained by simulating the whole procedure as summarized by Figs. 1-3 with an

exact analytic solution. That is, as per Fig.1 the scattering matrix is a function of the three impedances. The simulation for computing Z_s involved a Monte Carlo simulation of the procedure illustrated in Fig. 2; the internal medium was the shell structure and to emulate a laboratory experiment, the external medium was air. (We had previously shown that this procedure to determine Z_s actually produced the required *in vacuo* result [2]). The other two impedances are easily computed using the external shape of the object and the acoustical properties of water for the "outer fluid" for Z_i and Z_a, thereby verifying that measurements from the holographic laboratory procedure could be translated to a water loaded scattering result.

3. CONSTRUCTING THE LABORATORY FACILITY

The actual facility to obtain the measurements simulated in the previous section requires several components operating in conjunction to provide the complete system.

A skeletal scaffold is designed around the target dimensions, to which pairs of sensors will be mounted in close proximity to the objects surface (support for ~250 planned). This support structure is fabricated on a large form-factor 3D printer, providing the flexibility to accommodate targets of almost any shape.



(a) (b)

Figure 6: (a) 3D model depicting test target (inner blue/dark cylinder) and supporting sensor scaffold (outer white/light structure) to which the MEMS PCB units will be attached. (b) Actual scaffold and target constructed in a large form-factor 3D printer.

The sensors themselves are custom designed Printed Circuit Board (PCB) units (Fig. 7), utilizing pairs of digital MEMS microphones and complimentary logic for reliable data transmission over Low Voltage Differential Signalling (LVDS). The microphones are self-contained systems, providing signal conditioning, an analog-to-digital converter, decimation and anti-aliasing filters, and power management, all in a very small integrated package (4mm x 3mm x 1mm) capable of sampling rates up to 48kHz. This eliminates the need for any analog logic in the external data acquisition (DAQ) system, greatly reducing the cost and complexity, with the additional benefit of reduced susceptibility to noise since all sampling/conversions occur at the sensor end-point.

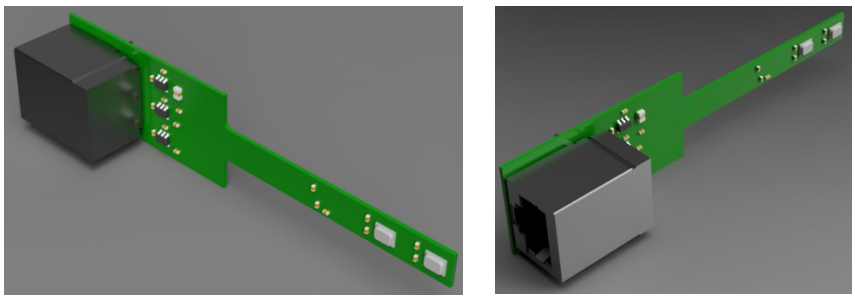


Figure 7: 3D renderings of the dual MEMS microphone PCB, ~10cm L x 2cm W. Signals are transmitted via LVDS over standard CAT-6 cabling

The DAQ unit driving theses sensors is now only responsible for handling the streams of binary data coming from the microphones, and providing the (also digital) sampling and base clock signals to them. This can be accomplished through logic defined on a Field Programmable Gate Array (FPGA) system, and is currently working with a small device capable of supporting up to 32 microphone pairs. Scaling the system out is accomplished by either adding more FPGA interfaces in parallel, or moving up to larger FPGA devices, with support for up to 128 dual-mic boards each. An optional multiplexing serializer/de-serializer (SerDes) can be interposed between the microphones and the FPGAs to reduce the number of wires required while also increasing data transmission distances.

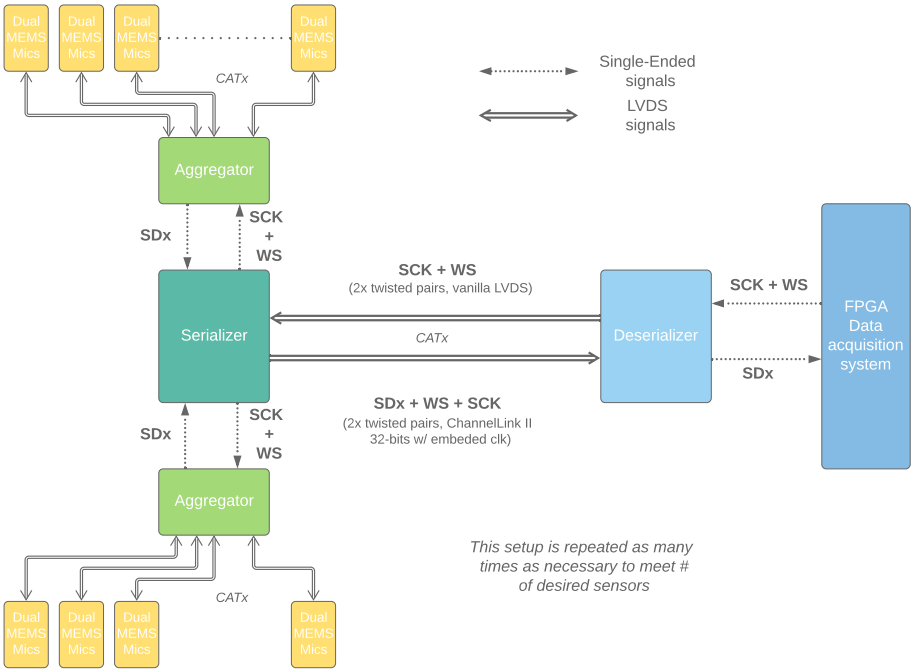


Figure 8: Schematic overview of full acoustic array acquisition system with optional SerDes interposer for extending data transmission distances and compressing the number of required wires/cables

To check the validity of the experimental set-up, a preliminary experiment using 10 pairs of digital MEMS microphones as the one shown on Figure 9 is first implemented to measure the response of a plastic capped pipe with a thickness d=2.5 mm, an outer radius r=40mm and a height h=150mm.

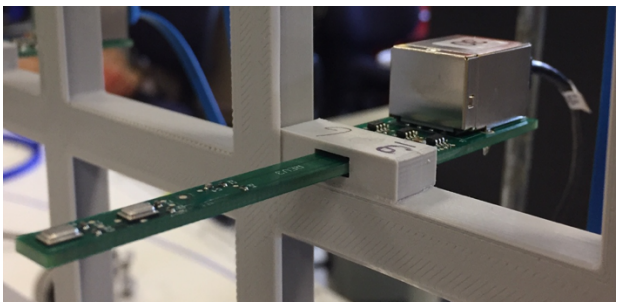


Figure 9: Zoom of the mounting system for holding the PCB that contains the MEMS microphones

As shown on Fig. 6, this target is embodied inside the scaffold that holds the PCBs containing the MEMS sensors (Fig. 8). Both structures, target and scaffold, are 3D printed using PLA plastic that has a density $\rho = 1250$ kg/m^3, a Young modulus $E = 3.5$ GPa and a Poisson ratio $\nu = 0.33$. Each PCB points toward the axis of the capped cylinder that is centred with the scaffold axis. The MEMS microphones are respectively located 5 mm and 15 mm off the target surface. Measurements are conducted by uniformly moving a white noise source around the {source + scaffold} in order to extract the capped pipe response (structural admittance/impedance) around its $n = 2$ mode following the approach described in section 2. According to numerical and analytical simulations, this mode occurs at 960.83 Hz (Figure 10) for the studied capped pipe when filled with air.

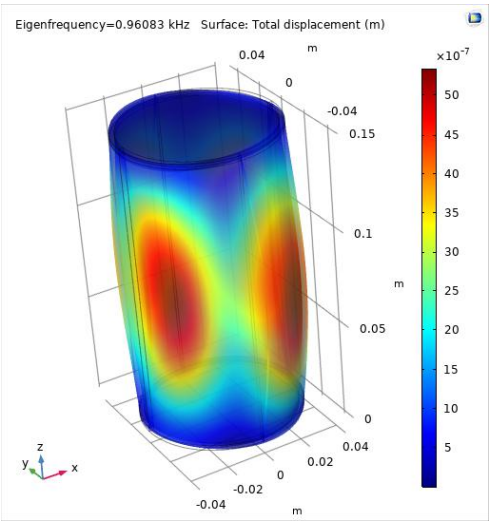


Figure 10: Mode n=2 of the capped pipe filled with air.

Once these preliminary tests are performed and validated, the next measurements will aim at estimating low and higher modes of the in-vacuo response of a complex shape target such as an unexploded ordnance. To do so, measurements will be performed with a larger array made of 250 MEMS microphone pairs like the one shown on **Error! Reference source not found.** Figure 9.

ACKNOWLEDGEMENTS

This research is supported by the U.S. Office of Naval Research.

REFERENCES

[1] Yu. I. Bobrovnitskii, Impedance theory of sound scattering: General relations, Acoust. Phys., 52(5), 2006, 513-517.

[2] S. T. Rakotonarivo, W. A. Kuperman and Earl G. Williams, Prediction of a body's structure impedance and scattering properties using correlation of random noise, J. Acoust. Soc. Am. 134(6), 2013, 4401-4411.

[3] I. Lucifredi and H. Schmidt, Subcritical scattering from buried elastic shells, J. Acoust. Soc. Am. 120(6), 2006, 3566-3583.

[4] G. V. Borgiotti, Effect of the compliance on the scattering of an elastic object immersed in fluid: A general formulation, J. Acoust. Soc. Am. 87(3), 1990, 1055-1061.

[5] C. F. Gaumond and T. Yoder, Determination of structural impedance from scattering data, J. Acoust. Soc. Am. 93(3), 1995, 1415-1422.

[6] Earl G. Williams, Jeffery D. Tippmann, Sandrine T. Rakotonarivo, Zachary J. Waters, Philippe Roux and W. A. Kuperman, Experimental estimation of in vacuo structural admittance using random sources in a non-anechoic room, J. Acoust. Soc. Am. 142, 2017, 103-109.

[7] Earl G. Williams, *Fourier Acoustics*, Academic Press, London, 1999.

[8] W. A. Veronesi and J. D. Maynard. Digital holographic reconstruction of sources with arbitrarily shaped surfaces. J. Acoust. Soc. Am., 85:588–598, 1989.

[9] N. Valdivia and E. Williams, Study of the comparison of the methods of equivalent sources and boundary element methods for near-field acoustic holography, J. Acoust. Soc. Am. 120, 2006, 36943705.

[10] Chuan-Xing Bi, Xin-Zhao Chen, and Jian Chen, Sound field separation technique based on equivalent source method and its application in nearfield acoustic holography, J. Acoust. Soc. Am. 123(3), 2008, 1472-1478.

[11] Efren Fernandez-Grande, Finn Jacobsen and Quentin Leclere, Sound field separation with sound pressure and particle velocity measurements, J. Acoust. Soc. Am. 132(6), 2012, 3818-3825.

[12] E. G. Williams, the nearfield acoustical holography (NAH) experimental method applied to vibration and radiation in light and heavy fluids, Computers & Structures, Vol 65, No. 3, pp 323-335, 1997.

DEVELOPMENT OF A MOORED ACOUSTIC ARRAY SYSTEM FOR EXPERIMENTAL ACOUSTIC IMAGING OF UNDERWATER ENVIRONMENT

Sung-Hoon Byun[a], Youngchul Choi[a], Sea-Moon Kim[a], Chong-Moo Lee[a], Kihun Kim[a], Sukmin Yoon[a], and Yeon-Seong Choo[b]

[a]KRISO, Daejeon, South Korea
[b]UST, Daejeon, South Korea

Sung-Hoon Byun, 32 Yuseong-gu 1312 beon-gil, Yuseong-gu, Daejeon, 34103, Korea, Fax number +82-42-866-3819, byunsh@kriso.re.kr

Abstract: *This paper introduces a moored-type underwater acoustic array system recently developed by KRISO for experimental acoustic imaging of underwater environment. It has a sixteen-element linear receiver array and four acoustic projectors which are capable of transmitting separate acoustic signals in synchronous manner. Because each projector can transmit a separate waveform, the multiple-input and multiple-output (MIMO) processing as well as the transmit beamforming can be utilized to enhance the acoustic imaging performance. Mechanically, it adopts two-body design of upper and lower bodies where the acoustic projectors and the receiver array are installed respectively. Active buoyancy control units inside the upper body maintains the total buoyancy and horizontal balance when the array system is deployed in the middle of water column. Principles of the developed system are explained, and preliminary experimental results in large-size water tank are discussed.*

Keywords: *underwater acoustic remote sensing, acoustic imaging, array signal processing*

1. INTRODUCTION

In order to detect and classify underwater sound sources and targets, acoustic arrays are commonly used. Recently, many researches have been carried out on underwater surveillance using acoustic array equipped on remotely operated unmanned system. In particular, with the advent of low-power underwater vehicles and advanced machine learning technology, it is attempted to use the autonomous underwater vehicle (AUV) for classifying underwater targets [1] and estimating undersea environmental information [2]. There also have been a lot of efforts to develop an underwater sound monitoring system which is usually installed on the seabed [3, 4]. However, most of those systems operate in passive mode and therefore cannot be used for active acoustic imaging without an external sound source.

In this paper, a new type of acoustic array system developed by KRISO is introduced. The new system was designed to deploy acoustic array horizontally in the water column. Being equipped with multiple acoustic projectors and a horizontal receiver array, it is able to generate both active and passive image of surrounding environment from a designated altitude from seabed. It adopts the two-body design where the receiver array is installed in the lower body and the acoustic projectors are in the upper body [5].

The main purpose of the system is to acquire experimental acoustic data for studying active and passive sonar imaging techniques. In particular, we are interested in target classification using broadband signaling and resolution enhancement by multiple acoustic projectors.

This paper introduces current status of system development and the result of preliminary experiment recently performed in large-size indoor water tank.

2. KRISO ACOUSTIC ARRAY SYSTEM

The KRISO acoustic array system (KAAS) is a moored-type horizontal array which is deployed afloat in the water column. Fig. 1(a) shows the concept of system operation, and Fig. 1(b) shows the underwater platform of KAAS with acoustic sensors denoted. The system is powered by batteries in the surface buoy and is remotely operated from the mother ship via RF communication.

KAAS has two-body hull and is designed to be neutrally buoyant in the water column. By placing the center of buoyancy above the center of mass, it is designed to have righting moment against heeling and thus sustain upright attitude. Inevitable buoyance difference caused by surrounding seawater density change are compensated by the buoyancy control units installed in the front and the rear caps of the upper body (Fig. 2). The buoyancy control units also help the system to be on an even keel horizontally.

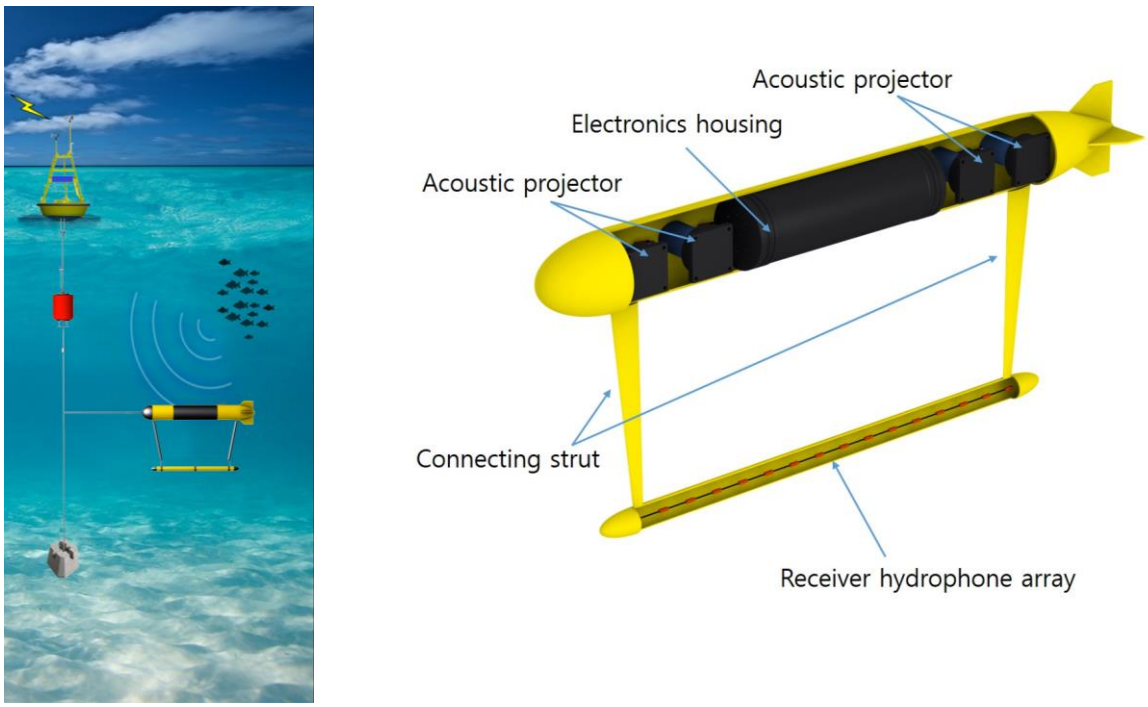
In the lower body, a sixteen-element uniform linear array receiver is located. The frequency range of the hydrophone array element is from 700 Hz to 12.5 kHz. The signals at the receiver array are sampled at a rate of 31.250 kHz. Sampled data are saved to the internal storage and can be retrieved via WIFI link at close distance or via communication cable for high-speed file transfer. The upper body has four Neptune T335 acoustic projectors whose useful frequency band is from 2 kHz to 8 kHz. Table 1 summarizes the technical specification of KAAS.

Because the transmitters are capable of sending separate waveforms, the multiple-input-multiple-output (MIMO) processing [6] can be utilized to enhance the angular resolution. In Fig. 3, the resolution enhancement of MIMO processing is demonstrated by a computer simulation [7]. It compares the performance of MIMO processing with that of the conventional single-input-multiple-output (SIMO) processing assuming the same transmitter and receiver dimension as KAAS. Two m-sequences of minimum peak aperiodic cross

correlation were selected as the probe signal and modulated by BPSK. The center frequency and bandwidth of the probe signal are 6 kHz and 4 kHz, respectively. The delay-and-sum method was used to find angle of arrival (AOA), and Fig. 3 shows the beam response for SIMO and MIMO processing. The result shows that AOAs of two sound sources at 0° and 4.1° are well-resolved for MIMO processing whereas SIMO fails to separate them. This angular resolution enhancement is achieved by the extended virtual aperture which is obtained using multiple transmitters spatially separated.

Max. water depth	100 m
Hydrophone frequency range	700 Hz to 12.5 kHz
Hydrophone spacing	12.5 cm
Number of hydrophones	16 channels
Sample rate	31.250 kHz
Data resolution	24 bits
Acoustic projectors	Neptune T335 × 4 Directional beam pattern (90 degrees)
Projector frequency range	2 kHz to 8 kHz
Functions	Remote control & data transmission via RF link Pressure, temperature, attitude sensors

Table 1: Specification of KRISO acoustic array system (KAAS).



(a) (b)

Fig. 1: The KRISO acoustic array system: (a) conceptual image of system operation and (b) system configuration of underwater platform.

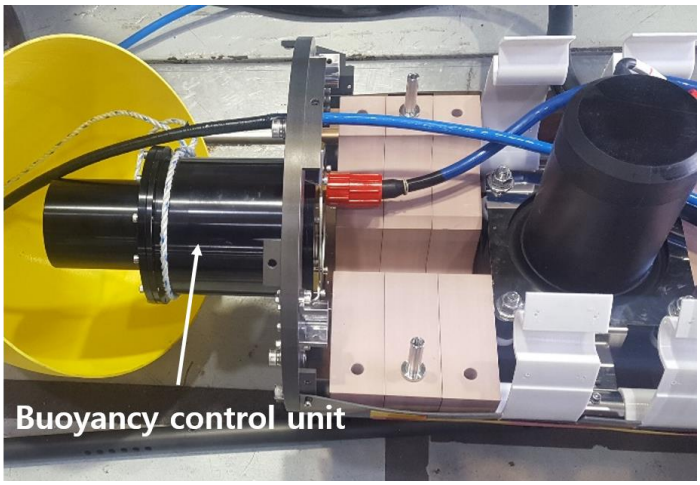


Fig. 2: Buoyancy control unit installed in the front cap of the upper body.

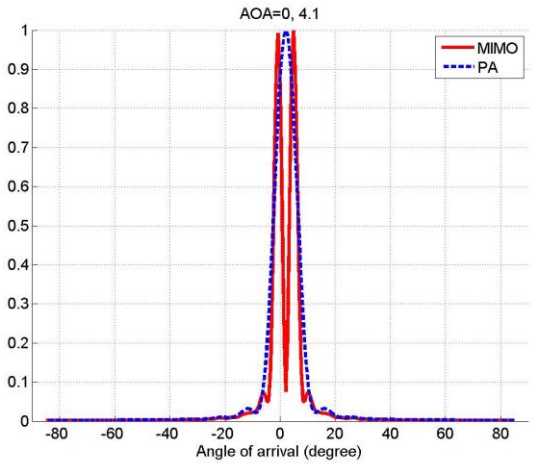


Fig. 3: Numerical comparison for the angular resolution of MIMO and SIMO. True AOAs are 0° and 4.1°.

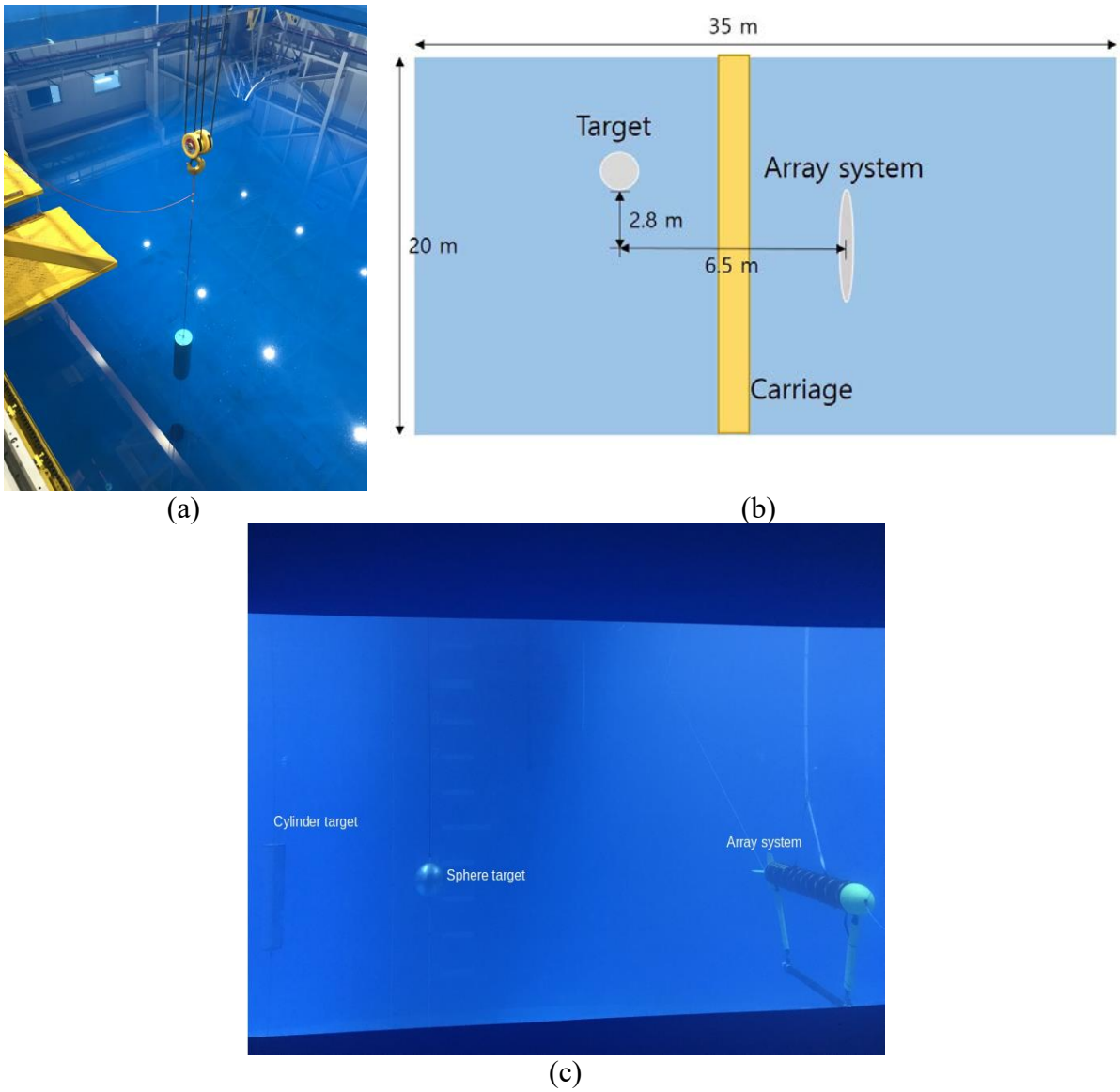
3. WATER TANK EXPERIMENT

In order to test operation of KAAS, an acoustic imaging experiment was carried out in large-size water tank in March 2019. A hollow aluminum cylinder of length 1.5 m and diameter 0.31 m was used as target. The shell thickness of the cylinder was 11 mm. Fig. 4(a) shows the installation of the cylinder target, and Fig. 4(b) describes the plan view of the target and array installation. Fig. 4(c) shows the setup of the target and KAAS in the experiment[1]. The water depth of the tank was 9 m, and both the cylinder and KAAS were installed such that their vertical center be located at the mid-depth.

Fig. 5 is the acoustic image obtained from the delay-and-sum beamforming. Only the SIMO processing result is discussed in this paper. In the experiment, tone pulses of varying length and frequency were used as probe signal. Fig. 5 shows the result when the probe signal of frequency 3.5 kHz and pulse length 700 μs was used. Once KAAS is installed, the acoustic data was acquired twice with and without the cylinder target in the water. Using the data

[1] The sphere target in Fig. 4(c) was withdrawn before data acquisition for simplifying target scattering condition.

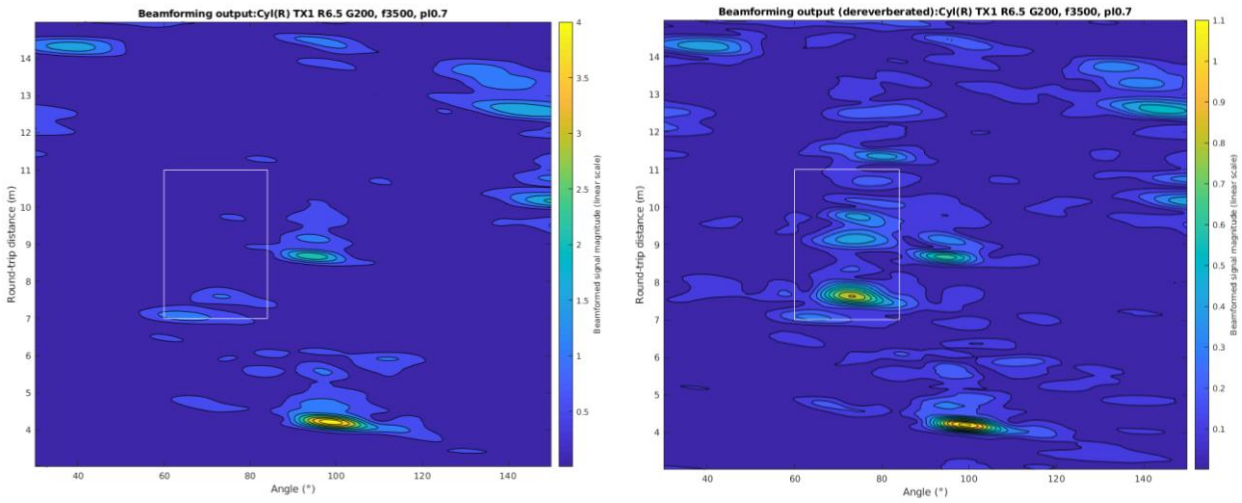
without target, we can estimate the reverberation-only signal and use it to reduce the reverberation in the target image. Fig. 5(a) shows the acoustic image of the original target signal. The white box denotes the range-angle bounds where signal scattered purely from the target, i.e. without any surface and bottom interactions, is expected. Fig. 5(b) shows the acoustic image after subtracting the reverberation from acoustic data of the target-existing case. Although the signals reflected from bottom and surface boundary at range 4 and 9 meters and angle 100° are not entirely removed, the target-scattered signal relatively stands out, and multiple arrivals by the elastic scattering [8, 9] are clearly revealed in the box. Examination of all other experiment data over broadband frequency band from 2 kHz to 12 kHz showed that the scattering strength is highly dependent on frequency. This will be analyzed more in the future.



(a) (b)

(c)

Fig. 4: Water tank experiment setup: (a) Installation of cylindrical aluminum shell, (b) plan view of experiment setup, and (c) photo of experiment setup.



(a) (b)

Fig. 5: Acoustic image of the hollow aluminium cylinder: (a) before removal of reverberation and (b) after removal of reverberation. Probe signal is the tone burst of frequency 3.5 kHz and pulse length 0.7 ms.

4. CONCLUSION

A new moored-type horizontal array system developed by KRISO was introduced with the result of an acoustic imaging test in water tank. MIMO array processing and broadband spectral characterization are possible by the developed system and are expected to provide enhanced acoustic classification of underwater targets. Those topics will be studied further by sea-side experiment scheduled in the latter half of this year.

5. ACKNOWLEDGEMENTS

This research was supported by the research project PES3180 funded by KRISO.

REFERENCES

[1] **Fischell, E. M., & Schmidt, H.,** Classification of underwater targets from autonomous underwater vehicle sampled bistatic acoustic scattered fields, *The Journal of the Acoustical Society of America, 138(6),* pp.3773-3784.

[2] **Nielsen, P. L., Muzi, L., & Siderius, M.**, Seabed characterization from ambient noise using short arrays and autonomous vehicles, *IEEE Journal of Oceanic Engineering, 42(4)*, pp.1094-1101, 2017.

[3] **Oh, S., Byun, S. H., Kim, S. M., Sung, S. Y., Kim, K., Lee, C. M., & Che, I. Y.,** Prototype development of an underwater sound measurement module using four hydrophones, In OCEANS 2015-MTS/IEEE Washington (pp. 1-4). IEEE, 2015.

[4] **McManus, S. J., & Green, D.**, Continued development of broadband passive bearing estimation. In OCEANS 2015-MTS/IEEE Washington, IEEE, 2015.

[5] **Lee, C. M., Kim, K., & Byun, S. H.**, Analysis and tests of the behavior of an underwater acoustic horizontal array platform, *Journal of Ocean Engineering and Technology*, 32(4), pp.222-227, 2018 (in Korean).

[6] **Li, J., & Stoica, P**., MIMO radar with colocated antennas. *IEEE Signal Processing Magazine*, *24*(5), 106-114, 2007.

[7] **Choi, Y. C., Byun, S. H., Lee, C. M., & Choo, Y. S.**, Experimental study on the angular resolution of MIMO sonar, *The Journal of the Acoustical Society of Korea, 38(1s),* p.241, 2019 (in Korean, Abstract only).

[8] **Anderson, S. D., Sabra, K. G., Zakharia, M. E., & Sessarego, J. P.,** Time-frequency analysis of the bistatic acoustic scattering from a spherical elastic shell, *The Journal of the Acoustical Society of America, 131(1),* pp.164-173, 2012.

[9] **Choo, Y. S., Byun, S. H., Kim, S. M. & Lee, K.**, Observation of Acoustic Echoes from Aluminum Hollow Sphere Using a Horizontal Line Array, In *the 6th Pacific Rim Underwater Acoustic Conference*, Taipei/Hualien, Taiwan, National Taiwan University, p.39, 2018.

Structured Session 11

Large Time-Bandwidth acoustic signals for target detection and tracking

Organiser(s): Tesei Alessandra

PASSIVE DETECTION AND BEARING-ONLY TRACKING OF LARGE-TIME BANDWIDTH SIGNALS USING AN AUV MOUNTED VECTOR SENSOR

Daniele S. Terracciano[a,d], Riccardo Costanzi[a,b,c], Vincenzo Manzari[a,d], Mirko Stifani[d], Andrea Caiti[a,b,c], Kevin LePage[e], Luigi Troiano[e]

[a]Department of Information Engineering (DII), University of Pisa, Italy
[b]Research Center "E. Piaggio", University of Pisa, Italy
[c]Interuniversity Center of Integrated Systems for the Marine Environment (ISME), Italy
[d]Naval Support and Experimentation Centre of Italian Navy (CSSN), La Spezia, Italy
[e]NATO STO Centre for Maritime Research and Experimentation (CMRE), La Spezia, Italy

Contact author: Daniele Terracciano, Department of Information Engineering, University of Pisa, Largo Lucio Lazzarino 2, 56122 Pisa, PEC address: ing.informazione@pec.unipi.it, mail: daniele.terracciano@ing.unipi.it

Abstract: *This paper presents experimental results of passive detection and bearing estimation of large time-bandwidth signals between 1.8 and 3.6 kHz using a DIFAR (Directional Frequency Analysis and Recording) vector sensor installed on the eFolaga Autonomous Underwater Vehicle (AUV). The bearing estimation method is based on the product between the pressure sensor and the two orthogonal dipole sensors of the DIFAR. It was implemented both in time and in frequency domain. Extensive data acquisition has been made in underwater gliding navigation, minimizing energy consumption. The collected data allowed to evaluate experimentally the bearing estimation performance in both surface-drifting and gliding mode. The data set was acquired during the Littoral Continuous Active Sonar 2018 (LCAS18) experiment, which took place off the coast of Elba Island, Italy, in November 2018. In this paper, the trial set-up is described. Experimental results on detection and the bearing estimation, both in time and in frequency domain, are presented. The obtained results, combined with the vehicle's persistence, suggest new approaches to acoustic surveillance in a completely autonomous way.*

Keywords: *AUV, Vector Sensor, Direction of Arrival Estimation, DIFAR.*

1. INTRODUCTION

Sonar systems can be divided into active and passive. In active sonar, the system emits a pulse of sound and listens for echoes. Conversly, a passive sonar system just listens to sounds emitted by the target that one is trying to detect. Active sonar can be subdivided into two categories: Continuous Active Sonar (CAS) and Pulse Active Sonar (PAS). Typically, in CAS long-duration waveforms are transmitted with a repetition interval similar to the one used with the traditional PAS. In PAS systems, a short continuous wave or a frequency modulated (FM) pulse is usually transmitted, followed by a relatively long transmission-free period of time to allow receiver to listen for the possible echoes. CAS for AntiSubmarine Warfare (ASW) in littoral waters could have many advantages with respect to the classical PAS. CAS systems transmit and listen for the possible echoes simultaneously, optimising the total energy of the signal and enhancing the detection and tracking performance. This results in the increased update rate of sonar contacts while maintaining the same Pulse Repetition Interval (PRI). Regardless of the specific system used (i.e., PAS or CAS), the state of the art in an active ASW is based upon the deployment of active/passive sonobuoys, on the use of hull-mounted and variable depth sonar deployed from surface ships and on the deployment of towed arrays from submarines. All of these systems can become components of multistatic applications. Recently, alternative approaches involving the use of Autonomous Underwater Vehicles (AUVs) have been suggested. This could lead to significant advantages such as savings on personnel costs, reduced workloads, reduced exposure to dangerous tasks and an improved decision-making under stress. This paper describes ongoing developments at the SEALab, a joint laboratory between the Naval Support and Experimentation Centre (CSSN) of the Italian Navy and the Interuniversity Center of Integrated Systems for the Marine Environment (ISME), in the use of an AUV equipped with an Acoustic Vector Sensor (AVS). Examples of detection and bearing estimation of underwater sources using AVS are addressed in [1]. Similar applications such as the use of a compact volumetric array mounted on an underwater glider have been investigated in [2]. These compact sensors are well suited to be used in light systems, where space is limited, such as an AUV. This paper shows that using a DIFAR (Directional Frequency Analysis and Recording) AVS integrated on the e-Folaga AUV [3] it is possible to track the azimuth of different types of acoustic signals in a multistatic scenario. Experimental results of passive detection and bearing estimation of large time-bandwidth signals, which allow extrapolation of the information in multiple frequency sub-bands, between 1.8 and 3.6 kHz are presented. The recent at-sea successes have demonstrated that the use of AUVs provides an alternative approach to acoustic surveillance. The paper is organized as follows: Section 2 describes the applied methodologies and the developed algorithms; In section 3 the experimental set-up is described; Section 4 reports a selection of the results obtained. Finally, conclusions are reported and discussed in section 5.

2. METHOD

The DIFAR AVS consists of a centrally placed omnidirectional hydrophone, two particle motion sensors arranged orthogonally around it and a built-in compass. In the original configuration the signal arriving at the sensors, together with the compass signal, were processed by the electronics of the sonobuoy forming the so-called “complex signal” to be transmitted via VHF [4]. The integration between the AUV and the AVS is based on the original DIFAR electronics: the modulated signal is acquired and stored within the developed acoustic payload. A pre-processing stage is necessary to demodulate the three signals from the sensors described above. Demodulation software has been implemented in MATLAB. Once the signals of the single sensors have been this way computed, the arctangent-based method [5] has been applied to estimate the bearing of an acoustic source. For an acoustic wave propagating

horizontally and arriving at the sonobuoy at an azimuthal angle β, the three sensor outputs can be written in the following form:

$$x_o(t) = x(t) \tag{1}$$

$$x_s(t) \approx x(t) \sin\beta \tag{2}$$

$$x_c(t) \approx x(t) \cos\beta \tag{3}$$

where the subscripts *o, s, c* denote omni, sine, and cosine [6]. The angle β is measured clockwise from north. The bearing of an acoustic wave arriving at the vector sensor from a certain direction β with respect to the North can be estimated in the time domain by:

$$\hat{\beta}(t) \approx \text{arctan2}\,[x_s(t) \cdot x_o(t)\,,\; x_c(t) \cdot x_o(t)] + \alpha \tag{4}$$

where $x_{\mathbf{o}}(t)$ is the signal acquired by the omni-directional hydrophone, $x_s(t)$ and $x_c(t)$ are the signal at the two particle motion sensors. α represents the angle on the horizontal plane between the magnetic and true North (magnetic declination due to the position on the Earth's surface), that is calculated by the implemented MATLAB software starting from the GPS position provided by the vehicle. The function arctan2 is the four-quadrant inverse tangent which returns values in the interval [-π, +π]. Differently from the arctangent, arctan2 uses the signs of both arguments to determine the quadrant of the result. In a similar way, the bearing estimator can be implemented in the frequency domain also:

$$\hat{\beta}(f) \approx \text{arctan2}\,[\text{real}\{X_s^*(f) \cdot X_o(f)\}\,,\; \text{real}\{X_c^*(f) \cdot X_o(f)\}] + \alpha \tag{5}$$

where real stands for the real part operator and the asterisk represents the complex-conjugate operator.

3. DESCRIPTION OF AT-SEA TESTS - LCAS'18 EXPERIMENT

The LCAS'18 (Littoral Continuous Active Sonar) experiment took place off the coast of Elba Island, Italy, in November 2018, in the context of a Multinational-Joint Research Project (LCAS MN-JRP) with the Centre for Maritime Research and Experimentation (CMRE). Water depth was between 100 and 200 meters. The research vessels NRV Alliance and CRV Leonardo took part in the experiment towing respectively an acoustic source capable of CAS - PAS transmissions over the frequency band of 1800 – 3600 Hz and an echo-repeater system which repeated the received signal transmitted by the Alliance in order to simulate a target. There was also a fixed source called DEMUS which transmitted PAS signals. CSSN staff was embarked on the N/O Astrea, a ship owned by the Italian Institute for Environmental Protection and Research (ISPRA), which was tasked by the CMRE. The experiment considered in this paper took place on November 24th-25th, 2018. The eFolaga AUV was deployed from N/O Astrea.

4. SELECTION OF EXPERIMENTAL RESULTS

A selection of results obtained by applying the described processing to data collected during the LCAS'18 experiment is reported. In addition to the vector sensor, the eFolaga AUV was equipped with an EvoLogics acoustic modem working in the frequency range 17 - 34 kHz. Furthermore, an EvoLogics USBL modem was deployed and towed from N/O Astrea in order to track the vehicle during underwater navigation. The vehicle also hosted an Idronaut CTD multiparameter probe to collect environmental data necessary to predict the propagation of sound in water.

4.1. PROCESSING THE SINGLE CAS-PAS SIGNAL

On November 24th, 2018, the NRV ALLIANCE towed a sonar source which was transmitting a CAS LFM in the bandwidth 1800 – 2600 Hz with a duration of 20 seconds and a Pulse Repetition Time (PRT) of 20 seconds. At the same time, the source was transmitting a PAS signal in the band 2.7 – 3.5 kHz with 1 second of duration. The PRT was the same. Fig. 1 (left) shows a photo of the vehicle during the deployment. An example of sound speed profile measured on November 25th is shown in Fig. 1 (right). It can be seen the profile is almost iso-velocity.

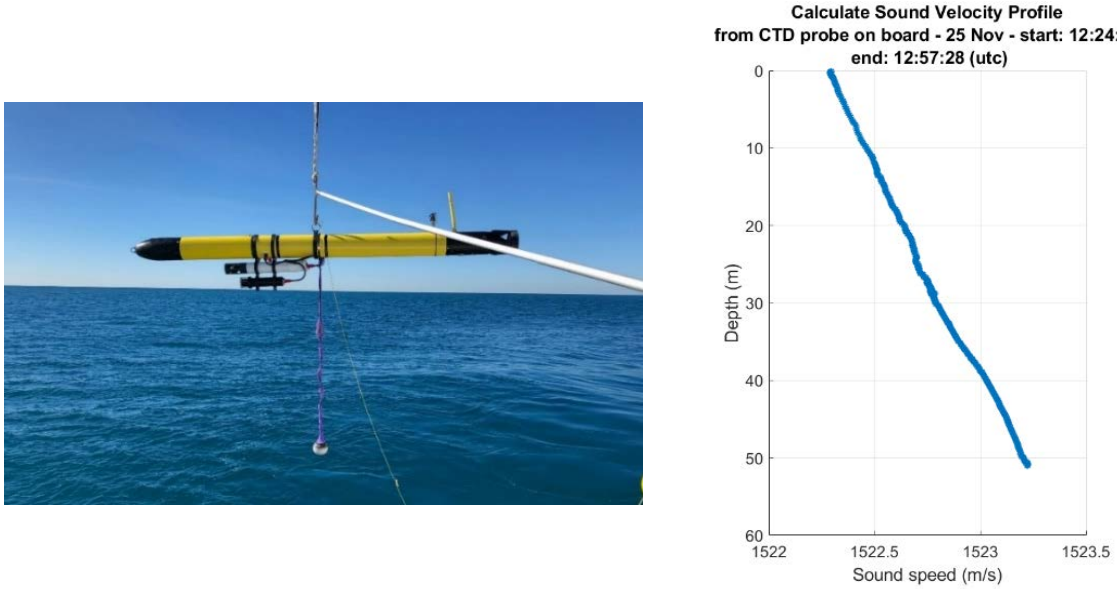


Fig. 1: (Left) Vehicle deployment. The two payloads: acoustic modem and acoustic vector sensor, are clearly visible. (Right) Sound Speed Profile measured from the CTD probe on board the vehicle.

A single CAS and PAS pulse has been selected in order to evaluate the detection and bearing performance of the developed system, applying both frequency and time-domain algorithms. The vehicle was on the surface during the data acquisition, waiting for a mission command by an operator. The acquired signal was filtered in the band 1.8 – 2.6 kHz for CAS signal and 2.7 – 3.5 kHz for the PAS. First, estimates were obtained in the frequency domain using (5) on the whole 20 seconds block of signal. If the calculated Signal to Noise Ratio (SNR) in the block was less than 5 dB the estimate was not considered. In order to reduce the number of estimates, we just considered one sample in a 1 Hz band, if detected. Figure 2 represents the estimates

obtained for the CAS signal emitted by the source on board Alliance, which was underway at 3.5 knots at an average distance of 12430 meters from the vehicle. The source can be considered static in the 20 seconds block of data. It can be seen that using the frequency domain estimator it is possible to obtain estimates reliable with the reference ground truth.

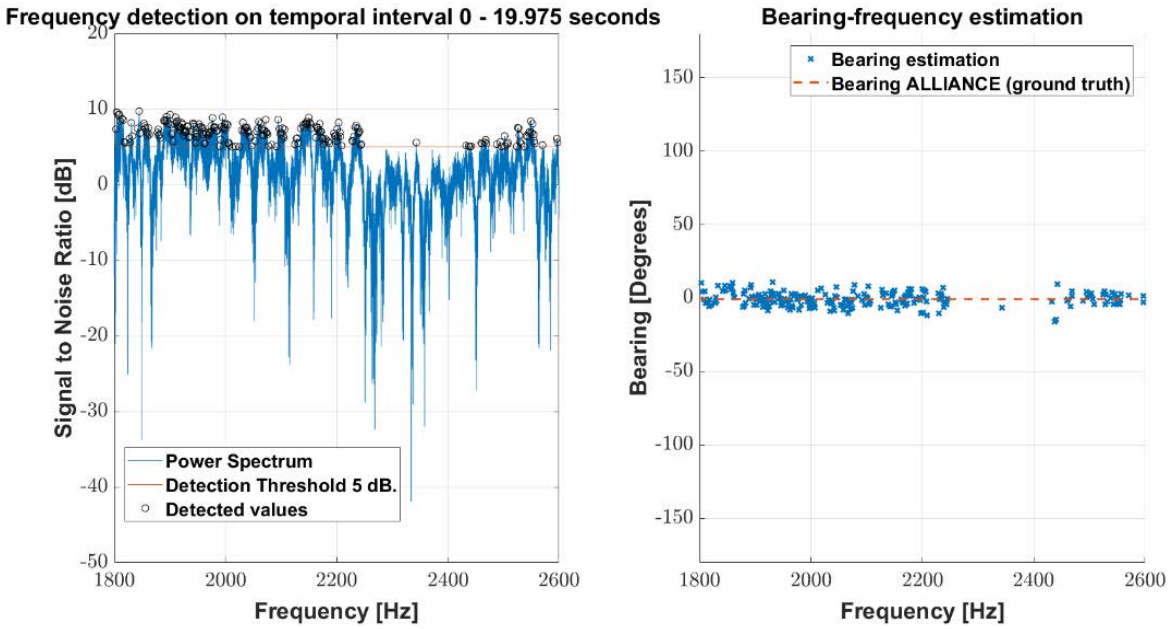


Fig. 2: (Left) Signal to Noise Ratio on the Omni sensor. (Right) Bearing-frequency estimates of a single CAS waveform.

Then we applied the described algorithm from (4) to estimate the bearing of the source in the time domain. Only one detection (if successful) per 0.5 seconds data block was considered. Figure 3 shows the obtained results:

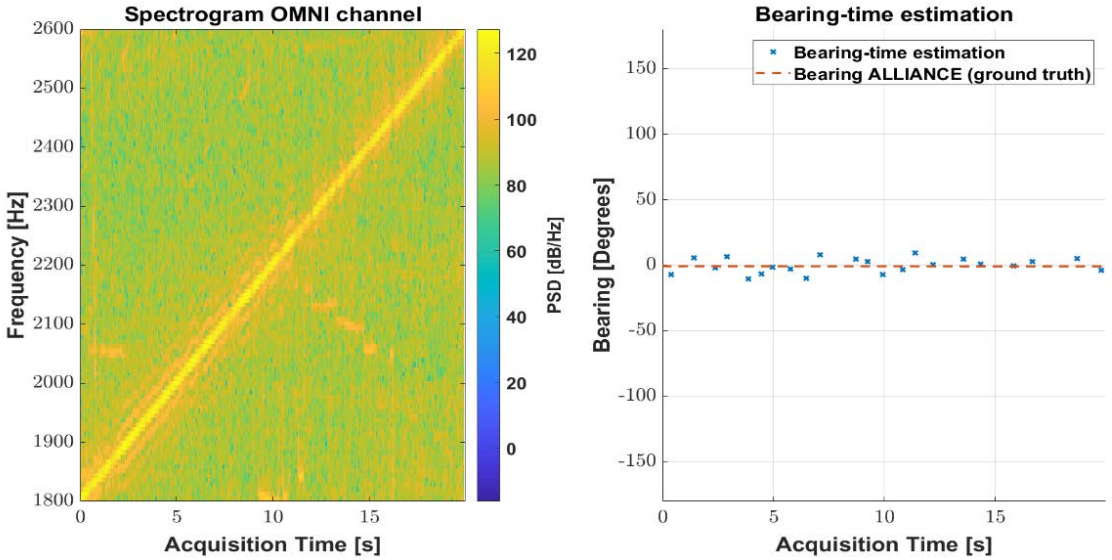


Fig. 3: (Left) Spectrogram of the received signal in which the CAS signal is clearly visible. (Right) Bearing-time estimates of the single CAS.

The same processing was applied to the PAS signal and finally, sub-band processing was applied to the CAS. The sub-bands were obtained by band-pass filtering the FFT of the signal of interest with the duration of the temporal blocks being proportional to the bandwidth. Each

sub-band was processed by a threshold detector as in the case of single signal. Table 1 summarizes the achieved results.

Number of Sub-bands	1	1	2		4			
ID	Single PAS	Single CAS	Sub-band CAS nr.1	Sub-band CAS nr.2	Sub-band CAS nr.1	Sub-band CAS nr.2	Sub-band CAS nr.3	Sub-band CAS nr.4
Time block length [s]	1	20	10	10	5	5	5	5
Frequency Start [kHz]	2.7	1.8	1.8	2.2	1.8	2.0	2.2	2.4
Frequency End [kHz]	3.5	2.6	2.2	2.6	2.0	2.2	2.4	2.6
Detection Threshold [dB]	5	5	5	5	5	5	5	5
Nr. Detections (time domain)	2	22	12	12	6	6	5	5
Nr. Detections (frequency domain)	85	232	122	89	43	55	35	35
Mean bearing-time error [degrees]	4.64	0.58	0.13	-0.02	-1.70	-1.22	-0.75	1.00
Mean bearing-freq. error [degrees]	5.35	0.1	-0.85	-0.02	-0.27	-1.73	-0.66	0.68
Std dev error time domain [degrees]	5.09	5.85	2.26	2.07	3.58	2.32	2.45	0.96
Std dev error frequency domain [degrees]	5.01	4.68	3.24	3.29	3.10	2.05	2.68	1.59

Table 1: Statistical indices of the applied processing on CAS, PAS, and sub-bands of a CAS.

The results are very promising in terms of bearing error especially when considering the large source-receiver distance and the oscillations of the sensor due to the vehicle's surface drift. Applying sub-band processing on the CAS waveform, results in an improvement in terms of standard deviation error with respect to the first case, both in time and frequency domain. This could be attributed to the higher SNR obtained on each sub-band; analysis over a shorter time duration was probably accompanied by smaller movements of the DIFAR sensor, effectively improving bearing estimates.

4.2. THE EFFECTS OF VEHICLE NAVIGATION ON DATA-PROCESSING

On November 25th, 2018, the NRV ALLIANCE, underway at 4.2 knots, with the source at 80m depth, transmitted a CAS LFM in the band 1800 – 2600 Hz with a duration of 18 seconds and a Pulse Repetition Time (PRT) of 20 seconds. The Alliance track is shown in figure 4.

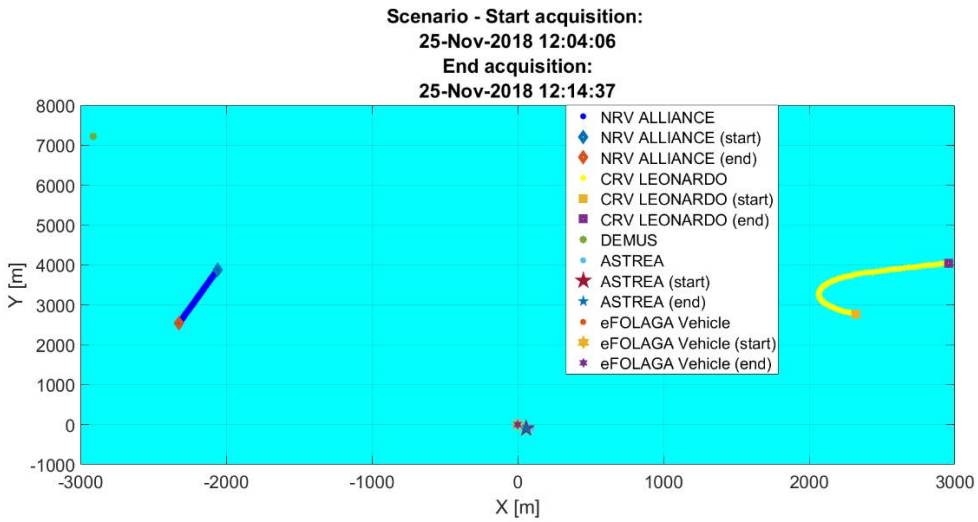


Fig. 4: Scenario of the selected experimental results. The vehicle is at the origin of the reference system. The blue trace is the NRV Alliance track which was towing the sound source.

Processing was accomplished by filtering the DIFAR signal in the sub-band 1800 – 2600 Hz in order to analyse the CAS signal. The distance between the vehicle and the Alliance varied between 4395 and 3443 meters, while the relative bearing with respect to the vehicle varied between 332 and 317 degrees. Detection contacts were extracted from the data (by applying (4)) when the SNR of the omnidirectional channel exceeded a threshold of 5 dB. Figure 5 (top) shows the extracted detection contacts and its bearings. The eFolaga tasks are shown in figure 5 (bottom) while it was acquiring the data. The vehicle started from the surface in a stationary mode, then it varied its buoyancy to reach a depth of 30 meters and started to perform gliding navigation between 30 and 50 meters.

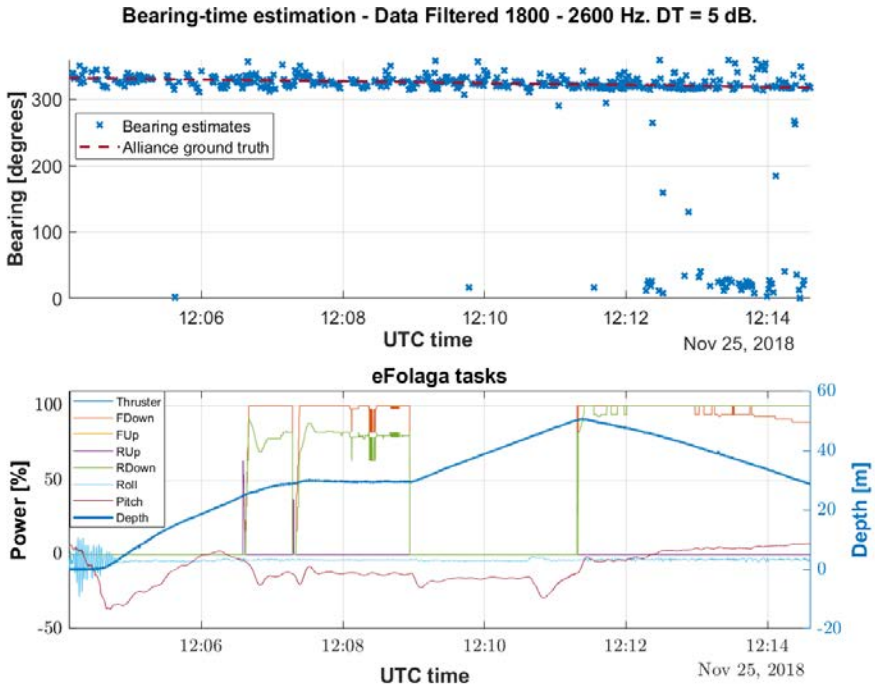


Fig. 5: (Top) Detection contacts and associated bearings. (Bottom) The eFolaga tasks while acquiring data.

At 12:11:30 (UTC) the vehicle activated the pumpjet in order to return to the surface, leading it to assume a positive pitch angle. This could have compromised subsequent bearing estimates, producing significant outliers. In addition, the ground truth was obtained from the Alliance GPS

and the last GPS fix of the vehicle when on the surface, due to the absence of transponder fixes in the temporal block considered. Considering the results before 12:11:30, there are 300 detections, with a mean bearing error of 0.6 degrees and a standard deviation of 19.6 degrees. Applying the sub-band processing in the range 1.8 - 2.2 kHz and 2.2 - 2.6 kHz and considering the same temporal length of the signal, we obtained a standard deviation error of 11.9 and 7 degrees respectively for the first and second sub-band signal. A mean bearing error for each sub-band of -2 and -2.7 degrees was observed. In this case, the detection events are respectively 213 and 188.

5. CONCLUSION

This paper discussed the capability of an AUV mounted vector sensor to estimate the bearing of real sources in a multistatic scenario. Time and frequency domain implementations of bearing estimation have been presented. It has been demonstrated, with field data, that a vector sensor integrated into an AUV is able to track different types of low frequency sources, while drifting on the surface and also during subsurface gliding navigation. Furthermore, the equipment used in the acoustic payload are of low cost and the implemented methods have low computational demand, making them suitable for use in real-time processing.

ACKNOWLEDGEMENTS

The authors would like to thank everyone involved in the LCAS'18 sea-trial, including the crew of the N/O Astrea whose professional skills made possible to work in synergy with all the deployed assets. They would also like to thank the engineering department and scientists of the CMRE which supported the implementation of the acoustic payload on board the eFolaga, supplying possible data-processing strategies. Finally, they thank all the SEALab members who helped the team during the missions at sea.

REFERENCES

[1] **P. Felisberto, P. Santos, S. M. Jesus,** "Tracking Source azimuth Using a Single Vector Sensor", In *Fourth International Conference on Sensor Technologies and Applications*, pp. 416 – 421, 2010.

[2] **A. Tesei, R. Been, D. Williams, et al.,** "Passive acoustic surveillance of surface vessels using tridimensional array on an underwater glider", In *OCEANS 2015*, Genova, pp. 1–8, May 2015.

[3] **A. Caffaz, A. Caiti, V. Calabrò, et al.,** "The enhanced Folaga: a hybrid AUV with modular payloads", in G.N. Roberts, R. Sutton (Eds.), *Further Advances in Unmanned Marine Vehicles*, IET, pp. 309 – 330, 2012.

[4] **A. Raganowicz, M. Rudnicki, R. Salamon**, "Processing the complex signal in the acoustic processor of a sonobuoy system", *Hydroacoustic*s, Vol. 8, pp. 163 – 170, 2005.

[5] **B. H. Maranda**, "The statistical accuracy of an arctangent bearing estimator", *in proc. IEEE Oceans Conf.*, vol. 4, pp. 2127–2132, 2003.

[6] **B. H. Maranda**, "Calibration Factors for DIFAR Processing", *Technical Memorandum, Defence Research Establishment Atlantic*, Nov. 2001.

HIGH DUTY CYCLE SONAR TRACKING PERFORMANCE AS A FUNCTION OF COHERENT PROCESSING INTERVAL FOR LCAS'15 DATA

D. J. Grimmett[a], J. J. Itschner[a], D. A. Abraham[b], L. Mazutti[a]

[a]NIWC Pacific, 53560 Hull Street, San Diego, CA, 92131, grimmett@spawar.navy.mil
[b]CausaSci LLC, P.O. Box 627, Ellicott City, MD 21041, UA, abrahad@ieee.org

***Abstract*:** *High Duty Cycle (HDC) sonar transmits with nearly 100% duty cycle. For LFM waveforms, this yields very large time-bandwidth products, with signal bandwidth swept over the entire transmission's ping repetition interval (PRI). In receive data processing, the PRI may be split up into shorter coherent processing intervals (CPIs), providing multiple detection opportunities per PRI. The potential advantage is an increased number of near continuous detection opportunities, leading to improved target localization, tracking, and classification, due to there being less time lapse between measurement scans. The corresponding disadvantage is that probability of detection and ranging accuracy may be lower per individual CPI detection opportunity. The choice of CPI for HDC sonar will influence detection and tracking performance.*

In this paper, the choice of CPI is evaluated using sonar data collected during the Littoral Continuous Active Sonar 2015 (LCAS'15) sea trial for a non-maneuvering surrogate target. A processing chain, including target tracker, is used to evaluate performance as a function of CPI. Typical track initiation algorithms (TIA) require setting parameters like SNR threshold and an M-of-N observation sequence to control the false track rates typical of clutter-rich environments. Previous analysis has been performed with fixed tracker parameters across different CPI settings, but here, we follow a more fair and operationally relevant comparison approach by specifying constant operationally relevant parameters for all cases, and by optimizing the tracker initiation M-of-N parameters for each individual case. Processing metrics such as probability of detection, and false alarm rate, as well as tracking metrics such as track-hold time, false track rate, and localization accuracy are reported. The relative advantages and disadvantages of reducing CPI are analyzed and explained for this dataset using these metrics at the output of a tracker.

***Keywords**: Continuous Active Sonar, Tracking, Bandwidth, Sonar, High Duty Cycle*

1. INTRODUCTION

Recently, there has been emerging interest in the concept of High Duty Cycle (HDC) Sonar. Unlike Pulsed Active Sonar (PAS), which listens for echoes in between short transmission bursts, HDC sonar attempts to detect echoes amidst the continual interference from source(s) transmitting with nearly 100% duty cycle. Like PAS systems, HDC sonar systems may employ a variety of signal types. In this paper, we focus on the evaluation of continuous-time linear frequency modulated (CTLFM) waveforms for run E14 of the Littoral Continuous Active Sonar 2015 (LCAS'15) seatrial. HDC sonar offers a new parameter for the receiver signal processing chain: the coherent processing interval (CPI), which also corresponds to an equivalent processing sub-bandwidth of the LFM sweeps. The performance of HDC sonar is assessed as a function of the various user-selected processing intervals/sub-bandwidths, at the output of a target tracker. Previous efforts [1] compared performance using fixed tracker parameters, like SNR thresholds and track initiation logic. In this paper, we make comparisons by using optimum values for the track initiation algorithm (TIA) per CPI case, and tuning the tracker SNR threshold to achieve a constant false track rate at the output of the tracker. Various metrics are computed and compared at the input and output of the tracker.

HDC processing is discussed in Section 2. Section 3 describes the LCAS'15 experiment. Section 4 discusses the processing method and section 5 shows results at the tracker output. Section 6 provides a summary and conclusions.

2. HIGH DUTY CYCLE PROCESSING

Both PAS and HDC waveform signals repeat with a cycle time, referred to as the ping repetition interval (T_{pri}). T_{pri} defines the maximum range at which targets are detectable without becoming obscured by or ambiguously associated with acoustic energy from previous waveform cycles. For the HDC LFM waveform, the signal sweeps across the entire available bandwidth over the duration of the T_{pri}. This enables very large time-bandwidth (TB) products: an order of magnitude or more than is typically available with a corresponding PAS waveform with the same T_{pri}. Theory suggests that increasing the time-bandwidth (TB) product in processing will improve resolution in the time and/or Doppler dimensions and thereby increase the SNR in reverberation and/or noise-limited conditions, respectively. This is done by reducing the acoustic background, either by increasing the signal duration (to reduce ambient noise) or by increasing the signal bandwidth (to reduce reverberation), or both, while leaving the signal level un-diminished. However, in practice, achieving such theoretical gains is not entirely realizable due to environmental multipath spreading (energy splitting loss), echo Doppler shift and echo distributions of extended (non-point) targets [2,3].

Alternatively, one may choose to successively process multiple smaller TB segments of the entire waveform cycle. In this case, the individual echo SNRs may be smaller, but it offers many more opportunities to detect with rapid update rate, potentially providing good performance at the output of a target tracker. HDC sonar offers this new processing parameter (not available with PAS), specified as the coherent processing interval/time (CPI), and denoted hereafter as $T_{p.}$ For LFM signals, T_p corresponds to a sub-bandwidth, B_p; these may be chosen to tune the performance of the sonar. T_p can be chosen within the bounds of: $0< T_p \leq T_{pri.,}$ (corresponding to $0<B_p<B$). The choice will be a trade-off between how much TB to use for echo SNR gain vs. the desired number of detection opportunities available within a single $T_{pri.}$ Fig. 1 (left) shows an example of the HDC processing interval. A common processing approach is to set up a bank of matched filters; one matched filter for each of the

selected sub-bands within a single cycle of the HDC LFM waveform. The sub-bands may be overlapped (in time/bandwidth) by about 50%, further increasing the number of detection scan opportunities, while maintaining measurements independence. Achieving more detection opportunities with a higher update rate can provide improvements in cumulative probability of detection, target initiation and holding, and target localization [4].

3. LCAS'15 EXPERIMENT

The LCAS'15 sea trial was conducted in September 2015, in shallow waters off the coast of La Spezia, Italy, in conjunction with an international research project with the Centre for Maritime Research and Experimentation (CMRE). Water depths ranged from 100-200m and reverberation-limited conditions were predominant. The research vessel R.V. Alliance towed an acoustic source capable of PAS and HDC transmissions over the frequency band of 1800-3400Hz. It also towed a monostatic triplet hydrophone receiver array. The R.V. Leonardo ship towed an echo repeater (E/R) system, which repeated the received HDC signals as a surrogate target.

The right hand image of Fig. 1 shows the geometry for run E14, which is analysed in this paper. The R.V. Alliance track is shown with heading of 122°T and speed of 3.5 kts, with the sonar source & receiver deployed at 50 meters depth. The E/R track is shown, traveling with heading 145°T at 3.2 kts. The run was designed to have the E/R at nearly constant bearing (63° T) relative to the source during the entire 1.3 hour run, with a target range-rate of -0.63 m/s (-1.2 kts). The transmitted signal was an LFM upsweep from 1800-2600Hz (B=800Hz) over 20 seconds, and repeating every 20 seconds (T_{pri}=20s). The E/R has a selectable target strength (TS), which is the amount of amplification that is applied to the repeated signal. For this data, the TS was set to 17 dB. The FORA receive array is a triplet array, which provides port/starboard discrimination of received acoustic energy. The received hydrophone data were beamformed by an on-board processing system in real-time.

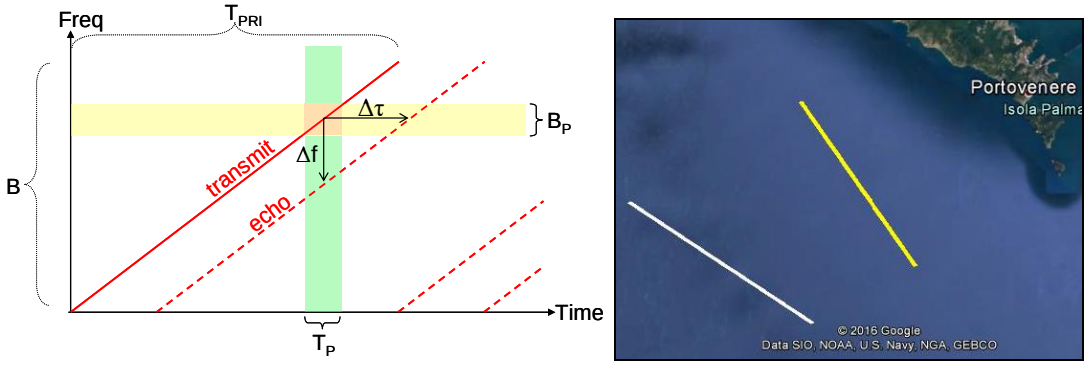


Fig. 1: Left-- Depiction of processing interval (green) and corresponding sub-band (yellow) for a continuous-time LFM signal in time and frequency. Right-- Geometry for run E14 of the LCAS'15 seatrial; Alliance (white) and E/R (yellow) tracks.

4. PROCESSING METHOD

HDC processing was accomplished using a bank of matched filters. The members of the replica bank correspond to a set of selected processing sub-bands, each with a bandwidth B_p at stepped-up center-frequencies to cover the total available signal bandwidth (B). The corresponding duration of each of the matched filter replicas is the processing time, T_p. In this paper, we evaluated the choice of T_p and B_p as a parameter, for the cases shown in Table 1. Also, the sub-bands were overlapped by about 50% in frequency (and equivalently

in time) to increase the detection scan rate, while still maintaining sample independence. The overlapping was not possible in the case of T_p=20s, because the sub-band cannot cross the T_{pri} boundary.

The matched filtering is applied to each of the processed beams, and the outputs of the replica bank are time-aligned to create a multi-scan detection image with echo time-delay forming the x-axis and scan time the y-axis. An example output is shown in Fig. 2 (left) for the single beam pointed at the target, where the direct blasts are clearly seen near zero seconds time delay. The target echoes are seen with decreasing time delays from 10-6 s, over the duration of the run. Each matched filtered beam of the data was processed with a one-dimensional split-window normalizer in time, with guard and noise bands of 0.2 seconds length. Detection contacts are extracted from the data by clustering any time-contiguous data exceeding a threshold of 10 dB, and with at least one excursion above a higher threshold of 12 dB. Temporal detection clusters from adjacent beams were clustered if their time-extents overlap. The resulting information extracted from the detection clusters contain the arrival time and beam angle of the echo peak, time- and beam-extents of the detection cluster, and peak signal-to-noise ratio (*SNR*). Fig. 2 (right) shows extracted detection contacts for all beams. Using truth reconstruction, we determine which of the contacts that are associated to the target and tag them, enabling the computation of various performance metrics.

	Case 1	Case 2	Case 3	Case 4	Case 5	Case 6	Case 7
T_p (sec)	1.25	2.5	3.33	5	6.67	10	20
B_p (Hz)	50	100	133	200	267	400	800
Overlap (%)	50	50	50	50	50	50	0
#scans/T_{pri}	31	15	11	7	5	3	1
N (scans in T_d)	95	47	35	23	17	11	3
K (scans)	95	47	35	23	17	11	3
M (scans)	32	21	18	13	11	8	2
h (dB)	14.13	15.15	15.3	15.7	15.5	15.6	19.25

Table 1: Test case processing intervals/sub-bands and tracker parameters.

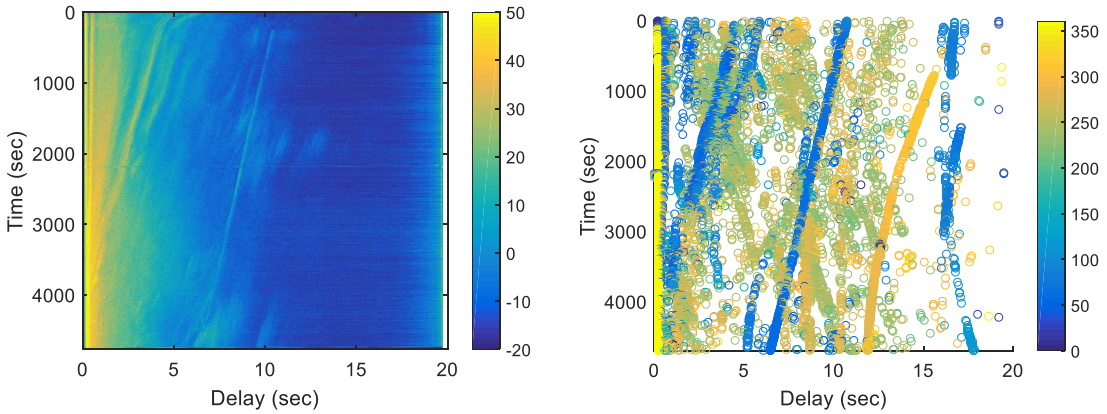


Fig. 2: Left-- Example HDC processing output for the target-pointing beam (T_p=3.33), output level in dB (in color) vs. scan-time vs. echo delay time. Right-- Example of extracted detection contacts above 15.5 dB, bearing (in color).

The processing was performed for each of the cases listed in Table 1, producing sets of detection contacts, per scan. A statistical analysis of the detection contacts for this data for different T_p cases has been done previously [1]. This showed that mean signal-to-noise ratio values increase somewhat with increasing T_p, but not to the extent predicted by theory. This is due the limitations in maintaining signal coherence in the acoustic channel due to time spreading/multipath [2,3].

5. TRACKING COMPARISONS

After the detection contacts were formed, they were input into a kinematic multi-target tracker [5]. We employ a simple but common track initiation algorithm (TIA). Tracks are confirmed by successful kinematic association of M detections above the tracker threshold h, within N sequential scans of the input data. Tracks are terminated after K consecutive scans where association was not successfully made.

In a previous analysis, comparative tracker performance (as a function of T_p) was obtained [1], however, it used fixed track initiation parameters (M, N, K, and h) for all cases. This may not be the most appropriate comparison method. In this paper, we choose to evaluate tracker performance using a different methodology which is better tied to operational requirements as follows: 1) we specify a constant, fixed time for track initiation, T_d, applicable to all cases, which results in a different N for each case, 2) we use a method [6,7] to determine an optimum setting of M, given N, for each case independently, and, 3) we specify a constant output false track rate (FTR) for all cases using the given M and N, and achieve it by adjusting the tracker input threshold h. For this study, we have chosen a track initiation time of T_d=60s (three times the T_{pri}). From this operational specification, the N values are derived consistent with 50% overlapping for each case. To simplify analysis, we have chosen the track kill parameter K to be equal to N. Optimum values of M were obtained from the method in [7], and the required levels of h were ascertained from iterations of tracker runs to achieve a constant $FTR \approx 22$ tracks/hr (which is ~30 tracks for the run duration), using those M and N values. All final parameters used for the tracking comparison are summarized in Table 1, and the results will now be presented, using various standard tracker metrics [8].

Fig. 3 (top left) shows the tracker input FAR (for contacts which are not tagged as originating from the target and above h), which is seen to increase exponentially with decreasing T_p, due to the increases in the number of detection scans. Also shown is the tracker output FTR, which does not include any of the "true" target track segments (identified by having a majority of their tracker updates being supplied by true target-tagged contacts). It is seen that the tracker achieves FTRs close to the specified 22/hr for all the T_p cases.

Fig. 3 (top right) shows the tracker input probability of detection (PD) as a function of T_p for the target tagged contacts above h. Input PD is computed as the ratio of the number scans detecting the target to the total number of scans. To better assess the limits of performance, the target-tagged contact SNRs were decremented by various amounts in post analysis and the tracker was re-run. This enables extension of comparisons to more challenging detection conditions not present in this data. The decrement values were 0, -2, -4, -6, -8, and -10 dB. The figure shows that better input PD is obtained around T_p =5-10 s, with it dropping at lower and higher T_p values. As the decrementing is applied, the input PD drops as expected until we reach a point where very few detections will be available for tracking the target.

Fig. 3 (bottom left) shows the PD at the output of the tracker. This is computed as the ratio of the number of scans contributing to true target tracks (including coasts) divided by the total number of scans. It may be thought of as the percentage of track holding time. The results show an expected drop in output PD as the target-contacts are decremented. The data show that PD is somewhat flat across many values of T_p, except at the lowest T_p case (1.25s) where

it is better, and at the highest T_p case (20s) where it is worse. The tracker appears to better improve PD (from input to output) for the lower T_p cases.

The tracker localization performance can be characterized by the mean track estimation error (estimated values versus true values) and by the area-of-uncertainty (AOU) within which the target exists with a certain probability. To quantify the AOU over the scenario duration and enable comparison between different contacts sets, we computed the mean of the cumulative sum of target track AOU over time, with a 99% probability of target containment. The mean localization error and AOU calculations are shown in Fig. 3 (bottom right), for the case without SNR decrementing. It is seen that there is a clear trend that both localization and localization uncertainty performance is greatly improved with shorter $T_{p,}$.

Fig. 4 shows the output plots of the tracker for each T_p case, where target SNRs were decremented by 4 dB. We see an equivalent number of approximately 22 false tracks per hour in each case, consistent with our operational specification. The true target tracking performance degrades with increased T_p, by the decrease in the percentage of track holding. In addition, there is an increase in tracker fragmentation resulting in multiple tracker output segments for the target, from no fragmentations for T_p=1.25 s to 4 fragmentations for T_p=20 s. Here the track segments are killed and sometimes reinitiated and this is another undesirable tracker behaviour to consider for performance. The false tracks show some consistency across cases, indicating that they are commonly viewing acoustic energy from clutter objects and/or environmental features producing it. False track's lengths tend to be longer with the lower T_p cases, consistent with the larger values of N and K used.

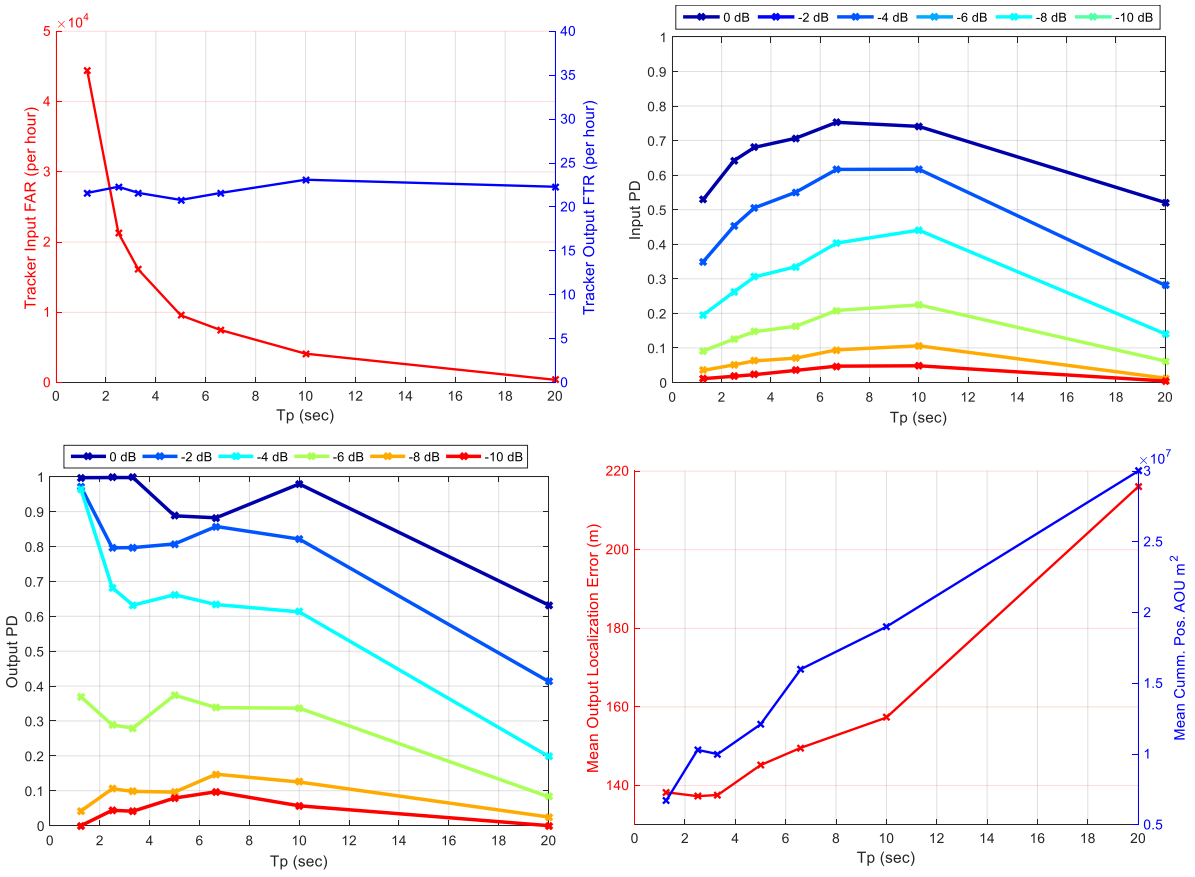


Fig. 3: Tracker metrics as a function of T_p. Top Left-- Tracker input false alarm rate (FAR) and tracker output false track rate (FTR) with no SNR decrement; Top Right-- tracker input probability of detection (PD) with various levels of decrementing; Bottom Left-- tracker output probability of detection with various levels of decrementing; Bottom Right-- tracker mean localization error and estimation uncertainty.

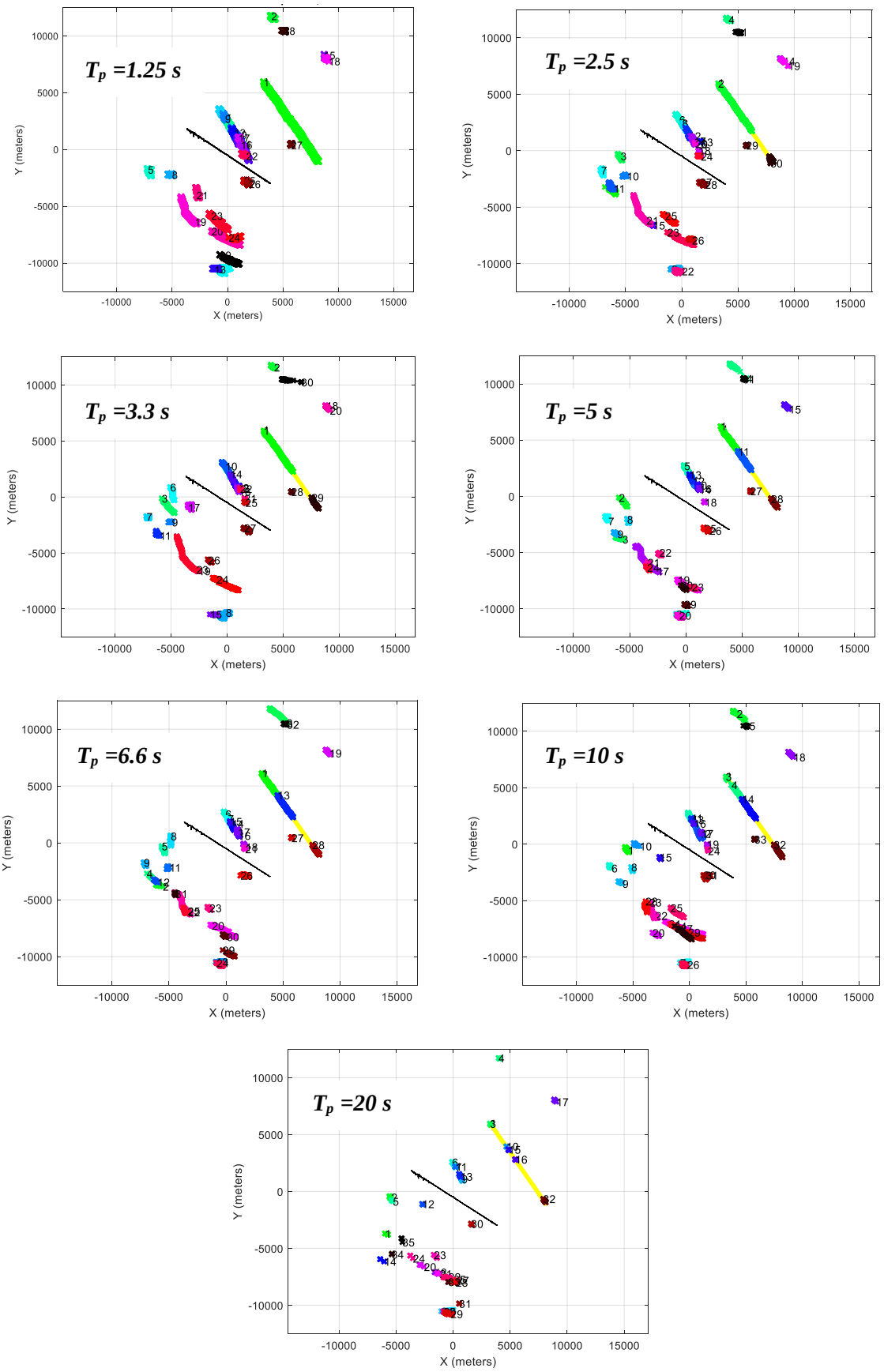


Fig. 4: Tracker output for the various T_p cases with ~30 output tracks; true target trajectory (yellow), ship trajectory (black), output tracks (numbered, with various colors).

6. SUMMARY AND CONCLUSIONS

The analysis of the LCAS'15 data offers insight into the tracking performance of HDC sonar as a function of a key new parameter: the HDC coherent processing interval, CPI (or T_p, or B_p). This parameter was investigated using a complete processing chain including kinematic tracker in order to evaluate processing chain end-to-end performance. The comparison approach was to specify the track initiation time and compare performance with constant output *FTR*, while optimizing the choice of *M*. The results show better tracking performance at lower values of T_p, in terms of target track holding, localization accuracy and localization uncertainty. The increased number of detection opportunities provided by shorter T_p offers improvement in localization. The tracker enhances the PD at lower T_p more than at high T_p. This comparison methodology may also be applied to evaluate how consistent performance is for different operational parameters (T_d and *FTR*).

7. ACKNOWLEDGEMENTS

We acknowledge the NATO CMRE LCAS Multinational Joint Research Project participants for their resources and support and in the planning, execution and analysis of this trial. Funding for this work was provided by ONR 321US.

REFERENCES

[1] **D. Grimmett, R. Plate**, High Duty Cycle Sonar Performance as a Function of Processing Time-Bandwidth for LCAS'15 Data, Editor, *in Proc. of the 5th International Conference on Underwater Acoustics*, Skiathos, Greece, July 2019.

[2] **R. Plate, D.J. Grimmett**, High Duty Cycle (HDC) Sonar Processing Interval and Bandwidth Effects for the TREX'13 Dataset, *Proc. of the MTS/IEEE Oceans'15 Conference,* volume (number), Genova, Italy, May, 2015.

[3] **D. Grimmett, R. Plate**, Temporal and Doppler Coherence Limits for the Underwater Acoustic Channel during the LCAS'15 High Duty Cycle Sonar Experiment, *Proc. of the MTS/IEEE Oceans'16 Conference*, September, 2016, Monterey, CA.

[4] **D. J. Grimmett,** Target AOU Growth Containment using LFM High Duty Cycle Sonar Editor, *in Proc. of the 2nd International Conference on Underwater Acoustics*, Rhodes, Greece, June, 2014.

[5] **S. Coraluppi, D. Grimmett**, Multistatic Sonar Tracking, *in Proc. Of the SPIE Conference of Signal Processing, Sensor Fusion, and Target Recognition XII*, April 2003, Orlando, FL, USA.

[6] **D. Abraham, D. Grimmett, J. Itschner**, Optimizing a Sliding M-OF-N Track Initializer in Clutter, Editor, *in Proc. of the 5th International Conference on Underwater Acoustics*, Skiathos, Greece, July 2019.

[7] **D. Abraham,** Optimization of M-of-N in heavy-tailed noise. In Proceedings of 2018 IEEE/MTS Oceans Conference, Charleston, SC, 2018.

[8] **S. Coraluppi**, D**. Grimmett, and P. de Theije**, Benchmark Evaluation of Multistatic Trackers, in *Proceedings of the 9th International Conference on Information Fusion*, July 2006, Florence, Italy.

OPTIMIZING A SLIDING M-OF-N TRACK INITIALIZER IN CLUTTER

Douglas A. Abraham[a], Douglas J. Grimmett[b] and Jonathan J. Itschner[b]

[a]CausaSci LLC, P.O. Box 627, Ellicott City, MD 21041, USA, abrahad@ieee.org
[b]SPAWAR Systems Center Pacific, 53560 Hull Street, San Diego, CA 92152, USA, grimmett@spawar.navy.mil

Abstract: ***In active sonar applications with moving targets, objects are tracked by associating and combining single-ping measurements (clusters) over short segments of time and space. A common track initialization algorithm (TIA) requires observing M single-ping clusters across any N consecutive pings within a local search region. Design of this TIA is straightforward when the background consists of false alarms (clusters) occurring randomly in the search space, but less tractable in the more realistic scenario of clutter tracks formed on echoes of physical objects (e.g., rock outcrops, fish schools, etc.). In this paper, a process is described for optimizing the sliding M-of-N TIA by choosing M and N to optimize target detection performance while using the cluster decision threshold to maintain a desired false-track rate in the presence of clutter events having a random duration. An example design is shown for a high-duty-cycle system with different coherent processing intervals. Although these result in different values of N, simulation testing illustrates how the design produces the desired false-track rate.***

Keywords: *tracking, track initialization, false-track rate, sliding M-of-N detector*

1. INTRODUCTION

The first step in many target tracking algorithms is to initialize tracks by associating and combining measurements over small regions of space and time. These track initialization algorithms (TIAs) typically use simple motion models and start tracks when the associated data satisfy a detection criteria. For example, it can be required that a measurement be observed within the tracker search gate in M of any consecutive N temporal updates [1, Sect. 3.6.2], which is known as a *sliding M-of-N* detection criterion. Design of the sliding M-of-N TIA entails choosing M, N, and the decision threshold (h) applied to form measurements at each update. Ideally, M and N are chosen to minimize the signal-to-noise power ratio (SNR) required to achieve a desired detection performance and h is chosen to achieve a desired false-

track rate (FTR) given M and N. In practice, M is often the only parameter chosen to optimize performance. When false alarms are dominated by clutter rather than diffuse background, the decision threshold h is typically chosen through trial-and-error to manage the quantity of clusters in each update without regard to M and N. If an average target track duration is known, it can be used to obtain N. When it is not, N is usually chosen heuristically to balance between robustness to signal fading (large N) or target maneuvers (small N). Although it is practical, this design process generally does not result in a constant false-track rate and is more complicated for high duty cycle (HDC) systems with sub-pulse processing [2,3] where the update rate (and therefore N) varies with the coherent processing interval (CPI).

In many scenarios, false tracks arise from physical objects within the scene (e.g., rock outcrops or fish schools in active sonar) rather than randomly occurring false detections arising from diffuse reverberation and noise. To handle the more realistic scenario, a design process is presented in this paper for the sliding M-of-N TIA by representing the occurrence of clutter events with a two-state Markov random process. The clutter-event model is presented in Sect. 2, along with the probability of the sliding M-of-N TIA detecting a clutter event, the average time between false tracks, and the proposed design process. A key requirement in the design is accurate modeling of the measurement decision statistic (typically the cluster peak normalized intensity). Although not presented, the generalized Pareto distribution (GPD) is used to characterize the thresholded cluster peak normalized intensity as was done in [4, 5]. In Sect. 3 optimization of the sliding M-of-N TIA is illustrated with an HDC application entailing different values of N and a simulation analysis used to demonstrate how the design process controls the rate of false tracks.

2. MODELING AND OPTIMIZING TRACK INITIALIZATION

Standard active sonar signal processing includes matched filtering the time series measured in each beam, normalization of the instantaneous intensity by the average background power, and application of a decision threshold to identify data that differs in power level from the background. The set of range/bearing points exceeding the decision threshold are then clustered prior to track initialization. The track initialization algorithm (TIA) associates clusters over multiple consecutive updates when they are consistent with an initial motion assumption (e.g., nearly constant velocity). With respect to cluster detection, this is similar to dividing the range/bearing space into a set of fixed regions and thresholding the peak normalized intensity within each. This suggests modeling track initialization as occurring over a number of independent *channels*,

$$N_{r\theta} \approx \frac{\text{\# beams} \times \text{range window}}{\text{cluster beam extent} \times \text{range extent}}, \tag{1}$$

simultaneously being tested for the beginning of a track. The cluster extents in range and bearing may be measured from real data or derived from the clustering algorithm parameters. Under this modeling assumption where the TIA runs separately on each individual channel simultaneously, the FTR required of the TIA is the system-level FTR (number of false tracks per unit time) divided by $N_{r\theta}$.

2.1. False tracks from clutter events

In many scenarios false tracks are produced by clutter arising from spatially isolated physical objects (e.g., rock outcrops, seaweed, or fish schools) rather than randomly occurring thresh-

old crossings from diffuse reverberation or ambient noise. This implies that clutter event clusters do not occur randomly (i.e., uniformly distributed) over time. However, it is reasonable to assume they are uniformly distributed over the spatial scene and so are equally likely to occur in any tracker channel. Within a given tracker channel, this clutter-event model describes a two-state random process where the data are either from diffuse background or a clutter event.

If the random process is Markovian (i.e., the statistical characterization of a future state can be described by the current state) and stationary, the dwell time in the diffuse-background or clutter-event states is a geometric random variable (using the alternative definition having a minimum of one sample [6, Ch. 23]) with success probability equal to the inverse of the average length. The probability mass function of the length of the ith clutter event (C_i) is then

$$f_{\mathrm{G}}[c; \bar{C}^{-1}] = \frac{1}{\bar{C}}\left(1 - \frac{1}{\bar{C}}\right)^{c-1} \quad \text{for } c = 1, 2, 3, \ldots \tag{2}$$

where $\bar{C}$ is the average length of a clutter event. Evidence supporting the geometric distribution (and therefore the Markov-random-process assumption) is found using data from the NATO Center for Maritime Research and Experimentation's (CMRE's) Littoral Continuous Active Sonar 2015 Experiment (LCAS15; see Sect. 5 for full acknowledgement). The data were processed for detection and through tracking to form a set of clutter tracks as described in [7]. The exceedance distribution function (EDF) of clutter-track length is shown in Fig. 1 as estimated from the LCAS15 data (along with a 90% confidence interval) and using the geometric model while conditioning on the track length being at least 17 updates long (17 was the shortest track length). Except for the shorter track lengths, the fit of the geometric model appears quite good. Note that the distribution of the length of a track produced by a sliding M-of-N detector is approximately geometric at large values (e.g., see the approximation in [8]). To ensure the results shown in Fig. 1 describe the clutter events and are not affected by the tracker, the EDF expected from the track-end logic (which required N consecutive coasts) is also shown using the approximation in [8]. With the length-distribution EDF of the tracker end-logic so close to one, the tracker is expected to produce much longer tracks than that seen in the data if the clutter event were to continue. As such, the clutter tracks are believed to end because the clutter event ends and are not affected by the tracker end logic.

The waiting time B_i before the ith clutter event is also modeled as a random variable. However, because false tracks are assumed to arise during clutter events and not during periods of diffuse background, only its mean $\bar{B}$ is required and no assumptions must be made about its distribution.

2.2. Average time between false tracks

The false-alarm performance metric of interest is the false-track rate (FTR), which is the number of false tracks observed per unit time. The TIA is designed using the inverse of this metric, $F = 1/\mathrm{FTR}$, which is the average time between false tracks. As previously noted, when the TIA operates on a single tracker channel, it is expected to observe a diffuse background interrupted at times by clutter events. In most scenarios false tracks will arise from the clutter events and not the diffuse background. However, the average extents of the background and clutter states should be included when designing the TIA. For example, if the diffuse background is much more prevalent than the clutter (i.e., $\bar{B} \gg \bar{C}$), the TIA can operate aggressively with respect to the desired FTR because it is so often encountering diffuse background and only rarely observes a clutter event.

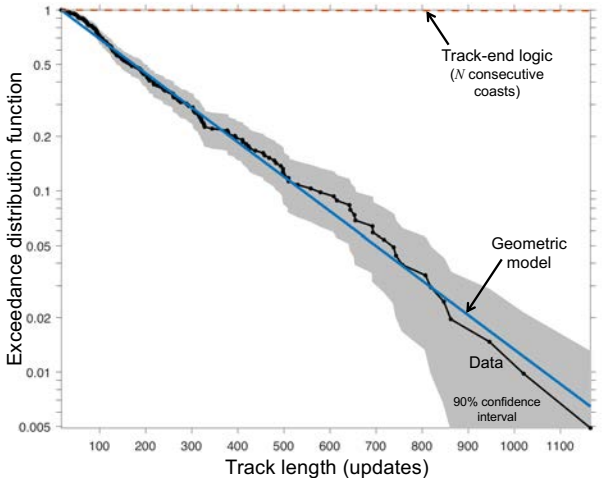


Fig. 1: Estimated and modeled exceedance distribution function of clutter track lengths formed from LCAS15 data with a CPI of $T_p = 5\,s$.

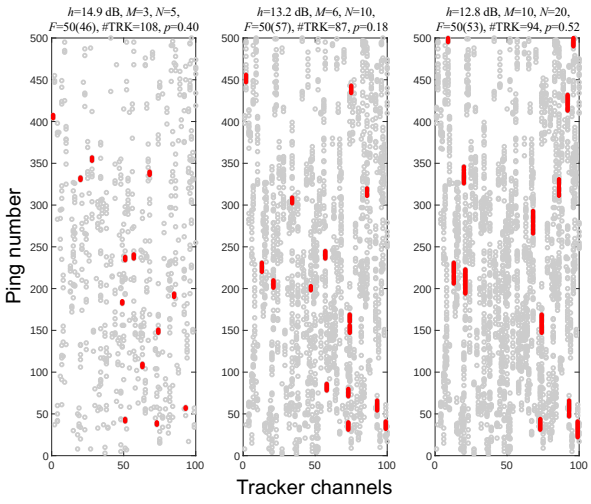


*Fig. 2: Simulated false clusters and tracks for design using $N = 5$, 10, *and* 20 *and an average of* $F = 50$ *samples between tracks.*

Once the ith clutter event occurs, the data feeding the TIA during the clutter event, X_c for $c = 1, \ldots C$, are assumed to come from a distribution $f_c(x)$ so the probability of observing a cluster is

$$p_0 = \int_h^\infty f_c(x)\,\mathrm{d}x, \tag{3}$$

where h is the cluster detection decision threshold. When the sliding M-of-N TIA is applied to these data, the probability of the TIA detecting the clutter event (i.e., producing a false track) within its C_i samples after averaging over the geometrically-distributed C_i can be approximated by

$$P_{\text{ft}} \approx \left\{ \sum_{c=0}^{N} \frac{1}{\bar{C}} \left(1 - \frac{1}{\bar{C}}\right)^{c-1} \left[1 - F_{\text{Bin}}(M-1; c, p_0)\right] \right\} + \left(1 - \frac{1}{\bar{C}}\right)^{N} \left[1 - \frac{\rho \tilde{p}^{N+1}}{\bar{C} - \tilde{p}(\bar{C}-1)}\right] \tag{4}$$

where F_{Bin} is the cumulative distribution function (CDF) of the binomial distribution, $\tilde{p} = (Q'_3/Q'_2)^{1/N}$, and $\rho = [Q'_2]^3/[Q'_3]^2$ with Q'_L depending on M, N, and p_0 as described in [8] (or see [9], [10, eqs. 4.4 & 4.5]). The latter term in (4) exploits Naus' approximation [8] for the probability of a sliding M-of-N test stopping within c samples.

Assuming each clutter event is independent of the others and identically distributed in terms of its length, the probability that the first false-track detection occurs in the ith clutter event is

$$\Pr\{\text{stop in } i\text{th clutter event}\} = (1 - P_{\text{ft}})^{i-1} P_{\text{ft}} \tag{5}$$

for $i = 1, 2, \ldots$, under the assumption that no TIA detections occur during the periods of diffuse background. This implies that I, the random stopping time of the TIA (in units of numbers of clutter events), is a geometric random variable with success probability P_{ft} and PDF as in (2) (replacing $1/\bar{C}$ with P_{ft}). The average number of clutter events before one produces a false track is therefore $1/P_{\text{ft}}$. This can then be used to form the average number of samples between

false tracks in a single tracker channel,

$$F_{\text{1-ch}} = E\left[\sum_{i=1}^{I} B_i + \sum_{i=1}^{I-1} C_i\right] = \bar{B}E[I] + \bar{C}E[I-1] = \frac{\bar{B}+\bar{C}}{P_{\text{ft}}} - \bar{C}, \tag{6}$$

where the beginning of the detected clutter event is taken as the time of the false track. Recall that this is related to the system-level average time between false tracks through $F_{\text{1-ch}} = N_{r\theta}F$.

2.3. Optimizing the track initializer

The objective in optimizing the TIA is to minimize the SNR required to achieve a desired detection performance specification while maintaining a desired false-track rate. If the false-track rate FTR_{h} is in units of false tracks per hour, then the desired average number of updates (e.g., pings or CPIs) between false tracks is

$$F = \frac{3600}{\text{FTR}_{\text{h}} \times T_{\text{up}}} \tag{7}$$

where T_{up} is the time between updates in units of seconds.

In most applications, the temporal extent over which the TIA is operated ($\sim NT_{\text{up}}$) is chosen to balance between robustness to signal fading and target maneuvers and produces a fixed value of N. Systems that vary the update rate yield a range of N over which the optimization must occur. For each value of N and for $M = 1, \ldots, N$, target detection performance must be assessed for a given SNR as follows.

1. Given M and N, find p_0 achieving

$$P_{\text{ft}} = \frac{\bar{B}+\bar{C}}{N_{r\theta}F + \bar{C}} \tag{8}$$

   as a functional inversion of (4).

2. Obtain the decision threshold h producing the desired p_0 as a functional inversion of (3). This requires modeling the clutter-cluster peak normalized intensity, which can be done using the GPD model as described in [4, 5].

3. Evaluate the probability of observing a target cluster as $p_1 = \int_h^\infty f_{\text{t}}(x; S)\,\mathrm{d}x$ for SNR S where $f_{\text{t}}(x; S)$ is the target-cluster peak normalized intensity, which can be approximated through the single-resolution-cell value when SNR is high enough.

4. Assess TIA target detection performance using p_1. Detection performance is quantified by the probability of detection for finite-duration signals or latency for infinite-duration signals.

When optimizing for a *design SNR*, the (M, N) combination maximizing the desired detection-performance measure is chosen. When optimizing to minimize the SNR required to achieve a performance specification, steps 3 and 4 are iterated for the given (M, N) combination to search over SNR until the desired performance is obtained. The (M, N) combination minimizing the SNR required to achieve the performance specification is then chosen.

3. DESIGN EXAMPLES

3.1. TIA optimization

The following parameters have been used to illustrate the design process for a high-duty-cycle active sonar system having a variable coherent processing interval (CPI):

Processing parameters:
CPI and spacing: $T_p = 5$ s or 1.25 s with 50% overlap
Track initialization window: $T_a = 60$ s yielding $N = 23$ or 95
Number of tracker channels: $N_{r\theta} = 1000$
Performance specification:
False-track rate: $\text{FTR}_\text{h} = 10$ per hour
Detection: static $P_d = 0.5$ or 0.9, latency equal to T_a
Signal and clutter modeling:
Signal model: deterministic or Gaussian-fluctuating point target
Clutter-event average length and spacing: $\bar{C} = 120$ s and $\bar{B} = 600$ s
Cluster intensity distribution: GPD parameters as estimated from the data with $h_0 = 12$ dB and coasting probability $q_c(h_0) = 0.6$

The SNR required to achieve each detection performance specification is shown in Fig. 3 for $T_p = 5$ and 1.25 s as a function of M for both signal models. For $T_p = 5$ s (left figure) it is seen that using $M = 10$ for the Gaussian signal required the least SNR to obtain each of the desired operating points (∇'s, solid black for P_d & colored for latency), whereas for the deterministic signal $M = 19$ was best for achieving $P_d = 0.5$ and $M = 18$ for $P_d = 0.9$ or latency equal to T_a. Also shown are the optimal values of M obtained using Shnidman's [11] method (■) and the minimax-optimal value for K-distributed clutter (▲) from [9] using $F = (\bar{B} + \bar{C})/P_\text{ft}$. The SNR loss in using the approximately optimal values of M appears to be small enough (generally < 1 dB, less when N is small) to be useful in practice (e.g., as they are or to initialize a search for the optimal, which may be preferred when N is large). In both design examples, the lower threshold (h_0) caused a limitation in the design at some point as M increased (i.e., the desired p_0 required a threshold $h < h_0$). In both cases, however, the optimal value of M was below the point of limitation. Interestingly, the SNR required to achieve latency equal to T_a (the dots in each figure) was nearly identical to that for achieving a static $P_d = 0.5$.

In comparing the two design cases it can be seen that a lower SNR is required when $T_p = 1.25$ s (~ 1.1 dB lower for the deterministic signal and ~ 3.2 dB lower for the Gaussian-fluctuating signal to achieve $P_d = 0.5$). Countering this is the increase in SNR achieved by the longer CPI, which is only expected to be proportionate (6 dB increase in SNR when going from $T_p = 1.25$ s to 5 s) when there is no coherence loss or energy spreading loss (e.g., see [2]). When coupled with a spreading-loss model [12], the procedure presented here thus allows optimization over N while controlling false-track rate.

3.2. Controlling false-track rate

To illustrate how the tuning process controls the false-track rate, contact-level data were simulated using the GPD with parameters $h_0 = 12$ dB, $\gamma = 0.5$, $\lambda_0 = 5$, and $q_c(h_0) = 0.6$ over $N_{r\theta} = 100$ tracker channels for $N_p = 5000$ pings. The average clutter-event length was set to $\bar{C} = 48$ samples with an average of $\bar{B} = 240$ samples separating them. Three different TIAs were then designed for $N = 5$, 10, and 20 with M chosen according to Shnidman's rule

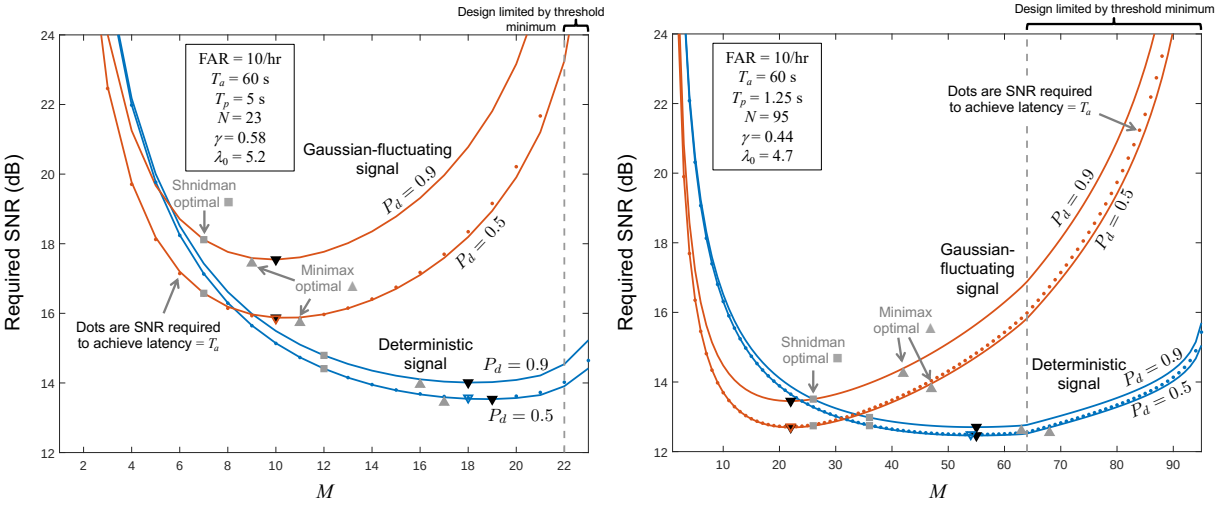


Fig. 3: SNR required to achieve a desired performance specification as a function of M for $T_p = 5\,s$ yielding $N = 23$ (left) and $T_p = 1.25\,s$ yielding $N = 95$/ (right).

for a deterministic signal. In each case, the desired average number of updates between false tracks was $F = 50$. Ten percent of the simulated data are shown in Fig. 2 where the gray circles represent clusters passed to the TIA and the connected red dots represent tracks that are formed. The TIAs with larger values of M (generally corresponding to designs with a larger value of N) have lower decision thresholds [12.8 dB for the $(10, 20)$ TIA vice 14.9 dB for $(3, 5)$] and so produce longer tracks.

The false-track counts over the complete simulation (108, 87, and 94, respectively, for $N = 5$, 10, and 20) yield p-values of 0.40, 0.18, and 0.52 probability of observing a count farther from the expected number (100) based on the design FTR and assuming a Poisson-distributed count. This suggests the design process successfully controls the false-track rate. Although not shown, similar results (p-values of 0.20, 0.18, and 0.74) were seen when the $(6, 10)$ TIA was designed for three different false-track rates ($F = 10$, 50, and 250 pings between false tracks).

4. CONCLUSIONS

An approach for the design of a sliding M-of-N track initialization algorithm (TIA) was presented where M and N are chosen to minimize the SNR required to achieve a detection performance specification and the cluster-level detection decision threshold is chosen to control the false-track rate. A two-state Markov random process was used to represent clutter-event occurrences, which were assumed to be the dominant source of false tracks. This model implies the clutter events have a geometrically distributed length, support for which was obtained by analyzing data from CMRE's LCAS15 experiment. The peak normalized intensity of clutter clusters was modeled using a generalized Pareto distribution (GPD), which was also supported by the LCAS15 data although not shown here. Design examples illustrated how to optimize the TIA and how it successfully controls false-track rate.

5. ACKNOWLEDGEMENTS

This work was sponsored by the Office of Naval Research; Code 321 Undersea Signal Processing.

Parts of this work were made possible by the LCAS Multi-National Joint Research Project (MN-JRP), including as Participants the NATO Centre for Maritime Research and Experimentation, the Defence Science and Technology Organisation (AUS), the Department of National Defence of Canada Defence Research and Development Canada (CAN), the Defence Science and Technology Laboratory (GBR), Centro di Supporto e Sperimentazione Navale-Italian Navy (ITA), the Norwegian Defence Research Establishment (NOR), the Defence Technology Agency (NZL), and the Office of Naval Research (USA).

REFERENCES

[1] A. Farina and F. A. Studer. *Radar Data Processing: Volume 1—Introduction and Tracking*. John Wiley & Sons, 1985.

[2] S. M. Murphy and P. C. Hines. Sub-band processing of continuous active sonar signals in shallow water. In *Proceedings of 2015 MTS/IEEE Oceans Conference*, pages 1–4, Genova, Italy, May 2015.

[3] R. Plate and D. Grimmett. High duty cycle (HDC) sonar processing interval and bandwidth effects for the TREX'13 dataset. In *Proceedings of 2015 MTS/IEEE Oceans Conference*, pages 1–10, Genova, Italy, May 2015.

[4] B. R. La Cour. Statistical characterization of active sonar reverberation using extreme value theory. *IEEE Journal of Oceanic Engineering*, 29(2):310–316, 2004.

[5] J. M. Gelb, R. E. Heath, and G. L. Tipple. Statistics of distinct clutter classes in mid-frequency active sonar. *IEEE Journal of Oceanic Engineering*, 35(2):220–229, April 2010.

[6] C. Forbes, M. Evans, N. Hastings, and B. Peacock. *Statistical Distributions*. Wiley, Hoboken, New Jersey, fourth edition, 2011.

[7] D. Grimmett and R. Plate. High duty cycle sonar performance as a function of processing time-bandwidth for LCAS'15 data. In *Proceedings of the Underwater Acoustics Conference & Exhibition*, pages 185–192, Skiathos, Greece, September 2017.

[8] J. I. Naus. Approximations for distributions of scan statistics. *Journal of the American Statistical Association*, 77(377):177–183, 1982.

[9] D. A. Abraham. Optimization of M-of-N detectors in heavy-tailed noise. In *Proceedings of 2018 IEEE/MTS Oceans Conference*, Charleston, SC, 2018.

[10] J. Glaz, J. Naus, and S. Wallenstein. *Scan Statistics*. Springer-Verlag, New York, 2001.

[11] D. A. Shnidman. Binary integration for Swerling target fluctuations. *IEEE Transactions on Aerospace and Electronic Systems*, 34(3):1043–1053, 1998.

[12] D. E. Weston. Correlation loss in echo ranging. *Journal of the Acoustical Society of America*, 37(1):119–124, January 1965.

IMPROVED TRACKING OF A SURROGATE TARGET USING CONTINUOUS ACTIVE SONAR

Jeffrey R. Bates[ab], Gaetano Canepa[a], Alessandra Tesei[a]

[a]Science and Technology Organization - Centre for Maritime Research and Experimentation, La Spezia, SP, ITALY
[b]now at Defence Research and Development Canada, Dartmouth, NS, CANADA

Contact: Jeffrey R. Bates DRDC 9 Grove St. Dartmouth NS, B3A 3C5
Tel: +1-(902)-407-0523, email: Jeffrey.Bates@forces.gc.ca

Abstract: *Increasing the duty cycle of traditional Pulsed Active Sonar (PAS) to approach that of a Continuous Active Sonar (CAS) mode is being investigated for Anti-Submarine Warfare applications including littoral scenarios. CAS mode offers the potential advantage of increasing the target update rate through sub-band processing to improve tracking performance. A sea trial was carried out by the Littoral CAS Multi-National Joint Research Project in the gulf of Taranto in October of 2016. LFM PAS and CAS active sonar waveforms were simultaneously transmitted by the surface ship NRV ALLIANCE, to detect a surrogate target (echo repeater) towed by the surface ship CRV LEONARDO. In this work multi-static echo returns of the CAS and PAS waveforms, received by an autonomous underwater vehicle towing a linear array, are analysed at the output of an M-of-N distributed multi-hypothesis tracker. The CAS waveform is sub-banded into seven 5 second long sub-pulses with a 50% overlap. To simulate a more realistic target, the signal to noise ratio of the echoes from the echo-repeater target were adjusted based on a simple bi-static target strength model in post processing. The results demonstrate that, in the measured environment, CAS can reduce the false alarm rate compared to a conventionally processed PAS waveform at the output of a distributed multi-hypothesis tracker.*

Keywords: *Continuous Active Sonar, Tracking, High Duty Cycle, Continuous time LFM, Echo Repeater, Littoral*

1. INTRODUCTION

Interest in increasing the duty cycle of traditional pulse active sonar (PAS) to a continuous active sonar (CAS) mode has arisen recently for anti-submarine warfare (ASW) applications including littoral scenarios [1]. In PAS systems, a sonar signal is transmitted for a short duration followed by a long listening duration (upper frequency band of Figure 1). In CAS systems, a sonar signal is transmitted continuously while simultaneously listening for echoes (lower frequency band of Figure 1). CAS mode offers the potential advantage of increasing the target update rate through sub-band processing [1-3] to improve tracking performance [4]. However this advantage needs to be experimentally confirmed as reducing the sub-band duration reduces the energy per ping which can negatively impact the detection performance. Sub-bands can have a narrower bandwidth, as is the case for linearly frequency modulated (LFM) waveforms, which can also negatively impact the detection performance in reverberation limited environments.

This paper will compare tracking performance of simultaneously transmitted CAS and PAS waveforms against a surrogate echo repeater target. The Signal to Reverberation Ratio (SRR) of the echoes from the surrogate target are adjusted in post processing based on a simple target model to make the comparison more realistic.

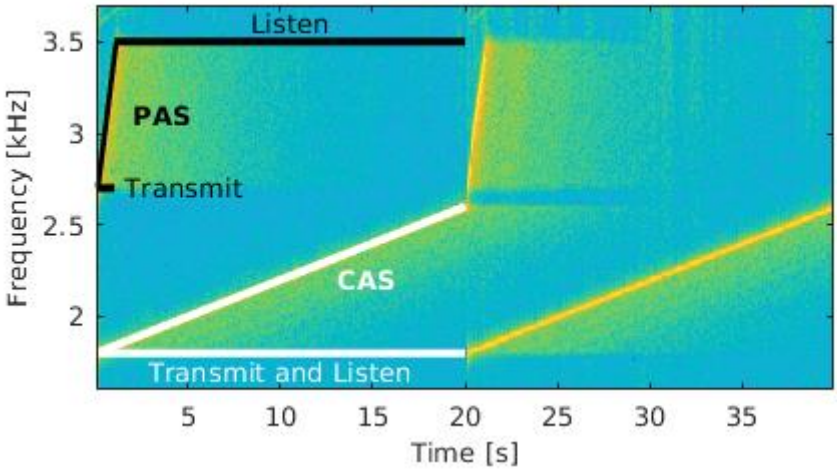


Figure 1: Spectrogram of an example LFM PAS (1 second long from 2.7-3.5 kHz, black labels) and LFM CAS (20 seconds long from 1.8-2.6 kHz, white labels) signals with a ping repetition interval of 20 seconds.

2. EXPERIMENT AND DATA ANALYSIS

In October 2016, the Littoral CAS (LCAS) Multi-National Joint Research Project (MN-JRP) held a sea trial off the coast of Taranto (Italy) to compare the detection capability of LFM PAS with LFM CAS. The NRV ALLIANCE attempted to detect an Echo Repeater (ER), acting as a surrogate target, towed by CRV LEONARDO.

On October 22, during run named ER-3, the NRV ALLIANCE towed a sonar source that transmitted a LFM PAS signal (from 2.7-3.5 kHz over 1 s) and a LFM CAS signal (from 1.8-2.6 kHz over 20 s with a source level $10\log_{10}(20s/1s)=13$ dB lower than the PAS signal) with a ping repetition interval of 20 s, as shown in Figure 1. Each pulse had equal total energy per ping. The source was towed at a depth of approximately 70 m. Ocean Explorer (OEX) Harpo, an Autonomous Underwater Vehicle (AUV), towed a linear array with 64 hydrophones at a depth of 85 m and was used as a bi-static receiver. The CRV LEONARDO towed an echo repeater at a depth of approximately 70 m.

The CRV LEONARDO sailed downslope and antiparallel to NRV ALLIANCE with a closest point of approach of approximately 6.2 km, as shown in Figure 2a. Both surface vessels travelled at approximately 3.5 knots (~1.75 m/s). OEX-C Harpo AUV travelled at 2 knots (~1 m/s). Figure 2a also shows the bathymetry of the operational area, acquired using an *EM 302 KONGSBERG* 30 kHz multibeam echo sounder.

The sound speed profiles were measured at 06:36UTC and 16:33UTC on October 22 using a *Sea-bird Electronics 9plus* conductivity, temperature, and depth (CTD) sensor and are shown in Figure 2b. The measured sound speed resulted in a downward refracting sound speed profile with a 35 m deep mixed layer. Note that source, receiver, and echo repeater were all below the thermocline.

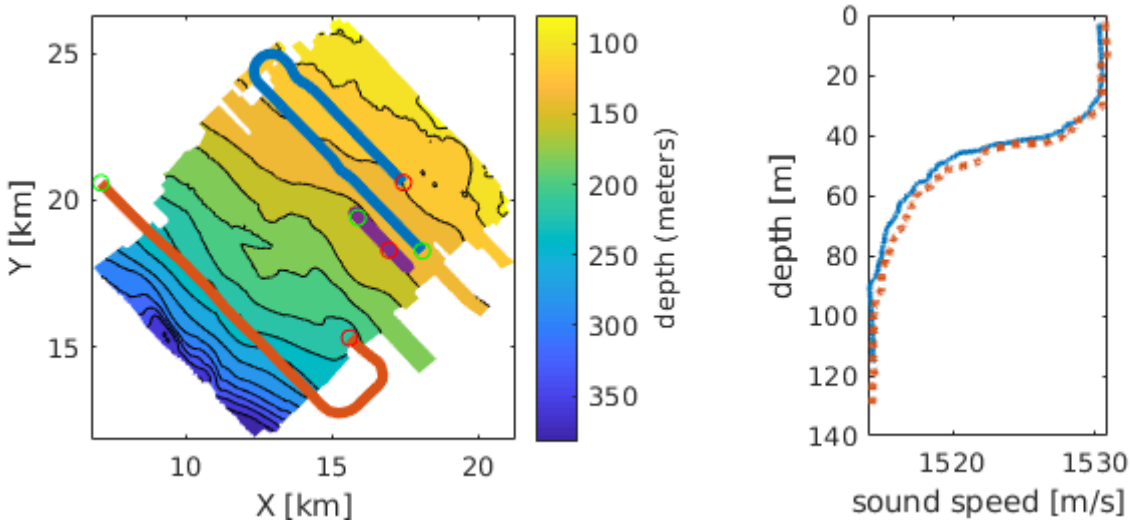


Figure 2: (a) NRV ALLIANCE (blue), CRV LEONARDO (red), OEX Harpo (purple) trajectory from green to red point. Background shows bathymetry of operational area. (b) Sound speed profile measured at 06:36UTC (blue) and 16:33UTC (dashed red) on October 22.

The sea conditions were sea state 3 (significant wave height of 0.6 meters), with waves coming from the south and a dominant wave power spectral density of approximately 0.4 m^2/Hz at 0.16 Hz, measured using a *Datawell oceanographic instruments MKIII* moored directional wave rider.

The hydrophone array data acquired by OEX-C Harpo were first beamformed into 64 cosine spaced beams. Next, the data were Matched filtered with a single replica for PAS and 7 sub-band replicas with Hann windows and a 50 % temporal overlap for CAS. The SRR was

estimated using a sliding window median filter with a duration of 400 ms (normalisation). A threshold (discussed below) was applied to the normalised data followed by clustering. The resulting contacts were sent to the Centre for Maritime Research and Experimentation (CMRE) Distributed Multi-Hypothesis Tracker [5]. The DMHT is a multi-hypothesis M-of-N tracker, where M contacts out of N opportunities are required to initialize a track [6].

Three values for N were selected for CAS and PAS respectively, as shown in Table 1. Note that values of N for CAS and PAS are equal as measured in duration (seconds). Values for M were estimated using recent work on sliding M of N detectors by Abraham [7][8] and the parameters in Table 1. The estimated values of M as calculated by Abraham [7][8] are within 2 of the approximation given by Shnidman [9],

$$M_{opt} = 10^b N^a, \tag{1}$$

Using the Swerling II target model (with a=0.91 and b=-0.38) [9]. An initiated track was killed when the number of sequential missed detections exceeded a parameter K. K was set to N-M to best approximate a sliding M-of-N detector.

Initial values of the threshold (T) (square brackets in Table 1) were also estimated using work by Abraham [7][8] and the parameters in Table 1. To obtain a Receiver Operating Characteristic (ROC) curve the threshold was varied around the initial values by the values in the curly brackets in Table 1. Each value in square brackets in Table 1 is used with the corresponding value for a different parameter. For example, the following tracker parameters were used with N=84 for the CAS waveform; M=22, K=62, and thresholds of 1.5,2,3,6, and 9 dB above the initial estimate of 11.8 dB.

Parameter	*Value*
N	PAS: [6,8,12] CAS: PAS x $7_{\text{sub-bands}=}$[42,56,84]
M (Estimated using [7])	PAS: [2,3,4] CAS: [12,16,22]
K (Max missed detections=N-M)	PAS: [4,5,8] CAS: [30,40,62]
T (starting point Estimated using [7])	PAS: [14.5, 13.3, 12.7] +{0,0.5,1,2,3,6,9,12,15} dB CAS:[12.3, 11.97, 11.8] +{1.5,2,3,6,9} dB
Process noise	0.001 m^2/s^3
Spatial gate probability	99 %
Tracker depth	2
Signal modal type	Gaussian fluctuating
Independent samples in normalizer	126
Number of cosine spaced beams	64
Valid target bistatic range (R)	3<R<25.5 km
Contact time delay uncertainty (σ_τ)	0.03 s
Contact bearing uncertainty (σ_Θ)	¼ of beam spacing

Table 1: Processing parameters.

In shallow water environments with high compact clutter on the sea floor, the tracker often has a number of false tracks that are stationary. These tracks are fixed in space and therefore should have a velocity of 0 m/s. At each point along a track, the DMHT provides an estimate of the track velocity and an uncertainty associated. For the purpose of this analysis, a track is assumed stationary and is discarded if the velocity of the track is equal to 0 m/s within the estimated uncertainty for a majority of the track duration (greater than 68%).

The surrogate target was omnidirectional, which is unrealistic. To make the comparison of CAS with PAS more realistic, the target echoes were degraded (or enhanced) based on a simple target model [10] and on the known tactical geometry (Figure 3) in post processing. The target echoes were identified as the strongest SRR contact within ±0.75 seconds and ±4 beam of the expected target location.

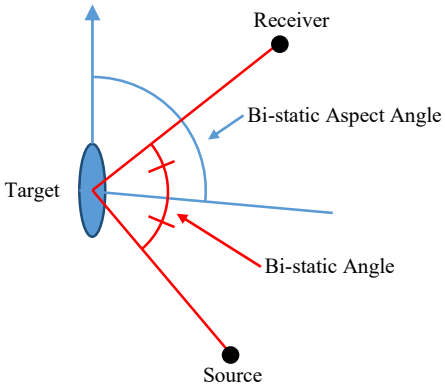


Figure 3: Bistatic active sonar geometry

3. EXPERIMENTAL RESULTS

Figure 4a shows the ROC curve for PAS and CAS with different values of N before adjustment of the target echoes. Each point along the curve gives the percent tracked time on target (TOT) and the average number of false alarms per minute using one set of tracker parameters. The tracker input threshold is varied while keeping all other parameters constant to generate each curve. Each ROC curve is colour coded by the different values of N as measured in duration (seconds). The continuous lines indicate CAS and the dashed lines indicate PAS. Figure 4b shows the tracking result with N=12 at the operating point indicated by the red circle in Figure 4a. The Green, blue, and dashed red lines in Figure 4b indicate the trajectory of the NRV ALLIANCE (source), OEX-C Harpo (receiver), and CRV LEONARDO (ER target) respectively. The solid red lines indicate the tracks.

The OEX-C Harpo towed a linear towed array which has port/starboard ambiguity. This ambiguity causes the tracks indicated by the black arrows in Figure 4b. Note that these excellent results (near perfect TOT and FAR) are not realistic due to the omnidirectional characteristic of the ER.

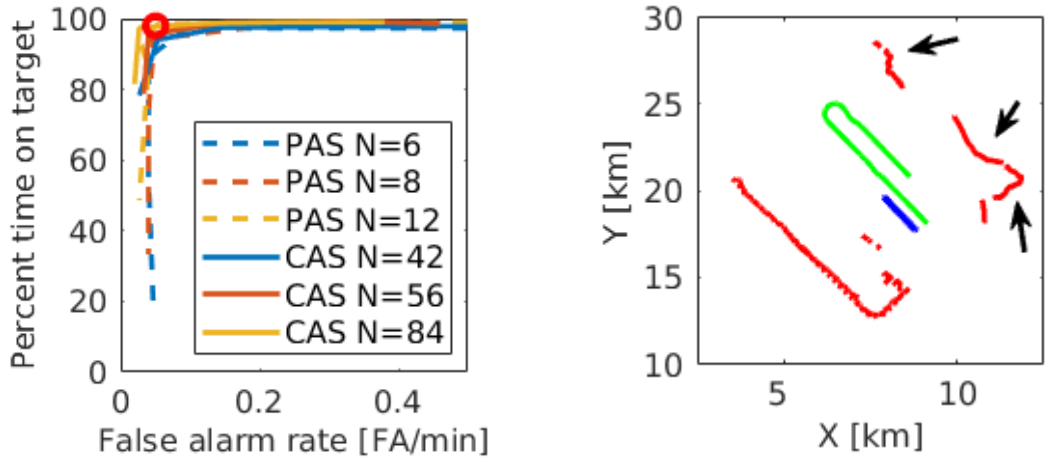


Figure 4: (a) ROC curve at the output of the tracker for 3 different values of N for CAS and PAS. Each point is given by the percent time on target and average false alarm rate for varying thresholds. Red circle indicates the results shown in (b). (b) Tracker results for N=12, M=4, T=18.7 dB resulting in FAR 0.05 min^{-1} and a time on target of 98%. Green, blue, and dashed red lines indicate the trajectory of the NRV ALLIANCE (source), OEX Harpo (receiver), and CRV LEONARDO (ER target) respectively. The non-stationary tracks are shown in red.

To compensate for the high echo repeater target strength, the target echoes were adjusted based on a simple target model [10] as described above. Figure 5 shows the ROC curve for PAS and CAS waveforms against the echo repeater target with adjusted echo SRR. Note that the CAS waveform outperforms the PAS waveform at the output of the tracker, as it has a higher TOT for a given FAR for all N.

Figure 6a and Figure 6b show the tracking results from the best CAS and PAS operating points in Figure 5 respectively (as indicated by the solid and dashed arrows). Note that there are approximately half the number of false alarms in CAS when compared to PAS and the time on target is approximately equal.

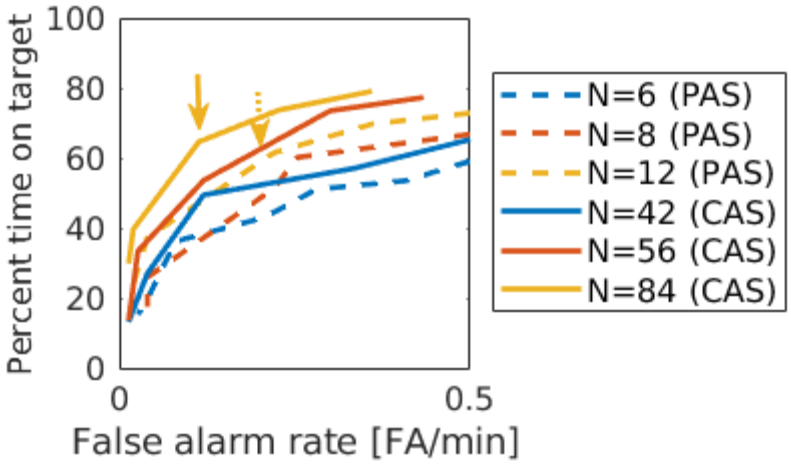


Figure 5: ROC curve for PAS (dashed lines) and CAS (solid lines). The matching colours have equal value of N as measured in seconds rather than updates. The solid and dashed arrows represent the operating points shown in Figure 6.

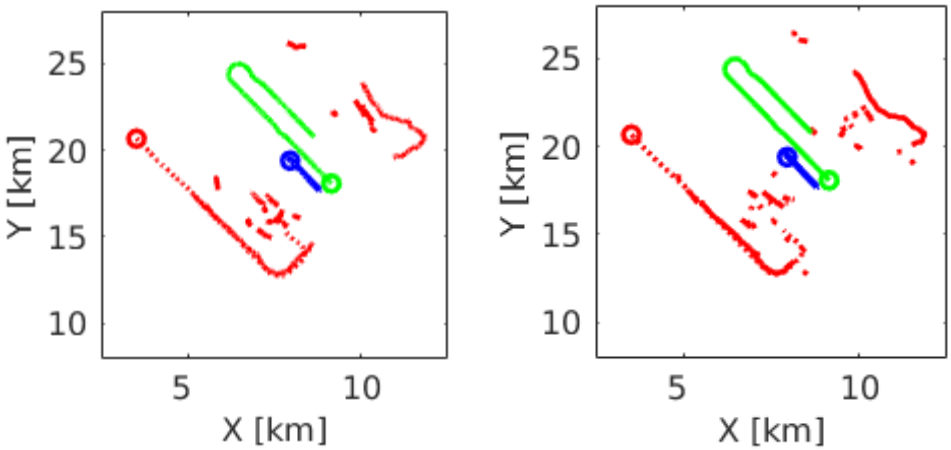


Figure 6: CAS vs. PAS tracker result with N=4 minutes. (a) CAS with N=84, M=22, and T=14.8, resulting in 7 false alarms per hour and 65% TOT. (b) PAS with N=12, M=4, T=15.7 dB, resulting in 13 false alarms per hour and 62% TOT.

4. CONCLUSIONS

A LFM CAS waveform was demonstrated to have fewer false alarms and equivalent time on target at the output of a tracker when compared with a LFM PAS waveform with equivalent bandwidth and energy per ping. The result was determined experimentally in a littoral environment with the echo repeater target strength adjusted in post processing to represent more realistic operating conditions. Reducing the false track rate is especially important for AUV platforms where decision making process needs to be automated due to the minimal ability for humans to directly interpret the AUV's underwater picture. Future work involves investigating if the results hold for more realistic targets and scenarios in a wide variety of

environments. These results should also be investigated with respect to scenarios with a human in the loop.

5. ACKNOWLEDGEMENTS

This work was funded by NATO Allied Command Transformation (ACT) Future Solutions Branch under the Autonomous Security Network Programme. This work was made possible by the LCAS Multi-National Joint Research Project (MN-JRP), including as participants the NATO Centre for Maritime Research and Experimentation, the Defence Science and Technology Organisation (AUS), the Department of National Defence of Canada Defence Research and Development Canada (CAN), the Defence Science and Technology Laboratory (GBR), Centro di Supporto e Sperimentazione Navale-Italian Navy (ITA), the Norwegian Defence Research Establishment (NOR), the Defence Technology Agency (NZL), and the Office of Naval Research (USA).

REFERENCES

[1] **P.C. Hines**, Experimental comparison of continuous active and pulsed active sonars in littoral waters, In *Proc. 1st International Conference and Exhibition on Underwater Acoustics*, Corfu, Greece, pp. 51-58, 2013.

[2] **S.M. Murphy P.C. Hines**, Sub-band processing of continuous active sonar signals in shallow water, In *Oceans 2015 - Genova*, Genova, Italy, pp. 1-4, 2015.

[3] **R. Plate and D. Grimmett**, High Duty Cycle (HDC) sonar processing interval and bandwidth effects for the TREX'13 dataset, In *Oceans 2015 - Genova*, Genova, Italy, pp. 1-10, 2015.

[4] **D. Grimmett**, Target AOU Growth Containment using LFM High Duty Cycle Sonar, In *Proc. Of the 2nd International Conference on Underwater Acoustics*, Rhodes, Greece, pp. 839-846, 2014.

[5] **C. Carthel, S. Coraluppi,** The NURC Distributed Multi-Hypothesis Tracker (DMHT): Scientific User Documentation, 2007.

[6] **S. Coraluppi and C. Carthel**, Distributed tracking in multistatic sonar, *IEEE Transactions on Aerospace and Electronic Systems*, vol. 41, no. 3, pp. 1138-1147, July 2005.

[7] **D. A. Abraham,** Optimization of m-of-n detectors in heavy-tailed noise. In Proc. IEEE/MTS OCEANS18, Charleston, US, 2018.

[8] **D. A. Abraham,** Analysis and Design of Sliding m-of-n Detectors. Technical report, CausaSci LLC, 2011.

[9] **D. A. Shnidman**. Binary integration for swerling target fluctuations. IEEE Transactions on Aerospace and Electronic Systems, 34(3):1043–1053, July 1998.

[10] **D. Grimmett et. al.** AMOC Multistatic Decision Aid Methodologies and Cross-Evaluation. *TTCP Technical Report*, TR-MAR-8-2012, 2012.

IMPROVED ACTIVE SONAR EXPERIMENT FOR MEASURING MATCHED-FILTER LOSS VS BANDWIDTH AND DURATION

Stefan M. Murphy[a], Paul C. Hines[b], Matthew E. W. Coffin[c], Jeffrey R. Bates[a], Kevin D. LePage[d]

[a]Defence Research and Development Canada, 9 Grove Street, Dartmouth, NS B2Y3Z7, Canada
[b]Dalhousie University, Electrical and Computer Engineering Department, 1360 Barrington Street, Halifax, NS B3H4R2, Canada
[c]GeoSpectrum Technologies Inc., 10 Akerley Blvd., Unit 19, Dartmouth, NS B3B1J4, Canada
[d]Centre for Maritime Research and Experimentation, Viale San Bartolomeo, 400, 19126 La Spezia (SP), Italy

Abstract: *Preliminary results are presented from a fixed-geometry experiment conducted during the Littoral Continuous Active Sonar 2018 (LCAS18) sea trial that was led by the Centre for Maritime Research and Experimentation (CMRE) in November 2018. The objective of the experiment was to measure environmental matched-filter loss as a function of bandwidth and duration independently in shallow water. A stationary source transmitted LFM waveforms with varying bandwidth and duration (up to 2048 Hz and 64 s), which were received on stationary hydrophones at ranges of approximately 100, 200, 300, 5000, 10,000, and 20,000 m (125-m water depth, 75-m source and receiver depths). The experiment was similar to one conducted during the LCAS16 trial, the main difference being that bandwidth was increased to improve the resolution of individual propagation paths, such as the surface reflection, which exhibited matched-filter loss that increased with increasing duration. This is an expected result because motion-related distortion occurs when the surface varies on a timescale shorter than the pulse duration. Furthermore, the LCAS18 experiment employed more hydrophones than LCAS16 in order to capture multiple surface grazing angles. At steeper grazing angles the effective roughness/motion of the surface is greater, so the matched-filter loss is expected to increase with increasing grazing angle.*

Keywords: *active sonar, detection, large time-bandwidth, LFM*

© Her Majesty the Queen in Right of Canada, Department of National Defence, 2019.

1. INTRODUCTION

This paper presents the details of an experiment conducted during the Littoral Continuous Active Sonar 2018 (LCAS18) sea trial, held approximately 20 km off shore from Piombino, Italy. The Centre for Maritime Research and Experimentation (CMRE) led the sea trial. The experiment is an improved version of a similar experiment conducted during the Littoral Continuous Active Sonar 2016 (LCAS16) sea trial, the details of which were presented at the previous Underwater Acoustics Conference and Exhibition in 2017 [1].

The purpose of the experiment was to measure matched-filter loss due to propagation distortion as a function of bandwidth (B) and duration (T) – the two parameters that dictate the performance of an active sonar waveform. The matched-filter loss due to the distortion incurred during the reflection from a rough, moving sea surface is of particular interest, especially for large BT signals. During both LCAS16 and LCAS18, two sequences of linear frequency modulation (LFM) waveforms were transmitted from a moored source and received on moored hydrophones. The first sequence held the duration constant and varied the bandwidth to measure the received level as a function of bandwidth, while the second sequence held the bandwidth constant and varied the duration to measure the dependence on duration. The bandwidth in the second sequence was kept small (B = 100 Hz) during LCAS16 to minimize bandwidth effects while examining the dependence on duration. However, the poor range resolution associated with the small bandwidth made it difficult to separate the surface reflection from other arrivals such as the bottom reflection. In LCAS18 a larger bandwidth (B = 2048 Hz) was selected to further separate the arrivals.

This paper highlights the improvements gained by using larger bandwidth during LCAS18 over the results from LCAS16.

2. EXPERIMENT

The experiment considered in this paper is a fixed-geometry experiment that employed CMRE's DEMUS source, which transmitted a sequence of LFMs (Table 1) that was received on six hydrophones located approximately 110 m, 220 m, 330 m, 5000 m, 10000 m, and 20000 m from the source. All equipment was moored to the sea bottom for stability. The source and receivers were deployed at a depth of 75 m in a 125-m water column.

The DEMUS source has a maximum transmit duration of 8 s. Signals with longer duration, up to T = 64 s, were also transmitted from sources deployed from NRV ALLIANCE and CRV LEONARDO during the LCAS18 trial.

The close-range hydrophones were included in the experiment to allow separation of arrivals, which become more closely spaced and unresolvable at longer range. The five shortest propagation paths were calculated assuming constant sound speed profile with c = 1520 m/s. Fig. 1a and Fig. 1b show the diagrams for the closest hydrophone in LCAS16 (range = 89 m) and LCAS18 (range = 110 m), respectively. The main difference is that the grazing angle of the surface reflection is smaller for LCAS18 (54° versus 66° for LCAS16). A smaller grazing angle was selected because the vertical beamwidth of the DEMUS transducers is 82° between -3 dB points, resulting in the source level rolling off at grazing angles above 49°. The smaller grazing angle therefore increased the surface reflection level, facilitating measurement. Another difference from LCAS16 is that the source and receiver were placed at the same depth, resulting in the same arrival time for the surface-bottom and bottom-surface paths.

Index	Transmit time (s re start time)	Duration (s)	Bandwidth (Hz)	Source level (nominal, dB)
1	0	0.25	4	199
2	5	0.25	8	199
3	10	0.25	16	199
4	15	0.25	32	199
5	20	0.25	64	199
6	25	0.25	128	199
7	30	0.25	256	199
8	35	0.25	512	199
9	40	0.25	1024	199
10	45	0.25	2048	199
11	50	0.25	2048	199
12	55	0.50	2048	196
13	65	1.00	2048	193
14	75	2.00	2048	190
15	90	4.00	2048	187
16	120	8.00	2048	184
repeat	180			

Table 1: Sequence of LFM waveforms transmitted from the DEMUS source during LCAS18. The sequence is the same as that transmitted during LCAS16, except that larger bandwidth was used for pings 11–16.

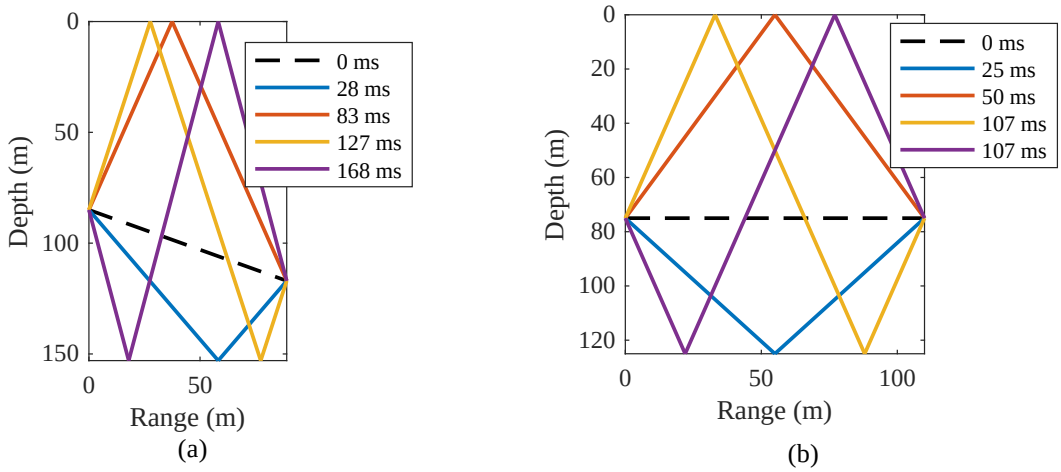


Fig. 1: Ray diagrams depicting left-to-right propagation from the DEMUS source to the closest icListen hydrophone for (a) LCAS16 (range = 89 m), (b) LCAS18 (range = 110 m). The axes are scaled proportionally so that the true angles of incidence at the surface and bottom are depicted.

Two additional close-range hydrophones were deployed during LCAS18 to make additional surface reflection measurements at different grazing angles. The 220-m hydrophone received a surface reflection with a grazing angle of 34°, and the grazing angle was decreased to 24° at 330 m. The Rayleigh parameter [2], a measure of the effective roughness of a surface, is proportional to the sine of the grazing angle, and the hydrophones were configured such that the sine of the grazing angle spanned a factor of two to achieve a

range of effective roughness. The matched-filter loss is expected to increase for surface reflections from rougher surfaces [3].

3. RESULTS

The improvement over the LCAS16 experiment in the measurement of the surface reflection level is evident by comparing Fig. 2 and Fig. 3. Fig. 2 was taken from the previous UACE paper [1] and shows the average matched-filter output for approximately 50 pings transmitted during run FX-1 on 19 October 2016 and received on the closest hydrophone (range = 89 m). The surface arrival was distinguishable with 100 Hz of bandwidth for the 0.25-s pulse (Fig. 2a, expected time delay of 0.083 s), but distortion in the surface reflection resulted in a large spread in the output for the 8-s pulse (Fig. 2b) and no local maximum at the expected delay.

Increasing the bandwidth from 100 Hz to 2048 Hz in LCAS18 resulted in improved resolution of arrivals at both 0.25 s and 8 s. The average matched-filter output for approximately 40 pings transmitted during run FX26-1 on 26 November 2018 and received on the closest hydrophone (range = 110 m) is shown in Fig. 3. The surface reflection (expected time delay of 0.050 s) shows evidence of distortion (time spread and decreased level) at 8 s, but a local maximum is still observable, as opposed to LCAS16.

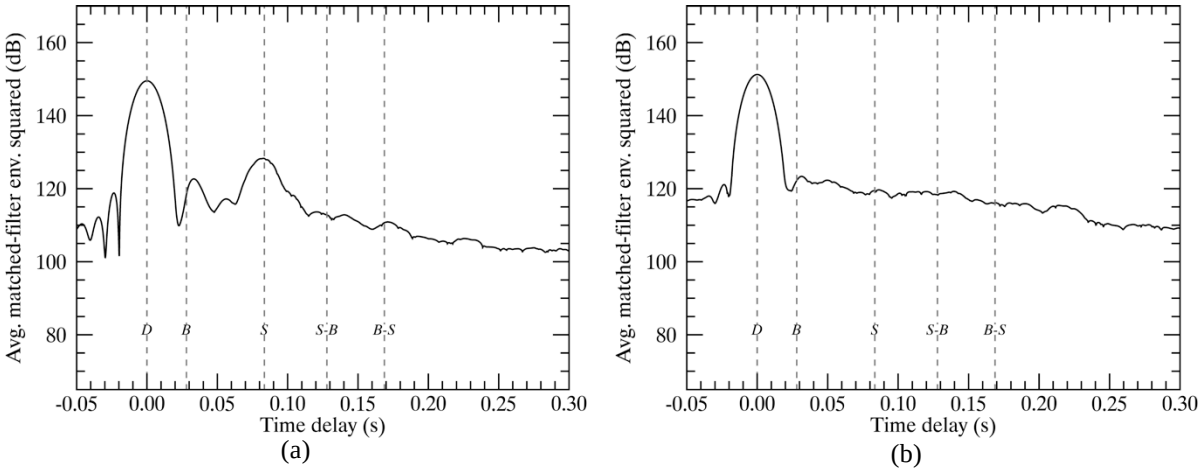


Fig. 2: LCAS16 average matched-filter for the LFM with 100 Hz of bandwidth and duration of (a) 0.25 s, (b) 8 s measured on the closest hydrophone (range = 89 m). At 8 s the surface reflection (expected time delay, 0.083 s) is distorted and no longer produces a local maximum. Figure taken from [1].

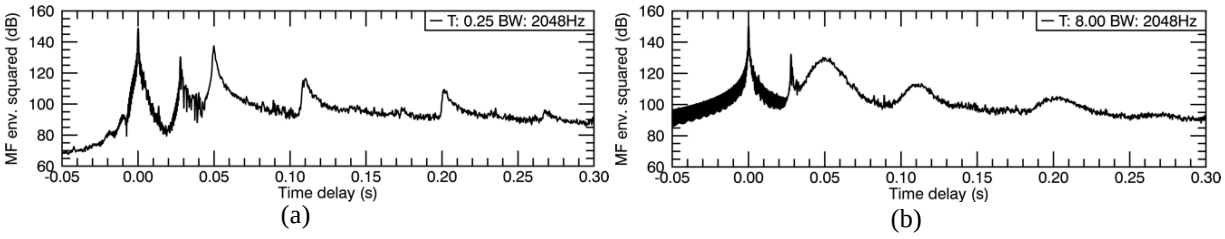


Fig. 3: LCAS18 average matched-filter output for the LFM with 2048 Hz of bandwidth and duration of (a) 0.25 s, (b) 8 s measured on the closest hydrophone (range = 110 m). The time spreading and decreased amplitude in the surface reflection of the 8-s signal (expected time delay, 0.050 s) is evidence of distortion, but a local maximum is still observable.

Finally, the boxplot from the previous UACE paper [1] is shown in Fig. 4a, showing the distributions of the received levels as a function of duration. The boxplot is produced from the same LCAS16 dataset used to produce Fig. 2, but here the levels are extracted from the matched-filter output from single pings rather than averaging the matched-filter output, and all durations are included. The bottom reflection (blue) has variability (vertical extent in the box) even though the sea bottom is stationary. The variability is due to interference with the variable surface reflection (red). The surface reflection is variable because the sea surface changes from ping to ping, and the poor resolution of the arrivals due to the small bandwidth results in the surface reflection interfering with the bottom reflection. On the other hand, with the increased bandwidth and resolution in LCAS18, the bottom reflection has low variability (Fig. 4b) as is expected from a reflection from a stationary boundary. The direct arrival (black) similarly has low variability, as expected, and the dependence of the direct arrival on duration observed in LCAS16 was removed by normalizing the signal amplitudes in the digital waveform files rather than attenuating the source level using the DEMUS controller.

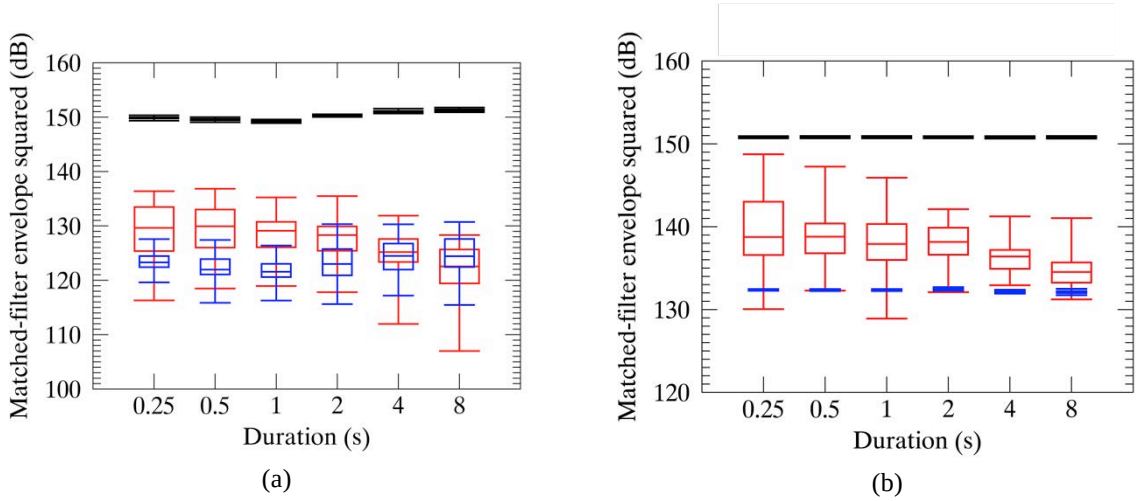


Fig. 4: Boxplot of received levels measured on the closest hydrophone in (a) LCAS16, figure taken from [1]*, (b) LCAS18. Direct (black), surface reflection (red), bottom reflection (blue). The bottom reflection has lower variability in LCAS18 than LCAS16 because the lower resolution in LCAS16 resulted in the distorted, variable surface reflection spreading into the bottom reflection.*

The trend of decreasing surface reflection level (or equivalently increased matched-filter loss) as a function of duration is observable in both the LCAS16 and LCAS18 boxplots (Fig. 4a and Fig. 4b, respectively). The trend is consistent with the theory that decorrelation in the surface reflection occurs when the pulse duration becomes significant relative to the period of surface waves, such that the surface moves within the pulse duration [3]. For LCAS16 and LCAS18 the spectrum of the surface heights measured with a wavebuoy revealed that most of the wave power was within wave periods of 2–6 s. The improved resolution of the LCAS18 experiment increases confidence in the measurement and may allow exploitation of the LCAS16 analysis where previously there was some uncertainty in the measurement of the received levels due to the poor resolution.

4. CONCLUSIONS AND FUTURE WORK

Preliminary results show that using larger bandwidth in LCAS18 (2048 Hz) compared to LCAS16 (100 Hz) improved the measurement of matched-filter loss as a function of duration by improving the resolution of arrivals received on a hydrophone at a range of approximately 100 m from the source. The bottom arrival was no longer affected by the distorted surface reflected at longer durations. The surface reflection was the only arrival with variability, and the median received level decreased with increasing duration, as expected. Bandwidth dependence was not explored in this paper, and analysis of the LCAS18 dataset is ongoing.

5. ACKNOWLEDGEMENTS

This work was made possible by the Littoral Continuous Active Sonar Multi-National Joint Research Project including participants CMRE (NATO), DSTG (AUS), DRDC (CAN), dstl (GBR), CSSN (ITA), FFI (NOR), DTA (NZL), and ONR (USA). The authors would like to thank all those involved in the LCAS18 sea trial, which was led by CMRE (Scientist in Charge: Kevin D. LePage). This work was funded in part by ONR Grant N62909-17-1-2090.

REFERENCES

[1] **S. M. Murphy**, "Preliminary results from an active sonar experiment for measuring matched-filter loss vs bandwidth and duration," In *Proceedings of the 4th Underwater Acoustics Conference and Exhibition*, Skiathos, Greece, pp. 153 –160, 2017.

[2] **R. J. Urick**, *Principles of underwater sound*, 3rd ed. McGraw-Hill, p. 193, 1983.

[3] **D. A. Abraham**, **S. M. Murphy**, **P. C. Hines**, and **A. P. Lyons**, "Matched-filter loss from time-varying rough-surface reflection with a small ensonified area," *IEEE J. Ocean. Eng.*, 43(2), pp. 506–522, 2017.

HIGH DUTY CYCLE ACTIVE SONAR USING BROADBAND DOPPLER-SENSITIVE WAVEFORMS: EXPLOITING A TRIPLET ARRAY FOR ATTENUATING DIRECT PATH INTERFERENCE

Michael Datum

General Dynamics Applied Physical Sciences Corp.
475 Bridge Street
Groton, CT 06340 USA
mdatum@aphysci.com

Abstract: *The class of active sonar waveforms that are Broadband and Doppler Sensitive (BBDS) is investigated for High Duty Cycle (HDC) sonar applications. BBDS waveforms include Pseudo Random Noise (PRN), Frequency Shift Keyed (FSK), and various phase modulated waveforms. The work here focuses on pseudo-random Minimum Shift Keyed (MSK) sequences, which provide good band constraint with efficient power levels, though much of the analysis applies to the entire class of waveforms. HDC sonar presents challenges for BBDS waveforms due to matched-filter sidelobe masking from the direct path. A technique is developed for suppressing the direct path as well its specular surface and bottom reflections, which exploits the properties of a triplet hydrophone array. Data from the Littoral Continuous Active Sonar 2015 (LCAS 15) experiment is analyzed, in which an echo repeater serves as the target.*

Keywords: *broadband waveforms, continuous active sonar, triplet array, high duty cycle sonar*

1. INTRODUCTION

Broadband Doppler sensitive waveforms

The continuous wave (CW) and frequency modulated (FM) waveforms are those most commonly used for active sonar. CW waveforms are sensitive to Doppler, but poor at resolving range, while FM waveforms resolve range well but are not sensitive to Doppler. Broadband Doppler sensitive (BBDS) waveforms can resolve both range and Doppler simultaneously, but typically suffer from matched filter sidelobes. BBDS waveforms include frequency shift keyed (FSK), which are often transmitted in a Costa's sequence [1], and various phase based methods, such as binary phase-shift keyed (BPSK) [2]. The BBDS waveform we analyze here is the minimum shift keyed (MSK) waveform, though the processing described can apply to any BBDS waveform.

MSK signalling, sometimes also called continuous phase frequency shift keying (CPFSK), was developed for digital communications. It employs both phase and frequency shift over many sub-pulses. In conventional MSK, the signal is encoded as two frequencies, f and $1.5f$, so that if the frequency is shifted from f to $1.5f$ or vice versa, the phase can be shifted by 180º (by multiplying by -1) if needed in order to maintain constant phase over the transition. The constant phase results in less spectral spread of the signal, while maintaining constant amplitude. Here we modify the MSK to allow arbitrary frequency choices for the two sub-pulse frequencies, which requires the phase to be computed at each transition to maintain constant phase. For a digital communications encryption, this would make decoding difficult, but here we need only maintain the transmit signal for matched filtering.

The MSK with bandwidth B, pulse length T, and center frequency f_0 is then generated as a sequence of sub-pulses, $\boldsymbol{s} = [\boldsymbol{s_1}\ \boldsymbol{s_2}\ \ldots\ ]$, each of duration $T_{sub} = 1/B$, computed by

$$s_k(n) = \cos\left[\frac{j2\pi f_k n}{f_s} + \phi_{k-1}\right] \quad n = 0,1,\ldots,[f_s T_{sub}] - 1, \quad k = 1,2,\ldots,\left\lfloor\frac{T}{T_{sub}}\right\rfloor \qquad (1)$$

Since the sub-pulse length results in sub-pulse bandwidth of $1/T_{sub}$, we choose the two frequencies to fill the band, and the phases for each sub-pulse to maintain constant phase,

$$f_k = \begin{cases} f_0 - \frac{B}{4} & if\ u_k = 0 \\ f_0 + \frac{B}{4} & if\ u_k = 1 \end{cases} \qquad \phi_k = mod[2\pi T_{sub} f_k + \phi_{k-1}, 2\pi] \qquad (2)$$

Where u_k randomly chosen with $P\{u_k = 0\} = P\{u_k = 1\} = 0.5$. In digital communications, the MSK is typically filtered with a Gaussian filter, which has zero overshoot step response. Here we filter with a more aggressive forward-backward (zero-phase) second order Butterworth filter to reduce spectral leakage at the expense of waveform extrema that reduces the RMS-to-peak ratio by about 1 dB.

Searching for an acoustic echo with Doppler sensitive waveforms entails matched filtering with a portion of the transmitted waveform that has been dilated in time to represent varying possible Dopplers of the echo. The ideal matched filter response can be characterized by the wideband ambiguity function (WAF) across varying time lag, τ, and Doppler, or range rate, $\dot{r}$,

$$\Psi(\tau,\alpha) = \sqrt{\alpha}\int_{-\infty}^{\infty} s(t)s^*[\alpha(t-\tau)]dt, \quad \alpha = \frac{c+\dot{r}}{c-\dot{r}}, \quad c \equiv sound\ speed \qquad (3)$$

The WAF for an 18 second filtered MSK with bandwidth 800 Hz and center frequency 2200 Hz, matched filtered with the full waveform is plotted in Figure 1, with power vs. range at zero Doppler, and maximum power across Doppler also plotted. Sidelobes, which have root-mean-square value a factor $T \cdot B$ lower than the peak, are evident. The lower right plot shows a close-

up of the main-lobe, which has range resolution of $\frac{c}{2B} \cong 0.5\ m$ and Doppler resolution of $\frac{c}{Tf_0} \cong 0.02\ kts$. Note that processing with only a portion of the waveform will reduce both range and Doppler resolution, while increasing sidelobe energy.

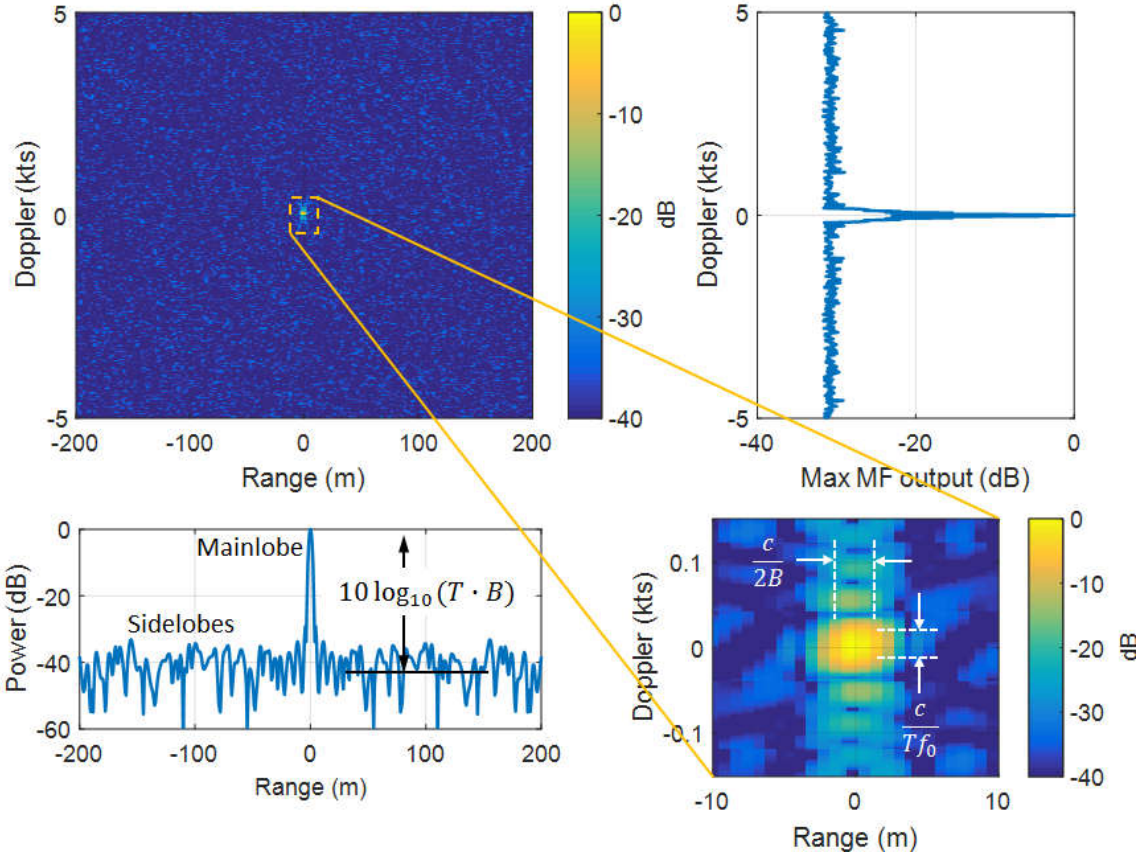


Figure 1: WAF for the filtered MSK across range and Doppler (upper left), the WAF power at zero Doppler (lower left), maximum WAF power over all range (upper right), and close-up of the main-lobe (lower right).

High duty cycle sonar and broadband Doppler sensitive waveforms

In high duty cycle (HDC) sonar, the probing transmit pulse is retransmitted at a rate such that matched filter search interval and transmit interval may overlap. Continuous active sonar (CAS) is a type of HDC sonar in which the transmit signal is repeated without delay. Figure 2 shows the post-beamformer spectrogram and matched filter output for both a LFM and MSK pulse, transmitted in shallow water with echo-repeater serving as target. For both waveforms, the repetition interval is 20 sec, with T = 18 sec and B = 800 Hz. The LFM spectrogram shows how the direct path transmission is still being received when the target echo first arrives. Although the data is beamformed, the off-axis beam response is high enough that the direct path energy is still significant.

The right half of Figure 2 depicts the primary difficulty with using BBDS waveforms for HDC sonar. The significant sidelobes for the MSK, about $10\log_{10}(TB)$ down from the peak, appear as noise-like and mask the typically much weaker target echo. In this example, the sidelobes would need to be reduced by about 30 dB to yield even a 10 dB signal to noise ratio (SNR), where "noise" is here the sidelobes. Moreover, the specular surface and bottom bounce energy from the source can arrive at much steeper angles. If a hydrophone line array is used, the conical beam shape can result in this strong bottom or surface reflection energy appearing in the near broadside beams typically where the primary target search is performed.

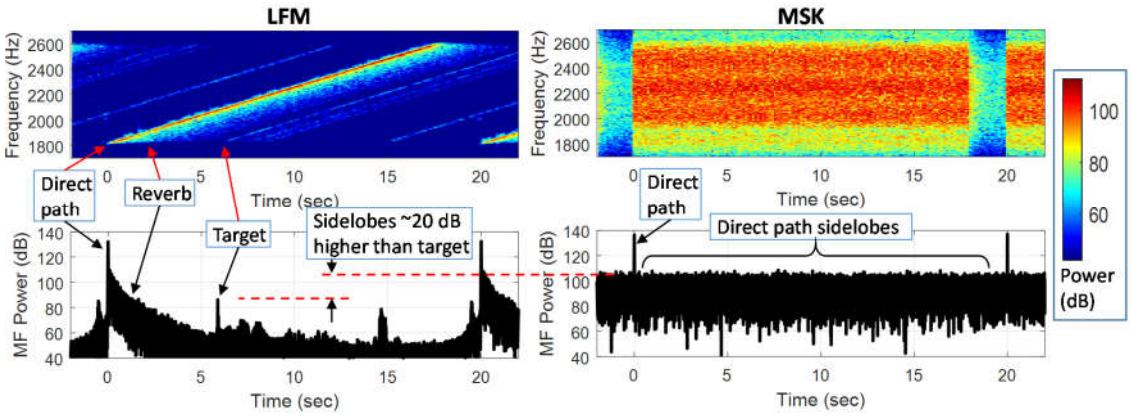


Figure 2: Example spectrograms (top) and zero Doppler matched filtered output (bottom) for both LFM (left), and MSK HDC (right) waveforms, with T=18 sec, B=800 Hz, repeated every 20 sec. In the LFM matched filter plot, the direct path, reverb, and target echo are clearly visible, while the matched filter sidelobes from the MSK direct path mask the target echo.

2. REDUCING DIRECT PATH INTERFERENCE

Reducing the strong direct path interference described above can be done by modifying the transmit waveform, by using temporal based techniques, or by exploiting spatial differences between the direct path and the desired search space. Modifying the waveform is currently being investigated by this and other authors [3], but will not be discussed here. Previous work in temporal based methods, sometimes called adaptive matched filtering, e.g. [4,5] have shown promise, but can be computationally expensive. Current research by the author includes implementation of the CLEAN algorithm [6], which requires less computation and has shown good results. Spatial based techniques include adaptive beamforming and adaptive noise cancellation, and will be the focus of this paper.

Spatial based methods of direct path interference reduction can be limited by spatial overlap of the interference and search space (as described above), by unknown spatial diversity of the target, and by temporal variation of the received signal in active sonar applications. We will begin with conventional and adaptive beamforming, and introduce a technique that takes advantage of properties of a triplet line array and the directivity of the primary source-to-receiver acoustic paths that make up the bulk of the interference.

Beamforming for interference rejection

Defining the steering vector $\mathbf{d}(k)$ as the set of complex phase terms at frequency bin k for aligning data from all hydrophones coming from a single beam direction, and defining the hydrophone data vector as $\mathbf{x}(k)$, the beam output of a conventional beamformer is computed as the projection of the data onto the desired steering vector, (suppressing the frequency bin index k),

$$y = \mathbf{d}^T\mathbf{x} \tag{4}$$

By shading the steering vector, the beam sidelobes of a conventional beamformer can be reduced significantly, but at the expense of a larger beam mainlobe, which can result in increased reverberation in the beam.

Adaptive beamforming methods sample the data over time and use the information to improve the beamforming, typically suppressing directional interferences. The Minimum Variance Distortionless Response (MVDR) beamformer estimates the steering vector by

$$\mathbf{w} = \frac{\mathrm{R}^{-1}\mathbf{d}}{\mathbf{d}^T\mathrm{R}^{-1}\mathbf{d}} \tag{5}$$

where $\mathrm{R} = E\{\mathbf{x}\mathbf{x}^T\}$ is the Cross Spectral Density Matrix (CSDM). The MVDR beamformer results in nulls steered towards any strong interferers, unless they are in the direction of the steering vector, which is always unit gain. Estimating R is typically done by averaging the data. Since the MSK waveform is continuously full-band, the estimate can be made over a portion of a ping, whereas for waveforms that vary over time, such as the LFM, multiple pings may be necessary to get a full-rank estimate.

For a horizontal triplet (or cardioid) array, which is a line array consisting of sets of hydrophones arranged in closely spaced equilateral triangles, the processing is typically designed to form a cardioid using each set with null steered to the side opposite the look direction [7]. This is used to disambiguate targets on the port or starboard sides of the array. Here processing is presented that instead uses the triplets to attenuate the direct source-to-receiver path interference as well as the specular surface and bottom bounce reflections, at the expense of now having no port-starboard ambiguity resolution.

It is first noted that the direct and specular surface/bottom reflected paths are largely confined to the vertical plane connecting the source and the midline of the array, as depicted in Figure 3. Also shown in the figure are several dipoles, which can be formed using the hydrophone triplets. The dipoles can be oriented such that their nulls are oriented on the direct and surface/bottom reflection interference plane. The properly calibrated dipole outputs can then be beamformed as a line array.

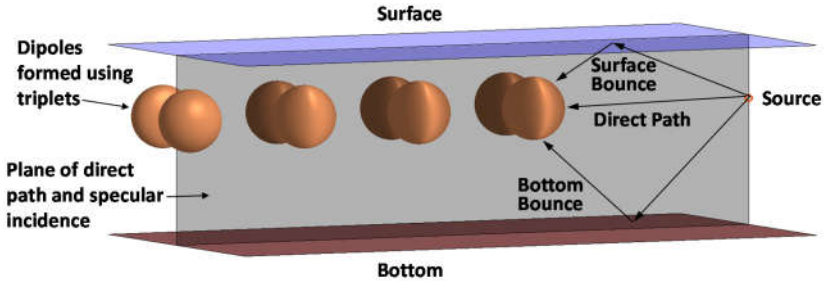


Figure 3: Illustration of direct and surface/bottom specular reflected interference, which are primarily directed along the vertical plane connecting the source and sensors. The hydrophone triplets can be used to form dipoles with nulls oriented on that same plane.

Formation of a dipole using a pair of closely spaced hydrophones can be achieved by differencing the two and scaling by the expected attenuation at the maximum response axis (MRA) of the dipole. Likewise, an orthogonally oriented dipole can be formed using the third hydrophone in the triplet and a scaled sum of the first two. The equations for generating the dipoles, with proper calibration for frequency f_0, are

$$d_1(t) = \frac{x_2(t) - x_3(t)}{2\sin(\pi f_0 s/c)} \qquad d_2(t) = \frac{x_1(t) - [x_2(t) + x_3(t)]/2\cos\left(\frac{\pi f_0 s}{c}\right)}{2\sin\left(\pi f_0 \sqrt{3} s/2c\right)} \tag{6}$$

where d_1 and d_2 are the horizontally and vertically oriented dipoles, respectively, and x_1, x_2, and x_3 are the three hydrophones in a single triplet with spacing s between hydrophones. The equations in (6) result in dipoles with centers offset by $\frac{\sqrt{3}}{4}s$, as illustrated in Figure 4. This will be negligible in terms of amplitude differences at target ranges, but will result in elevation dependent phase offset that will affect subsequent beamforming of the dipole data.

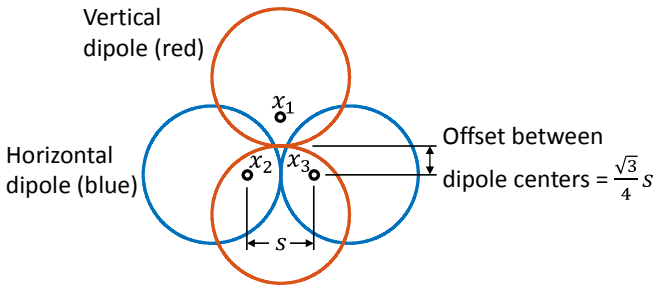


Figure 4: Illustration of the horizontal and vertical dipoles formed using the equations in (6).

The two dipoles can be closely approximated by $d_1 = \cos(\phi)$, $d_2 = \sin(\phi)$ where ϕ is the elevation on the plane perpendicular to the array centreline. To correct for possible roll of the array triplets, the dipoles are combined using the identity

$$d_\rho = \cos(\phi + \rho) = d_1 \cos(\rho) + d_2 \sin(\rho) \tag{7}$$

where ρ is the roll angle of the triplet, and d_ρ is the roll-corrected dipole.

3. EXPERIMENTAL RESULTS

The Littoral Continuous Active Sonar 2015 (LCAS 15) experiment was performed by an international team led by the NATO Centre for Maritime Research and Experimentation (CMRE). It took place off La Spezia, Italy in October 2015 where the bottom depth was upslope towards the target from 110 to 60 m. Both MSK and LFM waveforms were transmitted with the same pulse duration, 18 sec, and bandwidth, 800 Hz, centered at 2200 Hz, in similar geometries. The active source was towed about 150 m forward of the Five Octave Research Array (FORA), which had a set of 78 hydrophone triplets. An echo-repeater served as target, and was towed in the opposite direction at a closest point of approach of about 4500 m.

Both the LFM and MSK hydrophone data were processed to form dipoles using the equations in (6), and the measured roll of the array was used to rotate the dipole using equation (7) such that the dipole nulls were oriented vertically. To test the ability of the dipole technique to suppress the direct path and surface/bottom specular interference, the LFM results are first analyzed, with the matched filter output plotted on the lower left half of Figure 5 for both a single hydrophone (red) and a single dipole (black). The close-up around the direct path is plotted on the top, where it can be seen that the dipole direct path peak and surface/bottom specular energy, which is less than 100 m after the peak, are decreased by about 20 dB lower than the single hydrophone. The MSK waveform data was matched filtered, with the zero Doppler outputs plotted in the lower right of Figure 5. The target was expected to be at zero Doppler. Again the direct path peak for the dipole is about 20 dB lower than the single hydrophone, but it can be seen that the sidelobes are also decreased by 20 dB. The LFM energy near the target is decreased somewhat because the dipole is rejecting reverberation and ambient noise, but there are no significant sidelobes with the LFM. The target peak for the LFM is decreased by about 1 dB, possibly because the energy is not arriving in at the center of the dipole in the vertical direction. The target in the MSK case is still masked by the sidelobes from the direct path.

The MVDR beamformer described in equation (5) was applied to the 78 dipole outputs, treated as a line array, with the beam steered in the known direction of the target (near broadside). A MVDR Beamformer was also applied to all 234 hydrophones of the full volumetric array as comparison, this time with the beam steered towards the target in azimuth, but at zero elevation. Both MVDR Beamformer results are plotted in Figure 6, for both the LFM waveform (left) and MSK (right). Both MVDR beamformers suppressed the direct path

about 50 dB lower than the single dipole, and the surface/bottom specular energy by about 20 dB. The full volumetric MVDR also suppressed the target echo by about 20 dB. The MSK waveform dipole MVDR beamformed direct path was suppressed by over 50 dB, but two peaks occurred near where the direct path was. The sidelobe energy only decreased by about 30 dB from the single dipole. The full MVDR beamformer had similar multiple peaks, but the sidelobes were decreased by about 50 dB. The target was likely also suppressed for this case.

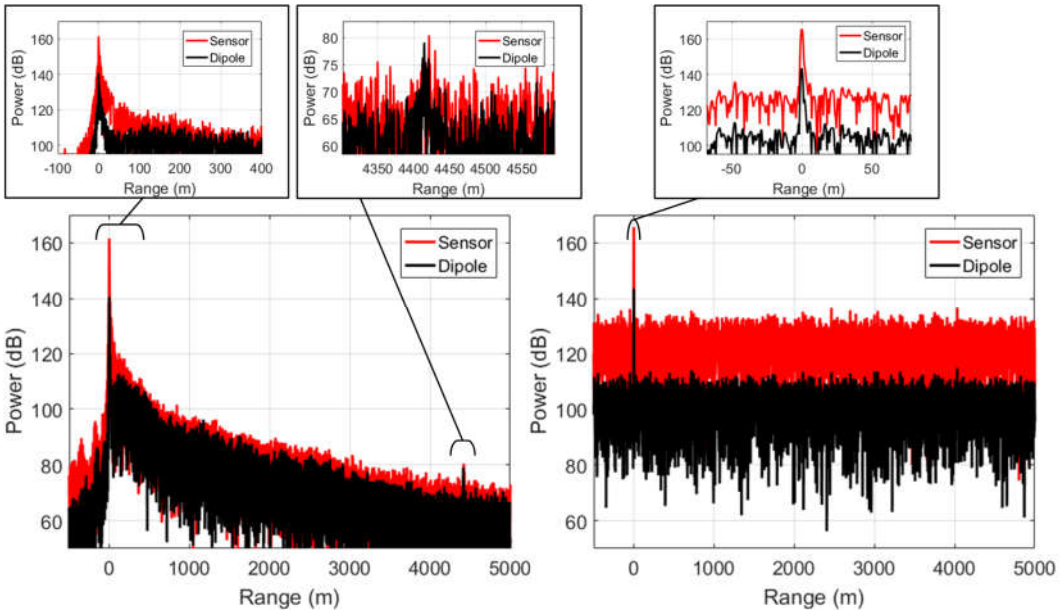


Figure 5: LFM (lower left) and MSK (lower right) matched filter outputs for single hydrophone (red) and a single dipole (black). Top plots show close-ups around the direct path and target peaks for the LFM and the direct path peak for the MSK. For both waveforms, the direct path and surface/bottom interaction (less than 100 m range) are suppressed by about 20 dB. The MSK shows a similar decrease in the sidelobes.

4. CONCLUSIONS

A method for reducing the direct path and the surface and bottom specular reflected interference in HDC sonar was introduced and experimentally demonstrated. The technique, which exploits the properties of a triplet hydrophone array, forms a set of orthogonal dipoles and steers them to form a null along the vertical plane where the direct and specular bounce paths are prevalent. The resulting set of steered dipoles were then beamformed as a line array. Since the steered dipoles where formed from dipoles with different phase centers, they had phase shift dependent on the roll correction and the arrival angle of the interference. A MVDR beamformer was used, since it estimates the phase of the strong interfering energy and steers nulls in those directions.

Results from the LCAS 15 experiment were analysed to test the algorithm, where both LFM and MSK HDC waveforms were transmitted. The LFM, which didn't suffer from matched filter sidelobe masking, allowed the effect on direct and specular paths and the target to be observed. About 20 dB of direct and specular interference suppression was seen for the individual dipoles, with only about 1 dB of target level decrease. For the dipole MVDR, there was about 50 dB of additional suppression of the direct path, and 30 dB of the specular, with about 1 dB more of target level decrease. The MSK signal, which had significant matched filter sidelobe masking, showed a decrease in direct path, and associated sidelobes, of about 20 dB for the dipole, and about 25 dB more decrease for the MVDR sidelobe levels.

A full volumetric MVDR beamformer was also implemented for comparison, which again showed significant reduction in the direct and specular paths, but also a significant reduction in

the target level. This is possibly because the target acoustic path did not arrive at zero elevation where the elevation of the full volumetric MVDR was, and was cancelled by the beamformer.

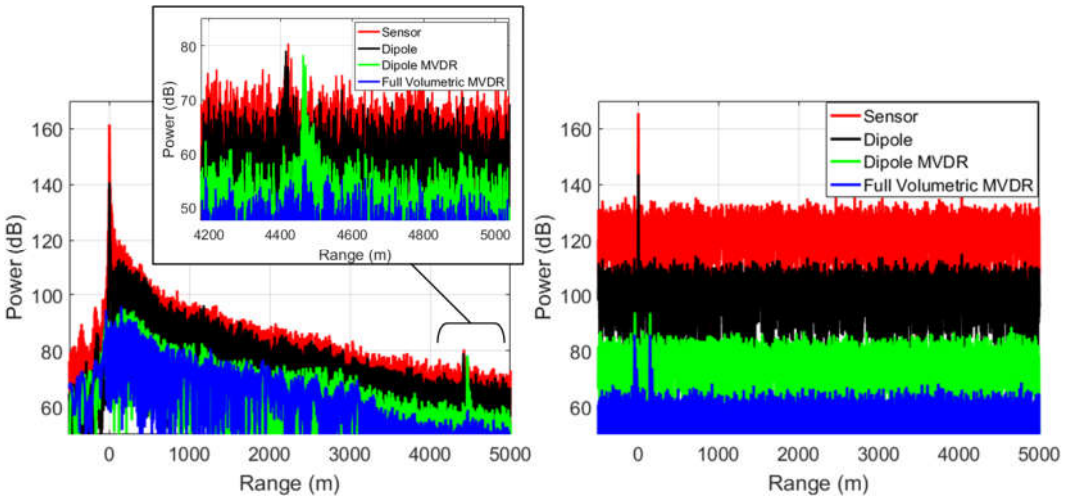


Figure 6: MVDR beamformer applied to the 78 dipoles after matched filtering (green) and a full volumetric MVDR beamforming applied to all 234 hydrophones (blue), for both the LFM waveform (lower left) and the MSK (lower right). Note that both the full volumetric and dipole beamformers suppresses the direct path interference well, but the full volumetric also supresses the target. The LFM waveform sidelobes are supressed, but still higher than the expected target level. The original single hydrophone and dipole are also plotted.

ACKNOWLEDGEMENTS

This work was funded by the Office of Naval Research Code 321. The LCAS 15 experiment could not have been possible without the efforts of NATO CMRE and the test participants.

REFERENCES

[1] **Costas, J. P.,** A study of a class of detection waveforms having nearly ideal range-Doppler ambiguity properties, *Proceedings of the IEEE,* 72 (8), pp. 996–1009, 1984.

[2] **Mathieu, E. and S. Beerens**, False-alarm reduction for low-frequency active sonar with BPSK pulses: Experimental results, *IEEE Journal of Oceanic Engineering,* 36 (1), pp. 53-60, 2011.

[3] **Hague, D. and J. Buck**, The generalized sinusoidal frequency-modulated waveform for active sonar, *IEEE Journal of Oceanic Engineering*, 42 (1), pp. 109-123, 2017.

[4] **Ling, J., Li, J., Stoica, P., and Datum, M.**, On probing waveforms and adaptive receivers for active sonar, *Journal of the Acoustical Society of America*, 129 (6), pp. 3640-51, 2011.

[5] **Lourey, S.**, Adaptive filtering for enhanced detection of continuous active sonar signals, In *4th Underwater Acoustics Conference and Exhibition*, Skiathos, Greece, ed. by John Papadakis, pp. 145-152, 2017.

[6] **Högbom, J.**, Aperture synthesis with a nonregular distribution of interferometer baselines, *Astron. Astrophys. Supplements*, vol. 15, pp. 417-426, 1974.

[7] **Baldacci, A., Haralabus, G., and van Velzen, M.**, Cardioid receive array calibration for active systems, *NATO Undersea Research Centre Technical Report NURC-PR-2006-015,* 2006.

Structured Session 13
Machine learning, compressive sensing and signal processing

Organiser(s): Xenaki Angeliki, Gerstoft Peter

VON MISES PRIOR FOR PHASE-NOISY DOA ESTIMATION: THE VITAMIN ALGORITHM

Guillaume Beaumont[a], Angélique Drémeau[a], Ronan Fablet[b]

[a]ENSTA Bretagne, Lab-STICC UMR 6285, CNRS, BREST, FRANCE
[b]IMT Atlantique, Lab-STICC UMR 6285, CNRS, BREST, FRANCE

guillaume.beaumont@ensta-bretagne.org

Abstract: *Sound waves in the ocean are affected by the space and time variabilities of the propagation medium. These fluctuations, mainly caused by internal waves such as tides and gyres, can lead to a loss of phase information in measured wave-fronts, and make hardly predictable the true location of a source. As a consequence, the performance of classical direction-of-arrival (DOA) estimation algorithms are significantly degraded. An important literature addresses this issue by considering either the phase as non-informative or the environment as a noise with no physical information. In this work, we propose to introduce a phase prior inspired by random fluctuation theories. This prior is combined with a sparsity assumption on the number of expected DOAs and exploited within a Bayesian framework. The contributions of such an approach are two-fold: by the use of suitable prior information (small number of DOAs and phase distortion), it allows an estimation of DOAs from a single snapshot, while simultaneously providing a posterior estimation of the mean fluctuations of the propagation medium. Bayesian inference can be performed in different ways. Among the different possible procedures, we chose here to resort to a Bethe approximation and a message-passing approach recently considered in compressive sensing setups. The resulting algorithm places in the continuation of our previous works. The main improvement lies in the probabilistic model used to describe the phase distortion. Here we use a Multivariate Von Mises distribution, more suitable to directional statistics and still fitting the simplified theory of phase fluctuation. Numerical experiments with synthetic datasets show that the proposed algorithm, dubbed as VITAMIN for ``Von mIses swepT Approximate Message passINg'', presents interesting performance compared to other state-of-the-art algorithms. In particular, in the considered experiments, VITAMIN behaves well regarding its robustness to additive noise and phase fluctuations.*

Keywords: *Compressed Sensing, DOA Estimation, Message Passing, WPRM, Bayesian Estimation.*

1. INTRODUCTION

Wave propagation through random media is at the heart of many applications (RADAR, acoustics, telecommunications…). Studies in this research field aim at characterizing the fluctuations of the propagation medium and their impact on a transmitted signal to improve associated processing. In this respect, the problem of direction-of-arrival (DOA) estimation occupies an important place in the literature. However, despite the large number of methods proposed, very few explicitly address the problem of fluctuating environments.

DOA estimation in well-known environments simply corrupted by additive white Gaussian noises constitute indeed the wide majority of the approaches. In that family, we find first the very popular beamforming approach [1], which relies on a simple inversion of the measurement matrix. Other methods put additional assumptions about the nature of the source signal. For example, some ‘high resolution’ techniques rely on the hypothesis of orthogonality between signal and noise subspaces like in the MUSIC algorithm [2]. More recent contributions propose to exploit a sparsity assumption on the number of DOA to recover, leading to so-called 'compressive' beamforming techniques [3].

To the best of our knowledge, DOA estimation in noisy environments has been mostly addressed from two major perspectives: the corrupting effect of the propagation medium on measurement is modelled either as a non-informative phase perturbation [4] or informative but uncorrelated phase noises [5].

Our previous work [6] started from this vein of methods. We tried however to go further by considering a perturbation model compatible with some perturbation regimes observed and defined by [7, 8]. Given a high-frequency approximation, we were able to modelize the perturbation as a multiplicative phase noise following a multivariate Gaussian law with a covariance matrix carrying the information related to the strength of the fluctuations. This model was exploited through a Message Passing Algorithm, resulting in a procedure named paSAMP [9].

In this paper, we refine our noise model to be more suitable for the issue of phase perturbation, using a Multivariate Von Mise Prior, more adapted to directional statistics [10]. As a result, we propose an improved version of paSAMP: the VITAMIN (for Von mIses swepT Approximate Message passINg) algorithm.

2. CHARACTERIZATION OF RANDOM FLUCTUATION IN THE OCEAN

We use here the results of works initiated in [7] and then updated in [8] to characterize the impact of multi-scale fluctuations of the ocean on a measured signal. Given a certain fluctuation strength of the internal waves, the signal can be corrupted as a function of its frequency, the propagation range and other interactions bottom-surface. Considering a high frequency approximation, we can define three saturation regimes which can be easily described through geometrical optics:

- The unsaturated regime: variations are not strong enough to alter the source ray. In this cas, there is no perturbation on the measured DOA.
- The partially saturated regime: stronger variations cause a diffraction phenomenon of the source ray. As a result, the sensors measure a coherent ray and multi-rays due to this spread. This spread is directly linked to the strength of the fluctuations and impacts the consistency of the wave propagated in the random medium. Beyond a so-called 'coherence-length’, we observe a loss of consistency, this length can be retrieved from measurement and easily modelled as a covariance structure within a random phase noise.

- The fully saturated regime: this regime can be observed when the variations are too strong, the micro-rays spread beyond the coherence ray. In that case, we observe a total loss of information on the phase noise statistics.

In this paper, we focus on DOA estimation in presence of a partially saturated regime.

3. FRAMEWORK

Observation model

Considering a *N* sensors array, one snapshot of the acoustic signal received on the *n-th* sensor can be written as:

$$y_n = e^{j\theta_n} \sum_{m=1}^{M} d_{nm} x_m + \eta_n \tag{1}$$

with θ_n the phase noise due to the spatial fluctuations of the medium, d_{nm} an element of the plane wave dictionary D with $d_m = [e^{j\frac{2\pi}{\lambda}\Delta\sin(\phi_m)} \dots e^{j\frac{2\pi}{\lambda}\Delta N\sin(\phi_m)}]^T$, Δ the sensor spacing and λ the signal wavelength. The aim here is to retrieve $x = [x_1, \dots, x_M]^T$ whose components index the atoms of D (i.e. the directions of arrival ϕ_m) in presence of phase noise and additive noise η_n.

Bayesian framework : prior assumptions

Prior on the sources

As a first assumption, we consider a small number of DOA: **x** is assumed to be sparse. Within a Bayesian framework, this constraint can be formulated as a Bernoulli-Gaussian prior on **x** [11], so that, for each x_m :

$$p(x_m) = \rho \mathscr{CN}(x_m; m_x, \sigma_x^2) + (1-\rho)\delta_0(x_m) \tag{2}$$

where ρ is the Bernoulli parameter, standing for the 'sparse rate' , i.e. the probability for x_m to be non-zero, $\mathscr{CN}(x_m; m_x, \sigma_x^2)$ stands for the circular Gaussian distribution with mean m_x and variance σ_x^2. Finally, δ_0 is the Dirac distribution.

Prior on the phase noise

As mentioned above, we choose the prior on θ_n with regard to previous works dealing with phase retrieval algorithms used for solving DOA estimation problem, studies [7,8] addressing the statistical impacts of the fluctuations on the measured signal and works about directional statistics [12,10]. In this respect, the multivariate Von Mises distribution appeared to be particularly suitable [10]:

$$p(\boldsymbol{\theta}) \propto \exp(\boldsymbol{\kappa}^T \mathbf{c}(\boldsymbol{\theta}, \boldsymbol{\mu}) - \mathbf{s}(\boldsymbol{\theta}, \boldsymbol{\mu})^T \Lambda \mathbf{s}(\boldsymbol{\theta}, \boldsymbol{\mu}) - \mathbf{c}(\boldsymbol{\theta}, \boldsymbol{\mu})^T \Lambda \mathbf{c}(\boldsymbol{\theta}, \boldsymbol{\mu})) \tag{3}$$

with parameters $\boldsymbol{\mu} = [\mu_1, \dots, \mu_M]^T, \boldsymbol{\kappa} = [\kappa_1, \dots, \kappa_M]^T$and Λ relative to a precision matrix, also introducing the cosine and sine vector relative to the angular noise, $\mathbf{c}(\boldsymbol{\theta}, \boldsymbol{\mu}) \triangleq [\cos(\theta_1 - \mu_1), \dots, \cos(\theta_M - \mu_M)]^T, \mathbf{s}(\boldsymbol{\theta}, \boldsymbol{\mu}) \triangleq [\sin(\theta_1 - \mu_1), \dots, \sin(\theta_M - \mu_M)]^T$.

Prior over the additive noise

Classically, we finally consider the additive noise η_n as a white gaussian noise, with zero mean and a variance σ^2.

4. BAYESIAN ESTIMATION OF THE DOA

Considering model (1)-(3), we can formulate the DOA estimation problem as a Minimum Mean Square Error problem:

$$\widehat{\mathbf{x}} = \underset{\widetilde{\mathbf{x}}}{\operatorname{argmin}} \int_{\mathbf{x}} ||\mathbf{x} - \widetilde{\mathbf{x}}||_2^2 \, p(\mathbf{x}\,|\,\mathbf{y}) d\mathbf{x} \tag{4}$$

where $p(\mathbf{x}\,|\,\mathbf{y}) = \int_{\theta} p(\mathbf{x}, \boldsymbol{\theta}\,|\,\mathbf{y}) d\boldsymbol{\theta}$ is the posterior distribution over $\mathbf{x}$ marginalized over the phase perturbation $\boldsymbol{\theta}$. Because of this marginalization, solving (4) leads to an intractable problem. One possible way to circumvent the issue is to search for an approximation of $p(\mathbf{x}, \boldsymbol{\theta}\,|\,\mathbf{y})$. More specifically, we propose here to resort to variational Bayesian approximations which try to approach $p(\mathbf{x}, \boldsymbol{\theta}\,|\,\mathbf{y})$ with some suitable factorisations minimizing the Kullback-Leibler divergence (i.e. the loss of information between the true distribution and the factorized one). Among them, we focus on the so-called Bethe approximation.

From Bethe approximation to the paSAMP and VITAMIN algorithms

The Bethe approximation relies on a factorisation of the posterior distribution of interest according to some clusters of variables. Minimizing the Kullback-Leibler divergence under such a penalization can then be well-handled by Message Passing algorithms [13], namely methods based on Belief Propagation. Among them, the Swept Approximate Message Passing algorithm [14] was proposed to solve non-linear but still component-wise problem (namely, measurements (1) are assumed to be independent from each other). In [6], we extended this approach to a Gaussian phase noise, leading to the paSAMP algorithm. Here, we adapt it to the multivariate Von Mises distribution (2). Due to space limitations, we omit the derivations of the algorithm. We refer however the reader to [15] for more details. We named the approach VITAMIN (for Von mIses swepT Approximate Message passINg) algorithm.

5. PROOF OF CONCEPT

In this section we discuss the performance of the VITAMIN algorithm to justify the interest in refining the phase noise model with more ‘directional-inspired’ methods.

For this, we run this algorithm on a set of simulated data according to a specific configuration. We want to recover the directions of arrival of k plane waves over a set of $N = 32$ potential angles with an antenna of $M = 32$ sensors. We consider here a simple setup where the phase noise obey a univariate Von Mises law. This corresponds to model (3) with parameter $\Lambda = 0_{32\times32}$. For the discussed result, we consider homogenous $\boldsymbol{\kappa}$ and set $\kappa_n = 4$ for all n, this value is equivalent to a Gaussian noise with a standard deviation of 0.25 radians, corresponding to an important angular perturbation.

We set the parameter $\lambda/\Delta = 4$ and for each of the k incident waves, each coefficient of $\mathbf{x}$ is designed as a realisation of distribution (2) with $m_x = 0 + j \times 0$, $\rho = K/M$ and $\sigma_x^2 = 0.1$.

We want to observe the contribution in terms of reconstruction performance of such a prior. To do this, we observe the normalized correlation $\frac{|\mathbf{x}^H \hat{\mathbf{x}}|}{\|\mathbf{x}\|\|\hat{\mathbf{x}}\|}$ between the true vector $\mathbf{x}$ and its estimate $\hat{\mathbf{x}}$ as a function of the additive noise variance and for different numbers of sources k. To obtain stable results we mean this performance index over 200 trials, corresponding to the number of realizations of $\mathbf{x}$ and angular noise.

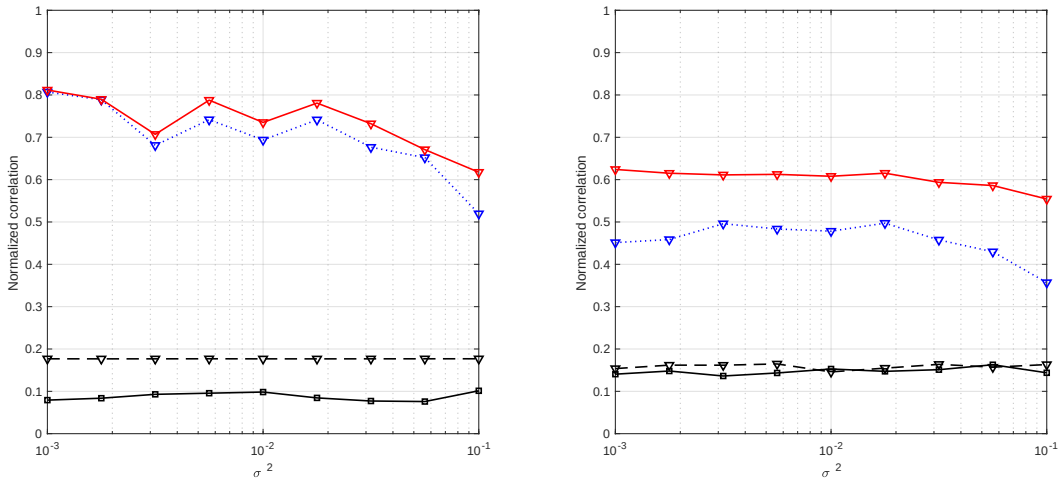


Figure 1: Normalized correlation regarding the additive noise variance σ^2. Here we observe the performance of conventional beamforming (squared line), prSAMP(dashed line), paSAMP(dotted line) and VITAMIN (triangle, solid line), one source (left) and ten sources (right).

Figure 1 illustrates the performance of VITAMIN and - even if the equivalence between the Von Mises distribution and the Gaussian distribution can be made for small variances - the importance of considering a directional prior in presence of phase noise. Indeed, we can see on this figure that VITAMIN outperforms the compressive beamforming and the prSAMP algorithm which do not integrate any informative prior over the phase noise. Moreover, the performance gap between VITAMIN and paSAMP (which exploits a Gaussian prior over the phase noise) tends to increase with the number of sources. This may due to the loss of information while considering an approximated prior: with a small number of sources, the loss is minimized but it tends to rise with the amount of information.

CONCLUSION

In this work, we proposed a new implementation of prSAMP with a modelization of phase noise from directional statistics. Such an approach can be justified by the fact that in such compressive sensing method, good prior knowledge is necessary to achieve perfect estimation of $\mathbf{x}$. After derivation of the calculations, we are able to propose the VITAMIN algorithm, allowing us to perform a better DOA estimation than algorithms which integrate a non-informative or Gaussian noise prior.

REFERENCES

[1] **D.H. Johnson and D.E. Dudgeon**, “Array Signal Processing: Concepts and Techniques”, *Prentice-Hall signal processing series*. P T R Prentice Hall, 1993.

[2] **R. O. Schmidt**, “Multiple emitter location and signal parameter estimation,” *IEEE transactions on antennas and propagation*, vol. 34, no. 3, pp. 276–280, 1986.

[3] **A. Xenaki, P. Gerstoft, and K. Mosegaard**, “Compressive beamforming” *The Journal of the Acoustical Society of America*, vol. 136, no. 1, pp. 260–271, 2014.

[4] **A. Paulraj and T. Kailath**, “Direction of arrival estimation by eigenstructure methods with unknown sensor gain and phase”, *IEEE International Conference on Acoustics, Speech, and Signal Processing*, 1985, pp. 640-643.

[5] **J. Ringelstein, A. B. Gershman and J.F. Bohme**, “Direction finding in random inhomogeneous media in the presence of multiplicative noise”, *IEEE Signal Process. Lett.*, 7(10): 269-272, October 2000.

[6] **G. Beaumont, R. Fablet, A. Drémeau**. “An Approximate Message Passing approach for DOA estimation in phase noisy environments” , *Int'l Conference on Latent Variable Analysis and Signal Separation (LVA/ICA)*, Guildford, UK, July 2018.

[7] **R. Dashen, S. M Flatté, W. H Munk, K. M Watson, and F. Zachariasen**, “Sound transmission through a fluctuating ocean”, *Cambridge University Press*, 2010.

[8] **John A. Colosi**, “Sound Propagation through the Stochastic Ocean”, *Cambridge University Press*, 2016.

[9] **A. Drémeau and C. Herzet**, “DOA estimation in structured phase-noisy environments” *IEEE International Conference on Acoustics, Speech, and Signal Processing*, 2016, pp. 3176–3180.

[10] **K. V. Mardia, G. Hughes, C. Taylor and H. Singh**, “A Multivariate Von Mises Distribution with Applications to Bioinformatics”,*The Canadian Journal of Statistics / La Revue Canadienne de Statistique*, 2008,Vol. 36, No. 1, pp. 99-109.

[11] **C. Soussen, J. Idier, D. Brie, J. Duan**. “From Bernoulli-Gaussian deconvolution to sparse signal restoration”. *IEEE Transactions on Signal Processing*, Institute of Electrical and Electronics Engineers, 2011, 59 (10), pp.4572-4584.

[12] **K. V. Mardia and P. E. Jupp**, “Directional statistics”, *John Wiley & Sons*, 2009.

[13] **D. L. Donoho, A. Maleki and A. Montanari**. “Message-passing algorithms for Compressed sensing’’, *Proceedings of the National Academy of Sciences Nov 2009*, 106 (45), pp. 18914-18919.

[14] **A. Manoel, F. Krzakala and E.W. Tramel**. “Swept Approximate Message Passing for Sparse Estimation’’. *International Conference on Machine Learning*, 2015, pp. 1123-1132.

[15] **G. Beaumont, R. Fablet, A. Drémeau**. “DOA estimation in fluctuating environments: an approximate message-passing approach - Technical report” *https://hal.archives-ouvertes.fr/hal-01624855v6*

HIGH-RESOLUTION LOW-FREQUENCY COMPRESSIVE SAS IMAGING WITH DISTRIBUTED OPTIMIZATION

Angeliki Xenaki[a], Yan Pailhas[a] & Ronan Hamon[a]

[a]Centre for Maritime Research and Experimentation, STO-NATO
Viale San Bartolomeo 400, 19126 La Spezia, Italy

Corresponding author: Angeliki Xenaki, email: Angeliki.Xenaki@cmre.nato.int

Abstract: *Synthetic aperture sonar (SAS) provides very high resolution acoustic imaging by processing coherently the backscattered acoustic signal recorded over several consecutive pings. Utilizing wideband high-frequency pulses, synthetic aperture processing can achieve centimetric range and cross-range resolution resulting in optical-like images of the seafloor reflectivity. Low frequency waves can be partly transmitted through objects or penetrate the seafloor providing information about internal structure and buried objects. Such frequency-specific information is crucial for improving the performance of automatic target recognition algorithms. Both sub-band processing and data reduction, however, degrade the SAS resolution. In this paper, SAS imaging is formulated as an ℓ_1-norm regularized least-squares optimization problem which improves the resolution by promoting parsimonious representations of the data. We use an algorithm based on the alternating direction method of multipliers (ADMM) to solve the optimization problem in a distributed and computationally efficient way. The resulting SAS image is the consensus outcome of collaborative filtering of the data from each ping. The potential of the proposed method for high-resolution, low-frequency SAS imaging is demonstrated with simulated data.*

Keywords: *SAS imaging, sparse reconstruction, ADMM, distributed optimization*

1. INTRODUCTION

Synthetic aperture sonar (SAS) combines coherently the backscattered echoes from successive acoustic pulses (pings) to produce high-resolution images of the seafloor with application in mine countermeasures, underwater archaeology or inspection of underwater installations [1]. To achieve the very-high resolution necessary for detection and classification of objects on the seafloor, SAS requires widebeam systems and wideband, high-frequency transmitted pulses at a high ping-repetition rate [1]. On the other hand, low frequencies can excite acoustic resonances in objects with structural symmetries or detect buried objects due to improved seafloor penetration [2]. Such low-frequency features are crucial for reducing the false alarm rate of automatic target recognition (ATR) algorithms in detection and classification of man-made objects. However, sub-band processing and reverberation reduce the resolution in conventional SAS imaging at low frequencies.

High-resolution imaging of low-frequency features is based on image denoising methods such as spatial filtering [3] or sparse feature selection through wavelet shrinkage [4]. This paper presents a signal processing method for high-resolution low-frequency SAS imaging based directly on the backscattered data. In particular, SAS imaging is formulated as a least-squares optimization problem regularized with an ℓ_1-norm penalty which promotes sparse solutions [5]. Since the backscattered data is naturally distributed over multiple pings, we use the alternating direction method of multipliers (ADMM) [6] to solve the optimization problem in a distributed way. The resulting consensus optimization problem involves minimizing a data fitting term per ping with the constraint that the local solutions agree to a global model for the SAS image. The proposed method provides high-resolution low-frequency SAS imaging while it allows for decentralized storage and processing of the large amount of data resulting from aperture synthesis.

In the following, vectors are represented by bold lowercase letters and matrices by bold uppercase letters. The symbols ^{T}, ^{H} denote the transpose and the Hermitian (i.e., conjugate transpose) operator respectively on vectors and matrices. The symbol * denotes simple conjugation. The ℓ_p-norm of a vector $\mathbf{x} \in \mathbb{C}^n$ is defined as $\|\mathbf{x}\|_p = (\sum_{i=1}^n |x_i|^p)^{1/p}$.

2. SAS GEOMETRY

The SAS geometry in strip-map mode is depicted in Fig. 1. In two-dimensional imaging, the seafloor lies on the xy-plane and it is characterized by the complex reflectivity function $s(\mathbf{r}_s)$, $\mathbf{r}_s = (x, y)$. The platform carrying an active sonar, comprising a configuration of transmitters and receivers, moves along a linear path, parallel to y-axis at height h from the seafloor plane. The origin of the coordinate system is located at the center of the aperture plane. To simplify the analysis, we assume that $h \ll r_0$, where r_0 is the range from the origin of the coordinate system to the center of the imaging area, so that the slant-range is approximately equal to the ground-range, i.e., the x-axis. Hence, the reconstruction of the seafloor reflectivity is depicted in slant-range - cross-range coordinates. In strip-map mode, the real aperture is steered towards broadside, i.e., the central axis of the real-aperture beampattern is perpendicular to the platform path [7].

The active sonar transmits a short pulse of duration τ_q, onwards referred to as ping, and records the backscattered echoes repeatedly as the platform moves along the track. The stop-and-hop approximation postulates that the platform is stationary during each ping transmission

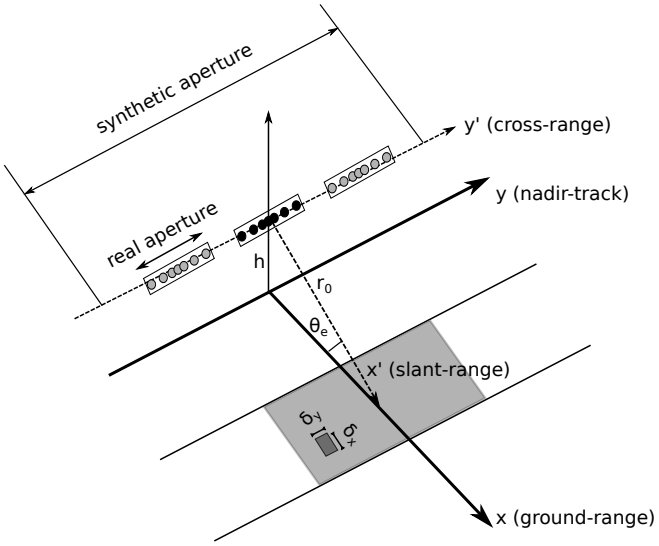


Fig. 1: Synthetic aperture sonar imaging geometry for strip-map mode.

and reception, before it jumps instantaneously to the next position [7].

The resolution of a SAS system is defined in the range and cross-range directions, indicated on Fig. 1 as δ_x and δ_y, respectively. The range resolution, obtained with matched filtering, is

$$\delta_x = \frac{c}{2\Delta f}. \tag{1}$$

The cross-range resolution depends on the apparent synthetic aperture length L_{SA},

$$\delta_y \approx \frac{\lambda \|\mathbf{r}_s\|_2}{2L_{\mathrm{SA}}}. \tag{2}$$

For a given real aperture length L, the corresponding synthetic aperture length is proportional to the wavelength λ and the range of the target [1],

$$L_{\mathrm{SA}} \approx \frac{\lambda \|\mathbf{r}_s\|_2}{L}. \tag{3}$$

Hence, from Eqs. (2) and (3), the cross-range resolution is independent of the wavelength and the range, $\delta_y \approx L/2$. Short physical apertures have broad beamwidths which allow the backscattered echoes from a target to be coherently integrated for a longer period improving the cross-range resolution.

3. SAS MODEL

Assuming a mono-static configuration, the signal d recorded in time t at a receiver located at $\mathbf{r}_r$ is the superposition of the backscattered echoes from all scatterers within the insonified area S and can be modeled as [7],

$$d(t,\mathbf{r}_r) = \int_S q\left(t - \frac{2\|\mathbf{r}_s - \mathbf{r}_r\|_2}{c}\right) s(\mathbf{r}_s)\mathrm{d}\mathbf{r}_s, \tag{4}$$

where q is the transmitted pulse, s is the complex scalar reflectivity field and c is the sound speed in the medium. The frequency response of the recorded signal (4) is obtained through the Fourier transform as,

$$d(f,\mathbf{r}_r) = \mathcal{F}\left\{d(t,\mathbf{r}_r)\right\} = q(f)\int_S e^{-j2\pi f 2\|\mathbf{r}_s-\mathbf{r}_r\|_2/c} s(\mathbf{r}_s)\mathrm{d}\mathbf{r}_s. \tag{5}$$

The matched filtered frequency response is computed by multiplying the recorded signal (5) by the complex conjugate of the transmitted pulse,

$$d_{mf}(f,\mathbf{r}_r) = q^*(f)q(f)\int_S e^{-j2\pi f 2\|\mathbf{r}_s-\mathbf{r}_r\|_2/c} s(\mathbf{r}_s)\mathrm{d}\mathbf{r}_s. \tag{6}$$

For completeness, we can include an amplitude factor $G(f,\mathbf{r}_r,\mathbf{r}_s) = G_t(f,\mathbf{r}_s)G_r(f,\mathbf{r}_s)/\|\mathbf{r}_s - \mathbf{r}_r\|_2^2$ accounting for the shading function of the transmitter array $G_t(f,\mathbf{r}_s)$ and the receiver array $G_r(f,\mathbf{r}_s)$ and the attenuation due to the spherical spreading over the two-way wave propagation distance to obtain the matched filtered response,

$$d_{mf}(f,\mathbf{r}_r) = \|q(f)\|_2^2\int_S G(f,\mathbf{r}_r,\mathbf{r}_s)e^{-j2\pi f 2\|\mathbf{r}_s-\mathbf{r}_r\|_2/c} s(\mathbf{r}_s)\mathrm{d}\mathbf{r}_s. \tag{7}$$

Discretizing the reflectivity field into N pixels, the matched-filtered data model (7) at a given ping can be written in a matrix-vector formulation,

$$\mathbf{d}(p,f) = \mathbf{A}(p,f)\mathbf{s}(p,f) + \mathbf{n}(p,f), \tag{8}$$

where $\mathbf{d} \in \mathbb{C}^M$ is the vector of the matched filtered measurements at frequency f for all M receivers comprising the real aperture at ping p, $\mathbf{s} \in \mathbb{C}^N$ is the unknown vector of the complex reflectivity values over a two-dimensional grid of N pixels and $\mathbf{n} \in \mathbb{C}^M$ is the additive noise vector. The matrix $\mathbf{A} \in \mathbb{C}^{M\times N}$ maps the unknown reflectivity $\mathbf{s}$ to the observations $\mathbf{d}$ and has as columns the steering vectors,

$$\mathbf{a}(\mathbf{r}_s,f,p) = \left[e^{-j2\pi f 2\|\mathbf{r}_s-\mathbf{r}_1\|_2/c}, \cdots e^{-j2\pi f 2\|\mathbf{r}_s-\mathbf{r}_M\|_2/c}\right]^T, \tag{9}$$

which describe the propagation delay from the sth scatterer to all the M sensors on the real aperture at ping p. Note that we have incorporated the gain factors, $\|q(f)\|_2^2$ and $G(f,\mathbf{r}_r,\mathbf{r}_s)$, into the reflectivity vector $\mathbf{s}$. The frequency, f, and ping, p, dependency of the quantities in Eq. (8) are made implicit in the following to simplify notation.

4. SAS IMAGING

SAS imaging refers to the inverse problem of reconstructing the reflectivity field $\mathbf{s}$, given the sensing matrix $\mathbf{A}$ and a set of data $\mathbf{d}$ over several frequencies and pings.

4.1. Conventional beamforming

An estimate $\widehat{\mathbf{s}}$ of the reflectivity field can be obtained by spatial filtering the array data $\mathbf{d}$. Conventional (delay-and-sum) beamforming (CBF) uses the steering vectors (9) as spatial

weights to combine the sensor outputs coherently, enhancing the signal at the look-direction from the ubiquitous noise. In SAS imaging, CBF provides the reflectivity estimate,

$$\widehat{\mathbf{s}}_{\text{CBF}} = \sum_{i=1}^{P} \sum_{j=1}^{F} \mathbf{A}^H(i,j)\mathbf{d}(i,j), \tag{10}$$

by combining coherently the sensor outputs over P pings and F frequencies.

4.2. Sparse signal reconstruction with ADMM

Assuming there are only a few strong scatterers in the reflectivity field ($K \ll N$), problem (8) can be solved as a sparse reconstruction problem with convex optimization. The resulting ℓ_1-norm regularized least-squares is known as the least absolute shrinkage and selection operator (lasso) [5],

$$\min_{\mathbf{s}} \frac{1}{2}\|\mathbf{A}\mathbf{s}-\mathbf{d}\|_2^2 + \mu\|\mathbf{s}\|_1, \tag{11}$$

where $\mu > 0$ is a regularization parameter controlling the relative importance between the quadratic data fitting term and the ℓ_1-norm constraint.

Here, we solve problem (11) with the alternating direction method of multipliers (ADMM) [6] which is an efficient convex optimization solver for problems with a very large number of model parameters N. Accounting for separable measurements over several pings and frequencies, the lasso problem (11) is reformulated as,

$$\begin{aligned} &\min_{\mathbf{s},\mathbf{z}} \frac{1}{2}\sum_{i=1}^{P}\sum_{j=1}^{F}\|\mathbf{A}_{ij}\mathbf{s}_{ij}-\mathbf{d}_{ij}\|_2^2 + \mu\|\mathbf{z}\|_1 \\ &\text{subject to} \quad \mathbf{s}_{ij}-\mathbf{z}=0, \quad \text{for} \quad i=1,\cdots,P, \quad j=1,\cdots,F. \end{aligned} \tag{12}$$

Problem (12) is a consensus problem, since the constraint imposes that the local reflectivity variables $\mathbf{s}_{ij}$ related to the data set from each ping and each frequency should be equal to the global variable $\mathbf{z}$. Consensus optimization promotes collaborative filtering as the P data sets over the frequency band of interest are collaborating to develop a global model for $\mathbf{z}$.

The ADMM solution for the consensus problem (12) consists of the iterations [6],

$$\begin{aligned} \mathbf{s}_{ij}^{k+1} &= \left(\mathbf{A}_{ij}^H\mathbf{A}_{ij} + \rho\mathbf{I}\right)^{-1}\left(\mathbf{A}_{ij}^H\mathbf{d}_{ij} + \rho(\mathbf{z}^k - \mathbf{u}_{ij}^k)\right) \\ \mathbf{z}^{k+1} &= S_{\mu/(\rho PF)}\left(\bar{\mathbf{s}}^{k+1} + \bar{\mathbf{u}}^k\right) \\ \mathbf{u}_{ij}^{k+1} &= \mathbf{u}_{ij}^k + \mathbf{s}_{ij}^{k+1} - \mathbf{z}^{k+1}, \end{aligned} \tag{13}$$

where $\rho > 0$ and $\mu > 0$ are regularization parameters and S denotes a soft-thresholding operator defined as $S_\kappa(\alpha) = (\alpha/|\alpha|)\max(|\alpha|-\kappa, 0)$ for $\alpha \in \mathbb{C}$, $\kappa \in \mathbb{R}$. Note that the overline operator in the $\mathbf{z}$-update step denotes averaging over the P pings and F frequencies, $\bar{\mathbf{v}} = 1/(PF)\sum_{i=1}^{P}\sum_{j=1}^{F}\mathbf{v}_{ij}$. The $\mathbf{s}$ and $\mathbf{u}$-variable update steps in (13) are independent for each ping $i = 1,\cdots,P$ and for each frequency $j = 1,\cdots,F$.

In the following, the ADMM algorithm is initialized with $\mathbf{s}_{ij}^0 = \mathbf{A}_{ij}^H\mathbf{d}_{ij}$, $\mathbf{z}^0 = \mathbf{0}$ and $\mathbf{u}_{ij}^0 = \mathbf{0}$ for $i = 1,\cdots,P$ and $j = 1,\cdots,F$. The algorithm terminates when $\|e^k\|_2 \leq \varepsilon_{tol}$, where $\|e^k\|_2^2 = \sum_{i=1}^{P}\sum_{j=1}^{F}\|\mathbf{s}_{ij}^k - \mathbf{z}^k\|$ is the norm of the residual for the feasibility of the primal problem and $\varepsilon_{tol}^k = \varepsilon_{abs}\sqrt{N} + \varepsilon_{rel}\max(\|\bar{\mathbf{s}}^k\|_2, \|\mathbf{z}^k\|_2)$ is a tolerance bound [6].

4.3. Results

We demonstrate the resolution limitations of sub-band SAS imaging and the potential of the proposed beamforming method with simulated data. For the simulations, we employ a SAS system with a linear receiver array composed of 12 independent transducers. The phase center approximation (PCA) [8] replaces a single-transmitter/multiple-receivers bistatic configuration with a monostatic one comprising virtual sensors located at the middle of the distance between each transmitter-receiver pair on the actual array. The resulting PCA array has half the length of the receiver array. The transmitted signal is a linear frequency modulated (LFM) pulse of duration τ_q with bandwidth Δf,

$$q(t) = w(t)e^{j2\pi\left(f_l + \frac{\Delta f}{2\tau_p}t\right)t}, \tag{14}$$

where $w(t)$ is a Tukey (tapered cosine) window and f_l is the chirp's lower frequency.

First, we assume a single point scatterer at an arbitrary location $\mathbf{r}_s = (9, 0.5)$ m on the imaging grid with reflectivity $s(\mathbf{r}_s) = 1$. Figure 2 shows the broadband and narrowband SAS reconstruction with conventional beamforming (10), (a)-(b), and the lasso implemented with the ADMM algorithm (13), (c)-(d). In broadband processing, both conventional beamforming and the ADMM solution provide high-resolution SAS imaging. However, the resolution of conventional beamforming degrades significantly in narrowband processing.

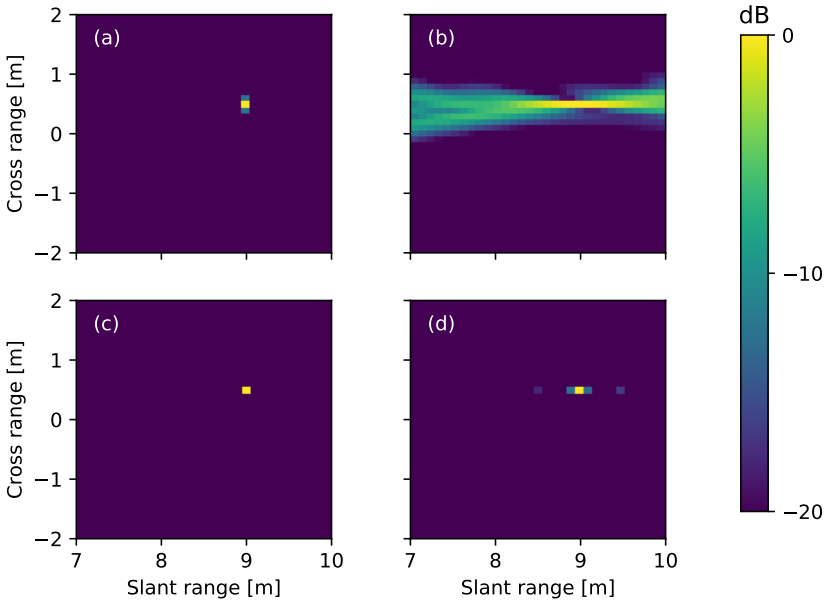


Fig. 2: SAS imaging point spread function (psf). Conventional beamforming (a) broadband ($\Delta f \approx 20$ kHz centered at 13 kHz) and (b) narrowband processing ($\Delta f \approx 10$ Hz centered at 13 kHz). Sparse reconstruction (c) broadband and (d) narrowband processing.

Consider now a more complex scenario where the seafloor comprises a distribution of strong scatterers embedded in a random field of weak scatterers as depicted in Fig. 3 (a). Here we consider an isotropic random field [9] with characteristic length 0.2 m and exponential covariance with zero mean and standard deviation equal to -20 dB relative to the reflectivity of

the strong scatterers. The signal-to-noise ratio due to additive noise is 20 dB. Sub-band processing ($7-10$ kHz) and reverberation degrade the resolution of CBF [Fig. 3 (b)], while sparse reconstruction [Fig. 3 (c)] provides a more accurate estimate of the reflectivity field. Figure 4 shows the convergence of the ADMM algorithm for the SAS reconstruction in Fig. 3 (c). The tolerance bound for the termination criterion is calculated with $\varepsilon_{abs} = 10^{-3}$ and $\varepsilon_{rel} = 10^{-2}$. The fast convergence of the ADMM iterative solution (within 10 iterations) is very useful for practical applications.

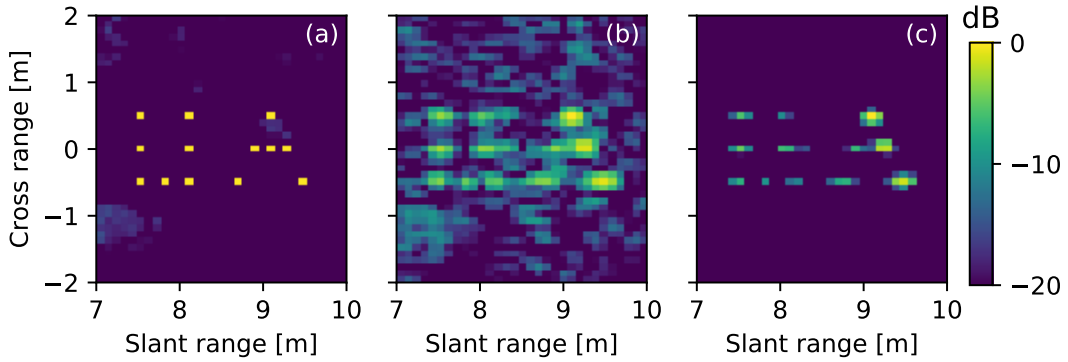


Fig. 3: Sub-band ($7-10$ kHz) SAS imaging. (a) Reflectivity field comprising a distribution of strong scatterers on a weak scattering background. (b) CBF reconstruction and (c) sparse signal reconstruction with the ADMM algorithm.

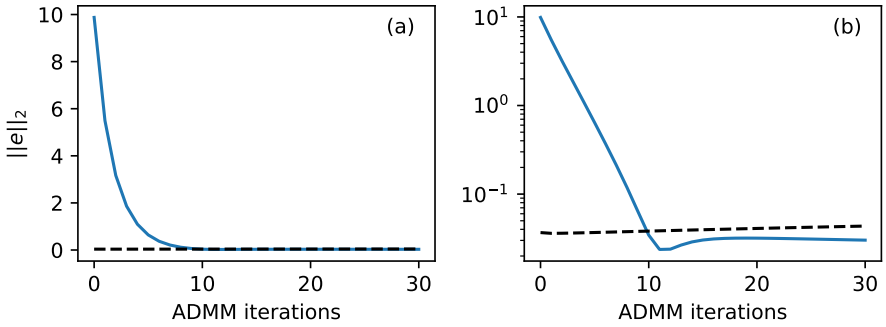


Fig. 4: Convergence of the ADMM algorithm. The primal residual norm $\|e^k\|_2$ (solid line) decreases to the tolerance bound ε_{tol}^k (dashed line) within 10 iterations, in (a) linear and (b) logarithmic scale.

5. CONCLUSION

Low-frequency SAS imaging can provide important information for the classification of man-made objects. However, sub-band low-frequency processing comes at the expense of reduced resolution in conventional beamforming. Sparse reconstruction with distributed optimization is shown to improve significantly the resolution in sub-band processing indicating the great potential of the method for high-resolution low-frequency SAS imaging.

ACKNOWLEDGEMENT

This work was performed under the Project SAC000905–High Resolution Low Frequency Synthetic Aperture Sonar (HRLFSAS) of the STO-CMRE Programme of Work, funded by the NATO Allied Command Transformation.

REFERENCES

[1] R. E. Hansen. *Sonar Systems*, chapter 1, pages 3–28. InTechOpen, Croatia, 2011.

[2] A. Tesei, A. Maguer, W. Fox, R. Lim, and H. Schmidt. Measurements and modeling of acoustic scattering from partially and completely buried spherical shells. *J. Acoust. Soc. Am.*, 112(5):1817–1830, 2002.

[3] T. M. Marston, P. L. Marston, and K. L. Williams. Scattering resonances, filtering with reversible sas processing, and applications of quantitative ray theory. In *OCEANS 2010 MTS/IEEE SEATTLE*, pages 1–9, 2010.

[4] A. J. Hunter and R. van Vossen. Sonar target enhancement by shrinkage of incoherent wavelet coefficients. *J. Acoust. Soc. Am.*, 135(1):262–268, 2014.

[5] R. Tibshirani. Regression shrinkage and selection via the lasso. *J. R. Statist.Soc. B*, 58(1):267–288, 1996.

[6] S. Boyd, E. Parikh, N.and Chu, B. Peleato, and J. Eckstein. Distributed optimization and statistical learning via the alternating direction method of multipliers. *Foundations and Trends® in Machine learning*, 3(1):1–122, 2011.

[7] P. T. Gough and D. W. Hawkins. Unified framework for modern synthetic aperture imaging algorithms. *Int J Imaging Syst Technol*, 8(4):343–358, 1997.

[8] A. Bellettini and M. A. Pinto. Theoretical accuracy of synthetic aperture sonar micronavigation using a displaced phase-center antenna. *IEEE J Oceanic Eng*, 27(4):780–789, 2002.

[9] A. Xenaki, P. Gerstoft, and K. Mosegaard. Modeling and detection of oil in sea water. *J. Acoust. Soc. Am.*, 134(4):2790–2798, 2013.

Structured Session 14
Environmental acoustics and noise

Organiser(s): Barclay David

AMBIENT NOISE OBSERVATIONS DURING A LARGE STORM EVENT IN SBCEX17

W.S. Hodgkiss[a] and D.E. Ensberg[a]

[a]Marine Physical Laboratory, Scripps Institution of Oceanography, La Jolla, CA

W.S. Hodgkiss, Marine Physical Laboratory, Scripps Institution of Oceanography, La Jolla, CA, 92093-0701, FAX: 1-858-822-0665, EMail: whodgkiss@ucsd.edu

Abstract: *The Seabed Characterization Experiment 2017 (SBCEX17) was carried out on the New England shelf in an area known as the "mud patch" during the months of March-April 2017. The experiment site was located ~120 km south of the Woods Hole Oceanographic Institution in water ~75 m deep. Two, 16-element, vertical receiving arrays were deployed ~6 km apart by the Marine Physical Laboratory and recorded source transmissions and ambient noise over the period 22 March - 3 April. Near the end of these deployments, a large storm passed over the area with winds building from 10 kts to 50 kts then calming over a 2-day period (31 March - 2 April). This paper presents the calibrated noise observations as a function of wind speed during that 2-day period.*

Keywords: *environmental acoustics, ambient noise, breaking waves, rain*

1. INTRODUCTION

The spatial and temporal structure of ambient noise in the ocean has been of interest for some time. The general characterizations provided by Knudsen [1] and Wenz [2] and summary by Urick [3] provide the backdrop for site-specific levels that are driven by a number of local/regional environmental factors including propagation. At low frequency, distant shipping tends to dominate the spectral characteristics. Above a few hundred Hz and into the kHz region, wind driven sea surface effects (e.g. bubbles injected into the upper water column by breaking waves) dominate. Overlapping this band and extending up to a few tens of kHz, rain has a substantial impact on ambient noise levels. In addition, noise of biological origin may be significant depending on the region and season.

Of specific interest here is the impact of significant wind mixed with rain on observations of shallow water ambient noise. Wind effects alone result in a spectral structure with a -5 to -6 dB/octave slope along with a logarithmic dependence on wind speed [2]-[5]. The addition of rain tends to both raise and flatten the spectral structure below 10 kHz [6-8].

2. SBCEX17 EXPERIMENT

The Seabed Characterization Experiment 2017 (SBCEX17) was carried out on the New England shelf in an area known as the “mud patch” during the months of March-April 2017. The experiment site was located ~120 km south of the Woods Hole Oceanographic Institution in water ~75 m deep (see Fig. 1). Near the end of the experiment, a large storm passed over the area with winds building from 10 kts to 50 kts then calming over the 2-day period 31 March (JD 090) - 2 April (JD 092). Here we present the calibrated noise observations as a function of wind speed during that 2-day period.

During SBCEX17, two 16-element, vertical receiving arrays were deployed by the Marine Physical Laboratory and recorded source transmissions and ambient noise over the period 22 March - 3 April. VLA1 was deployed in the center of the experiment region (see Fig. 1) and VLA2 was deployed ~6 km to the SE. The analysis presented here is from El. #13 of VLA1 (located ~14 m off the seafloor). Essentially, the same characteristics were observed at VLA2.

3. STORM EVENT AMBIENT NOISE OBSERVATIONS

A large storm passed through the experiment area over the 2-day period 31 March (JD 090) - 2 April (JD 092). As shown in Fig. 2, the winds increased from 10 kts (5 m/s) to ~50 kts (~25 m/s) late on JD 090 through early on JD 091, dropped then increased rapidly mid-day on JD 091, then calmed on into JD 092.

A spectrogram from El. #13 of VLA1 over this period is shown in Fig. 3 with the spectral levels averaged over 300 s. The tonals seen at 0.5 kHz increments between 1.5-4.0 kHz through ~2200 UTC on JD 090 were projected as part of our source transmissions. At that point, the transmissions were secured due to the building weather conditions. Fig. 4 provides a waterfall plot of cuts through the spectrogram in Fig. 3. Some contamination of the spectral structure is seen due to the tonal transmissions early in the period and likely mooring motion during portions of the storm event.

The waterfall of cuts through the spectrogram are displayed as scatter plots of spectral level versus log wind speed in Fig. 5a at 0.25, 1.0, and 4.0 kHz. Fig. 5b provides a similar scatter plot at 0.5, 2.0, and 8.0 kHz. There is substantial scatter at 250 Hz (see also Fig. 4). The storm event included precipitation. Thus, the observations here include both the impact of

a wind-driven sea surface (bubbles injected into the upper water column by breaking waves) as well as rain.

4. SUMMARY

The SBCEX17 experiment provided opportunistic observations of ambient noise in the hundreds of Hz to 10 kHz frequency band generated by a combination of wind-driven sea surface effects as well as rain. While roughly a linear relationship between spectral level and log wind speed is apparent (as would be expected by wind effects alone), the additional impact of rain is to raise these levels.

5. ACKNOWLEDGEMENTS

This work was supported by the Office of Naval Research, grants N00014-16-1-2773 and N00014-18-1-2118.

REFERENCES

[1] **V.O. Knudsen, R.S. Alford, and J.W. Emling**, "Underwater ambient noise," *J. Marine Research 7*, pp. 410-429, 1948.
[2] **G.M. Wenz**, "Acoustic ambient noise in the ocean: Spectra and sources," *J. Acoust. Soc. Am.* 34(12), pp. 1936-1956, 1962.
[3] **R.J. Urick**, *Principles of Underwater Sound (3rd. Ed.)*, McGraw-Hill, pp. 202-236, 1983.
[4] **S. Vagle, W.G. Large, and D.M. Farmer**, "An evaluation of the WOTAN technique of inferring oceanic winds from underwater ambient sound," J. Atmos. Oceanic Technol. 7, pp. 576-595, 1990.
[5] **D.H. Cato and S. Tavener**, "Ambient sea noise dependence on local, regional, and geostrophic wind speeds: Implications for forecasting noise," *Applied Acoustics* 51(3), pp. 317-338, 1997.
[6] **J.A. Nystuen**, "Rainfall measurements using underwater ambient noise," J. Acoust. Soc. Am. 79(4), pp. 972-962, 1986.
[7] **B.B. Ma, J.A. Nystuen, and R-C. Lien**, "Prediction of underwater sound levels from rain and wind," J. Acoust. Soc. Am. 117(6), pp. 3555-3565, 2005.
[8] **B.B. Ma and J.A. Nystuen**, "Passive acoustic detection and measurement of rainfall at sea," J. Atmos. Oceanic Technol. 22, pp. 1225-1248, 2005.

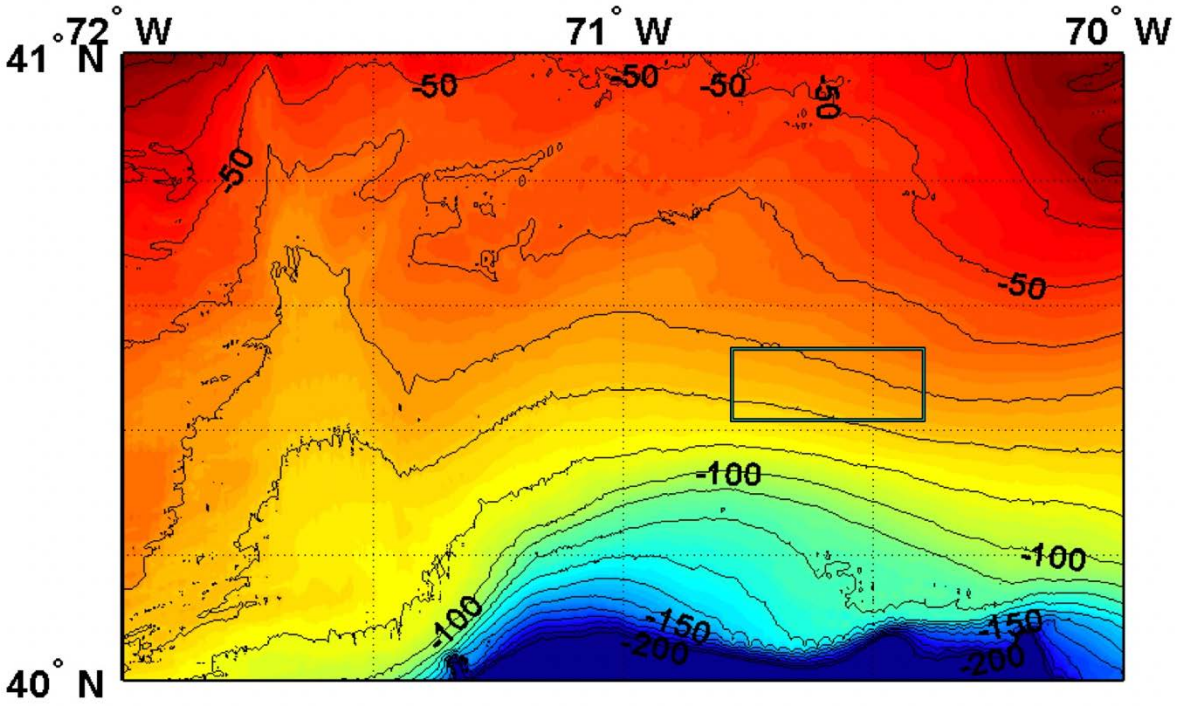


Fig. 1: SBCEX17 location ~100 km SE of Block Island, RI, and ~100 km due south of Martha's Vineyard, MA. Center of survey box (~10 km N/S and ~30 km E/W) is approximately 40-28N, 70-36W and water depth 75 m.

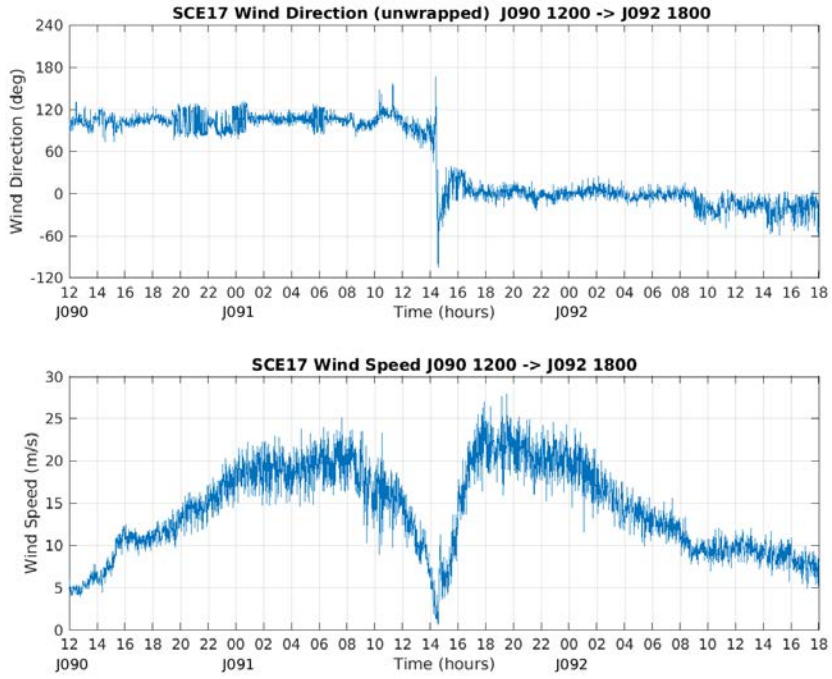


Fig. 2: Wind speed and direction during the SBCEX17 storm event JD 090-092.

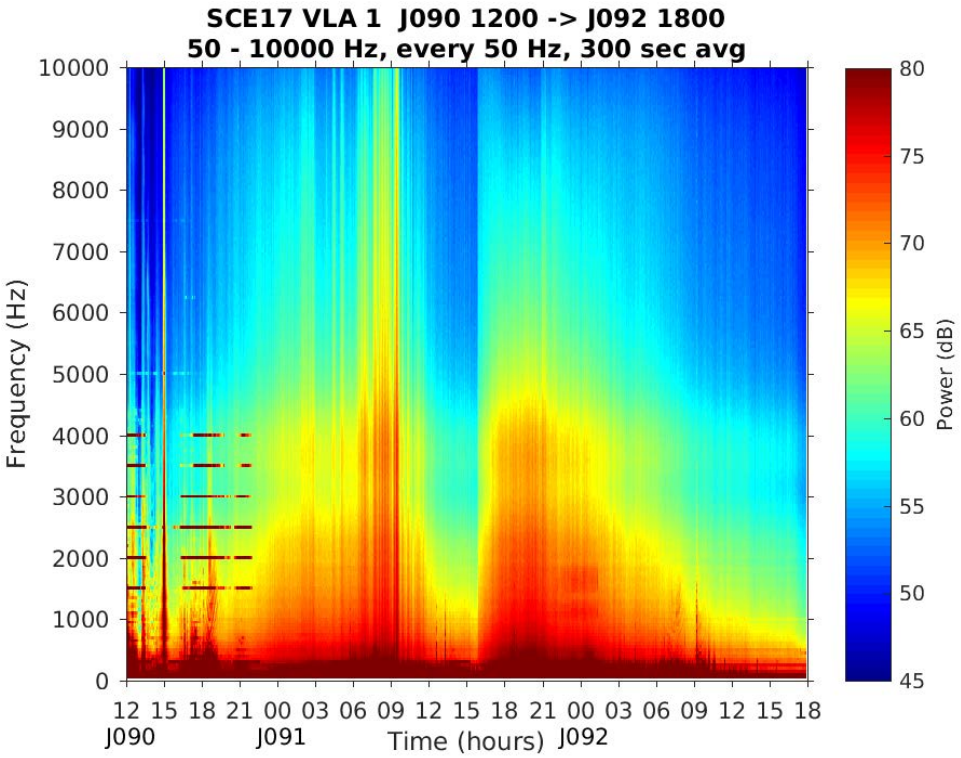


Fig. 3: VLA1 single hydrophone spectrogram during the SBCEX17 storm event.

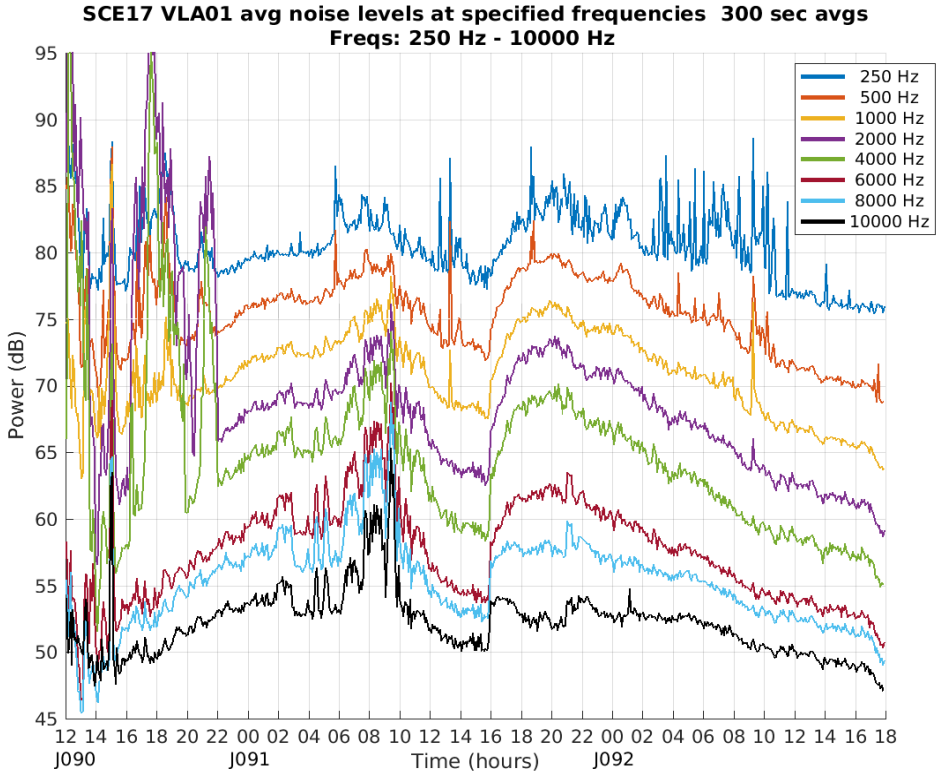


Fig. 4: Waterfall of cuts acrossVLA1 single hydrophone spectrogram.

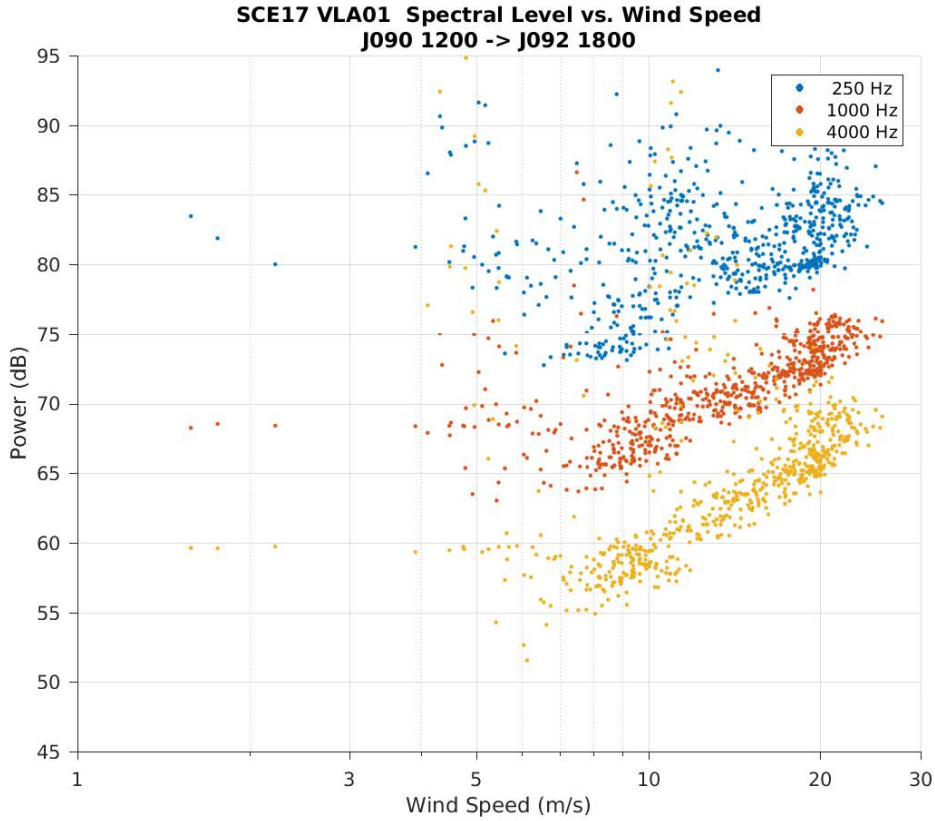


Fig. 5a: Scatter plot of VLA1 single hydrophone spectral level vs. wind speed (log scale).

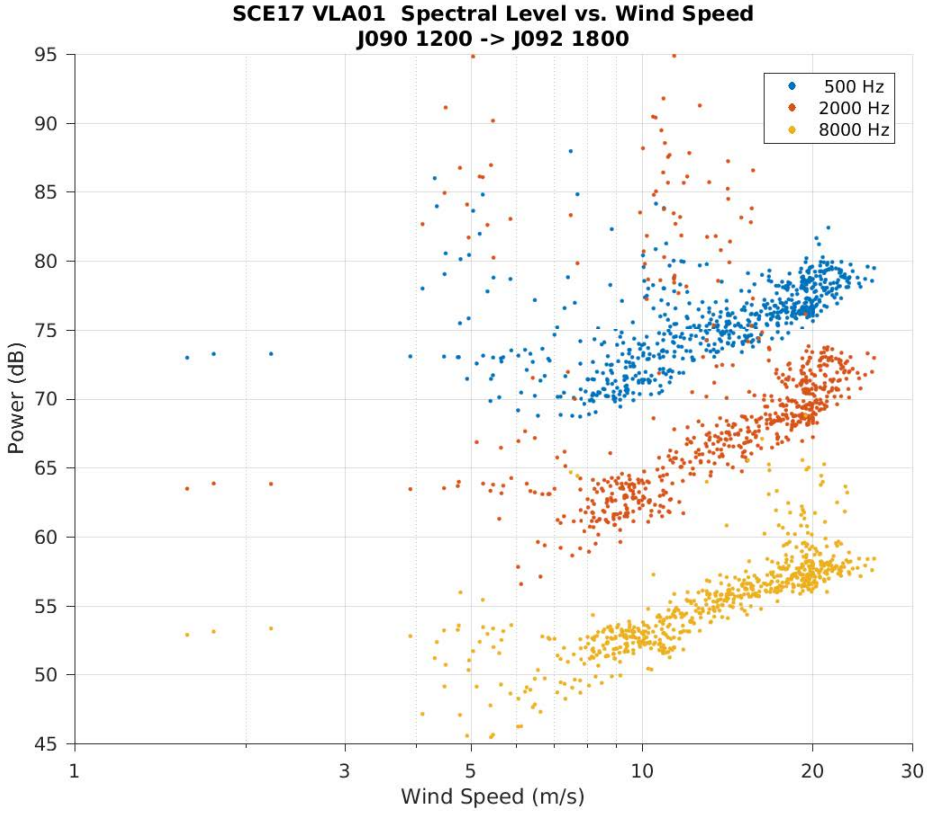


Fig. 5b: Scatter plot of VLA1 single hydrophone spectral level vs. wind speed (log scale).

IDENTIFICATION OF HIGH NOISE ZONES WITH A 3D PILE DRIVING NOISE MODEL

Jonas von Pein, Elin Klages, Stephan Lippert, Otto von Estorff

Hamburg University of Technology (TUHH), Institute of Modelling and Computation,
Denickestr. 17, 21073 Hamburg, Germany, mailto: mub@tuhh.de

Abstract: *Piles are the state-of-the-art technology for fastening the foundations of offshore wind power plants to the sea-floor. Due to the ongoing construction and development of offshore wind farms, pile driving activities at sea are increasing. During the piling process high noise levels are emitted into the water. These levels are potentially harmful for the marine environment, wherefore limits for the noise levels apply. These limits can be complied with by the use of noise mitigation systems, e.g., bubble curtains. In order to assess, if such systems are needed, detailed pile driving noise models for the prediction of the underwater noise emissions are necessary. Typical pile driving noise models are based on the finite-element-method (FEM) for ranges up to 1 km and coupled to a far-field model for distances further away from the pile. The FE-models are set up rotationally symmetric. Therefore, only small changes of the bathymetry can be accounted for. In order to consider 3D-effects induced by a varying bathymetry, e.g. a full 3D parabolic equation (PE) model can be used for the far-field computation.*
At a construction site with a variable water depth, the identification of hydrophone locations for noise monitoring is not straightforward. Therefore, zones with high noise levels have to be identified in a reliable way.
Within this contribution results of pile driving noise computations for a real-life future pile driving scenario with a heavily changing bathymetry are shown. In the final step, the possibility of finding these high noise zones by the examination of the transmission loss plot of a point source is examined.

Keywords: *Pile Driving, Underwater Noise, Parabolic Equations, Finite Element Method, 3D-Modelling*

1. INTRODUCTION

Offshore infrastructures, e.g. offshore wind power plants, are mainly fastened to the sea-floor by piles. Percussive pile driving is commonly used to bring the pile to the final penetration depth and can be considered as the state-of-the-art technique. Each hammer strike induces a compressional wave running down the pile, being reflected at both ends and running up and down again until its energy is dissipated. This wave leads to radial deformations of the pile, which excite pressure waves into the water as well as compressional and shear waves into the soil. The resulting wave fronts and their interference lead to high sound pressure levels in the water, which are potentially harmful for the marine fauna, e.g. the harbour porpoise [1]. In order to protect the marine environment, limits for the sound levels apply in several countries. For instance, in the German Exclusive Economic zone, the limits are set at 750 m as 160 dB for the sound exposure level (SEL) and 190 dB for the peak sound pressure level (SPL_{peak}) [2]. The SEL and SPL_{peak} are computed with the time pressure series $p(t)$ by

$$\mathrm{SEL} = 10\log_{10}\left(\frac{1}{T_0}\int^{\infty}\frac{p(t)^2}{p_0^2}\,\mathrm{dt}\right)\mathrm{dB} \tag{1}$$

and

$$\mathrm{SPL_{peak}} = 10\log_{10}\left(\frac{\max(p(t)^2)}{p_0^2}\right)\mathrm{dB} \tag{2}$$

where $p_o = 1\mu Pa$ and $T_0 = 1s$. To assess the sound levels prior to construction, accurate predictions of the sound pressure levels are necessary. These predictions can be performed with numerical or analytical models. Thereby, the advantages of detailed numerical models are the possibility of optimizing the pile driving set-up, e.g., the hammer, and the revision of the necessary noise mitigation concept. Furthermore, a high physical insight regarding noise transmission and propagation is given.

One of the first modelling approaches has been suggested by Reinhall and Dahl [3]. Meanwhile, several researchers have developed their own approaches and many of them presented their methods at the benchmarking workshops COMPILE I and II [4], [5]. All of the applied models therein assumed a bathymetry that can be considered as rotationally symmetric. However, 3D-effects may have an influence on the sound pressure levels at locations with heavily changing bathymetries. In order to be able to take 3D-effects into account, a hybrid 3D pile driving noise model has been developed by the authors [6].

The hydrophones for the measurement of the occurring sound pressure levels are usually placed at 750 m and 1500 m [2]. If the bathymetry is flat, there are only small differences in the measurement results at hydrophone locations with different azimuthal angles φ and a constant range. However, if the bathymetry is heavily changing, the positioning and the computation of the sound pressure levels at these distances is not straightforward. Therefore, this contribution focusses on the identification of high noise levels at the different measurement distances. This is done with full 3D- and Nx2D-computations of the SEL and tried with the transmission loss (TL) plots of a point source. For the investigations a real-life pile driving scenario is used. The measurement data of the heavily changing bathymetry of the considered scenario is shown in fig. 1.

This contribution is organized as follows: First, the used modelling approach is briefly described. Second, the main details of the considered real-life pile driving scenario are listed and the high-noise zones at the measurement ranges are identified by full 3D- and Nx2D-computations and the differences between them are investigated. Finally, it is examined if the

high-noise zones can also be identified with the TL plots of a point source with a frequency of 100 Hz placed in the middle of the water column.

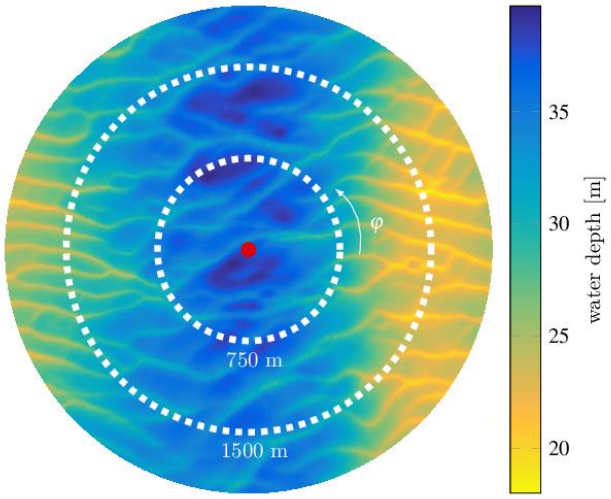


Fig.1: Measured bathymetry at the considered real-life pile driving location.

2. MODELLING APPROACH

The applied model is based on a hybrid modelling approach using the finite element method (FEM) for the close-range and a parabolic equation (PE) model for the far-field computation. With the PE model, Nx2D- and 3D-solutions can be computed. The necessary starting field is directly derived out of the results of the FE model. A detailed description and a validation of this modelling approach for a 2D pile driving scenario are given in [6].

The FE model is rotationally symmetric and computed in time domain. It is split into a pre-calculation and the main acoustical model. Within the pre-calculation, only the interaction between pile and hammer is considered. Therein, all hammer parts, which are relevant for the resulting impulse, e.g. ram mass, anvil, and anvil ring, are accurately discretized. Together with the pile, the pile head excitation can be computed, which is used later on as a boundary condition within the main acoustical model. The main acoustical model consists of the pile, the water column, and a linear-elastic layered soil profile. At the sea-surface, a zero-pressure boundary condition is used, while non-reflecting boundary conditions are applied at all other edges of the domain. A detailed description of the FE model is given in [7], [8]. The same approach is also used in another contribution within these proceedings [9].

The 3D far-field model is based on the split-step Padé technique, which was first introduced by Collins [10]. It is implemented in a cylindrical coordinate system. The exactness of the 3D computation highly depends on the approximation of the square root in eq. 3. With the identity matrices I, the depth-operator X, and the azimuthal-operator Y, the considered Taylor expansion of the square root is

$$\sqrt{I+X+Y} \cong -I + \sqrt{I+X} + \sqrt{I+Y}. \tag{3}$$

In this case occurring cross-terms are neglected. The depth operator X is computed according to [11] and an eighth-order central-difference scheme for the azimuthal operator Y is used, as introduced by Sturm et al. [12]. A stair-step approximation is employed for the occurring sloping bottoms and the higher order energy conserving PE formulation is used [11].

The resulting range marching procedure consists of two steps: First, the pressure at the next range step $r+\Delta r$ is computed for every considered azimuthal direction. Second, the one-way wave equation with the azimuthal operator is solved and the outgoing field is corrected by taking horizontal diffraction into account. A detailed description of these two steps are also given by Lin et al. [13] for a Cartesian coordinate system.

3. IDENTIFICATION OF HIGH NOISE ZONES

The considered pile is a conical monopile with a diameter of 8.7 m, an averaged constant wall thickness of 81 mm, an overall length of 69 m, and a penetration depth of 32 m. The used hammer is an IHC S-3000 at a strike energy of 2000 kJ. The water-depth is shown in fig. 1. In the following, this unmitigated pile driving scenario is used to show the identification of high-noise zones.

In order to identify the highest sound pressure noise levels at the distances of 750 m and 1500 m, the SEL is evaluated at these ranges with an Nx2D- and a 3D-computation. The corresponding results are shown in fig. 2. The results are evaluated up to a depth of 40 m, whereas the actual water depth is indicated by a black line.

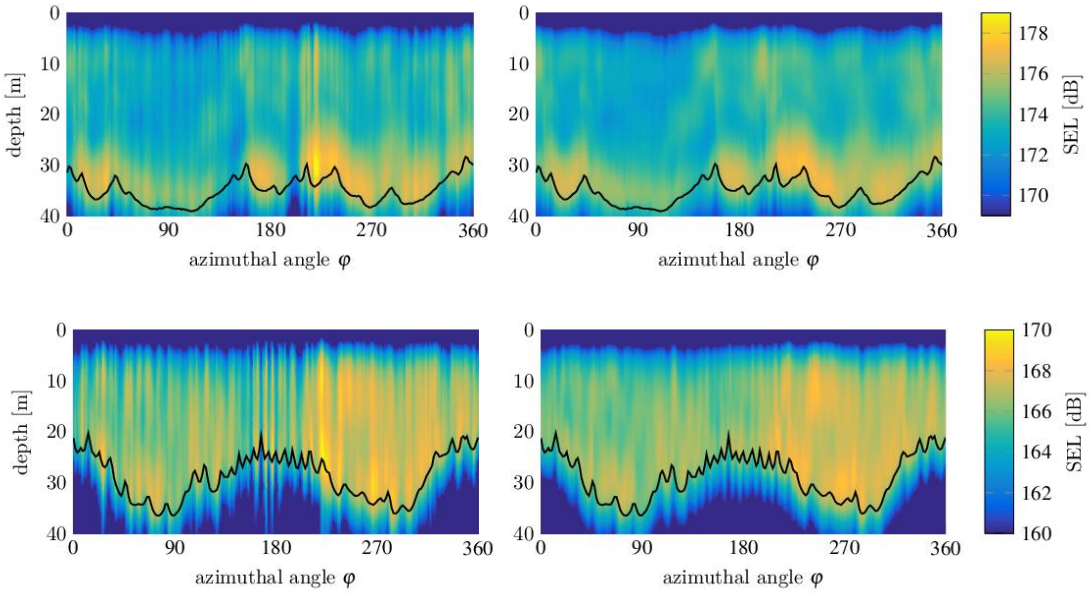


Fig.2: The 3D- (left) and Nx2D-results (right) of the SEL over depth and azimuth at 750 m (upper) and 1500 m (lower) together with the according water depth (black line).

At both distances the distribution of the SEL of the 3D- and Nx2D-results qualitatively has the same pattern. The evaluation of the results at 750 m clearly shows the existence of a high-noise zone between 212° and 237°, with the overall maximum of the 3D-results being 179.2 dB at 220°, which is about 1.6 dB higher than the maximum of the Nx2D-results. Another important aspect is that for φ>180° the SEL is generally higher. This indicates that the measurement direction should be chosen in the down-pointing canyon direction, compare fig. 1. These findings are also valid for a distance of 1500 m. Once again, the maximum of the SEL can be found around 220° with a difference between the Nx2D- and 3D-results of 2.2 dB and a SEL that is generally higher at φ>180°. Overall, the differences between the 3D- and Nx2D-results are in the range of ±3.5 dB at a distance of 750 m and +4.5 to -6.5 dB at 1500 m.

To check, if the identified angle of 220° is a reliable measurement position, the results need to be revised, to see if there are heavy oscillations along the radial direction. Therefore, the SEL is depicted over depth and range for an azimuthal angle of 220° in fig. 3. Once again, differences can clearly be seen between the Nx2D- and 3D-results, with the 3D-results being generally higher. Moreover, the 3D-results clearly show that the SEL does not oscillate much at the measurement positions 750±50 m and 1500±50 m at 2 m above the sea-floor when considering a possible uncertainty of ±50 m due to positioning inaccuracies of the submerged measurement system.

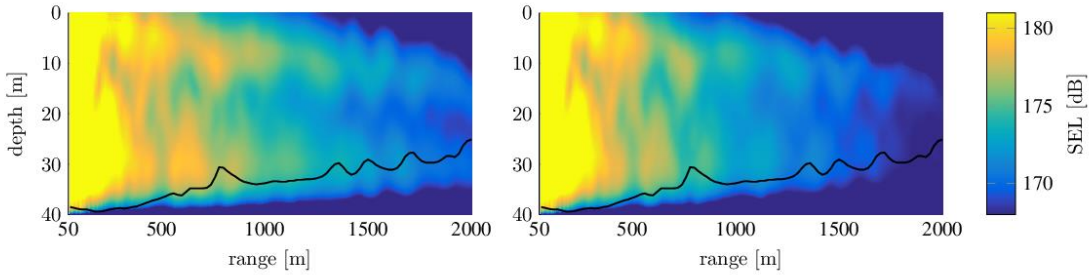


Fig.3: The 3D- (left) and Nx2D-results (right) of the SEL over depth and range at an azimuthal angle of φ=220°.

In order to have a reliable identification of the high-noise zone, an evaluation of the SEL in the horizontal plane at 2 m above the sea-floor, which corresponds to water depths of 32 m for the 750 m position and 27 m for the 1500 m position, from φ=180° to φ=360° is shown in fig. 4. For a better physical insight, the bathymetry is indicated with black isolines. The contour of the bathymetry clearly shows the influence of the radial oriented sand dune close to the pile, which seems to evoke the comparably higher SEL in the identified high-noise zones. Furthermore, it can be observed that the high-noise zone is shaped like a ray with a width of about 100 m at the range of 1500 m.

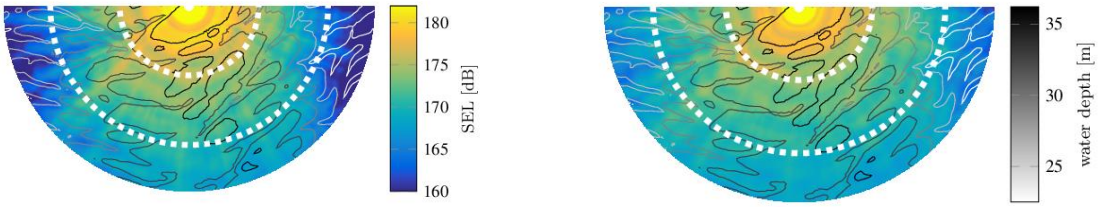


Fig.4: The 3D-results of the SEL evaluated at a corresponding water depth of 32 m (left) and 27 m (right) with the white circles at 750 m and 1500 m for 180° ≤ φ ≤ 360°.

The evaluation of the SEL in different planes clearly showed, that a reliable high-noise zone has been identified at φ=220 and that there are locally big influences of 3D-effects on the sound pressure levels.

The energy of pile driving noise radiation is mainly concentrated around 100 Hz. In fig. 4 the transmission loss (TL) for the considered measurement ranges over depth and azimuth is shown when using a point source with 100 Hz placed in the middle of the water column instead of a vibrating pile.

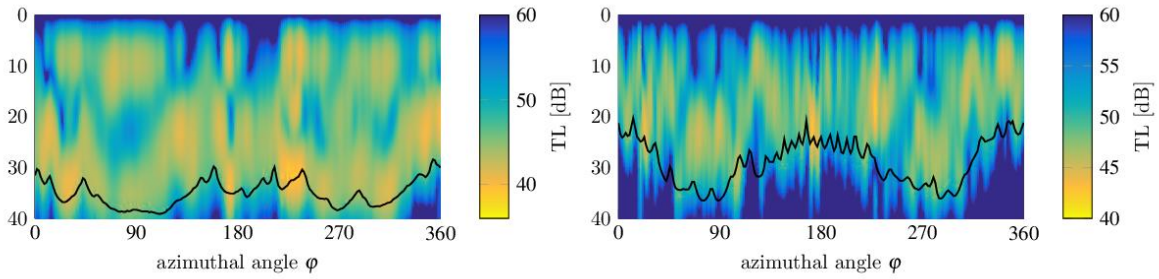


Fig.5: The 3D-results of the TL evaluated at 750 m (left) and 1500 m (right) of a point source with 100 Hz placed in the middle of the water column at 19 m below the sea-surface.

The results at 750 m clearly show a minimum of the TL at the identified high-noise zone around 220°. However, this finding cannot be reproduced for the distance of 1500 m, where none of the earlier identified effects can be seen. These results show that the TL plots of a single point source is not a valid measure to identify high-noise zones.

4. SUMMARY AND OUTLOOK

In this contribution the process of identifying high-noise zones at different measurement ranges for a pile driving location with a heavily varying bathymetry is shown. The comparison of the 3D- and Nx2D-results clearly indicated that Nx2D-computations are sufficient for a qualitative overview of high-noise zones, while full 3D-computations have to be conducted to get a good approximation of the highest sound pressure levels and the position of their occurrence. The comparison of the 3D- and Nx2D-results also showed that 3D-effects can locally lead to big differences in the considered sound pressure levels. Moreover, it can be observed that the radial-oriented sand dune close to the pile leads to higher noise levels at the measurement ranges. Furthermore, it is shown that high-noise zones can clearly be identified by evaluating the sound pressure levels in different planes and that these zones cannot be identified by only using a simplified point source representation as excitation.

The next step in the evolution of the presented 3D pile driving noise model is a validation with a real-life 3D pile driving case. Furthermore, the influence of uncertain parameters on the occurring 3D-effects and on the location of high-noise zones is going to be examined.

5. ACKNOWLEDGEMENTS

The authors would like to thank the company Ørsted Wind Power A/S for their friendly cooperation and valuable support.

REFERENCES

[1] **R. A. Kastelein, R. Gransier, M. A. T. Marijt, and L. Hoek**, Hearing frequency thresholds of harbor porpoises (Phocoena phocoena) temporarily affected by played back offshore pile driving sounds , *J. Acoust. Soc. Am.*, vol. 137, no. 2, pp. 556–564, 2015.

[2] **A. Müller and C. Zerbs**, “Offshore wind farms measuring instructions for underwater sound measurements. Current procedure application notes (Offshore-Windparks. Messvorschrift für Unterwasserschallmessungen. Aktuelle Vorgehensweise mit Anmerkungen. Anwendungshinweise), p. 39, 2011.

[3] **P. G. Reinhall and P. H. Dahl**, Underwater Mach wave radiation from impact pile driving: theory and observation, *J. Acoust. Soc. Am.*, vol. 130, no. 3, pp. 1209–1216, 2011.

[4] **S. Lippert, M. Nijhof, T. Lippert, D. Wilkes, A. Gavrilov, K. Heitmann, M. Ruhnau, O. Von Estorff, A. Schäfke, I. Schäfer, J. Ehrlich, A. MacGillivray, J. Park, W. Seong, M. A. Ainslie, C. De Jong, M. Wood, L. Wang, and P. Theobald**, COMPILE - A Generic Benchmark Case for Predictions of Marine Pile-Driving Noise, *IEEE J. Ocean. Eng.*, vol. 41, no. 4, pp. 1061–1071, 2016.

[5] **S. Lippert, O. von Estorff, M. J. J. Nijhof, and T. Lippert**, COMPILE II – A Benchmark of Pile Driving Noise Models against Offshore Measurements, in *Proceedings of Inter-Noise 2018, Chicago*, 2018.

[6] **J. von Pein, E. Klages, S. Lippert, and O. von Estorff**, A hybrid model for the 3D computation of pile driving noise, in *Proceedings of OCEANS, Marseille*, 2019.

[7] **S. Lippert, M. Huismann, M. Ruhnau, O. von Estorff, and K. van Zandwijk**, Prognosis of Underwater Pile Driving Noise for Submerged Skirt Piles of Jacket Structures, in *Proceedings of the UACE 2017 4th Underwater Acoustics Conference and Exhibition, Skiathos*, 2017.

[8] **K. Heitmann, S. Mallapur, T. Lippert, M. Ruhnau, S. Lippert, and O. von Estorff**, Numerical determination of equivalent damping parameters for a finite element model to predict the underwater noise due to offshore pile driving, in *Proceedings of EuroNoise 2015, Maastricht*, 2015, pp. 605–610.

[9] **E. Klages, J. von Pein, S. Lippert, and O. von Estorff**, An efficient model for offshore pile driving noise taking into account the hammer characteristics, in *Proceedings of the UACE 2019, 5th Underwater Acoustics Conference and Exhibition, Crete*, 2019.

[10] **M. D. Collins**, A split-step Padé solution for the parabolic equation method, *J. Acoust. Soc. Am.*, vol. 93, no. 4, pp. 1736–42, 1992.

[11] **M. D. Collins and E. K. Westwood**, A higher-order energy-conserving parabolic equqation for range-dependent ocean depth, sound speed, and density, *J. Acoust. Soc. Am.*, vol. 89, no. 3, pp. 1068–1075, 1991.

[12] **F. Sturm and J. a. Fawcett**, On the use of higher-order azimuthal schemes in 3-D PE modeling, *J. Acoust. Soc. Am.*, vol. 113, no. 6, pp. 3134–3145, 2003.

[13] **Y.-T. Lin, J. M. Collis, and T. F. Duda**, A three-dimensional parabolic equation model of sound propagation using higher-order operator splitting and Padé approximants., *J. Acoust. Soc. Am.*, vol. 132, no. 5, pp. EL364-70, 2012.

AN EFFICIENT MODEL FOR OFFSHORE PILE DRIVING NOISE TAKING INTO ACCOUNT THE HAMMER CHARACTERISTICS

Elin Klages, Jonas von Pein, Stephan Lippert, Otto von Estorff

Hamburg University of Technology, Institute of Modelling and Computation,
21073 Hamburg, Germany, e-mail: mub@tuhh.de

Abstract: *Pile driving of state-of-the-art piles for offshore wind farms requires the application of noise mitigation systems to assure that sound pressure levels fulfill official regulations. Currently applied are mainly sound mitigation systems reducing the propagation of the emitted sound, e.g., bubble curtains, rather than reducing the sound generation itself. However, rapidly increasing dimensions of wind turbines with even higher pile diameters demand additional measures to keep sound pressure levels within the defined limits. Therefore, the design of the hammer regarding its acoustic characteristics has recently gained attention.*

To optimize the hammer design, it is required to model the underwater sound pressure caused by the hammer impact. Here, the computation time is crucial to the overall optimization time. However, currently applied models to estimate the underwater sound pressure are either computationally expensive (finite element models) or do not allow for a detailed hammer design (analytical models).

Within this contribution, a computationally low-cost model, which is able to take modifications of the hammer into account, is presented. The model consists of two steps: In the first step, a finite element model is applied to compute the pile head acceleration. In the second step, a transfer function is used to obtain the sound pressure level based on the pile head acceleration.

Keywords: *Offshore pile driving, underwater noise, impact-hammer design, computationally low-cost model*

1. INTRODUCTION

Offshore wind energy is an important source of renewable energy. However, every construction of a new offshore wind park causes high underwater noise levels, threatening to harm marine mammals. Especially crucial is the piling of commonly applied monopiles that are driven into the sea bed using an impact hammer.

In order to protect the marine fauna, several countries have defined official limits for sound pressure levels during pile driving. Noise mitigations systems are usually applied to assure that sound pressure levels do not exceed these limits. However, the capacity of offshore wind turbines is increasing and so are pile diameters. To drive larger piles, more energy is required, thus more noise is emitted and sound mitigation measures at the pile driving location have to be extended. In view of this development, the modification of the sound source itself, i.e. hammer and pile, in order to decrease sound emission, has recently gained attention.

In order to design a hammer with improved acoustic characteristics, it is necessary to be able to estimate the sound pressure levels accurately. Several approaches, to model sound emission and propagation caused by offshore pile driving, exist. An overview can be found for example in [1]. In the context of hammer optimization, it is especially important that the chosen modelling approach includes the detailed hammer design. Furthermore, the calculation of the sound pressure levels has to be fast, to be suitable for an optimization. Considering these requirements, neither analytical models nor a detailed Finite-Element (FE) analysis can be applied here: While analytical models do not allow for a detailed consideration of small changes of the excitation signal, FE models for pile driving noise are simply too time-consuming to be used for multiple computations within an optimization. The present contribution aims to present an alternative model that is both, accurate and fast. The proposed model consists of two steps. The first step constitutes a FE analysis of the short hammer impact. In the second step, results of the FE analysis are applied to estimate sound pressure levels using a transfer function (TF) in the frequency domain.

2. ACOUSTIC OFFSHORE PILE DRIVING MODEL

To simulate the sound generation, emission, and propagation, a two-step model is applied. First, a FE model of hammer and pile is used to evaluate the hammer impact. The axial pile head velocity is then passed to the second model, used to obtain the underwater sound pressure caused by the vibrations of the pile. The second model may be a detailed FE model of the pile, water and sea bed or a TF based on the FE model. The modelling process is shown in Fig. 1. All three models will be shortly introduced in the following sections.

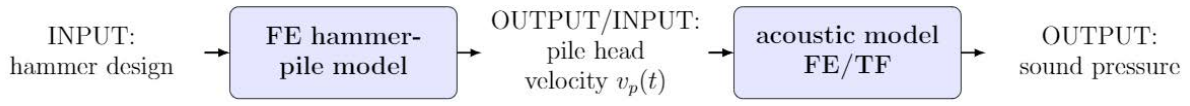


Fig. 1: Two steps to model the sound generation, emission and propagation caused by offshore pile driving. For the second step, either the FE model or the TF may be applied.

Separating the analysis of the impact and the sound propagation into two steps, is a common approach, as used in different ways for example in [2], [3]. In the latter, also transfer functions were discussed. However, in contrast, the present contribution focuses on replacing the second FE model, i.e., the actual acoustic model, with the TF to reduce simulation time during an optimization of the impact hammer.

2.1 FE model for hammer and pile

The first FE model serves to compute the pile head velocity caused by the hammer impact based on the hammer design. It includes only the main hammer components, anvil and impact weight, and the pile. A simplified illustration of exemplary hammer components can be found later on in Fig 3. The influence of water and sea bed on the pile head deformations are negligible and therefore not included in the model.

During pile driving, the anvil rests on the pile head and the impact weight is lifted up to fall afterwards on the anvil which transmits the impact to the pile. This process is repeated several hundred times for each pile, however, only one isolated impulse is modeled. For the purpose of modelling, the ram energy is defined via the initial velocity of the impact weight, here set to 1000kJ.

2.2 FE model for the acoustic propagation

The second FE model serves to compute the acoustic pressure based on the pile head velocity. It includes the pile, water, and the sea bed. The sea bed is modelled with layers with different sound velocities and densities, originally provided in the context of the project BORA for the offshore wind park BARD Offshore I. Further specifications of both FE models can be found in [4], [5].

2.3 Transfer function

Here, we assume that the dependency of sound emission on pile head deformation is at least approximately linear considering its representation in the frequency domain. The proposed TF relates the underwater sound pressure p at one specific position to the axial pile head acceleration a_p obtained from the FE hammer pile model, i.e.

$$TF(r,z,f) = \frac{p(r,z,f)}{a_p(f)}, \tag{1}$$

Here r refers to the distance to the pile, y to the z to the height over the sea bed, and f to the frequency.

To define the TF, the sound pressure values for at least one hammer design have to be known. Hence, although the TF is here presented as an alternative to the acoustic FE model, it is always based on the same and can therefore never fully replace it. The ram impulse with 1000kJ ram energy of the existing hammer MHU3500S, produced by MENCK, was simulated to obtain reference pressure values to define the TF.

3. COMPARISON OF MODELS

In order to discuss the accuracy of the proposed model, two case studies are presented in the following. In both cases, several simulations of the sound emission due to the hammer impact for different hammer designs were performed using the acoustic FE model and the TF to estimate the underwater sound pressure. The difference of the resulting sound pressure levels, ΔSEL and $\Delta\mathrm{SPL}_{\mathrm{Peak}}$, is then used to evaluate the performance of the TF.

For both case studies, a cylindrical pile with 70m length, 6.5m diameter and 80mm wall thickness serves as an example. The embedded length of the pile is 35m and the water depth is

30m. The TF was evaluated in 200m distance to the pile and 2m above the sea bed. The two following sound pressure levels were applied: The sound exposure level (SEL) defined as

$$\mathrm{SEL} = 10\log_{10}\left(\frac{1}{T}\int_0^T \frac{p(t)^2}{p_0^2}\,dt\right)[dB] \tag{2}$$

and the peak sound pressure level ($\mathrm{SPL_{Peak}}$) defined as

$$\mathrm{SPL_{Peak}} = 20\log_{10}\left(\frac{\max(|p(t)|)}{p_0}\right)[dB], \tag{3}$$

where p_0 is the reference pressure of p_0 = 1µPa and T is the reference time of 1s.

3.1 Case study: Variation of the material of the hammer components

The first case study includes 300 variations of the material of the hammer components, i.e. the density ρ and Young's modulus E of both hammer components. Every hammer design was thus defined via the parameter vector: $\theta = [\rho_{Anvil}, E_{Anvil}, \rho_{Weight}, E_{Weight}]$. The samples were randomly distributed and the parameter space was restricted via $\rho_{min} = 0.5\rho_0$, $\rho_{max} = 1.5\rho_0$ and $E_{min} = 0.5E_0$, $E_{max} = 1.5E_0$. The shape and the original material values ρ_0, E_0 of the hammer MHU3500S were used.

The distribution of the error of the TF is shown in Fig. 2. The results show good agreement of both models. Even the largest error of the SEL is smaller than 0.5dB. Errors in the $\mathrm{SPL_{Peak}}$ are larger, up to 2.1dB, but still small considering the difficulty in predicting the $\mathrm{SPL_{Peak}}$. However, since the shape of the hammer components in the case study was the same as used to define the TF, the error might be unrealistically small for other hammer designs.

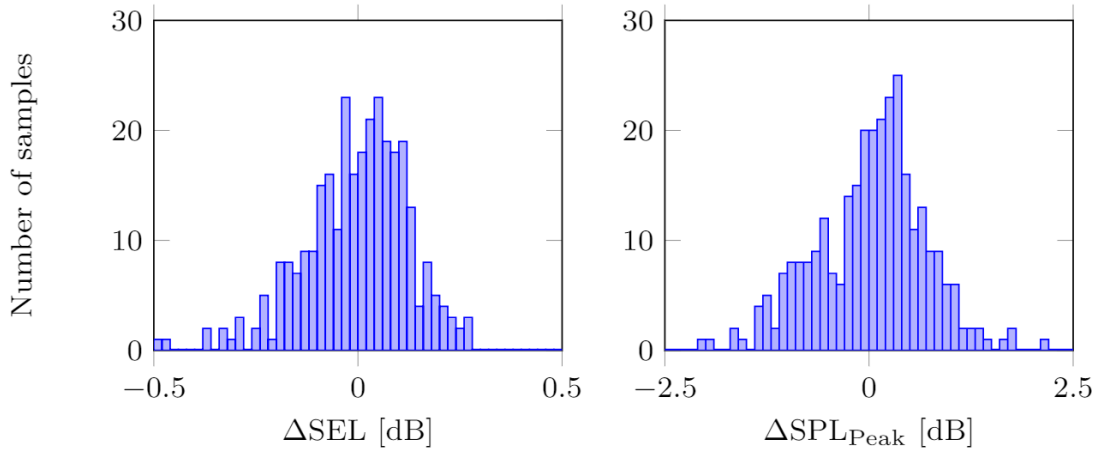


Fig. 2: Error of the TF for the material parameter study: $\Delta SEL = SEL_{FEM} - SEL_{TF}$ $\Delta SPL_{Peak} = SPL_{Peak,FEM} - SPL_{Peak,TF}$

3.2 Case study: Variation of the shape of the hammer components

In contrast to the previously presented case study, this section discusses the performance of the TF for different shapes of the hammer components. For this purpose, the cross section of the shape of the hammer components was defined via a polygon. A visualization of exemplary hammer components defined as polygons is shown in Fig. 3. Axis symmetry was assumed. The shape was described by 13 parameters. 198 samples were randomly distributed. The parameter

space was restricted by the maximum height h and diameter d for each component, i.e. $h_{anvil} = 2m$, $d_{anvil} = 8m$ and $h_{weight} = 15m$, $d_{weight} = 4m$. The corresponding differences in sound pressure levels are shown in Fig. 4.

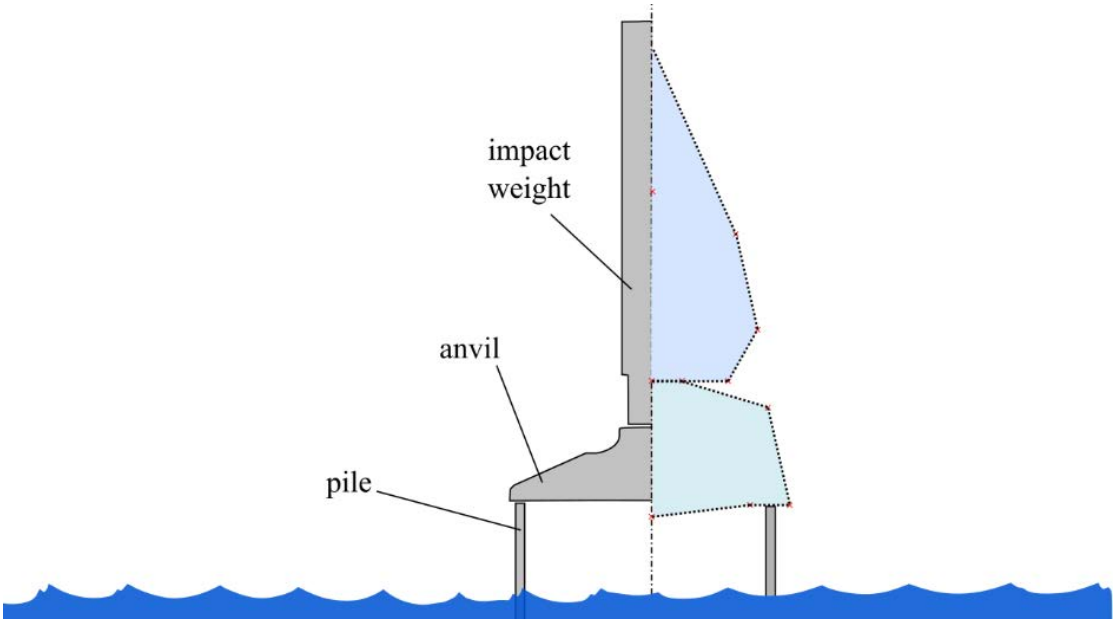


Fig. 3 A simplified illustration of the axis symmetric original hammer components at the left side and one example of the polygon parameterization at the right side. The pile is here approximated as a hollow cylinder.

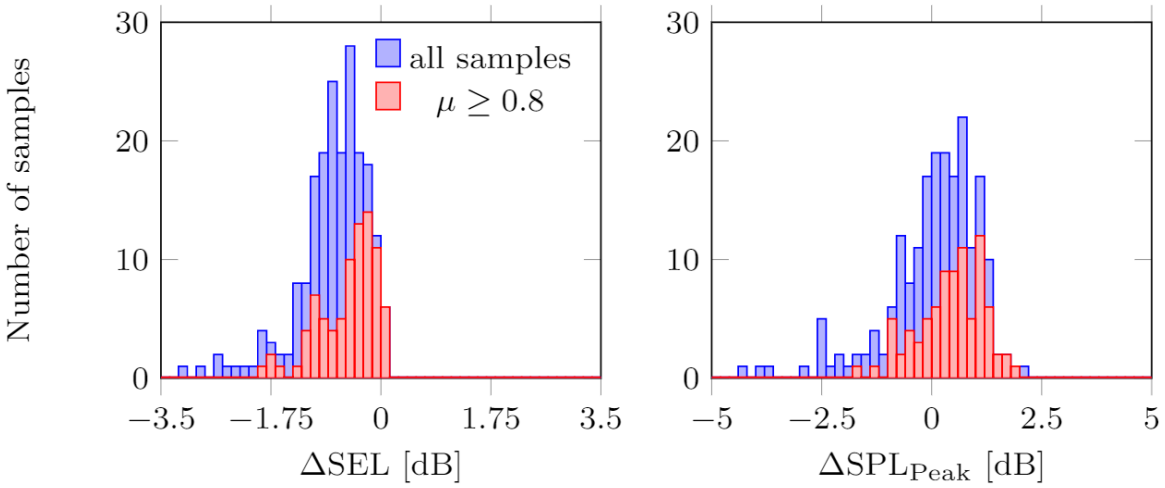


Fig. 4: Error of the TF for the parameter study of the shape of the hammer components: $\Delta SEL = SEL_{FEM} - SEL_{TF}$ $\Delta SPL_{Peak} = SPL_{Peak,FEM} - SPL_{Peak,TF}$. Red bars refer to the error distribution, considering only hammers with an efficiency μ of at least 0.8.

In comparison to the previous case study, errors are larger, but still indicate general good agreement of the TF and FE model as no extreme outliers occurred. If only hammers with a driving efficiency of at least 0.8 are considered, the maximum error is even less than 2dB for both sound pressure levels, the SEL and the SPL_{Peak}. However, even deviations of only 2dB might hinder an optimization, if it affects the comparison of the acoustic characteristics of hammer designs.

4. CONCLUSIONS

The estimation of sound pressure levels based on a linear TF in the frequency domain were discussed. The use of the TF for two exemplary case studies showed overall promising results and therefore support the approach of a linear TF in the frequency domain. However, the results of the second case study indicate that the here applied reference pressure based on an existing hammer might cause larger errors if the hammer of choice is too different from the original one. Future work will be directed to model the sound emission and propagation in the frequency domain to obtain a more accurate TF.

5. ACKNOWLEDGEMENTS

The presented research is part of the collaborative research project "*Investigation of primary measures for the reduction of underwater noise emission during offshore pile driving"* involving the companies Novicos GmbH and MENCK GmbH as well as the Hamburg University of Technology. The authors gratefully acknowledge the project funding by the Federal Ministry for Economic Affairs and Energy due to an act of the German Parliament (Project No. 0324262).

REFERENCES

[1] **Stephan Lippert et al.,** *COMPILE – A generic benchmark case for predictions of marine pile-driving noise*, IEE Journal of oceanic engineering, Vol. 41, pp. 1061 – 1071, 2016.

[2] **Per G. Reinhall, Peter H. Dahl**, *Underwater Mach wave radiation from impact pile driving: Theory and observation*, The Journal of the Acoustical Society of America, Vol. 130, pp. 1209 – 3011, 2011.

[3] **Mario Zampolli et al**, *Validation of finite element computations for the quantitative prediction of underwater noise from impact pile driving,* The Journal of the Acoustical Society of America, Vol. 133, pp. 72 - 81, 2013.

[4] **Kristof Heitmann**, *Vorhersage des Unterwasserschalls bei Offshore-Rammarbeiten unter Berücksichtigung von Schallminderungsmaßnahmen*, Shaker Verlag, 2017.

[5] **Kristof Heitmann et al.**, *Numerical determination of equivalent damping parameters for a finite element modelt o predict the underwater noise due to offshore pile driving*, In Euronoise 2015, Maastricht, Netherlands, pp. 605 – 610, 2015.

Structured Session 15
Acoustics of marine renewable energy developments

Organiser(s): Robinson Stephen, Lepper Paul, Blondel Philippe

DEVELOPMENT OF ACOUSTIC DOPPLER FISH MONITORING FOR APPLICATIONS IN HIGH-ENERGY TIDAL CHANNELS

Muriel Dunn[a], Len Zedel[a], Greg Trowse[b]

[a] Department of Physics and Physical Oceanography, Memorial University of Newfoundland, St. John's, NL
[b] Luna Ocean Consulting Ltd., Westport, NS.

Muriel Dunn, Chemistry-Physics Building, 283 Prince Philip Drive, St. John's, NL, A1B 3X7, Canada. mbdunn@mun.ca

Abstract: *Acoustic Doppler profiler systems (ADCPs) are the standard instrument used to monitor ocean currents. These instruments also detect signals scattered by fish, but these signals are normally treated as noise and rejected by ADCP data processing techniques. Those rejected signals do however contain information on fish movement providing an opportunity to extend the application of ADCP technology. The added capability of the ADCP provides a monitoring tool for fish activity and presence in areas that may be impacted by future in-stream hydro energy development projects. We explore this capability through a 37-day deployment of a self-contained bottom-mounted frame equipped with a 600 kHz RD Instruments Workhorse ADCP alongside a 120 kHz BioSonics DTX Submersible Split Beam Echo Sounder system. The deployment took place in Grand Passage, Nova Scotia, at a depth of 25m, where the tidal range is ~5m, and the currents are up to 2.5m/s. We chose this site because it is located in a tidal channel that is identified as having the potential for in-stream tidal generation. Anticipating possible interference, we selected different frequencies and regulated the duty cycles to overlap for half of the total sampling time to assure the collection of uncontaminated data. The split-beam echo sounder shows plumes of scatterers, presumably bubbles, emanating from the surface. Discrete targets are detected throughout the water column within fish schools and as individuals. The corresponding ADCP data detects the same fish schools by using coinciding instances of high intensity and high correlation. The ADCP signal has a lower range resolution but shows less contamination from surface bubbles and weaker scatterers. We present observations for both instruments and contrast their capabilities.*

Keywords: *Renewable energy, acoustic Doppler current profiler, fish detectability*

1. INTRODUCTION

Signals received by ADCPs contain backscatter from a variety of objects in the water column, including fish, zooplankton, sediments, bubbles and the surface or bottom. As the instrument is used for water velocity measurements, typically all signals that differ significantly in echo intensity between the four beams are rejected to reduce fish bias in velocity data [1]. Efforts to use Doppler sonar for fish velocity measurements before the 2000s used low frequency, long pulses and narrow bandwidths [2]. Though Doppler shift methods were said to, theoretically, be promising in gathering information for fish behaviour, the techniques and instruments had not been developed adequately for this purpose. Demer (2000) suggested that ADCPs need to achieve higher velocity and range resolution and showed that a higher frequency and autocorrelation for the detection of pulse shifts wouldaccomplish that. Demer also identified a need to modify parameters and data processing as well as carefully selecting survey sites with fish schools matched to the size of the processing bins [3].

Zedel and Cyr-Racine (2009) presented an alternative approach to analyzing Doppler sonar data using a least-squares based algorithm which analyzes each acoustic beam individually to extract both fish and water velocities, even when fish are intermittently present [4]. Even with a suitable processing algorithm, the challenge remains to identify the presence of fish in ADCP data accurately. The need for such an evaluation motivates this study which uses the opportunity presented by the need to monitor fish presence and behaviour in regions of in-stream tidal energy generation. Such areas are inherently difficult for sampling when using conventional boat mounted acoustic surveys.

This paper reports on a month-long deployment of a collocated bottom-mounted ADCP and split-beam echosounder to evaluate fish detectability in ADCP data.

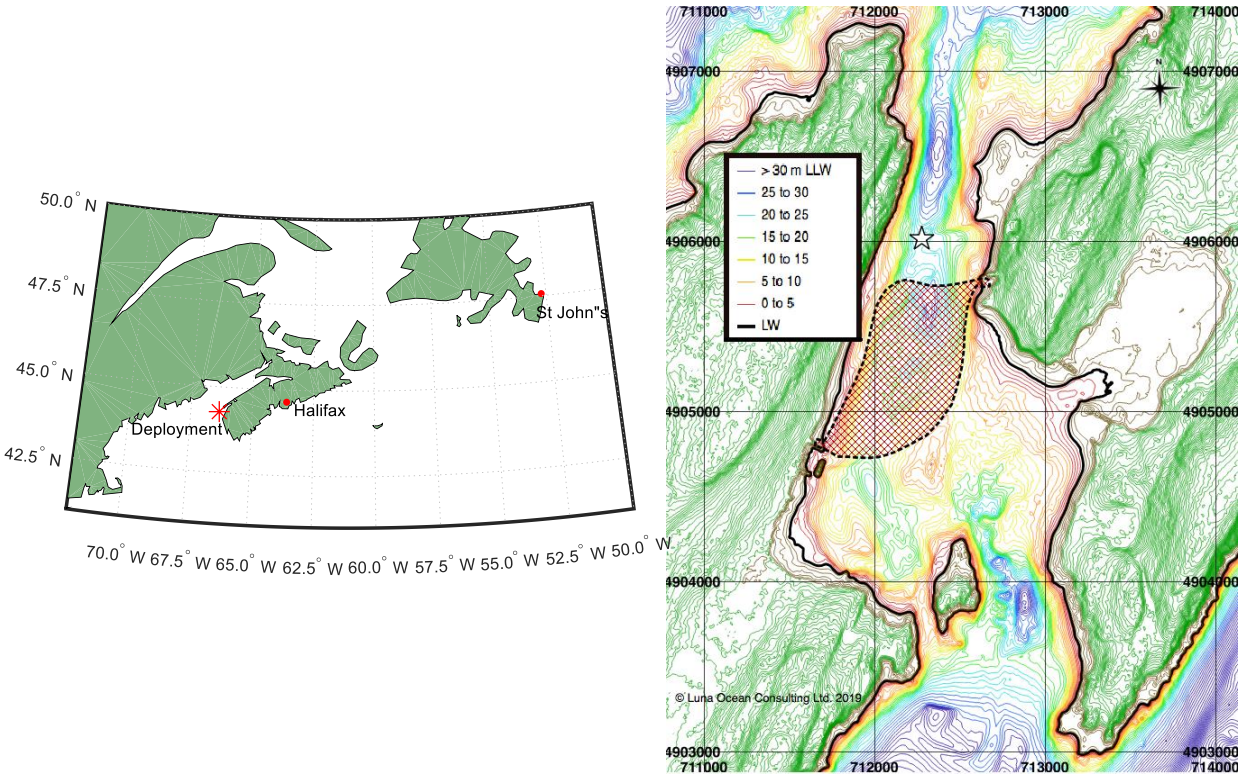


Fig.1: Experimental site. Left: location of the deployment in Nova Scotia. Right: deployment location in Grand Passage (STAR), (extent of the ferry route is the chequered red area).

2. METHODOLOGY

2.1 Experimental Site & Deployment

Grand Passage is a tidal channel in Nova Scotia, Canada that is identified as having the potential for in-stream tidal developments. Prior studies of fish presence in high-energy tidal channels have identified common survey challenges to be acoustic scattering from near-surface bubbles. The study by Melvin & Cochrane (2014) recommends deploying "an autonomous, stationary, bottom-mounted echo-sounder" to overcome these challenges [5]. This experimental site further motivates that approach because it has frequent boat and ferry traffic. A long-term bottom-deployment also allows for inter-survey data which can validate the "snapshot" measurements from conventional surveys and separate the diurnal and tidally induced fish behaviour. The bottom-mounted self-contained frame was deployed at 25m depth and positioned, as shown in Figure 1; note the location selected to avoid interference from the ferry traffic.

The frame was mounted with an RD Instruments 600kHz acoustic Doppler current profiler and a BioSonicsDTX Submersible system with 120kHz split-beam echosounder, as shown in Figure 2. The system was deployed for 37 days, from September 21st, 2018 14:30 to October 29th, 2018 13:54. The acoustic instruments were installed as close as possible to facilitate direct comparison between both datasets.

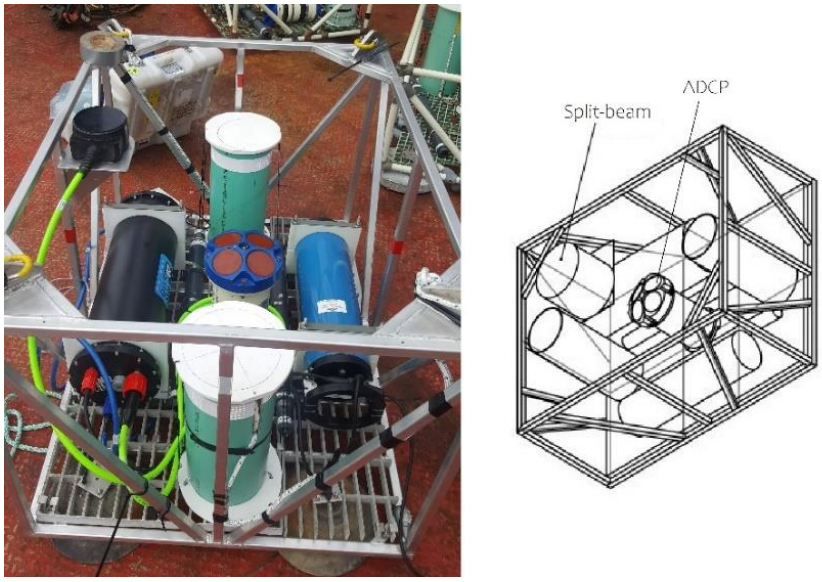


Fig.2: Left: A picture of the frame before the deployment. Right: Sketch of the frame.

2.2 Instrument configuration and calibration

A common problem when operating two nearby acoustic instruments is interference between the two instruments. We chose widely separated frequencies to mitigate this problem (120kHz for split-beam and 600kHz for the ADCP). Nevertheless, we observed contamination in the split-beam sonar data during lab tests. Therefore, in addition to the separate frequencies, we staggered the duty cycle to ensure the collection of both individual uncontaminated data as well as simultaneous measurements. The ADCP was set to collect at one ping per second with 1m bins with no averaging of the profile data; the sampling duty cycle was 20 minutes on and 20 minutes off. The split-beam sonar was configured to transmit four pings per seconds at a 0.1ms

pulse duration. The staggered duty cycle was set up by an initial 10 minutes lag relative to the ADCP and a 20 minutes on and 40 minutes off duty cycle.

The ADCP compass was calibrated the day before the deployment using the conventional rotation of the mounted frame [6]. The ADCP backscatter calibration coefficients were taken from a January 2018 laboratory calibration. The split-beam was calibrated with a 33.2mm diameter tungsten carbide sphere in the days immediately following the retrieval of the frame; the calculated offset of 1.1dB was applied to the dataset.

2.3 Data Processing

2.3.1 Acoustic Doppler current profiler

Backscatter data were corrected to volume backscatter coefficients using the procedure outlined by Deines (1999) [7]. The presence of fish in the Doppler sonar data can be indicated by volume backscatter levels exceeding a specified threshold, but properties unique to the broadband Doppler system allow discrimination of discrete targets as opposed to volume backscatter. Broadband Doppler systems transmit pulse pairs with a known lag; the phase of the received echoes is used to extract velocity. The magnitude of the autocorrelation of the received pulses is a measure of the quality of the signal. When coincident with high volume backscatter signal, a strong correlation suggests an acoustically discrete target, distinct from the median value correlation characteristic of a cloud of bubbles or a more extensive school of fish [8]

The volume backscatter and correlation thresholds, -45dB and 135 counts respectively, are applied to each beam individually for fish detection; an example is shown in Figure 3. To place the correlation threshold into context, normal volume backscatter data would have an average correlation of 128. Conversely; water targets are identified as signals below either the intensity or correlation thresholds. Note in particular the clear agreement in backscatter structure when comparing the Doppler sonar data (Fig 3a) with the split-beam data (Fig 3c).

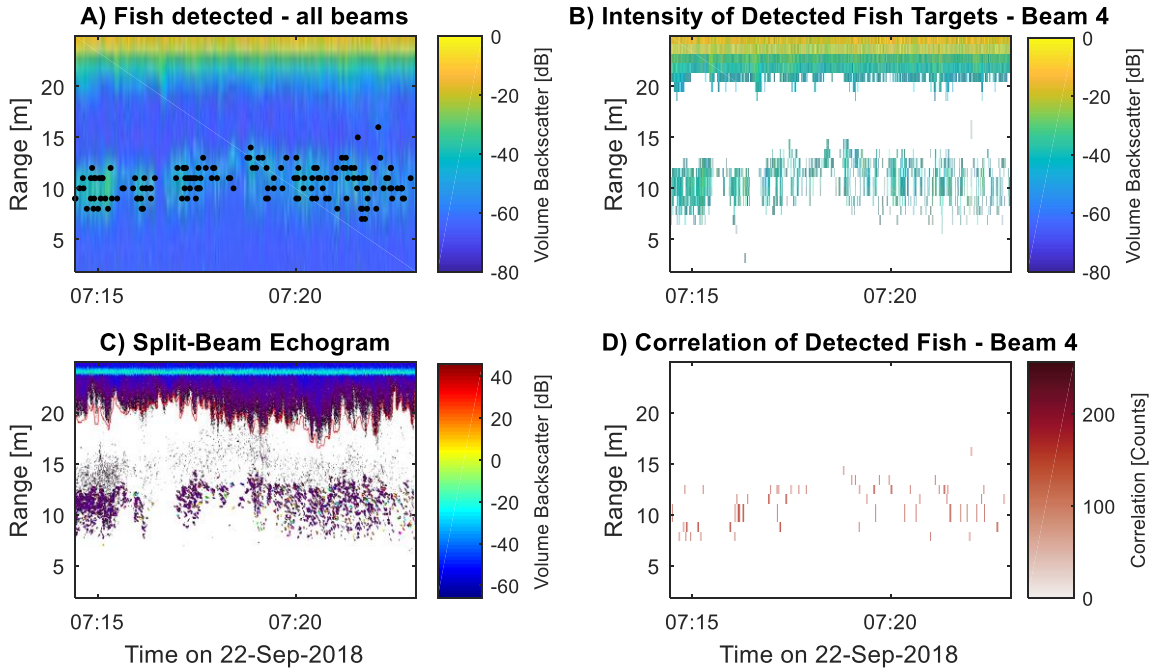


Fig.3: a) A volume backscatter echogram for a fish school from the ADCP with the identified fish targets (.) from all four beams b) identifies the remaining data after the backscatter threshold (-45dB) is applied, c) the corresponding split-beam signal and d) identifies the remaining data after the backscatter and correlation thresholds (135 counts).

2.3.2 Split-beam echo sounder

Sonar5-Pro [9], a post-processing tool for echosounder data was used to process the split-beam data. A surface exclusion line is determined by using the bottom detection algorithm but generally requires manual adjustment for areas of combined fish and bubbles signals. The Cross-Filter Detector algorithm was used to identify the SED (single echo detections) and to combine them into fish tracks. This algorithm is composed of two filters: a foreground filter that smooths over the stronger signal with a running mean and a background filter that smooths the weaker signal and adds an offset to minimize the intensity of the weaker signal even further. The combination of these filters isolates the targets into SEDs. These targets are then combined into fish tracks, using the automatic fish tracking algorithm, based on proximity of targets, and length, speed and path of tracks. Only the SEDs included in tracks, and the whole tracks themselves were used to compare with the fish targets identified in the ADCP data.

3. RESULTS

A total of 37h of simultaneous data were collected between September 21st and October 1st in 10 minutes intervals. The accepted fish detections for both instruments were averaged over 2-hour time bins and 2m depth bins to make a comparison.

A particular challenge in strong tidal flows is the occurrence of near-surface bubble plumes [5] which are often hard to distinguish from fish (or plankton) targets. With the Doppler sonar, we used the requirement of high signal correlations to distinguish discrete targets from bubble clouds. The capability is demonstrated through the data present in Figure 3, note the difference between Fig 3b and 3d, where the correlation threshold effectively removes the bubble plumes. For split-beam sonar data, most bubbles were avoided by using the surface exclusion line algorithm. That algorithm is not always correct and requires a user to review areas of spread bubble plumes or regions where fish and bubbles are mixed. In these areas, it becomes a somewhat arbitrary delineation to distinguish desirable data from bubble clouds. This process is irreproducible and time-consuming.

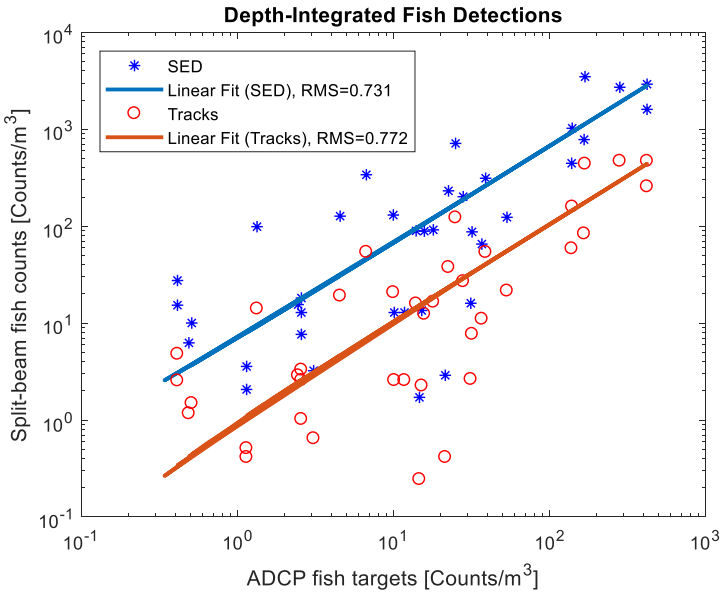


Fig.4: Linear regression analysis for comparison of ADCP fish targets dataset to split-beam fish track counts and SED within fish tracks count.

The ADCP and the split-beam sonar were evaluated by comparing depth-integrated counts over 2h time intervals. A linear regression model (Figure 4) between the two data sets has a slope of 1.04 ± 0.03 for the fish tracks and 6.7 ± 0.2 for the SED. The SEDs and fish track comparison show that there are on average seven single echo detections per track. The fish tracks are a slightly better representation of fish targets in the ADCP data and more representative of fish counts. Overall, the tracks provide a strong agreement with a cross-correlation of 0.881. Discrepancies in counts between the instruments would be expected due to differences in sampling volumes, operating frequency, and measured product.

4. FURTHER WORK

This data demonstrates that ADCP can detect fish in providing agreement with the industry standard, split-beam echosounder, for the conditions sample in Grand Passage. The ADCP also provides an alternative processing approach for dealing with near-surface bubbles that eliminates the need for the more operator intensive process of determining an exclusion line. Further work will focus on extracting fish velocity from the targets in the ADCP data and comparing those with velocities from fish tracks in split-beam data.

5. ACKNOWLEDGEMENTS

This research was conducted as part of a Master's project with Memorial University of Newfoundland, funded by OERA. We would like to thank Mark Downey for his help with the deployment and his instrumentation expertise and Richard Cheel for designing the frame and his invaluable help throughout the deployment and retrieval.

REFERENCES

[1] **Freitag, H., Plimpton, P. and McPhaden, M.** Evaluation of an ADCP fish-bias rejection algorithm *Proceedings of OCEANS'93*. IEEE, 1993.
[2] **Holliday, D.** Two applications of the Doppler effect in the study of fish schools. *Rapp. P.-v. Reun. Cons. Int. Explor. Mer,* 171, 1977, 21.
[3] **Demer, D., Barange, M. and Boyd, A.** Measurements of three-dimensional fish school velocities with an acoustic Doppler current profiler. *Fisheries Research* 47.2-3, 2000, 201.
[4] **Zedel, L. and Cyr-Racine, F.**. Extracting fish and water velocity from Doppler profiler data. *ICES Journal of Marine Science,* 66, 2009, 1849.
[5] **Melvin and Cochrane**, Final Report: Investigating the Vertical Distribution, Movement and Abundance of Fish in the Vicinity of Proposed Tidal Power Energy Conversion Devices. 2014
[6] **Instruments, R. D.** Workhorse Sentinel ADCP user's guide. 2001.
[7] **Deines, K.** Backscatter estimation using broadband acoustic Doppler current profilers. *Proceedings of the IEEE Sixth Working Conference on Current Measurement (Cat. No. 99CH36331)*. IEEE, 1999.
[8] **Tollefsen, C., Zedel, L.,** Evaluation of a Doppler sonar system for fisheries applications, *ICES Journal of Marine Science*, Volume 60, Issue 3, 2003, 692.
[9] **Balk, H. and Lindem**, Sonar4 and Sonar5-Pro post-processing systems, Operator manual version 604, CageEye AS, 2017.

PERFORMANCE CHARACTERISTICS OF A VECTOR SENSOR ARRAY IN AN ENERGETIC TIDAL CHANNEL

Kaustubha Raghukumar, Grace Chang[a], Frank Spada[a], Craig Jones[a], Jesse Spence[b], Sean Griffin[c], Jesse Roberts[d]

[a]Integral Consulting Inc., 200 Washington Street, Suite 201, Santa Cruz, CA 95062, USA
[b]Noise Control Engineering, LLC, 799 Middlesex Turnpike, Billerica, MA 01821, USA
[c]Proteus Technologies, 1040 Old Spanish Trail, Suite 7, Slidell, LA 70458, USA
[d]Sandia National Laboratories, P.O. Box 5800, Albuquerque, NM 87185-0101, USA

Kaustubha Raghukumar, 200 Washington Street, Suite 201, Santa Cruz, CA 95062 USA
Phone number: +1 831 466 9630, kraghukumar@integral-corp.com

Abstract: *A compact three-dimensional vector sensor array (termed the NoiseSpotter) was recently developed with the goal of characterizing and localizing sources of sound in energetic environments such as those where marine renewable energy devices are likely to be located. The three vector sensors on the NoiseSpotter are mounted on a bottom platform with each sensor suspended inside an optional flow noise removal shield. The multiple pressure and particle velocity channels on the NoiseSpotter are simultaneously sampled and stored on-board to enable coherent array processing of vector sensor array data.*

A series of field trials were conducted where the NoiseSpotter was deployed on a bottom platform in an 8 m deep tidal channel in Sequim Bay, Washington. Pure tones were transmitted from a drifting vessel whose distance from the bottom platform varied between 50 m and 500 m. The effect of flow noise on vector sensor array performance is quantified along with the detectability of low intensity sound in an energetic environment. Flow noise removal efficiency for each channel of every vector sensor is demonstrated using multiple metrics derived from the active and reactive intensities computed using the pressure-velocity cross-spectral density matrix. A flow noise removal shield is shown to improve the detectability of low intensity sound such as those that are expected to be emitted by marine renewable energy devices.

Keywords: *vector sensor array, particle motion, marine renewable energy, flow noise*

1. INTRODUCTION

In support of monitoring technologies to evaluate the potential environmental effects of marine and hydrokinetic (MHK) energy devices, a compact three-dimensional array of acoustic vector sensors (termed the NoiseSpotter) was developed that characterizes, classifies, and provides accurate location information for anthropogenic and natural sounds. By virtue of measuring the acoustic pressure and three-dimensional particle velocity, a vector sensor array (VSA) provides a compact means of achieving sound source localization, and thereby help characterize sound specific to a source [1]. This localization ability is key to characterizing sounds from MHK devices, which have been found to emit low intensity sounds on the order of 106-109 dB re 1 µPa in the frequency band 125-250 Hz and undetectable above the ambient noise outside this band [2].

Operational deployments of the NoiseSpotter are likely to occur in ocean regions with energetic flows induced by wave- or tidally-induced currents. The strong flows can induce non-acoustic pressure fluctuations that lead to contamination of acoustic signals. Flow noise contamination can be particularly acute with vector sensors due to saturation of the built-in accelerometer signal by energetic flows.

To facilitate NoiseSpotter deployments in energetic environments, a flow noise removal shield was developed and tested in a tidal channel in Washington, USA. Using a series of controlled source playbacks, the efficiency of the flow noise removal system is demonstrated using quantitative metrics that utilize the off-diagonal elements of the pressure-velocity cross spectral density matrix.

2. BACKGROUND

Vector sensor measurements consist of four measured quantities that represent acoustic pressure and particle velocity, represented as $\mathbf{A}(\boldsymbol{x},t) = [p, v_x, v_y, v_z]$, where the particle velocity components are expressed in units of pressure via the scaling ρc, where ρ is the density of sea water (1000 kg/m^3), and c is the nominal speed of sound in sea water (1500 m/s). Velocity components are typically measured in a local frame of reference and transformed to an earth-based frame of reference using Eulerean angles measured by an in-built or collocated inertial motion unit.

The Fourier transform of the time series in $\mathbf{A}(\boldsymbol{x},t)$ is given by $\mathbf{A}(\boldsymbol{x},\omega)$. The cross-spectral density matrix $\mathbf{S}(\omega)$ is then given by the ensemble-averaged outer product of the vector $\mathbf{A}(\boldsymbol{x},\omega)$. Individual components of the cross-spectral density matrix can be expressed as $S_{ij}(\mathbf{x},\omega) = A_i(\mathbf{x},\omega)A_j^*(\mathbf{x},\omega)$. Assuming ergodicity, $\mathbf{S}(\mathbf{x},\omega)$ can be calculated by averaging successive snapshots of $\mathbf{A}(\boldsymbol{x},\omega)$ computed over an interval of time. $\mathbf{S}(\mathbf{x},\omega)$ can then be decomposed into its real and imaginary components as $\mathbf{S}(\mathbf{x},\omega) = \mathbf{C}(\mathbf{x},\omega)+i\ \mathbf{Q}(\mathbf{x},\omega)$, where $\mathbf{C}(\mathbf{x},\omega)$ and $\mathbf{Q}(\mathbf{x},\omega)$ represent the in-phase and quadrature components of the individual elements of the cross-spectral density matrix. For example, the off-diagonal elements $\mathbf{S}_{1j}(\mathbf{x},\omega)$ represent the pressure-velocity cross-spectra whose in-phase and quadrature elements have been related to physical quantities that represent acoustic power flow [3]. The in-phase components $\mathbf{C}_{1j}(\mathbf{x},\omega)$, termed the ***active intensity***, represents the net power being propagated by the acoustic field. The quadrature component, $\mathbf{Q}_{1j}(\mathbf{x},\omega)$, termed the ***reactive intensity***, relates pressure and particle velocity components that are orthogonal to each other, and represents spatially heterogeneous power flow [3].

A number of metrics to describe the non-acoustic contributions to acoustic propagation can be derived using the reactive intensity components of the cross-power spectral density matrix. For example, one can derive the metric [4],

$$R_j \equiv \frac{\rho_0 c_0 Q_{1j}(\omega)}{C_{11}(\omega)}, \tag{1}$$

where R_j is the scaled ratio of the reactive intensity to the acoustic pressure autospectrum. For propagating acoustic signals, the metric R_j when sampled over time can be expected to cluster around a mean value, where the magnitude of this mean value depends on the level of spatial heterogeneity in the signal. In the event of non-acoustic contamination by flow noise, the phase relationship between the pressure and particle velocity signals is random and the distribution of R_j is uniformly spread over a range of values. Therefore, an examination of the distribution of R_j can provide an indication of the degree of non-acoustic contamination.

An additional metric to evaluate the contribution of the non-acoustic component can be defined [4] that arises from the relationship between the particle velocity cross-spectra and active and reactive intensity vectors:

$$M_{21} = \frac{|Q_{34}(\omega)| - \left|\left(\frac{C_{1[2,3,4]}(\omega) \times Q_{1[2,3,4]}(\omega)}{S_{11}(\omega)}\right)_x\right|}{|Q_{34}(\omega)| + \left|\left(\frac{C_{1[2,3,4]}(\omega) \times Q_{1[2,3,4]}(\omega)}{S_{11}(\omega)}\right)_x\right|},$$

$$M_{22} = \frac{|Q_{42}(\omega)| - \left|\left(\frac{C_{1[2,3,4]}(\omega) \times Q_{1[2,3,4]}(\omega)}{S_{11}(\omega)}\right)_y\right|}{|Q_{42}(\omega)| + \left|\left(\frac{C_{1[2,3,4]}(\omega) \times Q_{1[2,3,4]}(\omega)}{S_{11}(\omega)}\right)_y\right|}, \tag{2}$$

$$M_{23} = \frac{|Q_{23}(\omega)| - \left|\left(\frac{C_{1[2,3,4]}(\omega) \times Q_{1[2,3,4]}(\omega)}{S_{11}(\omega)}\right)_z\right|}{|Q_{23}(\omega)| + \left|\left(\frac{C_{1[2,3,4]}(\omega) \times Q_{1[2,3,4]}(\omega)}{S_{11}(\omega)}\right)_z\right|}.$$

The notation $X_{1[2,3,4]}$ represents the off-diagonal elements of the matrix **X**, arranged as a vector, and '×' is the vector cross-product. Values of M_{2j} that deviate significantly from zero are considered to be a flag of non-acoustic contamination.

3. EXPERIMENT

The VSA was deployed at the mouth of Sequim Bay in Washington, USA on a bottom platform in a water depth of 8 m with respect to the mean sea level. This location is an energetic tidal channel, where the tidal excursion during the deployment was 2.5 m. Sensors on the VSA consisted of two Geospectrum M20-040 vector sensors and one Geospectrum M020-100 vector sensor that also measures sensor orientation. In this paper, sensor data from the M20-100 are analysed for flow noise contamination. The sensors are sensitive to acoustic frequencies in the 50 Hz- 5 kHz range, with a flat frequency response on the pressure channel, and a peak in the response at 1 kHz on the particle velocity channels. The flow noise shields were constructed of 1050 ballistic nylon wrapped around a baffled PVC tube in which a vector sensor was suspended. The flow shield was in place during an outgoing tide (Figure 1), and removed from the PVC baffle during the subsequent rising tide. Low-frequency

sinusoidal pulses and frequency sweeps were transmitted using a sound source on board a boat that drifted past the sensor platform at distance that ranged from 50 m to 500 m.

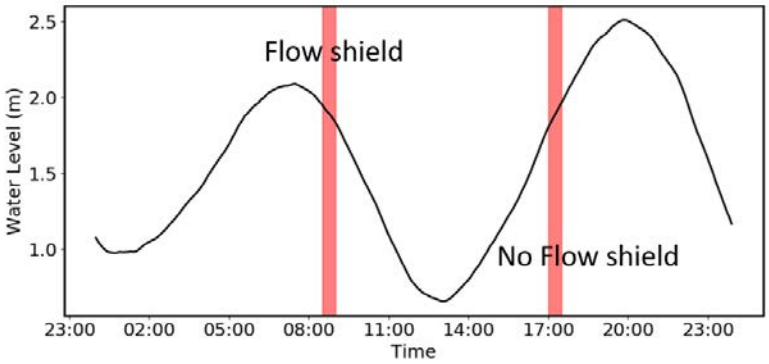


Figure 1: Tidal water level over the course of the field test on August 30, 2018.

4. RESULTS

Particle velocity and pressure frequency spectra were calculated with and without the flow noise removal shield (Figure 2).

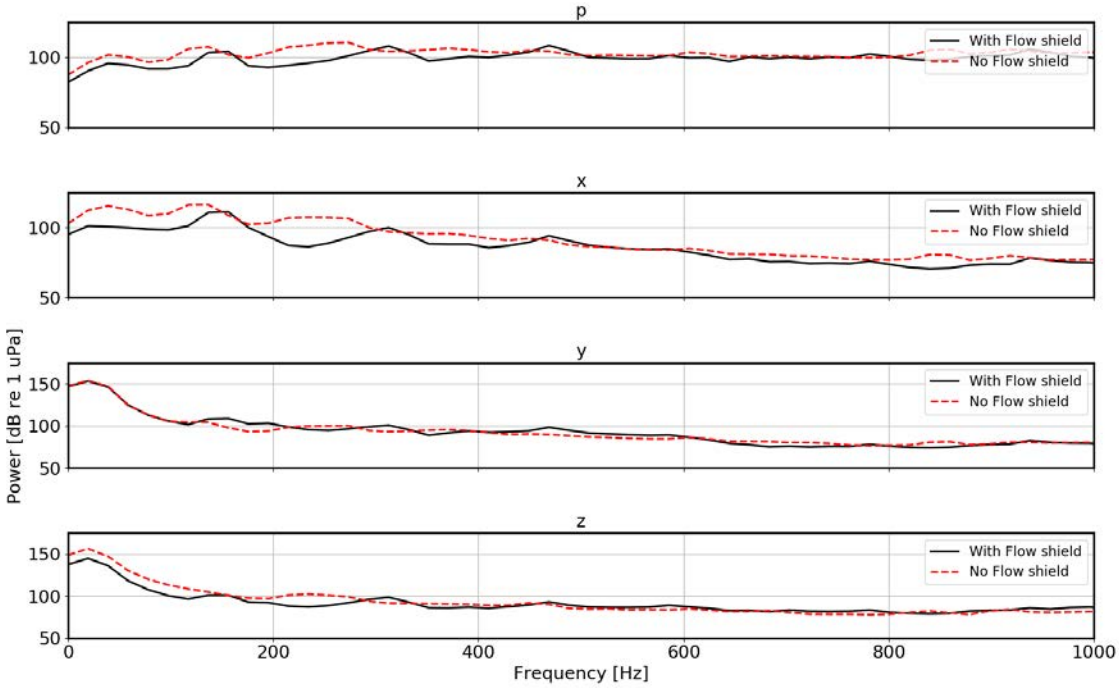


Figure 2: Frequency spectra for the pressure and particle velocity channels, with and without the flow shield.

Improvements in flow noise reduction are seen in the primary flow noise frequency band of 0-500 Hz on the pressure, x-, and z-particle velocity channels. Little to no change is observed for the y-particle velocity channel, attributed to the flow being orthogonal to the y-axis.

The probability distribution of R_j (Equation 1) is computed over a 30-minute period during each tidal cycle and is shown in Figure 3. The distribution markedly clusters around zero for the x-channel with the flow shield, consistent with the lowering of flow noise seen in the frequency spectra (Figure 2). No improvements are seen on the y-channel, while improvements in the z-channel are seen below 100 Hz where the R_j distribution without the flow shield is somewhat more randomly distributed than that without the flow shield. In general, low mean values of the R_j indicate a spatially homogeneous signal.

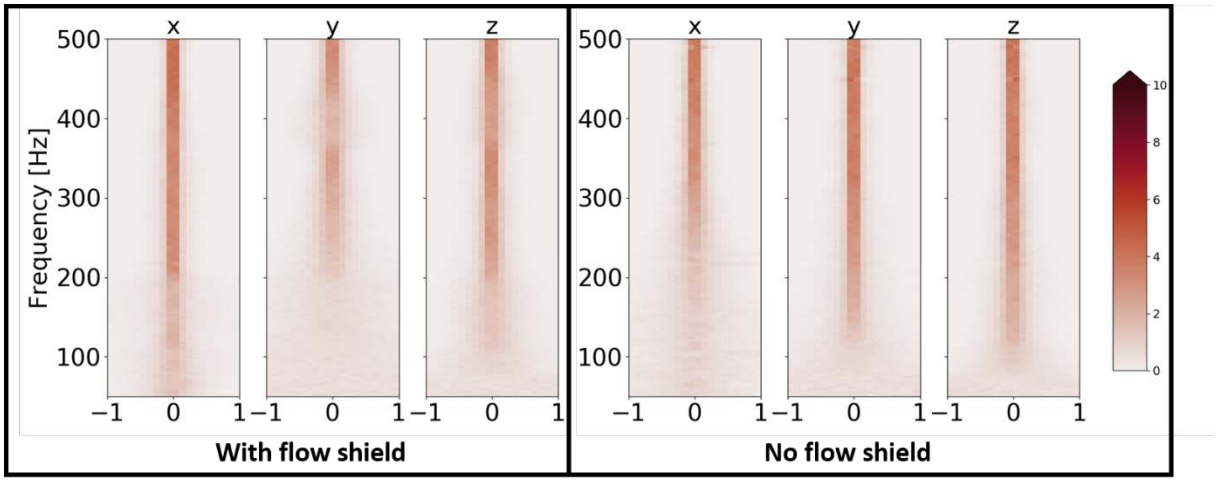


Figure 3: Probability distribution of R_j metric, with and without a flow shield.

Figure 4 shows the probability distribution of the M_{2j} metric, with and without the flow shield. A marked contrast is seen in the distributions with and without the flow shields. Distributions with the flow shield are seen to cluster around zero between 0-250 Hz, and no significant deviations towards higher values are observed. In contrast, the M_{2j} distributions without the flow shield are seen to cluster towards a value of 1 over much of the 0-500 Hz range shown, indicating the presence of non-acoustic signal contamination.

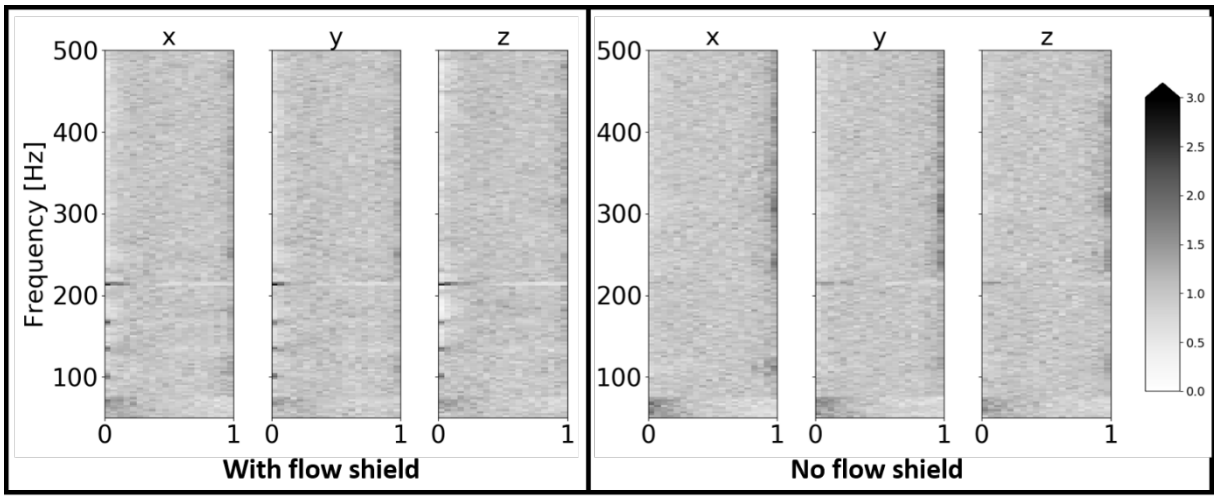


Figure 4: Probability distribution of M_{2j} metric, with and without a flow shield.

Figure 5 compares spectrograms of frequency sweeps as received on the pressure channel of a vector sensor, which illustrates the significant signal degradation in the absence of the flow noise removal shield. A visibly higher noise floor is seen in the absence of the flow shield, indicating significant degradation of signal detectability in the absence of the flow shield. Of particular interest is the low frequency portion of the spectrogram where the presence of a flow shield noticeably lowers the low frequency noise floor.

5. CONCLUSIONS

A field test of a vector sensor array was conducted in an energetic tidal channel where controlled source sweeps were transmitted over a full tidal cycle. Efficiency of a flow noise shield is demonstrated using analytical metrics [3,4] of vector sensor measurements of pressure and particle velocity. Improvements in the spectral levels and probability

distributions of the reactive ratio are observed. Spectrogram signal-to-noise and particle velocity cross-spectral metrics show significant improvements with the flow shield installed. Use of the flow shield on vector sensor arrays in energetic ocean environments is critical to improving acoustic measurements

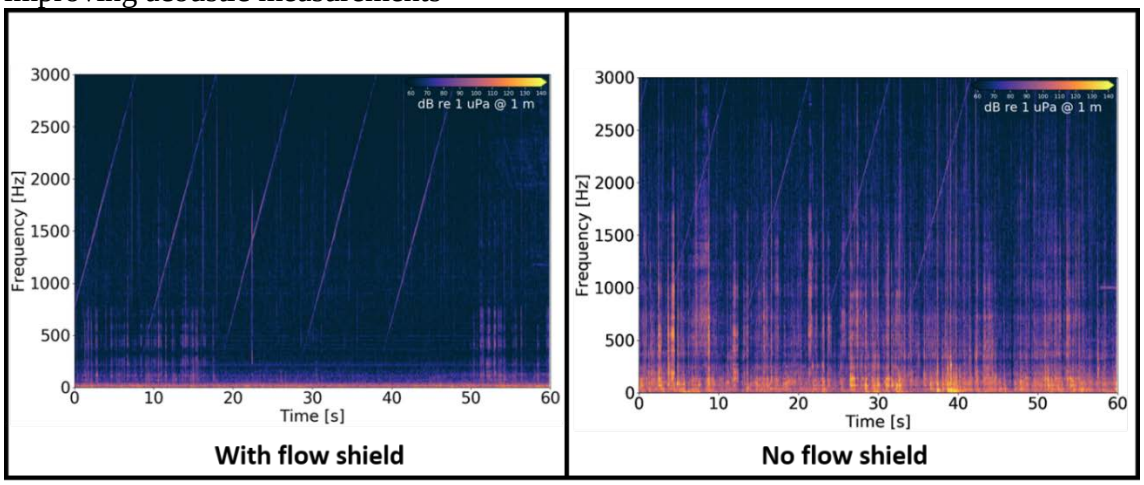


Figure 5: Received controlled source transmissions on the pressure channel of the vector sensor, with and without the flow shield.

6. ACKNOWLEDGEMENTS

The authors would like to thank the staff and crew at Pacific Northwest National Laboratories for a successful field effort. This material is based on work supported by the U.S. Department of Energy's Office of Energy Efficiency and Renewable Energy under the Water Power Program Award Number DE-EE0007822. This was prepared as an account of work sponsored by an agency of the United States Government. Neither the United States Government nor any agency thereof, nor any of their employees, makes any warranty, express or implied, or assumes any legal liability or responsibility for the accuracy, completeness, or usefulness of any information, apparatus, product, or process disclosed, or represents that its use would not infringe privately owned rights. Reference herein to any specific commercial product, process, or service by trade name, trademark, manufacturer, or otherwise does not necessarily constitute or imply its endorsement, recommendation, or favoring by the United States Government or any agency thereof. The views and opinions of authors expressed herein do not necessarily state or reflect those of the United States Government or any agency thereof.

REFERENCES

[1] Santos, P., Felisberto, P., and Hursky, P. Source localization with vector sensor array during the Makai Experiment, In *2nd International Conference and Exhibition on "Underwater Acoustic Measurements: Technologies and Results"*, Heraklion, Greece, 25–29 June 2007; pp. 985–990.

[2] Tougaard, J. 2015. Underwater noise from wave energy converters is unlikely to affect marine mammals. PloS One 10(7):e0132391

[3] D'Spain, G. 1990. Energetics of the deep ocean's infrasonic sound field. Ph.D. thesis, University of California, San Diego.

[4] Thode, A., Skinner, J., Scott, P., Roswell, J. 2010. Tracking sperm whales with a towed acoustic sensor. J. Acoust. Soc. Am. 128(5), 2681-2694.

WAVE PROPAGATION IN SOFT SOLID HALF SPACES AND EVANESCENT PRESSURES IN OVERLYING WATER

Richard (Dick) Hazelwood, Patrick Macey

R&V Hazelwood Associates LLP, Guildford GU2 8UT, UK
PACSYS Ltd, Strelley Hall, Nottingham, NG8 6PE, UK

Dr R A Hazelwood, 14 Ash Grove, Guildford GU2 8UT, UK, dick@r-vhazelwood.co.uk, aconic@zen.co.uk

Abstract:
Typical sedimentary seabeds have very slow shear wave speeds which increase with depth. This can be modeled with a linear depth profile of the shear wave speed. A simpler model has uniform solid material under a fluid half space, both extending to infinity as described by Scholte. Finite element modeling has been used to study both, when the solid is deformed by an impact, simulating piling or dredging actions .Off shore piling is used for wind turbine installation, and the consequences to seabed wildlife are associated with the wave energy which is radiated outward.
In addition to the ground roll interface waves, as discussed at earlier conferences, we find other wave forms which may also contribute to the vibrations in seabed sediments and the evanescent pressures they create in adjacent water. Wave propagation in the linear graded solid model can be predicted using circular ray pathways, all of which have their centre at the same height above the seabed. This is controlled by the shear speed profile.

Keywords: *Seismic interface waves, Half space model, Water particle velocity, piling, dredging*

1. INTRODUCTION

Previous studies showed how the propagation of seismic interface waves depends on the nature of the seabed [1],[2]. They led to the modelling of a saturated sedimentary seabed by a modified infinite half space. Rayleigh [3] described a simple half space of a uniform solid under a vacuum and Scholte [4] showed that similar interface waves would be seen when the upper half space was a fluid.

A more realistic model uses a graded solid, where the material shear wave speed increases linearly with depth. This model supports a special wavelet which propagates well if suitably excited. This is described as a Morphing Mexican Hat (MMH) form. It is efficiently excited by the Ricker form (a.k.a. Mexican Hat), of a suitable period, to repeatedly morph via a hump to a dip (inverted), and back, without dissipating energy into a longer period. In contrast we discuss the consequence of using a wavelet with a shorter period, which then expands in time, with a greater loss of peak intensity than predicted by cylindrical spreading.

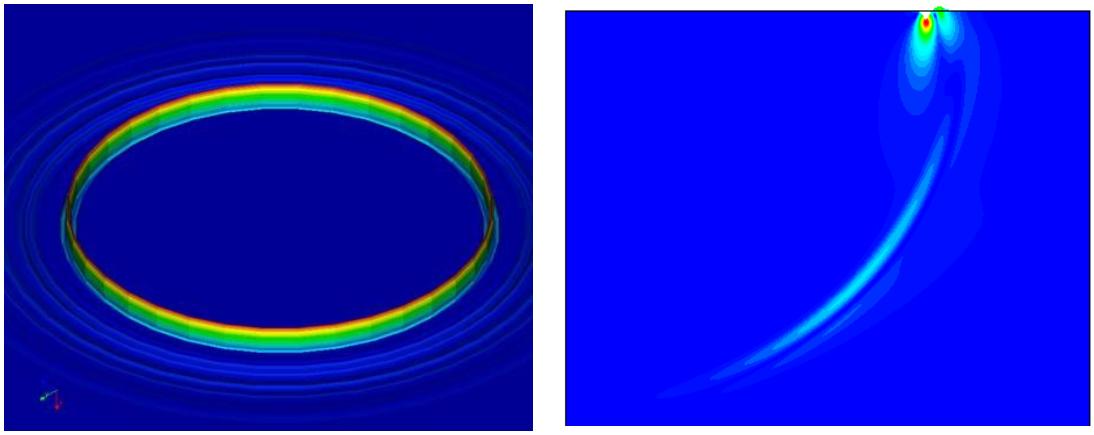


Fig 1: Two views of a seismic wavelet in an axisymmetric model. In the view from above, the axis of symmetry is central, whereas it is on the left in the cross section, showing the energy radiating from the interface into the depths for a Scholte model with uniform solid material. Whilst the most intense vibration occurs at the surface, a shear wave arc propagates into the depths. The vibration amplitude is colour coded, and the deformation exaggerated for clarity. After 1.25s, the interface wave in the 2nd view has reached a radius of almost 150m.

The axisymmetry assumed in these finite element (FE) models allows results to be presented as a cross section in two dimensions (2D), and then enlarged to show details.

2. THE SIMULATION OF THE IMPACT AND THE AIRY PHASE

The earlier work on pile driving represented the piling impact as a force on the substrate around a circular pile base, shown as a point on the 2D view, radius RP, in the FE model.

Model	RP= 0m	RP= 0.5m	RP= 1m	RP= 2m	RP= 4m
Energy	680J	657J	593J	409J	161J

Table 1: The energy accepted by the solid as a function of radius for the excitation

However, wavelet forms as seen in the far field showed little dependency on the radius of the node to which the vertical force was applied. A confirmatory study showed how the energy accepted by the solid, as this radius was decreased, showed a limit case at radius zero.

This simplification then allowed attention to be placed on the time profile of the applied force. Shearer [5] stated that seismologists often use the Ricker wavelet in their simulations

$$R_k(T) = K\, e^{\frac{-T^2}{2}} (1 - T^2) \qquad \text{where } T = \frac{2(t - t_0)}{\tau} \tag{1}$$

Here the time has been scaled by the use of a pulse width τ, about a centre maximum at time t_0. The central peak lies between two zeroes, occurring when $T^2 = 1$ or $t - t_0 = +/- \tau/2$. This shape is often called the Mexican Hat. The peak force K was always set to 1MN.

The zero/zero time τ, or pulse width, then governs the frequency spectrum of the energy of excitation. This can affect the speed of the interface wave in the graded model. Half space models with a uniform solid show no such effect, and are thus unrealistic, whereas many more realistic assumptions provide dramatic dispersion of input waves.

In earlier work a more realistic model used data on shear wave speed profiles with depth, taken from reviews by Hamilton [6] of measured values from various seabed types. Later it was found that a linear gradient of material shear speeds yielded a MMH wavelet, which propagated with little loss. By using a Ricker excitation, the interface wave was seen to morph from a hump to a dip and back at a rate determined by the shear speed profile.

The modelling ignored any absorption, but gave a good fit to a cylindrical energy spreading rule, with successive hump forms correlating well in their shape. This gave precise values for the group velocity, between two symmetric humps, smaller than the value of the shear wave speed as set in the model (often 128m/s). However, for these material values, there was a clear minimum seen when the width τ of the excitation was around 35ms.

	Pulse width τ ms	Transit speed ms^{-1}	Hump #1 width ms	Hump #2 width ms
1	16	117.89	15.4	16.6
2	20	117.74	18.8	20.4
3	25	117.5	23	24
4	32	117.38	29	29
5	40	117.39	36	36
6	50	117.60	45	45
7	64	117.92	56.3	58
8	80	118.79	70.4	74
9	100	119.47	86	88

Table 2. Wavelet properties taken from runs with different Ricker drive pulse widths.

The investigation of the shorter pulses was limited by the break-up of the resultant wavelets with distance, as dispersion caused them to be spread in time. An improved model has allowed the pulse widths to be further reduced, whilst still allowing sufficient correlation to better determine the group speed.

Note that the width (zero/zero times) of successive symmetric hump forms increases with time and distance when well away from the minimum in transit speed. At the minimum speed this wavelet expansion was also minimised.

This minimum is an example of what Shearer [5] describes as an Airy phase. Earth's geology is also layered, but on a much larger scale, leading to stable propagation of a variety of earthquake forms, including the interface wave (Rayleigh wave) with its strong horizontal motion, so destructive to buildings. Note the time scale is in minutes not millisconds.

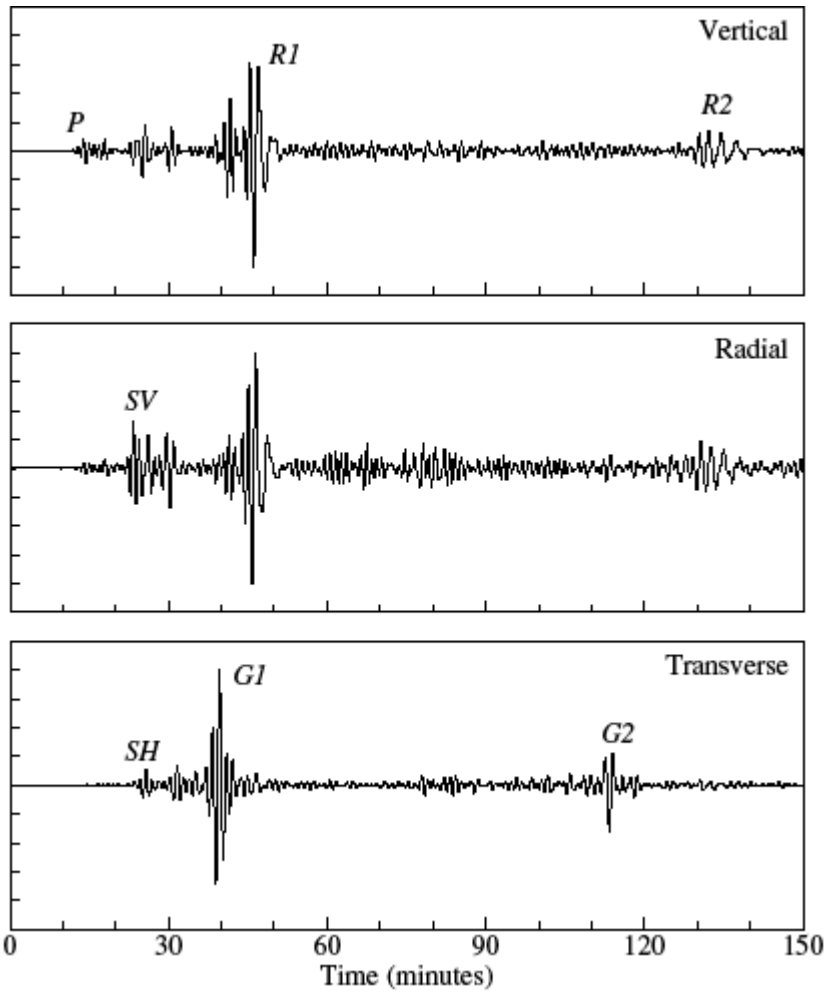


Fig 2: An example of a powerful earthquake as recorded after propagation across the Pacific ocean in 1989. Taken from Shearer [5] with permission. Waves include dominant Rayleigh (R1,R2) types as well as shear (SV and SH) and Love waves (G1,G2).

3. RESULTS FROM A MORE DETAILED FE MODEL

The mathematical model which gives a stably propagating, but morphing MMH compact form has a smooth linear increase in material stiffness with depth, d, as set by the shear wave speed function, $V_s(d)$. This is set by the interface value (d=0) and the gradient with depth, g_r. The gradient has been shown to control the morphing rate

Shear speed gradient (s^{-1})	1	2	4	8	16	32
Morphing frequency (Hz)	0.335	0.748	1.488	2.912	5.682	10.91

Table 3: The variation of the morphing frequency with the shear wave speed gradient.

A gradient of 4 (m/s)/m (also shown as s^{-1}) was often convenient, and a fairly good fit to the measured data reported by Hamilton [6]. The regular morphing occurs at 1.488Hz for this gradient. These MMH wavelets are an extreme example of the way wave groups are seen to progress with their peaks moving through the group envelope due to the difference between group velocity and phase velocity.

The finite elements of the FE model have material properties set in layers, but each successive layer of elements has its own different property. Recent models use 56 different values to better approximate the smooth curve of the physical model

4. RAYS IN A LINEAR GRADIENT FOLLOW ARCS OF CIRCLES

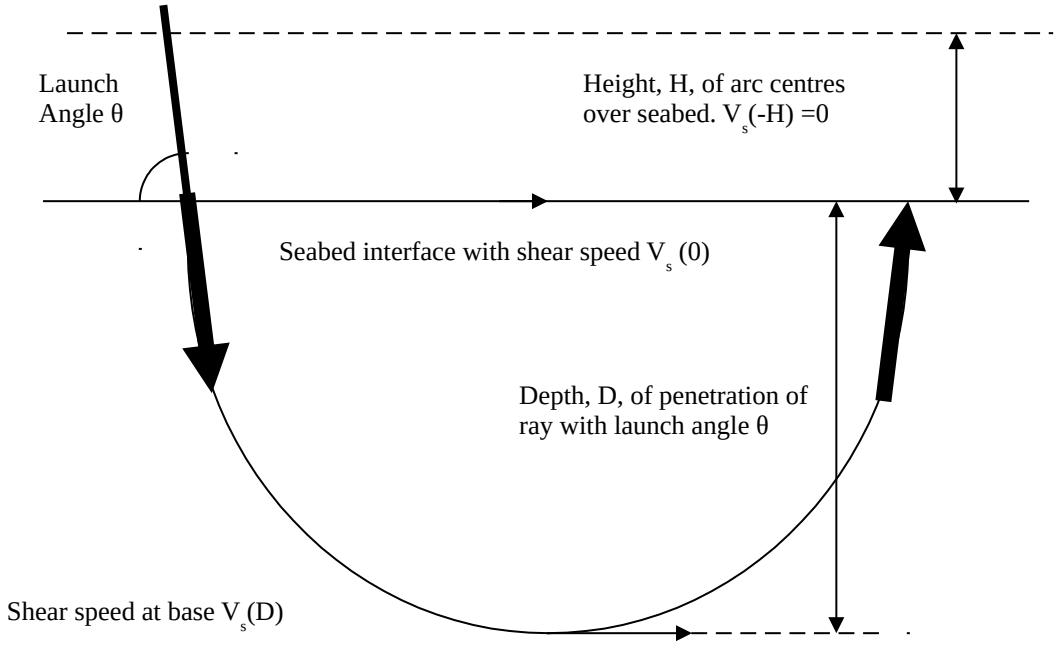


Fig 3: Rays (and corresponding plane waves) being refracted back to the interface

Plane pressure waves in water are well known to suffer refraction. Their paths can be analysed by ray tracing in most circumstances. Shearer [5] discussed the use of ray tracing for plane shear waves in solids. Whereas the shear waves in a Scholte model (Fig 1) pass down into the depths, they will be refracted by a shear speed depth gradient, just as sound pressure waves are refracted by the gradient of sound speed in water. Kinsler et al [7] showed that for a mixed layer, the refraction due to increasing pressure with depth gives ray paths as arcs of circles.

Snell's law leads to a constant "horizontal slowness" dependent on the launch angle θ (Shearer). This ray constant then controls the arc paths as shown in Fig 3. All ray paths are centred at the same height H above the interface, which is the height at which the shear speed function $V_s(d)$ becomes zero if extrapolated. D is the maximum depth for each ray which depends on θ. The travel time for the return to the interface (d=0) will also depend on θ.

5. A SHORTER WAVELET IS DISPERSED IN A GRADED MEDIUM

Whilst earlier studies concentrated on the properties of the compact MMH wavelet, seen at the Airy phase around periods ~ 35ms, dispersion occurs for pulses with different frequency contents. A Ricker wave of width τ = 8ms is shown to have expanded to give many zero crossing times in plots of vibration displacement. This model "fg5w" uses 56 different material properties for the finely graded interface elements, as seen in Fig 4. Data is computed for every successive 0.4ms step in the 3.2 second long transient analysis. The smallest solid elements are 0.25m deep by 0.2m radially, much finer than those used earlier, to allow the pulse width to be reduced. Poisson's ratio for the solid starts close to 0.5 but tends to 0.25 at infinity. The solid density is 2250 kg/m^3, and its pressure wave speed is 1520m/s at the interface. Water pressure speed is 1500m/s, and water density is set at 1000kg/ m^3.

The detailed view in Fig 4, of the state at 1.6s, after 4000 steps, only shows 5m depth of overlying water and 7m depth of sedimentary seabed. The gap between them is for clarity.

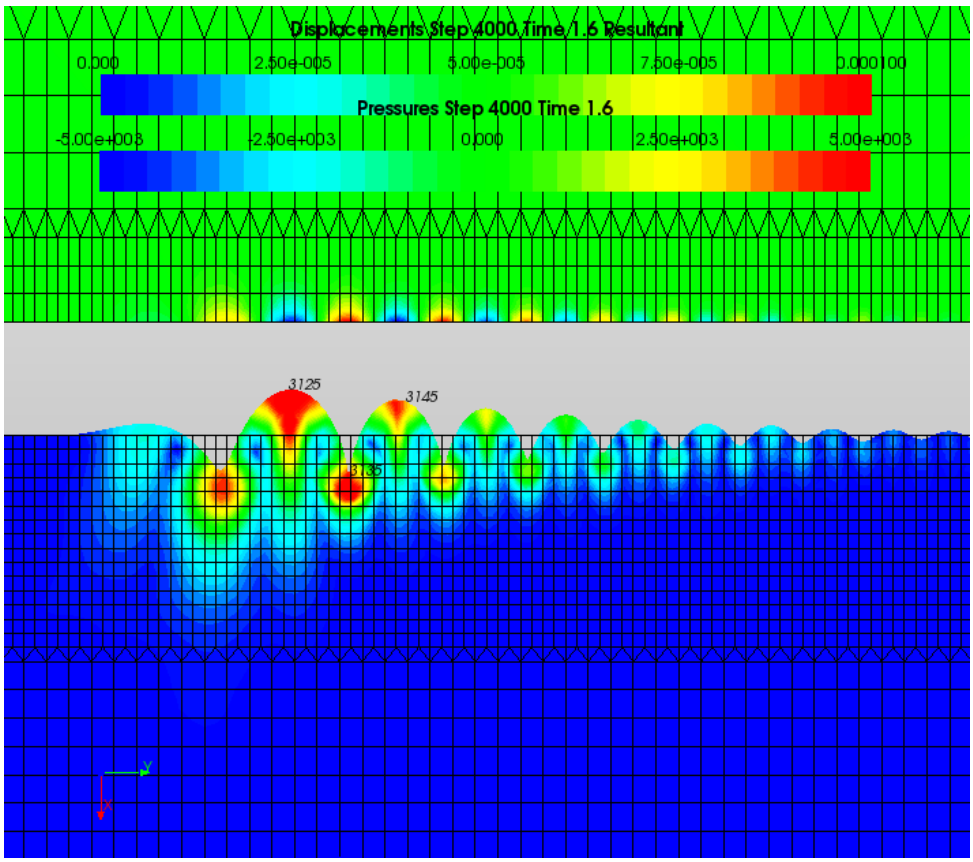


Fig 4: The displacement in the solid and pressures in the overlying water. Deformations are exaggerated. Peak pressures exceed 500Pa, and displacements exceed 100μm

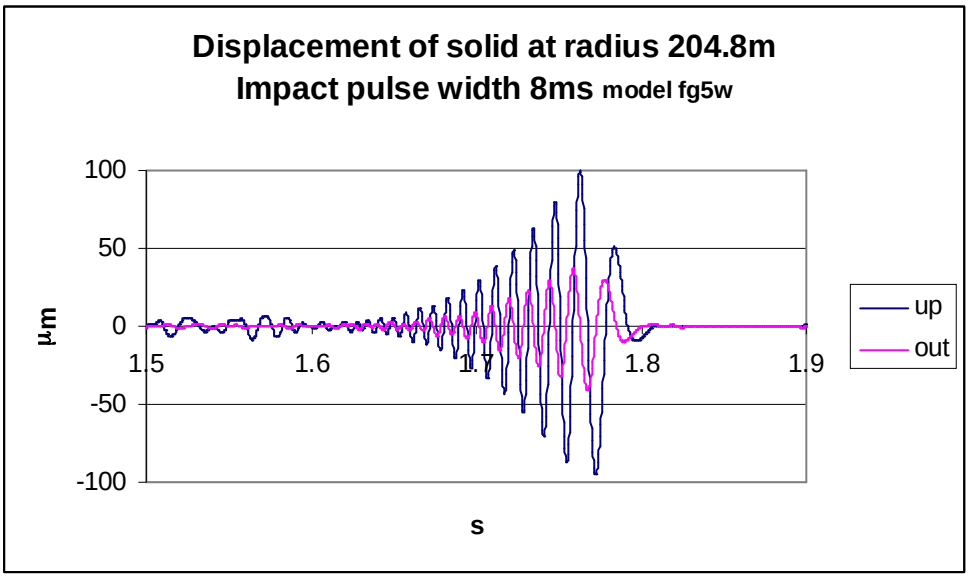


Fig 5: Despite having expanded in time to show many zero crossings, the upward displacement remains out of phase with the radial outward displacement. This retrograde ellipsoidal motion has a maximum inward velocity as upward displacement peaks.

6. THE EVANESCENT PRESSURES CLOSE TO THE SEABED

The acoustic pressures in the water close to the seabed rapidly reduce as heights increase

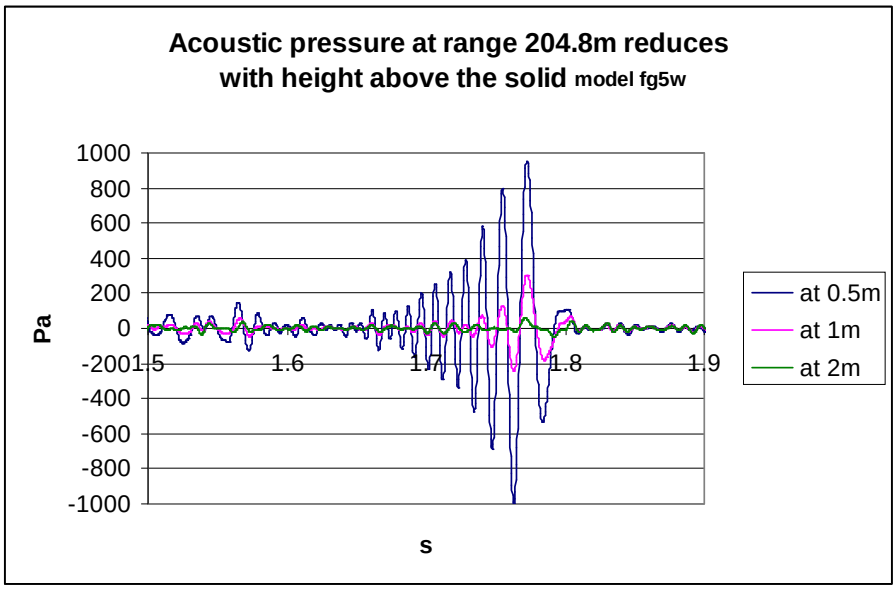


Fig 6: The acoustic pressures predicted by model run fg5w at three different heights

The pressure measured by hydrophone can be used to assess the solid motion

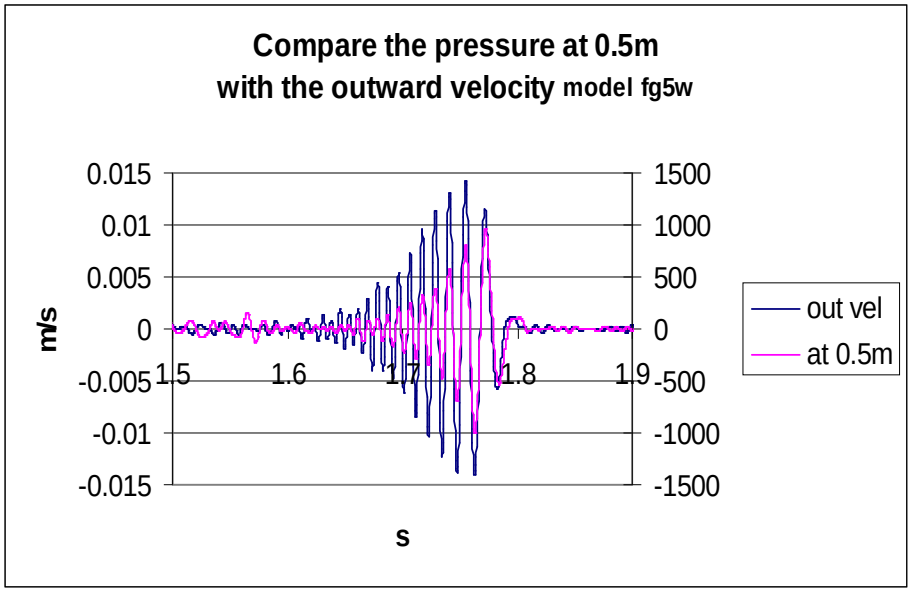


Fig 7: There is a good match between the times of zero crossings for predicted water pressures (right axis) and the outward velocity of the solid beneath (left axis).

The peak evanescent acoustic pressure p_E = -999Pa (mauve) corresponds to u_h = -13.7 mm/s outward velocity of the solid (largest negative peaks). The ratio is 72920 Pa/(m/s). This has the units of an impedance and can be compared to a typical specific acoustic impedance in seawater of 1.5 MPa/(m/s). As the hydrophone is raised, this p_E/u_h ratio will be reduced.

Strong seabed motion may thus be sensed by the detection of these evanescent pressure measurements, whose characteristics should allow them to be distinguished from other pressure waves. The times of the evanescent zero crossings are independent of the height above the seabed.

7. LINKING WATER PARTICLE VELOCITIES TO ACOUSTIC PRESSURE

The motion of the water near the seabed mimics that of the solid, but with larger horizontal motion. Vertical motions must be the same at the interface, but decay with height above it. However, the constraint on horizontal motion of the solid, as seen by the typical ellipsoidal paths is not present for the fluid, giving a substantial amplification of this key parameter.

Horizontal water particle velocities, u_h, for the MMH wavelet were modelled, and found to closely mimic the evanescent acoustic pressures, p_E, at the same point, given little or no dispersion. Theory then gives this ratio as proportional to the evanescent wavelet speeds, V_E, and the density of the water, ρ. This ratio does not change with height over the seabed

$$\frac{p_E}{u_h} = \rho V_E \qquad (2)$$

Note the similarity to the relation for a bulk pressure wave. A measured evanescent acoustic pressure thus predicts a much larger water particle velocity than that indicated for the same value bulk pressure wave, by a typical factor of the ratio of wave speeds 1500/117.4, more than a factor 12 larger. Some experimental confirmation has been achieved.

Current work involves further investigation of this link, hoping to be able to detect and measure the presence of ground roll vibrations using the more convenient deployment of a seabed mounted hydrophone array. Ideally this should be done in conjunction with the seabed geophone sledge.

8. ACKNOWLEDGEMENTS

The authors are grateful to Peter Shearer for permission to use his figure

REFERENCES

1. **Hazelwood, R.A. Macey, P.C**. Modelling water motion near seismic waves propagating across a graded seabed, as generated by man-made impacts. *J. Mar. Sci. Eng.*, 4(3), 47, 2016
2. **Hazelwood, R.A. Macey, P.C. Robinson S.P. Wang L. S.** Optimal transmission of interface vibration wavelets- a simulation of seabed responses. *J. Mar. Sci. Eng.*, 6, 61, 2018
3. **Rayleigh, L**. Interface waves. *Proc. Lond. Math. Soc.*, 17, 4–11, 1887.
4. **Scholte, J.G**. On true and pseudo Rayleigh waves. *Proc. K. Ned. Akad. Wet. Amst*., 52, 652–653, 1949.
5. **Shearer, P.M**. *Introduction to Seismology*; Cambridge University Press: Cambridge, UK, 1999
6. **Hamilton, E.L**. Vp/Vs and Poisson's ratio in marine sediments and rocks. *J. Acoust. Soc. Am.*, 66, 1093–1101, 1979.
7. **Kinsler L.E. Frey A.R. Coppens A.B. Sanders J.V**. *Fundamentals of Acoustics* 3rd Ed, John Wiley & Sons, New York, 1980

UNDERWATER NOISE GENERATED BY OFFSHORE PILE DRIVING: A PILE-SOIL-WATER VIBROACOUSTIC MODEL BASED ON A MODE MATCHING METHOD

Apostolos Tsouvalas, Yaxi Peng, Andrei V. Metrikine

Department of Engineering Structures, Faculty of Civil Engineering and Geosciences, Delft University of Technology

Corresponding author's email: Y.Peng@tudelft.nl

Abstract: *In this paper, a pile-water-soil model is developed for the prediction of sound generated due to impact piling. The complete model consists of two modules: i) a near-source module aiming at the accurate description of the pile-water-soil interaction together with the sound generation and propagation in the vicinity of the pile; and ii) a far-from-source module aiming at the propagation of the wave field at larger distances. The input to the far-from-source module is provided by the near-source module through a boundary integral formulation.*

Keywords: *underwater noise, offshore pile driving, acousto-elastic medium, mode matching, boundary integral*

1. INTRODUCTION

The underwater noise generated during the installation of foundation piles offshore has been an issue of serious concern mainly due to the rapid developments in the offshore wind industry. The noise pollution itself poses a threat to the marine fauna [1], especially when one considers the large foundation piles, i.e. pile diameters exceeding 7m and lengths of about 80m, that have been installed lately. In order to comply with the strict regulations imposed by several countries, the offshore industry strives to keep the noise levels to within acceptable limits. Various noise mitigation systems [2] have been employed to date aiming at the effective blockage of the noise transmission in the seawater while new ones are under development. To assist in the control of hydro-sound emission, underwater noise prediction becomes essential.

During the last decade, several models have been developed for noise prediction due to impact piling [3]. Reinhall and Dahl [4] were the first to examine systematically the noise generated by impact pile driving. By means of finite element (FE) simulations, they concluded that the sound waves in the seawater originate from the radial expansion of the pile surface caused by the compressional waves travelling downwards the pile at supersonic speed; the latter radiate waves in the water in the form of Mach cones. This observation was later confirmed by noise measurements [2]. Soon after, a wavenumber integration model was proposed by Lippert and Lippert [5] for the noise radiation due to pile driving, in which the pile was not modelled explicitly but substituted by a vertical array of point sources emitting

sound with a phase delay trying to mimic the waves travelling downwards the pile after the hammer impact. The results were generally found to be in good qualitative agreement with those of more detailed FE simulations.

In most available models [3], a two-step approach is adopted to model the entire noise path from the noise source (pile) to the receiver, the latter often positioned at large distances from the pile. A near-source model, based on either finite elements or finite differences, is usually employed for sound generation purposes. Subsequently, a far-from-source module is used to propagate sound at larger distances based on the normal-mode method, the wavenumber integration method or the parabolic equation method. The numerical predictions by the different models are basically consistent with each other [3]. With only a few exemptions [6,7], the seabed is customarily approximated by an equivalent acoustic fluid with extra attenuation. However, it is well-known that the pile-driving sources located in the seafloor are not purely compressional in nature, but emit both compressional, shear and interface waves [8]. Next to that, a detailed description of the soil is essential to correctly capture the noise source characteristics (pile vibrations) in the first place.

In contrast to the models described above, a semi-analytical pile-water-soil interaction model was developed by Tsouvalas and Metrikine [7], which includes a three-dimensional description of the water-saturated seabed as a layered elastic medium. In this model, the significance of the seabed-water interface waves (Scholte waves) was also investigated for the first time; the model predictions were also confirmed by collected measurement data [9]. The primary noise transmission path is in the water column in the form of Mach cones, while the secondary noise path is attributed mainly to Scholte waves which propagate along the seabed-water interface and, possibly, also to waves that are reflected in deeper soil layers and leak energy back to the water column. Examining the various noise transmission paths is key to the effective blockage of the noise propagation by exploiting the proper functioning of noise mitigation systems.

In this paper, the authors present a computationally efficient method for the prediction of the generation and propagation of the sound field associated with impact piling at large (from the pile) distances. The complete model consists of two modules: i) a near-source module aiming at the accurate description of the pile-water-soil interaction together with the sound generation and propagation in the vicinity of the pile; and ii) a far-from-source module aiming at the propagation of the wave field at larger distances with high accuracy. The input to the far-from- source module is provided by the near-source module through a boundary integral formulation. The structure of the paper is as follows. In Section 2, the descriptions of the near-source module and the far-from-source module are given. In Section 3, two case studies are analysed for both near-source module and the far-from-source module. Finally, Section 4 gives an overview of the main conclusions of the paper and the future work planned.

2. DESCRIPTION OF THE MODEL

2.1. Near-source module

The pile-water-soil coupled vibroacoustic model is used for the near-field prediction of the underwater noise induced by offshore impact pile driving. It is based on a three-dimensional semi-analytical model developed by Tsouvalas and Metrikine [7]. The complete system consists of the pile interacting with a layered acousto-elastic medium as shown in Fig. 1. The shell vibration is described by a linear high-order shell theory [10]. The shell is of finite length and occupies the domain $0 \leq z \leq L$. The fluid is modelled as a three-dimensional inviscid

compressible medium and occupies the domain $z_0 < z < z_1$ with a pressure release boundary at $z = z_0$. The soil is described as a three-dimensional horizontally stratified elastic continuum that occupies the domain $z_1 < z < H$ and is terminated at z = H with a rigid boundary. The effect of the rigid boundary is insignificant in the near-source range

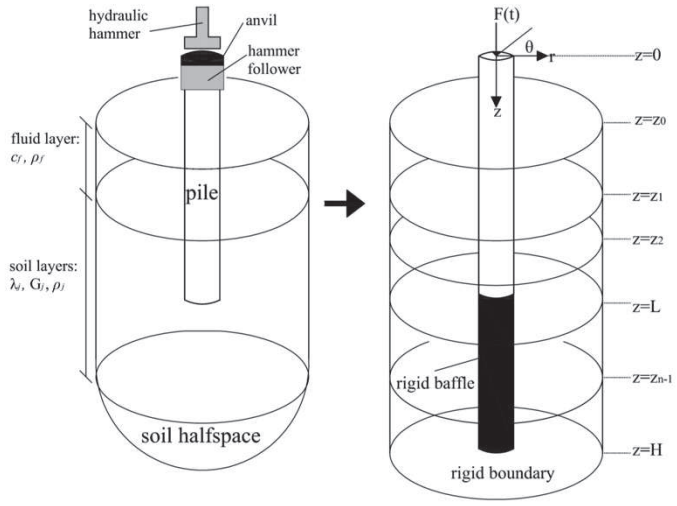


Fig. 1 Geometry depiction of the near-source model by Tsouvalas and Metrikine [9].

A modal decomposition is applied both for the shell structure and the acousto-elastic waveguide. The modal expansion of the shell structure is introduced as:

$$\tilde{u}_{p,k}(z,\omega) = \sum_{m=1}^{\infty} A_m U_{km}(z) \tag{1}$$

The vertical eigenfunctions $U_{km}(z)$ satisfy the boundary conditions at $z = 0 \sim L$. The expressions for the displacement and stress field in the waveguide, which inherently satisfy the boundary conditions and interface conditions, as well as the conditions at $r \to \infty$:

$$\tilde{p}_f(r,z,\omega) = \sum_{p=1}^{\infty} C_p H_0^{(2)}(k_r^{(p)} r)\tilde{p}_{f,p}(z) \tag{2}$$

The displacement and stress fields in the soil part of the waveguide can be expressed in the similar formulations as shown in [7], which are omitted here for the sake of brevity. The term k_r denotes the horizontal wavenumber, which is the solution of the dispersion. In Eqs. 1~2, the only unknowns are the coefficients of the modal expansions A_m and C_p. A system of infinite algebraic equations with respect to the unknown coefficients C_p can be obtained as explained in [7]:

$$\sum_{p=1}^{\infty} C_p \left(L_{qp} + k_r^{(q)} H_1^{(2)}\left(k_r^{(q)} R\right)\gamma_q \delta_{qp} - \sum_{m=1}^{\infty} \frac{R_{mq} Q_{mp}}{I_m} \right) = \sum_{m=1}^{\infty} \frac{F_m Q_{mp}}{I_m} \tag{3}$$

A detailed derivation of the terms L_{qp}, γ_q , Q_{mp}, R_{mq} and I_m introduced in Eq. 3 is given in [7] together with some explanation of the physical significance of each term. Finally, the coefficients of the shell structure are given by:

$$A_m = \frac{F_m + \sum_{p=1}^{\infty} C_p R_{mp}}{I_m} \tag{4}$$

The method presented above allows the coupling of the two sub-systems, namely the pile structure and the layered acousto-elastic medium. The solution method used in the near-source module gives great flexibility in examining various installation configurations. Due to the fact that the eigensolutions of the pile and seabed-water medium need to be solved only once for a

certain location, different installations scenarios, i.e. hammer force, pile penetration depths, etc., require only part of the solution to be evaluated, i.e. Eqs. 3~4. In fact, this allows one to examine multiple configurations with minimum computational effort. By coupling the near-source module to the far-from-source module, the complete model can also treat accurately complex soil conditions over larger radial distances.

2.2. Far-from-source module

In the far-from-source module, the environment is modelled as a fluid layer overlaying a layered elastic half-space. The input to the far-from-source module is provided by the near-source module. The far-from-source module aims to propagate the wave field at larger distances including the consideration of more complex soil conditions, i.e. frequency-dependent soil attenuation, which can be important for sound predictions at large distances.

Within the assumption of a cylindrically symmetric field, the acoustic field can be expressed by the displacement potential $\tilde{\phi}_f$ for the fluid, the displacement compressional potential $\tilde{\phi}_s$ and shear potential $\tilde{\boldsymbol{\psi}}_s$ = [0, $\tilde{\psi}_s$, 0] for the soil in frequency domain. The wave propagation in the fluid and soil medium can be described by the following displacement potentials:

$$\left[\nabla^2 + k_\chi^2(z)\right]\tilde{\varepsilon}_\chi\,(r,z,\omega) = \tilde{S}_{\omega\chi}(r_0,z_0,\omega)\frac{\delta(r-r_0,z-z_0)}{2\pi r} \tag{5}$$

in which $\tilde{\varepsilon}_\chi$ is one of the displacement potential functions $\tilde{\phi}_f$, $\tilde{\phi}_s$ and $\tilde{\psi}_s$ with the index $\chi = f,s,p$, k_χ $(=\frac{\omega}{c_\chi})$ are the medium wavenumbers for the fluid, the compressional or the shear potentials in the soil, respectively. The terms $\tilde{S}_{\omega\chi}$ are source strengths of the corresponding potential functions. Applying the forward Hankel transform in Eq. 5, the depth-separated wave equations in the wavenumber domain are obtained. The solutions for the displacement potentials in the wavenumber domain at each layer can be expressed as:

$$\hat{\varepsilon}_\chi(k_r,z) = \hat{S}_{\omega\chi}\frac{e^{-ik_{z,\chi}|z-z_s|}}{4\pi i k_{z,\chi}} + A_{\chi,1}(k_r)e^{ik_{z,\chi}Z} + A_{\chi,2}(k_r)e^{-ik_{z,\chi}Z} \tag{6}$$

in which the vertical wavenumbers are denoted as $k_{z,\chi} = \left(k_\chi^2 - k_r^2\right)^{1/2}$, the coefficients $A_{\chi,n}$ are the undetermined complex constants. The solutions for the potentials in the half-space consists of the particular solution to the source term and the general solution to the homogeneous equation with the waves propagating solely along the positive z-direction ensuring the radiation condition z → ∞. The condition $\Im(k_{z,p}) < 0$ and $\Im(k_{z,s}) < 0$ are imposed so that the field decays exponentially in depth [11].

Finally, the displacement potentials in frequency domain can be found by applying the inverse Hankel transform. According to the *Cauchy's* theorem and the residue theorem, the representations of the tensor of the Green's functions in both fluid and soil layers are given as:

$$\tilde{\varepsilon}_{\chi,k}^{g}(r,r_0,\omega) = -\pi i\sum_{m=1}^{M} Res\left(\hat{\varepsilon}_{\chi,k}^{g}(r_0,\omega)\right)H_0^{(2)}\left(k_r^{(m)}r\right) + \frac{1}{2}\int_{L_\alpha}\hat{\varepsilon}_{\chi,k}^{g}(r_0,\omega)H_0^{(2)}(k_r r)k_r dk_r + \frac{1}{2}\int_{L_\beta}\hat{\varepsilon}_{\chi,k}^{g}(r_0,\omega)H_0^{(2)}(k_r r)k_r dk_r \tag{7}$$

in which $\tilde{\varepsilon}_{\chi,k}^{g}$ with the index g denotes the Green's function with $\tilde{\varepsilon}$ being one of the displacement potential function, the index $\chi(=f,s,p)$ represents the location of the receiver and the index $k(=f,s,p)$ represents the location and type of the source with f indicating the

volume source in the fluid, p indicating compressional wave source and s indicating shear wave source in the soil, respectively.

Consider a cylindrical surface surrounding the pile at close proximity, and the case of a fluid layer overlaying a horizontally stratified linearly elastic half-space. The complete wave field characterized by the Green's function for the sources emitting both compressional waves and shear waves and the resulting amplitude of displacement potentials on the cylindrical surface from the pile driving, which are connected through the boundary integral equation as:

$$\tilde{\varepsilon}_{\chi}(\boldsymbol{r},\omega) = \sum_{k=f,s,p} \int_{S_k} \left[\tilde{\varepsilon}^{g}_{\chi,k}(\boldsymbol{r},\boldsymbol{r}_0,\omega) \frac{\partial \tilde{\varepsilon}_k(\boldsymbol{r}_0,\omega)}{\partial \boldsymbol{n}} - \tilde{\varepsilon}_k(\boldsymbol{r}_0,\omega) \frac{\partial \tilde{\varepsilon}^{g}_{\chi,k}(\boldsymbol{r},\boldsymbol{r}_0,\omega)}{\partial \boldsymbol{n}} \right] dS_0 \qquad (8)$$

in which $\tilde{\varepsilon}_k(\boldsymbol{r}_0,\omega)$ can be readily obtained from the near-source module (section 2.1).

3. CASE STUDIES

3.1. Case study 1: predictions of the near-source module

The predictions of the near-source module have been compared to data available in the literature from several measurement campaigns [8]. This section aims at examining the existence of an overlaying marine sediment layer (which is rather fluidised and thin) on the noise predictions for some typical seabed stratifications. In contrast to most other studies, which focus on the prediction of the pressure levels in the seawater region, the focus here is shifted towards an energy flux analysis which is believe to be key in the understanding of the noise transmission paths in the water and through the soil.

Case	Properties	Depth (m)	Density (kg/m^3)	c_L (m/s)	c_T (m/s)	α_p (dB/ λ)	α_s (dB/ λ)
Case study 1	Fluid	39.9	1000	1500	-	-	-
	Marine sediment	1.5	1540	1551	62	1.36	5.46
	Soil layer	78.5	1970	1967	468	0.27	1.09
Case study 2	Fluid	10	1000	1500	-	-	-
	Soil Half-space	-	1970	1845.7	130.2	1.00	2.00

Table 1: Properties of the acousto-elastic medium for case study 1 and 2.

The model consists of a pile with the length of L = 76.9 m, a diameter of D = 8 m, and a wall thickness of 90 mm, which is driven into the seabed through a water column, with the depth of H = 39.9 m, having a final penetration depth of L_p = 32.71 m. Table 1 contains all relevant properties of the system. In this analysis, the hammer and anvil are not modelled explicitly but replaced by a given smoothed exponential forcing function. As shown in Fig. 2 (a), a smoothed exponential force is used which results in approximately 1750 kJ input energy to the system which is a typical energy needed to drive piles of such dimension deep into the soil.

For the validation study, the acousto-elastic layer consists of one fluid layer and two soil layers. The marine sediment layer is described by a fluidized thin soil layer at the upper part of the seabed. In this analysis, the hammer and anvil are not modelled, but replaced by a force function applied at the pile head. In Fig. 2 (b), the total energy along the cross section of the acousto-elastic medium is normalized with the peak amplitude due to the existence of the

interface waves. The results indicate the contribution of the energy in the fluid and the soil domains for different horizontal distances from the pile. The energy carried by *Scholte waves* start to decay as soon as the interface waves propagate away from the pile surface. On the contrary, the amplitude of the pressure waves in the fluid decays much slower at large distances. The energy along the vertical coordinate grows steeply at the level of transition from fluid to marine sediment layer and from thin sediment layer to the soil layer due to the abrupt change in the impedance of the medium. As can be seen from the pressure evolution in Fig. 2 (c), higher pressure levels are found in the vicinity of the pile surface. Then the pressure levels start to decay rapidly as the waves radiate away from the pile. The Sound Exposure Level (SEL) are obtained for the 100 receiver points at radial distances up to 200m. Based on the logarithmic curve fitting of sound radiation over distances, the sound pressure level at 750 m distance from the pile are predicted as 182.4 dB.

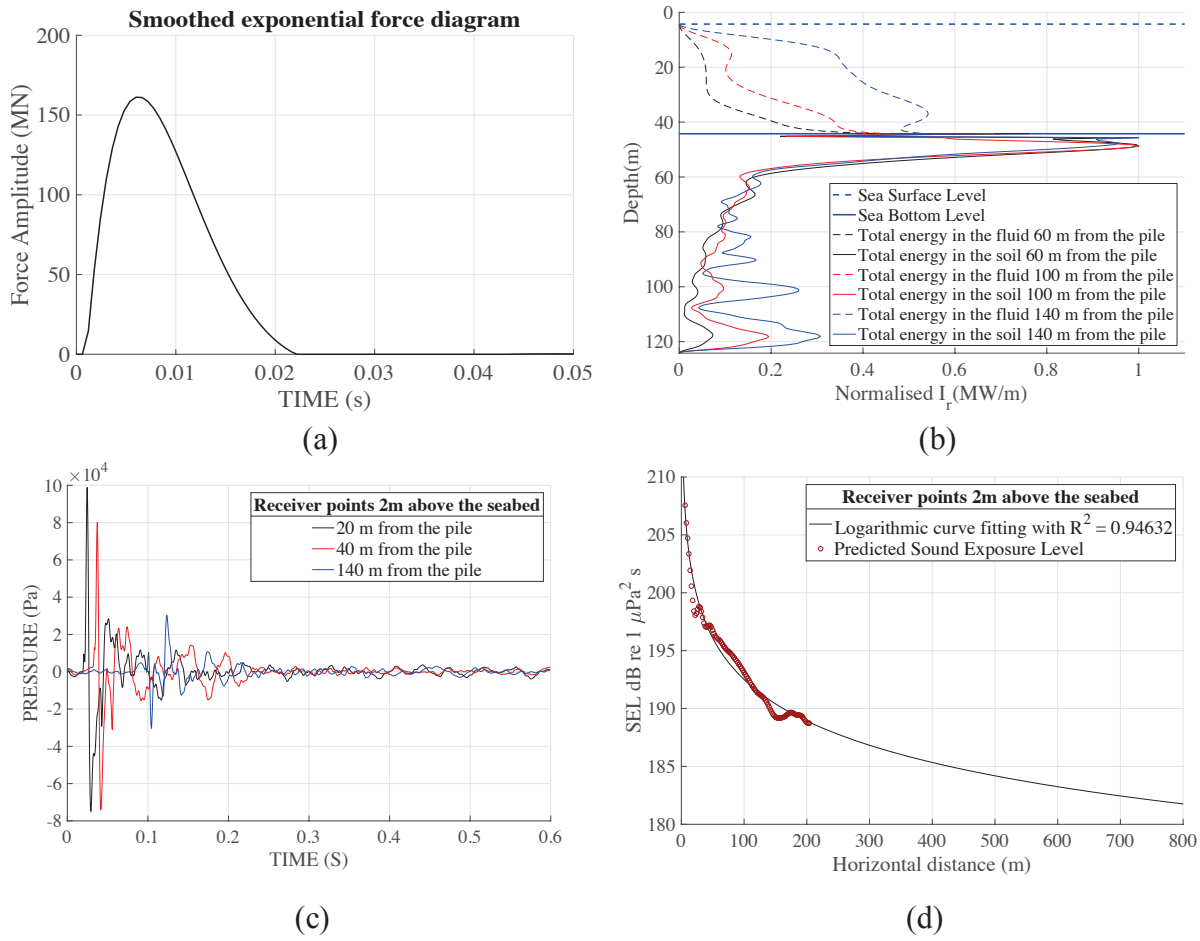


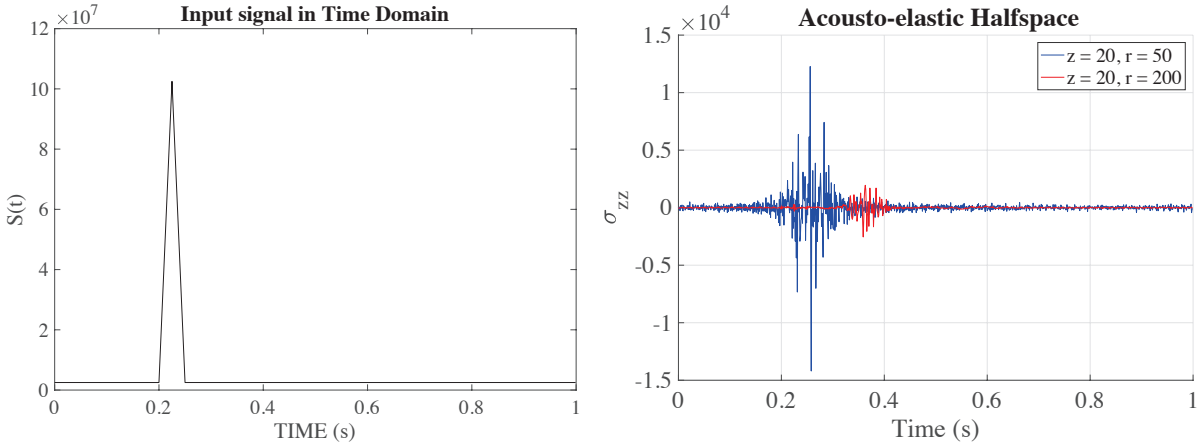
Fig. 2: (a) Force diagram for the smoothed exponential force function with an estimated blow energy of around 1750 kJ; (b) normalised total energy along the cross section of the fluid-soil domain at different horizontal positions; (c) pressure evolution with time; (d) predicted Sound Exposure Level (SEL) at different radial distances from the pile.

3.2. Case study 2: predictions of the far-from-source module

In this section, the sound radiation from pile driving is reproduced by a vertical distribution of time-delayed ring sources with the method proposed by Reinhall and Dahl [4]. The time

delay of the i_{th} source located at the cylindrical cross section $r_0 = 5m$ is determined by its depth and the speed of the pile bulge wave $c_b = 5080\ m/s$, as $\Delta\tau_i = z_i/c_b$.

The sources are defined as volume sources in the fluid and the soil with the source strength being the volume-injection amplitude in the unit of m^3 emitting compressional waves as shown in Fig.3 (a). In this case study, 60 ring sources at a spacing of 0.25m is distributed from the sea surface to the bottom of the pile. The penetration depth of the pile is assumed to be 5m. The ocean environment is described as one fluid layer overlaying a soil half-space. The material properties of the acousto-elastic domain and the geometry of the domain are summarised in Table 1.



(a) (b)

Fig. 3 Case study 2: (a) Input signal for the source (without time delay); (b) the normal stress σ_{zz} in the soil at 20m below the sea surface.

As shown in the Fig. 3 (b), the evolution of the pressure field in time is consistent with the appropriate arrival times of the wave fronts at different horizontal distances. The results presented here aim at solely proving the validity of the concept. In the next work, the input data from the near-source module will be inserted in Eq. 8 to propagate the wave field at large distances using the far-from-source module.

4. RESULTS AND FUTURE WORK

The paper establishes a computationally efficient method for noise predictions over large horizontal distances due to offshore pile driving. The complete model consists of a near-source module and a far-from- source module. The former aims at describing accurately the pile- soil-water interaction and the wave field generated at the surrounding acousto-elastic domain at close distances from the pile (~ $200 - 300$ m). The latter module aims at the propagation of this wave field at larger distances from the pile (~ $5 - 10$ km) provided that bathymetry changes are insignificant. The mathematical statement of the complete problem is presented and the adopted method of solution is described in great detail. Results from both the near-source module and far-from-source module are presented for a typical installation case encountered in the offshore wind sector. Future work will focus on the coupling of the pile-driving sources along the cylindrical surface to the far-from-source module.

5. ACKNOWLEDGEMENTS

The authors gratefully acknowledge China Scholarship Council (CSC) for financing this research project.

REFERENCES

[1] **Bailey, H., Senior, B., Simmons, D., Rusin, J., Picken, G., Thompson, P.M.**, Assessing underwater noise levels during pile-driving at an offshore windfarm and its potential effects on marine mammals, *Marine Pollution Bulletin*, 60, 888-897, 2006.

[2] **Bruns, B., Stein, P., Kuhn, C., Sychla, H., Gattermann, J.**, Hydro sound measurements during the installation of large diameter offshore piles using combinations of independent noise mitigation systems, In *Proceedings of the Inter-noise 2014 Conference*, Melbourne, Australia, 110, 2014.

[3] **Lippert, S., Lippert, T., Heitmann, K., Ruhnau, M., Von Estorff, O., Nijhof, M., Theobald, P.**, COMPILE - A Generic Benchmark Case for Predictions of Marine Pile-Driving Noise, *IEEE Journal of Oceanic Engineering*, 41(4) 1061-1071, 2016.

[4] **Per G. Reinhall, Peter H. Dahl.**, Underwater mach wave radiation from impact pile driving: Theory and observation, *The Journal of the Acoustical Society of America*, 130(3) 1209-1216, 2011.

[5] **Lippert, T. and Lippert, S.**, Modeling of pile driving noise by means of wavenumber integration, *Acoustic Australia*, 40(3) 178-182, 2012.

[6] **Fricke, M. B., Rolfes, R.**, Towards a complete physically based forecast model for underwater noise related to impact pile driving, *The Journal of the Acoustical Society of America*, 137(3), 1564-1575, 2015.

[7] **Tsouvalas, A., Metrikine, A. V.**, A three-dimensional vibroacoustic model for the prediction of underwater noise from offshore pile driving, *Journal of Sound and Vibration*, 333(8) 2283-2311, 2014.

[8] **Nealy, J. L., Collis, J. M., Frank, S. D.**, Normal mode solutions for seismo-acoustic propagation resulting from shear and combined wave point sources, *The Journal of the Acoustical Society of America*, 139(4) 95, 2016.

[9] **Tsouvalas, A., Metrikine, A.**, Structure-Borne Wave Radiation by Impact and Vibratory Piling in Offshore Installations: From Sound Prediction to Auditory Damage, *Journal of Marine Science and Engineering*, 4(3) 44, 2016.

[10] **Kaplunov, J. D., Kossovich, L. Y., Nolde, E. V.**, *Dynamics of thin walled elastic bodies*, San Diego: Academic Press, 1998.

[11] **Achenbach, J. D.**, *Wave propagation in elastic solids*, Amsterdam, New York: North-Holland Pub. Co.; American Elsevier Pub. Co, 1973.

Structured Session 16

Advances in acoustic measurement systems: Technologies and applications

Organiser(s): Tesei Alessandra

LOW-FREQUENCY PASSIVE ACOUSTIC SURVEY OF SHIP TRAFFIC USING A GLIDER EQUIPPED WITH DIRECTIONAL SENSORS

Alessandra Tesei[a], Pietro Stinco[a], Richard Dreo[a], Michele Micheli[a], Bartolome Garau[a], Roberto Petroccia[a], Diego Pinzani[a], Alberto Grati[a], Alain Maguer[a]

[a] NATO STO Centre for Maritime Research and Experimentation (CMRE), La Spezia, Italy

Alessandra Tesei, NATO STO CMRE, Viale S. Bartolomeo 400, 19126 La Spezia, Italy.
alessandra.tesei@cmre.nato.int

Abstract: *The problem of underwater, long-term acoustic monitoring of a defined sea area has an important role in many civilian and defence applications. The concept of passive acoustic survey using a small volumetric array on board a mobile platform has been proven at CMRE since 2012 by using compact acoustic antennas installed on mobile unmanned vehicles, such as buoyancy gliders and wavegliders. Using gliders may provide covertness, quietness, persistence, wide area coverage, real-time, continuous monitoring aimed at detection and tracking of noise sources. The present activity extends the previous work by integrating in a Slocum glider, for the first time at CMRE, an acoustic vector sensor, namely the 3D GeoSpectrum M20-040. This sensor is able to provide directionality in the band from few Hz to 3 kHz, despite its limited size. The glider has been equipped also with an acoustic modem, able to communicate with a USBL deployed from a mother ship or a gateway. Through the USBL, a Control Station can get R/T measurements of the glider position and receive its detection alarms during the underwater missions, without need of surfacing.*
First at-sea tests of navigation, underwater communications and acoustic data collection were conducted during REP18Med trials (Palmaria Island, Italy, Oct. 2018) with one of CMRE gliders hosting an M20-040 and an acoustic modem. Estimating the smoothness of the glider navigation is fundamental to understand whether a glider is suitable to conduct passive survey with a sensor sensitive to acceleration. The USBL position measurements were compared to the estimate achieved by filtering the proprioceptive data collected on-board the glider, corrected with the available GPS fixes. Having accurate positioning of the platform is a fundamental condition to fuse data among more gliders.
The paper will provide a detailed analysis of the system and of the processing chain, along with at-sea results.

Keywords: *passive underwater acoustic monitoring, acoustic vector sensors, buoyancy glider, cognitive communication architecture, advanced autonomy*

1. INTRODUCTION

The problem of underwater, long-term acoustic monitoring of a defined sea area has an important role in many civilian and defence applications, ranging from good smuggling and illegal immigration to anti-submarine warfare, maritime security and protection of high value assets. Passive acoustic surveillance in a confined area of interest may be achieved by using a network of sensorized underwater stations moored on the seabed in front of a strategic coastal area or a choke point, or by using a network of mobile smart, long-endurance platforms. The latter solution is more complex, but allows portability, flexibility and re-configurability of such a monitoring acoustic system.

NATO STO CMRE has long experience in passive acoustic monitoring of vessels, in particular small fast boats, with mobile robots such as buoyancy gliders and wavegliders [1]. This work extends previous detection and localization capabilities to low-frequency noise sources, such as big, slow vessels. In the proposed solution, acoustic antenna of hydrophones with large element spacing is replaced by compact directional hydrophones (namely, acoustic vector sensors) hosted on a team of low-power, long-endurance platforms, such as gliders. The team of such robots behaves as slave of a central-node (possibly a waveglider), having a surf that could allow continuous air/sat communication with a remote Command&Control (C^2) Station (on a mother ship or on land). The utmost features of a glider are: covertness, quietness, navigation stability. However, it has limited power and room for hosting payloads, its manoeuvrability is limited, and its navigation system too basic to allow accurate positioning. Since 2010 CMRE has been gaining extensive experience in operating gliders: CMRE owns a glider fleet consisting of nine TWR Slocum gliders [2]. The Slocum glider is an underwater, unmanned vehicle driven along saw-tooth vertical paths (yo-yos) by varying its buoyancy and moving its centre of mass at the inflection.

For the first time at CMRE one Slocum glider was equipped with an Acoustic Vector Sensor (AVS) from Geospectrum, in particular a tri-dimensional M20-040 AVS [3] able to sense radiated noise from sources emitting in the frequency band from few Hz to 3 kHz and to provide their direction of arrival through simple signal processing algorithms. Unlike scalar pressure sensors, AVSs measure the amplitude and phase of acoustic particle motions in a given direction, i.e. these sensors are capable of acquiring both the acoustic pressure and the Cartesian components of the particle velocity using one omni-directional pressure sensor and three (or two) orthogonally co-located directional sensors, respectively [4]. Compared with conventional pressure sensors array, an AVS shows advantages in its small size and light weight even when it is tri-dimensional and works at very low frequency. Furthermore, its beampattern is approximately constant with frequency in the working band. Hence, an AVS is more attractive for installation on small UUVs than traditional sensor arrays, when it is needed to work at low frequencies and have 3D directivity. However, being sensitive to particle velocity and acceleration, they are sensitive also to possible mechanical vibrations and interference originating from the host platform. For this reason a buoyancy glider is a very good candidate as hosting mobile platform.

The glider hosts also a mid-frequency (MF) underwater acoustic modem (18-34 kHz) from Evologics [5] and is aided by the possibility to be back-seat driven and to cooperate within a network of robots. The latter capability was made possible by using MOOS-IvP middleware architecture software [6] on-board the glider. The Cognitive Communication Architecture (CCA) recently developed at CMRE [7] was also installed and interfaced with the MOOS-IvP middleware to facilitate the communication between the glider and a USBL modem deployed from a support ship (eventually a waveglider gateway). The USBL allows the real time positioning of the glider underwater, further than sending commands to the glider and

receiving the navigation glider data. In the future, when the acoustic data processing is implemented on board, it will also receive its detection results in real time.

This paper describes the system and the signal processing algorithms developed to analyse the acoustic vector sensor data in order to find the direction of arrival of targets of interest; it also provides preliminary results achieved from the post-analysis of recent tests at sea.

2. A SLOCUM GLIDER EQUIPPED WITH NEW SENSORS AND NEW CAPABILITIES

One of CMRE gliders has been modified in order to conduct low-frequency underwater acoustic survey of ship traffic. The new devices included in the glider (see Fig. 1) are:

- a tri-dimensional (3D) AVS on the nose of the glider;
- an MF underwater acoustic modem on top of the glider.

From software point of view, the main modifications applied to the glider include:

- integration of the electronic payload devoted to the data acquisition, storage and processing of the AVS acoustic data;
- an updated version of the glider firmware provided by TWR, which allows the scientific payload CPU to communicate to the glider control to get glider navigation and status data and send new commands;
- integration of MOOS-IvP middleware architecture [6] to convert the glider in an actual autonomous robot, able to make its own decision and to be a node of an autonomous network with other gliders and/or other kinds of vehicles (wavegliders, UUVs, etc.);
- integration of the Cognitive Communication Architecture developed at CMRE [7];
- no real-time acoustic data processing is embedded on-board yet. This is part of next activities. The acoustic data will be processed on-board along with the glider proprioceptive data (roll, pitch, yaw) in order to provide not only contact alarms, but also DOA estimates of the detected targets in the North-East-Down (NED) reference frame. These results will be sent to the C^2 Station via the acoustic modem, according to the protocols selected through the CCA. The modem has been recently integrated into the glider back-seat through MOOS-IvP middleware architecture software and is used with the CCA.

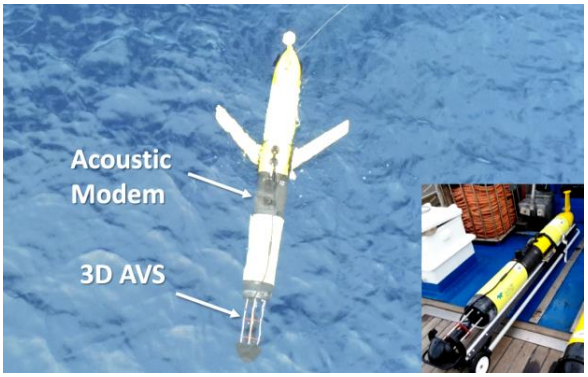


Fig.1: Photos of a CMRE Slocum glider equipped with a 3D AVS on its nose and an MF acoustic modem on top of a new central module.

2.1. The CMRE Cognitive Communication Architecture on board a buoyancy glider for the first time

The unique characteristics of underwater environments make the ability to communicate and build a network very challenging. The Cognitive Communications Architecture (CCA) developed by CMRE [7] aims at enhancing the reliability and robustness of current underwater networks. The main objective of this architecture is the creation of an underwater system that is able to learn and make "smart" decisions regarding the communication technologies and configurations to use, thus adapting and reacting, in a distributed and ad-hoc way, to dynamic changes in the network. The CCA is designed in a way that combines the traditional layered structure of the Open Systems Interconnection (OSI) paradigm with novel capabilities, such as the presence of multiple protocols at each layer of the stack and the extensive cross-layering across the whole stack. The availability of multiple protocols at each layer enables the implementation of smart and cognitive strategies that can autonomously reconfigure the protocol parameters and select the best current solution, adapting to the environmental picture.

An efficient and modular implementation of the CCA has been developed, specifically addressing: 1) usage during in-field operations; 2) deployment on various types of platforms with different computational and memory limitations; 3) interfacing with a wide range of hardware and software. Currently the CCA provides different Medium Access Control (MAC) and networking solutions, multiple communication technologies and services. Additionally, the CCA has been interfaced with different middleware architectures.

In its current implementation on the Slocum glider it is interfaced with MOOS-IvP middleware. At the present the network is limited to one glider and one gateway and the communication rate is very limited to maintain the glider as covert as possible. In particular:

- one two-ways message each 5 minutes is sent between the glider modem and the gateway USBL in order to know the current glider position
- when the signal processing chain is implemented on-board, we plan to make the glider send a detection and DOA message each 20 seconds during the full duration of a target detection.
- given the low probability of packet collisions due to the limited network traffic, the Aloha MAC has been selected to reduce the latency of messages and increase flexibility.

The CCA configuration is selected here in a simple configuration, with the perspective of a more complex network where the mother ship deploying the USBL will be replaced by a USV, which will play the double role of smart gateway and data fusion centre for a set of 2 or 3 gliders within its communication range.

3. THE SIGNAL PROCESSING CHAIN

Unlike scalar pressure sensors, AVSs measure the amplitude and phase of the medium's particle motion in a given direction. A three dimensional AVS consists of an omnidirectional acoustic pressure sensor that responds to the acoustic pressure, and three single-axis vector sensors that measure the three Cartesian components of the particle acceleration.

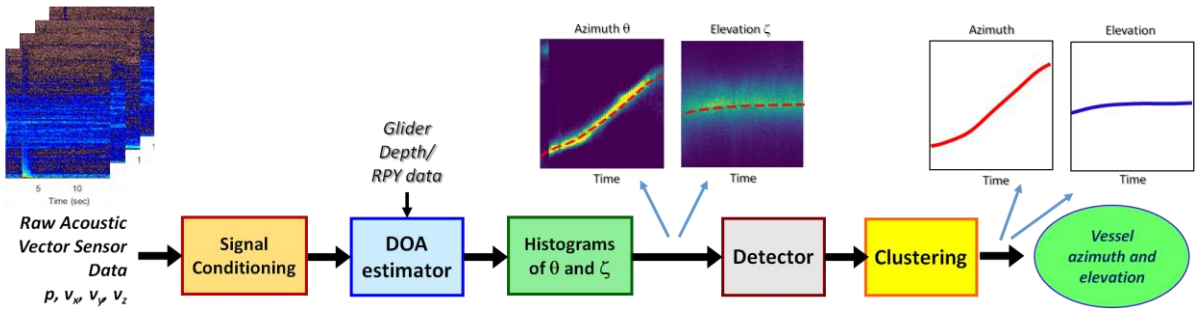


Fig.2: Signal processing chain for the passive acoustic detection of low-frequency noise sources and estimation of their direction of arrival in bearing and elevation.

The sensor was preliminarily tested in a test pool. The characterization of the sensor is presented in detail in [8].

The signal processing chain applied to AVS data is shown in the block diagram of Fig. 2.

The first step of the AVS receiver is signal conditioning, including phase compensation of the directional channels. The manufacturer provided a measured phase curve to make this compensation sufficiently accurate [3]. The Direction of Arrival (DOA) is directly measured using the intensity vector, defined as [9]:

$$\mathbf{I}(f, t) = 0.5\ \mathrm{Re}\{ S_p(f, t)\ \mathbf{S}_v^*(f, t)\}. \tag{1}$$

The intensity vector, also referred as the active intensity vector, is the real part of the complex intensity vector. It is possible to directly measure the DOA for each time-frequency, i.e., bearing $\theta(f, t)$ and elevation $\zeta(f, t)$, of the local net transport of sound energy with the inverse tangent functions of the active intensity, i.e.,

$$\begin{aligned} \theta(f, t) &= atan(\ I_x(f, t)\ /\ I_y(f, t)\ ) \\ \zeta(f, t) &= atan(\ (\ I_x^2(f, t) + I_y^2(f, t)\ )^{1/2}\ /\ I_z(f, t)\ ). \end{aligned} \tag{2}$$

Bearing and elevation are relative to the glider position and referred to its body frame. Elevation goes from 0° (up) to 180° (down), the glider is in the horizontal plane at elevation 90°. Bearing rotates clockwise from the nose of the glider.

Matrixes of bearing and elevations are obtained as time and frequency vary. At each time instant, the glider pitch, roll and heading are used to convert the bearing and elevation referred to the glider body frame into the azimuth and elevation in the NED reference system. To integrate the DOA angle along frequency, a histogram on the time/angle domain is computed over a band of interest. An example of the histogram images is shown in the block diagram of Fig. 2. The histograms are then normalized and a detection threshold is then applied to the images to keep only the stronger histogram values. A mathematical morphology filter is applied to the binary images in order to cluster the contacts and extract the final number of targets and related DOA estimates. If the histogram is computed over the whole 0-3kHz working bandwidth and all sources radiate broadband noise in the same bandwidth, only the strongest target can be detected. If the radiated noise from different sources has also a narrow-band component, then an analysis limited to specific sub-bands may make it possible to detect more than a target at a time if they have different DOAs. This will be subject of next research activities.

4. ACOUSTIC MEASUREMENTS AT SEA AND PRELIMINARY RESULTS

Local at-sea tests (Palmaria Island, Italy, March 18 and 25, 2019) were dedicated to acoustic data collection with Zoe TWR Slocum glider hosting an M020-40 AVS and an MF acoustic modem.

A USBL was deployed from the support boat when she was silent in drifting mode.

During part of the experiments, the support boat played the role of noise-radiating target by conducting runs around the glider path; it was equipped with a GPS antenna and the recorder GPS data are used as ground-truth. Figure 3 shows the navigation of the glider and of the support boat during one of these tests that lasted about 15 minutes, starting on March 25 at 13:00; the boat speed was about 5-6 kn. During this test the glider was yo-yoing at a distance from the support boat varying between 30 m and 540 m. The glider was sailing South and the support ship started to run from its rear; then it started to turn clock-wise around the glider twice, at different ranges. The glider navigation was extremely smooth during diving and climbing in terms of pitch and roll, more instable in terms of heading. The latter phenomenon will be further investigated.

The signal processing results are shown up to the angle histogram along time. This is a work in progress. In Figs. 4 and 5 (a) the azimuth and elevation are computed using Eq. (3) as the time and frequency vary in the full working band of the sensor. For long segments of time the angle remains very coherent along the full frequency band. Interesting fringes due to the Lloyd mirror effect are evident in the elevation image. The incoherent segments correspond to periods when the glider was inflecting or when the target boat was too far away compared to its source level (range >200 m). Figures 4 and 5 (b) show the histograms of azimuth and elevation as time varies. Whenever there is a good coherence in the wideband range, the angle curves are clearly visible on the histograms. The shape of the curves are in good agreement with the ground-truth, i.e., the elevation and azimuth computed from the glider and target navigation logs. We notice that the wideband coherence in azimuth is lost quite fast: 200 m in the analysed run. The azimuth measurement with the histogram method is then inefficient here, because of the presence of a big and noisy merchant ship in the vicinity of the glider. The signal of this ship is clearly visible on the spectrograms and we can see her azimuth basically varying from 140° (around minute 4) to 100° (at minute 15) on the histogram representation (Fig. 4(b) – green dashed line). The target azimuth is then lost for distance higher than 200 m because of a too low SNR.

5. CONCLUSIONS AND FUTURE ACTIVITIES

The paper has addressed the description of a glider that has been significantly modified to host and integrate an AVS and an acoustic modem. The aim is real-time monitoring of ship traffic, i.e., the detection and estimate of the direction of arrival of noise sources (vessels) in an area. Work in progress on the broadband analysis of the acoustic data has been presented. Next activities will include the completion of the signal processing chain, its implementation in real time on-board the glider and investigation of on narrow-band analysis in the lowest part of the frequency band (<300Hz) in order to discriminate several simultaneous sources.

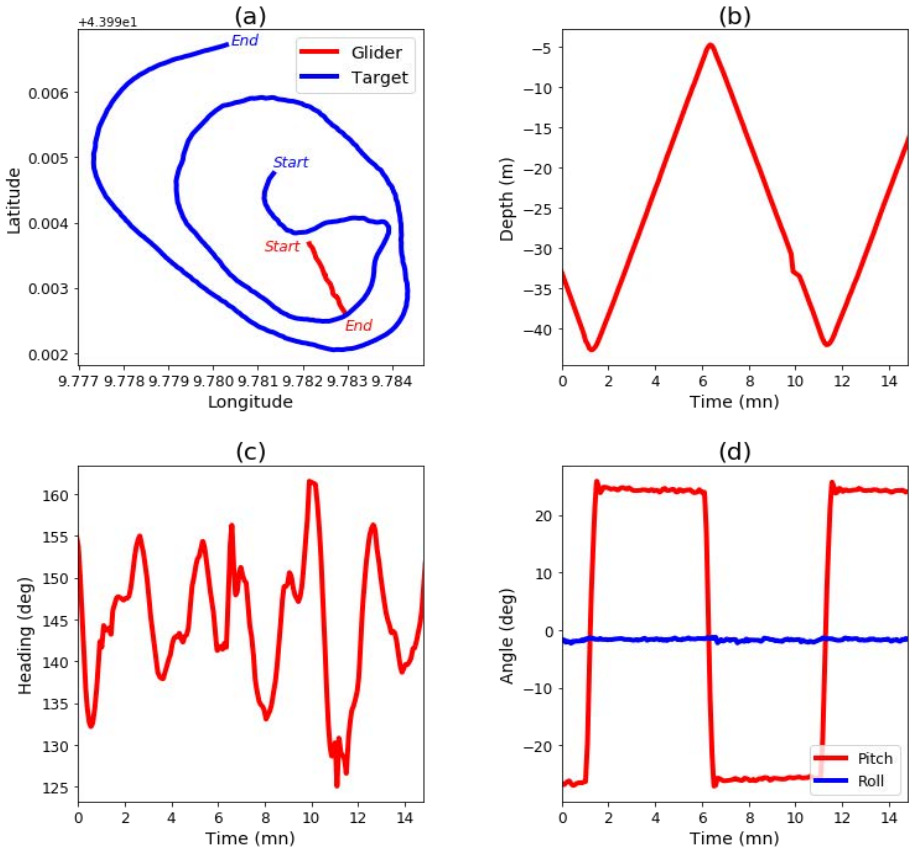


Fig.3: (a) Trajectories of TWR Slocum Glider Zoe (red) and of the support boat (blue) in one of the tests on March 25, 2019, off Palmaria Island, Italy; the run started at 13:00 (b) Depth (m) of the glider along the experiment. The orientation of the glider are in the two bottom plots: (c) heading, (d) pitch and roll.

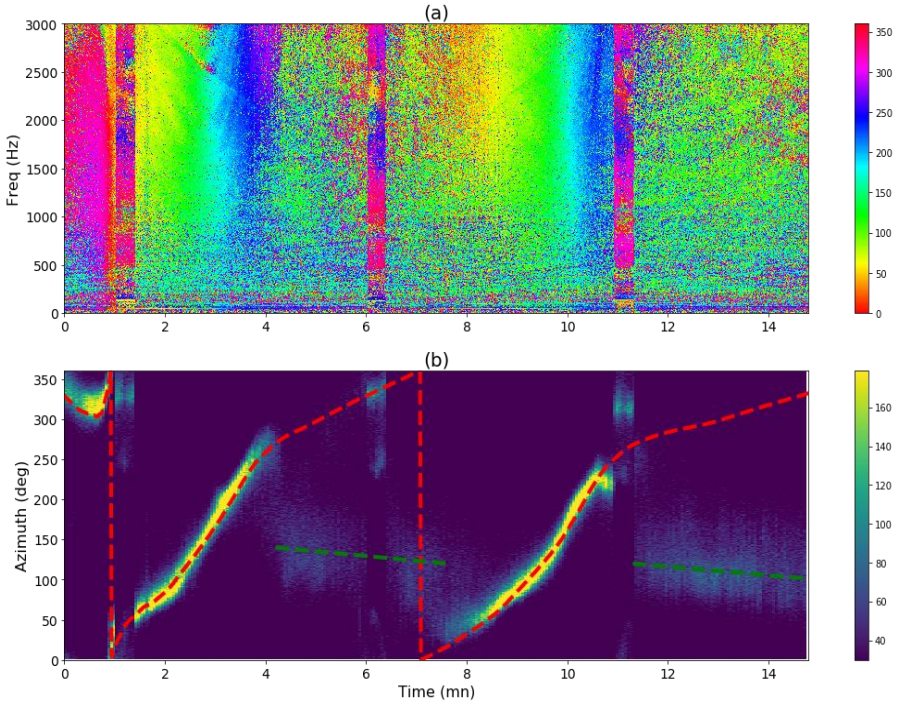


Fig.4: (a) Estimated azimuth as time and frequency vary during the run described in Fig. 3. The vertical stripes after minutes 1, 6 and 11 correspond to glider inflection periods, in which data are saturated and cannot be used. (b) Histogram of the azimuth computed over the frequency band 0 to 3 kHz. The ground-truth is superimposed as a red dashed line. Green dashed line represents the azimuth of a big merchant ship sailing in the area.

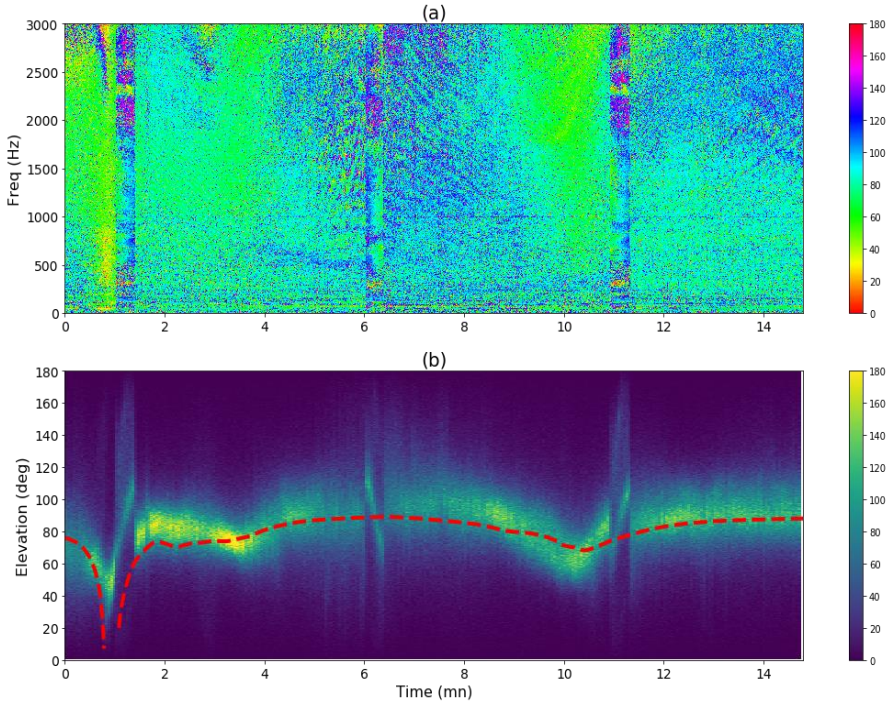


Fig.5: (a) Elevation as time and frequency vary (run in Fig. 3). (b) Histogram of the elevation computed over frequency. The ground-truth is superimposed as a red dashed line.

6. ACKNOWLEDGEMENTS

The authors wish to thank for their fruitful help all CMRE personnel involved in the preparation and conduction of at-sea tests. Grateful thanks go to Matt Dempsey and Bruce Armstrong from GeoSpectrum for their support in gaining experience on the M20-040 sensor, and to Massimo Scorcia from Muggiano Diving for his help during our latest test at sea. This work was funded by NATO Allied Command for Transformation.

REFERENCES

[1] **A. Tesei, R Been and F. Meyer**, Continuous real-time acoustic surveillance of fast surface vessels, In Procs. of UACE'17, Skiathos, Sept. 2017.
[2] http://www.teledynemarine.com/Slocum-glider
[3] **B. Armstrong**, *Directional Hydrophones*, Geospectrum Technical Document 2018-464.
[4] **A. Nehoray, E. Paldi,** Acoustic Vector-Sensor Array Processing, *IEEE Tr. on Signal Processing*, Vol. 42 (9), 1994.
[5] https://evologics.de/acoustic-modem/18-34
[6] **M.R. Benjamin, H. Schmidt, P.M. Newman and J.J. Leonard**, Autonomy for Unmanned Marine Vehicles with MOOS-IvP, in *Marine Robot Autonomy* (M.L. Seto Edt.), Springer, 2013.
[7] **R. Petroccia, G. Zappa, T. Furfaro, J. Alves, and L. DAmaro**, Development of a Software-Defined and Cognitive Communications Architecture at CMRE, In Procs. Of *MTS/IEEE OCEANS'18*, Charleston, USA, 2018.
[8] **A. Tesei, P. Stinco, M. Micheli, B. Garau, S. Biagini, L. Troiano, P. Guerrini**, A buoyancy glider equipped with a tri-dimensional acoustic vector sensor for real-time underwater passive acoustic monitoring at low frequency, In Procs. Of MTS/IEEE OCEANS19 – Marseille, June 2019.
[9] **F.J. Fahy**, *Sound Intensity* (2nd edition), E & FN Spon, London 1995.

PASSIVE ACOUSTIC MONITORING USING A TOWED ARRAY FROM A WAVE-PROPELLED USV

Alfie Anthony Treloar[a], Alan Hunter[a], Jan Bujalka[bc], Phil Johnston[bc]

[a]University of Bath, Bath, BA2 7AY, United Kingdom
[b]Seiche Ltd., Bradworthy, Devon, EX22 7SF, United Kingdom
[c]AutoNaut Ltd., Chichester, West Sussex PO20 7EJ, United Kingdom

Contact Author: Alfie Anthony Treloar, A.O.Anthony.Treloar@bath.ac.uk

Abstract: *The use of towed hydrophone arrays deployed from wave-propelled autonomous surface vehicles presents a unique opportunity for long-duration, wide-area passive acoustic underwater surveillance. Example applications include marine mammal monitoring for environmental surveys and mitigation zone enforcement, as well as port and harbour security. However, the intermittent nature of propulsion inherent to these platforms exacerbates the problem of uncertainty in the array profile, which can cause inaccurate bearing estimates, misdetections, and false alarms in beamforming estimates. Data from simulation and from the Unmanned Warrior '16 trial has been used to understand and quantify the array motion, and investigate potential techniques for improvement. Our method generates a probabilistic distribution of potential array shapes by means of a particle filter and then refines these by maximising the beamformer response. Following validation with simulated data, the method was applied to the experimental data and suggested that the array was curved and inclined by approximately -35° in this case.*

Keywords: *passive acoustic monitoring, towed array, wave-propelled, unmanned surface vehicle*

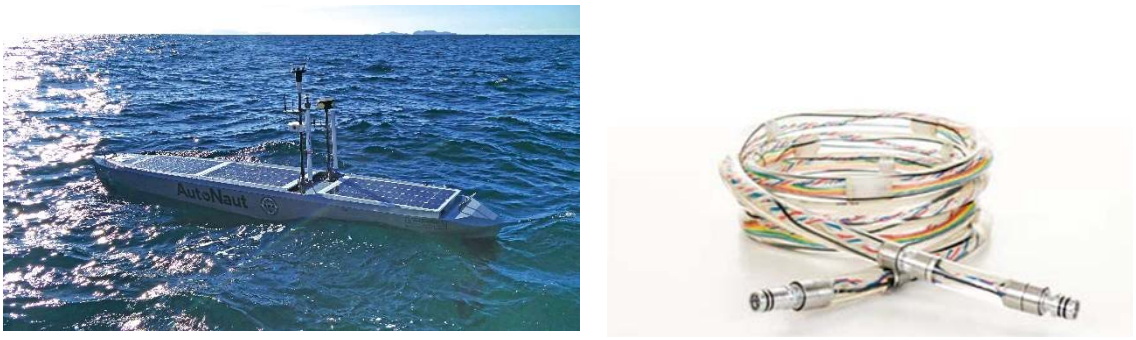
1. INTRODUCTION

The AutoNaut is a wave-propelled unmanned surface vehicle (USV) which presents a unique opportunity for passive acoustic monitoring (PAM). It enable a reduction in the cost of wide-area persistent monitoring compared to traditional vessels due to the reduced human oversight required. Furthermore, it is capable of more versatile modes of operation than buoy or seabed-deployed hydrophones. This would make the vessel uniquely suited for tasks such as port and harbour security, environmental surveys, and marine mammal monitoring around mitigation zones of noisy anthropogenic activities. However, the platform presents certain challenges.

Acoustic localisation techniques, such as beamforming, require accurate knowledge of the position of each sensor of an array. The relatively low tow speed of the vessel and the intermittent motion inherent to wave-propulsion can significantly perturb the array shape away from the ideal of a horizontally towed straight array. Unless compensated for, this could introduce bearing errors, and spurious or ambiguous detection peaks in beamforming estimates. On the other hand, there are benefits to operating a non-linear array. When used to estimate the direction of arrival of a sound source, a straight array has a left-right ambiguity that a more complex shape would not have.

In this work we use the AutoNaut towing the Seiche digital thin line array (DTLA), pictured in Fig. 1. The AutoNaut converts the hull motion caused by waves into propulsive thrust using a unique system of keel-mounted foils. Using solar panels for power and operating autonomously or remotely by satellite, this vessel can operate for up to months at a time [1]. The Seiche DTLA is a customisable array consisting of up to 32 hydrophones and able to be instrumented with compasses, heading and depth sensors at selected points along the array.

The purpose of this paper is to investigate and overcome the challenges operating a towed array from the AutoNaut USV. Using a combination of simulation and experimental trial data, the array motion is quantified and different array configurations are assessed for their suitability, with a view to optimally configuring the array for the operational and power requirements.



(a) *(b)*

Fig. 1: (a) AutoNaut USV and (b) Seiche digital thin line array

2. METHODOLOGY

The trial data used to investigate this problem is the Unmanned Warrior ’16 trial (UW16), in which an AutoNaut towed an 8-hydrophone array, instrumented with a compass and heading sensor at the tail end, in the presence of an autonomous underwater vehicle (AUV) in a known location emitting tonal signals at various frequencies (approximately 400Hz, 800Hz, 1500Hz and 1600Hz).

To simplify the problem, the array has been modelled as a series of ball-jointed sections, described by their inter-element azimuth and elevation, and constrained by a fixed inter-element distance. A two-stage method has been followed to estimate the array shape.

A particle filter [2] is used to propose likely candidate array shapes, by combining the probability density functions (PDFs) from acoustic inter-element time delay estimates and from the heading sensors along the array. Following this, the MVDR [3] beamformer response at a given frequency (1500Hz) is estimated for these shapes and the candidate with the maximum intensity is selected. To independently assess the performance of the shape estimate, the beamformer response has also been used as a metric, utilising the estimate from a different frequency (1000Hz) simulated at a different bearing.

3. RESULTS

Three possible array configurations were devised, as illustrated in Fig. 2: (a) configuration 1 – the array is instrumented with a heading sensor at the tail end (co-located with hydrophone pair 7-8) and there is no sound source used in the particle filter estimation; (b) configuration 2 – the array is instrumented the same as configuration 1 but a sound source in a known direction is included in the particle filter estimate; and (c) configuration 3 – where the array is instrumented at both ends (co-located with hydrophones 1-2 and 7-8) and a sound source is utilised, as in configuration 2. The first two of these configurations are intended to represent the UW16 configuration, while the third would be a candidate for a potential improvement to assess for future testing. The data that has been simulated is representative of the conditions of the UW16 test with regards to the heading and pitching of the array, and the bearing of the sound source.

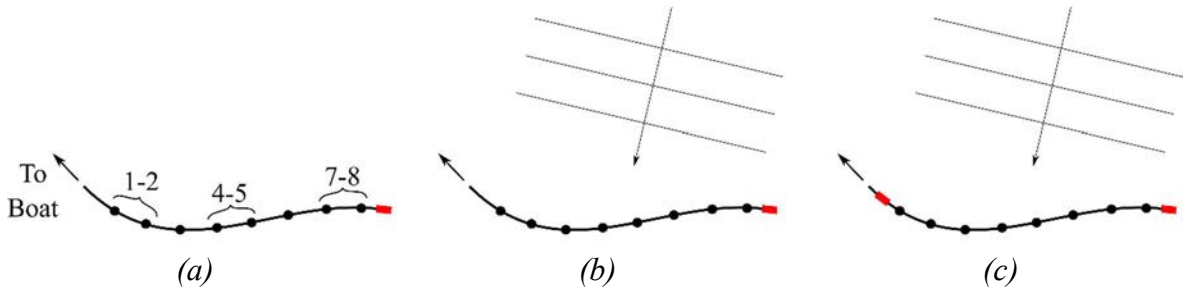


Fig. 2: Simulated array configurations, with black circles denoting hydrophones and red rectangles denoting heading sensors

The particle filter estimates are shown in Fig. 3. As can be seen from Fig. 3(a), with only a heading sensor at one end the spread of possible candidates is quite diffuse, and the mean position does not necessarily coincide with the true position. This shows the necessity of the use of the second stage of beamfomer maximisation, which can result in a more accurate estimate if there is a sound source present. As shown in Fig. 3(b), having a sound source in a known location narrows the distribution, in this case, in the horizontal plane. As would be expected, a second heading sensor tightened the distribution further, decreasing the search space further and improving the chance of the correct array shape being selected, as shown in Fig. 3(c).

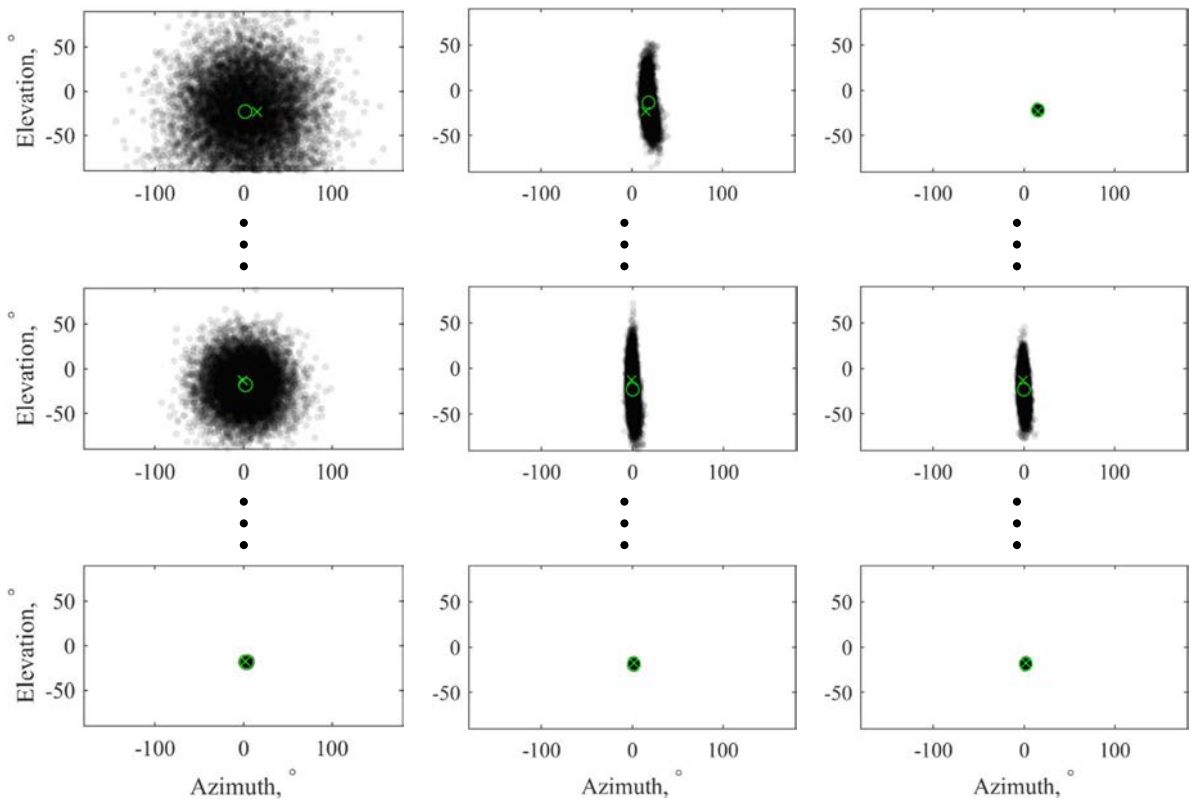


Fig. 3: Particle filter estimates for adjacent hydrophone pairs, with hydrophones 1-2 on the top row, 4-5 in the middle row and 7-8 on the bottom row. (a), (b) and (c) are the outputs for configurations 1, 2 and 3 respectively. The green cross is the true position and the green circle is the mean value of the particle filter output.

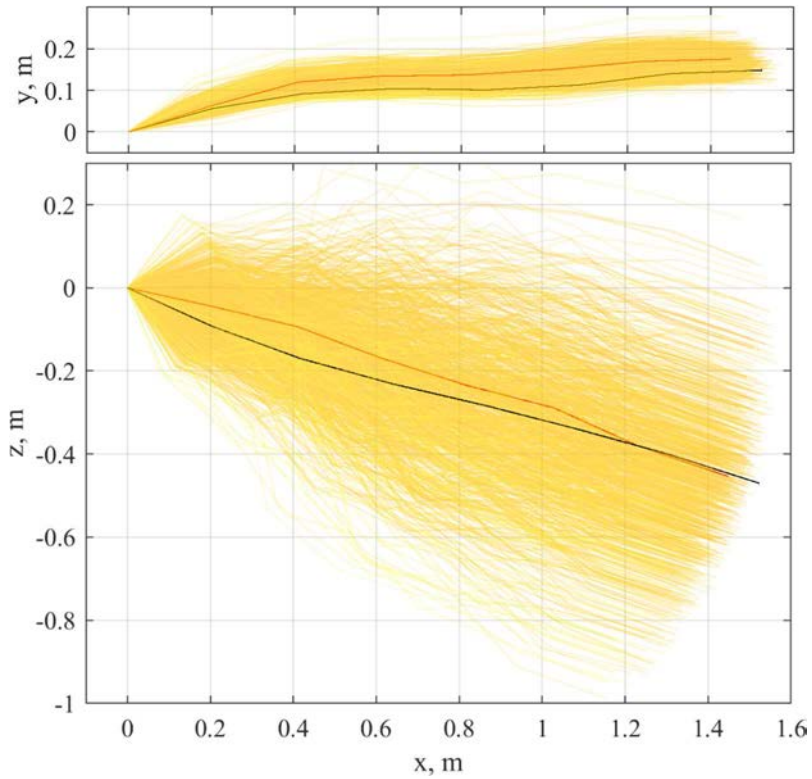


Fig. 4: Array shape estimates from data simulated with configuration 2 for a single instant of time. Candidates in yellow, true shape in black and the selected shape in red.

To resample into Cartesian space, randomised combinations are selected from each hydrophone pair's distribution to create a representative distribution of array shape candidates, shown in Fig. 4. As can be seen, the spread in the x-y plane is narrower than the spread in the x-z plane. Also shown on these figures is the disparity between the true shape and the beamformer optimal estimate.

The beamforming estimates, shown in Fig. 5, show the effect of utilising the method with each of the configurations. Also shown is the beamformer output for the uncompensated shape, which assumes a straight array oriented according to the simulated heading sensor on the end, and the optimal, which is utilising the true array shape. Configuration 1 shows very little improvement on the uncompensated shape, but the estimates approach optimal with configuration 3. Also, because of the limits on the x axis, this figure does not show the effect of the straight array assumption, with the ambiguity in detection peaks present only in the uncompensated beamformer estimate.

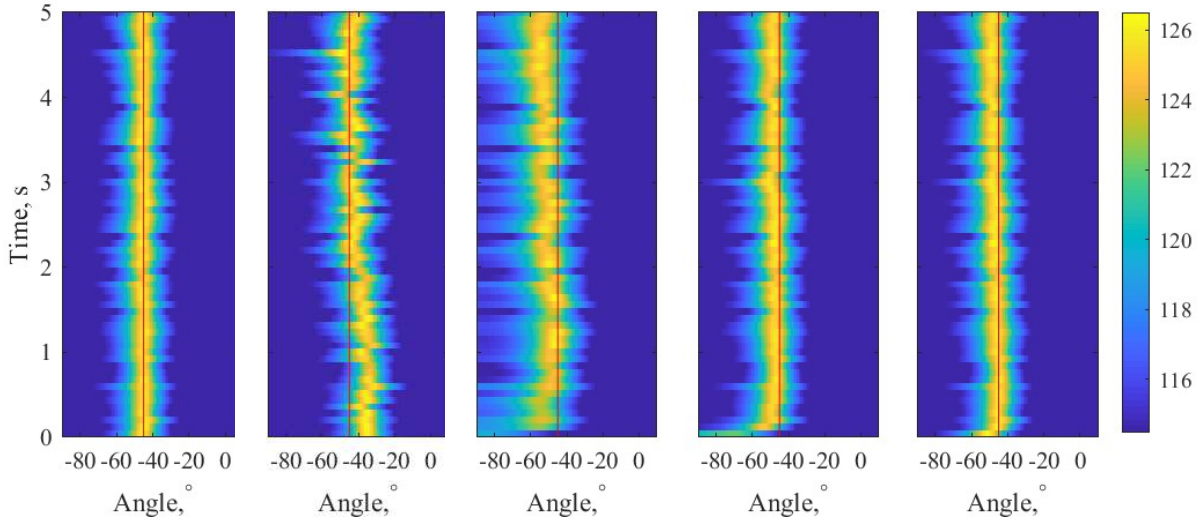


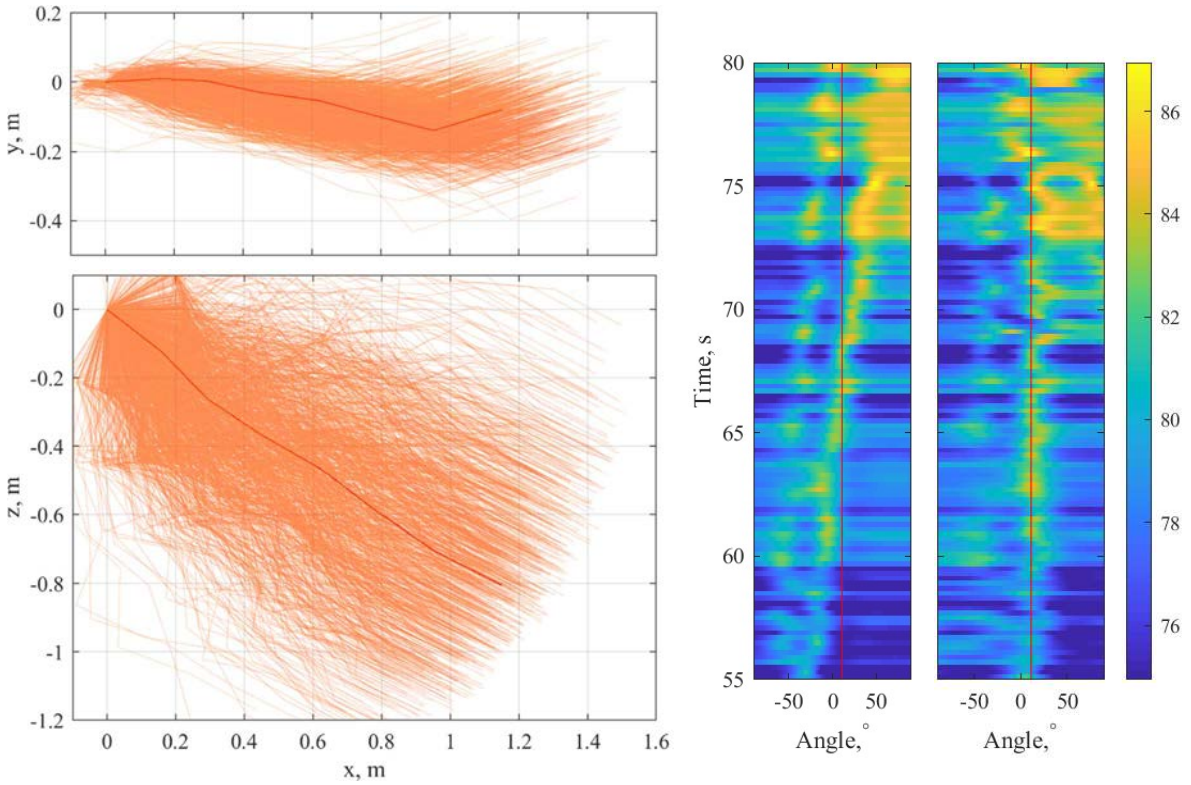
Fig. 5: Beamformer outputs for validation frequency. Target has been simulated at a bearing of -45° as indicated by the red line. (a) is using the true array shape, (b) is the uncompensated estimate, (c), (d) and (e) are the results of configurations 1, 2 and 3, respectively

Fig. 6 shows the results of applying the methods to experimental data. For periods of high SNR the method produces results consistent with that of the simulation, and suggests the perturbation of the array is a varying curve at a downward incline of approximately 35°, an instant of which is shown in Fig. 6(a). Shown in Fig. 6(b) and Fig. 6(c) is the improvement to the beamforming as a result of utilising the array shape estimate. The target is expected at a bearing of 11° and can be seen to be more consistently tracked when the compensated shape is used.

4. CONCLUSIONS & FUTURE WORK

This work has presented the results of investigating the array motion from a towed array deployed from an AutoNaut USV. Our method uses a particle filter followed by beamformer output maximisation, which was validated in simulation. This generated a distribution of potential array shapes which, in the scenario of the experimental data, allowed more precise resolution in the x-y plane. The effect of an improvement to the array configuration was

demonstrated, showing that extra instrumentation at another point in the array could improve accuracy of the estimate. Application of the method to experimental data suggested that the array had a curved horizontal shape which was inclined downwards by approximately 35°, consistent with what would be expected.



(a) *(b)* *(c)*

Fig. 6: Results of application of the array shape estimation method to the experimental data. (a) shows a single estimate of the array shape at high SNR at t = 62.7s. (b) and (c) respectively show the uncompensated and the compensated beamformer estimates.

Further work is to be carried out in order to quantify the array motion more accurately, including further experimental investigation with more sound sources and/or a more instrumented array. This will be preceded by an analysis into the influence of sound source bearing and array inclination, in order to establish performance limits for PAM from this vehicle. The method itself is also intended to be improved upon by implementing the particle filter in Cartesian space to enable the application of more realistic physical priors.

REFERENCES

[1] **Johnston, P. & Pierpoint, C.,** "Deployment of a passive acoustic monitoring (PAM) array from the AutoNaut wave-propelled unmanned surface vessel (USV)", In *OCEANS 2017 - Aberdeen*, Aberdeen, IEEE, pp.1-4, 2017.

[2] **Doucet, Arnaud & Johansen, Adam., "**A Tutorial on Particle Filtering and Smoothing: Fifteen Years Later", *The Oxford Handbook of Nonlinear Filtering,* Dan Crisan and Boris Rozovskii, Oxford Handbooks, pp.656-704, 2011.

[3] **Pillai, S. U. & Burrus, C. S.**, *Array Signal Processing*. Springer New York, 1989

MODEL-BASED 3D MICRO-NAVIGATION AND BATHYMETRY ESTIMATION FOR INTERFEROMETRIC SYNTHETIC APERTURE SONAR

Benjamin Thomas[a], Alan Hunter[a], Samantha Dugelay[b]

[a]University of Bath, Claverton Down, Bath, BA2 7AY, UK
[b]NATO STO CMRE, Viale S. Bartolomeo, 400, 19126 La Spezia SP, IT

Contact author: Benjamin Thomas, b.w.thomas@bath.ac.uk

Abstract: *Sub-wavelength navigation information is vital for the formation of all synthetic aperture sonar (SAS) data products. This challenging requirement can be achieved using the redundant phase centre (RPC) or displaced phase centre antenna (DPCA) micro-navigation algorithm, which uses cross-correlation of signals with inter-ping coherence to estimate time delays and hence make navigation estimates. In this paper a new approach to micro-navigation for interferometric synthetic aperture sonar is introduced. The algorithm makes 3D vehicle position estimates for each sonar ping by making use of time delays measured between all possible pairs of redundant phase centre arrays, using both interferometric arrays on each side of the vehicle. Simultaneous estimation of coarse bathymetry allows the SAS images to be projected onto ground-range. The method is based on non-linear minimization of the difference in modelled and measured time delays and surges between redundant phase centre arrays. The approach is demonstrated using data collected by the CMRE MUSCLE AUV using its 270-330 kHz SAS during the MANEX'14 experiment. SAS images have been projected onto the coarsely estimated bathymetry, and interferograms have been formed. The coarse bathymetry estimate and vehicle navigation estimate are validated by the quality of the image focussing and the near-zero phase of the interferogram. The method has the potential to improve through-the-sensor navigation aiding and to increase the accuracy of single-pass bathymetry estimation. Future development of the algorithm for repeat-pass operation has the potential to enable repeat-pass track registration in three dimensions. The method is therefore an important step towards improved coherent change detection and high resolution bathymetry estimation.*

Keywords: *Synthetic Aperture Sonar, Micro-navigation, Interferometry*

1. INTRODUCTION

Synthetic aperture sonar (SAS) is an advanced acoustic imaging technology capable of imaging sea-floor swathes of hundreds of meters with centimetre-scale resolution. The coherent processing requires the trajectory of the sonar to be known to within a fraction of a wavelength. This requirement can be achieved using the redundant phase centre (RPC) or displaced phase centre antenna (DPCA) micro-navigation algorithm [1]. RPCs are overlapping portions of the virtual monostatic array used to approximate the true bi-static geometry of multi-receiver SAS.

The RPC micro-navigation algorithm utilizes time delays measured between signals received by RPC arrays to make navigation estimates. However, in reality these time delays are also a function of bathymetry and medium fluctuations. Isolation of this 'triad of confounding factors' [2] enables accurate estimation of vehicle navigation and sea-floor bathymetry.

Many SAS-equipped autonomous underwater vehicles (AUVs) have a pair of vertically separated receiver arrays on each side of the vehicle. Typically, the RPC micro-navigation algorithm is applied to only one array per side, with independent measurements sway and surge made at multiple range windows. The navigation estimates are used to generate images for each pair of arrays, and the interferogram formed between the image pairs is used to generate bathymetry estimates. However, this two-stage process may incompletely isolate the phase contributions from navigation and bathymetry, which may corrupt their estimates. Developments to RPC micro-navigation have included heave estimation using dual-sided SAS [3], [4]. However, these make a flat bathymetry assumption and hence the navigation estimates may contain bathymetry-induced errors.

This paper describes a one-stage simultaneous micro-navigation and coarse bathymetry estimation technique for single-pass interferometric SAS. The method involves least-squares minimization of the difference between measured and modelled time delays and surges between RPC arrays. The method leverages the mutual information contained in the time delay estimates made at all range windows between all possible inter-ping and intra-ping (interferometric) RPC pairs. A similar technique was demonstrated in earlier preliminary work [2], where time delays measured between inter-pass RPC arrays on a single side of the vehicle were used to estimate inter-pass array displacements in sway and heave between individual pairs of pings of different passes. However, in that work the vehicle paths were not estimated due to the absence of coupling between adjacent pings. In the current work, coupling between pings is achieved by introducing measured and modelled surge between RPC arrays into the method, which allows estimation of the vehicle path.

The technique is demonstrated using data collected by the CMRE MUSCLE AUV using its 270-330 kHz SAS during the MANEX'14 experiment. The new method has been used to make estimates of vehicle navigation and coarse bathymetry. SAS images are formed onto the coarse bathymetry estimate, which is validated by forming interferograms between the image pairs.

2. MICRO-NAVIGATION METHOD

The new micro-navigation method is based upon a non-linear least-squares minimization of measured and modelled surges and time delays between RPC arrays. The use of all of the available surges and time delays between RPC array pairs allows the vehicle translations in surge, sway and heave to be measured from the sonar data, while at the same time making a coarse bathymetry estimate. The angular rotations of the vehicle in roll, pitch and yaw are measured by the inertial navigation system (INS). Fig. 1a shows the possible pairs of RPC arrays between which surge and time delays can be measured on each side of the vehicle, for an interferometric SAS. This shows that measurements of four inter-array surges and six inter-array time delays can be made per side, ping and range window. The fusion of all of these measurements enables simultaneous 3D micro-navigation and bathymetry estimation.

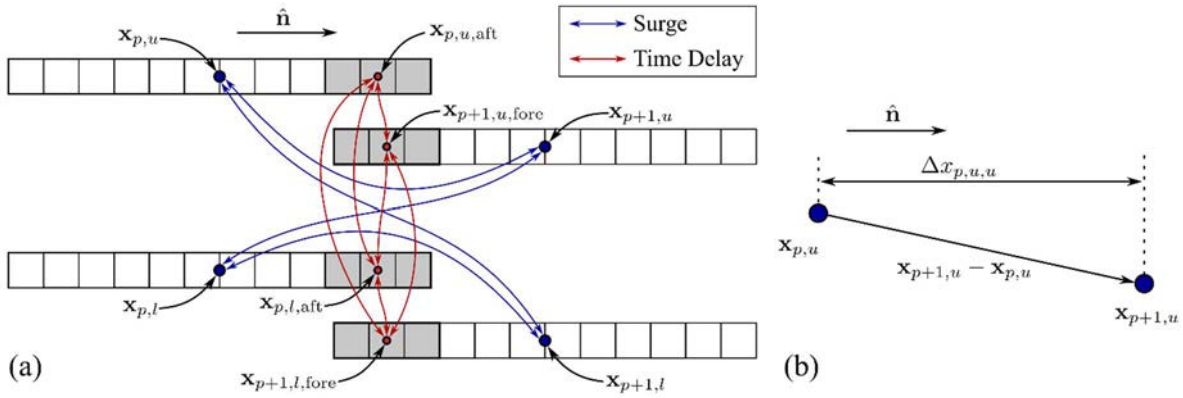


Fig. 1 – (a) Overlapping phase centre arrays between subsequent pings. Arrows join the pairs of phase centre arrays between which surges and time delays are measured. (b) Modelled surge between the upper phase centre arrays of two pings.

2.1. Surge Measurement and Modelling

The received signals are short-time windowed, producing signals corresponding to small range windows. Surge measurement is performed using the method described in [3] at every range window. Cross-correlation of the windowed signals is performed for a number of candidate surge values, corresponding to integer multiples of the distance between phase centres. Interpolation using a quadratic kernel is then used to refine each estimate. Finally, a weighted mean of the surge estimates at all range windows gives the inter-array surge.

The modelled inter-array surge is the length of the projection of the vector between two array centres in the direction of the platform orientation. For example, the modelled surge between the upper array of ping p and the upper array of ping $p+1$ is given by

$$\Delta x_{p,u,u} = \left\| (\boldsymbol{x}_{p,u} - \boldsymbol{x}_{p+1,u}) \cdot \hat{\boldsymbol{n}}_p \right\|, \tag{1}$$

as shown in Fig. 1b, where $\boldsymbol{x}_{p,u}$ and $\boldsymbol{x}_{p+1,u}$ denote the modelled position of the centre of the upper phase centre array on pings p and $p+1$ respectively, and

$$\hat{\boldsymbol{n}}_p = \begin{pmatrix} \cos(\psi_p) & -\sin(\psi_p) & 0 \\ \sin(\psi_p) & \cos(\psi_p) & 0 \\ 0 & 0 & 1 \end{pmatrix} \begin{pmatrix} \cos(\phi_p) & 0 & \sin(\phi_p) \\ 0 & 1 & 0 \\ -\sin(\phi_p) & 0 & \cos(\phi_p) \end{pmatrix} \begin{pmatrix} 1 \\ 0 \\ 0 \end{pmatrix}, \tag{2}$$

is the modelled platform orientation on ping p, where ψ_p and ϕ_p are the yaw and pitch of the vehicle on ping p.

2.2. Time Delay Measurement and Modelling

Measurement of the time delay between signals received by RPC arrays is achieved by finding the maximum of their cross-correlation function. The time delay measurements are split into an integer number of phase cycles, plus a fraction of a phase cycle. Care must be taken to ensure that any errors in the phase cycle number estimate are detected and corrected [5].

The complexity of the time delay model must be chosen depending on the application. Here we consider a model which does not employ the phase centre assumption i.e. propagation paths are modelled from the transmitter to the sea-floor and back to the receiving transducers. However, the stop-and-hop assumption is used, which assumes that the vehicle is stationary while the signal is transmitted and received, and then moves instantly to the position of the next ping. This has been shown to be a reasonable assumption for the MUSCLE AUV [6].

Consider the fore-most upper array elements of ping p and the aft-most upper array elements of ping $p+1$ that collect coherent signals due to the overlap of their corresponding phase centres. The locations of the centres of these sub-arrays are denoted by $\boldsymbol{x}_{p,u,\text{fore}}$ and $\boldsymbol{x}_{p+1,u,\text{aft}}$ respectively. The positions of the transmitter on pings p and $p+1$ are denoted by $\boldsymbol{x}_{\text{tx},p}$ and $\boldsymbol{x}_{\text{tx},p+1}$ respectively. Consider a modelled location on the sea-floor $\boldsymbol{x}_{f,p}$, which is constrained to lie on the plane passing through $\boldsymbol{x}_{p,\text{mid}}$ with normal vector $\hat{\boldsymbol{n}}_p$, where

$$\boldsymbol{x}_{p,\text{mid}} = \left(\boldsymbol{x}_{p,u,\text{fore}} + \boldsymbol{x}_{p+1,u,\text{aft}} + \boldsymbol{x}_{\text{tx},p} + \boldsymbol{x}_{\text{tx},p+1}\right)/4 \tag{4}$$

is the mid-point of the RPC arrays formed by pings p and $p+1$.

Two-way travel times from the transmitter, to the sea-floor location, and back to the redundant elements of the receiving arrays for pings p and $p+1$ are given by (5) and (6), where c is the medium propagation speed.

$$t_{p,u,\text{fore}} = \left(\left\|\boldsymbol{x}_{\text{tx},p} - \boldsymbol{x}_{f,p}\right\| + \left\|\boldsymbol{x}_{p,u,\text{fore}} - \boldsymbol{x}_{f,p}\right\|\right)/c \tag{5}$$

$$t_{p+1,u,\text{aft}} = \left(\left\|\boldsymbol{x}_{\text{tx},p+1} - \boldsymbol{x}_{f,p}\right\| + \left\|\boldsymbol{x}_{p+1,u,\text{aft}} - \boldsymbol{x}_{f,p}\right\|\right)/c \tag{6}$$

The difference in modelled two-way travel times for this pair of RPC arrays is then given by

$$\Delta t_{p,u,\text{fore},p+1,u,\text{aft}} = t_{p+1,u,\text{aft}} - t_{p,u,\text{fore}} \,. \tag{7}$$

2.3. Least-squares minimization

The coarse bathymetry and navigation estimates are generated by minimizing the differences between modelled and measured time delays and surges. On each iteration, the models for inter-array surges and time delays are linearized about the current navigation and bathymetry estimate. The linearized model is then solved to estimate updated vehicle and sea-floor positions. This process is iterated until convergence is achieved, and results in 3D estimates of the vehicle position for each ping and a coarsely sampled point-cloud of bathymetry estimates.

3. RESULTS

The new simultaneous micro-navigation and bathymetry estimation method has been applied to data collected by the CMRE MUSCLE AUV using its 270-330 kHz SAS during the MANEX'14 experiment. The vehicle was programmed to follow a straight line at a constant distance above the sea-floor with a speed of 1.4 m/s. SAS images have been generated using the navigation estimated by the new method, onto the coarse bathymetry estimate. The resulting navigation estimates from the new method are compared with those measured by the on-board navigation hardware in Fig. 2.

The smoothly-varying micro-navigation estimate in Fig. 2a follows a similar shape to that measured by the navigation hardware. The difference between the navigation hardware and micro-navigation estimates appears to arise from an integrated constant sway rate offset. However, it is not possible to attribute the error to either the navigation hardware or the micro-navigation estimate. Fig. 2c shows the sway rates, which shows that the navigation hardware estimates are severely quantised, whereas the micro-navigation estimates vary smoothly. The vehicle depth estimated by the micro-navigation method in Fig. 2b also varies smoothly, but seems to decrease slightly more rapidly than the measurement made by the depth sensor. This could be due to incorrectly modelled sonar mounting position on the platform, an incorrect sound speed assumption, or inaccurate sonar calibration. The depth rates shown in Fig. 2d show severe quantisation of the depth sensor, while the micro-navigation estimate varies smoothly.

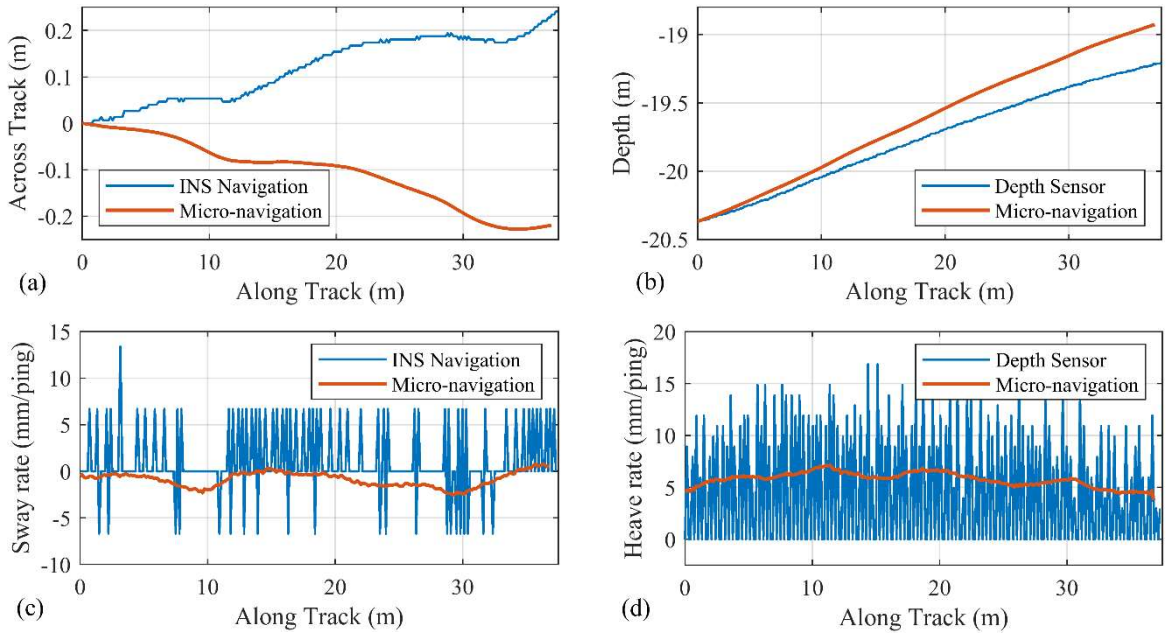


Fig. 2 – (a) Vehicle path (b) Vehicle depth (c) Sway rate (d) Heave rate, estimated by the navigation hardware and the new micro-navigation method.

The port-side SAS image projected onto the coarse bathymetry estimate is shown in Fig. 3. The scene is predominantly gently sloping and includes a pipe and concrete blocks. Colour encodes the deviation of the coarse bathymetry estimate from the best-fitting plane through the coarse bathymetry. This reveals some scouring around the proud objects.

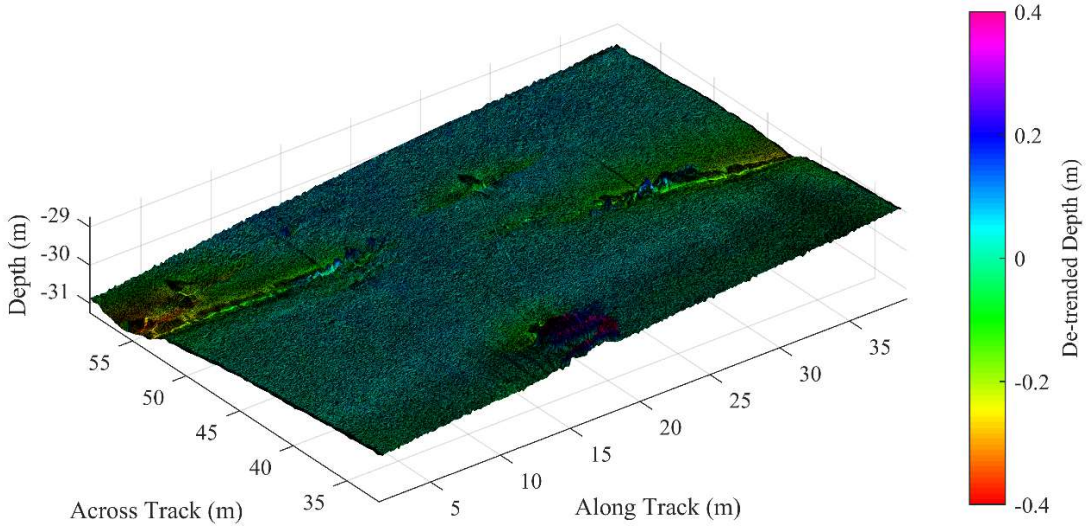


Fig. 3 – SAS image on coarse bathymetry. Colour encodes deviation from sloping plane.

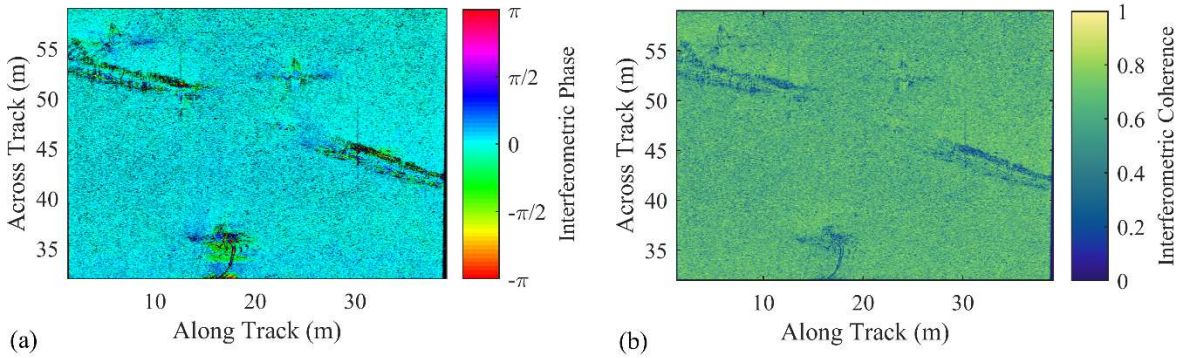


Fig. 4 – Interferogram (a) phase (b) magnitude

The interferogram formed between images generated from the upper and lower arrays is shown in Fig. 4. Zero interferogram phase indicates that the estimated bathymetry is accurate. The result shows near-zero phase over most of the scene, deviating only in high complexity regions. The phase of the interferogram could be used to improve the coarse bathymetry estimate. The interferogram magnitude is high, suggesting that the images are well registered.

4. CONCLUSION AND FURTHER WORK

Simultaneous 3D micro-navigation and bathymetry estimation for single-pass InSAS has been demonstrated using data collected by the CMRE MUSCLE AUV using its 270-330 kHz SAS during the MANEX'14 experiment. It is not possible to compare the navigation estimate against ground-truth. However, the focussed images, the near-zero interferometric phase and the high interferometric coherence validate the navigation and coarse bathymetry estimates.

The isolation of navigation and bathymetry information achieved by the new method has the potential to improve vehicle navigation estimation and the quality of single-pass interferometric bathymetry estimates. Further work will involve estimation of fine bathymetry using the single-pass interferogram. Additionally, estimation of medium propagation speed and fusion of measurements from the navigation hardware will be included in the method, potentially improving through-the-sensor navigation aiding [7]. The method will also be developed for repeat-pass SAS operations, which has the potential to improve coherent change detection and enable much higher resolution bathymetry estimation.

5. ACKNOWLEDGEMENTS

The authors would like to thank the Centre for Maritime Research and Experimentation for the MANEX'14 data and the Autonomous Mine Countermeasures team scientists, engineers and the crew of NRV Alliance for their support in collecting the data. The trial and CMRE's work are funded by the NATO Allied Command Transformation.

REFERENCES

[1] D. Billon and F. Fohanno, "Theoretical performance and experimental results for synthetic aperture sonar self-calibration," *IEEE Ocean. Eng. Soc. Ocean. Conf. Proc. (Cat. No.98CH36259)*, vol. 2, pp. 965–970, 1998.

[2] B. Thomas, A. J. Hunter, and S. Dugelay, "Repeat-pass micro-navigation and bathymetry estimation using interferometric synthetic aperture sonar," in *IOA Synthetic Aperture Sonar and Synthetic Aperture Radar*, 2018.

[3] D. A. Cook, "Synthetic Aperture Sonar Motion Estimation and Compensation," Georgia Institute of Technology, 2007.

[4] H. Schmaljohann *et al.*, "Dual-sided micronavigation for synthetic aperture sonar," in *1st International Conference and Exhibition on Underwater Acoustics*, 2013, pp. 119–126.

[5] S. Leier, "Signal processing techniques for seafloor ground-range imaging using synthetic aperture sonar systems," Technische Universität Darmstadt, 2014.

[6] Y. Pailhas, S. Dugelay, and C. Capus, "Impact of temporal Doppler on synthetic aperture sonar imagery," *J. Acoust. Soc. Am.*, vol. 143, no. 1, pp. 318–329, 2018.

[7] W. A. Connors, A. J. Hunter, and J. Dillon, "Increasing Navigation Effectiveness in GPS Denied Environments Using Through-The-Sensor SAS Techniques," in *4th International Conference on Synthetic Aperture Sonar and Synthetic Aperture Radar 2018*, 2018, pp. 99–106.

TRANSMISSION PATTERN OPTIMIZATION MODEL FOR CONFORMAL CONTOUR DESIGN

Christoph Zimmer[a], Nils Theuerkauf[b], Dieter Kraus[c], Anton Kummert[d]

[a] Bergische Universität Wuppertal, Rainer Gruenter Str. 21 42119 Wuppertal, Germany
[b] ATLAS ELEKTRONIK GmbH, Sebaldsbrücker Heerstr 235, 28309 Bremen, Germany
[c] Hochschule Bremen, Neustadswall 30, 28199 Bremen, Germany
[d] Bergische Universität Wuppertal, Rainer Gruenter Str. 21 42119 Wuppertal, Germany

Contact: Christoph.Zimmer@atlas-elektronik.com

Abstract: *To achieve desired transmission or reception characteristics either optimized amplitude and phase shadings are assigned to each transducer of a linear array or a conformal transducer placement is applied avoiding the necessity of individually driven channels. For higher frequency applications a desired characteristic can also be obtained by conformal shaping of a single transducer.*
In order to design a conformal transducer with differing horizontal and vertical requirements and a large bandwidth a three-dimensional contour needs to be optimized using numerical optimization techniques. To reduce manufacturing and curvature constraints the resulting contour is milled onto a single composite ceramic stack which also results in the ceramics polarization direction being no longer orthogonal to the conformal surface. To model the resulting acoustical behavior at moderate complexity we chose to adapt a discrete source model by attaching an inherent element characteristic which is differing for each source as a result of the local gradient for the surface contour. Our approach is to apply a linear combination of two characteristics- one along the main vibration direction and hence in main direction of the ceramic and the second orthogonal on the conformal surface to obtain a realistic overall result. These characteristics are acquired based on exemplary FEM simulations using simplified two-dimensional setups for a limited set of sloping angles.
The optimization results are verified by measurements obtained with two differing transducers manufactured using the optimized contours. With only minor deviations from the simulation results we present a promising method for conformal contour optimization which can also be applied easily to other applications, element sizes or desired transmission characteristics if required.

Keywords: *Conformal Transducer, Optimization, Beampattern Calculation*

1. INTRODUCTION

Desired transducer or antenna characteristics can be achieved by a variety of methods where either element positions which are typically obtained by applying numerical optimization techniques which require a sufficient transmission pattern model. Optimum drive- or arrangement calculation by local [1]-[2], or global [3] numerical optimization techniques as well as their comparison [4] has been of major interest in the last decades till recent applying the well-known point source model [5]. If a constant characteristic is required the beam shaping is preferably achieved by conformal placement of the transducers avoiding the necessity of separated- and individually driven elements.

In this work we apply numerical optimization to design the conformal contour of a relatively small single transducer to achieve a desired transmission characteristic over a large frequency domain. To reduce manufacturing and curvature constraints the resulting contour is milled onto a single composite ceramic stack which also results in the ceramics polarization direction being no longer orthogonal to the conformal surface which is considered by applying a sophisticated element characteristic. Two contours are optimized for differing requirements and the design is validated by comparing simulation results to test measurements.

2. CONTOUR SPECIFICATION

For this design we describe the contour of the transducer by a polynomial which in general allows every continuous shape and hence a problem specific solution. The contour height y is given by

$$y(x) = \sum_{i=1}^{N} p_i x^i . \tag{1}$$

where x is the length coordinate centered around $x = 0$ and p_i are the polynomial coefficients which are the parameters to be optimized. For this work we consider only symmetric beampattern requirements and hence all odd p_i are equal to zero. Nevertheless, also asymmetric contours are possible which also results in a more complex optimization due to the increased number of optimization parameters. The order N of the polynomial is chosen as tradeoff between shape synthesizability and optimization complexity and hence is problem specific.

Nevertheless, the flexibility of the polynomial description also allows undesired contours which e.g. cannot be manufactured or do not fit secondary requirements. Hence a constrained optimization is applied further specified in Section 5.

3. TRANSDUCER TRANSMISSION PATTERN CALCULATION

With the aim to design the beampattern of a single element the success is mainly depending on the accuracy of the applied model. Moreover, the model should also cause low computation costs if included into a numerical optimization routine. Hence, we apply the discrete source model described in [5] where the obtained contour is sampled equidistantly with in total N sources and extend it by applying a special element characteristic $c(\varphi, f)$. For a later comparison with tank experiments the transmission characteristic is calculated range dependent, where the complex beampattern at elevation $\theta = 0°$ is given by

$$b(\varphi, f \mid r) = \gamma \sum_{n=1}^{N} \frac{1}{r_n(\varphi \mid r)} c(\varphi, f) e^{jkr_n(\varphi \mid r)} . \tag{2}$$

Here γ is a normalization parameter, $k = 2\pi f / c$ denotes the wavenumber, r and φ are the polar coordinates of the test probe measured relative to the element center and r_n represents

the distance between the n-th point source on the surface of the element and the test probe. The logarithm of the squared magnitude of $b(\varphi, f \mid r)$ is called beampattern.

$$B(\varphi, f \mid r) = 10\log_{10}\left(\left|b(\varphi, f \mid r)\right|^2\right) \tag{3}$$

The conducted test measurements motivated a more sophisticated modeling of the element characteristic. Due to the chosen design in which the ceramic rods are no longer normal to the transducer surface, we model the element characteristic by a linear combination of a forward component $c_f(\varphi, f)$ and a surface normal component $c_n(\varphi, f)$, i.e.

$$c(\varphi, f) = \alpha c_f(\varphi, f) + (1-\alpha)c_n(\varphi, f)\,. \tag{4}$$

The design parameter α as well as the characteristics c_f and c_n are chosen to match exemplary FEM simulation results obtained with simplified two-dimensional models.

4. NUMERICAL OPTIMIZATION

The applicability of a contour is evaluated by comparing the resulting beampattern $B(\varphi, f \mid r)$ to a desired beampattern $\hat{B}(\varphi, f)$. As cost function the magnitude squared deviation is applied, i.e.

$$c = \int_b \int_{\varphi_s} \left| B(\varphi, f \mid r) - \hat{B}(\varphi, f) \right| d\varphi\, df \tag{5}$$

where φ_s is the desired operating sector for the transducer and b the corresponding bandwidth. The cost function is minimized using the MATLAB optimization toolbox. Furthermore linear constraints are added to control the maximum contour height, maximum sloping and ensure the convexity of the obtained solution.

For this work we depict two example contours in Fig. 1 which are obtained by numerical optimizations for different specifications. ‚Contour 1„ should provide a constant opening angle with an approximately parabolic main lobe. ‚Contour 2„ should achieve a flat and low ripple operating sector of 30° in total with least possible sensitivity elsewhere. The contour lengths were selected due to secondary specifications.

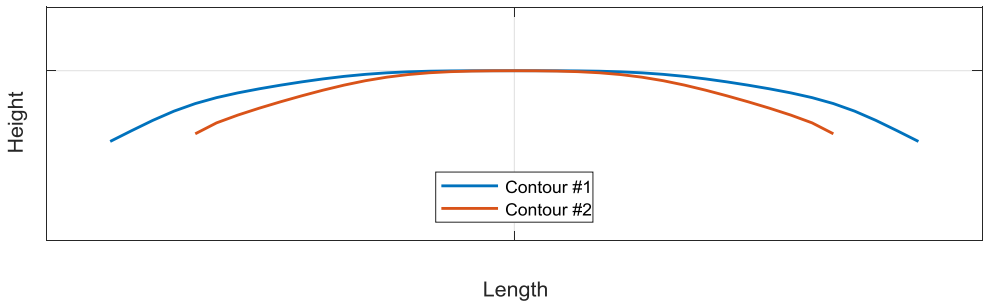


Fig.1: ‚Contour 1' and ‚Contour 2' obtained applying numerical optimization for two different design goals

5. MEASUREMENT EVALUATION

The simulated and measured beampattern alongside with the desired beampattern shape is shown in Fig. 2 for ‚Contour 1„ and in Fig. 3 for ‚Contour 2„ for a set of six frequencies.

For ‚Contour 1„ in Fig. 2 the approximation of the cosine shaped desired pattern is least optimal for the lowest frequency due to the low effect of the curvature on comparably low frequencies. The approximation achieves good results for the frequencies in subplot c) to f). The

measurement results fit well to the simulation while the sensitivity for larger angels tends to be lower than expected. The largest deviation is visible in subplot a) and cannot be explained with the applied model.

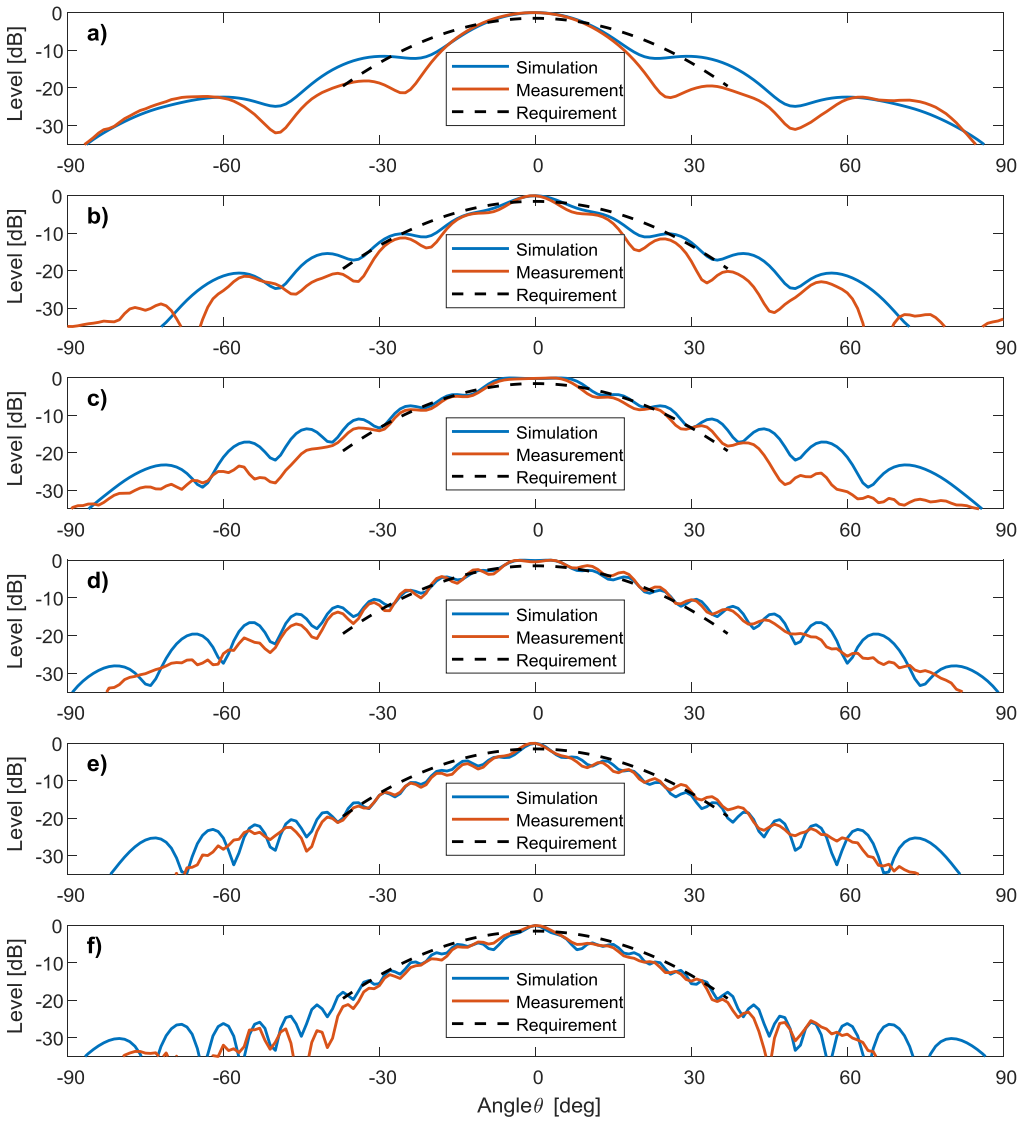


Fig.2: Comparison between Calculated and Measured Beampattern of ‚Contour 1' for frequencies $f = f_0, 2f_0, ..., 6f_0$ *with the lowest in plot a) to the highest in plot f)*

For ‚Contour 2„ in Fig. 3 the approximation of the flat top desired pattern is least optimal in subplot b) which results from the low effect of the curvature while in subplot a) the obtained main lobe already provides the desired behaviour. The approximation achieves excellent results for the frequencies in subplot c) to f). The measurement results also fit well to the simulation with comparable results to the ones achieved with ‚Contour 1„ besides that the deviation from the model in subplot a) insures as desired by the optimization goal an even lower sensitivity outside of the operating sector.

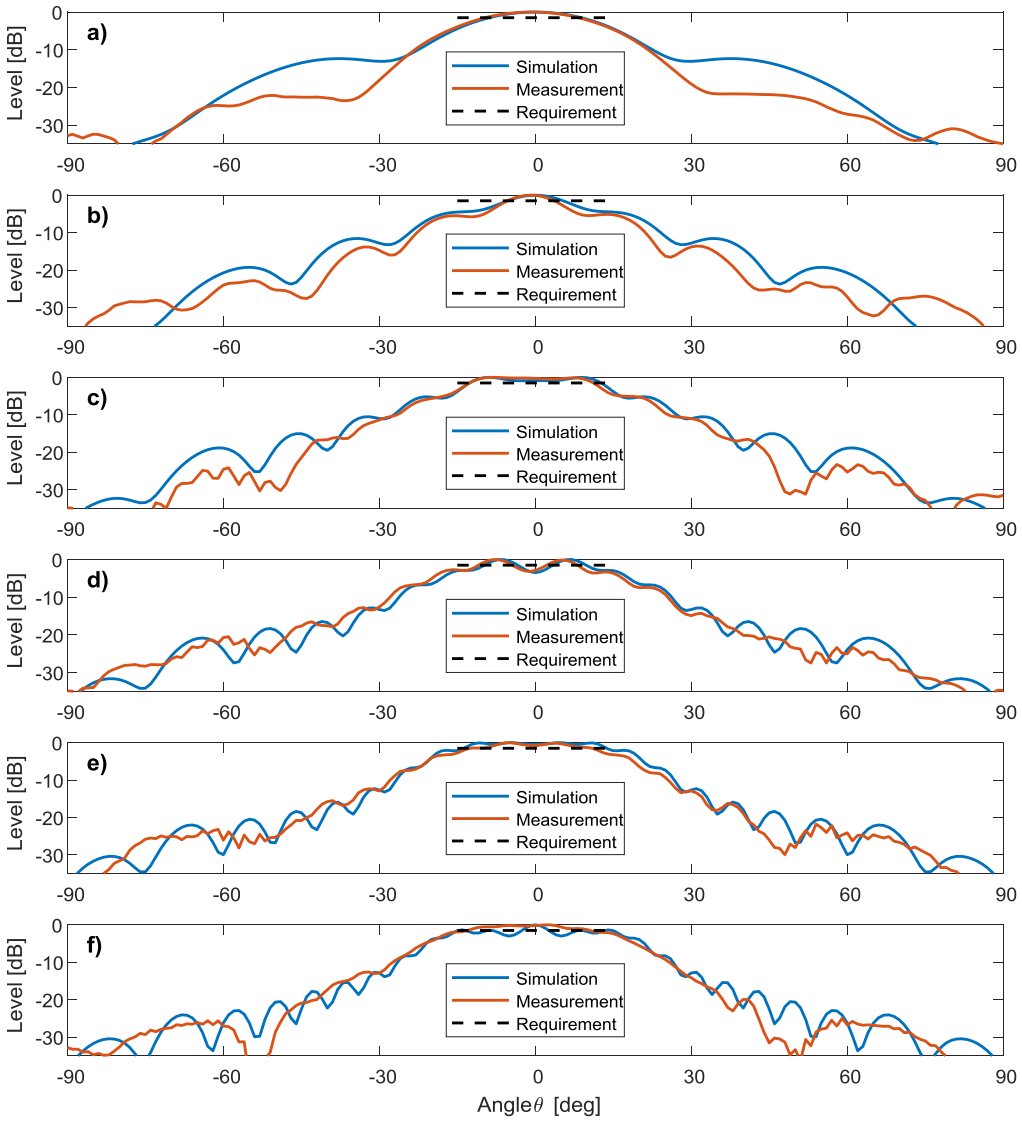


Fig.3: Comparison between Calculated and Measured Beampattern of ‚Contour 2' for frequencies $f = f_0, 2f_0, ..., 6f_0$ with the lowest in plot a) to the highest in plot f)

6. CONCLUSION

In this paper we showed results for the optimization of a conformal contour of a compact ceramic to achieve a desired transmission characteristic over a large bandwitdh. The applied discrete source model was enhanced by a sophisticated element characteristic to obtain an overall realistic result. With the compact size of the transducer the approximation of the desired sensitivity characteristic was less optimal for lower frequencies but showed a good approximation from medium to high frequencies for the two investigated cases. The modeled behavior matched well with conducted measurements where only the low frequency behavior showed larger deviations. Hence the proposed modeling can also applied for differing required characteristics. Further improvements could be achieved by further exploiting exemplary FEM simulations for more realistic element characteristics.

REFERENCES

[1] **H. Lebret, S. Boyd**, "Antenna Array Pattern Synthesis via Convex Optimization", *IEEE Transactions on Signal Processing*, Vol. 45, No. 3, 1997.
[2] **O. Bucci, G. D'Elia, G. Mazzarella, G. Panariello**, "Antenna Pattern Synthesis: A New General Approach", *Proceedings of the IEEE*, Vol. 82, No.3, 1994.
[3] **E. Rajo-Iglesias, O. Quevedo-Teruel**, "Linear Array Synthesis Using an Ant-Colony-Optimization Based Algorithm", *IEEE Antennas and Propagation Magazine*, Vol 49, No. 2, 2007.
[4] **S. Jayaprakasam, S. Kamal, C. Yeow, M. Yusof**, "Beampattern Optimization in Distributed Beamforming using Multiobjective and Metaheuristic Method", *IEEE Symposium on Wireless Technology and Applications*, 2014
[5] C. Sherman, J. Butler, "Transducers and Arrays for Underwater Sound", Springer, Chapter 5

SYNTHETIC APERTURE SONAR FOR A LOW-COST AGILE PLATFORM: PRELIMINARY RESULTS

Ciaran Sanford[a], Alan Hunter[a], Allan Willcox[b]

[a] University of Bath, Bath, BA2 7AY, United Kingdom
[b] Picotech Ltd, Meadow Hayes, Dorset SP7 0JW, United Kingdom

Contact Author: Ciaran Sanford, C.Sanford@bath.ac.uk

Abstract: *Synthetic aperture sonar (SAS) imaging systems are at the cutting edge of underwater sensing technology. They are capable of producing extremely high-resolution images independent of range and frequency. However, conventional platforms carrying SAS hardware are typically large, slow, non-agile platforms. Furthermore, these systems are inherently high cost, owing to the need for specialised components. In this paper, we present preliminary results from a low-cost agile remotely operated vehicle (ROV). The platform utilises a repurposed forward looking sonar (FLS) as SAS hardware. We have performed experiments with the ROV at a swimming pool with a series of targets deployed at close range. Coherence between pings is demonstrated and synthetic aperture images are shown which, despite some defocusing, show an improved resolution compared to conventional sector scan images. These latest results are also compared with previous results from a rail.*

Keywords: *Synthetic aperture sonar, remotely operated vehicle, agile platform, off-the-shelf, curved transmitter, near-field, widebeam*

1. INTRODUCTION

Synthetic Aperture Sonar (SAS) is a state-of-the-art seafloor imaging technique for underwater systems. Coherent summation of echo data along the path traversed by the sonar produces images with constant across-track resolution that is independent of range and frequency [1]. Images generated by SAS systems are typically far more detailed and higher resolution than conventional sector scan images. However, coherent summation requires the trajectory of the sonar to be known to sub-wavelength precision [2], meaning data-driven navigation techniques are required.

Conventionally, SAS payloads are operated from large, non-agile platforms following linear paths. Coupled with the need for a high-quality inertial navigation system (INS) to help satisfy the strict navigation requirements of the technique, this drives the cost of SAS systems to the point where low cost commercial off-the-shelf (COTS) systems are non-existent. The development of small, agile, low cost platforms would enable shallow water civilian applications, such as underwater crime scene investigation [3].

In this paper, we present a low-cost SAS system that is operated from a commercially available remotely operated vehicle (ROV). The SAS hardware is a repurposed low cost forward looking sonar (FLS). As an intermediate step towards the agile platform, a small linear rail was constructed. Data from the rail carrying the same SAS hardware is also presented.

2. SAS IMAGING HARDWARE

Our hardware is the Picotech FLS40 [4]. This is a COTS system designed for civilian applications, e.g., small fishing boats. The specifications of the system are shown in Table 1. The range resolution of SAS, as with a sector scan, is defined by $\delta y = c/2B$, where c is the speed of propagation and B is bandwidth. This gives a range resolution of roughly 1.9 cm for the Picotech system. However, the along-track resolution δx of a sector scan is dependent on range. With a full aperture SAS it is determined only by the spacing between receiver elements d, such that $\delta x = d/2$. The small spacing in the Picotech receive array gives a theoretical resolution of around 2.3 mm along track.

Picotech FLS40 Specifications	
Centre Frequency	500kHz
Bandwidth	40kHz
Azimuth field of view	40°
Maximum range	70m
Ping rate	10Hz
Receive array length	0.13m
Receive elements	31
Receive element spacing	4.45mm

Table 1: Specifications of the Picotech FLS40.

The typical method for data-driven navigation is the redundant phase centre (RPC) micro-navigation method (also known as DPCA) [5]. However, repurposing an FLS presents further challenges. Firstly, the curved transmission surface causes errors when navigating and blurring when imaging. This can be compensated for as described in [6]. Secondly, the target applications for the system naturally lead to near-field geometries, which need to be considered when using micro-navigation.

3. RAIL EXPERIMENT

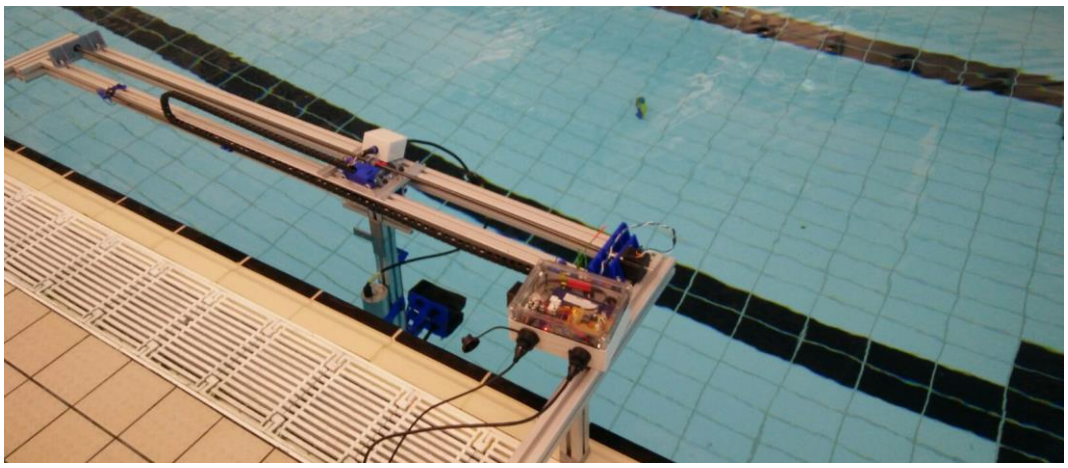
In the first experiment, the FLS was operated from a small linear rail (figure 1a), giving a known trajectory to aid navigation. The rail is constructed from COTS components and 3D printed parts, and is around 1.3m long, giving a synthetic aperture roughly 10 times the length of the FLS40 physical aperture. The transducer was mounted facing broadside at 11° below horizontal. This placed the centre of the footprint at a range of approximately 4.5 m. The rail moves at 6mm per second, meaning the advance per ping is far less than the phase centre array length. This provided a choice of RPC arrays for correlation. The experiment was conducted in a swimming pool, as this provided a controlled environment. The target field consisted of small metal rings of diameter 5 cm, as well as an acrylic retroreflector 20 cm across (figure 1b).

Cross correlations were performed with an RPC array of 20 receiving elements. The data was divided into overlapping range bins of length 0.75 m and the normalised coherence at the midpoint of each range was calculated (fig 1c). RPC micro-navigation has been applied to the data and a SAS image generated (fig 1e). For comparison, a conventional sector-scan image of the same scene has been generated (fig 1d). The SAS image shows considerable improvement in resolution, on the sector scan. The target field is visible, along with the lines between the pool tiles. There is some defocussing, which may be caused by uncompensated navigation errors. This may be due to a combination of the FLS40's curved projector and near-field effects.

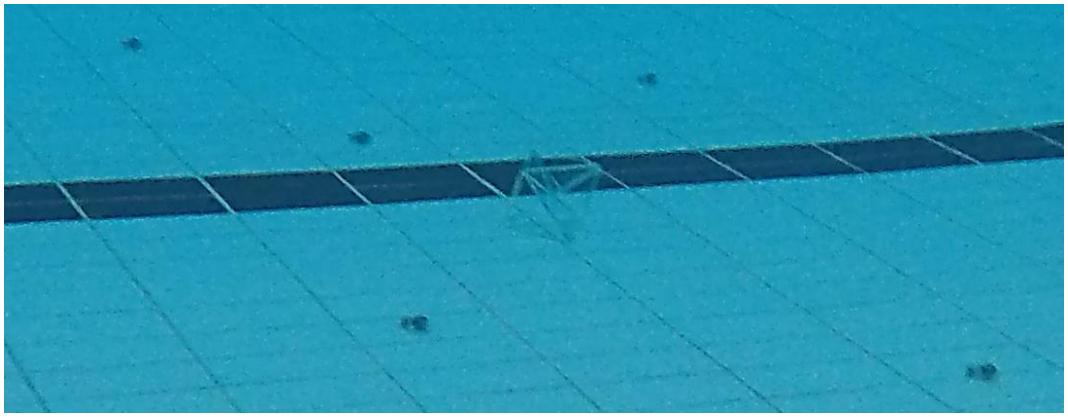
4. ROV EXPERIMENT

The second experiment used an ROV made by Blue Robotics (figure 2a). This is a low cost, COTS design and is capable of lateral motion in all directions. The FLS-40 was mounted underneath the vehicle, at 20º below horizontal. For this experiment, the ROV was driven at its top speed of 1m/s. The experimental setup was similar to that of the first experiment, with a target field placed roughly in the middle of the transducer footprint. Due to the increased depression angle, the target footprint was smaller and closer to the ROV, centred at a range of 3.5 m. The targets were small metal hemispheres with a variety of diameters, and a patch of artificial grass to simulate a seafloor (figure 2b).

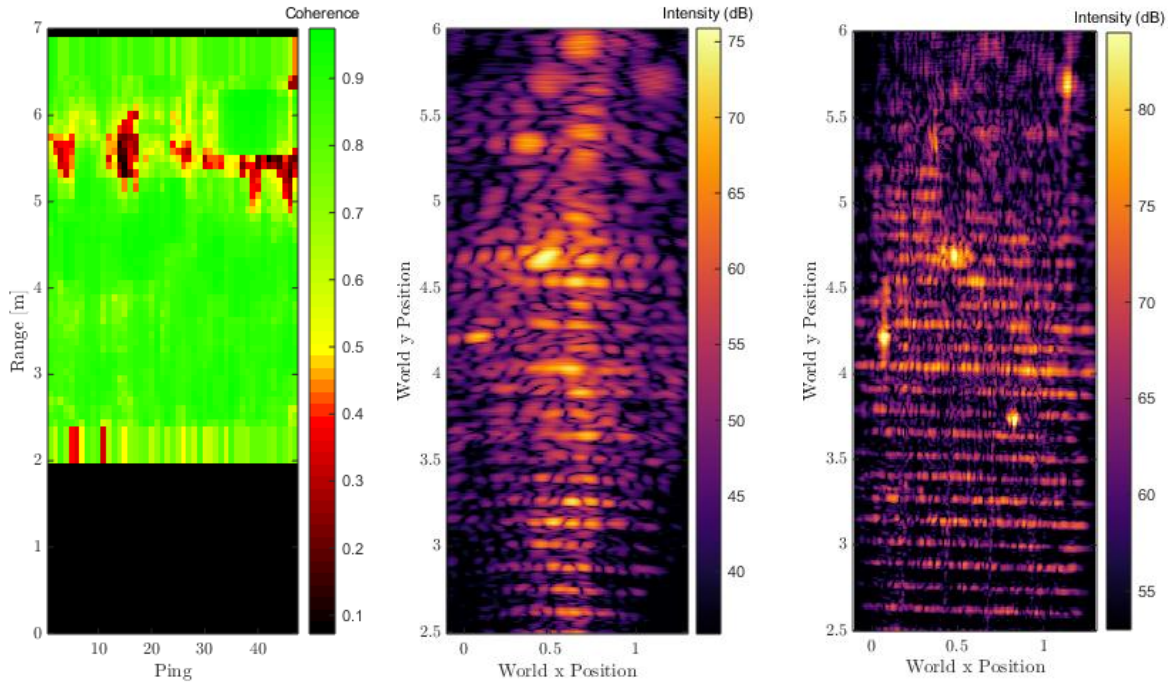
The speed of the vehicle is variable, and unlike the rail, there is no fixed RPC array length between pings. The range was divided into range bins of 0.75 m as before, and cross-correlating the data shows again that good coherence is achieved with the ROV across 90 pings (figure 2c), despite the unconstrained path. Again, RPC micro-navigation has been applied to the data and a SAS image generated (figure 2e), with a sector-scan comparison (figure 1d). The SAS image again shows significant resolution improvement, with the target field visible, particularly the patch of artificial grass. The image is defocussed and this may once again be due to uncompensated navigation errors and near-field effects.



(a)



(b)



(c) (d) (e)

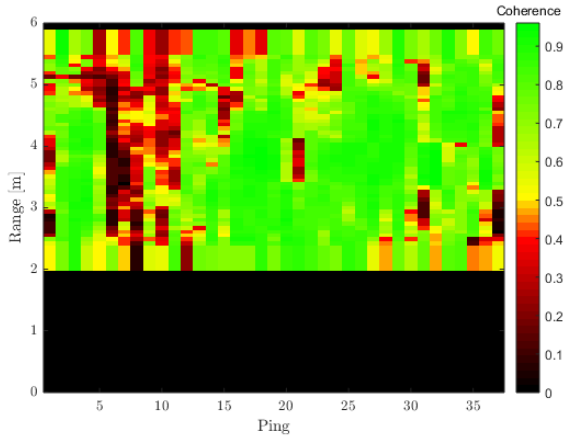
Fig 1: Photos and images from the first pool experiment. (a) The rail at poolside. (b) Target field of metal rings and an acrylic retroreflector. (c) Inter-ping coherence from the rail data. (d) Sector-scan image of the target field alongside (e) a SAS image of the same scene.



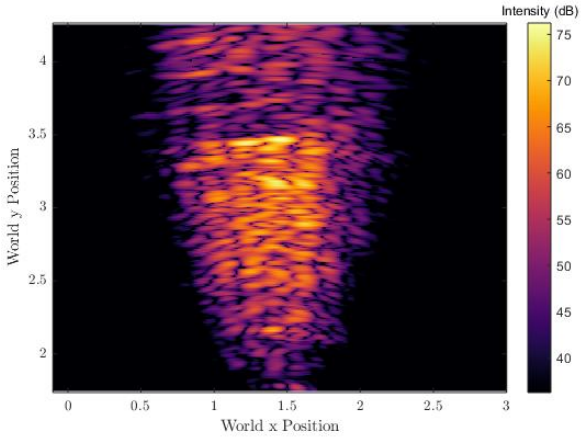
(a)



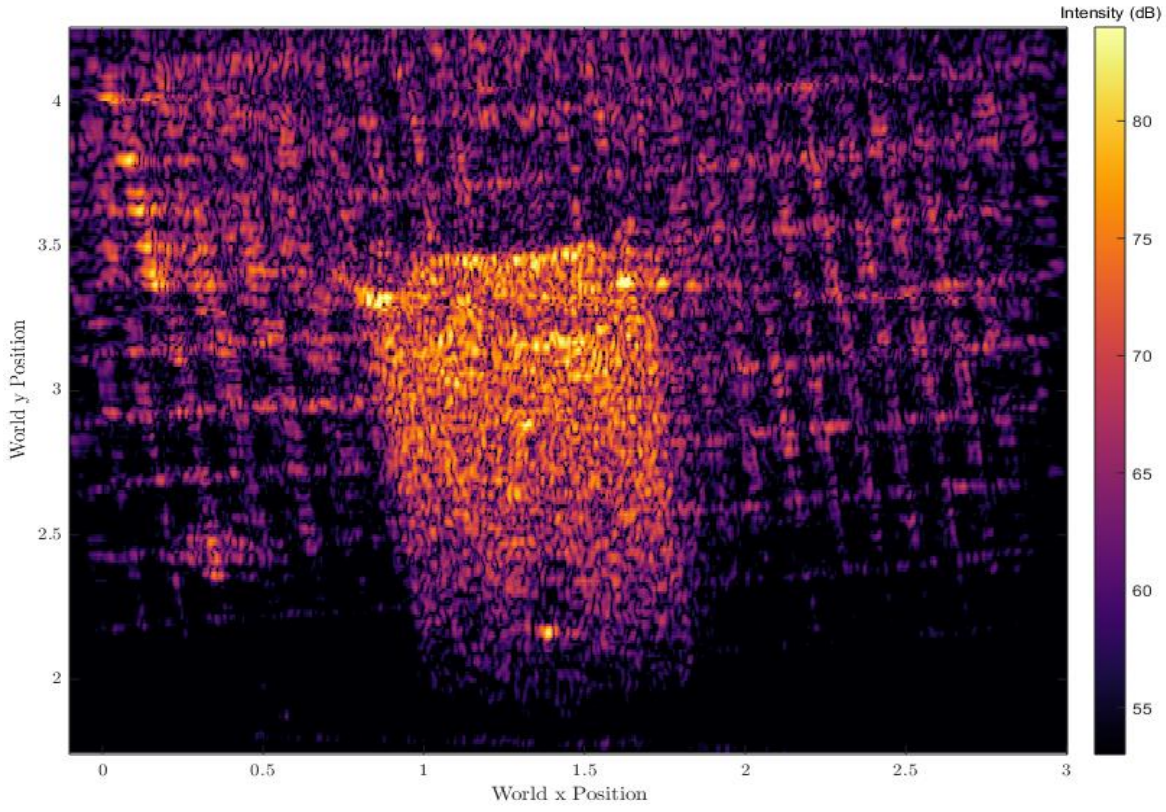
(b)



(c)



(d)



(e)

Fig 2: Photos and images from the second pool experiment. (a) The ROV. (b) Target field of hemispherical metal objects and an artificial grass floor. (c) Inter-ping coherence from the ROV data. (d) Sector-scan image of the target field alongside (e) a SAS image of the same scene.

5. CONCLUSIONS AND FUTURE WORK

We have shown that a small form factor, COTS sector-scan sonar can be repurposed into a higher resolution system using SAS techniques. Both the rail and the ROV show high coherence between pings, allowing for the use of conventional navigation methods such as RPC micro-navigation. SAS images have been generated from both platforms, displaying an increase in resolution compared to the conventional sector-scan images. However, they are defocussed, and this is likely to be due to navigation errors.

The repurposed FLS presents challenges, primarily navigation and imaging errors caused by the curved projector. There is also near-field geometry to consider. Future work will focus on overcoming these challenges and producing focussed images at full system resolution.

6. ACKNOWLEDGEMENTS

Mr Sanford is grateful to Bath alumnus, Mr Gareth Hamilton-Fletcher, for funding his PhD studentship. The authors appreciate support from the Metropolitan Police in the application of this work to underwater crime scene investigation.

REFERENCES

[1] **Hansen, R. E.**, "Introduction to Synthetic Aperture Sonar", *Sonar Systems*, Nikolai Kolev, IntechOpen, pp. 10-11, 2011.

[2] **Gough, P. T., & Miller, M. A.,** "Displaced ping imaging autofocus for a multi-hydrophone SAS," *IEE Proc. - Radar Sonar Navig.*, vol. 151, no. 3, pp. 163, 2004.

[3] **Metcalfe, B., Thomas, B., Treloar, A., Rymansaib, Z., Hunter, A., and Wilson, P.,** "A compact, low-cost unmanned surface vehicle for shallow inshore applications". *Intell. Syst. Conf.,* pp. 961–968, 2017.

[4] **Willcox, A.**, "Picotech Miniature Multibeam Sonar," 2016, Available at: https://www.picotech-ltd.com/PicoFLS-40 [Accessed October 2016];

[5] **Cook, D. A.**, "Synthetic Aperture Sonar Motion Estimation and Compensation," *Masters Thesis*, pp. 90-94, 2007.

[6] **Sanford, C., Hunter, A. J., & Willcox, A.**, "Synthetic aperture sonar phase correction for a curved projector", *4th International Conference on Synthetic Aperture Sonar and Synthetic Aperture Radar*, Lerici, Italy, IOA, vol. 4, pp. 1-8, 2018

MULTI-BEAM DOPPLER SONAR FOR MEASURING 2-D VELOCITIES IN A SWATH: SWATHDOP

Mahdi Razaz[a], Len Zedel[b], Alex Hay[c]

[a]Department of Marine Sciences, University of Georgia, Athens, 30602 Georgia

[b]Physics and Physical Oceanography, Memorial University of Newfoundland, St. John's, NL, A1B 3X7, Canada

[c]Department of Oceanography, Dalhousie University, Halifax, NS, B3H 4R2, Canada

Len Zedel, Physics and Physical Oceanography, St. John's, NL, A1B 3X7, Canada. Fax. 709 737 8739, zedel@mun.ca

Abstract: *Doppler sonar profiling systems normally employ an array of diverging acoustic beams and measure velocity profiles subject to assumptions about flow homogeneity over the sampled volume. On smaller length scales where homogeneity cannot be assumed, bistatic beam geometries are employed to create (near) coincident component measurements that allow velocity profiles over a limited range. For either approach, measurement of flow spatial structure in more than one dimension requires the use of multiple instruments or requires physically scanning with a single instrument with the assumption of flow stationarity. We are interested in understanding sediment transport over bedforms where flow evolves continuously both in time and space. For this purpose we are developing a pulse-to-pulse coherent swath Doppler system by combining a steerable receiver array with fan beam transmitters in a bistatic configuration. The system operates at 500 kHz with 10% bandwidth sampling transmit pulses at 1.5 ms intervals. The software-defined radio data acquisition and control system limits us at present to 8 independent receiver channels, giving a sample domain that measures 2-D velocities in a ~0.8 m by ~0.8 m region and allows a resolution of about ~3 cm in the plane of the swath. A coherent sonar simulation model was used to test beamforming algorithms and data inversion methods. We report on prototype trials made at the St. Anthony Falls Laboratory main flume facility with observations of 1-m deep unidirectional flow at speeds of order 1 m s^{-1} over evolving bedforms.*

Keywords: *Doppler Sonar; Velocity; Pulse-to-pulse; Coherent; Bistatic; Multi-beam; Beamforming*

1. INTRODUCTION

Doppler sonar used for oceanographic purposes normally employs a series of diverging acoustic beams where each beam is able to measure a single velocity component. By arranging a number of beams with different orientations, multiple velocity components can be measured and these observations can be inverted to determine the 3-component velocity. The trade-offs between measurement accuracy and profiling range result in practical systems with 3 to 5 acoustic beams tilted at angles of between 20 and 45° away from vertical. An essential assumption in this configuration is that the flow is homogeneous over the volume sampled by the diverging beams so that all of the beams are measuring components of the same velocity [1]. In the context of measuring ocean current profiles, this assumption is easily met.

In smaller scale flow environments, the velocity will not be homogeneous over the span of the diverging acoustic beams and the conventional Doppler profiler geometry is not suitable. For such applications, velocity measurements are made using Doppler velocimeters where the multiple acoustic beams are oriented to converge on a single sample volume. These systems provide high precision velocity measurements but can provide velocity profiles over a comparatively short distance interval along one spatial dimension (Nortek Vectrino [2], MFDop [3], Sontek Argonaut-ADV [4], ADVP [5]).

The sampling of structures that evolve in both time and space using standard Doppler beam geometries requires multiple synchronised instruments in a spatially-distributed array [6], [7]). An acoustic geometry capable of simultaneous measurements at multiple locations in 2d space is provided by multi-beam sonar (see for example [8], [9]), which can be configured to extract Doppler velocity estimates [10]. We have configured such a system – the SwathDop -- to enable velocity measurement in near-bottom flow for the purpose of studying sediment transport processes.

2. SYSTEM CONFIGURATION

The SwathDop consists of two fan-beam transmitters mounted 0.568 m to either side of an 8-element receiver array (see Fig. 1). Operating at 500 kHz, pulses are transmitted alternately from each transmitter and recorded by the central receiver array. The beam pattern of the receiver array has a ~4.9° (3 dB) beam width in the xz plane. The 2d measurement domain is sampled using steer angles between +20° to -20° in 4° increments. The measurement domain extends nominally 0.8 m below the instrument with a horizontal extent of 0.8 m but the velocity and spatial resolution vary with position.

In order to extract two component velocities, measurements from the two (essentially independent) bistatic sonar systems must be combined. In addition, the individual sample volumes for the two sonars do not overlap and so data must be interpolated to a common sample space. The actual velocity magnitude is determined by combining bistatic measurements u_1 and u_2 as follows:

$$\alpha_1 = \tan^{-1}\left[\frac{1}{\sin\gamma}\left(\frac{u_2}{u_1} - \cos\gamma\right)\right] \quad (1)$$

$$\alpha_2 = \tan^{-1}\left[\frac{1}{\sin\gamma}\left(\frac{u_1}{u_2} - \cos\gamma\right)\right] \quad (2)$$

$$\gamma = \alpha_1 + \alpha_2 = \psi_1 + \psi_2 \quad (3)$$

$$U = \frac{1}{2}\left(\frac{u_1}{\cos\alpha_1} + \frac{u_2}{\cos\alpha_2}\right), \tag{4}$$

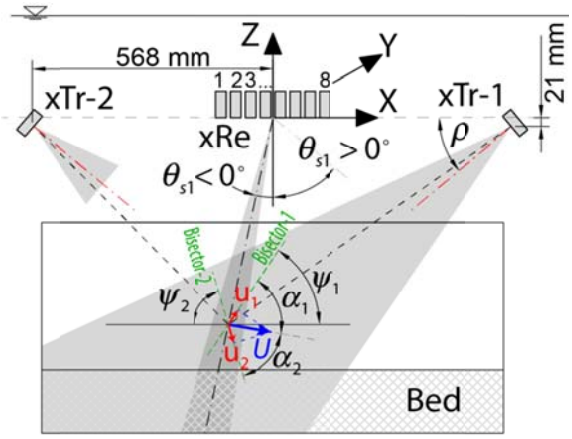


Fig. 1: SwathDop geometry.

here, angles α_1, α_2, ψ_1, ψ_2, and γ are defined in Fig. 1. The cartesian components are then given by:

$$\begin{aligned} u &= U\cos\varphi \\ w &= U\sin\varphi \\ \varphi &= \psi_1 - \alpha_1 \end{aligned} \tag{5}$$

3. MODEL EVALUATION

The expected performance of the SwathDop concept was investigated by using a model of coherent Doppler operation [11]. The model was used to develop beamforming methods and to test the required signal processing algorithms and velocity extraction algorithms (Equations 1-5). Transducer sidelobes are a challenge for multibeam sonar operation and ultimately limit the range of sample volumes that can be resolved by the system. Fig. 2 presents the bistatic beam intersection predicted by the model for a 12° steer angle.

As a demonstration of system sampling, the model was used to simulate velocity measurements with a logarithmic velocity profile over a boundary located at 0.7 m below the receiving array (see Fig. 2). Sampled velocities (black dots) are shown in comparison to the input velocity profile for steer-angles of -12, -4, 4, and 12° in Fig. 3. In general there is pleasing agreement through the profile with noticeable deviations near bottom and at the top of the sample domain.

4. LABORATORY TRIALS

Based on the model results, a design geometry was chosen and implemented on a prototype SwathDop system. The prototype was tested in the St. Anthony Falls Laboratory main flume facility; the main flume is 84 m by 2.75 m by ~ 1m (length by width by depth) and allows a discharge of order 1 $m^3 s^{-1}$ with flow speeds of order 1 m s^{-1} (see Fig. 4).

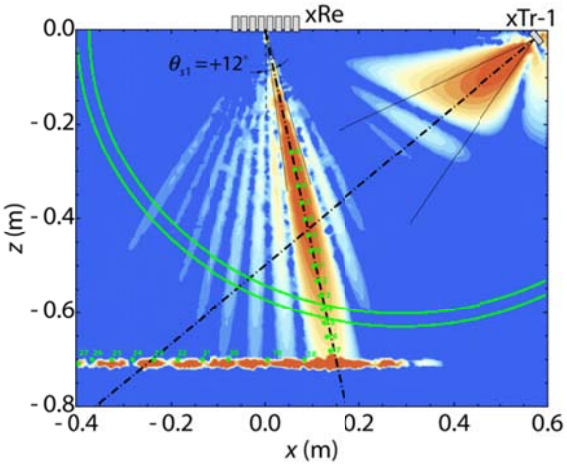


Fig. 2: SwathDop bistatic beam pattern. Here, the beam for the receive array (centered at x=0, z=0) has been steered to 12° off axis. . Warmer colours indicate higher amplitude response. The high amplitude signal at z = -0.7 m is caused by the bottom return.

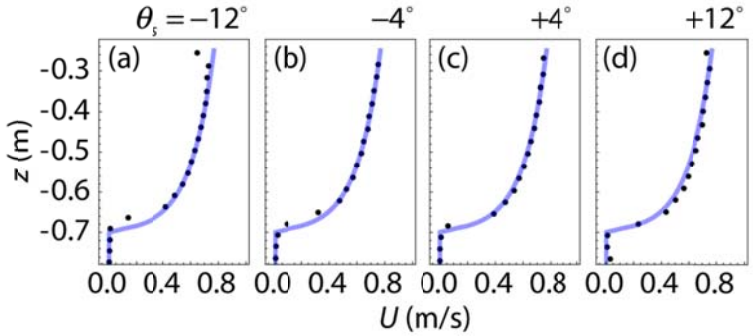


Fig. 3: Model results from sampling logarithmic velocity profile.

The SwathDop was positioned so that the transducers were ~0.7 m above a mobile sand bed with median particle diameter of 0.4 mm. For the results presented here, dunes with length of about 2 m and amplitudes of about 0.10 m were present and moving through the test area. Additional flow speed measurements were made with a Nortek Vectrino ADV. A rotary pencil beam was used to determine bedforms. In addition, independent (although not concurrent) measurements of velocity profiles were made using the MFDop velocity profiler [3].

Despite high concentrations of acoustic scatterers in the water column, the SwathDop system realised low signal levels giving rise to low signal to noise ratios in the phase measurements required for Doppler velocity processing. Only data from one of the two transmitters provided data of an adequate quality to extract data and as a result, it was not possible to extract flow direction information. In order to generate velocity profiles from the resulting data, it was assumed that the flow was horizontal. Given the presence of significant bedforms (where slopes on the lee-side of dunes were as high as 30°) the assumption of horizontal flow could result in substantial bias especially near the bottom.

5. SYSTEM PERFORMANCE

System performance was evaluated by generating averaged velocity profiles at different steer angles. An example set of profiles for steer angles of 0, 4, 8 and 12° is shown in Fig. 5 (red dots). A somewhat uniform velocity of about 0.8 m s^{-1} is seen down to about 0.1 m

above bottom where there is a rapid decrease to 0 m s^{-1}. The profile shape does not match the typical law-of-the-wall profile that was used in the model simulation trials, but comparison with the MFDop profiles collected during similar flow conditions validates this profile shape (see solid lines in Fig. 5); this profile shape is consistent with theory for flow over bedforms presented by [12].



Fig. 4: St. Anthony Falls Laboratory main flume.

6. SUMMARY/CONCLUSIONS

This paper has reported on development of a new multi-beam sonar system that enables the measurement of velocity profiles over a swath; the SwathDop. The instrument operates by using two fan beam acoustic projectors offset to either side of a central 8 element receiver array. By transmitting pulses alternately from each projector, 2-D velocity estimates can be constructed from the two independent bistatic velocity fields. Simulations of the system indicated that reasonable measurements were possible using steer angles ranging over $\pm 12°$ (see Fig. 2). Field scale laboratory trials of the system were undertaken in St. Anthony Falls Laboratory in a 1.0 m deep flow at 0.8 m s^{-1} over a mobile bed of 0.4 mm diameter sediment. Operating in this environment we struggled to achieve an adequate signal level in the receiving array. This problem was caused by the need for greater amplifier gain in the receive circuits and also by limits to the transmit power of the projectors; this is an area of system operation that needs to be improved. Even when working with the low signal levels, measured profiles provided good agreement over steer angles from 0-12° and these profiles agreed with independent velocity profiles collected during similar flow conditions, and with the predicted vertical structure of flow over dune fields.

7. ACKNOWEDGEMENTS

The authors should like to acknowledge Saint Anthony Falls Hydraulic Laboratory for the access to the facility and the excellent support that made this research possible. Technical support from Richard Cheel and Walter Judge are also gratefully acknowledged. Funding was provided through a grant from the Atlantic Canada Opportunities Agency (contract 193499).

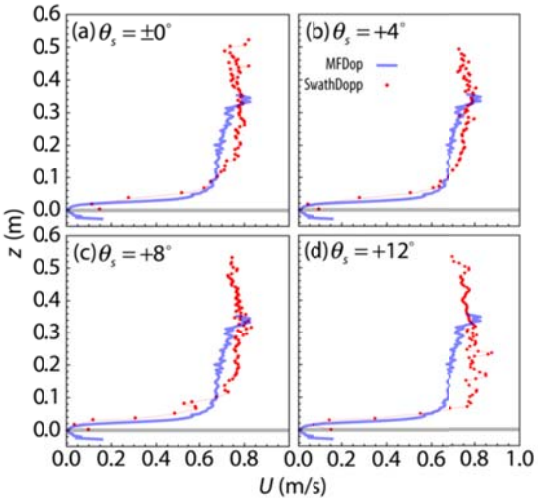


Fig. 5 SwathDop Velocity profiles measured at selected steer angles compared to independent observations from MFdop.

REFERENCES

[1] **Gordon, R.L.**, Acoustic Doppler Current Profiler, Principles of Operation, a Practical Primer, RD Instruments, San Diego, 52 pp, 1996.

[2] **Zedel, L., and A. Hay**, Turbulence measurements in a jet: Comparing the Vectrino and the Vectrino II. IEEE/OES/CWTM 10th Current, Waves and Turbulence Measurement (CWTM). DOI: 10.1109/CWTM.2011.5759547, 2011.

[3] **Zedel, L., and A.E. Hay**, Multi-Frequency, Pulse-to-pulse Coherent Doppler Sonar. IEEE Journal of Oceanic Engineering. DOI: 10.1109/JOE.2010.2066710, 2010.

[4] **Hogg, N.G.., D.E. Frye**, Performance of a New Generation of Acoustic Current Meters. Journal of Physical Oceanography, 37, 148-161, 2007.

[5] **Hurther, D., & Lemmin, U.,** Shear stress statistics and wall similarity analysis in turbulent boundary layers using a high-resolution 3-D ADVP. IEEE Journal of Oceanic Engineering, 25(4), 446-457, 2000.

[6] **Hurther, D., and Thorne, P.**, Suspension and near-bed load sediment transport processes above a migrating, sand-rippled bed under shoaling waves. J. Geophys. Res. 116, C07001, DOI:10.1029/2010JC006774, 2011.

[7] **Hare, J., A.E. Hay, L. Zedel, R. Cheel**, Observations of the Space-time Structure of Flow and Stress over Orbital-scale ripples. JGR-Oceans, 119, 1876-1898, 2014.

[8] **Gerlotto, F., M. Soria, P. Freon,** From two dimensions to three: the use of multibeam sonar for a new approach in fisheries acoustics. Canadian Journal of Fisheries and Aquatic Science. 56, 6-12, 1999.

[9] **Hughes, J.E., L.A. Mayer, D.E. Well**, Shallow-Water Imaging Multibeam Sonars: A New Tool for Investigating Seafloor Processesin the Coastal Zone and on the Continental Shelf. Marine Geophysical Researches 18, 607-629, 1996.

[10] **Smith, JA, J.L. Largier**, Observations of nearshore circulation: Rip currents. JGR 100, C6. 10,967-10,975, 1995.

[11] **Zedel, L.**, Modelling Pulse-to-pulse Coherent Doppler Sonar, J. Atmos. Oceanic Tech., 25, 1834-1844, 2008.

[12] **Nelson, J. M., & Smith, J. D.,** Mechanics of flow over ripples and dunes. Journal of Geophysical Research: Oceans, 94(C6), 8146-8162, 1989.

Structured Session 17

Modeling techniques for underwater acoustic scattering and propagation

Organiser(s): Gunderson Aaron, Isakson Marcia

SEMI-ANALYTIC MODELING OF SOUND PROPAGATION AND NOISE CROSS-CORRELATIONS IN A COASTAL OCEAN

Oleg A. Godin[a]

[a]Naval Postgraduate School, Monterey, CA, USA

Contact author: Oleg A. Godin, Physics Department, Naval Postgraduate School, 833 Dyer Road, Bldg 232, Monterey, CA 93943, USA. Fax: 831-656-2834. Email: oagodin@nps.edu.

Abstract: *Sound propagation in the coastal ocean over ranges large compared to water depth involves multiple interactions with the ocean surface and bottom. Bathymetric variations and time-dependence of the ocean surface lead to 3-D (such as horizontal refraction) and 4-D (arising from an evolution of the environmental parameters with time) effects being more pronounced in the coastal ocean than in typical deep-water settings. Understanding and modeling sound propagation in horizontally inhomogeneous ocean with time-dependent parameters remains a challenging problem. In this paper, we investigate 3-D and 4-D propagation effects from the prospective of acoustic remote sensing. Analytical techniques are employed to quantify the effects of horizontal refraction on amplitudes and travel times of adiabatic normal modes. Depending on orientation of the propagation path relative to the prevailing seafloor slope, different patterns emerge of the systematic deviation of apparent dispersion curves of adiabatic modes from the dispersion curves in the range-independent waveguide. It is found that, when mode travel times are used as input information for geoacoustic inversions, moderate bottom slopes can lead to large errors in retrieved geoacoustic parameters and cause a positive bias in the bottom sound speed estimates if the horizontal refraction is ignored. In passive acoustic remote sensing, two-point noise cross-correlation functions replace acoustic fields due to a compact controlled sound source as the probing signals which interrogate the environment. Noise averaging times that are necessary to measure two-point cross-correlation functions are much larger than the acoustic propagation times between the two points. As a result, 4-D effects prove to be much stronger in the passive than active remote sensing regime. It will be shown how wind waves and tides limit the usable frequency band of passive acoustic remote sensing in the coastal ocean.*

Keywords: *range-dependent waveguides, horizontal refraction, noise interferometry*

INTRODUCTION

This brief paper provides a sample of the material to be discussed in the conference presentation. Section 2 illustrates the effects of the waveguide range dependence and horizontal refraction of sound on normal mode dispersion, manifestations of these effects when time-warping [1] is applied to isolate modal components of the acoustic field, and their implications for geoacoustic inversions. Section 3 gives an example of the distortions of the empirical Green's function retrieved from noise cross-correlations in a coastal ocean due to motion of the ocean surface during noise averaging.

DISPERSION OF ADIABATIC NORMAL MODES IN A COASTAL WEDGE

Consider guided sound propagation in a homogeneous fluid layer with boundaries, the normal impedances of which depend only on the angle of incidence of a plane wave but not on wave frequency. Examples of such boundaries include pressure-release and rigid surfaces as well as interfaces with homogeneous fluid or solid half-spaces. It is easy to see that, when written in terms of phase speed of normal modes, dispersion equation of such a waveguide contains frequency ω only in the combination ωH, where H is thickness of the fluid layer.

Let sound propagate in a coastal wedge with a strait coastline. Horizontal coordinates x and y are perpendicular and parallel to the coastline, respectively. Water depth $H(x)$ increases linearly with increasing x. In the adiabatic approximation [2], travel time of n-th normal mode is

$$T_n = \int \frac{dx}{u_n} = \cot\alpha \int_{H_1}^{H_2} \frac{dH}{u_n(\omega, H)}. \tag{1}$$

Here H_1 and H_2 are the water depths at the source and receiver locations, $H_1 < H_2$; α is the angle that the seafloor makes with the horizontal plane; and $u_n(\omega, H)$ is the group speed of the local normal mode.

When sound speed in water is constant, phase and group speeds c_n and u_n are functions of ωH in an ideal wedge with pressure-release and/or rigid boundaries and in a penetrable wedge with a pressure-release surface and homogeneous fluid or solid bottom. Then,

$$\frac{1}{u_n} = \frac{1}{c_n} + \omega\left(\frac{\partial}{\partial\omega}\frac{1}{c_n}\right)_H = \frac{1}{c_n} + \omega H \frac{d}{d(\omega H)}\frac{1}{c_n} = \frac{1}{c_n} + H\left(\frac{\partial}{\partial H}\frac{1}{c_n}\right)_\omega = \left(\frac{\partial}{\partial H}\frac{H}{c_n}\right)_\omega. \tag{2}$$

Substitution of the right-most side in Eq. (2) into Eq. (1) gives a closed-form expression for the mode travel time:

$$T_n = \left[\frac{H_2}{c_n(\omega, H_2)} - \frac{H_1}{c_n(\omega, H_1)}\right]\cot\alpha. \tag{3}$$

It is straightforward to extend this result to a more complicated bathymetry, where water depth is piece-wise linear function of x. Then, mode travel time is given by the sum of

contributions Eq. (3) in each segment with a constant bottom slope, the slope α being different in each segment.

In the more general case, when sound propagates at an angle to the seafloor slope,

$$T_n = \int \frac{dl}{u_n} = \int \frac{\sqrt{k_x^2 + k_y^2}}{k_x} \frac{dx}{u_n} = \omega \cot\alpha \int \frac{dH}{u_n \sqrt{\omega^2 - c_n^2 k_y^2}}. \quad (4)$$

Here l stands for arc length along a horizontal (modal) ray; k_x and k_y are the x and y components of the mode's wave vector, and k_y =const. on the horizontal ray. The integral in Eq. (4) is readily evaluated in a closed form in the ideal wedge but numerical integration is needed in the case of the penetrable wedge.

Figure 1 illustrates dependence of mode travel time on frequency at upslope/downslope sound propagation in the penetrable wedge. The most apparent difference between the dispersion curves in the wedge and the Pekeris waveguide with the same average depth is the disappearance (for modes n = 2, 3, 4) or contraction (for mode 1) of the anomalous dispersion part of the curves. In addition, at normal dispersion, instantaneous frequencies tend to be higher, at a given travel time, in the wedge. Another important difference from the range-independent case is the large decrease in the maximum travel time. This can be attributed to the minimum group speed occurring at different frequencies at different depths, so that at all frequencies only a small portion of the entire up- or downslope propagation path is covered at near-minimum group speeds. In the warped domain, contraction of the frequency range or complete disappearance of the anomalous dispersion gives the warping results in the penetrable wedge a much closer resemblance to the results in the range-independent ideal waveguide, where the warped dispersion curves are horizontal lines, than in the case of the Pekeris waveguide.

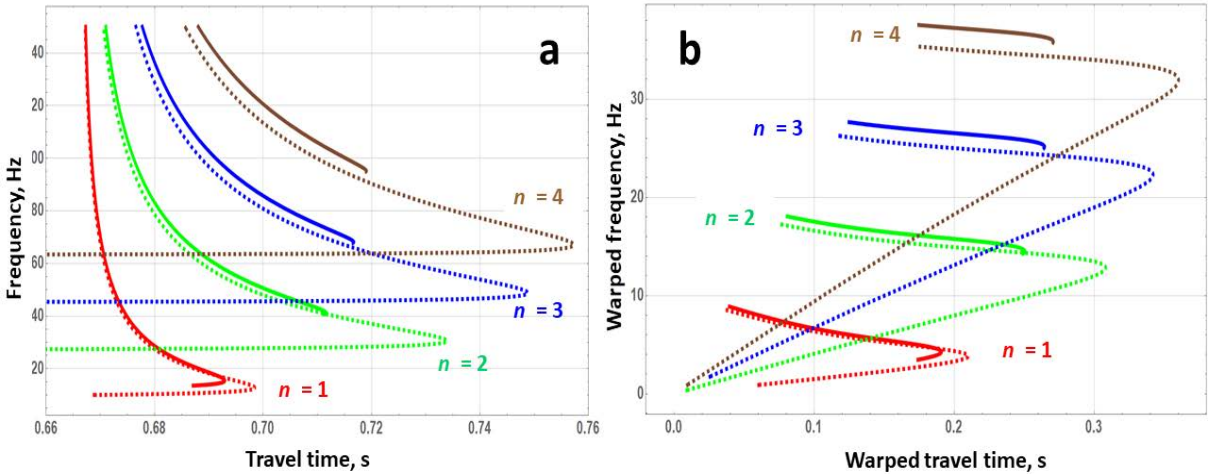


Fig.1: Dispersion curves of the first four adiabatic normal modes in the physical (a) and warped (b) domains at upslope or downslope propagation in a penetrable wedge with a fluid bottom. Source and receiver depths are 50 m and 100 m. Sound speeds in the water column and bottom are c =1500 m/s and c_b =1800 m/s, respectively; the ratio of bottom and water densities m = 2.2. Dashed lines show dispersion curves of normal modes in a range-independent, 75 m-deep waveguide with the same water and bottom parameters and at the same propagation range of 999.167 m.

Figure 2 illustrates modal dispersion at cross-range propagation. Normal modes in a wedge experience stronger dispersion than at propagation over the same range in the Pekeris waveguide with the same physical parameters. This leads to an increase of the received signal duration. In particular, for a fixed frequency range in the normal dispersion band, the

maximum travel time is greatly increased compared to the Pekeris waveguide. Lower frequencies are responsible for later arrivals and are more sensitive to the seafloor slope. In contrast, travel times at higher frequencies, where the value of the group speed approaches the sound speed in water, are insensitive to the slope. The adiabatic mode's travel time reaches its maximum at a higher frequency at cross-slope propagation than in the Pekeris waveguide. At all frequencies considered, sound propagates slower in the wedge than in the Pekeris waveguide. This should be contrasted with the Fermat's principle-related *decrease* in the mode's eikonal (phase) due to horizontal refraction [3].

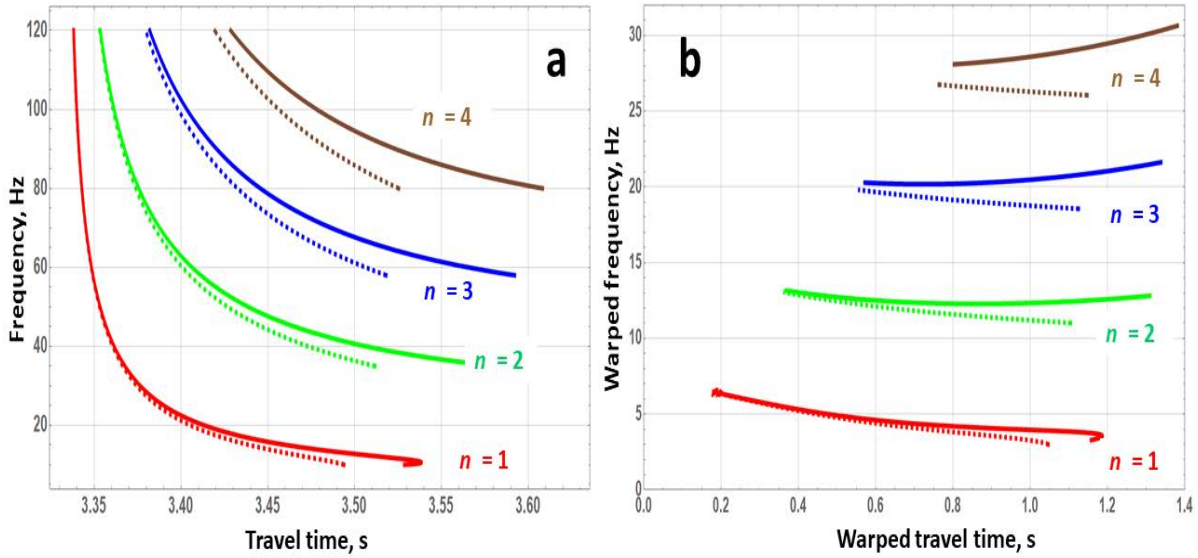


Fig.2: Same as in Fig. 1 but at cross-slope propagation. Source and receiver depths are 100 m. Dashed lines show dispersion curves of normal modes in a range-independent Pekeris waveguide with the same water and bottom parameters and depth of 75 m, at the same propagation range of 5000 m. The dispersion curves are shown in the frequency bands 10–120, 35–120, 58–120, and 80–120 Hz for modes 1, 2, 3, and 4, respectively.

LONR-RANGE NOISE CORRELATIONS AND LOSS OF COHERENCE IN NONSTATIONARY OCEAN

The ocean is a dynamic environment, physical parameters of which evolve in time. In acoustics, the ocean can be often treated as a "frozen" medium with time-independent parameters as long as no appreciable changes occur during the *sound travel time*. This is not the case in acoustic noise interferometry, where the "frozen" medium approximation is justified only when no appreciable changes occur during the much larger *noise averaging time* that is necessary for emergence of an approximation to the deterministic Green's function from cross-correlation functions of diffuse noise. Time-dependence of environmental parameters leads to a deterioration of the long-range correlations of diffuse noise, which underlie the noise interferometry and its applications to passive ocean remote sensing.

Under rather general assumptions, the problem of quantifying the loss of noise coherence in a dynamic ocean proves to be mathematically equivalent to calculating the mean field due to a deterministic point source in an inhomogeneous medium with either random or periodic in time parameters [4]. Figure 3 illustrates coherence loss in a coastal ocean, which is modelled as a Pekeris waveguide, in the presence of tides. To a good accuracy, tides change the water depth simultaneously along the entire sound propagation path between the two receivers involved in evaluation of the noise cross-correlations. A loss of coherence occurs

primarily because the normal mode phase advance at propagation between the receivers changes with the water depth. The coherence loss of individual normal mode components of

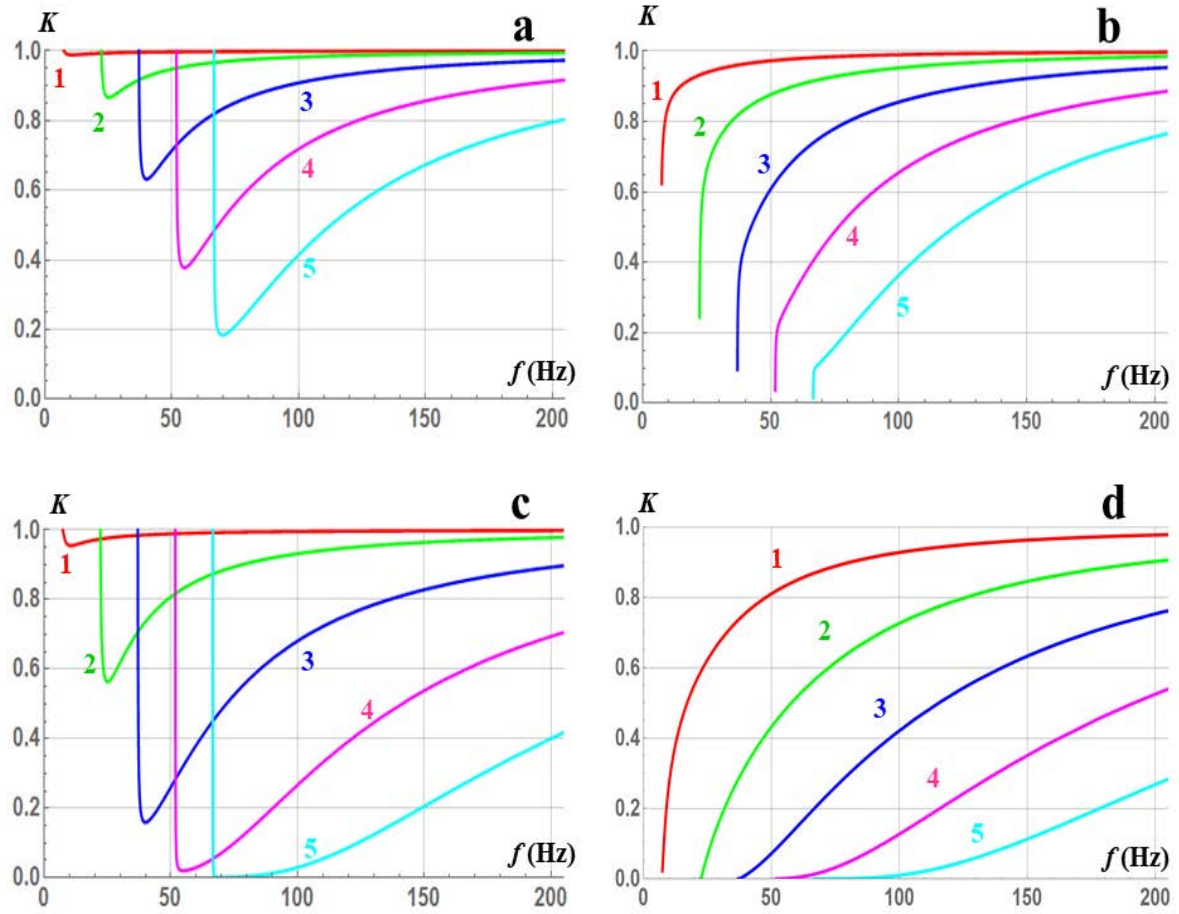


Fig.3: Loss of coherence of normal mode components of noise cross-correlations in a Pekeris waveguide due to ocean surface motion and sound attenuation in the ocean bottom. (a), (c) Coherence loss due to ocean surface motion alone with sound attenuation being negligible. (b), (d) Combined effect of bottom attenuation and surface motion. Horizontal separation of hydrophones is 5 km in panels (a), (b), and 10 km in panels (c), (d). Tidal changes of water depth are modeled as a Gaussian random process with RMS elevation of 0.5 m. Water depth is 100 m; sound speeds in water and fluid bottom are 1537.4 m/s and 1800 m/s; the ratio of bottom and water densities is 2.2. Sound attenuation in the bottom is 0.2 dB/wavelength in panels (b) and (d). Each curve is marked by the order n = 1, 2, 3, 4, 5 of the respective normal mode.

the two-point noise cross-correlation function rapidly increases with range (Figs. 3a, c) similar to the coherence loss of individual surface-reflected rays with a fixed angle of incidence [4]. The trend of the coherence loss to increase with mode order in Fig. 3 is analogous to the increase in coherence loss with angle of incidence of surface-reflected ray arrivals. However, frequency dependence of the coherence loss proves to be rather different for rays and normal modes. For normal modes, the frequency dependence is distinctly non-monotone when absorption is negligible, with zero coherence loss at the cutoff frequency and in the high-frequency limit and a pronounced maximum of the coherence loss at frequencies slightly above the cutoff. This peculiar frequency dependence can be traced back to the fact that the sensitivity of the mode phase to surface elevations is controlled by the derivative of the mode wavenumber, ω/c_n, with respect to water depth H, and

$$\left(\frac{\partial}{\partial H}\frac{\omega}{c_n}\right)_{\omega} = \omega\left(\frac{\partial}{\partial H}\frac{1}{c_n}\right)_{\omega} = \frac{\omega^2}{H}\left(\frac{\partial}{\partial \omega}\frac{1}{c_n}\right)_{H} = \frac{\omega}{H}\left(\frac{1}{u_n} - \frac{1}{c_n}\right). \quad (5)$$

The right-most side of Eq. (5) is zero at mode cutoff and in the high-frequency limit.

Sound absorption in the bottom adds to the coherence loss (Fig. 3b, c) due to exponential decay with range of normal mode amplitudes in the empirical Green's function retrieved from noise cross-correlations. In the Pekeris waveguide, normal mode penetration into the bottom is largest at cutoff and steadily decreases with frequency; at a given frequency, bottom penetration increases with the normal mode order. These properties of normal modes are reflected in the dependencies of the coherence loss on sound frequency and mode order. Note the sharp contrast between frequency dependencies near the mode cutoff of the coherence loss with (Fig. 3b, d) and without (Fig. 3a, c) account for the absorption. In a more realistic scenario, where the bottom attenuation and ocean surface nonstationarity are present simultaneously, the two mechanisms of coherence loss combine and, for the waveguide parameters and the hydrophone separation considered, result in the coherence losses that steadily decrease with frequency and increase with mode order n. Comparison of Figs. 3a–d shows that relative significance of the two mechanisms varies depending on ω an n. However, the relative significance of tides vs. bottom attenuation always increases with increasing horizontal separation of hydrophones.

ACKNOWLEDGEMENTS

This work was supported by the National Science Foundation, grant OCE1657430, and the Office of Naval Research, awards N00014-18-WX-01725 and N00014-19-WX-00462.

REFERENCES

[1] **J. Bonnel and N. R. Chapman**, Geoacoustic inversion in a dispersive waveguide using warping operators, *J. Acoust. Soc. Am.*, 130 (2), pp. EL101–EL107, 2011.

[2] **L. M. Brekhovskikh, and O. A. Godin,** *Acoustics of Layered Media. 2 Point Sources and Bounded Beams*, 2nd edn., Springer, pp. 243–319, 1998.

[3] **O. A. Godin**, A 2-D description of sound propagation in a horizontally-inhomogeneous ocean, *J. Comput. Acoust.*, 10 (1), pp. 123–151, 2002.

[4] **O. A. Godin**, Acoustic noise interferometry in a time-dependent coastal ocean, *J. Acoust. Soc. Am.*, 143 (2), pp. 595–604, 2018.

EXCITATION AND PROPAGATION OF WHISPERING GALLERY WAVES IN VICINITY OF CURVILINEAR ISOBATHS IN SHALLOW WATER

Katsnelson B.[1], Petrov P.[2]

[1] L. Charney School of Marine Sciences, University of Haifa, Israel, 3498838 Haifa,
[2] Far East University, Vladivostok, Russia

Contact author: Boris Katsnelson
University of Haifa, 199 Aba Khoushy Ave., Mount Carmel, Haifa 3498839, Israel
e-mail: bkatsnels@univ.haifa.ac.il

Abstract: *Sound signals propagation in a shallow-water area with bowl-like bottom relief which can be part of an underwater canyon, a bay, a lagoon or a lake is studied. Such area is characterized by curvilinear (in particular circular) isobaths with the depth increasing towards their center of curvature (inner part of the bowl). Manifestation of horizontal refraction in this case consists in the existence of whispering gallery waves (WGWs) localized in some vicinity of isobaths. Main attention is paid to conditions and criteria of excitation of such waves by a point source and specific features of their propagation. It is shown that WGWs can be excited by a source localized both inside the area with bowl-like bathymetry and in its exterior. The latter case can take place due to the "tunneling" of sound wave to the inner part of the bowl from the exterior. Efficiency of the tunneling is estimated for realistic waveguide models. The amplitude of excited WGWs depends on the sound frequency, on the position of the source and parameters of the waveguide, in particular, on the curvature radius of isobaths. Modal structure of whispering gallery beam is analyzed both in an analytical form and using numerical modeling within the framework of Parabolic Equation approach. The respective azimuthal wavenumbers and radial mode functions are computed. Dispersion of such waves is also investigated, and the possibility of their experimental observation is discussed.. [This work was supported by Israel Science Foundation, grant 565/15].*

Keywords: *shallow water acoustics, horizontal refraction, whispering gallery*

1. INTRODUCTION

In the paper as an example shallow water waveguide is considered with rotational symmetry (Fig.1). It is characterized by curvilinear (in particular circular) isobaths with depth increasing toward center of curvature (inner part of bowl).

Let's consider waveguide with changing depth:

$$h_1(r) = \begin{cases} h_1, r < r_1 \\ h_2, r > r_2 \end{cases} \tag{1}$$

and some transition segment $r_1 < r < r_2$. If $r_1 = r_2$ then we have step-like bathymetry.

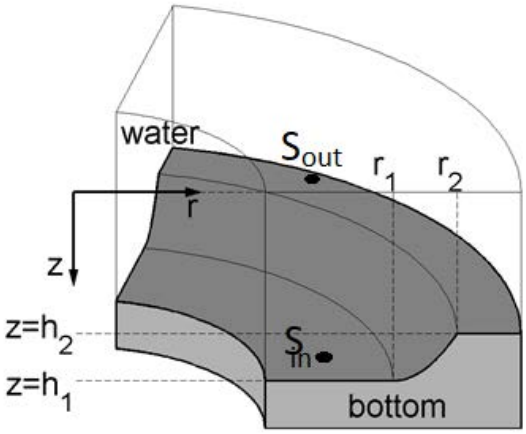


Fig.1. Shallow water waveguide

2. WHISPERING GALLERY MODES

Our goal is to consider possibility of formation of waves localized near the circular (generally speaking curvilinear) isobaths, in other words whispering gallery waves. In theory amplitude of the sound field $P(x, y, z)$ formed by the source with the constant frequency is found in the form of decomposition over adiabatic vertical modes

$$P(x, y, z) = \sum_{j=1}^{N_m} A_j(r, \theta)\phi_j(r, z)\,, \tag{2}$$

where local (adiabatic) eigenfunctions $\phi_j(r, z)$ and the corresponding horizontal wavenumbers $q_j(r)$ can be found via solution of the Sturm problem for every waveguide cross-section. Amplitudes $A_j(r, \theta)$ depending on mode number and frequency describe distribution of acoustic intensity of the corresponding waveguide mode in horizontal plane and satisfy equation

$$\frac{1}{r}\frac{\partial}{\partial r}\left(r\frac{\partial A_j}{\partial r}\right) + \frac{1}{r^2}\frac{\partial^2 A_j}{\partial \theta^2} + q_j^{\,2} P = 0 \tag{3}$$

Amplitudes A_j can be found as decomposition over radial modes $R_\nu(r)$

$$A(r,\theta) = \sum_\nu R_\nu(r)\psi_\nu(\theta) \quad (4)$$

Some of radial modes, with big values of numbers ν~2500 have specific shape with maximum in area of boundary/transition segment and correspond to the whispering gallery modes. At the same time for these modes for low and mid frequency parameter qr~ 10^3-10^4 >>1 and radial modes can be described by Debye asymptotic expression [Abramowitz, Stegun]. In the Fig.2 these modes $R_\nu(r)$ are shown for step-like bathymetry where $r_1 = r_2$ = 6 km, $h_1 = 24$m, $h_2 = 26$m, in this case they are expressed through the Bessel functions. Remark that radial modes in the Fig.2 have only outgoing waves in area $r > r_2$, they can be excited by the source placed inside of deep part of the waveguide (S_{in} in the Fig.1). Outgoing waves in shallow water of can arise as "tunneling".

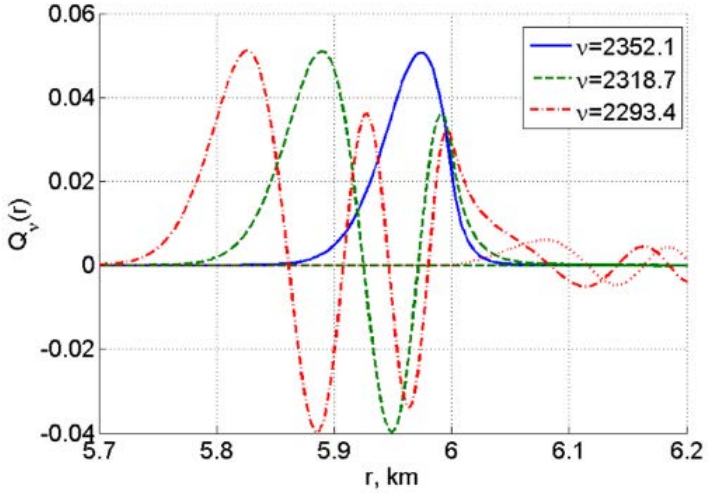


Fig.2. Radial modes, localized in vicinity of boundary between two areas with constant depth

It means that all WGM are leaking (see Fig.3) it correspond to modification of Fresnel's laws and the absence of total reflection for curvilinear boundary [Hentshel et al, 2002] in the case of horizontal rays and vertical modes or imaginary part of eigen values $q_j(r)$. It is clear that for WGM $\mathrm{Im}q_j(r) \ll \mathrm{Re}q_j(r)$

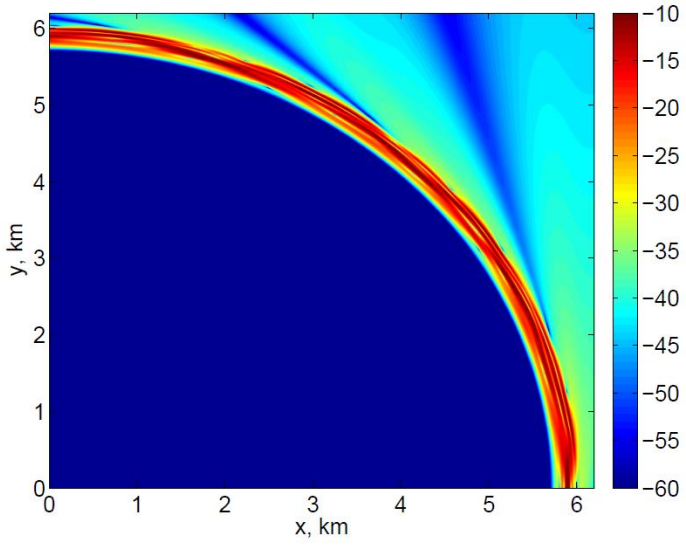


Fig.3 Sound field from the point source, placed inside of deeper part (S_{in})

Rather interesting phenomena for given waveguide is possibility for excitation of WGM by the source, placed in area of smaller depth (source S_{out}) in the Fig.1.

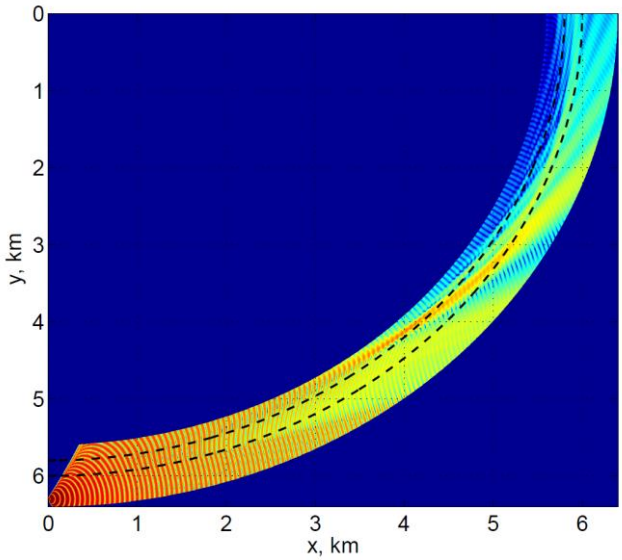


Fig.4 Sound field in horizontal plane excited by the source S_{out}

It means that we can find radial modes $R_\nu(r)$, which contain outgoing and incoming waves in area $r > r_2$. Excitation of WGM by the source, placed in shallow part of the waveguide (Fig.1) corresponds to the so called tunnel effect in quantum mechanics. In the Fig.4 such distribution of the sound field is shown, obtained within the framework of Parabolic equation in horizontal plane, which is derived from Eq(3) by standard way. We can see close distribution of the sound field in horizontal plane in the Fig.3 and Fig.4

3. REFERENCES

Abramowitz & Stegun . Handbook of Mathematical Functions, , Dover Publications, fifth printing

M. Hentschel and H. Schomerus. (2002) Fresnel laws at curved dielectric interfaces of microresonators. Phys. Rev. E, V. 65, 045603~R, DOI: 10.1103/PhysRevE.65.045603.

ACOUSTIC WAVE SCATTERING FROM DYNAMIC ROUGH SEA-SURFACES USING THE FINITE-DIFFERENCE TIME-DOMAIN METHOD AND PIERSON-MOSKOWITZ FREQUENCY SPECTRUM

Alex Higgins[a], Martin Siderius[a]

[a]NEAR-Lab, Electrical and Computer Engineering Department, Portland State University,
PO Box 751 – ECE
Portland, OR 97207-0751

Alex Higgins, higginja@ece.pdx.edu email, 1-503-725-3807 fax
Northwest Electromagnetics and Acoustics Research Laboratory
PO Box 751 – ECE NEAR-Lab
Portland, OR 97207-0751

Abstract: *Most models for underwater acoustic propagation typically assume the sea-surface to be either perfectly smooth or rough but "frozen" in time. Long duration transmissions on the order of tens of seconds are being considered for next-generation sonar. These types of signals improve target resolution and tracking. However, they can interact with the sea-surface at many different wave displacements during transmission. This violates the frozen surface assumption and causes anomalies in the received signal which introduce additional transmission losses and Doppler effects. Full wave propagation models can be used to better understand the mechanisms behind these anomalies. This understanding leads to better system design and enhanced performance without having to perform expensive at-sea experiments. In this paper, a finite-difference time-domain (FDTD) method is developed to model the impact of both roughness and motion of the sea-surface. The FDTD method is a full-wave numeric technique that allows an arbitrary function to define the boundary points within the computational space. Surface motion is accomplished by modifying these boundary points at each time step. The rough, time-evolving sea-surface is modeled using a Pierson-Moskowitz (PM) frequency spectrum, which is simple to implement and fully defined by wind speed and direction. Results from FDTD simulations of static rough sea-surfaces are compared to a previously established integral equation solution method to evaluate the validity of the approach. Agreement is also demonstrated for FDTD simulations of a dynamic rough sea-surface and a theoretic statistical model. [Work supported by the Office of Naval Research]*

Keywords: *Underwater acoustic propagation; Finite-difference time-domain; Pierson-Moskowitz frequency spectrum; Dynamic rough sea-surface*

INTRODUCTION

Over the past few decades interest has increased in creating an internet of underwater things[1] (IoUT). Doing so would greatly alleviate difficulties in underwater exploration and monitoring by removing the necessity of tethering underwater vehicles and sensor systems. Due to rapid attenuation underwater electromagnetic solutions cannot be directly transferred from land to underwater channels. In this regime acoustic modem are predominately used for communications. These types of systems are hindered by their high bit error rates and long propagation delays. Additionally, sound speed variations in depth can cause shadow zones and loss in connectivity. Due to the large coverage areas and variations in the channel, measurements are not feasible. Modeling techniques are therefore needed to offer insights and drive the design of acoustic communication systems that can mitigate these issues.

Long duration signals on the order of tens of seconds are being considered for the next-generation[2] of SONAR. These types of signals improve target resolution and tracking. However, they interact with the sea-surface at many different displacements along the sea-surface during their transmission. This violates the frozen boundary assumption of most modeling techniques and causes anomalies in the received signal that add to transmission losses and introduce Doppler effects. Adding realistic motion to the sea-surface boundary would increase the accuracy of the model and provide insights into the mechanisms of the observed anomalies. These insights drive decisions that help SONAR designers build more robust systems.

A modeling technique that is capable of handling boundary roughness and motion is required. The finite-difference time-domain (FDTD) method fits these requirements. In the next section, the FDTD method for scalar acoustic pressure fields is discussed. In this section model results from a modified Image method (M-IM), Integral equation (IE) approach and Kirchhoff approximation (KA) are compared to FDTD simulations. Then, random rough sea-surfaces are discused. Models capable of simulating static random roughness are compared. Then the spectral approach[3] proposed by Pierson-Moskowitz (P-M) is combined with the FDTD method to simulate realistic dynamic rough sea-surfaces.

FINITE-DIFFERENCE TIME-DOMAIN METHOD

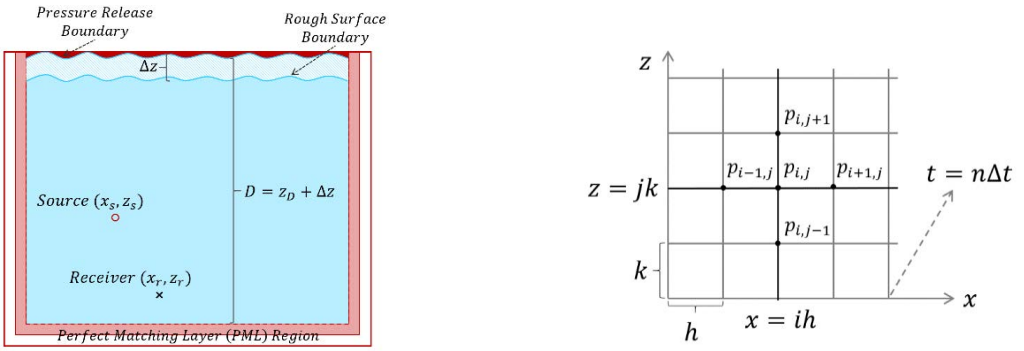
The finite-difference time-domain method is a well establish numeric technique that is used to approximate the wave equation. In its general form it can be applied to solve any ordinary and partial differential equation. It has been used extensively in electromagnetics to simulate Maxwell's equations[4]. Typically used for propagation and scattering problems that include complicated boundary conditions or geometries, it offers insights as to how fields interact spatially and temporally and is capable of ultra-broadband solutions in a single simulation. The FDTD method has also been used in seismic exploration and in underwater acoustics. Practical examples include; seismic propagation around faults zones or areas which contain potential oil and gas traps or acoustic interactions with elastic bottoms and scattering from geometric irregularities such as keels and leads on the underside of Artic ice cover.

In this section the wave equation which governs seismo-acoustic propagation is implemented using central finite-differences over a two-dimensional mesh that represents an ocean half-space, as shown in Fig. 1. The two dimensional (2D) scalar wave equation for an acoustic pressure field produced by a transient line source is

$$\frac{\partial^2}{\partial x^2}p(x,z;t)+\frac{\partial^2}{\partial z^2}p(x,z;t)-\frac{1}{v_c}\frac{\partial^2}{\partial t^2}p(x,z;t)=-S(t)\delta(x-x_s)\delta(z-z_s), \qquad (1)$$

where p is the acoustic pressure, x and z are spatial coordinates within the computation grid, t is time, v_c is the acoustic velocity, $S(t)$ is an arbitrary time dependent line source function and

(x_s, z_s) are the source position. Equation (1) is a second-order partial differential equation describing acoustic propagation. By discretization of the independent variables the differential operators are locally approximating by finite-differences. Discretization for the ocean half-space is shown in Fig. 1-b. Where a rectangular mesh over the entire computation domain is defined as $(x_i, z_j; t_n) = (ih, jk; n\Delta t)$, $i = 0 \cdots N$, $j = 0 \cdots M$ and $n = 0 \cdots T$.



(a) Ocean half-space *(b) Finite-difference computation domain*

Fig. 1: Ocean half-space and computation domain diagrams for two-dimensional finite-difference time-domain simulations.

Conforming to this definition, the spatial and temporal operators in (1) are replaced by their central finite-differences. Solving the discretized wave equation for the scalar pressure at the next time-step $p_{i,j}^{n+1}$ provides

$$p_{i,j}^{n+1} = u^2\left(p_{i-1,j}^{n} + p_{i+1,j}^{n} + p_{i,j-1}^{n} + p_{i,j+1}^{n}\right) + 2(1 - 2u^2)p_{i,j}^{n} - p_{i,j}^{n-1}, \qquad (2)$$

where n is the time-step index, i is the range index, j is the depth index and $u = v_c n/i$. The right-side of (2) is referred to as the updated part of the equation. The acoustic pressure at the next time-step t_{n+1} gets updated with the finite-difference of the current time-step t_n and the previous t_{n-1}. In this manner, the field is approximated for all grid points in the mesh and marched/stepped forward in time. At any given time-step only knowledge of the current and previous time-step are needed, with exception to the boundaries along the left $(x = x_0, z)$, bottom $(x, z = z_M)$ and right $(x = x_N, z)$ edges of the mesh. These are special cases for (2) in which there is no adjacent pressure value.

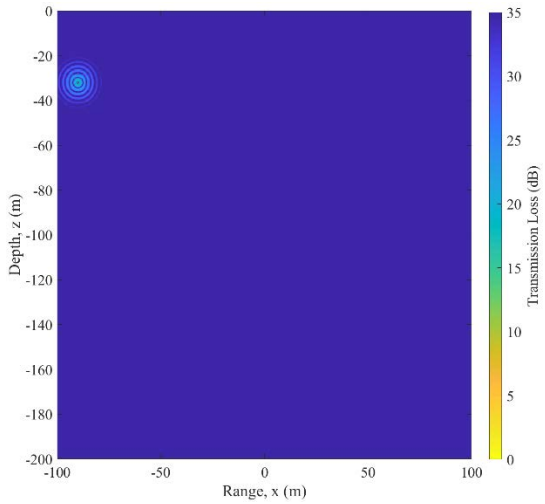
The ocean half-space model (Fig. 1) dictates that the boundary along the sea-surface be pressure-release. This is implemented using a Dirichlet boundary condition, effectively maintaining that the mesh points along the sea-surface are zero. This will ensure that (2) is unbalanced at $p_{i,j+1}^{n} = 0$. Resulting in the next time-step being offset by the same amount. This is analogous to reflection. Along the left, right and bottom edges we have arbitrary boundary conditions. For all three of these cases the field needs to continue propagating as if it did not encounter a boundary. To enforce this type of behaviour while maintaining the integrity of the incident pressure point a perfect-matching layer (PML) is implemented around the edges. This type of boundary condition requires a minimum of two additional prior time-steps in order to cancel only the reflected amount at the boundary point. This is analogous to rapidly attenuating the field over two time-steps.

A high-level algorithm for the 2D FDTD simulations presented throughout this work is summarized in Table. 1. A baseline 2D FDTD simulation of a smooth static sea-surface is

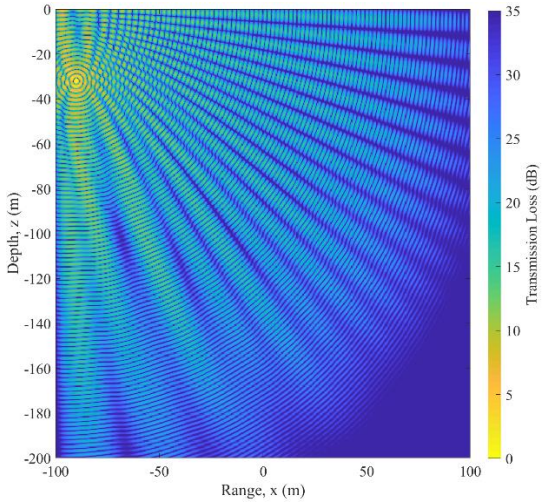
Step	*Description*
1	Determine highest acoustic frequency of interest
2	Initialize the computation domain
3	Determine arbitrary source function
4	Determine finite-difference for each mesh point at time-step t_n
5	Store points of interest for post-processing
6	Advance pressure fields, i.e. $p_{i,j}^{n} = p_{i,j}^{n+1}$
7	Inject source function value at time-step t_{n+1}
8	Repeat steps 3 – 6 until event of fields has occurred.

Table 1: High-level finite-difference time-domain algorithm.

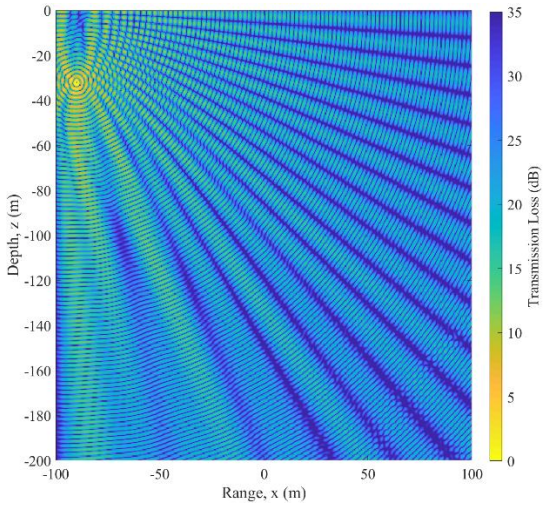
shown in Fig. 2. The source function is a unity amplitude sinusoidal tone $f_s = 375\ Hz$ located at $(x_s, z_s) = (-90, -32)$. A Tukey window was used with $\alpha = 0.075$ to ease the beginning and ending transitions of the source function. Using a wavelength divisor of 10 sets the mesh spacing equal to $0.4\ m$. A rectangular mesh was chosen for simplicity, other approaches are available but are outside the scope of the work present here. To enforce stability of the PML boundary conditions the acoustic wave needs to propagate one wavelength over two time-steps $\Delta t = 0.4/(2v_c) = 0.133\ ms$. After $t = 21\ ms$ the source has radially propagated $32\ m$ and exhibits $30\ dB$ transmission loss due to geometric spreading. This is observed in Fig. 2a where the field $\sim 12\ m$ away from the source is in the $30 - 35\ dB$ range. At $t = 0.168\ ms$ the field along z_s has reflected at the sea-surface and propagated $252\ m$. This is seen the Fig. 2b where the field extends beyond the computation space at $z = -200\ m$. The total pressure clearly shows a pattern of nulls due to interference by the direct path from the source and the sea-surface multipaths. Following a sea-surface reflected path from the lower bottom-right corner of the computation space to the source traces out $\sim 232.35\ m$. This is less than the distance previously stated directly under the source. Fig. 2b demonstrates this behaviour as the extent of the wave front is in the bottom-right corner of the computation space. When the simulation reaches a steady-state the entire computation space is filled with the total field and the familiar Lloyds Mirror pattern is easily identifiable in Fig. 2c.



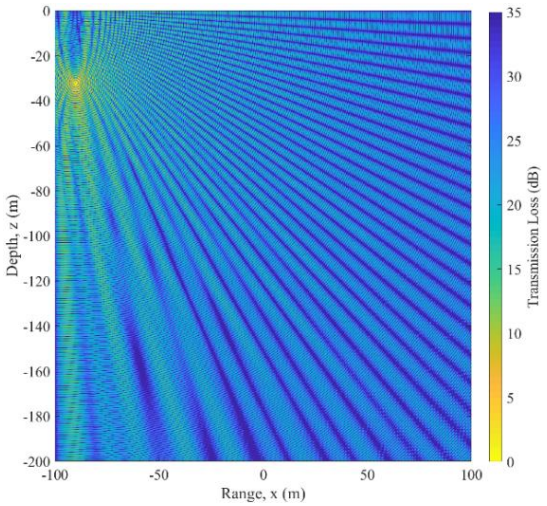
(a) t = 0.021 s, f_s = 375 Hz



(b) t = 0.168 s, f_s = 375 Hz



(c) $t = 0.478\ s, f_s = 375\ Hz$



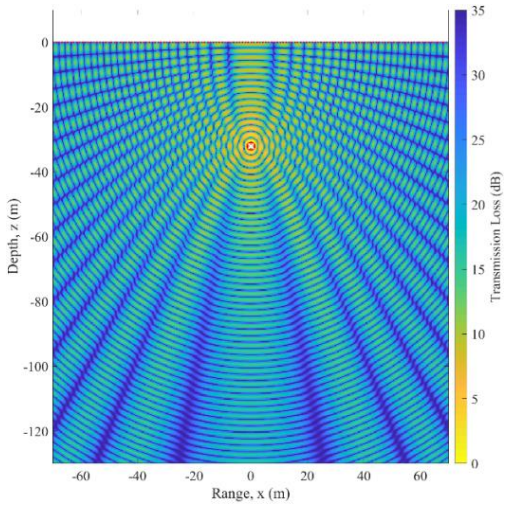
(d) $t = 0.478\ s, f_s = 750\ Hz$

Fig. 2: Pressure field at varying times for a 2D finite-difference time-domain simulation of a smooth static sea-surface.

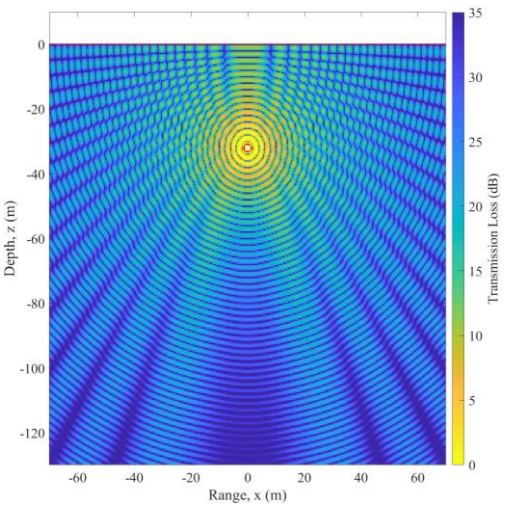
This same scenario happens when the simulation is run and the frequency is doubled (Fig. 2d).

The 2D FDTD implementation is further verified by comparing the results to three other numeric techniques; Image method[6], Kirchhoff approximation and Integral equation[7]. These techniques numerically solve the Helmholtz equation with solutions in the time-harmonic form. Finite-difference time-domain simulations must reach steady-state before the results can be compared to these models. This is demonstrated in Fig. 3 for the same tonal source function located at $(x_s, z_s) = (0, -32)$. All three techniques exhibit the expected interference pattern by a static smooth sea-surface. The IE and KA have less than $0.04\ \%$ average difference across the computation space. The Image method has slightly more overall transmission loss which can be attributed to normalization errors introduced by a singularity at the source point. Additionally, the FDTD method shows less transmission losses directly below the source due to the continuous time source function.

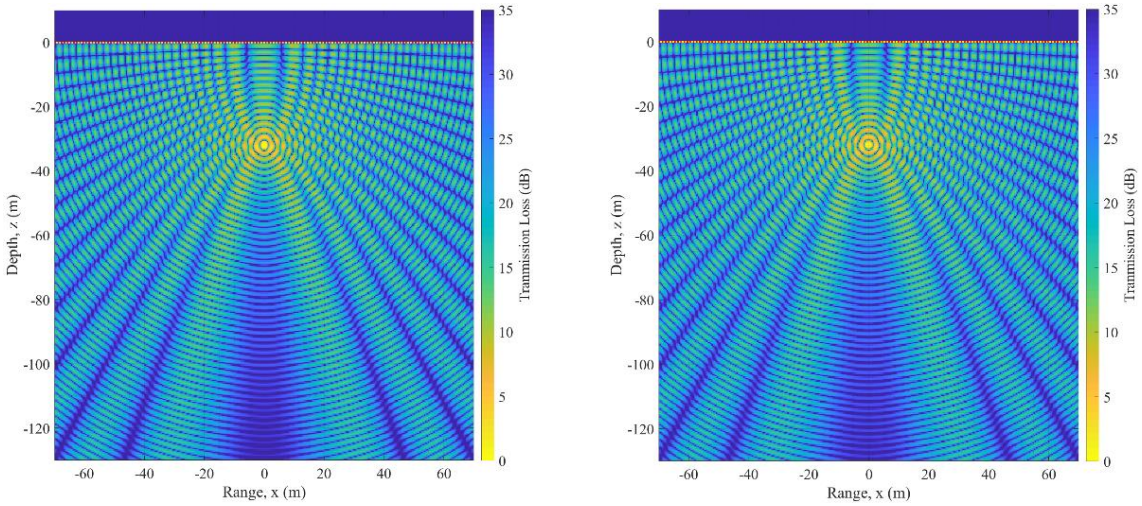
With confidence that the 2D FDTD implementation properly simulates the acoustic physics of the ocean half-space a more realistic sea-surface model is desired. In the following section two random rough sea-surface models are discussed. First static sea-surfaces generated by a Gaussian roughness model then a fully developed wind sea model produced by P-M frequency spectrum.



(a) Finite-difference time-domain



(b) Modified Image method



(c) Integral equation method *(d) Kirchhoff approximation*

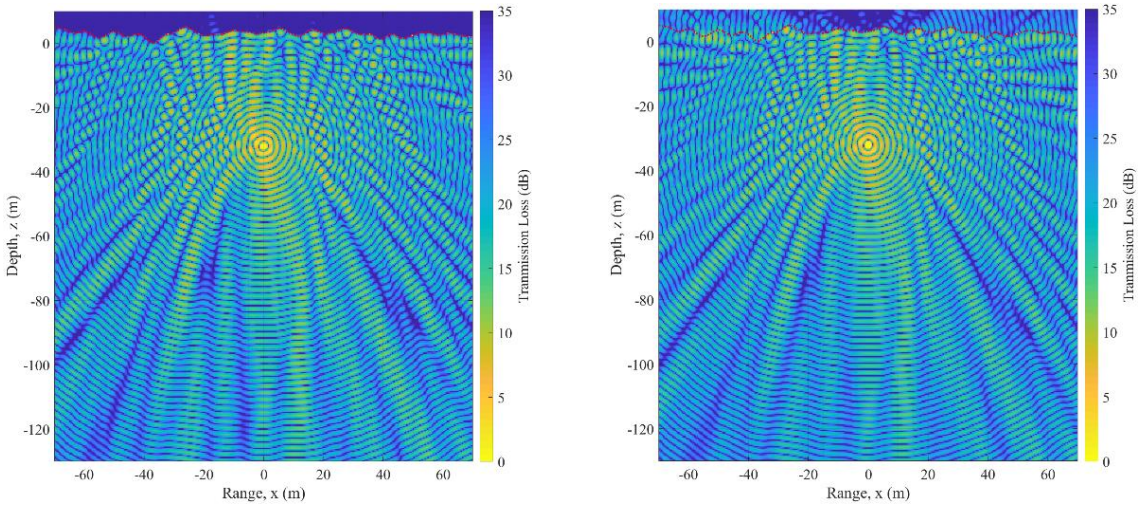
Fig. 3: Comparison of pressure field determined by different models for a static smooth sea-surface t = 0.082 s, f_s = 375 Hz.

RANDOM ROUGH SEA-SURFACES

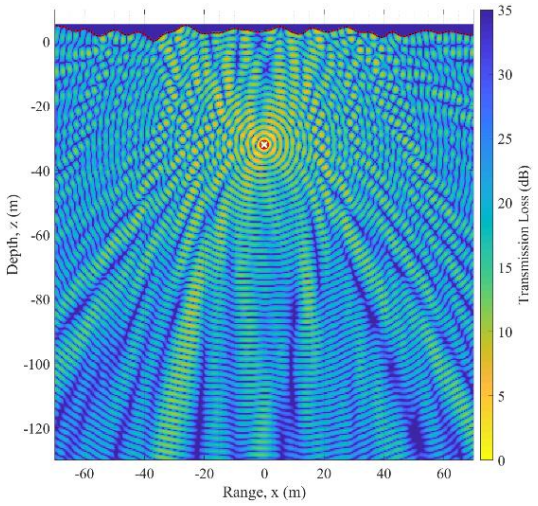
A more realistic sea-surface model would include roughness and motion to mimic gravity waves produced by the fluctuations of fluids. To start the sea-surface is extended to the static Gaussian roughness model[6] and then to a fully developed wind seas model as described by the P-M spectrum[3].

The Image method is unable to handle scattering due to roughness along the sea-surface boundary. This is implicit in its formalization which only takes into account specular reflections by placing the source "image" at a mirrored position above the boundary. The IE and KA include scattering terms and can be compared to 2D FDTD simulations that include a random Gaussian roughness model for a static sea-surface. Both the IE and KA provide solutions that are time-harmonic and therefore are currently unable to handle dynamic sea-surfaces.

The static Gaussian rough sea-surface is defined by a root-mean-square wave height $h_{rms} = 0.212\,\lambda$ and coorelation length of $l_x = 0.9\,\lambda$. The techniques compared use the same static Gaussian rough sea-surface. The computation grid has been limited to $x = [-70..70]$, $z = [-140..0]$. The same source function and position were used as in the prior section. The steady-state field of the FDTD simulation occurs at times $t > 0.124\,s$.



(a) Integral equation method t = 0.167 s *(b) Kirchhoff approximation t = 0.167 s*

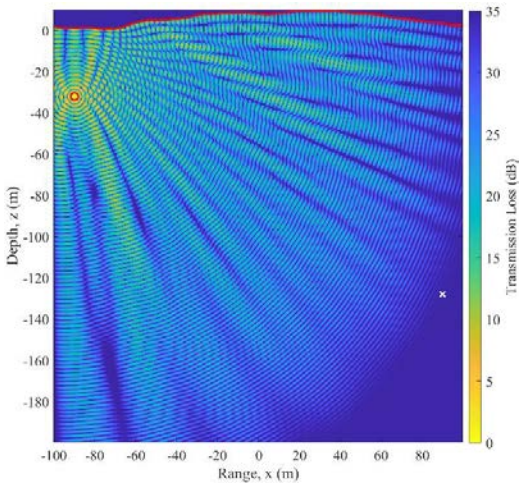


(c) Finite-difference time-domain t = 0.162 s

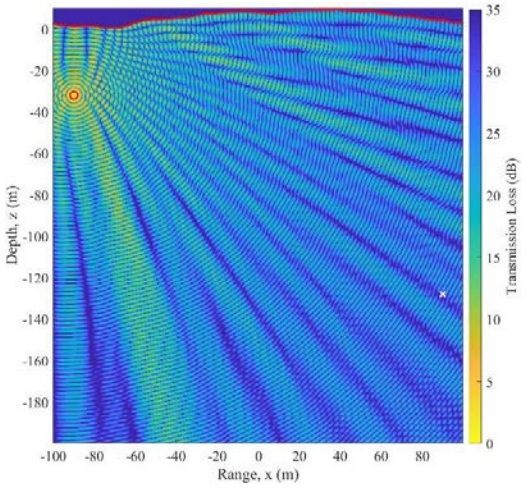
Fig. 4: Comparison of pressure field determined by different models for a static rough Gaussian sea-surface f_s = 375 Hz.

Discrepancies in the FDTD field and the IE and KA in Fig. 4 are due to slight differences in Δt. In the FDTD case $\Delta t = 0.4/(2v_c) = 1.33\overline{3}\ ms$ and for the IE and KA $\Delta t = 1.3\ ms$. This causes a phase offset of $3.33\overline{3}\ \mu s$ between the fields in Fig. 4a-b and Fig. 4c which is less than one FDTD time-step.

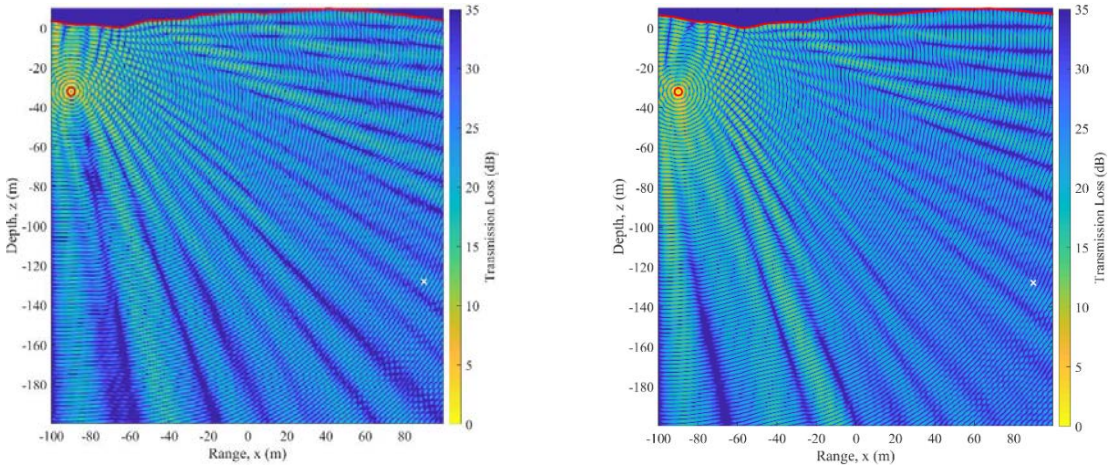
The P-M spectrum approach is well suited for modeling rough, time-evolving sea-surfaces. It is relatively simple to implement and fully defines the sea-surface by wind speed and direction. Preliminary results for 2D FDTD simulations using a P-M spectrum to generate a dynamic rough sea-surface boundary are shown in Fig. 5. The same tonal source function located at $(x_s, z_s) = (-90, -32)$ was used for these simulations. The P-M spectrum was generated using a wind velocity $v_w = 22.6\ m/s$ and a dominant wind direction $\phi_w = 0^\circ$. These parameters where chosen to mimic a Beaufort Sea State (SS10) which is considered storm condition wind forces. Using an extreme case accentuates the motion of the sea-surface over the relatively short duration of simulation. For the simulations in Fig. 5 the peak wave travels approximately $12\ m$ in the positive x-direction. This is further indicated by the static white x-marker located at $(x, z) = (90, -128)$ in Fig. 5b-c which passes through a null as the sea-surface minimum advances.



(a) t = 0.168 s



(b) t = 0.478 s



(c) t = 0.942 s *(d) t = 2.140 s*

Fig. 5: Pressure field at increasing times for a 2D finite-difference time-domain simulation of a rough dynamic sea-surface modelled by a Pierson-Moskowitz spectrum.

CONCLUSIONS

The finite-difference time-domain method has been implements for acoustic wave propagation and scattering within an ocean half-space. This technique has been compared to other numeric methods for smooth and rough Gaussian static sea-surfaces. The IM is unable to handle specular scattering due to its requirement of placing a fictions source at a mirrored location above the sea-surface boundary. The IE and KA are well suited for static random sea-surfaces but lack realistic surface wave motion in their formalizations and suffer from potential loss in generality due to conversions from their time-harmonic solutions. The FDTD method determines the pressure field at a marched-step time indices which easily accommodates boundary motion. The well-established P-M frequency spectrum provides realistic dynamic sea-surfaces and has been used incorporated into FDTD simulations. Insights gained by FDTD simulations with realistic sea-surfaces provide a practical and cost effective way to guide design decisions for acoustic modem and next-generation SONAR systems.

ACKNOWLEGMENTS

This work has been funded by the United States Office of Navy Research (ONR).

REFERENCES

[1] **M. C. Domingo**, "An overview of the internet of underwater things," Journal of Network and Computer Applications, vol. (35-6), pp. 1879 – 1890, 2012.

[2] **D. A. Abraham, S. M. Murphy, P. C. Hines, and A. P. Lyons**, "Matched filter loss from time-varying rough-surface reflection with a small effective ensonified area," IEEE Journal of Oceanic Engineering, vol. (43-2), pp. 506 – 522, 2018.

[3] **W. J. Pierson, Jr and L. Moskowitz**, A proposed spectral form for fully developed wind seas based on the similarity theory of S. A. Kitaigorodskii, New York University Bronx Department of Meteorology and Oceanography, Tech. Rep. AD0421610, 1963.

[4] **K. Yee**, Numerical solution of initial boundary value problems involving Maxwell's equations in isotropic media, *IEEE Transactions on Antennas and Propagation*, vol. (14), pp. 302 – 307, 1966.

[5] **F. B. Jensen, W. A. Kuperman, M. B. Porter, and H. Schmidt**, *Computational Ocean Acoustics*, 2nd ed, R. T. Beyer, Springer Publishing Company, pp.394 – 406, 2011.

[6] **E. I. Thorsos**, "The validity of the Kirchhoff approximation for rough surface scattering using a Gaussian roughness spectrum," The Journal of the Acoustical Society of America, vol. (83-1), pp. 78 – 92, 1988.

SEA-SURFACE SCATTERING OF A CONTINUOUS WAVE IN THE 1 TO 200 HZ FREQUENCY RANGE

Iannis Bennaceur[a], Xavier Cristol[a]

[a]THALES Defense Mission Systems FRANCE

525 route des Dolines, 06560 Valbonne FRANCE.
iannis.bennaceur@fr.thalesgroup.com

Abstract: *The purpose of this paper is the scattering of a continuous wave in the 1 to 200 Hz low frequency range by the fully developed swell of the Atlantic Ocean in a deep-water configuration. Considering the scales of the problem, we use the small-perturbation method coupled with the normal-mode theory and an asymptotic analysis to derive the first order spatio-temporal scattered pressure field p_1. This approach, greatly inspired by Labianca and Harper, allows us to express p_1 depending on the normal-mode functions and their associated wave-numbers that we compute numerically using an in-house modal propagation code called MOCTESUMA. This code may be run for an ocean waveguide with any particular sound-speed profile and takes into account the propagation into multiple-layers sea-bottom. First, we compare the computed power spectral density of pressure fluctuations with the one measured experimentally in the Sargasso Sea [1]. In a second phase we compare the propagation losses undergone by the scattered field and the non-perturbed field in the shadow zone appearing when the acoustic source is located in the summer thermocline. Finally we look at the level of scattered energy on both sides of the scattering mechanism cut-off ratio $\Gamma/k_0 = 2$, depending on the source immersion.*

Keywords: *Underwater acoustic modelling, sea-surface scattering, low-frequency range, deep-water acoustic propagation*

1. INTRODUCTION AND METHOD

The scattering of acoustic waves by rough surfaces has been widely studied in the past decades [2] and results to amplitude and phase modulation as well as a spatial and spectral re-distribution of the acoustic energy. The resolution method for a scattering problem depends both on the emitted wave and on the rough surface scales. In this study, we consider the scattering of low-frequency emissions (f_0 from 1 to 200 Hz meaning a wavelength λ_0 varying between 7.5 and 1500 m) by the fully developed swell which typical scales h and L, respectively the root-mean square value of the surface height fluctuations and their horizontal scale, vary from 1.3 10^{-3} to 1.2 m and from 0.21 to 200 m depending on the sea-state. Since $h/\lambda_0 \ll 1$ and $h/L \ll 1$, we use the small perturbation method. This method consists in evaluating the first terms of the perturbed pressure field Taylor development with h as small parameter. Here we focus on the computation of the first order term p_1 which gives a good approximation of the energy re-distributed on frequencies adjacent to the carrier.

We have followed [3] to derive the exact integral solution of the scattered pressure field p_1 (cf. equation 15(b) of [3]) before leading the same asymptotic analysis as [4] valid for source-receiver distances higher than 2.5 km, using equation (2) p.399 of [5] to obtain a simplified expression for p_1. The derivation of p_1 is made under the hypothesis that the swell is a sinusoidal wave $u(x,t) = 2\cos(\Gamma x - \Omega t)$ with Γ and Ω respectively the wave-number and pulsation of the swell that propagates in the $\boldsymbol{e}_x$ direction at the velocity $V_S = g/\Omega$ with g the gravity constant. Furthermore, the source and acoustic receiver are static. The major difference with previous works ([3], [4], [6] and [7]) lies in the use of the in-house modal propagation code MOCTESUMA for the computation of modal functions $u_m(\omega)$ and associated wavenumbers $K_m(\omega)$ of ocean waveguides with any particular sound-speed profile. Also we add an imaginary part in $K_m(\omega)$ enabling the convergence of the computation and we do not consider that $\omega_0 \pm \Omega \approx \omega_0$ anymore.

2. RESULTS

The total pressure field, truncated at the first order term in h, may be expressed as :

$$p(\boldsymbol{r},t) = p_0(\boldsymbol{r},t) + hp_1(\boldsymbol{r},t) = T_0(\boldsymbol{r})\mathrm{e}^{-i\omega_0 t} + T_1^-(\boldsymbol{r})\mathrm{e}^{-i(\omega_0-\Omega)t} + T_1^+(\boldsymbol{r})\mathrm{e}^{-i(\omega_0+\Omega)t} \quad (1)$$

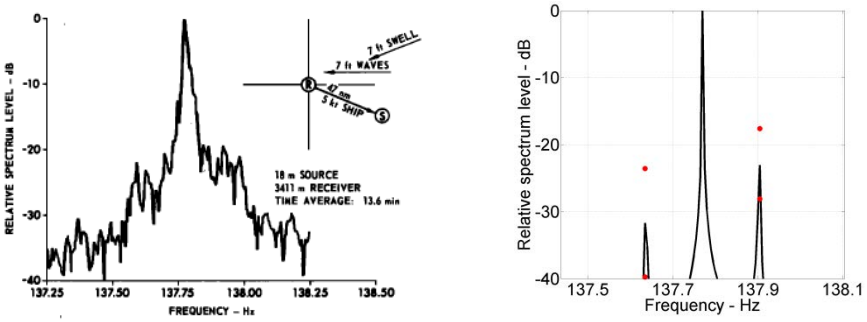
where the quantities T_0, T_1^- and T_1^+ respectively give the level of energy at the source frequency ω_0 and within the side-lobes centred at $\omega_0 \pm \Omega$. All the computations have been realised with a seabed that presents a relatively soft muddy first layer with a porosity of 65%, a density of 1.41 tonne/m^3 and an upper velocity of compression P-waves of 1534 m/s.

2.1. Comparison to Shooter & Mitchell measurements

The authors in ref. [1] have conducted an experiment in the Sargasso Sea during the summer period to highlight the effect of the scattering of a continuous wave (CW) by the agitated sea-surface. They have hauled an acoustic source immersed at 18 m, emitting at 138 Hz, at a speed of 5 knots and computed the power spectral densities (PSD) of pressure fluctuations received at a depth of 3411 (cf. *Fig 1(a)*) and 4789 m. They have showed the spectral re-distribution of the acoustic energy into side-lobes, located between 0.1 and 0.2 Hz away from the Doppler shifted source frequency, which are typical frequencies of the swell.

Moreover, the PSD exhibits a dissymmetry between the levels of its two side-lobes due to the fact that the receiver is more deeply immersed than the source.

For the purpose of supporting our theoretical and numerical approach, we have computed the PSD of the pressure field expressed by (1) in a configuration as close as the one of the experimental campaign in order to compare the level of the side-lobes. According to the environmental data described in [1], we have estimated the sea-state to be around 4 and 5 during the experiment, meaning a wind speed of 10.3 m. Using the JONSWAP model, we have computed the pressure field with $\Omega = 0.84$ rad/s, $h = 0.54$ m and $\Gamma = 0.072$ m^{-1}. *Fig. 1(b)* shows the computed spatially averaged spectra, artificially shifted by -0.23 Hz to take into account the Doppler effect, along with a measure of the spatial spectra's dispersion. The level of the right side-lobe is very close to the experimental one whereas the level of the left side-lobe is a bit lower. Furthermore, our computation exhibits the same side-lobes level dissymmetry.



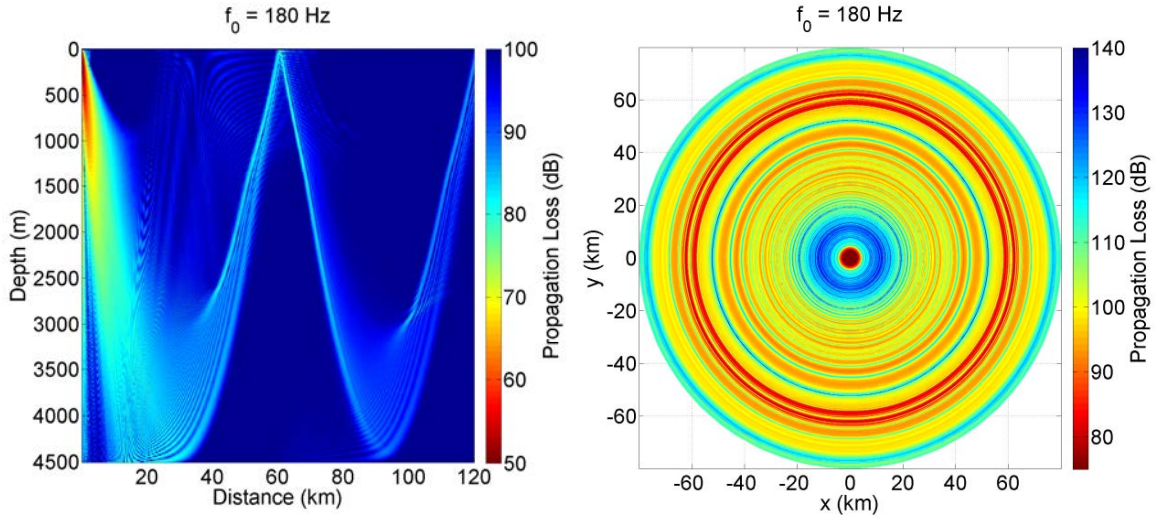
(a) *(b)*

Fig.1: Power spectral densities (a) from [7] and (b) computed.

2.2. Shadow zone filling by the scattered pressure field

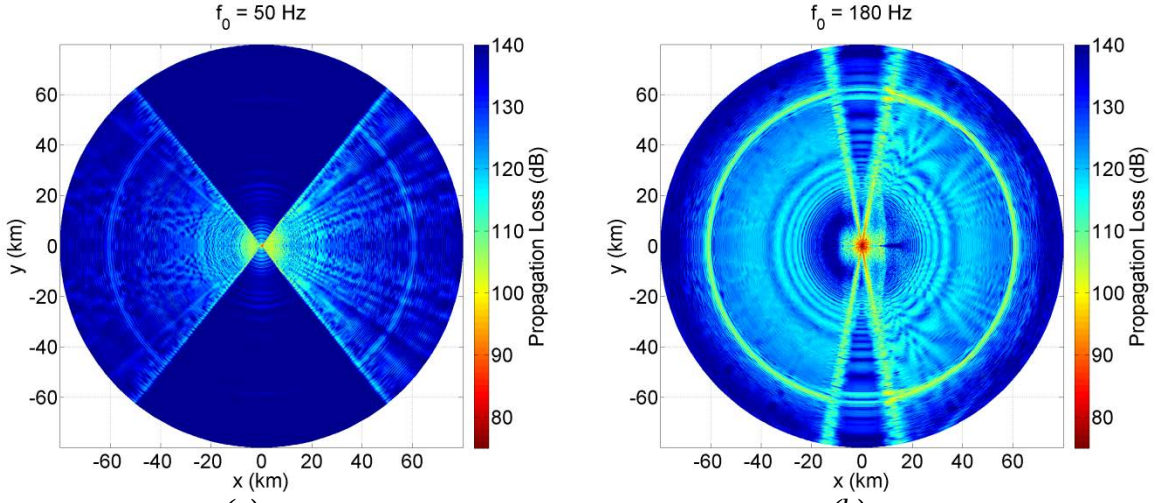
In this section we compute the terms T_0, T_1^- and T_1^+ of eq. (1) with a deep-water, north Atlantic sound-speed profile during the summer period, with a source immersed at $z_0 = 5$ m emitting at $f_0 = 50$ or 180 Hz and a receiver immersed at $z_R = 300$ m. We choose a sea-state of 3 leading to $\Omega = 1.6$ rad/s, $h = 0.15$ m and $\Gamma = 0.26$ m^{-1}. *Fig.2(a)* represents the propagation losses in the vertical plane if the sea were perfectly flat ($-20\log_{10}|4\pi T_0|$) for a source emitting at 180 Hz. We observe a strong shadow zone spreading from 3 km to 20 km in range and from 0 to 1000 m in depth and a strong decrease of the propagation losses around 60 km, region called the first convergence zone. *Fig.2(b)* represents the propagation losses in the horizontal plane, the source being located at $x_0 = y_0 = 0$ m. Since the sound-speed profile is uniform in this plane, the propagation losses present a revolution symmetry around the source location. We clearly observe the shadow zone for the radii between 3 and 20 km as well as the first convergence zone around 60 km.

Let us focus now on the scattered pressure field. We plot on *Fig.3* the propagation losses related to the left side-lobe ($-20\log_{10}|4\pi T_1^-|$) in the horizontal plane for the source emitting at 50 and 180 Hz. We recall that the swell progresses in the $\boldsymbol{e}_x$ direction. At 50 Hz, we see that the level of scattered energy is relatively high (low propagation losses) for a specific angle of aperture with respect to the swell propagation direction and strongly decreases after a "*critical angle*" $\theta_c \approx \pm 54°$. The spatial distribution of the scattered energy for the $x > 0$ looks like the one for the $x < 0$ but is not exactly the same since the plane $x = 0$ is not a plane of symmetry. At 180 Hz, θ_c is higher, approximately equal to ±81° and the scattered energy level difference on both sides of the *critical angle* is lower. Furthermore, we notice that the level of scattered energy is globally higher in the directions defined by the *critical angle* than elsewhere, especially for distances lower than 15 km. Finally, we observe that the level of scattered energy increases around the first convergence zone.



(a) *(b)*

Fig.2: Propagation losses for a source emitting at 180 Hz in (a) the vertical and (b) the horizontal plane.



(a) *(b)*

Fig.3: Propagation losses of the left side-lobe for (a) f_0 =50 and (b) f_0 =180 Hz.

We have noticed that the *critical angle* is close to the Bragg resonance angle $\psi = \operatorname{acos} \Gamma/2k_0$, whose definition and physical implications are illustrated in [9]. Considering that the grazing angle of incident rays on the sea-surface are low ($k_{iz}^* \to 0$) according to the considered source-receiver distances, we find, using the wave-number diagrams approach [8], that a necessary condition for the first order scattering to occur is that $k_{ix}^* > \Gamma/2k_0$ inducing $\theta < \psi$ with k_{ix}^* the normalized incident wave-number component in the $\boldsymbol{e}_x$ direction.

We now compare the propagation losses undergone by the pressure field $p_0$with the ones undergone by the scattered pressure field at $f_0 - \Omega$ inside the shadow zone by plotting on *Fig.4* the quantity $\Delta^- = -20 \log_{10} |T_1^-/T_0|$ in a dB scale. We have assigned the value $\Delta^- = 0$ when the propagation losses associated with the left side-lobe are higher than 100 dB in order to focus only on the relatively low level of propagation losses. We then observe that the level of propagation losses associated with hp_1 is, in the directions of the critical angle, 5 to 30 dB lower than the ones of p_0 for a source-receiver distance going from 5 to 20 km. This means that the shadow zone is filled up by the scattered pressure field on the critical angle directions. This may have an impact on detection in the shadow zone; an array processing may fail to detect at f_0 whereas it would have detected at $f_0 - \Omega$. Such filling is observed, on a smaller scale, from $f_0 = 130$ Hz. The truthfulness of such observation may be questionable since, in the small-perturbation theory, hp_1 is supposed to always be way lower than p_0. This is indeed

the case for the vast majority of receiver positions, frequencies and environmental configurations tested but our approach may still fail when getting close to the *critical angle*. It would be worth validating this observation, either with another theoretical approach or with a dedicated experiment.

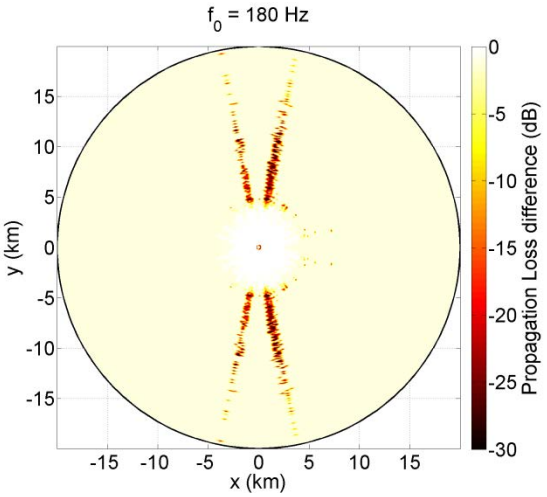
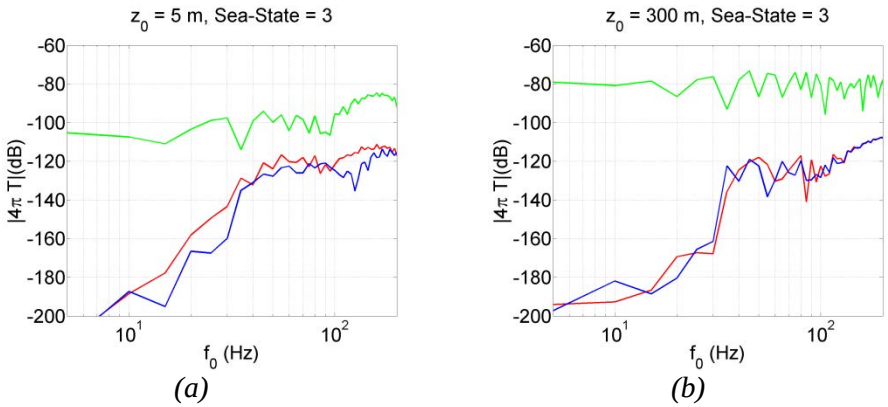


Fig.4: $-20\log_{10}|T_1^-/T_0|$ *for* f_0 *=180 Hz.*

2.3. Cut-off frequency of the scattering mechanism

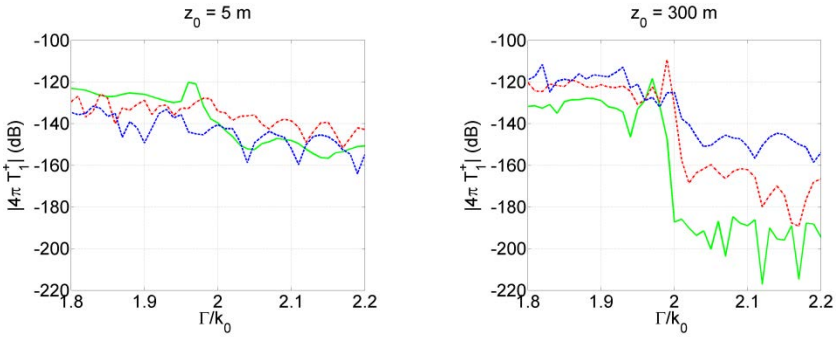
Fig.5 represents 4π times T_0, T_1^- and T_1^+ computed for a source immersed at 5 and 300 m against f_0 at the receiving position (x_R, y_R, z_R) = (60,0,0.3) km, in the same environmental configuration than the previous section. At this receiving location, the scattered energy remains 20 to 40 dB lower than the energy carried at f_0, depending on the source frequency and immersion. Furthermore, for $z_0 = 300$ m, we notice a strong increase of about 40 dB of the scattered energy at $f_0 = 30$ Hz. At this frequency, the ratio $\Gamma/k_0 \approx 2$. The authors in [8] had already identified this cut-off value from which the first order term p_1 is drastically reduced and gave a physical interpretation based on wave-number diagrams and ray trajectories. When we consider a source immersed at 5 m (*Fig.5(a)*), we observe that the level of scattered energy decrease in a more progressive way, especially the right side-lobe.



(a) *(b)*

Fig.5: T_0*: (---),* T_1^-*: (---) and* T_1^+*: (---) against* f_0 *for a source immersed at (a) 5 and (b) 300 m.*

To have a better look at the scattered energy decrease on both sides of the cut-off ratio, we plot on *Fig.6* $|4\pi T_1^+|$ against Γ/k_0 for the sea-states 1, 3 and 5. For the source immersed at 300 m, the decline of the scattered energy is significant when Γ/k_0 is exceeded, especially when the sea-state is equal to 1 or 3, whereas it is smoother when the source is located in the thermocline. At this time, we are not able to explain this observation.



(a) *(b)*

Fig.3: T_1^+ computed for sea-states equal to 1:(---), 3:(-- --) and 5: (- · -) against Γ/k_0 for a source immersed at (a) 5 and (b) 300 m.

5. CONCLUSION

In this paper we studied the scattering of a continuous wave in the 1 to 200 low frequency range by the fully developed swell of the Atlantic Ocean in deep-water configurations. We used the small-perturbation method coupled with the normal-mode theory and an asymptotic analysis to derive the first order spatio-temporal scattered pressure field p_1. Our approach splits off from [3] by the use of an in-house code that provides the modal functions allowing the computation of p_1 for any waveguides. As a first step, we compared favorably the side-lobes level issued from our computation with the ones measured experimentally by [1] in the Sargasso Sea. Then we showed that the shadow zone observed when the source is located in the summer thermocline is filled up by the scattered pressure field from 130 Hz, on the directions defined by the Bragg resonance angle. Finally, we showed that the collapse of p_1 when $\Gamma/k_0 > 2$ may be relatively smooth when the source is located in the thermocline.

6. REFERENCES

[1] **Shooter J. A., Mitchell S. K.**, Observations of acoustics sidebands in cw tones received at long ranges, *J. Acoust. Soc. Am.*, volume (90), pp. 829-832, 1975.

[2] **Voronovitch A. G.**, *Wave scattering from Rough Surfaces*, Berlin: Springer-Verlag, 1994.

[3] **Labianca F. M., Harper E. Y.**, Connection between various small-waveheight solutions of the problem of scattering from the ocean surface, *J. Acoust. Soc. Am.*, volume (62), pp. 1144-1157, 1977.

[4] **Labianca F. M., Harper E. Y.**, Sideband structure of sound from a harmonic point source scattered by a rough surface moving over an upward-refracting ocean, *J. Acoust. Soc. Am.*, volume (61), pp. 378-389, 1977.

[5] **Felsen L. B., Marcuvitz N.**, *Radiation and Scattering of Waves.* New York: Wiley-IEEE Press, 1994.

[6] **Harper E. Y., Labianca F. M.**, Perturbation theory for scattering of sound from a point source by a moving rough surface in the presence of refraction, *J. Acoust. Soc. Am.*, volume (57), pp. 1044-1051, 1975.

[7] **Harper E. Y., Labianca F. M.**, Scattering of sound from a point source by a rough surface progressing over an isovelocity ocean, *J. Acoust. Soc. Am.*, volume (58), pp. 349-364, 1975.

[8] **Labianca F. M., Harper E. Y.**, Asymptotic theory of scattering by a rough surface progressing over an inhomogeneous ocean, *J. Acoust. Soc. Am.*, volume (59), pp. 799-812, 1976.

SOUND SPEED AND ATTENUATION PREDICTIONS USING THE CORRECTED BIOT MODEL FOR GAS-BEARING MARINE SEDIMENTS

Guangying Zheng[a,b], Chuanxiu Xu[a,b], You shao[a,b]

[a]Hangzhou Applied Acoustics Research Institute, No. 715, Pingfeng Road, Xihu District, 310023, Hangzhou, P.R. China
[b]Science and Technology on Sonar Laboratory, No. 715, Pingfeng Road, Xihu District, 310023, Hangzhou, P.R. China

Guangying Zheng, 276454158@qq.com

Abstract: *As is well known, a small volume of gas bubbles existing in a sediment can greatly change the sound speed and attenuation in marine sediment. In this work, to investigate the sound propagation in a gas-bearing marine sediment, we integrate the volume vibrations of bubbles in pore water into the continuity equation of pore-fluid filtration in porous medium based on Biot theory, so as to obtain the continuity equation of pore-fluid filtration with bubble pulsation. On this basis, according to the relationship between the instantaneous radius of bubble and the background pressure of the medium under the linear vibration of bubble, as well as the equations of motion of the fluid medium and porous medium, a new displacement vector wave equation of porous medium under the influence of bubble is derived, which establishes the model for the sound speed dispersion and attenuation prediction under the gas-bearing sediments. The acoustic properties of gas-bearing sediments show three distinct zones of frequency-dependent behavior in numerical analysis. For the insonifying frequency below the gas-bubble resonance frequency, the phase velocity is lower, and the attenuation coefficient is significantly higher than that in non-gassy sediments. A transition zone near the resonance can be observed, in which the phase velocity rapidly increases. In particular, the phase velocity can highly exceed the non-gassy velocity at the resonance frequency. The attenuation is highest at frequencies close to the gas-bubble resonance frequency, which depends mainly on the bubble radius. Above the resonance, the phase velocity approaches a constant value similar to the non-gassy sediment, whereas the attenuation is higher than non-gassy attenuation and increases with the increasing frequency.*

Keywords: *gas-bearing marine sediment, sound speed, attenuation*

1. INTRODUCTION

It is well known that the presence of a small volume of gas bubbles in marine sediments can lead to a poor acoustic penetration[1]. And physical properties of gassy sediments are of interest to a number of offshore activities, including drilling operations and the siting of seafloor structures[2].

Three types[3,4] of gas bubbles in gassy sediments are generally considered as illustrated in Fig. 1(i.e., interstitial, reservoir, and sediment-displacing bubbles).

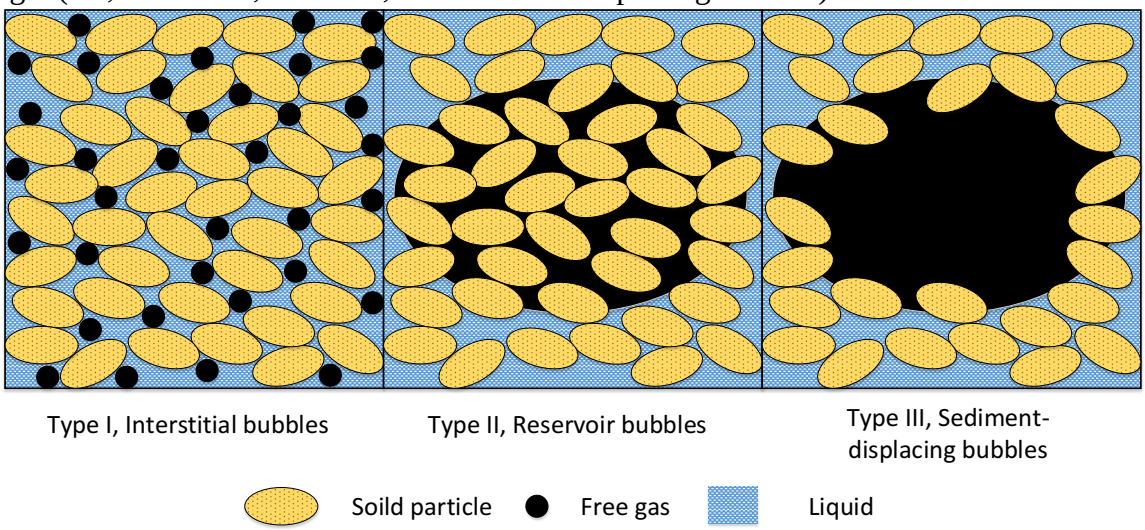


FIG. 1: Generic bubble classification for bubbles in sediments.

The most frequently used model for predicting acoustic scattering, sound speed and attenuation in gas-bearing marine sediments is proposed by Anderson and Hampton[5,6], The applicability of this model is limited to linear gas bubble pulsations, and leaves ambiguities for the inverse problem because of the plus/minus sign entering the expression of the complex sound speed. This sign ambiguity may result in the presence of both positive and negative bubble counts when inverting broadband acoustic data.

Recently, Zheng and Huang[7] developed a geoacoustic model to predict the acoustic response in gas-bearing sediments based on the Biot model and gas-bubble pulsations. This corrected model can be used to predict the sound speed and attenuation of the marine sediments of type I and type III, and can be used to estimate bubble size distributions through a full acoustic inversion. This paper reviews the method to predict the sound speed and attenuation using the corrected Biot model, and the acoustic response of these two type sediments is analysed.

2. MODELLING GAS-BEARING MARINE SEDIMENTS USING THE CORRECTED BIOT MODEL

2.1. Corrected Biot wave equation

The corrective poro-elastic equations derived by Zheng and Huang[7] are shown in Eqs. (1) and (2),

$$G_b\nabla^2\mathbf{u}+\left[H-G_b\right]\nabla\left(\nabla\cdot\mathbf{u}\right)-C\nabla\left(\nabla\cdot\mathbf{v}\right)-\beta C\nabla\beta_g=\frac{\partial^2}{\partial t^2}\left(\rho\mathbf{u}-\rho_w\mathbf{v}\right), \tag{1}$$

$$C\nabla\left(\nabla\cdot\mathbf{u}\right)-M\nabla\left(\nabla\cdot\mathbf{v}\right)-\beta M\nabla\beta_g=\frac{\partial^2}{\partial t^2}\left(\rho_w\mathbf{u}-\frac{\alpha\rho_w}{\beta}\mathbf{v}\right)-\frac{\eta F}{\kappa}\frac{\partial\mathbf{v}}{\partial t}, \tag{2}$$

where H, C and M denote the Biot elastic moduli, $\mathbf{u}$ denotes the absolute displacement vector of the solid framework, $\mathbf{v}$ denotes the relative displacement vector of the pore fluid relative to the solid framework, ρ is the density of the porous medium mixture, ρ_w is the density of pore fluid, η denotes the viscosity coefficient of the pore water, β is the porosity, κ denotes the permeability, α is the tortuosity, F denotes the high frequency complex correction factor, and β_g is the dynamic gas bubble void fraction.

Comparing these variables with the original Biot wave equation, two terms that involve $\nabla\beta_g$ have been introduced, which are again related to gas-bubble pulsations. In order to eliminate this gradient of the gas-bubble void fraction (i.e., $\nabla\beta_g$), the equation of motion of the effective fluid, which involves the effective sound pressure p_{eff} and the effective displacement $\mathbf{u}_{\text{eff}}=\mathbf{u}-\mathbf{v}$, is written as

$$-\nabla p_{\text{eff}}=\rho_{\text{eff}}\ddot{\mathbf{u}}_{\text{eff}}=\rho_{\text{eff}}\left(\ddot{\mathbf{u}}-\ddot{\mathbf{v}}\right), \tag{3}$$

where the effective density is

$$\rho_{\text{eff}}=\frac{\rho\tilde{\rho}_0-\rho_w^2}{\rho+\tilde{\rho}_0-2\rho_w}, \tag{4}$$

$$\tilde{\rho}_0=\frac{\alpha\rho_w}{\beta}-\frac{iF\eta}{\kappa\omega}. \tag{5}$$

The gas-bubble void fraction can be denoted as $\beta_g=4N\pi R^3/3$ by using N to denote the bubble number per unit volume. The relationship between the instantaneous radius of bubbles R and the effective perturbation pressure p_{eff} under the linear vibration of bubbles is given in, and ignoring higher-order perturbations:

$$\nabla\beta_g=-\frac{4\pi NR_0}{\rho\left(\omega_0^2-\omega^2+2ib_{\text{tot}}\omega\right)}\nabla p_{\text{eff}}, \tag{6}$$

where ω_0 and b_{tot} are the bubble resonance frequency and damping term, respectively, for type I gas-bearing sediments, air-bubble pulsations in pore water, which are given by Commander[8],

$$\omega_0^2=\left[\operatorname{Re}\phi-2\sigma/\left(aP_{in,0}\right)\right]P_{in,0}/\rho_w a^2, \tag{7}$$

$$b_{\text{tot}}=2\eta/\left(\rho_w a^2\right)+\omega^2 a/\left(2c\right)+\operatorname{Im}\left(P_{in,0}\phi\right)/\left(2\omega\rho_w a^2\right), \tag{8}$$

On the other hand, for type III gas-bearing sediments, air-bubble pulsations in saturated sediments, which are given by Yang and Church[9], the resonance frequency of gas bubble pulsations in a viscoelastic medium,

$$\omega_0^2=\left(3p_{g0}\operatorname{Re}\left(\phi\right)-\frac{2\sigma}{R_0}+4G_0\right)\Big/\left(\rho_0R_0^2+\frac{4\eta_0R_0}{c_0}\right). \tag{9}$$

The damping term b_{tot}, which is sum of the viscous damping, thermal damping, radiation damping, interfacial damping and elastic damping. These damping terms are denoted as follows:

$$b_{\text{tot}} = b_{\text{vis}} + b_{\text{P-th}} + b_{\text{rad}} + b_{\text{int}} + b_{\text{el}}, \tag{10}$$

$$b_{\text{vis}} = 2\eta_0 \Big/ \left(\rho_0 R_0^2 + \frac{4\eta_0 R_0}{c_0} \right), \tag{11}$$

$$b_{\text{P-th}} = \left(\frac{3p_{g_0}\,\text{Im}(\phi)}{2\omega} \right) \Big/ \left(\rho_0 R_0^2 + \frac{4\eta_0 R_0}{c_0} \right), \tag{12}$$

$$b_{\text{rad}} = \left(\frac{\rho_0 \omega^2 R_0^3}{2c_0} \right) \Big/ \left(\rho_0 R_0^2 + \frac{4\eta_0 R_0}{c_0} \right), \tag{13}$$

$$b_{\text{int}} = -\sigma \Big/ \left(\rho_0 c_0 R_0^2 + 4\eta_0 R_0 \right), \tag{14}$$

$$b_{\text{el}} = 2G_s \Big/ \left(\rho_0 c_0 R_0 + 4\eta_0 R_0 \right), \tag{15}$$

where the complex polytropic function ϕ is denoted as follows:

$$\phi = 3\gamma_g \Big/ 1 - 3\left(\gamma_g - 1\right) \text{i}\chi \left[\left(\text{i}/\chi \right)^{1/2} \coth\left(\text{i}/\chi \right)^{1/2} - 1 \right], \tag{16}$$

where σ is Surface tension, $\chi = D/\omega R_0^2$, D is the thermal diffusivity of gas, and γ_g denotes the ratio of specific heats.

Substituting Eqs. (3) and (6) into Eqs. (1) and (2), the following equations are obtained,

$$G_b \nabla^2 \mathbf{u} + \left[H - G_b \right] \nabla \left(\nabla \cdot \mathbf{u} \right) - C \nabla \left(\nabla \cdot \mathbf{v} \right) = \frac{\partial^2}{\partial t^2} \left(\left(\rho + \gamma\tilde{\rho} \right) \mathbf{u} - \left(\rho_w + \gamma\tilde{\rho} \right) \mathbf{v} \right), \tag{17}$$

$$C \nabla \left(\nabla \cdot \mathbf{u} \right) - M \nabla \left(\nabla \cdot \mathbf{v} \right) = \frac{\partial^2}{\partial t^2} \left(\left(\tilde{\rho} + \rho_w \right) \mathbf{u} - \frac{\alpha \left(\rho_w + \tilde{\rho} \right)}{\beta} \mathbf{v} \right) - \frac{\eta F}{\kappa} \frac{\partial \mathbf{v}}{\partial t}, \tag{18}$$

where $\tilde{\rho} = \dfrac{4\pi N R_0 M \beta}{\left(\omega_0^2 - \omega^2 + 2ib_{\text{tot}}\omega \right)} \dfrac{\rho_{\text{eff}}}{\rho}$, $\gamma = 1 - \dfrac{K_w}{K_s}$.

Eqs. (17) and (18) can be written in another form:

$$\frac{G_b}{\text{ratio}_2} \nabla^2 \mathbf{u} + \frac{\left[H - G_b \right]}{\text{ratio}_2} \nabla \left(\nabla \cdot \mathbf{u} \right) - \frac{C}{\text{ratio}_2} \nabla \left(\nabla \cdot \mathbf{v} \right) = \frac{\partial^2}{\partial t^2} \left(\frac{\left(\rho + \gamma\tilde{\rho} \right)}{\left(\rho_w + \gamma\tilde{\rho} \right)} \rho_w \mathbf{u} - \rho_w \mathbf{v} \right), \tag{19}$$

$$\frac{C}{\text{ratio}_1} \nabla \left(\nabla \cdot \mathbf{u} \right) - \frac{M}{\text{ratio}_1} \nabla \left(\nabla \cdot \mathbf{v} \right) = \frac{\partial^2}{\partial t^2} \left(\rho_w \mathbf{u} - \frac{\alpha \rho_w}{\beta} \mathbf{v} \right) - \frac{\eta F}{\text{ratio}_1 \kappa} \frac{\partial \mathbf{v}}{\partial t}, \tag{20}$$

where $\text{ratio}_1 = \left(\rho_w + \tilde{\rho} \right) / \rho_w$ and $\text{ratio}_2 = \left(\rho_w + \gamma\tilde{\rho} \right) / \rho_w$.

It should be noted that ratio_1 and ratio_2 are both complex, with the moduli larger than 1, as long as the bubble volume fraction is not zero. Eqs. (19) and (20), show that the bubble volume vibration can be seen to alter the fluid compressibility, which leads to a decrease in the effective elastic modulus of the porous medium. Although the effective density of the porous medium is effectively unchanged by the presence of extremely small bubbles, there is a significant decrease in the speed of sound in the medium. Moreover, additional dissipation mechanisms are involved in the imaginary part of $\tilde{\rho}$ in Eqs. (17) and (18), which are due to the radiation, interfacial, viscous, thermal, and elastic damping of the pulsating air bubbles.

Note that if $\beta_g = 0$, there are no bubbles in the porous medium; the bubble number per unit volume is $N = 0$. In that case, Eqs. (17) and(18) become identical to the Biot equations. Thus, the present theory is tantamount to Biot theory when the gas-bubble pulsation is unaccounted for.

3. RESULTS

3.1. Acoustic response of type I gas-bearing sediments

	parameters	values	parameters	values
Biot model parameters	Grain diameter	0.128mm/0.781mm	Fluid viscosity	1.002×10^{-3}Pa·s
	Grain density	2517 kg/m^3	porosity	0.439
	Grain bulk modulus	5.1×10^{10} Pa	permeability	2.54×10^{-10} m^2
	Fluid density	999 kg/m^3	Pore size	1.53×10^{-4} m
	Fluid bulk modulus	2.193×10^{9} Pa	Structure factor	1.35
	Frame bulk modulus	5.31×10^{7} Pa	Frame shear modulus	5.58×10^{6} Pa
	Longitudinal logarithmic decrement	0.15	Shear logarithmic decrement	0.15
Gas bubble parameters	Gas density	1.1691 kg/m^3	Thermal diffusivity	2.4×10^{-5} m^2/s
	Gas velocity	340 m/s	Surface tension	72.75×10^{3} N/m
	Equilibrium pressure	1.01×10^{5} Pa	ratio of specific heat	1.4

Table 1: Model input parameters for gas-bearing sediments.

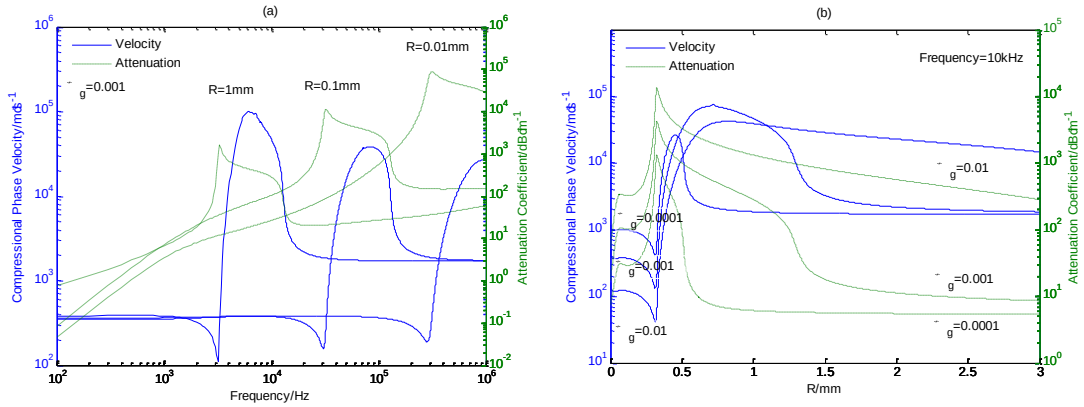


Fig. 2: Acoustic response of gas-bearing sediments according to the model in this paper. (a) Variation in acoustic velocity and attenuation coefficient with frequency for a range of gas bubble sizes(constant gas content 0.001) and (b) Variation in acoustic velocity and attenuation coefficient with bubble radius for a range of gas contents(constant excitation frequency of 10kHz).

A typical set of response curves in Fig. 2 shows three distinct zones of frequency-dependent behavior. These model input parameters in Table 1 were measured from sediment samples in our experiment, and a delta-function bubble size distribution is provided. For frequencies below resonance, the velocity is significantly reduced and the attenuation is higher than that in gas-free sediments. Near resonance, a transition zone is seen, where phase velocity dramatically increases. At resonance, the gassy sediment is highly dispersive and the velocity can greatly exceed the gas-free velocity, which has not been measured in field data. Attenuation is highest at a frequency near the bubble resonance frequency, which is primarily dependent on the radius of the bubble. Above the resonance frequency, the bubbles scatter the sound and the acoustic response essentially that of the surrounding medium, so the velocity remains constant at a value commensurate with the gas-free sediment, while the attenuation is higher than in gas-free sediment and increases with frequency. Note that the attenuation coefficient calculated here is related to acoustical bubble scattering(which also includes terms for fluid viscous damping at the bubble walls, bubble radiation damping and bubble gas

thermal damping) and the dissipation due to the relative motion between pore fluid and framework.

3.2. Acoustic response of type III gas-bearing sediments

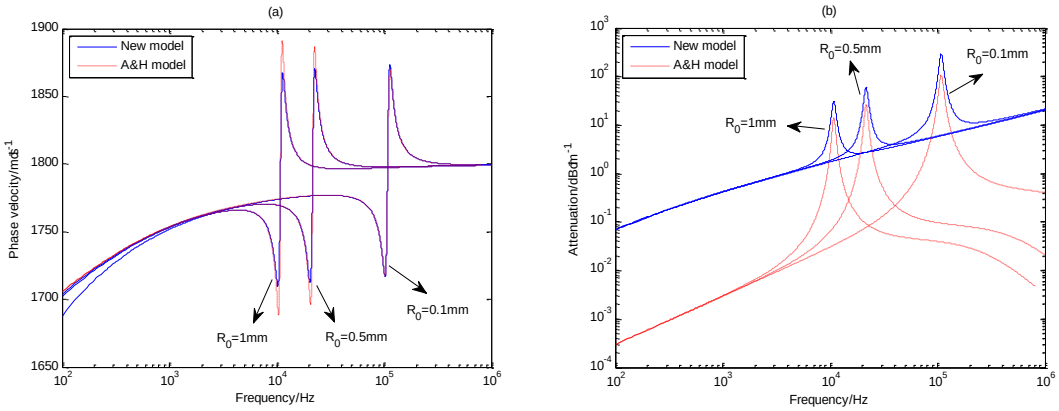


FIG. 3: (a) Sound speed and (b) attenuation as frequency functions for a series of mono-dispersed bubble populations, which all have a void fraction of 10^{-5} (i.e., the radius for each bubble labeled in the figure). The solid line denotes the results calculated by the proposed model, whereas the dashed line denotes the results of the A&H model.

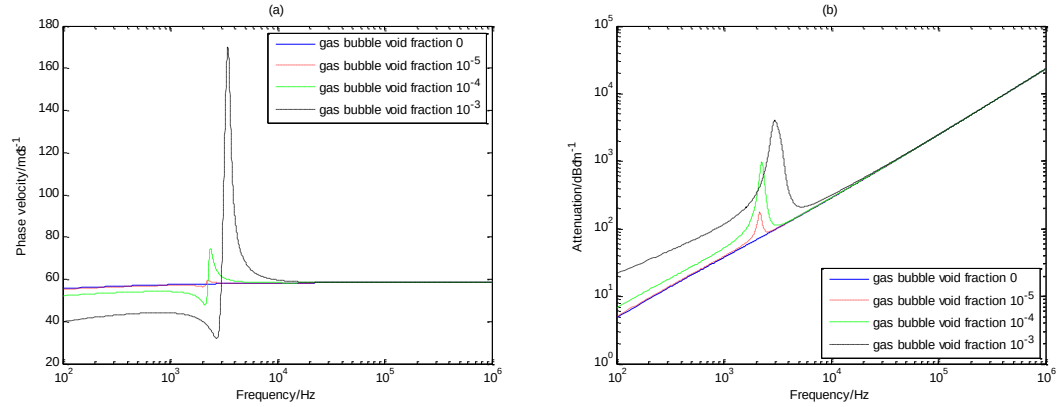


FIG. 4: Variation in the (a) shear wave phase velocity and (b) attenuation coefficient with frequency for a range of gas contents (constant gas-bubble radius of 5 mm).

Fig. 3 shows a comparison of the sound speed and attenuation for the fast wave between the proposed model and the A&H model. Notably, significant differences between the predictions of these two models are shown in Fig.3b. The current model predicts higher attenuation than the results predicted by the A&H model. The main reason for this scenario is that the current model involves more dissipation regimes: the relative motion between the pore water and solid frame, elastic damping, and interface damping. The main advantage of the current model is that its expression that predicts the velocity does not contain sign ambiguity and can be applied to an inversion model, which requires simultaneous information on sound speed and attenuation data.

What's more, the current model can be used to predict the phase velocity and attenuation coefficient of a shear wave(Fig. 4).The shear wave response curves show similar frequency-dependent behavior to that of a fast wave. The phase velocity is lower than that in gas-free sediments because the insonifying frequency is lower than the resonance frequency of the bubbles. The phase velocity at the resonance can significantly exceed the non-gassy velocity, and attenuation is the highest.

4. CONCLUSIONS

This study presents the corrected Biot model for gas-bearing marine sediments. This model can be used to predict the sound speed and attenuation of longitudinal and shear waves in the presence of linear bubble pulsations in gassy marine sediments. Numerical results for the phase velocity and attenuation coefficient show similar frequency dependencies for type I and type III sediments, longitudinal and shear waves. By contrast, the results for the attenuation of fast waves show a significant difference due to the additional damping regimes comparing to the A&H model. The current model has three major advantages: 1) this current model is applicable to the two type of marine sediments; 2) It can predict sound speeds, attenuation coefficients, and reflection coefficients for fast, slow, and shear waves; 3) It can also be utilized in inversion models that require simultaneous data on sound speed and attenuation.

5. ACKNOWLEDGEMENTS

This work was supported by the National Natural Science Foundation of China (Grant No. 61471327). This work was funded by the National Defense Science and Technology Innovation Zone.

REFERENCES

[1] **P. Fleischer, T. Orsi, M. Richardson, and A. Anderson**, Distribution of free gas in marine sediments: a global overview, *GeoMarine Letters*, volume 21, pp. 103–122, 2001.
[2] **G. C. Sills and S. J. Wheeler**, The significance of gas for offshore operations, *Continental Shelf Research*, volume 12, pp. 1239-1250, 1992.
[3] **G. B. N. Robb, T. G. Leighton, J. K. Dix, A. I. Best, V. F. Humphrey and P. R. White**, Measuring bubble populations in gassy marine sediments: a review, Futures in Acoustics: Today's Research-Tomorrow's Careers. *Proceedings of the Institute of Acoustics Spring Conference*, volume 28, pp. 60–68, 2006.
[4] **A. L. Anderson, F. Abegg, J. A. Hawkins, M. E. Duncan and A. P. Lyons**, Bubble populations and acoustic interaction with the gassy floor of Eckernförde bay, *Continental Shelf Research*, volume 18, pp. 1807–1838, 1998.
[5] **A. L. Anderson and L. D. Hampton**, Acoustics of gas-bearing sediments. I. Background, *Journal of the Acoustical Society of America*, volume 67, pp. 1865–1889, 1980.
[6] **A. L. Anderson and L. D. Hampton**, Acoustics of gas-bearing sediment. II. Measurements and models," *Journal of the Acoustical Society of America*, volume 67, pp. 1890–1903, 1980.
[7] **G. Y. Zheng and Y. W. Huang**, Effect of linear bubble vibration on wave propagation in unsaturated porous medium containing air bubbles, *Acta Physica. Sinica*, volume, 65, pp. 234301, 2016.
[8] **K. W. Commander and A. Prosperetti**, Linear pressure waves in bubbly liquids: Comparison between theory and experiment, *Journal of the Acoustical Society of America*, volume 85, pp. 732–746, 1989.
[9] **X. Yang and C. C. Church**, A model for dynamics of gas bubbles in soft tissue, *Journal of the Acoustical Society of America*, volume 118, pp. 3595–3606, 2005.

ACOUSTIC SCATTERING FROM AN OBJECT IN A MUD LAYER OF A SHALLOW WATER WAVEGUIDE

Steven G. Kargl, Kevin L. Williams, Aubrey L. Espana

Applied Physics Laboratory, University of Washington, 1013 NE 40th St., Seattle WA 98105-6698 USA

Steven G. Kargl, Applied Physics Laboratory, University of Washington, 1013 NE 40th St., Seattle WA 98105-6698 USA, FAX: 206-543-1300, kargl@uw.edu

Abstract: *Bay Experiment 2014 (BAYEX14) collected low-frequency synthetic aperture sonar (SAS) data in St. Andrew's Bay, Panama City, FL. Inert ordnance, scientific targets, and some clutter objects were distributed in the field of view of the SAS system. The environment is roughly characterized by a 7-m water depth with a mud layer over a sand sediment subbottom. The layer thickness varies from 15 to 30 cm. All objects deployed in BAYEX14 sank into the mud layer. Large targets were partially buried and came to rest on the underlying sand sediment; while small targets were completely buried. Modifications to the APL-UW target in the environment response (TIER) model were required to account for propagation paths within the mud layer. Simulations and comparisons to BAYEX14 data suggest that the primary contribution to the received scattered signal is the direct scattering ray path. The SAS platform was near the middle of the water column. For objects with horizontal ranges from the SAS platform that exceed a few water depths, an air-water reflected ray path can significantly alter the scattered signal and, under calm conditions, ocean surface bounce target images can be formed. These topics will be the focus of this paper. [Work supported by SERDP and ONR.]*

Keywords: *Synthetic aperture sonar, Unexploded ordnance, mud layer.*

1. INTRODUCTION

Although disposal of munitions in coastal waters was discontinued during the 1970's, environmental, economical, and recreational impact persist [1]. Overfield and Symons note that over 2100 underwater sites are likely to contain shipwrecks, munitions dumpsites, radiological waste, abandoned pipelines, and wellheads [2]. Of those sites, verification has been completed on approximately 50% with contemporary records (e.g., ship logs). Although not all sites listed in the Resources and Undersea Threats (RUST) database contain discarded munitions, RUST also may not contain a comprehensive list of current and former US military training sites. In any event, there is a clear need for cost-effective surveys of underwater sites. Schwartz and Brandenburg summarize the current technologies available for underwater unexploded ordnance (UXO) applications [3]. Their Table 1 includes chemical sensors, metal detection, and sonar. Chemical sensors and metal detection are typically restricted to very short ranges; while sonar technologies considered in [3] are limited in range or are limited by poor penetration into sediments due to the sonar's high frequency.

Low-frequency (LF) sonar in underwater UXO remediation activities has been considered by researchers at the Naval Research Laboratory [4,5] and by our group at the Applied Physics Laboratory, University of Washington (APL-UW) [6-10]. Sound below 50 kHz has three advantages. First, it can propagate to hundreds of meters with little attenuation loss. Second, low frequencies can penetrate into sediments, and have the potential to detect buried objects. Third, and importantly, low frequencies can couple into an elastic response of an object. This response can then be utilized in classification schemes.

Much of our previous efforts focused on LF synthetic aperture sonar (SAS) to ensonify underwater objects resting on a water-sediment interface. Field experiments with numerous objects (including inert UXO, scientific targets, and clutter objects) have been conducted. Data were used to validate finite-element (FE) models and a fast ray-based model [6-10]. This research demonstrated that the environment within which an object is found must be considered when determining its elastic response. Combining acoustic scattering amplitudes from FE simulations with the fast ray-model has led to the target-in-the-environment-response (TIER) model. When an object becomes buried within a sediment, the TIER model requires modifications. During Bay Experiment 2014 (BAYEX14), all targets were partially or fully buried in a thin mud layer above a sandy subbottom. This paper discusses modifications to the TIER model to account for propagation under BAYEX14 conditions. Section 2 describes BAYEX14. Section 3 outlines the TIER model and discusses the modifications required to account for propagation within the mud layer. Section 4 provides simulations that show the mud layer's effect on an object's response and effects of an air-water reflected path. Section 5 summarizes.

2. BAY EXPERIMENT 2014

BAYEX14 was conducted in St. Andrew's Bay, Panama City, FL in late Spring of 2014. The environment is characterized by a 7 to 8 m water depth with a mud layer over a sandy subbottom. The thickness of the mud layer varies from 15 to 30 cm. The water in the bay is brackish due to tidal exchange and inflow of freshwater. This environment provided two unique situations not encountered in our previous field measurements; namely, the mud layer and the air-water interface could not be ignored under certain conditions.

The *Research Vessel (RV) Sharp* was placed in a four-point moor with a westward heading. APL-UW's rail-tower sonar platform was deployed parallel to the *RV Sharp* off her starboard side. The rail provided a 40-m SAS aperture with target fields placed north of the

rail in the field-of-view of the sonar. The tower moved along the rail at 5 cm/s, and simultaneously transmitted 1-30 and 110-190 kHz linear-frequency-modulated (LFM) pulses with a 2 Hz repetition frequency.

Divers installed a fixed grid of lightweight cords from 5 to 40 m in 5 m intervals. Objects were placed at grid locations with specified orientations. Adjacent objects have sufficient separation such that multiple scattering can be ignored. A target field could contain 10 to 28 objects during the collection of SAS data. All objects deployed in BAYEX14 sank into a mud layer coming to rest on a sandy subbottom. Large objects were partially buried; while small objects were completely buried. The source and receiver were located approximately 3.8 m above the subbottom, which coincided with the nominal mid column of the waveguide. With this source/receiver location and under calm conditions an air-water reflected acoustic path can contribute to the measured acoustic scattered pressure. Thus, the mud layer and shallow water environment posed new requirements on our TIER model.

3. MODIFIED TIER MODEL

When the depth of a homogeneous waveguide is much larger than a wavelength of sound, the Green function for propagation can be represented by a superposition of image sources reflected through the waveguide's boundaries. Likewise, a receiver in the waveguide can be represented by a superposition of image receivers. The TIER model utilizes image sources and receivers to represent the propagation associated with acoustic scattering from an object within a waveguide. A detailed description of the TIER model is available in [7]. Here, we simply give a brief description.

With r_i, r_j, and r_t representing source, receiver, and object locations, the physical source (receiver) corresponds to $i = 0$ ($j = 0$) and its images have $i > 0$ ($j > 0$). The distance between a source and object is $d_{ti} = |r_t - r_i|$, and $d_{jt} = |r_j - r_t|$ is the distances between a receiver and object. The propagation time delay along the ray joining a source and object is $t_{ti} = d_{ti} / c_1$, and the time delay for the object to receiver is $t_{jt} = d_{jt} / c_1$. The sound speed in water is c_1. The total scattering pressure is then the superposition of contributions of form:

$$P_{ij}(\omega) = \left[\frac{A_{jt}}{d_{jt}}\exp(i\omega t_{jt})\right]\left[\frac{A_{ti}}{d_{ti}}\exp(i\omega t_{ti})\right] f(k_i, k_j, \omega) r_0 P_{src}(\omega). \quad (1)$$

A_{jt} and A_{ti} account for source and receiver beam patterns and any interaction of a ray with the boundaries of the waveguide. In (1), the scattering process is a multiplication of the free-field scattering amplitude, $f(k_i,k_j,\omega)$, with the spectrum of the transmitted pulse, $P_{src}(\omega)$. The incident and scattered wave vectors, associated with source i and receiver j, are k_i and k_j, respectively. These wave vectors are defined within a target-centered coordinate geometry. Finally, r_0 is a reference distance associated with calibration of the source.

The distance between the actual source and actual receiver on the APL-UW sonar platform is much smaller than the slant range to an object, so the source and receiver are assumed to be co-located. In our experiments prior to BAYEX14, the air-water interface can be ignored, because rays that interact with this interface are removed by time-gating the received signals (see below). Under these conditions, only four rays contribute to the total scattered pressure. With S, R, T, and B denoting the source, receiver, target, and bottom, the 4 rays are given by S→T→R (direct scattering path), S→B→T→R and S→T→B→R (reciprocal paths with one bottom bounce), and S→B→T→B→R (double bounce path). The arrow denotes direction of propagation. The conditions of BAYEX14 [10] required modifications to the TIER model.

Consider a uniform layer bounded above by water and below by a homogeneous subbottom. Assume a layer thickness of h and an origin of the coordinate system in the interface separating the layer and subbottom. The layer permits additional ray paths to reach

an object. For a source (or receiver) at a finite horizontal range R from an object within the layer, refracted ray paths exist and satisfy

$$(z_s - h)\cot\theta_{m,1} + mh\cot\theta_{m,2} + (h - z_t)\cot\theta_{m,2} - R = 0\,, \qquad m \text{ even}, \tag{2}$$

$$(z_s - h)\cot\theta_{m,1} + mh\cot\theta_{m,2} + z_t\cot\theta_{m,2} - R = 0\,, \qquad m \text{ odd}, \tag{3}$$

where z_s and z_t are the z coordinates of the source and object. The integer m enumerates the number of internal reflections within the layer. That is, path 0 crosses the water-layer interface, but otherwise does not interact with a boundary; while path 1 reflects once from the layer-subbottom interface (see Fig. 1). To describe the scattering process, it is convenient to write 0→1 to mean an incident path 0 is scattered into an outgoing path 1. For ray m, an incident grazing angle $\theta_{m,1}$ is related to an angle of refraction $\theta_{m,2}$ via Snell's laws, $\cos\theta_{m,2} = \nu \cos\theta_{m,2}$, where the real index of refraction is $\nu = c_1 / c_2$. The speed of sound in the layer is c_2. Snell's law allows one to eliminate $\theta_{m,2}$ from (2) and (3), and then solve the resulting transcendental equation for $\theta_{m,1}$. The length of a ray's path within the water is

$$d_{m,1} = (z_s - h)\csc\theta_{m,1}, \tag{4}$$

and the total length of a ray's path in the layer is

$$d_{m,2} = (mh - z_t + h)\csc\theta_{m,2}, \qquad \text{m even}, \tag{5}$$

$$d_{m,2} = (mh + z_t)\csc\theta_{m,2}, \qquad \text{m odd}, \tag{6}$$

Finally, mud has a fairly high acoustic absorption in comparison to water. For that portion of a ray path in mud, the absorption loss is given by

$$loss_{m,2} = \exp(-\delta d_{m,2}\omega / c_2)\,, \tag{7}$$

where δ is a dimensionless loss parameter.

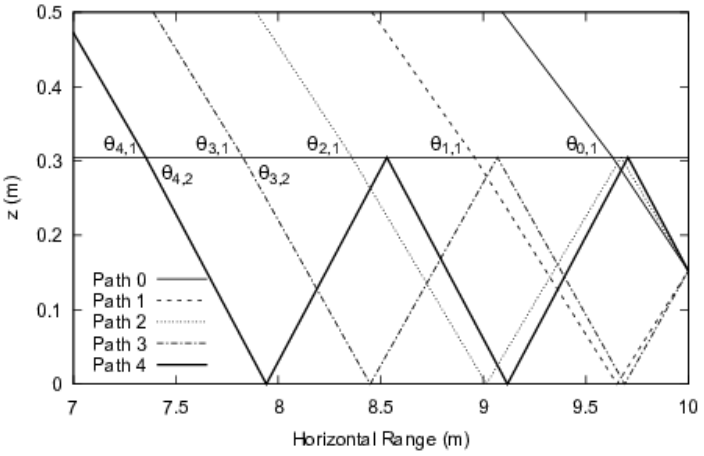


Fig. 1. Five ray paths for a BAYEX14 simulation with an object at a 10 m horizontal range. The layer-subbottom interface is at z = 0. The horizontal black line indicates the water-layer interface. Physical properties of mud are close to those of water, so the ray paths are only slightly refracted crossing the water-layer interface. For clarity, refraction angles $\theta_{0,2}$, $\theta_{1,2}$, and $\theta_{2,2}$ have been omitted.

4. MODEL-DATA COMPARSION

In BAYEX14, the speeds of sound in water and mud were c_1= 1530 m/s and c_2 = 1504 m/s, respectively. For mud, the loss parameter, δ, is typically in the range of 0.01 to 0.02. A solid aluminum cylinder (2 ft length by 1 ft diameter) was placed at a horizontal range of R = 20 m where the layer thickness is $h \approx 0.16$ m. Co-located source/receiver heights are z_s = 3.8 m and

the target center has z_t = 0.1524 m. As a ray propagates in the layer, acoustic energy is absorbed by the layer. Using (5) - (7) with δ = 0.01, one-way absorption losses for individual paths are shown in Table 1.

m	$\theta_{m,1}$ (deg)	$d_{m,1}$ (m)	$d_{m,2}$ (m)	dB 1 kHz	dB 10 kHz	dB 20 kHz	dB 30 kHz
0	10.33	20.30	0.030	-0.01	-0.11	-0.22	-0.33
1	10.93	19.20	1.194	-0.43	-4.33	-8.67	-13.00
2	10.96	19.14	1.250	-0.45	-4.54	-9.07	-13.61
3	11.59	18.11	2.345	-0.85	-8.51	-17.02	-25.53
4	11.62	18.06	2.398	-0.87	-8.70	-17.40	-26.10

Table 1. One-way absorption loss in mud for rays to those depicted in Fig. 1. The last four columns contain the loss at the specified frequency. Note, this loss does not account for reflection and transmission coefficients at the lower and upper boundaries of the layer.

The target strength (TS) for the aluminum cylinder under different environmental conditions is displayed in Fig. 2. The simulation conditions are those that match the above BAYEX14 conditions with the cylinder at R = 20 m. Fig. 2a and 2c correspond to a broadside orientation of the cylinder while Fig. 2b and 2d are for an end-on orientation. The free-field result (black line) is the direct scattering in the absence of any boundaries (i.e., S→T→R). The blue line in Fig. 2a and 2b is the scattering from the cylinder sitting proud on the subbottom in the absence of a mud layer. The green, red, and cyan lines in Fig. 2a and 2b are the TS for the cylinder in the mud layer with δ = 0.00, 0.01, and 0.02, respectively. In Fig. 2c and 2d, the 0→0, 0→1 + 1→0, and 1→1 ray contributions to the TS for a cylinder in the mud

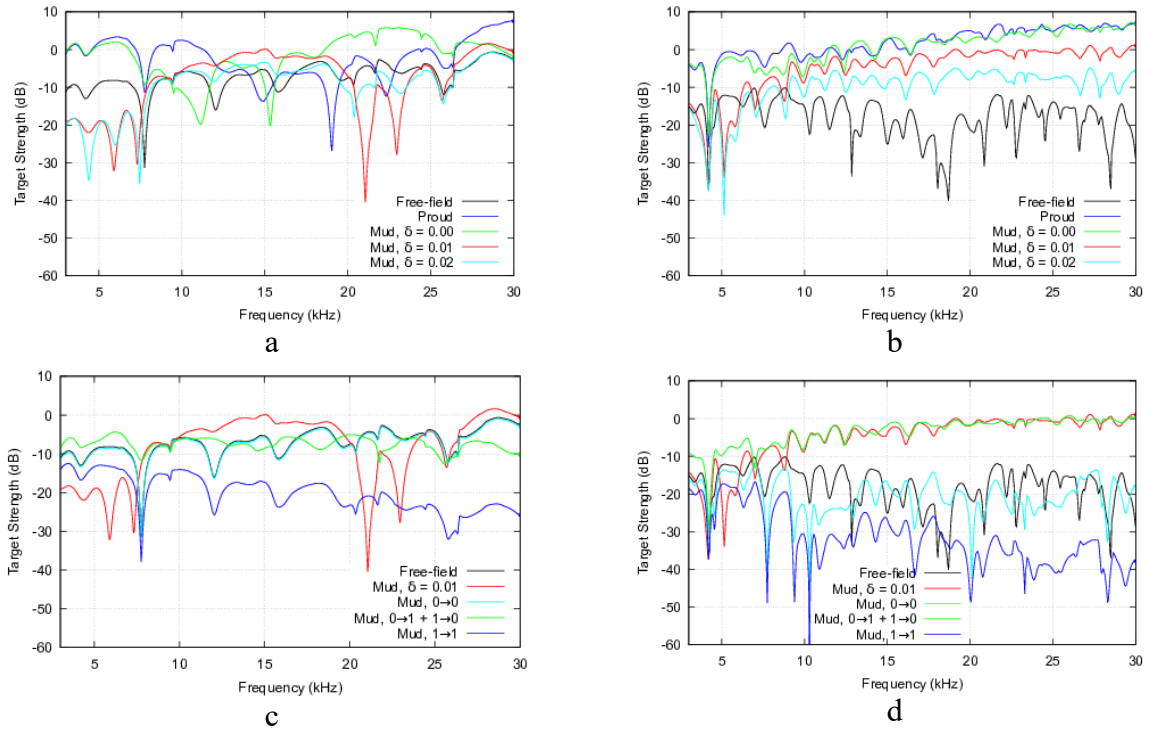


Fig. 2. TIER model TS simulations of the scattering from a 2:1 solid aluminum cylinder: a. cylinder in broadside orientation; b. cylinder in end-on orientation; c. broadside orientation for free-field scattering and scattering in mud layer with δ = 0.01; and, d. end-on orientation for free-field scattering and scattering in mud layer with δ = 0.01. Individual path contributions 0→0, 0→1 + 1→0, and 1→1 are also shown in c and d.

layer are depicted. This allows one to see the significance of 0→0, 0→1 + 1→0, and 1→1 contributions, and shows the frequency dependence of the absorption loss (e.g., the 1→1 path is significantly lower than the 0→1 + 1→0 paths).

In the shallow water environment of BAYEX14 with objects deployed to a 40 m horizontal range and source/receiver near the middle of the water column, reflections from the air-water interface are unavoidable for the type of broad beamwidth transducers used in BAYEX14. In the following TIER simulations, we ignore the mud layer and consider the superposition of $P_{ij}(\omega)$ as given in (1) with $i_{max} = j_{max} = 1$ and $i_{max} = j_{max} = 2$. The former case is a simulation for the four ray paths S→T→R, etc. with an image source and image receiver below the water-sediment interface. The latter case includes nine contributions where an additional image source and image receiver occur above the air-water interface. The simulations are for a 3:1 aluminum cylinder at the centre of a circular SAS (CSAS) path. A CSAS simulation allows the TIER model to generate a full 360° acoustic colour (AC) template (i.e., TS as a function of aspect angle and frequency) with a single simulation. The transmitted LFM pulse spans 1-30 kHz with a pulse duration of 6 ms. Fig. 3 shows the TIER model results for the simulations with the cylinder at the centre of CSAS paths with 10 and 40 m radii. Here, the time signals have been pulse compressed. The red box denotes that portion of the time signals used in the construction of SAS images and AC templates. Column b shows that the air-water interface contributions can be time-gated out; while column d shows an unavoidable

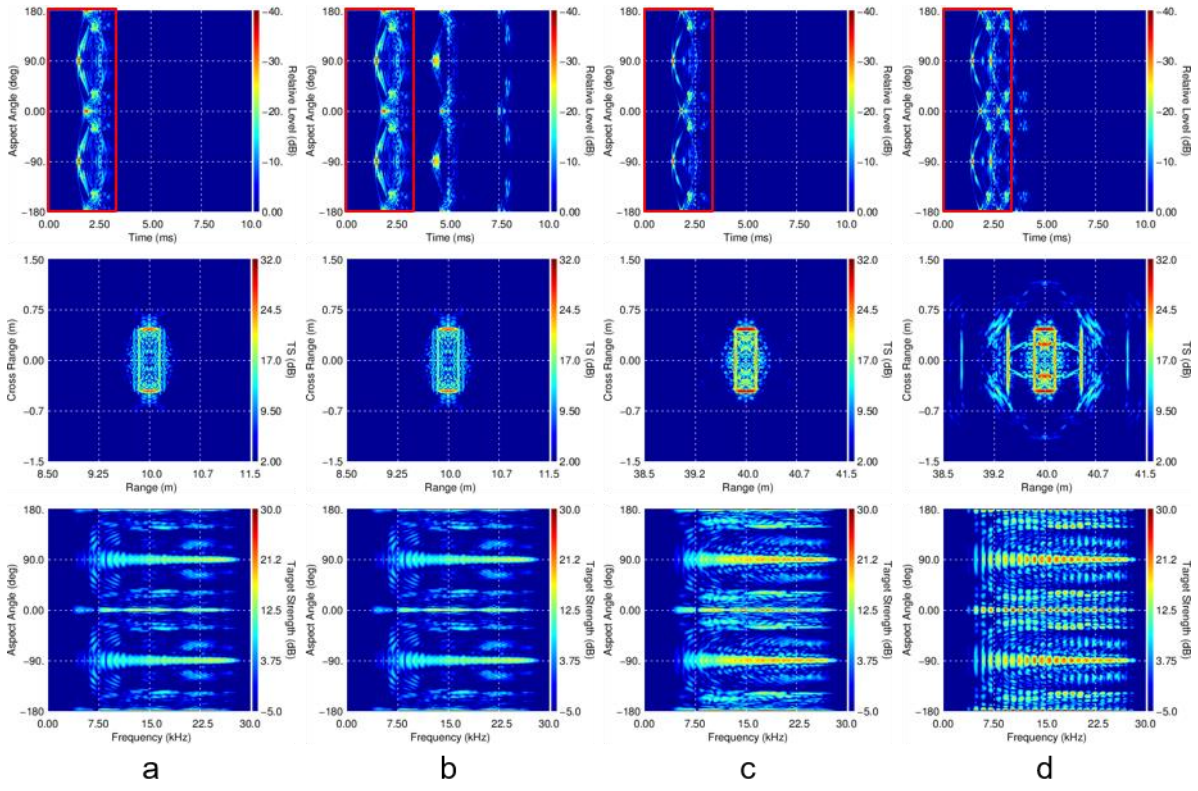


Fig. 3. CSAS TIER simulations for 3:1 aluminum cylinder. Columns a and b are for a 10 m radius CSAS path. Columns c and d are for 40 m radius CSAS path. Columns a and c have $i_{max} = j_{max} = 1$. Columns b and d have $i_{max} = j_{max} = 2$. Top row is the pulse-compressed scattered signals. Middle row is the SAS images constructed from the portion of the time signals in the red box. Bottom row is the AC templates for the portion of time signals in the red box.

overlap of air-water interface contributions within the time window of interest. This overlap causes what appear to be artefacts in the SAS image (column d, middle). The coherent SAS processing that focuses the $i_{max} = j_{max} = 1$ data does not properly account for the propagation

phase delay associated with the image source and image receiver above the air-water interface. Inspection of the time signals in Fig 3 (column b and d) reveals that the late-time arrivals from the air-water interface have a constant lag. Instead of constructing a SAS image from the primary returns at a reference distance, R, associated with the actual source/receiver location, the air-water arrivals can be used to construct a focused image at reference distance associated with the image source/receiver in air, $R + c_1 \times \text{lag}$. When these time-domain data are converted into a AC template, it is observed that the air-water interface contribution causes a modulation in the TS (see Fig. 3d, bottom). AC templates are often used in classification schemes. If a lack of recognition of the modulation exists during training and/or testing, then classification likely may fail for an object in shallow water.

5. SUMMARY

Inspection of Table 1 and Fig. 2 reveals that for objects placed at horizontal ranges that exceed a few water depths, the upper portion of the frequency band of the LF LFM pulse is extensively attenuated. The scattering amplitude in (1) determines the directionality of the scattered acoustic field. For co-located source/receiver, this means for an incident acoustic field that propagates along say path 0 in Fig. 1, a portion of its acoustic energy may be scattered into paths 0, 1, 2, … For the case of a nominally half-buried cylinder, the free-field result and 0→0 are nearly identical at broadside (see Fig. 2c) and have the same general level in an end-on orientation (see Fig. 2d). More importantly, Table 1 suggests that paths with multiple internal reflections become insignificant through absorption loss. It is also observed that for a given path length in the mud layer, high frequencies suffer significant absorption loss. This then yields reduced effective bandwidth of the LFM pulse, which degrades SAS image resolution.

A shallow water environment can impact the SAS image and the AC template for an object that is placed several water depths in horizontal range from the SAS platform, because air-water interface reflected paths can contribute under calm conditions. For BAYEX14, the water depth is about 8 m with broad-beamwidth source and receiver near mid-column. For objects in the 25 to 40 m horizontal range, SAS images display artefacts and AC templates show a modulation.

6. ACKNOWLEDGEMENTS

The research reported was jointly funded by the Strategic Environmental Research and Development Program (SERDP) and the Office of Naval Research (ONR). BAYEX14 was conducted in collaboration with the Naval Surface Warfare Center, Panama City Division.

REFERENCES

[1] **TP Long**, A global prospective on underwater munitions, *Mar. Technol. Soc. J.*, 43, pp. 5-10, 2009.

[2] **ML Overfield, LC Symons**, The use of the RUST database to inventory, monitor, and assess risk from Undersea Threats, *Mar. Technol. Soc. J.*, 43, pp. 33-40, 2009.

[3] **A Schwartz, E Brandeburg**, An overview of underwater technologies for operations involving underwater munitions, *Mar. Technol. Soc. J.*, 43, pp. 62-75, 2009.

[4] **JA Bucaro, BH Houston, M Saniga, LR Dragonette, T Yoder, S Dey, L Kraus, L Carin**, Broadband acoustic scattering measurements of underwater unexploded ordnance (UXO), *J. Acoust. Soc. Am.*, 123, pp. 738-746, 2008.

[5] **JA Bucaro; H Simpson, L Kraus, LR Dragonette, T Yoder, BH Houston**, Bistatic scattering from submerged unexploded ordnance lying on a sediment, *J. Acoust. Soc. Am.,* 126, pp. 2315-2323, 2009.

[6] **SG Kargl, KL Williams, TM Marston, JL Kennedy, JL Lopes**, Acoustic response of unexploded ordnance (UXO) and cylindrical targets, in *Proc. OCEANS 2010 MTS/IEEE*, Seattle WA, pp. 6, DOI: 10.1109/OCEANS.2010.5664392.

[7] **SG Kargl, AL Espana, KL Williams, JL Kennedy, JL Lopes**, Scattering from objects at a water sediment interface: Experiment, high-speed and high-fidelity models, and physical insight, *IEEE J. Ocean. Eng*., 40, pp. 632-642, 2015.

[8] **M Zampolli, AL Espana, KL Williams, SG Kargl, EI Thorsos, JL Lopes, JL Kennedy**, **PL Marston**, Low- to mid-frequency scattering from elastic objects on a sand sea floor: Simulation of frequency and aspect dependent structural echoes, *J. Comp. Acoust*., 20, p. 1240007 (14 pp.), 2012, DOI: 10.1142/S0218396X12400073.

[9] **KL Williams, SG Kargl, EI Thorsos, DS Burnett, JL Lopes, M Zampolli, PL Marston**, Acoustic scattering from a solid aluminum cylinder in contact with a sand sediment: Measurements, modeling, and interpretation, *J. Acoust. Soc. Am*., 127, pp. 3356-3371, 2010.

[10] **KL Williams,** Buried targets in layered media: A combined finite element/physical acoustics model and comparison to data on a half buried 2:1 cylinder, *J. Acoust. Soc. Am*., 140, EL504 (2016); https://doi.org/10.1121/1.4971324

THREE-DIMENSIONAL FINITE ELEMENT MODELING TECHNIQUES FOR UNDERWATER ACOUSTIC SCATTERING SIMULATIONS

Aaron Gunderson[a], Marcia Isakson[a], and Anthony Bonomo[a]

[a]Applied Research Laboratories: The University of Texas at Austin

Contact:
Aaron Gunderson
10,000 Burnet Rd.
Austin, TX 78758
aarong@arlut.utexas.edu

Abstract: *Finite element (FE) modeling is a technique ideally suited for the evaluation and prediction of acoustic scattering and propagation in complicated underwater environments, but requires consideration to keep the problem computationally feasible and efficient when solving over long ranges. Two-dimensional FE solvers are often preferred for efficiency, but are limited to symmetric targets and environments. This work will demonstrate a number of techniques for three-dimensional (3D) FE modeling which facilitate highly accurate evaluation of large-scale 3D scattering solutions from elastic targets in complicated ocean environments. A recently developed numerical Green's function determination technique allows the 3D FE domain to be kept small, while capturing far-field scattering results through the Helmholtz-Kirchhoff integral. Analytic forms of Green's functions are generally known for only a set of simple, canonical environments, and approximations are often applied for more general problems. By determining Green's functions numerically, analytic forms need not be known or imposed ahead of time, and may be determined accurately. A nontraditional scattering formulation is also adopted, which has been shown to improve FE model accuracy in the context of seafloor interface environments. This work will also explore the use of tapered plane wave approaches, Floquet-Bloch formulations, and other approximations within simulations involving targets in a rough or variable interface environment. A 3D model of target scattering in complex seafloor environments which applies these various techniques can be both efficient and accurate, and may strongly aid with underwater object detection and characterization.* *This work has been supported by the U.S. Office of Naval Research, Ocean Acoustics division, by IR&D funding from Applied Research Laboratories: The University of Texas at Austin, and by the SMART scholarship provided by the American Society for Engineering Education.*

Keywords: *Scattering, three-dimensional, modeling, finite elements*

1. Introduction

Finite element (FE) modeling is ideally suited for underwater acoustic scattering problems, due to the complexity and variability of seafloor environments. Effects such as interface roughness and bathymetry, seafloor layering, and interface clutter can strongly contribute to the acoustic scattering, and models must be able to properly account for these contributions. FE models are not restricted by any degree of environmental complexity, and therefore can replicate the exact three-dimensional (3D) configuration of the seafloor environment, giving highly accurate scattering predictions. The tradeoff for high solution accuracy is generally considered to be the computation time of 3D FE modeling, which grows rapidly with the size of the physical domain considered. To encompass distance scales associated with ocean environments, two-dimensional (2D) FE techniques[1,2] are often favored over 3D, although at a distinct cost. By using 2D FE models to predict scattering within a 3D environment, environmental symmetries must be assumed with respect to at least one coordinate, and the true variability of the environment cannot be imposed within the model. This article discusses a number of 3D FE modeling techniques, which yield far-field scattering solutions within reasonable time frames. In particular, an original numerical Green's function determination method is utilized, which enables far-field solutions to be rapidly determined within any environment. These techniques are applied within the context of modeling acoustic scattering from elastic targets in seafloor environments, with generalizable target/environment configurations, and with application to underwater object detection and classification. Near-field and far-field techniques are discussed in Sections 2 and 3, respectively. Section 4 applies these techniques to 3D models of target scattering, and further applications are discussed in the conclusion.

2. Near-Field techniques

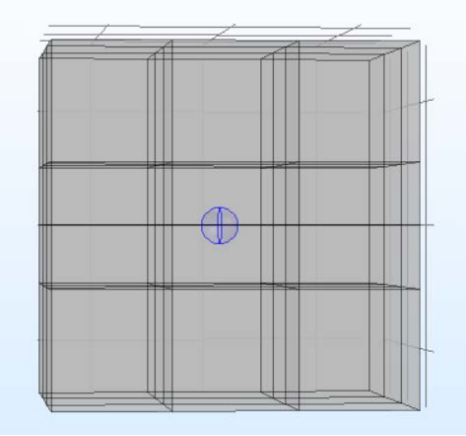


Fig.1: 3D FE domain for modeling acoustic scattering by an elastic sphere (blue), half buried in sediment. The flat, horizontal seafloor interface separates water subdomains from sediment subdomains, and runs through the sphere equator. All external subdomains are PMLs.

FE models require artificial truncation of the physical domain in order to solve, and the truncating boundary must not scatter or reflect outgoing radiation in order to satisfy the Sommerfeld radiation condition. A common solution is to place Bérenger Perfectly Matched Layers (PMLs)[1] at the edges of the domain, which fully absorb outgoing radiation and

simulate an infinite environment. Applying PMLs in such a way as shown in Fig. 1 allows the outgoing radiation to be absorbed in every direction at the edge of the model domain. PMLs are among the most widely used radiation absorption mechanisms within FE modeling, but a unique issue with PMLs arises in the context of modeling seafloor environments. The seafloor interface extends over the entire breadth of the FE domain, and necessarily must intersect the edge of the PMLs. This is problematic because the operation of a PML is inherently wavelength specific. Since the acoustic wavelength is different in the water and sediment environments, the PMLs adjacent to water and sediment must be customized differently. At PML-interface junctions, artificial reflections occur due to radiation from one environment meeting the PML associated with the other environment. These artificial reflections can reenter the FE domain, and have been observed[3] to contribute significantly to the scattering solution.

A method of reducing the artificial scattering from PML-interface junctions is to solve the problem using the fully scattered field formulation (FSFF),[4] also known as the interior transmission formulation.[3] In the FSFF, the solutions for the fields reflected by and transmitted through the interface are prescribed in addition to the incident field, and the target scattering alone is solved. This is in contrast to the usual scattered field formulation (SFF) in which the incident field alone is prescribed, and all other fields are determined through solving. The FSFF has been shown[3] to strongly improve FE solutions for buried target scattering when PMLs are used. For the case of a flat interface, analytic forms of the reflected and transmitted fields are known and may be prescribed within the FSFF framework. More complicated interfaces will be discussed in Sec. 4.

Alternatively, reflections from PMLs can be avoided by tailoring the incident field in such a way that the radiated fields incident upon the PML-interface junctions are minimized. Artificial tapers to incident fields are often imposed, such as the Gaussian or modified-Gaussian tapers of Thorsos et al.[5,6] The challenge is to use a wide enough taper that the target scattering is unaffected, while simultaneously keeping the FE domain large enough the incident, reflected, and transmitted fields go to zero at the domain edges. Tapers can therefore require much larger 3D computational FE domains, and much longer solution times than other methods. Another alternative is to remove the PMLs from the edge of the FE domain adjacent to the interface, and replace them with periodic boundary conditions (PBCs) to simulate an infinite domain. Floquet-Bloch PBCs have previously been used in FE scattering models with very good success.[7] The issue with PBCs is the inclusion of artificial Bragg resonances for which the periodicity is an integer number of wavelengths. The size of the FE domain must be chosen so that these resonances are outside the frequency range of interest for the problem.

3. Far-Field techniques

Far-field scattering solutions are often achieved using near-field FE models through the use of the Helmholtz-Kirchhoff (H-K) integral:

$$p_{\text{far}}(\vec{x},\omega) = \frac{1}{4\pi}\int_{S_0}\left[\frac{\partial G(\vec{x},\vec{x}_0,\omega)}{\partial n}p(\vec{x}_0,\omega) - G(\vec{x},\vec{x}_0,\omega)\frac{\partial p(\vec{x}_0,\omega)}{\partial n}\right]dS. \quad (1)$$

Eq. (1) gives the far-field scattering, evaluated at far-field point $\vec{x}$ and at frequency ω, where $\vec{x}$ can be outside the FE domain. The equation contains a contour integral over an arbitrary 3D contour S_0, which completely surround the target and may extend through the interface. The integrand contains the near-field solution $p(\vec{x}_0,\omega)$, evaluated at point $\vec{x}_0 \in S_0$, and the Green's

function $G(\vec{x}, \vec{x}_0, \omega)$ connecting the points $\vec{x}_0$ and $\vec{x}$, and their partial derivatives relative to the contour's outward-pointing normal $\vec{n}$. Use of the H-K integral allows the contour and the FE domain to be kept as small as possible, extending as little as a fraction of a wavelength outside the target. In this way, the far-field receiver location need not be included within the FE domain. Likewise, a far-field point source may also be excluded from the FE domain, by imposing a plane wave to be incident from the direction of the source. Thus, if the Green's function of the target's environment is known, only the target and a small portion of the environment in its immediate vicinity need to be included within the FE domain, keeping the 3D FE solution computationally efficient. The H-K contour may be discretized and the integral may be solved numerically within the F-E model, yielding far-field scattering solutions for any desired location of source and receiver.

Analytic forms of Green's functions are known for a set of canonical, relatively simple environments, while simplifying approximations are often used for more complicated environments.[8] The error associated with analytic Green's function approximations grows with the complexity of the environment, and in many cases makes the solution unusable. Various numerical or experimental Green's function determination methods have also been proposed,[9,10] which generally require a cross-correlation or convolution of field measurements made at multiple points in space, or at the same point at different instances in time. A newly-developed Green's function determination method allows the Green's function to be determined rapidly within the near-field FE model, using only a single field measurement and without requiring further mathematical processing. This method therefore introduces an enormous time saving measure for 3D FE modeling, which requires the Green's function to be determined at many discrete points around a 3D H-K contour. It also may be applied within any environment, and the only simplifying approximation made is that the receiver is in the far-field of the target. In this method, the Green's function $G(\vec{x}, \vec{x}_0, \omega)$ is obtained by placing a point source of frequency ω at the receiver location $\vec{x}$, and using the FE model to determine the field transmitted to the contour point $\vec{x}_0$. This field is, by definition, equal to $G(\vec{x}_0, \vec{x}, \omega)$ whose reciprocal Green's function $G(\vec{x}, \vec{x}_0, \omega)$ is determined by applying the reciprocity condition [Eq. (2.274) of Ref. 8]. As with the source location, the far-field receiver location need not be located within the FE domain. A plane wave from the receiver direction may instead be imposed, provided that phase information of the incoming wave is carefully preserved, based on the actual distance traveled between $\vec{x}$ and $\vec{x}_0$.

4. 3D finite element results

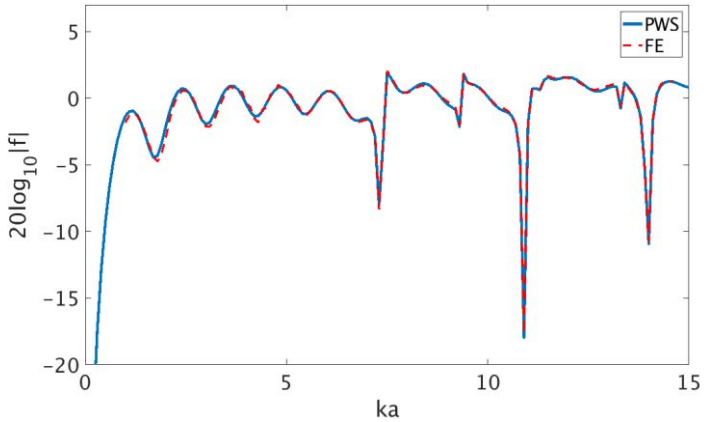


Fig.2: Scattering amplitude for a tungsten carbide sphere in water, as a function of frequency in terms of ka. Scattering amplitude is in terms of the decibel magnitude of the backscattering form function, f. Results for a partial wave series (PWS) and 3D finite element (FE) model are shown.

3D FE modeling was applied to the problem of acoustic scattering by an elastic, tungsten carbide sphere in a free-field infinite water column, using COMSOL Multiphysics® software. The model was developed with the domain construction depicted in Fig. 1, with water material properties prescribed on both sides of the sphere. The FSFF technique was applied, although the free-field nature of the problem would have permitted use of the SFF just as well. The scattering was solved for the case of a co-located far-field point source and receiver point, using the H-K integral and the numerical Green's function determination method presented in Sec. 3. The source/receiver point was chosen to be well in the far-field of the sphere, and was not included in the FE domain. Plane waves were imposed from the direction of the source/receiver, both as the incident field and to determine the Green's function at each point around the H-K contour. A cubic lattice of contour points surrounding the sphere was chosen as the H-K contour, with a maximum contour point spacing of λ/12.8 or smaller, at all wavelengths λ. Far-field scattering was evaluated in terms of the backscattering form function[11,12] f, which is related to the complex far-field scattered pressure p_{far} and the complex incident field p_{inc} in the following way:

$$p_{\text{far}} = p_{\text{inc}} \left(\frac{a}{2r}\right) f e^{ikr}. \tag{2}$$

In Eq. (2), a is the sphere radius, r is the range from source/receiver to target, and k is the acoustic wavenumber. Results are shown in Fig. 1, depicting good agreement between the FE result and an analytic partial wave series (PWS) scattering solution.[13] Both results are plotted as a function of incident frequency in terms of the dimensionless product ka.

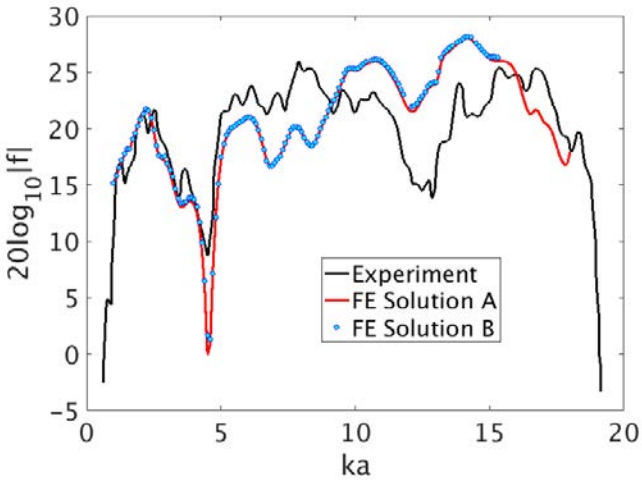


Fig.3: Scattering amplitude for an aluminum cylinder sitting flat (proud) on sand, as a function of frequency in terms of ka. Scattering amplitude is in terms of the decibel magnitude of the backscattering form function, f. Results for an experiment, and two 3D FE models. Solutions A and B are described in Sec. 4.

A 3D FE model of acoustic backscattering from an aluminum cylinder resting flat (proud) on sand was also created. The cylinder had a 2:1 length to diameter ratio, and sound was incident at a 21.5° grazing angle. The same 3D FE techniques and methodology were applied to this problem as to the problem of the sphere in Fig. 2, with the exception that the subdomains beneath the cylinder were given sand properties instead of those of water. Analytic forms of the reflected and transmitted fields at the interface were prescribed within the FSFF. The result is shown in Fig. 3 in red (called Solution A), and is compared to an experimental result from the same cylinder published by Williams et al. in Ref 14. Scattering amplitudes in terms of

target strength from Ref. 14 have been converted to form function notation. While distinct differences between the experimental and FE results are visible, they may largely be attributed to either (a) variations in sediment properties, or (b) variations in sediment surface structure that were not captured by the model. The model assumed a flat interface, and despite the experimental team's efforts to smooth the interface, some surface structure may be assumed to have been present in the experiment. Even modest amounts of surface roughness or changing bathymetry can strongly affect the scattering.

While interface roughness and structure may be imposed within FE models, an issue arises when attempting to apply the FSFF in such situations. Analytic forms of the reflected and transmitted fields are not generally known for complex interface geometries, and cannot consequently be applied within the FSFF. Another approach is to solve for these fields numerically, prior to prescribing them within the FSFF. These fields can be solved within the 3D FE framework by removing the target and solving the same problem using the SFF formulation; however, caution must be taken once again to avoid the artificial reflections associated with PML-interface junctions. Approaches such as artificially tapering the incident wave, applying PBCs to domain edges, or applying the analytic small slope approximation may all be used to solve for the reflected and transmitted fields. Solution B in Fig. 3 displays the result obtained when the 3D FE model was solved by prescribing numerically obtained fields, instead of analytic formulations as in Solution A. The fields were obtained in this case by applying Floquet-Bloch PBCs to the domain edges. This solution gives very similar results at all frequencies to Solution A. The numerical approach to solving for the reflected and transmitted fields is therefore a reasonable approach, and use of the FSFF need not be viewed as a hindrance to solving complex interface problems with 3D FE models.

5. Conclusion

3D finite element solutions have been evaluated for elastic targets in seafloor environments, using a number of techniques to keep the 3D modeling efficient and capable of producing far-field scattering results. In particular, a numerical Green's function determination method was used, which allows the far-field solution to be determined through the Helmholtz-Kirchhoff integral, by way of a single field measurement within the FE model. This step does not add a significant amount of time to the near-field solution, and is therefore quite beneficial when evaluating the H-K integrand at many locations along the discretized 3D H-K contour. The fully scattered field formulation (FSFF) also significantly increases solution accuracy, but does require solving numerically for additional fields prior to prescribing them within the FE model in the context of non-flat interface environments. With these techniques in place, the stage is now set for highly accurate 3D modeling of targets within complex seafloor interfaces. The interface height function for all results presented here has been constrained to the flat interface scenario of $z = 0$, but everything is in place for this constraint to be removed, allowing any kind of interface structure to be considered. Small-scale roughness, large-scale variable bathymetry, seafloor layering, and clutter may be incorporated into the model. It will be of great interest to see how the first tests of the model fare against experimentally acquired scattering data from real targets in a variety of environmental contexts. If all goes well, 3D FE modeling could soon provide significant application to the field of underwater target recognition and classification, by its ability to generate highly accurate synthetic data for training purposes.

6. Acknowledgements

This work has been supported by the U.S. Office of Naval Research, Ocean Acoustics division, by IR&D funding from Applied Research Laboratories: The University of Texas at Austin, and by the SMART scholarship provided by the American Society for Engineering Education.

REFERENCES

[1] **M. Zampolli, A. Tesei, F. B. Jensen, N. Malm, and J. B. Blottmann III**, "A computationally efficient finite element model with perfectly matched layers applied to scattering from axially symmetric objects," *J. Acoust. Soc. Am.*, volume 122, pp. 1472-1485, 2007.

[2] **M. J. Isakson, B. Goldsberry, and N. P. Chotiros**, "A three-dimensional, longitudinally-invariant finite element model for acoustic propagation in shallow water waveguides," *J. Acoust. Soc. Am.*, volume 136, pp. EL206-EL211, 2014.

[3] **S. Dey, W. G. Szymsczak, A. Sarkissian, and J. A. Bucaro**, "Scattering from targets in three-dimensional littoral and surf-zone environments with multi-layered elastic sediments based on an interior transmission formulation," *Comput. Methods Appl. Mech. Engrg.*, volume 260, pp. 24-39, 2013.

[4] **A. L. Bonomo**, "An evaluation of competing geoacoustic models and their applicability to sandy ocean sediments," Ph.D. dissertation, The University of Texas at Austin, Austin, TX, 2017.

[5] **E. I. Thorsos**, "The validity of the Kirchhoff approximation for rough surface scattering using a Gaussian roughness spectrum," *J. Acoust. Soc. Am.*, volume 83, pp. 78-92, 1988.

[6] **J. V. Toporkov, R. S. Awadallah, and G. S. Brown**, "Issues related to the use of a Gaussian-like incident field for low-grazing-angle scattering," *J. Opt. Soc. Am.*, volume 16, pp. 176-187, 1999.

[7] **A. C. Hennion, R. Bossut, J. N. Decarpigny, and C. Audoly**, "Analysis of the scattering of a plane wave by a periodic elastic structure using the finite element method: Application to compliant tube gratings," *J. Acoust. Soc. Am.*, volume 87, pp. 1861-1870, 1990.

[8] **F. B. Jensen, W. A. Kuperman, M. B. Porter, and H. Schmidt**, *Computational ocean acoustics, 2nd Ed.*, Springer, pp. 233-525, 2011.

[9] **O. I. Lobkis and R. L. Weaver**, "On the emergence of the Green's function in the correlations of a diffuse field," *J. Acoust. Soc. Am.*, volume 110, pp. 3011-3017, 2001.

[10] **A. Colombi, L. Boschi, P. Roux, and M. Campillo**, "Green's function retrieval through cross-correlations in a two-dimensional complex reverberating medium," *J. Acoust. Soc. Am.*, volume 135, pp. 1034-1043, 2014.

[11] **A. M. Gunderson, A. L. España, and P. L. Marston**, "Spectral analysis of bistatic scattering from underwater elastic cylinders and spheres," *J. Acoust. Soc. Am.*, volume 142, pp. 110-115, 2017.

[12] **A. L. España, K. L. Williams, D. S. Plotnick, and P. L. Marston**, "Acoustic scattering from a water-filled cylindrical shell: Measurements, modeling, and interpretation," *J. Acoust. Soc. Am.*, volume 136, pp. 109-121, 2014.

[13] **P. L. Marston**, "Acoustic beam scattering and excitation of sphere resonance: Bessel beam example," *J. Acoust. Soc. Am.*, volume 122, pp. 247-252, 2007.

[14] **K. L. Williams, S. G. Kargl, E. I. Thorsos, D. S. Burnett, J. L. Lopes, M. Zampolli, and P. L. Marston**, "Acoustic scattering from a solid aluminum cylinder in contact with a sand sediment: Measurements, modeling, and interpretation," *J. Acoust. Soc. Am.*, volume 127, pp. 3356-3371, 2010.

Structured Session 18

Multibeam Echo Sounding: Bathymetry and sediment Classification

Organiser(s): Simons Dick, Snellen Mirjam

SEAFLOOR SEDIMENT CHARACTERIZATION USING MULTIBEAM ECHOSOUNDERS WITHOUT GRAB SAMPLING: OPPORTUNITIES AND CHALLENGES

Alireza Amiri-Simkooei[a], Leo Koop[a], Mirjam Snellen[a], and Dick G. Simons[a]

[a] Acoustics Group, Faculty of Aerospace Engineering, Delft University of Technology, Delft, 2629 HS, The Netherlands, email: a.amirisimkooei@tudelft.nl

Abstract: *In the last two decades, the use of multibeam echosounders has been growing for seafloor mapping and characterization. The former uses bathymetry data whereas the latter makes use of backscatter data. The use of backscatter data has been the subject of intensive research to gain insight into seafloor composition using either empirical or model-based methods. Model-based methods employ the available physical models for predicting the backscatter strength and determine the seafloor geoacoustic parameters in an inversion algorithm using optimization methods. These methods allow for direct coupling between the backscatter curve and sediment characteristics. But the methods usually suffer from a shortcoming associated to uncalibrated sonars, which is referred to as calibration curve. Grab samples at reference areas are required to estimate the calibration curve. A question may arise as to whether, or to what extent, the calibration curve can be estimated without grab sampling. Knowing that the calibration curve is an unknown function of incident angle, in principle, one can approximate it using the available estimation and optimization theories. This is elaborated in this paper and its opportunities and challenges will be addressed. The potential benefit is twofold. 1) The huge amount of MBES backscatter currently available in many hydrographic organizations can directly be used for seafloor characterization. 2) The available multiple-frequency MBESs can further improve the performance of the inversion process. There are also challenges to be addressed. 1) Estimation of the calibration curve is an unstable process because it is merely based on observed backscatter data without using grab samples. 2) The physical models, and component parts thereof, are not usually well-behaved functions, possibly due to their discontinuities or discontinuity of their derivatives. These issues will be elaborated in this paper.*

Keywords: Multibeam echosounder (MBES), Backscatter data, Angular calibration curve (ACC), Sediment mean grain size.

1. INTRODUCTION

Multibeam echosounders (MBESs) data have been intensively used in many marine research problems over the last decades. Two kinds of information are widely provided by an MBES: bathymetry and backscatter data. MBES-derived bathymetric data are used to map the topographic features of the seafloor for a wide range of applications such as maintaining safe navigation, off-shore construction and studying seafloor structure and morphology. Information on the seafloor composition can mainly be obtained from the backscatter data. The use of MBES backscatter data is prone to a few sources of fluctuations and uncertainties. They can be considered as deterministic effects, to be compensated for in a functional model. Unmodelled effects such as noise are to be taken into consideration in the stochastic model.

Although the stochastic nature of backscatter data can be an interesting research field by its own, the focus of this study is on all deterministic effects. We therefore reduce the backscatter fluctuations due to noise by an averaging procedure. The deterministic fluctuation of backscatter data, showing an angular dependence, is a function of seafloor sediment type, acoustic signal frequency, and calibration of the MBES. This is further investigated in the present study.

There are methods widely used to characterize seafloor using the backscatter data. The methods can be classified into two main categories as 'empirical methods' and 'model-based methods'. The model-based methods use available physical models and characterize the seafloor by maximizing the match between modelled and observed backscatter signal. These methods optimize an objective function for seafloor type or parameters indicative for seafloor type. These methods allow for direct coupling between the backscatter data and sediment characteristics if the MBES sensitivity is known. This is however not usually the case, indicating that the correction on the backscatter curve (backscatter as a function of angle) is to be estimated prior to the optimization process [1,2]. The empirical methods make use of a few statistical features extracted from the data, possibly after dividing the area/data into small regions/groups. The principal component analysis (PCA), linked with clustering algorithms—k-means for instance—can be used to classify backscatter data [3,4]. The clustering algorithms aim at partitioning observations into a few clusters in which each observation belongs to one cluster satisfying some pre-defined criteria. As a result, the outcome of clustering algorithms is a qualitative comparative description of the seafloor sediment distribution (e.g. finer, fine, coarse, and coarser). The advantage of the empirical methods is their ease of implementation and use. The complication is that ground truth is usually required to associate the classification results to sediment physical parameters such as mean grain size.

This contribution considers the model-based seafloor characterization methods. We aim at determining seafloor parameters based on the available physical model interrelating backscatter data with sediment geoacoustic parameters. Among such models, the model suggested by Jackson et al. [5] is frequently used in geoacoustic inversion algorithms. This model states that the total backscatter strength is a combination of the interface roughness scattering and volume scattering. Such a model-based method uses the backscatter data at the entire angular range, known as angular response curve (ARC). There is a complication that the observed backscatter curve, as a function of angle, is not always calibrated. Therefore the angular correction curve (ACC) is to be applied to the received backscatter. The ACC is usually determined by the calibration of the MBES in flat areas, having homogenous sediment types and known grain sizes values. This is achieved through the application of the angular range analysis (ARA) to the observed backscatter data [2]. This contribution attempts to avoid grab samples when estimating the ACC.

The above methods thus require grab samples to characterize sediment types. We elaborate on characterizing the seafloor without grab samples. Having the available physics-based models, one can predict the backscatter data for different sediment types, frequencies and incident angles. Given the frequency of the multibeam system, the angular response curve is affected by two main factors: 1) the sediment type, 2) the ACC as a function of incident angle. To estimate the calibration curve without grab sampling, we will employ the available advanced estimation and optimization methods. We propose a method to approximate the calibration curve of MBES by employing high-order polynomials as a function of incident angle. Having the ACC available, an inversion procedure can be implemented to estimate the geoacoustic parameters of the entire survey area.

The remainder of this paper is structured as follows. Section 2 proposes an algorithm to estimate the calibration curve of the sonar system. This section will then apply the method to a MBES data set collected in the Brown Bank area of the North Sea in 2017. Section 3 provides some opportunities and challenges of the proposed algorithm. The conclusions are presented in Section 4.

2. METHODOLOGY AND RESULTS

2.1 Methodology

This section presents our algorithm for estimating the sonar calibration curve. In many engineering problems, fitting a curve in one-dimensional (1D) space to a set of randomly scattered data points is a commonly encountered problem. The calibration curve is an unknown function of sonar beam angle, which is to be estimated using only the backscatter data, without grab sampling. Having an irregular data set, one can use an approximating function to obtain the function values at specific intermediate points. When the data are contaminated with random noise—backscatter data for instance—approximation provides more accurate results than interpolation. The approximation can be accomplished by using high-order polynomial functions. A more elegant alternative, to be considered for future research, is to use a spline function consisting of piecewise low-order polynomial segments connected together at known knots under some continuity conditions.

We hypothesize that the calibration curve of the sonar system is a function of signal frequency and grazing angle. The difference between the observed (BS^o) and modeled (BS^m) backscatter data is considered to be the calibration curve. One then has $C(f,\theta) = BS^o(f,\theta,AC) - BS^m(f,\theta,M_z,w_2,\sigma_2)$ where f is the signal frequency, θ is the incident angle, AC is the acoustic class number, see Ref. [6], and M_z, w_2 and σ_2 are the sediment mean grain size, spectral strength, and volume scattering parameter, respectively [7]. For a given frequency f, the above equation simplifies to

$$C(\theta) = BS^o(\theta,AC) - BS^m(\theta,M_z,w_2,\sigma_2) \quad (1)$$

This is the basis model considered to estimate the calibration curve. As a function of angular range, a high-order polynomial is employed

$$C(\theta) = a_0 + a_1\theta + a_2\theta^2 + \cdots + a_p\theta^p \quad (2)$$

Choosing an appropriate value for p is a challenging problem. Too small values can lead to under-parameterization and hence not capturing all variations along the angular range. Too large values can lead to the problem of instability and high oscillations of the approximating function, known as Runge's phenomenon [8]. The use of spline functions can resolve the above two problems.

The polynomial coefficients $a_0,\dots,a_p$ in Eq. (2) are unknown. To estimate them, one requires the backscatter data at the entire angular range, say $\theta_j = -65,\dots,65$ ($j = 1,\dots,\mathrm{m}$), with m the number of beam angles at which the backscatter data are observed. This will then make a linear model $y = Ax + e$, where y is an m-vector of observations, A is the $\mathrm{m} \times (\mathrm{n} = \mathrm{p}+1)$ design matrix, and e is an m-vector of observation errors. At a specific incident angle, θ_j, the j$^{\text{th}}$ entry of y is $y_j = BS^o(\theta_j,AC) - BS^m(\theta_j,M_z,w_2,\sigma_2)$, and its corresponding row of the design matrix is $A_j = [1,\theta_j,\theta_j^2,\dots,\theta_j^p]$. In principle, when the number of observations m is larger than the number of unknown parameters n (i.e., $\mathrm{m} > \mathrm{n}$, having redundancy in the linear model), one can use the least squares method to estimate the coefficients of the polynomial. There are however two complications regarding the implementation of the above problem. The details are as follows:

(1) The observed BS^o is directly available, while the modeled BS^m is a function of the unknowns M_z, w_2 and σ_2. One way out of this dilemma is to use the backscatter data at grab sample positions at which M_z (and thereby w_2 and σ_2) are known (see [9]). We however propose to estimate the three geoacoustic parameters along with the polynomial coefficients in an optimization method—differential evolution (DE) algorithm for example [10].

(2) So far we assumed, the observation vector y consists of one backscatter curve relating to one acoustic class: $BS^o(\theta,AC)$. This is however not sufficient because 1D data (even with

arbitrary values for M_z, w_2 and σ_2) can be captured with a high-order polynomial. This indicates that the estimated calibration curve cannot be stable, when dealing with only one acoustic class. To ensure the stability of the results, backscatter curves for more than one acoustic class are required. The number of acoustic classes can thus ensure the redundancy and hence stability of the estimation of the calibration curve. Therefore the observation vector y should take into consideration the backscatter curve of all identified acoustic classes, i.e. $BS^o(\theta_j, AC_i), i = 1, \dots, I$, where I is the number of ACs [6]. This accordingly allows the geoacoustic parameters M_z^i, w_2^i and $\sigma_2^i, i = 1, \dots, I$ to vary among different acoustic classes.

After estimating the calibration curve, the method proposed by Ref. [9] is used to estimate the three geoacoustic parameters for the entire area.

2.2 Results

The Brown Bank, located in the North Sea, was surveyed using the Kongsberg EM 302 MBES system. The survey was conducted by the Royal Netherlands Institute for Sea Research (NIOZ) vessel, the Pelagia, from Oct. 27 to Nov. 03, 2017. The settings of the MBES were as follows: Central frequency of 30 kHz, Beam opening angles of 2° and 1° in the across and along track directions, respectively, Pulse length of 750 µs. The beam coverage of 432 beams was set to equidistant. A swath opening angle of 130° was used, with port and starboard coverage both being 65°.

The proposed algorithm was implemented to estimate the calibration curve. Prior to the optimization process, we implemented the Bayesian method, Ref. [6], to identify number of acoustic classes. Four acoustic classes were identified. Figure 1 shows the Bayesian acoustic classification results of the survey area, with some grab samples as ground truth. Lower acoustic class number (e.g. class no. 1) corresponds to lower backscatter value, whereas higher class (e.g. class no. 4) corresponds to higher backscatter value. The four classes make in general four backscatter curves, each having three unknown geoacoustic parameters (in total 12), but only one set of common coefficients for the calibration curve in Eq. (2) for which we set $p = 10$. This optimization process is implemented using the differential evolution (DE) method, see Ref. [10]. The search is performed to simultaneously estimate the 12 geoacoustic parameters along with the coefficients of the 10-degree polynomial in the optimization method.

The optimization process of estimating the calibration curve was repeated over 100 independent runs. Each run will then give the polynomial coefficients in Eq. (2). The results are presented in Fig. 2. There are some variations, among the 100 runs, when estimating the calibration curves. These variations could be associated to various sources of uncertainty among which sampling bias is the main contributor. Such a bias is averaged out through averaging over the 100 independent runs. The mean curve over all 100 runs is thus used as the backscatter curve correction of the sonar system for the subsequent inversion process using the DE optimization method.

After estimating the calibration curve, the observed backscatter curves of the entire area were used to perform the inversion. Three geoacoustic parameters M_z, w_2 and σ_2 were searched for using the DE optimization method. The parameters were constrained as $-1 \leq M_z \leq 9$, $0 \leq w_2 \leq 0.02$ and $0.00001 \leq \sigma_2 \leq 0.02$. Figure 3 shows the inverted values of w_2 and σ_2 versus those inverted for M_z. As a function of M_z, the range of variations of w_2 and σ_2 differs from the empirical model predictions proposed by APL-UW model [7]. The reported relations with M_z are known to be rather weak as there is a considerable range of variations in these two parameters and hence they are not much correlated with M_z [7]. This further confirms that the optimization is to be performed by at least the three parameters M_z, w_2 and σ_2. The parameters w_2 and σ_2 can provide further insight into seafloor structure and sediment composition, respectively. This is the subject of further research in the future.

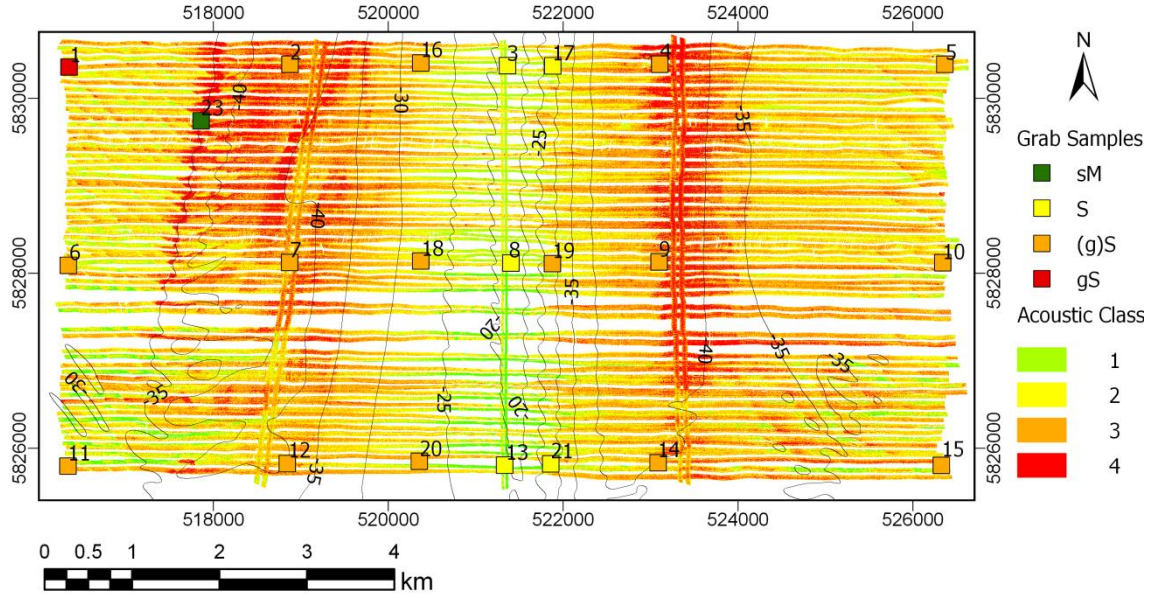


Fig. 1. *Bayesian classification map along with grab samples based on Folk scheme. Four acoustic classes ranging from lowest backscatters (green) to highest values (red), figure from Koop et al. (2019).*

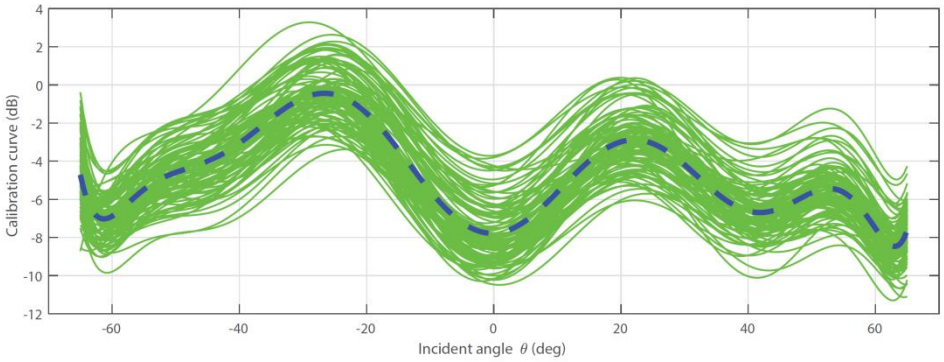


Fig. 2. *Calibration curve expressed as 10-degree polynomial in Eq. (2) obtained for 100 independent runs (green solid lines) along with their average curve (blue dashed line).*

3. OPPORTUNITIES AND CHALLENGES

The use of the proposed method can have a few potential benefits of which we point out two major issues. Seafloor characterization using MBES backscatter data usually requires grab samples to estimate the calibration curve. This can be avoided if the proposed algorithm is applied to MBES data for seafloor characterization. The huge amount of MBES backscatter currently available in many hydrographic organizations can directly be used for seafloor characterization. Further, the performance of the proposed algorithm can be improved if multiple-frequency MBES data are available. This can open new research areas in this field.

In Refs. [7] and [11], empirical representations of geoacoustical parameters in terms of the mean grain size M_z have been offered. They empirically relate M_z to the geoacoustical characteristics of the upper few centimetres of the sediments. There are specific empirical polynomial models that relate ratio of sediment mass density to water mass density (ρ), ratio of sediment sound speed to water sound speed (v), sediment sound speed attenuation coefficient as a contributor to loss parameter δ (i.e. α_2/f). Although the expressions for these parameters are continuous over the entire mean grain size ranging from $M_z = -1$ to $M_z = 9$, their derivative are not continuous in the entire domain of definition.

A differentiable function is the one whose derivative exists at each point in its domain of definition $M_z \in [-1, 9]$. The graph of the empirical representation of the geoacoustical parameters shows sharp corners (see later Fig. 4), indicating that they are not differentiable in their entire domain. Having a smooth and differentiable function makes the subsequent optimization methods more stable and efficient when implementing geoacoustic inversion algorithms. Some of the optimization methods, based on iterative algorithms, require not only evaluation of the function values but also their higher-order derivatives. This study makes the bridge for implementing new optimization methods.

To further highlight the importance of a smooth function in the optimization process, we further investigate some of the inverted parameters w_2 and σ_2 versus estimated M_z (Fig. 3). It is observed that a kind of discontinuity exists in the estimated values for both parameters w_2 and σ_2 at $M_z = 1$. A similar observation has been also reported by Ref. [9] at $M_z = 5.3$ for MBES data at higher frequency, i.e. f = 300 kHz. These kinds of discontinuities or bias in the estimates of the inverted parameters are due to the empirical relations expressing ρ and ν as a function of M_z. We observe that both ρ and ν have sharp corners, indicating a sudden change in their rates both at $M_z = 1$ and $M_z = 5.3$ (see Fig. 4). An approximating function using the cubic spline theory handles this problem.

We now present our proposal to make the above empirical formulas differentiable up to and including the second order. This is achieved based on an approximation of the above empirical representations using the cubic spline theory. Such splines consist of a series of piecewise third-order polynomial connected to each other at some intermediate points, known as knots. The consecutive pieces are joined together at the knots such that the first and second derivatives of the fitted curves are also continuous at these points. The method used is based on the least squares cubic spline approximation [12].

For each of the above parameters (i.e. $\rho, \nu, \alpha_2/f$ and w_2) a separate spline function is used. Each spline consists of a few cubic polynomials of the form $f_i(M_z) = a_{0i} + a_{1i}M_z + a_{2i}M_z^2 + a_{3i}M_z^3$, connected to each other. The coefficients $a_{ji}, j = 0,1,2,3$ of these third-order polynomials are presented in Table 1. The final spline function, consisting of all polynomials connected to each other, is presented in Fig. 4, for each of the above parameters. They closely follow their original representations, but now having continuous first and second order derivatives in their domain of definition $M_z \in [-1, 9]$.

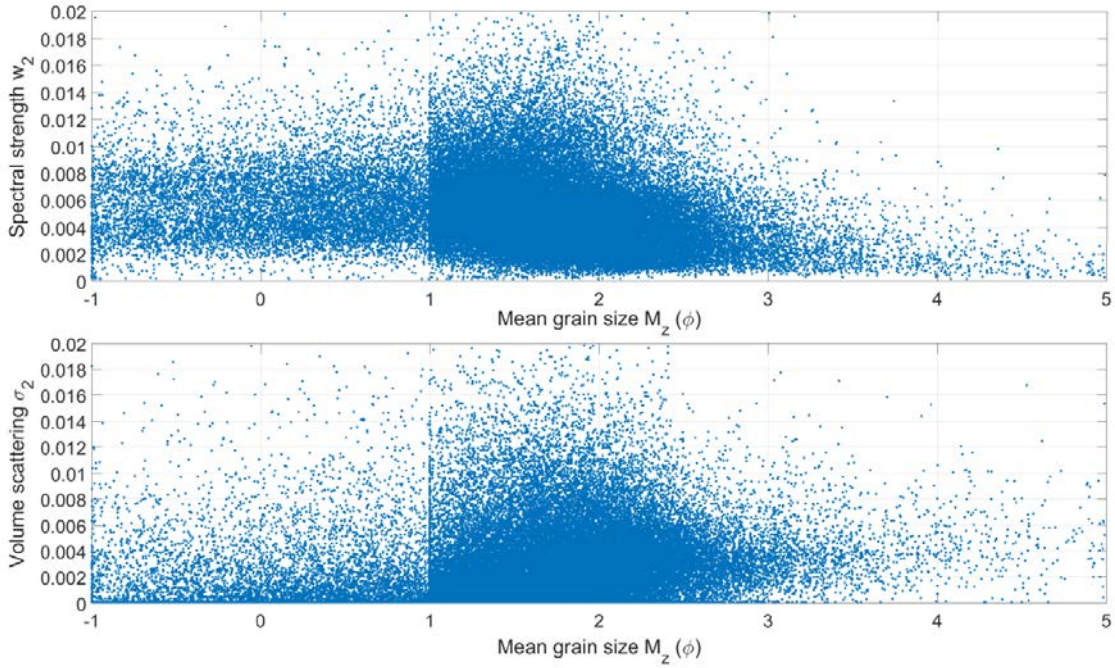


Fig. 3. *Inverted spectral strength w_2 (top) and volume scattering parameter σ_2 (bottom) versus estimated mean grain size M_z*

Table 1. *Polynomial coefficients of spline function for four geoacoustic parameters* $\rho, \nu, \alpha_2/f$ and w_2*:* $f_i(M_z) = a_{0i} + a_{1i}M_z + a_{2i}M_z^2 + a_{3i}M_z^3$*, connected to each other at some intermediate points*

Parameter	i	M_z range	a_{0i}	a_{1i}	a_{2i}	a_{3i}
ρ	1	[-1, 1]	2.363149906	-0.201790117	-0.056492156	0.016180867
	2	[1, 2.5]	1.794316816	1.110551799	-0.974676718	0.190856603
	3	[2.5, 5.3]	1.995533627	-0.224930836	-0.002874679	0.002935133
	4	[5.3, 9]	1.234233881	-0.020216334	0.001181053	-4.29060E-06
ν	1	[-1, 1]	1.285222133	-0.057546455	-0.005178733	0.000628855
	2	[1, 2.5]	1.244269004	0.038686795	-0.074785846	0.014955847
	3	[2.5, 5.3]	1.196631647	-0.001627891	-0.019668166	0.002407916
	4	[5.3, 9]	1.051173569	-0.013612915	0.000389345	2.71798E-05
α_2/f	1	[-1, 0]	0.455599999	2.07592E-09	1.43323E-08	1.26182E-08
	2	[0, 2.6]	0.455599999	2.07593E-09	0.012262365	-0.000966864
	3	[2.6, 4.3]	2.786522897	-2.265631606	0.720622671	-0.070880176
	4	[4.3, 6]	-27.66322511	17.3075376	-3.442709462	0.221737223
	5	[6, 9]	0.834517646	-0.174873566	0.00994903	-1.73210E-05
w_2	1	[-1, 2]	0.008933068	-0.003704703	0.000364354	6.46530E-05
	2	[2, 5]	0.006238244	-0.001091583	-0.000227648	4.42271E-05
	3	[5, 9]	0.001050034	-0.000123598	7.74266E-06	-6.48982E-08

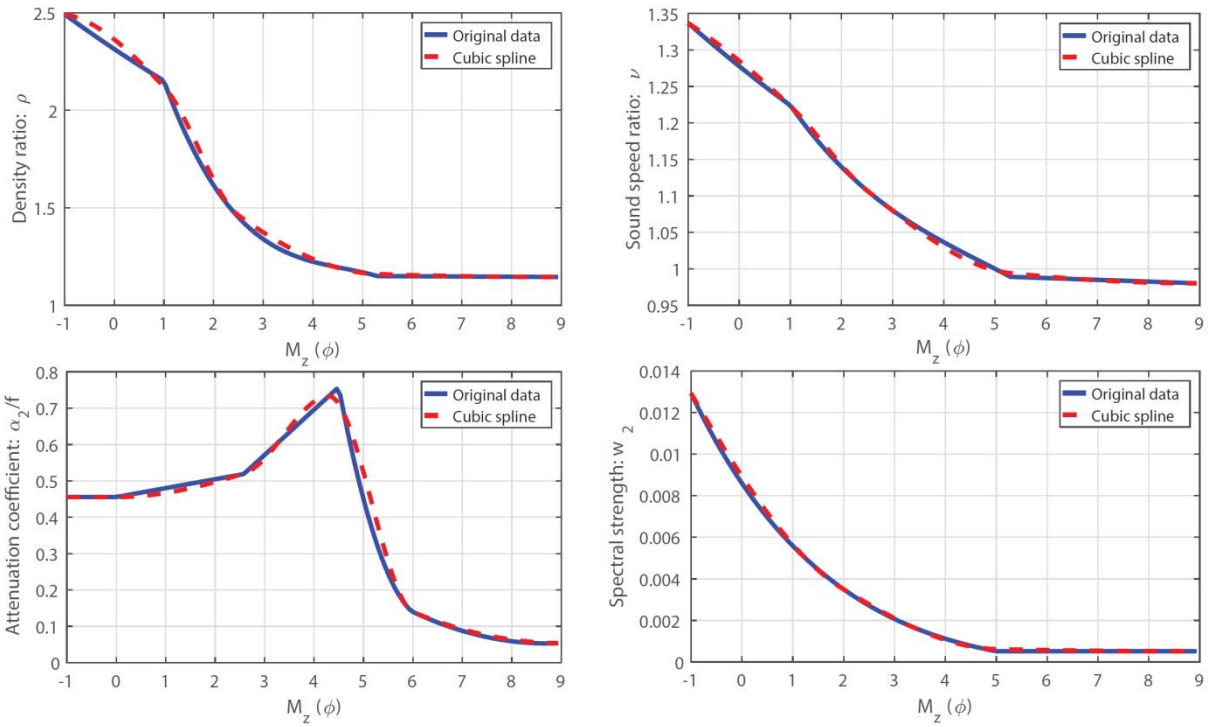


Fig. 4. *Empirical representations of four geoacoustical parameters, Ref. [6], along with their best approximation using spline functions; ratio* ρ *of sediment mass density to water mass density (top-left), ratio* ν *of sediment sound speed to water sound speed (top-right), sediment sound speed attenuation coefficient* α_2/f *(bottom-left), and spectral strength (bottom-right).*

CONCLUSIONS

Model-based methods were employed to estimate seafloor geoacoustic parameters in an inversion algorithm using an optimization method. The model-based methods usually suffer from a shortcoming associated to uncalibrated sonars. Grab samples at reference areas are usually required to estimate the calibration curve. This study presented an algorithm to

estimate the calibration curve without grab sampling. Knowing that the calibration curve is an unknown function of incident angle, in principle, one can approximate it using the available estimation and optimization theories. The method was successfully applied to the MBES backscatter data collected at the North Sea. The potential benefit of the proposed method is twofold. A large amount of MBES backscatter currently available in many hydrographic organizations can directly be used for seafloor characterization. The available multiple-frequency MBESs can further improve the performance of the inversion process. We also highlighted a few challenges. The calibration curve estimation is an unstable process when there are no grab samples or reference areas. Also, the available empirical physical models are not usually well-behaved functions, possibly due to their discontinuities or discontinuity of their derivatives. We addressed this issue by approximating them using cubic spline functions.

Acknowledgments: We would like to thank RobWitbaard for being the chief scientist during the data gathering cruise and the crew of the NIOZ vessel the Pelagia for their assistance during the acquisition of the data. Karline Soetaert of NIOZ is acknowledged for her role in organizing the cruise, as well as Tom Ysebaert, who also coordinated the particle size analysis of the grab samples. Peter van Breugel was key in performing the particle size analysis in the NIOZ lab. We also thank Leendert Dorst and Daniëlle van Kuijk of the Hydrographic Service within the Royal Netherlands Navy for making full coverage bathymetry data of the Brown Bank area available. We acknowledge the Gieskes-Strijbis Fonds for the financial support of the DISCLOSE project, within which this research took place.

References

[1] Clarke, J.H., Danforth, B., Valentine, P. (1997) Areal seabed classification using backscatter angular response at 95 kHz. In, SACLANTCEN Conf on High Frequency Acoustics in Shallow Water (pp. 243-250)

[2] Fonseca, L., Mayer, L. (2007) Remote estimation of surficial seafloor properties through the application angular range analysis to multibeam sonar data. *Mar. Geophys. Res*. 28 (2), 119–126.

[3] Brown, C.J., Todd, B.J., Kostylev, V.E., Pickrill, R.A. (2011) Image-based classification of multibeam sonar backscatter data for objective surficial sediment mapping of Georges Bank, Canada. *Continental Shelf Research*, 31, S110-S119

[4] Eleftherakis, D., Amiri-Simkooei, A., Snellen, M., Simons, D.G. (2012) Improving riverbed sediment classification using backscatter and depth residual features of multi-beam echo-sounder systems. *The Journal of the Acoustical Society of America*, 131, 3710-3725

[5] Jackson, D.R., Winebrenner, D.P., Ishimaru, A. (1986) Application of the composite roughness model to high-frequency bottom backscattering. *The Journal of the Acoustical Society of America*, 79 (5), 1410–1422.

[6] Simons, D.G., Snellen, M. (2009) A Bayesian approach to seafloor classification using multi-beam echo-sounder backscatter data. *Applied Acoustics*, 70, 1258-1268

[7] APL-UW model (1994) High-Frequency Ocean Environmental Acoustics Models Handbook, edited by K. L. Williams (http://www.dtic.mil/docs/citations/ADB199453, APL-UW technical report, 1994), No. APL-UW 9407.

[8] Runge, C. (1901) Über empirische Funktionen und die Interpolation zwischen äquidistanten Ordinaten, *Zeitschrift für Mathematik und Physik*, 46: 224–243.

[9] Snellen M., D. Eleftherakis, A.R. Amiri-Simkooei, R.L. Koomans, D.G. Simons (2013) An inter-comparison of sediment classification methods based on multi-beam echo-sounder backscatter and sediment natural radioactivity data, *The Journal of the Acoustical Society of America*, 134 (2), 959-970

[10] Snellen M. and D.G. Simons (2008) An assessment of the performance of global optimisation methods for geoacoustic inversion, *Journal of Computational Acoustics*, 16(2), pp. 199–223

[11] Hamilton, E. (1974) Prediction of deep-sea sediment properties: state-of-the-art. In: Inderbitzen, A.L. (Ed.), Deep-Sea Sediments, Physical and Mechanical Properties. Plenum Press, New York, pp. 1–43.

[12] Zangeneh-Nejad F., A. R. Amiri-Simkooei, M. A. Sharifi and J. Asgari (2017) Cycle slip detection and repair of undifferenced single-frequency GPS carrier phase observations, *GPS Solutions*, 21(4):1593–1603.

SEABED SCATTERING CROSS SECTION ESTIMATION USING THE RESON SEABAT T50: A NUMERICAL EVALUATION OF THE FOOTPRINT ERROR WHEN USING A ZERO-SLOPE ASSUMPTION IN THE ALONG-TRACK DIRECTION

Gorm Wendelboe

Teledyne RESON

Contact author: Gorm.Wendelboe@Teledyne.com, Teledyne RESON A/S, Fabriksvangen 13, 3550 Slangerup, Denmark. Phone +45 4738 0022.

Abstract: *The bottom scattering cross section estimated by the RESON SeaBat T50 multibeam echosounder (MBES) includes an estimate of the insonified area, which is obtained by assuming the seabed has a vanishing slope in the along-track direction. In this paper, the validity of this assumption is investigated for different along-track slopes, depths, and continuous wave (CW) pulse durations using a numerical model. It is demonstrated how the errors are largest around normal incidence and rapidly decrease as steering angle increases. The errors can be reduced by increasing the CW pulse duration. For example, at 400kHz, a 40μs CW pulse transmitted over a nadir-depth of 35m will, for seafloors with along-track slopes of 5% and 15%, yield errors of 1.5 and 5dB, respectively. If, however, the duration of the CW pulse is increased to 100μs, the resulting errors are reduced to 0.05 and 1.5dB, respectively. Finally, a brief description is given of how the estimated footprint areas can be removed from the estimated scattering cross section values and replaced by the user's own estimates.*

Keywords: *multibeam echosounder, seabed scattering strength, insonified area.*

1. INTRODUCTION

Over the recent decades, various acoustic measurements have shown that the seabed back-scattering strength S_b obtained at frequencies between 20-500kHz depends on whether the seabed consists of sand, gravel, mud, rock, gravel, or a mixture of those [1]-[6]. Species present on top of or inside the sediment may also have an influence on S_b [7]. The scattering strength varies with the angle of incidence and it may vary with the acoustic frequency depending on sediment type. The scattering strength is a physical property of the seabed, and the acquisition of S_b requires a calibrated sonar [8]. The SeaBat T50 multibeam echosounder (MBES) provides estimates of the seabed scattering strength [6]. The estimates of the insonified area are based on the assumption that the seabed has zero slope in the along-track direction, which may lead to incorrect S_b-estimates. Here, the validity of the assumption is assessed using a numerical model, in which the MBES beam patterns are projected on a seafloor plane, and where the footprint area will be calculated as the convolution of the transmitted tone-burst with the seafloor as a function of time. The approach is particularly important close to nadir [9][10]. Along-track slopes between 2% -15% (≈ 1° - 9°) are considered.

2. A 3D NUMERICAL MODEL OF THE INSONIFIED AREA

The model will consider an MBES transmitting a continuous waveform (CW) pulse, also known as a tone-burst, of duration τ with carrier frequency $f_c = 400$kHz onto a plane and horizontal seabed.
Figure 1(a) shows the applied coordinate system. The x-axis is pointing in the across-track direction, the y-axis in the along-track direction, and the z-axis upwards. The origin is located at the center of the receiver (Rx), and with zero pitch angle, i.e., $\alpha = 0$, the center of the transmitter (Tx) is located at $\vec{r}_{Tx}(0) = [0\ y_{Tx}\ 0]^T$. Roll, heave, and heading are not included. A point on the seafloor is given by the vector $\vec{r} = \begin{bmatrix} r_x & r_y & -H \end{bmatrix}^T$, where H is the depth.

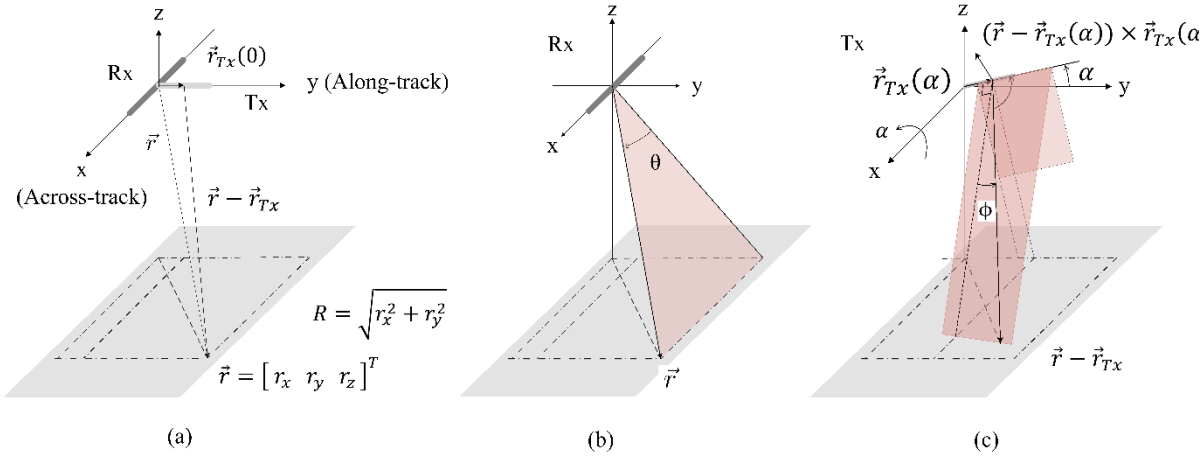


Figure 1: Geometry applied (a), the angle θ used for the Rx beamformer beam pattern (b), and the angle ϕ used for the Tx beam pattern (c).

The Tx sensitivity is assumed constant in the across-track direction between -65° and 65°, and the Rx sensitivity is assumed constant in the along-track direction between -20° and 20°. Thus, Tx and Rx are represented as line arrays, i.e., the arrays that are rotationally symmetric around their main axes. The beam patterns of interest are the beamformed Rx beam pattern in the

across-track direction, with a 3dB beam width of approximately 0.5°/cos(θ_s), where θ_s is the steering angle, and the Tx beam pattern in the along-track direction with a 3dB opening angle of 1°. The purpose is to project the beam patterns onto discrete points on the seabed. The far-field beamformed Rx beam pattern b_{Rx} is obtained by the following expression [11]:

$$b_{Rx} = \sum_{n=1}^{N_0} w_n e^{-iknd(\sin(\theta)-\sin(\theta_s))} \tag{1}$$

where $N_0 = 256$ is the number of channels, and w_n is the energy-normalized shading coefficient for the n'th channel; here the receiver shading is a Chebyshev window with a sidelobe suppression magnitude factor of 30dB. Next, in Eq. (1) i is the imaginary number, $k = 2\pi f_c/c$ is the wave number obtained with a speed of sound $c = 1500$ m/s, $d = 1.6$mm is the sensor spacing. Finally, θ_s is the steering angle, and θ is the angle of the incoming field from the point $\vec{r}$, where $\sin(\theta) = r_x/|\vec{r}|$, see, e.g., Figure 1(b). For any given point on the seabed the corresponding b_{Rx} value is obtained using Eq. (1). An example of the receiver beam pattern for a steering angle of 20° is shown in Figure 2 (left).
The far-field beam pattern of the transmitter in the along-track direction b_{Tx} is obtained from a look-up table with values populated by a company proprietary model. b_{Tx} is shown in Figure 2 (right). An along-track sloping seafloor is simulated by rotating the transmit array around the x-axis by the angle α. The along-track transmit beam angle ϕ is equal to zero at the center of the Tx along-track beam, and for any point on the horizontal seabed plane it is computed from the cross-product between the vector from the Tx center to the seabed point and the vector from the origin to the Tx center, i.e.,

$$\phi = \frac{\pi}{2} - \sin^{-1}\left(\frac{\left|\left(\vec{r} - \vec{r}_{Tx}(\alpha)\right) \times \vec{r}_{Tx}(\alpha)\right|}{|\vec{r} - \vec{r}_{Tx}(\alpha)|\,|\vec{r}_{Tx}(\alpha)|}\right) \tag{2}$$

see, e.g., Figure 1(c).

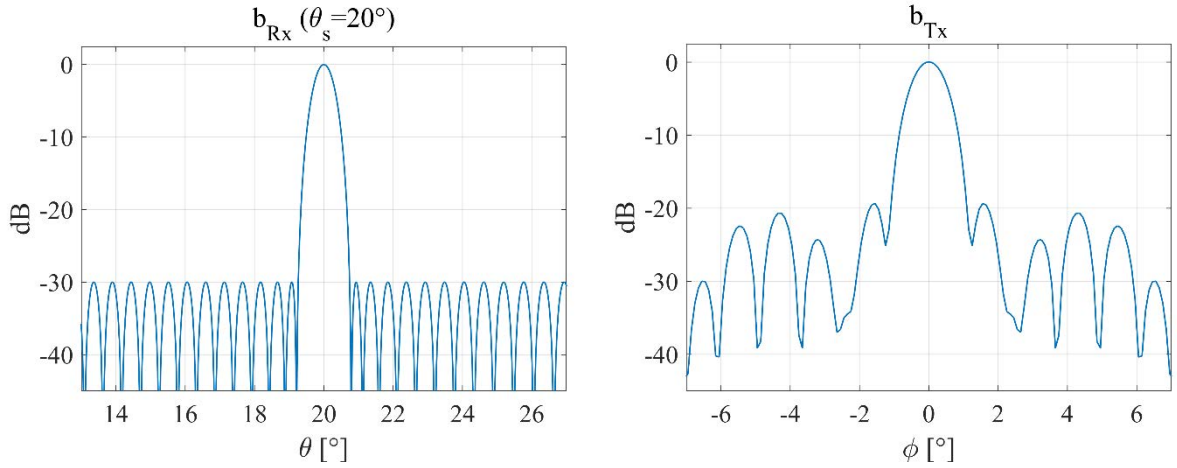


Figure 2: Across-track beam pattern of the Rx beam former (left) Along-track Tx beam pattern (right) both at 400 kHz.

The integration area is reduced to a region around the point where the center beam of the transmitter crosses the center of the steered beam on the seabed. For illustrative purposes, the area covers what corresponds to $\pm 5\theta_{3dB}$ in the across-track direction and $\pm 5\phi_{3dB}$ in the along-track direction.

Close to nadir, the seabed plane is divided into rectangular grids with a size governed by the width of the main beams. The angular resolution is $\Delta\theta = \theta_{3dB}/30 = 0.5°/30$, and the resolution in the across-track direction yields

$$\Delta x = H\,[\tan(\theta_s - \theta_{3dB} + \Delta\theta) - \tan(\theta_s - \theta_{3dB})] \tag{3}$$

Equivalently, $\Delta\phi = \phi_{3dB}/60 = 1°/60$, and the resolution in the along-track direction, Δy, is obtained by replacing θ_{3dB} with ϕ_{3dB} and setting $\theta_s = 0$ in Eq. (3). The instantaneous footprint area is obtained as the product of the projected Tx and Rx beam pattern squared and integrated over the tone-burst projected area on the seabed at a given point in time (see, e.g., Eq. G.4, p. 495, [5]). Using the seabed model, the insonified area is expressed as

$$A(n, \theta_s, H) = \Delta x\,\Delta y \sum \left\{ b_{Tx}^2(x_i, y_j)\; b_{Rx}^2(x_i, y_j; \theta_s) \middle| R_1 \le \sqrt{x_i^2 + y_j^2} \le R_2 \right\} \tag{4}$$

where n is the sample number, i and j are indices of the discrete x - and y points respectively, and

$$R_1 = \left\{ \sqrt{\left(n\Delta r_{T_s} - \Delta r_\tau\right)^2 - H^2} \;\middle|\; n \ge (H + \Delta r_\tau)/\Delta r_{T_s} \right\} \tag{5}$$

(otherwise $R_1 = 0$), that is, the ground range distance from the origin to the rear edge of the pulse on the seabed plane (see, e.g., Figure 1(a)); $\Delta r_{T_s} = c\,T_s/2$ is the sampling range resolution, and T_s is the sampling time; $\Delta r_\tau = c\tau/2$ is the physical range resolution, and τ is the tone-burst duration. Finally, in Eq. (4), R_2 is the front edge of the pulse on the seabed, and it is given by

$$R_2 = \left\{ \sqrt{\left(n\Delta r_{T_s}\right)^2 - H^2} \;\middle|\; n \ge H/\Delta r_{T_s} \right\} \tag{6}$$

(otherwise $R_2 = 0$). For simplicity, the offset y_{Tx} is not included in Eqs. (4)-(6); the impact of this approximation is considered to induce insignificant offsets of the integration areas. Cartesian coordinates are applied up to an angle, which corresponds to the maximum disk size multiplied by a factor ν, i.e.,

$$\theta_T = \nu \cos^{-1}\left(\frac{H}{H + \Delta r_\tau}\right) \tag{7}$$

where $\nu = 5$ is applied. For $\theta_s > \theta_T$, integration is carried out using polar coordinates so that

$$A(n, \theta_s, H) = R_n\,\Delta R_n\,\Delta\alpha \sum_{m=1}^{M} b_{Tx}^2(n, j)\; b_{Rx}^2(n, j; \theta_s) \tag{8}$$

where n is the sample number, $R_n = \sqrt{r_n^2 - H^2}$ is the ground range, $\Delta R(n, \theta_s) = \Delta r_\tau / \cos(\theta_g)$ is the pulse projected on the seafloor, $m = 1,2,..,M$ is the index of an angular sub-sector out of M sectors. Each sector has a radial resolution of $\Delta\alpha = \Delta\phi_{3dB}/30$ =1°/30. The beam patterns are projected onto the seabed points with coordinates$(R(n)\cos(\alpha_m), R(n)\sin(\alpha_m))$.

3. SIMULATION RESULTS

All simulations have been made with $f_c = 400$kHz. The along-track seabed slopes are presented as linear percentage slopes. For example, a slope of 10% corresponds to a bottom that changes the depth by 10m over a distance of 100m. The distance between the origin and the center of the Tx is set to y_{Tx} = 0.25m. The sampling time used in the simulations is T_s = 5.76μs.

Figure 3(a-c) shows the time progression of the footprint area for the beam with steering angle θ_s = 2°. Figure 3(d) shows total area as a function of time. The duration of the tone-burst is τ = 40μs, and the depth is H=35m. Three instances in time after the front side of the signal has reached the seabed are shown. At time t_1= 20μs (a) the footprint area is a small disk containing the main lobe of the combined 2D beam pattern; the total area is approximately 20dB below the maximum value (d). At time t_2 = 56μs the insonified area is an annulus (b), and where the insonified area includes the main lobe of the combined beam pattern, and the total area has reached the maximum of -6.5dB re 1 (d). At t_3 = 80μs the annulus is moving out of the main lobe of the combined beam pattern, and the total area has, at this point in time, already been reduced by approximately 10dB since time t_2 (d). The blue dotted line in Figure 3(d) represents the total area obtained with the 3D numerical model presented in the previous section. The red dotted line is the total area produced by the 2.5D algorithm applied for the SeaBat T50; a model that does not include side-lobes.

Figure 4 shows the maximum insonified area as a function of beam angle for six different along-track slopes at a depth of 35m. Figure 4(a) shows for the case where the tone-burst has a duration of τ = 40μs: At the nadir beam a 5% sloping bottom yields an error of 1.5dB when compared to the bottom with 0% slope; at 7% the error is about 2.5dB, and at 15% it is about 5dB. As the steering angle increases the errors decrease and become insignificant above θ_s = 35°. Figure 4(b) shows the results for a similar investigation, but with τ = 100 μs: A 5% sloping bottom does not produce an error at the nadir beam; a 7% sloping bottom only yields an insignificant error of about 0.1dB, and at 15º it is about 1.7dB. Thus, by increasing the duration of the tone-burst the error will decrease.

Figure 5 shows the relative error of the maximum footprint area at nadir as a function of depth. Figure 5(a) shows the error for a tone-burst duration of τ = 40μs: If the error must be less than 1dB, then at 30m and 50m the slope is allowed to be up to 5% and 3%, respectively. Figure 5(b) shows the errors when τ = 100μs: If the error must be less than 1dB, then at 30m and 50m the slope is allowed to be up to 11% and 7%, respectively.

Figure 6 shows the relative error of the maximum footprint at nadir as a function of tone-burst duration. Figure 6(a) shows the expected errors at a depth of 20m. If τ>120μs the errors will be negligible even for slopes up to 15%. Figure 6(b) shows the expected footprint errors at a depth of 35m; if τ>120μs the errors will be negligible for slopes up to 7%.

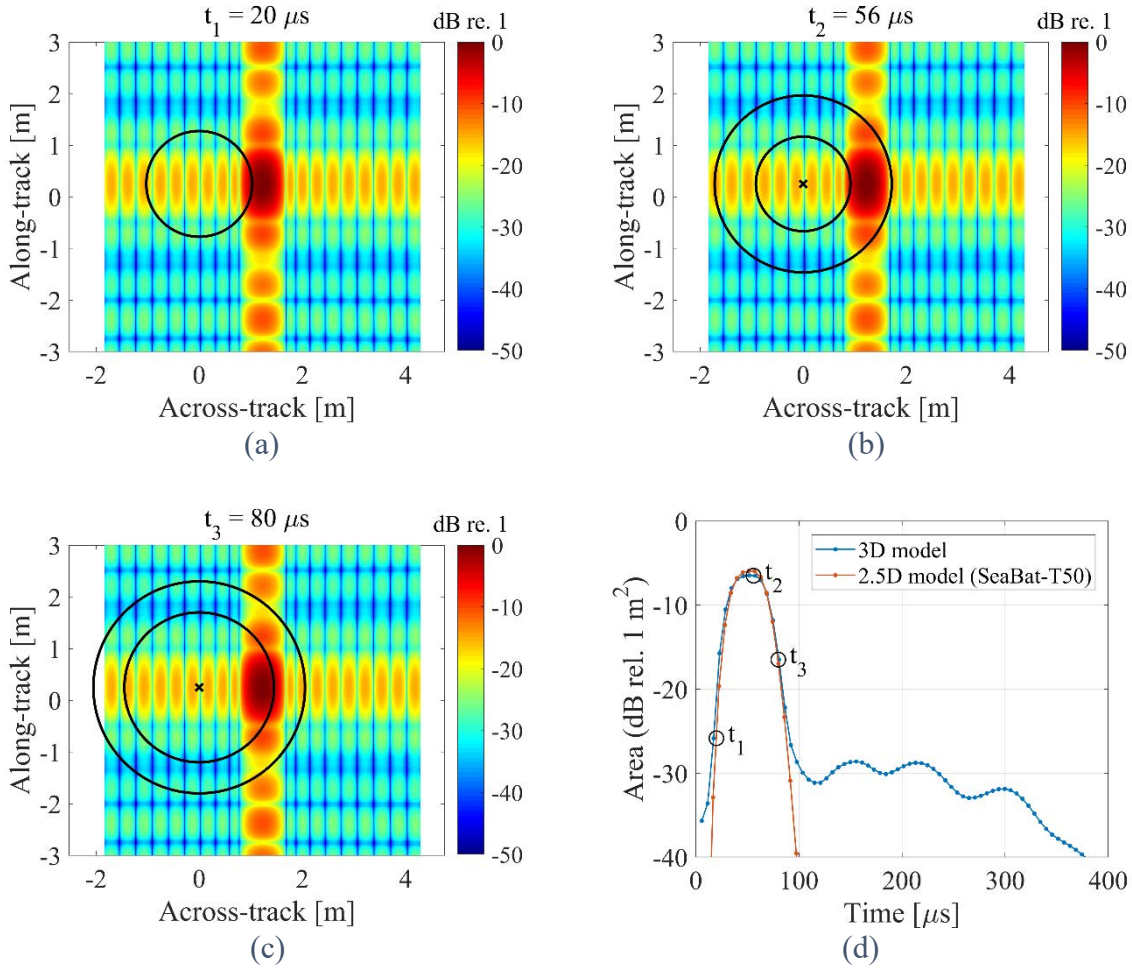


Figure 3: Time evolvement of the footprint area at θ_s = 2° on a non-sloping seabed. The tone-burst center frequency is f_c =400kHz, τ =40μs, and H =35m. Figures 1(a)-1(c) show the insonified area at three different points in time after the front side of the pulse has reached the seabed. Finally, Figure 1(d) shows the footprint area as a function of time.

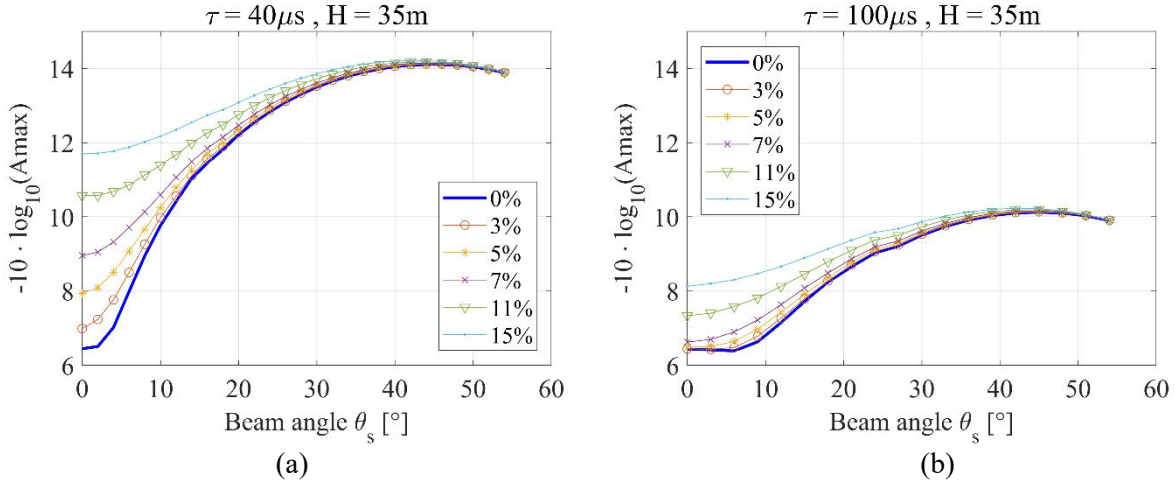


Figure 4: The maximum insonified area as a function of beam angle for six different seabed slopes in the along-track direction

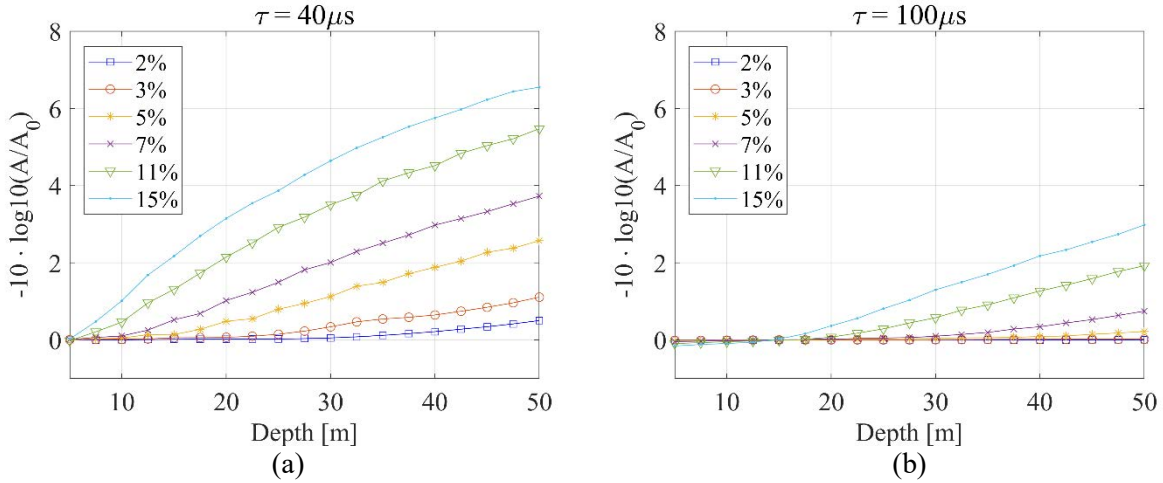


Figure 5: Relative error of the maximum insonified area within the nadir beam as a function of depth. The reference area A_0 is the area of a non-sloping seafloor.

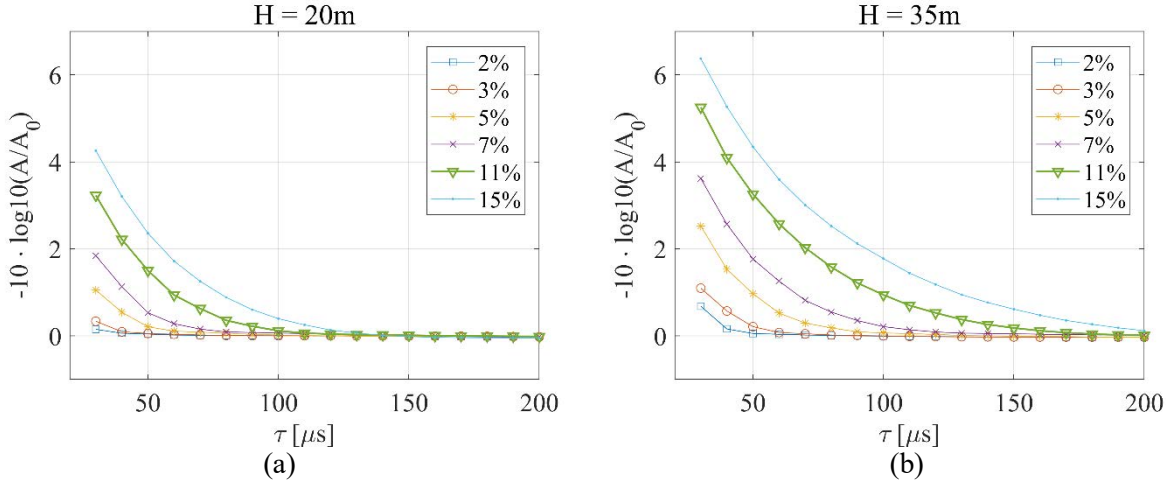


Figure 6: Relative error of the maximum insonified area within the nadir beam as a function of tone-burst duration. The reference area A_0 is the area of a non-sloping seafloor.

4. PROCESSING OPTION FOR THE MBES USER

For each S_b -value stored in the T50 datagram (Record 7058) [12] the associated footprint area value A_{T50} is also stored. It is possible to replace A_{T50} with an alternative footprint value, for instance based on a 3D bottom geometry produced by survey software packages such as QPS™ or Teledyne CARIS™. The scattering cross section is obtained from the scattering strength by $\sigma = 10^{(S_b/10)}$, where $\sigma = K_{T50}/A_{T50}$, and where K_{T50} is a factor that depends on environmental conditions and other MBES parameters. The modified scattering cross section can be obtained by

$$\sigma_m = \sigma A_{T50}/A_m \tag{9}$$

where A_m is the alternative footprint area. The grazing angle, i.e., the angle between incoming field and the seabed surface, is not included in the datagram, but it is crucial for further analysis. Thus, if the σ -values obtained from the T50 datagram are selected for analysis, the grazing angle can be obtained from the datagram that includes the bottom detection points (Record 7027), and from which the height profile obtained from a ping can be used to estimate the grazing angles.

5. SUMMARY

The algorithm, which estimates S_b for SeaBat T50 data, neglects the slope of the seabed in the along-track direction. Consequently, surveys over areas with high topographic variations or depth gradients in the along-track direction may lead to flawed S_b-estimates. The errors are dominant near normal incidence, and they will decrease with increasing angle of incidence at the outer beams. The errors increase with increasing along-track gradients and with depth. However, if the duration of the transmitted CW pulse is increased the errors are reduced significantly. Thus, for best possible backscatter performance is it recommended to use CW pulses with durations between 80-200µs depending on the depth and the seabed topography. Alternatively, it is possible for the user to replace the footprint values with the user's own estimates.

REFERENCES

[1] **C.M. McKinney, C.D. Anderson**, Measurements of backscattering of sound from the ocean bottom, *J. Acoust. Soc. Am.*, 36 (1), pp. 158-163, 1964.

[2] **P.D. Mourad, D.R. Jackson, A**, High frequency sonar models for bottom backscatter and forward loss, In *Proc. OCEANS*, pp. 1168-1175, 1989.

[3] **D.G. Simons, M. Snellen**, High frequency measurements of bottom backscattering strength in the North Sea: Correlation with grain size, shell content and gravel content, In *Boundary Influences in High Frequency, Shallow Water Acoustics,* University of Bath, pp. 177-184, 2005.

[4] **T.C. Weber, L.G. Ward**, Observations of backscatter from sand and gravel seafloors between 170 and 250 kHz, *J. Acoust. Soc. Am.*, 138 (4), pp. 2169-2180, 2015.

[5] **D.R. Jackson, M.D. Richardson**, *High-Frequency Seafloor Acoustics*, Springer, 2007.

[6] **G. Wendelboe**, Backscattering from a sandy seabed measured by a calibrated multibeam echosounder in the 190–400 kHz frequency range, *Marine Geophysical Research*, 39 (1-2), pp. 105-120, 2018.

[7] **M.S. Ballard, K.M. Lee**, The acoustics of marine sediments, *Acoustics Today*, 13 (3), pp. 11-18, 2017.

[8] **G. Larmarche, X. Lurton**, Introduction to the Special Issue "Seafloor backscatter data from swath mapping echosounders: from technological development to novel applications", *Marine Geophysical Research*, 39 (1-2), pp. 1-3, 2018.

[9] **D. Jackson, B.T. Hefner, A. Ivakin, G. Wendelboe**, Seafloor characterisation using physics-based inversion of multibeam sonar data, In *Proc. 11th European Conference on Underwater Acoustics (ECUA 2012)*, Edinburgh, pp. 258-263, 2012.

[10] **L. Bjørnø**, *Applied Underwater Acoustics*, T.H. Neighbors and D. Bradley, Elsevier, pp. 532-535, 2017.

[11] **P. S. Naidu**, *Sensor array signal processing*, CRC Press, Elsevier, pp. 75-94, 2001.

[12] **Teledyne-RESON**, Data Format Definition Document. 7k Data Format, https://www.teledyne-pds.com/faq-2/where-can-i-find-the-latest-teledyne-reson-7k-dfd/

ASSESSMENT OF RELIABILITY OF MULTI-BEAM ECHO-SOUNDER BATHYMETRIC UNCERTAINTY PREDICTION MODELS

Tannaz H. Mohammadloo[a], Mirjam Snellen [a], Alireza Amiri-Simkooei[a], Dick G. Simons[a]

[a]Acoustics Group, ANCE, Department of Control & Operations, Faculty of Aerospace Engineering, Delft University of Technology, Kluyverweg 1, 2629 HS, Delft, The Netherlands

Tannaz H. Mohammadloo, Kluyverweg 1, 2629 HS, Delft, The Netherlands, 0031 15 2787399, T.Hajimohammadloo@tudelft.nl

Abstract: *Nowadays Multi-Beam Echo-Sounder (MBES) systems are used for obtaining information of the sea/river bed bathymetry and sediment composition. For the latter, use is usually made of the backscatter strength and depth derivatives, such as depth residuals. However, the depth derivatives are affected by the uncertainties inherent to the MBES varying with the sensors used, survey configuration and operational environment. Although models are available for the vertical uncertainty prediction, the question is how well these models can capture the estimated uncertainties of real observations. The present contribution addresses this issue by comparing the measured with modelled depth uncertainty accounting for the most recent insights of the error contributors. Data was acquired in water depths of around 2m, 10m and 30m with pulse lengths of 27 µs, 54 µs and 134 µs in the Oosterschelde estuary, the Netherlands, enabling the assessment of depth and pulse length dependence of the uncertainties. In general, the predicted and measured uncertainties are in the same order of magnitude. With increasing depth the discrepancy between the modelled and measured uncertainties increases. The effect of changing pulse length is found to be captured by the model, except for the angles close to nadir. The most dominant contributors to the vertical uncertainty are those induced by the angle of impact and range measurements. These contributors thus require further investigation to obtain a more realistic estimate of the vertical uncertainties.*

Keywords: *Multibeam Echosounder Derived Depth, Bathymetric Uncertainty Prediction, Inherent MBES Uncertainty Sources*

1. INTRODUCTION

Multibeam echosounders (MBESs) have become the most valuable tool for seafloor mapping providing a good coverage and high resolution bathymetrty and acoustic backscatter datasets within a relatively short time [1]. The applications of these datasets are numerous, including offshore activities such as building wind farms at sea, the support of dredging operations, safe navigation, and the study of marine geological and biological systems [2], [3], [4], [5]. The MBES measurements used for obtaining such information are backscatter strength and depth derivatives, such as depth residuals. However, similar to any type of measured quantity, they are contaminated by uncertainties.

Obtaining a realistic a priori estimate of depth uncertainties is thus of importance as lacking information can lead to mistakenly classifying the uncertainties and assigning different sediment types to measurement having actually the same sediment composition, but different uncertainties. The realistic uncertainty description is also used for survey planning to assess whether the required survey standards can be met in a specific measurements campaign. Other applications of a-priori estimates of the vertical uncertainty include, but are not limited to, bathymetric gridding, [6], used for coastal inundation modelling, [7]. Efforts have been thus put forward to predict the depth uncertainties [8], [7], [9] and [10]. However, considering the fast development of MBES systems, there is a need to investigate the reliability of MBES depth uncertainty prediction models using real measurements to obtain an insight into their agreements and possible discrepancies and to highlight direction for future improvements.

The present contribution makes the first steps toward such a comparison and it is organized as the following. Section 2 gives a short description of the equations used for quantifying the depth uncertainties followed by the result in Section 3. The conclusions are given in Section 4.

2. DESCRIPTION OF THE DEPTH UNCERTAINTY PREDICTION MODEL

In an MBES system the depth of an underlying surface is determined using the travel time of a transmitted signal. A wide bundle of sound is transmitted perpendicular to the direction of vessel movement. Using electronic beam-steering at reception, the MBES can distinguish between incoming angles of sound on the transducer, [11]. The steering angle is noted by θ_s and the resulting beams have opening angles ψ_y and ψ_x in the across-track and along-track directions respectively. The depth below the transducer, d, is determined as

$$d = r \cos P \cos(\theta_s + R + \theta_{\text{mount}}) = r \cos P \cos \theta \tag{1}$$

with θ_{mount}, R and P being the across track angle under which the MBES is mounted on the vessel, roll and pitch angle, respectively. Three angles represent rotations around the depth-axis and can be combined in a single rotation $\theta = \theta_s + R + \theta_{\text{mount}}$. Uncertainty with regard to the exact values of the parameters used for depth calculation induces a depth uncertainty. Here, a short description of the contributions is given (an interested reader might refer to [8] for a complete derivation of all equations).

I. **Echo-Sounder contribution** which can be divided into range and angular errors. The former is induced by uncertainties in the measured travel time of the signal and speed

of sound. The across-track angular error is due to the uncertainty in the measurement of the angle of impact of the incoming sound wave at the transducer array. The combined uncertainty, σ^2_{EchSou}, reads as

$$\sigma^2_{EchSou} = (cos\ P\ cos\ \theta)^2 \left[\sigma^2_{r_{meas}} + \left(\frac{r_{meas}}{v_{meas}}\right)^2 \sigma^2_{v_{meas}}\right] + (r\ sin\ \theta\ cos\ P)^2 \sigma^2_{\theta_{meas}} \quad (2)$$

where $\sigma^2_{r_{\text{meas}}}$ is the error in the measured distance (r_{meas}). It depends on the range sampling resolution and pulse length. Equation (2) is valid under the assumption that the true sound speed in the water (v) does not deviate too much from the measured average sound speed in the water column (v_{meas}). $\sigma^2_{\theta_{\text{meas}}}$ is the random error in the measurements of the impact angle and depends on the measurement method (phase or amplitude detection), as

$$\sigma_{\theta_{\text{meas}}} = \begin{cases} \dfrac{\psi_y}{12} & \text{Amplitude detection} \\ \dfrac{0.2\psi_y}{\sqrt{n_p}} & \text{Phase detection} \end{cases} \quad (3)$$

with n_p the number of phase samples, defined as $\left(\frac{d\psi_y}{\cos^2\theta}\right)/\left(\frac{\tau v}{2\sin\theta}\right)$ where τ indicates the pulse length. In Ref. [8], it is indicated that the phase detection is applied for situations in which $n_p > 12$. For the present contribution, the detection type is chosen automatically based on the minimum of angular measurements errors induced by the amplitude and phase detection. Equation (3) does not take the impact of a particular pulse shape into account. An alternative approach presented in [9] does account for the uncertainties in the detection instant in the interferometry step using the coherence coefficient which is a measure for the correlation between the two received signals at the two sub-arrays. In this case the pulse shape is taken into account.

II. **Angular Motion Sensor contribution** due to the uncertainty in the measurement of roll and pitch denoted by $\sigma^2_{R_{meas}}$ and $\sigma^2_{P_{meas}}$, respectively. The resulting random depth error reads as

$$\sigma^2_{\text{Ang_Mot}} = (r \cos P \sin\theta)^2 \sigma^2_{R_{\text{meas}}} + (r \cos\theta \sin P)^2 \sigma^2_{P_{\text{meas}}} \quad (4)$$

In case of applying roll and pitch corrections during beamforming, a second pair of roll and pitch errors are added due to account for the errors made by this stabilization.

III. **Motion Sensor/Transducer Alignment contribution** due to incorrect alignment of the motion sensor, i.e., roll (ΔR_{Align}) and pitch (ΔP_{Align}), with the MBES transducer and induces a depth uncertainty as

$$\sigma^2_{\text{MotSen_Align}} = (r \cos P \sin\theta)^2 \sigma^2_{\Delta R_{\text{Align}}} + (r \cos\theta \sin P)^2 \sigma^2_{\Delta P_{\text{Align}}} \quad (5)$$

where the first and second terms in Eq. (5) indicate the contribution of roll and pitch incorrect alignment, respectively. Again, if mechanical pitch and roll stabilization is active, a second pair of $\sigma^2_{\Delta R_{\text{align}}}$ and $\sigma^2_{\Delta P_{\text{align}}}$ is added to Eq. (5).

IV. **Sound Speed contribution** due to errors in the sound speed at the transducer, $\sigma^2_{v,s}$, and that of the water column, $\sigma^2_{v,p}$. These uncertainties induce uncertainty in the steering angle and consequently the measured depth. The contribution reads as

$$\sigma^2_{\text{SoundSpeed}} = (r \cos P \sin\theta)^2 \left[\left(\frac{\tan\theta_s}{v_s} \right)^2 \sigma^2_{v,s} + \left(\frac{\tan\theta}{2v_p} \right)^2 \sigma^2_{v,p} \right] \tag{6}$$

where the first term in brackets in Eq. (6) represents errors in the beam steering angle due to fluctuations of the sound speed at the transducer and depends on the angle relative to the normal of the transducer, θ_s, and v_s is the surface sound speed. The second term in bracket in Eq. (6) is the contribution of the non-uniform sound speed profile to the random depth error. Varying sound speed in the water column result in the deviation of the sound waves from straight lines. This is accounted for in the MBES processing but uncertainties in the water column sound speed profile measurements induce errors in the resulting bathymetry. The above expression for the quantification of this errors source is based on the assumption a two-layer sound speed profile.

V. **Heave contribution** due to measurements error of heave and roll and pitch errors. The depth uncertainty due to the heave contribution reads as

$$\sigma^2_H = \max(a^2, (bH_{\text{meas}})^2) + \sigma^2_{H_{\text{Induced}}} \tag{7}$$

where the first term in Eq. (7) represents the uncertainty in the heave measurements with a being a static component in meters and b a variable component. In case of using the Global Navigation Satellite System (GNSS) sensor for heave measurements, the first term is substituted with the uncertainty of the sensor's z-component. Heave induced uncertainty is due to the errors in the roll and pitch measurements, their alignment and the fact that the vertical reference unit, VRU, (or GNSS sensor in case of using it for heave determination) is not located at the same position as the transducer resulting in a deviation between the measured heave and the heave at the transducer. The corresponding induced depth uncertainty reads as

$$\begin{aligned} \sigma^2_{H_{\text{Induced}}} = {} & (x \cos P - y \sin R \sin P - z \cos R \sin P)^2 \left(\sigma^2_{P_{\text{meas}}} + \sigma^2_{\Delta P_{\text{Align}}} \right) \\ & + (y \cos R \cos P - z \sin R \cos P)^2 \left(\sigma^2_{R_{\text{meas}}} + \sigma^2_{\Delta R_{\text{Align}}} \right) \\ & + \sin^2 P \sigma^2_x + \sin^2 R \cos^2 P \sigma^2_y + (1 - \cos R \cos P)^2 \sigma^2_z \end{aligned} \tag{8}$$

where x, y, and z are the offset coordinates between the transducer and VRU. Here, σ^2_x, σ^2_y and σ^2_z are the errors in the measurement of the distance between the VRU and MBES. In case the vertical positioning is carried out using the GNSS and the position corrections are received from Real Time Kinematic (RTK) services, the depth relative to the vertical datum is derived and accounting for height offset, such as dynamic

draft and tidal variations, in not of importance. Otherwise, a separate contribution will be added, see [8].

Assuming the above contributors are uncorrelated, the total depth error is calculated as

$$\sigma_d^2 = \sqrt{\sigma_{EchSou}^2 + \sigma_{\text{Ang_Mot}}^2 + \sigma_{\text{MotSen_Align}}^2 + \sigma_{\text{SoundSpeed}}^2 + \sigma_H^2} \tag{9}$$

3. RESULTS

This section focuses on quantifying the predicted depth uncertainties for different environmental conditions and operation setting. The predictions are derived for a situation where the EM2040c MBES (manufactured by Kongsberg) is used, and its characteristic are thus used as the input parameters, see [12]. In addition to the MBES characteristics, information regarding the uncertainties of the sound speed measurements and motion sensors are of importance. For this study a case is considered where the inertial navigation sensor and sound velocity profiler used are Phins (manufactured by iXblue) with nominal roll and pitch accuracies equalling 0.01° and miniSVP (manufactured by Valeport) with a nominal accuracy of 0.02m/s, respectively, see [13] and [14]. However, from measurements in different locations (inland waterways and the North Sea), the uncertainty of the latter was found to be 0.2m/s, and hence this value is chosen as a more realistic description of the system's accuracy. The sound velocity profile acquired was almost constant through the water column equalling 1515 m/s. Shown in Fig. 1 is the total predicted vertical uncertainty as a function of depth for pulse lengths of 27 μs, (a), and 134 μs, (b) for 4 different beam angles. As seen, an increase in the pulse length deteriorates the vertical accuracy for all beam angles. For beams close to nadir, the increased uncertainty with depth (black solid line) is negligible, however, as the beam angle increases, the vertical uncertainty increases to a larger extent.

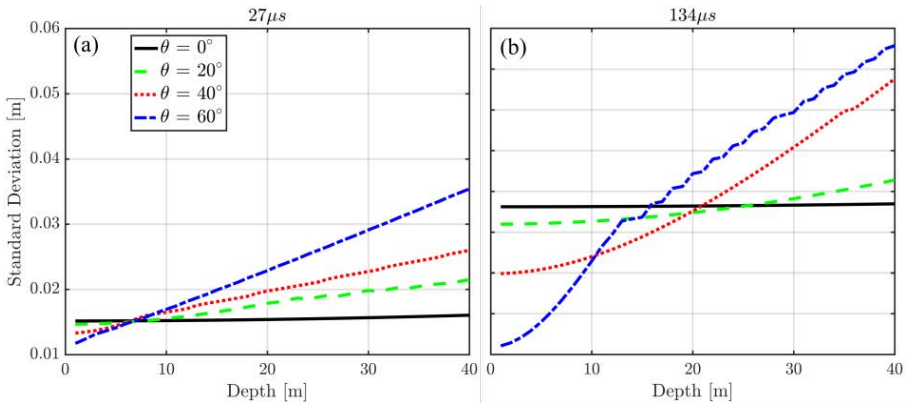


Fig. 1: Predicted depth uncertainty as a function of depth for pulse length of 27 μs (a) *and 134 μs* (b)

Shown in Fig. 2 is the total vertical uncertainty predicted as a function of pulse length for depths of 2 m, (a), and 30 m, (b). For the depth of 2 m and shortest pulse length, the predicted uncertainty is almost equal for all the beam angles. As the pulse length increases, the discrepancy between the predictions for varying beam angle increases with the predictions being larger at nadir. As one moves to deeper depths, (b), the behavior of the predictions changes compared to those of the shallower depth. This means that for the shortest pulse length, the uncertainty increases toward the outer parts of the swath. As seen, for the beam

away from nadir (20° (green), 40° (red) and 60° (blue)) the predictions show almost equal increase in the uncertainty with the pulse length. However, this is not the case for shallower depth as the rate of the increase with the pulse length decreases towards the outer parts of the swath.

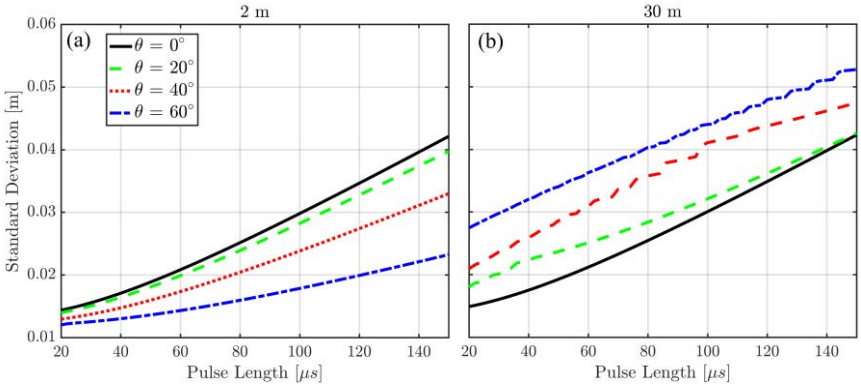


Fig. 2: Predicted depth uncertainty as a function of pulse length for water depth of 2 m (a) *and 30 m* (b)

The assessment of the dependency of the predicted uncertainties to depth, beam angle and pulse length indicates that varying MBES settings and operational environments can significantly affect the vertical uncertainties. Therefore, a realistic description of this parameter is needed for employing the depth derivatives, such as depth residuals ([4] and [15]), as a potential classifier in seafloor sediment classification methods. This means that for a certain MBES setting and operational environment, lacking knowledge of the vertical uncertainties can lead to interpreting the observed depth variations as varying sediment types although they might be induced by the depth uncertainty sources inherent to the MBES.

To assess the reliability of the uncertainty prediction model, the predicted depth uncertainty is compared to that measured. Shown in Fig. 3 is the measured (blue) and total (cyan) predicted vertical standard deviation in water depth of 10 m with pulse length of 27 µs (a) and 134 µs (b). The contribution of the individual sources is also shown. The black vertical lines indicate the beam angle where the switch from the amplitude to phase detection occurs based on the minimum standard deviation induced by both detection methods. The blue squares and asterisks represent the amplitude and phase detection based on the measurements, respectively. The theoretical beam angle corresponding to the change in the bottom detection method does not coincide with the one found for the measurements. This indicates that the criteria used for obtaining this transition point require modification possibly by accounting for the characteristics of the received signal.

As the pulse length increases, a broader range of beam angles around nadir (both based on predictions and measurements) use amplitude detection which is due to the phenomenon referred to as the baseline decorrelation. Longer pulse length means larger footprints on the seafloor, and hence a more fluctuating directivity pattern resulting in a noisy estimate of the zero-crossing of the phase difference (used for the phase detection). Therefore, amplitude detection becomes the preferred bottom detection approach. Generally, for both pulse lengths, the predicted and measured uncertainties are in the same order of magnitude with larger uncertainties for longer pulse lengths (b). For the shorter pulse length, there is a good agreement for the beams larger than 10° and the discrepancies occur for the beams closer to nadir. Potential improvements in the agreement can be obtained by further investigation of the term associated to the echosounder contribution (see the black circles) as 1) it is the most

dominant uncertainty source and 2) it depends on the bottom detection approach. As for the measurements with the longer pulse length, slightly better agreement between the measured and modelled uncertainties is obtained for starboard. The larger variations in depth uncertainty for the port side can be due to the existence of a strong bottom morphology. Here, the results are derived by subtracting the mean depth per small surfaces. However, for some areas, this will not fully account for the changes in the bathymetry induced due to the presence of local slopes. One approach to address this issue is to fit a bi-quadratic or linear function to the measurements located within small surfaces and calculate the standard deviation which is now under further investigation.

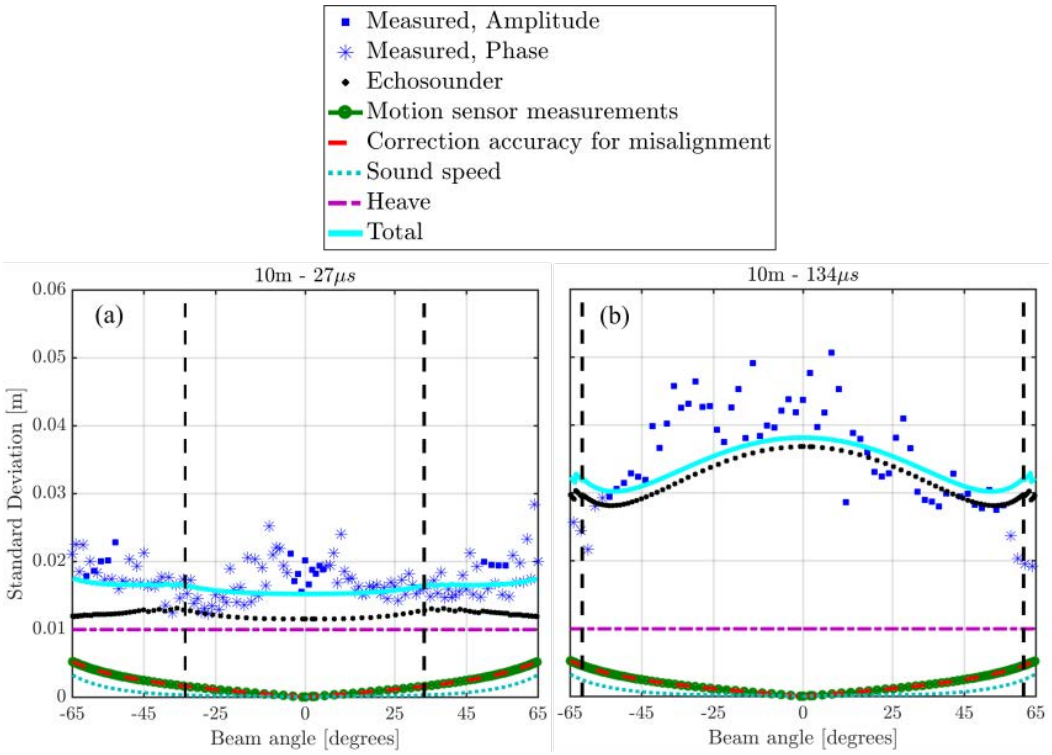


Fig. 3. Measured vertical standard deviation and those predicted for water depth of 10 m and pulse lengths of 27 µs (a) and 134 µs (b). The black vertical lines shows the location the beam angle where the switch from amplitude to the phase detection occurs according to the criterion of minimum standard deviation.

4. CONCLUSIONS

The performance of the sediment classification approaches can be potentially improved by including the depth derivatives, such as depth residuals. However, these depth measurements are contaminated by the uncertainties in the measured depths depending on a number of parameters, such as survey configuration. A realistic description of the vertical uncertainties is thus required to ensure that the variation of the depth derivatives is due to the variation in the sediment type and not induced by the vertical uncertainties. The modelled and measured vertical standard deviation are thus compared to assess their agreement and directions for possible improvements. In general, the predicted and measured uncertainties are in the same order of magnitude. Vertical uncertainty increases with both an increasing pulse length and depth. To obtain a better agreement between the predicted and measured uncertainties, one can 1) account for the presence of local slopes as the model is developed assuming a flat

seafloor, and 2) further investigate the contribution of the echosounder as it is the most dominant error source with dependency on the detection method.

REFERENCES

[1] V. Lecours, M. F. J. Dolan, A. Micallef and V. L. Lucieer, "A review of marine geomorphometry, the quantitative study of the seafloor," *Hydrology amd Earth System Science,* vol. 20, p. 3207–3244, 2016.

[2] J. J. Daniell, P. T. Harris, M. G. Hughes, M. Hemer and A. Heap, "The potential impact of bedform migration on seagrass communities," *Continental Shelf Research,* vol. 28, no. 16, p. 2188–2202, 2008.

[3] V. E. Kostylev, B. J. Todd, G. B. J. Fader, R. C. Courtney, G. D. M. Cameron and R. A. Pickrill, "Benthic habitat mapping on the Scotian Shelf based on multibeam bathymetry, surficial geology and sea floor photographs," *Marine Ecology Progress Series,* vol. 219, pp. 121-137, 2001.

[4] D. Eleftherakis, A. R. Amiri-Simkooei, M. Snellen and D. G. Simons, "Improving riverbed sediment classification using backscatter and depth residual features of multi-beam echo-sounder systems," *J. Acoust. Soc. Am. ,* vol. 131, no. 5, pp. 3710-3725, 2012.

[5] J. E. Hughes Clarke, L. A. Mayer and D. E. Wells, "Shallow-water imaging multibeam sonars: A new tool for investigating seafloor processes in the coastal zone and on the continental shelf," *Marine Geophysical Researches,* vol. 18, no. 6, p. 607–629, 1996.

[6] B. R. Calder and L. A. Mayer, "Automatic processing of high-rate, high-density multibeam echosounder data," *Geochem Geophys Geosyst,* vol. 4, no. 6, pp. 1048-1069, 2003.

[7] R. Hare, B. Eakins, C. Amante and L. A. Taylor, "Modeling bathymetric uncertainty," in *US Hydro 2011*, Tampa, FL, 2011.

[8] R. Hare, "Error Budget Analysis for US Naval Oceanographic Office (NAVOCEANO) Hydrographic Survey Systems," Hydrographic Science Research Center (HSRC), Mississippi, 2001.

[9] T. H. Mohammadloo, M. Snellen and D. G. Simons, "Multi-beam echo-sounder bathymetric measurements: Implications of using frequency modulated pulses," *The Journal of the Acoustical Society of America,* vol. 144, no. 2, pp. 842-860, 2018.

[10] X. Lurton and J. M. Augustin, "A measurement quality factor for swath bathymetry sounders," *IEEE J. Ocean. Eng.,* vol. 35, no. 4, pp. 852-862, 2010.

[11] X. Lurton, An Introduction to Underwater Acoustics, Principles and Applications, Second edition, Springer-Verlag Berlin Heidelberg, 2010, pp. 167-224, 225-270.

[12] Kongsberg, *EM 2040C,* Kongsberg, 2017.

[13] *Phins: FOG-based high-performance inertial navigation system,* iXblue, March 2017.

[14] *miniSVP - Sound Velocity Profiler,* Valeport, May 2016.

[15] D. Eleftherakis, M. Snellen, A. Amiri-Simkooei and D. G. Simons, "Observations regarding coarse sediment classification based on multi-beam echo-sounder's backscatter strength and depth residuals in Dutch rivers," *Journal of Acoustical Society of America,* vol. 135, p. 3305, 2014.

MULTIBEAM AND SINGLEBEAM MULTIFREQUENCY CLASSIFICATION OF BOTTOM HABITATS - THE COMPLEMENTATION OF TWO APPROACHES

Jaroslaw Tegowski[a], Lukasz Janowski[a], Karolina Trzcinska[a], Maria Rucinska-Zjadacz[a], Pawel Pocwiardowski[b], Klaudia Kusek[a]

[a]Institute of Oceanography, University of Gdansk, al. Marszalka Pilsudskiego 46, 81-378 Gdynia, Poland
[b]NORBIT-Poland Sp. z o.o., al. Niepodleglosci 813-815/24, Sopot, Poland

Jaroslaw Tegowski, Institute of Oceanography, University of Gdansk, al. Marszalka Pilsudskiego 46, 81-378 Gdynia, Poland, fax: +48585236678, email: j.tegowski@ug.edu.pl

Abstract: *The development of multi-frequency multi-beam (MBES) and single-beam (SBE) echosounders has enabled progress in acoustical classification methods for bottom sediments and habitats. In this study we present the results of habitat classification based on the image analysis of bathymetry and backscattering strength maps recorded by MBES NORBIT iWBMS (model STX) at frequencies of 150kHz and 400kHz and analyses of echo envelopes recorded by SBE Simrad EK 80 at frequencies of 38kHz, 120kHz and 333kHz. The survey was carried out in the South Baltic Sea on an area of approximately 1.2 km2, where the southern boundary of the study polygon was 1 km distant from the Rowy harbour. The Rowy area is characterized by diverse habitat conditions and presence of marine vegetation unique in this part of the Baltic Sea. The MBES data approach benefit from object-based image analysis and development of K Nearest Neighbour supervised classifier. Another data set was calculated for single-beam echosounder signals, including echo energy parameters and wavelet transform parameters for all the three frequencies. Automatic classification methods utilized fuzzy logic and k-means algorithms. Based on the ground-truth samples and ROV seafloor images we have identified six habitat classes and selected the most relevant features of the bathymetric and backscatter data. The results of the valid classification reached almost 80%, demonstrating that the combination of measurements with multi and single beam echosounders as well as multifrequency registrations can advance progress in habitat mapping, which is one of the goals of the ECOMAP EU BONUS project.*

Keywords: *Multibeam echosounder, singlebeam echosounder, bottom habitats, multifrequency classification*

INTRODUCTION

Recently, leading manufacturers of echosounders and sonars have been equipping their devices with the ability to measure on different frequencies of the transmitted acoustic signals. As in the case of multispectral satellite measurements of the Earth's surface, multispectral acoustic methods should significantly increase the amount of information about the bottom and help in the remote sensing classification of sediments and habitats.

In the scope of the ECOMAP EU project (Baltic Sea environmental assessments by opto-acoustic remote sensing, mapping, and monitoring), bottom research was carried out in the Rowy test area using the NORBIT iWBMS STX multibeam and the Simrad EK80 singlebeam echosounders. Both echosounders can operate in multifrequency mode, giving new possibilities for non-invasive recognition and classification of benthic habitats. Analysis of the data recorded with a singlebeam echosounder provided additional information for the classification of bottom habitats using a multibeam echosounder.

STUDY SITE

The study site is located in the shallow marine area of the Polish part of the Southern Baltic Sea in the close neighbourhood of the Rowy harbour at the coast (Fig. 1). The area is characterized by low depths, from 4 to 20 m below sea level. Considering its relatively small spatial extent, the morphology of the seabed consists of crests and valleys of complex shapes. The bathymetry deepens from south-east to north-west direction concealing the main shoal at the center of the area. This moraine structure is made of boulders and gravels on outcrops of glacial tills partly covered by red algae communities. Large boulders are commonly colonized by dense cover of *Mytilus trossulus* bivalves. Previous research confirms existence of other substratum outside the glacial tills outcrops, that are: sands, very fine sands, fine sands, sandy gravels and gravelly sands [1].

MATERIALS AND METHODS

Underwater acoustic data were collected using multibeam echosounder (MBES) equipment (Norbit iWBMS) mounted on the Zelint research motor boat. Scientific surveys took place in 27 and 28 of May 2018 using two working frequencies: 150 kHz and 400 kHz. The MBES device was supplemented by integrated Applanix Wave Master GNSS/INS navigation system. All measurements were carried out with sweep time of 500 μs and maximum ping rate of 30 Hz. Design of surveys included maintenance of a constant speed of 5.5-6 knots and complete spatial coverage of the area.

Single-beam Simrad EK 80 echosounder measurements took place in 20 and 21 October 2018 and were carried out during the cruise rv Oceanograf to the Rowy area. The measurements were carried out simultaneously for three frequencies of the transmitted signal at frequencies of 38kHz, 120kHz and 333kHz. The SBE data were processed using the Sonar5 software and own programs written in Matlab.

Multibeam echosounder (MBES) bathymetry and backscatter datasets were processed using QPS Qimera and Fledermaus Geocoder Toolbox (FMGT) software. The first software was used for bathymetry processing, including data cleaning and generation of bathymetry grids. Bathymetry grid raster for 400 kHz dataset had 0.5 m cell size, while for 150 kHz it had 0.75

m pixel size. The same resolutions per frequency were used to generate backscatter mosaic grids. They were created using FMGT software and following settings: 'flat' type of Angle Varying Gain AVG correction with window size of 300 and 'blend' style of overlapping lines management. Methods of backscatter data processing were described in details in Schimel et al. [2]. Bathymetry of the area based on 400 kHz frequency was shown at the Fig. 1. Maps of backscatter intensity for both working frequencies are visible at Fig. 2. Mentioned MBES

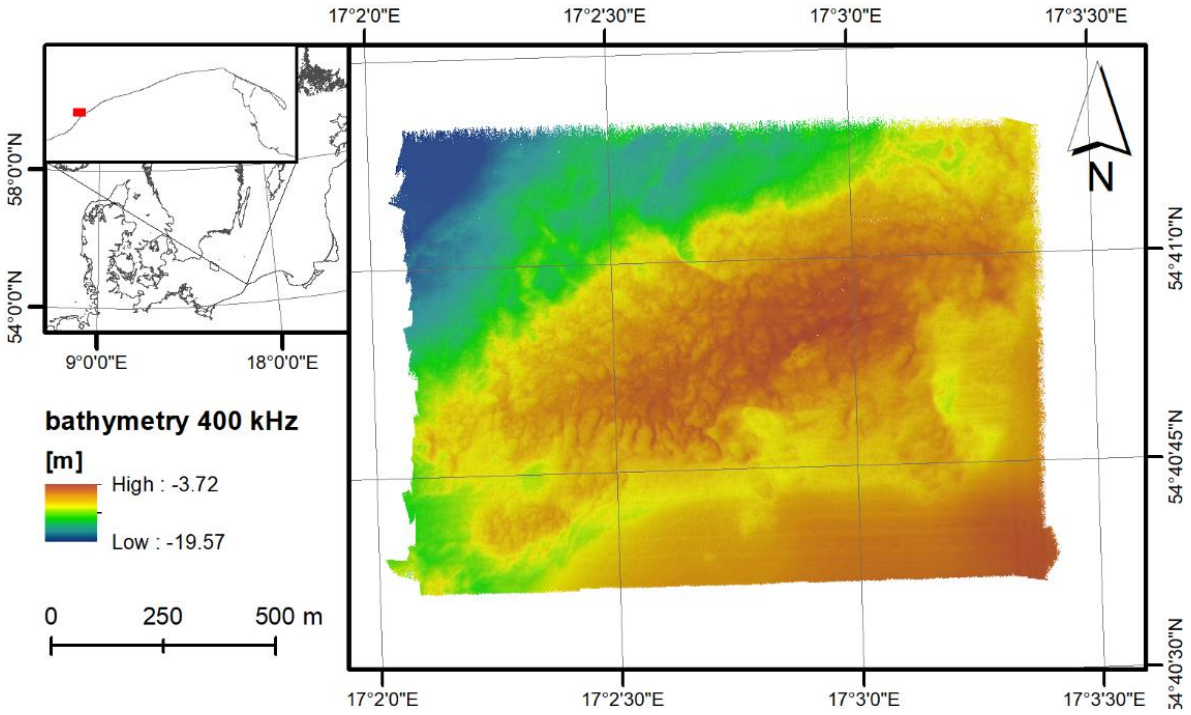


Fig. 1: Site location within the Polish coast of the Baltic Sea (left), bathymetry of the area generated from 400 kHz MBES measurements (right).

datasets in conjunction with ground-truth samples were used for further habitat mapping.

Ground-truth *in situ* information was gathered from sediment samples and ROV video inspections. We adopted habitat identification scheme from the work of Janowski et al. [1].

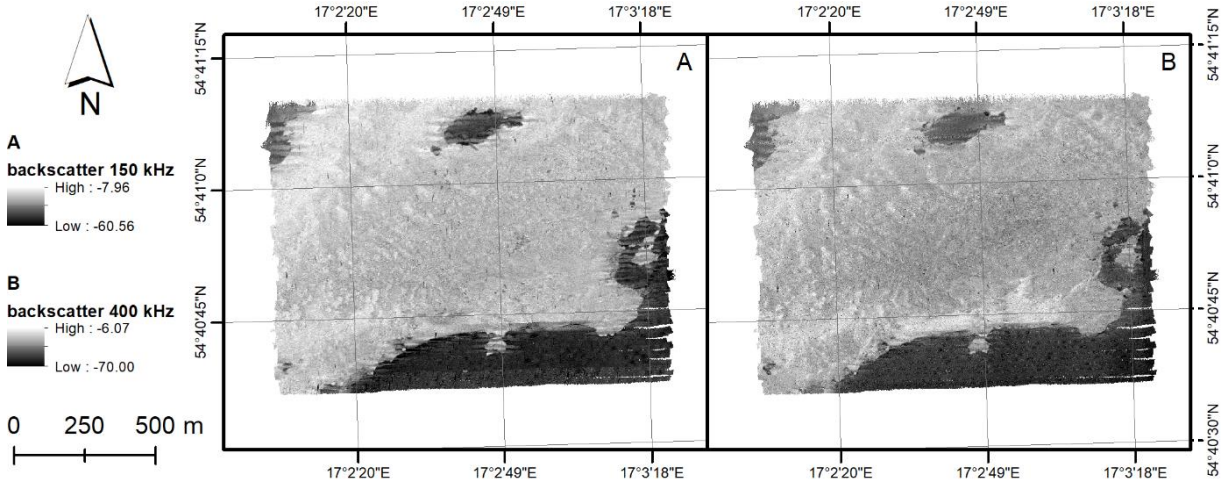


Fig. 2: Backscatter intensity grids generated using FMGT from MBES measurements for two frequencies: 150 kHz (A) and 400 kHz (B).

Abovementioned template separated properties of multibeam echosounder backscatter for five acoustic facies, including class of boulders (B), red algae (R), sandy gravels and gravelly sands (SG_GS), sands (S), very fine and fine sands (VFS), and additional class of artificial structures (A). Separation for five numbers of ground-truth classes was justified from an acoustic point of view considering distribution of MBES backscatter intensity.

Methodology of image analysis presented herein was performed on a basis of Object-Based Image Analysis (OBIA) and supervised classification of created segments using K Nearest Neighbour (KNN) classification method. We generated image objects of backscatter mosaic images using bottom-up region merging technique, named multiresolution segmentation. Segments creation started when single pixels of similar backscatter values were merged into larger areas. They grow until reaching the homogeneity criterion, described in details in Benz et al. [3]. The main parameter influencing the homogeneity criterion is scale, defining relative size of generated image objects. In this study we adopted scale 3 and highly common values of other homogeneity parameters used for creation of segments in benthic habitat mapping [4-6].

Ground-truth samples allowed us to perform supervised classification of segmented image. We used training samples form the division into training and validation samples from Janowski et al. [1] to train K Nearest Neighbour (KNN) supervised classifier [7]. Mentioned algorithm allows to assign class for a certain segment based on K number of nearest neighbours. In our case we defined K=1, so each image object was classified depending on the location of its nearest training sample. The classifier analysed dependencies between labelled training data in feature space consisting of four MBES datasets: bathymetry 150 kHz, bathymetry 400 kHz, backscatter 150 kHz and backscatter 400 kHz.

Generated results were compared with spatial locations of validation subset of ground-truth samples supporting creation of confusion matrix. Performance of classification was evaluated using accuracy assessment statistics based on estimated errors [8]. Measures calculated in this study included: user's and producer's accuracy, overall accuracy and Kappa Index of Agreement [9].

We have selected a polygon from a map of benthic habitats created with a known precision, in which we compared and tested the results with the classification of the singlebeam echosounder (SBES).

The map of benthic habitats created with known precision was the basis for the selection of a testing area in which we studied the results of SBE habitat classification. The polygon area was selected along SBE transects and its spatial location is visible as black frame over the result in Fig. 5, where an example of echograms recorded on three frequencies is shown in Fig. 4.

SBE data were subjected to an analysis consisting in the extraction of consecutive envelopes of echo pulses and computation of a set of their wavelet transform parameters [10]. These

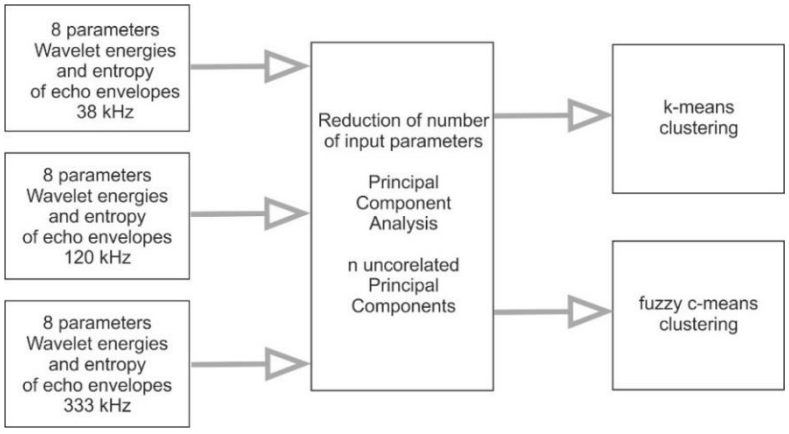


Fig. 3: Classification scheme for bottom habitats - SBE dataset.

parameters were then an input to Principal Component Analysis and further to classification procedures of k-means and fuzzy c-means. Fig. 3 shows habitats classification diagram used for data collected by SBE.

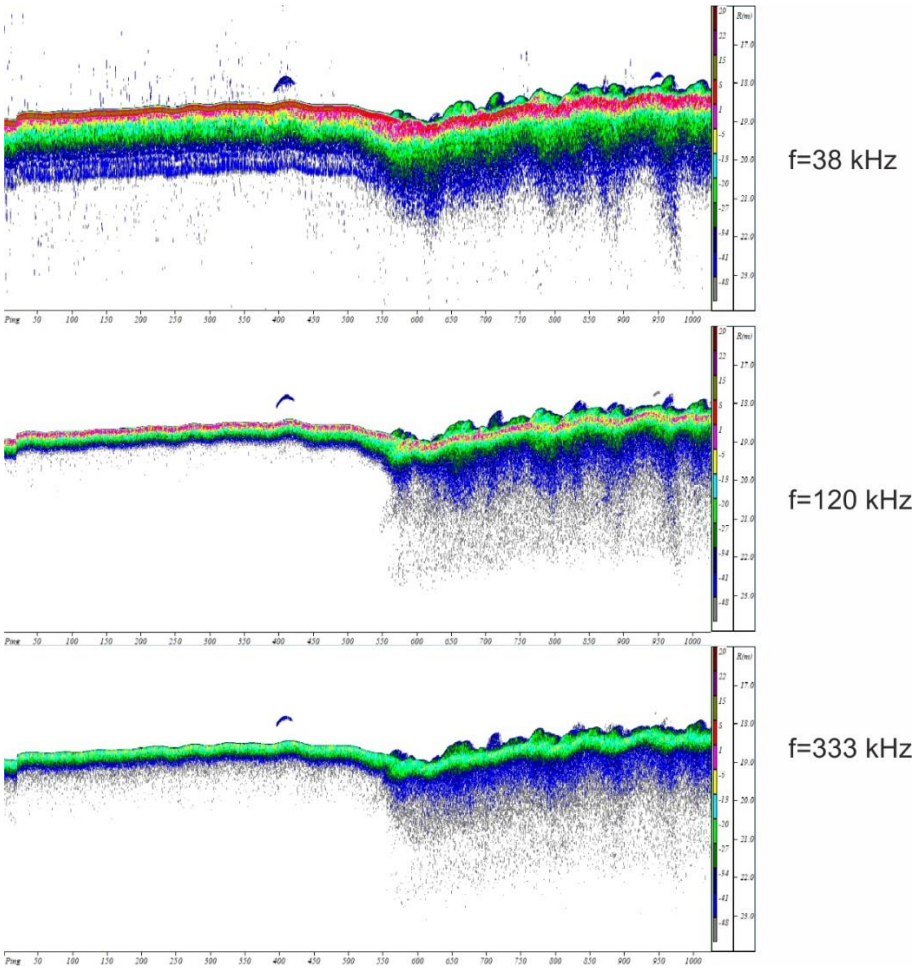


Fig.4: Example of echograms recorded in the Rowy area with the use of SBE operating simultaneously on three frequencies - 38kHz, 120 kHz and 333 kHz.

Developed benthic habitat map of the Rowy area is visible in Fig. 5. It clearly distinguishes properties of MBES datasets, like the central convex spot of red algae occurrence or stronger backscatter absorption in sand and very fine sand classes. Spatial delineation between B and SG_GS classes suggests depth related dependence, which is evident after comparison with MBES bathymetry of the area (Fig. 1).

For the data recorded by the singlebeam echosounder, it was checked how many evident habitats can be separated on the area marked with the frame depicted in Fig. 5. As shown in Fig. 6, in the space of parameters formed by three vectors containing wavelet energies and entropy of echo envelopes recorded on three frequencies, four clusters corresponding to the habitats visible in the area marked with a frame in Figure 5 are clearly marked. Sands (S),

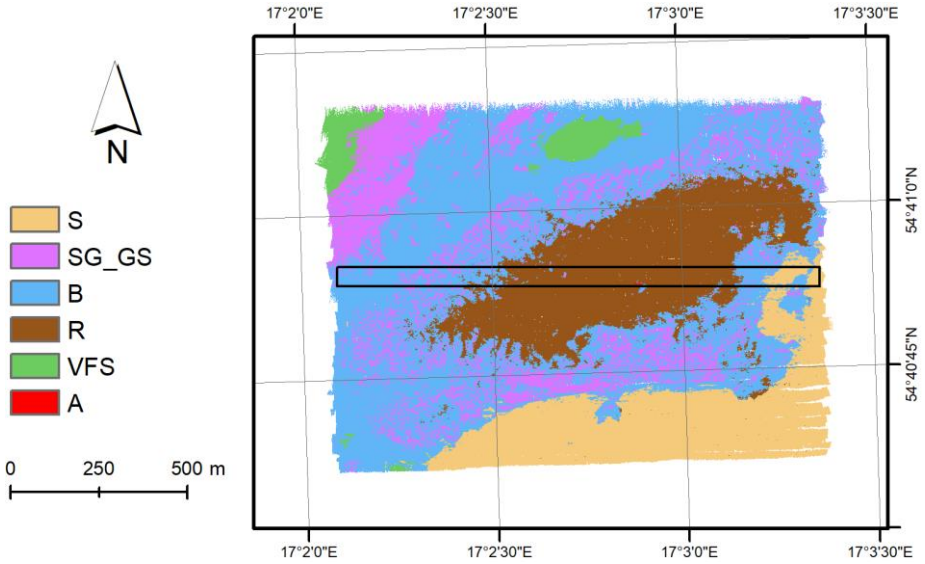


Fig.5: Result of Object-Based Image Analysis for the Rowy area using KNN classifier and multiresolution segmentation scale 3. Black frame represents spatial extent for comparison between MBES and SBES

boulders (B), red algae (R) and gravelly sands (SG-GS) were found in the framed area. We have additionally tested a number of spectral, energy and wavelet parameters of echo envelopes. It was found that wavelet energies and wavelet entropy were sufficient for correct classification of habitats using SBE data.

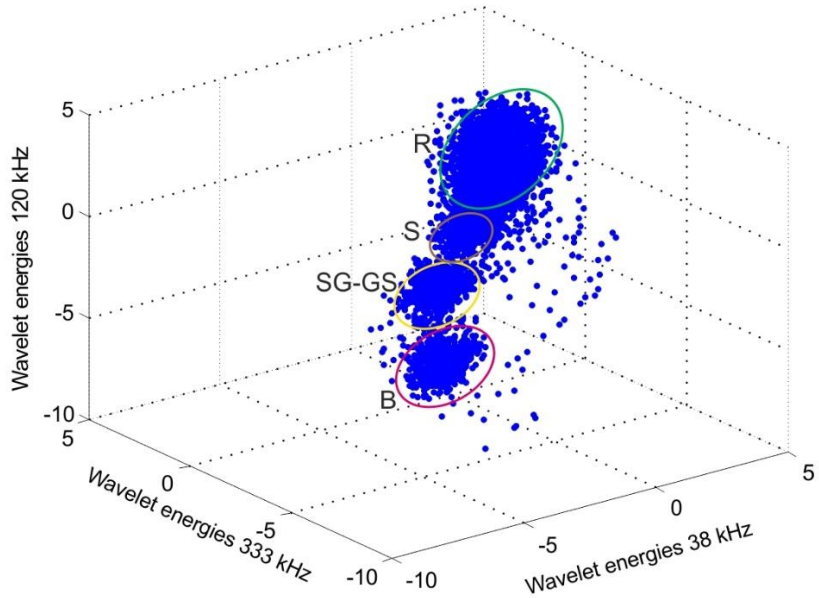


Fig.6: Wavelet energies plot containing four clusters indicating separate features of seafloor sound reflectivity on the area marked with the frame depicted in Fig. 5.

Confusion matrix and accuracy assessment statistics confirm high prediction performance of the KNN classifier based on multifrequency MBES dataset (Table 1). Overall accuracy measure shows 79%, whereas Kappa statistic indicates that classification conformity was significantly greater than random.

Confusion matrix						
User \ Producer Class	S	SG_GS	B	R	VFS	Sum
S	14.3	0.0	0.0	0.0	0.0	14.3
SG_GS	0.0	7.1	7.1	0.0	0.0	14.3
B	7.1	7.1	28.6	0.0	0.0	42.9
R	0.0	0.0	0.0	21.4	0.0	21.4
VFS	0.0	0.0	0.0	0.0	7.1	7.1
Sum	21.4	14.3	35.7	21.4	7.1	100.0
Accuracy assessment						
Producer’s	0.67	0.50	0.80	1.00	1.00	
User’s	1.00	0.50	0.67	1.00	1.00	
Overall Accuracy	0.79					
KIA	0.71					

Table 1: Confusion matrix and accuracy assessment results. Confusion matrix values were presented as percentages.

DISCUSSION

This study presents methodological aspect of MBES classification for benthic habitat mapping. Based on previous experiences in the study area [1], we developed a simple mapping procedure that benefits from multifrequency MBES datasets and is still precise. Our approach assumes simplification of previous developed benthic habitat mapping workflow by omission of the feature extraction and selection procedures and arbitrary selection of only primary attributes of MBES backscatter. Majority of benthic habitat mapping research confirms that MBES bathymetry and backscatter are the most important of all features and therefore we assume that in some cases they may be enough to perform successful supervised classification of benthic habitats [11], especially for multifrequency MBES datasets. Therefore, we confirm usefulness of more than one frequency to benthic habitat mapping, but on the other hand, omission of feature extraction and selection steps for traditional single frequency MBES datasets may require a further study.

The additional use of multifrequency SBE data for classification confirmed its usefulness for classification of bottom habitats. Parallel use of two hydroacoustic systems is particularly useful in case of difficulties in classification with high spatial resolution.

CONCLUSIONS

Both MBES and SBE bottom imagery segmentation schemes have many promising features which allow them to be applied for extracting bottom habitats. The first method, based on image analysis, allows quick habitat recognition, while the second method, based on envelope

analysis, can be used for accurate classification with high resolution, especially in places with uncertain habitat identification results. The multi-frequency data has enabled progress in acoustical classification methods for bottom sediments and habitats.

ACKNOWLEDGEMENTS

This research was funded by EU BONUS-185 ECOMAP project (Baltic Sea environmental assessments by opto-acoustic remote sensing, mapping, and monitoring) and co-financed by the National Centre for Research and Development no. BONUS-BB/ECOMAP/07/2017.

REFERENCES

[1] **Janowski, L., Trzcinska, K., Tegowski, J., Kruss, A., Rucinska-Zjadacz, M., Pocwiardowski, P.,** Nearshore Benthic Habitat Mapping Based on Multi-Frequency, Multibeam Echosounder Data Using a Combined Object-Based Approach: A Case Study from the Rowy Site in the Southern Baltic Sea, *Remote Sensing*, 10, 1983, 2018.

[2] **Schimel, A.C.G., Beaudoin, J., Parnum, I.M., Le Bas, T., Schmidt, V., Keith, G., Ierodiaconou, D.,** Multibeam sonar backscatter data processing, *Marine Geophysical Research*, 39, 121-137, 2018.

[3] **Benz, U.C., Hofmann, P., Willhauck, G., Lingenfelder, I., Heynen, M.,** Multi-resolution, object-oriented fuzzy analysis of remote sensing data for GIS-ready information, *ISPRS Journal of Photogrammetry and Remote Sensing*, 58, 239-258, 2004.

[4] **Janowski, L., Tegowski, J., Nowak, J.,** Seafloor mapping based on multibeam echosounder bathymetry and backscatter data using Object-Based Image Analysis: a case study from the Rewal site, the Southern Baltic, *Oceanological and Hydrobiological Studies*, 47, 248-259, 2018.

[5] **Lucieer, V., Hill, N.A., Barrett, N.S., Nichol, S.,** Do marine substrates 'look' and 'sound' the same? Supervised classification of multibeam acoustic data using autonomous underwater vehicle images, *Estuarine, Coastal and Shelf Science*, 117, 94-106, 2013.

[6] **Montereale Gavazzi, G., Madricardo, F., Janowski, L., Kruss, A., Blondel, P., Sigovini, M., Foglini, F.,** Evaluation of seabed mapping methods for fine-scale classification of extremely shallow benthic habitats – Application to the Venice Lagoon, Italy, *Estuarine, Coastal and Shelf Science*, 170, 45-60, 2016.

[7] **Bremner, D., Demaine, E., Erickson, J., Iacono, J., Langerman, S., Morin, P., Toussaint, G.,** Output-Sensitive Algorithms for Computing Nearest-Neighbour Decision Boundaries, *Discrete & Computational Geometry*, 33, 593-604, 2005.

[8] **Foody, G.M.,** Status of land cover classification accuracy assessment, *Remote Sensing of Environment*, 80, 185-201, 2002.

[9] **Cohen, J.,** A Coefficient of Agreement for Nominal Scales, *Educational and Psychological Measurement*, 20, 37-46, 1960.

[10] **Ostrovsky, I., Tegowski, J.,** Hydroacoustic analysis of spatial and temporal variability of bottom sediment characteristics in Lake Kinneret in relation to water level fluctuation, *Geo-Marine Letters*, 30 (3-4), 261-269, 2010.

[11] **Diesing, M., Mitchell, P., Stephens, D.,** Image-based seabed classification: what can we learn from terrestrial remote sensing?, *ICES Journal of Marine Science: Journal du Conseil*, 73, 2425-2441, 2016.

MBES DATA SIMULATION: ASSESSMENT BY DIRECT COMPARISON WITH A HIGH-RESOLUTION MULTI-SETTINGS WRECK SURVEY.

Antoine Blachet[a], Ruth Plets[b], Fabio Sacchetti[c], Andreas Austeng[a], Alan J Hunter[a,d], Roy E Hansen[a,e]

[a]University of Oslo, P.O. Box 1080 Blindern, N-0316 Oslo, Norway.
[b]Ulster University, School of Geography and Environmental Sciences, Coleraine, BT52 1SA, Northern Ireland.
[c]INFOMAR, Marine Institute, Oranmore, Co. Galway H91 R673, Republic of Ireland.
[d]University of Bath, Bath BA2 7AY, U.K.
[e]Norwegian Defence Research Establishment (FFI), Kjeller, Norway.

Antoine Blachet, University of Oslo, Department of Informatics, P.O. Box 1080 Blindern, N-0316 Oslo, Norway. Email: antoinbl@ifi.uio.no

Abstract: *Simulation is a valuable tool when developing new sonar designs or survey strategies. By avoiding expensive and time-consuming sea trials, simulations can help to test and identify the optimum acquisition settings, especially when dealing with complex bathymetry. In this contribution, a simulator output consisting of synthetic Multi-Beam Echo-Sounder (MBES) water-column data is compared against high-resolution real data. The simulator allows the user to specify array geometry, pulse type and a point-based seabed model. In 2015, a 92 meters WWI wreck (SS Polwell) located in the Irish Sea was mapped using various multibeam acquisition settings, including multiple frequencies, modes, pulse rates, angular sectors, beam spacing, bandwidth and bottom detection modes. The survey configurations have been replicated in the simulator. We provide a ready to use framework for generating the data. The array imitates a Kongsberg EM-2040 and the scenario encapsulates the effects of key acquisition settings. The input model is an ultra-dense point cloud of the wreck created from a combination of all MBES data acquired in 2015. Moreover, the signal processing is designed to match the embedded system. Examples of synthetic water-column images are presented and compared with the original survey measurements. Finally, system-specific artifacts such as sidelobes are examined in more detail. Based on the outcome of the modelling experiment, this simulator can be used to advise hydrographers and researchers on the optimum survey strategy to image objects exposed on the seabed.*
Keywords: *Simulation, Sonar, Ultrasound, Multi-beam echo sounder, shipwreck, INFOMAR.*

1. MBES DATA SIMULATOR:

Sonar data simulation is a valuable asset for acoustic engineers and hydrographic surveyors. Firstly, it reduces time, cost and uncertainty when developing a new sonar system. Secondly it helps to validate the optimum system settings and survey strategy before a specific mission. In a previous contribution [1], we introduced a simulator which is able to generate sonar data at various processing stages. The program uses the ultrasound package Field II [2], [3] to model the wave-field radiated by any array design with arbitrary geometry and pulse shape. The scene is modelled as an extended scatterer target [4]. Finally, it integrates reliable Multi-Beam Echo Sounder (MBES) signal processing algorithms [5]. For a more complete description of the simulator, the reader is invited to read [1].

Sidelobes and thermal noise levels are determined by the characteristics of the sonar array. Therefore, it is necessary to verify that these features are contained in the synthetic water column images.

In this contribution we assess the quality of the simulated data by comparing them with real survey data. A very dense multi-setting wreck (*SS Polwell*) point cloud is used to generate the extended scatterer input model. Then we compare the nature of water-column data generated with different sonar settings. Finally, we compare the accuracy of the bottom detection algorithms.

2. POLWELL DATASET

The real MBES dataset used, was acquired over a WWI metal wreck (*SS Polwell*) located on a 30m deep sandy seabed in the Irish Sea. The ship is 92m long and has a maximum width of 12m. The original purpose of the *Polwell* survey was to investigate the effect of acquisition settings and survey design strategies for optimal imaging of wrecks. The mapping process has been repeated several times (84 passes) with various aspect angles and sonar settings. It includes multiple frequencies, pulse length, swath width and bottom detection algorithms. Detailed information about the *Polwell* survey is available in [6].

Multibeam data were acquired using Kongsberg Maritime Seafloor Information System and standard multibeam acquisition procedures were followed. data were imported and edited in Caris HIPS & SIPS v9.0 hydrographic package [7]. Combinations of automated and manual processing procedures were applied to carefully preserve the ship structure. Finally, an ultra-dense point-cloud was produced combining all cleaned soundings falling within an uncertainty of IHO Order 1a [8] (Fig. 1 left).

3. SIMULATION SETUP

The simulation setup was designed to reproduce the real measurements and emulate the effect of the MBES acquisition settings. We generated synthetic data from two specific swaths. Their locations are presented in Fig. 1 and match the georeferenced positions of the Research Vessel in the *Polwell* survey.

At the first location (Site A), the transmit mainlobe penetrated between the broken wreck structure while the transmit sidelobes illuminated the deck and a part of the internal ship structure. At the second site (Site B), the sonar is located near the stern, 10m away from the deck. In this example the transmit mainlobe illuminated the wreck deck and the mast. The starboard part of the hull and a portion of the seabed were hidden by the shadow of the wreck.

The simulated array geometry was a Mill's cross array similar to a Kongsberg EM2040 used on the research vessel [9]. Table 1 describes the various sonar settings used in the three different simulation scenarios. The point-cloud density provided a significant number of scatters per resolution cell. The amplitude of each point was modelled as a random gaussian

variable. For simplicity, the acoustic shadow was simulated by removing the scatterers not located in the sonar line of sight. Such process can be automated using terrain analysis algorithms (e.g. viewshed [10])

The signal processing, from raw channels data to depth sounding, was performed is the time domain [11]. White Gaussian Noise (WGN) uncorrelated between channels was added on the Rx channels to simulate the effect of thermal noise. Raw channel data were bandpassed and matched-filtered [4]. Water-column image generation was done with the ultrasound processing toolbox USTB [5]. Dynamic focusing beamforming was performed in the nearfield. Dolph–Chebyshev windows were designed to keep the transmit and receive sidelobe level at -40dB. Finally, bottom depth was estimated with the centre of gravity method [11], [12]. The estimation was obtained from the weighted sum of the signal amplitude 10 dB under the maximum value. We expect slightly reduced performance compared to the internal EM2040 bottom detector algorithm which relies on multiple detection methods [11]. Nevertheless, the method provides a satisfactory level of accuracy for the scope of this study.

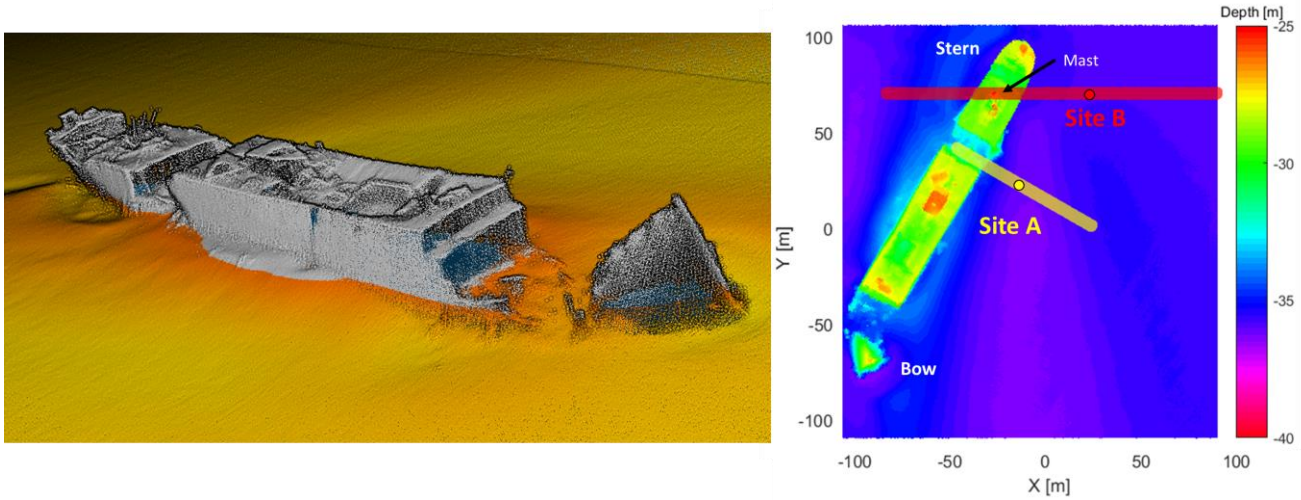


Fig.1: Left: Point Cloud generated from the multi-settings survey data.
Right: Location of the simulated scenarios. Colour overlay indicates the transmit mainlobe footprint. Circular markers indicate the sonar position at the surface.

Scenarios / **Parameters**	*1*	*2*	*3*
Site location	A	A	B
Nominal frequency	200 kHz	400 kHz	400 kHz
Swath opening angle	60 deg	60 deg	110 deg
Rx resolution	1.5 deg	0.7 deg	0.7 deg
Tx resolution	1.5 deg	0.7 deg	0.7 deg
Pulse resolution	52.5mm	37.5mm	37.5mm
Pulse length	70µs	50 µs	50 µs

Table 1: Key parameters used to emulate the real data.

4. RESULTS

We compare real and simulated water-column images and consider the performance of the bottom detection algorithms. Fig. 2 and Fig. 3 show the beamformed images of scenarios 1 and 2. The spatial location and energy content of the sonar mainlobe is comparable between real and synthetic data. Increasing the nominal frequency provides the expected angular resolution gain. Moreover, the scenarios successfully captured the undesired inherent characteristic of the MBES array: the transmit sidelobe generates a ghost image of the wreck deck and its internal structure 5m above the seafloor. The echo is visible at -40dB under the peak amplitude value. Furthermore, the nadir specular reflection induces a strong receive sidelobe located in the water-column at a constant radius.

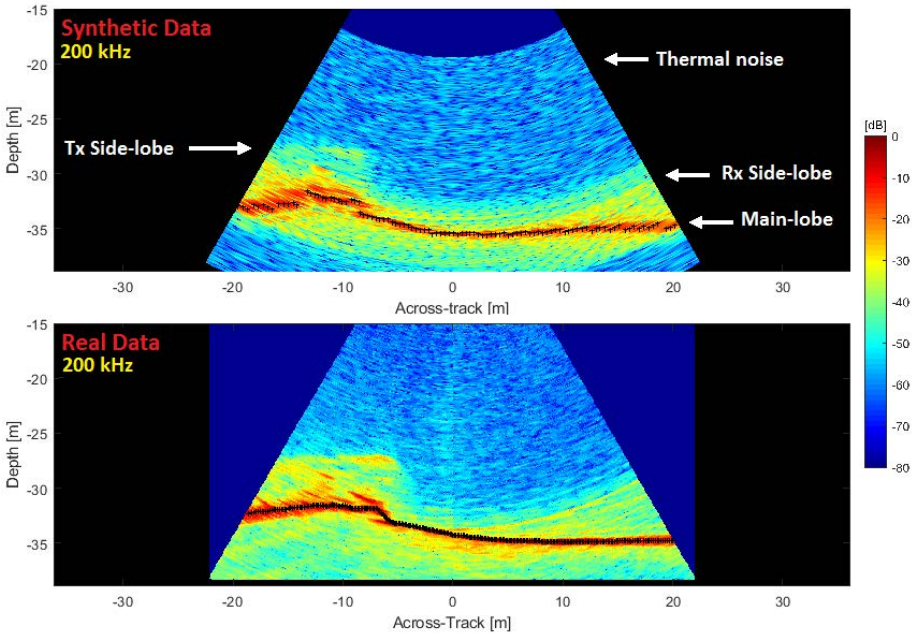


Fig. 2: Scenario 1: Upper: simulated water-column data. Lower: Real water-column data. The black markers "+" indicates the detected sea bottom.

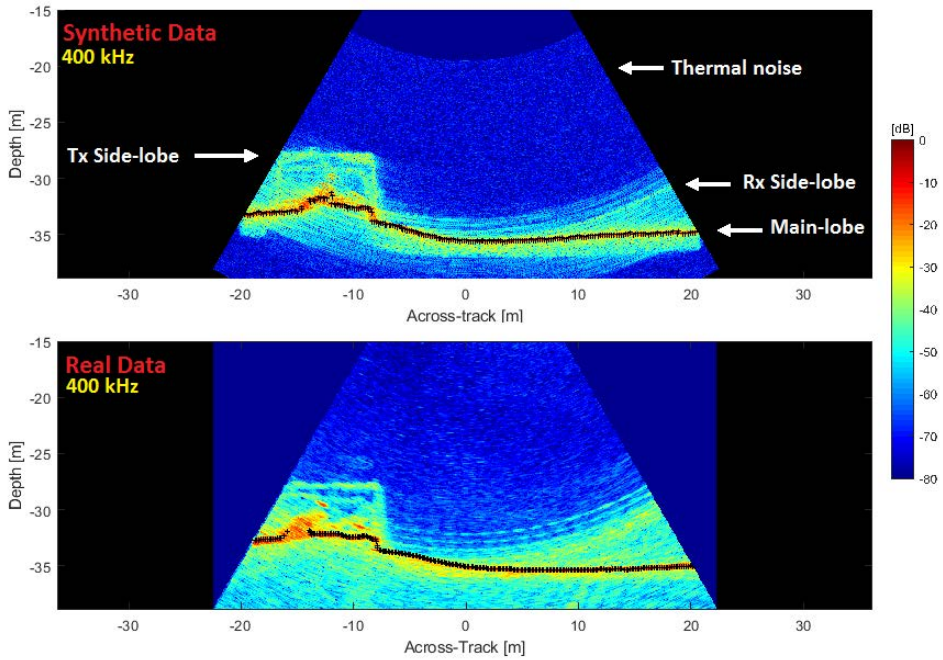


Fig. 3: Scenario2: Upper: simulated water-column data. Lower: Real water-column data. The black markers "+" indicates the detected sea bottom.

Fig. 4 shows the water-column images obtained in scenario 3. As observed in the previous example, the location and energy content of the sonar mainlobe is correctly emulated. The narrow angular resolution provided by the 400 kHz mode managed to image and detect the strong scatterer that coincide with the mast location. Acoustic shadow was generated by discarding the scatterers not located in the sonar line of sight. This solution provided satisfactory results since the aspect of shadow on the hull and the seabed appeared to be reproduced.

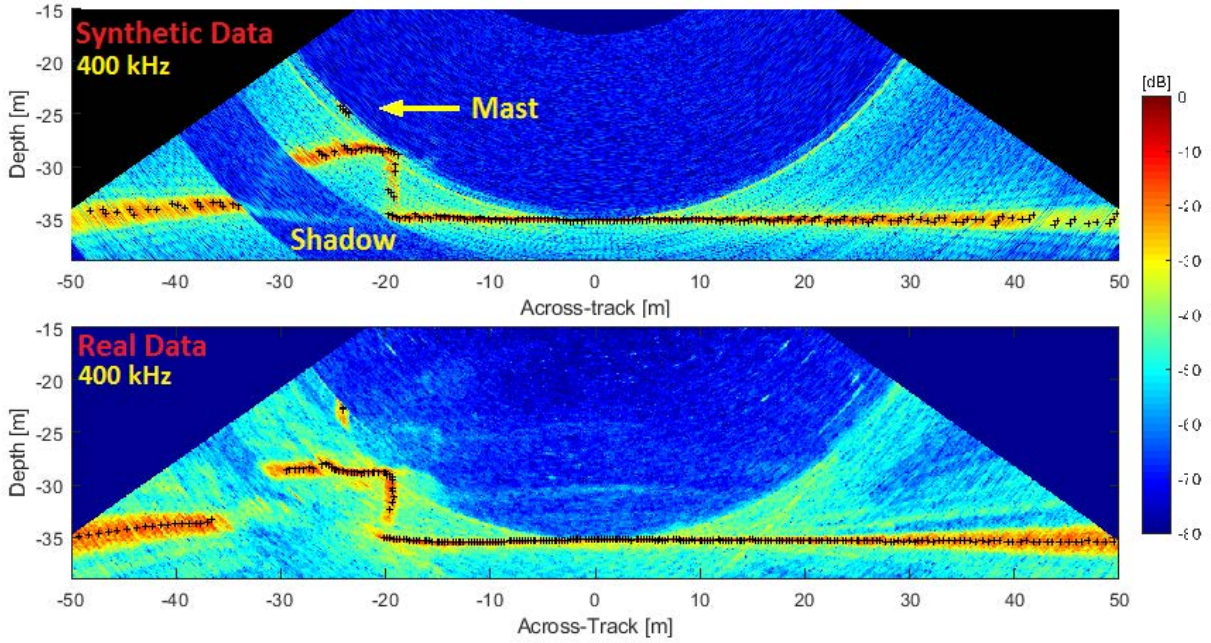


Fig. 4: Scenario3: Upper: simulated water-column data. Lower: Real water-column data. The black markers "+" indicates the detected sea bottom.

Finally, a comparison of bottom detection results is shown in Fig. 5. For the real data the depth was estimated with the "minimum depth" detection mode [13]. This mode solves ambiguous multi-detections by selecting the echo with the shallowest depth. The simulation used only the centre of gravity detector for simplicity. In all cases, the 200 kHz mode identified the ship structure with a reduced accuracy. As expected, the centre of gravity method produced less accurate results on the wreck structure and for steering angles beyond 25 degrees. A depth difference of 0.5 m, starting at 7m across track from nadir is visible in scenarios 1 and 2 on Fig. 5. We interpret this as an effect of an imperfect orientation of the mainlobe corridor in the simulation. The detection performance of the internal EM2040 bottom detector is interpreted as an effect of its possible advanced complexity: multiple-detection methods (leading edge, centre of gravity and phase difference) [9] and additional post-processing techniques (smoothing and cleaning) produced a more precise depth sounding.

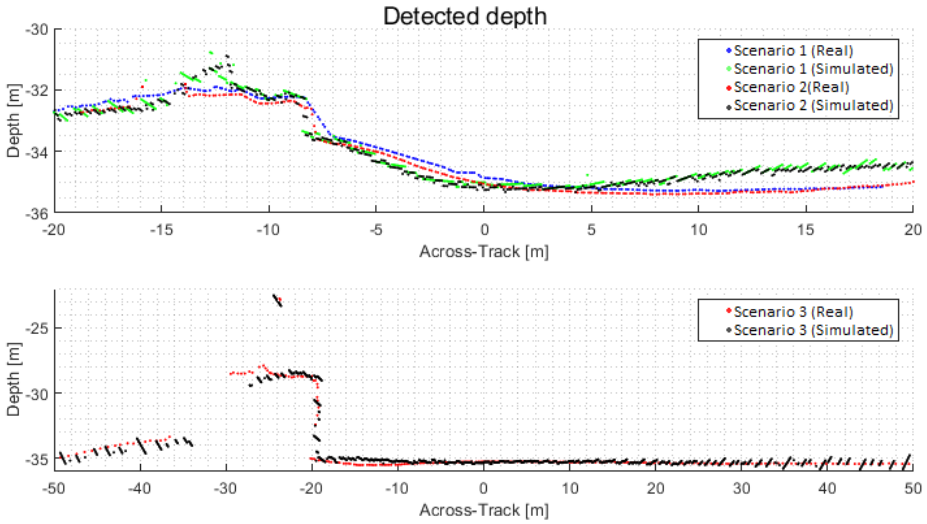


Fig. 5: Estimated depth after bottom detection. For real data the depth was estimated via the constructor bottom detector with minimum depth mode.

5. DISCUSSION

The current study demonstrates the possibility to generate MBES water-column data and detection for a specific choice of sonar parameters. In addition to this work, motion induced perturbation such as Doppler can be simulated.

We consider two main applications: Firstly, this tool offers to acoustical engineers the possibility to experiment easily with new system design such as antenna geometry and pulse type. A simulator provides by definition the real ground-truthing. It offers to compare accurately various signal processing algorithms and tailor the processing chain for a given application. The second application is geared towards hydrographic surveyors and researchers desiring to benchmark and optimize the survey and acquisition settings prior to a survey. This work demonstrated that a point cloud or a digital terrain model populated with scatterers was sufficient for simulating water-column data.

Finally, this simulation tool can be used for training of humans or algorithms to various tasks such as interpretation and processing of MBES data.

6. CONCLUSION

We studied the possibility to emulate MBES data at various processing stages. The comparison was done against a high-quality multi-settings MBES wreck dataset. The study has considered the effect of acquisition settings on the characteristics of water-column images. We provided a large body of examples representative of the features encountered in wreck surveying missions. Results demonstrated a satisfying match between real and synthetic data. The structure of water-column data was reproduced with system specific artefacts while the bottom detection identified the ship framework with a similar level of details.

7. DOWNLOADABLE RESOURCES

The simulator and a simple MATLAB tutorial can be downloaded at the address: http://www.ustb.no/publications/multibeam-sonar-simulation/

Please refer to [1] and this paper if you decide to use the simulator for any academic purpose.

The ultrasound simulator field-II can be downloaded at: http://field-ii.dk//.

8. ACKNOWLEDGEMENTS

This research was supported by the Centre for Innovative Ultrasound Solutions (CIUS) and the Research Council of Norway, project code: 237887.
The authors thank Ole Marius Hoel Rindal and the USTB team for their support.
We thank the Ulster University for the scientific contribution and for the use of the *Polwell* dataset.
Multibeam data collection was supported by the Marine Institute of Ireland's ship-time programme (APP-CV15009: World-War-I shipwreck in the Irish Sea: commemoration, visualization and heritage management), under the INFOMAR program. INFOMAR is a joint venture between the Geological Survey Ireland and the Marine Institute, funded by the Department of Communications, Climate Action and Environment.

REFERENCES

[1] **Blachet, Antoine, et al**, Sonar data simulation with application to multi-beam echo sounders. In: *Underwater Acoustics Conference and Exhibition*, Skiathos, Greece, September 2017.
[2] **Jensen, Jørgen Arendt**, Field: A Program for Simulating Ultrasound Systems, *Paper presented at the 10th Nordic-Baltic Conference on Biomedical Imaging Published in Medical & Biological Engineering & Computing, pp. 351-353, Volume 34, Supplement 1, Part 1, 1996.*
[3] **Jensen, Jørgen Arendt and Svendsen, Niels Bruun**, Calculation of pressure fields from arbitrarily shaped, apodized, and excited ultrasound transducers, *IEEE Trans. Ultrason., Ferroelec., Freq. Contr., 39, pp. 262-267, 1992.*
[4] **Richards, Mark A**, *Fundamentals of radar signal processing*. McGraw-Hill Education, 2005.
[5] **Rodriguez-Morales, Alfonso, et al**, The ultrasound toolbox. In: *2017 IEEE International Ultrasonics Symposium (IUS)*. IEEE, 2017. p. 1-4.
[6] **Westley, Kieran, et al**, Optimising protocols for high-definition imaging of historic shipwrecks using multibeam echosounder. *Archaeological and Anthropological Sciences*, 1-17.
[7] **Teledyne Caris**, Product description (May 2019): https://www.teledynecaris.com/en/products/hips-and-sips/
[8] **UK Maritime and Coastguard Agency**, UK Civil Hydrographic Programme Survey Specifications 2018.
[9] **Kongsberg Maritime**, EM-2040 product datasheet (May 2019): https://www.kongsberg.com/contentassets/e8fa4f09f25f4b1e86eda52cc1355dc7/443810_em2040_mkii_data_sheet.pdf
[10] **Kim, Young-Hoon, Rana, Sanjay, Wise, Steve**, Exploring multiple viewshed analysis using terrain features and optimisation techniques. *Computers & Geosciences*, 2004, 30.9-10: 1019-1032.
[11] **Lurton, Xavier**, *An introduction to underwater acoustics: principles and applications*. Springer Science & Business Media, 2010, p. 359.
[12] **Lurton, Xavier and Augustin, Jean-Marie**, A measurement quality factor for swath bathymetry sounders. *IEEE Journal of Oceanic Engineering*, 2010, vol. 35, no 4, p. 852-862.
[13] **Kongsberg Maritime,** Instruction manual: EM Series Multibeam Echo Sounder, EM datagram formats, (2019).

Structured Session 19
Situation-adaptive distributed networked systems

Organiser(s): Ehlers Frank, Schulz Arne

DISTRIBUTED FUSION IN UNDERWATER SENSOR NETWORKS: FUSING BEARING INFORMATION

Roald Otnes[a], Per Zetterberg[b], Stephane Blouin[c], Magnus Lundberg Nordenvaad[b], Håvard Austad[a], Elin Dombestein[a]

[a]Norwegian Defence Research Establishment (FFI), Horten, Norway
[b]Swedish Defence Research Agency (FOI), Kista, Sweden
[c]Defence Research and Development Canada (DRDC) Atlantic, Dartmouth, NS, Canada

Roald Otnes, Norwegian Defence Research Establishment (FFI), PO box 115, NO-3191 Horten, Norway, email: roald.otnes@ffi.no

Abstract: *In underwater sensor networks, distributed data fusion may be more efficient than centralized fusion because the limited data transmission capacity can make it difficult to collect all required sensor information at a centralized fusion centre. In this paper, we investigate three distributed fusion techniques applied to a network of passive acoustic underwater sensor nodes. We focus on the process of having a node combining its own bearing-to-target information with bearing-to-target information received from another node. In one of the techniques, we approximate the uncertainty in crossfixes in Cartesian coordinates by a Gaussian distribution with their second-order statistics derived from an exact distribution. The bearings and covariance matrixes are fed into a Kalman filter for tracking. The other methods are a particle filter using an exact distribution, and a distributed particle filter using an approximate likelihood representation. The performance of the methods is investigated on simulated data as well as on real-world data collected by seafloor sensor nodes during a Stockholm Archipelago sea trial in the trilateral collaborative project DUSN (Distributed Underwater Sensor Networks) between Canada, Norway, and Sweden.*

Keywords: *Underwater sensor networks, data fusion, tracking*

© Her Majesty the Queen in Right of Canada, Department of National Defence, 2019

1. INTRODUCTION

Distributed fusion in underwater sensor networks is a main topic in the trilateral collaborative project DUSN (Distributed Underwater Sensor Networks) between Canada, Norway, and Sweden. Distributed data fusion may be more efficient than centralized fusion because the limited data transmission capacity can make it difficult to collect all required sensor information at a centralized fusion centre.

Small and easily deployable underwater sensor nodes equipped with passive acoustic sensors provide bearing-only estimates, with limited accuracy due to small array sizes. In this paper we focus on one step of distributed fusion, where a sensor node has received bearing-to-target information deemed worthy of reporting from another node, and combines it with its own bearing-to-target information. We investigate the problem through a case study using real-world data, and also using idealized synthetic data for the same scenario.

2. CASE STUDIES

2.1. Real-world data

At a DUSN sea trial in September 2018, underwater sensor nodes from Canada, Norway, and Sweden were deployed in an area in the Stockholm archipelago. We here use data from the Norwegian NILUS (Networked Intelligent Underwater Sensors) sensor nodes [1][2], which are equipped with a tetrahedral hydrophone array and local signal processing [3], which enables them to estimate bearing to target(s) and also to produce an estimate of the uncertainty in the bearing estimates.

Fig. 1 (left) shows the case study geometry. In a littoral area, three NILUS nodes were deployed on the sea floor in the marked positions. A surface vessel passed through the sensor field from North to South along the indicated trajectory.

Each sensor node estimated at least one bearing and bearing uncertainty every 5 s, as shown in Fig. 1 (right). There was also an algorithm running in the sensor nodes determining which bearing estimates were worthy of reporting to other nodes, typically in a time interval around CPA (closest point of approach). The bearings marked with blue dots were transmitted to the other nodes along with their uncertainties. We also see some detections of other targets farther away, but these bearings were not transmitted to other nodes.

We focus on node 1 receiving the “blue” bearings from nodes 2 and/or 3. Node 1 can combine bearings from other nodes with *all* its own bearing estimates, not only the “blue” ones. Herein lies a possible benefit of distributed fusion over centralized: In a centralized fusion scheme it would put a heavy toll on the communication network to always transmit all bearing estimates (and not only the “blue” ones) to the fusion centre, whereas in distributed fusion each node’s local fusion processor can also make use of the information it did not find worthy of reporting just based on its own knowledge.

Fig. 2 shows histograms of bearing errors in selected time intervals in the real-world data set. Note that the data sets are small, and their uncertainty value σ represents both an unknown (local) bias value and variation from sample to sample, therefore they do not fit well to an analytical zero-mean probability density function (pdf) with σ as standard deviation. We apply the analytical zero-mean von Mises pdf in further tracking, acknowledging that we thereby make a coarse approximation. The von Mises distribution [4] is more suitable to circular data than the Gauss distribution, and as Fig. 2 shows they are quite similar when we do not focus on the tails.

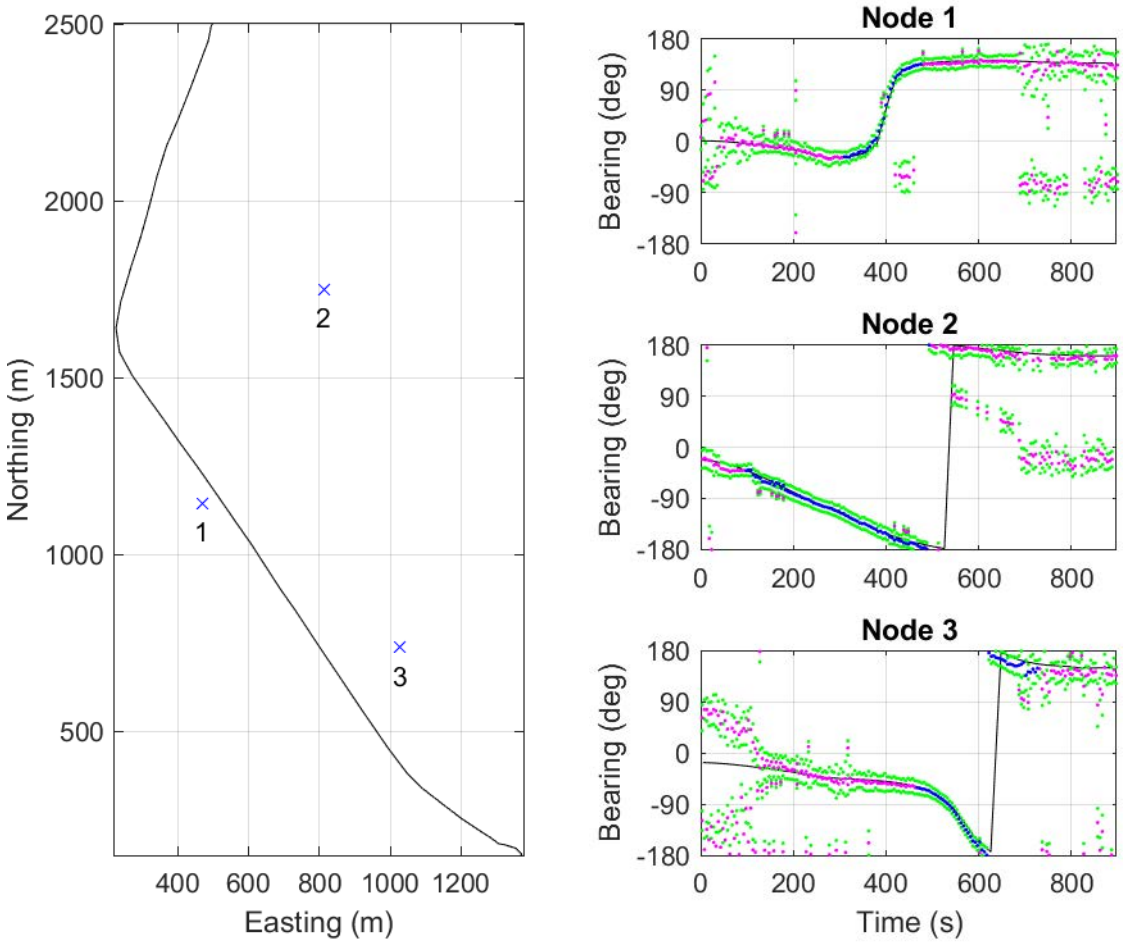


Fig. 1: ***Left:*** *Case study geometry. Crosses denote seafloor sensor nodes, black line shows target's GPS track.* ***Right:*** *Bearing estimates (magenta and blue dots) computed by the three nodes. Blue dots show bearings reported to the other nodes. Green dots show bearing uncertainty (±1σ) estimated by the nodes. Black lines show actual bearing to target.*

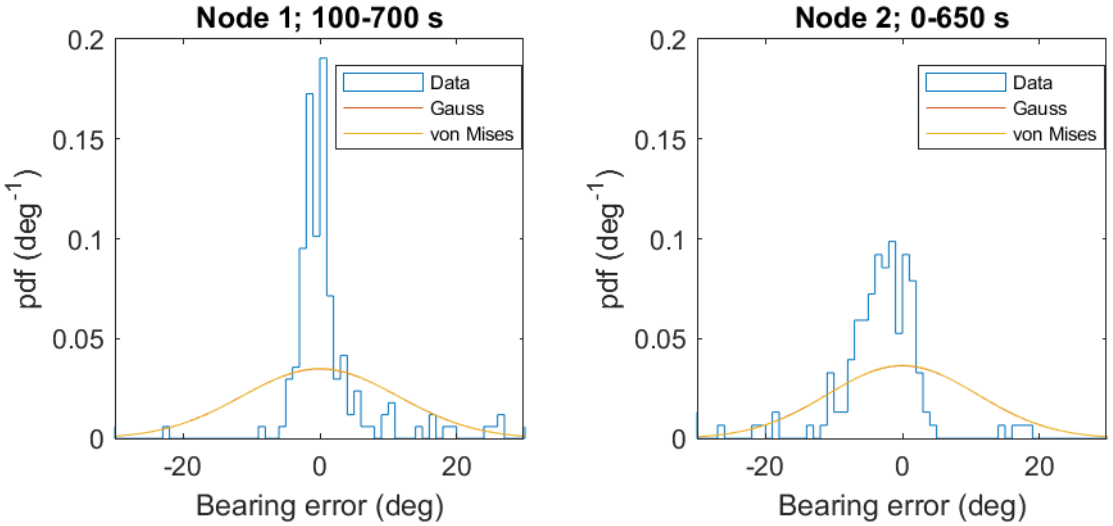


Fig. 2: Histograms of bearing errors over selected time intervals, along with Gauss and von Mises distributions (almost overlapping curves) with the average σ value reported as uncertainty over the same intervals. There are also sporadic bearing errors outside the plotted x axis limits.

2.2. Synthetic data

To also assess algorithm performance on a cleaner but less realistic data set, we generate synthetic data corresponding to the same geometry as the real-world data set, shown in Fig. 1 (left). We assume each node produces a bearing estimate every 5 s, drawn from a pdf which is a mixture between a uniform distribution and a von Mises distribution: $p(\theta) = \alpha \mathrm{U}(-\pi, \pi) + (1-\alpha)\mathrm{vM}(\mu, \kappa)$ [11], where U(a,b) is the uniform distribution from a to b, and vM(μ,κ) is the von Mises distribution with mean μ and an equivalent concentration parameter κ computed from the standard deviation σ using Eqns. (3.30) and (4.40) in [4].

The uniformly distributed element of the mixture model corresponds to the possibility of detecting other targets or noise instead of the target of interest. We let the distributed fusion processor know the standard deviation σ, but let it assume α to be zero. In the real-world data set of Fig. 1 (right), we see that α is close to zero when the target of interest is near CPA (closest point of approach), but larger elsewhere. We assume that node 2 and 3 send bearings to node 1 for the same time intervals as for the real-world data set (blue points in Fig. 1).

2.3. Communication pattern

The communication pattern in the scenario described above consists of three messages: Node 2 and node 3 each send one message with a series of "blue" bearing estimates[1]. These two messages are received by node 1, which combines with its own bearing estimates, runs a tracker on the data, and produces a third message with track information which is transmitted further in the network. This is one step of a larger distributed fusion approach, the remainder of which is outside the scope of this paper.

3. TRADITIONAL TRACKING BASED ON SECOND-ORDER STATISTICS

From the estimates of bearings and bearing uncertainties from the two nodes at a point in time, we compute the crossfix and its covariance matrix using Eqns. (8)-(14) in [5]. The covariance matrix represents the second-order statistics, which can be represented by uncertainty ellipses. This constitutes an approximation, as the actual pdf will be more complicated. To compute the actual pdf numerically for comparison, we assume that the target position is *a priori* uniformly distributed on a Cartesian grid, except in regions close to a node (to avoid singularities). It can then be shown that, on the supported region, we have

$$p(x,y \mid \theta_1, \theta_2) \propto p_1(\theta_1(x,y)) p_2(\theta_2(x,y)) \left| J(x,y) \right| \tag{1}$$

$$\left| J(x,y) \right| = \frac{(y-y_2)(x-x_1) - (y-y_1)(x-x_2)}{r_1^2 r_2^2}$$

where θ_i and r_i are the bearing and distance from node i to each point (x,y), $p_i(\theta)$ are the bearing pdfs, (x_i,y_i) are the node positions, and $|J(x,y)|$ is the determinant of the Jacobian given by Eqns. (12)-(14) in [5]. In Fig. 3 we show an example comparison between the actual pdf and the uncertainty ellipses assuming second-order statistics only, where the non-elliptical nature of the actual pdf can be clearly seen.

[1] Bearings can be exchanged between nodes more often, but communicating one message for every 5-s time step between bearing estimates would probably be too frequent for an underwater acoustic communication network.

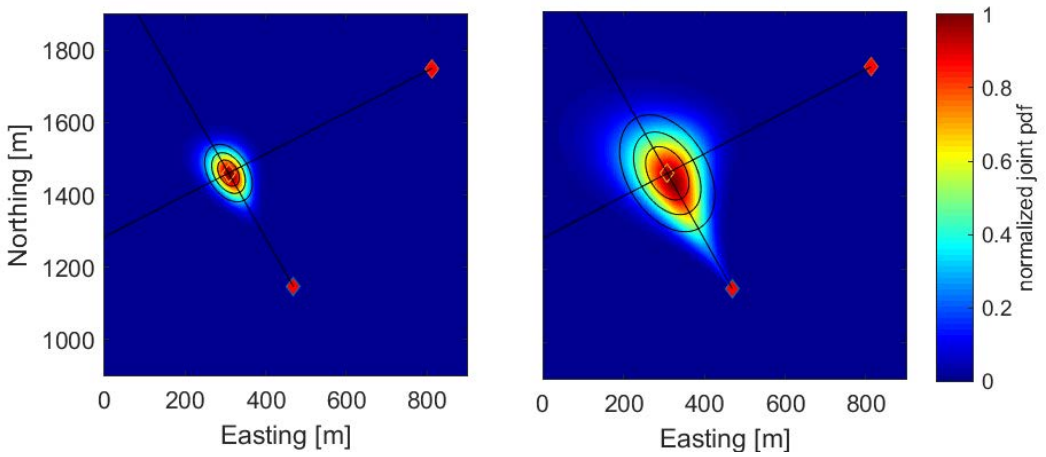


Fig. 3: Crossfix and pdfs for a point along the target trajectory, assuming von Mises distributed bearings with σ=5° (left) and σ=10° (right). The error ellipses shown indicate 25%, 50% and 75% quantiles if we use second-order statistics only.

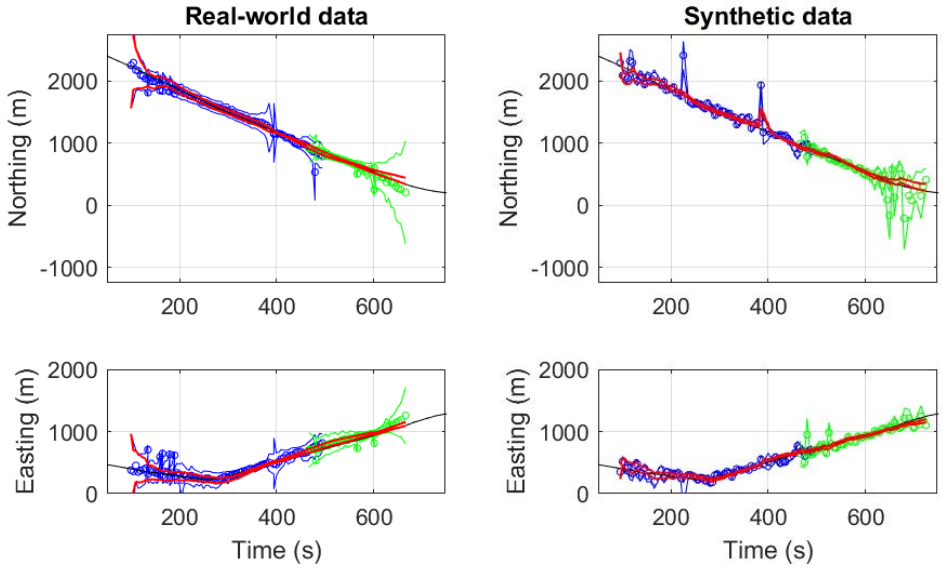


Fig. 4: Crossfixes and Kalman filter track computed by node 1. Blue(green): Crossfixes by combining own bearings with those received from node 2(3). Circles indicate crossfix position and lines indicate position ±1 std.dev. along each direction. Red: Track output from Kalman filter. Position not shown; lines indicate position ±1 std.dev. along each direction. Black line: Actual target track

We let our node 1 compute crossfixes (x,y) and covariance matrixes **R** based on its own stored bearing estimates (all points for node 1 in Fig. 1) and the estimates received from nodes 2 and 3 (blue points in Fig. 1), for pairs of bearings which are sufficiently close in time. The crossfixes are used as measurements in a Kalman filter, along with covariance matrices representing the measurement uncertainty. Sometimes a bearing from node 2 and a bearing from node 3 are matched with the same bearing from node 1. We neglect the fact that these two crossfixes are statistically dependent. Sometimes the bearings may not cross or the crossfix uncertainty is very large (>1000 m) in which case they are discarded.

Fig. 4 shows the result from node 1 crossfixing its own bearings with bearings received from nodes 2 and 3, in blue and green, respectively. A state-space model with four states (the x- and y- coordinates and their derivatives) is used together with a constant velocity motion model. The output from the Kalman filter tracker is shown in red in Fig. 4. For clarity we do not show the track coordinate here, but only the lines that represent the uncertainty.

For the real-world data, when comparing the crossfixes to ground truth they are always within the reported uncertainty. This uncertainty is larger when the target is farthest from node 1 because (a) node 1's own bearing uncertainty then becomes larger, and (2) the geometry becomes more collinear. The tracker output is within the reported uncertainty compared to ground truth. For the synthetic data (with parameters α=0.08 and σ=5°), the outliers due to non-zero α have too small reported uncertainties, and sometimes confuse the tracker. However, it quickly converges towards the correct track again.

4. PARTICLE FILTER APPROACHES

4.1. Basic particle filter

Particle filters are based on the idea of discretizing the probability distribution of the target state vector. This enables non-linear measurement equations and non-Gaussian noise to be easily included into the framework. This is utilized here to update the particles directly from the bearing estimates without estimating the cross-fixes. This enables a more flexible utilization of the measurement data with no explicit demand for time alignment of measurement data, and allows us to do measurement update even with bearings from a single node only (for introduction to particle filters for tracking, see [8]). We also avoid re-using the same bearing as describe above for the Kalman filter. The particle filter used here is similar to the basic particle filter of [11]. One difference with [11] is the initialization. Here we initialize the particles based on the first measurement in a pie-shaped area assuming a distance from the node of 15 to 1500 meters and an azimuth angle distributed according to the von Mises distribution. The particles are naturally propagated through the process update equation. The update step is done by calculating the likelihood of the latest arrived measurement with respect to each particle which is followed by systematic resampling. The likelihood is calculated using the von Mises distribution with α=0 and κ obtained from the uncertainty estimate of the bearing estimator.

The particle filter was applied to the real dataset described above. The root-mean squared (RMS) error of the Kalman filter was 42.8 m while for the particle filter described here it is 56.3 m. This is a bit surprising given all the benefits of the particle filter we just described. However, this could be due to modelling errors or be unique to this data set.

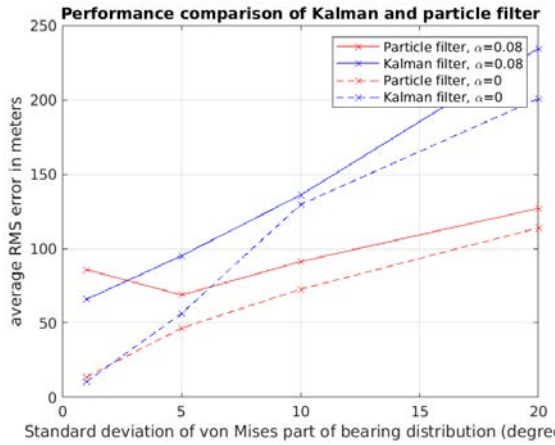


Fig. 5: Comparison of basic particle filter and Kalman filter on synthetic data. Both filters apply α=0 in all cases, while they are given the correct standard deviation.

To assess our earlier claims of the advantages of particle filters, we did a simulation study using the same target track but synthetic bearing data using the mixture model of Sec. 2.2.

The results are shown in Fig. 5 for different values of σ and α. The average RMS error over ten runs are consistently better for the particle than the Kalman filter except for σ=1° and α=0.08. In this case, the particles sometimes get stuck in a point due to uniformly distributed bearings – and the filter is unable to recover. Note that even though the average RMS values (over ten runs) for the particle filter is better than Kalman, a few runs shows a better performance for the Kalman filter.

4.2. Distributed Particle Filter

In this section, we investigate a Distributed Particle Filter (DPF) (developed in [6]) and assess its performance against the real dataset described in Section 2. This filter falls in the category of constraint sufficient statistics (CSS) schemes. Indeed, rather weak constraints must be satisfied [7] for approximating the Global Sufficient Statistics (GSS) through the computation of Local Sufficient Statistics (LSS). Those local statistics are meant to represent the likelihood function as seen by individual nodes. The bootstrap approach [10] is used for the Sequential Importance Sampling (SIS) and re-sampling is performed at each time step based on the Systemic Resampling algorithm of [8]. Regardless of the number of particles used, only the six LSS values need to be communicated to other nodes. Like the basic particle filter described above, but unlike the Kalman filter, no bearing measurement is used twice.

All nodes (including node 1) locally run the DPF algorithm described above. Moreover, we assume that all other nodes hear the bearings transmitted by one node. For convenience purposes, we here also assume that LSS values are exchanged amongst all nodes at every time step. A time-driven approach is taken here, but the approach could also be implemented as playback of past data after receiving a series of bearings from another node. In summary, at each time step each node receives and only uses: (a) the latest LSS values from other nodes, and (b) its own and most recent bearing. In addition to this, a node sometimes receives bearings from one or many other nodes. In real applications, LSS values could only be transmitted along with new bearing data.

The proposed approach uses the conventional discrete-time constant velocity (CV) target motion developed in [9] along with counter-clockwise coordinated turns (CCT) as proposed in [8]. In that setup, the filter state vector is comprised of the estimated target position and velocity, in the latitude and longitude space (the other two filters operate in the X-Y space).

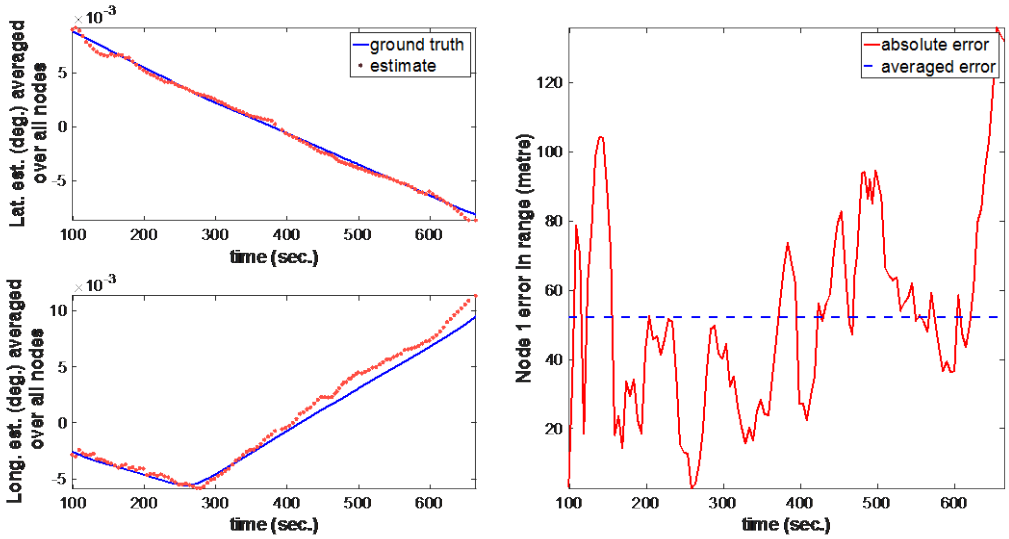


Fig. 6: Simulation results of the Distributed Particle Filter with the real dataset. Left: de-referenced latitude and longitude of both the target and the averaged (over all nodes) target position estimate. Right: Time evolution of the root mean squared (RMS) error from node 1.

Fig. 6 shows results of applying this DPF to the real dataset with 50,000 particles (using 1,000 particles only leads to marginally worse results). The averaged RMS error is 52 m, which is comparable to the other two schemes.

5. CONCLUDING REMARKS

We have discussed three different techniques of locally fusing measurements in bearing-only trackers. Moreover, real and synthetic datasets are used for performing an initial comparison of their relative performances. The synthetic datasets have bearings based on a mixture of uniform and von Mises distributions.

Even though each tracker has distinct internal processing approaches and use of measurement data, they have comparable performance on the real data set. Over synthetic datasets, the basic particle filter seems to outperform the Kalman filter in most cases.

Future work will include analysis of the performance and extensions of the proposed bearing-only trackers, and to experimentally validate the present results.

REFERENCES

[1] **R. Otnes**, NILUS – An Underwater Acoustic Sensor Network Demonstrator System, In *10th International Mine Warfare Technology Symposium*, Monterey, CA, USA, 2012. Online: https://www.ffi.no/no/Publikasjoner/Documents/NILUS2012.pdf

[2] **R. Otnes, E. v. d. Spek, M. E. G. D. Colin, H. S. Dol, C. E. Solberg**, Easily deployable underwater sensor nodes – the NILUS MK 2 Demonstrator System, In *UDT Europe*, Oslo, Norway, 2016.
Online: https://www.ffi.no/no/Publikasjoner/Documents/NILUS_UDT_Europe_2016.pdf

[3] **R. Otnes, J. Eastwood, M. E. G. D. Colin**, Using GStreamer for acoustic signal processing in deployable sensor nodes, In *MTS/IEEE Oceans*, Genoa, Italy, 2016.

[4] **N. I. Fisher**, *Statistical Analysis of Circular Data*, Cambridge University Press, 1996.

[5] **E. Taghavi, R. Tharmarasa, T. Kirubarajan, M. McDonald**, Multisensor-Multitarget Bearing-Only Sensor Registration, *IEEE Tr Aerospace and Electronic Systems*, 52 (4), pp. 1654-1666, 2016.

[6] J. Y. Yu, M. J. Coates, M. G. Rabbat, S. Blouin, A Distributed Particle Filter for Bearings-Only Tracking on Spherical Surfaces, *IEEE Signal Processing Letters*, 23 (3), pp. 326-330, 2016**.**

[7] **A. Mohammadi, A. Asif,** A constraint sufficient statistics based distributed particle filter for bearing only tracking" *IEEE Int. Conf. Communications*, pp. 3670-3675 Jun. 2012.

[8] **B. Ristic, S. Arulampalam, N. J. Gordon,** *Beyond the Kalman filter: Particle filters for tracking applications,* Artech House, 2004.

[9] **Y. Bar-Shalom, X. R. Li, T. Kirubarajan,** *Estimation with Applications to Tracking and Navigation*, Wiley, 2004.

[10] **O. Hlinka, F. Hlawatsch, P. M. Djuric**, Distributed particle filtering in agent networks: A survey, classification, and comparison, *IEEE Signal Processing Magazine*, 30 (1), pp. 61-81, 2013.

[11] **E. Rabe, E. Gudmundson, M. L. Nordenvaad**. Target tracking using bearings-only sensor nodes and a mixture model, in *MTS/IEEE Oceans*, Aberdeen, UK, 2017.

A BAYESIAN INFORMATION FUSION APPROACH TO NAVAL MINE-HUNTING SYSTEM OF SYSTEMS OPERATION PLANNING AND EVALUATION

Ruben Strenzke[a], Christopher Strode[a]

[a]NATO Centre for Maritime Research and Experimentation

Contact author: Ruben Strenzke, STO CMRE, Viale San Bartolomeo, 400,
19126 La Spezia, Italy; Tel.: +39 0187 527 447; ruben.strenzke@cmre.nato.int

Abstract: *Planning and evaluating naval mine-hunting missions requires a situational picture. This picture shall include the information gathered by modern image-producing sonar sensors. Therein, a central component must fuse the information gathered by the sensors of a system of heterogeneous systems. We hence propose a novel framework for planning and evaluation for a mine-hunting system of systems. The framework calculates a geo-referenced mine presence belief by applying Bayesian statistics on detections and through-the-sensor performance self-assessment information. Thus, a mine presence probability map and an information availability map are produced; the latter showing the general confidence in either mine presence or absence. Furthermore, the framework can determine the number of future sensor looks necessary to achieve a certain target risk for vessels that are transiting the area of interest. This is done by simulation on sensor performance predictions to drive the mine presence belief to a context-derivable lower or upper threshold, which results in a sensor-specific future effort map. We describe the algorithms that generate the three before-mentioned map types from pre-processed performance assessment and target recognition data - without relying on any prior knowledge on mine density. Furthermore, we present results from simulation experiments involving systematic deviations of performance self-assessment from the actual performance. The results suggest that the geo-referenced fusion of multiple independent data collection runs improves the information availability per cell and the estimated number of mines - even if there is a constant high bias in performance self-assessment.*

Keywords: *Naval Mines, Mine-Hunting, Through-the-Sensor Performance Assessment, Planning, Evaluation, Bayesian Statistics, AUV, UUV*

1. INTRODUCTION

Current operational approaches for the Planning and Evaluation (P&E) of naval Mine Counter Measures (MCM) operations [1, 2] were developed for manned vessels with forward looking mine-hunting sonars. These sonars do not produce lasting still images that can be analysed at any point in time later on. Each part of the area of interest (AOI) is worked on by exactly one such vessel, which will immediately pursue every detection (D) of a Mine-Like Echo with the ordered follow-up actions: classification (C), identification (ID), and neutralisation (NE).

In contrast, modern systems employ side-looking sonars that produce images for onboard or post-mission analysis. Such analyses allow Through-the-Sensor (TTS) performance assessment [3], and the result can be displayed in a 2D grid map of the seafloor [4]. Furthermore, multiple modern MCM vehicles are able to operate concurrently in the same part of the AOI - e.g. Autonomous Underwater Vehicles (AUVs) that are specialised on one or more of the mine-hunting phases (D+C, ID, NE). This means that the phases are decoupled, and detections that were established in the survey phase can be left untreated in following phases - at least for some time. As a consequence the need to fuse interim mine-hunting results arises.

In the context of our work on Planning and Evaluation for System of Systems (PESOS), the scenario we are interested in includes a System of Systems consisting of heterogeneous mine-hunting AUVs, which operate in the same area with different sensors (including side-looking sonars). Our goal in this work is to develop an information fusion approach that helps creating an MCM P&E situational picture. It shall be able to handle the mentioned multi-phase scenario and make use of TTS performance assessment. In addition, we show that the information produced during the evaluation process can be used as basis for decision-making and planning.

2. OVERVIEW OF THE PLANNING AND EVALUATION FRAMEWORK

The risk to vessels transiting an AOI (short: transitors) to be struck by a mine (short: risk) is the essential measure for decision making in MCM operations. Hence, the situational picture for MCM P&E must include a Mine Presence Probability Map (MP-Map), which allows deriving this risk for a specific transit route. To determine the geo-specific mine presence probability $P(M)$ first an estimation concerning the total number of mines present in the AOI n has to be established (see Fig. 1). This leads to a probability mass function (PMF) $p(n)$. Then $P(M)$ can be determined from the mathematical expectation $E(n)$ and any information collected from that cell: mine detections (passing a classification score threshold), TTS estimated probability of detecting and correctly classifying a mine (P_{DC}), and TTS estimated false alarm rate (P_{FA}), i.e. the probability of reporting a detection where there is no mine.

The availability of information can differ in certain parts of the AOI due to past effort, possibly contradicting results, and sensor performance. Hence, we add to the situational picture a geo-referenced information availability I and associated with it an Information Availability Map (IA-Map). Finally, we demonstrate how the planning of future MCM effort can be performed in principle. To this end, we determine the number of additional looks $L_{S,R}$ necessary to reduce the risk to a target value R with a sensor S. As input the geo-specific sensor performance prediction is needed, and the output can be displayed in a Future Effort Map (FE-Map). This feature is represented by dashed lines in Fig. 1 because it is for demonstration purpose only.

The multi-phase aspect of MCM operations is handled in the following way. All results of DC and ID looks are fused into the MP- and IA-Maps. NE task effectiveness and affordable effort has to be estimated (e.g. by a human operator). The FE-Map is generated based on this input and the target risk. If the map is generated for a survey AUV, then small spots on

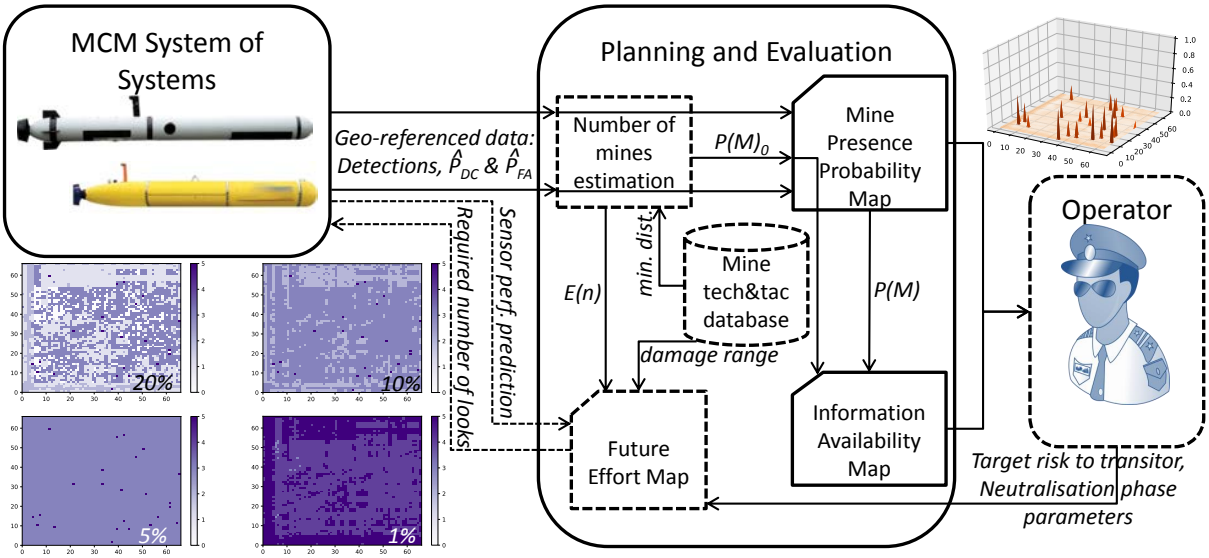


Fig. 1: Data flow in our Planning and Evaluation framework and examples of a Mine Presence probability Map (upper right) and Future Effort Maps (lower left, indicating the number of future sensor looks required to achieve a target risk, such as 20%, 10%, 5%, 1%).

the FE-Map with high number of future looks (e.g. 5 in Fig. 1) should be prioritised as re-visit locations for a different sensor with a higher predicted $\hat{P}_{DC}$ and lower $\hat{P}_{FA}$ (such as an ID AUV). In case NE tasks strictly depend on preceding ID tasks, ID effectiveness and affordable effort must be integrated into the NE effectiveness and affordable effort (as input for generating the FE-Map). Finally, the MP-Map plays is the indicator for NE task planning. If again ID tasks are coupled to NE tasks, then the MP-Map also has to be used for ID task planning.

3. MODEL AND ALGORITHMS

The P&E model is grid-based, and each cell can hold at most one mine and/or one detection (depending on the context). All P&E steps are completely based on Bayesian statistics.

The remainder of this chapter describes the algorithms to determine first the PMF for the number of mines $p(n)$, secondly the cell-specific mine presence probability $P(M)$, thirdly the cell-specific information availability I, and fourthly the cell- and sensor-specific future number of looks necessary for risk reduction $L_{S,R}$.

3.1. Estimating the number of mines present

The number of mines present can be determined with an optimal unbiased estimator based on Bayes' theorem. Inputs for the estimator are looks on cells inside the AOI, which can be generated by covering the cell with a Synthetic Aperture Sonar (SAS) tile or an electro-optical video frame etc. For every look on a cell we perform Bayesian updating of beliefs [5] concerning n, which are stored in the PMF $p(n)$ (1). The underlying assumption is that the mine density in the area covered is representative for the overall AOI. In the likelihood [5] function (2), every possible n is associated with a $P(M)=\frac{n}{cells_{AOI}}$. The function also takes the binary detection vector $\vec{DC}$, and its TTS performance context: $\vec{\hat{P}}_{DC}$ and $\vec{\hat{P}}_{FA}$ (for looks l on cells with x/y coordinate indices i, j). $p(n)$ may be updated at any time on receiving further information.

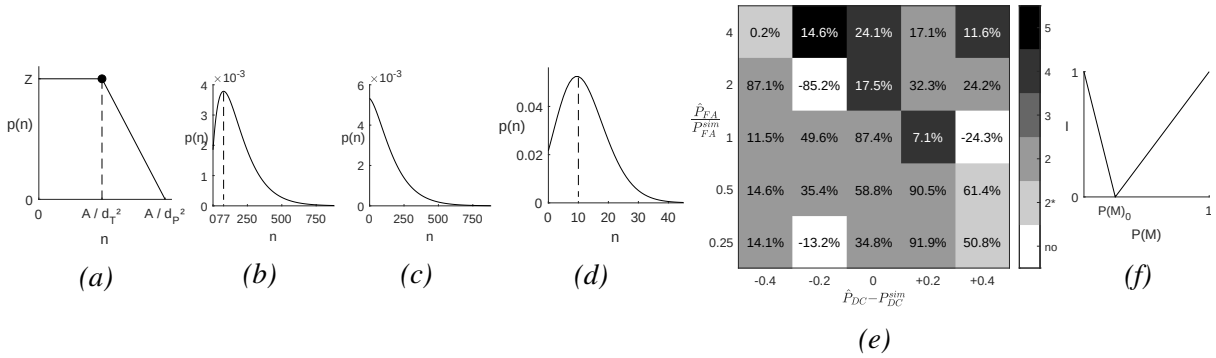


Fig. 2: ***(a)*** *Initial beliefs concerning the number of mines present as PMF $p(n)$, shaped by physical and tactical minimum mine distances d_P and d_T (A: area, Z: normalisation).* ***(b)*** *$p(n)$ for an AOI consisting of 50 SAS tiles, calculated after analysing only a single SAS tile containing one detection. $\hat{P}_{DC}$ was 0.5, and $\hat{P}_{FA}$ was 0.0005, both uniformly. $E(n)$=179.89.* ***(c)*** *$p(n)$ after changing $\hat{P}_{DC}$ to 0.1 for the cell with the detection. $E(n)$=145.29.* ***(d)*** *$p(n)$ after analysing 50 SAS tiles, all with the parameters mentioned in (b). 16 detections in total, the most probable result if n=9. $\arg\max_n p(n)$ =10 and $E(n)$=12.36.* ***(e)*** *Percentage of how close the sum of all P(M) in the AOI gets to the actual n after 5 passes over the AOI, compared to only 1 pass. 25 configurations performance estimation deviations. Also shows the number of passes that led to the first improvement over baseline (no: no improvement after 5 passes; 2*: after fusing later passes, the result was intermediately worse).* ***(f)*** *Cell-specific information availability I as function of $P(M)$ and uniform $P(M)_0$=$\frac{E(n)}{cells_{AOI}}$*

The initial prior distribution $p(n)_{iniprior}$ holds before there is any sensor information from the AOI. It is shaped by a physical minimum mine distance d_P is used as a hard upper limit to n. In addition, a tactical minimum mine distance d_T is introduced, which is less likely to be undercut than to be overrun (linear degradation, see Fig. 2a). The resulting initial prior distribution is deemed appropriate for all kinds of MCM operations, as it does not rule out any physically possible number of mines, and it allows modelling tactical considerations.

$$p(n \mid \vec{DC}, \vec{\hat{P}}_{DC}, \vec{\hat{P}}_{FA}) \propto p(n)_{iniprior} \times P(\vec{DC} \mid n, \vec{\hat{P}}_{DC}, \vec{\hat{P}}_{FA}) \tag{1}$$

$$P(DC_{i,j,l} \mid n, \hat{P}^{DC}_{i,j,l}, \hat{P}^{FA}_{i,j,l}) = \begin{cases} \frac{n}{cells_{AOI}} \cdot \hat{P}^{DC}_{i,j,l} + (1 - \frac{n}{cells_{AOI}}) \cdot \hat{P}^{FA}_{i,j,l} & \text{if } DC_{i,j,l}=1 \\ \frac{n}{cells_{AOI}} \cdot (1 - \hat{P}^{DC}_{i,j,l}) + (1 - \frac{n}{cells_{AOI}}) \cdot (1 - \hat{P}^{FA}_{i,j,l}) & \text{if } DC_{i,j,l}=0 \end{cases} \tag{2}$$

For demonstration we created an example scenario, in which the AOI had 150×150 cells with 3×3m size, and it contained 9 randomly placed mines. d_P was set to 3 m, and d_T to 30 m. In order to avoid any influence of the mine locations on the results, P_{DC} and P_{FA} were uniform over all cells (P^{sim}_{DC}=0.5 , P^{sim}_{FA}=0.0005). Fig. 2b shows the updated $p(n)$ after examining the first SAS tile containing one detection. For Fig. 2c we set a different $\hat{P}_{DC}$=0.1 for the cell with DC=1 to show that each the TTS context of each detection plays a role. If instead another cell (with DC=0) was chosen to have $\hat{P}_{DC}$=0.1, then $p(n)$ would look similar to Fig. 2b, but $E(n)$=180.23 instead of 179.89. Hence, the difference between Fig. 2b and 2c is the effect of evaluating DC in the concrete TTS context. Fig. 2d shows the outcome after analysing all 50 SAS tiles with the same attributes, but only 15 additional detections, which is the most probable outcome for an overall n=9. Both $E(n)$=12.36 and $\arg\max_n p(n)$ =10 are very close to n=9 in a solution space of $0 \leq \hat{n} < 22500$.

3.2. Evaluating the mine presence probability

From $p(n)$ it is possible to derive a uniform prior $P(M)_0$ for each cell via the expectation of n (3). After that, we can perform cell-specific Bayesian updates on $P(M)$ for every look l ($1 \leq l \leq l_{max}$) that included the corresponding cell (4). The result of this iterative process can be displayed by means of an MP-Map as shown in Fig. 1 in 3D.

$$P(M)_0 = \frac{E(n)}{cells_{AOI}} \tag{3}$$

$$\forall l{:}P(M \mid DC)_l = \begin{cases} \frac{P(M)_{[l-1]} \cdot \hat{P}_l^{DC}}{P(M)_{[l-1]} \cdot \hat{P}_l^{DC} + (1-P(M)_{[l-1]}) \cdot \hat{P}_l^{FA}} & \text{if } DC_l{=}1 \\ \frac{P(M)_{[l-1]} \cdot (1-\hat{P}_l^{DC})}{P(M)_{[l-1]} \cdot (1-\hat{P}_l^{DC}) + (1-P(M)_{[l-1]}) \cdot (1-\hat{P}_l^{FA})} & \text{if } DC_l{=}0 \end{cases} \tag{4}$$

We conducted sensitivity analyses regarding the quality of the MP-Map after fusing the information from multiple passes over the AOI. To this end, we generated 25 configurations: five relations of simulated P_{DC}^{sim} to TTS-assessed $\hat{P}_{DC}$ combined with five relations of P_{FA}^{sim} to $\hat{P}_{FA}$. The AOI had the same characteristics as described for the number of mines estimation experiments. For each configuration, we performed ten randomised runs of data collection/fusion. As quality measure we chose the distance reduction $\Delta\hat{n}$ [%] of the construct $\sum P(M)$ (i.e. the sum of all $P(M)$ in the AOI) gets to the actual n. $\sum P(M)$ after five passes is compared to the baseline, which is $\sum P(M)$ after the first pass (5). These results and the lowest number of passes to improve the outcome are shown in Figure 2e. In all configurations with systematic overestimation of P_{FA}, we found that $\sum P(M)$ came closer to n than $E(n)$ did (because $p(0)$ became larger with every additional pass). This effect set in usually after the second pass over the AOI already, and only in one configuration after the third. After the first pass, i.e. before any cell-specific fusion, $E(n)$ was always higher than $\sum P(M)$, but the difference was always below 0.835 [mines].

$$\Delta\hat{n}[\%] = \frac{|\sum n - P(M)_{l=1}| - |n - \sum P(M)_{l=5}|}{|n - \sum P(M)_{l=1}|} \cdot 100 \tag{5}$$

3.3. Evaluating the information availability

The goal of an MCM operation is to localise mines, which means to maximise the certainty concerning mine existence or absence at any position. Therefore, the information that we want to gather is directly related to $P(M)$. We base the geo-referenced information availability measure on the difference of $P(M)$ and $P(M)_0$. Hence, for cells never looked at $I{=}0$, because their $P(M)$ was never updated by (4) to differ from $P(M)_0$. For obvious reasons, I reaches the maximum 1 in case of total certainty regarding mine presence or absence, i.e. $P(M){=}1 \vee P(M){=}0$. We apply two linear scales for $P(M){>}P(M)_0$ and $P(M){<}P(M)_0$ (see Fig. 2f).

We conducted sensitivity analyses regarding the effect on information availability by fusing the information delivered from two passes over the AOI. To this end, we used the same parameters and the 25 configurations for the deviations of TTS assessment as in Section 3.2 and performed ten randomised runs of data collection per configuration. The fusion was shown to improve I averaged over all cells by either 0.09, 0.21, or 0.25 - depending solely on $\hat{P}_{DC}$.

Table 1 shows the possible developments of $P(M)$ and I over two looks, assuming $P(M)_0$ remains unchanged. Again, the same parameters were used. When $P_{DC}{=}0.5 \wedge P_{DC} \gg P_{FA} \wedge P_{DC} > P(M)_0$, then every $DC{=}0$ event lets $P(M)$ fall to $\approx 50\%$ of the previous value, hence

Table 1: Results for P(M) and information availability I after one and two looks on a cell with different detection and classification outcomes $\vec{DC}$. $\hat{P}_{DC}$=0.5 , $\hat{P}_{FA}$=0.0005.

	$\vec{DC}=(0)$		$\vec{DC}=(1)$		$\vec{DC}=(0,0)$		$\vec{DC}=(0,1)$		$\vec{DC}=(1,1)$	
$P(M)_0$	$P(M)$	I	$P(M)$	I	$P(M)$	I	$P(M)$	I	$P(M)$	I
0.0004	0.0002	0.4997	0.2858	0.2859	0.0001	0.7497	0.1668	0.1669	0.9975	0.9979

decreasing the distance of I to 1 by $\approx 50\%$. In contrast to that, cells with true or false alarms end up with $P(M) \gg P(M)_0$, so that $I \approx P(M)$. For DC=0 events, I develops over multiple looks like $1-\underline{P}_{DC}$ (i.e. P_{DC} aggregated over multiple looks) as long as $P_{DC} \gg P_{FA}$ and $P_{DC} > P(M)_0$. Although I could therefore in principle be used as the maximisation objective for combined coverage and detection revisit planning, we propose to plan on a target risk in the following.

3.4. Estimating the future survey and identification effort

If it is possible to estimate future sensor performance, e.g. from past performance, then we can determine for every cell the future number of looks $L_{S,R}$ necessary to probably achieve a certain target risk with this sensor. Risk reduction is two-fold: For empty cells we require a confidence on mine absence; and for mines we want to reduce the risk of remaining unneutralised (i.e. it either does not become the target of any NE attempt or all attempts fail).

We define $thresh_{empty}$ as the value to be undercut by the $P(M)$ that is predicted after simulating future effort. Its value can be determined as shown by (6) to (7): via the target risk R^{empty}_{total} and the number of cells in which the presence of a mine would pose a threat to the transitor (cells to cross length-wise c, potentially dangerous cells width-wise per crossing step m, determined by mine damage range $r_{damage[cells]}$ to both sides of the ship, hence $\times$ 2).

$$m=2 \cdot r_{damage[cells]} \quad ; \quad R^{empty}_{step}=1-(1-R^{empty}_{cell})^{m} \quad ; \quad R^{empty}_{total}=1-(1-R^{empty}_{step})^{c} \tag{6}$$

$$thresh_{empty}=R^{empty}_{cell}=1-\sqrt[c \cdot m]{1-R^{empty}_{total}} \tag{7}$$

When a cell's $P(M)$ surpasses $thresh_{mine}$ (which is higher than $thresh_{empty}$), this serves as an indicator to perform NE attempts. Because the number of NE attempts available is usually limited by certain factors, a high $thresh_{mine}$ is needed to achieve a low R^{empty}_{total}. This can be explained by filtering out false alarms that would otherwise be targeted by NE tasks, thereby reducing the number of attempts on actual mines and increasing remaining risk. As first step to determine $thresh_{mine}$, in this uniform approach we demand the risk posed by cells with mines to be reduced to a similar value as that of empty cells, and the remaining risks depends on the probability of not trying or (repeated) failing of NE attempts - hence (8), where $f_N \in \mathbb{R}_{\geq 0}$ is the average number of attempts per cell where we suspect a mine, i.e. where $P(M) > thresh_{mine}$. (9) describes how to determine f_N in case either less than one attempt is needed on average or more than one. In realistic examples of sparsely populated minefields, R^{mine}_{cell} will already be very low compared to the product of reacquisition and NE success probabilities $P_{RN} \cdot P_N$. Then f_N is high, and hence it is better to target for successful NE only of mines along a single route, which can be either generic or specific. This is described in (10), where $cells_{alongRoute}$ refers to the specific channel made up geometrically by $c \times m$. As shown in (11), $thresh_{mine}$ can then be determined by distributing $\hat{n}$ as $P(M)$ over the number of cells that will be visited for NE v_N, which can be derived from f_N and the number of NE tasks available t_N.

$$R^{mine}_{cell} \equiv R^{empty}_{cell} \; ; \; R^{mine}_{cell} = 1-f_N \cdot P_{RN}P_N \text{ if } f_N \leq 1 \; ; \; R^{mine}_{cell} = (1-P_{RN}P_N)^{f_N} \text{ if } f_N > 1 \tag{8}$$

$$\implies f_N = \begin{cases} \frac{1-R_{cell}^{empty}}{P_{RN}P_N} & \text{if } R_{cell}^{empty} \geq 1-P_{RN}P_N \\ \frac{\log(R_{cell}^{empty})}{\log(1-P_{RN}P_N)} & \text{if } R_{cell}^{empty} < 1-P_{RN}P_N \end{cases} \tag{9}$$

$$\hat{n}_{alongRoute}^{generic} = \frac{E(n)\cdot c \cdot m}{cells_{AOI}} \quad ; \quad \hat{n}_{alongRoute}^{specific} = \sum_{\forall cells_{alongRoute}} P(M) \tag{10}$$

$$thresh_{mine} = \frac{\hat{n}_{alongRoute}}{v_N} \quad ; \quad v_N = \frac{t_N}{f_N} \tag{11}$$

We now determine the number of future sensor looks $L_{S,R}$ that with at least a probability of p_{min} (e.g. 50%) achieve that: $P(M)$ undercuts $thresh_{empty}$ if the cell is empty, and $P(M)$ surpasses $thresh_{mine}$ if there is a mine. For every cell with $thresh_{empty} < P(M) < thresh_{mine}$, $L_{S,R}$ is iteratively incremented from 1 upwards with abort criteria as described below. In every iteration two Bernoulli experiments are made with predicted P_{DC} and P_{FA} for a specific sensor in the geographical context: It is simulated that the cell is empty (with the success case $DC=0$), and it simulated that there is a mine (with the success case $DC=1$). In each simulation all combinations of numbers of $DC=0$ and $DC=1$ events are processed by iterative Bayesian updating (as in (4)), wherein the current $P(M)$ of the cell serves as prior. We then sum up the occurrence probabilities of all combinations by which the predicted $P(M)$ passes the corresponding *thresh*. If that sum surpasses p_{min} for the mine and empty case, then $L_{S,R}$ has been found for that cell. Otherwise the next higher $L_{S,R}$ has to be tested.

Thus, for a specific sensor and a certain target risk value, an FE-Map as displayed in Fig. 1 can be generated. It shows in where how much effort is needed to reduce risk to a target value, but it is neither suited to replace track planning, nor is it suited as input for track planning. This is because a certain track pattern leads to different numbers of looks for different cells (due to overlaps and gaps between SAS tiles) and at the same time to range-dependent effects on P_{DC} per cell [4]. However, inside this framework, a track planner could iterate over its parameters, thereby influencing $L_{S,R}$ and P_{DC} to reach the thresholds.

4. CONCLUSION, RELATED AND FUTURE WORK

We have described a framework that performs the whole MCM P&E loop, with the exception of track/path plan generation. Its novelty is that it works with detailed geo-referenced maps - in addition to the classical statistical measures. By means of the experiments presented, we have shown that even if the AUVs' performance assessment has a high deviation from actual performance, data fusion from multiple passes or vehicles has a positive effect on information on mine presence or absence. With the FE-Map, we demonstrated how sensor performance prediction can be used for the planning of MCM effort based on risk to transitors.

The TTS performance assessment required by our approach has been performed on the estimated probability of detection and correct classification of a mine already [4]. In addition, similar to [6] we have proposed that TTS performance assessment be performed also for the false alarm rate. We applied a grid-based approach, as it is done in [7]. Their concept of a "search channel" treats detections and non-detections for every grid cell over time as Bayesian update on the associated mine presence belief. Although our approach is similar in that, it differs through introducing: first, a solution for the important question of the prior mine presence belief, and secondly, mine presence probability thresholds for planning on risk.

Future work includes analysing the impact of navigational error (i.e. probability distributions of the AUV position) on the geo-referenced mine presence probability. There is a cell-size

effect when treating navigational error and when calculating the risk - both needs to be taken into account. The proposed approach can be improved in terms of computational speed by finding a non-optimal unbiased estimator. The estimation of false alarm rates and the possibility of reproducible false alarms in the survey phase (e.g. rocks with mine-like shapes) should be target of future research in the context of real sensor data. Related to that is the analysis of false alarm geographic distribution patterns, especially in comparison with realistic mine-laying patterns. Also, the exploitation of classification scores should be considered in the likelihood function - in contrast to treating every detection that passes a classification threshold in a binary way. In that context it is also relevant that the scores might systematically depend on aspect angle. Furthermore, the FE-Map points to the requirement that a future planning component needs to perform mixed-sensor planning. If the FE-Map is generated for an ID AUV with P_{DC} high and P_{FA} low enough so that all cells show the future number of looks is 1, then ID task optimisation is pointless. Instead, many cells might need to be part of an additional survey before planning ID tasks, if the survey sensor has a wider field of view. Related to that is also the unsolved topic of sensor performance prediction models (i.e. dealing with past performance, environmental conditions, aspect angle, range etc.). Finally, to apply the framework to different operating navies, standards for data exchange need to be defined and tested under real world conditions.

5. ACKNOWLEDGEMENTS

This work was supported by NATO ACT. The authors have taken up ideas exchanged and approaches discussed in the context of the MCM P&E Joint Research Project, especially from FFI (Norwegian Defence Research Establishment) and the German Navy.

REFERENCES

[1] Washburn, Alan R. ”Mine Warfare Models.” (2007).

[2] Cramer, Megan. *Understanding information uncertainty within the context of a net-centric data model: A mine warfare example.* Naval Sea Systems Command Washington DC Mine Warfare Program Office (PMS 495), 2008.

[3] Harris, Mike, et al. ”AQS-20 Through-the-Sensor (TTS) performance assessment.” *OCEANS 2005. Proceedings of MTS/IEEE.* IEEE, 2005.

[4] Gips, Bart, Strode, Christopher, and Dugelay, Samantha. ”Residual Risk Maps for Performance Assessment of Autonomous Mine Countermeasures using Synthetic Aperture Sonar”. *Proceedings of the Insitute of Acoustics.* 2018.

[5] Lynch, Scott M. *Introduction to applied Bayesian statistics and estimation for social scientists.* Springer Science & Business Media, 2007.

[6] Geilhufe, M., Connors, W. A., and Midtgaard, Ø. ”Through-the-sensor performance evaluation for modern mine hunting operations.” *Proc. Undersea Defence Technology.* Lillestrøm, Norway. 2016.

[7] Baylog, John G., and Wettergren, Thomas A. ”A ROC-Based Approach for Developing Optimal Strategies in UUV Search Planning.” *IEEE Journal of Oceanic Eng.* 2017.

ACOUSTIC MODELLING KNOWLEDGE FOR DESIGN AND SPECIFICATION OF SITUATION-ADAPTIVE DISTRIBUTED NETWORKED SYSTEMS

Frank Ehlers

Bundeswehr Technical Centre for Ships and Naval Weapons,
Maritime Technology and Research (WTD 71)

Contact author: Frank Ehlers, WTD 71, Klausdorfer Weg 2-24, 24148 Kiel, Germany;
frankehlers@bundeswehr.org

Abstract: *The design and specification of situation-adaptive distributed networked systems has to take the ability of the system to generate plans on the basis of its own assessments into account, i.e. considering the evaluation results from previous missions. Acoustic modelling should be the core of this planning and evaluation process. However, sophisticated detailed modelling is not computationally feasible at the level of design decision making because the optimization loops involved in adaptive planning and in the design and specification process are already demanding for the high-dimensionality of parameter sets found for realistic operational scenarios. On the other hand, just relying on fast modelling (e.g. insertion of the Sonar Equation) at the level of design decision making does not exploit the benefits of adaptability built into the system, hence might lead to wrong decisions regarding the selection of designs (resulting also in wrong decisions on plans and specifications). The aim of this paper is to generate a general recommendation on how to deal with acoustic modelling for design and specification of situation-adaptive distributed networked systems.*

Keywords: *Acoustic modelling, planning and evaluation, design and specification*

MOTIVATION

Underwater acoustic measurements are extremely important for the navigation and telemetry of autonomous underwater vehicles (AUVs). Underwater acoustic measurements are also a major element of distributed networked systems, e.g. as part of a surveillance systems looking for intruders. Combining networks with degrees of freedoms AUVs have or equipping AUVs with the sensors of distributed networks seems to be the natural follow-on research, given the demonstrated success of both concepts [1]. Such situation-adaptive distributed networked systems inherit the importance of underwater acoustic measurements from their parent systems, plus the ability of the system to generate plans on the basis of its own assessment. This ability has to be taken into account when designing and specifying situation-adaptive distributed networked systems: A clever plan might overcome limits of low quality sensor measurements, resulting in procurement costs efficiency and/or robustness of the system. Planning can be translated into mathematics as optimization regarding system degrees of freedom, assessment as optimization of model parameters regarding previous measurements. Hence, acoustic modelling is onboard the distributed networked system and the influence of its quality on the overall performance of the system has to be assessed when looking at designs and specifications for such systems. A very important aspect there is to take into account that only a few measurement samples might be available onboard an autonomous asset, hence model input errors and expected model output error have to be balanced. Furthermore, when a system reaches the level of an industrial product, verification and validation processes have to look into the details of acoustic modelling.

Simulations and analytical calculations are taking place in acoustic modelling, finite elements on one end of the scale (high-fidelity, processor power consuming), sonar equation calculation at the other end of the scale (general, fast). And in between there is a continuum of more exact (but slower) or more general (but faster) approaches. Certainly, for the verification and validation aim, the fastest solution seems appealing, since it has to be taken into account the simulation result onboard the network asset given its measurement in a simulated environment with a large number of situational (environmental) parameters. Unfortunately, details count: E.g. in Anti-Submarine Warfare (ASW) the “sonar range of the day” has been proven to be of limited use in a multistatic shallow water environment, or in Mine Countermeasures (MCM) the “look through the sensor” approach seems to be favorable when planning ahead missions.

In this paper, we are trying to compile a survey (in particular from the own, signal processing and data fusion driven, perspective) on acoustic modelling approaches in the realm of distributed sensor networks and AUVs. ASW and MCM are serving as example application areas. The aim is to generate a general recommendation on how to deal with acoustic modelling for design and specification of situation-adaptive distributed networked systems.

The remainder of this paper is organized as follows: In the next section, we explain how design and specification have to be linked. Then, we take a look at previous approaches in ASW and MCM dealing with estimating system performance facing the difficulty of environmental variability. Next, we formulate a concept called “Uncertainty Absorption” to discuss how situation-adaptive distributed networked systems can be characterized. Then, the predicted Bayesian effect of deeper modelling layers is suggested as core of an autonomous acoustic modelling. We conclude giving a final recommendation based on the discussions in the previous sections.

DESIGN AND SPECIFICATION

In [2], the ERE (Effectiveness, Robustness of evaluation, Efficiency) methodology has been developed. Fig. 1 is summarizing the approach. In its core, ERE is a reinforcement learning loop, aiming at operating at a given level of effectiveness while maximizing efficiency. In order to achieve this aim, a robust way of evaluating the effectiveness and efficiency is mandatory. Details of the system are captured in a realization of a NATO Architecture Framework, evaluations are made possible through a maintenance of independence between internal modules, and a Reasoner Module is making final decisions on activating or not specific behaviors.

Acoustic modelling is part of all modules listed in Fig. 1. For example, the "Estimator" has a sensor model with parameters to be set according to the conditions of sound transmission. Any action of the Independence Plan has to be evaluated according to its effect on the performance (e.g. diving deeper could lead to entering a favorable sound channel). All environmental details have to be stored in an organized manner, e.g. by an ontology fitting into the NATO Architecture Framework.

The overall system has to be verified and validated. Therefore, all parts have to be examined at their "atomic" level, where "atomic" means that a reasonable and understood physical model is available to analytically/stochastically justify all numerical parameter values set in the Verification and Validation step.

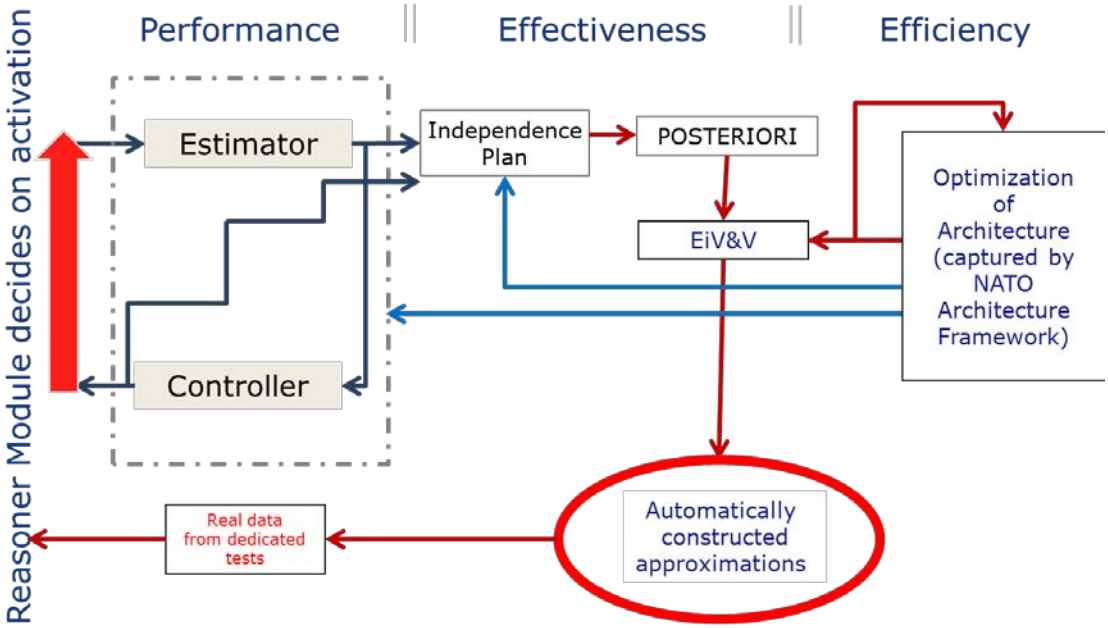


Fig. 1: Sensor employment solutions are evaluated under a variety of situations including the ability of sensors to adapt to changes. Adding Efficient independent Verification & Validation (EiV&V) to the standard learning scheme ensures solution effectiveness and allows for comparison of results leading to the best co-ordination method inside the networked system.

SURVEY

- Single system: The SONAR equation combines in logarithmic units (i. e., units of decibels relative to the standard reference of energy flux density of rms pressure of 1μPa integrated over a period of one second), the following terms:

    - SNRout = (S − TL1 − TL2) − (N − AG) + TS which define signal excess where:

        - S: source energy flux density at a range of 1 m from the source;
        - TL: propagation loss for the range separating the source and the target (TL1) and the target and the receiver (TL2);
        - N: noise energy flux density at the receiving array;
        - AG: array gain that provides a quantitative measure of the coherence of the signal of interest with respect to the coherence of the noise across the receiving array;
        - TS: target strength whose value strongly depends on the aspect of the target to the source receiver pair [3].

    - The SONAR equation can be treated as “atomic” level if all assumptions for its application are valid. Resolution of sonar systems has to be taken into account, in higher frequencies (without resonance effects of the object structure) facet models of objects can be established.

- Environmentally adaptive systems: The maritime environment affects the acoustic measurements. Detailed models exist in many cases, e.g. matched-filter loss from time-varying rough-surface reflections [4] or the effect of internal waves in MCM [5], just to name two. Looking through the sensor is a technique that extracts environmental information from the sonar data. However, the effect of the feedback of these estimated parameters into the system has to be taken into account. Does matched-filter loss affect a specific ASW mission? Do internal waves affect a specific MCM mission?

- Distributed systems: The fusion of multistatic homogeneous or heterogeneous ASW systems has been studied e.g. in [3]. Its performance has been evaluated by a list of values [6], but not based on the actual effect on the given ASW mission goals. In fact, depending on the behavior of the sensors e.g. track length might be very important (in case of a reachability based hunting behavior) or less important (in case of a percolation based hunting behavior). In other words, performance measures are linked to behaviors (called Independent Plans in Fig.1).

  Also in MCM SAS multi-pass applications can be translated into the PHD data fusion and tracking domain [7], e.g. via the reconstruction/simulation proposed in [8].
  The use of Compressive Sensing in [7] is one path towards distributed networked systems with real-time fusion under communication constraints. Of course,

information theoretic approaches are needed to decide whether or not measurement information from one location is needed at another location.

- Situation-adaptive distributed networked systems: The focus is set on decision making in terms of sensor management and platform movements regarding the operational objective. Defining autonomous systems as systems capable to make decisions beyond the foresight of developers, programmers and operators, situation-adaptive distributed networked systems could be seen as located in both, the sensor management realm (with foreseen actions of the system) and those autonomous systems that have "assured autonomy" (meaning here, that they cannot harm the overall operational objective by following some strict rules in their state space).

For ASW, two different approaches have been tried to implement a design decision making:
A) tracking performance with simulated targets included in evaluating multistatic sonar systems with high-fidelity modelling, but non-sophisticated tracking [9], and
B) an information theoretical approach simple sensor model, but actually executing target tracking with Particle Filters in the simulation [10]. Combining both approaches is computationally too challenging when following a straight-forward approach.

For MCM, a fine-scale simulation/reconstruction is proposed in [8], another approach by inserting artificial mines in real data and using operational ATR [11] Is there a similar implementation gap as for ASW when straight-forward combination of both approach is tried? Probably, yes, because performing simulations for all possible fine-scale variations of the MCM-environment is too challenging.

Summarizing the finding in this survey: Well-understood physics (linked to many environmental and system-internal details) on the one side has to be connected to operational specifications on the other side, whereby the linkage cannot generally be implemented in a straight-forward manner.
In the next section, we propose the concept of "Uncertainty Absorption" as a tool to characterize approaches to implementing this details-to-specification connectivity.

UNCERTAINTY ABSORPTION

Referring to Fig. 1, the ERE methodology can be interpreted as a system design process where effectiveness is preserved by uncertainty absorption. There are several tools that can be used (as templates) within the design process, some of them are listed here as examples. The idea behind these uncertainty absorption templates is that their parameters span the workings space for the design process (instead of the actual state space of the assets of the distributed system), i.e. by such transformation "invariant" (or independent) variables can be exploited in order to generate new "atomic" elements for which analytical calculations/simulations are available (for these new atomic elements the Bayes effect of more detailed acoustic modelling can be used as decision criterion on whether or not such more detailed acoustic modelling should be started or not).
Imagine a surveillance area with a grid of small grid size. For ASW, the area has to be scanned simultaneously everywhere, for MCM, there is also the choice for a sequential search (because mines do not move). The simplest, but very inefficient system design is

positioning a sensor in each grid cell. Saving sensors, one might use active sound with higher stand-off ranges.

- Matched Filters are absorbing noise regarding the echoes of the active sound and uncertainty regarding the resolution.

In the surveillance, ASW targets or MCM echo highlights on larger objects are moving and need to be concatenated.

- The tracking approach has Cramer Rao lower bounds which can be used to construct decision making algorithms of how good the estimation is depending on the geometrical situation, i.e. the tracking algorithm is an uncertainty absorber.

For the localisation on the global surveillance grid, source-receiver localisation is necessary.

- Source receiver localisation: SAS, SLAT [12], and SLAM algorithms absorb the uncertainty of own localisation.

For track-and-trail (ASW) or re-localisation (MCM) a reachability of the object tracked has to be ensured.

- Reachability analysis absorbs all uncertainty of target movement (given observability of the target)

Since sensor performance might be degraded, non-concatenated tracks (in ASW) or multiple passes (in MCM) might be necessary to be handled.

- Percolation analysis absorbs uncertainty regarding the effectiveness of the surveillance mission.

Each of these templates contains acoustic modelling (e.g. waves affect the Matched Filter performance, internal waves affect the SAS processing). Acoustic modelling results contain the uncertainty of its input data. Hence, the question arises how this uncertainty can be absorbed.

Look-through-the-sensor and the platforms autonomy to act according to this sensor information gathering seems to be one reasonable approach for this uncertainty absorption. This means that the AUV has to decide on the level of uncertainty of the look-through-the-sensor and modelling information, i.e. the AUV has to answer the question when the overall performance starts to degrade due to improper estimates and improper modelling.

THE PREDICTED EFFECT OF DEEPER MODELLING LAYERS AS CORE OF AN AUTONOMOUS ACOUSTIC MODELLING

As concluded in the previous section, a (Bayes) decision making on whether to go into deeper layers of modelling/more look-through-the-sensor or not has to be performed on board the AUV. The ERE concept of Uncertainty Absorption provides “atomic” modules with known statistics that link the potential decisions to the system-wide effectiveness. However, actual data sets (or high-fidelity simulations) can only be produced in a very limited amount. This situation is comparable to medical investigations comparing studies of treatment with studies of no treatment.

Meta-analyses of clinical trials targeting rare events face particular challenges when the data lack adequate numbers of events for all treatment arms. Especially when the number of studies is low, standard meta-analysis methods can lead to serious distortions because of such data sparsity. To overcome this, [13] suggests the use of weakly informative priors (WIP) for the treatment effect parameter of a Bayesian meta-analysis model.

In the implemented execution phase, a correct modelling/look-through-the-sensor level can be examined by the AUV via checking (with given statistical guidelines) the effect of the current level compared with a next higher level.

In the design-specification phase the execution is to be modelled, hence correct levels are not yet known, and the effect has to be studied. Operational scenarios are the equivalent of medical studies (with and without treatment). An example is given in [14, p. 124]. If the same design should be able to handle various scenarios (which might lead to overall efficiency), hierarchical models can be used to combine the outcome of dedicated tests at sea or of high-fidelity simulations. To perform this mathematical operation, the basic statistics to generate the appropriate re-sampling statistics have to be known, i.e. Indendence Plans (as in Fig. 1) have to be available. Obviously, a fix-point algorithm is entered here, where approximated solutions are re-entered into the system to produce better solutions. The solution of this algorithm determines finally the level of autonomy (in terms of how wide or specific the rule sets are) a system has to have to reach its operational goal.

Stated differently, the effect of better acoustic modelling has been based on a low number of samples, hence “automatically constructed approximations” (as in Fig. 1) have to be used to base the decision on. These “automatically constructed approximations” stem from the Uncertainty Absorbing templates which already reduce the parameter space the decision depends on.

This discussion leads back to the survey section, in particular to the statement on situation-adaptive distributed networked systems: Do these systems need to store (and take with them) the complete knowledge of the entire operation? Certainly, for a fully autonomous operation the calculations have to check for effects within their entire (unconstraint) action space. On the other hand, such fully autonomous systems are then free of any programming bounds. Verification and validation seems to be impossible with the numerical tools we have available today. Instead, when following the ERE methodology, the autonomy plus the need for the autonomous systems to being able to make decisions given their limited amount of data and modelling capability, results in a set of rules for the autonomous system which makes possible its verification and validation and takes away the autonomy to perform actions that have never been foreseen by developers, programmers or operators.

RECOMMENDATIONS

The maritime environment is highly variable in space and time. Pure modelling with historical data can introduce huge errors into planning processes. Therefore, the autonomy via the look-through-the-sensor concept is pushed forward to the executing sensor platform. This autonomy is absorbing the uncertainty given by the environment.

However, this autonomy comes with a price: either access on each asset to the entire system plus (unrealistic) computational processing needs on each asset, or an extensive concatenation phase of design and specification where the autonomy is then finally bound by a rule set (“assured autonomy”).

This second option (“assured autonomy”) seems to be a viable way ahead. However, the concatenation phase has to deliver (like a mathematical proof) a complete chain of arguments, any hole in this chain will make the verification and validation process become invalid. Acoustic modelling is an inherent part of this chain and is used in the sensor

models, in the target models, and in the look-through-the-sensor estimations. Furthermore, consistency is needed: The concatenation phase has to take the optimal choices of the autonomous systems and they have to be able to make these optimal choices in the real implementation.

For some systems, the core (or atomic) elements of the models are relatively easy (like reflection of high frequency sound on a facet), for other systems the acoustic modelling is very challenging (like low frequency coupling of sediment and multi-component partially buried mine-like object). As depicted in Fig. 1, "real data from dedicated tests" is needed to step forward and make core (or atomic) models available for these difficult acoustic problems.

REFERENCES

[1] F. Martin-Lauzer, M. Stevenson, S. Jespers and F. Ehlers, Coalition of ASW Sensors, In *Defence Technology Asia*, Singapore, 2007.
[2] Frank Ehlers, Evaluating the Effectiveness of Coordination Methods for Distributed Mobile Sensors, STO Scientific Publications, SET-199, May 2016.
[3] M. Daun and F. Ehlers, Tracking algorithms for multistatic sonar systems, *EURASIP Journal on Advances in Signal Processing*, 2010 (1), 2010.
[4] [Abraham, Douglas A.; Murphy, Stefan M.; Hines, Paul C.; Lyons, Anthony P., Matched-Filter Loss from Time-Varying Rough-Surface Reflection with a Small Effective Ensonified Area, IEEE Journal of Oceanic Engineering, vol. 43, issue 2, pp. 506-522, 2017.]
[5] Hansen, Roy & P. Lyons, Anthony & Olsmo Saebo, Torstein & John Callow, Hayden & A. Cook, Daniel. (2014). The Effect of Internal Wave-Related Features on Synthetic Aperture Sonar. IEEE Journal of Oceanic Engineering. 40. 1-11. 10.1109/JOE.2014.2340351.
[6] D. Grimmet, S. Coraluppi, B. L. Cour, C. Hempel, T. Lang, P. Theije and P. Willet, MSTWG multistatic tracker evaluation using simulated scenario data sets, *11th International Conference on Information Fusion*, 2008.
[7] Frank Ehlers, "Application of Compressive Sensing on Sonar Data for Unexploded Ordnance under Sediment," SET-265 Specialist Meeting on "Compressive Sensing Applications", Salamanca, 05/2019.
[8] E. Coiras, J. Groen, Simulation and 3D Reconstruction of Side-Looking Sonar Images, In Advances in Sonar Technology, Sergio Rui Silva (Ed.), DOI - 10.5772/39406, IntechOpen, 2009.
[9] Julian Klinner, Frank Ehlers, Operation Specific Tailoring of Scenario Data for Underwater Threat Analysis, Future Security 2014, Berlin, Germany; 09/2014.
[10] F. Ehlers, Particle Filter for Information Management in an Autonomously Operating Activated Distributed Sensor Network, in Proceedings of OCEANS 2007, June 2007.
[11] Oliver Daniell, Jose Vazquez, Estimation of detection/classification performance in sonar imagery using textural features and self-organising maps, in Proceedings of OCEANS 2017.
[12] Broetje, Martina & Broetje, Lars & Ehlers, Frank. (2018). Parameter state estimation for bistatic sonar systems. IET Radar, Sonar & Navigation. 12. 10.1049/iet-rsn.2017.0426.
[13] Burak Kürsad Günhan, Christian Röver, Tim Friede, Meta-analysis of few studies involving rare events, arXiv:1809.04407v1 [stat.AP] 12 Sep 2018.
[14] A. Gelman, J. Carlin, H. Stern, D. Dunson, A. Vehtari, D. Rubin, Bayesian Data Analysis, 3rd Edition, CRC, 2014.

Structured Session 20

Sonar performance modeling and verification. Applications to active and passive sonar

Organiser(s): Colin Mathieu, Prior Mark, Heaney Kevin, Ellis Dale

PREDICTING INTERNAL WAVE PACKET CHARACTERISTICS AND ACOUSTIC SIGNAL COHERENCE

Timothy F. Duda[a], Arthur E. Newhall[a], Karl R. Helfrich[a], Weifeng Gordon Zhang[a], Ying-Tsong Lin[a], and Pierre F. J. Lermusiaux[b]

[a]Woods Hole Oceanographic Institution, Woods Hole, MA, USA
[b]Massachusetts Institute of Technology, Cambridge, MA, USA

Contact author Timothy Duda, WHOI AOPE Dept., Woods Hole, MA 02543, USA, v: 1-508 289 2495, tduda@whoi.edu

Abstract: *A handful of experiments, theoretical studies and simulation studies have shown that packets of nonlinear internal waves, which are commonly found in shallow water areas, can have strong impacts on propagating sound. Impacts include rapid changes in the temporal and spatial coherence of the sound, and the occurrence of strongly focused sound accompanied by shadow zones with little or no sound energy. Moreover, the acoustic effects can be anisotropic, so that sound traveling in one direction geographically will have different characteristics than sound traveling another direction (for instance, along and across internal wave crests). To better apply this knowledge to the use of sound, we have developed a system of linked models to study our ability to predict the appearance of the internal wave packets, and to predict characteristics such as packet speed and direction, wave size, and wave shape. The model system links three fluid models: a primitive equation model, an internal tide model, and a nonhydrostatic internal wave model. These are linked in turn to a 3D acoustic propagation model. Output from the model system will be shown, including comparison with experimental data from the Shallow Water 2006 program. Acoustic field and acoustic parameter predictions from the system will also be shown and will be compared with experimental results.*

Keywords: *Nonlinear internal waves, ocean dynamical modeling, three-dimensional underwater acoustic propagation, acoustic field coherence*

INTRODUCTION

Nonlinear internal waves with strong currents and dramatic vertical displacements have been found to impact many oceanographic processes, and have been given a great deal of attention. Because they move stratified water vertically they create large and moving sound-speed anomalies centered at the pycnocline, and thus impact propagating sound. Many studies have shown the effects, through both theory (for example [1,2]) and experiment (for example [3-6]). In many situations, the three-dimensional (3D) nature of the internal waves is key to the acoustic effects [2-5].

The processes by which the waves affect sound are now well understood. However, ultimate impacts on the sound field vary widely depending on many parameters. These include the angle between the internal wave direction and the sound propagation direction, the amplitude (vertical excursion) of the internal waves, the wavelength, and whether the waves appear in isolation or in groups. Therefore, to predict the general patterns of internal wave effects on underwater sound in any given area, some basic properties of the waves at that location would need to be known, starting with such basic things as wave presence or absence, and wave direction. Moving beyond general patterns, specific acoustic effects at a given time and place might be predictable in detail if the waves could be predicted in detail.

Here, we review the basics of a system to study factors controlling the detailed behavior of the waves, to quantify their predictability. The system can also provide wave predictions given enough input data to drive the system towards a reliable state estimate that can run forward in time. The ability of the system to make predictions of sound field properties such as intensity level and coherence will be demonstrated but not tested directly against data for accuracy. Thus far, the major recent contributions from this research may be quantification of the internal tides and the nonlinear wave formation variability. The pronounced acoustic effects that the waves have, once they are formed, have been studied in the past few years and this part of the research effort may be further along.

LINKED MULTIPHYSICS MODELS

The system links three physical oceanographic models, each valid within a specific dynamic range and under a specific set of dynamical approximations. These are (1) a primitive equation computational flow model, (2) a ray-based model of internal tide modal propagation, and (3) a mode-based model of nonlinear nonhydrostatic wave evolution. When the models are linked, the system embeds packets of nonlinear nonhydrostatic internal waves (NNIW) into large-scale ocean flow fields. Internal tides are simply internal gravity waves of tidal frequency, which appear where tidal flows efficiently provide energy to the vertical oscillations of internal waves. The system can be considered a hybrid physical model; the term hybrid been used for models of processed like El Nino/Southern Oscillation (ENSO) but the term is not rigorous. The merged environmental fields (background and NNIW) are then processed to form a simulated environment for 3D acoustic modeling; and the acoustic simulation is the final step. The basics of the system are described in a paper written for the 2014 Underwater Acoustics Conference [7] and a recent paper gives a more complete explanation [8]. Our name for the system is the IODA-A model, because it is the main system put together under the Integrated Ocean Dynamics and Acoustics Project [7].

The modeling rests on 3D ocean fields of eddies, fronts, other mesoscale features simulated with tidal forcing included. The tides are necessary because they force the features that can be transformed dynamically into predicted NNIW.

The ocean fields from model (1), calculated using the nonlinear primitive equations with hydrostatic pressure, can be either constrained by data and meant to be predictive, or fully idealized with analytic boundary and flow descriptions, or somewhere between these. Certain features of the large-scale flow known to be important to NNIW formation and propagation are extracted from the flow fields to take the next steps to compute and then embed the NNIW.

There are six families of operations involved in linking the component models and then computing the sound field. (1) Regional modeling must be performed. Fields from a regional model with surface tides and internal tides are needed. (2) Estimation of a background state (with no internal waves) in a region of interest for internal-wave modeling is required. This required separation of internal waves from a background state suffers because of entangled time and spatial scales. An isopycnal surface tracking method is adopted for this operation. (3) Internal tides in the regional model must be characterized. Internal-tide signals must be extracted from the full field of isopycnal displacements (position differences from the estimated background state) at critical locations, and their properties tabulated. This forms input for internal tide and NNIW propagation analysis. Internal tide propagation trajectories (rays of mode-one waves) are computed at this time. (4) The extended rotation-modified Korteweg-de Vries nonhydrostatic wave model (eKdVf model) is run along the internal-tide modal rays. It is initialized and constrained by the background state and the characterized internal tides. (5) The regional model and eKdVf fields are merged into a set of volumetric ocean state snapshots. (6) Lastly, 3D acoustic simulations are run with the split-step Fourier parabolic equation (PE) method [9].

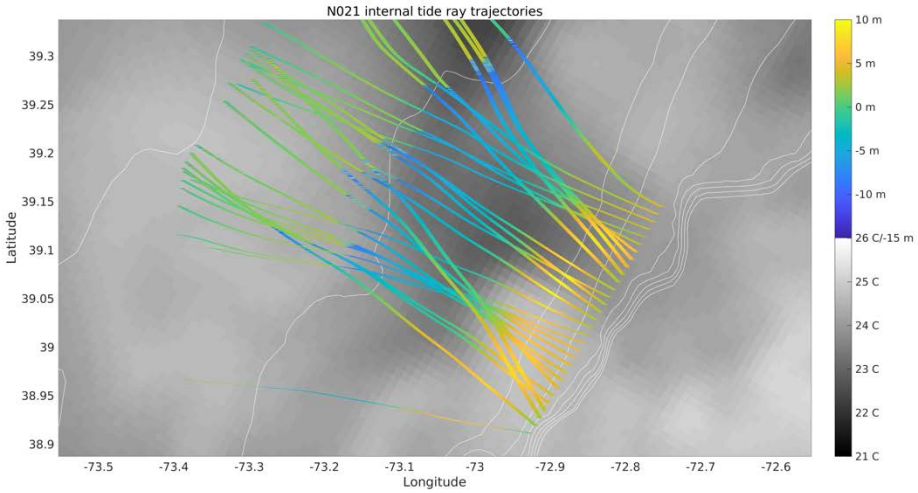


Fig. 1: Internal-tide mode-one rays computed from the model are plotted. The background field that is shown is the surface temperature of the MIT-MSEAS model. The color along the rays shows mode amplitude from the eKdVf model. Bathymetry in shallow water is contoured, none are shown in the rapidly deepening water to the southeast.

Fig. 1 shows mode-one internal tide rays initiated at the outer continental shelf, at the site of the ONR Shallow-Water 2006 experiment [10] and traced shoreward with refraction determined by the mode-one phase velocity field. The regional model used for this ray calculation is the MIT MSEAS data-assimilating model [11]. The area is east of New Jersey and Delaware Bay, USA. Mode-one internal waves have vertical displacement that are of uniform sign at all depths, appear to be an oscillation of the main thermocline, and are also similar to interfacial waves in a two-layer system. The rays are started in a cross-shelf zone where internal tides show flux divergence. This is the so-called critical zone where bathymetric slope transitions from low and *subcritical* in the shallow water to the northwest,

to steep and *supercritica*l to the southeast. Here, critical means that the near-seabed internal tide energy flux direction, in a vertical plane, is parallel to the seafloor. This is where internal tides are formed via barotropic tidal motion. Not all continental shelf edges and slopes exhibit this transcritical slope behavior, but most do, so the model had good applicability. The rays in Fig. 1, which model wave energy moving inshore to the northwest of the critical slope, are initiated at horizontal angles determined by a beamforming-type examination of internal tide motions in the area. Mode-one rays are shown and used exclusively in this modeling because a large fraction of internal-wave energy on continental shelves is mode-one, usually more than 50 percent, and often much more than that.

Fig. 2 shows a snapshot of internal tides and NNIW computed along the rays of Fig. 1 with the eKdVf model and then interpolated to fill more of the area. The 3D sound-speed field with wave perturbations can be built from this wave-amplitude field $\eta(x,y,t)$ via

$$c(x,y,z,t) = c_B\big(x,y,z-\varsigma(x,y,z,t)\big) \tag{1}$$

where the modeled internal-tide and displacement at each location is given by

$$\varsigma(x,y,z,t) = \eta(x,y,t)\phi_{\boldsymbol{B}}(x,y,z) \tag{2}$$

Here, c_B is the background sound-speed structure for a time window of the regional model determined by an averaging process that removes internal tides and gives background temperature (T) and salinity (S), η is the mode-one internal wave field snapshot from eKdVf (includes both internal tides and NNIW), and ϕ_B are the mode-one internal wave normal modes from the background T and S. The subtidal time-dependence of c_B and ϕ_B are suppressed.

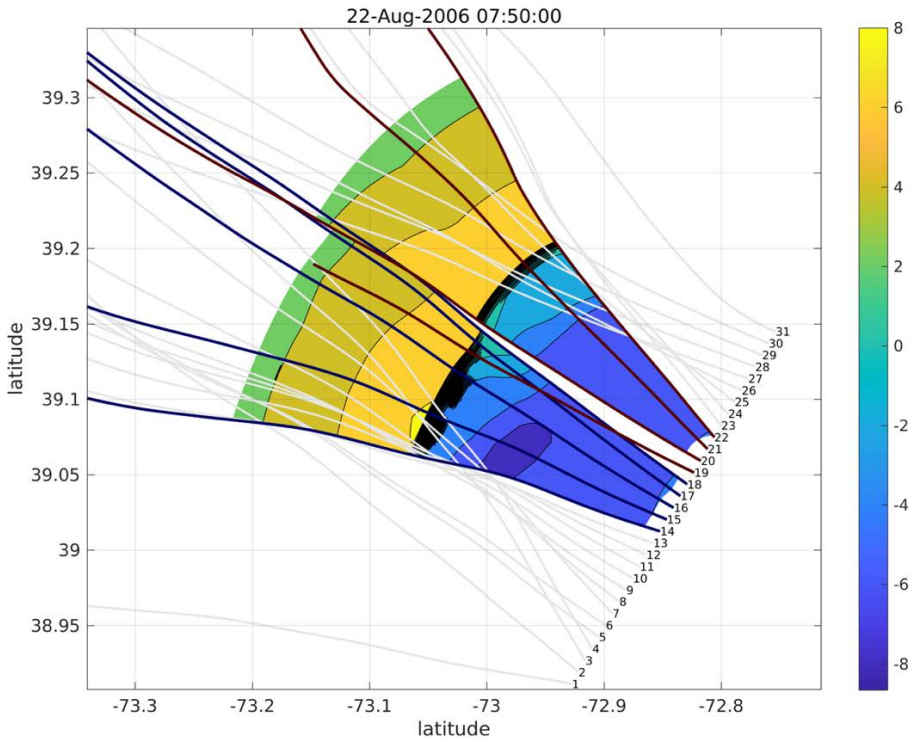


Fig. 2: Internal tides of order 30-km wavelength and short NNIW of order 300-m wavelength computed using the eKdVf model are shown. The model is run independently along each ray, then the results are examined to find wave crests common across rays and can be grouped to form wave crests similar to what is seen in nature. After the crests are identified, 3D sound-speed fields can be built from this. Many rays do not show NNIW development (not shown).

ACOUSTIC MODELING

The final step of the joint ocean/acoustic estimation procedure is to run the 3D acoustic simulation. Fig. 3 shows a rectangular domain for the Cartesian 3D PE for a packet of NNIW from the area depicted in Fig. 2, although for a different time. The figure also shows the intensity of the simulated 1000-Hz field at one depth, and the incoherent depth average intensity that shows sound refraction in the NNIW.

The acoustic field from the PE is now analyzed to show the effects of the NNIW on horizontal coherence. The correlation length L is derived from the correlation function

$$C(\Delta y; x, y, z) = \langle \psi(x,y)\psi^*(x,y+\Delta y)\rangle \Big/ \langle \psi(x,y)\psi^*(x,y)\rangle \tag{3}$$

for the acoustic field ψ by determining the spatial lag Δy where C drops to exp(-1) from a value of unity at zero lag. The correlation length in the y direction is shown in Fig. 4. This is computed by using 50-m long groups of data, so L longer than 50 m is not computed. Values of 50 m indicate full field coherence in the y direction. In the NNIW, L drops to order 5 or 10 meters, only a few wavelengths. The figure also shows signal strength (upper right) and signal strength after coherent field summation by plane-wave beamforming in the direction to the source. The beamforming is not fully effective in the NNIW, and is even less effective in an area in the NNIW "shadow". At the lower right the figure shows the gain from the coherent summation beamforming, measured with respect to the theoretical gain of 10 log10(N) where N is 66 elements in each 50-m array. Fig 5. Shows statistics of horizontal array gain degradation in selected portions of the modeled region, namely away from, within, and in the shadow of NNIW,

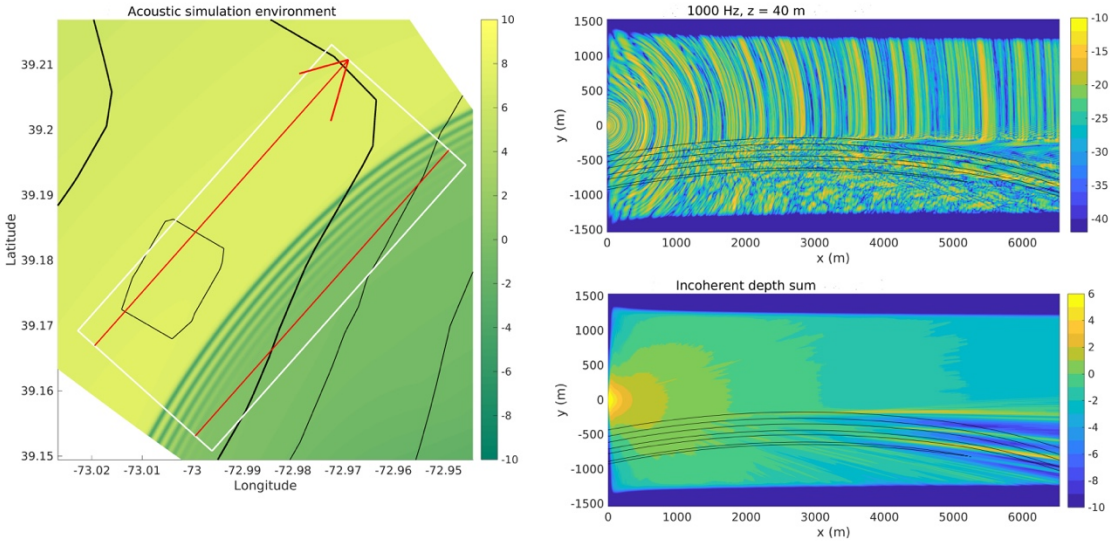


Fig. 3: Left: the rectangle shows the domain for a 1000-Hz PE simulation. The color shows the wave amplitude field η(x,y,t). The NNIW are waves of depression with downward displacements (dark color, green). Bathymetry is contoured; a closed 62-m contour (mound is shown, along with the thicker 74-m contour, and deeper 76 and 78 m contours. Upper right: The sound field intensity at 40-m depth is shown. Lower right: The depth-averaged intensity in the water is shown. Source is 60-m deep at (0,0).

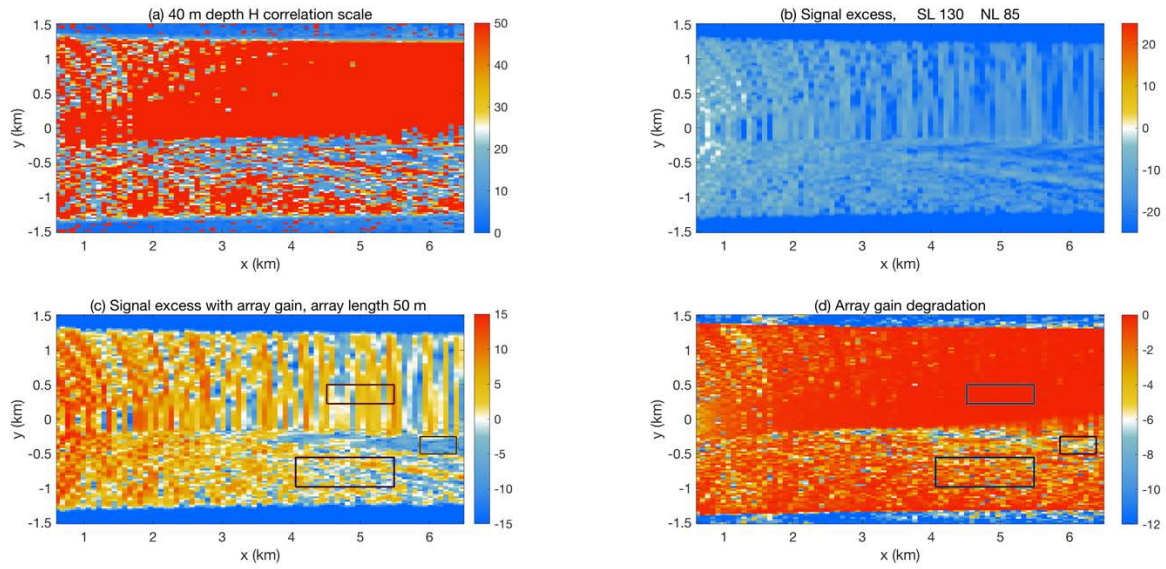


Fig. 4: Upper left: For 1000-Hz sound at 40-m depth in the simulation (Fig, 3), the field correlation length in the y-direction is plotted for the domain. 50-m long groups of points (synthetic arrays) are used. Upper right: The mean sound intensity in each synthetic array is shown. This is a scaled version of intensity, signal excess SE=SL-TL-NL. Lower left: Signal excess after beamforming is shown, SEB=SL-TL-NL+AG, where AG is the achieved array gain. Lower right: The array gain degradation is shown, AG-TG where TG is theoretical gain.

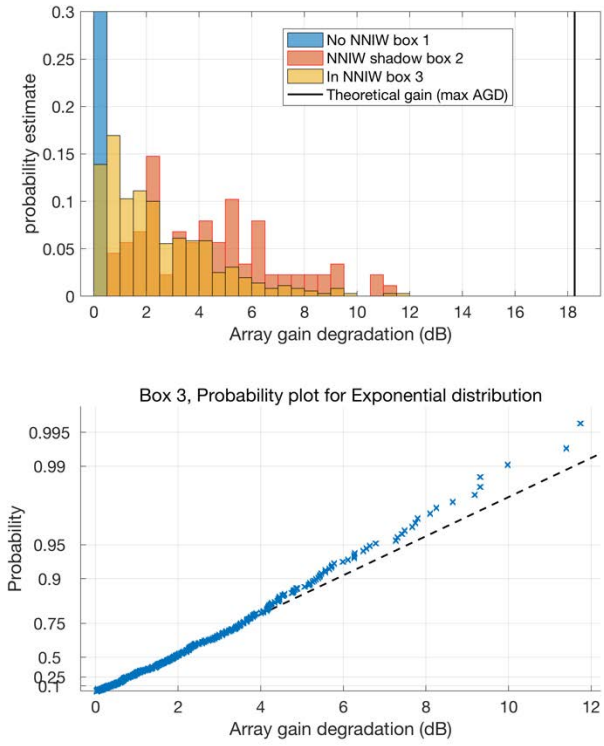


Fig. 5: Statistics of the array gain degradations shown in Fig. 4d are shown, with AGD= TG-AG. Histograms of AGD in three domain boxes are shown at the top, with the boxes shown in Fig. 4. One box shows AG within 0.5 dB of TG always, away from the NNIW. The other two boxes show significant AGD very often. At the bottom, the cumulative distribution of the AGD in box 3 (in NNIW) exceed 4 dB 25 percent of the time, and 5 dB 10 percent of the time.

DISCUSSION AND SUMMARY

A number of questions have arisen from this work. One is that NNIW form on some rays and not others, although the environmental conditions only vary slightly. The eKdVf partial differential equation model (can be used for any mode, mode one modeled here) has many parameters that are complicated functions of the environment, including the quadratic nonlinear term, the cubic nonlinear tern, and the dispersion term, and it would be informative to study the relationship between wave formation and the parameters with the parameters linked in the way that they are for data-constrained modeled ocean environments.

In addition, the initial conditions of the eKdVf, which are the internal-wave displacements at the ray origins, have been calculated to be consistent with internal-tide waves forces locally by barotropic tidal currents. Field observations strongly suggest that these local barotropic tidal currents are not the only source of internal tides and the NNIW they spawn in the SW06 area, and probably other areas [12]. The tidally-forced internal waves are beams in the vertical, and are made of many vertical modes. The beam moves shoreward and undergo mode coupling and loss in nature such that mainly mode one remains after less than a half wavelength or so of propagation, so the energy scaling of the eKdVf initial conditions is *ad hoc*. The other probable sources of mode-one shelf internal tidal energy are mode-one incident internal waves arriving from the deep ocean, known to occur from field studies, and virtually certain to form NNIW packets on the shelf [12]. These are not included in the eKdVf initialization. A scheme would be needed to extract these from the regional model fields and then include them into the eKdVf wave simulations. These are already mode one, and may nonlinearly combine with the multi-mode internal tides converting to mode-one waves just inshore of the critical-zone ray origins, so some research may be necessary to consistently drive the eKdVf with these two classes of onshore-directed wave energy.

The main purpose of the model system is to locate NNIW, determine their amplitudes, packet parameters, propagation direction, and speed. If this were possible to do reliably, then the acoustic effects of NNIW known from previous work and amenable to PE simulation can be incorporated into detailed high-resolution acoustic condition predictions in shallow water areas of interest.

ACKNOWLEDGEMENTS

This work was supported by Department of Defense Multidisciplinary University Initiative (MURI) grant N00014-11-1-0701, managed by the Office of Naval Research Ocean Acoustics Program, and National Science Foundation Grant OCE-1060430. Manuscript preparation was supported by ONR Ocean Acoustics grants N00014-17-1-2624 and N00014-17-1-2692. PFJL also thanks ONR and NSF for research support under grants N00014-13-1-0518 and OCE-1061160.

REFERENCES

[1] **Preisig, J. C., and T. F. Duda,** Coupled acoustic mode propagation through continental shelf internal solitary waves, *IEEE J. Oceanic Eng.*, volume 22, pp. 256-269, 1997.

[2] **Lin, Y.-T., T. F. Duda, and J. F. Lynch,** Acoustic mode radiation from the termination of a truncated nonlinear internal gravity wave duct in a shallow ocean area, *J. Acoust. Soc. Am.*, volume 126, pp. 1752-1765, 2009.

[3] **Duda, T. F., Y.-T. Lin and D. B. Reeder,** Observationally constrained modeling of sound in curved ocean internal waves: Examination of deep ducting and surface ducting at short range**,** *J. Acoust. Soc. Am.*, volume 130, pp. 1173-1187, 2011.

[4] **Badiey, M., B. G. Katsnelson, J. F. Lynch, S. Pereselkov and W. L. Siegmann,** Measurement and modeling of three-dimensional sound intensity variations due to shallow-water internal waves, *J. Acoust. Soc. Am.*, volume 117, pp. 613–625, 2005.

[5] **Duda, T. F., J. M. Collis, Y.-T. Lin, A. E. Newhall, J. F. Lynch and H. A. DeFerrari,** Horizontal coherence of low-frequency fixed-path sound in a continental shelf region with internal-wave activity, *J. Acoust. Soc. Am.*, volume 131, pp. 1782-1797, 2012.

[6] **Headrick, R. H., J. F. Lynch, J. N. Kemp, K. von der Heydt, J. Apel, M. Badiey, C.-S. Chiu, S. Finette, M. Orr, B. Pasewark, A. Turgut, S. Wolf, and D. Tielbuerger,** Acoustic normal mode fluctuation statistics in the 1995 SWARM internal wave scattering experiment, *J. Acoust. Soc. Am.*, volume 107, pp. 201-220, 2000.

[7] **Duda, T. F., Y.-T. Lin, A, E, Newhall, K. R. Helfrich, W. G. Zhang, M. Badiey, P. F. J. Lermusiaux, J. A. Colosi and J. F. Lynch,** The "Integrated Ocean Dynamics and Acoustics" (IODA) hybrid modeling effort, in UA2014, *Proceedings of the 2nd International Underwater Acoustics Conference and Exhibition*, Rhodes, Greece, Edited by John S. Papadakis & Leif Bjørnø, 2014.

[8] **Duda, T. F., Y.-T. Lin, A. E. Newhall, K. R. Helfrich, J. F. Lynch, W. G. Zhang, P. F. J. Lermusiaux, and J. Wilkin**, Multiscale multiphysics data-informed modeling for three-dimensional ocean acoustic simulation and prediction, *J. Acoust. Soc. Am.*, submitted, 2019.

[9] **Lin, Y.-T., T. F. Duda and A. E. Newhall,** Three-dimensional sound propagation models using the parabolic-equation approximation and the split-step Fourier method, *J. Comput. Acoust.*, volume 21, p. 1250018, http://dx.doi.org/10.1142/S0218396X1250018X, 2013.

[10] **Tang, D. J., J. N. Moum, J. F. Lynch, P. Abbot, R. Chapman, P. Dahl, T. Duda, G. Gawarkiewicz, S. Glenn, J. A. Goff, H. Graber, J. Kemp, A. Maffei, J. Nash and A. Newhall**, Shallow Water 2006: a joint acoustic propagation/nonlinear internal wave physics experiment, *Oceanography*, volume 20(4), pp. 156-167, 2007.

[11] **Haley, P. J., Jr. and P. F. J. Lermusiaux, P. F. J.,** Multiscale two-way embedding schemes for free-surface primitive-equations in the Multidisciplinary Simulation, Estimation and Assimilation System, *Ocean Dynamics*, volume 60, pp. 1497-1537, 2010.

[12] **Nash, J. D., S. M. Kelly, E. L. Shroyer, J. N. Moum and T. F. Duda,** The unpredictable nature of internal tides on continental shelves, *J. Phys. Oceanogr., 42,* 1981-2000, doi: http://dx.doi.org/10.1175/JPO-D-12-028.1, 2012.

ESTIMATING RANGE DEPENDENT SEDIMENT THICKNESS AND REFLECTION COEFFICIENTS FROM BATHYMETRIC DATA FOR IMPROVED SONAR PERFORMANCE MODELLING

Dan Henrik Sekse Stender[a], André A. Søvik[a]

[a]Norwegian Defence Research establishment (FFI), PO Box 115, 3191 Horten, Norway

Dan Henrik Sekse Stender, Norwegian Defence Research establishment (FFI), PO Box 115, 3191 Horten, Norway, Dan-Henrik.Stender@ffi.no

Abstract: *Knowledge about the underwater environment is critical to anti-submarine warfare operations in littoral waters. The sonar settings and depth selections can significantly affect the predicted sonar performance. Bathymetry and sound speed profiles can be found or measured on site, whereas the geoacoustic properties of the seabed usually rely on sporadic historical data. Sediment thickness is important for low- to-mid-frequency active sonars, which cannot be found in the traditional sediment databases where only the top layer is sampled. The thickness of sediment deposit in an area will, among other things, depend on the shearing angle of the sediment and the slope of the bottom profile. Utilising available environmental information, such as granular size and bathymetry, an estimate of geoacoustic properties along the bottom profile can be made. When using a sonar performance model, a reflection coefficient for the bottom interface is required. The reflection coefficient is frequency-dependent and depends on the substructure of the bottom. The available information is utilised in a simple and fast calculation which gives the environmental parameters along a bottom profile to be used in a sonar performance model. The goal is to improve the accuracy of the predicted sonar ranges without making extensive measurements of the sea floor. We find that there seems to be a strong correlation between the slope of the sea bottom and the sediment thickness in the area of the North Sea west of Marstein. Furthermore, the background level towards the Norwegian coast is modelled, using a range dependent sediment profile, and compared to sonar data from the same region. Finally, the modelled background level with a range dependent sediment profile is compared to previous models with range independent sediment profiles.*

Keywords: *Sonar, Modelling, Sound propagation, Bathymetry, Sediments*

1. INTRODUCTION

In underwater acoustics, environmental control is a key factor in producing realistic simulations and predictions. During anti-submarine warfare (ASW) operations, only a limited time is available for data collection and model fitting, but a necessity for sound propagation modelling in realistic prediction of sonar ranges at various settings. Other than weather data and sound speed measurements, a rough dataset with measured depths in the area and a basic knowledge of the most common/probable sediment(s) is all the environmental information that can be assumed to be available.

Measurements of sediment properties and thickness have been extensively conducted in the North Sea along with backscatter and various other experiments. Some of this data was used in [1], where they, among other things, investigated the relationship between grain size in the sediment and its acoustic classification. Although there appears to be no correlation between the backscatter from a sediment layer and its grain size, there are studies of the correlation between grain size and critical friction angle of sand and soil [2],[3]. Without the knowledge of the critical friction angle of various sediments, the next best thing would be to compare the slope of the bottom to the thickness of the sediment layer. A correlation here will mean it can be possible to estimate the sediment thickness solely from knowing the bottom structures and a general knowledge about the seabed in the area.

For sonars operating in the low- to-mid-frequency range, the thickness of the sediment layer can play a vital role as the sound can be transmitted through the sediment layer and be reflected by harder subcrop, resulting in lower bottom loss [4]. In the littoral waters of the North Sea, the upper and underlying layers are Holocene marine sediments and Quaternary sediments respectively [1]. By estimating the slopes at which the sonar would see the subcrop, improved sound propagation modelling would be possible, especially in the complex environment towards the coast, without the need for costly and time consuming measurements. Furthermore, such a result could be utilised in other areas where the sediment properties are similar but only the depth profiles are available.

2. DATA

An area in the North Sea, west of Marstein, has been thoroughly mapped by the Norwegian Defence Research Establishment (FFI) between 2003 and 2008. In a geophysical survey, in September 2005 and February 2006, a parametric Kongsberg Maritime Topas PS 018 sonar, transmitting a 20ms 2-4kHz chirp pulse, and high resolution seismic equipment, two $40in^3$ with single channel streamer, were utilised to map the Quaternary layer sequence. These sediment data were acquired on a coarse survey grid with a total track length of approximately 2500km, along with 39 sonobuoy drops which gathered wide-angle seismic data.

In addition to the sediment thickness dataset we used a 60m resolution bottom depth map from the same North Sea region, gathered in the same time period. The multibeam echosounder used to map the area was a 95kHz Kongsberg Maritime EM 1002 which has 111 beams and a $2^o \times 2^o$ 3dB beamwidth [1]. Both the bathymetry map and the sediment thickness data can be seen in Fig. 1, where the outline of the sediment thickness data is shown in red on the depth data in the left panel. The right panel shows the sediment data.

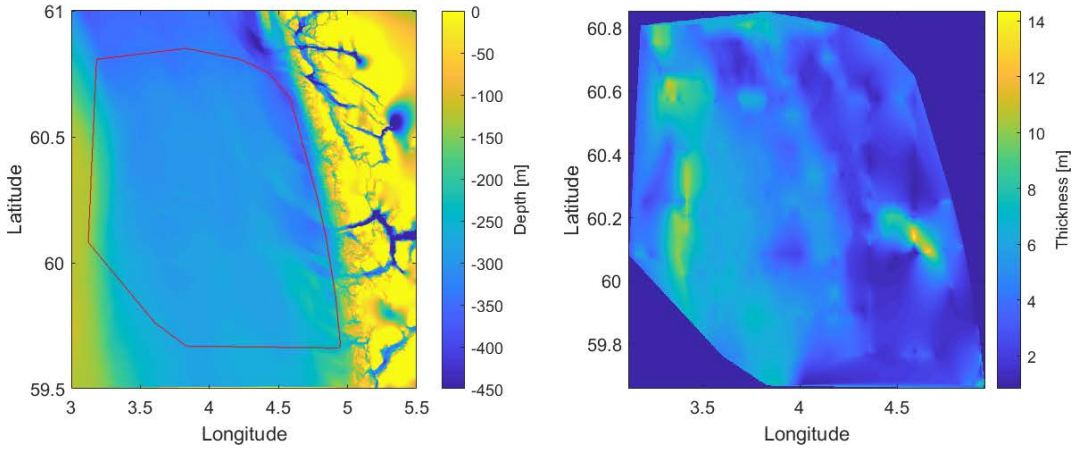


Fig.1: The bottom depth data, left panel, with the outline of area of the sediment data (red). The right panel contains the sediment data.

Finally, an experiment from the New Array Technology 3 (NAT3) program, Clutter Experiment 2 (CEX02), was used for testing and validation of the method. The NAT3 program was a joint collaboration between Thales Underwater Systems, TNO, FFI, and the French, Dutch, and Norwegian navies, where several experiments were conducted. One of the experiments, CEX02, was conducted in the Norwegian Trench in September 2002 with an active low-frequency towed array sonar system towed by FFIs research vessel, H. U. Sverdrup II. The receiver array consisted of equally spaced triplet hydrophones, while a towed body, the TNO Socrates source, transmitted a two second long hyperbolic, frequency modulated pulse every 90 seconds for two hours (79 transmissions). The received hydrophone data were processed up to a pre-tracking level following the steps in [5].

3. METHOD

Correlation of the sediment thickness with the bottom slope is sensitive to the resolution of the two maps. High resolution depth data results in a very uneven bottom with steep slopes on scales smaller than can be seen in the sediment map. In our case, the depth map has a resolution of 60m, while the sediment map is only at roughly 200m, meaning that the first step is to downscale the bottom map to roughly 20m resolution. Furthermore, the position, in latitude and longitude, of every data point in the sediment map is extracted and interpolated onto the downscaled depth map where the total slope of the position can be calculated. This result in a sediment thickness to bottom slope correlation which can be used to fit a function which best describes the relationship between the bottom slope and sediment thickness of this area. Because of the very high density of samples at minor slope angles compared to steeper slopes, the function fitting was done in an iterative process. First the fitting was done with all samples, which gives a very highly correlating fit for low slope angles. This was used to set the starting point (A) of an exponential decay function,

$$Y=Ae^{\lambda x}, \tag{1}$$

where Y is the sediment thickness, A is the sediment thickness at 0^o slope, λ is the decay factor, and x is the slope in degrees, before fitting the rest of the function to the mean sediment thickness in bins of increasing bin size for steeper slope angles. The increasing bin size is also to account for the lack of data at steep angles and the possibility of bins with a single sample contributing heavily to the fitting. This iterative fitting process gives an

exponential decay function which performs well at both low slope angles, where there is a lot of data, and towards steeper slope angles, with sparse data sampling.

Finally, this function can be used along with the CEX02 dataset, to estimate the sediment thickness towards the shore in a detailed bottom profile in order to improve on the sound propagation models for this experiment. The function for estimating the sediment thickness in terms of the slope of the bottom surface is used to determine a slope limit where the sediment becomes acoustically transparent. The slope limit is determined by a qualitative assessment of reflection coefficient for a simple 3-layer environment, water-sediment-bedrock, easily computed by the OASES code [6], [7]. This allows us to simplify the bottom model and treat it as a uniform half-space composed of sediment or bedrock. The bottom loss as a function of grazing angle is calculated using an analytical expression for the Rayleigh reflection coefficient [8]. The background level will be modelled with two different sediment profiles, one range independent, seeing only the upper sediment layer, and one range dependent, varying between the upper sediment layer and the bedrock, depending on the slope of the profile. The physical parameters for the upper sediment layer (Holocene) and Quaternary/ bedrock layer is presented in Table 1. The geoacoustic properties of the bedrock are assumed to be similar to mudstone [9]. The acoustic model was compared to measured background levels in CEX02 similar to the work done in [10], where a range independent bottom loss model was used. The acoustic propagation model used is the acoustic raytracer Lybin [11].

Parameter	Value
Holocene	
Lambert's coefficient, μ (dB)	-18
Sound speed, c_{sed} (m/s)	1505
Density, ρ_{sed} (kg/m^3)	1.5
Attenuation, α_{sed} (dB/λ)	0.15
Quaternary/ bedrock	
Lambert's coefficient, μ (dB)	-18
Sound speed, c_{sed} (m/s)	2050
Density, ρ_{sed} (kg/m^3)	1.5
Attenuation, α_{sed} (dB/λ)	0.15

Table 1: Environmental parameters

4. RESULTS

A bottom profile with a cross section that displays a decrease in depth along the profile is shown in Fig. 2, along with the sediment thickness along the profile. The resolution along the x-axis is roughly 200m, and the profiles clearly show a decrease in sediment thickness for an increasingly inclined slope. The largest sediment thickness, of 10.46m, is found at roughly 15000m, where the slope is 0.14^o, whereas, the minimum sediment thickness, of 3.38m, is seen at approximately 22700m, with a slope of almost 0.6^o.

Figure 3 displays a density plot of all sediment thickness data and the corresponding slope at that location. The raw data indicates a clear correlation between an increase in slope resulting in a decrease of sediment thickness, which is only enhanced by the black stars which mark the weighted bin values. Furthermore, we see, in purple, the solid line marking the iterative exponential decay fit, which was locked to a starting position of 4.6m sediment thickness at 0^o slope by fitting all data points before fitting the decay of the curve to the weighted bin values. The dashed lines represent a fit of the 75 and 25 percentile of the binned data. These curves will all tend towards zero at steeper slopes if extrapolated.

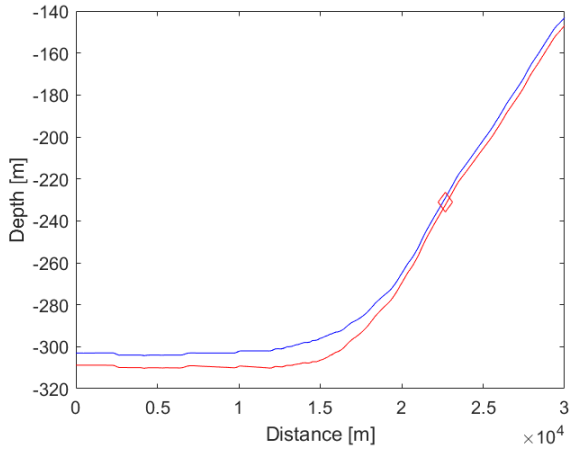


Fig.2: Depth profile in the North Sea (blue) along with a sediment thickness profile (red). The point with the thinnest sediment thickness is marked with a red diamond.

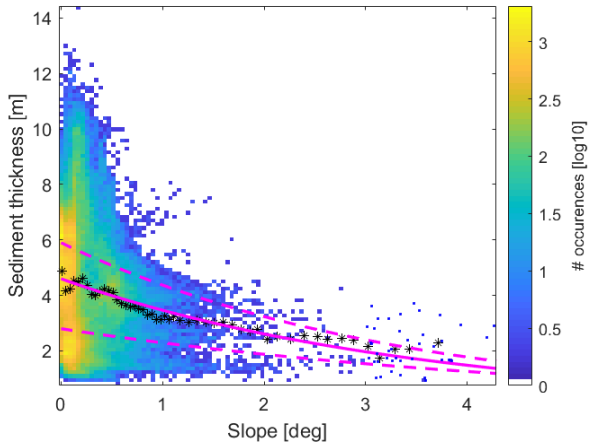


Fig.3: A density map of the relationship between bottom slope and sediment thickness. The average of different bins are shown as black stars, while the iterative exponential decay fit is shown as a purple solid line. The two dashed lines mark the exponential decay fit of the 75 and 25 percentiles of the bins.

Utilising the fitting parameters from Fig. 3, an acoustic propagation analysis based on the CEX02 data can be performed with an estimated sediment thickness for a given slope on the bottom profile. A comparison of measured and modelled background levels, for range independent and range dependent bottom loss models are shown in Fig. 4. The models compares well with the measurements the first 6km where the bottom profile is relatively flat. At greater ranges the models underestimates the background levels most likely due to increased backscattering not accounted for in the model. In Fig. 5 we see a statistical comparison of the CEX02 modelled and measured reverberation level analysis done with a range independent bottom loss model, as done in [10], and with a range dependent bottom loss model, in the left and right panel, respectively. The figures show a clear discrepancy between the two bottom loss models, with the range independent bottom loss model displaying a stronger correlation with measured reverberation level data compared to a range dependent bottom loss model, correlating the slope with sediment thickness. Surprisingly, the range dependent bottom loss model overestimates the reverberation levels for ranges greater than 10km, ranges at which our model predicts a thin to non-existing sediment layer, and show significantly greater spread in the error distribution at same ranges. The error is defined as

$$e_{RL} = BL - RNL, \tag{2}$$

where *BL* is the measured background level and *RNL* is the modelled reverberation and noise level.

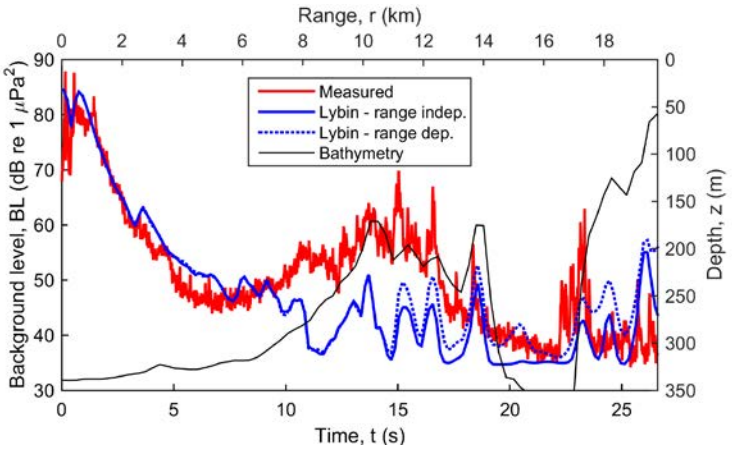


Fig. 4: Comparison of modelled and simulated background level in a beam directed towards the coast. The bottom profile is included as a visual guide.

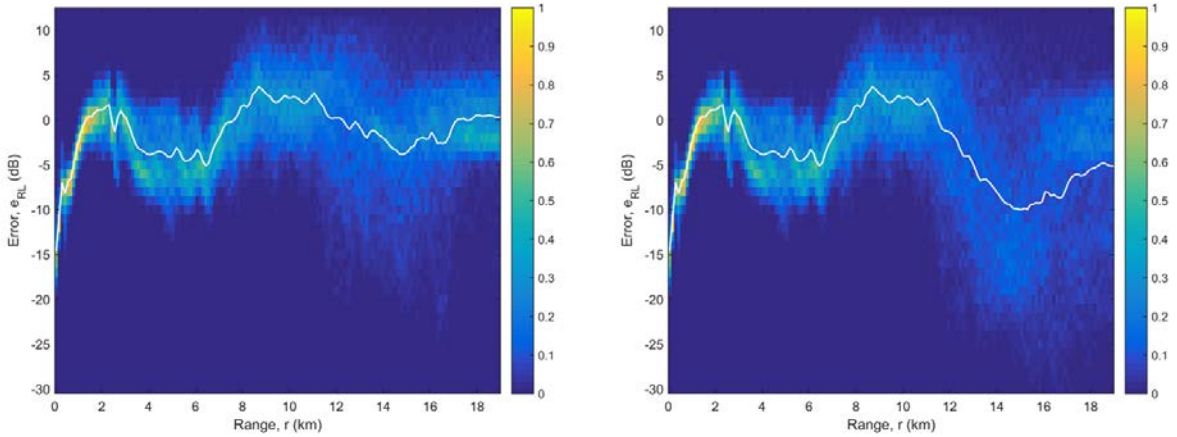


Fig.5: Normalised error distribution (in dB) for reverberation estimates with Lybin as a function of range. A range independent bottom loss model is utilised in the left panel, while a range dependent bottom loss model, correlating the slope with sediment thickness is utilised in the right panel. The white line represents the average error.

5. DISCUSSION

From the initial investigation based on the visual correlation from Fig. 2, it seems natural that for an increase in slope we see a decrease in the sediment thickness. However, the looks in Fig. 2 is extremely deceiving, with a variation in depth, y-axis, of 150 meters, while the variation in distance, x-axis, is 30 000 meters. This means that what seems like an extreme incline, actually is a slowly increasing slope over several thousand meters. This becomes apparent when finding that the maximum slope at any point of the bottom profile is approximately 0.7^{o}. This indicates that a larger statistical sample than a few bottom profiles is required in order to find a relationship, if any, between the slope of a surface and its sediment thickness.

In Fig. 3, the slope at every point of the bottom data has been calculated and interpolated onto the sediment thickness map. The resulting dataset contains approximately $1.9x10^5$ data points. Visually, Fig. 3 indicates a clear relationship between the slope of the surface and its sediment thickness. And the average values of the bins only amplify this impression. However, when attempting to fit a function to the dataset, the picture is not as simple. An exponential decay seems to provide the best fit to the dataset. But if the fitting is done on the average bin values, it becomes very flat, as the same weight is given to the later bins, with less than 100 data points, as the earliest bins, with tens of thousands data points in each bin. Another method is to fit the exponential decay to the entire dataset. This obviously gives a very good fit at very shallow slopes, as this part has a high density of data points. However, the function seems to overfit to the earlier data and end up decaying towards zero sediment thickness extremely fast. By recognising that the fit on the entire dataset does in fact fit almost perfectly for shallow slopes, we can use this value to fix one parameter, the starting point (A), before fitting the rest of Eq. 1 to the average values of the bins. This results in a good fit to both the oversampled shallow slope cases and the undersampled steep slopes. The resulting exponential decay fit indicates a relationship between the slope of a surface and its sediment thickness that will tend towards zero sediment thickness at slopes of more than 10^o.

Employing the exponential fit found from the data in Fig. 3, the sediment thickness in the area can be estimated based solely on the slope of the bottom surface. This is implemented as one of the input parameters to the acoustic propagation model Lybin, where the modelled background level is compared to the measured background level from CEX02, right panel in Fig. 5. Here we see that by including the estimated sediment thickness from our results, the modelled background level performs worse at long ranges than the use of highly tuned range independent sediments [10]. However, it should be noted that there are many sources of error in the modelling, and the experiment was conducted in an area with highly varying oceanographic conditions. Furthermore, Lambert's law was used as a scattering kernel, where Lambert's coefficient was set to be constant along the profiles.

Although the range dependent model has an overall worse performance than the range independent model, individual samples, Fig. 4, indicate a higher correlation at certain ranges with the range dependent model. From our results it looks as if the sediments seen by the sonar on the upslopes towards the coast are softer than the bedrock properties used here. Furthermore, the models do not have enough degrees of freedom to account for the variations in the geoacoustic properties of the bottom. A similar model should be used to include a range dependent backscattering model.

6. CONCLUSION

By comparing seismic data and depth profiles, we have been able to find a relationship between the slope of the ocean floor and the thickness of the sediment present. This was done in an area in the Norwegian Trench with a relatively uniform sediment population consisting of mainly silt, sand and clay. The resulting relationship was then exploited in an attempt to improve upon previous acoustic modelling of backscatter in the area. The use of estimated sediment thickness in the models did not improve the modelled background level compared to previous range independent models. Whether this is due to the properties of the sediments in the upslopes towards the coast or other oceanographic properties is unknown. Although this is presenting a much quicker way of doing relatively accurate modelling of acoustic propagation based on bottom parameters. The method has only been tested in a very limited area with a relatively uniform sediment type and a very flat bottom.

Future work would have to expand the work done here by attempting to find relationships between the bottom slope and sediment thickness in other areas with a variation of sediments.

It would also be interesting to see whether different sediments have different relationships between slope and thickness. In Fig. 3 it is possible to imagine three distinct peaks of different sediment thicknesses at shallow slopes, and also possible to follow these peaks in what looks like three separate exponential decays. We hope to be able to follow up on this dataset and examine whether there is a link between these apparent peaks and their decays and certain positions in the map with particular bottom and/or sediment properties. Finally, we want to examine more closely the fact that soft range independent sediments provide a more accurate model of the background level towards the coast and upslopes than a range dependent model changing between the soft sediment type and bedrock.

REFERENCES

[1] **Eidem, E. J. & Landmark, K.**, Acoustic seabed classification using QTC IMPACT on single-beam echo sounder data from the Norwegian Channel, northern North Sea, *Continental Shelf Research*, 68, pp. 1-14, 2013.

[2] **Kara, E. M., Meghachou, M., & Aboubekr, N.**, Contribution of particles size ranges to sand friction, *Engineering, Technology & Applied Science Research*, 3, pp. 497-501, 2013.

[3] **Arvanitidis, C., Steiakakis, E., & Agioutantis, Z.**, Peak Friction Angle of Soils as a Function of Grain Size, *Geotechnical and Geological Engineering*, 37, pp. 1155-1167, 2019.

[4] **Jensen, F. B., Kuperman, W. A., Porter, M. B., & Schmidt, H.,** *Computational Ocean Acoustics*, Springer Science & Business Media, 2000.

[5] **Beerens, S. & Boek, W.**, A robust algorithm for LFAS target classification, *Undersea Defence Technology-UDT Europe*, 2007.

[6] **Schmidt, H.**, SAFARI: Seismo-Acoustic Fast Field Algorithm for Range-Independent Environments. User's Guide, 1988.

[7] **Schmidt, H.**, OASES Version 3.1. User Guide and Reference Manual. Department of Ocean Engineering Massachusetts Institute of Technology. February 20, 2004.

[8] **Kinsler, L. E., Frey, A. R., Coppens, A. B., & Sanders, J. V.**, *Fundamentals of Acoustics*, John Wiley \& Sons, Inc, pp. 560, 1999.

[9] **Ainslie, M. A.**, *Principles of sonar performance modelling*, Springer, pp. 800, 2010.

[10] **Søvik, A. A. & Hjelmervik, K. T.**, Comparison of measured and modelled reverberation and echo level in littoral waters, In *OCEANS 2017 - Aberdeen*, pp. 1-6, 2017.

[11] **Dombestein, E. & Wegger, K. E.**, Predicting sonar false alarm rate inflation using acoustic modeling and a high-resolution terrain model, FFI, 2014.

MODEL BENCHMARKING RESULTS FOR SHIP NOISE IN SHALLOW WATER

Bas Binnerts[a], Christ de Jong[a], Ilkka Karasalo[b], Martin Östberg[b], Thomas Folegot[c], Dominique Clorennec[c], Michael A. Ainslie[d1], Graham Warner[d2], Lian Wang[e]

[a] TNO – P.O. Box 96864, NL-2509 JG The Hague
[b] FOI – Gullfossgatan 6, SE-16490 Stockholm
[c] Quiet-Oceans – 525 av Alexis de Rochon, Plouzane, France
[d1] JASCO Applied Sciences – Mergenthaler Allee 15-21, 65760 Eschborn, Germany
[d2] JASCO Applied Sciences – 2305-4464 Markham St, Victoria BC, V8Z 7X8, Canada
[e] NPL – Hampton Road, Teddington, TW11 0LW, UK

Bas Binnerts, TNO - P.O. Box 96864, NL-2509 JG The Hague, bas.binnerts@tno.nl

Abstract: *To support North Sea countries to comply with EU legislation, a framework for a fully operational joint monitoring programme for ambient noise in the North Sea is developed in the Interreg Joint Monitoring Programme for Ambient Noise North Sea (JOMOPANS). A key task in the project is to develop and demonstrate verified and validated modelling methods applicable for generating maps of ambient noise in the North Sea, with a focus on ships and wind as the dominant sources of sound.*

Within the project a wide range of acoustic propagation model implementations from the JOMOPANS project partners are verified by means of a comparison of the output for two well-defined benchmark scenarios based on the modelling scenarios developed for the Weston Memorial Workshop. The model types considered are based on energy-flux integration, analytical and numerical mode solvers, parabolic equation range step integration, ray tracking and wavenumber integration. Recommendations on the use of these models are given and limitations are discussed. The acoustic metric considered is the depth-averaged sound pressure level in one-third octave (base 10) bands from 10 Hz to 20 kHz.

The results show that the majority of the tested models are in agreement for a range-independent shallow water environment, providing a reliable benchmark solution for the future verification of other propagation models. The observed agreement gives confidence that these models are correctly configured and able to provide numerically correct solutions. For a range-dependent environment however, a significant uncertainty remains. The solutions provided in this paper can be used as a reference to select the optimal compromise between reducing the computational complexity and increasing the model precision for the propagation of sound in shallow water.

Keywords: *Underwater acoustics, Propagation modelling, benchmarking scenarios, model verification, Ambient noise, JOMOPANS project*

1. INTRODUCTION

To support North Sea countries to comply with EU legislation, a framework for a fully operational joint monitoring programme for ambient noise in the North Sea is developed in the Interreg Joint Monitoring Programme for Ambient Noise North Sea (JOMOPANS). A key task in the project is to select verified and validated modelling methods applicable for generating maps of ambient noise in the North Sea, with a focus on ships and wind as the dominant sources of sound. Accurate modelling of underwater ambient noise and being able to quantify the uncertainty in the model predictions are both relevant for the assessment of good environmental status as well as for sonar performance modelling.

In JOMOPANS the uncertainty in the complete ship noise modelling chain (from AIS data to noise maps) will be assessed against long term acoustic measurements at various measurement locations. This uncertainty results from limitations in the quality of available input data from ships and environment as well as in the applicability of the selected source and propagation models. Requirements for the model accuracy should be balanced against the uncertainties related with the input data, and will be set later in the project. The applicability of different underwater sound propagation models is verified by comparing their output against trusted reference solutions for two synthetic test cases. The two considered test cases are derived from previous benchmarking studies [1][2][3]. These were based on test cases defined in the Weston Memorial workshop [4]. The test cases were modified to be more representative for shallow water ship noise predictions in the full frequency range of interest for JOMOPANS (one-third octave (base 10) bands from 10 Hz to 20 kHz). A selection of the models was also compared against results published in [1][2], which showed good agreement and gives trust in the correct implementation and configuration of the models.

In section 2, the two test cases are detailed. Next, the propagation models that are compared are described in section 3. In section 4, the modelling results are compared to quantify the uncertainty of the model predictions. Finally, the results are discussed and conclusions on the applicability of the models for propagation modelling in shallow water are drawn in section 5.

2. TEST CASE DESCRIPTION

Two synthetic test cases were selected: one range-independent and one range-dependent. Comparing the model output for these two cases serves two objectives:

- to obtain a trusted solution with an associated uncertainty for the depth-averaged sound pressure level (SPL), for all one-third octave (base 10) bands from 10 Hz to 20 kHz
- to use this trusted solution to quantify the error of the propagation models for the two considered test cases.

The geometry and source depth are altered from the Weston Memorial workshop [4] case 1 and 4, to be more representative for ship modelling (5 m source depth) and for the North Sea (shallow water). Figure 1 shows the geometry for the two cases. The output metric is the broadband and one-third octave (base 10) band (‘OTO’) SPL, depth averaged over the water column (average of squared sound pressure). All one-third octave bands from 10 Hz to

20 kHz are considered. To make the results representative for ship noise modelling, the Wales and Heitmeyer source spectrum [3] for merchant shipping is used:

$$L_{s,f}(f) = 230\ \text{dB} - 10\log_{10}\left(\left(\frac{f}{1\ \text{Hz}}\right)^{3.594}\right)\text{dB} + 10\log_{10}\left(\left(1+\left(\frac{f}{340\ \text{Hz}}\right)^{2}\right)^{0.917}\right)\text{dB}$$

At frequencies below 30 Hz a constant value $L_{S,f}$ (f=30 Hz) is used and the equation is used outside its validity range (1.2 kHz) up to 20 kHz. The OTO band monopole source level $L_{S,\text{OTO}}$ is defined by integration of the spectral density over the bandwidth.

Furthermore, a single frequency (band centre frequency) was used for calculating the results in each band to reduce the computational complexity of the benchmarking effort. The water was modelled as iso-velocity (c_w=1500 m/s) and iso-density (ρ_w=1000 kg/m^3). The absorption of the seawater is specified according to the Ainslie-McColm model [3]. The seabed is a homogenous sandy infinite fluid half space (c_s=1700m/s, ρ_s=2000 kg/m^3, α_s=0.5 dB/λ). The water surface was smooth (perfectly reflecting).

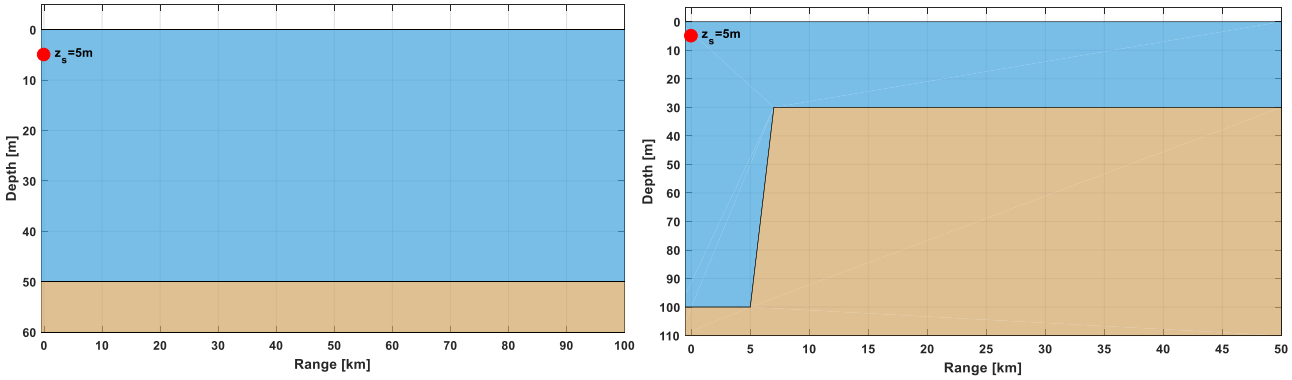


Figure 1. Schematic representation of the test case 1 (left) and test case 2 (right) environment. The red dot indicates the source position at 5 m depth. The upslope bathymetry (100 m to 30 m) starts at 5 km and ends at 7 km, corresponding to a 2 degrees slope.

3. DESCRIPTION OF MODELS

In this section the models tested in this work are introduced. An overview of the models is presented in Table 1, indicating the model type and the frequency range for which modelling results are included in this paper. A more detailed description of the models is described hereafter. For all models, the results where provided at a 100 m range resolution, starting at 100 m.

TNO-Aquarius 3 (Aq3): is based on the hybrid propagation model 'Soprano' for range-dependent shallow waveguides [2]. It combines the accuracy of an analytical incoherent adiabatic range-dependent normal mode model for the first five modes with the speed of Weston's flux integral approach for higher modes. A 0.5 m depth resolution was used to calculate the depth-averaged propagation loss.

TNO-Aquarius 4 (Aq4): The Aquarius 4 model is an adiabatic normal mode propagation model based on KrakenC model [5]. The KrakenC rootfinder is used to compute a mode lookup-table with a 1 m bathymetric resolution. Aquarius 4 matches the modes given the local water depth along the range trajectory. Leaky modes are not taken into account. A 0.5 m depth resolution was used to calculate the depth-averaged propagation loss.

QO-QUONOPS: The QUONOPS range dependent propagation model uses the parabolic equation (PE) solution (RAMsurf model) [6] at low frequencies and the BELLHOP ray tracing program [5] at frequencies of 2 kHz and higher. A 0.5 m depth resolution was used to

model the depth averaged propagation loss. The RAMSurf model used a frequency-dependent discretisation and 8 Padé terms. Bellhop was run using 300k gaussian beams and a 89 degrees opening angle.

FOI-JEPE: JEPE (Jeltsch energy-conserving PE) is a wide-angle parabolic equation code [7] for computing the acoustic field in a range dependent environment composed of fluid media. It uses a transparent boundary condition at the deep boundary to avoid unnecessary computational cost associated with the use of artificial damping layers. The discretisation depends on frequency.

FOI-REV3D: REV3D [8] is a ray-based program for computation of transmission loss in 3D environments. The bottom is discretised by a rectangular grid using bilinear interpolation of the depth between grid points.

FOI-XFEM: XFEM is a hybrid method for range-independent media composed of multiple fluid and solid layers [9]. It is based on discretization of the depth-dependent wave equation with exact finite elements and computation of the wavenumber integral within a user-specified accuracy by adaptive variable-order quadrature with error control [10]. The solution can alternatively be obtained as a sum of normal modes and branch cut integrals, using adaptive winding number integration for searching modes in the complex plane [11]. In test case 1 the bound for the relative error in the transform and branch-cut integrals was set to 1.E-7. The solution was computed by wavenumber integration for the 7 lowest frequencies, and by modes and branch-cut integrals for higher frequencies.

FOI-RPRESS: RPRESS is a hybrid method for range-independent multi-layered fluid-solid media. It handles the depth-dependent wave equation with a compound matrix technique [12], using the same methods as XFEM for transform integration and mode search.

JASCO-MONM: MONM is a wide-angle split step Padé PE solution to the acoustic wave equation [6] based on a version of the U.S. Naval Research Laboratory's Range-dependent Acoustic Model (RAM), which has been modified to account for a solid seabed [13]. The PE computation range and depth spacing was frequency dependent. A 2 m depth resolution was used to calculate the depth-averaged propagation loss.

NPL-OASES: OASES applies wavenumber integration techniques to calculate propagation loss in horizontally stratified fluid and elastic media [5]. It can also deal with range-dependent propagation problems [14]. For the range-dependent test case 2, results above 1 kHz were omitted as the modelled propagation loss started to show unexplained unstable behaviour.

	Model name	**Model type**	**Frequency range**
TNO	Aquarius 3 (Aq3)	Range dependent hybrid analytical mode sum + flux integral model	32 Hz ≤ f ≤ 20 kHz
	Aquarius 4 (Aq4)	Range dependent numerical mode model using mode lookup table	10 Hz ≤ f ≤ 20 kHz
QO	QUONOPS	Range dependent split step Padé PE	10 Hz ≤ f < 2 kHz
		Range dependent coherent Gaussian rays	2 kHz ≤ f < 20 kHz
FOI	JEPE	Range dependent Jeltsch energy-conserving PE	10 Hz ≤ f ≤ 10 kHz
	REV3D	Range dependent coherent 3D rays	200 Hz ≤ f ≤ 20 kHz
	XFEM	Range independent wavenumber integration at 7 lowest bands, normal modes + branch-cut integration at higher bands.	10 Hz – 20 kHz
	RPRESS	Range independent wavenumber integration	10 Hz – 10 kHz
NPL	OASES	Range dependent wavenumber integration.	10 Hz ≤ f ≤ 20 kHz
JASCO	MONM	Range dependent split step Padé PE	10 Hz ≤ f ≤ 20 kHz

Table 1: overview of models that have been compared for test cases 1 and 2.

4. RESULTS

In this section the model predictions for the two test cases (section 2) are compared. Figure 2 illustrates the depth averaged SPL for the TNO-Aq3, QO-QUONOPS and FOI-XFEM models test case 1. From this type of representation it can be observed that model results are similar, but quantitative assessment of differences is difficult due to the large dynamic range.

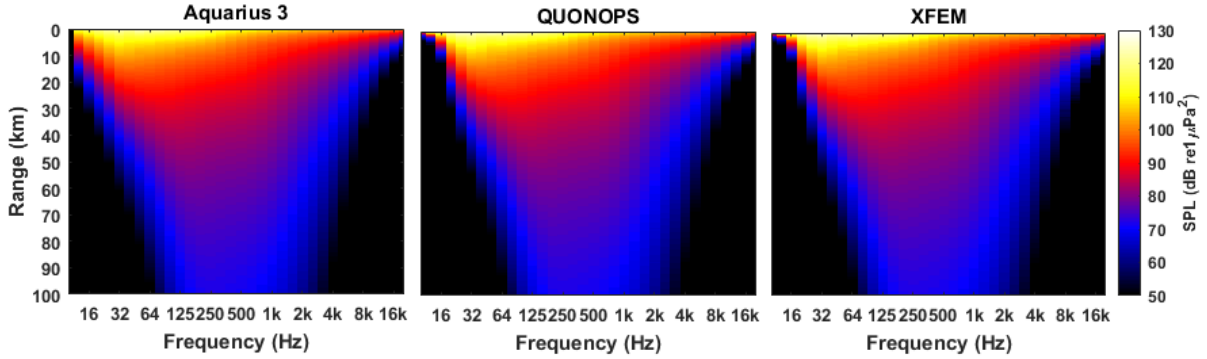


Figure 2: Depth-averaged SPL versus range and OTO band for 3 of the tested models.

In order to make a quantitative assessment of the model agreements for ship noise, figure 3 (top 2 plots) shows the modelled broadband depth-averaged SPL. The normalised representation (ΔSPL) below these makes it possible to observe differences smaller than a few dB. Note that the choice for the reference model (in this case Aquarius 3) is arbitrary, and does not say anything about the accuracy of the reference model itself. The bottom 4 plots show OTO spectra of the depth-averaged SPL at 10 and 40 km range.

For the range-independent case, it is observed that at distances larger than 500 m, all models except REV3D & Aquarius 3 are in agreement, with broadband differences smaller than 0.5 dB and OTO level differences in the bands from 20 Hz to 10 kHz smaller than 1 dB. The ray approximation in REV3D is not valid at low frequencies and observed to deviate from the other models at frequencies below about 300 Hz for the two test cases. The analytical approximation to the mode shapes in Aq3 leads to deviating results at frequencies below 50 Hz. At ranges shorter than 500 m, the Aq4 and JEPE results deviate from the other PE and wavenumber integration models. The ensemble of model predictions from the QUONOPS, MONM, OASES, XFEM and RPRESS is considered to be the correct solution (with a 0.2 dB associated uncertainty) for test case 1.

For the range-dependent case, it is observed that at distances up to 5 km (where the upslope bathymetry starts) the QUONOPS, MONM, OASES and Aquarius model predictions show a larger spread than for test case 1, in which the water depth was half that of test case 2. In this case the QUONOPS and MONM results overlap. The OASES results are 1 dB higher. At ranges between 1 km and 5 km, the maximum observed difference with the JEPE and Aq4 models is 1 dB. The difference between the model predictions increases towards shorter ranges. Beyond 5 km (where the range-dependence starts) the difference between the PE models is less than 0.5 dB. An explanation for the difference observed between the PE and Aquarius model predictions beyond 5 km is the adiabatic approximation used by the Aquarius models. Because only the PE models are in agreement, assessment of their absolute accuracy is uncertain. It is expected that the PE models are correctly configured given their close agreement.

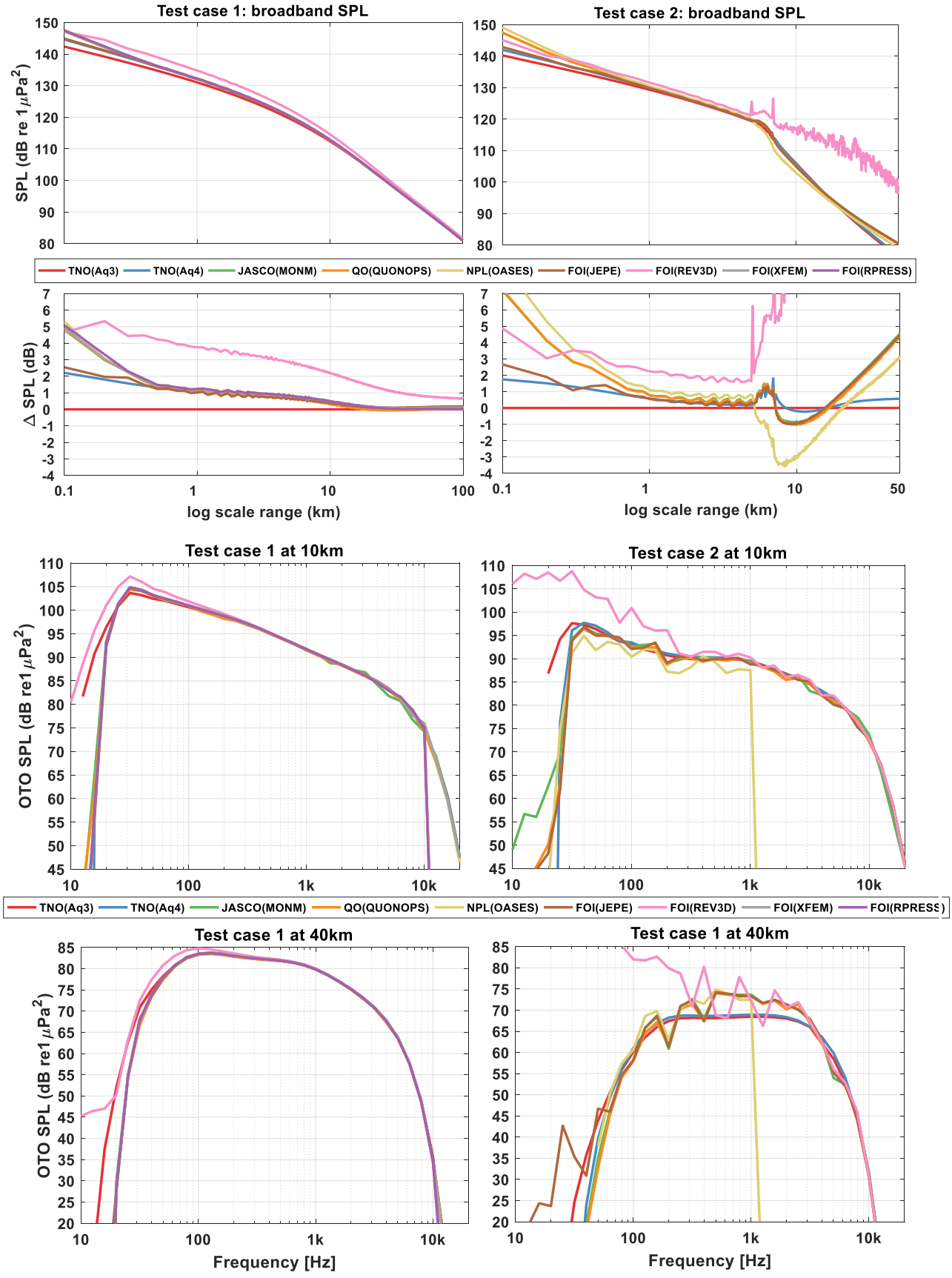


Figure 3: broadband (top 4) and spectral (bottom 4) modelling results for the two test cases

In order to gain further confidence in the correctness of the PE results, a comparison against other model types (e.g. finite element (FE) or coupled mode models) is desirable, but was outside of the scope of this paper. With regard to the range dependent OASES results it should be noted that contributions from bands above 1 kHz were omitted due to observed unstable model behaviour at the start of the slope, which provides a possible explanation for the underestimation of the broadband results observed after 5 km with respect to the PE predictions.

For the range-dependent case, it is observed that the QUONOPS, JEPE and MONM model predictions are similar (with differences smaller than 3 dB above 80 Hz). The Aq3 and Aq4 results are similar to the PE models at 10 km, but the predicted SPL at 40 km at frequencies between 500 Hz and 3 kHz is lower by ~5 dB. This observed bias may be caused by the adiabatic mode assumption used by these models. A comparison of a coupled mode or a FE simulation would strengthen this hypothesis. Below 1 kHz the range-dependent OASES model deviates from the PE models by about 5 dB. At 2 kHz and above, the QUONOPS model uses a ray approach, which lead to the same results as the JEPE and MONM PE models.

5. DISCUSSION AND CONCLUSIONS

For the range-independent test case 1 a reference solution was obtained with an associated uncertainty of 0.2 dB for all tested frequencies. For test range-dependent case 2, the predictions of PE and adiabatic mode/hybrid mode flux models differ up to ~5 dB at 40 km. Further comparison against other model types such as FE and coupled modes and comparison with existing benchmarks such as [2] are recommended to reduce the uncertainty of this reference solution. Furthermore, the strong variability observed for the range dependent case is expected to reduce when an average value for the OTO bands is calculated using more frequencies which is expected to reduce the difference with incoherent models such as the Aquarius 3 and 4 models.

While the model benchmarking described in this paper helped to better understand the accuracy and limitations of the tested models, a good agreement for the selected test cases does not by default guarantee a good performance for other scenarios. The results published in this paper were configured with great care to provide optimal results for the selected test cases. Given the (numerical) complexity of the tested models, the optimal configuration depends on the environment. In particular at low frequencies and in shallow water (near and below the cut-off frequency) and in range-dependent environments, great care should be taken to check the stability, convergence and applicability of propagation models.

Regarding the applicability of the tested models for modelling underwater noise, the required model accuracy should be balanced against the uncertainties related to the input data from environment as well as sources. Generally speaking, using a more accurate model (configuration) will require more computational resources. For large scale noise mapping, this will affect other model parameters such as the temporal and spatial resolution of the modelling. During the remainder of the JOMOPANS project, the uncertainty associated with other modelling parameters relevant for large scale noise modelling will be investigated. These insights will be used to assess the applicability of the various model types tested in this study.

REFERENCES

[1] **E.T. Küsel, M. Siderius**, *Comparison of Propagation Models for the Characterization of Sound Pressure Fields*, IEEE Journal of oceanic engineering, 2019

[2] **H.Ö. Sertlek,** *"ARIA OF THE DUTCH NORTH SEA: Propagation, source and sound mapping simulations for the Dutch North Sea",* Leiden: PhD Thesis, 2016

[3] **M.E.G.D. Colin, M.A. Ainslie, B. Binnerts, C.A.F. de Jong, I. Karasalo, M. Östberg, H.Ö. Sertlek, T. Folegot, D. Clorennec**, *Definition and results of test cases for shipping sound maps,* IEEE, 2015

[4] **M.A. Ainslie**, *Editorial: Validation of Sonar Performance Assessment Tools*, in Validation of Sonar Performance Assessment Tools: In Memory of David E Weston, M. A. Ainslie, Ed. Clare College, Cambridge, UK. 7–9 Apr 2010, pp. 2-6, 2010

[5] **F.B. Jensen, W.A. Kuperman, M. B. Porter. H. Schmidt,** *Computational Ocean Acoustics*, Springer, 2011

[6] **M.D. Collins**, *A split-step Padé solution for the parabolic equation method,* Journal of the Acoustical Society of America 93(4): 1736-1742, 2010

[7] **E. Larsson, L. Abrahamsson.** Helmholtz and parabolic equation solutions to a benchmark problem in ocean acoustic. The Journal of the Acoustical Society of America **113**, 2446 (2003) pp 2446-2454

[8] **S.M. Ivansson**, *Stochastic ray-trace computations of transmission loss and reverberation in 3-D range-dependent environments,* In Proc. 8th European Conference on Underwater Acoustics, Faro, Portugal, S.M. Jesus and O.C. Rodriguez (eds.), pp. 131-136, 2006.

[9] **I. Karasalo,** *Exact finite elements for wave propagation in range-independent fluid-solid media*, Journal of Sound and Vibration 172(5), pp. 671-688, 1994

[10] **S. Ivansson, I. Karasalo**, *A high-order adaptive integration method for wave propagation in range-independent fluid-solid media*, JASA 92(3), pp 1569-1577, 1992

[11] **S. Ivansson, I. Karasalo**, *Computation of modal wavenumbers using an adaptive winding-number integral method with error control*, Journal of Sound and Vibration, 161(1), pp. 173-180, 1993

[12] **S. Ivansson**, *Seismo-acoustic wave-fields: Compound-matrix methods for range-independent fluid-solid media*, Dr Techn. thesis, Royal Institute Of Technology, S-100 44 Stockholm 70, Sweden, 1994.

[13] **Z.Y. Zhang, C.T. Tindle**, *Improved equivalent fluid approximations for a low shear speed ocean bottom*, Journal of the Acoustical Society of America 98(6): 3391-3396, 1995

[14] **J.T. Goh, H. Schmidt**, *A hybrid coupled wavenumber integration approach to range-dependent seismo-acoustic propagation code*, Journal of the Acoustical Society of America Vol. 100, 1409-1420, 1996

MODELLING NOISE FROM WIND, RAIN AND DISTANT SHIPPING IN SCENARIOS OF VARYING COMPLEXITY.

Mark K. Prior [a], Mathieu E.G.D. Colin [a] and Martijn W.G. van Riet [a]

[a] Acoustics and Sonar Department, TNO, Oude Waalsdorperweg 63, 2597 AK Den Haag

Contact Author: M. Prior, Acoustics and Sonar Department, TNO, Oude Waalsdorperweg 63, 2597 AK Den Haag. Email: mark.prior@tno.nl

Abstract: *Passive sonars attempt to detect sound radiated by vessels of interest. This detection takes place against a background of noise, with important sources of noise including distant shipping, rain falling on the sea surface and breaking waves and bursting bubbles associated with sea-surface waves. The estimation of these noises is therefore an important part of the prediction of the likely performance of passive sonars. Mathematical models are available for the prediction of noise and these represent a combination of descriptions of the level and directionality of radiated noise, the propagation of sound between source and receiver and the convolution of receiver beam patterns and the directivity of the noise field at the receiver. These processes vary with acoustic frequency and environmental properties such as water depth, seabed type, sea-water sound-speed profile, precipitation rate and wind speed. The important physical processes are not straightforward to model and all prediction tools are, to some extent, approximations. When assessing model legitimacy, reference solutions are necessary to demonstrate model accuracy. Predictions of rain, wind and distant-shipping noise are presented in a simple environment previously developed for the purposes of verifying sonar-performance models. An existing reference solution for rain noise is used, along with a novel expression for the noise from distant shipping. Calculations are extended to more complicated scenarios including non-uniform shipping distributions and beam-patterns for generic arrays.*

Keywords: *Ambient Noise, Rain Noise, Surface Noise, Shipping Noise*

1. INTRODUCTION

The calculation of underwater acoustic ambient noise is challenging and requires good models for acoustic propagation, accurate descriptions of noise sources and detailed knowledge of the properties of the acoustic receiver. The dominant sources of noise are known to vary with frequency and environmental conditions [1] and it is common to think of distant shipping as the dominant source of low-frequency noise while rain and wind become more important at higher frequencies. The specific frequency at which this change in dominant source occurs depends on many factors, including the beam pattern of the receiving sonar.

In this paper, an approach is described by which expressions for the absolute level and directivity of noise sources are taken from the literature and combined with a propagation model to predict the directivity of noise incident on a receiver. This field is then convolved with receiver beam-patterns to provide in-beam noise levels for single-hydrophone and line-array receivers.

The following section sets out definitions and standards used in the calculation of ambient noise and describes the formulae taken from the literature for sources of shipping and sea-surface noise. It then describes the method by which these source formulae are combined with a propagation model and descriptions of receiver beam-patterns. Section 3 describes a reference solution for rain noise, also taken from the literature, that is used as a test-case for the modelling method. It then describes the derivation of a novel reference solution for shipping noise in similar environments. Predictions made by the ambient-noise modelling approach are compared with the reference solutions in Section 4 and conclusions drawn. Example results for more complicated scenarios – for which no reference solution currently exists – are also described to illustrate the flexibility of the numerical approach.

2. TERMINOLOGY AND ALGORITHMS

Standard terminology was followed in that ambient noise was defined as “sound except acoustic self-noise and except sound associated with a specified signal” [2]. This ties the definition of noise to the concept of a signal whose detection is sought.

In the case of rain and wind noise, the terminology is unambiguous but further clarification is required for shipping noise. Passive sonars attempt to detect vessels’ radiated noise and the signal is therefore of the same nature as the noise which might obscure its detection. If a ship can be detected by a passive sonar it consequently ceases to be a source of ambient noise. Its sound may remain an undesired part of the acoustic field because it is not from the vessel being sought but as such it becomes a ‘false target’ rather than a source of noise. Consequently, the term ‘*distant* shipping noise’ is used here to make clear that the noise under consideration is only that from ships that are far enough away that the sonar is unable to detect them as discrete sources of sound. The distance at which this transition occurs is determined by the properties of the sonar under study.

The formulation followed here for the prediction of sea-surface noise follows those of Chapman [3] and Harrison [4]. The sea surface is considered to be a sheet of dipole sources that extends infinitely and uniformly in all directions. As such, the sea-surface noise field is isotropic in horizontal angle but varies with vertical angle because of source directivity and angular dependence in acoustic propagation. This propagation is modelled by a ray-theoretic approach in which the sound arriving within a given angular increment is an infinite summation over the contribution of patches of sea-surface whose distances from the receiving array are integer multiples of the ray-cycle distance at the angle of interest. Formulae for the source strength per

unit area of sea surface are taken from formulae developed by APL [5] and discussed in Ainslie [6]. An example result is shown in Fig. 1.

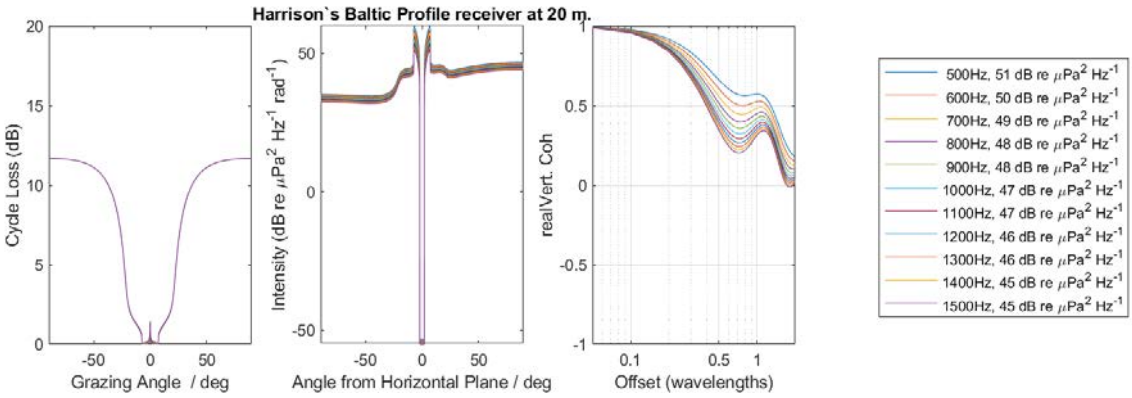


Fig.1: Vertical distribution of sound from sea-surface noise sources incident on a receiver

The left panel shows the loss per cycle range as a function of vertical angle. This is symmetric about the horizontal and rises for larger (absolute) angles because of increased reflection loss at the seabed. The spike in loss around the horizontal is a consequence of absorption in the very long cycle ranges associated with near-horizontal paths. The middle panel shows the distribution of noise with vertical angle. This is asymmetric about the horizontal because upward rays have undergone one more bottom reflection than downward rays at the same angle. The peaks in noise close to zero angle are a consequence of the Baltic-Sea sound-speed profile that was used in the calculations of Harrison, [4] and which was also used in the calculation whose results are shown here. The angles closest to the horizontal have no noise associated with them because there is no path from surface to receiver at these angles due to in-water refraction. The right panel shows the real part of the vertical coherence of the acoustic field [3]. This parameter is important in the design of arrays with vertical aperture and its calculation was the motivation for the development of Harrison and Chapman's methods.

Shipping noise requires a separate formulation. It is more important at lower frequencies and the low associated absorption loss means that distant ships may make significant contributions to the total noise field. Source strengths were calculated using the formula of Wales and Heitmeyer [7] and with a dipole directivity pattern assumed. The sea-surface area surrounding the receiver was split into an irregular pattern of facets whose area was used in combination with a density of ships to produce a source strength for each facet. Source density was set to zero below a critical range within which ships would act as false targets, rather than sources of noise. Sound was propagated from each facet to the receiver using a formula based on the concept of acoustic flux [8], [9], [10]. This formula yields a distribution of sound with vertical angle at the receiver that can be convolved with the receiver beam pattern. The method of facets allows for the straightforward incorporation of inhomogeneous distributions of shipping such as fishing grounds and shipping lanes.

3. REFERENCE SOLUTIONS

The process of developing a numerical model for ambient noise requires successful incorporation of source, propagation and receiver descriptions. The first and second of these factors depend on environmental properties such as water-depth, wind-speed and seabed type. Correct implementation of source and receiver descriptions requires detailed treatments of all normalisation and calibration parameters to ensure that the final in-beam noise is expressed in absolute terms rather than relative decibels. This process is challenging and has scope for errors of implementation and interpretation. As such it is important that the predictions of numerical

models should be verified (shown to correctly implement their baseline algorithms) and validated (shown to produce accurate absolute levels).

An important step in the verification/validation process is comparison with reference solutions. These may take the form of highly accurate numerical solutions or closed-form mathematical expressions which, in well-defined circumstances, represent accurate solutions to the problem under study. Two closed-form reference solutions were considered here: one for rain noise, taken from the literature, and one for distant-shipping noise that was developed especially for this purpose.

The reference solution for rain-noise was taken from [11]. It was developed in one of a series of standard environments that were produced for use in model verification and validation [12]. The particular environment, 'Weston I' considered here represents a horizontally invariant environment in which 100 m of isovelocity water overlies a sand halfspace. The wind-speed is set to be zero and the only source of noise is rain which falls at a rate of 1 mm/Hr. The reference solution for shipping noise was developed for this study and is now described.

Considerations of acoustic flux allow the depth-averaged acoustic intensity, I, measured by an omnidirectional hydrophone, due to a dipole source at the surface and at range r to be expressed as an integral over vertical angle θ [10].

$$I = \frac{4}{Hr} e^{-\beta r} \int_0^{\frac{\pi}{2}} \frac{S_a \sin^2\theta}{D(\theta) sin\theta} e^{\frac{2r}{D(\theta)} \ln[|V(\theta)|]} cos\theta d\theta \tag{1}$$

Where H is the water depth, S_a is the source strength, $D(\theta)$ is the cycle range of a ray, β is the volume-absorption coefficient and $V(\theta)$ is the seabed reflection coefficient. This can be simplified to a standard form under approximations of small angles [10] and restriction of the upper limit of the angular integral to the seabed critical angle θ_c . This yields

$$I = \frac{S_a}{2Hra} e^{-\beta r} \left(\sqrt{\frac{\pi}{a}} \mathrm{erf}\left(\sqrt{a\theta_c}\right) - 2\theta_c e^{-a\theta_c^2} \right); a = \frac{rs}{H} \tag{2}$$

Where s is the gradient of reflection coefficient at grazing incidence, expressed in Nepers per radian. The noise intensity from distant shipping over all ranges is

$$N_{Sh} = \int_{r_c}^{\infty} I(r) n \, 2\pi r \, dr \tag{3}$$

Where n is the (spatially invariant) density of ships and r_c is shortest range at which ships will not be discriminated as discrete sources and their noise will form part of the background noise field. This can be reduced to a closed-form expression on the assumption that r_c is O(10^4m)

$$N_{Sh} = \sqrt{\frac{\pi^3 H\beta}{s^3}} n S_a \left(\sqrt{\pi}(\mathrm{erf}(a_c) - 1) + \frac{e^{-a_c^2}}{a_c} \right); a_c = \sqrt{\beta r_c} \tag{3}$$

This represents a reference against which numerical-model predictions can be compared for the special case of a uniform shipping density in the Weston-I environment. Examples of this comparison are given in the following section.

4. EXAMPLE RESULTS

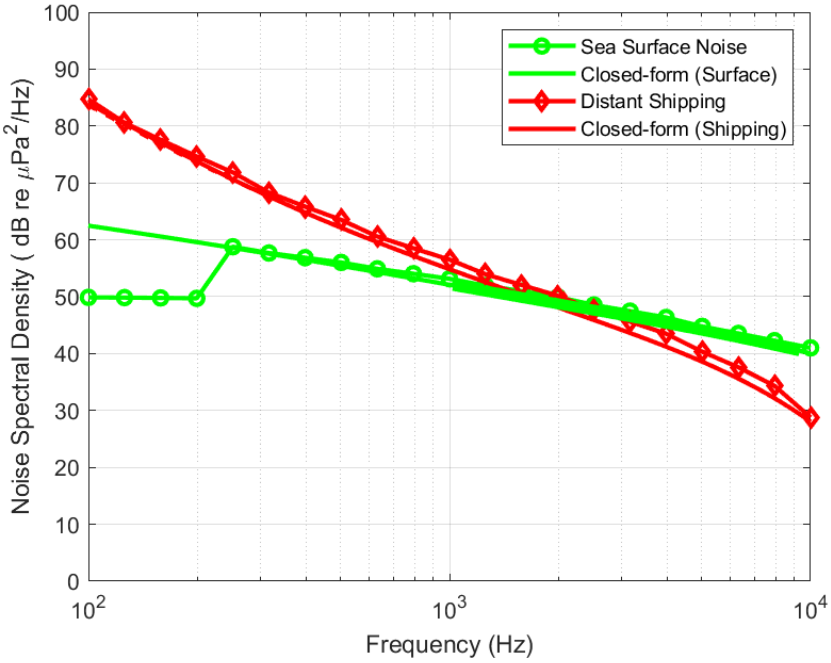


Fig.2: Comparison of numerical model predictions with closed-form reference solutions

Fig. 2 shows the ambient noise predicted for an omnidirectional hydrophone in the Weston-I environment. The green line is the noise from the reference solution for rain noise [11] and the thicker portion of the line shows the frequency regime for which it is quoted as being valid. The green line with circle markers is the numerical model's prediction of the same noise, calculated by integrating the noise distribution over vertical angle. The two lines are shown to agree well in the region of validity for the reference solution. The two diverge at low frequencies because the formula for the source strength of rain noise does not extend below 200 Hz [6] and the noise predicted by the numerical model defaults to a 'low sea-state' value associated with the wind noise formula. The red line shows the reference solution for shipping noise developed in the previous section. This is shown to be higher at lower frequencies, following the Wales-Heitmeyer spectrum. The red line with diamond markers shows the predictions made by the numerical model for the Weston-I environment. Good agreement is shown and the small discrepancy (<2dB) is a consequence of the full integration over angle performed by the numerical propagation model, compared to the small-angle approximation implicit in the reference solution. The agreement between the numerical model and the reference solutions is taken to be supportive of the hypothesis of model validity.

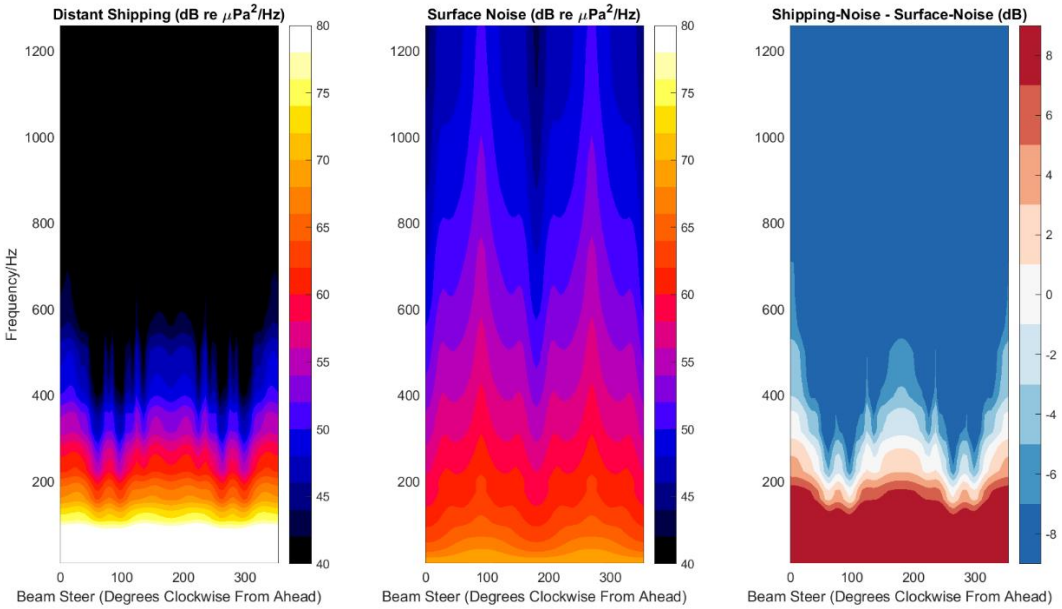


Fig.3: Numerical model predictions for a line-array receiver in the Weston-I environment.

Fig. 3 shows numerical model predictions of noise received on a line array in the Weston-I environment with a wind-speed of 8 ms^{-1} and a rain rate of 0.1 mm/Hr. No reference solution exists for these conditions but the model's agreement for the reference case with the single receiver means that, as a working hypothesis, it may be assumed to be valid. The left panel shows shaded colours of noise as a function of beam-steer-angle on the x-axis and frequency on the y-axis. The noise is higher at low frequencies and rises for the beams steered at forward (0^o) and rear (180^o) directions. The line array is 'ambiguous' in the sense that arrivals from port and starboard are indistinguishable and this causes the symmetry observed about 180^o. The middle panel shows sea-surface noise across beams and frequency. Although the noise does not vary with horizontal angle, in-beam noise is shown to vary with beam steer and broadside beams (90^o and 270^o) are shown to have highest noise. This is a consequence of the three-dimensional nature of beams formed by line arrays. A beam steered at 30^o from forward actually forms a cone that is as responsive to horizontal sound arriving at a bearing of 30^o as it is to sound travelling at a vertical angle of 30^o from directly ahead of the array. The broadside beams are thus narrow in horizontal angle but broad in vertical angle. The right panel in Fig. 3 shows the decibel difference between the two types of noise. Whereas conventional wisdom refers to shipping noise being dominant at low frequency, the shapes of the contours in the panel show that the frequency at which the two types of noise become equal actually varies with the steer direction of the beams. Broadside beams are dominated by surface noise at lower frequencies than forward and rear beams.

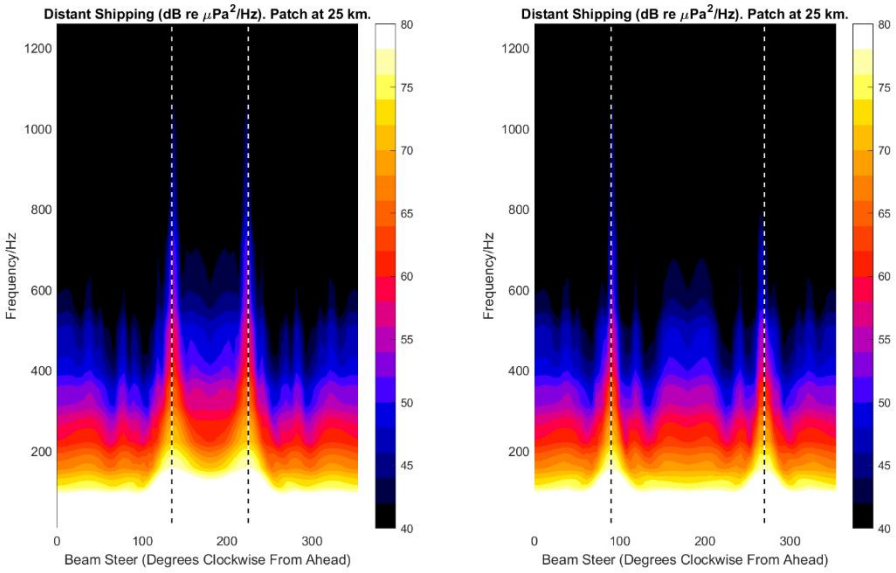


Fig.4: Distant-shipping noise predictions for environments with a small patch of high shipping density added to a uniform background. Dashed lines show the relative bearing of the patch (and the ambiguous bearing) in two cases: off-broadside (left) and broadside (right).

Fig. 4 shows shaded images of in-beam noise for a case where a patch of high shipping density was added to the environment. This simulates what would occur in the vicinity of an area of concentrated shipping activity, such as a fishing-ground or an area of oil production. The right pane shows the effects of the patch when it is at a relative bearing of 90º, i.e. in the broadside beam. A narrow, symmetric beam of noise is centred around the true bearing of the patch, shown by the dotted line. The ambiguous nature of the line array makes a similar pattern appear around 270º. The left panel shows the effect of the same patch when its relative bearing is 135º. The amplitude of the increased noise is similar to the broadside case in the beam closest to the true bearing but the shape of the fall-off of noise with beam steer is now asymmetric. This is because of the broader beams that are steered in directions close to the rear. The beams are in fact so large that the two noise-peaks at the actual and ambiguous bearings merge in the rear beam, whose noise is increased by the patch, despite the 45º angular separation between the patch and the beam-steer. No reference solution exists for this situation but the case is useful to demonstrate that the combination of noise-source distribution, propagation and beamforming gives physically sensible results.

CONCLUSIONS

Closed-form reference solutions are a useful tool in the verification and validation processes that are an important part of the development of numerical models of underwater ambient noise. Expressions for the noise from rain and distant shipping were compared against model predictions and shown to be in close (<2dB) agreement. The same model, run in the same environment but with a line-array receiver, showed how sea-surface noise varied with beam-steer in the horizontal, even though the surface-noise field itself does not vary with horizontal angle. This means that the frequency at which surface noise becomes greater than distant-shipping noise is a function not only of wind-speed, rain-rate and shipping density but also of beam-steer. Broadside beams receive a greater amount of surface noise than forward and rear beams formed from the same array. This work was sponsored by the Defence Materiel Organisation of The Netherlands.

ACKNOWLEDGEMENTS

This work was sponsored by the Defence Materiel Organisation of The Netherlands.

REFERENCES

[1] **Wenz, G. M**. "Acoustic ambient noise in the ocean: Spectra and sources." *The Journal of the Acoustical Society of America* 34(12), pp 1936-1956, 1962.
[2] **ISO**. "ISO 18405 Underwater Acoustics—Terminology." (2017).
[3] **Chapman, D.**, "Surface-generated noise in shallow water: A model." A B Wood Medal Lecture, Proceedings of the Institute of Acoustics, 9, pp 1-l1, 1988.
[4] **Harrison, C. H.** "CANARY: A simple model of ambient noise and coherence." *Applied Acoustics* 51, no. 3, pp 289-315, 1997.
[5] **Jackson, D. R.** "APL-UW high-frequency ocean environmental acoustic models handbook." Applied Physics Laboratory, University of Washington, Technical Report 9407 (1994).
[6] **Ainslie, M. A**. *Principles of sonar performance modelling*. Berlin: Springer, 2010.
[7] **Wales, S. C., and R. M. Heitmeyer**. "An ensemble source spectra model for merchant ship-radiated noise." *The Journal of the Acoustical Society of America* 111(3) pp 1211-1231, 2002.
[8] **Macpherson, J. D., and M. J. Daintith**. "Practical Model of Shallow-Water Acoustic Propagation." *The Journal of the Acoustical Society of America* 41(4A), pp 850-854, 1967.
[9] **Weston, D. E.** "Acoustic flux formulas for range-dependent ocean ducts." *The Journal of the Acoustical Society of America* 68(1), pp 269-281, 1980.
[10] **L. M. Brekhovskikh and Lysanov, Y**., *Fundamentals of ocean acoustics*. AIP Press, 2003.
[11] **Ainslie, M. A., C. H. Harrison, and M. Zampolli**. "An analytical solution for signal, background and signal to background ratio for a low frequency active sonar in a Pekeris waveguide satisfying Lambert's rule." In *4th International Conference and Exhibition on Underwater Acoustic Measurements: Technologies & Results*, pp. 491-498. 2011.
[12] **Sertlek, H. O., and M. A. Ainslie**. "Propagation loss model comparisons on selected scenarios from the Weston memorial workshop." In *Proceedings of 1st International Conference on Underwater Acoustics (UAC), 23-28 June 2013, Corfu, Greece*, pp 441-448. 2013.

VERTICAL ARRAY GAIN IN SHALLOW WATER

Mathieu E.G.D. Colin, , Mark K. Prior, S. Peter. Beerens

TNO, Oude Waalsdorperweg 63, 2597 AK The Hague, THE NETHERLANDS

Abstract: *Detecting sound in the ocean is greatly improved by hydrophone array processing. Until recently, operating large arrays required cumbersome data acquisition systems and processing computers. Thanks to miniaturisation of electronics and improvements in computing power, array size is now limited by practicalities of deploying large physical apertures rather than the difficulties of the associated electronics. This allows improving signal to noise ratio, in particular against ambient noise. An important component of ambient noise is noise originating from the sea surface, which is strongly anisotropic.*

The detection performance of an array can be quantified by the directivity index which is easy to compute but difficult to measure or the array gain which is easily measurable but challenging to model. Directivity index is defined for isotropic noise, while array gain, which determines the actual performance of the system in a given environment, is defined for any noise directionality. Extending the vertical or horizontal aperture of an array may result in any an increased directivity index but array gain will also be affected by signal coherence and noise anisotropy. These two characteristics are in turn influenced by all the environmental parameters related to acoustic propagation (water column, surface and seafloor parameters).

In this paper, we use semi analytical formulas of array gain to study array gain against surface noise in simple shallow water environments. In particular we quantify the relation between array gain, aperture and geo-acoustic parameters and compare it with directivity index.

Keywords: *sonar performance modelling, vertical array*

1. INTRODUCTION

In "back-of-the envelope" sonar performance computations and manufacturers' brochures, sonar receiving array performance is often quantified in terms of directivity index (DI) instead of array gain (AG). This makes sense as the former is easy to compute as it is only a property of the sonar while the latter depends on both the environment and the source and requires more complex computations that are case-specific. In the case of a horizontal line array, DI is a good approximation for AG in most cases. However, for an array with vertical directivity (i.e. for a horizontal line array in bearings towards end-fire or an array with vertical aperture), the directionality of the signal to be detected and that of the noise have a large influence on AG.

In this paper, we concentrate on the AG of vertical line arrays, and use simple modelling to quantify its departure from DI as a function of source range and environmental parameters. The array aperture is left as a free parameters in order to assess the added value of a longer array. A similar but more in-depth analysis presenting comparable results is provided by Rachel Hamson in [1] using different types of models and comparison with measured data.

In Section 2, we recall definitions for array gain and directivity index. The detail of array gain computation in the considered environments is given in section 3. In section 4, we use the presented formula to analyse the behaviour of array gain and its departure from directivity index in a typical shallow water environment.

2. DEFINITIONS

Array gain is defined in [2] as the difference in SNR level for a single hydrophone and after array processing (beamforming):

$$AG = SNR_{hydro} - SNR_{bf}. \tag{1}$$

We express SNR level in terms of difference of sound pressure level of noise and signal:

$$SNR = 10 \log_{10} \frac{Q_s}{Q_n}, \tag{2}$$

where Q_n and Q_s are the mean square pressure of noise and signal respectively.

From these expression, it is clear that the source factors of noise and signal all cancel out when the difference in SNR is computed, and we will therefore omit them for the rest of the paper. The mean square pressure in a given beam after beamforming is the integral over all solid angles of all the contributions of noise or signal:

$$Q = \int_{\Omega} dQB(\varphi,\theta)\mathrm{d}\Omega = \int_{0}^{2\pi} \int_{-\frac{\pi}{2}}^{\frac{\pi}{2}} dQB(\varphi,\theta) \cos\theta \, \mathrm{d}\theta \mathrm{d}\varphi \,, \tag{3}$$

where φ and θ are azimuth and elevation (positive upwards), respectively, B the array beampattern and dQ is the mean square pressure contribution per solid angle.

Directivity index is a special case of array gain, as it is defined as array gain for a plane wave against isotropic noise [2]. In this case, the expression of array gain simplifies to

$$AG_{iso} = DI = -10\log_{10}\int_{-\frac{\pi}{2}}^{\frac{\pi}{2}}\int_{0}^{2\pi} B(\varphi,\theta)\mathrm{d}\varphi\cos\theta\,\mathrm{d}\theta. \quad (4)$$

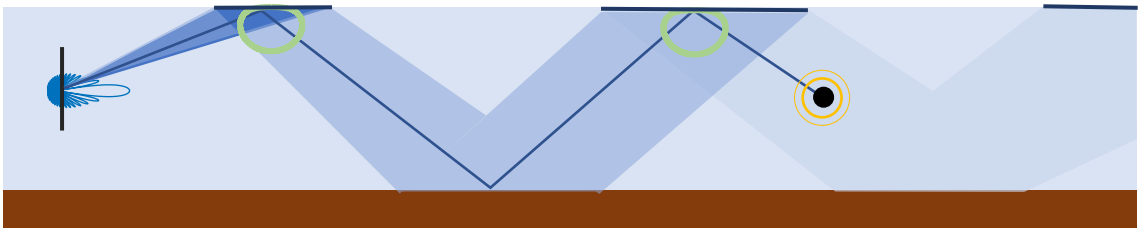
The beampattern $B(\varphi,\theta)$ (as defined in [2]) of most arrays can be readily calculated using techniques presented in [3]. In this paper, we will concentrate on the added value of the vertical aperture of arrays, and therefore restrict ourselves the properties of vertical line arrays. In the rest of the paper, we assume the beamforming carried out is the unweighted delay-and-sum beamformer. For a continuous unweighted vertical line array steered at broadside (horizontal), the beampattern is:

$$B(\varphi,\theta) = \mathrm{sinc}^2\left(\frac{2\pi L}{2\lambda}\sin\theta\right), \quad (5)$$

where λ is the wavelength, L the array length and sinc is the cardinal sine function ($\sin x/x$).

3. ARRAY GAIN IN A SHALLOW WATER ENVIRONMENT

In this section we will recall formulas from literature for angular contributions of signal and noise in a shallow water waveguide.



3.1. Signal

Let us first consider the signal contribution. The mean square pressure contribution per solid angle to the total received signal after beamforming is,

$$dQ_S = S(\varphi,\theta)B(\varphi,\theta)F(\theta), \quad (6)$$

where $S(\varphi,\theta)$ is the source factor (1 $\mu\mathrm{Pa}^2\mathrm{m}^2/\mathrm{ste}$ for this paper) and $F(\theta)$ is the propagation factor for a single eigenray:

$$F(\theta) = \frac{\cos^2\theta}{r^2}\exp\left(-\frac{2\alpha r}{\cos\theta}\right)|R(\theta)|^{\frac{r}{H}\tan\theta}, \quad (7)$$

where r is the source range, α the volume absorption in water, $R(\theta)$ the seafloor amplitude reflection coefficient. The exponent of the reflection coefficient accounts for the $\frac{r}{2H}\tan\theta$ reflections at the seafloor and $r/\cos\theta$ is the eigenray path length. Following [4],

we compute the total mean square pressure as a continuous sum of incoherent eigenrays over all solid angles.

Computing array gain involves computing the signal mean square pressure before and after beamforming. We use omni-directional hydrophones and therefore use $B(\varphi,\theta)=1$ to compute the mean square pressure before beamforming. While it is possible to obtain a closed form solution for this integral by making simplifications on the beampattern and the reflection coefficient [2], we choose to evaluate it numerically to allow using arbitrary beampatterns and reflection coefficients. The resulting $F(\theta)$ function is plotted in Fig. 2 (solid and dashed black lines), together with the critical angle (black mixed line) and the reflection coefficient for the chosen environment (see section 4 for environmental description).

3.2. Noise

To compute the noise contribution, we use Chapman's work [5] on noise directionality. He shows that the summed contributions of successive patches of surface dipoles radiating to the receiver within a solid angle (Fig. 1) result in an infinite series which elegantly simplifies in the following expressions:

$$dQ_N(\theta<0)=\frac{B(\varphi,\theta)S_0\sin\theta\,|R^2(\varphi)|}{1-|R^2(\theta)|} \tag{8}$$

$$dQ_N(\theta>0)=\frac{B(\varphi,\theta)S_0\sin\theta}{1-|R^2(\theta)|}. \tag{9}$$

where S_0 is an areic source level term disappearing in the AG computation.

In this paper, we neglect absorption, but treatment of absorption and other phenomena are treated extensively by Harrison [6][7]. The resulting noise directionality ($dQ_n(\theta)$) is plotted in Fig. 2.

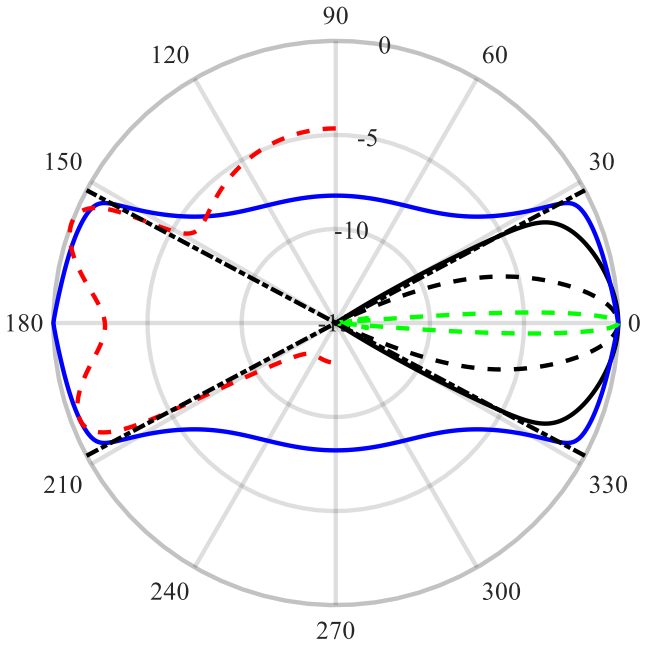


Fig.2: Red dashed line noise directivity, blue reflection gain (i.e. reflection loss but always negative so that adding the gain reduces the level), black signal directivity for a source at range 1 km (solid line), 10 km (dashed line), green dashed line, directivity pattern of a 10λ vertical array

3.3. Array Gain

The array gain is computed by integrating all angular contributions over solid angle:

$$AG = 10\log_{10}\left(\frac{\int_\Omega dQ_{S,bf}\mathrm{d}\Omega \int_\Omega dQ_{N,hydro}\mathrm{d}\Omega}{\int_\Omega dQ_{S,hydro}\mathrm{d}\Omega \int_\Omega dQ_{N,bf}\mathrm{d}\Omega}\right), \quad (10)$$

where the suffix *hydro* corresponds to the mean square pressure for a single hydrophone (i.e. $B(\varphi,\theta)=1$) and *bf*, the mean square pressure after beamforming. In Fig. 2, the elements of the integrands of equation (10) are plotted in a polar format. This plot seems to indicate that all contributions are strongly affected by the critical angle and the signal directionality depends strongly on the source range. In the following section, we will therefore look at the sensitivity of array gain, for different array lengths, to these parameters. We will further look at the influence of wind as wind speed and surface roughness are usually affecting all terms of the sonar equation.

4. PARAMETER VARIATION

The basic shallow water environment used in this paper is that used for the David Weston Memorial Workshop on sonar performance modelling [8]. Additionally, some environmental parameters are varied.

4.1. Effect of source range

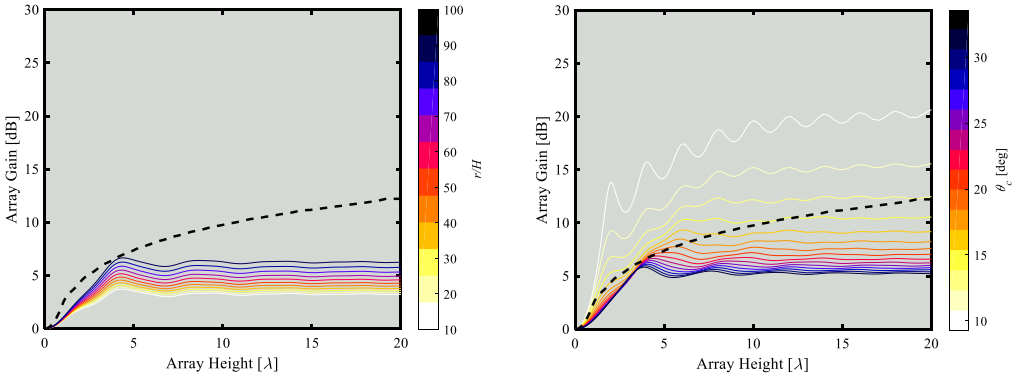


Fig.3: Left: Directivity Index (dashed line) and Array Gain as a function of target range (in number of water depths) and array height (in wave lengths). Right: same for varying seafloor critical angle.

As shown in Fig. 2, the signal contribution becomes more directional with increasing source range. We computed AG for a source range increasing from ten to one hundred times the water depth (100 m). The results are shown in the left panel of Fig. 3. The dark lines correspond to the furthest range and the bright lines to the closest range. A few observations

can be made: In this case, array gain is always less than directivity index. Also, while DI keeps increasing with array length, AG saturates at about four wavelengths, whatever the source range. The saturating value depends on the source range, with a further source allowing increased AG. This can be understood by considering Fig 2.: as the source range increases, steeper paths get more attenuated and the signal is more directional around the horizontal. A longer array only over-resolves the signal resulting in no increased array gain.

4.2. Effect of critical angle

The critical angle has a more complex influence than source range, as it influences both signal and noise. In the right frame of Fig. 3, the critical angle of the sediment is varied from around 9 deg to about 33 deg (other geo-acoustic parameters such as sediment density and compressional attenuation are fixed to the values from [8]). Array gain saturates around four wavelengths for faster sediments and a bit more for slower sediments. For slower sediments, (brighter lines), array gain can even be higher than directivity index. What this implies for the performance of a sonar would require an analysis including shipping noise [9].

4.3. Effect of wind

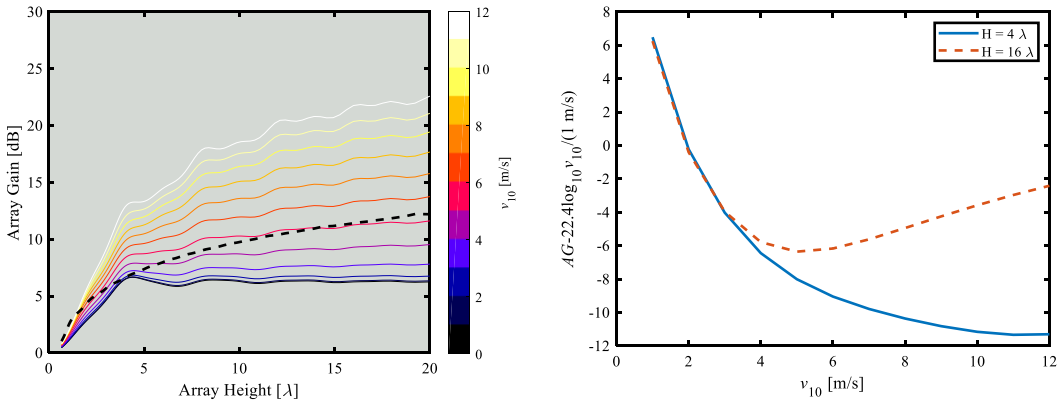


Fig.3: Left: Directivity Index (dashed line) and Array Gain as a function of wind speed and array height (in wave lengths). Right: array gain minus noise increase due to wind speed as a function of wind speed for two array heights.

We carried out a similar analysis including surface loss due to wind, using the reflection coefficient from [2], with a wind speed at an altitude of 10 m from 0 m/s to 12 m/s. As one can expect, a mechanism similar to that of the increasing critical angle is visible in the results in Fig. 3. An increase in wind strips down the higher angle paths thereby increasing the array gain. As this may suggest that detection performance increases as wind speed increases, we attempted to consider the net effect on SNR without having to compute a full sonar equation. The mean-squared pressure areic source factor due to wind-generated surface noise from [2] is proportional to $v_{10}^{2.24}$, therefore we plotted $AG - 22.4 \log_{10}(v_{10}/1\ \mathrm{m/s})$ as a proxy for an hypothetical SNR, for two array lengths, in the right panel of Fig. 4. For both array lengths, an increase in wind only results in a degradation in SNR in comparison to the low wind case. For the longest array (16 λ), the SNR is increasing again beyond 5 m/s, but the resulting SNR is still small compared to a situation without wind.

5. CONCLUSION

Using simple formulae from literature we have shown how array gain can be computed for a shallow water environment. With these formula we analysed the sensibility of array gain to a few parameters (source range, sediment critical angle and wind speed) and compared it to directivity index.

This has shown that, as far as vertical aperture is concerned, directivity index is not a very good approximation of array gain. Furthermore, array gain seems to level off with increasing array length quicker than directivity index (with an array length around 4 λ) for the cases considered here. Finally, as an exercise in modelling, we have shown that while an increase in wind speed results in more array gain, it only results in an increase in SNR beyond a certain wind speed.

In general, the estimation of the performance of an array with vertical aperture requires taking into account the directionality of noise and signal to meaningfully reduce uncertainty in sonar performance prediction.

ACKNOWLEDGEMENTS

This work was sponsored by the Defence Materiel Organisation of The Netherlands. The authors are indebted to M. Ainslie and S. van IJsselmuide for useful suggestions and discussions.

REFERENCES

[1] **Hamson, R. M.** (1980). The theoretical limitations of a passive vertical line array in shallow water, *The Journal of the Acoustical Society of America,* 68(1), July 1980.

[2] **Ainslie, M. A.** (2010) *Principles of sonar performance modelling,* Springer

[3] **Queen, W. C.** (1970). The directivity of sonar receiving arrays. *The Journal of the Acoustical Society of America,* 47(3A), 711-720.

[4] **Harrison, C. H.** (2003). Closed-form expressions for ocean reverberation and signal excess with mode stripping and Lambert's law. *The Journal of the Acoustical Society of America*, 114(5), 2744-2756.

[5] **Chapman, D. M. F.** (1987) Surface-generated noise in shallow water: a model, *Proc. IOA* Vol. 9, Part 4,

[6] **Harrison, C. H.** (1997). CANARY: A simple model of ambient noise and coherence. *Applied Acoustics*, 51(3), 289-315.

[7] **Harrison, C. H.** (1996). Formulas for ambient noise level and coherence. *The Journal of the Acoustical Society of America*, 99(4), 2055-2066.

[8] **Zampolli, M., Ainslie, M. A., & Schippers, P.** (2010). Scenarios for benchmarking range-dependent active sonar performance models, Validation of Sonar Performance Assessment Tools: In Memory of David E Weston, 7th–9th April 2010 Clare College, Cambridge, UK, 53-63.

[9] **Prior, M. K., Colin, M. E. G. D., Riet, van M. W. G.** (2019) Modelling noise from wind, rain and distant shipping in scenarios of varying complexity, *Proceedings of UACE 2019*, Hersonissos, Greece

ENVIRONMENT DEPENDENT TRANSITION FREQUENCIES FOR RAM AND BELLHOP

Iris E. Hartstra[a], Erik Salomons[a], Mathieu E.G.D. Colin[a] and Mark K. Prior[a]

[a] TNO, Oude Waalsdorperweg 63, 2597 AK The Hague, THE NETHERLANDS

Abstract: *Passive-sonar-performance modelling requires the accurate estimation of the acoustic field for a broad range of frequencies in various environments. In this paper, we assess the suitability of a Gaussian Beam (Bellhop) and Parabolic Equation model (RAM), whereby we focus primarily on computational efficiency.*
For Parabolic Equation (PE) models the computation time increases with the number of grid-points required to provide accurate results. Since the grid-size scales to the wavelength, the computation time generally increases with frequency. The computation time of Gaussian Beam models increases primarily with longer maximum range. Since lower frequencies result in relevant acoustic intensities at larger distances, this results in a computation time increase in case of lower frequencies.
Our aim is to estimate a single-run 'transition frequency' that determines which model is optimal in terms of computational costs, while ensuring that each model is subjected to a convergence criterion we set at 1 dB. We only consider single-frequency runs in this paper. The transition frequencies are estimated for three different scenarios that vary in depth and sound speed profile (SSP). We find that RAM is the computationally efficient choice up to a transition frequency of about 11 kHz and 12 kHz in the case of the shallow water scenarios: Weston Case 1 and 4, respectively. For the deep water scenario, a Munk profile truncated at 1 km depth, RAM is found to be the most efficient choice up to about 4.5 kHz.

Keywords: *sonar performance, computation time, parabolic equation model, Gaussian beam model, transition frequency*

1. INTRODUCTION

Passive-sonar-performance modelling is required to estimate the ability of a passive sonar system to detect a target in an operational environment. These models aim to provide reliable spatial maps of probability of detection within an acceptable length of computation time. In recent years, the bandwidth of hydrophones has increased significantly, especially towards the higher frequency range. This advancement demands a reassessment of the operational practicality of different acoustic propagation models as a function of frequency and environmental parameters (such as water depth).

In this paper we compare two widely used and benchmarked models that are based on distinct physical approximations: the Gaussian Beam (GB) model of Bellhop [1] and the Parabolic Equation (PE) model RAM [2].

Gaussian Beams are solved in a two-step approach, of which the first entails the numerical integration of ray trajectories throughout the medium and the second the computation of the associated intensity along and in the vicinity of the rays. The coherent form of Gaussian Beams has a low frequency limitation in terms of computation time, because the accurate reconstruction of model interference patterns at low frequencies requires a very large number of rays. The computation time of both coherent and incoherent GB models increases with increasing propagation distance, because the ray trajectories are traced further out. This will lead to a longer computation time for lower frequencies, because lower frequency waves are less affected by absorption and thus propagate further out than high frequency waves. In this paper, we will use the incoherent form of Bellhop, because we consider acoustic intensities.

The PE model solves the full one-way wave equation by marching an initial field solution (the starter field), resolved for all depths at zero range, in the range direction. Since the 'marching steps' are a function of wavelength, we expect the computation time of this model to increase with frequency. However, as in the case of GB models, we expect this effect to be curbed by the fact that the maximum range at which PL values remain relevant is lower for higher frequencies.

We conduct convergence tests and depth-averaged intensity comparisons to closed-form solutions for three different scenarios, of which the first two are based on examples of the Weston Memorial Workshop: the Weston Case 1 is a homogeneous Pekeris waveguide with 100 metre water depth [3], and the Weston Case 4 is the same as 1, but contains a wedge that linearly rises to a depth of 30 metres between 5 and 7 km range [3]. The third scenario is a deep water environment: we adapt the original Munk profile [4] by placing the bottom at 1 km depth. We use the same environmental parameters (e.g. coarse-grained sediment, SSP, etc.) as described in [5]. However, instead of having a constant maximum range, we vary the maximum range as a function of frequency in order to limit the propagation loss (at maximum range) to values that are rendered relevant for sonar applications (~75-100 dB re m^2). The frequencies we consider are 100, 500, 1000, 4000, 10000, 15000 and 20000 Hz. By monitoring the computation time of the respective models as a function of these frequencies, we aim to estimate a single-run transition frequency for each environmental scenario.

2. THEORY

2.1. Parabolic Equation model

The Parabolic Equation model (PE model) is an efficient numerical method for calculating sound propagation from a point source to a distant receiver in a refracting medium [6]. The sound pressure field is calculated as a function of range and depth on a rectangular grid. The PE model can be used for situations with range-dependent medium properties. The field is calculated in steps along the range axis. A change of a medium property at a certain range is taken into account by a change in the parameters of the propagation formulas. Of practical interest is range dependence of the sound speed profile and the water depth. It should be emphasized that the PE model is not subject to a high-frequency approximation (which is the case for ray models), so PE is particularly useful and efficient for sound propagation at lower frequencies.

For the study described in this paper we employed the efficient split step Padé PE model developed by Collins [7]. We make use of a Fortran version of this PE model, which is referred to as RAM PE (RAM stands for Range-dependent Acoustic Model) [2].

2.2. Gaussian Beam model

The full derivation of the Helmholtz equation can be formulated in terms of an infinite series of equations [1,6]. The governing equation for the Gaussian Beam model follows by considering two main equations of this series: the Eikonal equation (ray or travel time solutions), and the transport equation (intensity).

In a first step, the Eikonal equation is solved, yielding a ray fan which provides travel time and ray angle information throughout the medium and represents a 'high-frequency approximation' of the acoustic field. The bending of the rays is controlled by the variations in sound speed of the medium according to Snell's law.

In the next step, the transport equation is solved to obtain a solution for the amplitude of the acoustic pressure field along the rays, which varies due to geometrical spreading and focusing. The amplitude in the vicinity of the ray can be derived by taking the ray central axis as maximum value and decreasing it by a Gaussian shape in the perpendicular direction from the ray axis. The width of this Gaussian shape is computed by the dynamic ray equations, which are a function of the local ray density and sound speed variations. The intensity distribution, obtained by summing the resulting beams, respects low frequency effects such as shadow zones and is unaffected by caustics [1].

2.3. Closed-form solutions

We compare the PL calculations of Bellhop and RAM with closed-form expressions that are based on mode-stripping. These expressions can be rigorously simplified by using the fact that higher order modes experience more attenuation [8]). We use the range-independent closed-form expression from [8] (Eq. 4 in [8]) for the range-independent cases 1 and 3. For the range-dependent case 4, we use the range-dependent closed-form expression from [9] (Eq. 21 in [9]).

3. EXPERIMENTS

For the three different scenarios defined in the introduction we run both RAM and Bellhop for different frequencies (first row in Table 1). To prevent the intensity of the acoustic field to reach values that are rendered insignificant for sonar applications, we allow the maximum range to vary as a function of frequency using an empirical relation (second row in Table 1). The fact that Bellhop has the option to calculate only an incoherent solution allows us to use a larger grid-size in the vertical direction, which saves computation time. For RAM we use the Nyquist criterion to define the grid-size in the vertical direction (remaining rows of Table 1). Both models are subjected to convergence tests for each different scenario and frequency. The model settings that result in a convergence within a criterion of 1 dB are used for the experiments that serve to estimate the transition frequency. This criterion provides sufficient practical accuracy, because it is a small value when compared to the uncertainty of environmental input data as discussed in [10]. The (possible) intersection of the computation time of Bellhop and RAM will serve to interpret the transition frequency.

Table 1: The maximum range varies as function of frequency. The vertical grid-size for Bellhop's receiver output grid varies by scenario, whereas for RAM it varies as function of frequency: it is equal to the spatial Nyquist criterion.

Frequency [Hz]		100	500	1000	4000	10000	15000	20000
MaxRange [km]		200	76	50	22	13	10	8
Bell dzOut [m]	Scen 1	2	2	2	2	2	2	2
	Scen 2	2	2	2	2	2	2	2
	Scen 3	10	10	10	10	10	10	10
RAM dzOut [m]		7.5	1.5	0.75	0.1875	0.075	0.05	0.0375

3.1. Convergence tests

The RAM PE model has several numerical parameters, which must be optimized in order to achieve accurate results in an efficient way. Important parameters are the horizontal and vertical grid-sizes Δr and Δz of the computation grid. We found that the horizontal grid-size Δr may be chosen as large as 10λ (where λ is the wavelength), for frequencies in the range 50-4000 Hz. For the vertical grid-size Δz smaller values must be used, ranging from 0.1λ at 50 Hz to 1.0λ at 4000 Hz.

These optimized values were determined by convergence tests where the depth-averaged propagation loss was considered as a function of range. Due to the complex nature of PE convergence, we limited the test method to a visual assessment. The criterion was that the propagation loss should not change by more than about 1 dB if smaller values were used for the horizontal and vertical grid-size. We found that choosing the vertical grid-size too small, smaller than 0.01λ, led to inaccurate results.

There were also other numerical parameters which we varied in the convergence tests. These include: i) the number of Padé terms (we used 8 terms for the calculations reported here), ii) the thickness of the sediment (we used 20λ for the calculations reported here), and iii) some parameters of the absorption layer below the sediment (we followed the approach described in [6]). For the convergence tests we also considered the results of convergence tests performed by [9] and [11].

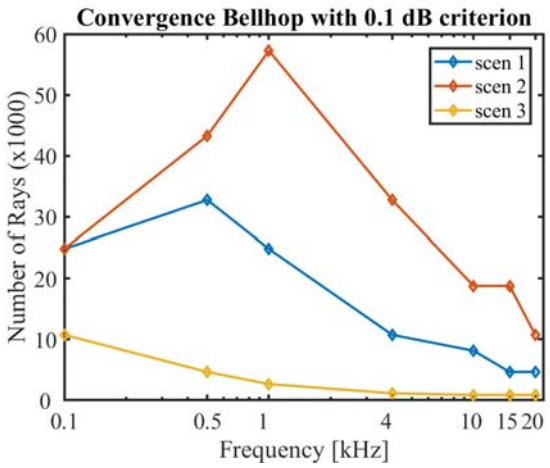


Figure 1a Number of rays required per frequency and scenario for Bellhop to converge within 0.1 dB. NB: different y axis limits are used than in figure 1b.

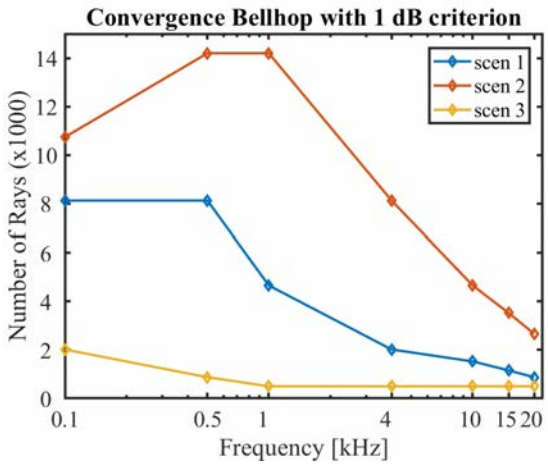


Figure 1b Number of rays required per frequency and scenario for Bellhop to converge within 1 dB. NB: different y axis limits are used than in figure 1a.

For the Gaussian Beam model, Bellhop, we determine the optimal number of rays necessary to reach convergence of the depth-averaged PL at one kilometre short of the maximum range. Figure 1a shows the convergence results for a criterion of 0.1 dB. However, we use the number of rays that yields a convergence of 1 dB (Figure 1b) for the experiments conducted in this paper to determine the transition frequency per scenario.

3.2. Relative depth averages

For the first scenario at 100 Hz, the depth-averaged results of RAM deviate from the closed-form solution by less than 1 dB for ranges up to about 35 km, beyond which RAM starts to increasingly deviate, reaching a value of about 6 dB at the maximum range of 200 km (Figure 2a). Bellhop deviates between 1-2 dB until about 130 km, beyond which it reaches a deviation of about 3 dB at 200 km range. At 4000 Hz both RAM and Bellhop hardly deviate. For the second scenario: at 100 Hz, both Bellhop and RAM differ significantly from the closed form solution: RAM by about 3 dB in the 100-metre-deep zone, which increases to more than 6 dB for the 30-metre-deep zone, and Bellhop by about 1 dB in the 100-metre-deep zone, which increases to about 6 dB in the 30-metre-deep zone (Figure 2c). At 4000 Hz, both models do not deviate from the closed-form solution by more than a dB (Figure 2d).

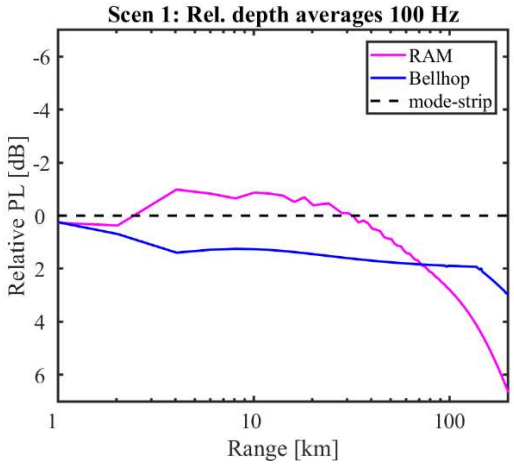


Figure 2a

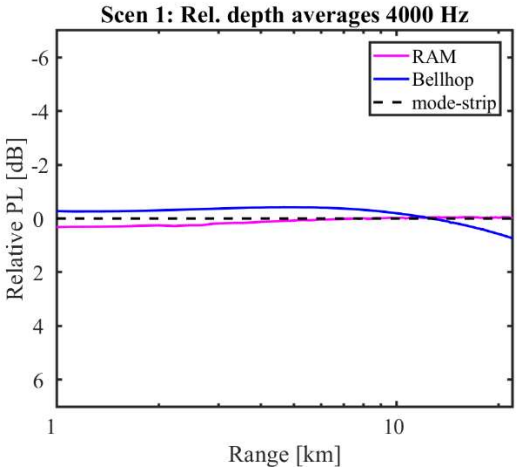


Figure 2b

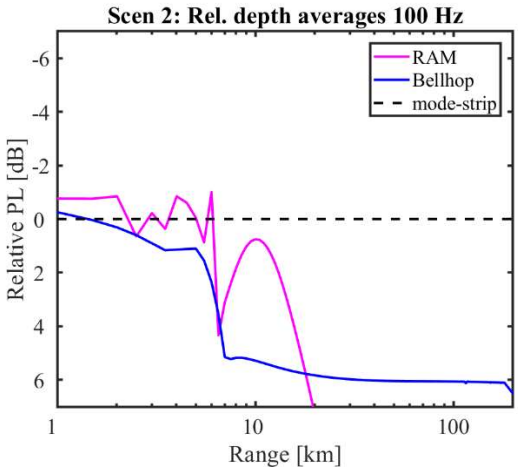


Figure 2c

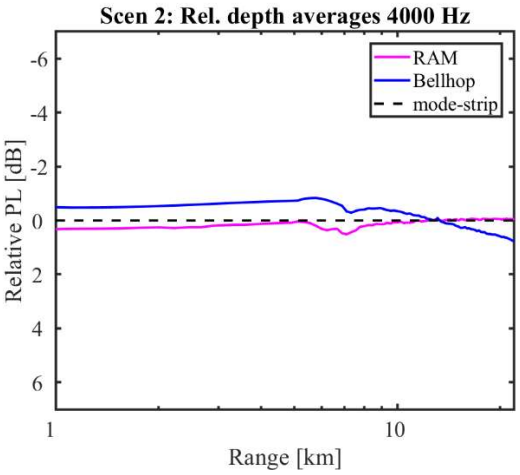


Figure 2d

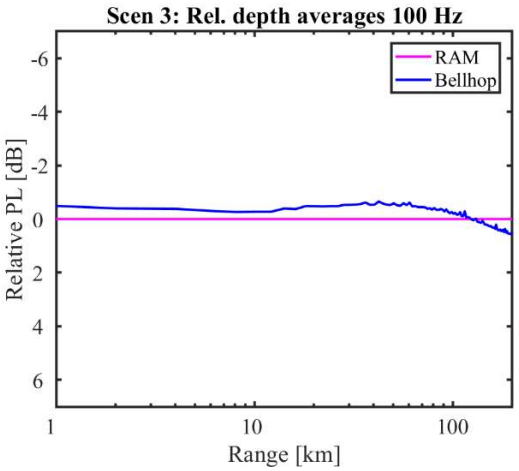


Figure 2e

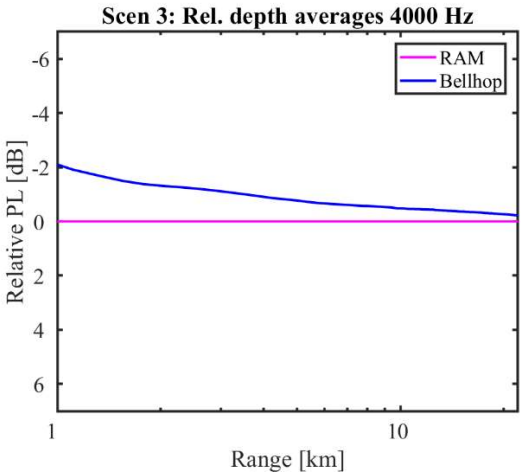


Figure 2f

Figure 2 Figures a-d show depth-averaged PL with respect to the closed-form solutions for the two Weston scenarios for 100 and 4000 Hz. Not that the maximum range varies as a function of frequency (see Table 1). Figures e and f show depth-averaged PL of Bellhop with respect to RAM for the deep water scenario.

For the third scenario, we only analyzed the averaged PL difference between the two models, because we do not have a closed-form solution for a Munk profile. For 100 Hz, the models give almost the same result, while for 4000 Hz Bellhop deviates by about 2 dB from RAM for the smaller ranges (Figures 2e and 2f, respectively).

3.1. Single-run transition frequency

We estimate the transition frequency by comparing the computation times of both models for a single-frequency run. The transition frequency per scenario is defined as the frequency above which RAM has a longer computation time than Bellhop, and thus becomes less practical for single-frequency applications. Table 2 displays the single-run transition frequencies we found per scenario number. Figure 3 shows how the transition frequency is estimated from the intersection of the two computation time curves of Bellhop and RAM for the deep water scenario: the intersection occurs around 4.5 kHz.

Table 2 Single-run transition frequency estimates for each scenario.

Scenario	Transition Frequency [kHz]
1 Weston	11
2 Weston, wedge	12
3 Deep water	4.5

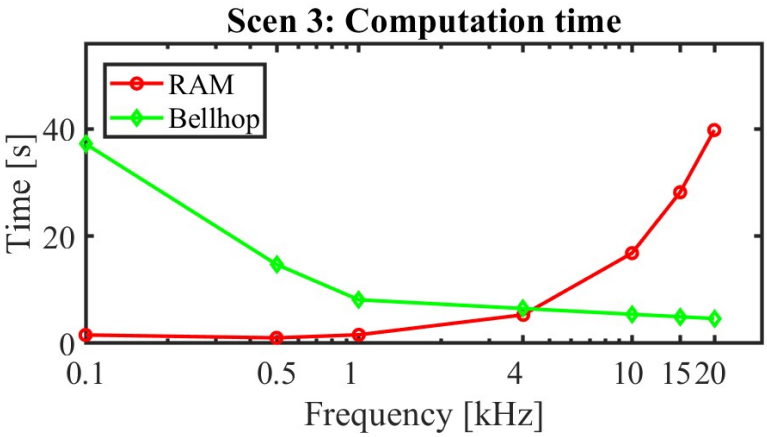


Figure 3 Computation time for a single-frequency run of RAM and Bellhop for the deep water scenario 3. The intersection occurs around 4.5 kHz, which is interpreted as the single-run transition frequency for this scenario.

4. DISCUSSION AND CONCLUSIONS

Both Bellhop and RAM deviated from the closed-form solution in some of the cases considered. The deviations for Bellhop were especially large for the Weston Case 4 (wedge) at 100 Hz in the 30-metre-deep zone. In this same scenario, RAM shows the largest deviation as well and to a greater extent than Bellhop. This specific example may indicate an issue with the use of single precision the *fortran* version of the RAM code. The single-

run transition frequencies displayed in Table 2 show that RAM is the most efficient choice in the case of scenarios 1 and 2 for frequencies up to about 12 kHz. However, in the case of deep water, Bellhop is more efficient than RAM above a frequency of 4.5 kHz. This is expected, because RAM requires considerable more grid-points for computing deep water solutions.
As a final note, we emphasize that the transition frequencies we present in this paper are only valid for single-frequency runs. When for instance time resolution is required, the transition frequencies could turn out to be very different, because multiple frequency runs are necessary in this case for RAM [3].

Acknowledgement
This work was sponsored by the Defence Materiel Organisation of The Netherlands.

REFERENCES

[1] **Porter, M. B. and Bucker, H. P.** (1987). Gaussian beam tracing for computing ocean acoustic fields. The Journal of the Acoustical Society of America, 82(4), 1349-1359.
[2] Fortran code for RAM PE by M. Collins and is available at the Open Acoustics Library, http://oalib.hlsresearch.com/PE/RAM/. The code is called ram.f, version 1.5.
[3] **M. Zampolli, M. A. Ainslie, P. Schippers** (2010). Scenarios for benchmarking range-dependent active sonar performance models. *Ainslie, MA, Validation of Sonar Performance Assessment Tools: In Memory of David E Weston,* 2010
[4] **Munk, W. H.** (1974). Sound channel in an exponentially stratified ocean, with application to SOFAR. The Journal of the Acoustical Society of America, 55(2), 220-226.
[5] **H.Ö. Sertlek, M.A. Ainslie, K.D., Heaney** (2018). Analytical and Numerical Propagation Loss Predictions for Gradually Range-Dependent Isospeed Waveguides. *IEEE Journal of Oceanic Engineering.*
[6] **F.B. Jensen, W.A. Kuperman, M.B. Porter, H. Schmidt,** "Computational Ocean Acoustics", Springer, 2011
[7] **M.D. Collins**, "A split-step Padé solution for the parabolic equation method", J. Acoust. Soc. Am. **93**, 1736–1742 (1993).
[8] **C.H. Harrison** (2003). Closed-form expressions for ocean reverberation and signal excess with mode stripping and Lambert's law. *J. Acoust. Soc. Am. 114 (5)*
[9] **H.Ö. Sertlek and M.A. Ainslie**, "Propagation loss model comparisons on selected scenarios from the Weston Memorial Workshop", *Proc. first international conference and exhibition on underwater acoustics, UAC 2013, Corfu, Greece.*
[10] **B. Binnerts, C. de Jong, I. Karasalo, M. Östberg, T. Folegot, D. Clorennec, M. Ainsley, A. MacGillivray, G. Warner, L. Wang,** "Model benchmarking results for ship noise in shallow water", *Proc. fifth international conference and exhibition on underwater acoustics, UAC 2019, Hersonissos, Greece*
[11] **E.T. Küsel and M. Siderius,** "Comparison of propagation models for the characterization of sound pressure fields", *IEEE Journal of Oceanic Engineering, DOI 10.1109/JOE.2018.2884107*

REVERBERATION MODEL-DATA COMPARISONS AND ESTIMATED SCATTERING STRENGTHS IN THE VICINITY OF THE TREX13 SITE

Dale D. Ellis

Department of Physics, Mount Allison University, Sackville, NB, Canada

Contact: Dale D. Ellis, 18 Hugh Allen Drive, Dartmouth, NS, Canada B2W 2K8
email: daledellis@gmail.com

Abstract:
During the 2013 Target and Reverberation Experiment (TREX13) reverberation and target echo data were collected using a fixed source and fixed horizontal array deployed in shallow water in the Gulf of Mexico. Various pulses in the 1.8 to 3.6 kHz frequency band were sent, day and night over a 4-week period, and an extensive analysis of the reverberation data and environmental measurements made. Results by various authors were collected in the recent TREX13 Special Issue of the IEEE Journal of Oceanic Engineering. Ellis et al. used a normal-mode Reverberation and Target Echo model [IEEE JOE, 42, 344–361, 2017] to perform model-data comparisons and extract a scattering strength (based on Lambert's rule) along the relatively-flat Reverberation Track. The beams of the horizontal array, can be steered at all azimuths, so in this paper we look at model-data comparisons along other radials, using a different scattering function. As well as propagation effects, the model takes into consideration the frequency and angular dependence of the beam patterns, so an estimate of the range and azimuthal dependence of the scattering can be extracted. Scattering anomalies point to regions where additional environmental measurements would be worthwhile.

Keywords: *TREX Experiment, reverberation, range-dependent modelling, normal modes, scattering functions, Gulf of Mexico, towed array*

1. INTRODUCTION

TREX was a series of Target and Reverberation Experiments sponsored by the US Office of Naval Research (ONR) in the Gulf of Mexico off Panama City, Florida, USA. Their unique feature was a fixed source and fixed receivers deployed in about 20 m of water, with the acoustic experiments being complemented by an extensive set of environmental measurements. These measurements were to facilitate the understanding of the underlying reverberation and clutter mechanisms, and to support quantitative modelling. The reverberation experiments were primarily organized by the Applied Physics Laboratory at the University of Washington (APL/UW). Extensive environmental measurements were made before, during, and after the main experiment. Results from various authors have been collected in a Special Issue of the IEEE Journal of Oceanic Engineering [1].

The main focus was the reverberation experiments, where various pulses in the 1.8 to 3.6 kHz frequency band were sent, day and night for about four weeks in April and May 2013, and received on a horizontal line array. An extensive analysis of the reverberation data has been made by Yang et al. [2]. Modelling efforts by Ellis et al. [3] concentrated on interpretation of the data, calibration of the matched filter output, and estimation of scattering strengths. For that work a normal-mode Reverberation and Target Echo model was used to perform model-data comparisons and extract a scattering strength (based on Lambert's rule) along the relatively-flat Reverberation Track.

The beams of the horizontal array, can be steered at all azimuths, so in this paper model-data comparisons are made along other radials, using a different scattering function. As well as propagation effects, the model takes into consideration the frequency and angular dependence of the beam patterns, so an estimate of the range and azimuthal dependence of the scattering can be extracted. Scattering anomalies point to regions where additional environmental measurements would be worthwhile.

2. TREX OVERVIEW

Figure 1 shows the TREX13 site and deployments. The source and FORA triplet array [4] were fixed near the bottom in about 20 m water, moored to research vessel *R/V Sharp*. The data were received on the 48-element array deployed horizontally in a fixed position about 2.1 m above the bottom. Each of the elements were triplets, so the "left-right" ambiguity was resolved, and beams could be formed in the full 360° azimuth. The 0.2-m spacing between the elements made the aliasing frequency about 3.8 kHz for a sound speed of 1525 m/s. At half-wavelength spacing the 48 elements can be used to produce approximately 96 independent beams, though generally more were processed.

The omnidirectional ITC-2015 source, also fixed, was deployed nearby, 1.2 m above the bottom. Typical pulses were CWs at 1.9, 2.7, and 3.6 kHz, and LFMs in the bands 1.9–2.0, 2.7–2.8, 3.4–3.5, 1.8–2.7, and 2.7–3.6 kHz. The pulses were 1 s duration and 10% Tukey-shaded at each end. The source levels varied slightly over the band, but were roughly 197 dB re 1μPa at 1 m, and produced reverberation which dropped into the noise after 5 to 10 s, depending on conditions.

3. SOME REVERBERATION DATA

In this paper, we use data processed by Yang [2], with uniformly-weighted beams steered every degree of azimuth, except for 5 degrees near each endfire where the triplet processing [5] was potentially inaccurate. For the results here, beams at 3° intervals were selected.

For each beam, the frequency-domain processing gave a reverberation estimate at time intervals of $(\text{bandwidth})^{-1}$. To smooth the fluctuations of an individual ping for display, the intensity over 19 time points was averaged using with a Hann window.

A few pings with low noise and low volume reverberation from fish were selected from overnight Run 79 (May 9–10) and Run 124 (May 15–16). For these deployments, the array heading was 353°T. For Run 79 there were 4 LFMs of interest, each ping of the same type being repeated every 6 minutes. For Run 124 there were two 900-Hz bandwidth LFMs which alternated every 40 s.

Figure 2 shows the reverberation from a 1.8–2.7 kHz LFM on a polar plot, superimposed on bathymetric contours spaced at 2 m intervals. For the overlay, the beams are mapped into azimuth, and time is mapped into range. The data for each beam have been flattened by multiplying by $(\text{time})^3$, which is slightly less than the reverberation dropoff. This allows a reduced dynamic range for the colour scale, so more features to be seen. Note the high reverberation near the shoreline (white bathymetric contours to the northeast of the array); the reverberation from it also appears faintly on the ambiguous beams to the northwest. Many other scattering features can be seen.

Figure 3 shows the flattened reverberation at short time from the 2.7–3.6 kHz LFM for a selection of beams to the southeast of the array in the general direction of the Reverberation Track (upper plot), and for a selection of beams to the west of the array (lower plot). The reverberation to the southeast (upper plot) is associated with the sand waves of the detailed bathymetry [3, 2]; Figure 4 illustrates the correlation along the Reverberation Track from previous analysis. The reverberation to the west (lower plot of Figure 3) shows similar structure, but the reverberation "peaks and valleys" are closer together, and not so obvious.

4. DATA-MODEL COMPARISON

The Target and Reverberation Model [3] was used to compare with the data. It is a bistatic range-dependent reverberation model that uses adiabatic normal modes for propagation and an empirical function for the scattering. Ray-mode analogies are used to obtain the grazing angles for the scattering function. In [3] the scattering function used was Lambert's rule: $S_b(\theta, \theta') = \mu_2 \sin\theta \sin\theta'$, where the θs are the incident and scattered grazing angles. Figure 4 (left) shows

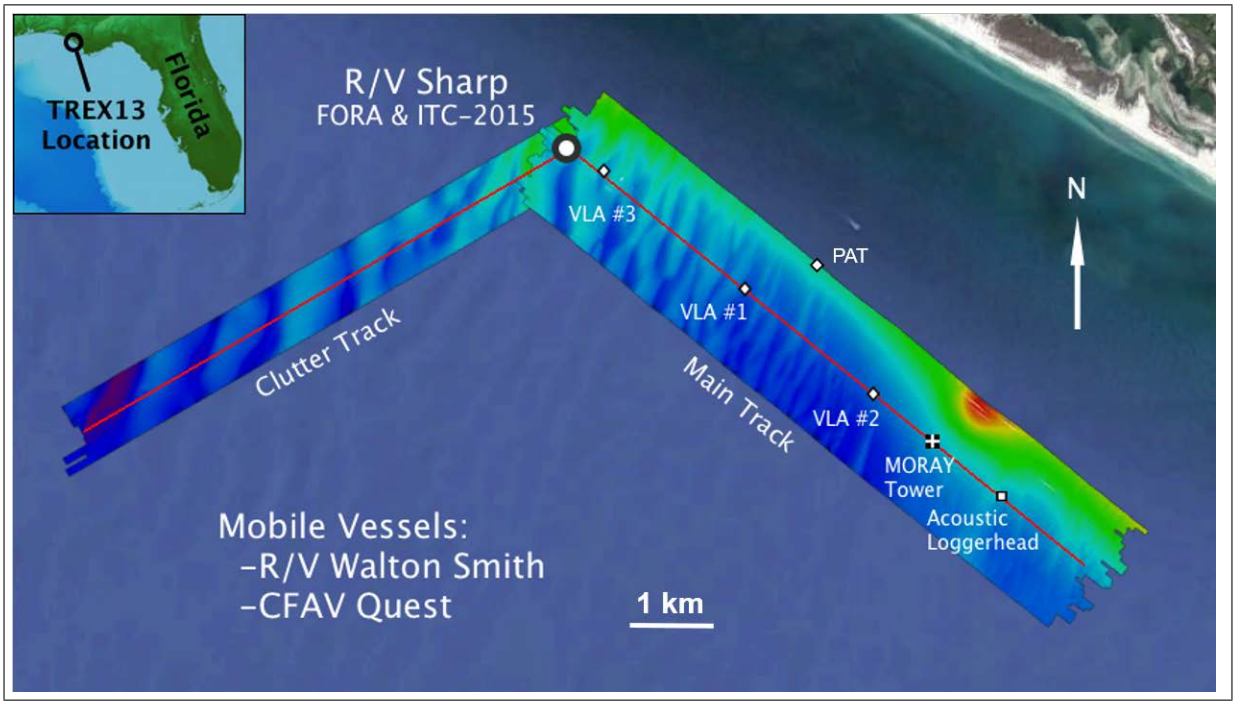


Fig. 1: TREX site showing bathymetry and deployments. The ITC-2015 source and FORA horizontal array are fixed near the bottom in about 20 m water. Water depths range from 12 m (red) to 21 m (dark blue). The Main Track is about 7 km and of nearly constant depth; sand dunes are 1–2 m in height, and several hundred meters apart.

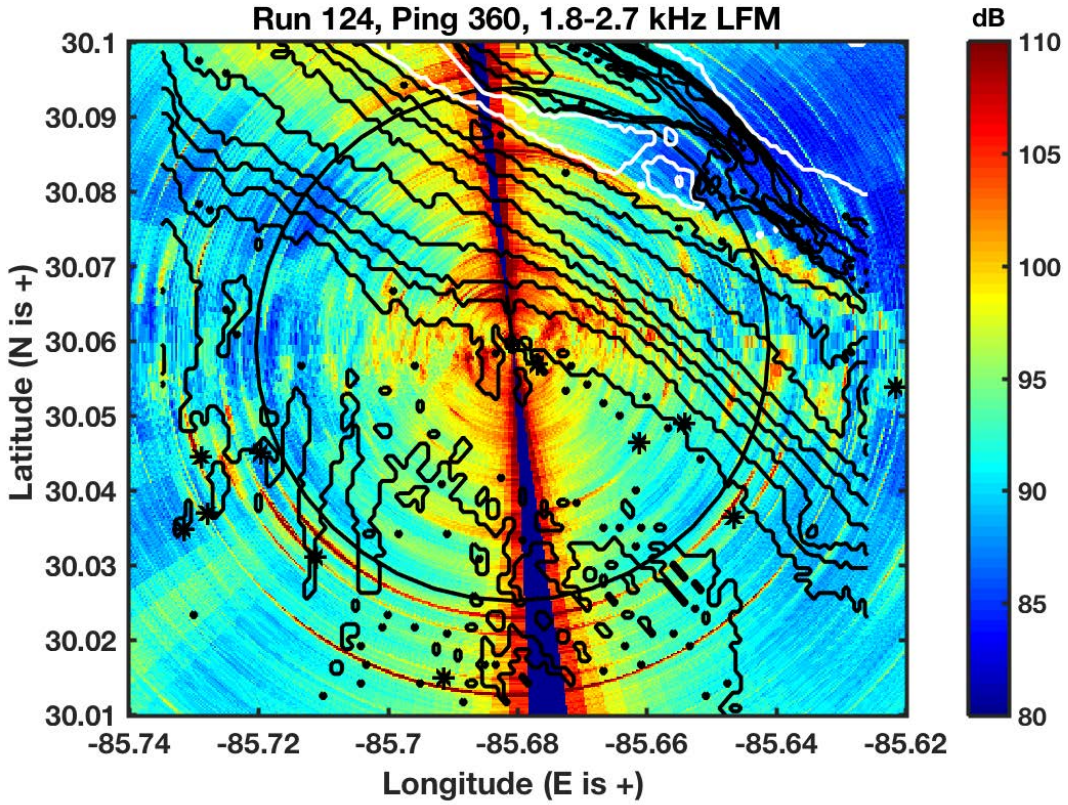


Fig. 2: Polar plot of flattened reverberation for one ping the 1.8-2.7 kHz pulse in Run 124. The source and receiver are at the centre, and the circle corresponds to a time of 5 s (3.8 km).

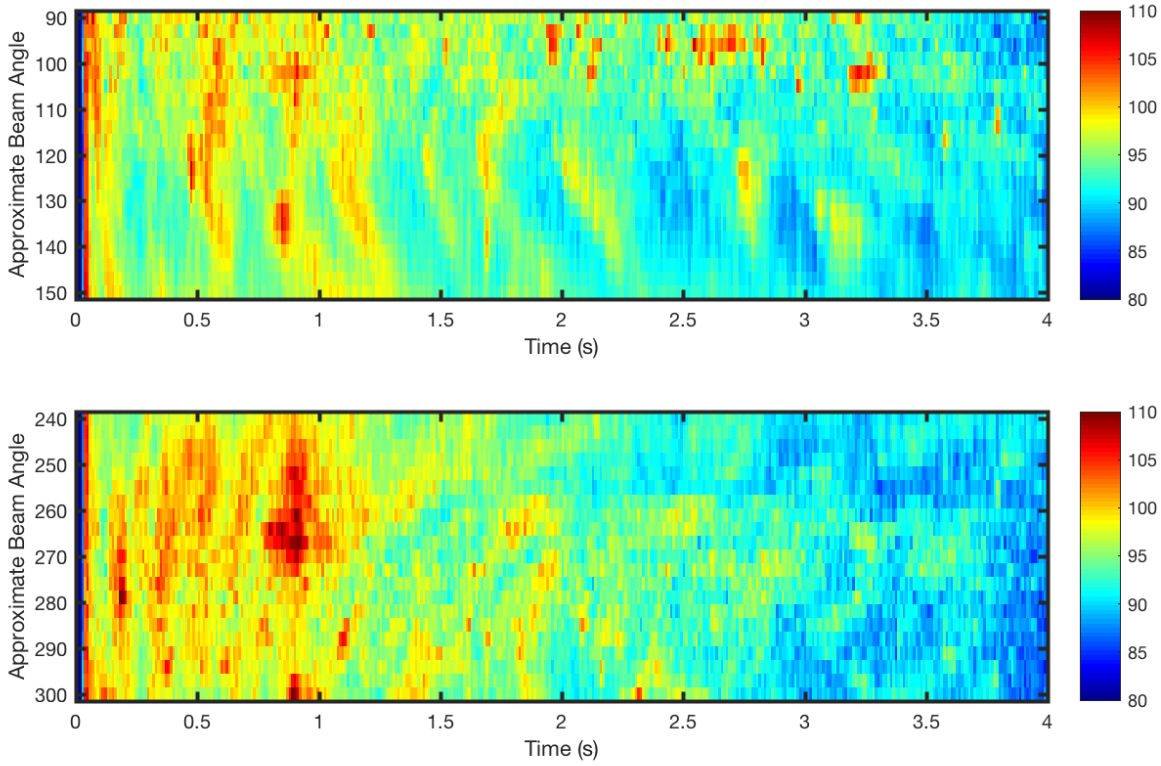


Fig. 3: Plot of reverberation from the 1.8–2.7 kHz LFM for a selection of beams: in the vicinity of the Reverberation Track (upper), and to the west of the array (lower).

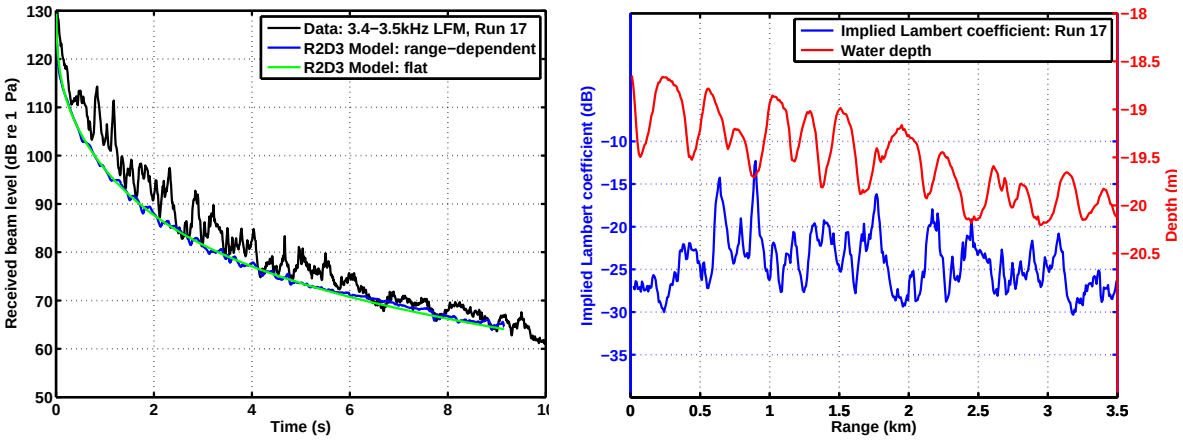


Fig. 4: (Left) Model-data comparison along the Reverberation Track for an earlier data set, and (right) the implied scattering strength compared with the bathymetry.

a model-data comparison along the Reverberation Track from that earlier work using a constant Lambert coefficient, along with the implied scattering strength (right) required to fit the data.

In this paper a different scattering function is used: $S_b(\theta, \theta') = \mu_3 (\sin\theta \sin\theta')^{3/2}$, which gives a reverberation decay of $r^{-3.5}$ for Pekeris environment [6], and provides better agreement with the slope of the measured data [7].

From a TREX13 Workshop, a "Strawman" environment was proposed (B.T. Hefner, Private communication, Sept. 2016) with water depth 19.6 m, constant water sound speed 1525 m/s, and a bottom halfspace with sound speed 1660 m/s, and density ratio 1.9. The bottom attenuation had a wide variance, and 0.5 dB/m-kHz was used here. The bathymetry from a NOAA database which has ∼90 m resolution was used for the calculations in this paper.

Figures 5 and 6 show model–data comparisons in two frequency bands for four beam angles (one in each quadrant). For the calculations, a constant scattering strength was used at each frequency. For the 1.8–2.7 kHz LFM a value of $\mu_3 = -21$ dB provided a reasonable fit for three of the beams (Figure 5). The model calculations did not include background noise which may be affecting the data at the longer times shown. For the 2.7–3.6 kHz LFM, a stronger scattering coefficient $\mu_3 = -16$ dB was needed. Again, it provides a reasonable fit (Figure 6) to the lower envelope of the data in three of the quadrants, but also falls too low for the beam looking shoreward to the northeast.

The cause of this is not known: it could be increased scattering due to the bottom or surface; it could be that the bathymetry is in error; or it could be that the modes near cutoff are beaming into the bottom causing sub-bottom volume scattering that is not included in the model. Figure 7 shows reverberation on a beam looking shoreward for 4 frequency bands. At 4 s there is a quick drop off of reverberation. There may be a frequency-dependent mode cutoff, with the lower frequencies being cut off a little earlier.

5. DISCUSSION AND SUMMARY

The directional dependence of the towed array, along with the time resolution of the reverberation, make it a very useful tool for Rapid Environmental Assessment and surveying an area [8], identifying features for further investigation.

The previous analysis of the TREX13 reverberation data concentrated on the Reverberation Track. Using high-resolution bathymetry, spikes in the reverberation along the Reverberation Track were shown to be correlated troughs in the sand dunes.

Here we have taken a look at other bearings using beams of the FORA array. Similar patterns in the reverberation are seen to the west of the source-receiver. However, more detailed bathymetry

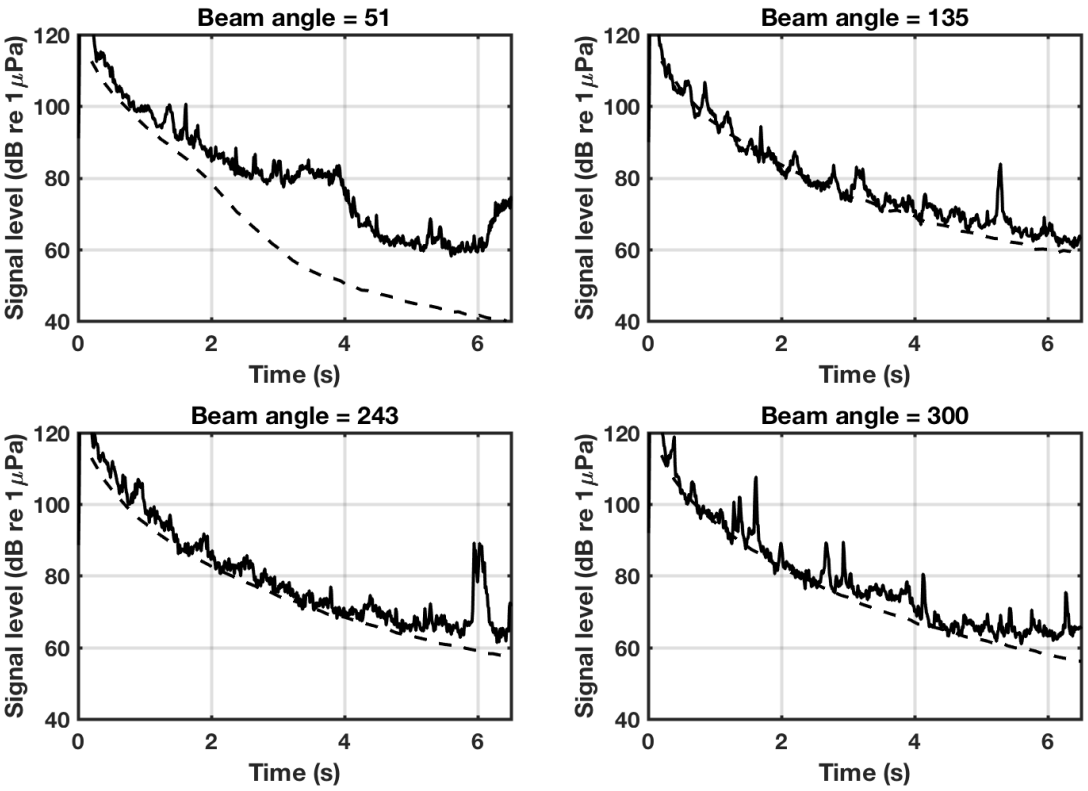


Fig. 5: Model-data comparison on selected beam angles for 1.8–2.7 kHz LFM.

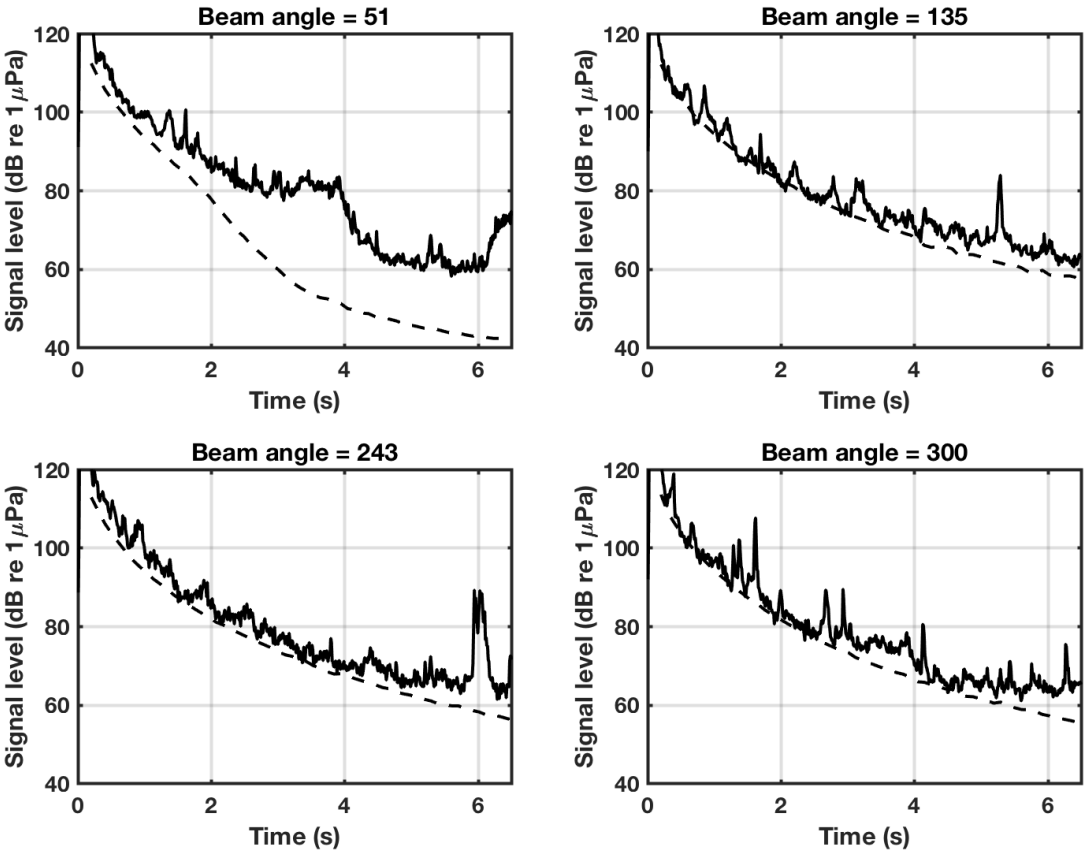


Fig. 6: Model-data comparison on selected beam angles for 2.7–3.6 kHz LFM.

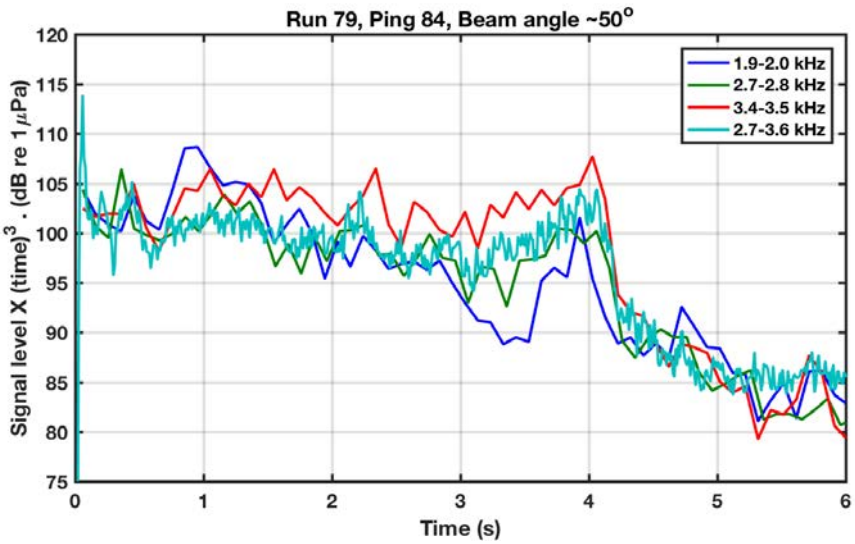


Fig. 7: Comparison of reverberation at different frequencies for shoreward beam.

would be needed to make a correlation.

Initial estimates of the bottom Lambert scattering strength were made in Ref. [3]. There seems to be some indication that the reverberation fits a $\sin^3\theta$ backscattering law which gives a $r^{-3.5}$ range dependence. This is midway between the commonly used $\sin^2\theta$ of Lambert's rule, and the low-angle $\sin^4\theta$ given by perturbation theory. The physics-based scattering function from perturbation theory should be incorporated into the model, and used with estimates of the roughness scattering parameters obtained along the Reverberation Track.

As discussed near the end of the previous section, the behaviour of the scattering near the shore is interesting and requires more investigation.

Work is continuing to look at the data in more detail, and to refine the model predictions.

Model-data differences point to regions where additional environmental measurements would be worthwhile.

ACKNOWLEDGEMENTS

The work was supported by the US Office of Naval Research, Ocean Acoustics, Code 32.

Todd Hefner, DJ Tang and Kevin Williams from Applied Physics Laboratory, University of Washington planned and directed the TREX13 experiments. John Preston of ARL/PSU was instrumental in preparing the FORA array, and ensuring the data were of highest possible quality. Jie, Yang, DJ Tang, Todd Hefner, and other co-workers from APL/UW provided many valuable inputs and insights.

REFERENCES

[1] **B. T. Hefner and D. Tang**, Guest editorial: Target and Reverberation Experiment 2013 (TREX13)—Part I, *IEEE J. Oceanic Eng.*, 42(2):247–249, 2017. Also, Part II. *IEEE J. Oceanic Eng.*, 42(4):757–758, 2017.

[2] **J. Yang, D. Tang, B. T. Hefner, K. L. Williams, and J. R. Preston**, Overview of mid-frequency reverberation data acquired during the Target and Reverberation Experiment 2013. *IEEE J. Oceanic Eng.*, 43:563–585, 2018.

[3] **D. D. Ellis, J. Yang, J. R. Preston, and S. Pecknold**, A normal mode reverberation and target echo model to interpret towed array data in the Target and Reverberation Experiments. *IEEE J. Oceanic Eng.*, 42(2):344–361, 2017.

[4] **K. M. Becker and J. R. Preston**, The ONR Five Octave Research Array (FORA) at Penn State. In *Oceans 2003 Proceedings*, pages 2607–2610. Oceanic Engineering Society, IEEE, September 2003.

[5] **G. Haralabus and A. Baldacci**, Unambiguous triplet array beamforming and calibration algorithms to facilitate an environmentally adaptive active sonar concept. In *Proceedings Oceans 2006*, 2006.

[6] **M. A. Ainslie and D. D. Ellis**, Echo, reverberation, and echo-to-reverberation ratio for a short pulse in a range-dependent Pekeris waveguide. *IEEE J. Oceanic Eng.*, 42(2):362–372, 2017.

[7] **D. D. Ellis**, Modelling bottom scattering and target echoes from data collected during the 2013 Target and Reverberation Experiment. In J. S. Papadakis, editor, *4th Underwater Acoustic Conference and Exhibition: Proceedings*, pages 245–252, 2017. Conference held at Island of Skiathos, Greece, 3–8 September 2017.

[8] **J. R. Preston and D. D. Ellis**, Extracting bottom information from towed-array reverberation data Part I: Measurement methodology. *J. Mar. Syst.*, 78:S359–S371, 2009. Also, Part II, Modelling methodology, pp. S372-S381.

UNCERTAINTY ANALYSIS IN SONAR PERFORMANCE MODELLING BY LATIN HYPERCUBE SAMPLING

Robert Sigg and Jörgen Pihl

Swedish Defence Research Institute, 164 90 Stockholm, Sweden

Jörgen Pihl, Swedish Defence Research Institute, 164 90 Stockholm, Sweden.
Fax: +46 5550 3569, email: jorgen.pihl@foi.se

Abstract: *We have studied the possibility to use stratified sampling for uncertainty analysis applied to underwater applications. The method is called Latin Hypercube Sampling (LHS) and the idea behind this approach is to sample only a representative part of the probability distributions so that the number of runs can be reduced significantly. Usually, the number of runs are in the order of 50-100 compared to traditional Monte Carlo sampling where you have millions of runs. An important issue is the difference between uncertainty and sensitivity analysis, which we demonstrate with an active acoustic scenario. Thereafter, we show how we can use LHS in an area where you have quite large uncertainties in the geo-acoustic properties. We have identified the need of presenting the uncertainties to the user in an easy understandable way in a single plot. A new visualization parameter is defined, TPOD (Total Probability of Detection), to meet this requirement. Our studies using LHS show that it is easy to apply and give useful insight in complex uncertainty dependencies. However, for relevant output we need to have good knowledge about the individual parameter probability distributions, both regarding absolute values and representative distributions.*

Keywords: *Sonar, performance calculations, uncertainty analysis, Latin Hypercube Sampling*

INTRODUCTION

Many years of research in underwater acoustics, together with development of fast computers and efficient algorithms have resulted in that we today can do truthful simulations of our sensor systems, and do performance predictions with high precision.

However, good quality predictions are only possible if the input data is well known, i.e. the errors in the parameters are small. Unfortunately this is not always the case, some parameters such as the geo-acoustic bottom and sub-bottom parameters are sometimes not well known.

The calculations you normally do in performance predictions show the probability of detection (POD) for a given set of parameters, as a function of distance and depth, giving the detection distance for your sonar, or the counter-detection distance for a possible threat. Now, due to uncertainties in the input parameters, this value need not be the most representative. However, it can often be sufficient to just know this value, for example when setting the optimal depth for a variable depth sonar (VDS). But in some situations we also need to know the uncertainty in the calculations. For example, a submarine exposed to ASW wants to know if the hunting ship has a chance to detect it or not, in order to be able to navigate safely or to be able to take calculated risks to escape the situation. Then it is important to know not only the most probable detection distance, but also the minimum and maximum distances.

Uncertainties in complex calculations, especially those using nonlinear models, are not only dependent on individual input errors, but also on how parameters in combination affect the end result. We have therefore studied how to calculate these uncertainties correctly.

To define the concept of *uncertainty* analysis, we compare it with the concept of *sensitivity* analysis. As described in [1] *sensitivity* analysis is performed by perturbing one parameter, while keeping all other parameters fixed. On the other hand, in *uncertainty* analysis several parameters are varied at the same time and in this way the entire output space can be studied. One can say that the sensitivity analysis is local, while the uncertainty analysis takes a global perspective.

As also pointed out in [1] there are three main areas regarding uncertainties; parameter uncertainties, structural uncertainties (model errors) and stochastic uncertainties. The two former are mainly due to the lack of knowledge regarding parameters or how physical processes are simplified in the model used. Such uncertainties can be reduced with better knowledge of parameter values and better physical approximations in the model. Stochastic uncertainties or, in other words, the variability of natural phenomena cannot be eliminated. Through increased knowledge, however, one can get a better understanding of these uncertainties. In this report, we have primarily studied the influence of parameter uncertainties.

LATIN HYPERCUBE SAMPLING

The basic approach behind Latin Hypercube Sampling (LHS) is to divide the probability distributions into a number of bins, each with equal probability, where the number of bins is an arbitrary value set by the user. This is called stratification. Each stratification can only be used once when combining the parameters included in the uncertainty analysis which means that the number of runs will be equal to the stratification value [2].

Given the stratification value the idea is to compute a large enough number of parameter combinations to cover the most important uncertainty features (Fig.1). After that the wave propagation model is run for every combination computed by LHS. The advantage of LHS is that the number of dispersion calculations is significantly reduced compared to Monte-Carlo methods (MCM). In LHS, we typically talk about 50-100 runs while in brute force MCM the number are millions. The selection of the stratification number is dependent on the specific global uncertainty analysis, and typically, with an increased number of parameters with

uncertainties the more stratifications you need. Many times you have to study the specific problem in order to select the proper stratification number.

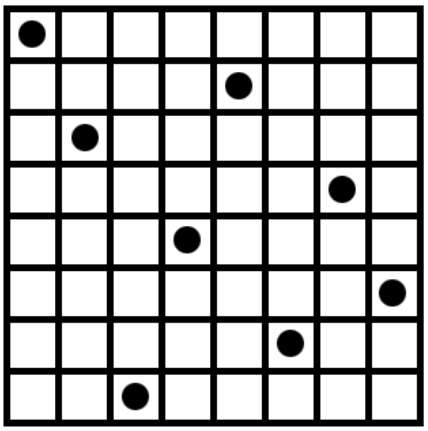


Fig.1: A two-parameter problem with a stratification of 8. The total number of combinations are 64 (as required for a Monte-Carlo simulation). However, the LHS method generates 8 evenly distributed combinations (black dots).

Both LHS and MCM requires knowledge of the parameter uncertainties and their probability distributions. These distributions depend on the nature of the physical problem. In this project we have assumed that the parameter distribution is normal.

UNCERTAINTY ANALYSIS COMPARED TO SENSITIVITY ANALYSIS

In order to gain an understanding of the uncertainties in the result, it is useful to supplement the uncertainty analysis with a sensitivity analysis. To illustrate this, we present results from an uncertainty analysis where we imagine that we have an active VDS sonar searching for a submarine. We study uncertainties in three parameters: the VDS dome depth, the ambient noise, and Lambert's backscattering coefficient. We use a ray-trace model (MultiMoc) for sonar performance calculations, and LHS is used to generate global uncertainty. This is then compared to runs where we fix all parameters except the one that is varied.

Normally, results from sonar performance calculations are displayed as POD. It is calculated based on the assumption that the detection probability follows the so-called ROC curve (Receiver Operating Characteristic). Now, when we have an ensemble of calculations, we have chosen to visualize the result as the "total" POD, *TPOD*, which we also think is the simplest presentation method. If the TPOD is 90%, it means that 90% of the individual runs in the LHS analysis have a detection probability over a given threshold. The threshold we have used in our studies is 50%, which is normally used in performance calculations for surveillance sonar. Thus, if the TPOD is 10%, it means that 10% of the individual runs in the LHS analysis have a detection probability above the 50% threshold. Thus we take into account both favorable and poorer propagation conditions.

In the uncertainty analysis, the parameters have been assigned a normal distribution which is described by an average value and a standard deviation. Regarding Lambert's back scattering coefficient, a fairly large range is chosen which extends from hard rock bottom to sand. Figure 2 shows the result from calculations in a typical summer situation in the Baltic, with a well-developed thermocline at about 20 m.

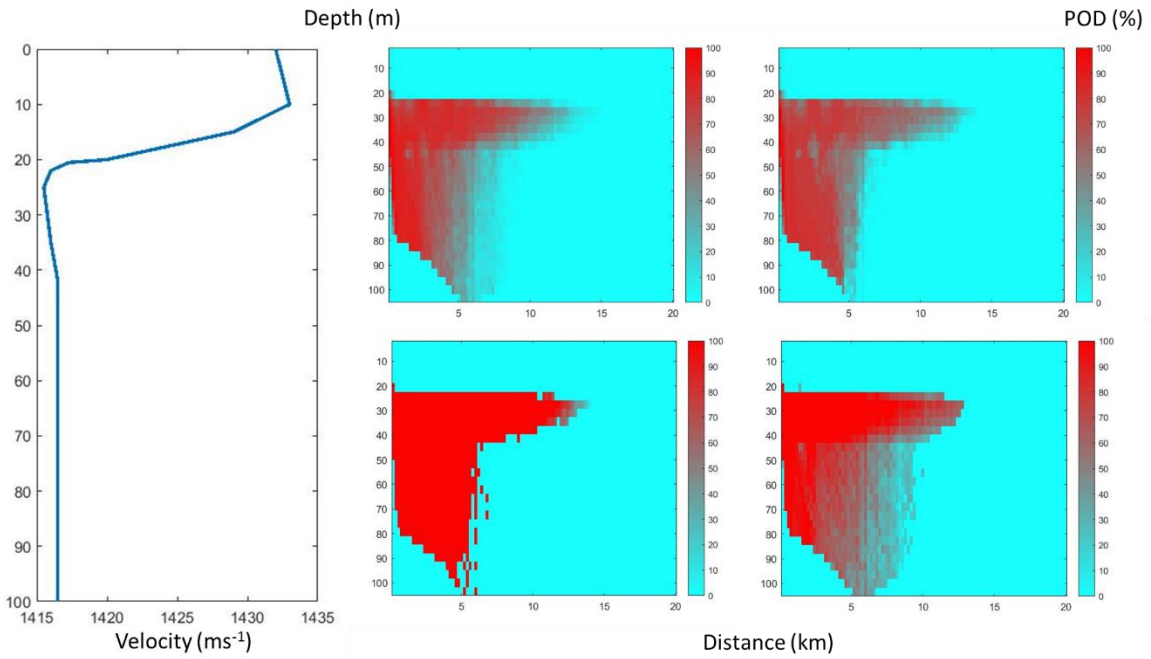


Fig. 2: Detection distance (TPOD) for the uncertainty analysis (top left), sensitivity to ambient noise (bottom left), sensitivity to transmitter depth (top right) and sensitivity to Lambert's coefficient (bottom right).

The TPOD from the uncertainty analysis (Fig.2, top left) shows that to be really sure of detection, the target should be within 2-3 km from the transmitter and in the sound channel up to 6 km. In some of the runs, detection can take place in longer distances, out to 6-12 km. The transition zone between always discovered to rarely detected is approximately 3-5 km. However, this says nothing about which parameter combinations give short and long ranges, respectively. Therefore, there is a need to make a comparison with a sensitivity analysis.

First, we keep Lambert's coefficient and the transmitter depth constant, and the ambient noise varies linearly. In this case, there is very little sensitivity to the ambient noise (Fig.2, bottom left). When we vary the ambient noise there is no variation in detection distances, and the transition zone between always detected to not-detected is short. In addition, in a normal surveillance situation, it is quite easy to measure the ambient noise with sufficient accuracy. The global uncertainty therefore depends very little on this parameter.

When the transmission depth is varied a greater effect is obtained (Fig. 2, top right). This image begins to resemble the global uncertainty analysis (top left) and it tells us that the distance of detection depends strongly on the transmitter depth, which is a typical behavior in shallow waters.

Lastly, we vary Lambert's coefficient, which also has a large impact on the detection distance (Figure 2, bottom right). The detection distance is strongly dependent on the bottom characteristics.

All in all, we can conclude that this is a reverberation-limited case where we also have a sensitivity to the transmitter depth, depending on the sound velocity curve. In order to get a complete picture of how the performance calculations depend on the input parameters, it is helpful to have both a global uncertainty analysis complemented with a sensitivity study. Thus, from a tactical perspective, it would be desirable if a combination of these calculations can be visualized. One way to visualize the results is demonstrated in the example below.

EXAMPLE: SAFE COUNTER-DETECTION

In our example a submarine is out on an exploration mission in a shallow area which is guarded by bottom-mounted passive surveillance sonar. The question now is how close we dare to go without risk of discovery. We know the positions and the capability of the systems relatively well, so we can calculate their detection distances provided we also have correct values for environmental parameters. We assume that the sound velocity in the water and the ambient noise is known. However the geo-acoustic parameters of the sediment layers is not well known. As the performance of a passive low-frequency sonar in shallow water greatly depends on the bottom characteristics, we need to make some assumptions regarding the sediment parameter values, and the possible errors in those assumptions. The best thing we can do is to assume that the area is similar to another known area with a similar geological structure. The assumed parameter values are given in table 1.

Parameter	Mean value	Standard deviation
Sound speed	1480 m/s	100 m/s
Density	1400 kg/m^3	50 kg/m^3
Absorption	0.2 dB/λ	0.1 dB/λ
Layer thickness	50 m	40 m

Table 1: Parameter values for LHS-calculations.

In this case, the calculations show that up to 3 km from the sensor there is a great risk of detection, but if one is to be absolutely sure of passing unnoticed it is necessary to pass at least 6 km distance, given the uncertainties estimated.

A sensitivity analysis has also been carried out where the sound velocity in the sediment layer has been varied within a given interval, and all other parameters are set to the mean value (table 1). Fig. 3 shows the mean value (black-solid line) and the standard deviation (black-dotted line) plotted from this sensitivity analysis for detection distances. The lines illustrate that part of the variations in detection distances is captured by the sensitivity analysis.

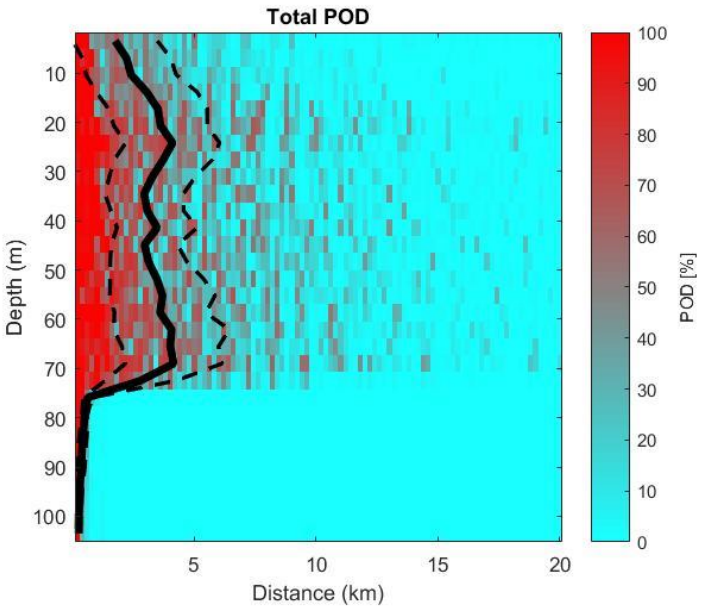


Fig. 3: The TPOD for detection (blue and red colours) by a qualified sonar compared to a sensitivity analysis where only the sound velocity profile is varied: Mean value (solid black line) and standard deviations (dotted lines).

We find that the TPOD becomes an effective way of analyzing the detection distance from an uncertainty perspective. Instead of analyzing 50 different POD plots, we can visualize the same information in a single figure. These calculations are not particularly heavy, and it is fully realistic to introduce these in tactical support systems.

CONCLUSIONS

Our study of the LHS method shows that it is very useful for understanding how uncertainties in input data affect complicated propagation calculations. In our example, we show important aspects such as input uncertainties and its distributions, as well as the importance of choosing the right stratification. Practical experience shows that a suitable stratification for LHS is somewhere between 50 - 100.

However, the uncertainty analysis will depend on good estimates of the parameter uncertainties, both regarding size and what the distribution looks like. In these studies, we have made the assumption that parameter values are normally distributed, but studies are needed to investigate if this really is the case.

In our example, we show how large the variations in detection distance predictions can be, with reasonable values of input data. In an ordinary single calculation of the detection distance, the uncertainty in the result makes it necessary to address safety margins. A calculation with LHS gives all possible outcomes, so the result can be used with greater confidence. We believe that it would be beneficial to introduce LHS into our operational tactical support systems. Here, we propose that the concept of TPOD is introduced, which is an effective way of visualizing the uncertainty in the calculations.

REFERENCES

[1] **J. Burman, N. Brännström, O. Björnham, P. Lindgren, L. Persson, P. von Shoenberg, L. Thaning,** Osäkerheter i observationer och beräkningar, *FOI-R3764—SE,* Swedish Defence Research Institute, 2013.

[2] **McKay, M.D., Conover W.J., Beckman R.J.,** A comparison of three methods for selecting values of input variables in the analysis of output from a computer code. *Technometrics* 21, 239, 1979.

Structured Session 21
Target Echo Strength-Measurements and Modelling

Organiser(s): Williams Duncan, Nunn David, Nijhof Marten

PRELIMINARY TARGET MEASUREMENTS FROM A PROTOTYPE MULTISPECTRAL SYNTHETIC APERTURE SONAR

Zuhayr Rymansaib[a], Alan Hunter[a], Christopher Bowen[a], Jeremy Dillon[b], Richard Charron[b], David Shea[b]

[a] University of Bath, Bath BA2 7AY, United Kingdom
[b] Kraken Robotic Systems Inc., St John's, NL A1N 4P6, Canada

Contact author: Alan Hunter, a.j.hunter@bath.ac.uk

Abstract: *The AquaPix Multispectral Synthetic Aperture Sonar (SAS) is a next-generation seafloor imaging product in development by Kraken Robotic Systems Inc. It will operate in multiple bands widely spaced over a wide acoustic spectrum, enabling acoustic spectroscopy, buried object detection, and enhanced target classification. This paper presents early results from opportunistic target measurements carried out during development and testing. Various multispectral data products are presented from an aluminium pipe target suspended in the water column in a controlled lake experiment. The data products include circular SAS images from multiple spectral bands, a multispectral image fusion, and an acoustic colour signature. The multispectral imagery is shown to simultaneously expose the acoustic features of the target corresponding to its geometric shape and its elastic response. These early results demonstrate the feasibility and potential of the system, which is expected to provide a powerful new capability in seafloor mapping.*

Keywords: *Synthetic aperture sonar, multispectral, target scattering*

1. INTRODUCTION

The AquaPix Multispectral SAS will operate in multiple spectral bands from approximately 2-5 kHz in the audible region up to 200 kHz in the ultrasonic region [1]. SAS images from the high-frequency bands will provide the high resolution and high contrast already offered by conventional SAS [2]. The other bands will provide an enhanced capability to characterise the seafloor via acoustic spectroscopy (as in satellite and airborne electromagnetic multispectral systems [3]). Moreover, the low frequency bands will penetrate beneath the seafloor to enable detection of buried objects and inside objects to excite resonant modes specific to internal structures and composition.

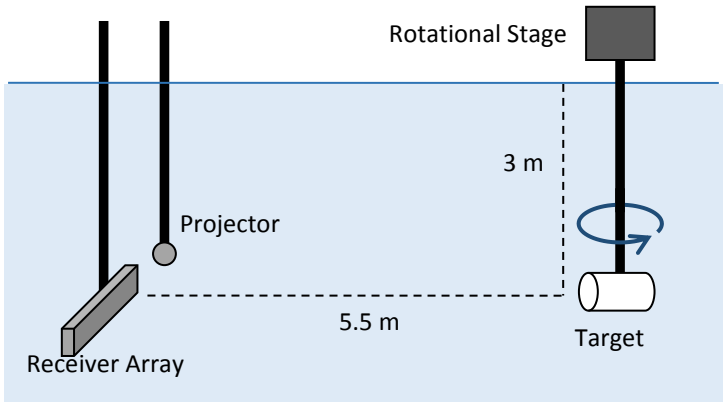
Opportunistic target measurements have been made using a basic prototype of the AquaPix Multispectral SAS during early development and testing. A simple aluminium pipe target was selected with a 12-inch outer diameter, 24 inch length, and 0.5-inch wall thickness; this resembles an aluminum pipe target deployed in related US studies [4,5].

2. EXPERIMENTAL METHOD

The experiment was carried out from a pontoon in the Kelk Lake underwater testing facility in the UK. Ideally, the measurements would have been made in the free field. However, for simplicity, the target was bolted to a pole via a welded flange and suspended from the rotational stage on the pontoon. (In a dedicated experiment, more effort would have been made to minimise the influence of the mounting structure.). Two projectors covering the bandwidth from 15 kHz to 120 kHz and the wideband receiver array were suspended from poles at a distance of 5.5 m from the target. The target was suspended at a depth of 3 m and the water depth was approximately 9 m. An illustration of the experimental geometry and a photograph of the aluminium pipe target is shown in Fig. 1.

The target was rotated through 360 deg and wideband acoustic scattering measurements were made at increments of 0.25 deg. Repeated "baseline" measurements were then made without the target but with the pole and flange only. The purpose of these measurements was to determine the influence of the mounting structure and other reverberation for baseline subtraction.

(a)



(b)



***Fig. 1: Experimental setup**: (a) measurement geometry; (b) aluminium pipe target suspended from the rotational stage.*

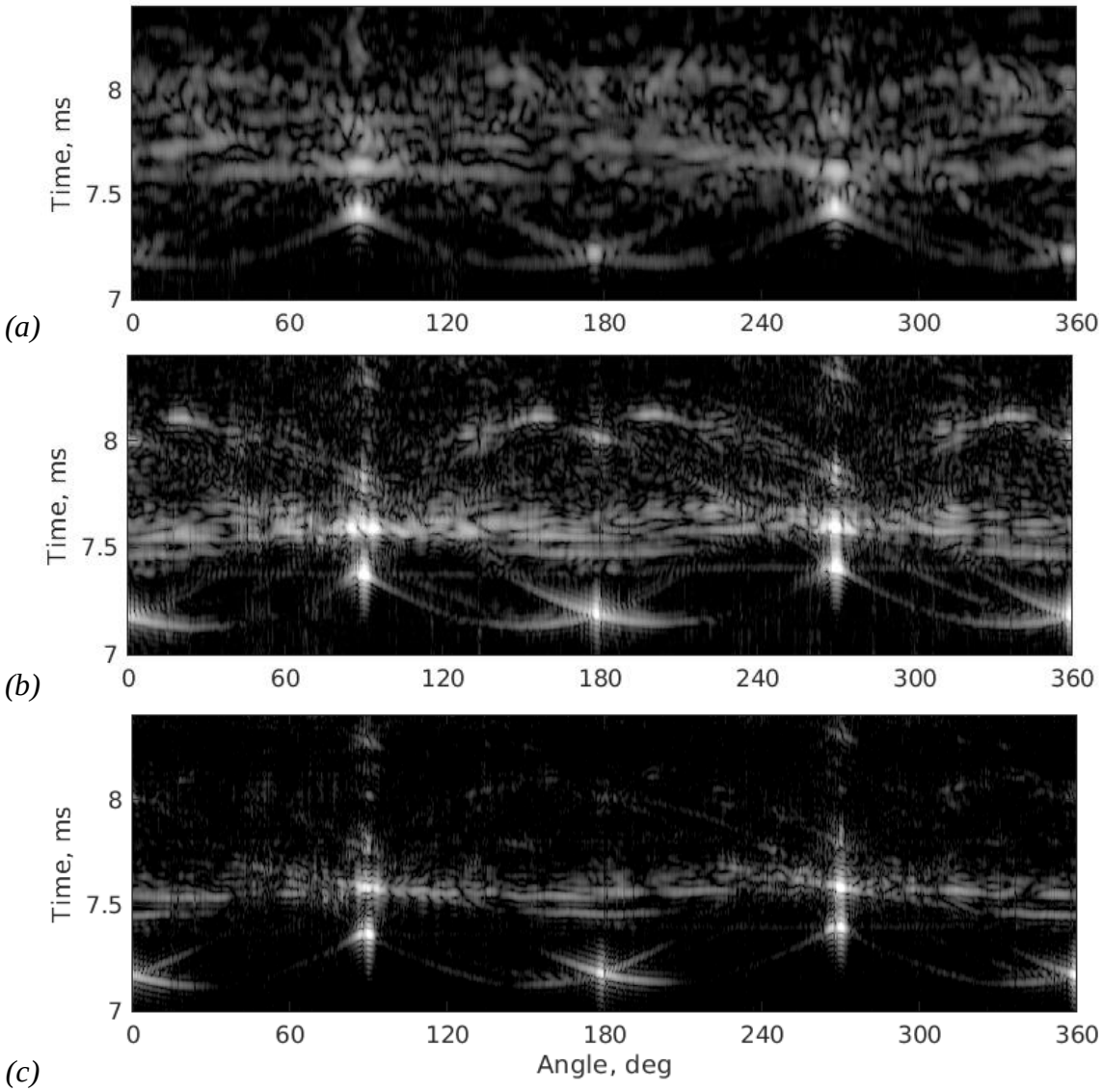


Fig. 2: Multispectral circular SAS data *from the aluminium pipe target and mounting structure over a 40 dB dynamic range: (a) 15-40 kHz; (b) 40-80 kHz; and (c) 80-120 kHz. (Baseline data and baseline subtraction are not shown.)*

3. PRELIIMINARY RESULTS

The raw echo data is shown in Fig. 2 for three spectral bands: 15-40 kHz, 40-80 kHz, and 80-120 kHz. These bands were selected for convenience due to the opportunistic nature of the experiment and we have chosen to denote them as “low”, “medium”, and “high”-frequency (LF, MF, and HF). The raw data have been processed into various useful data products: 1) circular SAS images from each band, 2) a false-colour image fusion from all three bands, and 3) the acoustic colour signature from all bands.

The circular SAS images from each band are shown in Fig. 3(a-i). The baseline subtraction was reasonably effective at removing the influence of the mounting structure. The images from the different bands were observed to exhibit different characteristics. The HF band shows the basic geometrical structure whereas the MF and LF bands contain non-geometric features that we attribute to elastic scattering. In the MF band, strong features can be observed in the internal corners of the target image. In the LF band, what appears to be resonant “ringing” can be observed behind the geometrical features However, further analysis is required to properly explain these observations.

A false-colour image fusion was created by encoding the three spectral bands into three RGB colour channels: LF – red, MF – green, and HF – blue. This is shown in the bottom row of Fig. 3(j-l). It presents a more compact and intuitive representation of the multispectral imagery. The popular acoustic colour representation [6,7] is also provided in Fig. 4, showing the angle and frequency dependent scattering characteristics of the target.

4. SUMMARY

Preliminary results from the AquaPix Multispectral SAS prototype have been presented. These provide an early indication of the types of data product that will be generated by this new product. Multispectral image fusion conveys literal *acoustic colour* information by encoding it together with the high resolution SAS images into a single RGB image. The aluminium pipe test target was shown to exhibit different acoustic characteristics in the different spectral bands and this highlights the added value of multispectral SAS for enhanced target classification.

5. ACKNOWLEDGEMENTS

The authors acknowledge Alba Ultrasound (UK) for producing the prototype wideband receiver array. They are also grateful to Mr Ian Bayles at Neptune Sonar (UK) for his assistance during the experiments. Dr Rymansaib and Dr Hunter thank the UK Engineering and Physical Sciences Research Council (EPSRC) for their financial support under grant no. IAA-322.

REFERENCES

[1] **Kraken Robotic Systems Inc.**, Kraken Announces AquaPix Multispectral SAS, *Press Release*, https://krakenrobotics.com/kraken-announces-aquapix-multispectral-sas, 14 May, 2018.

[2] **D. Shea, P. Crocker, J. Dillon, and S. Chapman**, AquaPix - a low-cost interferometric synthetic aperture sonar for AUVs: sea trials and results, In *18th International Symposium on Unmanned Untethered Submersible Technology*, Portsmouth NH, USA, August 2013.

[3] **N. Yokoya, C. Grohnfeldt, and J. Chanussot**, Hyperspectral and Multispectral Data Fusion, *IEEE Remote Sensing and Geoscience Magazine*, 5 (2), June 2017.

[4] **K.L. Williams, S.G. Kargl, E.I. Thorsos, D.S. Burnett, J.L. Lopes, M. Zampolli, and P.L. Marston**, Acoustic scattering from a solid aluminum cylinder in contact with sand sediment: measurements, modelling, and interpretation, *Journal of the Acoustical Society of America*, 127 (6), June 2010.

[5] **K.L. Williams, S.G. Kargl, and E.I. Thorsos**, TREX13 target experiments and case study: comparison of aluminum cylinder data to combined finite element / physical acoustics modeling, *Journal of the Acoustical Society of America*, 136 (4), October 2014.

[6] **A.J. Hunter, R. van Vossen, B.A.J. Quesson, and A.L.D Beckers**, Acoustic signatures of underwater UXO measured by low frequency broadband SAS, In *1st International Conference and Exhibition on Underwater Acoustics*, Corfu, Greece, June 2013.

[7] **T.M. Marston, P.L. Marston, and K.L. Williams**, Scattering resonances, filtering with reversible SAS processing, and applications of quantitative ray theory, In *IEEE/MTS Oceans Conference*, Seattle WA, USA, September 2010.

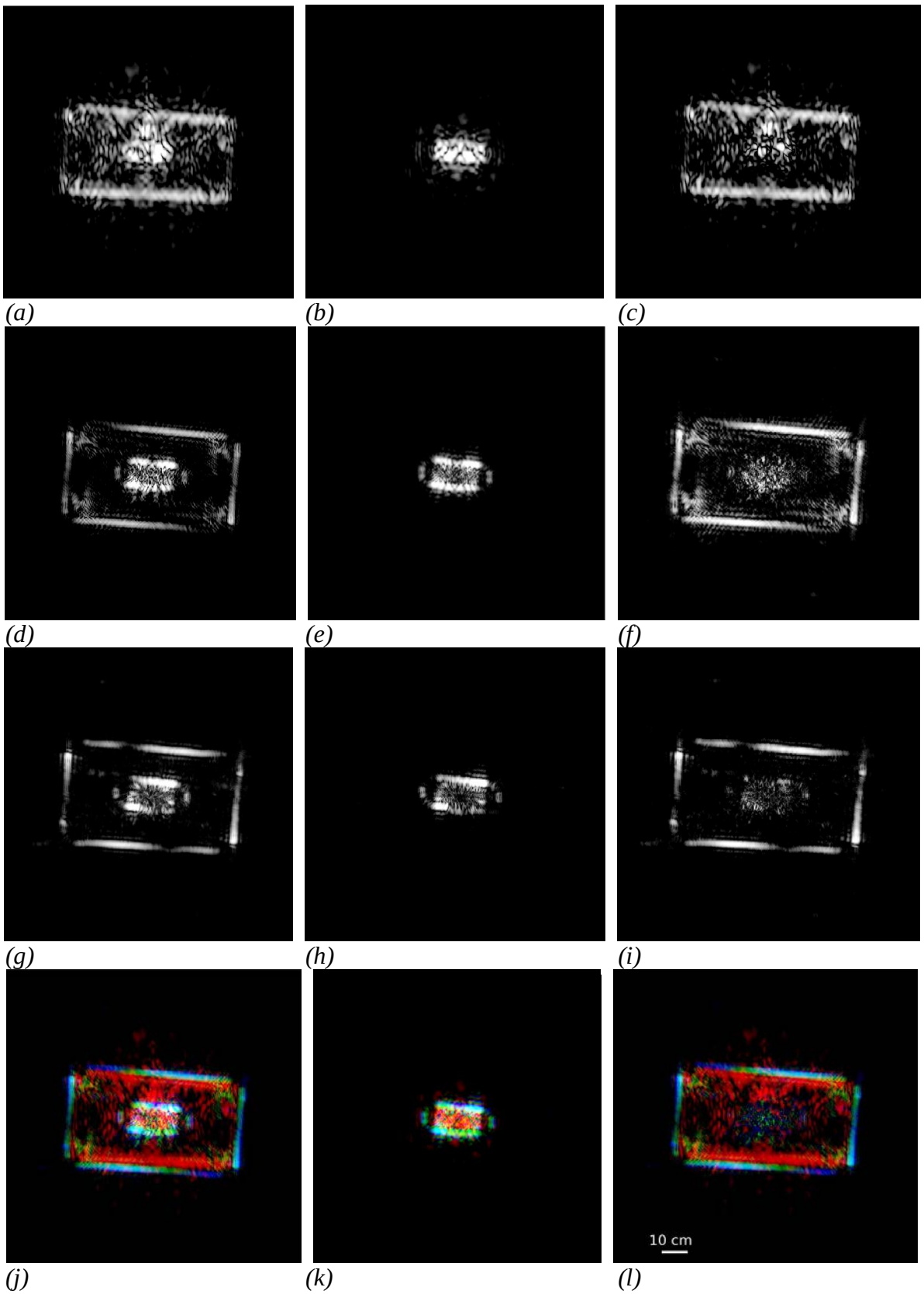


Fig. 3: Multispectral circular SAS images *of the aluminium pipe target over a 10 dB dynamic range: (a,b,c) 15-40 kHz; (d,e,f) 40-80 kHz; (g,h,i) 80-120 kHz; (j,k,l) multi-band fusion with the images from the three bands encoded in red, green, and blue channels respectively; (left column) target and mounting structure; (middle column) baseline with mounting structure only; (right column) target after baseline subtraction.*

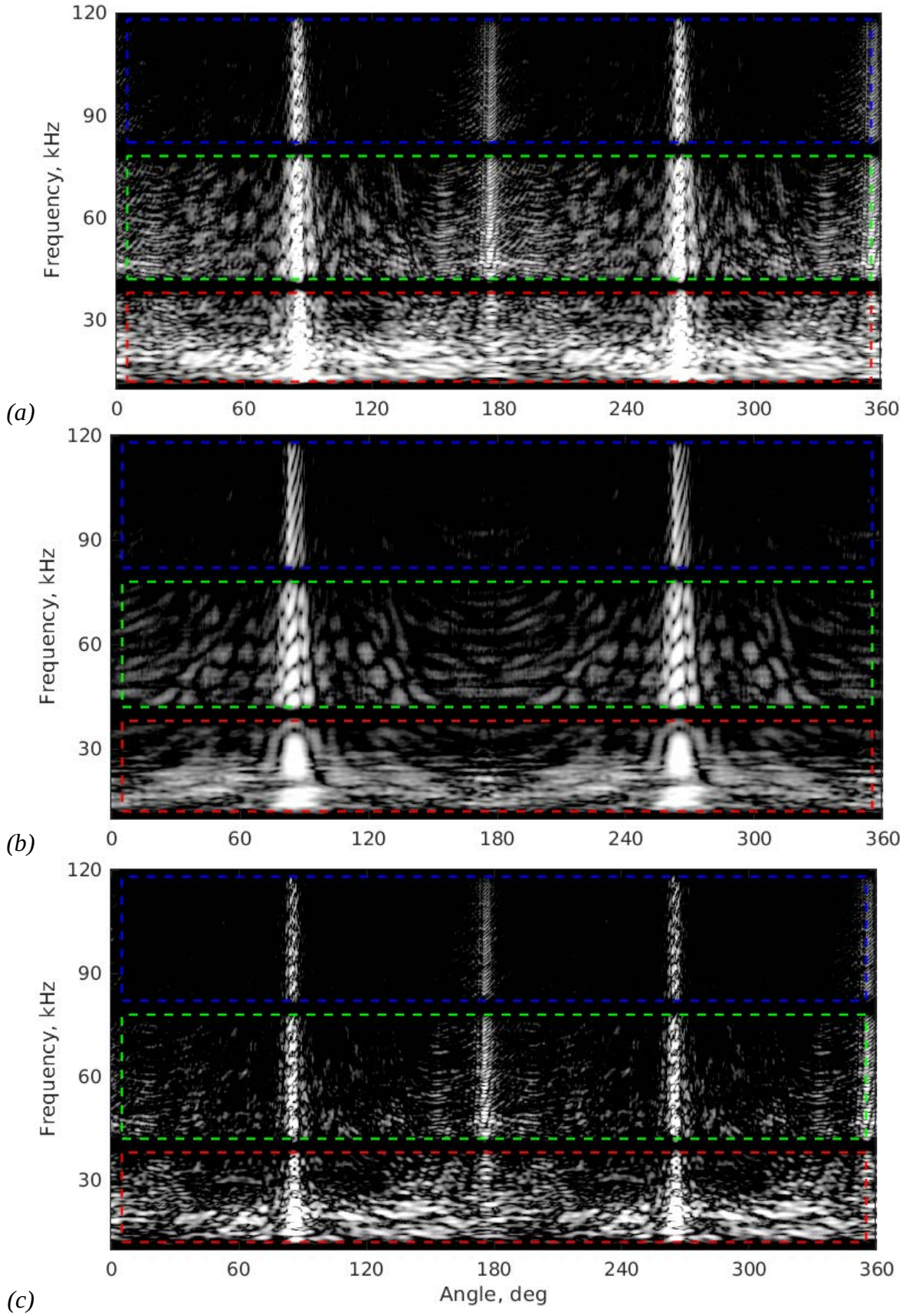


Fig. 4: Acoustic colour signature *of the aluminium pipe target over a 10 dB dynamic range: (a) target and mounting structure; (b) baseline with mounting structure only; and (c) target after baseline subtraction. The red, green, and blue boxes indicate the three spectral regions selected for multispectral image fusion.*

COMPARING TARGET ECHO STRENGTH MODELS OF A GENERIC SUBMARINE

A.C. Curtis, D. Nigro, R.J. Harter, M.J. Stirland

Thales UK, Ocean House, Templecombe, Somerset BA8 0DH, UK
tel: +44(0)1963 372039
email: alan.curtis@uk.thalesgroup.com

Abstract: *Thales UK carries out work associated with the underwater acoustic signatures of a variety of platforms, with typical dimensions ranging from a few metres to hundreds of metres, and covering frequencies from a few Hz to hundreds of kHz. Supporting these projects is a comprehensive target echo strength capability, including in-water test facilities and modelling tools. This paper discusses some of the different types of model available to calculate the target echo strength of underwater objects.*
Modelling tools are used for different purposes ranging from initial concept - stage design through to more detailed assessments of specific signature features and signature reduction measures. The models employed include analytic models based on simple, rigid geometric shapes; models for complex rigid bodies based on geometric optics methods; physical optics models for elastic bodies; and finite element analysis for arbitrary elastic bodies. The tools can be applied at differing levels of complexity and fidelity to detail, and may assume perfect reflection or utilise a full elastic solution. The use of these models is discussed, and the paper also describes a number of methods for representing the target echo strength predictions, including graphs of aspect - dependent integrated echo intensity; "hourglass" plots of echo intensity as a function of time of arrival and aspect; and frequency - azimuth plots.
The use of these modelling tools is demonstrated with the aid of particular examples, and results are presented for the predicted target echo strength of the BeTSSi generic submarine, which was the subject of an international collaborative workshop at The Hague in 2016. The paper discusses the differences between the predicted results from the various models, and considers the significance of these differences when selecting methods and applying the tools at different frequencies and for different purposes.

Keywords: *Target Echo Strength, submarine, BeTSSi, modelling*

1. TYPES OF TARGET STRENGTH MODEL

Many workers have practical reasons for wishing to predict and understand the acoustic Target Echo Strength (TES) of objects in water; modelling tools are used for different purposes and at different stages in the development of systems. Different tools are employed to provide predictions at differing levels of complexity and fidelity to detail appropriate to the needs, which may range from exploration of major parameters at the stage of initial concept studies, to detailed models of specific structures used in the assessment of final designs.

1.1. Empirical models

In the initial stages of a project, estimates may be obtained from empirical relationships such as the general trend of TES against displacement derived from a body of measurements or model results. Alternatively, a comparison with a similar target with known TES may provide a good basis for estimation.

1.2. Analytic Solutions.

The TES of any rigid body of canonical shape can be computed exactly by solution of the wave equation with the relevant boundary conditions at the target surface in a suitable coordinate system. This is only practicable for simple shapes; exact solutions exist for a sphere and a cylinder, but other closed form solutions can be obtained as approximations, valid under specified conditions such as the solution for an arbitrarily curved convex surface with large radii of curvature [1] (where “large” means with respect to the acoustic wavelength). Formal methods have also been used to derive analytic solutions for some more complex objects formed from the combination of primitive shapes (e.g. a cone-sphere) where appropriate conformal transformations can be identified, but these have limited applicability in TES problems. One way in which the analytic solutions (exact or approximate) can be used to address real-life scattering problems is by creation of a model representing the target as a combination of simple shapes, and combining the scattered pressures from each shape calculated separately [2]. This method neglects the influence of the “missing” surfaces in the solution for each primitive shape and no formal treatment of the errors introduced by the method seems to have been published, but the technique allows a rapid determination of the relative importance of different parts of the target. Thales UK has developed the THREBITS modelling tool utilising this approach and successfully used it in the early design optimisation studies of a number of underwater systems. This tool provides results quickly, and therefore permits the exploration and comparison of the TES of a range of geometries.

1.3. Geometric Acoustics

Geometric acoustics or ray methods are applicable where the target dimensions are much greater than the acoustic wavelength; the scattered field can be represented as an expansion in terms of inverse frequency, in which the first term is the geometric acoustics result. The basis of the method is the computation of the range of angles over which a bundle of rays (assumed to be parallel when approaching the target) is spread after reflection – each ray being reflected at the angle given by the law of reflection. The number of scattered rays passing through a unit surface in a given direction gives the scattered field pressure in that direction. Modelling

tools using this method can deal with complex target geometries including re-entrant or concave surfaces and have relatively short computation times, making this the method of choice for high frequency solutions and reverberant cavities. The target is considered to be a purely passive geometric object and there is no consideration of effects due to the dynamic response of the scatterer. In many applications, this is an adequate approximation - for example when modelling a submarine clad with pressure-release tiling. The effects of absorption can be approximated by inclusion of an appropriate reflection coefficient at the surface, which may be dependent on the angle of incidence. The basic ray tracing approach allows only specular reflection and predicts hard shadow edges. The use of a finite number of rays means that some reflection paths will always be missed, and the method tends to be inaccurate over regions where the scatterer has high curvature. There is no way to determine the number of rays needed to achieve a given accuracy; in spite of these limitations, comparisons between ray model results and exact solutions often indicate better agreement than the underlying assumptions would suggest [3].

1.4. Physical Acoustics extensions to Geometric Acoustics Models

Ray theory does not describe phenomena such as interference and diffraction, and fails to account for the presence of a scattered field in a shadow region where there is no direct line of sight, which can be accounted for by energy scattered or diffracted at the target surface. Physical acoustics methods take into account these phenomena and thereby improve the predictions, particularly at lower frequencies. Some physical acoustics models add second-order terms to the geometric acoustics result to represent the effects of diffuse reflections. A common approach is to launch rays in non-specular directions with the overall spatial distribution of energy obeying Lambert's Law, with the amplitude described by effective scattering coefficient. Diffraction arises where incident rays strike edges, resulting in a distribution of energy in a range of directions; or are at grazing incidence to surfaces, resulting in the generation of creeping waves which follow the surface. Various laws of diffraction are used to characterise the diffracted rays, including the Geometrical Theory of Diffraction (GTD) [4]. This introduces additional rays using diffraction coefficients determined from canonical problems such as the infinite wedge. The GTD allows for propagation around obstacles and into shadow zones, but fails near reflection and shadow boundaries. This is overcome by the Uniform Theory of Diffraction [5] through the use of transition functions that provide for a continuous and bounded diffracted field.

1.5. Tangent Plane Approximations

Kirchhoff / Tangent Plane (KTP) approximation methods solve the Helmholtz-Kirchhoff integral by dividing the target surface into a mesh of plane elements or facets. Using the Kirchhoff approximation, the pressure and particle velocity on each element are approximated with the values that would exist if the surface was infinite in extent. The reflection from each element can then be found analytically and the TES of the surface can be calculated as the coherent sum of the contributions from the individual elements. The method can be applied to rigid surfaces, or angle-dependent reflection coefficients may be applied to represent real materials. Advantages include rapid execution times even with complex geometry; the disadvantages include the treatment of the surface as a purely passive scatterer, without fluid/structure interaction effects such as resonances, and the lack of edge diffraction effects. The method is less accurate for bistatic TES, particularly forward scattering, because the assumption is made that the acoustic pressure is zero on all elements of the surface in the shadow zone on the far side of the target from the source. Thales UK has implemented this

approach in the SCATTER model which incorporates approximate methods for bounding the TES resulting from penetration of surfaces and subsequent scattering.

1.6. Numerical solutions of the wave equation

Both boundary element (BE) and finite element (FE) methods have been applied to develop numerical solutions for the TES. FE uses elements to discretise the entire domain leading to harmonic solutions of the wave equation with the relevant boundary conditions. BE discretises the scattering surface and solves the Helmholtz-Kirchhoff integral equation; the solution in the fluid domain can then be obtained by integration over a surface. In both methods the necessary discretisation is dependent on the frequency, rather than the geometry, and in FE a sufficient volume of the fluid domain must be meshed to avoid near-field effects. BE methods avoid the need to mesh the domain but are more computation-intensive for a given number of nodes. Both approaches are thus restricted to comparatively low frequencies by the computation time and memory requirements. Care must be taken when using commercial general purpose FE packages for underwater TES calculations because approaches typically taken to reduce computation overheads, which may be acceptable to the majority of users, are not necessarily appropriate to modelling of highly fluid-loaded elastic structures. For this reason, Thales UK prefers to utilise codes such as PAFEC and the proprietary tools FELINE and SuperFELINE which were developed specifically for applications involving fluid loaded structures.

2. THE BETSSI SUBMARINE TARGET

This paper demonstrates the use of some of the models available to Thales UK, using the example of the Benchmark Target Strength Simulation (BeTSSi) generic submarine model which was the subject of a collaborative workshop at The Hague in 2016 comparing the predictions of different models from a number of teams. The BeTSSi Submarine definition was developed by FWG in Germany [6] and was designed to facilitate an international workshop held at Kiel, Germany in 2002 [7] to compare numerical codes for prediction of TES. The model is a simplified generic representation of a typical diesel-electric submarine of around 1700 Tonnes displacement, with the external geometry simplified to ease the creation of input descriptions for different models, and with limited internal structure – in particular, rib stiffeners and internal decks are omitted. The model does however include a representation of free-flooded regions containing structures including bulkheads and decks, torpedo tubes and a sonar flat in the bow area and a variety of simple structures in the fin. The external form of the model and the internal components are shown in Fig. 1.

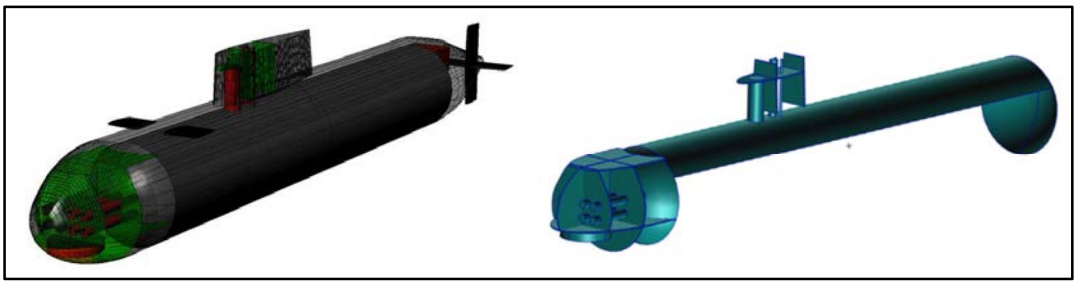


Fig. 1: The BeTSSi submarine model. Left: overall view, right: internal structures.

3. BETSSI MODEL RESULTS

3.1. Analytic model: THREBITS (with simplified geometry)

The first result shows the prediction by the Thales THREBITS tool, using a hemi-ellipsoid, cylinder and truncated cone, surmounted by a vertical ellipsoidal cylinder, to represent the BeTSSi submarine external form. The individual TES contributions from these elements have closed-form results which are computed and added coherently to produce the results shown in Fig. 2. The contribution of the individual elements can also be assessed; for example, the contribution of the hemi-ellipsoid element representing the bow is shown. The THREBITS model does not require any surface generation and meshing and this makes it cheap to run to compare different hull forms. For example, the overall length can be increased, resulting in a stronger broadside TES peak and movement of the tail-cone peak as shown (at lower angular resolution) in the upper right plot of Fig. 2. The THREBITS model can also provide bistatic predictions, by utilising more elaborate equations; sample bistatic results are also shown in Fig. 2.

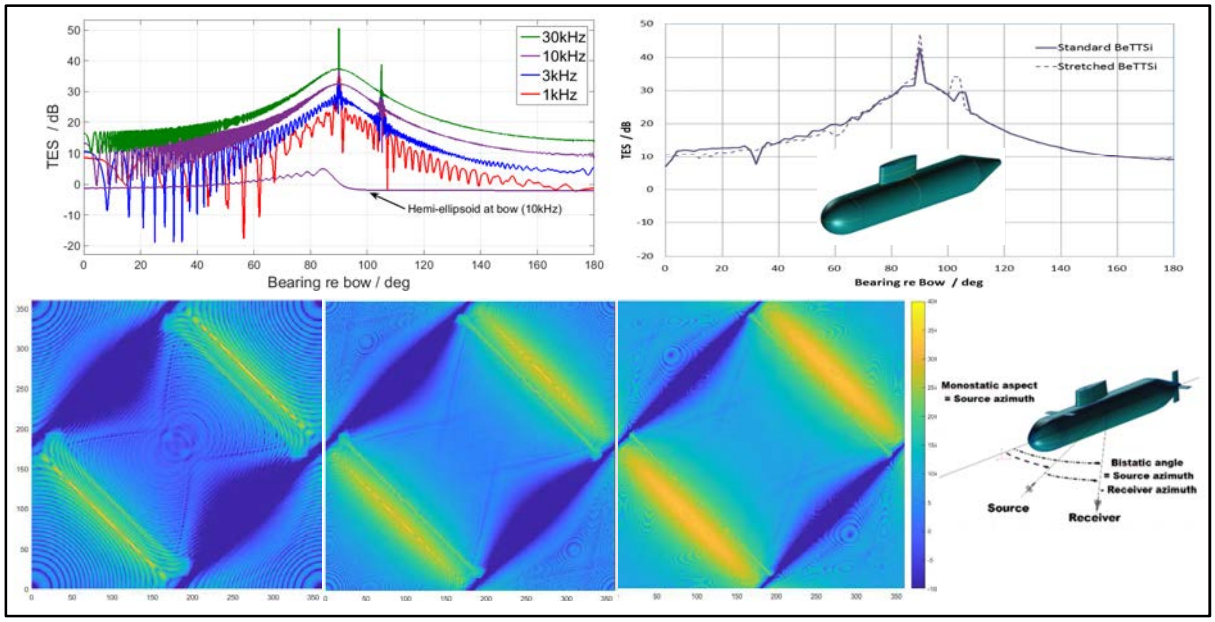


Fig. 2: Analytic THREBITS TES predictions for a simplified BeTSSi submarine model. Upper left: monostatic TES prediction; upper right: effects of changing length (10kHz); inset: simplified model. Lower: bistatic TES prediction (ordinate: receiver angle; co-ordinate: source angle); left: 1kHz; centre left: 3kHz; centre right: 10kHz; right: angle definitions.

Analysis of these results demonstrate that the largest peaks in the TES are generated by the beam-on reflection from the cylindrical section and the reflection from the tail cone at the cone semi-angle. Comparison with the plots for individual components shows that the fin dominates over most of the azimuthal range. For example, at 10kHz the hemi-ellipsoid at the bow contributes just -1dB at 0 deg (bow-on) rising to a maximum of 5dB at 90 deg. At angles in the bow quarter (between 0 deg and 90 deg), the combination of the reflections from the front of the hemi-ellipsoid and the leading edge of the fin results in interference fringes. In the aft quarter, such fringes are only evident at the lower frequencies as at higher frequency the tail cone response is confined to a narrow range of angles. Note also that the truncated cone was not terminated by a disc so there is no strong reflection at 180 deg.

3.2. Tangent Plane Model: SCATTER (with simplified geometry)

The simple analytic THREBITS model results shown above can be compared with the results of a KTP model of the same geometry (with the exception that here the tail cone is closed at the end), calculated using the Thales SCATTER model (Fig. 3).

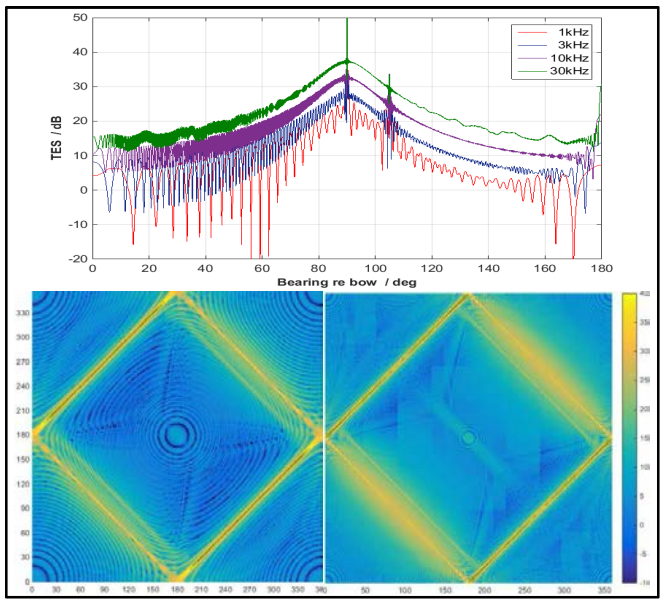


Fig. 3: SCATTER TES predictions for the simplified BeTSSi submarine model. Upper: monostatic TES. Lower: bistatic TES (axes as Fig. 2); left: 1kHz; right: 3kHz.

Apart from the features close to stern-on which are associated with the closure of the tail-cone, the broad characteristics of the results (Fig. 3) are the same although at the highest frequency the result shows some ripples which are an indication that a finer mesh geometry is required to ensure the facet representing the local surface reflects with the correct phase.

3.3. FE Model: SuperFELINE (axisymmetric approximation)

In the Thales SuperFELINE model the solution is decomposed into circumferential Fourier modes which allow more rapid solution for axisymmetric structures. Fig. 4 shows results of a prediction for an axisymmetric representation of the BeTSSi submarine.

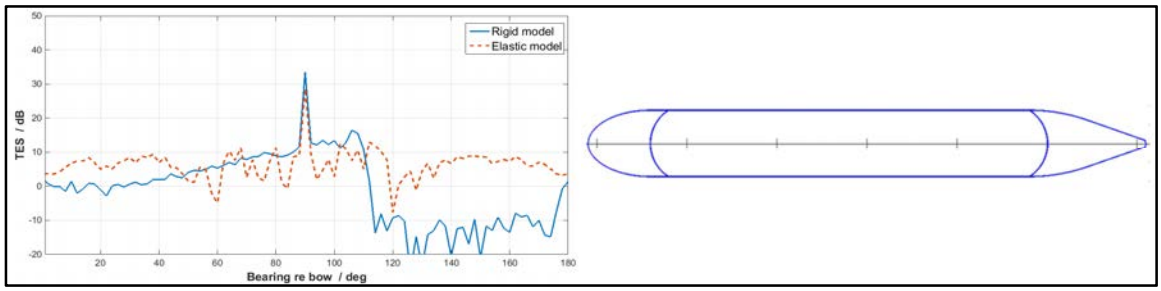


Fig. 4: SuperFELINE predictions for an axisymmetric representation of the BeTSSi submarine model. Left: TES at 1kHz; right: the model geometry.

The example results in Fig. 4 have been computed at reduced angular resolution and show the difference between the TES of a rigid structure and a fully elastic structure. Where applicable, this method shows features associated with resonances and modal behaviour, and in the example the effects of penetration through the outer casing are clearly seen.

3.4. Tangent Plane Model: SCATTER with true geometry

The SCATTER model uses the KTP method and can be applied to arbitrarily complex geometry, and this section gives results for a SCATTER model of the true BeTSSi geometry as defined in Fig. 1. The Thales implementation of the method includes an approximate treatment of acoustic penetration by calculating the average transmitted intensity through the outer surface, followed by scattering by any underlying structure. Fig. 5 below shows the SCATTER result for the true BeTSSi true geometry with both rigid boundaries and realistic elastic boundaries, resulting in transmission into internal spaces.

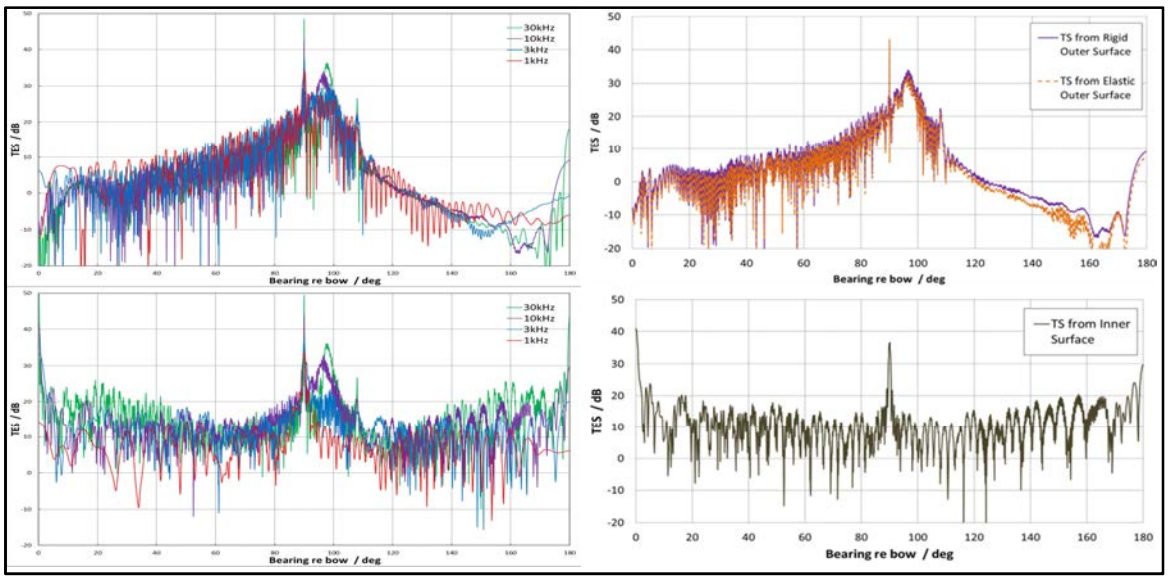


Fig. 5: SCATTER predictions for an exact BeTSSi submarine model. Upper left: rigid boundaries; upper right: TES from outer surface only at 10kHz, rigid and elastic. Lower left: resultant TES for full elastic model; lower right: TES from inner structure at 10kHz.

The major differences between these results and the earlier results for the simplified geometry arise from the more accurate representation of the fin – using the true NACA geometry rather than an ellipsoid results in an asymmetric TES with a peak around 97 deg, and significantly lower levels in the stern quarter. The simpler model is however shown to be sufficiently accurate for many purposes. The addition of penetration effects produces new peaks, notably at 0 deg and 180 deg attributed to internal bulkheads, and significantly higher levels elsewhere due to the complex internal structure.

The SCATTER model also allows results to be presented in other formats, which can be useful aids to understanding the TES. Fig. 6 shows an “hourglass” or downrange plot which shows the time of arrival of each part of the reflected signal. The plot has been annotated to show which part of the structure gives rise to each reflection. Also shown is a frequency-azimuth plot which shows the dependence of TES on frequency, an elevation-azimuth plot which shows the TES in two dimensions, and a phase map which shows the relative phase of the signal contributions from various parts of the target. The elevation-azimuth plot and phase map both highlight the significant reflection from the fin at small elevation angles.

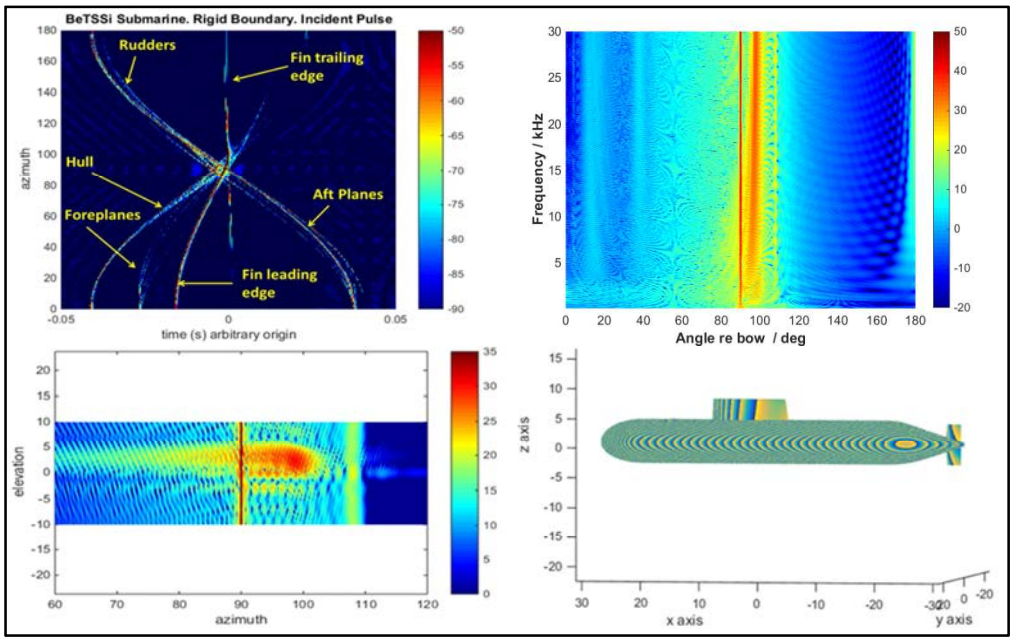


Fig. 6: Other representations of SCATTER predictions. Upper left: downrange plot for rigid model; upper right: Frequency-Azimuth plot for full elastic model. Lower left: Elevation-Azimuth plot; lower right: phase map (100 deg azimuth, 2.5 deg elevation, 3kHz).

4. ACKNOWLEDGEMENTS

The authors wish to acknowledge the contribution of many colleagues at Thales UK and with other experts in the field, in particular D Nunn and D Williams of DSTL.

REFERENCES

[1] **J.J. Bowman, T. Senior, P. Uslenghi**, *"Electromagnetic and Acoustic Scattering by Simple Shapes"*, North-Holland Publishing (1969)

[2] **D.M. Drumheller, L.E. Gilroy and M.G. Hazen**, *"The Bistatic Acoustic Simple Integrated Structure (BASIS) Target Strength Model"*, Technical Report NRL/FR-MM/7140-02-10,019, US Naval Research Laboratory (2002)

[3] **L. Gilroy & I. Karasalo**, *"Target Echo Strength Software Benchmarking: Tasks 1 and 2 Under Canada-Netherlands-Sweden Project Arrangement on Target Echo Strength"*, Report DRDC-RDDC-2017-R091, DRDC (2017)

[4] **J. B. Keller**, "Geometrical theory of diffraction", *J. Opt. Soc. Am.* 52(2), 116–130 (1962).

[5] **R. Kouyoumjian & P. Pathak**, "A uniform geometrical theory of diffraction for an edge in a perfectly conducting surface", *Proc. IEEE* 62(11), 1448–1461 (1974).

[6] **Ch. Fiedler and H.G. Schneider**, *"BeTSSi-Sub – Benchmark Target Strength Simulation Submarine"*, Technical Report, FGW (Kiel 2002).

[7] **H.G. Schneider, R. Berg, L. Gilroy, I. Karasalo, I. MacGillivray, M. TerMorshuizen, A. Volker**, "Acoustic scattering by a submarine: Results from a benchmark target strength simulation workshop", In *10th International Congress on Sound and Vibration*, Stockholm, 7-10 July 2003, eds. H. Boden, A. Nilsson, International Institute of Acoustics and Vibration (2003)

ACOUSTIC SCATTERING FROM THIN-WALLED CYLINDERS: EXPERIMENTAL VALIDATION OF A NOVEL BOUNDARY ELEMENT METHOD

Anatoli Tsinovoy[a], Evgeny Chernokozhin[b], Matan Kahanov[a], Amir Boag[b]

[a] Rafael Advanced Defence Systems Ltd., POB 2250(19), Haifa, 3102102 Israel
[b] Tel Aviv University, Tel Aviv, 6997801 Israel

Anatoli Tsinovoy, Rafael Advanced Defence Systems Ltd., POB 2250(19), Haifa, 3102102 Israel, Fax: +972-733355895
E-mail: anatolt@rafael.co.il

Abstract: *We measured the monostatic target echo strength (TES) of a thin-walled aluminium cylinder, flooded with water, as a function of azimuth aspect angle and frequency. We present the near field estimate of the TES. Various scattering mechanisms are observed and delineated. In order to facilitate comparison with theory, reduced sets of data points encompassing the most prominent scattering features were chosen. These reduced sets were simulated using a novel Boundary Element Method for acoustically thin targets. As the approach does not take elastic waves into account, a rich comparison is found, with some features being well-accounted for, while others are absent. Of note is the acoustic regime explored, with the cylinder length and radius, L and R, large with respect to the wavelength λ, L,R>> λ, but the wall thickness t is small with respect to the wavelength. This allows us to explore the regime t<<λ that has not been extensively studied in experiment.*

Keywords: *Target Echo Strength; Numerical Modelling; Boundary Element Method*

1. INTRODUCTION

Knowledge of the acoustic target echo strength (TES) of underwater bodies is essential for many underwater applications. In the design phase of underwater vehicles and assemblies the TES is often a design goal, achieved using validated theoretical models. Though for some models validation by comparison to exact solutions (Finite Element Methods, Method of Moments) is possible, for many scattering objects and frequencies such calculations are intractable. As a result, validation of some theoretical models must be performed by comparison with experiments. Here we present measurements of the monostatic target echo strength of a thin-walled aluminium cylinder, flooded with water, as a function of azimuth aspect angle and frequency, performed in the acoustic tank at the Israeli national underwater test facility.

As the length of the cylinder was large with respect to the wavelengths measured, some scattering features were measured in the near field, and others in the far field.

Our measurements are compared with the predictions of a novel Boundary Element Method based on the Multilevel Nonuniform Grid approach for acoustically thin targets [1]. As the approach does not take elastic or guided waves into account, a rich comparison is found, with most features being well-accounted for, while others are absent.

2. METHODS

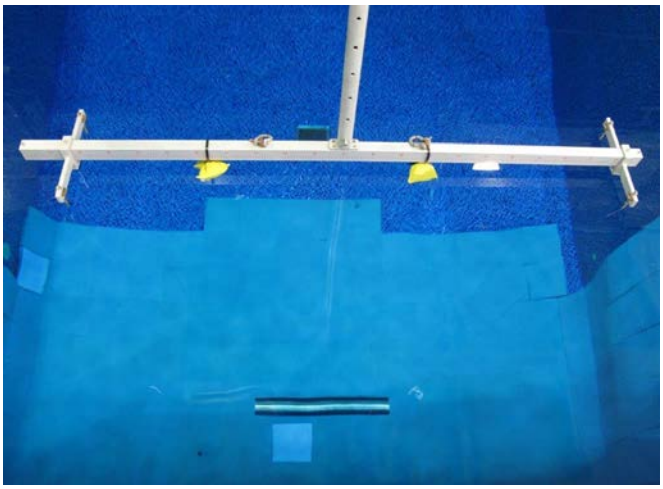


Fig. 1: Experimental setup, cylinder flooded to 97% by volume, lowered to a depth of 5m.

The target was illuminated using a directional transducer with a resonant frequency of 25 kHz. The transmission signal was a pulse with linear frequency modulation spanning the range 20 kHz to 50 kHz with a duration of 250 ms. Matched-filtering allowed separation in the time domain between the target echo and reverberations from the acoustic tank despite the tank being much smaller than the acoustic length of the transmitted pulse. A separate measurement of the tank reverberation response was performed and coherently subtracted from the target response. This reduced interfering signals further. The measurements were carried out in two configurations. The transmitter was positioned 8.5m from the target. An omnidirectional hydrophone was placed 4.5m

from the transmitter along the line connecting the transmitter and target, this is the "**quasi monostatic configuration**". A directional hydrophone was placed 1.5m next to the transmitter, forming a bistatic angle of $2\beta \approx 10°$, this is the "**slightly bistatic configuration**". All measurements are in a plane containing the cylinder's axis of symmetry (zero elevation) (see Fig. 1). The flat end-caps of the cylinder have radius R=8.4cm and thickness $t_{\text{End-cap}}$=3mm. The side of the cylinder has length L=1.27m and thickness t_{Side}=0.68mm.

The target echo pressure $p_{rec}(\varphi, f)$ is equal to the source pressure level $R_{\text{ref}}\, p(R_{\text{ref}})$ (usually reported as the pressure at 1 m, multiplied by 1 m) with two way propagation to the target. This relation is easily inverted for a near field estimate for the TES:

$$S(\varphi, f) \equiv \frac{R_{\text{Tx-Target}} R_{\text{Target-Rx}} e^{-i\frac{2\pi f}{c_w}\left(R_{\text{Tx-Target}} + R_{\text{Target-Rx}}\right)} p_{rec}(\varphi, f)}{R_{\text{ref}}\, p(R_{\text{ref}})} \tag{1}$$

where φ denotes the observation angle (see Fig. 2) and c_w is the speed of sound in water. In the limit where the distances of the transmitter and the receiver from the target, $R_{\text{Tx-Target}}, R_{\text{Target-Rx}}$, tend to infinity, this is exactly the TES.

Extraction of the TES from the received echo voltage requires knowing the transmitted waveform and the product of the transmitter and receiver responses. For the quasi monostatic configuration, the calibration is a trivial task, as the transmitted signal is directly incident on the receiver. Calibration in the slightly bistatic configuration is performed using the echo from a target of known TES (a single small Tungsten-Carbide sphere) placed at the position of the target, following the procedure presented in [2].

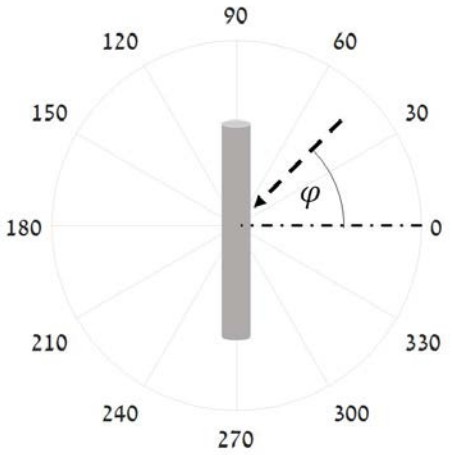


Fig. 2: Measurement geometry, end-cap incidence is at φ=90°, broadside incidence is at φ=0°.

In the theoretical calculations, the cylinders are simulated as thin inertial shells in which the elastic effects are neglected. Under the assumption that the thickness of the shell is constant, the scattered field is entirely determined by the pressure discontinuity across the shell, $p^+ - p^-$, which is proportional to the normal velocity. The air-filled cylinder is simulated as a hollow shell, in which $p^- = 0$; in this case, we have a problem of scattering by an impedance surface, formulated as an integral equation with respect to the outer pressure, p^+. In the case of the flooded cylinder, we reduce the problem to an integral equation with respect to the pressure discontinuity distribution. The integral equations are discretized using the Boundary Element Method and are solved using the Multilevel Nonuniform Grid (MLNG) approach [1], which belongs to the class of "fast" methods and can be applied to fairly large scatterers. The resulting surface distributions are then used to calculate the scattered field at the observation points and the corresponding target strengths.

3. RESULTS

The measurements were carried out at intervals of 0.4° in φ, while the angular Nyquist sampling interval for our system was $\Delta\varphi_{\min} = {360^o}/{2kd+10} \approx 0.66^o$. The far field distance at broadside incidence is on the order of 15m, and 0.5m for end-cap incidence. This means that we are in the far field with respect to end-cap incidence, but in the near field with respect to broadside incidence. Our measurements span a large bandwidth, so the band-limited impulse response of the target can be analysed alongside the frequency response. Results from the slightly bistatic configuration are presented in Fig. 3.

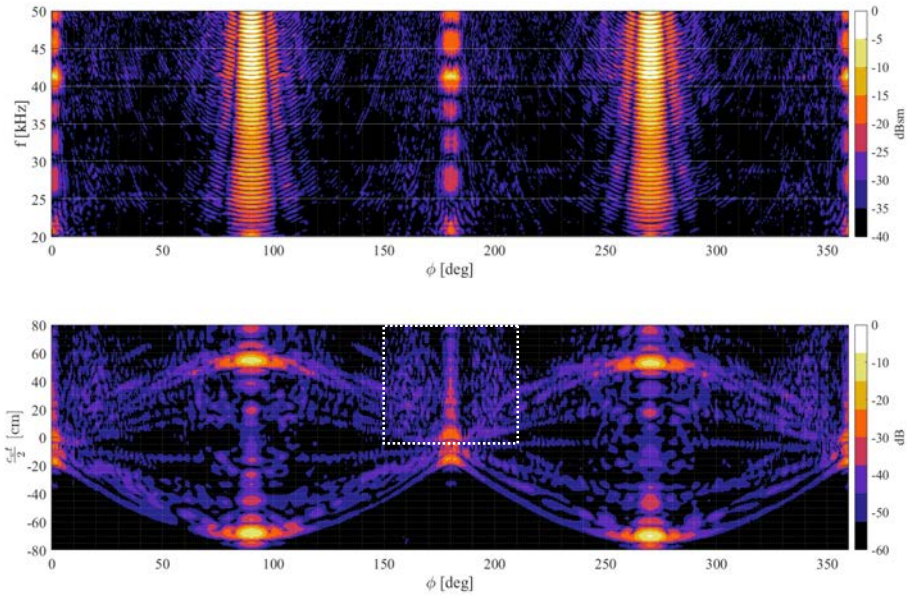


Fig. 3: TES as observed in the slightly bistatic configuration. (top) $S(f,\varphi)$ in dBsm. (bottom) $\widetilde{S}(t,\varphi)$, the Fourier transform counterpart of $S(f,\varphi)$, in dB relative to its maximum value, with the time axis scaled to the acoustic distance. Note that we compensated for the bistatic angle, by aligning the broadside echo with 0°.

Several features can be identified:

1. The echo at end-cap incidence is composed of two distinct returns. The acoustic signal is partially returned from one end-cap, and partially transmitted through the cylinder interior until it is scattered by the second end-cap. This shows as a pronounced beating in the TES with $\Delta f = {1}/{t_{\text{round-trip}}} = {c_w}/{2L} \approx 600\,\text{Hz}$.
2. The echo at broadside incidence is composed of several distinct returns also leading to a beating pattern in the TES, at $\Delta f \approx 4500\,\text{Hz}$. This corresponds to partial reflection from the cylindrical shell with transmission and subsequent reflection from the opposite end of the shell.

3. As previously shown by España et al. [3], at angles up to the shear wave coupling angle, $\gamma_T = 27°$, away from broadside incidence, there is significant scattering from guided helical waves. This feature is much more easily discerned in the time domain plot where it has been highlighted in Fig. 3 around $\varphi = 180º$. Returns associated with meridional waves are also visible in the time domain plot as distinct curves.

The simulation was carried out with incoming plane-waves, rather than with a spherical source, but with the receivers properly placed in their near field positions. In Fig. 4 we present a comparison between experiment and theory for a single frequency, $f = 27$kHz, at all incidence angles. The simulated results assumed nominal values for the speed of sound in water and for the density of aluminium. A fitting procedure was carried out in order to determine the best-fit frequency in the experimental results close to $f = 27$kHz.

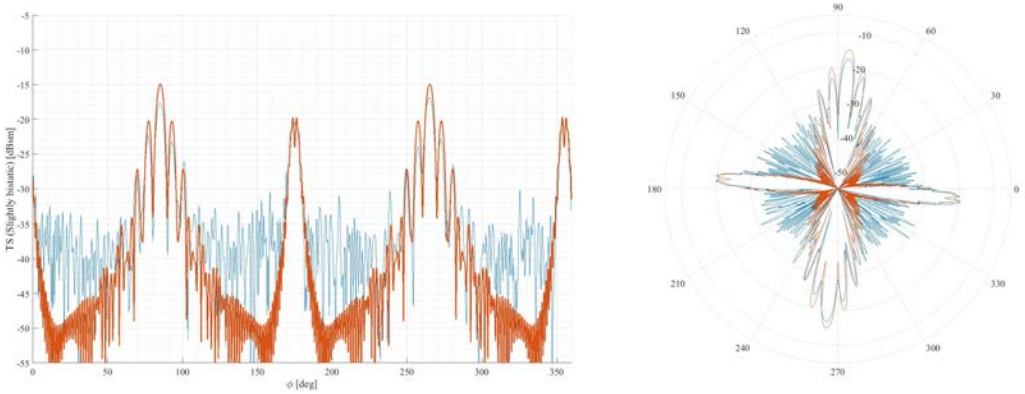


*Fig. 4: (**red**) Simulation at f=27kHz, (blue) experiment at f=27.41kHz, for the slightly bistatic configuration, Cartesian and polar plots.*

There is an excellent agreement both around broadside and end-cap incidence, demonstrating that all relevant scattering mechanisms are described by the model. The most significant discrepancy is in the guided waves around broadside incidence. The experimental uncertainty is at around -45 dBsm, so the difference is significant.

A difference of 20 m/sec in the speed of sound fully accounts for the shift in frequency. Subsequently, we scale the experimental frequency axis by a factor of (27.41 kHz/27 kHz).

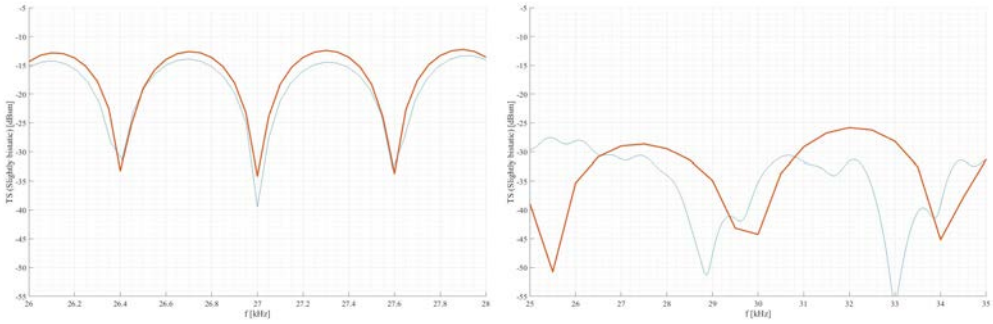


Fig. 5: (red) Simulation, (blue) experiment, for the slightly bistatic configuration at (left) end-cap incidence and (right) broadside incidence.

In Fig. 5 we present cuts along the frequency axis at end-cap and broadside incidences, with the experimental frequency axis properly scaled.

For end-cap incidence an excellent agreement is observed, both in amplitude and in beating frequency. This shows that the reflection and transmission amplitudes of the end-caps are predicted properly by the model as well as the interference between these reflections. For broadside incidence, an adequate agreement is observed, with the deep nulls observed in experiment being reproduced, albeit at slightly offset frequencies. This may imply that in addition to the waves accounted for by the model, some elastic waves may contribute at broadside incidence.

4. SUMMARY

The monostatic target echo strength of a thin-walled aluminium cylinder flooded with water was measured. The results were then used to validate a novel Boundary Element Method simulation appropriate for acoustically thin targets. Non-elastic features of the scattering were predicted with good accuracy, and an excellent agreement with the experiment results was observed where it was expected. As the elastic features are, at present, not modelled, they were absent from the model results.

5. ACKNOWLEDGEMENTS

The authors are grateful to the Israeli national underwater test facility at Rafael Advanced Defence Systems Ltd., Haifa, Israel.

REFERENCES

[1] **E. Chernokozhin, Y. Brick, A. Boag**, A Fast and Stable Solver for Acoustic Scattering Problems Based on the Nonuniform Grid Approach, *J. Acoust. Soc. Am.*, 139 (1), pp. 472-480, 2016.

[2] **T. K. Stanton, D. Chu**, Calibration of broadband active acoustic systems using a single standard spherical target, *J. Acoust. Soc. Am.*, 124 (1), pp. 128-136, 2008.

[3] **A. L. España, K. L. Williams, D.S. Plotnick, P. L. Marston**, Acoustic scattering from a water-filled cylindrical shell: Measurements, modeling, and interpretation, *J. Acoust. Soc. Am.*, 136(1), pp. 109-121, 2014.

TARGET ECHO STRENGTH OF A SCALED STEEL BODY WITH INNER STRUCTURE AND THIN HULL

Arne Stoltenberg, Ingo Schäfer

German Federal Armed Forces Technical Centre for Ships and Naval Weapons, Maritime Technology and Research (WTD 71),
Acoustic Modelling, Berliner Strasse 115, 24340 Eckernförde, Germany

Email: ArneStoltenberg@Bundeswehr.org, Ingo5Schaefer@Bundeswehr.org

Abstract: *A scaled model of a steel cone under a thin metal sheet was constructed, built and its monostatic target echo strength has been measured in a water tank. In parallel the target echo strength of the same body was calculated with various numerical methods (BEM, FEM, ray-tracing). The comparison of both results showed some differences under certain aspect angles due to some experimental challenges. With an improved experimental setup these differences could be minimised.*

Keywords: *target echo strength, scaled body, thin hull, experiment modelling comparison*

1. INTRODUCTION

The size of the target strength of a body determines its detectability for active sonar systems. The determination and diminishment of the target strength is a dominant topic for all sonar applications, from Anti Submarine Warfare to repelling mammals from fishernets. Contemporary calculation models allow different successful approaches to determine the target strength via the solution of the Helmholtz equation. These increasingly complex calculation models require increasingly complex validation experiments for their verification.

In this paper a scaled steel cone with a one-sided triple mirror was covered with a thin (compared to the used wavelength) cylindrical steel sheet. The dependency of the target strength on the aspect angle was determined experimentally and also calculated with a boundary element method (BEM) and a ray traycing method (BEAM). The computational and experimental results have been compared and interesting angles have been identified.

2. BASICS

In its simplified form the sonar equation is given by:

$$RL = SL - 2 \cdot TL + TS$$

where RL denotes the received level, SL the source level, TL the transmission loss and TS the target echo strength, as in [1]. Solving for TS yields:

$$TS = RL - SL + 2 \cdot TL$$

The case of neglectable TL (at a distance of 1 m, TL is 0 dB) gives:

$$TS = RL - SL$$

such that TS can be evaluated easily from measurements of RL and SL.

3. TANK EXPERIMENT

The water tank of WTD 71 is a 5 m x 5 m x 3 m tank built of concrete with rubber sound absorbers at the walls, in order to suppress multiple reflections. By placing the transmitter / receiver unit in the centre of the water volume the runtime between emission of the signal and arrival of the reflected signal at the receiver can be maximised to appoximately 2 ms.

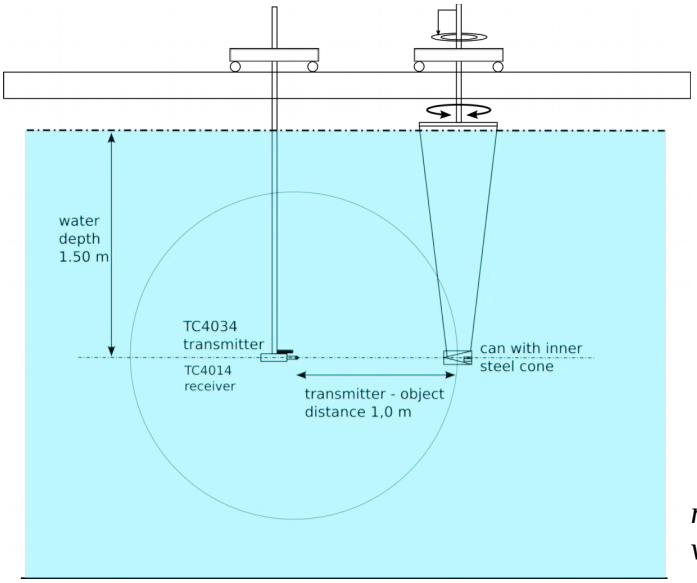




Fig. 1: left: t*ank experiment transmitter/receiver in the centre of the water volume, above: steel cone and can*

The object consists of a massive steel cone with a length of 100 mm, a diameter of 50 mm and an aperture angle of 2 x 14 ° on a round bottom steel plate (1 mm) with 57 mm diameter with a twofold triple mirror in the right side of the cone. This cone was embedded within a hollow cylinder, made from a thin 0.08 mm steel sheet (part of a can), representing the hull. Transmitter and receiver of the experiment were arranged vertically above each other with a mutual distance of 26 mm and located at the position in the centre of the water volume, as shown in Fig. 1. Strictly speaking, this represents a bistatic situation with an aperture angle of 1.5 ° at 1 m distance, which was regarded as approximately monostatic with respect to the vertical direction.

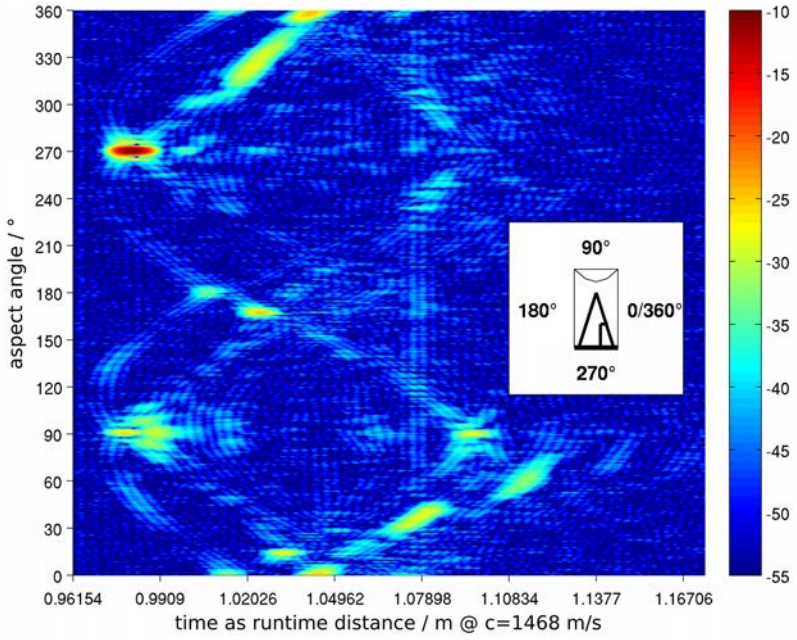


Fig. 2: *time-resolved contributions to the target echo strength of the object vs. aspect angle*

The object was rotated horizontally within the water in steps of 1 °, and at each aspect angle the resulting reflections were recorded as time series. From the cross-correlation between the reflected time series and the transmitted signal the impulse response at the given aspect angle can be obtained. From the known transmit and receive sensitivities of the transceivers the real target echo strength of the object can be computed. Fig. 3 shows the monostatically calculated and the experimentally obtained target echo strength.

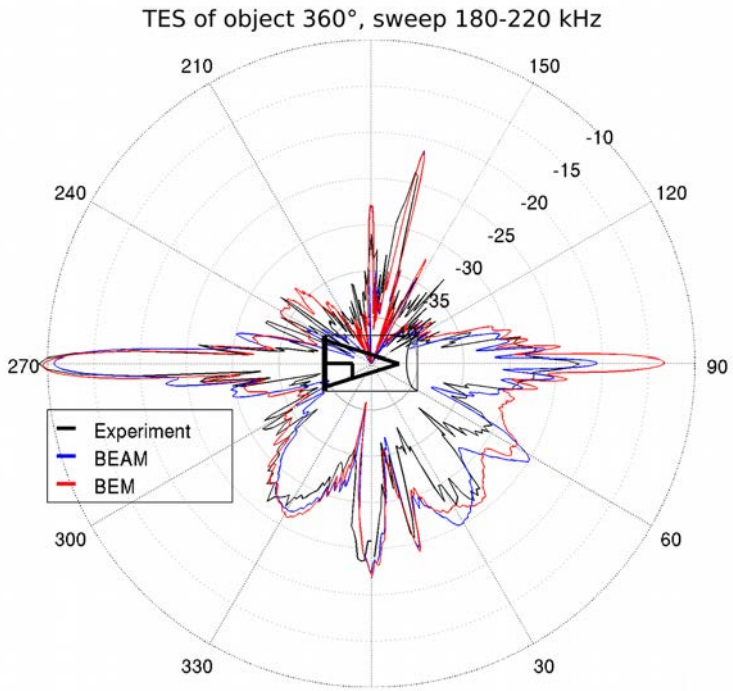


Fig. 3: *polar plot of target echo strength of the object, resulting from monostatic BEM and BEAM calculations and from the experiment*

When compared to the calculated monostatic target echo strength (as shown in Fig. 3), the most important reflections of this object are given in the following table:

Aspect Angle	Reflection
0 °	Triple mirror (as double mirror), Hull
14 °	Cone surface
30 ° - 45 °	Triple mirror (left)
45 ° - 65 °	Triple mirror (right + bottom refl.)
90 °	Horn effect + Bottom reflection (see below)
152 °	Multiple reflexion Cone surface - Hull
166 °	Cone surface (180 ° - 14 °)
180 °	Hull
270 °	Bottom plate of the Cone
310 ° - 345 °	Triple mirror (right)

Table 1: Reflections of the object, depending on the aspect angle.

4. MODELLING THE TARGET ECHO STRENGTH

Nearly all reflections found in the experiment could be confirmed by the computational modelling. The greatest difference between the two modelling methods and the experiment occurred at the aspect angle of 90 °. At this angle BEM and BEAM give target strengths of -14 dB and -21 dB, respectively, while the experiment provides a value of -23 dB. Due to this disagreement, further evaluation and modification of the experiment were performed. It was realised that the energy of the wave, when hitting the cone exactly along the cone axis, is integrated up over the cross section of the cone along the cone surface (horn effect). This integrated energy is nearly completely reflected at the circular bottom plate ring of the object, thereby producing the relatively high target strength of -14 dB. This interpretation was confirmed by FEM analysis, shown in Fig. 5.

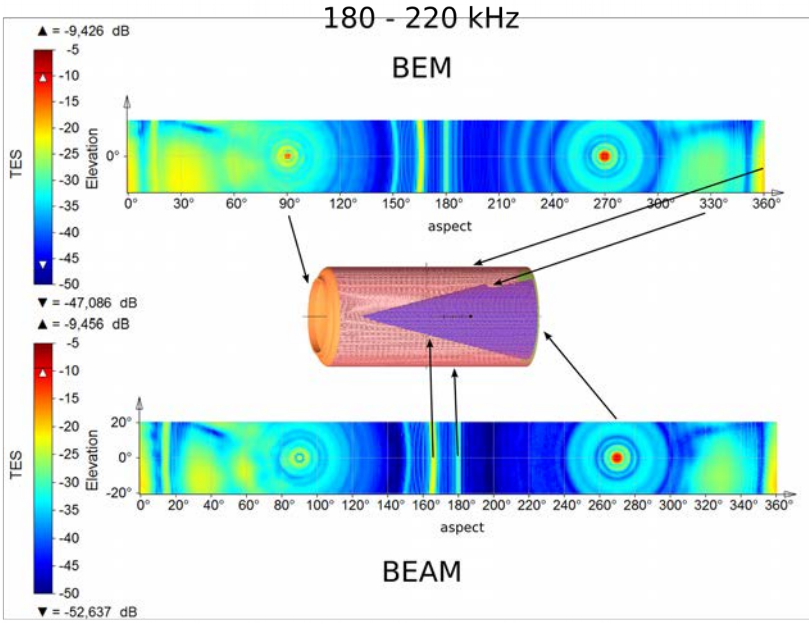
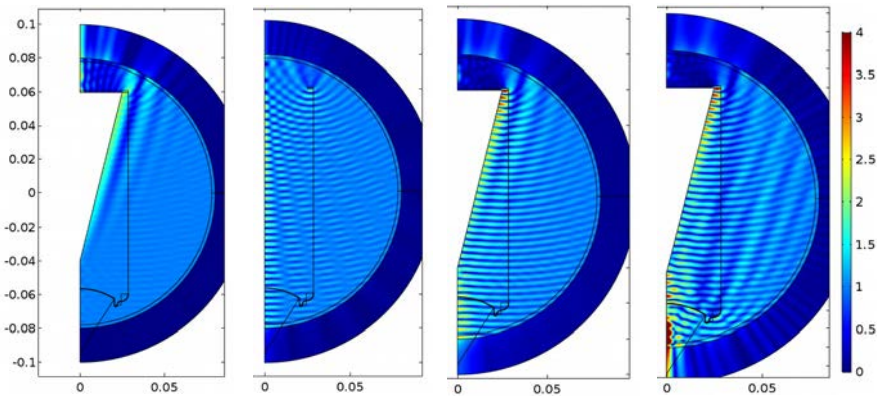


Fig. 4: *numerical BEM and BEAM calculation in comparison of aspect and elevation angle of the target object*

In the experiment the target strength reflection at 90 ° consists of two contributions, the contribution of the reflection of the thicker indentation at the lower end of the can (shown at the top of the inset of Fig. 2) and the contribution of the above stated horn effect / bottom ring reflection (occurring later in time in Fig. 2). These contributions sum up to the total target echo strength.



only cone surface (horn effect) TS = -34 dB	only bottom circle ring TS = -21 dB	cone + circle ring TS = -12 dB	cone + circle ring + hull TS = -14 dB

Fig.5: Results of Finite Element Modelling of reflections at aspect angle of 90 °, considering only parts of the object

Regarding the discrepancy between calculated models and experiment, it was found that the monostatic approximation of the actually bistatic experimental situation was incorrect. The small vertical distance between transmitter and receiver results in a considerable difference of the target strength at an aspect angle of 90 °. To compensate for this unwanted bistatic effect, an additional transmitter was placed at the same vertical distance under the receiver, in order to render the transmitting field symmetric with respect to the receiver plane. Due to interference effects two in-phase transmitters cause a transmission field with Moiré effects occurring in different positions of space. Outside of the cancelation zones of the Moiré pattern, the symmetric transmission field can be used, after a recalibration step. Repetition of the measurements, including this modification (this time only with the inner steel cone without the hull) provided an increased target strength of -14.4 dB at the aspect angle of 90 ° (see Fig. 7), in concordance with the results of the numeric modelling.

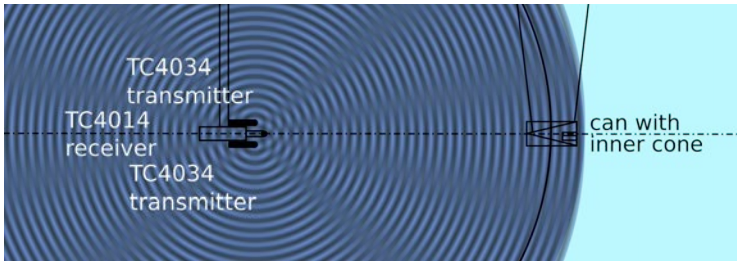


Fig. 6: *Moiré pattern of the transmitted field for the experiment with two transmitters; note the symmetry w.r.t. the receiver plane*

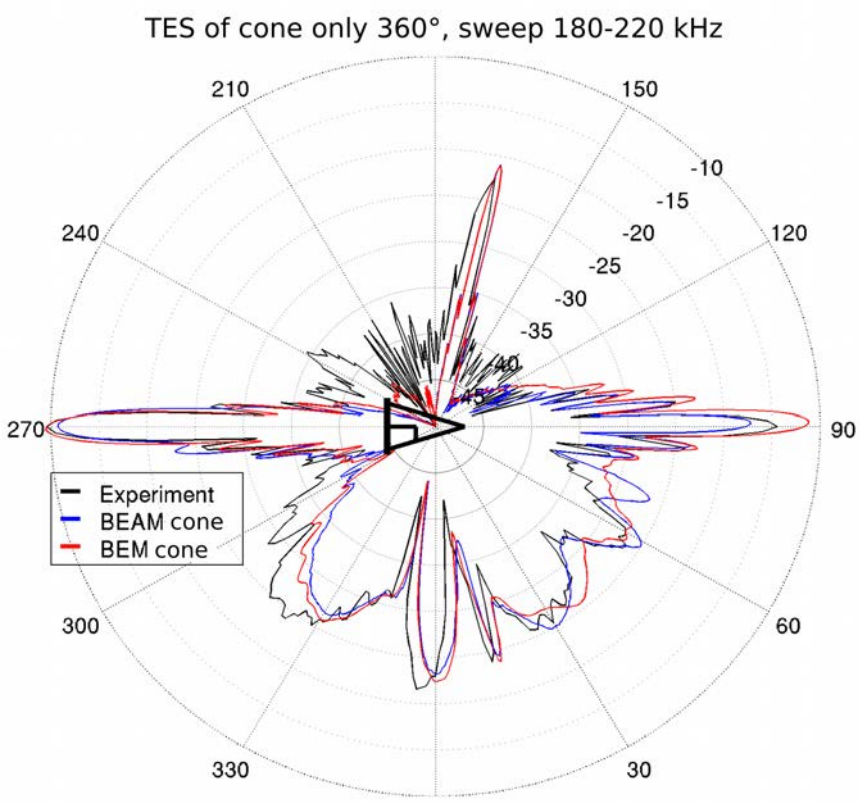


Fig. 7: *polar plot of target echo strength of the object (steel cone without hull), resulting from monostatic BEM and BEAM calculations and from the experiment*

5. RESULTS

The target echo strength (TS) of a scaled body consisting of a massive steel cone structure and a thin steel sheet hull was determined as a function of aspect angle through numerical modelling and experiment. The experiment was performed in a water tank and compared with the calculated TS of different calculation methods (BEM, BEAM, FEM). After compensation for an unwanted bistatic effect within the experiment, good to very good agreement (better than 2~dB over a wide interval of angles) between theoretical and experimental results for determining the target echo strength has been achieved.

REFERENCES

[1] **Robert J. Urick:**, Principles of underwater sound, 3rd edition, Peninsula Publishing, LosAltos, California, 1983

INFLUENCE OF FLUID-STRUCTURE COUPLING ON TARGET ECHO STRENGTH SIMULATION

Ingo Schäfer[a], Jan Ehrlich[a], Ralf Burgschweiger[b], Martin Ochmann[b]

[a] WTD 71, Berliner Straße 115, 24340 Eckernförde, Germany
[b] Beuth Hochschule für Technik, Luxemburger Straße 10, 13353 Berlin, Germany

Jan Ehrlich, Bundeswehr Technical Centre for Ships, Naval Weapons, Maritime Research and Technology (WTD 71), Berliner Straße 115, 24340 Eckernförde, Germany, Fax: +494316074150, janehrlich@bundeswehr.org

Abstract: *A combined Boundary Element – Finite Element method for the calculation of the Target Echo Strength (TES) of an underwater object is presented. For the calculation of TES in the high frequency range it is not necessary to consider fluid-structure-coupling. In this case it is possible to use a raytracing based algorithm together with a Kirchhoff scattering approximation. Better results can be obtained by using a method like the BEM, that is able to include the influence of the mass of object as a thin shell. But for the low frequency region the elastic response of the object has to be considered as well. This demands the application of a full fluid-structure interaction, which can be done with a BEM-FEM coupling. Three different formulations for this coupling will be explained and compared. Results of calculations for a test object consisting of a water-filled steel cylinder with one semi-spherical end cap with the different coupling algorithms will be presented. The coupled approach makes it possible to detect TES highlights at several frequencies that are caused by eigenmodes. It will be shown that only some eigenmodes are able to radiate. The presented BEM-FEM approach is able to calculate the TES of models consisting of more than a million elements.*

1.1. ***Keywords:*** *Target Echo Strength, FEM, BEM, coupling*

1. INTRODUCTION

Target echo strength is a quantity that describes the backscattered energy of an object in water in the far field, excited by an incident acoustic wave. The physically most precise method to calculate this is the finite element method (FEM) that takes the fluid structure coupling of the object with the surrounding water into account. The problem with this approach is that the computational load gets enormous quickly for three dimensional calculations because the full 3D domain including the water has to be discretised. A usual method to circumnavigate this problem is using the boundary element method (BEM). The equations are derived from the Helmholtz equation, cast as integral equation in the weak form, by application of the Gauss integral theorem. The advantage of the BEM is that for the resulting equations only the surface of the object and not the fluid domain has to discretised. This reduces the problem to a two-dimensional one which. The disadvantage is that both the structural response of the object to the excitation and the fluid structure coupling are neglected. As one way to remedy the latter at least partially for thin structures the so-called mass inertia coupling can be used. Thereby the mass of the thin structure gives an inertia boundary condition for the coupling of the fluids on the front and the back of the object [1]. In order to also consider the response of the excited structure itself and its effect on the fluid a FEM method has to be used. This is especially important at low frequencies where discrete resonances of the structure are important. In order to retain the advantage of the BEM not having to discretise the 3D fluid domain a coupling between FEM and BEM has to be made. Foundations for FEM and BEM for acoustics can be found in [2]. In the following such a method is proposed for structures that can be modelled with thin shells and three approaches for the solution of the resulting matrix equations are explained. Calculations for a test structure in water are presented.

2. FLUID STRUCTURE COUPLING

The presented approach for this task is based on an already existing BEM code that can handle direct and indirect BEM formulations. It uses a BEM collocation formulation with constant basis functions and triangular elements. For the indirect BEM formulation which is appropriate for thin structures, the unknowns are the acoustic normal velocity $\vec{v}$ and the step of pressure δp between the front and the back of the object. For constant elements the unknowns are placed in the centre of the object.

For the FEM description of the object a formulation is chosen that uses Love-Kirchhoff plate theory. This means that the object is not discretized with three-dimensional solid elements but with two-dimensional shell elements which leads to the restriction to objects with thin structures. For these elements the unknowns are the translational degrees of freedom w_x, w_y, w_z and the rotational degrees of freedom φ_x, φ_y and φ_z. These unknowns are placed on the corners of the triangular elements. Moreover, the discretisation of the object is not necessarily the same for FEM and BEM. In order to apply the fluid structure coupling in this case a mortar coupling is used. The idea is to distribute the loads onto the other DOFs taking into account the geometric positions of the respective nodes and the element size.

The equation governing the FEM model is

$$(\mathbf{K} - \omega^2 \mathbf{M}) \begin{bmatrix} \vec{\varphi} \\ \vec{w} \end{bmatrix} = \mathbf{K}_f \begin{bmatrix} \vec{\varphi} \\ \vec{w} \end{bmatrix} = \mathbf{K}_f \, \vec{x} = \begin{bmatrix} \mathbf{K}_{\varphi\varphi} & \mathbf{K}_{\varphi w} \\ \mathbf{K}_{w\varphi} & \mathbf{K}_{ww} \end{bmatrix} \begin{bmatrix} \vec{\varphi} \\ \vec{w} \end{bmatrix} = \begin{bmatrix} 0 \\ \vec{f} \end{bmatrix} \tag{1}$$

with the mass matrix **M** and the stiffness matrix **K** that give the resulting matrix $\mathbf{K_f}$, the excitation force $\vec{f}$. The matrix $\mathbf{K_f}$ can be split into four submatrices that either describe the coupling of translational DOFs and rotational DOFs or the cross couplings. The matrices are sparse, as it is usual for FEM matrices.

The indirect BEM equation is given by

$$-\rho c \cdot \overrightarrow{v_n} + \boldsymbol{J}_B \cdot \overrightarrow{\delta v_n} + \boldsymbol{F}_B \cdot \overrightarrow{\delta p} = -\rho c \, \vec{v}_{inc} \tag{2}$$

with the variables normal velocity $\overrightarrow{v_n} = (\vec{v}_x, \vec{v}_y, \vec{v}_z)$, step of pressure between front and back $\overrightarrow{\delta p}$ (double layer potential) and step of velocity $\overrightarrow{\delta v_n}$. The latter is assumed to be zero since in the shell formulation the velocity is equal on both sides. Therefore, the equation simplifies to

$$-\rho c \cdot \overrightarrow{v_n} + \boldsymbol{F}_B \cdot \overrightarrow{\delta p} = -\rho c \, \vec{v}_{inc} \tag{3}$$

where $\boldsymbol{F}_B$ is the fully populated BEM matrix. The coupling of FEM and BEM is done by linking the force term $\vec{f}$ of the FEM to the jump of pressure $\overrightarrow{\delta p}$ of the BEM and the translations $\vec{w}$ to the velocity $\vec{v}$ via coupling matrices $\mathbf{T}_1$ and $\mathbf{T}_2$ as

$$\vec{v} = \mathbf{T}_1 \cdot \vec{w} \quad \text{and} \quad \vec{f} = \mathbf{T}_2 \cdot \Delta\vec{p} \tag{4}$$

This leads to the coupled matrix equation

$$\begin{bmatrix} \mathbf{K}_{\varphi\varphi} & \mathbf{K}_{\varphi w} & 0 \\ \mathbf{K}_{w\varphi} & \mathbf{K}_{ww} & \mathbf{T}_2 \\ 0 & -\rho c \mathbf{T}_1 & \mathbf{F}_B \end{bmatrix} \begin{bmatrix} \vec{\varphi} \\ \vec{w} \\ \overrightarrow{\delta p} \end{bmatrix} = \begin{bmatrix} 0 \\ 0 \\ -\rho c \, \vec{v}_{inc} \end{bmatrix} \tag{5}$$

or

$$\begin{bmatrix} \mathbf{K}_f & \mathbf{T'}_2 \\ -\rho c \mathbf{T'}_1 & \mathbf{F}_B \end{bmatrix} \begin{bmatrix} \vec{\mathrm{x}} \\ \overrightarrow{\delta p} \end{bmatrix} = \begin{bmatrix} 0 \\ -\rho c \, \vec{v}_{inc} \end{bmatrix} \tag{6}$$

with the shorter notation of $\vec{x} = [\vec{\varphi}, \vec{w}]^T$ from equation (1). The coupling matrices $\mathbf{T}_1$ and $\mathbf{T}_2$ are replaced with $\mathbf{T'}_1 = [0, \mathbf{T}_1]$ and $\mathbf{T'}_2 = [0, \mathbf{T}_2]^{\mathrm{T}}$.

3. SOLUTION STRATEGIES

Equation (6) is a matrix equation with the left hand matrix consisting of the large sparse FEM matrix $\mathbf{K}_f$, the smaller but fully populated BEM matrix $\mathbf{F}_B$ and two sparse coupling matrices $\mathbf{T'}_1$ and $\mathbf{T'}_2$. There are several possible methods to solve this equation.

The straightforward way is a direct solution of the matrix equation (6). The resulting matrix is very large und needs a lot of memory for the decomposition. It is also not easy to solve since it consists of a sparse part and a fully populated part. Treating the whole matrix as a sparse matrix demands a lot of memory.

An alternative method uses the Schur approach. This can be done by inverting the upper equation of (6) to $\vec{x} = -\mathbf{K}_f^{-1} \, \mathbf{T'}_2 \cdot \overrightarrow{\partial p}$ (Schur complement) and inserting it into the lower equation. This leads to the Schur equation

$$\rho c \mathbf{T'}_1 \mathbf{K}_f^{-1} \mathbf{T'}_2 \cdot \overrightarrow{\partial p} + \mathbf{F}_B \cdot \overrightarrow{\partial p} = -\rho c \, \vec{v}_{inc} \tag{7}$$

The difficult part would be the inversion of the large FEM matrix $\mathbf{K}_f$. But by using an iterative solution strategy it can be avoided to do the matrix inversion explicitly. Instead only matrix vector products with $\mathbf{K}_f$ have to be calculated. But this method still uses the large FEM matrix.

A way to reduce the effective size of the matrix can be found by using the eigenmodes of the uncoupled FEM equation (dry modes). A given number of the lowest eigenmodes can be extracted from $\mathbf{K}_f$ with modest numerical effort. These correspond to the resonances of the structure in vacuum. With the eigenvectors a matrix $\boldsymbol{\psi}$ can be formed that has the dimension number of DOFs times number of eigenvectors (N_{DOF} x N_{ev}), in contrast to the square matrix $\mathbf{K}_f$ which has the dimension N_{DOF} x N_{DOF}. With this matrix $\boldsymbol{\psi}$ a transformation of $\mathbf{K}_f$ can be made that results in transformed matrices $\mathbf{H}_{ev}$ with the reduced size of N_{ev} x N_{ev}

$$\mathbf{H}_{ev} = \boldsymbol{\Psi}_{ev}^T \cdot \mathbf{K}_f \cdot \boldsymbol{\Psi}_{ev} \tag{8}$$

$\mathbf{H}_{ev}$ is diagonal and small and can be inverted much more easily than $\mathbf{K}_f$. This leads to the final equation for the modal approach

$$(-\rho c \, \mathbf{T'}_1 \, \boldsymbol{\Psi}_{ev} \, \mathbf{H}_{ev}^{-1} \, \boldsymbol{\Psi}_{ev}^T \, \mathbf{T'}_2 + \mathbf{F}_B) \cdot \overrightarrow{\partial p} = -\rho c \, \vec{v}_{inc} \tag{9}$$

The physical meaning of this approximation is that all results for the coupled equation are linear combinations of the modes, i.e. the vibration patterns of the uncoupled system.

All three equations (6), (7) and (9) have a similar structure with a matrix times the solution vector $\overrightarrow{\partial p}$ on the left hand side and the incident sound velocity $\vec{v}_{inc}$ on the right hand side. Table 1 gives an overview of the proposed solution methods, its characteristics and applicability.

Method	*BEM*	*Sparse*	*Schur*	*Modes*
Memory size	small	large	large	small
Realistic results	+	++	++	++
Solver	direct iterative	direct	iterative	direct iterative
Frequency regime	medium high	low	low medium	low medium
Fast multipole method	yes	no	yes	yes

Table 1: Solution methods for TES calculations and its characteristics

4. EXAMPLE

In order to examine the procedures a test body was devised. It consists of a half open steel cylinder with the thickness of 6 mm with a hemispherical end cap of the same thickness on one side. The other side is open. The cylinder has a diameter of 0.5 m and the whole structure is 1 m long and immersed in water.

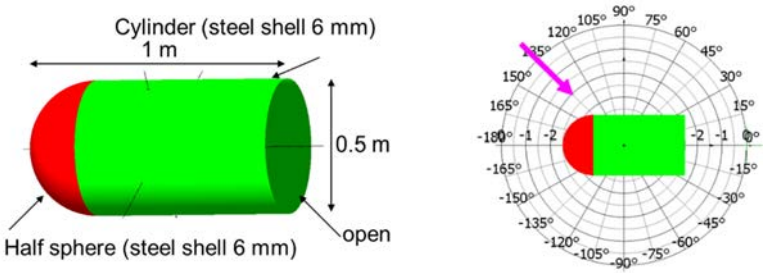


Figure 1: Test structure with open cylinder and hemispherical end cap (left) and direction of insonification.

The target echo strength of this test body was calculated for insonification from 135° aspect angle and 0° elevation angle using the above methods for a frequency range from 300 Hz to 1000 Hz. As a reference TES was calculated with the commercial FEM code Comsol in a fully coupled 3D calculation. Besides the TES calculation, the eigenmodes of the uncoupled und the coupled structure in water were calculated.

5. RESULTS

The problem could not be solved by solving equation (6) with a direct solver for sparse matrices due to memory and time restrictions. The Schur approach and the eigenmode approach were used for the calculation of TES, the latter with different numbers of dry eigenmodes used for the expansion. Fig. 2 shows the results for the calculations compared with the Comsol FEM calculation.

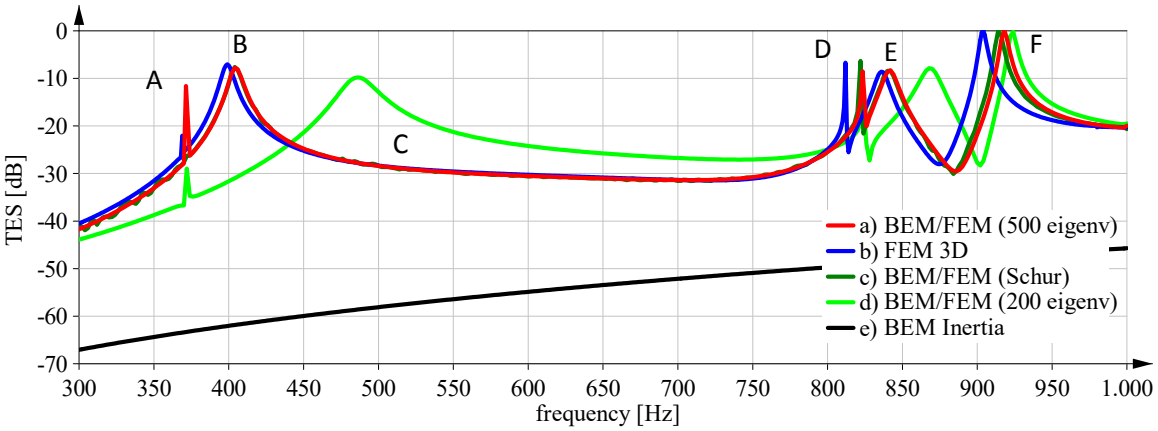


Figure 2: TES calculation results for the test structure with FEM 3D calcualtion, FEM/BEM coupling with Schur and modes and BEM inertia coupling.

Several things can be seen in the graph. The blue Comsol result can be considered to be the reference. All results of methods with full coupling show a broadly similar shape. The curves all have a few distinct sharp and broad peaks that correspond to resonances, where the vibration of the structure and, hence, backscatter is stronger. The BEM inertia result (black curve) is incorrect in this frequency range and underestimates TES by at least 20 dB. The result of the mode calculation with 200 eigenmodes (green curve) is also insufficient. The resonance peaks are at incorrect frequencies. The results of the Schur calculation and the mode calculation with 500 eigenmodes are very similar to each other and differ only slightly from the Comsol result. This proves the success of the coupled BEM/FEM calculations.

For the eigenmode approach, which is the fastest of the three, the number of eigenmodes has to be considerably higher than 200 for this example and the frequency range considered. The discrepancy of the results from the Comsol result are probably due to the fact that we used shell elements from Love-Kirchhoff plate theory whereas Comsol used Reissner-Mindlin shell elements. The difference between these formulations requires further investigation.

All results show a relatively smooth curve with a few distinct peaks at resonances. But when you calculate the eigenmodes of the coupled problem, you find a much greater number of modes in the frequency range considered that do not contribute visibly to the TES curve. These modes are obviously not radiating. Comsol gave the ability to produce pictures of the eigenmodes found for the dry modes. Table 2 shows a selected number of eigenfrequencies for the dry case (in vacuum), the wet case and the case of a rigid structure in water for the corresponding modes. For important modes pictures of vibrating shape of the modes are shown above and labelled. The letters correspond to the ones in Fig. 1. For the dry modes the number of the mode is added in parentheses.

For all modes the frequency is lower in the coupled case due to the fluid loading of the structure. This phenomenon is well known. These are the only modes where the eigenfrequency has a non-negligible imaginary part. This reflects the radiation into the far-field of these modes which corresponds to a loss of energy of the mode and hence an imaginary part. The next similarity of these modes is that their mode shape shows a larger distance between maxima and minima than for the other modes. One example of a non-radiating mode is C at 946 Hz dry / 516 Hz wet. If you attribute a wavelength to the mode shapes defined the longitudinal difference between maxima and minima on the structure and compare it to the acoustic wavelength in water you find that the mode wavelength is in the order of the water wavelength or larger for the radiating modes and much smaller for the non-radiating modes.

There are two radiating modes that have no equivalent in the dry calculation but in the sound hard calculation. The can be seen as a kind of Helmholtz resonators that are not present in the dry calculation. They roughly correspond to a quarter water wavelength and a half water wavelength fitting in the length of the structure. In the dry (in vacuum) calculation this condition is not met since there is no medium with an acoustical wavelength present.

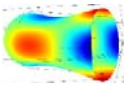
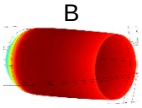
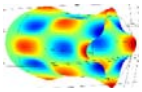
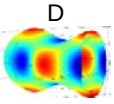
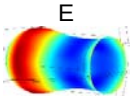
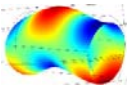
		A	B	C		D	E	F
								
dry mode	71 (7)	**780 (21)**		**946 (27)**	1394	**1704 (53)**		**1780 (55)**
wet mode	32	**369+0.01i**	**399+4i**	**516**	845	**812+0.2i**	**836+5i**	**903+2i**
rigid			**354+5i**				**1070+50i**	

Table 2: Eigenfrequencies of selected modes in the dry, wet and rigid calculation in Hz and mode shapes above. The order of the dry modes is added in parentheses

The monostatic TES calculation was repeated for other all aspect angles from 0° to 180° and frequencies from 100 Hz to 1 kHz. The results in Fig. 3 show the magnitude of the calculated TES over the aspect angles. The magnitude distribution of peaks reveals the principal vibration shapes of the resonances. The first radiating mode A has a dipole characteristic with a main direction around 90°. The broader Helmholtz resonator mode B also has this pattern. The same applies to the next sharp peak D. The second order Helmholtz

mode E, however, has a minimum at broadside and maxima at the front and the back. The first bending mode F has its main radiation direction at 45°/135°.

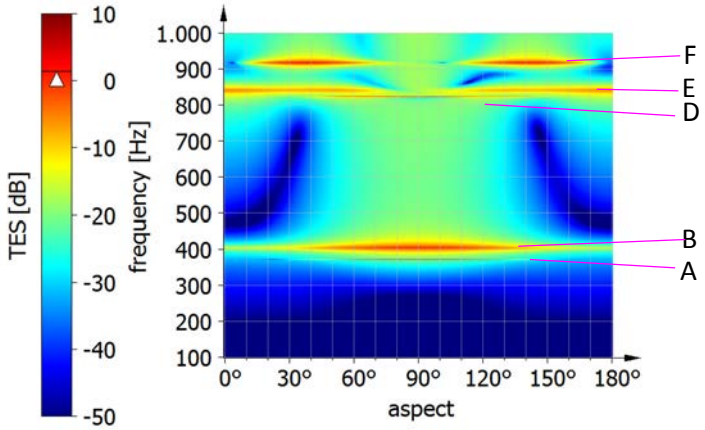


Figure 3: Monostatic TES calculation over frequency for aspect angles from 0° to 180°.

6. SUMMARY AND OUTLOOK

A coupled FEM / BEM method for the calculation of target echo strength of thin structures in the low frequency regime was described. Three methods for the solution of the coupled matrix equations were presented. The direct solution is hardly practicable because the matrix gets too big. The Schur method improves on that and the mode leads to the smallest matrix to solve. Calculations for a test structure were presented and compared to results of a finite element calculation with a commercial code. The results of the Schur method and the modal decomposition agreed fairly well with the results of the FEM calculation. Remaining discrepancies of resonance frequencies are probably due to the different FEM shell element types that were used.

The mode calculations revealed that although there is vast number of modes in the frequency range considered only a few of them are radiating modes and dominate target echo strength. The mode calculations show that it was not sufficient to include only 200 dry modes. The question arises whether all dry modes have to be used for the modal expansion or if it is sufficient to include only radiating modes. After knowing which modes are radiating, subsequent calculations with these modes and the lowest modes indicate that this seems to be the case. In order to automate this approach, it would be necessary to find a criterion for the dry modes to determine whether it would be radiating or not in water. This idea will be pursued in future.

REFERENCES

[1] Burgschweiger R., Schäfer I., Ochmann M., Implementation and results of a mass inertia coupling as an extension of the BEM for thin shells, in *Proceedings of ISVC 22,* Florence, Italy, 2015.

[2] Marburg S., Nolte B. (ed.), *Computational Acoustics of Noise Propagation in Fluids - Finite and Boundary Element Methods*, Springer, Berlin, 2008.

ANECHOIC COATING DESIGN KNOWLEDGE FIELDS

Martin Uitdenbogerd

Netherlands Ministry of Defence Herculeslaan 1
Postbox 90125 3509BB Utrecht Netherlands

jm.uitdenbogerd@mindef.nl

Abstract: *One of threats for submarines is active sonar from surface ships. Anechoic coating is used to passively protect the submarine from this. Research and development are necessary to get optimal Anechoic coating design. This paper will introduce an overview of knowledge fields that apply for Anechoic coating design. This is based on four pillars:*

1 Operational use.
2 Applied Materials.
3 Measurements and Calculations. 4 Integration and maintenance

The paper describes briefly the different pillars and shows how Research and Development is applied to get operational anechoic coatings.

Keywords: Anechoic Coatings TS Tiles Target Echo Strength

1. INTRODUCTION

Modern submarines are mostly coated with Anechoic tiles. The reflection of acoustic waves from surface ship sonars back to the Sonar source is reduced by absorption or by scattering in directions other than the direction of the source. The development of those Anechoic coatings can be structured by road mapping so that all operational requirements are covered. The Defence Material Organisation of NL MoD uses road mapping to determine its research and development activities.

2. OPERATIONAL USE

The operational requirements of the submarine are the starting point for the requirements for the applied anechoic coating. Related to Anechoic materials the operational diving depth is one of the relevant parameters. This will determine the pressure dependency of the material. Deformation by static pressure will change the acoustic properties of the anechoic coating. This deformation will also set the requirements for gluing and aging of the coating.

Another factor is the expected sonar threat. These days several sonar systems are available such as LFAS (Low Frequency Active Sonar, towed behind surface ships), HMS (Hull Mounted Sonar), HELRAS (Helicopter Long Range Active Sonar, dipping sonars) and torpedo sonars. Each threat comes with a different frequency and detection range. The anechoic coating should be developed for the frequency ranges of the expected active sonar threats.

3. APPLIED MATERIALS

The development of materials is the key factor for anechoic coatings. The relation between the chemical parameters and the acoustic performances should be determined. The material should be buoyancy neutral so it has less influence on the buoyancy of the submarine. The density of anechoic coatings varies between 1100 and 1500 kg/m^3. Coatings that contain air are usually good reflectors due to the acoustic impedance mismatch with water. The acoustic performance of these coatings changes a lot with diving depth. The materials that "absorb" acoustic waves are usually thicker and around ¼ of the wave length of interest.

4. MEASUREMENTS AND CALCULATIONS

The acoustic performance can be measured in acoustic tubes with transducers and hydrophones to determine the reflection, transmission and absorption of the anechoic materials.

For material modelling the shear and bulk modules should be determined in order to reconstruct the material master curves in the relevant range of frequency, temperature and pressure. Shear and bulk modules can be measured with a DMTA (Dynamic Mechanical Thermal Analysis) apparatus, with a laboratory test rig for measuring the dynamic transfer stiffness of resilient mountings, and by measuring the longitudinal wave speed with ultrasound.

The material properties and their pressure dependency can be taken into account when modelling and calculating the Target Strength (TS) of a submarine. The optimisation of the TS will require several iterations.

5. INTEGRATION AND MAINTENANCE

Integration into the submarine design. Anechoic coatings will add extra weight to the submarine which should be compensated by extra volume. Also the previous mentioned deformation of the anechoic coatings will change the buoyancy of the submarine which must be compensated with pumps and ballast tanks. Absorption coatings are usually applied on structures that are air backed, such as the pressure hull. Reflection materials are applied on water backed structures, like the sail. But also combinations of reflection and absorption materials are applied. The shaping of the ship in combination with Anechoic coatings will also influence it's TS. Modern submarines have "Stealth" shapes at the sails and shaped hulls.

Maintenance will ensure that the performance of the anechoic coating is maintained. For example inspections of the hull underneath the cladding to detect corrosion. Also measuring the coating separately and the whole submarine to ensure the TS performance in relation with the operational requirements.

6. CONCLUSION

The different knowledge fields are the basis for developing Anechoic coatings and give guidance for Research and Development projects. Developing an anechoic coating for a submarine is an integral process.

Structured Session 22
Vector Hydrophone Research

Organiser(s): Yang Desen

AN ESTIMATION ALGORITHM OF DOA FOR VECTOR SENSOR ARRAY BASED ON TENSOR THEORY

Song Li[a,b,c], Zhe Chen[a,b,c], Desen Yang[a,b,c]

[a]Acoustic Science and Technology Laboratory, Harbin Engineering University, Harbin 150001,China;
[b]Key Laboratory of Marine Information Acquisition and Security(Harbin Engineering University),Ministry of Industry and Information Technology; Harbin 150001, China;
[c]College of Underwater Acoustic Engineering, Harbin Engineering University, Harbin 150001, China

SongLi, Room 1103, College of Underwater Acoustic Engineering, Harbin Engineering University, Harbin 150001, China; E-mail: songli@hrbeu.edu.cn

Abstract: *In order to solve the problem that direction of arrival estimate performance of traditional direction of arrival (DOA) estimation algorithm in the case of low signal to noise ratio is degradation. In this paper, a DOA estimation algorithm based on tensor decomposition for vector hydrophone array signals is proposed. The tensor analysis model is introduced to establish the tensor model of the vector hydrophone array signal, the signal subspace is derived by tensor decomposition, which combines the traditional DOA estimation algorithm to estimate the sound source. The DOA estimation algorithm based on tensor decomposition for vector hydrophone array signals in the noise suppression and Signal subspace estimation superior than the traditional DOA estimation algorithm. In simulation, the proposed algorithm is compared with the traditional DOA estimation algorithm, and the results show the effectiveness of the proposed algorithm.*

Keywords: *Tensor decomposition, Vector hydrophone array, Direction of arrival estimation*

1. INTRODUCTION

Nowadays, accurate orientation of the target's orientation is one of the key issues that must be addressed in many future areas. In the underwater acoustic signal processing, in order to determine the direction of arrival (DOA) of the sound wave, the sound field is usually spatially sampled using a vector hydrophone array, and spatial spectrum estimation is performed. Traditional methods of azimuth estimation include subspace algorithms such as MUSIC algorithm and ESPRIT algorithm. The traditional azimuth estimation method has poor performance at low SNR because these algorithms use the particle velocity and sound pressure as parallel data to expand into a vector form, and do not make full use of the sound pressure output from the acoustic vector sensor. The orthogonal relationship between the components of the vibration velocity, therefore, an effective way to solve the above problem is to introduce a tensor operation.

As a unified language for multi-dimensional signal processing, tensor has incomparable advantages for high-dimensional algebraic operations. Compared with matrix or vector, tensor decomposition model is more suitable for multi-dimensional structure of real signal. An important model in tensor decomposition is Tucker tensor decomposition. Tucker tensor decomposition is a high-order singular value decomposition, which focuses on acquiring information feature subspace and retaining the orthogonality of the algorithm.

The current tensor decomposition algorithm is mainly used in image processing. In array signal processing, it is mainly used in electromagnetic vector signals. In the literature, the tensor method is introduced in vector array signal processing, and the tensor is applied in the polarization sensitive array. Combined with the MUSIC algorithm, the vector MUSIC signal algorithm using tensor operation is proposed. The literature introduces the Tucker decomposition model to construct a Kronecker product approximation method as a pre-regulator for image processing. The literature introduces the Tucker tensor decomposition model into motion recognition, and its application extends from static images to dynamic images. The paper proposes a tensor-based real-valued subspace method for estimating the target wavelength direction (DOD) and direction of arrival (DOA) in multiple-input multiple-output (MIMO) radar. In this paper, the received acoustic vector signal data is reconstructed, the tensor model is established, and the corresponding tensor signal subspace is obtained by tensor decomposition, which combines the traditional azimuth estimation method to estimate the sound source. The azimuth estimation algorithm based on tensor decomposition theory proposed in this paper has better noise suppression ability for acoustic vector array signals, which can improve the accuracy of azimuth estimation accuracy.

2. TENSOR DECOMPOSITION THRORY

The n-mode expansion of a tensor is the tensor expanded into a matrix as a column in n-mode. $A_{(n)}(1 \le n \le N)$ is the matrix of n-mode expansion for the tensor $A \in C^{I_1 \times I_2 \times \ldots \times I_N}$,and the following relationship exists between element (i_n, j) and $(i_1, i_2, \ldots, i_N)$:

$$j = 1 + \sum_{\substack{k=1 \\ k \neq n}}^{N} (i_k - 1) J_k, J_k = \prod_{\substack{m=1 \\ m \neq n}}^{k-1} I_m \tag{1}$$

A new tensor is made by $A \in C^{I_1 \times I_2 \times \ldots \times I_N}$ and matrix $U = C^{J_N \times I_N}$

$$B = A \times_n U \in C^{I_1 \times I_2 \times \ldots \times I_{n-1} \times J_n \times I_{n+1} \times \ldots \times I_N} \tag{2}$$

$$b_{i_1, i_2, \ldots, j_n, \ldots, i_N} = \sum_{i_n} a_{i_1, i_2, \ldots, j_n, \ldots, i_N} u_{j_n i_n} \tag{3}$$

3. ACOUSTIC VECTOR SENSOR ARRAY TENSOR MODEL

It is assumed that the signal satisfies the narrow-band far-field plane wave condition, and the incident signals are statistically independent. The background noise received by each array element is Gaussian white noise, and the correlated time radius of the noise is smaller than the time interval of data acquisition. The background noise received by each array element is independent.

There are k signals satisfying the conditions of the narrow-band far-field plane wave incident on an equidistant linear array composed of M vector sensors. The incident angle is (θ_k, φ_k), k=1,2,…, K, and θ_k, φ_k are the azimuth angle and pitch angle of the kth signal. The number of array elements of the linear array is greater than the number of sound source signals。

If the $a(\Theta_k) \circ u_k$ can be looked as a slice, then the direction tensor $A(\Theta)$ will be got.

$$A(:,:,k)=\begin{bmatrix} 1 & \cos\theta_k\cos\varphi_k & \sin\theta_k\cos\varphi_k & \sin\varphi_k \\ e^{-j\frac{2\pi}{\lambda}d\sin\varphi_k} & e^{-j\frac{2\pi}{\lambda}d\sin\varphi_k}\cdot\cos\theta_k\cos\varphi_k & e^{-j\frac{2\pi}{\lambda}d\sin\varphi_k}\cdot\sin\theta_k\cos\varphi_k & e^{-j\frac{2\pi}{\lambda}d\sin\varphi_k}\cdot\sin\varphi_k \\ \vdots & \vdots & \vdots & \vdots \\ e^{-j\frac{2\pi}{\lambda}d(M-1)\sin\varphi_k} & e^{-j\frac{2\pi}{\lambda}d(M-1)\sin\varphi_k}\cdot\cos\theta_k\cos\varphi_k & e^{-j\frac{2\pi}{\lambda}d(M-1)\sin\varphi_k}\cdot\sin\theta_k\cos\varphi_k & e^{-j\frac{2\pi}{\lambda}d(M-1)\sin\varphi_k}\cdot\sin\varphi_k \end{bmatrix} \tag{4}$$

$A(:,:,k)$ is a slice of the tensor $A(\Theta)$ at the 3th dimensional, and k=1,2,…, K. then $A(:,:,k)=A_K$ is defined. A third-order tensor output model is constructed under L snapshots,

$$X = A\times_3 S^T + N \tag{5}$$

In this formula, $\times_3$ is represented product of tensor and the 3-modulus matrix, and $A\in C^{M\times 4\times K}$, $X\in C^{M\times 4\times L}$, $N\in C^{M\times 4\times L}$.

Obtained in the measurement tensor model output X high order tensor Singular Value Decomposition

$$X = S\times_1 U_1\times_2 U_2\times_3 U_3 \tag{6}$$

$S\in C^{M\times 4\times L}$ is the core tensor of tensor X under singular value decomposition, and $U_1\in C^{M\times M}$ is the left singular vector matrix of tensor X under singular value decomposition in 1-mode. The formula below is satisfied,

$$X_{(1)} = U_1\cdot\Sigma_1\cdot V_1^H \tag{7}$$

At the same theory, $U_2\in C^{4\times 4}$ is the left singular vector matrix of tensor X under singular value decomposition in 2-mode, and $X_{(2)}=U_2\cdot\Sigma_2\cdot V_2^H$ is satisfied; $U_3\in C^{L\times L}$ is the left singular vector matrix of tensor X under singular value decomposition in 2-mode, and $X_{(3)}=U_3\cdot\Sigma_3\cdot V_3^H$ is satisfied.

The we cut off the left singular matrix of tensor X under singular value decomposition in n-mode, and $U_{1S}\in C^{M\times K}$, $U_{2S}\in C^{4\times K}$, $U_{3S}\in C^{L\times K}$ are obtained which are made of the column vectors corresponding to K larger singular values are chosen. Then $U_{1N}\in C^{M\times(M-K)}$, $U_{2N}\in C^{4\times(4-K)}$, $U_{3N}\in C^{L\times(L-K)}$ are obtained by the other columns.

So we can have that

$$X_{(1)} \approx U_{1S} \cdot \Sigma_{1S} \cdot V_{1S}^{H} \tag{8}$$

$$X_{(2)} \approx U_{2S} \cdot \Sigma_{2S} \cdot V_{2S}^{H} \tag{9}$$

$$X_{(3)} \approx U_{3S} \cdot \Sigma_{3S} \cdot V_{3S}^{H} \tag{10}$$

In this formula， $\Sigma_{ns}(n=1,2,3)$ are the diagonal matrix consisting of K singular values of the n-mode expansion of the tensor X, respectively.

$$X = S \times_1 U_{1S} \times_2 U_{2S} \times_3 U_{3S} \tag{11}$$

So the core tensor can be defined as

$$S_S = X \times_1 U_{1S}^{H} \times_2 U_{2S}^{H} \times_3 U_{3S}^{H} \tag{12}$$

Which is

$$X = S_S \times_1 U_{1S} \times_2 U_{2S} \times_3 U_{3S} \tag{13}$$

We define the tensor signal subspace as

$$U_S = S_S \times_1 U_{1S} \times_2 U_{2S} \tag{14}$$

Since the tensor model steering matrix is

$$A_K = a(\theta_k) \circ u_k \tag{15}$$

We could define the following formula at the tensor mode, which are 1-mode Signal subspace is U_{1S}, 2-mode Signal subspace is U_{2S}， and 1-mode noise subspace is U_{1N}, 2-mode noise subspace is U_{2N}：

$$U_{1S}U_{1S}^{H} = \text{span}(a(\theta_1), a(\theta_2), \cdots, a(\theta_k)) \tag{16}$$

$$U_{1S}U_{1S}^{H} = \text{span}(u_1, u_2, \cdots, u_k) \tag{17}$$

So we can know that

$$U_{1N}U_{1N}^{H} \cdot a(\theta_k) = 0 \tag{18}$$

$$U_{2N}U_{2N}^{H} \cdot u_k = 0 \tag{19}$$

According to the tensor model, the relationship between the steering matrix and the noise subspace can be expressed as:

$$A_K \times_1 U_{1N}U_{1N}^{H} = 0 \tag{20}$$

$$A_K \times_2 U_{2N}U_{2N}^{H} = 0 \tag{21}$$

It can be seen that the column vector of the tensor model array response matrix is orthogonal to the 1-mode noise subspace, and the row vector is orthogonal to the 2-mode noise subspace, which is called dual mode orthogonality.

So the spectral estimation formula based on tensor decomposition azimuth estimation algorithm is obtained.

$$P_{MUSIC}(\theta,\varphi) = \frac{1}{\left\| A \times_1 U_{1N}U_{1N}^{H} \times_2 U_{2N}U_{2N}^{H} \right\|} \tag{22}$$

4. SIMULATION ANALYSIS

In this simulation analysis, the acoustic vector sensor array uses a half-wavelength equidistant linear vertical array. By comparing the effectiveness of the traditional MUSIC algorithm and the performance verification experiment based on the tensor decomposition azimuth estimation algorithm. And condition of the simulation are: the number of elements M=8，the distance between the neighboring elements d=λ/2, the azimuth angle and pitch angle both are 45°, the centre frequency is 300Hz，the snapshot L=1024，the background is White Gaussian Noise and SNR is -5dB。

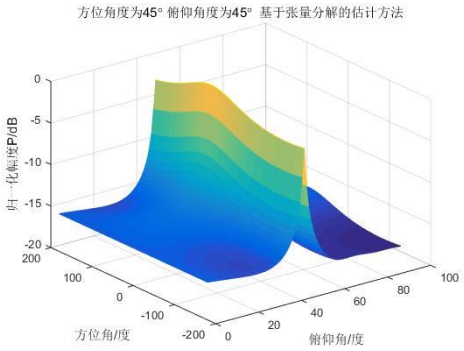


Fig.1: Three-dimensional simulation diagram based on MUSIC algorithm

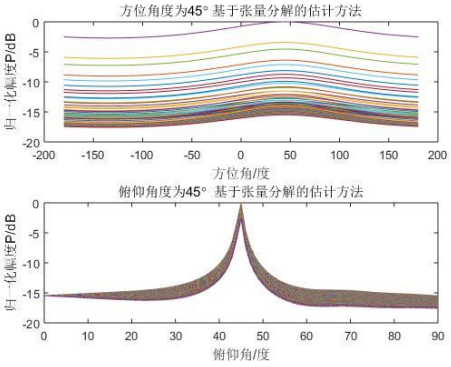


Fig.2: Simulation diagram based on MUSIC algorithm

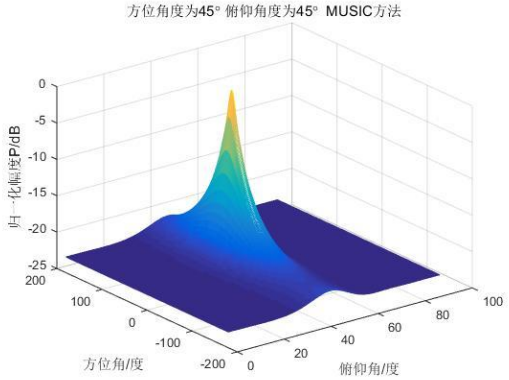


Fig.3: Three-dimensional simulation diagram based on tensor decomposition azimuth estimation algorithm

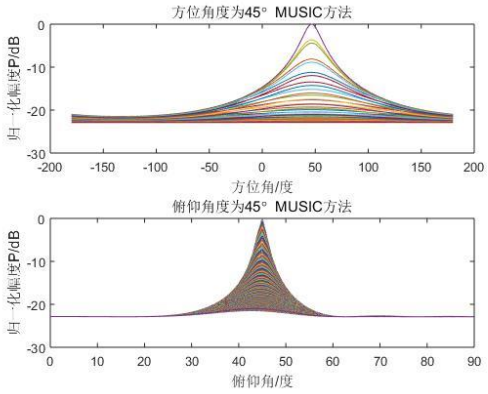


Fig.4: Simulation diagram based on tensor decomposition azimuth estimation algorithm

Figure 1 and Figure 2 are simulation diagrams of the MUSIC algorithm. It can be seen from the figure that the azimuth estimation performance is poor at low SNR. Figures 3 and 4 are simulation diagrams based on the tensor decomposition orientation estimation algorithm. It can be seen that under the same simulation conditions, the tensor decomposition based orientation estimation algorithm has lower side lobes, higher spectral peaks, and the estimation accuracy is greatly improved. Therefore, the proposed algorithm has great engineering application value.

5. CONCLUTION

The traditional azimuth estimation method has certain errors in estimating the signal subspace and the noise subspace, resulting in the accuracy of the estimated sound source incident angle is not high. A tensor decomposition based azimuth estimation algorithm proposed in this paper can better suppress noise due to high-order singular value decomposition, and has better noise suppression ability for sound vector array signals, which can improve low signal-to-noise ratio. The performance of the time orientation estimate.

6. ACKNOWLEDGEMENTS

This paper is funded by the National Natural Science Foundation of China (Grant No. 11674074) and Stable Supporting Fund of Acoustics Science and Technology Laboratory (No. SSJSWDZC2018003).

REFERENCES

[1] **Schmidt R O.** A signal subspace approach to multiple emitter location and spectral estimation,[D].Stanford Univ.,Stanford,CA, 1981.
[2] **Paulraj A** , Roy R , Kailath T . A subspace rotation approach to signal parameter estimation[J]. Proceedings of the IEEE, 1986, 74(7):1044-1046.
[3] **Tucker L R**. Extension of factor analysis to three-dimensional matrices[C].Contributions to Mathematical Psychology. 1964.
[4] **Tucker L R**. Some mathematical notes on three-mode factor analysis[J]. Psychometrika, 1966, 31(3):279-311.
[5] **Sidiropoulos N D**. Generalizing Caratheodory's uniqueness of harmonic parameterization to N dimensions[J]. 2001，47（4）：1687-1690.

[6] **Liang J L, Liu D, Zhang J Y**. Joint frequency,2-D DOA,and polarization estimation using parallel factor analysis[J]. Science in China, 2009, 52(10):1891-1904.
[7] **Guo X, Miron S, Brie D, et al**. A CANDECOMP/PARAFAC Perspective on Uniqueness of DOA Estimation Using a Vector Sensor Array[J]. IEEE Transactions on Signal Processing, 2011, 59(7):3475-3481.
[8] **Miron S , Bihan N L , Jérôme I. Mars**. Vector-Sensor MUSIC for Polarized Seismic Sources Localization[J]. Eurasip Journal on Advances in Signal Processing, 2005, 2005(1):1-11.
[9] **Nagy J G, Kilmer M E**. Kronecker product approximation for preconditioning in three-dimensional imaging applications[M]. IEEE Press, 2006.
[10] **Vasilescu M A O** . Human motion signatures: analysis, synthesis, recognition[C]. International Conference on Pattern Recognition. IEEE, 2002.
[11] **Wang X , Wang W , Liu J , et al**. Tensor-based real-valued subspace approach for angle estimation in bistatic MIMO radar with unknown mutual coupling[J]. Signal Processing, 2015, 116:152-158.

A NEW ACOUSTIC PAYLOAD FOR GLIDERS

Lionel Uzan[a], Fabien Pellet[a]

[a]ALSEAMAR, 60 avenue Olivier Perroy, 13790, Rousset, FRANCE

Lionel Uzan, ALSEAMAR, 60 avenue Olivier Perroy, 13790, Rousset, FRANCE, e-mail: luzan@alseamar-alcen.com
Fabien Pellet, ALSEAMAR, 60 avenue Olivier Perroy, 13790, Rousset, FRANCE, e-mail : fpellet@alseamar-alcen.com

Abstract: *With the support of the DGA, the aim of the AGLIMMS (Acoustic GLIders Mission Management System) project, is to efficiently coordinate a fleet of underwater gliders whose missions are to obtain physical, chemical, biological and/or acoustic measurements on a large 3D sea area. This paper describes the acoustic part under development and especially the passive acoustic results with the classification part.*

Keywords: *Glider, hydrophone array, underwater acoustic, classification, deep learning*

1. INTRODUCTION

The underwater glider, as a silent platform, has opened a new way to explore passive acoustic domain. Indeed, without external propeller or moving part, it navigates using only gravity and buoyancy. So, except during transition phases (surface and deepest point), the self-generated noise is very limited.

For example, it can be used in the Marine Strategy Framework Directive (MSFD) to measure environmental noise level, or to evaluate the biological features as marine mammal's status (number, localisation…).

Other important point to take into account is that sending information is only available at surface through a satellite communication and the piloting is done by an on-shore control team.

Some acoustic payload, adapted for gliders, are already available for measuring the underwater anthropogenic noise level, or detecting few species of marine mammals, but either the power consumption is too high or the software and algorithmic part are proprietary.

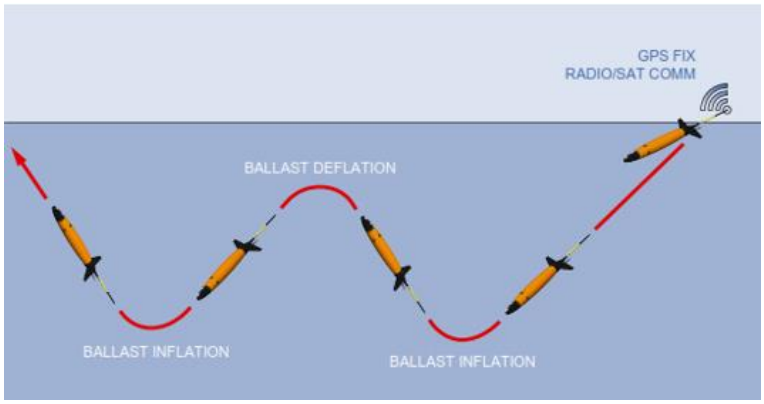


Fig.1: Glider principle

In this document, we only deal with the classification aspect, as this is a real breakthrough. Indeed, the use of deep learning inside a low power microcontroller is quite new, and it opens new possibilities to make easier the classification of acoustic events.

2. PAYLOAD DESIGN

In order to optimise the integration with the SeaExplorer glider, a new acoustic payload was developed to intend new possibilities. Indeed, the main asset of a glider is the endurance, so a special effort was done on the very low power electronic boards to maintain this point with a consumption of 1.7 W.

Moreover, to ensure a very good signal quality, the EMC point has also been taking into account. The system can deal with 8 hydrophones and this is a real breakthrough compared to the equivalent system on the market: the antenna gain (according to the mechanical design) can increase the detection range. The main specifications of the system are:

- sampling frequency up to 192 kHz
- storage on 2 TB of memory
- bandwidth: 10 Hz to 85 kHz
- ADC: 24 bits
- extra sensors input (CTD, SVP…)
- Some embedded application:

- audio recording
- environmental noise level measurement at normalized frequencies (for example 63 and 125 Hz) on 1 hydrophone
- detect an acoustic anomaly
- localize by giving a direction
- classify
- modify the mission following detection and measurement



Fig.2: Hydrophones mounted on the glider

The first mechanical design includes:

- 4 hydrophones in the nose in line array with a tuning frequency of 19200 kHz
- 4 hydrophones in planar array on the wings

On the modify mission point, two aspects will be available:

- as the glider can transmit information by satellite communication only at surface, it is planned, during a dive and in case of detection, to reach the surface as quickly as possible to send a message to the ground control.
- following sensor measurement as sound velocity, the glider could adapt its mission to stay into a favourable water layer.

3. PRESENTATION OF AN ASSESSMENT AT SEA

A campaign of measurement in the Mediterranean Sea was done between the 2nd and 10th of April, 2019.

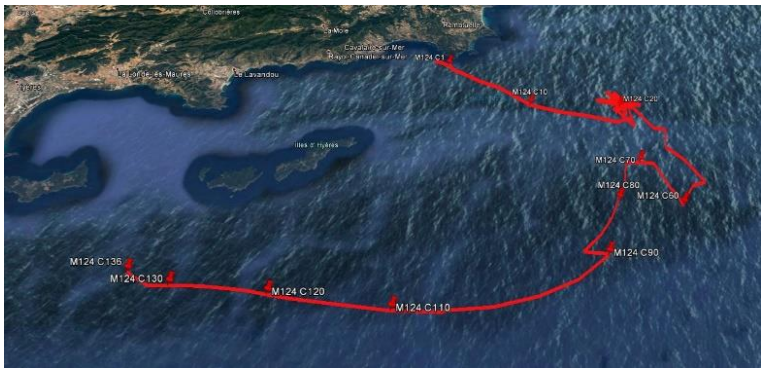


Fig.3: Track of the SeaExplorer (from Cavalaire to South of Porquerolles Island)

The main part of the measurement was done during a virtual mooring: the glider flights always around a fixed position.

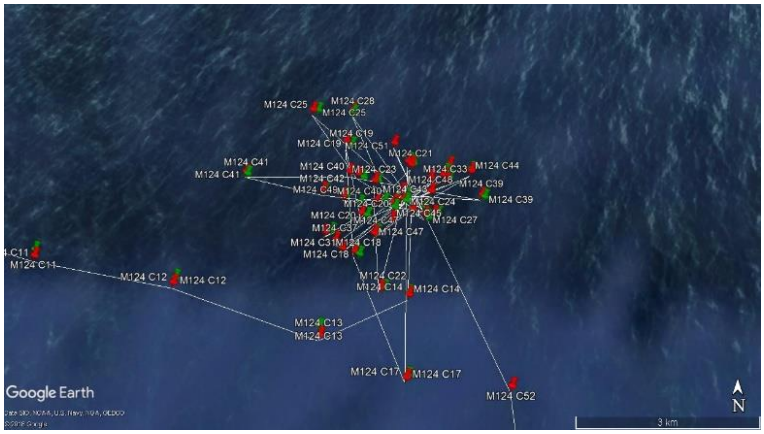


Fig.4: Virtual mooring at South of Cavalaire

There are some remarkable phases of flight that have been applied to the vehicle:

- Different vertical speed (11, 20 and 31 cm/s) for simple yo until 700 m depth: the vertical speed is modified by changing the weight in water with the ballast volume.
- Drift at several depth (100, 300 and 500 meters): during a drift the depth is controlled and some modification of the ballast volume can be done.

The recorder was configured with a sampling frequency of 96 kHz in order to save storage space.

4. SOUND CLASSIFICATION

A very important aspect of the acoustic payload developed into the AGLIMMS project, is the ability of classify acoustic events in real time. So, a particular effort was done to the choice of the microcontroller, on one hand for the best compromise power/consumption and on the other hand for the algorithmic skills. Indeed, the selected microcontroller can deal with deep learning technics as prediction using a pre-learned model.

The first step was to create a sample database for the model training, so, using the large amount of collected acoustic data, a list of categories was defined: boat, mammals click in HF (Fig. 5), dolphin whistle, rain (Fig. 6), normal ambient noise, SeaExplorer internal events (pump, actuator moves). The samples were selected manually with a proprietary software developed for this purpose. There are some samples taken for the learning.

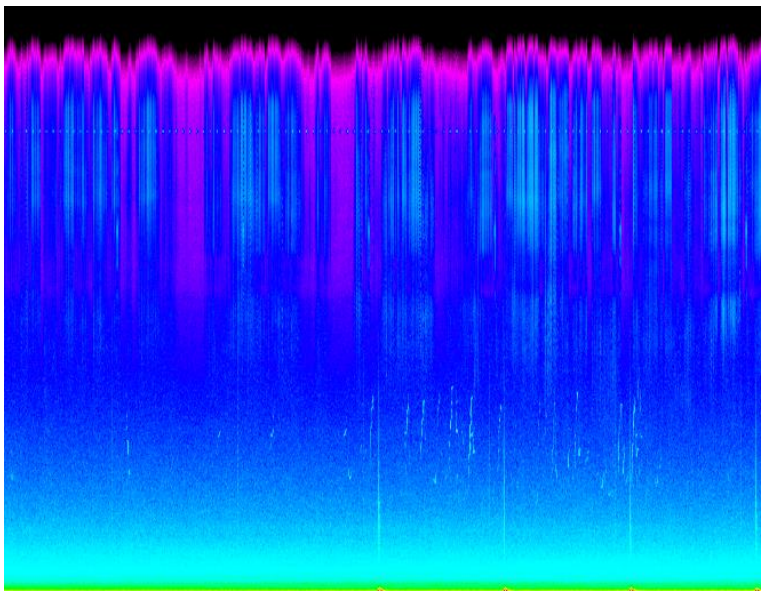


Fig. 5: Spectrogram of dolphin whistles and mammal clicks

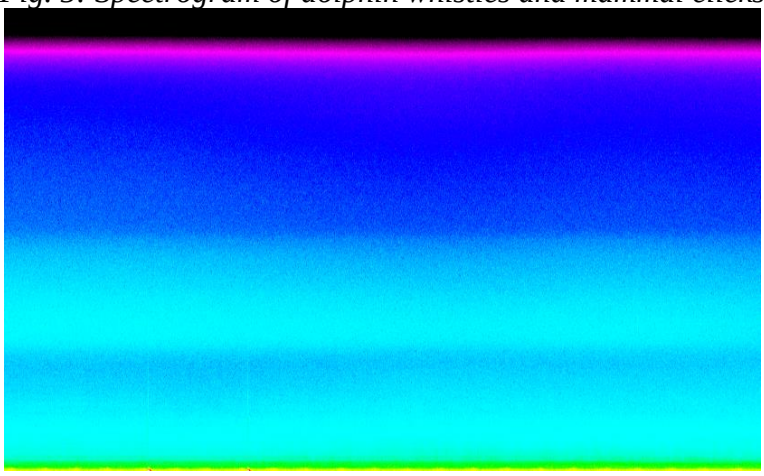


Fig. 6: Spectrogram of the underwater noise caused by the rain

In [1], several odontocetes click frequency range are described, but it seems that there is no matching with a species living in Mediterranean Sea.

The rain noise spectra shown in Fig. 7 can be compared to the spectra given in [2] with the "bump" starting at 14 kHz.

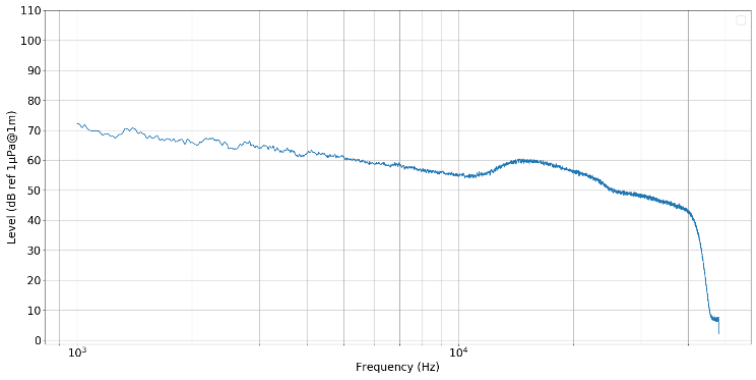


Fig. 7: Noise spectra produced by rain

Then, after the database creation, some relevant features have to be defined dealing with the model dimension:

- 1D with data vector as input,
- 2D with image as input.

The deep learning process can probably give better results with image than vector but as the microcontroller as a very limited memory size, the 1D is the only acceptable solution with a model and weight file of few dozen KB against dozens of MB.

In [3], several features are proposed, but after an evaluation of several features with the confusion matrix, a set of features was selected. For the moment, this choice cannot be revealed because performance tests are in progress in order to tune the features parameters. For example, the features used for the following results are calculated for the whole bandwidth. According to the linear hydrophone array into the nose, the bandwidth could be reduced around 19200 Hz, but it will, probably, redefined the categories.

After a training on several thousand data (with a GPU on a desktop computer), the model and the weight matrix are uploaded to the microcontroller to evaluate the performance in term of computation time as the real time aspect is critical. The calculation time to process 1 second of data is around 35 ms including the features extraction and the prediction at a sampling frequency of 96 kHz. The results are checked with the ones produced by equivalent algorithm on the desktop computer and the two delivered the same prediction for the same test sample.

To evaluate the efficiency of the deep learning technic on the classification, we superimpose on the spectrogram, the result of the prediction as color line at the top. The length of the color line is proportional to the prediction score.

The green line that can be seen in the Fig. 9 and Fig. 10 is the depth of the SeaExplorer. The actuators are categorized into “angular” and “linear” that corresponds to the movement of the battery pack. The angular movement is the rotation of this pack and this allows the vehicle to change is heading. The linear movement is the translation along the lubber line and this allows the modification of the pitch. The noise category gathers all the moment without any disturbance.

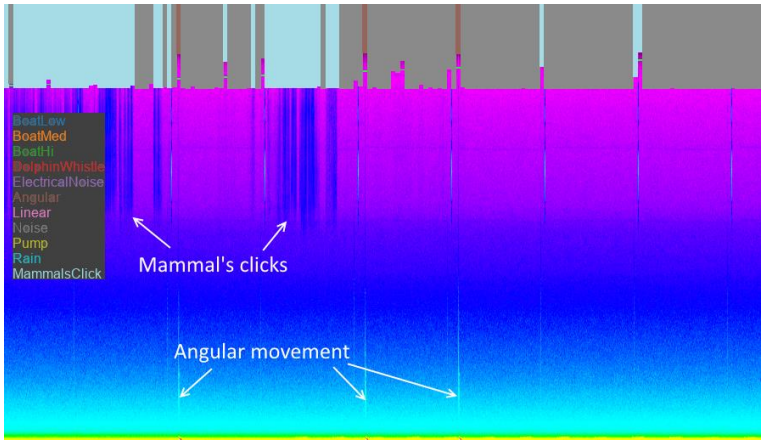


Fig. 8: Detection of mammals clicks

The boat detection is split in 3 categories (low, medium or high level) following the noise level generated. This choice is purely arbitrary and a specific study on this point must be done.

On Fig. 8, the mammal’s clicks are well detected except at the end with 3 false detections: the event is classified as “MammalsClick” instead of Angular.

On Fig. 9, the deep learning prediction hesitates between the 2 levels of boat (low or medium). Probably the noise level generated by the ship(s) is as close to one as to the other category. This is reinforced by the fact that the prediction score can be low. Indeed, the prediction algorithm gives a score for each category, but two can have a relatively close score (only the maximum is displayed).

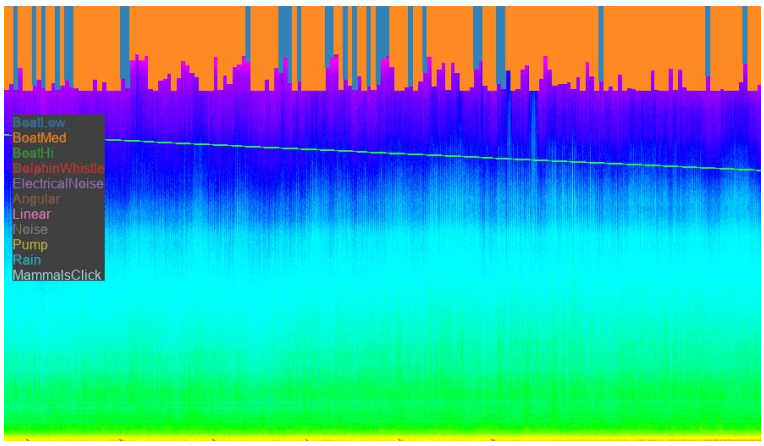


Fig. 9: Detection of boat

Finally, the rain is perfectly detected on Fig. 10.

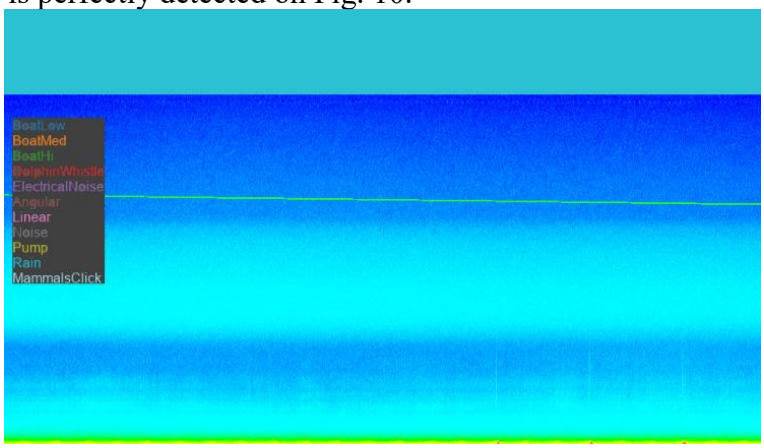


Fig. 10: Detection of rain

The classification using deep learning is quite promising because, firstly, it gives good results and secondly, because it can be embedded into microcontroller.

5. CONCLUSION

At this point, we don't use the hydrophone array to increase the detection range. Indeed, the hydrophone array in the nose is tuned for a frequency of 19200 Hz. So, coupling the array (with +6 dB as array gain) to get the direction of the source and the classification could be very interesting. The two software components are already developed into the microcontroller, but separately, so, a merge is necessary.

A demonstration with three SeaExplorer operating in a formation is planned late 2019 in the Mediterranean Sea. It will highlight the whole detection, localisation, classification process, and in case of "abnormal sound" detected (for example boat) modify the glider's behaviour to reach the surface and send an alarm message to the glider pilot on shore.

ACKNOWLEDGMENT

This work is partially founded by the French defence procurement agency DGA.

REFERENCES

[1] **Morisaka, T., & Connor, R. C.** (2007). Predation by killer whales (Orcinus orca) and the evolution of whistle loss and narrow-band high frequency clicks in odontocetes. *Journal of evolutionary biology*, *20*(4), 1439-1458

[2] **Scrimger, J. A., Evans, D. J., McBean, G. A., Farmer, D. M., & Kerman, B. R.** (1987). Underwater noise due to rain, hail, and snow. *The Journal of the Acoustical Society of America*, *81*(1), 79-86

[3] **Malfante, M., Dalla Mura, M., Mars, J. I., & Gervaise, C.** (2016). Automatic fish sounds classification. *The Journal of the Acoustical Society of America*, *139*(4), 2115-2116

DEVELOPMENT OF LOW-NOISE VECTOR SENSOR USING BENDING MODE RELAXOR FERROELECTRIC SINGLE CRYSTAL MATERIALS

Zhi Li[a,b]

[a] School of Marine Science and Technology, Northwest Polytechnical University
[b] Acoustics Science and Technology Laboratory, Harbin Engineering University

No. 127, West Youyi Road, Xi'an, Shaanxi, 710072, P. R. China
E-mail: zhili@hrbeu.edu.cn

Abstract: *With the development of vector sonar technology, the performance requirements for the vector sensors are gradually increasing, especially for the low-noise, high-sensitivity characteristics at low frequencies. Relaxor ferroelectric single crystal has higher piezoelectric coefficient and lower dielectric loss compared with piezoelectric ceramic, which can make the performance fundamentally improved. The [011] cut relaxor ferroelectric single crystal is proposed to develop the vector sensor in this paper. The dual-beam structure was designed to match the bending mode and anisotropic characteristics of the material. An inertial type vector sensor prototype was developed and characterized. The sensitivity of the prototype can reach to -215.2dB@100Hz, while the working frequency band is 20Hz~1000Hz. The dipole directivity pattern with null depth less than -30dB is obtained. The equivalent noise pressure level is significantly lower than the Knudsen ambient noise level of sea state zero (SS0) above 100Hz band, in which are 55.5dB@100Hz and 45.9dB@200Hz, respectively. This prototype provides the possibility to detect the low-noise target at low frequency.*

Keywords: *Vector sensor, low-noise, relaxor ferroelectric single crystal, bending mode.*

1. INTRODUCITON

Recently, the development of multi-pole vector sensor array technology provided novel approach for remoting detection at low frequency. The high requirements for the vector sensor become urgent, that is, not only higher sensitivity but also lower self-noise [1-3]. The self-noise of the vector sensor system in practice comes from vector sensor itself and the pre-amplifier [4,5]. More specifically, the self-noise of vector sensor is the fundamental noise limit of the system [6].

The self-noise of the vector sensor generally refers to the intrinsic noise caused by the materials and structures itself, which cannot be eliminated and unrelated to the environment [7]. In general, the self-noise of piezoelectric vector sensors is related to the dielectric loss and piezoelectric constant of the material. The lower dielectric loss can significantly reduce the self-noise. However, the performance of vector sensor based on conventional piezoelectric ceramics (PZT) cannot be improved further owning to the properties of materials. Currently, the self-noise of vector sensor, equivalent noise pressure level (*ENPL*, in dB ref. 1μPa/√Hz), is mostly higher than the Knudsen Sea state zero (SS0) ambient noise spectral level in particularly at low frequencies [8-10].

The ternary relaxor ferroelectric single crystal xPb($In_{1/2}Nb_{1/2}$) O_3-yPb ($Mg_{1/3}Nb_{2/3}$)O_3-$z$$PbTiO_3$ (PIN-PMN-PT or PIMNT) is proposed as the active material for low-noise vector sensor in view of its lower dielectric loss and higher piezoelectric constant compared with PZT. A dual-beam structure is designed for matching the bending mode and anisotropic characteristics of PIMNT. The vector sensor prototype is developed and measured in this paper.

2. LOW-NOISE CONSIDERATION AND DEVICE DESIGN

The self-noise of the vector sensor, consisting of electric-thermal noise and mechanical-thermal noise uncorrelated to each other is described as the equivalent noise pressure is given by [5]

$$\overline{P_n^2} = 4k_B T\left[\frac{\tan\delta}{\omega C_p M_p^2} + \frac{\omega_0(\rho c)^2}{mQ\omega^2}\right] \tag{1}$$

where the first term is electric-thermal noise and the second term is mechanical-thermal noise, respectively. k_B (1.38×10^{-23} J/K) is Boltzmann's constant and T (K) is absolute temperature. The electric-thermal noise is caused by active losses in the piezoelectric crystal material, tanδ (%), the dielectric loss. The mechanical thermal noise is created by the mechanical resistance of the damped harmonic oscillator system of the vector sensor, which due to the mechanism of Brownian Motion. However, the mechanical thermal noise commonly can be neglected due to the inertial mass of the vector sensor is millimetre scale. The total self-noise is frequently dominant by the electric-thermal noise, which is concern to dielectric loss of the piezoelectric crystal material, the capacitance C_p (pF) and the pressure sensitivity M_p (dB re. 1V/μPa) of the vector sensor.

The pressure sensitivity generally proportional to its operating mode piezoelectric coefficient d and inversely proportional to the permittivity coefficient ε^T. The *ENPL* also depends on the mode in which the material is used [7]. For instance, the *ENPL* of vector sensor operating in longitudinal mode is respected to

$$ENPL = 10\log\left(\overline{P_n^2}\right) \sim \frac{\varepsilon_{33}^T \cdot \tan\delta}{d_{33}^2} \tag{2}$$

The bending mode and shear mode are similar to this equation. The lower *ENPL* can be obtained by using lower dielectric loss and higher piezoelectric constant. PIMNT is quite suitable for the requirements. The same structure and same size vector sensor with different operating mode are employed for examining the improvement of *ENPL* by using PIMNT substitute for PZT. PIMNT presents different piezoelectric/dielectric performance according to different poled direction. The parameters in various operating mode of different poled PIMNT and PZT-5H are shown in Table 1.

Mode	Material	*d* [pC/N]	ε	tanδ [%]	Δ*ENPL* [dB]	REF
Longitudinal	$[001]_c$ PIMNT	1510	4400	0.6	12.2	[11]
	PZT-5H	593	3401	2		[7]
Bending	$[011]_c$ PIMNT	-1781	4361	0.6	20.4	[12]
	PZT-5H	-274	3399	2		[7]
Shear	$[011]_c$ PIMNT	3354	6814	0.6	14.9	[12]
	PZT-5H	741	3124	2		[7]

Table 1: Parameters in various operating mode of different poled PIMNT and PZT-5H.

As shown in Table 1, the $[011]_c$ PIMNT operating in the bending mode can bring the greatest improvement of *ENPL* by substituting the piezoelectric material. In addition, bending mode is generally used in low frequency applications to obtain higher sensitivity. The high pressure sensitivity is necessary for the inertial type vector sensor especially at low frequency due to the sensitivity will be decreased by 6dB/oct with frequency declining.

The $[011]_c$ PIMNT has different piezoelectric constant along 32 and 31 orientation. The conventional flexural disk design using bending mode is not appropriate for $[011]_c$ PIMNT. The rectangular $[011]_c$ PIMNT presents great piezoelectric properties along 32 orientation. On the other hand, cantilever is the basic structure of flexural beam. However, the inertial type vector sensors are used as neutral buoyancy body which are easily interfered by twisting force. The cantilever is easily affected by this kind of force. The bending dual-beam accelerometer for inertial type vector sensor is proposed for low-noise application at low frequency. The bending accelerometer is operating in 32-mode of the $[011]_c$ PIMNT. The dual-beam has stronger anti-twisting force compared with cantilever, which can improve the stability and anti-interference ability of the vector sensor in actual applications.

Four pieces of $[011]_c$ PIMNT are employed in bending dual-beam design shown in Fig. 1. The d_{32} orientation along the length of the beam and the poling direction is perpendicular to the beam. The parallel of the crystals can increase the total capacitance to decrease coupling condition with pre-amplifier. The arrangement of accelerometer case and base with dual-beam are shown below as well.

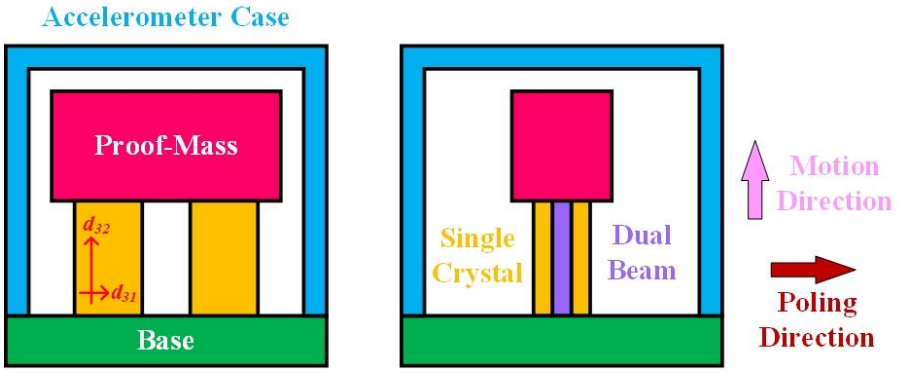


Fig.1: Schematic diagram of dual-beam accelerometer.

The finite element method (FEM) is employed to calculate the sensitivity of the vector sensor. The inertial type vector sensor is co-vibrating with water particle, and the vibration transmits into the vector sensor body then acts on the accelerometer case. We can use the FEM solution of acceleration sensitivity instead of complex multi-physics coupled calculation. The incident acoustic particle acceleration, as the motion direction in Fig. 1, is set on the whole accelerometer case with amplitude a_i (m/s^2) at all analysis frequencies f (Hz). The dielectric, piezoelectric constants and elastic parameters of PIMNT used in FEM are referenced on [11]. The pressure sensitivity level L_M is calculated as

$$L_M = 20\log(M_p) = 20\log(\frac{2\pi f V_o}{\rho c a_i}) - 120 \quad \text{(dB re. 1V/μPa)} \tag{3}$$

where V_0 is the average electric potential of piezoelectric material.

3. PROTOTYPE MANUFACTURED AND PREFORMANCE CHARACTERIZATION

The vector sensor is comprised of the bending mode dual-beam accelerometer and the built-in pre-amplifier (Fig. 2). The accelerometer consisting of bending dual-beam, base and case are made by aluminium alloy. The single crystal (9×6×1 mm) is glued to the beam of the same size. The case and base are bonded together to constitute the complete accelerometer, which has the diameter of 38 mm and the height of 45 mm. The wires lead from the base side to the pre-amplifier with diameter of 35 mm. The accelerometer and the pre-amplifier are assembled on the potting mould which is used to fabricated the polyurethane waterproof coat of the vector sensor. The cylinder vector sensor prototype has diameter of 50 mm and height of 110 mm as shown in Fig. 3.

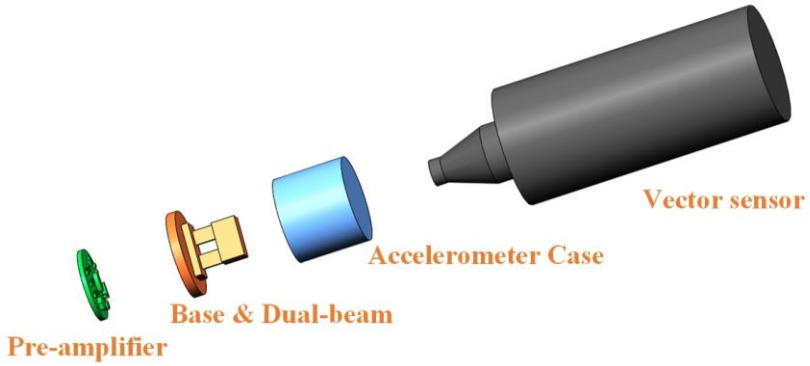


Fig.2: Construction scheme of the vector sensor.



Fig.3: Vector sensor prototype.

The sensitivity and directivity of the prototype were measured in the standing wave tube for evaluating the low frequency characteristic (Fig. 4). The prototype was suspended on the support bracket with spring. The main axis of the prototype was toward the projector settled on the bottom of the tube when measuring sensitivity. The reference hydrophone B&K 8104 was used to comparison with the prototype to determine the pressure sensitivity. The rotating device was employed to evaluate the directivity from 0° to 360° by the interval of 10°.

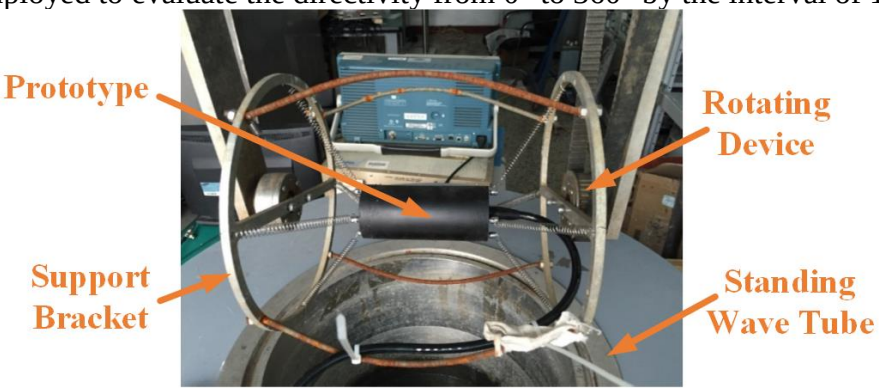
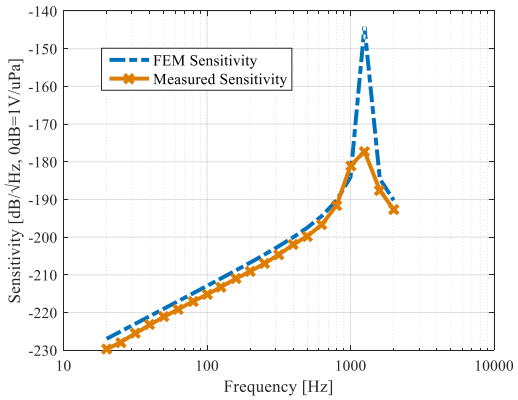


Fig.4: Arrangement of vector sensor sensitivity and directivity measurement.

Fig. 5 presents the measured pressure sensitivity in comparison with that from the FEM solutions. The working frequency band is approximately 20Hz~1000Hz, and the pressure sensitivity without pre-amplifier is -215.2dB@100Hz. The tendency of the two curves are in good agreement except that the overall value of measured sensitivity is slightly lower than that of simulation. The possible reason is that the density of the prototype is greater than water. The negative buoyancy makes sensitivity decreasing. The measured directivity at 100Hz presents in clear dipole pattern (Fig. 6). The null depth is less than -30dB and heterogeneity of main axis is less than 1dB.



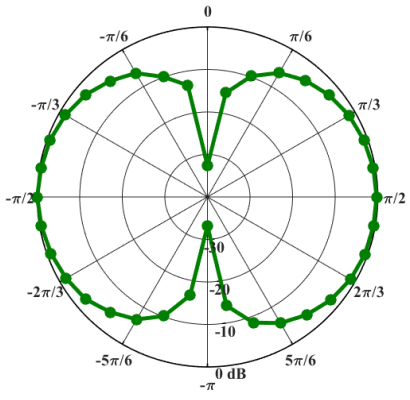


Fig.5: Experimental and theoretical sensitivity. *Fig.6: Measured directivity at 100Hz.*

The vector senor of inertial type is sensitive to both sound pressure and vibration. These kinds of interferences can easily be introduced into the measurement if there is no isolation. The equipment for measuring self-noise of vector sensor was developed as Fig. 7. The acrylic

tank using vacuum gauge and vacuum pump creates a vacuum environment for sound insulation. The thin copper was coated outside of the acrylic tank for electromagnetic shield. The tank placed on the steel base and the air spring settled under the base for vibration isolating. The prototype was suspended by elastic band inside the tank. All instruments like low-noise amplifier (5113), data acquisition (NI 9239) and battery were placed in the tank. The air had been evacuated from the tank using vacuum pump before recorded the data. The self-noise data was stored in a USB flash disk and then processed on the computer.

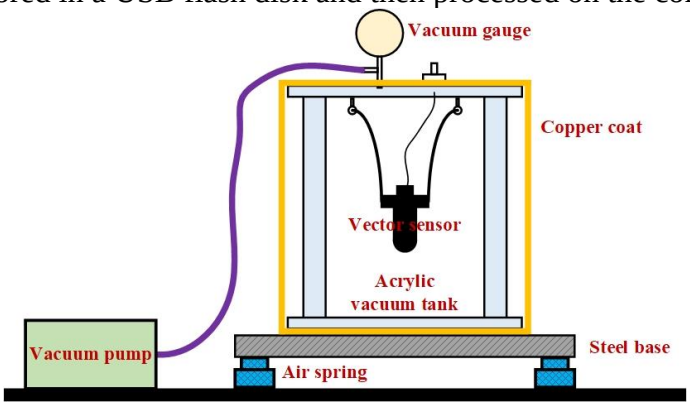


Fig.7: Schematic of vector sensor self-noise measured equipment.

The *ENPL* of prototype is represented and compared to Knudsen SS0 in Fig. 8. The measured *ENPL* is significantly less than that of Knudsen SS0 above 100Hz in which reaches to 55.5dB@100Hz and 45.9dB@200Hz, respectively. The vibration interference has a great influence below 60Hz due to the passive vibration isolation in laboratory cannot achieve good results in this band.

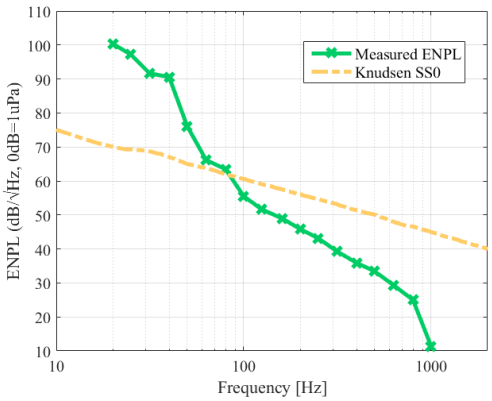


Fig.8: Experimental ENPL of vector sensor prototype compared with Knudsen SS0.

4. CONCLUSION

The development of inertial type vector sensor by using relaxor ferroelectric single crystal material is reported in this paper. The dual-beam structure vector sensor for matching the $[011]_c$ bending mode single crystal is studied, and the prototype is manufactured. The measurement results indicate that pressure sensitivity of the prototype is -215.2dB@100Hz and the working frequency band is 20Hz~1000Hz, which are in good agreement with the FEM solution. The directivity shows good dipole pattern with null depth less than -30dB. The obtained *ENPL* are 55.5dB@100Hz and 45.9dB@200Hz, respectively. The *ENPL* is significantly less than that of Knudsen SS0 above 100Hz which indicate the vector sensor prototype has low-noise performance at low frequency. This prototype provides the possibility to detect the low-noise target at low frequency.

5. ACKNOWLEDGEMENTS

This work was supported by the Fund of Acoustics Science and Technology Laboratory. Special thanks to Prof. Xu and Prof. Wang from Xi'an Jiaotong University for supporting the relaxor ferroelectric single crystal materials.

REFERENCES

[1] **S. Yang,** Directional pattern of a cross vector sensor array, *J. Acoust. Soc. Am.*, 131(4), pp. 3484-3484, 2012.

[2] **X. Guo, S. Yang and S. Miron,** Low-frequency beamforming for a miniaturized aperture three-by-three uniform rectangular array of acoustic vector sensors, *J. Acoust. Soc. Am.*, 138(6), pp. 3873-3883, 2015.

[3] **X. Guo, S. Miron, Y. Yang, et al.,** An upper bound for the directivity index of superdirective acoustic vector sensor array, *J. Acoust. Soc. Am.*, 140(5), pp. EL410-EL415, 2016.

[4] **T. B. Gabrielson,** Modelling and measuring self‐noise in velocity and acceleration sensors. In *AIP Conference Proceedings CONF-9509298*, Vol. 368, pp. 1-48, 1996.

[5] **Z. LI, S. Yang and H. CHEN,** Low-noise design of piezoelectric vector sensor. *ACTA ACUSTICA*, 2018(4), pp. 432-444, 2018.

[6] **T. B. Gabrielson,** Fundamental Noise Limits for Miniature Acoustic and Vibration Sensors, *J. Sound. Vib.*, 117(4), pp. 405-410, 1995.

[7] **J. L. Butler and C. H. Sherman,** *Transducers and arrays for underwater sound*. Springer International Publishing, pp. 551-552, 2016.

[8] **K. R. Howard, W. K. Thomas, J. K. Patrick and T. B. Gabrielson,** A microfabricated electron-tunneling accelerometer as a directional underwater acoustic, *American Institute of Physics Conference Proceedings*, 368, pp. 57-68, 1996.

[9] **P. A. Wlodkowski, F. Schloss,** Advances in acoustic particle velocity sensors, *Workshop Directional Acoustic sensors*, Newport, RI, April. 2001.

[10] **F. Edalafar, S. Azimi, A. Q. A. Qureshi, et al.,** A wideband, low-noise accelerometer for sonar wave detection, *IEEE Sens. J.*, 18(2), pp. 508-516, 2018.

[10] **S. Zhang, and F. Li,** High performance ferroelectric relaxor-PbTiO3 single crystals: Status and perspective. *J. App. Phys.*, 111(3), pp. 2, 2012.

[11] **E. Sun, S. Zhang, J. Luo, et al.,** Elastic, dielectric, and piezoelectric constants of $Pb(In_{1/2}Nb_{1/2})$ O_3-Pb $(Mg_{1/3}Nb_{2/3})O_3$-$PbTiO_3$ single crystal poled along $[011]_c$. *Appl. Phys. Lett.*, 97(3), pp. 032902, 2010.

Regular Session 23
Mine countermeasures

EVALUATING HUMAN/MACHINE INTERACTION FOR UNDERWATER THREAT CLASSIFICATION: A CASE STUDY

Olga Lopera Tellez[a],

[a] Department of Communication, Information, Systems and Sensors, Royal Military Academy,1000 Brussels, Belgium

olopera@rma.ac.be

Abstract: *In this paper, expert deminers and automated algorithms are charged with the task of analysing sonar images collected during real mine countermeasures exercises in order to classify targets. Images are collected using synthetic aperture sonar (SAS) and side scan sonar (SSS), covering a test area on the Belgian Continental Shelf. A total of 1241 images (with 847 detection opportunities) collected from different sonar systems, each of them covering the entire area, are used. Image resolution is divided in three categories: (1) up to 5cm pixel size, (2) over 5cm until 10cm pixel size, (3) larger than 10cm pixel size. Data are analysed in different ways by the expert operators and the algorithms. Results demonstrate how challenging underwater threat recognition still is, and highlight the utility of considering the human operator as an integral part of the automatic underwater object recognition process, as well as how automated algorithms can extend and complement human performances.*

Keywords: *mine countermeasures; synthetic aperture sonar; side-scan sonar; automatic target classification; human-in-the-loop*

1. INTRODUCTION

The need to maintain maritime freedom of manoeuvre implies a requirement for maritime capability to survey littoral waters, sea line of communications, choke points, structures, ports and harbours. Currently, these maritime capabilities include high-resolution sonar systems such as side-scan sonar (SSS) and synthetic aperture sonar (SAS) for imaging the seabed and the water column in order to detect and identify underwater objects which might threaten safety of navigation. Although automatic object recognition algorithms have been developed for and are applied in different remote-sensing imaging applications, object-recognition from acoustic/optical imagery in this maritime application is still performed almost exclusively by human operators. There is still a long way to see these automatic algorithms being fully trusted to take the place of human analysts [1]. To facilitate this process, [2] suggests the development of methods by which humans and computers can work in concert to achieve improved performance.

In this paper, human experts and algorithms are charged with the task of analysing the same database of acoustic images. The later are collected by unmanned maritime vehicle systems equipped with SSS and SAS, tasked with naval mine hunting and route surveillance operations during real mine countermeasures (MCM) exercises. The group of human experts is composed by 4 deminers with 7 to 25 years of experience in sonar imaging and 2 scientists with 10 years of experience in sonar imaging. Two classification algorithms are used, one based on Markov Chain Monte Carlo [3] and a second one based on Adaptive Boosting Decision Trees [4]. The test area is located on the Belgian Continental Shelf, between the Thorton bank and the Goote Bank. This test area is selected based on the long term stability of its physical characteristics. Different objects (exercise-mines and friendly objects) are deployed at different locations. Data are recorded using different SAS and SSS systems, and data are categorized by their resolution: (1) up to 5cm pixel size, (2) over 5cm until 10 cm pixel size and (3) larger than 10cm pixel size.

This study is a continuation of the analysis presented in [5,6]. In [5], data collected during object-detection trials (mine hunting trials) are analysed in order to create a connection between seafloor characterisation maps and prediction of object-detection performance. Results demonstrate that trends can be established between environmental parameters and the detection performance (in accordance with the analysis presented in [7]). In [6], a preliminary analysis of the target detection performances of human vs machine was carried out with a limited acoustic image database, and the classification performance was not yet evaluated. This paper goes forward with the evaluation of different human/machine interaction strategies to improve classification performance.

This paper is divided as follows. Section 2 describes the test area based on the analysis of ground truthing measurements presented in [8]. The sonar systems and their data are introduced in Section 3. Section 4 introduces the algorithms used to process and analyse the data and a discussion of the results and further work is presented in Section 5.

2. TEST AREA AND ENVIRONMETAL ASSESSMENT

2.1. Test area description

The area is located between the Goote bank and the Thorton bank, a central area on the Belgian Continental shelf, 17 NM off the Belgian coast (Ostend). It is 2NM² and presents 20 to 30 meter of water depth. At the left side of Fig. 1, the location of this area is shown with a

dark green rectangle. Its corresponding bathymetry map is shown at the right side of Fig. 1. In the later, sandwaves with height between 2 to 4 meter and wavelength around 150 meters are recognized. They are distributed Northeast and Northwest of the area. A low flat area is present Southworth between those sandwaves and the nearby Goote bank area.

For the environmental assessment of this area, during a scientific survey with the oceanographic Research Vessel Belgica A962, 32 sediment samples were collected. The analysis of these samples is introduced in the next Session.

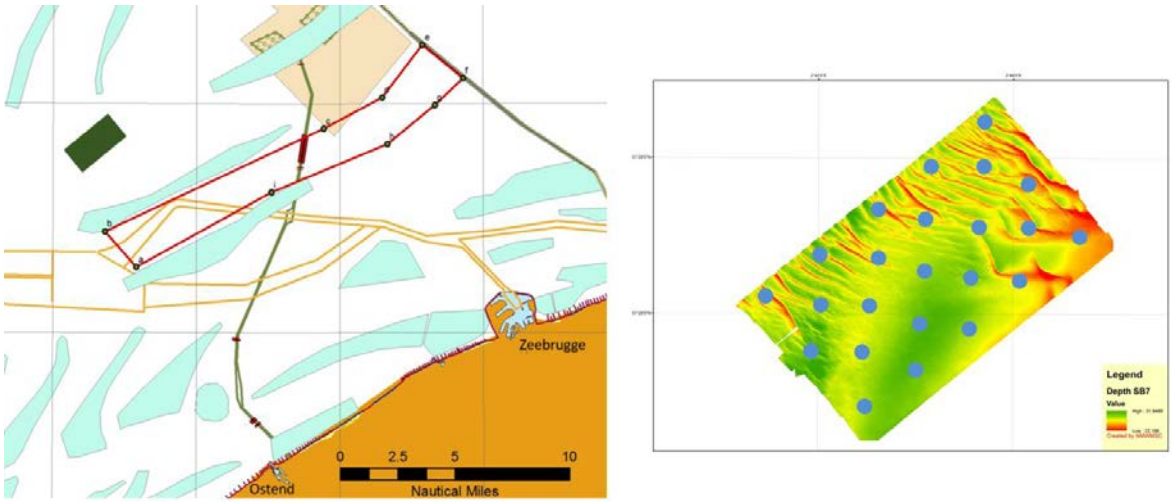


Fig.1: Left: Test area marked by a green box between the Goote bank and Thorton bank. Right: Bathymetric map of the test area, where 32 sampling stations are indicated by blue circles. Distance between the samples varies between 500 and 600m.

2.2. Sampling analysis

In the analysis the collected samples, not only the grains size distribution of the sediments over the area were considered, but also shell distribution, carbonate content distribution, gravel distribution and presence of benthic organisms. Regarding the shells, a distinction was made between entire shells, shell fragments and shell hash. Shell hash is considered being accumulation and abundance of small fragments with dimension less than 4mm.

Considering the shell distribution, abundance of shells is found where bedforms are largely developed, whilst complete absence of shells is noticed at the transition zone between the most western sandwaves and the gully. Shell fragments distribution follows the shells distribution although the fragments are better aligned with the currents directions. Shell hash is mainly founded where abundance of shells is, though a good level of shell hash is found in the gully where nor shells nor shell fragments are present. The hypothesis is that the shell hash in the southern part of the area could be accumulated after being transported by the local currents.

The distribution of the carbonate content is in line with the shell, shell fragments, and shell hash distribution. Regarding tubeworms, they are concentrated where concentration of shell fragments and shell hash is high; this is in response to their nature to construct their main housing with small shell fragments. Echinidae are mainly found where large bedforms are developed and gravels are mainly founded into the gully.

The Grain size analysis of the 32 samples was conducted considering the mixture sand and carbonate into the sediments. Only the organic material was eliminated by chemical treatment. The sediment results had shown a granulometry in a range between 350 and 700 μm corresponding to coarse sand in the Wentworth scale. In the test area the coarseness increases going towards southeast.

The coarseness is accentuated by the presence of the carbonate into the sediments. Proof of that is given by the samples with higher values of granulometry. For those samples, consistent high level of shell hash was found into their mixture.

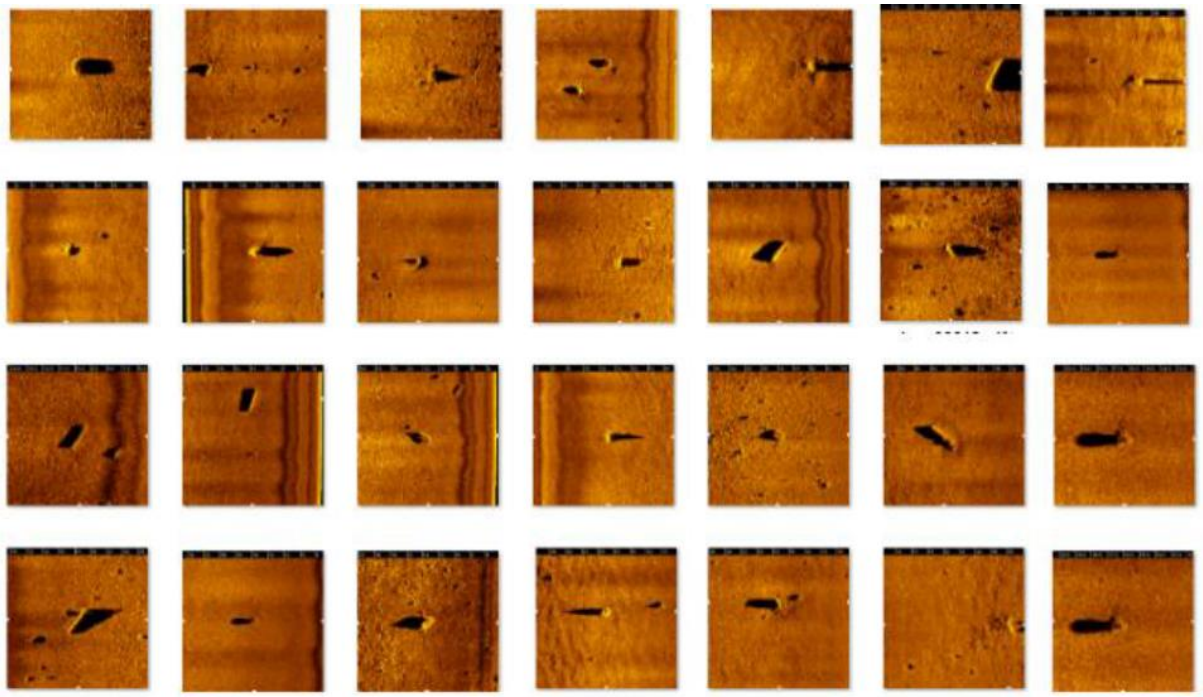


Fig.2: Some thumbnails of SSS data

3. MEASUREMENT SETUP

Data gathered by different SAS and SSS systems are used for this study. The centre frequency of the systems ranges from 100kHz to 300kHz. Some examples of the images provided byone the SSS systems can be seen in Fig. 2.

A total of 31 mine-like objects were deployed (including Manta, Cylindrical, Rockan and Moored exercise mines) on the seabed and in the water column. They were located at different positions distributed all over the test area. In order to give an idea of the dimensions of the objects, their description is presented in Table 1. A few friendly objects were also deployed, including oil barrels and metallic cages. It is worth noting that positions where unknown to the operators and the algorithms during the object recognition process and were released afterwards for the analysis.

Target	Dimensions
Manta mine (MM)	Height: 44 cm Diameter: 98 cm
Cylindrical mine (GM)	Length: 1,60 m Diameter: 50 cm
Rockan mine (RC)	Width : 100 cm Length: 80 cm Height: 40 cm
Moored mine (MM)	Length: 100 cm Diameter: 75 cm

Table 1: Geometrical characteristics of the deployed mine-like objects.

4. METHODOLOGY

4.1. Target detection and classification

In order to detect objects of interest, the algorithm used here focuses mainly on the geometrical configuration of the highlight and shadow cast on the seafloor. The methodology presented in [3] is applied, which segments the shadow and highlight using a combination of fuzzy sets and mathematical morphology. A number of geometrical features are then extracted from these areas, and are then used to classify targets from real data against a previously compiled database of mine-like objects (MLO) and friendly-objects (FO) features using a Monte Carlo Markov Chain approach proposed in [3] and the Adaptive Boosting Decision Trees proposed in [4].

In MCM, there is an increasing interest in having methodologies for automatic seafloor characterization related to mine-hunting difficulty. Several authors have started developing image processing techniques based on acoustic images [9-11]. Generally speaking, these techniques evaluate the pixel values and classify them following segmentation, feature extraction techniques, statistical models, amongst other approaches. More recently, [7] presented a seafloor characterization approach based on lacunarity with very promising results. The lacunarity of a set of pixels in a grayscale image is the ratio of the variance of the pixel values to the square of the mean of the pixel values. It has several forms of being calculated. In [7], a new, fast technique based on integral- image representations is proposed and validated using thousands of HR sonar images with diverse seafloor conditions. This technique has been applied in [5,8] for the evaluation of the segmentation results compared with ground truthing measurements (sediment analysis, video imaging, sediment profile imagery and diving).

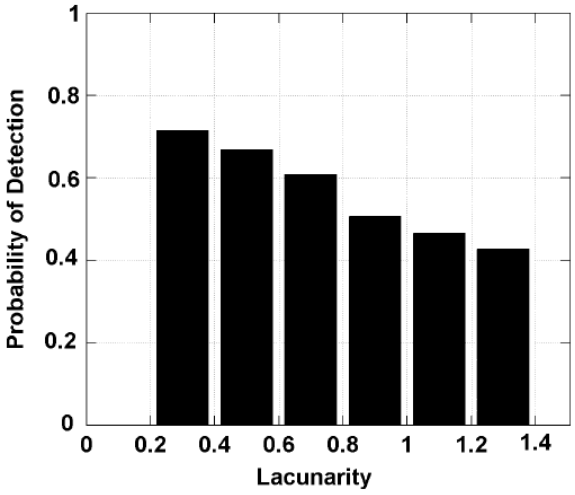


Fig. 3: Probability of detection for the detection program as a function of lacunarity [5].

4.2. Data processing strategies

Three different strategies were tested. In the first one, the complete data set is processed by the detection and classification programs. Time to complete the process is count and the probability of detection and classification are calculated separately for each classification algorithm. For the second approach, human experts are asked to process the entire database. Their timing is also counted and their detection and classification probabilities are also calculated. Finally, the data set is divided into two soil categories: "benign" and "complicated", based on the lacunarity results presented in [5], and the algorithms process one part of the data while human/machine combination processes the other part.

In [7], it was shown that the probability of detection decreases as the lacunarity increases. Results found in [5] are in accordance with the later (see Fig. 3). High values of lacunarity mean that the pixel-intensity variation is high, and after studying probability of detection in such seafloors, they are categorized as "complicated". Seafloors with low values of lacunarity are categorized as "benign".

Sonar data collected in the test area presented a high variation in the lacunarity values [5]. Several zones could be identified and well correlated with the environmental parameters. Where a high concentration of complete shells and benthos were found, high lacunarity values (higher than 1) were calculated. Presence of shell hash also increments the lacunarity values (between 1.1 and 1.4). This could indicate that shell hash increase the sediment (scatterer) size in average and therefore the seafloor becomes more "complicated". The latter is accordance with the hypothesis found in [7] where lacunarity values increased with sediment size.

5. DISCUSSION

The probability of detection is shown in Fig 4 for the operators (Op) and algorithm (ATD). Note that, in order to simplify the graph, the operators are not considered individually but their average performance is used as a single expert. The graph shows results as a function of mine type and pixel size. Not surprisingly, it can be seen that the probability of detection decreases with the resolution. Results drastically decrease for the lowest resolution, with exception of the detection by the operator and the ATD of the cylindrical mine (GM) in such conditions. This can be explained by the geometry and dimensions of the cylindrical mine,

which are larger compared to the manta and rockan mines. The detection algorithm performs slightly better than the human expert, except for the manta mine (MA) and the moored mine (MM, not presented in the graph).

The probability of classification is shown in Fig 5 for the operators (Op, averaged as well) and both algorithms (ATC1 and ATC2). Performance of both algorithms is similar and they outperform the operator, except for the manta mine (MA) and the moored mine (MM, not presented in the graph). None of the later mine was correctly classified by the algorithms since it is not included in the training database. Although cylindrical mines (GM) were detected for images with a pixel size larger than 10cm, none of them were correctly classified by the operator nor by the ATC algorithms. For the later, this can be explained by the fact that algorithms were trained using images with pixel size smaller than 5cm. For the cylindrical and rockan mines, it can also be seen that operators performed better for the images with pixel size between 5 and 10cm than for images with better resolution. This can be explained by the fact that the majority of images in the 5-10cm pixel size category comes from the sonar system they are used to work with.

For the last part of the analysis and following the lacunarity, data are divided between ‘benign’ and ‘complicated’. For the test area considered here, the area with the lowest lacunarity values (between 0.2 and 0.4), i.e., scoring the highest probability of detection (0.7) is categorized as “benign”. This corresponds to almost 30% of the dataset. The rest of the area is considered as “complicated” (probability of detection lower than 0.7). Data included inside the “benign” soils are treated by the detection and classification algorithms directly, while detection in the “complicated” soils is first performed by the human operators and their results used as input for the classification algorithm. Following this strategy, the number of false alarms is drastically reduced by 73% and the number of misdetection is reduced by 48%, compared with the first strategy. It is worth noting that for this strategy, time of processing is doubled during the analysis of the human operator in combination with the algorithm, compared with processing using only the algorithms. The extra time added when passing from one strategy to another also depends on the experience of the operators with the type of images (working with previously unseen images, i.e., not previously used for training operators, which is the case in this study) as well as the size of the data to be processed by the operator only (corresponding to the “complicated” soils). The selection of the threshold between ‘benign’ and ‘complicated’ soils could therefore play an important role in the timing. These are crucial factors that would have to be considered for the planning and evaluation of a mission.

Further work needs to be done to improve the detection and classification algorithms, and to consider a different approach such as deep learning. Future MCM capabilities will integrate different systems for autonomous detection and classification of targets. This study opens a discussion for the importance of human-in-the-loop, in conditions such as presence of targets unknown for the ATC algorithm or difficult environmental conditions.

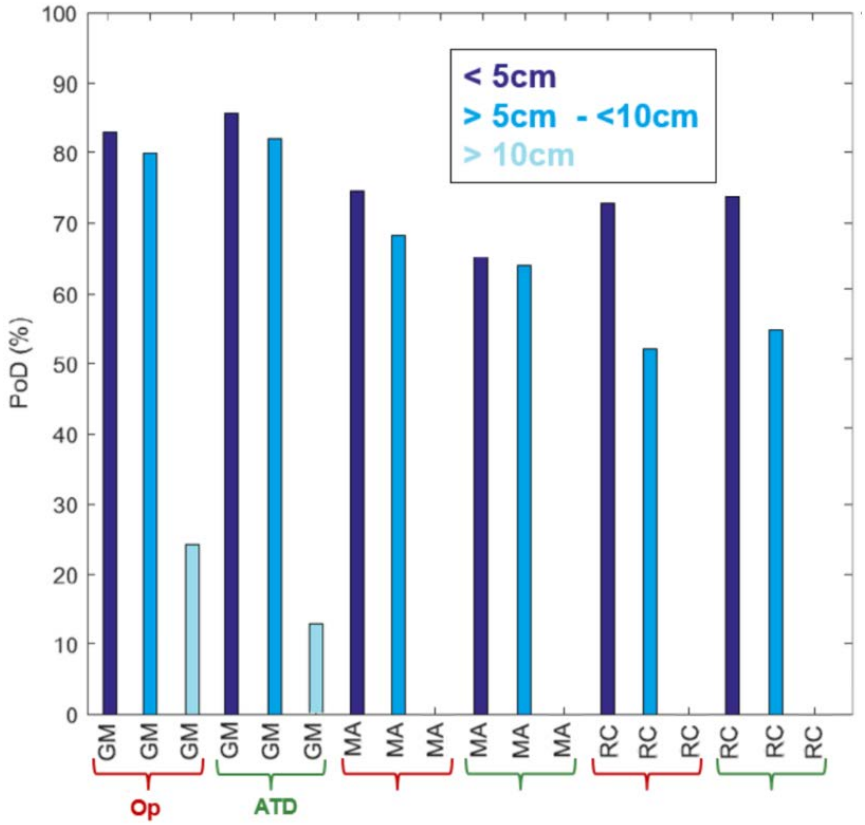


Fig. 4: Probability of detection for operators (BE Op) and algorithm (ATD) as a function of mine type and image resolution.

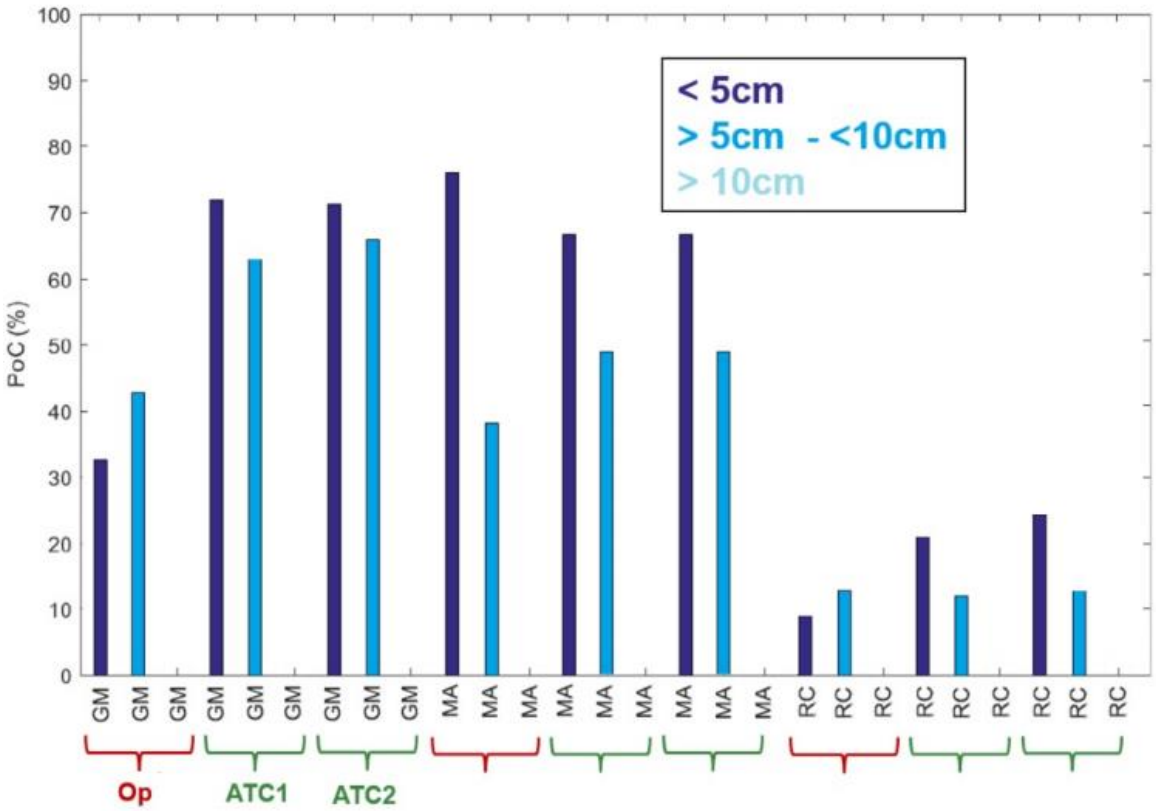


Fig. 5: Probability of classification for operators (BE Op) and algorithms (ATC1, ATC2) as a function of mine type and image resolution.

6. ACKNOWLEDGMENT

The authors would like to thank CMRE STO for giving us access to part of the MUSCLE database from the Autonomous Undersea Surveillance group in order to train our algorithms and for allowing us to use their lacunarity software. The authors would like to thank also the human experts involved in the experiment as well as the crews of RV Belgica [12] and the different Belgian Navy vessels involved in data collection for their time and efforts in contributing to this study.

REFERENCES

[1] J. Stack, "Automation for underwater mine recognition: Current trends and future strategy," in SPIE Defense, Security, and Sensing, vol. 8017, 2011.
[2] D. Williams, M. Couillard, and S. Dugelay, "On Human Perception and Automatic Target Recognition: Strategies for Human-Computer Cooperation", in International Conference on Pattern Recognition, 2014.
[3] Lopera, O., A. Borghgraef and E. Mersch; The Special Case of Sea Mines, in Mine Action, Beumier C, ed. InTech 2017, pp 251-279.
[4] J. Isaacs, "Sonar Automatic Target Recognition for UXO Remediation," Naval Surface Warfare Center PCD, Proceedings of the Institute of Acoustics, Vol. 36, 2014.
[5] O. Lopera and S. Papili, "Sea-floor characterization related to object-detection performance of sonar systems: a case study", in Oceans 2017, Aberdeen, UK, 2017
[6] O. Lopera, "Human in the loop for autonomous underwater threat recognition", in Oceans 2018, Charleston SC, 2018
[7] D. Williams, "Fast Unsupervised Seafloor Characterization in Sonar Imagery Using Lacunarity", IEEE transactions on Geoscience and Remote Sensing, Vol. 53, No. 11, pp. 6022-6034, 2015.
[8] O. Lopera and S. Papili, "An introductory study of the impact of environmental parameters in the performances of imaging sonar systems", in Oceans 2016, Monterey, CA, 2016.
[9] L. Sha, and L. Nolte, "Effects of environmental uncertainties on sonar detection performance prediction," The Journal of the Acoustical Society of America, vol. 117, no. 4, pp. 1942–1953, 2005.
[10] D. Williams and E. Fakiris, "Exploiting environmental information for improved underwater target classification in sonar imagery," IEEE Transactions on Geoscience and Remote Sensing, vol. 52, no. 10, pp. 6284–6297, 2014.
[11] X. Lurton, and G. Lamarche, "Backscatter measurements by seafloor-mapping sonars: Guidelines and Recommendations". Geohab, Eastsound, WA, USA. 200pp. 2015.
[12] http://www.howbigisbelgica.be

ENABLING AUTONOMOUS MINE COUNTERMEASURES FOR THE NATO ALLIANCE

Samantha Dugelay[a], David Williams[a], Thomas Furfaro[a], Jose Melo[a], Veronika Yordanova[a], Christopher Strode[a], Bart Gips[a], and Yan Pailhas[a]

[a]NATO Centre for Maritime Research and Experimentation (CMRE)

CMRE, Viale San Bartolomeo, 400, La Spezia, Itlay
Samantha.Dugelay@cmre.nato.int

Abstract: *As many more nations actively transition their mine countermeasures (MCM) capability towards autonomous systems, the NATO Centre for Maritime Research and Experimentation (CMRE) continues to research the utilisation of robotics in the minefield to deliver doctrinally relevant autonomy and on-board intelligence with a view to deliver a NATO capability.*
This review paper will present an overview of the CMRE approach to autonomous mine countermeasures. In particular, this paper will highlight the development of specific enabling technologies regarding sensors, automatic target recognition, autonomy, and in situ planning and evaluation.
These specialised and multi-disciplinary activities are brought together into a system-of-systems approach, which will enable future war fighting capability to adapt to mission specifics and environmental conditions. With a system-of-systems concept come additional particularities and difficulties such as passing target location and its accuracy from one vehicle to another, collaborative autonomy, interoperability and the performance evaluation of a set of heterogeneous vehicles.

Keywords: *NATO, Mine countermeasures, autonomy, robotics, automatic target recognition, synthetic aperture sonar, planning and evaluation, interoperability, target location accuracy.*

1. INTRODUCTION

The Centre for Maritime Research and Experimentation (CMRE) is working to transform the way mine countermeasures are conducted from a post-Cold War approach that focuses on post-operations clearance using surface ships, to a quickly deployable, autonomous system that is scalable, cost effective, and minimizes risk to personnel. Recently, work in the Autonomous Naval Mine Countermeasures group (ANMCM) at the Centre has focused on using AUVs for mine hunting, including developing techniques for handling the large data rates associated with modern high-resolution sonar and developing AUV systems that make decisions based on data that is gathered *in situ*. Now, the Centre's emphasis is expanding from using AUVs in mine hunting to using AUVs in mine identification, developing a network of collaborating heterogeneous vehicles and continued development of novel sensors. This strategy is one that is adopted by many nations and CMRE is committed to supporting these efforts; the Centre's advantage is the ability to rapidly prototype and test new algorithms, concepts and systems at sea, work with nations to develop NATO interoperability and standards and exploit the vast amount of at sea data acquired in a variety of environments

This paper will give an overview of the program of work undertaken within the ANMCM group. CMRE is advocating for multi-phase system-of-systems MCM missions comprising multiple heterogeneous unmanned systems. One such operational example is the Italian Mine hunting Exercise (MINEX) 2018 as shown in Figure 1. However, in such a system-of-system (SOS) MCM scenario, the accuracy on the location of each of the detected targets will naturally affect subsequent phases of a system-of-systems MCM missions, and the problem needs to be addressed from a SOS point of view. The CMRE fleet of vehicles currently comprises:

- the **MUSCLE**, a 21" Bluefin vehicle equipped with a Thales, UK synthetic aperture sonar which focuses mainly on wide area survey and provides a detection and classification capability,
- the Black Collaborative Autonomy Testbed (**Black CAT**) equipped with a forward look 900kHz Blueview sonar, a 2.25 MHZ Blueview multibeam echo-sounder and an optical camera, mainly utilised to test collaborative behaviours, reacquisition of a target and gathering additional information on target,
- the Bi-modal Identification Or Neutralisation DemOnstor (**BIONDO**), a SPARUS vehicle equipped with an ARIS camera, which is employed for acoustic identification and to simulate the behaviours of a neutralisation vehicle.

Each vehicle is equipped with different system adapted to carry out a particular phase or set of tasks with a typical mine hunting scenario; however, the fundamental enabling technologies remain the same:

- the development of on board perception which includes for example on board sonar image processing, automatic target recognition, and target clustering,
- the implementation of *in situ* performance evaluation based on the data, outputs from the ATR and target clustering,
- the increase in vehicle capability to make decisions and to collaborate with our systems.

Additionally, CMRE is building a novel low frequency synthetic aperture sonar concept to tackle the problem of buried targets and difficult environments with a particularly high false alarm rate.

The remainder of the paper is organised as follows: section 2 will present the work related to on board perception, in particular related to the CMRE MUSCLE and the exploitation of the synthetic aperture sonar images produced in real-time on board the vehicle; section 3 will explore the development of in situ performance evaluation, while section 4 will describe the autonomy and the collaborative framework which brings all the aspects of modern mine hunting together. Section 5 will briefly introduce the low frequency sonar to complete the program overview. Section 6 will conclude and offer some thoughts on the evolving CMRE program of work and the transfer knowledge to nations.

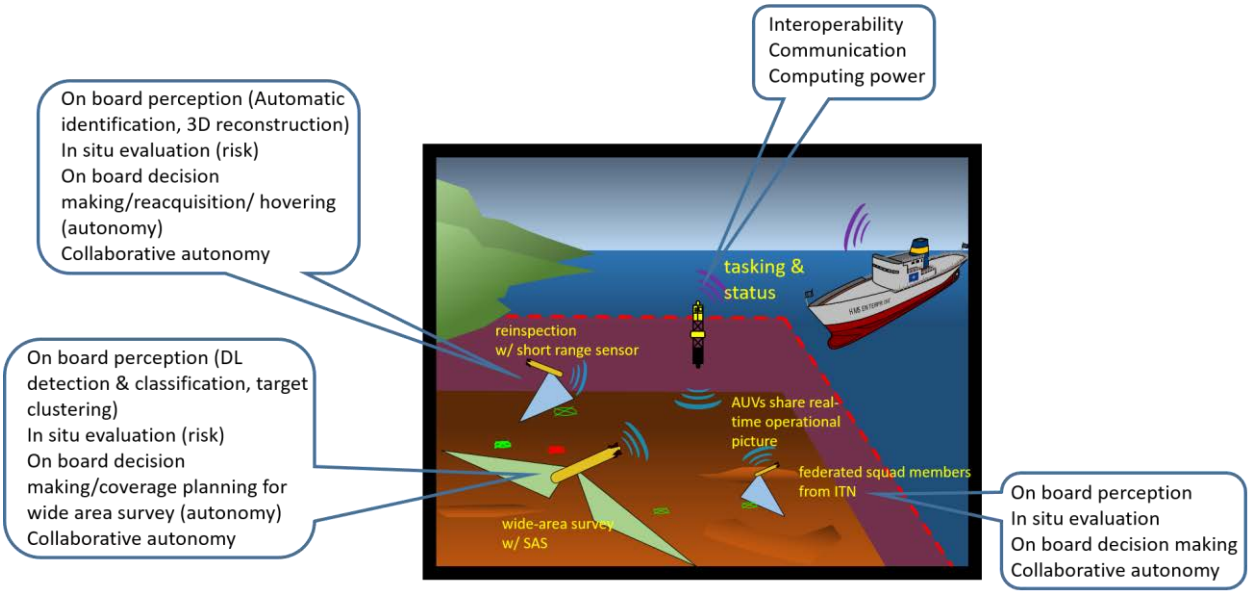


Fig.1: CMRE ANMCM program of work overview shown in an operational view utilised during Italian MINEX 2018.

2. ON BOARD PERCEPTION

2.1. Automatic target recognition

For several years, automatic target recognition research at CMRE has focused on the use of convolutional neural networks (CNNs) [1]. This vision led to CMRE being the first in the underwater MCM community to pursue such an approach [2], which has since been adopted by many other research groups around the world. But unlike most of these others, CMRE has continued to eschew the use of "off-the-shelf" networks trained on optical imagery, instead opting to leverage a large in-house database of MUSCLE synthetic aperture sonar (SAS) imagery that has been collected over the last decade during sea experiments in various locations. At the same time, we have incorporated extensive domain expertise into the network design, which has enabled the successful development of tremendously smaller networks (trained "from scratch") that still achieve excellent classification performance [2-3]. This philosophy of tailoring the algorithms to the specific sonar modality has also facilitated the use of alternative data representations with CNNs [4-6], including low-frequency

acoustic-color data [7]. Relying on off-the-shelf networks, in contrast, would have closed these rich research avenues. Our work has also demonstrated the applicability of transfer learning, showing the feasibility of applying to other sonar sensors the CNNs that have been trained on MUSCLE data [8-9]. As such, there are promising opportunities for transitioning the CMRE-developed CNNs to similar, but distinct, systems of NATO nations in the near future.

2.2. Target clustering

The goal of Target Clustering algorithms is to merge multiple detections of the same target into a single entity, or cluster. Ideally, the formed cluster will benefit from the multiple detections of the same target, by having a better estimate of the target's position. In order to do so, clustering algorithms usually build on data provided by an ATR software or from a human operator. In particular, they can use information of the location of a given detection in a tile, together with an associated score. These detections are fused into multiple target clusters, taking into account the estimated navigational drift of the vehicle. However, in some situations the ATR can fail completely to detect the target. On the other hand, the ATR can sometimes detect a target but assign it a low score which then, depending on the acceptance threshold, can cause a target to remain disregarded. Figure 2 provides a schematic diagram of the interface between ATR and Target Clustering.

In an ongoing effort to address Target Clustering, CMRE is proposing a newly developed probabilistic target clustering algorithm. Motivations for a probabilistic algorithm are two-folded. First, it is desirable that the target clustering process provides not only the location of a given target, but also an indication of the uncertainty of such estimation, in a mathematically sound and robust approach. Secondly, the use of a probabilistic framework also favours a closer integration with other aspects related with target location accuracy, as for example navigation accuracy of autonomous vehicles, exploration and target reacquisition search behaviours, or even planning and evaluation for systems of systems MCM operations. For instance, the navigation accuracy of a vehicle will have a definite impact on the location of the targets it detects. At the same time, knowledge of the location of a target as well as its uncertainty can be very relevant, particularly in multi-vehicle MCM missions, where surveying and target reacquisition tasks might be performed by different vehicles.

The proposed algorithm, based on a Probability Hypothesis Density (PHD) filter, uses Random Finite Sets (RFS) to model both the collection of individual target states and the collection of observations. Perhaps the biggest advantage of the PHD filter, is the fact that it does not require an explicit data association step. When addressing problems such as target clustering or multiple target tracking, characterized by multiple simultaneous observations, the data association step can be quite cumbersome, and even computationally very demanding or even intractable. At the same time, the usage of RFS, as opposed to random vectors, is a more suitable formulation for addressing varying number of targets, target (dis)appearance and spawning, the presence of clutter and association uncertainty, false alarms and missed detections or even extended targets.

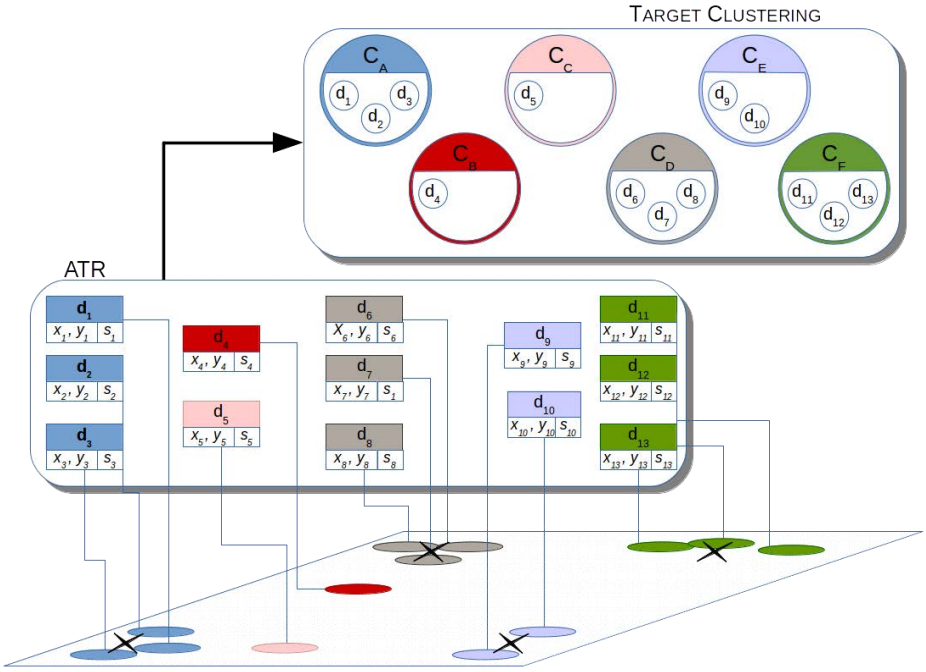


Fig. 2: ATR and Target Clustering algorithms. The ATR algorithm provides 11 detections of existing targets, and false alarms. The Target Clustering algorithm merges the 13 detections into 6 different clusters, corresponding to the 4 existing targets, and to the 2 false alarms.

3. IN SITU PERFORMANCE EVALUATION

At the CMRE we developed an in situ performance evaluation framework, which aims to predict the probability of the ATR *not* detecting a target. We combine these probabilities into a Residual risk map (RRM) of the survey area [10]. RRMs give us a way to quantify the performance of the AUV during a mine-hunting mission. Similar to currently available software such as MCM Expert and DARE, these RRMs can aid in estimating the percentage of targets that have been detected. Unlike the methodology currently in use, the RRM framework is designed to properly handle side-looking sonar imagery and, instead of providing a single number expressing risk or coverage, the RRM can be used to identify which parts of the survey area should be revisited for closer inspection, or if time and resources do not permit this, which areas should be avoided. The algorithm through which we can construct the RRM is based on the range, i.e. the distance between the sonar sensor and the target, but crucially also on *through-the-sensor* features such as ping-to-ping correlation, and metrics that are sensitive to the texture of the image that in turn are correlated with different types of sea bottoms [11]. The algorithm is flexible in the sense that it is agnostic to the specific sensor hardware and ATR type used, as long as we have reference data to constrain model parameters. This means that RRMs can be generated by multiple AUVs that are not necessarily identical in load-out. This is ideally suited for cases where we want to deploy multiple assets in parallel to accelerate the survey.

Through the use of Bayesian statistics, we not solely have a point estimate of our RRM (i.e. a single number per grid cell), but we also calculate a confidence interval. This means that the presence or absence of certain features, e.g. the presence of acoustic shadows, will not only tell us how strongly the probability of detection will increase or decrease, but it will also tell us the amount of uncertainty it will introduce in our estimate. This can be particularly

useful when we wish to fuse RRMs from different vehicles with different sensors, since we can use these uncertainty estimates to weight their contributions to the combined RRM.

Fig 3 shows an example RRM. The homogeneous red areas indicate grid cells not covered during the survey. The vertical green strip in the left hand side of the RRM is the results of the MUSCLE covering this strip twice, leading to an increase in the probability of detection. Finally, red and orange "veins" running through the RRM are the result of sand ripples being present there, causing a decrease in the probability of detection. To bring down the estimated residual risk, these areas should be revisited and viewed from a different angle to avoid the acoustic shadows caused by the sand ripples.

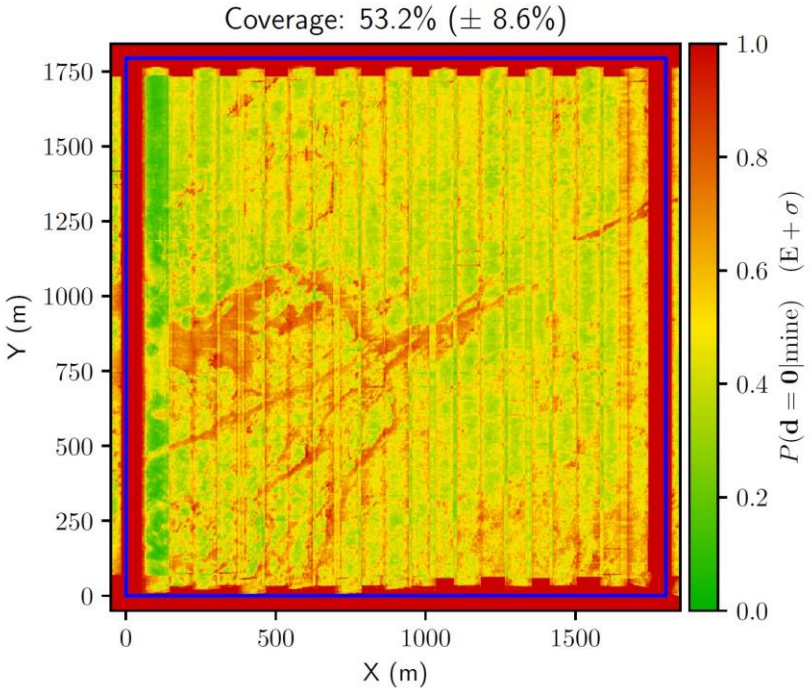


*Fig. 3: RRM constructed from data recorded by the MUSCLE during ESPMINEX18. The colour values express the probability of a hypothetical target going undetected. To integrate our uncertainty estimates into a single map, we penalize uncertain areas by adding the uncertainty (σ) to the expected value (*E*). The blue border indicates the borders of the survey area.*

4. AUTONOMY

Autonomy is the mechanism through which human operators can be displaced or altogether removed from a mine countermeasures mission. Autonomy situated aboard unmanned systems uses sensor information and the results of signal processing algorithms (e.g. those described in Section 2), and algorithms for adaptation and intelligent decision making to drive mission execution. In our programme, we delineate two layers of autonomy --- single and multi-agent. Single agent autonomy encompasses the autonomy solution(s) onboard a single asset for performing any of the tasks that said platform might perform, e.g. [12-14]. The multi-agent layer has a larger scope, and is responsible for the management of multiple autonomous single-agents to perform missions collaboratively [15]. In this section we discuss an example of a current single-agent autonomy solution, adaptive survey planning for improved data quality; and in general terms the approach we take to multi-system collaborative mission execution.

4.1. Adaptive Survey

CMRE has developed a coverage path planning approach for the MUSCLE that combines efficiency and through-the-sensor metrics to inform the track orientation of an AUV [12]. Following the results from the RRM in Figure 3 [rrm map], a considerable decrease in probability of detection is caused by sand ripples on the seabed. Employing an adaptive survey instead of a predefined path allows the vehicle to react immediately to unfavourable environmental conditions and could eliminate the need for revisiting the area.

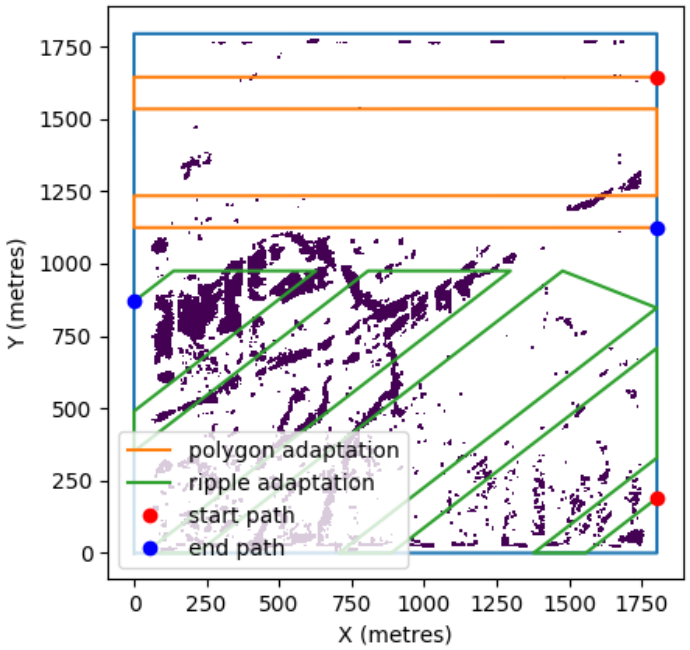


Fig. 4: Adaptive survey based on RRM data products from ESPMINEX18. The simulated mission starts with the orange tracks and takes as an input only the spatial parameters of the survey area – the tracks are adapted to the survey area shape. With each track line, a layer of the RRM map from Fig. 1 is processed and updated. The AUV adapts to the discovered sand ripples by changing its tracks orientation, shown in green, and collects the data at an angle that optimises the data quality [12].

Figure 4 gives an example of an AUV adaptive survey using data products derived from the *in situ* performance evaluation shown in Figure 3 [rrm map]. At the beginning of the mission, it is assumed that only the spatial and temporal parameters of the mission are known to the AUV, but no seabed information is available in advance. The orange path of the vehicle adapts to the search area shape, with the aim to improve resource efficiency. Once a sand ripple field has been detected, the AUV changes its track orientation and follows a path along the ripples' ridges. At the new angle the vehicle can collect sonar data with less shadows, and increase the probability of target detection. Developing and improving new adaptive survey approaches allows collecting more reliable and high-quality data. Such strategies will also aid the safe waterspace management and efficient collaboration in a shared operational area for a heterogeneous network of manned and unmanned assets.

4.2. Collaborative autonomy

The rationale behind using multiple agents to perform mine clearance is the overall goal of accelerating mission execution. Given that a mine clearance mission includes dynamic, highly heterogeneous tasks (from wide area survey to target revisit and identification), the creation of a federated squad allows the specialisation of systems for specific tasks, and allows for a greater rate of clearance. Our approach, architecturally, delineates a layered separation between the execution of tasks (known as capabilities) and the invocation or allocation of those tasks, at a network level, as depicted in Figure 5.

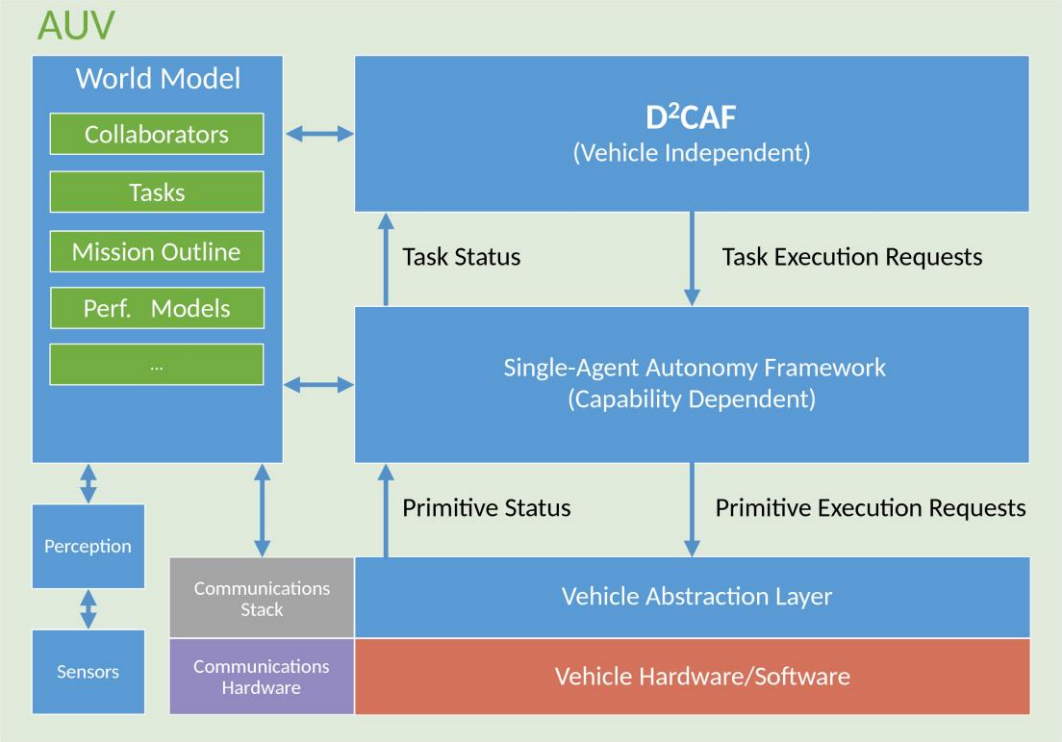


Fig 5: Layered architecture of CMRE's ANMCM assets. D2CAF, our solution for managing task allocation and dissemination within a heterogeneous squad, sits above single-agent frameworks, which might be different for each asset. The task execution interface (the lines between the upper two layers) shares the same interaction model between systems, independently of how the tasks themselves are performed.

The multi-agent layer is responsible for the management of the squad-level task objectives, their decomposition and dissemination within the fleet, and the allocation of the objectives to appropriate members of the squad. The single-agent layer simply provides a task interface, exposing its internal capability of task execution, to be invoked by higher-level decision-making. In this way, the intelligence or novelty of task execution is compartmentalized in a modular away, separate from the mechanisms which decide to invoke the execution of such a task. We have developed a framework, the Distributed/Decoupled Collaborative Autonomy Framework (D^2CAF), [15], which provides infrastructure and tools in which to house prototype algorithms handling the distributed task allocation problem. This framework has a task-centric model, where tasks represent work to be done in relation to a higher level mission goal, and the performance of such tasks can and must be scheduled and allocated to platforms

that have appropriate capabilities. The framework itself is not domain specific, with domain specialisation being represented by the definition of a task dictionary --- the framework itself does not care about the specifics of the task types, but only about the abstract representation of the performance of those types. The framework is designed to allow *distributed* algorithms to be embedded, without a centralized master node. Moreover the framework can be used to amalgamate various systems into a federated squad by *decoupling* the task execution and allocation problems, and even allowing D^2CAF agents to run in systems other than those autonomous systems that they represent. This configuration allows legacy assets to be incorporated into a more performant squad using off-the-shelf interfaces for command and control.

5. HIGH RESOLUTION LOW FREQUENCY SYNTHETIC APERTURE SONAR

Over the last decade, Synthetic Aperture Sonar (SAS) has become a tool of choice for Mine Counter Measure (MCM) operations. The high resolution acoustic imaging output coupled with a constant resolution in range has drastically improved Automatic Target Recognition (ATR) algorithm results in term of detection rate and probability of false alarm. A major effort in research and development has been made for the high frequency SAS systems which provide surfacic information of the seabed and prone objects. Improvised Explosive Device (IED) and buried targets however still may remain extremely challenging to detect and classify especially in difficult and cluttered environments. A Low Frequency (LF) system aims to counteract this particular problem: lower frequencies provide greater sound penetration into the seabed and the potential target, permitting additional detection and recognition information; LF also propagates further in water, potentially allowing longer imaging range.

The CMRE has been developing his own high resolution low frequency synthetic aperture sonar (HR-LFSAS) prototype to tackle the problem of underwater mine classification and identification. The design of this system is based on a 2D transmitter array and a 2D receiver array, where elements can be driven individually. The development of such a system is not without challenges [16], but it also solves intrinsic problems linked to low frequencies such as size, bandwidth or energy output [17]. The 2D array receiver is also fundamental as it allows 3D data collection, which is one of the main interesting features that low frequency systems offer.

Over the last year, the HR-LFSAS team has developed theoretical tools to better understand and exploit the LF information gathered by such a system. These include:

- a study of the SAS PSF (Point Spread Function) [18], which is in essence the building block of SAS imagery and is fundamental for multi-chromatic analysis;
- the design and the impact of the waveforms [19] in order to maximise the efficiency of the system; and,
- the potential advantages of super-resolution imaging algorithms [20] for operators or for improving the performance of automatic recognition algorithms improved.

An important aspect of the development and the improvement of the system resides in realistic representations of the interactions between LF acoustic waves and an object of interest. Part of our effort is focusing on developing realistic, physics-based acoustic wave simulators [21–23] to apprehend the complex backscattering phenomena, enable the elaboration of a large simulated database and develop efficient strategies for information extraction. In particular, new ATR algorithms benefit greatly from synthetic representative

datasets. As an example, we showed in simulation the potential of the LF system to differentiate materials of an object [24].

Although the LFSAS prototype is still in construction, several trials have taken place in 2018 including the first phase of the calibration of the transmitter array [25] at Loch Goil in Scotland, and the rail-based TORHEX'18 (Target Oriented Rail-based Experiment) [17, 26] at La Spezia, Italy. TORHEX'18 was focused on acquiring relevant scientific data with the upgraded hardware, and the full transmitter array. The rail facility was utilised to acquire data for LF aperture synthesis, and the first LFSAS images of relevant objects have been analysed and processed showing the great potential of this system for MCM operations.

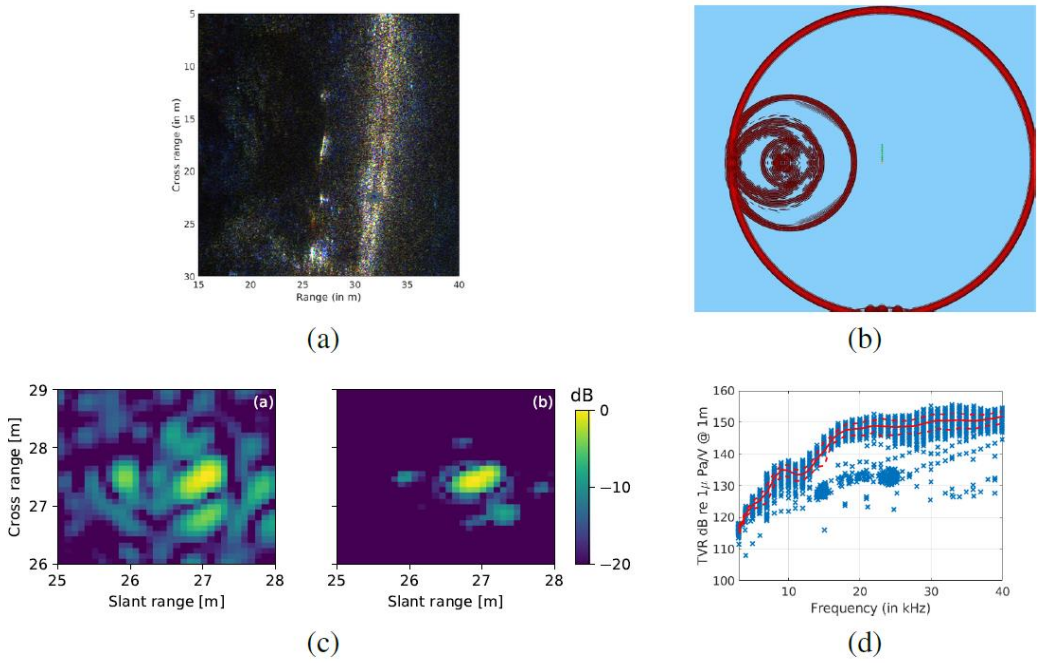


Fig 6: (a) Multi-chromatic LFSAS image from TORHEX'18. (b) PVC shell response computed with SPECFEM2D. (c) Sparse LFSAS image reconstruction with the DMM algorithm. (d) Statistical Transmit Voltage Response

6. CONCLUSIONS AND FUTURE PROSPECTS

The CMRE mine countermeasures program of work is based on a multi-disciplinary approach, which develops complementary techniques to bring together heterogeneous autonomous systems and ensure the best possible outcome of a system-of-systems mission. The strength of the centre is its ability to rapidly prototype new algorithms and concepts at sea in realistic conditions. The ANMCM group will continue to develop further autonomy, automatic identification, navigation remediation, and low frequency solutions for difficult cluttered environments and buried targets.

The work will seek to expand its operational envelope to very shallow waters, over-the-horizon overt and covert and address the potential new mine threats that may challenge the current technologies. This will entail the development of new high resolution technologies to address the very shallow water conditions, adaptable vehicles to difficult surf zone environments and the increase in automated machine intelligence and decision making capabilities.

The CMRE regularly releases papers and reports to highlight the advances of the research and will periodically release software relating to the work undertaken. In particular, a first version of D2CAF is now downloadable for national defence laboratories if eligible. The centre continues to work in bi-lateral efforts with nations actively to transfer knowledge and algorithms for particular national systems. The Centre is also an active participant in NATO working groups focused on Naval Mine Warfare applications and regularly promotes novel and modern products such as the risk maps to operators and command and control.

7. ACKNOWLEDGEMENTS

The work is funded by the NATO Allied Command Transformation Future Solutions and is enriched by the numerous interactions with the Nations who have supported our work and participated in our trials.

REFERENCES

[1] **Y. LeCun, Y. Bengio, and G. Hinton**, "Deep learning," Nature, vol. 521, no. 7553, pp. 436, 2015.
[2] **D. Williams**, "Underwater target classification in synthetic aperture sonar imagery using deep convolutional neural networks," in Proceedings of the 23rd International Conference on Pattern Recognition (ICPR), 2016.
[3] **D. Williams**, "Demystifying deep convolutional neural networks for sonar image classification," in Proceedings of the Underwater Acoustics Conference, 2017.
[4] **D. Williams**, "Exploiting Phase Information in Synthetic Aperture Sonar Images for Target Classification," in Proceedings of IEEE OCEANS, 2018.
[5] **I. Gerg and D. Williams**, "Additional Representations for Improving Synthetic Aperture Sonar Classification Using Convolutional Neural Networks," Proceedings of the 4th International Conference on Synthetic Aperture Sonar and Synthetic Aperture Radar, Vol. 40, Pt. 2, pp. 11-22, Lerici, Italy, September 2018.
[6] **D. Williams, R. Hamon, and I. Gerg**, "On the Benefit of Multiple Representations with Convolutional Neural Networks for Improved Target Classification Using Sonar Data," in Proceedings of the Underwater Acoustics Conference, 2019.
[7] **D. Williams**, "Acoustic-Color-Based Convolutional Neural Networks for UXO Classification with Low-Frequency Sonar," in Proceedings of the Underwater Acoustics Conference, 2019.
[8] **D. Williams**, "Convolutional Neural Network Transfer Learning for Underwater Object Classification," in Proceedings of the 4th International Conference on Synthetic Aperture Sonar and Synthetic Aperture Radar, Vol. 40, Pt. 2, pp. 123-131, 2018.
[9] **D. Williams**, "Transfer Learning with SAS-Image Convolutional Neural Networks for Improved Underwater Target Classification," to appear in the Proceedings of the IEEE International Geoscience and Remote Sensing Symposium (IGARSS), 2019.
[10] **B. Gips**, Bayesian Seafloor Characterization from SAS Imagery, In 5th Underwater Acoustics Conference & Exhibition, 2019.
[11] **B. Gips, C. Strode, S. Dugelay**, Residual Risk Maps for Performance Assessment of Autonomous Mine Countermeasures Using Synthetic Aperture Sonar, In *Proceedings of the Institute of Acoustics*, 40, 47-56, 2018.

[12] **V.Yordanova, B. Gips, T. Furfaro, S. Dugelay**, Coverage Path Planning for Mine Countermeasures: Adapting Track Orientation, In IEEE/MTS OCEANS 2019, Marseille, pp. 1-7, 2019.
[13] **D. Machado, T. Furfaro, S. Dugelay**, Micro-bathymetry data acquisition for 3d reconstruction of objects on the sea floor, In *OCEANS 2017-Aberdeen*. Aberdeen Scotland UK, IEEE, pp. 1-7, 2017.
[14] **D. P. Williams, F. Baralli, M. Micheli, S. Vasoli**, Adaptive underwater sonar surveys in the presence of strong currents, In *2016 IEEE International Conference on Robotics and Automation (ICRA)*, Stockholm Sweden, IEEE, pp. 2604-2611, 2016.
[15] **T. Furfaro**, A Distributed Framework for Embedded Collaborative Autonomy, In *OCEANS 2018 MTS/IEEE Charleston*, Charleston SC USA, IEEE, pp. 1-6, 2018.
[16] **S. Fioravanti, F. Aglietti, A. Carta, A. Sapienza, and Y. Pailhas**, Modular design of a 2D transmitting array for an advance low frequency synthetic aperture sonar. In *OCEANS 2019* - MTS/IEEE Marseille, pages 1–6, Jun 2019.
[17] **Y. Pailhas, S. Fioravanti, and S. Dugelay**, The high resolution low frequency synthetic aperture sonar (HR-LFSAS) project. In *SAR/SAS conference, Institute of Acoustics*, volume 40, pages 66–72, 2018.
[18] **Y. Pailhas,** 2D & 3D, centred & offset, circular synthetic aperture sonar point spread function. In *UACE2019*, Hersonissos, Crete, pages 1–8, Jul 2019.
[19] **Y. Pailhas**, Waveform design for low frequency frequency synthetic aperture sonar. In *UACE2019*, Hersonissos, Crete, pages 1–6, Jul 2019.
[20] **A. Xenaki, Y. Pailhas, and R. Hamon**, High-resolution low-frequency compressive SAS imaging with distributed optimization. In *UACE2019*, Hersonissos, Crete, pages 1–8, July 2019.
[21] **P. Cristini, Y. Pailhas, R. Hamon, A. Xenaki, and G. Urso**, Influence of the sediment characteristics and of the level of burial on the acoustic response of a hollow cylinder in shallow water. In *OCEANS 2019* - MTS/IEEE Marseille, pages 1–6, Jun 2019.
[22] **P. Cristini, Y. Pailhas, R. Hamon, A. Xenaki, and G. Urso**, Modification of the acoustic response of a partially buried hollow cylinder as a function of the sediment characteristics and of the level of burial. In *UACE2019*, Hersonissos, Crete, pages 1–8, Jul 2019.
[23] **Y. Pailhas, P. Cristini, R. Hamon, A. Xenaki, and G. Urso**, On the importance of accurate numerical tools in sonar development: the low frequency case. In *OCEANS 2019* - MTS/IEEE Marseille, pages 1–6, Jun 2019.
[24] **R. Hamon, Y. Pailhas, A. Xenaki, P. Cristini, and G. Urso,** Classification and characterization of objects made of different materials from numerical acoustic responses using convolutional neural networks. In *UACE2019*, Hersonissos, Crete, pages 1–9, Jul 2019.
[25] **Y. Pailhas, S. Fioravanti, F. Aglietti, D. Galietti, A. Carta, and A. Sapienza**, Low Frequency SAS 2D transmitter array calibration. In *OCEANS 2019* - MTS/IEEE Marseille, pages 1–6, Jun 2019.
[26] **Y. Pailhas**, TORHEX'18 sub-dataset description. Internal report CMRE-DA-2019-001, CMRE, 2019.

Marine ecosystem engineers: a challenge for mine countermeasure

Sonia Papili [1,2], Yves Dupont[3], Vera Van Lancker [2,4]

[1]Belgian Defence, Marinebasis Zeebrugge, Graaf Jansdijk 1, 8380 Zeebrugge, Belgium
[2]Ghent University, Department of Geology, Renard Centre of Marine Geology, Krijgslaan 281-S8, 9000, Gent Belgium.
[3]Belgian Defence, MR Naval Systems, Everestraat 1, 1140 Brussels, Belgium.
[4]Royal Belgian Institute of Natural Sciences. Operational Directorate Natural Environment, Vautierstraat 29, 1000 Brussels, Belgium.

Sonia Papili. Belgian Defence, Marinebasis Zeebrugge, Graaf Jansdijk 1, 8380 Zeebrugge, Belgium. E.Mail: sonia.papili@mil.be

Abstract: *Worldwide the marine environment is exploited increasingly and new challenges arise for communication, transportation, blue energy, seabed mining, aquaculture and coastal tourism. Meanwhile, the world of mine countermeasure is deeply changing as well, in terms of tactics, planning, sea monitoring, recognition and neutralization of threats. Human activities are increasingly regulated to steer exploitation towards most efficient, safe and sustainable ways. Safeguarding biodiversity is key and needs monitoring using most time- and cost-efficient ways. Biogenic reefs often form hotspots of biodiversity and therefore are important in the assessment of good environmental status of the marine environment (e.g.,Europe's Marine Strategy Framework Directive (MSFD; Directive 2008/56/EC). As ecosystem engineers they modify, create or define habitats by altering the habitat's physical properties. From a military perspective, this poses challenges for mine countermeasure. First, biogenic reefs can hide man-made objects or even built on them. Secondly, they are visualized on sonar images showing mostly features with comparable dimensions to man-made targets; and lastly, their scattered spatial distribution makes monitoring and detection difficult.*

To provide assistance in discriminating seabed from man-made targets, a comprehensive table is constructed collecting the most recent and significant acoustic images showing the characteristic acoustic signature of a group of structural ecosystem engineers such as seagrass beds or tubeworms and evaluating the impact for mine countermeasure.

Key words: *Ecosystem engineers, mine countermeasure, remote sensing, biogenic reefs*

Methodology

Wever and Jenkins [1] provided evidence of biology affecting severely naval operations at sea, showing also that prediction capabilities can be mismatching if biological effects on the seafloor are not taken into account. Here, we demonstrate how ecosystem engineers modify the habitat and how those affect acoustic imagery. Results from a number of surveys are shown.
Sonar images were recorded using the Autonomous Unmanned Vehicle (AUV) REMUS 100 by Hydroid, equipped with a Side-Scan Sonar (SSS) using a very-high frequency of 900 kHz. Multibeam imagery (Kongsberg Simrad EM 1002 recording at frequency of 99kHz) was used as well.

Recordings with the REMUS 100 were performed in 2014 in Spain and in June 2016 in Belgian waters. The REMUS was programmed to fly 3 m above the seafloor at a velocity of 3 kn. Data were processed with the dedicated Hydroid software packages Sea Scan PC review and SSPC

data (Marine Sonic technology, Ltd. 2011). Recordings with the Multibeam EM 1002 data from 2007 were acquired with the research vessel A962 RV Belgica.
Main results are compiled into a comprehensive table in which different parameters are listed: used sonar and the frequency; type of ecosystem engineer; picture of the organisms; illustration of their spatial distribution and corresponding sonar images.

Ecosystem engineers

Not all ecosystem engineers are considered biogenic reefs *s.s.* [2], however any species modifying the seabed may affect acoustic imagery and be challenging in the context of mine countermeasures. Since seamines are found mostly in shallow waters (<50m), ecosystem engineers living in shallow waters were taking into consideration for this study. Three types of ecosystem engineers are presented: the polychaete *Lanice conchilega*, and the bivalve *Ensis directus*, widespread occurring in the North Sea, and the seagrass *Posidonia oceanica,* being of high value in the Mediterranean region.

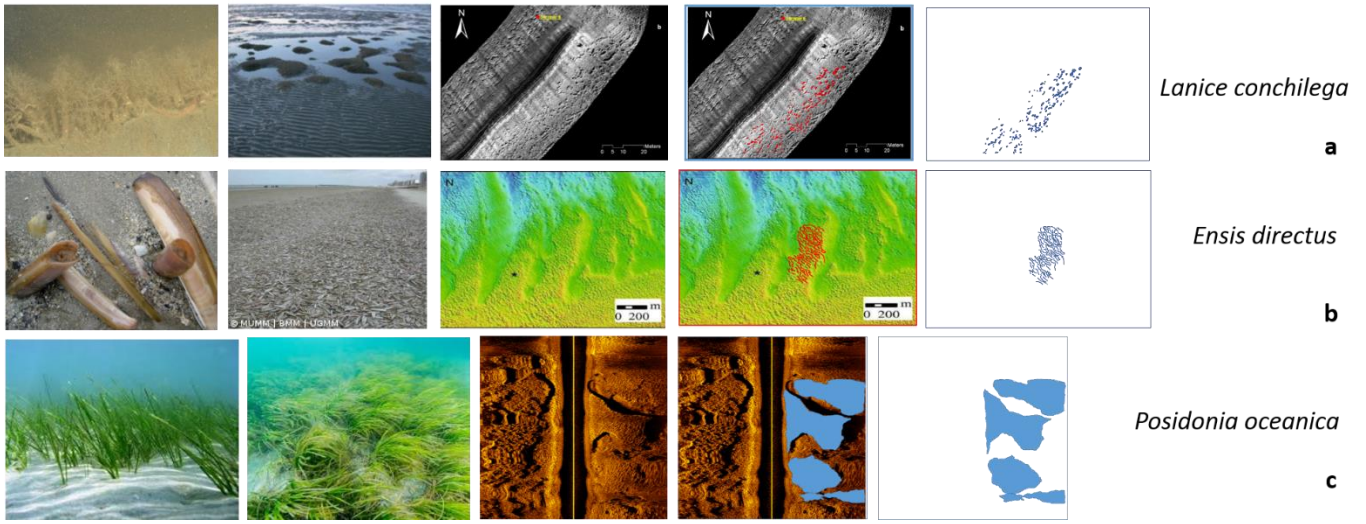
L. conchilega (Pallas, 1766) is a tubeworm typically occurring in the *Abra alba* community of the Belgian part of the North Sea (BPNS) and is strongly linked to shallow muddy to fine sands and medium sands, as well as to the deeper fine sands [3]. *L. conchilega* builds its tube with particles consisting of calcium carbonate grains (shell hash), up to 60-80 % of its volume [4]. The tube has a typical diameter of 0.5 cm and a length of up to 65 cm, although the tubes are mostly around 20 cm. The tubes protrude up to 4 cm above the sediment and have tentacles that ensure the feeding process [5]. *L. conchilega* is considered an ecosystem engineer since, when occurring in colonies, the tubes and tentacles are able to modify the near-bed hydrodynamic flow [6]. The reproduction peak of the species is in Spring, with two smaller peaks in Summer and Autumn [3].
E. directus (Conrad, 1843), also belongs to the *A. alba* community. Originating from North-Eastern America, the species started to invade the North Sea reaching the German Bight in the late 1970s and is spreading in Belgian waters since the 1980s [7]. Along the BPNS, stable adult populations were found in the vicinity of sandbanks, as also along the ebb tidal delta of the Westerschelde estuary [8]. The species tolerates a wide range of environmental conditions, but prefers slightly muddy fine sands in shallow waters where phyto-plankton is present [8]. The species can reach lengths of up to 16 cm and has a life stage of up to 5 years [8]. It has a high adaptability to environmental conditions, although it seems to avoid zones of higher sediment dynamics such as bedforms [9]. Its spawning period is in May and June [8].
Seagrass meadows [10] are formed from submersed marine angiosperms growing mainly on sandy or muddy substrates in shallow coastal and estuarine waters. Highly productive habitats are formed that also provide shelter to many organisms [10]. Apart from spawning grounds, they host larval and juvenile stages of many fish, mollusks and crustaceans [11,12], stabilizing bottom sediments and fixing carbon via photosynthesis [13]. An example is *Posidonia oceanicae* (Linnaeus, 1813) and is characteristic of the infralittoral zone of the Mediterranean in water depths from 0 to 40 meters. It can be found on soft or hard substrates and is tolerant to temperature variation and water movement, but are sensitive to desalination. They host mollusks, echinoderms and different species of fish.

Results

Some examples are given here of the acoustic signature of the ecosystem engineers described above. Their appearance is sketched from the sonar images allowing easy intercomparison. Depending on the type of organism and their lifecycles, the signature varies.

Table 1: Acoustic signature of ecosystem engineers derived by high frequency and very high frequency sonar images (b in [14]).

ID	Ecosystem engineer	Location	year	sonar type	frequency
a	*Lanice conchilega*	West diep gully (North Sea)	2016	SSS Remus 100 Kongsberg Hydroid	900 kHz
b	*Ensis directus*	Vlakte van de Raan (North Sea)	2007	MB EM1002 Kongsberg Simrad	95kHz
c	*Posidonia oceanica*	Spain (Mediterranean Sea)	2014	SSS Remus 100 Kongsberg Hydroid	900 kHz



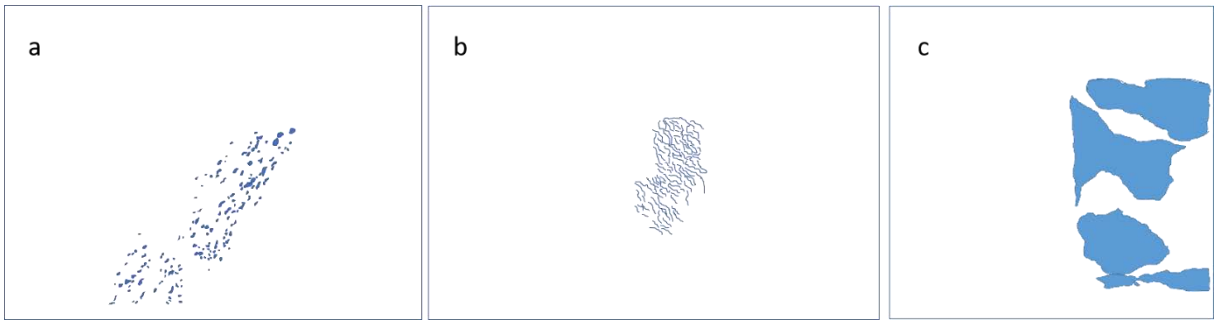


Fig.1: signatures of a) L.conchilega; b) E.directus; c) P.oceanica

The way dense colonies of tubeworms is ensonified is mostly described as rounded or elongated features and occurring in patches [15]. However, revisiting and discretizing, the signatures show that the spatial distribution of *L. conchilega* mostly follows the major axes of the main course of the autonomous vehicle aligned with the main tidal stream. This is not the case for colonies of *E. directus* that mainly develop against the main current direction. In both cases, the highly irregular shape and irregular distribution clearly sets them apart from regular bedforms, such as ripples.

Posidonia oceanica occupies large areas and the resulting features are large and compact. A preferential alignment is not evident.

For the search and detection of seamines this is highly valuable information.

Conclusion

Biological influence has been widely ignored in mine countermeasures, though it may impact considerably the sonar imagery and mask the presence of mines. However, there is large variability in the way organisms are imaged acoustically depending on a number of parameters that hitherto were not considered in a naval operational context: e.g., type of sediment, scale and shape of patchiness, linearity, spatial distribution, as well as seasonality.

During mine searches, it is important to have rapid assessment tools, including data bases with existing knowledge on the areas of interest, as well as the parameters influencing the signature as listed above. Additionally, it is envisioned to create a seafloor atlas illustrating ecosystem engineer's signatures on sonar images.

Approaching an era during which unmanned capabilities, automatic target detection and robotica will be used increasingly for mine countermeasures, it is crucial to supply to machines also environmental information with high level of accuracy and considering both physical and biological processes, as well as their interaction.

Acknowledgements

The authors thank Belgian Science Policy (BELSPO) for the use of the RV A962 Belgica and Flanders Marine Institute (VLIZ) for the use of RV Simon Stevin. The crew of both vessels is warmly thanked for their support. A special thanks goes to the VSW and REA Division of the NMCM department of the Belgian Navy for assistance during the remote sensing recordings. This paper contributes to the projects MRN015 funded by the Belgian Ministry of Defence, Royal Higher Institute for Defence. It also contributes to the project INDI67 (BELSPO, contract BR/143/A2/INDI67), and the SEACoP consortium in particular.

References

1. Wever, Th.F. & C.J. Jenkins, 2013. The Necessity of Entering Biological Effects on the Seafloor into Models and Doctrine for Navy Applications. Wehrtechnischer Bericht WTD71-0072/2013. 0-27.
2. Berke, S.K., 2010. Functional groups of ecosystem engineers: a proposed classification with comments on current issues. Oxford University Press on behalf of the Society for Integrative and Comparative Biology. Vol.50-2. 147-157.
3. Van Hoey G., 2006. Spatio-temporal variability within the macrobenthic Abra alba community, with the emphasis on the structuring role of Lanice conchilega. Ghent University: 0-187.
4. Fournier, J., C. Bonnot-Courtois, B. Caline, N. Desroy, S. Dubois, S. Etienne, L. Godet, J.B. Le Cam, M. Noernberg, & B Tessier, 2009. Calcium carbonate trapping by Sabellaria alveolata and Lanice conchilega and reef volume estimation: Preliminary results.

5. Callaway, R., 2003. Juveniles stick to adults: recruitment of the tube-dwelling polychaete Lanice conchilega (Pallas, 1766). Hydrobiologia 503:121– 130. doi:10.1023/B:HYDR.0000008494.20908.87
6. Rabaut, M., K. Guilini, G. Van Hoey, M. Vincx, & S. Degraer, 2007. A bioengineered soft-bottom environment: The impact of Lanice conchilega on the benthic species-specific densities and community structure. Estuarine Coastal and Shelf Science 75: 525-536
7. Kerckhof F. & E. Dumolin, 1987. Eerste vondsten van de Amerikaanse zwaardschede *Ensis directus* (Conrad, 1843) langs de Belgische kust. De Strandvlo 7(2): 51-52.
8. Houziaux J.-S., J. Craeymeersch, B. Merckx, F. Kerckhof, V. Van Lancker, W. Courtens, E. Stienen, J. Perdon, P.C. Goudswaard, G. Van Hoey, L. Vigin, K. Hostens, M. Vincx & S. Degraer 2012. 'EnSIS' - Ecosystem Sensitivity to Invasive Species. Final Report. Brussels: Belgian Science Policy Office. – Research Programme Science for a Sustainable Development:0-105.
9. Van Lancker, V., J.S. Houziaux, M. Baeye, D. Van den Eynde, M. Rabaut, K. Troost, T. Vermaas & T.A.G.P. van Dijk, 2013. Biogeomorphology in the field: bedforms and species, a mystic relationship. In: Van Lancker, V. & T. Garlan, (eds.). Conference Proceedings Marine and River Dune Dynamics, MARID IV, April 2013, Bruges, Belgium: 277-283.
10. Hamana M., Komatsu T., 2016. Real-Time classification of seagrass meadows on flat bottom with bathymetric data measured by a narrow multibeam sonar system. Remote sensing. Vol.8, 96. Doi: 10.3390/ rs8020096
11. Jackson, E.L.; Rowden, A.A.; Attrill, M.J.; Bossey, S.; Jones, M. The importance of seagrass beds as a habitat for fishery species. Oceanogr. Mar. Biol. 2001, 39, 269–304. 7.
12. Bertelli, C.M.; Unsworsth, R.K.F. Protecting the hand that feeds us: Seagrass (Zostera marina) serves as commercial juvenile fish habitat. Mar. Pollut. Bull. 2014, 83, 425–429.
13. Short, F.T.; Beth, P.; Livingstone, S.R.; Carpenter, K.E.; Salomão, B.; Bujang, J.S.; Calumpong, H.P.; Carruthers, T.J.B.; Coles, R.G.; Dennison, W.C.; et al. Extinction risk assessment of the world‘s seagrass species. Biol. Conserv. 2011, 144, 1961–1971.
14. Van Lancker, V. 2017. "Bedforms as Benthic Habitats: living on the edge, chaos, order and complexity." Atlas of Bedforms in the Western Mediterranean. Springer, Cham, 2017. 195-198.
15. Degraer S., G. Moerkerke, M. Rabaut, G.Van Hoey, I. Du Four , M. Vincx, J-P. Henriet & V. Van Lancker, 2008. Very-high resolution side-scan sonar mapping of biogenic reefs of the tube-worm Lanice conchilega. Remote Sensing Environ 112:3323–3328. doi:10.1016/j.rse.2007.12.012

Regular Session 24
Inversion methods in underwater acoustics

ENHANCED SONAR IMAGE RESOLUTION USING COMPRESSIVE SENSING MODELLING

Andreas Gällström[a,b] , Louise Rixon Fuchs[a,c] and Christer Larsson[a,b]

[a] Saab AB, SE-581 88 Linköping, Sweden
[b] Department of Electrical and Information Technology, Lund University, P.O. Box 118, SE-221 00 Lund, Sweden
[c] KTH Royal Institute of Technology, School of Electrical Engineering and Computer Science, Teknikringen 14, SE-100 44 Stockholm, Sweden

Contact author: Andreas Gällström, Saab AB, SE-581 88 Linköping, Sweden.
Email: andreas.gallstrom@saabgroup.com

Abstract: *The sonar image resolution is classically limited by the sonar array dimensions. There are several techniques to enhance the resolution; most common is the synthetic aperture sonar (SAS) technique where several pings are added coherently to achieve a longer array and thereby higher cross range resolution. This leads to high requirements on navigation accuracy, but the different autofocus techniques in general also require collecting overlapping data. This limits the acquisition speed when covering a specific area.*
We investigate the possibility to enhance the resolution in images processed from one ping measurement in this paper using compressive sensing methods.
A model consisting of isotropic point scatterers is used for the imaged target. The point scatterer amplitudes are frequency and angle independent. We assume only direct paths between the scatterers and the transmitter/receiver in the inverse problem formulation. The solution to this system of equations turns out to be naturally sparse, i.e., relatively few scatterers are required to describe the measured signal.
The sparsity means that L1 optimization and methods from compressive sensing (CS) can be used to solve the inverse problem efficiently. We use the basis pursuit denoise algorithm (BPDN) as implemented in the SPGL1 package to solve the optimization problem.
We present results based on CS on measurements collected at Saab. The measurements are collected using the experimental platform Sapphires in freshwater Lake Vättern. Images processed using classical back projection algorithms are compared to sonar images with enhanced resolution using CS, with a 10 times improvement in cross range resolution.

Keywords: *Sonar, imaging, resolution, Compressive Sensing, Synthetic Aperture Sonar*

1. INTRODUCTION

The enhancement of the spatial resolution in sonar imaging is a classical research field in array signal processing with several different approaches, one example being Synthetic Aperture Sonar (SAS) systems, where data from a number of subsequent measurements are combined through signal processing, resulting in an increased along-track resolution in SAS-imaging. The imaging is often performed using the back-projection algorithm in practice. The back-projection algorithm is a fast and robust method to solve the inverse problem, which gives reliable results. The drawback with back-projection is that it suffers from resolution and ambiguity limitations related to the frequency bandwidth, aperture size and sampling step sizes.

Methods that can extract more information from the available data have been developed in Compressive Sensing (CS). These methods are based on minimizing the l_1-norm of the solution and require that the solution of the inverse problem, in this case the SAS-image, is relatively sparse.

The paper is organized in the following way: Chapter 2 is a brief introduction to CS and the model used in this work. In chapter 3, two examples showing the utilization of this framework is shown – demonstrating possibilities of these techniques for sonar data.

2. COMPRESSIVE SENSING

Non-stringently expressed, the Nyquist-Shannon sampling theorem states that the sampling rate of a time-continuous signal has to be twice its highest frequency in order to ensure reconstruction. Therefore, it comes as a surprise that, under certain assumptions, it is possible to reconstruct signals when the number of available measurements is smaller than expected based on the Nyquist-Shannon theorem. The underlying assumptions for this is based on that the signal is sparse in some domain, in this case the sonar image.

A signal is called sparse if most of its components are zero. Another perspective on this is that many signals are compressible, i.e. they can be well approximated by sparse signals. This explains why the family of different compression techniques (such as JPEG, MPEG, or MP3) work so well.

The rise of interest in leveraging CS for signal processing applications has several reasons: a combination of development of theory, faster available algorithms, and faster computers. The field was pioneered by Candés et al in a publication 2004[1]. One early publication reporting an application in magnetic resonance imaging can be found in [2].

2.1 Problem Formulation

CS can be applied to several sonar frameworks. In this work, a transmitter sends out a properly designed acoustic signal, the sonar pulse, which is scattered from objects, for example on the sea floor. An array of receivers then acquires the acoustic signal resulting from the scattered waves. This can be modelled as an inverse problem:

$$Ax = y, \tag{1}$$

where the forward operator $A \in \mathbb{C}^{mxN}$, vector $x \in \mathbb{C}^N$ is the process variable, and measured sonar signal $y \in \mathbb{C}^m$. N and m are the dimensions of the operators. Normally, this problem is underdetermined (m<<N).

The problem to find the sparsest solution is formulated as an optimization based on the l_0 norm. This is, in general an NP-hard problem, therefore the optimization problem is relaxed to the l_1-norm:

$$\min\|x\|_1 \; subj.\; to \; \|Ax - y\|_2 \leq \sigma \tag{2}$$

Where the indices 1 and 2 denote the l_1 and l_2-norms, respectively, and σ is an estimate of the noise.
In this work, the quadratic constrained l_1-minimization problem has been used, in the SPGL1 implementation ([3]). The relaxation step is defined according to [1].
The model is based on isotropic and frequency independent point scatterers. Equation (3) shows the general expression for the forward-propagator acting on x, also taking into account the travel distance $|r - r'|$, frequency ω and at time t(see for example reference [5] for more information).

$$Ax = \frac{x\left(t - \frac{|r - r'|}{c}\right)}{|r - r'|^2} e^{i\omega t\left(t - \frac{|r - r'|}{c}\right)} \tag{3}$$

In this formalism, the inverse forward-propagator (i.e. back-propagator) acting on y is defined as:

$$\hat{A}^{-1}y = \sum_{n=1}^{m} w_n y_n(t) \tag{4}$$

The back-propagator is the classical delay-and-sum (see for example reference [4]), where $y_n(t)$ is the measured sonar signal from element n at time t, w_n is an appropriate window function coefficient. Both the forward-propagator and the back-propagator are used in the minimization algorithm described above.
The output from the minimization algorithm is the vector $x \in \mathbb{C}^N$, describing the sonar image. The results can be visualized using the forward projector for a specific array setup (i.e. the same geometry and configuration as used for the collecting the sonar signal) or another – synthetic-array with different geometry, for example longer array with more elements to achieve higher resolution.

3. RESULTS AND DISCUSSION

The measurements are collected using the experimental platform Sapphires in the freshwater Lake Vättern. Sapphires has a side-looking sonar array giving a SAS resolution of <4x4 cm, using conventional back-projection, combining data from several pings using auto-focussing. Results using the method described above are presented, both from one ping data and from a combination of several pings. To simplify comparisons, all measurements are covering the same objects, namely a rope loop. The images show $\|C\|_2^{1/3}$, to decrease the dynamics in the results (C being the complex valued back-projected sonar image).

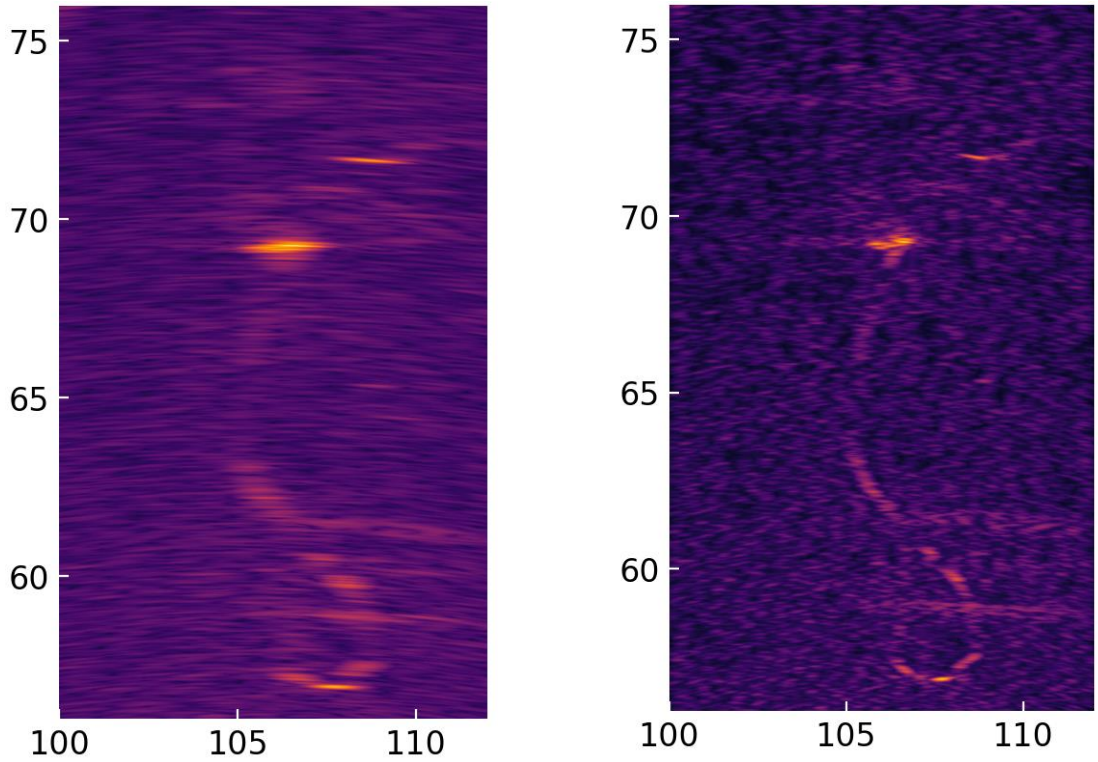


Fig. 1, Enhanced resolution from one ping data. Left image showing delay-and-sum on raw measurement data, right the enhanced image based on CS-results.

An example result is visualized in figure 1, where the image to the left shows the image using the delay-and-sum formulation on the measurement data. The image to the right shows the CS result. The CS results have been achieved using the results from the minimization together with the forward- and backwards-propagator for a synthetically extended array (but keeping the inter-distance between the receivers). In this case, the synthetic aperture is 16 times longer than the measurement aperture.

The resolution is significantly enhanced by using the model described above together with the l_1-minimization.

Worth mentioning is that the sparsity is generally in this study is around 10%, i.e. 90% of the vector x is zero-valued.

In order to compare with the more traditional synthetic aperture sonar images, different measurements covering the same area are used. In this case, the measurement apertures are not overlapping; the apertures do not partially overlap but are separated with several meters. This prevents the use of most of the traditional micro-navigation/autofocus techniques. Figure 2 shows two results; the left image is constructed using traditional techniques but incoherently added. The image to the right shows the results using CS based on the same measurement data as the left images, and here each measurement is used as input for optimization algorithm and thereby synthetic sonar data is achieved the same way as described above. The results from the three measurements are also incoherently added in this image.

We have demonstrated that CS is a promising tool for improving the spatial resolution in sonar imaging, for both one-measurement techniques as well as multiple measurements techniques (such as SAS). For alternative methods, see for example [6] using Deep Learning based methods.

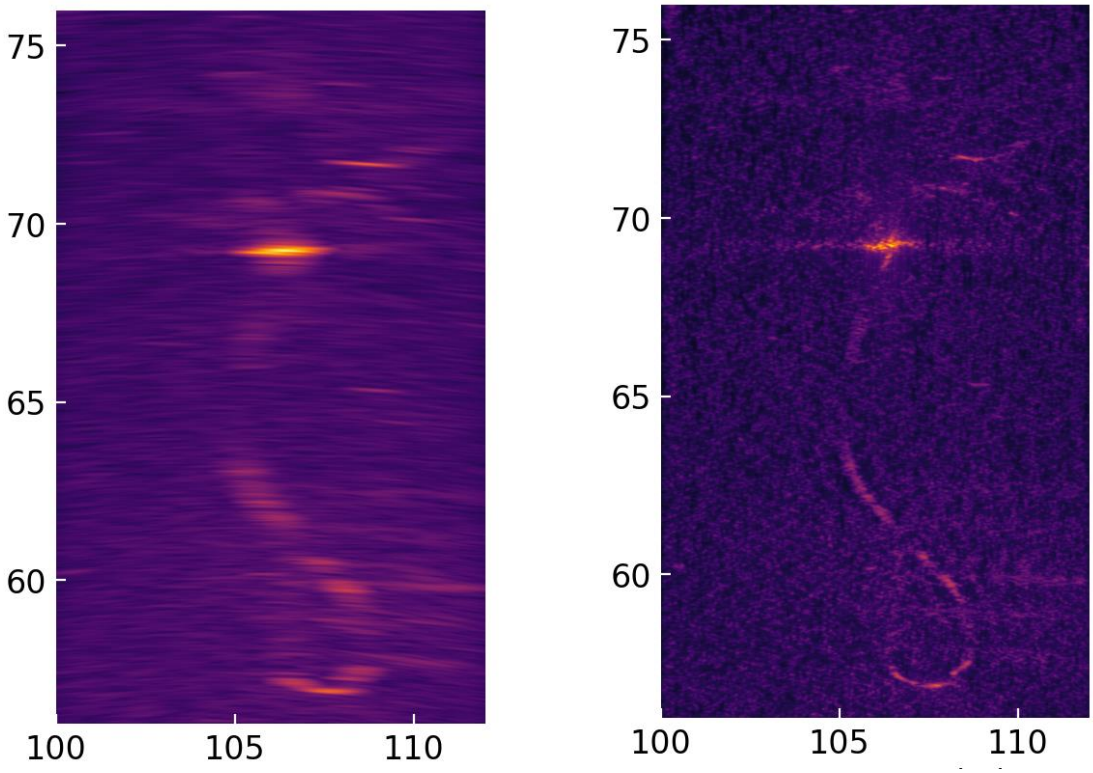


Fig. 2, *Enhanced resolution from three data measurements. Left image showing delay-and-sum on raw measurement data, right the enhanced image based on CS-results.*

ACKNOWLEDGEMENTS

This work was supported by the Swedish Foundation for Strategic Research through Strategic Mobility grants.

REFERENCES

[1] **E.J. Candés, J. Romberg, T. Tau**, *IEEE Trans. Inform. Theory*, 52 489-509 (2004)
[2] **M. Lustig, D. Donoho, J. M. Pauly,** *Magn. Reson. Med.*, 58 1182-95 (2007)
[3] **E. van den Berg, M. P. Friedlander**, *SIAM J. on Scientific Computing*, 31(2): 890-912 (2008)
[4] **R. E. Hansen**, Introduction to Synthetic Aperture Sonar, Sonar System, Prof. Nikolai Kolev (ed.) (2011), ISBN: 978-953-307-345-3
[5] **R. J. Urick**, principles of underwater sound, 3rd edition (1983), ISBN: 9780932146625
[6] **L. Rixon Fuchs, C. Larsson, A. Gällström**, Deep Learning based Technique for enhanced sonar imaging, In *UACE 2019, Crete-Greece*, 2019

APPLICATION OF MARKOV-CHAIN MONTE CARLO PARAMETER-SET IDENTIFICATION TO DESIGN AND INVERSION

Sven M. Ivansson[a]

[a]SE-11529 Stockholm, Sweden

Sven M. Ivansson, SE-11529 Stockholm, Sweden; email sven.ivansson@gmail.com

Abstract: *In this paper, Markov-chain Monte Carlo (MCMC) sampling is used to identify sets in parameter space defined by the smallness of some "misfit" function. Two applications are given. The first concerns design of Alberich anechoic coatings with identification of coatings achieving a given maximum reflectance within a given frequency band. The layer-multiple-scattering (LMS) computational method is extended to cover three or more cavity types in the rubber coating. Three types turn out to improve the broad-band echo reduction, but no further improvement is obtained with four. Correlations among favourable design parameters are identified. The preferable cavity sizes typically increase with the rubber shear-wave velocity, but the smallest cavities are smaller than expected from a consideration of the resonance frequency of an isolated cavity. Effects of multiple scattering may explain this. The second application is about inversion uncertainty, with an example concerning determination of seismo-acoustic material parameters from backscattering measurements. With the a priori information that the difference between data and replica be within a certain error-norm bound, marginal estimates of the model parameters are computed. An interpretation is given in terms of Bayesian inversion with a certain simple data-error distribution, that does not involve additional data-error covariance parameters to be estimated.*

Keywords: *Anechoic coating, layer-multiple-scattering method, reflection/transmission matrix, Bayesian inversion*

1. INTRODUCTION AND SUMMARY

As detailed in [1], the Markov-chain Monte Carlo (MCMC) method, *e.g.*, [2], can be used to identify sets $G = \{\mathbf{p}: g(\mathbf{p}) < \varepsilon\}$, where $g(\cdot)$ is a computable function, in a space of parameter vectors $\mathbf{p}=(p_1,p_2,...)$. Volume-weighted projections of G onto parameter axes and two-dimensional parameter planes are thereby useful for visualization. An application to design of Alberich anechoic coatings was included in [1], using the layer-multiple-scattering (LMS) method [3],[4] for computation of the pertinent function $g(\cdot)$ defined as the maximum reflectance within a certain frequency band. Specifically, the coated structure was viewed as a phononic crystal (PC) slab for which the LMS method provided reflection/transmission (R/T) matrices for plane waves. The rubber-layer coatings contained long cylinder cavities of $S = 2$ sizes, with axes in a lateral direction.

The present paper includes an extension of this coating application to cavities of $S = 3$, or more, sizes. Secton 2 gives the details of the needed extension of the LMS method, and Sec. 3 provides coating-design results. The third cavity size improves the broad-band performance, but there is no further improvement with $S = 4$. As expected, for favourable coatings with $S = 3$, the sizes of the largest and medium cavities are positively correlated with the rubber shear speed. For the smallest cavities, however, there is a negative correlation, and they are much smaller than expected from a consideration of single-cavity resonances. This appears to be due to multiple scattering among the coating-layer cavities.

The MCMC identification of parameter sets can also be useful for assessment of inversion uncertainty. Section 4 gives an example, based on [5], concerning determination of seismo-acoustic material parameters from backscattering measurements in a water tank. Parameter values compatible with the measurements are identified. The approach can be reformulated in a Bayesian context, with a particularly simple data-error distribution. Sharper uncertainty estimates might result by using additional knowledge about the data errors, but estimation of additional data-error covariance parameters is avoided.

2. R/T MATRICES FOR A PC SLAB

The LMS method for computing R/T matrices for a PC slab with infinite cylindrical scatterers, detailed in [6], [7, Sec. III], and [1, Sec. III.C], is here extended to an arbitrary number S of scatterers within the unit cell of length d. In a Cartesian xyz coordinate system for position vectors $\mathbf{r} = (x,y,z)$, the cylinder axes are parallel to the y-axis, and cylinders of type σ=1,2,..,S appear at $\mathbf{r}_\sigma + \mathbf{R}$ where $\mathbf{r}_\sigma = (x_\sigma,0,0)$ and $\mathbf{R} = m(d,0,0)$ with m running through the integers. Figure 1 shows a coating example with $S = 3$.

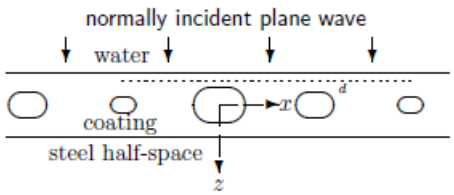


Fig.1: Coating containing cylindrical scatterers of three sizes between a steel and a water half-space. The medium is independent of y and periodic with period d in x.

The angular frequency of an insonifying plane wave is $\omega > 0$. At first, the scatterers are in an otherwise homogeneous anelastic solid whole-space with wavenumbers k_p and k_s for sound and shear waves, respectively, and with basic cylindrical displacement-vector

solutions $\mathbf{u}_{l\kappa}^{0P}(\mathbf{r})$ and $\mathbf{u}_{l\kappa}^{+P}(\mathbf{r})$ for regular (involving J_l) and outgoing (involving $H_l^{(1)}$) waves, respectively, as defined in [6]. P=L,M,N indicates wave type, l=0,±1,±2,.. angular order, and the real number κ controls the exp(iκy) dependence on y. $T_\sigma = \{(T_\sigma)_{l;l'}^{PP'}\}$ is the transition (T) matrix for a scatterer of type σ located at the origin. For a scatterer of type σ at $\mathbf{r}_\sigma$+$\mathbf{R}$, exp[i$\mathbf{k}_\parallel$·($\mathbf{r}_\sigma$+$\mathbf{R}$)] $\mathbf{b}_\sigma^+$ gives the expansion coefficients for its scattered field in terms of $\mathbf{u}_{l\kappa}^{+P}(\mathbf{r}-\mathbf{r}_\sigma-\mathbf{R})$, and exp[i$\mathbf{k}_\parallel$·($\mathbf{r}_j$+$\mathbf{R}$)] $\mathbf{b}_{\sigma\nu}^0$ gives the expansion coefficients for the scattered field from all other scatterers of type ν in terms of $\mathbf{u}_{l\kappa}^{0P}(\mathbf{r}-\mathbf{r}_\sigma-\mathbf{R})$. For σ=1,2,..,S,

$$\mathbf{b}_\sigma^+ = T_\sigma \cdot (\mathbf{a}_0 + \textstyle\sum_{\nu=1}^{S} \mathbf{b}_{\sigma\nu}^0)\ . \tag{1}$$

Here, $\mathbf{a}_0 = \{(a_0)_{l\kappa}^{0P}\}$ gives the coefficients for expansion of the incident plane wave with horizontal wavenumber $\mathbf{k}_\parallel = (k_{\parallel x},\kappa,0)$ in regular waves $\mathbf{u}_{l\kappa}^{0P}(\mathbf{r})$. Equation (1) gives the following linear equation system for determination of the $\mathbf{b}_\sigma^+ = \{(b_\sigma^+)_l^P\}$, σ=1,2,..,S:

$$\mathbf{b}_\sigma^+ = T_\sigma \cdot \left(\mathbf{a}_0 + \Omega^0 \cdot \mathbf{b}_\sigma^+ + \textstyle\sum_{\nu=1,\nu\neq\sigma}^{S} Q_{\sigma\nu} \cdot \mathbf{b}_\nu^+\right)\ . \tag{2}$$

Here, Ω^0 and $Q_{\sigma\nu}$ are lattice translation matrices such that $\mathbf{b}_{\sigma\sigma}^0 = \Omega^0 \cdot \mathbf{b}_\sigma^+$ and $\mathbf{b}_{\sigma\nu}^0 = Q_{\sigma\nu} \cdot \mathbf{b}_\nu^+$ for $\nu \neq \sigma$. With $p = \left(k_p^2 - \kappa^2\right)^{1/2}$, $q = (k_s^2 - \kappa^2)^{1/2}$, and $\nu \neq \sigma$, their nonzero elements are

$$\begin{aligned}
&(\Omega^0)_{l;l'}^{LL} = \Theta_{l-l'}(0; k_{||x}d, pd) \qquad (\Omega^0)_{l;l'}^{MM} = (\Omega^0)_{l;l'}^{NN} = \Theta_{l-l'}(0; k_{||x}d, qd)\\
&(Q_{\sigma\nu})_{l;l'}^{LL} = \Theta_{l-l'}\left((x_\nu - x_\sigma)/d; k_{||x}d, pd\right)\\
&(Q_{\sigma\nu})_{l;l'}^{MM} = (Q_{\sigma\nu})_{l;l'}^{NN} = \Theta_{l-l'}\left((x_\nu - x_\sigma)/d; k_{||x}d, qd\right)
\end{aligned} \tag{3}$$

where, for the dependence exp(−iωt) on time t, Im(p),Im(q) > 0 and, with sgn(0) = 0,

$$\Theta_l(x; k_{||x}d, kd) = \textstyle\sum_m \left(\frac{\mathrm{sgn}(x+m)}{\mathrm{i}}\right)^l \exp\left(\mathrm{i}k_{||x}d(x+m)\right) \mathrm{H}_l^{(1)}(kd|x+m|)\ . \tag{4}$$

Equations (3) follow from the Graf addition theorem for Bessel functions, expressed as

$$\mathrm{H}_l^{(1)}(kr_{x+m})\mathrm{e}^{\mathrm{i}l\theta_{x+m}} = \textstyle\sum_n \mathrm{H}_{l-n}^{(1)}(kd|x+m|)\left(\frac{\mathrm{sgn}(x+m)}{\mathrm{i}}\right)^{l-n} \mathrm{J}_n(kr)\mathrm{e}^{\mathrm{i}n\theta} \tag{5}$$

for integers l and m, complex nonvanishing k with Im(k) > 0, and polar coordinate representations r(sin(θ),cos(θ)) = r_{x+m}(sin(θ_{x+m}),cos(θ_{x+m})) + (d(x+m),0) with $r < d\ |x+m|$.

Using [6, Eq. (12)], essentially the Poisson summation formula, the total scattered field $\mathbf{u}_{\mathrm{sc}}(\mathbf{r}) = \sum_{\sigma=1}^{S}\sum_{Pl}(b_\sigma^+)_l^P \sum_{\mathbf{R}} \exp\left(i\mathbf{k}_{||} \cdot (\mathbf{r}_\sigma + \mathbf{R})\right) \mathbf{u}_{lk}^{+P}(\mathbf{r}-\mathbf{r}_\sigma-\mathbf{R})$ can be expressed in terms of plane waves of different types P,SV,SH (j_{sc}=1,2,3, respectively), directions along the z-axis (s_{sc}=+/− for positive/negative), and horizontal wavenumbers $\mathbf{k}_\parallel$ + (2πm_{sc}/d,0,0), where m_{sc} runs over the integers. This provides the desired plane-wave R/T matrices, but incident plane waves for all j_{inc}=1,2,3, s_{inc}=+/−, and integers m_{inc} must be considered. For a PC slab with several scatterer or layer interfaces, parallel to the xy-plane, R/T matrices for the different interfaces can be combined recursively to form a total R/T matrix, *e.g.*, [4].

The matrices Ω^0 are independent of m_{inc}, where $\mathbf{k}_\parallel$ + (2πm_{inc}/d,0,0) is the horizontal wavenumber of the incident plane wave, while (for each m_{inc}) the matrices $Q_{\sigma\nu}$ depend on σ and ν only through $x_\nu - x_\sigma$. For the special case with uniform scatterer location according to x_σ = (σ−1)d/S, σ = 1,..,S, Eqs. (3)-(4) show that $Q_{\sigma\nu} = Q_{1\,\nu+1-\sigma}$ if $\sigma < \nu$, $Q_{\sigma\nu} = Q_{1\,\nu+1+S-\sigma}$ if $\nu < \sigma$, $Q_{\sigma\nu}$ is periodic with period S in m_{inc} which can be used to treat the

different m_{inc} in an order that minimizes the needed updates of the $Q_{\sigma\nu}$, and that $\Omega^0 + Q_{1\,2} + Q_{1\,3} + .. + Q_{1\,S} = \Omega^0_S$ where Ω^0_S is "the Ω^0 computed with d replaced by d/S" (Ω^0_S is of course periodic with period S in m_{inc}, but it is not independent of m_{inc}). For the special case when $k_{\|x} = 0$, $(\Omega^0)^{PP'}_{l;l'}$ vanishes if $l - l'$ is odd, "$(Q_{\sigma\nu})^{PP'}_{l;l'}$ computed for m_{inc}" = $(-1)^{l-l'}$ "$(Q_{\nu\sigma})^{PP'}_{l;l'}$ computed for $-m_{\text{inc}}$", and $(Q_{\sigma\nu})^{PP'}_{l;l'}$ vanishes if $|x_\nu - x_\sigma| = d/2$, m_{inc} is even, and $l - l'$ is odd. These observations are helpful to reduce the computational work.

Finally, a comment about the case when the scatterers of type σ=1,2,..,S get displaced an amount ζ_σ in the z-axis direction relative to the wave center used for computation of their T-matrices T_σ. The equation system (2) is then modified to

$$[S(\zeta_\sigma)]^{\mathrm{T}} \cdot \mathbf{b}^+_\sigma = T_\sigma \cdot [S(\zeta_\sigma)]^{\mathrm{T}} \cdot \left(\mathbf{a}_0 + \Omega^0 \cdot \mathbf{b}^+_\sigma + \textstyle\sum_{\nu=1,\nu\neq\sigma}^{S} Q_{\sigma\nu} \cdot \mathbf{b}^+_\nu\right) \qquad (6)$$

where the orthogonal matrices $S(\zeta)$ are defined as in [1, Sec. III.C]. It is appropriate in this case to introduce new "effective" lattice translation matrices $[S(\zeta_\sigma)]^{\mathrm{T}} \cdot \Omega^0 = \Omega^0 \cdot [S(\zeta_\sigma)]^{\mathrm{T}}$ and $[S(\zeta_\sigma)]^{\mathrm{T}} \cdot Q_{\sigma\nu} = Q_{\sigma\nu} \cdot [S(\zeta_\sigma)]^{\mathrm{T}}$, with elements that depend on l, l' through the difference $l - l'$ only, *cf.* [1, Sec. III.C].

3. COATING DESIGN

A coating design example from [1] is here modified to $S = 3$ uniformly located cavity types, as in Fig. 1. The steel parameters are 5850 and 3230 m/s for the sound and shear-wave speeds, respectively, and 7.7 kg/dm^3 for the density. The water sound speed is 1480 m/s. Each cylindrical cavity has a superelliptical cross section with symmetry half-axes of lengths a and b in the z- and x-directions, respectively. A coating with small reflectance in the frequency band 8-22 kHz is desired. At first, a vector $\mathbf{p}$ with six design parameters, $\mathbf{p} = (p_1,p_2,p_3,p_{3x},p_4,p_5)$ is varied, by differential evolution, to minimize the maximum reflectance in the band. The parameters are, with their variation intervals in brackets: Lattice period $p_1 = d$ [4-160 mm], coating thickness $p_2 = H$ [1-12 mm], length-scale quotient between the medium-sized and largest cavities p_3 [0.15-1.0], length-scale quotient between the smallest and medium-sized cavities p_{3x} [0.15-1.0] cavity excentricity parameter $p_4 = a/b$ [0.4-1.0], and rubber shear-wave speed $p_5 = \beta$ [60-400 m/s]. All cavities appear in the middle of the coating. The largest, medium-sized, and smallest ones have half-axes a_1, $a_2 = p_3\, a_1$, and $a_3 = p_{3x}\, a_2$, respectively, in the z-axis direction. The rubber compressional-wave absorption is, in each case, set to the lowest value consistent with the physical constraint for the bulk modulus. In this initial optimization, the rubber shear-wave absorption is 25 dB/wavelength, while the sound speed and density of the rubber agree with those of the water.

The lowest curve (at 15 kHz) in left panel of Fig. 2 shows the reflectance at optimum, with maximum −38.6 dB in the 8-22 kHz band. The other two curves, with larger reflectance maxima, concern $S = 1$ and 2. Extension to $S = 4$ did not improve the $S = 3$ result.

Next, the design parameter space is extended with rubber shear-wave absorption $p_6 = \delta$ [1-25 dB/wavelength], sound speed $p_7 = \alpha$ [1400-1600 m/s], and density $p_8 = \rho$ [0.9-1.3 kg/dm^3]. Moreover, with $S = 3$ cavity types, a simple variable transformation, *cf.* [1, Secs. II.C and IV.A], is applied to replace the parameters p_2,p_3,p_{3x} with the cylinder-size parameters a_1,a_2,a_3. The MCMC sampling method is used to identify the set G' in the extended and modified design space for which the 8-22 kHz band reflectance falls below −30 dB. The right panel of Fig. 2 shows projections of G' onto the β-a_1, β-a_2, β-a_3 planes. As expected [1, Sec. IV.A], β-a_1 as well as β-a_2 are positively correlated, and the corresponding contours mainly appear between the indicated $\omega a/\beta = 0.3$ lines, at 8 kHz

(upper line) and 22 kHz (lower line), for approximate single-cavity absorption cross-section maxima. Surprisingly, however, the β-a_3 contours mainly fall below the $\omega a/\beta = 0.3$ line for 22 kHz, and they indicate a negative correlation between β and a_3. The reason appears to be complicated effects of multiple scattering among the cavities. The three ring symbols in the figure indicate β, a_1, a_2, a_3 values at the optimum (for $S = 3$) from the left panel. With a much larger a_3 value, the three plus symbols indicate corresponding values for an optimization done by artificially ignoring multiple scattering among the cavities (setting pertinent Ω^0 and $Q_{\sigma\nu}$ from Sec. 2 to zero matrices).

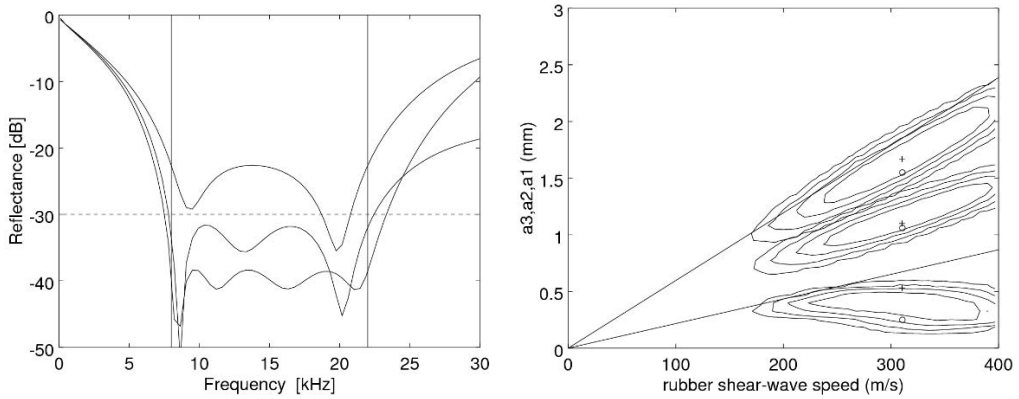


Fig.2: Left panel: reflectance curves obtained by minimizing the maximum reflectance in the indicated 8-22 kHz band; there are three curves, with improving results, for S = 1,2,3, respectively. Right panel: projections onto the β-a_1, β-a_2, β-a_3 planes of the set G′ with favourable coatings; for each of a_1, a_2, a_3, there are four contours enclosing minimal regions including 65%, 85%, 95%, and 99%, respectively, of the coatings in G′.

Further projections of G' (not shown) demonstrate that, for the favourable coatings: the lattice period d is concentrated around 50 mm; the excentricity parameter a/b appears in the interval (0.5,0.6) and it is negatively correlated with β, a_1, and a_2; the rubber shear-wave absorption δ is greater than 20 dB, while the reflectance is rather insensitive to the considered values of the negatively correlated rubber parameters α and ρ.

4. INVERSION UNCERTAINTY

Suppose that a data vector **d** has been obtained from some measurements, and consider the inverse problem to determine an underlying model parameter vector **p**. Without any errors, $\mathbf{d} = g_0(\mathbf{p})$ would hold, for a known computable forward-model function g_0. If an error-limit norm $\|\cdot\|$ with an error limit ε is also known, such that $\|\mathbf{d} - g_0(\mathbf{p})\| < \varepsilon$, the inversion uncertainty can be assessed by using MCMC sampling to identify the model set $G = \{\mathbf{p}: \|\mathbf{d} - g_0(\mathbf{p})\| < \varepsilon\}$.

Figure 12a in [5] shows a time trace, **d**, obtained by backscattering from a resin solid sphere in a certain tank-measurement configuration, devised to allow inversion of the resin parameters p_1 (compressional-wave speed), p_2 (shear-wave speed), p_3 (compressional-wave absorption), p_4 (shear-wave absorption). With the maximum norm and $\varepsilon = 4$ % (2 %) of the time-trace maximum, the solid (dashed) curves in Fig. 3 are histograms of volume-weighted projections of the corresponding set G onto the parameter axes. Such histograms can be useful for assessing inversion uncertainty and for designing measurement setups.

Finally a comment on the relation to Bayesian inversion. With standard notation, *e.g.*, [2], $P(\mathbf{p}|\mathbf{d}) \sim P(\mathbf{d}|\mathbf{p})\ P(\mathbf{p})$ according to Bayes' rule. With a uniform prior distribution $P(\mathbf{p})$ and with $P(\mathbf{d}|\mathbf{p}) \sim \exp(-E(\mathbf{p}))$ with the error or misfit function $E(\mathbf{p}) = 0$ when **p** is in $G = \{\mathbf{p}: \|\mathbf{d} - g_0(\mathbf{p})\| < \varepsilon\}$ and $+\infty$ when it is not, it follows that $P(\mathbf{p}|\mathbf{d}) \sim \chi_G(\mathbf{p})$, the characteristic

function of the set *G*. In Bayesian terminology, the projections in Fig. 3 of *G* onto the parameter axes are one-dimensional marginal posterior probability distributions.

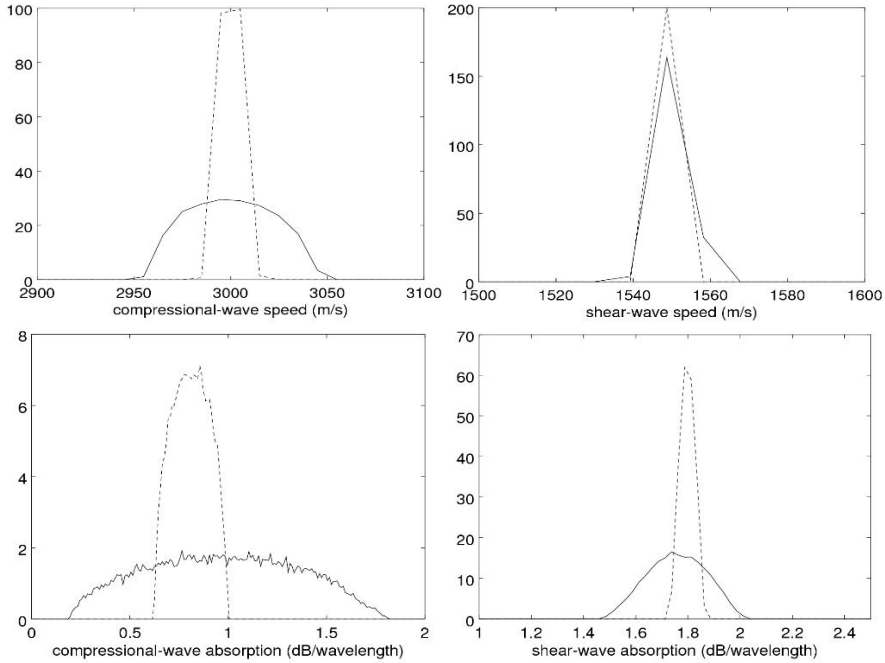


Fig.3: Histograms of projections onto the parameter axes of a set G of resin-parameter models compatible with certain backscatter measurements. The solid and dashed histograms concern different data-error limits, with halved limits for the dashed ones.

5. ACKNOWLEDGEMENTS

This work builds on experience gained while the author was with the Swedish Defence Research Agency. Stan Dosso provided one of his subroutines for MCMC model sampling.

REFERENCES

[1] **S.M. Ivansson**, Markov-chain Monte Carlo identification of favourable design choices with application to anechoic coatings, *J. Acoust. Soc. Am.*, 135 (6), pp. 3338-3351, 2014.
[2] **S.E. Dosso,** Quantifying uncertainty in geoacoustic inversion. I. A fast Gibbs sampler approach, *J. Acoust. Soc. Am.*, 111 (1), pp. 129-142, 2002.
[3] **R. Sainidou, N. Stefanou, I.E. Psarobas, A. Modinos**, A layer-multiple-scattering method for phononic crystals and heterostructures of such, *Comput. Phys. Commun.*, 166, pp. 197-240, 2005.
[4] **J.B. Pendry**, *Low Energ Electron Diffraction*, Academic Press, 1974.
[5] **A. Tesei, P. Guerrini, M. Zampolli**, Tank measurements of scattering from a resin-filled fiberglass spherical shell with internal flaws, *J. Acoust. Soc. Am.*, 124 (2), pp. 827-840, 2008.
[6] **S.M. Ivansson**, Designing 2D phononic crystal slabs with transmission gaps for solid angle as well as frequency variation, *Adv. Acoust. Vib.*, 2009, 317890, 2009.
[7] **S.M. Ivansson**, Anechoic coatings obtained from two- and three-dimensional monopole resonance diffraction gratings, *J. Acoust. Soc. Am.*, 131 (4), pp. 2622-2637, 2012.

Regular Session 25
Signal and image processing

BELOW-BAND SIGNAL PROCESSING FOR LOCALIZING DISTANT SOURCES IN A NOISY DEEP OCEAN

David J. Geroski[a], David R. Dowling[b]

[a]David J. Geroski (ATTN: Alesha Thomas)
Applied Physics Program
1301 Beal Avenue
Ann Arbor MI, 48109
[b]David R. Dowling
Department of Mechanical Engineering
1231 Beal Avenue
Ann Arbor, MI 48109

Abstract: *Frequency Difference Source Localization (FDSL) methods have proven successful for localizing sources both in the deep ocean and in the shallow ocean using recordings from a vertical array of hydrophones. These source localization algorithms are based upon the phase coherence of a product of recorded complex field values, termed autoproducts, at frequencies below the recordings' bandwidth. Similar to Matched Field Processing (MFP), the measured autoproduct is correlated to a replica that is calculated based on the user's knowledge of the acoustic environment. These below-band source localization methods are nonlinear and sacrifice in-band spatial resolution for robustness to environmental mismatch. Past frequency-difference localization efforts utilized high signal-to-noise ratio (SNR) data to demonstrate robustness to mismatch. This paper explores the performance of FDSL in the presence of noise. Specifically, simulated noise and noise measured during the PhilSea10 experiment are added to both simulated and measured pings to determine the SNR below which localization performance begins to degrade. For the scenario considered here, the source was located 210 km from a vertical receiving array in a deep ocean environment with an active internal wave field. The source broadcast was a linear frequency sweep from 200 to 300 Hz. At high SNR (>20 dB) using single-digit-Hertz below-band frequencies, the source is correctly localized in all simulations, and in 97 out of 100 trials using single-broadcast ocean recordings. For simulated and measured forward signals distorted by simulated noise, this performance persists down to SNR's of –20 and –14 dB, respectively. For measured forward signals with elevated levels of measured noise, successful performance persists down to –8 dB SNR.*

Keywords: *Source Localization, Nonlinear Signal Processing, Matched Field Processing*

1. INTRODUCTION

Passive acoustic localization of a distant unknown source is a common task in acoustic remote sensing in the ocean using hydrophone arrays (see Dowling and Sabra, 2015). One popular class of frequency-domain techniques for this task is Matched Field Processing, (MFP) which involves correlating measured fields with replica fields calculated using the known propagation physics of the acoustic environment (Bucker, 1976). MFP techniques have proven to be robust to many kinds of ocean noise (Debever and Kuperman 2007), and they work well when the acoustic environment between the source and receiving array is well known. However, a lack of sufficiently-complete environmental knowledge causes MFP to struggle in many scenarios of interest (Baggeroer et. al. 1993). This problem, known as *mismatch*, becomes more severe at higher frequencies and longer ranges, as the acoustic propagation becomes more sensitive to smaller environmental details at higher frequency, and includes larger regions of the imperfectly-known ocean environment at longer range.

Recently, this limitation has been mitigated in the shallow ocean using Frequency Difference MFP (FDMFP) to localize sources operating at high (f > 10 kHz) frequencies in a 103 m deep sound speed channel (Worthmann 2015, 2017). This technique involves constructing quadratic products of the measured signals and correlating them to lower frequency fields, where mismatch is less problematic. This article has two purposes: to introduce a mild revision of FDMFP, termed Frequency Difference Source Localization (FDSL), that allows distant acoustic sources to be localized in the deep ocean, and to test the noise rejection capabilities of FDSL. This performance is assessed with propagation data measured during the PhilSea10 experiment (Worcester et. al. 2013). In particular, this study focuses on localizing a single source, positioned 210 km downrange from a vertical array of transducers, that transmitted a frequency sweep signal (200 < f < 300 Hz) repeatedly over the course of several months. The results show that FDSL can be used to overcome mismatch in the deep ocean even at relatively low signal-to-noise ratios (SNRs).

The remainder of this paper is divided into three sections. Section 2 contains a summary of conventional MFP and FDSL, as well as descriptions of the signal processing techniques undertaken to produce the given results. Section 3 provides a brief description of the PhilSea10 experiment, the post processing used to artificially degrade the SNR achieved during the experiment, and the simulated and measured results of FDSL in this ocean environment. Section 4 summarizes this study, and states the conclusions drawn from it.

2. THEORY

The FDSL technique can be thought of as a variant of conventional MFP for array recorded acoustic signals. Given this, the most natural place to begin a discussion of this algorithm is with conventional, or Bartlett MFP (see Jensen et. al. 2011). Bartlett MFP is a spatial filtering process applied over a receiving array. Acoustic signals measured along the array from a source located at x_s, denoted in the frequency domain as $P_j(\omega)$ at angular frequency ω and for hydrophone j, are cross correlated with a weight vector $w_j(x_t,\omega)$ that represents the acoustic response of the (known) acoustic environment to a time-harmonic source transmitting from trial location x_t to hydrophone j. The trial-source location, x_t, is then varied over the region of interest to produce an ambiguity surface defined in (1).

$$B_c(x_t,\omega)=\Sigma_{i,j} w_i(x_t,\omega) R_{ij}(\omega) w_j^*(x_t,\omega) \tag{1}$$

$$R_{ij}(\omega)=\frac{P_i^*(\omega)P_j(\omega)}{\Sigma_i|P_i(\omega)|^2} \tag{2}$$

$$w_j(x_t,\omega)=G(\omega,x_t,x_j)(\Sigma_i|G(\omega,x_t,x_i)|^2)^{-\frac{1}{2}} \tag{3}$$

Here, $R_{ij}(\omega)$ in (2) is conventionally referred to as the cross-spectral density matrix (CSDM) (Baggeroer et. al. 1993) and is defined as such to make MFP independent of the source waveform. The asterisk in (1) and (2) indicates complex conjugation, and G is the calculated Green's function of the (known) environment for a source transmitting at x_t to a receiver at x_j. When defined this way, the ambiguity surface, B_c, is a positive, real, and bounded between 0 and 1, with 1 indicating a perfect match between the measured and calculated fields. Mismatch arises in (1) when $P_j(\omega)$ and $w_j(x_s,\omega)$ differ unintentionally. These differences tend to increase with frequency and source-receiver range. Some of these differences can be compensated by incoherently averaging through the measured signal bandwidth as in (4). Here the signal frequency is assumed to be bounded between Ω_L and Ω_H.

$$B_c(x_t)=<B_c(x_t,\omega)>_\omega=\frac{1}{\Omega_H-\Omega_L}\int_{\Omega_L}^{\Omega_H}B_c(x_t,\omega)d\omega \tag{4}$$

Frequency difference techniques, including FDSL, rely on analysing the CSDM of the frequency-difference autoproduct defined in (5) that is measured along the array, and correlating it to a weight vector that matches the physics of the autoproduct.

$$R_{ij}^{AP}(\Delta\omega)=\frac{<AP_i^*(\omega,\Delta\omega)AP_j(\omega,\Delta\omega)>_\omega}{\Sigma_i|<AP_i(\omega,\Delta\omega)>_\omega|^2} \tag{5}$$

$$AP_j(\omega,\Delta\omega)=P_j^*(\omega-0.5\Delta\omega)P_j(\omega+0.5\Delta\omega) \tag{6}$$

$$w_j(x_t,\Delta\omega)=\left|G_{modes}(\Delta\omega,x_t,x_j)\right|\arg(\Sigma_i|A_i|^2\exp(i\Delta\omega\tau_i)) \tag{7}$$

$$B_\Delta(x_t,\Delta\omega)=\Sigma_{i,j}w_i(x_t,\Delta\omega)R_{ij}^{AP}(\Delta\omega)w_j^*(x_t,\Delta\omega) \tag{8}$$

This processing is done by first taking a single sample of the autoproduct, as in (6), where the complex field values measured on one receiver are multiplied to form an autoproduct sample. This sample is then used to compute an autoproduct CSDM, and all samples available in the measured signal bandwidth are averaged and normalized to produce the final CSDM in (5). This CSDM is then cross correlated with the weight vector defined in (7). In (7), the amplitude of the weight vector is calculated using KRAKEN, a normal mode code, (Porter 1987), while its phase is derived from a ray code, Bellhop (Porter 1992). The amplitude follows that of FDMFP (Worthmann 2015), but the phase is derived from considerations of (6) when the measured field is well described as a sum of ray-path contribution with amplitude A_i and arrival times τ_i. The utility of the phase correction employed here is to remove the phase induced on a ray path which has been reflected by a barrier (Kinsler et. al. 2000) or which has passed through a caustic (Jensen et. al. 2011), as such phase corrections are absent from the measured autoproduct (Worthmann and Dowling 2018). Such processing is possible because the user has full control over how the weight vector is calculated in any MFP scheme.

3. EXPERIMENTAL SETUP & RESULTS

The experimental data used in this study was measured during the 2010-2011 Philippine Sea Experiment (PhilSea10) (Worcester et. al 2013). This was an underwater oceanographic

experiment, and the utility of the dataset for source localization research was unexpected. PhilSea10 included the collection of thousands of transmissions that came from a variety of sources. This study explores the first 120 pings (nominally the first 100 pings plus several others for snapshot averaging purposes) measured from the second closest source positioned 210 km downrange from the receiving array. The dataset used was provided to the authors by P. Worcester and M. Dzieciuch, lead scientists on the experiment, as matched-filtered time series for each hydrophone. This matched-filtering process technically requires knowledge of the source waveform, but it is here used only to achieve high SNR. All signal waveforms are scrambled across frequency by applying a random phase to each frequency bin to prevent source waveform information from reaching the signal processing steps. Additionally, the experimentalists also provided an acoustic sound speed profile measured near the receiving array, as well as nominal receiver positions for 149 elements in the receiving array. All calculations were done using this given information without alteration.

Based on this experimental geometry, the performance of conventional MFP and FDSL for both simulated and measured signals was calculated. In simulation, the pressure fields at the array were calculated using Bellhop. For MFP, 21 individual field samples (f = 200 Hz, 205 Hz, … , 300 Hz) from the measured bandwidth were used to construct the ambiguity surface. For FDSL, five difference frequency samples (Δf =1 Hz, 1.25 Hz, … , 2 Hz) were used to construct the ambiguity surface. Fig. 1 shows sample ambiguity surfaces calculated using measured field values for MFP and FDSL. The performance was also calculated for simulated fields, with results being similar to the results given in Fig. 2. In simulation, both

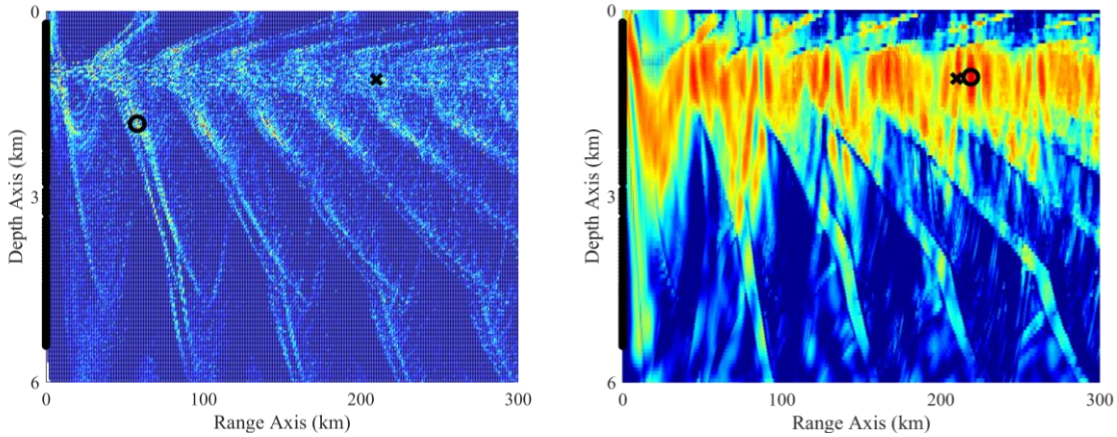


Figure 1: Ambiguity surfaces calculated applying (a) Bartlett MFP, and (b) FDSL to the first valid measurement of the given source during the PhilSea10 exercise.

MFP and FDSL successfully localize the relevant sources. However, in measurement, only FDSL successfully localizes the given sources within ±5% in range and depth. It is worth noting that FDSL shows approximately an 8 km range bias. This range error is seen in all localization results, and could possibly be corrected by taking into account bathymetric variations in the range-depth plane defined by the source and the vertical receiving array.

To demonstrate the robustness of FDSL to environmental mismatch, both types of processing were performed on the first 100 measured transmissions. The source localization results for both algorithms are shown in Fig. 2, along with a nominal localization success boundary that is an ellipse with axes defined by ±5% of the overall search range and depth (±15 km and ±300 m, respectively). These bounds are chosen to be reasonable and to indicate that the overall results are not obtained by chance. Initially, 97% of the trials are found to be successful for FDSL and 0% for MFP. Therefore, one final elementary signal processing step, snapshot averaging, was taken. Snapshot averaging is here taken to mean that ambiguity surfaces from successive pings were averaged. With two snapshot averaging, 100% localization success is achieved for FDSL. The localization performance of MFP did not improve for any amount of snapshot averaging (up to 20 snapshots).

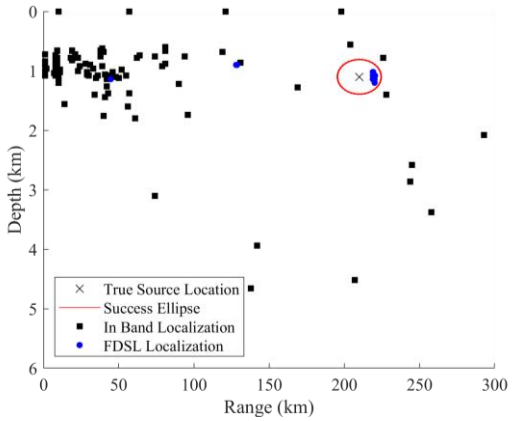


Figure 2: Scatter plot of source localization results from the first 100 pings transmitted by a source 210 km from the vertical receiving array during the PhilSea10 experiment. Conventional MFP does not localize the source. FDSL successfully localizes the source 97 times.

Given these localization results, the robustness of both conventional MFP and FDSL to elevated noise levels was tested. The noise level was varied here by adding either simulated or measured ocean noise. The simulated noise was created in the time domain by generating random numbers according to normal distributions with zero mean and unit standard deviation. This simulated time series was then Fourier transformed to place it into the frequency domain. The measured noise time series was collected during the experiment immediately before the measured signal was received. From here, either noise sample was multiplied by α according to (9) in order to give the desired SNR. This definition of SNR,

$$SNR(\alpha)=10\left(\log_{10}\left(\Sigma_i \left|P_i(\omega)\right|^2\right)- \log_{10}\left(\Sigma_i \left|\alpha N_i(\omega)\right|^2\right)\right) \quad (9)$$

is standard (Jensen et. al. 2011). The simulated performance of conventional MFP and FDSL in the presence of elevated levels of simulated noise is shown in Fig. 3. In addition to this, the

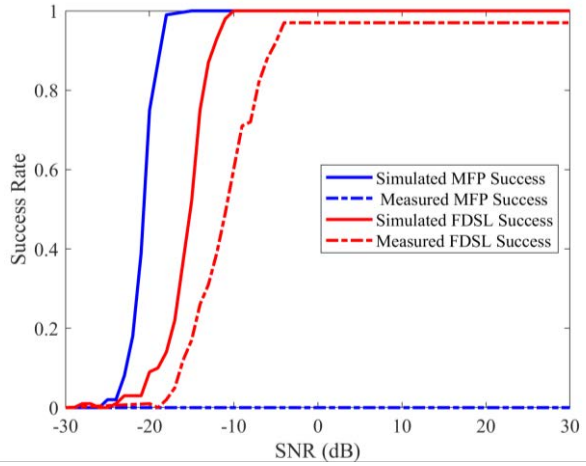


Figure 3: Noise Rejection capabilities of simulated and measured MFP and FDSL for -30<SNR<30. Simulations of both are conducted by using Bellhop to compute a forward field, and simulated noise is added to this field at a given SNR. Measurements of both are computed by adding measured noise to the given measured signal.

measured performance of MFP and FDSL in the presence of measured noise is also shown in Fig. 3. Here, success is determined by the percentage of successful localizations based on the success criterion defined in Fig. 2. The simulated results show that MFP has the best noise rejection capability. Despite this, MFP fails to successfully localize a source at any SNR using measured signals. FDSL, while not as robust to simulated noise as is MFP, is capable of

localizing sources down to SNRs of –8 dB or so in the presence of both simulated and measured noise.

4. SUMMARY AND CONCLUSIONS

Frequency-difference source localization (FDSL) is a new below-band technique for source localization in imperfectly known deep ocean environments that is akin to conventional matched field processing (MFP). FDSL successfully localizes a source positioned 210 km downrange from a vertical receiving array in the Philippine Sea using both simulated and measured data. In the chosen difference-frequency range, the performance of FDSL is robust to measured-field-to-calculated-field mismatch that is ubiquitous in long range acoustic propagation in the deep ocean. The noise rejection capabilities of both algorithms were also explored. Using simulated data, MFP rejects noise down to SNRs near –20 dB without mismatch, but fails to localize the source (at all SNRs) using PhilSea10 experimental data. However, using both simulated and experimental data, FDSL is able to successfully localize the source down to SNRs near –8 dB. Approaches that allow FDSL to inherit the greater noise rejection capabilities of MFP are now being explored.

REFERENCES

[1] **Dowling, D.R. and K. Sabra**, Acoustic Remote Sensing, *Ann. Rev. Fluid Mech.* 47, pp. 221-243, 2015.

[2] **Bucker**, Use of calculated sound fields and matched-field detection to locate sound sources in shallow water. *J. Acoust. Soc. Am.* 59, pp. 368, 1976.

[3] **Debever, C, and W.A. Kuperman**, Robust matched-field processing using a coherent broadband white noise constraint processore, *J. Acoust. Soc. Am.* 122, pp. 1979-1986, 2007.

[4] Baggeroer, A.B., W.A. Kuperman, and P.N. Mikhailevsky. An overview of matched field methods in ocean acoustics. *IEEE J. Ocean Eng.* 18, pp. 3018-3029, 1993.

[5] **Worthmann, B.M., H.C. Song, and D.R. Dowling**, High frequency source localization in a shallow ocean using frequency-difference matched field processing. *J. Acoust. Soc. Am.* 138, pp 3549, 2015.

[6] **Worthmann, B.M., H.C. Song, and D.R. Dowling,** Adaptive frequency-difference matched field processing for high frequency source localization in a noisy shallow ocean. *J. Acoust. Soc. Am.* 141, pp. 543-556, 2017.

[7] **Worcester, P.F., M.A. Dzieciuch, J.A. Mercer, R.K. Andrew, B.D. Dushaw, A.B. Baggeroer, K.D. Heaney, G.L. D'Spain, J.A. Colosi, R.A. Stephen, J.N. Kemp, B.M. Howe, L.J. van Uffelen, and K.E. Wage.** The North Pacific Acoustic Laboratory deep-water acoustic propagation experiments in the Philippine Sea, *J. Acoust. Soc. Am.,* 134(4), pp. 3359-3375, 2013.

[8] **Jensen, F.B., W.A. Kuperman, M.B. Porter, and H. Schmidt.** *Computational Ocean Acoustics, 2nd Ed.,* AIP, pp. 705-722, 2011.

[9] **Porter, M.B. and H.P. Bucker.** Gaussian beam tracing for computing ocean acoustic fields. *J. Acoust. Soc. Am.* 82, pp. 1349-1359, 1987.

[10] **Porter, M.** The KRAKEN normal mode program. Defense Technical Information Center (DTIC).

[11] **Kinsler, L.E., A.R. Frey, A.B. Coppens, J.V. Sanders,** *Fundamentals of Acoustics, 4th Ed.,* J. Wiley & Sons, 2000.

[12] **Worthmann, B.M. and D.R. Dowling.** The frequency-difference and frequency-sum acoustic-field autoproducts. *J. Acoust. Soc. Am.* 141, pp 4579, 2017.

SUBBSPACE TRACKING FOR DOMINANT MODE REJECTION BEAMFORMING

Gilles Gaonach[a], Arnaud Jaegler[a]

[a] Thales DMS France, 525 route des Dolines, 06 903 Sophia Antipolis Cedex

gilles.gaonach@fr.thalesgroup.com, arnaud.jaegler@fr.thalesgroup.com

Abstract: *Dominant mode rejection enables adaptive beamforming when the number of snapshots is limited. This situation typically occurs for the detection of transient signals in passive sonar processing. Moreover, the adaptive beamforming filter needs to be computed at a very high rate to adapt to the processed signal. This task is very demanding in terms of computation cost. However the processing only requires the first eigenvalues and eigenvectors, which may be computed recursively using subspace tracking algorithms. An implementation of a subspace tracking algorithm is here proposed. This implementation is based on previous studies and its numerical stability is tried out both on simulated and real data for dominant mode rejection beamforming. A comparison is finally made between conventional and dominant mode rejection in the context of transient detection.*

Keywords: *Adaptive beamforming, passive sonar, subspace tracking, dominant mode rejection beamforming*

INTRODUCTION

The main goal of passive sonar array processing is to detect low level signals by removing loud interferers and rejecting self-noise. The natural way to achieve this goal is to increase the array size. Yet, loud interferers limit the array gain for the detection of low level source through sidelobes jamming when the beamformer is conventional. On the opposite, sidelobes are kept under noise level when the array is adaptively processed by placing notches in the direction of these interferers. To this end, the adaptive processing, known as the Capon beamforming, computes the beamforming weights using the inverse of the noise covariance matrix. This noise covariance matrix is estimated with the received signal impinging the array, and the number of needed snapshots is linked to the number of sensors through the Capon statistics. To avoid SNR losses, the required number is at least three times the number

of sensors. Consequently, the larger the array is, the more time is needed to estimate the weights. However, at the same time, the data might only be stationary during short period of time, especially for large arrays, fast-changing environments or transient signals. Faster convergence of the adaptive processing is therefore required in these situations. This is achieved through the reduction of the adaptive degrees of freedom. Several techniques are available: subarray [1] or beamspace processing are the most common ones. Data dependent rank reduction is also popular and considered more optimal for rejection: krylov subspaces, or eigenspaces beamformer are the best examples. The dominant mode beamformer uses the dominant eigenvectors of the (badly) estimated covariance matrix, and use them to construct a better estimate by constructing the unknown minoring eigenspace as an uncorrelated noise, whom level is modelled or estimated.

Along with the need of rank reduction, adaptive filter weights computation is needed more often for fast-changing environment. Ultimately, this computation is processed at each new snapshot to adapt to very short transient signals. It might also serve as a basis for audio processing prior to inverse Fourier transform. To this end, minimizing computing costs are reached by using subspace tracking algorithms, which only calculate the dominant eigenvectors. The bottleneck of such recursive algorithms is the numerical stability. A fast and stable implementation is here used, and slightly modified to achieve exact equivalence with a direct method, that computes all the eigenvectors and eigenvalues of the sensors covariance matrix.

This paper is organized as follows. The first part presents the DMR beamformer, while the second part details the subspace tracking algorithm. Its numerical stability and precision are shown on sea signals, and the benefits over a conventional beamforming are discussed.

DOMINANT MODE REJECTION ADAPTIVE BEAMFORMER

The adaptive beamforming aims at maximising the output SNR beam, by minimizing the output power while maintaining the signal contribution in the steering direction:

$$\mathbf{h} = \arg\min \mathbf{h}^{+}\boldsymbol{\Gamma}\mathbf{h} \;\; s.t. \;\; \mathbf{h}^{+}\mathbf{d} = 1 \tag{1}$$

The solution to this optimization problem is the usual Capon filter:

$$\mathbf{h} = \frac{\boldsymbol{\Gamma}^{-1}\mathbf{d}}{\mathbf{d}^{+}\boldsymbol{\Gamma}^{-1}\mathbf{d}} \tag{2}$$

When the number of snapshots N is greater than the number of sensors n, the covariance matrix is estimated with the snapshots of the received signal vector $\mathbf{x}_i$:

$$\boldsymbol{\Gamma}_{\mathbf{SMI}} = \hat{\boldsymbol{\Gamma}} = \frac{\mathbf{1}}{\boldsymbol{K}}\sum_{\boldsymbol{i=1}}^{\boldsymbol{K}} \mathbf{x}_{\boldsymbol{i}}\mathbf{x}_{\boldsymbol{i}}^{+}, \boldsymbol{K} > \boldsymbol{n} \tag{3}$$

When this sample matrix inversion (SMI) is not feasible due to the snapshot deficiency or would involve high signal losses (K < 3n), the covariance matrix is estimated by using the r dominant eigenvectors $\mathbf{U}_s$ and eigenvalues $\boldsymbol{\Lambda}_s = \mathrm{diag}([\lambda_i]_{i\leq r})$ of $\hat{\boldsymbol{\Gamma}}$:

$$\boldsymbol{\Gamma}_{\boldsymbol{DMR}} = \mathbf{U}_s[\boldsymbol{\Lambda}_s - \sigma^2\,\mathbf{I}_r]\,\mathbf{U}_s{}^{+} + \sigma^2\,(\mathbf{I}_K - \mathbf{U}_s\mathbf{U}_s^{+}) \tag{4}$$

The number of dominant eigenvectors depends on the number of available snapshots and, as for Capon beamforming, this number of freedom degrees r should respect K > 2 r. The level of uncorrelated noise is either known (electrical noise) or estimated as the mean of lowest eigenvalues of the covariance matrix (possibly estimated using a greater number of snapshots). The adaptive filter is then computed using this constructed covariance matrix:

$$\mathbf{h_{DMR}} = \frac{\mathbf{\Gamma}_{DMR}^{-1}\mathbf{d}}{\mathbf{d}^{+}\mathbf{\Gamma}_{DMR}^{-1}\mathbf{d}} \tag{5}$$

The output of the DMR filter $\mathbf{w}_{\mathbf{DMR}}^{+}\mathbf{x}_{\boldsymbol{i}}$ is finally written as follows:

$$\mathbf{h}_{\mathbf{DMR}}^{+}\mathbf{x}_{\boldsymbol{i}} = \frac{\mathrm{d}^{+}\mathbf{U}_{\boldsymbol{s}}(\mathbf{\Lambda}_{\boldsymbol{s}} - \sigma^2\,\mathbf{I}_{\boldsymbol{r}})\mathbf{U}_{\boldsymbol{s}}{}^{+}\mathbf{x}_{\boldsymbol{i}} + \sigma^2\left(\mathbf{d}^{+}\mathbf{x}_i - \mathrm{d}^{+}\mathbf{U}_{\boldsymbol{s}}\mathbf{U}_{\boldsymbol{s}}{}^{+}\mathbf{x}_{\boldsymbol{i}}\right)}{\mathrm{d}^{+}\mathbf{U}_{\boldsymbol{s}}[\mathbf{\Lambda}_{\boldsymbol{s}} - \sigma^2\,\mathbf{I}_{\boldsymbol{r}}]\,\mathbf{U}_{\boldsymbol{s}}{}^{+}\mathbf{d} + \sigma^2\left(n - \mathrm{d}^{+}\mathbf{U}_{\boldsymbol{s}}\mathbf{U}_{\boldsymbol{s}}{}^{+}\mathbf{d}\right)} \tag{6}$$

In this last expression, the main computations are the following matrix product: $\mathbf{U}_{\boldsymbol{s}}{}^{+}\mathbf{x}_{\boldsymbol{i}}, \mathrm{d}^{+}\mathbf{U}_{\boldsymbol{s}}, \mathbf{d}^{+}\mathbf{x}_i$. It is also remarkable to notice that only the dominant eigenvectors and eigenvalues are needed to implement the dominant mode rejection beamforming. When the beams need to be computed very often, the snapshots are only partly renewed. In this case, subspace tracking algorithms might be used: new eigenvectors and eigenvalues are computed from the former ones instead of computing them again from the snapshots.

SUBSPACE TRACKING ALGORITHM

The goal of subspace tracking algorithm is to recursively compute an orthogonal projector $\mathbf{\Pi}(t)$ on the r dominant eigenvectors subspace of the rank modification of the covariance matrix:

$$\mathbf{C_{xx}}(t) = \beta\mathbf{C}_{xx}(t-1) + \mathbf{x}(\mathrm{t})\mathbf{x}(\mathrm{t})^{+}, \qquad \mathbf{C_{xx}}(t) \in \mathbb{C}^{n,n} \tag{7}$$

The covariance matrix $\mathbf{C_{xx}}(t)$ is linked to the covariance used in the beamforming by a scaling factor and β is the typical forgetting factor such that $0 < \beta < 1$. The rectangular window can be achieved with two successive rank one modifications.

This projector, $\mathbf{\Pi}(t) = \mathbf{W}(t)\mathbf{W}(t)^{+}$, constructed with the orthogonal basis $\mathbf{W}(t)$, maximises the generalized Rayleigh quotient $J\big(\mathbf{\Pi}(t)\big)$:

$$\mathbf{\Pi}(t) = \arg\max J\big(\mathbf{\Pi}(t)\big), \qquad J\big(\mathbf{\Pi}(t)\big) = \mathrm{Tr}\big(\mathbf{C}_{xx}(t)\mathbf{\Pi}(t)\big) \tag{8}$$

Let $\underline{\mathbf{\Pi}}(t) = \underline{\mathbf{W}}(t)\underline{\mathbf{W}}(t)^{+}$ now be the projector on the subspace at time t-1, augmented with the new vectors generated by the new snapshots. The augmented basis is expressed with the former basis as $\underline{\mathbf{W}}(t) = [\mathbf{W}(t-1)\ \ \mathbf{u}]$, where

$$\mathbf{u} = \mathrm{orth}(\mathbf{e}) \tag{9}$$

$$\mathbf{e} = (\mathbf{I}_K - \mathbf{W}(t-1)\mathbf{W}(t-1)^{+})\,\mathbf{x}(t) = \mathbf{x}(t) - \mathbf{W}(t-1)\mathbf{y}(\mathrm{t}) \tag{10}$$

$$\mathbf{y}(\mathrm{t}) = \mathbf{W}(t-1)^{+}\mathbf{x}(t)$$

The goal is now to find the vector **v** such that, as proposed in [2]:

$$\mathbf{\Pi}(t) = \underline{\mathbf{\Pi}}(t) - \mathbf{v}\mathbf{v}^{+} \tag{11}$$

To achieve the subspace reduction from the augmented basis, this vector $\mathbf{v}$ has to be orthogonal to the new basis. Yet, it is included in the vector space spanned by $\underline{\mathbf{W}}(t)$, and can therefore be expressed as $\mathbf{v} = \underline{\mathbf{W}}(t)\underline{\boldsymbol{\phi}}$. The Rayleigh coefficient is finally:

$$J\left(\mathbf{\Pi}(t)\right) = \mathrm{Tr}\left(\underline{\mathbf{C}}_{\mathbf{yy}}(t)\right) - \mathrm{Tr}\left(\underline{\boldsymbol{\phi}}\underline{\mathbf{C}}_{\mathbf{yy}}(t)\underline{\boldsymbol{\phi}}\right) \tag{12}$$

$$\text{with } \underline{\mathbf{C}}_{\mathbf{yy}}(t) = \underline{\mathbf{W}}(t)^{+}\mathbf{C}_{\mathbf{xx}}(t)\underline{\mathbf{W}}(t) = \begin{pmatrix} \beta\mathbf{C}_{\mathbf{yy}}(t-1) + \mathbf{y}(t)\mathbf{y}(t)^{+} & \mathbf{z} \\ \mathbf{z}^{+} & \gamma \end{pmatrix}$$

$$\mathbf{z} = \beta\,\mathbf{W}(t-1)^{+}\mathbf{C}_{xx}(t-1)\mathbf{u} + \mathbf{y}(t)\,\mathbf{u}^{+}\mathbf{x}(t)\mathbf{x}(t)^{+}\mathbf{u}$$

$$\gamma = \beta\mathbf{u}^{+}C_{xx}(t-1)\mathbf{u} + \mathbf{u}^{+}\mathbf{x}(t)\mathbf{x}(t)^{+}\mathbf{u}$$

This Rayleigh coefficient is therefore maximised when $\underline{\boldsymbol{\phi}}$ is chosen as the minoring eigenvectors of $\underline{\mathbf{C}}_{\mathbf{yy}}(t)$. The new (not necessarily orthogonal) basis $\mathbf{T}$ of the dominant eigenspace, linked to the orthogonal projector defined in equation 11, needs to be orthogonal to the vector $\mathbf{v}$. This constraint is only asymptotically respected in [2]. The following basis proposed here respects exactly this constraint:

$$\mathbf{T} = \mathbf{W}(t-1) - \mathbf{u}(\varphi^{+})^{-1}\boldsymbol{\phi}^{+}, \text{ with } \underline{\boldsymbol{\phi}} = \begin{pmatrix} \boldsymbol{\phi} \\ \varphi \end{pmatrix} \tag{13}$$

The update procedure now consists in orthonormalizing $\mathbf{T}$ to get the new basis $\mathbf{W}(t)$. This tricky point is major, as the level of orthogonality is fundamental for the adaptive beamforming. The proposed technique in [2] does not seem to be completely stable [3]. A stabilized version of the YAST algorithm has been proposed in [4], which does not modify the algorithm complexity. On the opposite, a full reorthogonalization increases the complexity of the algorithm to $\mathcal{O}(nr^2)$ instead of $\mathcal{O}(nr)$. However, this choice ensures the numerical stability. It also opens the way to a generalized rank k update, for which all the developments made above are compatible. In the context of beamforming, this generalisation allows for a more flexible choice of the filter update frequency. After all, the cost of full reorthogonalization is virtually similar to the eigenvectors computation cost of $\underline{\mathbf{C}}_{\mathbf{yy}}(t)$ when the rank r is not excessively smaller than the number of sensors.

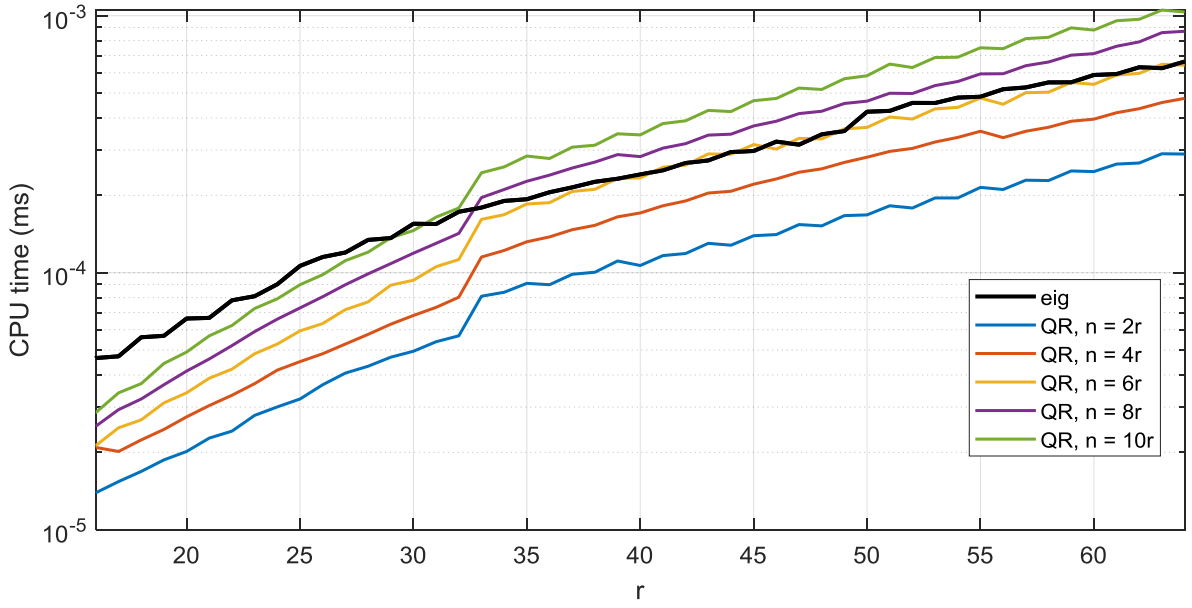


Fig.1: CPU time of orthogonalisation (single precision) and eigenvalue (double precision)

The choices of r and n corresponding to array processing make the cost of full reorthogonalization rather affordable. This full reorthogonalization avoids the risk of numerical instability. The gain on computation cost compared to a direct computation is still very comfortable. Fastest eigenvalues algorithms, such as "divide and conquer", achieve a computational complexity of $\mathcal{O}(n^{2.8})$ for flop counts [5]. Depending on the ratio n/r, the gain on computation costs is theoretically between 7 for n/r = 2 and 630 for n/r = 10.
Numerical stability has been assessed both on simulation and sea signals. As simulations reproduce with difficulty the variety of real signals (marine mammals, sonar emission, self-noise or even electronic glitches), all kind of arrays were processed with this algorithm. No sign of divergence between the recursive and the direct computation were noticed. The processing results from a 32 sensors towed array are presented here with a rank set to 16.

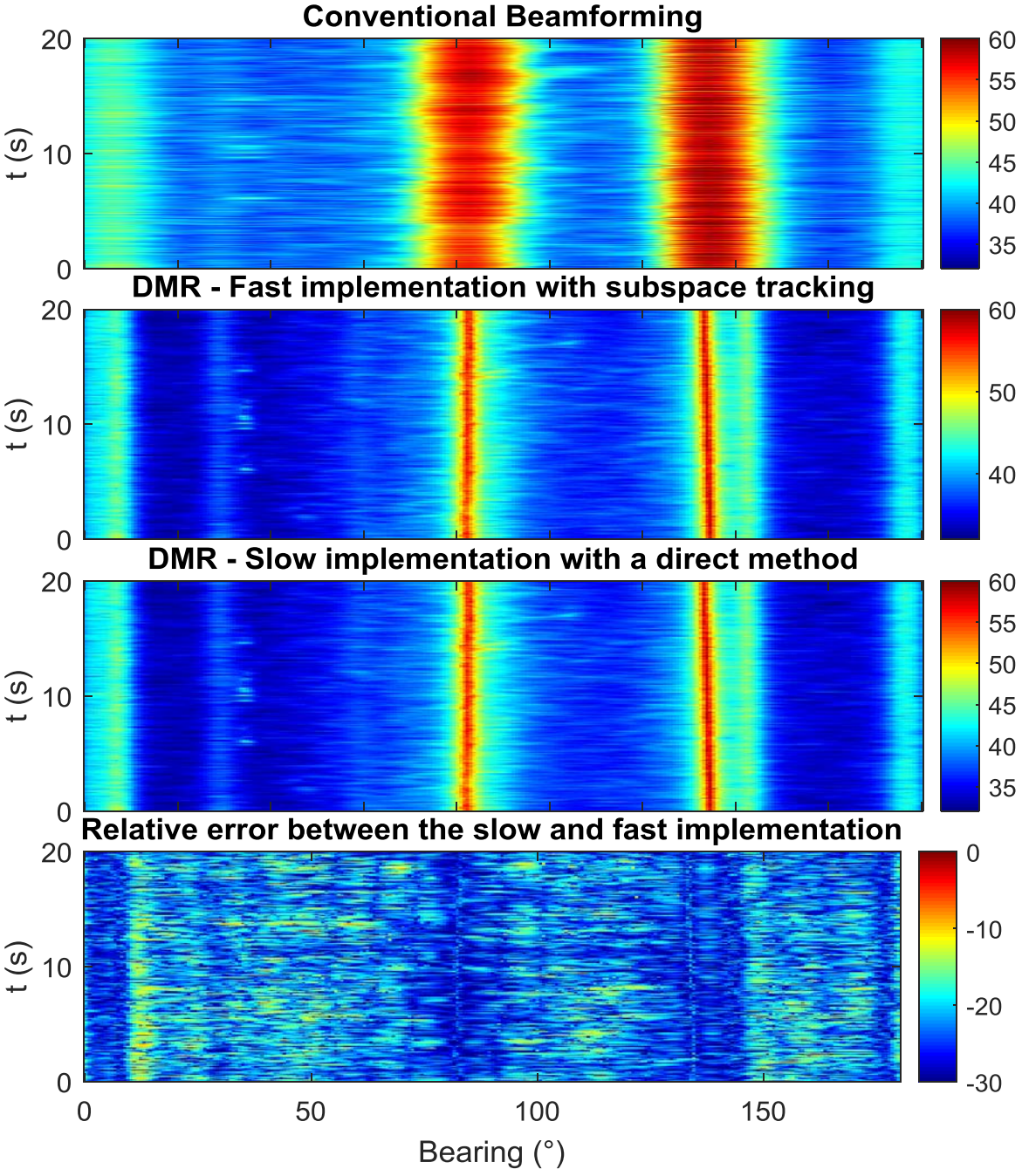


Fig.2: Broadband beams for conventional and DMR beamforming

The snapshots used for filter estimation are collected on 1 second time and 48 Hz band samples weighted by a rectangular window. The chosen rank, 16, respects the rule of thumb that dictates to set the rank, number of adaptive degree of freedom, as the third of the available independent snapshots. This choice made here is consistent with the traditional Capon statistics, requiring the number of snapshots to be three times the number of sensors.
The beams are formed every 125 ms. This very short integration time is adequate for the detection of very short transient signals. Through the proposed algorithm, the transient detection benefit from the loud interferer rejection of the adaptive beamforming, as shown on Fig. 2 at bearing 40°. Indeed, as shown on the last subplot, the fast implementation proposed here does not diverge from the direct implementation. Relative error is higher on the noise than on the sources. Indeed, a fully uncorrelated noise may admit several dominant subspaces.

CONCLUSION

In this paper, a subspace tracking algorithm has been proposed. Compared to previous studies, the proposed algorithm theoretically yields the same subspace as a direct implementation of the rank one modification of the covariance matrix, but with a highly reduced computation cost. A full reorthogonalization at each recursion ensures the numerical stability of the algorithm. For passive sonar applications, the cost of this full reorthogonalization of the basis remains reasonable. It also opens the way for a rank k modification.
This subspace algorithm has been applied to dominant mode rejection beamforming on passive sonar sea signal. Numerical stability is reached, and no divergence has been noticed when comparing the subspace tracking to a direct implementation. This recursive implementation thus emerges as an attractive solution to the dominant mode beamformer for detection of transient signals in the context of passive sonar processing, ensuring the rejection of the adaptive beamformer and the reactivity of a conventional one.

ACKNOWLEDGEMENTS

This work was supported by Direction Générale de l'Armement – Techniques Navales.

REFERENCES

[1] **G. Gaonach, M. Gehant**, Adaptive Subarrays beamforming, 2013 MTS/IEEE OCEAN.
[2] **R. Badeau, G. Richard and B. David,** "Fast and Stable YAST Algorithm for Principal and Minor Subspace Tracking," in *IEEE Transactions on Signal Processing*, vol. 56, no. 8, pp. 3437-3446, Aug. 2008.
[3] **M. Arjomandi-Lari and M. Karimi,** "Stability and convergence analysis of the YAST subspace tracking algorithm," *2010 5th International Symposium on Telecommunications*, Tehran, 2010, pp. 679-684.
[4] **Arjomandi-Lari, and M. Karimi,** "Generalized YAST algorithm for signal subspace tracking." *Signal Processing* 117 (2015): 82-95.
[5] **James W. Demmel, Osni A. Marques, Beresford N. Parlett, and Christof Vomel**. Performance and accuracy of LAPACK's symmetric tridiagonal eigensolvers. SIAM J. Sci. Comput., 30 (3):1508–1526, 2008

DEEP LEARNING BASED TECHNIQUE FOR ENHANCED SONAR IMAGING

Louise Rixon Fuchs[a,b], Christer Larsson[b,c], Andreas Gällström[b,c]

[a]KTH Royal Institute of Technology, School of Electrical Engineering and Computer Science, Teknikringen 14, SE-100 44 Stockholm, Sweden
[b]Saab, SE-581 88 Linköping, Sweden
[c] Department of Electrical and Information Technology, Lund University, P.O. Box 118, SE-221 00 Lund, Sweden

Contact author: Louise Rixon Fuchs, KTH Royal Institute of Technology, School of Electrical Engineering and Computer Science, Teknikringen 14, SE-100 44 Stockholm, Sweden.
Email: rixon@kth.se

Abstract: *Several beamforming techniques can be used to enhance the resolution of sonar images. Beamforming techniques can be divided into two types: data independent beamforming such as the delay-sum-beamformer, and data-dependent methods known as adaptive beamformers. Adaptive beamformers can often achieve higher resolution, but are more sensitive to errors. Several signals are processed from several consecutive pings. The signals are added coherently to achieve the same effect as having a longer array in synthetic aperture sonar (SAS). In general it can be said that a longer array gives a higher image resolution. SAS processing typically requires high navigation accuracy, and physical array-overlap between pings. This restriction on displacement between pings limits the area coverage rate for the vehicle carrying the SAS. We investigate the possibility to enhance sonar images from one ping measurements in this paper. This is done by using state-of-the art techniques from Image-to-Image translation, namely the conditional generative adversarial network (cGAN) Pix2Pix. The cGAN learns a mapping from an input to output image as well as a loss function to train the mapping. We test our concept by training a cGAN on simulated data, going from a short array (low resolution) to a longer array (high resolution). The method is evaluated using measured SAS-data collected by Saab with the experimental platform Sapphires in freshwater Lake Vättern.*

Keywords: *Sonar Imaging, Synthetic Aperture Sonar, Generative Adversarial Networks, Image Enhancement*

INTRODUCTION AND BACKGROUND

Synthetic aperture sonar (SAS) systems have been around since the 80s [1]. They are mostly used for creating high resolution maps of the seafloor, and for finding small objects on it such as in mine countermeasures (MCM) applications. The heavy attenuation of sound in water makes it desirable to have as high signal-to-noise ratio as possible. A high resolution and a high SNR can be achieved by coherently adding measurements from several pings as the sonar platform moves. The sonar image resolution is proportional to the array dimensions, where a longer array gives a higher resolution, in general. For SAS a longer synthetic array is created in order to create high resolution images from a short array sitting on an underwater vehicle. This demands high navigation accuracy since the position of the element in the synthetic array has to be determined with sub-wavelength accuracy. In addition to inertial navigation sensors, signal processing methods are used to correct for deviations from the nominal position. The use of signal processing methods to correct for position errors is commonly referred to as micro-navigation or autofocus. To apply micro-navigation there is often a restriction on the vehicle's displacement between pings, since some techniques require the sub-arrays to overlap between pings.

Numerous enhancement methods for imaging are available. Some examples of well-known methods developed for natural image processing include different filter methods for noise reduction or contrast enhancement [2]. Most work for SAS image enhancement is focused on the image reconstruction using methods for micro-navigation and autofocus [3]. Methods from deep learning have started to be applied for image enhancement purposes in recent years. For example convolutional neural networks (CNNs) have been applied to both natural images [4], medical images [5], RADAR [6], and to SONAR [7]. Generative Adversarial Networks (GANs) have also been used for denoising and image enhancement for medical imaging [5]. Image-to-image translation using GANs has been proposed for RADAR [8], where it was used to transform low resolution SAR imaging to its higher resolution counterpart. Enhancement of one ping SAS images seems to be a new field of research without many publications. In [9] one ping SAS image enhancement is performed using a compressive sensing method.

Our research questions for this paper are: Is it possible to transform a low resolution sonar image to its high resolution counterpart, using state-of-the art methods for Image-to-Image translation, and can sonar image enhancement benefit in other ways from using GANs?

METHODS

The work in this paper can be separated into two parts: one part using simulated data, and another part using measured sonar data. In common for the two parts however is the use of a conditional GAN (Pix2Pix) for paired image-to-image translation tasks. The Pix2Pix network is trained on sonar data generated using simulations.

Generative Adversarial Networks and conditional Generative Adversarial Networks: Generative Adversarial Networks (GANs), introduced by [10] is a framework for estimating generative models. It builds on the idea of having two adversary networks: a generator network G, and a discriminator network D. The generator produces new samples in a distribution in data space $G(z, \theta_g)$, where z is input noise, and θ_g are the parameters of a multilayer perceptron. The discriminator's role is to estimate the probability estimate of the data having been generated as opposed to it being real. Mathematically this process can be defined as having D and G play a two-player min-max game, seen in the equation below,

$$\min_G \max_D V(D,G) = E_{x\sim p_{data}(x)}[logD(x)] + E_{z\sim p_z(z)}[log(1-D(G(z)))] \quad (1)$$

where $p_z(z)$ is the prior on the input noise variables, $D(x)$ is the probability that the data x came from the data distribution rather than the generator's distribution p_g.

The min-max game ends when D and G cannot improve anymore, and the discriminator cannot distinguish between real, and fake samples, this happens when $p_g = p_{data}$, and $D(x) = 0.5$. There have been many variants developed since the original introduction of GANs in 2014. One of these variants is the conditional GAN (cGAN) which introduces a conditioning y on both G and D [11]. With this extra piece of information it becomes possible to direct the data generation process. The conditioning y could be for example the label of the data.

In this work a conditional GAN [12] is used to generate "artificial" high resolution sonar images from its low-resolution counterpart. This can also be explained as going from a short to a long phased array sensor. We then compare and evaluate the generated "artificial" images to their corresponding ground truth high resolution images. We use the implementation of Pix2Pix provided in [13].

Simulated data: Simulated SAS data is generated at the signal level for the proof of concept. An arbitrary number of point targets of different target strengths can be placed in a scene in the simulator. Parameters that can be defined in the simulator are: sound velocity, array dimensions, number of sonar elements in the array, source level of the transmitter, frequency content and pulse waveform. As a default we use a chirp with the same centre frequency as used in the experimental data acquired by the Sapphires SAS sensor. A SAS image is formed by a using a conventional back-projection algorithm on the individual sonar element signals.

Experiments: We create two kinds of datasets (A and B) for our experiments, where each scene in an image A_i corresponds to a scene in an image B_i. Dataset A holds sonar images created from a short array of 50 elements. The dataset B holds the corresponding sonar images for a longer array with 100 or more elements. The spacing between the elements is always the same so a 100 element long array is twice as long as a 50 element array. When generating the point targets in the scene their location and target strength are updated randomly for each image pair A_i and B_i. We generate 500 images for both A and B, and separate them into training (300 images), validation (100 images), and testing (100 images). The cGAN is then trained to learn how to go from dataset A to B.

Measured SAS data: The used experimental SAS data has been collected with the experimental platform Sapphires in freshwater Lake Vättern. The shorter array image for the measured SAS-data is translated through a cGAN network which has been trained using two datasets A and B (as above) containing simulated point scatters. We use a test image of a tripod processed from measured SAS data (Fig. 3) in our experiments. More details are given in the Results section of the paper.

RESULTS

The experiments performed can be divided into two parts. For the first part simulated point scatter data is used. For the second part, measured SAS data is used and transformed by a cGAN trained on the simulated data from the first experiment.

Simulated data: We study the effect of an Image-to-Image translation task for simulated point targets. The task is to go from a dataset A which holds images formed by a short array to a corresponding dataset B for images formed by a long array. The experiment is performed with one, three and 10 point targets in the respective runs. In each run the cGAN is trained with a dataset that has the same number of point targets in each image. The network is later evaluated on its validation data. An assessment of how well the output image from the cGAN corresponds to its target ground truth image is done using the metrics structural similarity (SSIM) index [14], and mean square error (MSE). The results are shown in Table 1. The SSIM metric is also taken between the datasets A and B as a benchmark to make sure that the high SSIM scores are not due to the datasets A and B being very similar. Note that increasing the number of point targets leads to a degradation in performance between the cGAN output and the ground truth in dataset B, see the reduced SSIM score and increased MSE score (Table 1). The dataset A corresponds to images from a short array 50 elements, and the dataset B corresponds to images from a long array of 100 elements, for this assessment. A visual example for a translation can be seen in Fig. 1 where the short array contains 50 elements and the long array 400 elements.

We also carry out experiments to investigate separation of closely spaced point targets. The cGAN appears to be able to separate closely spaced targets when the two targets have similar target strength (Fig. 2). In the case of having two closely spaced point targets with different target strength, the cGAN frequently translate the two targets as one target point located at the position of the strongest point target in the high-resolution domain. For this experiment the short array has 50 elements, while the long array has 400 elements.

We observe that translating simulated SAS images with more point targets (up to 10) with a cGAN trained on less point targets in each image also works well.

Table 1: Error measures for simulated point targets

SSIM between output image from GAN and corresponding ground truth image from dataset B.				
# Point targets	**SSIM mean**	**SSIM std**	**MSE mean**	**MSE std**
1	0.9862	0.0012	4.3500	4.3500
3	0.9475	0.0166	26.3825	13.2465
10	0.9455	0.0053	37.1433	5.4232
SSIM between A and B dataset for benchmark.				
# Point targets	**SSIM mean**	**SSIM std**	**MSE mean**	**MSE std**
1	0.6428	0.0076	113.4660	4.2450
3	0.7649	0.0324	117.5165	21.2098
10	0.8182	0.0207	125.7439	9.9929

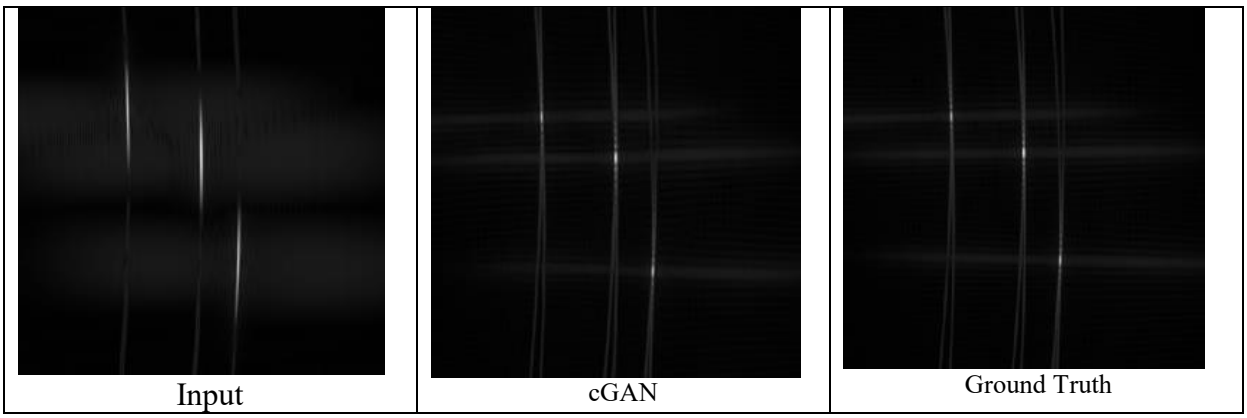


Fig. 1: Point targets. To the left is the depiction from the point targets using the short array. The middle image shows the output from the cGAN. To the right is the ground truth output from the long array.

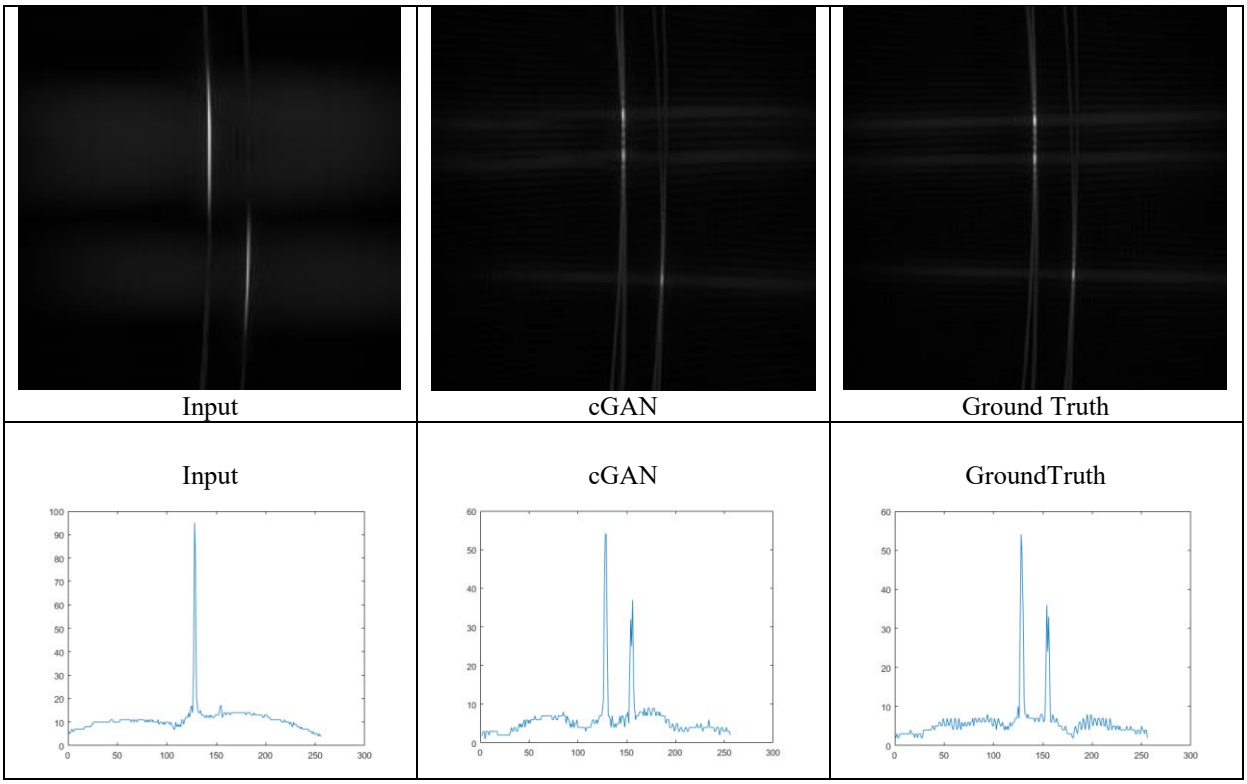


Fig. 2: Separation of closely spaced point targets. The two point targets in the leftmost image are closely spaced and cannot be distinguished as two separate targets. After being sent through the cGAN the output results in an image where the closely spaced targets are distinguishable as separate targets. Upper left (input short array).Upper middle, the output from the cGAN. Upper right (ground truth long array image). The lower row shows the distribution of intensities of a vertical slice from the position of the two closely spaced targets.

Measured Data: The purpose of the second experiment is to investigate if there are any advantages of using the cGAN applied to measured SAS data. We use our test image for all the runs of this experiment. A cGAN trained on scenes containing three point scatters is used. The translated ground truth SAS image appears to have a reduced background level (Fig. 3). For comparison we apply a traditional method for image enhancement, namely that of contrast stretching [2]. In addition we also apply some methods for denoising the image using

a convolutional neural network, a median filter and wavelet-transforms. One the evaluation measures used is entropy as introduced by Shannon [15]:

$$H(x) = -\sum_{i=1}^{N} p_i log_2 p_i, \quad (2)$$

where the p_i values are the probabilities of the different intensity levels for the grey-scaled image. Having a higher entropy number means there is more information in the image. Using entropy minimization can be used for autofocus of ISAR images [16]. Inspired by this we hypothesize that for a target to appear clearly in the image we want to have lower entropy, which should be achieved if signal leakage is removed and the background signal level is suppressed. A ratio between the background and target (Target to background ratio –TBR) is also calculated through taking the ratio between the mean value of the pixel intensities for an area containing the target and the mean pixel intensities for an area containing background. The same areas for background and target are used for all images in order to achieve comparable measurements. The results are summarized in Table 2. We can conclude that the use of cGAN reduces the entropy for the image, and gives the highest target-background ratio. The entropy was lowered further through pre-processing using Otsu thresholding [17] (with four threshold values).

Additionally we analyse the cGAN effect on the input image using the SSIM metric (Table 3). Note that the cGAN's SSIM score between the cGAN processed 50-element image, and the 100-element is higher than the SSIM score between the original 50-element image and the 100-element image. For this experiment the GAN was trained to go from 50-elements to 100-elements for scenes with three point targets.

Table 2 Evaluation measures for our SAS-test image made from 50 elements (leftmost column). The following columns shows evaluation measures for the SAS-test image processed in different ways, the rightmost columns holds the evaluation measures for a SAS-test image made from 100 elements.

	50-element	cGAN	Thres	Thres+cGAN	Median	CNN	Contrast	Wavelet	100-elements
Entropy	6.6957	6.0921	**5.0124**	5.3716	5.9507	6.0827	6.0169	6.0930	5.6615
TBR	1.5079	2.6287	4.1349	**4.8119**	1.5474	1.5087	2.1102	1.5080	1.6988

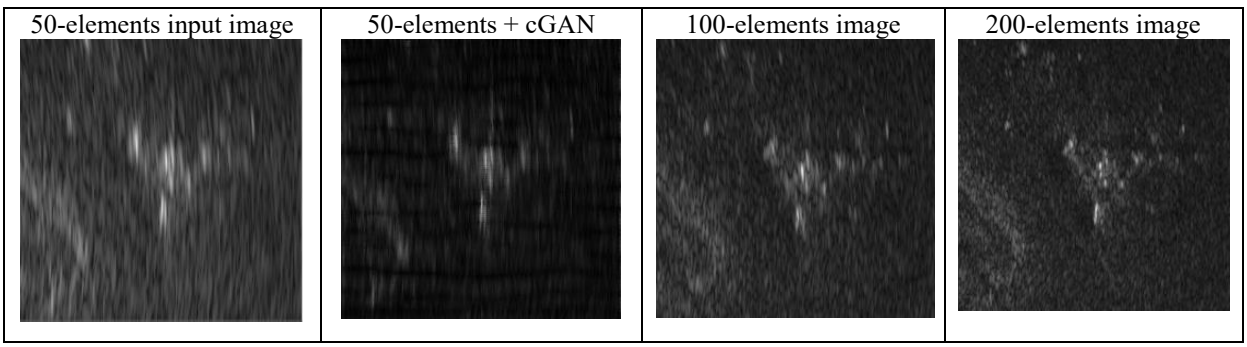


Figure 3 Input SAS image from 50-elements (left), output image after the cGAN (middle-left). SAS image from 100-elements (middle-right), and SAS image from 200-elements (right).

Table 3 SSIM for comparison of measured SAS data and cGAN

	50-element image	cGAN	100-element image
100-element image	0.3197	0.3456	1
200-element image	0.3205	0.3514	0.6232

CONCLUSION

We show that cGAN is a promising tool to enhance sonar imaging. In particular our contributions in this work are the following:

1. We demonstrate some capability for separation of point targets with cGANs.
2. We show that it is feasible to go from a low resolution sonar image produced from a (short-array) to its high resolution (long-array) counterpart with simulated data.

It is hard to conclude at this point that this method could lead to a relaxed requirement for array overlap for SAS in order to enable a higher platform speed. Some increased detection capabilities for sonar targets using cGANs for enhancement may also be possible. For further work it could be interesting to train the whole cGAN entirely on measured SAS data going from a short to long array.

ACKNOWLEDGEMENTS

This project is financed by the Swedish Maritime Robotic Centre (SMaRC) (IRC15-0046), a national centre funded by the Swedish Foundation for Strategic Research (SSF). This work was also supported by SSF through Strategic Mobility grants.

REFERENCES

[1] **M. P. Hayes and P. T. Gough,** Synthetic aperture sonar: A review of current status, *IEEE Journal of Oceanic Engineering*, 34(3), pp. 207-224, July 2009.
[2] **R. C. Gonzalez and R. E. Woods**, *Digital Image Processing (3rd Edition),* Prentice-Hall, Inc., Upper Saddle River, NJ, USA, 2006.
[3] **H. J. Callow.** *Signal processing for synthetic aperture sonar image enhancement*, PhD thesis, University of Canterbury, 2003.
[4] **V. Jain and S. Seung**, Natural image denoising with convolutional Networks, In *D. Koller, D. Schuurmans, Y. Bengio, and L. Bottou, editors, Advances in Neural Information Processing Systems 21,* pages 769-776. Curran Associates, Inc., 2009.
[5] **Q. Yang, P. Yan, Y. Zhang, H. Yu, Y. Shi, X. Mou, M. K Kalra, Y. Zhang, L. Sun, and G. Wang,** Low-dose ct image denoising using a generative adversarial network with

wasserstein distance and perceptual loss, *IEEE Transactions on Medical Imaging*, 37(6), pp 1348-1357, 2018.

[6] **P. Wang, H. Zhang, and V. M Patel**, Sar image despeckling using a convolutional neural network, *IEEE Signal Processing Letters*, 24(12), pp. 1763-1767, 2017

[7] **M. Sung, H. Joe, J. Kim, and S. Yu,** Convolutional neural network based resolution enhancement of underwater sonar image without losing working range of sonar sensors, In *2018 OCEANS -MTS/IEEE Kobe Techno-Oceans (OTO)*, pp.1-6, 2018.

[8] **D. Ao, CO Dumitru, G. Schwarz, and M. Datcu**, Dialectical gan for sar image translation: From sentinel-1 to terrasar-x, *Remote Sensing*, 10(10), 2018.

[9] **A. Gällström, L. Rixon Fuchs and C. Larsson**, Enhanced sonar image resolution using compressive sensing modelling, In *UACE 2019, Crete-Greece*, 2019.

[10] **I. Goodfellow, J. Pouget-Abadie, M. Mirza, B. Xu, D.Warde-Farley, S. Ozair, A. Courville, and Y. Bengio**, Generative adversarial nets, In *NIPS*, 2014.

[11] **M. Mirza and S. Osindero,** Conditional generative adversarial nets, *arXiv preprint arXiv:1411.1784***,** 2014.

[12] **P. Isola, J. Zhu, T. Zhou, A. A. Efros,** Image-to-image translation with conditional adversarial networks**,** In *2017 IEEE Conference on Computer Vision and Pattern Recognition, CVPR 2017*, *Honolulu, HI, USA, July 21-16, 2017*, pp. 5967-5976, 2017.

[13] Implementation of pix2pix. https://github.com/affinelayer/pix2pix-tensorflow. Accessed: 2019-03-26.

[14] **Z. Wang, A. C. Bovik, H. R. Sheikh, E. P. Simoncelli**, "Image quality assessment: From error visibility to structural similarity", *IEEE Trans. Image Process.*, vol. 13, no. 11, pp. 600-612, Apr. 2004.

[15] **Shannon, C. E.** , A mathematical theory of communication, *Bell Systems Technical Journal,* 27:379-423, 623-656, 1948.

[16] **L. Xi, L. Guosui and J. Ni**, Autofocusing of ISAR Images Based on Entropy Minimization, *IEEE Transactions on Aerospace and Electronic Systems,* vol. 35, no. 4, October 1999.

[17] **Otsu, N.**, A Threshold Selection Method from Gray-Level Histograms, *IEEE Transactions on Systems, Man, and Cybernetics*. Vol. 9, No. 1, 1979, pp. 62–66.

Regular Session 26
Sound propagation in shallow and deep water

STUDY ON THE PHASE OF REFLECTION COEFFICIENT OF MEDIUM WITH GRADIENT CHANGE OF ACOUSTIC IMPEDANCE

Bo Hu[a,b], Yimei Du[b], Moran Wang[b]

[a]Acoustic Science and Technology Laboratory, Harbin Engineering University, No.145, Nantong Street, Nangang District, Harbin, 150001, Heilongjiang, China
[b]College of Underwater Acoustic Engineering, Harbin Engineering University, No.145, Nantong Street, Nangang District, Harbin, 150001, Heilongjiang, China

Contact author: Bo Hu, College of Underwater Acoustic Engineering, Harbin Engineering University, No.145, Nantong Street, Nangang District, Harbin, 150001, Heilongjiang, China, fax: 0451-82531753, email: kidd1105@sina.com

Abstract: *Medium with gradient change of acoustic impedance is a new type acoustic structure which composed of several materials and has a continuous gradient composition and structure whose specific acoustic impedance varies smoothly across the layer. It has been used in various practical situations such as acoustic rectifiers, medical devices, weakening vibration and reducing noise. The purpose of this paper is to investigate the phase characteristics of reflection coefficient of medium with gradient change of impedance to make use of the sound pressure and vibration velocity of the wave. Exact solutions of the Helmholtz equation are derived for a typical density profile and sound-speed profile. The solutions in the medium are matched with solutions in the homogeneous upper and lower layers to derive analytical expressions for the phase of the reflection coefficient of a plane wave which incident from the upper medium. The phase of reflection coefficient in a variety of cases that of different frequencies and incident angles are examined. A number of simulation results are presented and comparison is made with computed results. The phase data can be used in the subsequent vector signal processing.*

Keywords: *Reflection coefficient phase, oblique incidence, gradient medium*

1. INTRODUCTION

Medium with gradient change of acoustic impedance has been developing rapidly because of its unusual material parameters [1]. Acoustic characteristics of different acoustic impedance distribution media was calculated by Pedersen [2]. The sound reflection and transmission of the anisotropic medium with multilayer composite structure was calculated by Caviglia [3]. Feng presented the micro fabrication of an acoustic impedance gradient matching layer on a spherically-shaped piezoelectric ultrasonic transducer [4]. Gómez investigate material requirements to produce impedance matching layers for air-coupled piezoelectric transducers, to identify materials that meet these requirements, and to propose the best solution to produce air-coupled piezoelectric transducers for the low megahertz frequency range [5]. Robins had studied the reflection of plane waves from a layer with varying density and sound speed profile [6,7]. A nondestructive method to determine the density of coating has been proposed by Zhao based on the ultrasonic reflection coefficient phase spectrum (URCPS) [8].

Although a large number of scholars have studied the acoustic properties of medium with gradient change of acoustic impedance, few studied the phase of reflection coefficient. Studying the phase of reflection coefficient of medium with gradient change of acoustic impedance is beneficial for us to understand its acoustic characteristics more comprehensively. This paper considers the reflection coefficient phase when an acoustic plane wave impinges an interface of gradient medium obliquely and shear wave effects are neglected. The relationship between the reflection coefficient phase of the gradient medium and the incident angles is derived by comparing the simulation results under different conditions.

2. THEORETICAL ANALYSIS

There are two semi-infinite homogeneous medium labled medium 1 and medium 3 respectively. Medium 2 is the medium with gradient change of acoustic impedance with continuously varying density and sound speed located between medium1 and medium 3. The incident plane wave is propagating in direction from medium 1 into the medium 2 and then transmits into medium 3.

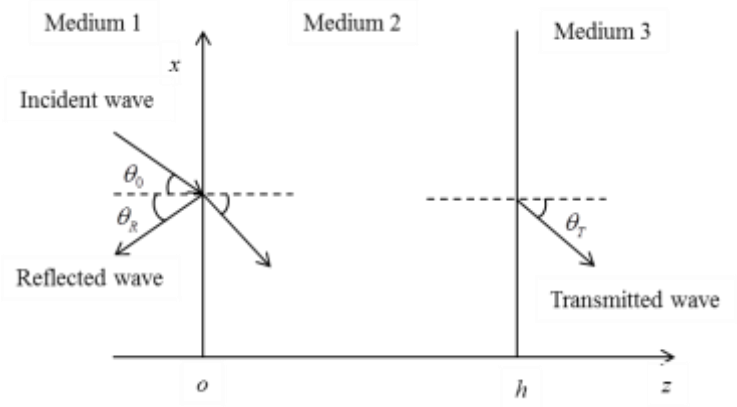


Fig.1: The diagram of wave propagating through the gradient medium.

In a medium with varying density, the Helmholtz equation takes the form

$$(\nabla^2 + k^2)p = (1/\rho)\nabla p \cdot \nabla \rho \tag{1}$$

where *k*, *p*, ρ means the wave number, sound pressure and density. Assuming that the density depends only on the coordinate *z*, Eq. (1) becomes

$$(\nabla^2 + k^2)P = (1/\rho)\frac{dP}{dz}\frac{\partial \rho}{\partial z} \tag{2}$$

Suppose that an incident acoustic wave traveling in the *z* direction written as Eq. (3) and the total pressure with addition of a wave of amplitude *R* in the medium1 is p_0

$$p = e^{ik_1(x\cos\theta_0 - z\sin\theta_0)},\ p_0 = e^{ik_1 x\cos\theta_0}(e^{ik_1 z\sin\theta_0} + Re^{ik_1 z\sin\theta_0}) \tag{3}$$

and θ_0 is the grazing angle. The *x* dependence is removed by writing the pressure in the medium2 as

$$p_2 = e^{ik_0 x\cos\theta_0} \cdot p_2(z) \tag{4}$$

Substitution in Eq. (2) leads to the following equation for p_2

$$\frac{d^2 p_2}{dz^2} - \frac{1}{\rho}\frac{d\rho}{dz}\frac{dp_2}{dz} + (\frac{\omega^2}{c^2} - k_1^2\cos^2\theta_1)p_2 = 0 \tag{5}$$

where k_1 is wave number in medium1. A variable q is defined and leads to the equation for q

$$q(z) = \rho^{-1/2} p_2(z) \tag{6}$$

$$\frac{d^2 q}{dz^2} + [\frac{\omega^2}{c^2} - k_1^2\cos^2\theta_1 + (\frac{1}{2\rho}\frac{d^2\rho}{dz^2} - \frac{3}{4}(\frac{1}{\rho}\frac{d\rho}{dz})^2]q = 0 \tag{7}$$

Robins has considered a more general class of density profiles, for which exact solutions of the Helmholtz equation can be found [6]. This class of profiles is described by the equation

$$\rho(z) = Ae^{\alpha z}/(e^{\alpha z} - a)^2 \tag{8}$$

By suitable choice of the constants A, a and α to achieve different density distributions. In order to solve the Eq. (7), we construct the Airy function. The sound speed profile in which the square of wave number varies linearly with is described as the following equation:

$$\frac{1}{c(z)^2} = (1 + \delta z)/c_1^2 \tag{9}$$

where c_1 is value of sound speed at midpoint of medium2, δ is a constant paremeter. With the sound speed profile given by Eq. (9), the equation for *q* becomes

$$\frac{d^2 q}{dz^2} + (k_2^2\delta z + k_2^2 - k_1^2\cos^2\theta_0 - \alpha^2/4)q = 0 \tag{10}$$

where $k_2 = \omega/c_2$. The solution for Eq. (10) is a combination of the Airy functions A_i , B_i

$$p_2 = e^{jk_2\cos\theta_2}\frac{e^{(1/2)\alpha z}}{e^{\alpha z}+a}\cdot[C_1\cdot A_i(\eta)+D_1\cdot B_i(\eta)] \tag{11}$$

where C_1 and D_1 are constants. η is the variable defined by Eq. (12)

$$\eta = -(k_2^2\delta)^{-2/3}(k_2^2\delta z + k_2^2 - k_1^2\cos^2\theta_0 - \alpha^2/4) \tag{12}$$

The value of reflection coefficient R is obtained by matching pressure and velocity at the interfaces of medium2,

$$R = -N_2/(D_2 e^{(ik_1 h\sin\theta_1)}) \tag{13}$$

N_2 and D_2 can be derived by substituting the boundry conditions in preesure equation and the reflection coefficient is the ratio of real part of R and imaginary part of R.

3. SIMULATIONS

The phase of reflection coefficient of medium with gradient change of acoustic impedance is examined in this part. The relationship between the reflection coefficient phase and frequency and incidence angle is obtained. The incident angle of acoustic wave is set from 0° to 15° in the frequency range 0-100 kHz. The Fig. 2 plots the reflection coefficient phase against frequency and incident angles for the same sound-speed and density profile.

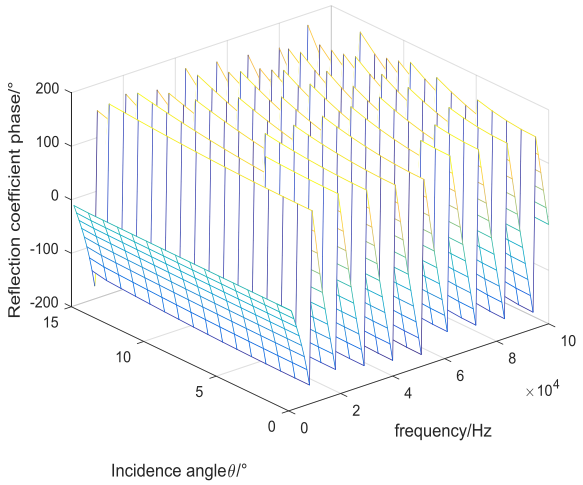


Fig. 2: Phase of reflection coefficient for different incident angles

From Fig. 2, it can be seen that the frequency and incidence angle of acoustic wave have a great influence on the phase of reflection coefficient of the medium with with gradient change of impedance. In the whole frequency range, the phase oscillates periodically with the frequency, and the amplitude and oscillation period of the reflection coefficient phase increase with the incident angle. In order to get the relationship between incident angle and reflection coefficient more intuitively, the acoustic characteristics of the medium are simulated with different incident angles: 0°, 5° and 10°. The comparison of reflection coefficient for three incident angles is shown in Fig. 3.

Fig. 3. shows that the three curves oscillate periodically in the full frequency band in three cases of incident angle. The extremum for different incident angles are almost the same. The

three curves vary similarly in the low-mid frequency band (1-20 kHz). In the mid-high (20-50 kHz) frequency band, the phase of reflection coefficient for incident angle $0°$ oscillates a little rapidly than that for $5°$ and $10°$.

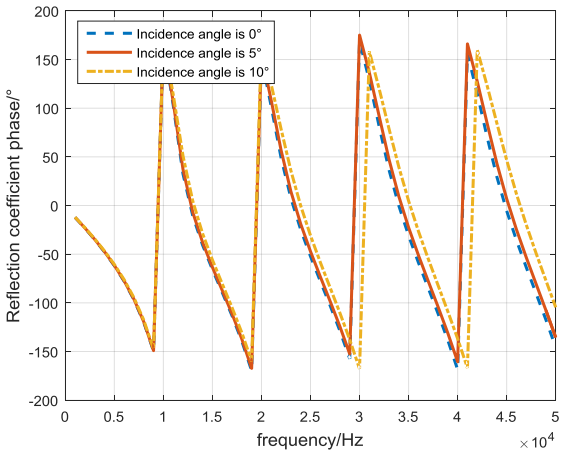
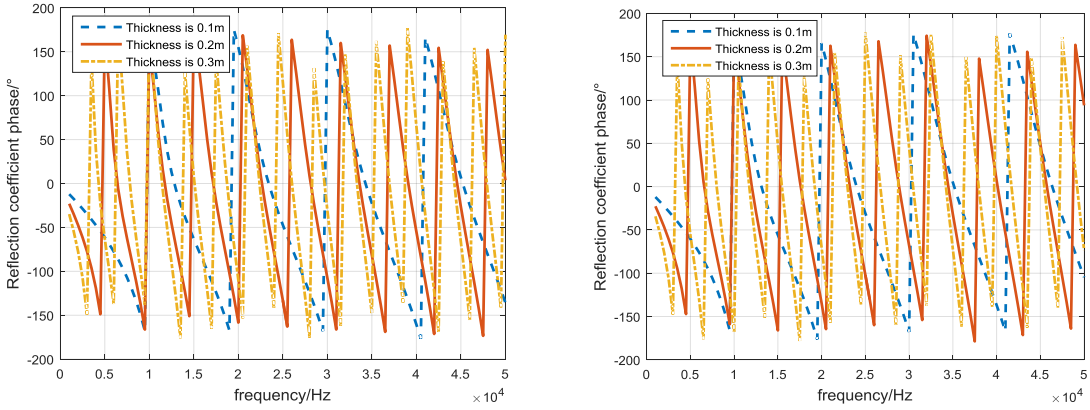


Fig. 3: Phase of reflection coefficient for different incident angles

Fig. 4 compares reflection coefficient phase of different thickness of medium when incident angles are $5°$ and $10°$ in the frequency range of 0-50 kHz. The width of medium 2 is set to be 10 cm, 20 cm and 30 cm and the impedance profile is concave curve along the thickness direction.



(a)The incidence angle is 5 ° *(b)The incidence angle is 10 °*

Fig. 4. Phase of reflection coefficient for different Thicknesses of medium

The three curves in Fig. 4 oscillate with frequency in the full frequency range when the incident angles are $5°$ and $10°$. The extremum and difference between the maximum and minimum of phase of three curves are the same with the increase of frequency. The oscillation period of 10 cm thickness medium is the largest, and that of 30 cm thickness is the smallest. It takes more time for sound wave to propagate through the medium need as the increase of the thickness of the medium and phase varies more rapidly with the frequency. The phase reaches the extreme value at a lower frequency and the oscillation period is shorter when the the medium thickness is lager.

4. CONCLUSION

In this paper the acoustic wave propagation model in the medium with gradient change of acoustic impedance is established and complex reflection coefficient is derived. There are almost the same extremum and change period of reflection coefficient phase for different incident angles. The larger thickness of the medium is, the more dramatically the reflection coefficient varies. The phase of reflection coefficient attains the extremum at a lower frequency and the variation period of it is smaller as increasing in the thickness of the medium with gradient change of impedance.

REFERENCES

[1] **Z. Gerhard**, **A. Schievenbusch**, Materials with an acoustic impedance gradient, *Materials Science Forum*, volume (308-311), pp. 533-538, 1999.

[2] **P. C. Pedersen**, **O. Tretiak**, **P. He**, Impedance-matching properties of an inhomogeneous matching layer with continuously changing acoustic impedance, *Journal of the Acoustical Society of America*, volume (72), pp. 327-336, 1982.

[3] **G. Caviglia**, **A. Morro**, Wave propagation in multilayered anisotropic solids, *International Journal of Engineering Science*, volume (38), pp. 847-863, 2000.

[4] **G. Feng**, **W. Liu**, A spherically-shaped PZT thin film ultrasonic transducer with an acoustic impedance gradient matching layer based on a micromachined periodically structured flexible substrate, *Sensors*, volume (13), pp. 13543-13559, 2013.

[5] **Gómez Alvarez-Arenas**, Acoustic impedance matching of piezoelectric transducers to the air, *IEEE Transactions on Ultrasonics Ferroelectrics & Frequency Control*, volume (51), pp. 624-633, 2004.

[6] **A. J. Robins**, Reflection of plane acoustic waves from a layer of varying density, *The Journal of the Acoustical Society of America*, volume (87), pp. 1546-1552, 1990.

[7] **A. J. Robins**, Reflection of a plane wave from a fluid layer with continuously varying density and sound speed, *Journal of the Acoustical Society of America*, volume (89), pp. 1686-1696, 1991.

[8] **Y. Zhao**, **X.M. Li**, **L. Lin**, **M.K. Lei**, Measurements of coating density using ultrasonic reflection coefficient phase spectrum, *Ultrasonics*, volume(51), pp. 596-601, 2011.

VARIABILITY OF THE SOUND FIELD IN THE PRESENCE OF INTERNAL KELVIN WAVES IN A STRATIFIED LAKE

Uzhansky E.[1], Katsnelson B.[1], Lunkov A.[2], Ostrovsky I.[3]

[1] L. Charney School of Marine Sciences, University of Haifa, Israel, 3498838 Haifa,
[2] Prokhorov General Physics Institute of the Russian Academy of Sciences, 38 Vavilova str. Moscow, 119991, Russia,
[3] Israel Oceanographic & Limnological Research, Yigal Alon Kinneret Limnological Lab., P.O. Box 447, Migdal 1495001, Israel

Contact author: Ernst Uzhansky
Room 270, Multi-Purpose Blvd., University of Haifa, 199 Aba Khoushy Ave., Mount Carmel, Haifa 3498839, Israel
e-mail: ernstuzhansky@gmail.com

Abstract: *The spatiotemporal variability of low- and mid-frequency sound field in the presence of internal Kelvin waves (IKWs) was studied in Lake Kinneret (Israel). Experimental measurements of the sound field were carried out using a vertical line array (VLA) consisting of ten hydrophones with 3 m spacing. The VLA was deployed in the deepest (37 m) part of the lake. Signals were transmitted from the source deployed at peripheral lake location at the distance of 5.5 km from the VLA at 5-m depth. Chirp signals (300 – 2000 Hz) were transmitted with 5 sec intervals during >24 hours (the period of the IKWs). IKWs were registered using three thermistor chains (TCs) positioned along the northwest transect at 10-m, 20-m and 37-m station depths. This setting allowed us to characterize the variations of thermal structure and the corresponding sound speed profile along the transect. The vertical structure of sound field obtained with the VLA shows correlation with temporal variability due to IKWs. The modeling of sound propagation was done using Parabolic Equation (PE) method, taking into account the parameters of bottom, lake bathymetry and variation of water temperature. The PE results showed close agreement with experimental measurements.* [This work was supported by Israel Science Foundation, grant 565/15].

Keywords: *Internal Waves, underwater acoustics.*

1. INTRODUCTION

Internal waves (IWs) populate various stratified aquatic systems from small reservoirs, such as lakes to the ocean. Water motions caused by IWs lead to an increase in turbulence and diapycnal mixing at the peripheral lake zones, especially in areas where the metalimnion (the thermocline) touches the bottom [1]. It results in enhanced vertical transport of solutes from the nutrient-rich hypolimnion (water below the thermocline) to the upper productive water layer, leading to increased primary productivity rates [2]. From acoustical point of view, IWs are one of the most important factors influencing sound propagation in the ocean. The acoustic effect of IWs in negligible at very short ranges but becomes important for path lengths of several kilometers [3]. The capability of acoustical methods in studying IW dynamics was demonstrated on the shelf zone of the ocean [4], while no such measurements were done in lakes.

The presence of a sharp thermocline and respective gradient in water density in the metalimnion are important for the development of various types of Internal Waves (e.g. Kelvin waves, Poincare waves, high-frequency gravitational waves) e.g. [5], [6]. Rotational internal Kelvin waves (IKWs) showed the most significant contribution to the internal waves spectra [7].

It was shown in [8], remarkable influence of IKWs on the sound propagation and some specific features of variation of interference pattern of the sound field.

2. MESUREMENTS AND INSTRUMENTAION

The study is carried out in a warm monomictic Lake Kinneret. It possesses typical shallow water waveguide properties (depth of ≈10 to 40 m, sound speed profile with a slight negative gradient). The lake bottom is represented as a less than 1 m thick gas-rich layer with low compressional wave velocity (≈300-500 m s^{-1}) lying above gas-free thick bottom with relatively high sound speed (1550 m s^{-1}). Parameters of the bottom were estimated from direct sediment sampling and acoustical sediment characterization [9]. During the winter temperature of the whole water body is about 16° C, while during the summer lake is strongly stratified.

In the following work we consider sound field propagation along the acoustic track (Fig. 1) from the source deployed at 5 m depth at Station T (7.5 m bottom depth) to the receiving system, i.e. Vertical Line Array of 10 hydrophones with 3 m spacing positioned at Stn. A (36 m bottom depth).

Experiment

The experiment was carried out at the end of June 2018 when sharp thermocline is presented (Fig. 2). Linear-frequency modulation pulses (Chirp) at 300 – 2000 Hz frequency band with 5 sec duration were transmitted for > 24 hours (the period of the IKW). Each cycle of 10 consequent pulses was repeated every 30 minutes from 17:45 June 26 till 22:00 June 27. No pulses were radiated from 03:30 till 11:45 on June 27. The recorded signals were cross-correlated with the radiated signals to obtain pulse response. The Hilbert transform was applied to extract the experimental pulse envelopes.

Three thermistor chains were deployed at three stations (H, F, A) to register temporal evolution of the water temperature, and thus, temporal variability of the IKW.

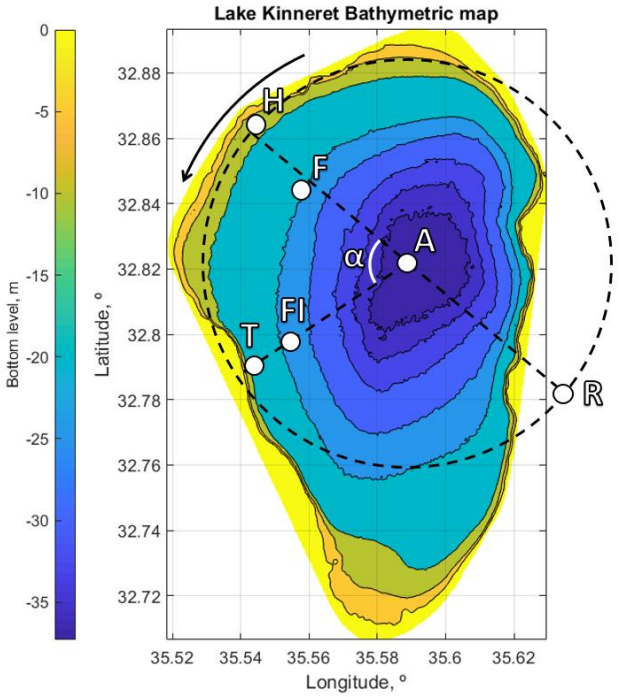


Fig. 2: Bathymetric map of Lake Kinneret and layout of the experiment. A – position of VLA. H, F, A – positions of thermistor strings. T denotes position of the sound source.

Simulation

Numerical modeling of the sound field was carried out for various thermocline positions for the full cycle of the IKW (i.e. 24 hrs). Temporal variability of the IKW was obtained from temperature data from thermistors chains. Sound field simulations were done with a Parabolic Equation approach using RAMs (M. Collins/NRL). Variation of bathymetry and layered structure of the bottom was considered as stationary (unperturbed) parameters. As a non-stationary (perturbed) component only water temperature variations were used. In our model we consider circular shape of the lake (dashed circle, Fig. 1) with radius TA, spatiotemporal variations of water temperature are similar for each radius of this circle (i.e. temperature variations at transect TA are the same as on the transect HA and have the corresponding shift in time).

Thermistor chains were deployed at the northwest transect, whereas acoustic track was positioned at the southwest. Considering period of the IKW 24 hours corresponding to 360º of phase shift, and the angle between these transects α, variations of the IKW at southwest transect were obtained from the +5 hours (i.e. 75º) phase shift of IKW from temperature sensors deployed at Stns. H, F, A.

3. RESULTS

Both simulated and experimental sound fields show similar behavior. First, sound field at the VLA is concentrated below the thermocline. Secondly, variability of sound field intensity is connected with vertical thermocline displacements. When thermocline is high, sound field is stretched and less intense. When thermocline is low, it presses the sound field down to the bottom, resulting in higher intensity of the sound field (Fig.3). Analysis of numerical modeling (Fig. 4) shows up to ≈1 km horizontal displacement of the sound field in vicinity to the VLA.

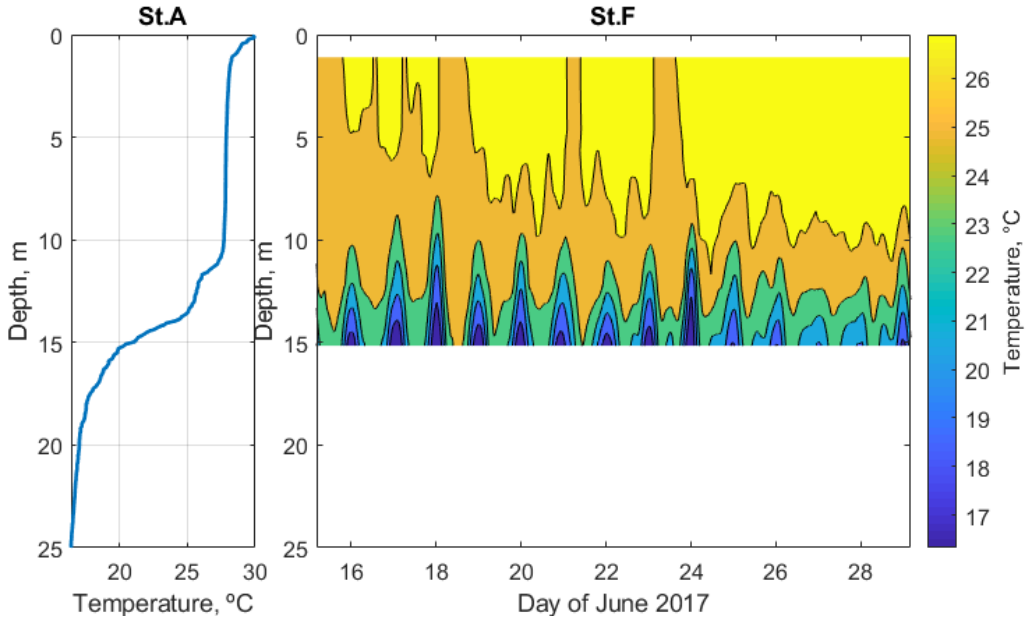


Fig.2: a) – temperature profile at Stn. A at the day of the experiment (26 June 2018) with CTD; b) – temperature profiles obtained at St. F in June 2017 with a thermistors chain.

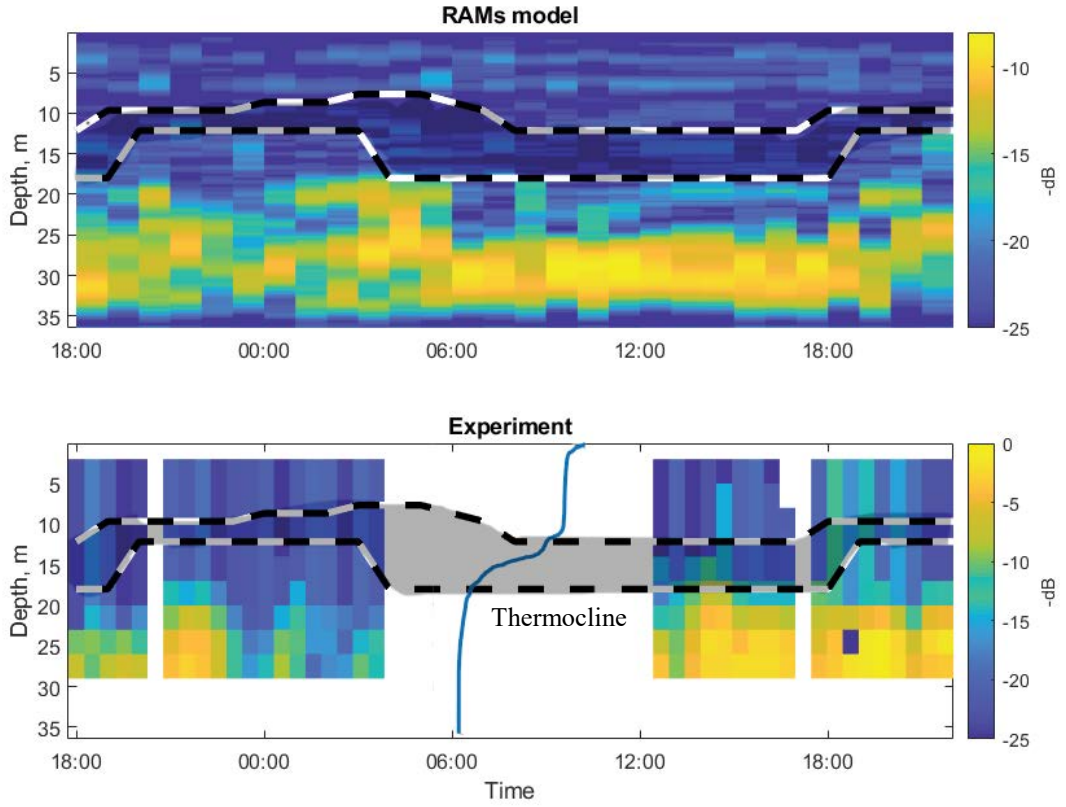


Fig.3: a) Transmission Loss at the VLA simulated with RAMs at frequency of 1 kHz, b) experimental sound intensity recorded on the VLA. White color depicts absence of data. Thermocline boundaries are depicted as dashed lines. In the center of is depicted typical thermocline curve.

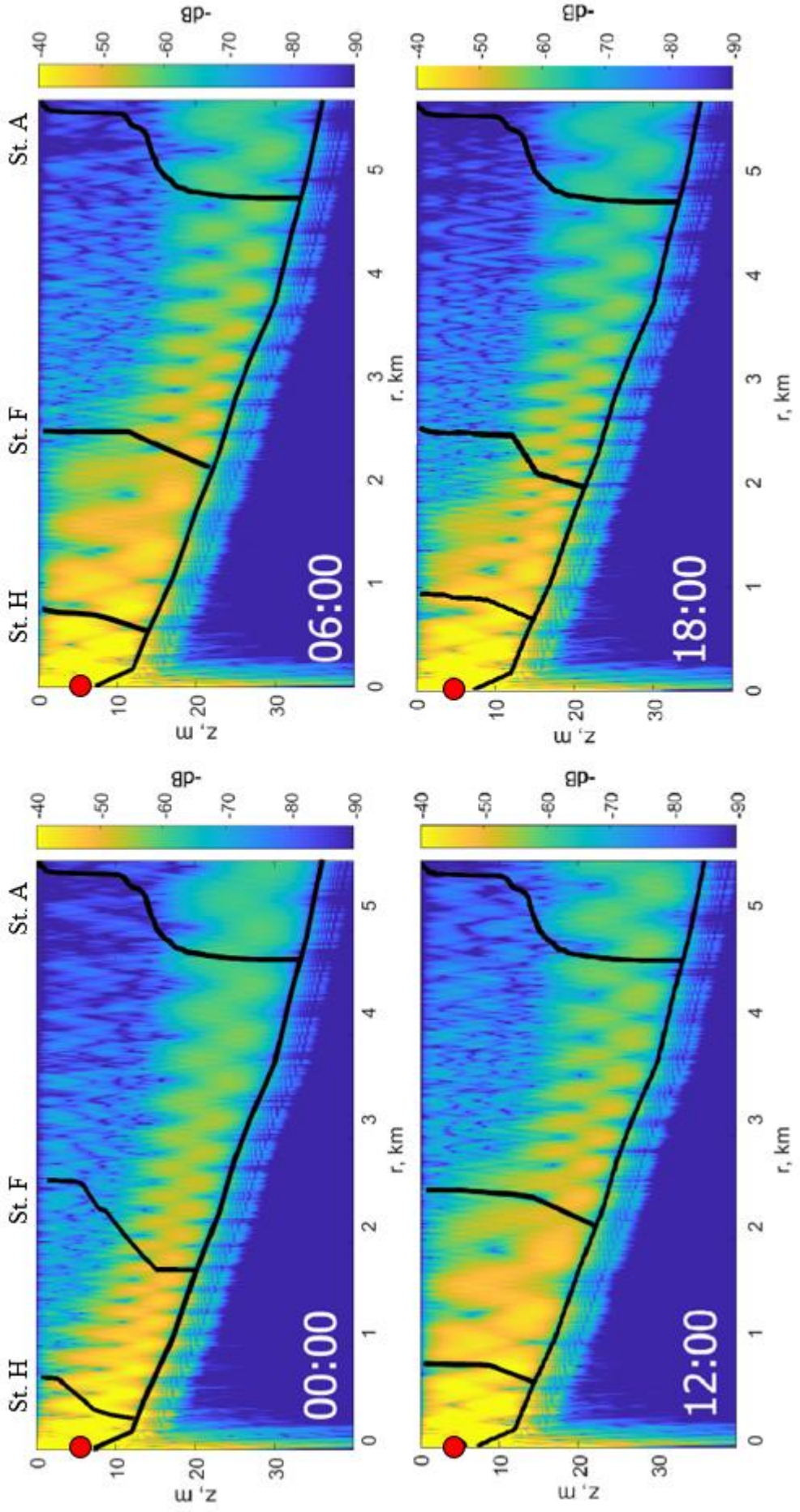


Fig4. Numerical model of Transmission Loss along the transect TA at four moments of time. Solid lines represent temperature profiles obtained with thermistors chain at Stations H, F, and A and shifted in time by +5 hrs. Sound source is depicted as a red circle

4. ACKNOWLEDGEMENTS

We would like to thank Dr. Pavel Petrov (Pacific Oceanological Institute, Vladivostok, Russia) for sharing his user-friendly RAMs (M. Collins/NRL) Matlab code and advices in operation.

5. REFERENCES

[1] **Lorke, A. (2007).** "Boundary mixing in the thermocline of a large lake," J. Geophys. Res. 112, C09019, doi:10.1029/2006JC004008.

[2] **Ostrovsky, I., and Sukenik, A. (2008).** "Spatial heterogeneity of biogeochemical parameters in a subtropical lake," in Monitoring and Modeling Lakes and Coastal Environments, edited by P. K. Mohanty (Springer, New York), pp. 79–90

[3] **Katsnelson, B., Petnikov, V., & Lynch, J. (2012).** *Fundamentals of shallow water acoustics*. *Springer* (Vol. 1). http://doi.org/10.1017/CBO9781107415324.004

[4] **Kuz'kin, V. M., Lin, Y-T., Lunkov, A. A., Lynch, J. F., and Petnikov, V. G. (2011).** "Frequency shifts of the sound field interference pattern on oceanic shelf in summer conditions," Acoust. Phys. 57(3), 381–390.

[5] **Pedlosky, J. (2003).** Waves in the Ocean and Atmosphere: Introduction to Wave Dynamics (Springer, Berlin), 268 pp.

[6] **Filatov, A., Terzevik, R., Zdorovennov, V., Vlasenko, V., Stashchuk, N., and Hutter, K. (2012).** Field Studies of Non-Linear Internal Waves in Lakes on the Globe, edited by K. Hutter (Springer, New York), pp. 23–103.

[7] **Lemckert C. J., and Imberger, J. (1998).** "Turbulent benthic boundary layer mixing events in fresh water lakes," in Physical Processes in Lakes and Oceans, Coastal and Estuarine Studies Series, edited by J. Imberger (AGU, Washington, DC), Vol. 54.

[8] **Katsnelson, B., Lunkov, A., & Ostrovsky, I. (2016).** Interference pattern of the sound field in the presence of an internal Kelvin wave in a stratified lake. *The Journal of the Acoustical Society of America*, *139*(2), 881–889. http://doi.org/10.1121/1.4941658

[9] **Katsnelson, B., Katsman, R., Lunkov, A., & Ostrovsky, I. (2017).** Acoustical methodology for determination of gas content in aquatic sediments, with application to Lake Kinneret, Israel, as a case study. *Limnology and Oceanography: Methods*, *15*(6), 531–541. https://doi.org/10.1002/lom3.10178

ACOUSTICAL SIGNAL HORIZONTAL REFRACTION IN THE COAST WEDGE

Igor Esipov[a] and Oleg Popov[b]

[a] Gubkin University of Oil and Gas, 65, Leninsky prosp., 119991, Moscow
[b]Institute of Atmosphere Physics, 3, Pyzhevsky line, 119017, Moscow

Igor Esipov, National University of Oil and Gas «Gubkin University», 65, Leninsky prosp., 119991, Moscow, FAX: +7 499 1268411, email address: igor.esipov@mail.ru.

Abstract: *The results of experimental research of acoustical pulse propagation along to the coastal wedge are presented here. The research has been done with extended bottom receiving array at the Black sea shallow water range. We defined the direction of arrival sequences of acoustical pulses, excited in water by seismic airgun. The acoustical pulses registration is provided by extended receiving array installed next to the bottom cross the coastal wedge isobaths. Seismoacoustical source moved from the array by the boat along to one of the isobaths. It is shown the variation of the receiving signal intensity distribution along to the array aperture both and variation of arrival angles with the distance increasing to the source.*

Keywords: *Bottom array, bathymetric acoustical refraction, shallow water sound propagation.*

1. INTRADUCTION AND EXPERIMENT SET UP

The problem of acoustical wave propagation in shallow water in zones with the complicated bottom relief is considered in frame so called 3D model of underwater sound propagation. When sea surface and bottom arrange a narrowing wedge, acoustical rays, going up this wedge have manifold reflections from the sea surface and inclined bottom and with every such a reflection from inclined bottom the ray slightly deflects to the most bottom inclination. That is viewing the process from the top, one could see the acoustical ray is crooked, or refraction takes place in horizon plane.

Specific features of such sound wave propagation in coastal wedge have been considered first in monography [1]. But up to the recent time there were only a few experimental researches with investigation of this theme. Now, with respect to the progress in the sea experiment technique, this problem attracts much more attention. The main attention is paid to sea shelf, where tides and internal waves are essential [2, 3]. Ocean waveguide variability in the horizon plane (due to bathymetry or sound speed propagation variability) leads to 3D effects, which are investigated theoretically and experimentally as for deep ocean [4], both and for shallow water [5,6]. It was shown manifold acoustical manifestations of horizontal refraction in the coastal wedge. Results of the first measurements of the horizontal angles of arrivals at the coastal wedge were shown at [7]. Further, research of variations in interference pattern in horizon plane in the coastal wedge has been done [8]. Another word there is no any problem of coastal wedge acoustical sounding in contemporary ocean acoustics without estimation of horizontal refraction.

Results of the experimental research of peculiar properties of the acoustical signals, registered by elongated bottom array in the coastal wedge are presented in this paper. Experiment has been done in the Black sea, at Gelendgik area in Blue bay area. Signal reception has been done by the bottom array as a chain of 50 receivers. The array was installed cross the isobaths (Fig. 1). The receiver #1 was at about 14 m depth, #25 – 23 m depth and #50 – 26 m depth. Distance between the receivers was fixed 12.5 m. The position of the receivers was defined by GPS. Air-gun was used as a source of acoustical signals. Air-gun was towed at 2.5-3 m depth by parallel and obliquely to the array. Air-gun transmitted acoustical pulses each 20 sec. Maximum distance of the air-gun from the array was 1037 m. The source position at the signal transmission was controlled by GPS. The main energy of air-gun transmission was in the frequency band of 10 – 500 Hz.

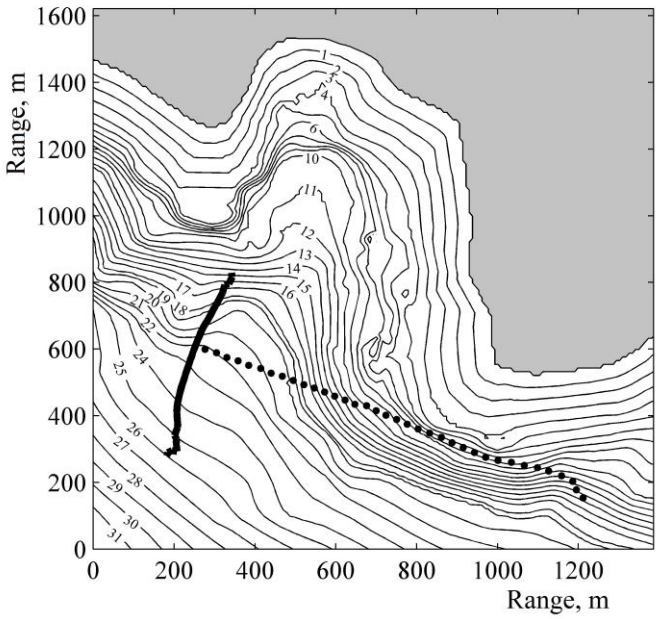


Fig.1. Bathymetry map of experimental range. Heavy line shows the array. Dots corresponds to the places of the signal transmission.

2. RESULTS OF THE EXPERIMENT

Sound speed profile (Fig. 2) provided near bottom sound propagation and well sound interaction with the bottom. Signal duration at the distance more then 300-400 m from the source was 0.15 s and more, which corresponded to multipath sound propagation. Angle of sound wave arrival was determined by correlation of the signals received by the pair of neighboring receivers and, in frame of the homogeneous medium model for small grazing angles we define the angle of the sound wave arrival. Variation of the wave angle arrivals is shown at Fig. 2. Angle of arrivals oscillates in time. That means the different arrivals which propagate by different paths reach the array at different angles. And angle of arrivals gradually falls in time duration of the signal up to 5 degrees at the distance to the source of 390 m. That is the signal tail formed by the rays, which arrived to the array from the other directions with respect to the head of the signal. The tail of the signal propagates along to arc from the signal source the array receivers. No monotonic type of arrival angle variation in time is related, probably, to the fact that the procedure of arrival angle determination is depending on not only by sound refraction in horizon plane, but and by the grazing angle in vertical plane, which is not defined in this experiment.

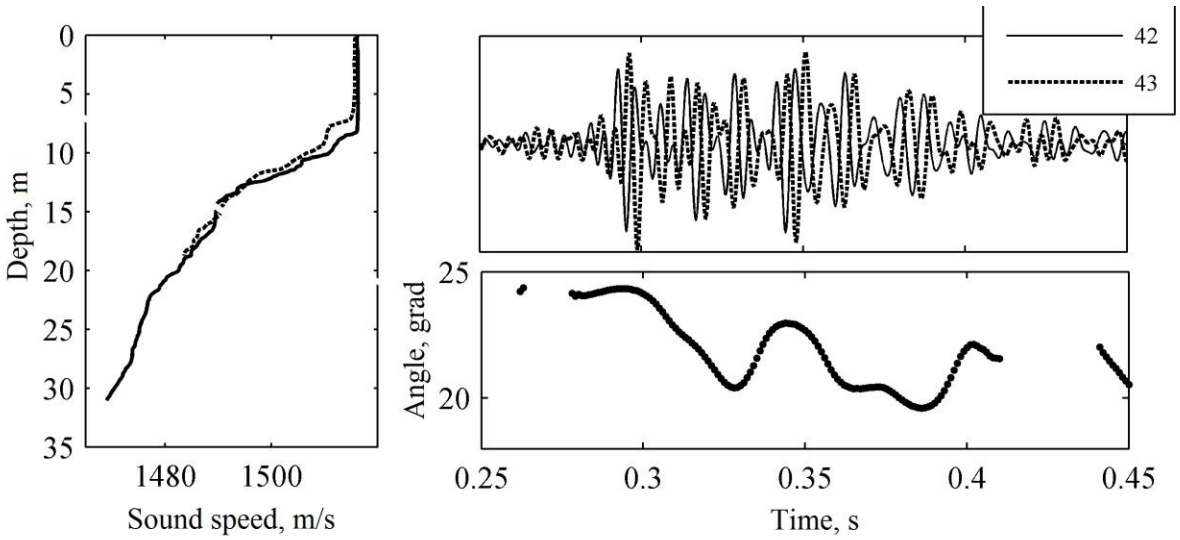


Fig.2. Sound speed profile (left). Sugnals for pair receivers N 42 and 43 and variation of the angle arrival for the acoustical signals (right)

Fig.3 shows the signal distribution through the array in frequency band 70-350 Hz for different distances to the source. It could be marked of the some peculiarity related to relative signal intensity increase at the edges of the array with the distance to the source. For smaller distances to the source as 27 m and 204 m signal intensity distribution through the receivers is quite obvious – the nearer receiver to the source, the higher intensity of the registered signals (Fig. 3 (I, II)). But, with the distance increasing the relative signal intensity at the edge of the array rises with respect to the signal intensity at center of the array (Fig. 3(III, IV)). And one could see at Fig. 3(IV) that signal intensity distribution is shifting to the higher numbers of the receivers, which corresponds to the deeper water part of the experimental area. This specific feature of the signal distribution through the array aperture could be related to the properties of bathymetric refraction in area of the experiment.

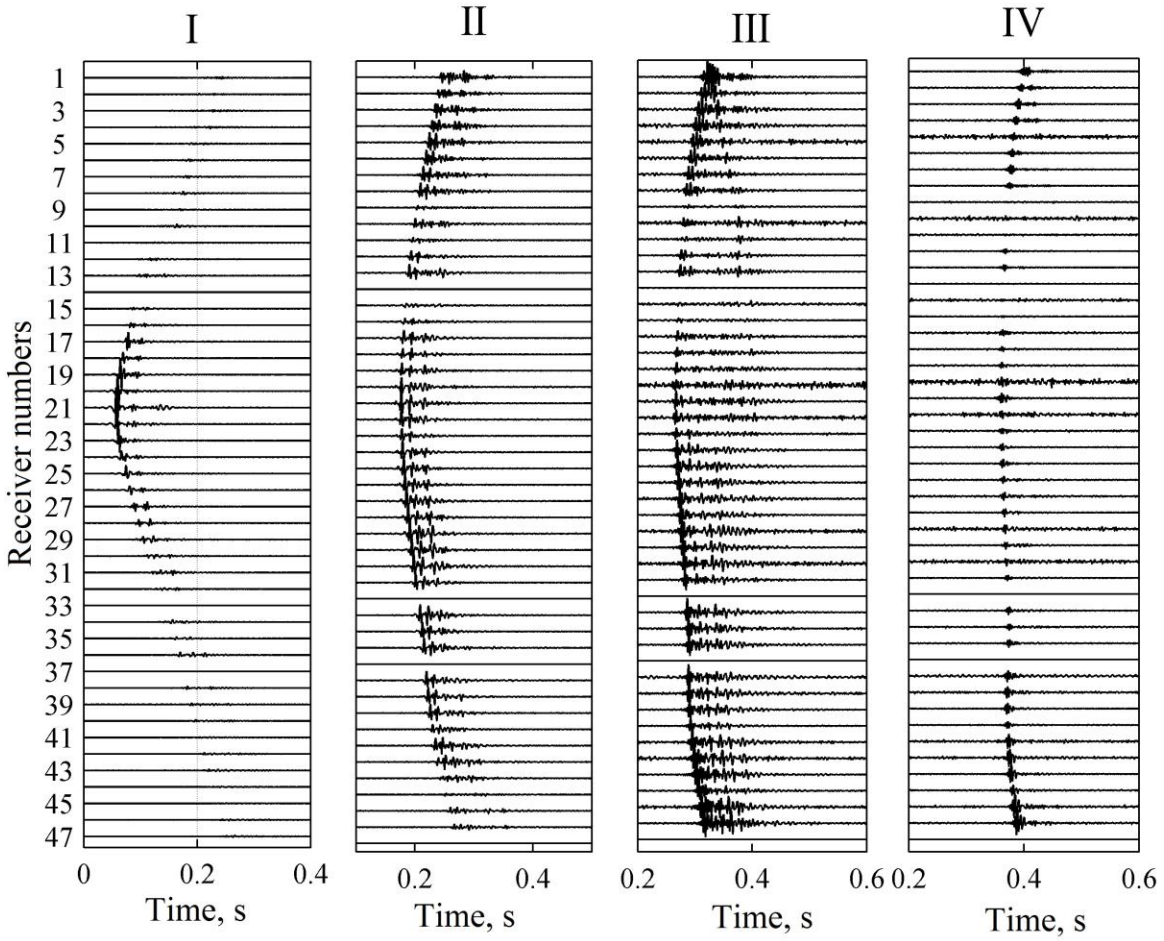


Fig.3. Signal distribution through the array. Distance to the source from the nearest receiver I – 27m, II -204m, III – 347m and IV – 485m

The result of the signal ray paths calculations by code of N. N. Komissarova [9] is shown at Fig. 4 for our experimental conditions. Could be seen that the rays are mostly concentrated at the deep water part of the array and at about of 1 km distance and at the grazing angle more than 8º there is no straight ray, which crosses the array. It corresponds to the very low level signal registered in the experiment at the distance more than 500 m.

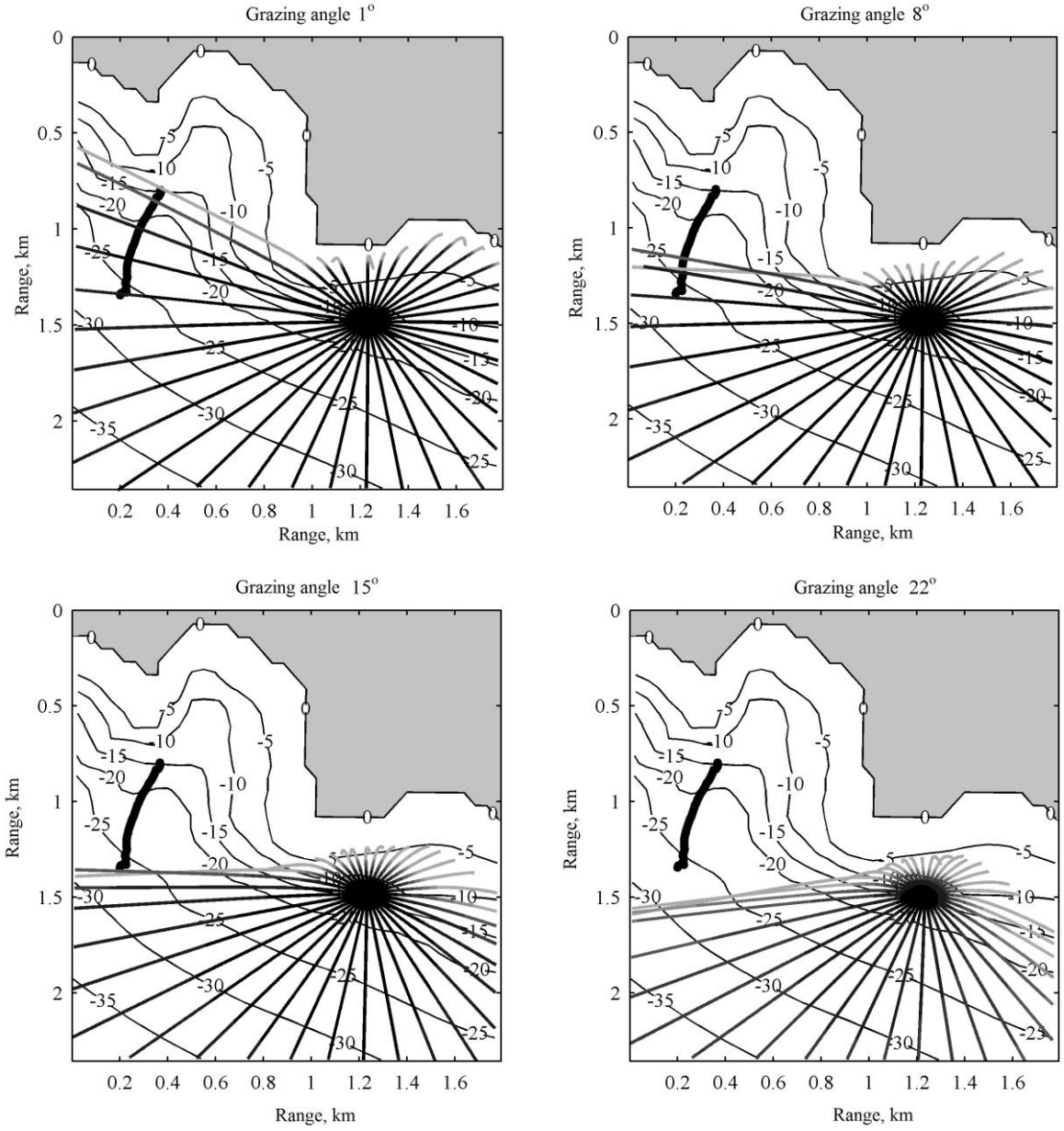


Fig. 4. Horizontal ray projection. View from the top.

3. CONCLUSION

Results of the experimental research lead us to the following conclusion.

Linear bottom array is a good instrument to investigate the horizon refraction at the coastal wedge. Procedure of cross-correlation of the signals received by the pair of neighboring receivers was used for the direction of sound wave arrival determination. This direction changes rather on the same sound pulse duration.

Horizon angle of arrivals oscillates in time. That means the different arrivals of the same signal propagate by different paths and reach the array at different angles.

Experiment reveals no monotonic signal arrival angle variation. That no monotonic type of arrival angle variation in time is related, probably, to the fact that the procedure of arrival angle determination is depending on not only by sound refraction in horizon plane, but and by the grazing angle in vertical plane, which is not defined in this experiment. To investigate 3D signal arrivals could be recommended to use the receivers, which could determine vector characteristics of the signal arrivals.

4. ACKNOWLEDGEMENTS

This research has been supported by Russian Foundation of Basic Research (RFBR projects 17-02-00434, 19-52-40004 and 16-29-02003).

REFERENCES

[1] **L.M. Brekhovskikh**. *Waves in Layered Media*. 2nd Ed. – Academic Press, 520 p. (1976).

[2] **B. G. Katsnel'son, S. A. Pereselkov**. Low-frequency horizontal acoustic refraction caused by internal wave solitons in a shallow sea. *Acoustical Physics*, 46(6), 684–691, (2000)

[3] **A. Yu. Shmelerv, A. A. Migulin and V. G. Petnikov**. Horizontal refraction of low frequency acoustic waves in the Barents Sea stationary acoustic track experiment. *J. Acoust. Soc. Am. 92*, 1003 (1992).

[4] **Collins, M. D., McDonald, B. E., Heaney, K. D., and Kuperman W. A**. Three-dimensional effects in global acoustics, *J. Acoust. Soc. Am*. 97, 1567–1575 (1995).

[5] **Heaney, K. D., and Murray, J. J.** Measurements of three dimensional propagation in a continental shelf environment. *J. Acoust. Soc. Am*. 125(3), 1394–1402 (2009).

[6] **Katsnel'son, B. G., Badiey, M., and Lynch, J.,** Horizontal refraction of sound in a shallow water and its experimental observations, *Acoust. Phys*. 53(3), 313–325 **.** (2007).

[7] **Doolittle, R., Tolstoy, A., and Buckingham, M. J.** Experimental confirmation of horizontal refraction from a point source in a wedge shaped ocean. *J. Acoust. Soc. Am.* 83(6), 2117–2125. (1988).

[8] **Badiey, M., Katsnelson, B. G., Lynch, J. F., Pereselkov, S., and Siegman, W. L.** Measurement and modeling of three-dimensional sound intensity variations due to shallow-water internal waves. *J. Acoust. Soc. Am*. 117(2), 613–625. (2005).

[9] **N. N. Komissarova**. Horizontal Refraction of Rays in a Coastal Zone at Different Sound Velocity Profiles. *Acoustical Physics*. 44(6), 698 – 704, (1998).

PARAMETRIC ARRAY SIGNAL COMPRESSION IN SHALLOW WATER WAVEGUIDE

Igor Esipov[a], Oleg Popov[b] and Gennady Soldatov[c]

[a] Gubkin University of Oil and Gas, 65, Leninsky prosp., 119991, Moscow
[b]Institute of Atmosphere Physics, 3, Pyzhevsky line, 119017, Moscow
[c]South Federal University, 2 Shevchenko str., 347928, Taganrog, Rostov reg.

Igor Esipov, National University of Oil and Gas «Gubkin University», 65, Leninsky prosp., 119991, Moscow, FAX: +7 499 1268411, email address: igor.esipov@mail.ru.

Abstract: *Results of experimental research of parametric array application for marine shallow water waveguide excitation by chirp modulated signal are presented. Acoustical signal of 1-3 ms duration is generated in frequency band of 7 kHz-15 kHz by parametric array with a primary frequency 150 kHz. Sharp directivity of the parametric array transmission provides a single mode underwater waveguide excitation in the whole frequency band. It was shown a frequency modulated signal changes it form due to shallow water waveguide dispersion. Chirp modulated signal compression experimentally shown for single mode signal propagation in shallow water. This signal is transmitted in single lobe along the path up to 750 waveguide thicknesses. Wide-frequency band signal compression increases the efficiency of waveguide propagation. Discussion of the efficiency parametric array application for shallow water marine sounding is presented as well.*

Keywords: *Parametric array, single mode excitation, waveguide sound speed dispersion, virtual acoustical barrier.*

1. INTRADUCTION AND EXPERIMENT SET UP

The parametric array (PA) is acoustical nonlinear transduction process, which develops in a medium through the interaction of co-linear, intense sound waves, called pump waves. PA is well known in oceanography as a tool for precision subbottom profiling. The specific feature for PA, is extremely narrow directivity pattern (several degrees in angular resolution normally) for low frequency acoustical signals [1]. The effective width of this directivity pattern is practically constant in a wide frequency range. Sounding signal is forming in the marine environment, which is stimulated by intensity modulated high frequency power acoustical pump. As a result the end-fire array is forming in the marine environment, which excites sharp directional signal radiation at modulation frequency. Such a low frequency signal, generated by parametrical means will propagate in underwater waveguide independently from the pump radiation. Due to non-resonance properties for low frequency signal generation, PA provides sounding signal transmission in extremely wide frequency band (more than 2 octaves). The main objective of this paper is to discuss the ability of such underwater array, working on the principles of nonlinear acoustics for shallow water long-range hydrographic research.

To our knowledge, there was only one actually long-range ocean experiment using a parametric array for up to 1000 km range signal propagation [2, 3]. This experiment was performed in the early 1990s in the region of Kamchatka and Kuril in the Pacific Ocean. The 6 m long and 2 m high side-scanning array in the bow of the ABK was used as a parametric array with pump wave power of 20 kW at the primary frequency of 3 kHz. This array transmitted parametric signals in a frequency range of 230-700 Hz. The parametric sonar was used to investigate synoptic eddy structure at far distances. A region of the Kuril Strait with typical ocean eddies was chosen for this experiment at the range of 400 km [3].

The research has been done in Taganrog bay, Azov sea in August 2018. Transmitting array was installed vertically at the bottom and could scan horizontally the bay by narrow beam with the rotating device. PA has been done as a mosaic of high frequency transmitting elements; half of them were exciting at pump frequency of 150 kHz and the other at frequency 5-20 kHz lower. Vertical size of the array was 30 cm and 20 cm – is it width. Electricity power of the transmitter was 1 kW for each pump frequency.

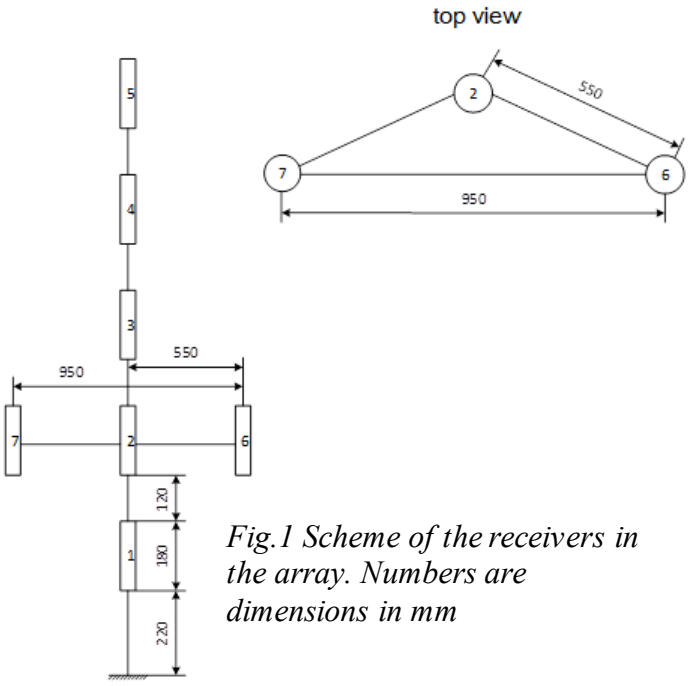


Fig.1 Scheme of the receivers in the array. Numbers are dimensions in mm

The receiving array was arranged as a vertical chain of five receivers, which were installed at the metal rod with interval of 30 cm. This rod as a part of rigid construction was installed at the bottom vertically and overlaps the whole waveguide. Two more receivers were attached at the level of the 2nd receiver, as it is shown at Fig. 1, to direction-finding of the receiving signals.

The sea depth at the range of experiments slightly changes at about 2 m. Vertical sound speed profile provided near-bottom signal propagation.

2. RESULTS OF THE EXPERIMENT

A sequence of acoustical pulses was transmitted by PA. The duration of a single pulse was from 0.7 ms to 3 ms, and the interval between pulses was about 300 ms. Signals were simultaneously received from all of the gages of the vertical array. The measurements were carried out for transmitter–receiver distances of 0.5 to 1.5 km. At the greater distance the signal amplitude decreases rapidly because the attenuation due to near-bottom propagation. The frequency–time characteristic for pulses with initial duration of 3 ms and a carrier frequency linearly modulated within 7–15 kHz was investigated while pulses propagate through the shallow-water waveguide. And at that time the frequency sweep in the transmitting signal was arranged from lower frequency to higher, which corresponds to normal shallow water dispersion.

As analysis shown, the choice of that frequency range for the signals was optimal for our experiment. It is known that waveguide dispersion increases with the frequency decrease, but at that the PA transmission efficiency falls. PA transmission efficiency increases with the frequency, but the dispersion rapidly decreases at the same time. PA transmission efficiency was sufficient to make an experimental research up to 1500 m with emphasized waveguide frequency dispersion for signals in chosen frequency range. Fig. 2 shows signals from the gages of the receiving array at 1000 m distance, while PA transmits linear frequency modulated pulses of 3 ms duration. One could see the main energy of PA signals in shallow water is concentrated at the middle and near-bottom part of the waveguide and the signals from the gages installed at the different levels of the array are proved in the phase, which is corresponded to the first mode of the waveguide excitation.

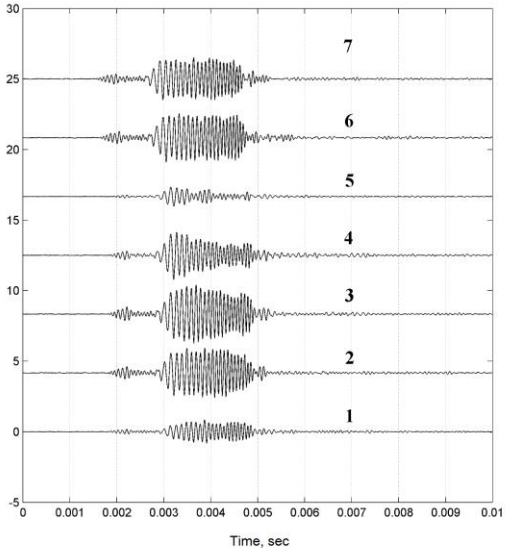


Fig.2. Oscillograms of the signals from the gages of the receiving array 1000 m distance. Numbers correspond to the gage number at Fig.1. Maximum level was registered at gages 2 and 3, which correspond to near-bottom propagation.

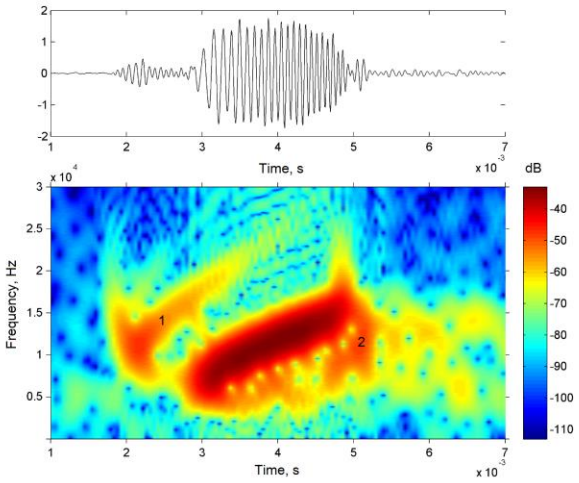


Fig. 3. Spectrogram for linear frequency modulated signal, received by the gage 2 at 1000 m distance. 1- is a forerunner, 2 is a reflection from the supporting boat. Signal level is in relative units. Forerunner corresponds to the second harmonic of the main body of the signal and propagates faster.

Oscillograms at Fig.2 show the typical special features related to the PA signal propagation in marine shallow water waveguide. One can mark a forerunner which runs faster than the main body of the signal. Forerunner is related to the second harmonics excitation in process of parametric signal transmission. It has higher frequencies and therefore runs faster. One could see that the main body of the registered signal lasts 2 ms, as while as the duration of the signal transmission was 3 ms. Wide frequency band signal became shorter at 1 ms while it propagates through the distance of 1000 m long. These specific features have been already marked earlier under investigation of PA signal propagation in shallow water waveguide [4, 5].

After analysis of the frequency dispersion of the waveguide sound transmission in that environmental conditions we could expect of full compression for wide frequency band parametric signal of 1.7 ms duration under transmission at 1500 m distance. We could note that the distances of 1000 m and 1500 m correspond to the far-distance propagation in full measure. Distance of the signal propagation excides the vertical scale of the marine waveguide in 500-750 times. Fig. 4 shows the result of wide frequency band signal compression. The signal forerunner is proved not so notable as it was at 1000 m distance because of attenuation, but the higher frequencies in forerunner came earlier that the lower ones. The main body of the signal with duration of 1.7 ms under transmission is compressed in the pulse of 0.4 ms duration after shallow water propagation (depth of the sea approx. 2 m) through the pass of 1500 m long. Signal compression occurs in more than 4 times in that experiment. After the compressed pulse one could see the signal reflection from the boat.

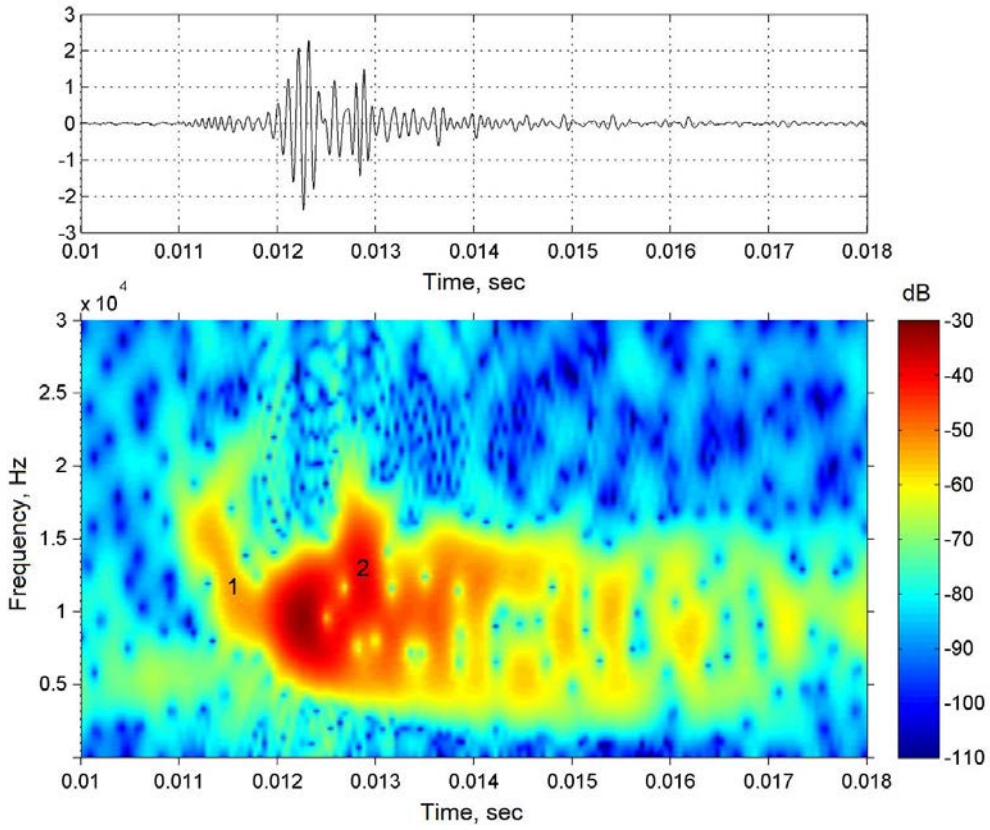


Fig. 4. Spectrogram for frequency modulated signal of 1.7 ms under transmission and received by the gage 2 at 1500 m distance. 1- is a forerunner, 2- is a reflection from the supporting boat. Signal level is in relative units.

3. SINGLE MODE FREQUENCY DISPERSION FOR A WIDE FREQUENCY BAND SIGNAL IN UNDERWATER WAVEGUIDE.

In shallow water the sound field usually consists of a series of modes exhibiting frequency dispersion of the speed of signal propagation. Mode dispersion in underwater waveguide means that the modes of the same number have different envelope speed of propagation at different carrier frequencies. The value of the dispersion depends, among others, on the vertical sound speed profile. The frequency dispersion provides either a spread in time of short broadband pulses that travel long distances, or concentration of acoustic signal energy within a short time interval when the frequency modulation of the signal corresponds to the dispersion conditions of the medium. Therefore wide frequency band signal changes it form in process of the waveguide propagation. Fig. 5 shows the results of the modeling of the signal form transformation for the propagation along the pass of 500 km long in the Black sea underwater waveguide. Sound speed minimum corresponds to 50-70 m depth for the Black sea environment conditions. Short acoustical pulse was excited in frequency band of 200-1200 Hz as the first mode of the typical Black sea waveguide. As one could see signal is rather short at the distance of 1 km (pulse duration less than 5 ms), but for distance of 500 km it duration becomes about 80 ms with emphasized frequency modulation corresponding to the waveguide dispersion. Pulse duration changes in 16 times in that example. Fig. 6 shows a proper spectrogram of the signal at 500 km distance. It shows the Black sea waveguide dispersion for the first mode signal propagation. Thus, if we excite the first mode as a signal of 80 ms in frequency band of 200-1200 Hz with frequency modulation corresponding to the waveguide dispersion, it could compress to the short pulse of 5 ms duration with a proper intensity increase. Note, the lower frequencies run faster than the higher ones for the Black sea underwater waveguide. Therefore, to get a full compression for the wide frequency signal in the Black sea underwater waveguide one should make a sweep of frequency modulation from high to lower frequencies in process of signal transmission.

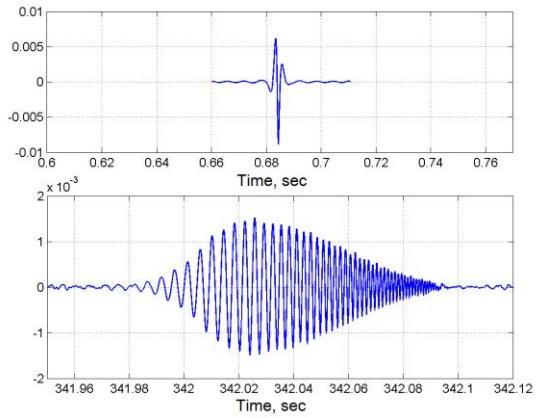


Fig. 5. Single mode shot pulse waveguide excitation in frequency band 200-1200 Hz. Top – signal at 1 km distance (the first mode). Bottom – signal at 500 km distance. X axis shows absolute time. Signal level – in relative units.

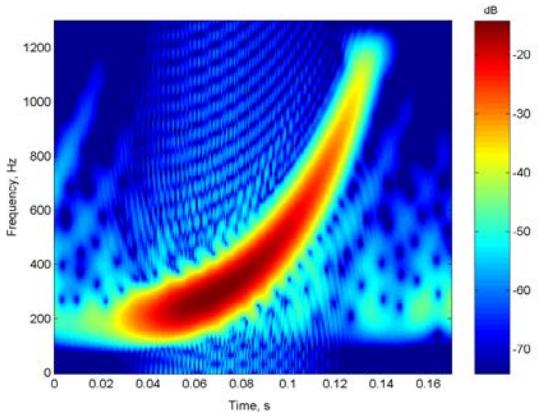


Fig. 6. Spectrogram for the signal of 200-1200 Hz frequency band. The first mode of the Black sea waveguide at 500 km distance. Spectrogram corresponds to signal shown at Fig. 5 bottom.

4. CONCLUSION

Results of the experimental research lead us to the following conclusion.

1. Parametric array application could provide acoustical single mode excitation in wide frequency band in the waveguide. Frequency band of PA signal modulation can reach an octave or rather more.
2. PA signal compression under it propagation in shallow water waveguide was experimentally shown.
3. Signal frequency modulation used in our experiments didn't correspond in the full measure of the experimentally measured wave guide dispersion. Therefore the compensation of the times propagation of the different frequencies at signal compression is proved not for the total frequency band of signal modulation and just only for limited number of frequency components. Experimentally signal was compressed in 4 times at distance of 1.5 km. Calculations show that in conditions of our experiment the signal could be compressed in 10 times.
4. Signal compression leads to relative increase of signal intensity in process of it propagation and to signal-to-noise gain for signal receiving. Therefore the parametric array could be the most effective instrument for the long-range acoustical propagation in shallow water [6].
5. Signal compression is pure linear acoustical process. But to realize it a single mode wide frequency band acoustical signal is needed in the waveguide. It is shown that such a signal could be excited in the marine waveguide due to sharp directed parametric array, operating on principals of nonlinear acoustic.

5. ACKNOWLEDGEMENTS

This research has been supported by Russian Foundation of Basic Research (RFBR projects 17-02-00434 and 16-29-02003).

REFERENCES

[1] **B. K. Novikov, O. V. Rudenko, V. I. Timoshenko**, *Nonlinear Underwater Acoustics*, (AIR-Press, NY, 1987).

[2] **I.B. Esipov, A. I. Kalachev, A. D. Sokolov, A. M. Sutin, and G. A. Sharonov**, Long-range propagation experiments with a powerful parametric source," *Acoust. Phys*. 40(1), 61−64 (1994).

[3] **I.B. Esipov, S.V. Zimenkov, A. I. Kalachev, and V. E. Nazarov**, Sensing of an ocean eddy by directional parametric radiation, *Acoust. Phys.* 39(1), 89−90 (1993).

[4] **I. B. Esipov, O. E. Popov, V. A. Voronin, and S. P. Tarasov**, Dispersion of the signal of a parametric array in shallow-water, *Acoust. Phys*. 55(1), 76–80 (2009).

[5] **Igor B. Esipov.** New approach to oceanography research on elongated paths on principals of nonlinear acoustics. *Proceedings of Meeting on Acoustics (POMA)*, 24, 1, 005005 (2016); htpp://dx.doi.org/10.1121/2.0000146.

[6] **I. B. Esipov, O. E. Popov, G. V. Kenigsberger, I. I. Sizov**. A parametric antenna for hydrophysical research on long-distance paths. *Bulletin of the Russian Academy of Sciences: Physics*, 80(10), 1209–1217, (2016)

COUPLING 3D ACOUSTIC PROPAGATION TO OPERATIONAL OCEAN CIRCULATION MODELS

Ilmer D. van Golde[a], Martha C.M. Guerreiro[a], Orlando C. Rodríguez[b], Luís S. Quaresma[a], Yann Stéphan[c]

[a]CMETOC–IH, Marinha, Rua das Trinas 49, 1249-093 Lisboa, Portugal
[b]FCT, Universidade do Algarve, Campus de Gambelas – Edifício 2, 8005-139 Faro, Portugal
[c]SHOM, CS 92803, 29228 Brest CEDEX2, France

Ilmer D. van Golde, Centro Meteorológico e Oceanográfico Naval (CMETOC), Instituto Hidrográfico, Rua das Trinas 49, 1249-093 Lisboa, Portugal, ilmer.golde@hidrografico.pt

Abstract: *An operational 3D underwater acoustic model is currently being implemented at the Portuguese Navy to estimate real-time ocean ambient noise levels. To achieve this goal, accurate noise source positioning and ocean structure dynamics is required. While noise source information can be obtained from real time AIS data, 3D ocean structure information cannot be obtained only from observations. As such, the present paper aims to be a preliminary study of the use of 3D numerical ocean circulation model, to provide the ocean structure required for operational underwater acoustic modelling.*
The HYCOM ocean circulation model allows for a hybrid vertical discretization of the ocean structure, enabling high resolution surface Z-levels while maintaining a good discretization of the deep ocean water masses through isopycnal layers. Operational HYCOM outputs are validated and evaluated as the source for the ocean profile required for acoustic modelling.

Keywords: *Ocean modelling, ocean-acoustic coupling, Mixed Layer Depth, numerical noise filtering.*

1. INTRODUCTION

The Maritime GEOMETOC Centre (CMETOC) of the Portuguese Navy is developing the SUBECO project, which, amongst others, aims the implementation of an operational underwater ambient noise model for the seas surrounding Western Iberia. AIS data will provide the noise source information while the environmental conditions will be obtained through a 3D operational ocean model.

The sound velocity in the ocean can be calculated from temperature, salinity and hydrostatic pressure. The propagation of sound in the ocean is mainly determined by the shape of the vertical sound velocity profile rather than the absolute values of sound velocity along the water column [1].

While the entire vertical ocean profile is important for accurate calculation of sound propagation, most of the noise resultant from shipping will be restricted in a surface duct. Sound travelling along a duct is prevented from spreading in depth and becomes confined by oceanographic parameters, the ocean surface and the sonic layer depth (SLD). Between these limits the effect of the increasing hydrostatic pressure is greater than the effect of the decreasing temperature and a positive sound velocity gradient exists downwards, with a maximum occurring at the SLD [2].

The SLD is usually placed near the mixed layer depth (MLD), with both often coinciding [3]. The MLD is hard to be precisely defined and as such an approximation is often derived through various methods. Even if many of these methods use temperature differences or gradients it is preferable to use density as this determines the stability of the water column and hence the degree of mixing [4].

2. OCEAN CIRCULATION MODEL

The Hybrid Coordinate Ocean Model (HYCOM) was developed to fulfil the need for an ocean model that allows a variable vertical coordinate scheme. The main distinguishing feature is the possibility to apply any combination of isopycnal vertical coordinates in deep stratified waters, high resolution Z-coordinates in the upper ocean and terrain-following sigma coordinates in shallow waters [5].

CMETOC runs the HYCOM model operationally for the Western Iberian Peninsula. The current configuration consists of 32 hybrid layers and uses ECMWF's model for atmospheric forcing and MERCATOR for boundary conditions.

3. RESULTS

An ocean temperature section along the 37.5ºN parallel, obtained by numerical modelling is represented in Fig. 1. As expected for a winter season, there is a non-stratified upper layer (MLD) followed by a temperature decrease around 200m depth, representing the first permanent thermocline. Around 1000m depth, warmer water masses are found along the west-Iberia margin, corresponding to Mediterranean Outflow veins flowing poleward [6]. Further down another increase in temperature gradient is observed, evidence of other permanent thermoclines, and finally, from approximately 2000m depth onwards, there is little change in the temperature structure, typical for deep waters. All the main structures that influence the acoustic propagation can be observed from the temperature profiles.

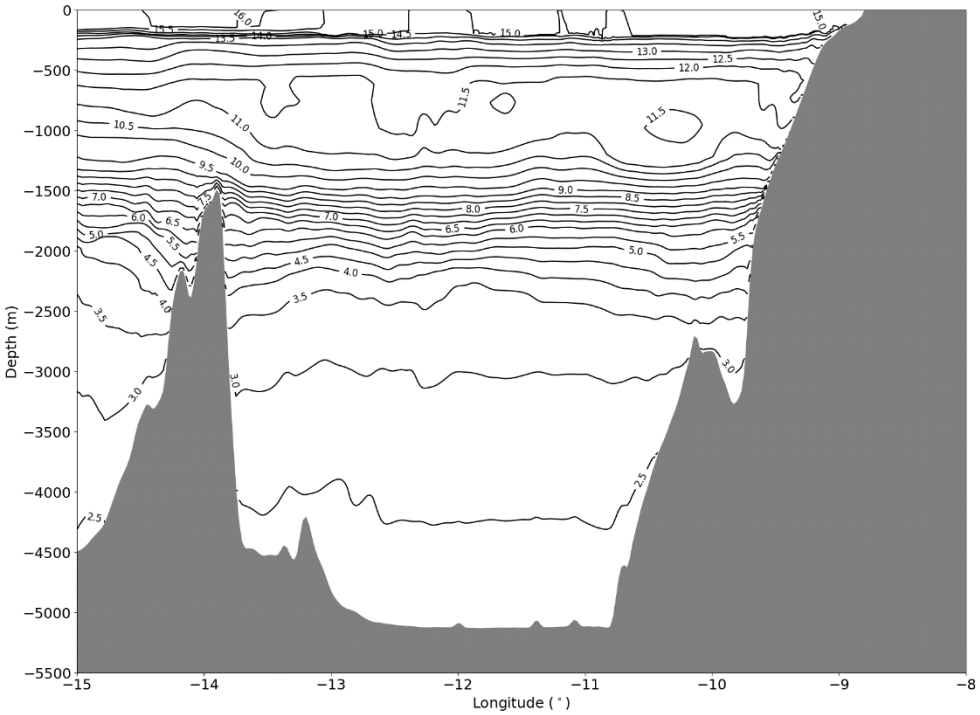


Fig. 1: HYCOM temperature output for 37.5ºN.

Higher frequency variation seems to be present near the upper layers of the ocean and a detailed look (Fig. 2) shows the occurrence of numerical noise above the mixed layer depth, as can be observed near 12ºW and 11ºW. Since sound velocity is very sensitive to temperature gradients [2], where even small changes of sound velocity can have significant impact on its propagation [1], this numerical noise is expected to highly impact the underwater ambient noise model solution.

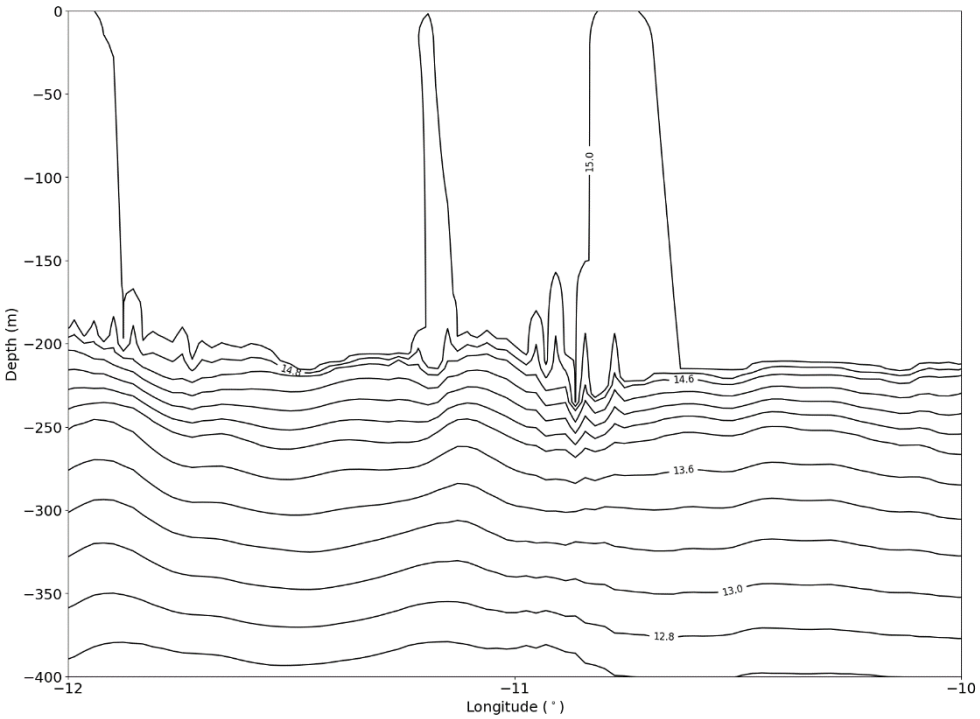


Fig. 2: Upper layers of HYCOM temperature output.

In Fig. 3 MLD is calculated by various methods. While differences are expected from each method, we can notice that all of them show solutions contaminated by numerical noise. The fluctuations in the derived MLD and, by approximation, in the SLD will have significant impact in the sound propagation solution. To demonstrate the adequacy of frequency domain filtering, a Wiener filter was applied to the mixed method MLD data. The Wiener filter was selected for its relative simplicity and ease of implementation [7]. The filtered data set is also represented in Fig. 3, showing a great improvement in noise reducing along this interface.

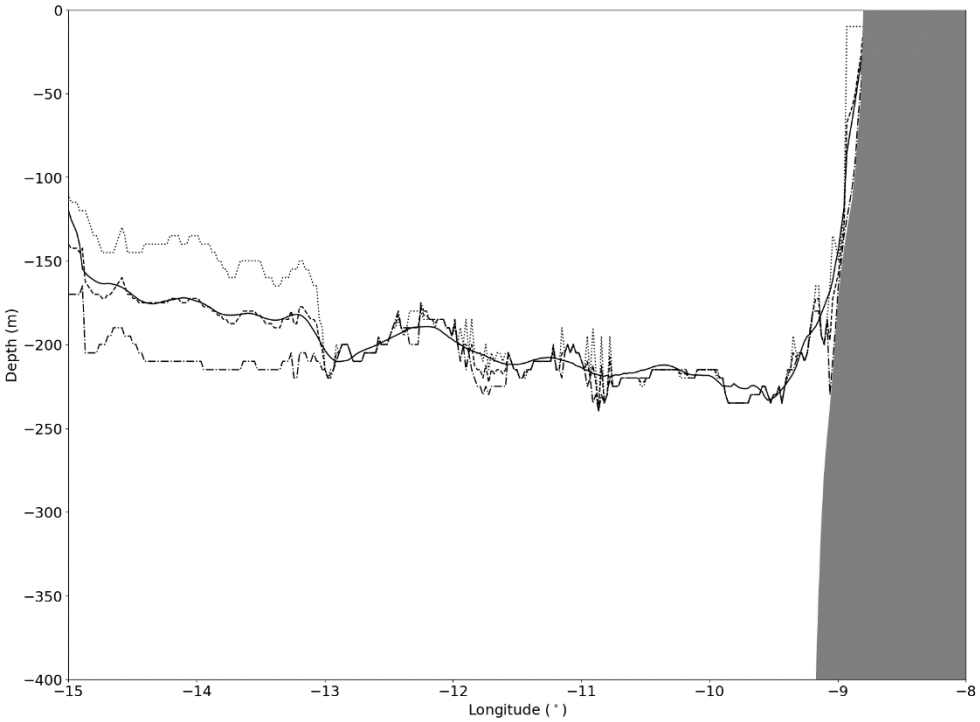


Fig. 3: MLD profiles calculated with the HYCOM output. The dotted line is MLD calculated via temperature difference, the dot-dash line is the MLD calculated via density gradient, the dashed line is a mixed MLD calculation via temperature difference and density gradient and the solid line is the mixed MLD calculation with a Wiener filter.

4. CONCLUSION

An operational numerical ocean circulation model can be a valid source of environmental information for an underwater acoustic propagation model. The preliminary results presented in the current study however suggest that numerical noise in ocean model's forecasts can significantly impact the underwater sound propagation solution, leading to inaccurate results.

Frequency domain filtering can mitigate the numerical noise introduced by the ocean circulation model. An in-depth study could lead to the establishment of an adequate filtering technique to be implemented with the operational coupling of an ocean circulation model and an acoustic propagation model.

5. ACKNOWLEDGEMENTS

This work was funded under the SUBECO project, financed by Portuguese Ministry of Defence.

REFERENCES

[1] **Brekhovskikh, L.M., Lysanov, Yu.P.**, *Fundamentals of Ocean Acoustics – Third Edition*, Springer, 2003.
[2] **Etter, P.C.,** *Underwater Acoustic Modeling and Simulation – Fifth Edition*, CRC Press, 2018.
[3] **Helber, R.W., Barron, C.N., Carnes, M.R., Zingarelli, R.A.**, Evaluating the sonic layer depth relative to the mixed layer depth, *Journal of Geophysical Research*, volume 113, 2008.
[4] **Thomson, R.E., Fine, I.V.,** Estimating Mixed Layer Depth from Oceanic Profile Data, Journal of Atmospheric and Oceanic Technology, volume 20, pp. 319-329, 2003.
[5] **Wallcraft, A.,** *Hybrid Coordinate Ocean Model (HYCOM) Version 2.1 User's Guide*, Naval Research Laboratory, 2003.
[6] **Iorga, M.C., Lozier, M.S.,** Signatures of the Mediterranean outflow from a North Atlantic climatology: 1. Salinity and density fields, *Journal of Geophysical Research*, volume 104, pp. 25,985-26,009, 1999
[7] **Blackledge, J.M.,** *Digital Signal Processing: Mathematical and Computational Methods, Software Development and Applications*, Horwood Publishing, 2006

TIME-FREQUENCY AND WARPING ANALYSIS OF THE SOUND FIELD MODAL COMPOSITION IN VARIABLE SHALLOW WATER ENVIRONMENT. SWARM'95 EXPERIMENT AS CASE STUDY.

Yarina M., Katsnelson B.

L. Charney School of Marine Sciences, University of Haifa, Israel, 3498838 Haifa,

Contact author: Marina Yarina
Room 270, Multi-Purpose Blvd., University of Haifa, 199 Aba Khoushy Ave., Mount Carmel, Haifa 3498839, Israel
e-mail: marina-malysheva@autorambler.ru

Abstract: *broadband air-gun data from SWARM'95 experiment in shallow water area of Atlantic shelf are used to analyze mode filtering using Warping Transform (WT). Sound intensity fluctuations in the presence of moving nonlinear internal waves are considered on the base of WT. Results are compared with mode filtering using vertical line array (VLA). It is shown that Warping Transform allows us to carry out mode filtering in shallow water environment, changing in time and space in the presence of moving nonlinear internal waves by single hydrophone only. Temporal variations of mode composition in given case have properties specific for manifestation of horizontal refraction in the form of focusing/defocusing in horizontal plane [This work was supported by Israel Science Foundation, grant 565/15].*

Keywords: *shallow water sound propagation, warping transform, horizontal refraction.*

1. INTRODUCTION

Experiment SWARM'95 [1] on the sound signals propagation in the shallow water waveguide was carried out in Atlantic shelf of USA by Woods Hole Oceanographic Institute (WHOI) and Naval Research Lab (NRL) and University of Delaware (UD). WE consider acoustic track (Fig.1) of the length ~ 15 km with the wideband source (air-gun) with the band ~ 30-300 Hz and vertical array (WHOI VLA). Acoustic track is approximately parallel to the beach). UD source is air-gun, located 12 m below the sea surface, radiated wideband signals every 60 sec. WHOI VLA contains 16 hydrophones, spanned the water column from 14.9 to 67.4 m, with hydrophone spacing 3.5 m [1]. During time of experiment a few trains of nonlinear

internal waves (NIW) were passing through acoustic track (Fig.1), producing sound intensity fluctuations registered by VLA. The most interesting observations were carried out in the presence of the nonlinear internal waves passing acoustic track, where fluctuations were registered due to the so called focusing/defocusing in horizontal plane takes place. In the Fig.3 intensity fluctuations are shown in the time interval 19:00 – 20:00 GMT. One of the main specific features of this phenomena is synchronicity of fluctuations for different waveguide modes, and the corresponding synchronicity of intensity fluctuations over depth, what we can see in the Fig.3. Theoretical explanation of this experiment was done in the paper [2] on the base of theoretical analysis using vertical line array, which allows us to filter waveguide modes on the base of standard methodology

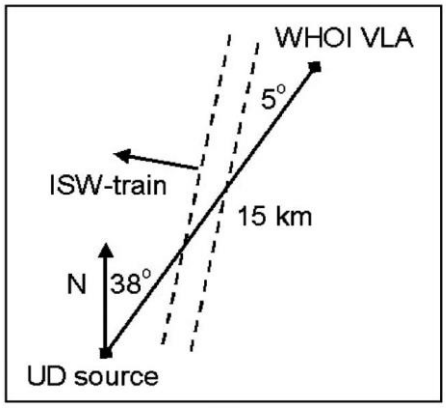


Fig.1. Layout of the SWARM'95 experiment

Let's consider sound field from the wideband source placed in the horizontal plane with coordinates (0,0). If there is train of NIW passing through acoustic track then sound field changes in time (T), on receiving array . Sound field on the VLA, placed at the point in horizontal plane with coordinate (x,y) has the form:

$$P\big(x,y,z;T)\big) = \sum_n a_n(T)\psi_n(z)\exp\big(iS(x,y)\big) \tag{1}$$

where $a(T)$ is amplitude of mode n, S – phase function (eikonal) in horizontal plane, describing horizontal rays. We can suppose that waveguide functions at the VLA practically do not change in time and all the variations of the sound field are provided by modal amplitudes $a_n(T)$.

Intensity of separate mode on the single hydrophone (or at the fixed depth z) is:

$$I_n = \left|a_n(T)\psi_n(z)\right|^2 \tag{2}$$

Experimental evidence of horizontal refraction was presented in the papers [1,2], where we can list specific features, characterizing fluctuations of the sound field just due to horizontal refraction, initiated by nonlinear internal waves:

(i) significant fluctuations of intensity with period ~ 12-15 min, corresponding to the Vaisala period for given temperature (density) profile, and in turn, to the period of NIW;
(ii) Synchronicity of fluctuations over depth (focusing/defocusing) for all the waveguide modes

In the Fig.3 total intensity (summarized over all the modes) is shown.

Let's consider modal decomposition of the sound field using sound field recorded by the single hydrophone only. In the Fig.2 spectrogram of pulse is shown, where we can see

dispersion curves, corresponding to four modes, giving contribution to the sound field.

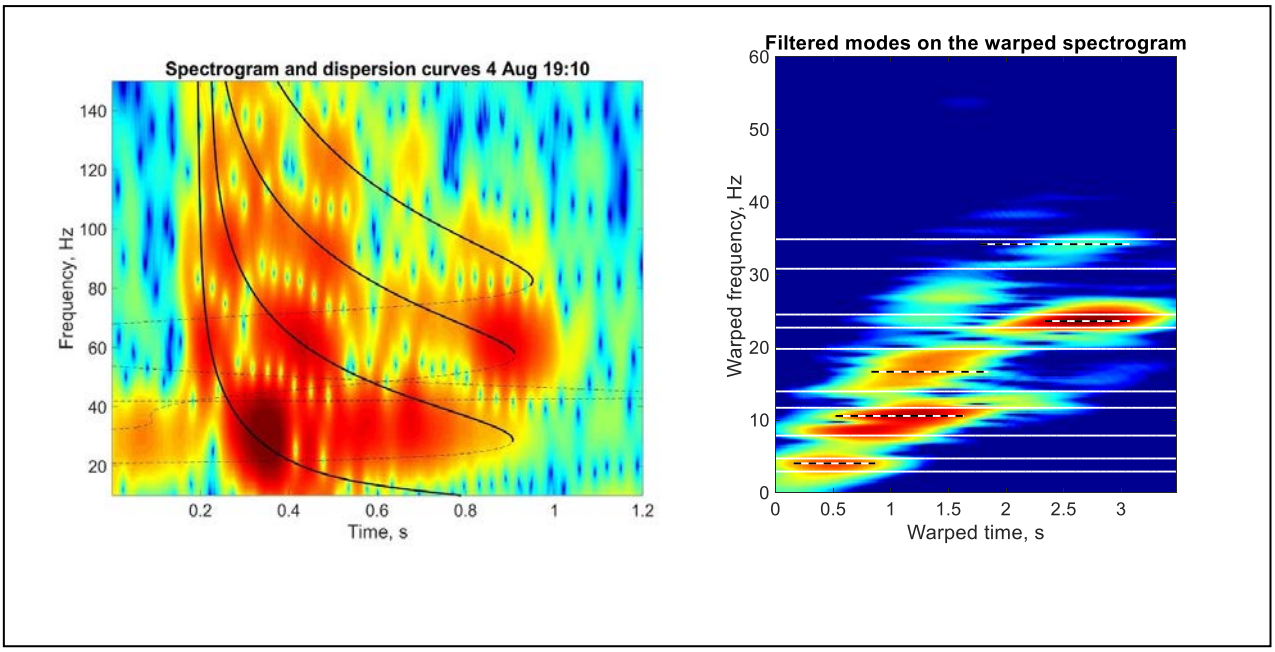


Fig.2 Spectrogram of one pulse of air-gun (left panel), solid lines show the corresponding frequency dependence of modal group velocities. Warping transform of spectrogram (right panel)

In order to get amplitude of separate mode let's use Warping Transform (WT) [3] The corresponding WT spectrogram is shown in the Fig.2

After application of the inverse Warping Transform it is possible to get amplitudes of each mode a_n and the corresponding modal intensity I_n. We got that different maximal values of intensities due to different values of eigen functions for given depth and synchronous variation in time for all four modes. Remark that for other depths of hydrophones there is the same behavior of modal intensities.

In the Fig. 3 temporal dependence for depth distribution of total intensity along with the corresponding functions for three lowest modes are shown. We can clearly see synchronicity of variation of different modes and synchronicity of variations over depth what acknowledge 3D nature of given phenomena.

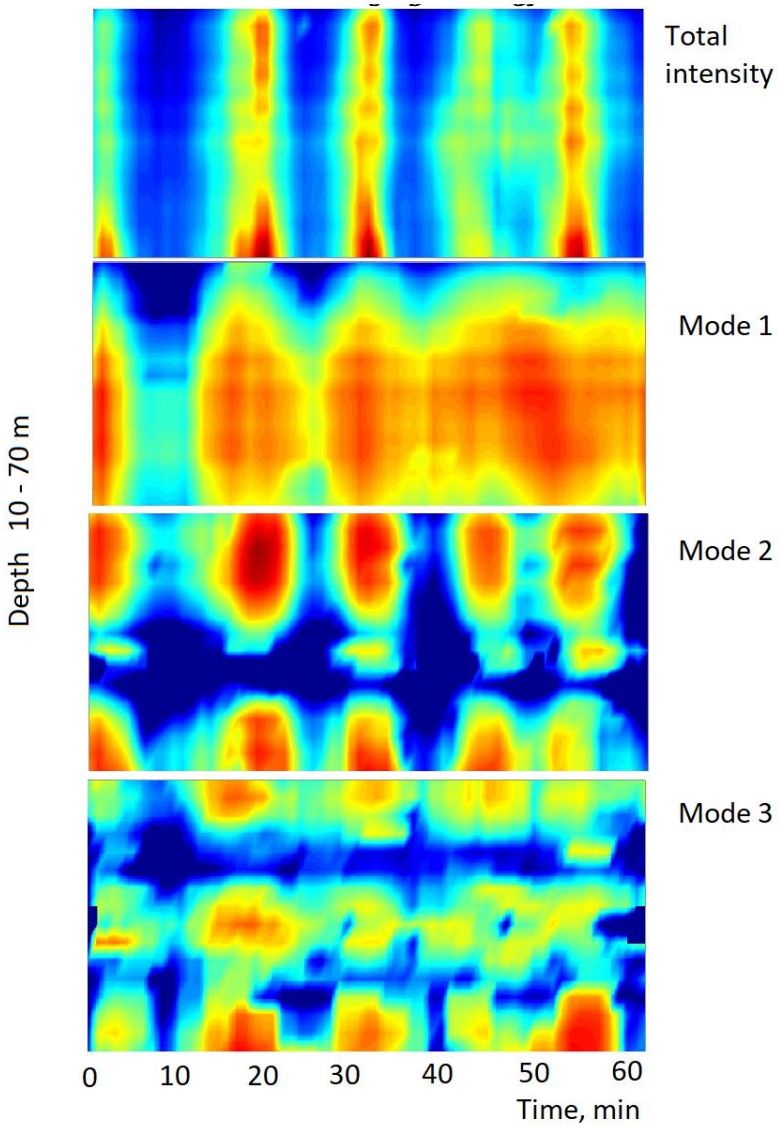


Fig.3. Temporal dependence of total intensity and intensities of the lowest three modes

Using these data we can find scintillation index for intensities of modes,

$$S_n^2(T) = \left(\left\langle I_n^2(T) \right\rangle - \left\langle I_n(T) \right\rangle^2 \right) / \left\langle I_n(T) \right\rangle^2 \tag{3}$$

which is proportional to the refraction index for the corresponding modes in horizontal plane. Results of calculations is shown in the Fig.4, which gives frequency dependencies close to obtained in [2]

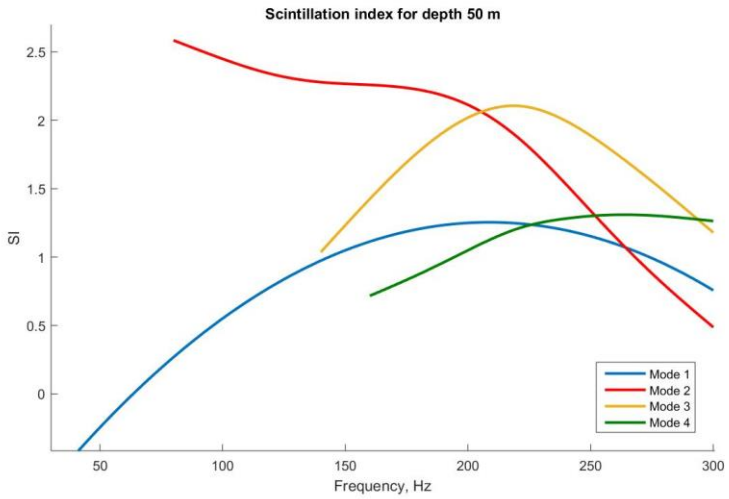


Fig.4. Scintillation index for four lowest modes as a function of frequency

REFERENCES

[1] **M. Badiey ; Y. Mu ; J. Lynch ; J. Apel ; S. Wolf.** Temporal and azimuthal dependence of sound propagation in shallow water with internal waves. IEEE JOE, v.27, 117-129, (2002)
[2] **Badiey M., Katsnelson B., Lynch J., Pereselkov S**. Frequency dependence and intensity fluctuations due to shallow water internal waves. J. Acoust. Soc. Am V.122(2) p.747-760, (2007).
[3]) **R. Baraniuk and D. Jones**, "Unitary equivalence: A new twist on signal processing," IEEE Trans. Signal Processing 43(10), 2269–2282 (1995)

First Authors' Index

Author	Page
Abraham Douglas	577
Abrahamsson Per	41
Amiri-Simkooei Alireza	767
Anthony Treloar Alfie	685
Asch Mark	3
Ballard Megan S.	499
Bates Jeffrey	585
Beaumont Guillaume	519, 609
Bennaceur Iannis	527, 735
Binnerts Bas	851
Bjørnø Irina	129
Blachet Antoine	799
Blom Koen	311
Blondel Philippe	9, 477, 491
Bousquet Jean-Francois	289
Bouzerdoum Abdesselam	179
Byun Sung-Hoon	551
Campagnaro Filippo	281
Chen Yi	81
Colin Mathieu	867
Cronin Stephen	335
Curtis Alan	905
D'Alès De Corbet Benoît	227
Dall'Osto David	453
Datum Michael	599
Diab Daher	383
Duda Timothy F	483, 835
Dugelay Samantha	975
Dunn Muriel	647
Ehlers Frank	825
Eller Anthony I.	461
Ellis Dale	883
Esipov Igor	1043, 1049
Fakiris Elias	351
Fattaccioli Dominique	509
Fornshell John	103, 109
Gällström Andreas	995
Gaonach Gilles	1015
Gavrilov Alexander	375
Geroski David	1009
Gips Bart	219

Author	Page
Godin Oleg A.	717
Gournia Charikleia	211
Grimmett Doug	569
Gunderson Aaron	757
H. Mohammadloo Tannaz	783
Hansen Roy Edgar	429
Hartstra Iris	875
Hazelwood Dick	659
Healy Cornelius	251
Herter Ulrich	163
Higgins Alex	727
Hodgkiss William	625
Hovem Jens M	95
Hu B O	1031
Iqbal Kashif	17
Isaev Alexander	61
Ivansson Sven	1001
Jaśniewicz Damian	123
Kargl Steven	413, 749
Katsnelson Boris	391, 723
Klages Elin	639
Kulgemeyer Tobias	437
Li Song	939
Li Zhengnan	265
Li Zhi	955
Linné Markus	67
Lopera Tellez Olga Lucia	965
Loranger Scott	115
Marcellin Simon	397
Mashoshin Andrei	171
Matveev Anton	75
Melo José	195
Menzel Peter	443
Morozs Nils	303
Murphy Stefan M.	593
Ødegaard Lars	359
Otnes Roald	809
P. Maia Lussac	327
Pailhas Yan	141, 155
Papili Sonia	987
Pelekanakis Konstantinos	271
Prior Mark	859
Quidu Isabelle	203

Author	Page
Raghukumar Kaustubha	653
Razaz Mahdi	709
Real Gaultier	535
Richardson Michael	405
Rixon Fuchs Louise	1021
Robinson Stephen	25, 467
Rymansaib Zuhayr	899
Sanford Ciaran	703
Sarkar Jit	543
Schaefer Ingo	925
Shen Lu	243
Sigg Robert	891
Sklivanitis George	319
Stender Dan Henrik Sekse	843
Stoltenberg Arne	919
Strenzke Ruben	817
Synnes Stig A V	147
Tegowski Jaroslaw	367, 791
Terracciano Daniele Sebino	561
Tesei Alessandra	677
Thomas Benjamin	691
Troiano Luigi	55
Tsinovoy Anatoli	913
Tsouvalas Apostolos	667
Uitdenbogerd Martin	933
Unal Deniz	297
Uzan Lionel	947
Uzhansky Ernst	1037
Van Golde Ilmer	1055
Von Pein Jonas	631
Wang Liansheng	89
Wang Shiquan	47
Ward Jacob	33
Wendelboe Gorm	775
Williams David	187, 421
Xenaki Angeliki	615
Yarina Marina	1061
Zhang Z.Y.	343
Zheng Guangying	741
Zhou Bin	235
Zhou Yuehai	259
Zimmer Christoph	697


FORTH
CCBS Greece
Conference tailor made